Environmental
Management
Nevada Program

DOE/EMNV--0039

Groundwater Flow and Contaminant Transport Model of Corrective Action Units 101 and 102: Central and Western Pahute Mesa, Nye County, Nevada

Revision No.: 1

July 2022

Approved for public release; further dissemination unlimited.

U.S. Department of Energy
Environmental Management Nevada Program

Available for sale to the public from:

U.S. Department of Commerce
National Technical Information Service
5301 Shawnee Road
Alexandria, VA 22312
Telephone: 800.553.6847
Fax: 703.605.6900
E-mail: *orders@ntis.gov*
Online Ordering: *http://www.ntis.gov/help/ordermethods.aspx*

Available electronically at *http://www.osti.gov/scitech*

Available for a processing fee to U.S. Department of Energy and its contractors, in paper, from:

U.S. Department of Energy
Office of Scientific and Technical Information
P.O. Box 62
Oak Ridge, TN 37831-0062
Phone: 865.576.8401
Fax: 865.576.5728
Email: *reports@adonis.osti.gov*

Reference herein to any specific commercial product, process, or service by trade name, trademark, manufacturer, or otherwise, does not necessarily constitute or imply its endorsement, recommendation, or favoring by the United States Government or any agency thereof or its contractors or subcontractors.

DOE/EMNV--0039

GROUNDWATER FLOW AND CONTAMINANT TRANSPORT MODEL OF CORRECTIVE ACTION UNITS 101 AND 102: CENTRAL AND WESTERN PAHUTE MESA, NYE COUNTY, NEVADA

U.S. Department of Energy, Environmental Management Nevada Program
Las Vegas, Nevada

Revision No.: 1

July 2022

Approved for public release; further dissemination unlimited.

GROUNDWATER FLOW AND CONTAMINANT TRANSPORT MODEL OF CORRECTIVE ACTION UNITS 101 AND 102: CENTRAL AND WESTERN PAHUTE MESA, NYE COUNTY, NEVADA

Approved by: JOHN MYERS Digitally signed by JOHN MYERS Date: 2022.07.05 14:01:50 -07'00' Date: _____

John Myers
Underground Test Area Activity Lead
EM Nevada Program

Approved by: WILHELM WILBORN Digitally signed by WILHELM WILBORN Date: 2022.07.05 14:05:10 -07'00' Date: _____

Bill R. Wilborn
Deputy Program Manager, Operations
EM Nevada Program

Table of Contents

List of Figures ix
List of Tables xl
List of Acronyms and Abbreviations xlii
Executive Summary ES-1

1.0 Introduction 1

1.1 UGTA Activity Background 4
1.1.1 UGTA Strategy Implementation for PM CAUs 6
1.2 Purpose, Objectives, and Scope 10
1.2.1 Purpose and Objectives 10
1.2.2 Scope 11
1.3 Major Data Collection and Analysis Activities in Phase II 11
1.4 Supporting Documents 14
1.5 Document Organization 14

2.0 PM Background 16

2.1 Physical Setting 16
2.2 PM-OV Geologic Setting 18
2.3 PM-OV Hydrogeologic Setting 21
2.3.1 Surface Water and Drainage at the NNSS 21
2.3.2 Groundwater Flow System 22
2.3.3 Hydrogeologic Framework 25
2.3.3.1 Hydrogeologic Units 27
2.3.3.2 Hydrostratigraphic Units 30
2.3.3.3 Structural Features 34
2.4 Summary of Underground Nuclear Testing at PM 35
2.5 Geochemistry and Flow Paths 37
2.5.1 Flow Path Evaluation 38
2.6 Previous Modeling Studies 42
2.6.1 Pre-Phase I Regional Groundwater Modeling 43
2.6.2 Phase I Modeling Study 43
2.6.3 Modeling Studies Performed during Phase II 44
2.6.3.1 USGS PM-OV Basin Delineation Model 45
2.6.3.2 USGS Volcanic Rock Characterization Model 50
2.6.3.3 LANL AMANZI Bench Area Model 53
2.6.3.4 USGS Death Valley Regional Groundwater Flow System Model 57
2.6.3.5 USGS HANDLEY Flow and ^{3}H Transport Model 61
2.6.4 Summary of Previous Modeling Studies Performed during Phase II 63

3.0 Flow and Transport Modeling Approach 67

Table of Contents *(Continued)*

3.1 Flow Model Approach . . . 70
3.2 Transport Model Approach . . . 71

4.0 Flow Model . . . 73

4.1 Hydrogeologic Data and Flow Model Conceptualization . . . 74
4.1.1 Groundwater Basin Area . . . 74
4.1.2 Recharge and Discharge . . . 76
4.1.3 Hydraulic Heads . . . 77
4.1.4 Subsurface Hydraulic Properties . . . 82
4.1.4.1 Hydraulic Conductivity . . . 82
4.1.4.2 Aquifer Storage . . . 89
4.1.5 Conceptual Flow Model Summary . . . 90
4.2 PM CAU Flow Model Development and Calibration . . . 92
4.2.1 Model Area and Numerical Grid . . . 92
4.2.2 Material Parameter Assignment . . . 94
4.2.3 Boundary Conditions . . . 95
4.2.4 Base Case Flow Model Calibration . . . 96
4.2.4.1 Observations Used for Model Calibration . . . 98
4.2.4.2 Calibration Results . . . 104
4.3 Flow Model Uncertainty Analysis . . . 124
4.3.1 Model Including All Faults . . . 124
4.3.2 Models with Alternative Recharge Distributions . . . 125
4.3.2.1 DVRFS3 Recharge Model . . . 129
4.3.2.2 INFILv3 Recharge Model . . . 134
4.3.3 Unconfined Model . . . 135
4.4 Flow Model Sensitivity Analysis . . . 139
4.4.1 Local Parameter Sensitivity Analysis . . . 143
4.4.2 Model Sensitivity Analysis of the SCCC Barrier Faults and Increased Black Mountain Recharge . . . 145
4.4.2.1 Model Sensitivity of SCCC Barrier Faults . . . 147
4.4.2.2 Model Sensitivity of Increased Black Mountain Recharge . . . 153
4.5 Flow Modeling Summary and Conclusions . . . 154

5.0 PM CAU Transport Model . . . 158

5.1 Unclassified HST . . . 158
5.1.1 Uncertainty in HST . . . 162
5.1.2 Screening Analysis . . . 163
5.1.3 Implementation of HST . . . 165
5.2 Conceptual Model . . . 166
5.2.1 Transport Processes . . . 167
5.2.1.1 Radioactive Decay . . . 167

Table of Contents *(Continued)*

5.2.1.2 Advective Transport of Dissolved RNs 168
5.2.1.3 Dual-Porosity Conceptualization of Fracture Transport 169
5.2.1.4 Dispersion 170
5.2.1.5 Matrix Diffusion 171
5.2.1.6 Matrix and Fracture Sorption 173
5.2.1.7 Colloid-Facilitated Transport 174
5.2.2 Transport Parameters and Distributions 176
5.2.2.1 Radioactive Decay Constants 176
5.2.2.2 Matrix Porosity 177
5.2.2.2.1 Role of Matrix Porosity in Contaminant Transport 178
5.2.2.2.2 Distributions Used in the PM CAU Transport Model 178
5.2.2.3 Effective Porosity 178
5.2.2.3.1 Role of Effective Porosity in Contaminant Transport 181
5.2.2.3.2 Distributions Used in the PM CAU Transport Model 182
5.2.2.4 Bulk Rock Density 185
5.2.2.4.1 Distributions Used in the PM CAU Transport Model 185
5.2.2.5 Fracture Spacing 185
5.2.2.6 Fracture Aperture 189
5.2.2.6.1 Role of Fracture Aperture in the PM CAU Transport Model 189
5.2.2.6.2 Distributions Used in the PM CAU Transport Model 189
5.2.2.7 Dispersivity 193
5.2.2.7.1 Role of Dispersivity 193
5.2.2.7.2 Dispersivity Values Used in the PM CAU Transport Model 193
5.2.2.8 Matrix Diffusion 194
5.2.2.8.1 Role of Matrix Diffusion 194
5.2.2.8.2 Diffusion Process and Tortuosity 194
5.2.2.8.3 Distributions Used in the PM CAU Transport Model 195
5.2.2.9 Matrix Sorption Parameters 196
5.2.2.9.1 Role of Matrix Sorption in Contaminant Transport Models 197

Table of Contents *(Continued)*

5.2.2.9.2 Distributions Used in the PM CAU Transport Model . . . 197
5.3 Summary of RN Observation Data . . . 198
5.4 Numerical Approach . . . 201
5.5 PM CAU Transport Model . . . 204
5.5.1 Calibration . . . 205
5.5.1.1 Observations Used for Model Calibration . . . 216
5.5.1.2 Objective Function Formulation . . . 218
5.5.1.3 Calibration Results . . . 219
5.5.1.3.1 Transport Parameter Estimates . . . 248
5.5.1.3.2 Extent of ^{3}H Contamination from Model Calibration . . . 254
5.5.1.4 Comparison of Other RNs to Observed Values . . . 254
5.5.1.4.1 ^{14}C Results . . . 266
5.5.1.4.2 ^{36}Cl Results . . . 268
5.5.1.4.3 ^{90}Sr Results . . . 269
5.5.1.4.4 ^{99}Tc Results . . . 271
5.5.1.4.5 ^{129}I Results . . . 274
5.5.1.4.6 ^{137}Cs Results . . . 277
5.5.1.4.7 U (Total) Results . . . 279
5.5.1.4.8 $^{239/240}$Pu Results . . . 282
5.5.2 Monte Carlo Transport Simulations . . . 286
5.5.2.1 Monte Carlo Results . . . 290
5.5.2.1.1 Results for Base Case Flow Model . . . 291
5.5.2.1.2 Results for INFILv3 Recharge Alternative Flow Model . . . 304
5.5.2.1.3 Results for DVRFS3 Recharge Alternative Flow Model . . . 312
5.5.2.1.4 Results for Alternative Flow Model Including All Faults . . . 317
5.6 Sensitivity Analysis . . . 321
5.6.1 Qualitative Analysis . . . 321
5.6.2 Local Parameter Sensitivity Analysis . . . 323
5.6.3 Sensitivity to Dispersion . . . 325
5.6.4 Sensitivity to Initial Pu Source Mass . . . 328
5.6.5 Sensitivity to Number of Particles . . . 332
5.7 CB Ensemble . . . 338
5.8 Summary . . . 345
6.0 CB Forecasts . . . 346
7.0 Summary and Conclusions . . . 361

Table of Contents *(Continued)*

7.1 Building Confidence in the PM CAU Flow and Transport Model 362
7.1.1 CAIP Specific Objectives 364
7.1.2 FFACO Modeling Topics 366
7.2 Summary of Results 372

8.0 References 374

Appendix A - Bibliography of Selected Phase II Investigations

A.1.0 Major Data Collection and Analysis Activities A-1

A.2.0 Bibliography of Well-Specific Phase II Investigations A-3

A.3.0 References Cited in Section A.1.0 . . . . . A-8

Appendix B - QAP Implementation

B.1.0 Implementation of QAP Requirements in the PM CAU Flow and Transport Model B-1

B.2.0 References B-20

Appendix C - Hydrostratigraphic Model Supporting Information

C.1.0 Description of the PM-OV Model Layers C-1

C.2.0 References C-19

Appendix D - PM CAU Underground Nuclear Testing

D.1.0 Underground Nuclear Test Information D-1

D.2.0 References D-6

Appendix E - PM CAU Flow and Transport Model Code Selection and Preprocessor Development

E.1.0 Code Selection E-1

E.1.1 Flow Model Code Selection E-1
E.1.1.1 General Attributes E-2
E.1.1.1.1 Fully 3-D E-2
E.1.1.1.2 Large Numbers of Nodes Capability E-2
E.1.1.1.3 Multiple Boundary Condition Options E-2
E.1.1.1.4 Transient Capability E-2
E.1.1.1.5 Efficient Solver E-3
E.1.1.1.6 Acceptable Numerical Accuracy E-3

Table of Contents *(Continued)*

E.1.1.1.7 Minimal Numerical Dispersion E-3
E.1.1.1.8 Acceptable Verification and Validation E-3
E.1.1.1.9 Access to Source Code E-3
E.1.1.2 Groundwater Flow Model Attributes E-4
E.1.1.2.1 Saturated Groundwater Flow E-4
E.1.1.2.2 Point and Distributed Sources and Sinks of Water E-4
E.1.1.2.3 Temperature Dependence E-4
E.1.1.2.4 Simulate Complex Geology E-4
E.1.1.3 Transport Model Attributes E-5
E.1.1.3.1 Advection, Dispersion, Sorption, and Matrix Diffusion E-5
E.1.1.3.2 Radioactive Decay E-5
E.1.1.3.3 Daughter Products E-5
E.1.1.4 Desirable Attributes E-5
E.1.1.4.1 Finite-Element Formulation E-6
E.1.1.4.2 Steady-State Capability E-6
E.1.1.4.3 Double-Porosity/Double-Permeability Formulation E-6
E.1.1.4.4 Multiple Solutes E-6
E.1.1.4.5 Established Preprocessors and Postprocessors E-7
E.1.1.5 History of Code Selection for the PM CAU E-7
E.1.1.6 Code Selection for the Phase II PM CAU Modeling E-8

E.2.0 MF6-Walkabout Development and Testing E-10

E.2.1 Summary E-10
E.2.2 Overview and Objectives E-10

E.3.0 MODFLOW and Walkabout E-11

E.3.1 MODFLOW E-11
E.3.2 Walkabout E-11
E.3.3 Incompatibility between MODFLOW6 and Walkabout E-12

E.4.0 Transfer of Information from Cell Centroids to Cell Vertices E-16

E.4.1 Calculations of Hydraulic Gradients and Velocities E-16
E.4.2 Transfer of Information from Cell Interface Centroids to Cell Vertices E-19
E.4.3 Application Example E-20

E.5.0 Preprocessor E-23

E.5.1 Structure E-23
E.5.2 Verifications E-24
E.5.2.1 Testing on a Uniform Grid – Boundary Corrections E-24
E.5.2.2 Testing on a Heterogeneous CAU Scale Grid E-28

Table of Contents *(Continued)*

E.6.0 References E-31

Appendix F - Hydrographs Comparing Simulated and Observed Drawdown from 16 MWATs at PM

F.1.0 Simulated and Observed Drawdown from 16 MWATs at PM F-1

F.1.1 Comparisons of Simulated and Observed Drawdowns in Response to Well ER-20-4 Main Pumping F-1
F.1.2 Comparisons of Simulated and Observed Drawdowns in Response to Well ER-20-7 Main Pumping F-2
F.1.3 Comparisons of Simulated and Observed Drawdowns in Response to Well ER-20-8-2 Main Pumping F-3
F.1.4 Comparisons of Simulated and Observed Drawdowns in Response to Well ER-20-8 Main Upper and Lower Pumping F-4
F.1.5 Comparisons of Simulated and Observed Drawdowns in Response to Well ER-20-11 Main Pumping F-6
F.1.6 Comparisons of Simulated and Observed Drawdowns in Response to Well ER-EC-11 Main Pumping F-9
F.1.7 Comparisons of Simulated and Observed Drawdowns in Response to Well ER-EC-12 Main Upper and Lower Pumping F-12
F.1.8 Comparisons of Simulated and Observed Drawdowns in Response to Well ER-EC-13LZ Main Pumping F-13
F.1.9 Comparisons of Simulated and Observed Drawdowns in Response to Well ER-EC-13 Main Upper Pumping F-14
F.1.10 Comparisons of Simulated and Observed Drawdowns in Response to Well ER-EC-14 Main Upper and Lower Pumping F-17
F.1.11 Comparisons of Simulated and Observed Drawdowns in Response to Well ER-EC-15 Main Upper, Intermediate, and Lower Pumping F-19
F.1.12 Drawdown Response Conclusions F-23

F.2.0 References F-25

Appendix G - Log K_d Distributions Used in the PM CAU Transport Model

G.1.0 Log K_d Distributions Used in the PM CAU Transport Model G-1

G.2.0 References G-21

Appendix H - Detailed Transport Results

H.1.0 Detailed Transport Results H-1

Table of Contents *(Continued)*

H.1.1 Modeled and Measured ^{3}H Concentrations versus Time from Calibrated PM CAU Transport Model H-2
H.1.2 Modeled and Measured ^{14}C Concentrations versus Time from Calibrated PM CAU Transport Model H-36
H.1.3 Modeled and Measured ^{36}Cl Concentrations versus Time from Calibrated PM CAU Transport Model H-44
H.1.4 Modeled and Measured ^{90}Sr Concentrations versus Time from Calibrated PM CAU Transport Model H-51
H.1.5 Modeled and Measured ^{99}Tc Concentrations versus Time from Calibrated PM CAU Transport Model H-56
H.1.6 Modeled and Measured ^{129}I Concentrations versus Time from Calibrated PM CAU Transport Model H-67
H.1.7 Modeled and Measured ^{137}Cs Concentrations versus Time from Calibrated PM CAU Transport Model H-78
H.1.8 Modeled and Measured U (Total) Concentrations versus Time from Calibrated PM CAU Transport Model H-84
H.1.9 Modeled and Measured $^{239/240}$Pu Concentrations versus Time from Calibrated PM CAU Transport Model H-95
H.1.10 Modeled $^{239/240}$Pu Concentrations versus Time from Calibrated PM CAU Transport Model at Locations Not Observed for Pu H-107

H.2.0 References H-114

Appendix I - Nevada Division of Environmental Protection Comments

List of Figures

Number	Title	Page
ES-1	Location of the PM CAUs	ES-2
ES-2	Map Showing PM Test Locations	ES-3
ES-3	Areal Extent and Mesh of the PM CAU Flow and Transport Model	ES-12
ES-4	Potentiometric Surface and Residuals of the PM CAU Flow Model	ES-14
ES-5	Modeled versus Measured Steady-State Heads for the PM CAU Flow Model	ES-15
ES-6	Groundwater Velocity Field and Simulated Groundwater Flow Paths from Underground Nuclear Tests in the PM CAU Flow Model	ES-16
ES-7	Simulated Extent of ^{3}H from Calibrated PM CAU Transport Model at 55 Years (2020)	ES-18
ES-8	Modeled versus Measured ^{3}H Concentrations for the PM CAU Transport Model	ES-19
ES-9	Ensemble of 1,000-Year Time-Cumulative Probability of Exceedance of MCLs CB Forecasts (Base Case on Top)	ES-21
ES-10	CB of Base Case Colored by Saturated Depth of Contamination (as Determined by MCL Exceedance for Relevant RNs)	ES-22
ES-11	CB of INFILv3 Recharge Alternative Flow Model Colored by Saturated Depth of Contamination (as Determined by MCL Exceedance for Relevant RNs)	ES-23
ES-12	CB of DVRFS3 Recharge Alternative Flow Model Colored by Saturated Depth of Contamination (as Determined by MCL Exceedance for Relevant RNs)	ES-24
ES-13	CB of Alternative Flow Model Including All Faults Colored by Saturated Depth of Contamination (as Determined by MCL Exceedance for Relevant RNs)	ES-25

List of Figures *(Continued)*

Number	Title	Page
ES-14	Average Fractional Exceedance Volume by RN for PM Base Case	ES-26
1-1	Location of the PM CAUs	2
1-2	FFACO UGTA Strategy Flowchart	7
1-3	Physiographic Features of the PM CAU Model	12
2-1	Structural Features of the PM-OV HFM	17
2-2	Groundwater Basins in and near the PM-OV HFM	19
2-3	Generalized Geologic Map of the PM-OV HFM and Surrounding Area	20
2-4	Features of the PM-OV Groundwater Basin	23
2-5	PM-OV Basin Steady-State Potentiometric Contour Map	24
2-6	PM Transmissivity Ranges	26
2-7	Cross Sections of HSUs through the PM-OV HFM Area	32
2-8	Map Showing PM Test Locations	36
2-9	Geochemistry Flow Paths Derived Using (a) Cl and (b) δ^2H of Wells and Springs	39
2-10	Locations of Select Wells and Places for Discussion of Geochemical Pathways	40
2-11	PM-OV Chloride Concentrations and Simulated Recharge Rates	46
2-12	PM-OV Groundwater Flow Paths Simulated by the Basin Delineation Model	48
2-13	PM-OV Transmissivity Distribution Simulated by Basin Delineation Model	49
2-14	Simulated Transmissivity Distribution from the Integrated Groundwater-Flow Model in the Area Investigated by the 16 MWATs	52
2-15	Flow Pathlines Simulated by the LANL AMANZI Bench Model	55
2-16	Simulated Distribution of ^3H above the 20,000-pCi/L MCL as of 2020	56

List of Figures *(Continued)*

Number	Title	Page
2-17	Predevelopment Water Budgets within and between Geographic Areas in the Death Valley Regional Flow System	58
2-18	Simulated 165-Year Advective-Flow Paths by DVRFS Model from 296 Underground Nuclear Tests Detonated near or below Water Table in NNSS	60
2-19	Cross Sections Showing Modified Hydrostratigraphic Framework, Hydraulic Conductivity, Combined Specific Yield and Specific Storage, and Effective Porosity	62
4-1	PM-OV Groundwater Basin Boundary and Boundary Flows	75
4-2	Potentiometric Surface, Steady-State Water-Level Sites from Wells, Spring Locations, and Structural Features within the PM Groundwater Basin	78
4-3	Structural Features near the Nuclear Testing Areas of PM	80
4-4	Pump- and Slug-Scale Aquifer Test Hydraulic Conductivity versus Depth	87
4-5	Areal Extent and Mesh of the PM CAU Flow Model	93
4-6	Recharge and Discharge Rates from the PM CAU Flow Model	97
4-7	Monitoring and Pumping Periods for the PM MWATs	100
4-8	Transmissivity Measurements within the PM CAU Flow Model Domain	103
4-9	Potentiometric Surface and Residuals of the PM CAU Flow Model	107
4-10	Modeled versus Measured Steady-State Heads for the PM CAU Flow Model	108
4-11	Modeled versus Measured Gradients for the PM CAU Flow Model	108
4-12	Measured and Simulated Water-Level Profiles Coincident with Flow Paths (red dashed lines are simulated heads)	109
4-13	Comparisons of Simulated and Observed Drawdowns in ER-EC-11 Intermediate	112

List of Figures *(Continued)*

Number	Title	Page
4-14	Simulated Transmissivity and Groundwater Flow Paths from Underground Nuclear Tests in the PM CAU Flow Model	113
4-15	Identifiability Index for Independent Parameters: (A) All Parameters and (B) Parameters with Identifiability Index Greater than or Equal to 0.5	115
4-16	Calibrated Hydraulic Conductivity as a Function of HGU	119
4-17	Groundwater Velocity Field and Simulated Groundwater Flow Paths from Underground Nuclear Tests in the PM CAU Flow Model	120
4-18	Cross Sections Showing HSUs and Flow Paths Originating from the HANDLEY, BENHAM, and MOLBO Detonations	121
4-19	Tests and Base Case Advective Travel Distances in Excess of 5 km after 200 Years	123
4-20	Potentiometric Surface and Residuals for the PM CAU Flow Model with All Faults Identified in the HFM	126
4-21	Comparisons of Simulated and Observed Drawdowns in ER-EC-11 Intermediate for a Model with All Faults Identified in the HFM	127
4-22	Simulated Transmissivity and Groundwater Flow Paths from Underground Nuclear Tests for a Model with All Faults Identified in the HFM	128
4-23	Base Case and Alternative Recharge Distributions: (A) Base Case, (B) DVRFS3, and (C) INFILv3	130
4-24	Potentiometric Surface and Residuals in a Model with Recharge from the USGS DVRFS3 Model	131
4-25	Comparisons of Simulated and Observed Drawdowns in ER-EC-11 Intermediate for a Model with Recharge from the USGS DVRFS3 Model	132

List of Figures *(Continued)*

Number	Title	Page
4-26	Simulated Transmissivity and Groundwater Flow Paths from Underground Nuclear Tests for a Model with Recharge from the USGS DVRFS3 Model	133
4-27	Potentiometric Surface and Residuals of a Model with Recharge from the INFILv3 Model	136
4-28	Comparisons of Simulated and Observed Drawdowns in ER-EC-11 Intermediate for a Model with Recharge from the INFILV3 Model	137
4-29	Simulated Transmissivity and Groundwater Flow Paths from Underground Nuclear Tests for a Model with Recharge from the INFILv3 Model	138
4-30	Potentiometric Surface, Residuals, and Mesh for a PM CAU Flow Model Using a Water Table Boundary Condition	140
4-31	Comparisons of Simulated and Observed Drawdowns in ER-EC-11 Intermediate for a Model Using a Water Table Boundary Condition	141
4-32	Simulated Transmissivity and Groundwater Flow Paths from Underground Nuclear Tests for a Model Using a Water Table Boundary Condition	142
4-33	Sensitivity and Identifiability for Model Parameters: (A) Hydraulic Conductivity and (B) Specific Storage	144
4-34	Head Residuals and Flow Path Sensitivity of the Base Case Model	148
4-35	Head Residuals and Flow Path Sensitivity of the All Faults Alternative Model	149
4-36	Head Residuals and Flow Path Sensitivity of the DVRFS3 Alternative Recharge Model	150
4-37	Head Residuals and Flow Path Sensitivity of the INFILv3 Alternative Recharge Model	151

List of Figures *(Continued)*

Number	Title	Page
4-38	Head Residuals and Flow Path Sensitivity of the Unconfined Alternative Model	152
5-1	^{3}H Relative to SDWA MCL in PM and Downgradient Groundwaters	200
5-2	Modeled versus Measured ^{3}H Concentrations for the PM CAU Transport Model	221
5-3	Modeled versus Measured ^{3}H Concentrations for the Postshot Holes in the PM CAU Transport Model	222
5-4	Modeled and Measured ^{3}H Concentrations versus Time at U-19ad_PS_1A	223
5-5	Modeled and Measured ^{3}H Concentrations versus Time at U-19e_PS_2D	223
5-6	Modeled and Measured ^{3}H Concentrations versus Time at U-19q_PS_1D	224
5-7	Modeled and Measured ^{3}H Concentrations versus Time at U-19v_PS_1D	224
5-8	Modeled and Measured ^{3}H Concentrations versus Time at U-20aa_PS_1D	225
5-9	Modeled and Measured ^{3}H Concentrations versus Time at U-20f_PS_1D	225
5-10	Modeled and Measured ^{3}H Concentrations versus Time at U-20i_PS_1D	226
5-11	Modeled and Measured ^{3}H Concentrations versus Time at U-20m_PS_1D	226
5-12	Modeled and Measured ^{3}H Concentrations vs Time at U-20n_PS_1D_o1Z	227
5-13	Modeled and Measured ^{3}H Concentrations versus Time at U-20n_PS_1D_o5Z	227
5-14	Modeled and Measured ^{3}H Concentrations versus Time at U-20n_PS_1D_o2	228
5-15	Modeled and Measured ^{3}H Concentrations versus Time at U-20n_PS_1D_o3Z	228
5-16	Modeled and Measured ^{3}H Concentrations versus Time at U-20n_PS_1D_m2	229

List of Figures *(Continued)*

Number	Title	Page
5-17	Modeled and Measured ^{3}H Concentrations versus Time at UE-20n_1_o2	229
5-18	Modeled versus Measured ^{3}H Concentrations for the Observation Locations near TYBO and BENHAM in the PM CAU Transport Model	230
5-19	Modeled and Measured ^{3}H Concentrations versus Time at ER-20-5-1_m1	231
5-20	Modeled and Measured ^{3}H Concentrations versus Time at ER-20-5-3_m1	231
5-21	Modeled and Measured ^{3}H Concentrations versus Time at ER-20-7_m1	232
5-22	Modeled versus Measured ^{3}H Concentrations for the Observation Locations near TYBO and BENHAM in the PM CAU Transport Model with Adjusted Observation Location for ER-20-5-3	233
5-23	Modeled versus Measured ^{3}H Concentrations for the Observation Locations near the Bench in the PM CAU Transport Model	234
5-24	Modeled and Measured ^{3}H Concentrations versus Time at ER-20-8_p1	235
5-25	Modeled and Measured ^{3}H Concentrations versus Time at ER-20-8_m2	235
5-26	Modeled and Measured ^{3}H Concentrations versus Time at ER-20-8_p3	236
5-27	Modeled and Measured ^{3}H Concentrations versus Time at ER-20-8-2_m1	236
5-28	Modeled and Measured ^{3}H Concentrations versus Time at ER-20-11_m1	237
5-29	Modeled and Measured ^{3}H Concentrations versus Time at ER-EC-11_p1	237
5-30	Modeled and Measured ^{3}H Concentrations versus Time at ER-EC-11_m2	238
5-31	Modeled and Measured ^{3}H Concentrations versus Time at ER-EC-11_p3	238
5-32	Modeled versus Measured ^{3}H Concentrations for Observation Locations near HANDLEY in the PM CAU Transport Model	239
5-33	Modeled and Measured ^{3}H Concentrations versus Time at ER-20-12_m1	240
5-34	Modeled and Measured ^{3}H Concentrations versus Time at ER-20-12_p1	240

List of Figures *(Continued)*

Number	Title	Page
5-35	Modeled and Measured ^{3}H Concentrations versus Time at ER-20-12_p2	241
5-36	Modeled and Measured ^{3}H Concentrations versus Time at ER-20-12_p3	241
5-37	Modeled and Measured ^{3}H Concentrations versus Time at ER-20-12_p4	242
5-38	Modeled and Measured ^{3}H Concentrations versus Time at PM-3_p1	242
5-39	Modeled and Measured ^{3}H Concentrations versus Time at PM-3_p2	243
5-40	Modeled versus Measured ^{3}H Concentrations for Observation Locations near BULLION in the PM CAU Transport Model	244
5-41	Modeled and Measured ^{3}H Concentrations versus Time at ER-20-6-1_p1	244
5-42	Modeled and Measured ^{3}H Concentrations versus Time at ER-20-6-2_p1	245
5-43	Modeled and Measured ^{3}H Concentrations versus Time at ER-20-6-3_p1	245
5-44	Modeled versus Measured ^{3}H Concentrations at Remaining Observation Locations with No Modeled ^{3}H in the PM CAU Transport Model	246
5-45	Modeled versus Measured ^{3}H Concentrations at Remaining Observation Locations with No Measured ^{3}H in the PM CAU Transport Model	247
5-46	Modeled versus Measured ^{3}H Concentrations at Remaining Observation Locations with No Measured ^{3}H in the PM CAU Transport Model with Adjusted Observation Location for ER-20-1	248
5-47	Identifiability Index for Effective Porosity Parameters	250
5-48	Identifiability Index for Matrix Porosity Parameters	251
5-49	Identifiability Index for Matrix Diffusion Coefficient Parameters	252
5-50	Identifiability Index for Fracture Aperture Parameters	253
5-51	Calibrated Effective Porosity Values	255
5-52	Calibrated Matrix Porosity Values	256

List of Figures *(Continued)*

Number	Title	Page
5-53	Calibrated Matrix Diffusion Coefficient Values	257
5-54	Calibrated Fracture Aperture Values	258
5-55	Calculated Fracture Spacing Values	259
5-56	Simulated Extent of ^{3}H Contamination from Calibrated PM CAU Transport Model at 55 Years (2020)	260
5-57	Modeled versus Measured ^{14}C Concentrations for the Postshot Holes in the PM CAU Transport Model	267
5-58	Modeled versus Measured ^{14}C Concentrations near the Bench in the PM CAU Transport Model	267
5-59	Modeled versus Measured ^{36}Cl Concentrations for the Postshot Holes in the PM CAU Transport Model	268
5-60	Modeled versus Measured ^{36}Cl Concentrations near the Bench in the PM CAU Transport Model	269
5-61	Modeled versus Measured ^{90}Sr Concentrations for the Postshot Holes in the PM CAU Transport Model	270
5-62	Modeled versus Measured ^{90}Sr Concentrations near HANDLEY in the PM CAU Transport Model	271
5-63	Modeled versus Measured ^{99}Tc Concentrations for the Postshot Holes in the PM CAU Transport Model	272
5-64	Modeled versus Measured ^{99}Tc Concentrations near the Bench in the PM CAU Transport Model	273
5-65	Modeled versus Measured ^{99}Tc Concentrations near HANDLEY in the PM CAU Transport Model	274
5-66	Modeled versus Measured ^{129}I Concentrations for the Postshot Holes in the PM CAU Transport Model	275

List of Figures *(Continued)*

Number	Title	Page
5-67	Modeled versus Measured ^{129}I Concentrations near the Bench in the PM CAU Transport Model	276
5-68	Modeled versus Measured ^{129}I Concentrations near HANDLEY in the PM CAU Transport Model	277
5-69	Modeled versus Measured ^{137}Cs Concentrations for the Postshot Holes in the PM CAU Transport Model	278
5-70	Modeled versus Measured ^{137}Cs Concentrations near the Bench in the PM CAU Transport Model	279
5-71	Modeled versus Measured U Concentrations for the Postshot Holes in the PM CAU Transport Model	280
5-72	Modeled versus Measured U Concentrations near the Bench in the PM CAU Transport Model	281
5-73	Modeled versus Measured U Concentrations near HANDLEY in the PM CAU Transport Model	282
5-74	Modeled versus Measured $^{239/240}$Pu Concentrations for the Postshot Holes in the PM CAU Transport Model	283
5-75	Modeled versus Measured $^{239/240}$Pu Concentrations near the Bench in the PM CAU Transport Model	284
5-76	Modeled versus Measured $^{239/240}$Pu Concentrations near HANDLEY in the PM CAU Transport Model	286
5-77	1,000-Year Time-Cumulative Probability of Exceedance of MCLs for PM Base Case	292
5-78	1,000-Year Time-Cumulative Probability of Exceedance of MCLs for PM Base Case (Beta Emitters)	293
5-79	1,000-Year Time-Cumulative Probability of Exceedance of MCLs for PM Base Case (Alpha Emitters)	294

List of Figures *(Continued)*

Number	Title	Page
5-80	1,000-Year Time-Cumulative Probability of Exceedance of MCLs for PM Base Case (U)	295
5-81	Probability of Exceedance of MCLs for the PM Flow Model Base Case (55 years)	296
5-82	Probability of Exceedance of MCLs for the PM Flow Model Base Case (60 years)	297
5-83	Probability of Exceedance of MCLs for the PM Flow Model Base Case (80 years)	298
5-84	Probability of Exceedance of MCLs for the PM Flow Model Base Case (100 years)	299
5-85	Probability of Exceedance of MCLs for the PM Flow Model Base Case (200 years)	300
5-86	Probability of Exceedance of MCLs for the PM Flow Model Base Case (300 years)	301
5-87	Probability of Exceedance of MCLs for the PM Flow Model Base Case (500 years)	302
5-88	Probability of Exceedance of MCLs for the PM Flow Model Base Case (1,000 years)	303
5-89	CB of Base Case Colored by Lowest Contaminated HSU	305
5-90	Lowest Contaminated HSUs in CB for Base Case Flow Model with Color Key for Figure 5-89	306
5-91	CB of Base Case Colored by Saturated Depth of Contamination	307
5-92	1,000-Year Time-Cumulative Probability of Exceedance of MCLs for PM INFILv3 Recharge Alternative Flow Model	308

List of Figures *(Continued)*

Number	Title	Page
5-93	CB of INFILv3 Recharge Alternative Flow Model Colored by Lowest Contaminated HSU	309
5-94	Lowest Contaminated HSUs in CB for INFILv3 Recharge Alternative Flow Model with Color Key for Figure 5-93	310
5-95	CB of INFILv3 Recharge Alternative Flow Model Colored by Saturated Depth of Contamination	311
5-96	1,000-Year Time-Cumulative Probability of Exceedance of MCLs for PM DVRFS3 Recharge Alternative Flow Model	313
5-97	CB of DVRFS3 Recharge Alternative Flow Model Colored by Lowest Contaminated HSU	314
5-98	Lowest Contaminated HSUs in CB for DVRFS3 Recharge Alternative Flow Model with Color Key for Figure 5-97	315
5-99	CB of DVRFS3 Recharge Alternative Flow Model Colored by Saturated Depth of Contamination	316
5-100	1,000-Year Time-Cumulative Probability of Exceedance of MCLs for PM Alternative Flow Model Including All Faults	318
5-101	CB of Alternative Flow Model Including All Faults Colored by Lowest Contaminated HSU	320
5-102	Lowest Contaminated HSUs in CB for Alternative Flow Model Including All Faults with Color Key for Figure 5-101	321
5-103	CB of Alternative Flow Model Including All Faults Colored by Saturated Depth of Contamination	322
5-104	Sensitivity and Identifiability for Transport Parameters	324
5-105	^{3}H Plumes above MCL from BENHAM at 55 Years for Varying Dispersivity Values	326

List of Figures *(Continued)*

Number	Title	Page
5-106	^{3}H Plumes above MCL from BENHAM at 55 Years for Varying Dispersivity Values	327
5-107	Peak Straight-Line Distance of ^{3}H above MCL from BENHAM at 55 Years for Varying Dispersivity Values	328
5-108	^{239}Pu Plumes above MCL from BENHAM at 55 Years with Minimum K_ds for Different Melt Glass Fractions	329
5-109	^{239}Pu Plumes above MCL from BENHAM at 55 Years with Maximum K_ds for Different Melt Glass Fractions	330
5-110	Peak Straight-Line Distance of ^{239}Pu above MCL from BENHAM at 55 Years for Different Melt Glass Fractions	332
5-111	^{3}H Plumes above MCL from BENHAM at 55 Years for Varying Numbers of Particles	333
5-112	Peak Straight-Line Distance of ^{3}H above MCL from BENHAM at 55 Years for Varying Numbers of Particles	334
5-113	Modeled and Measured ^{3}H Concentrations at ER-20-5-1_m1 for Varying Numbers of Particles	335
5-114	Modeled and Measured ^{3}H Concentrations at ER-20-7_m1 for Varying Numbers of Particles	336
5-115	Modeled and Measured ^{3}H Concentrations at ER-20-11_m1 for Varying Numbers of Particles	337
5-116	1,000-Year Time-Cumulative Probability of Exceedance of MCLs CB Forecasts	339
5-117	1,000-Year Time-Cumulative Probability of Exceedance of MCLs CB Forecasts	340
5-118	1,000-Year Time-Cumulative Probability of Exceedance of MCLs CB Forecasts	341

List of Figures *(Continued)*

Number	Title	Page
5-119	1,000-Year Time-Cumulative Probability of Exceedance of MCLs CB Forecasts	342
5-120	Distributions of Cumulative MCL Exceedance Volume for PM Base Case and Alternative Flow Models	343
5-121	Average Fractional Exceedance Volume by RN for PM Base Case	344
5-122	Average Fractional Exceedance Volume by RN Class for PM Base Case	344
6-1	1,000-Year Time-Cumulative Probability of Exceedance of MCLs CB Forecasts (Base Case on Top)	347
6-2	CB of Base Case Colored by Lowest Contaminated HSU	349
6-3	Lowest Contaminated HSUs in CB for Base Case Flow Model with Color Key for Figure 6-2	350
6-4	CB of Base Case Colored by Saturated Depth of Contamination	351
6-5	CB of INFILv3 Recharge Alternative Flow Model Colored by Lowest Contaminated HSU	352
6-6	Lowest Contaminated HSUs in CB for INFILv3 Recharge Alternative Flow Model with Color Key for Figure 6-5	353
6-7	CB of INFILv3 Recharge Alternative Flow Model Colored by Saturated Depth of Contamination	354
6-8	CB of DVRFS3 Recharge Alternative Flow Model Colored by Lowest Contaminated HSU	355
6-9	Lowest Contaminated HSUs in CB for DVRFS3 Recharge Alternative Flow Model with Color Key for Figure 6-8	356
6-10	CB of DVRFS3 Recharge Alternative Flow Model Colored by Saturated Depth of Contamination	357

List of Figures *(Continued)*

Number	Title	Page
6-11	CB of Alternative Flow Model Including All Faults Colored by Lowest Contaminated HSU	358
6-12	Lowest Contaminated HSUs in CB for Alternative Flow Model Including All Faults with Color Key for Figure 6-11	359
6-13	CB of Alternative Flow Model Including All Faults Colored by Saturated Depth of Contamination	360
E-1	MODFLOW Cell (basic cell)	E-13
E-1	MODFLOW Cell	E-13
E-1	MODFLOW Cell (DISU cell)	E-14
E-2	Tetrahedral Element	E-14
E-3	Subdivision of Hexahedral Element into Tetrahedral Elements (only one tetrahedral element is shown)	E-15
E-4	Treatment of Boundary Nodes and Elements	E-19
E-5	Typical DISV Cells	E-20
E-6	Flow Domain Discretization: Application Example	E-21
E-7	Comparison of Velocity Profiles	E-21
E-8	Comparison of Travel Distances	E-22
E-9	Flowchart of the Preprocessor	E-24
E-10	Comparison of Head Profiles	E-25
E-11	Comparison of Velocity Distribution before Adjustment	E-26
E-12	Velocity Distributions after Adjustment	E-26
E-13	Comparison between Particle Paths Generated by Walkabout and an Analytical Solution	E-27

List of Figures *(Continued)*

Number	Title	Page
E-14	Comparison of Calculated Flow Paths from MODPATH7 and Walkabout	E-29
E-15	Comparison of Calculated Flow Paths from MODPATH7 and Walkabout	E-30
F-1	Comparisons of Simulated and Observed Drawdowns in Response to Well ER-20-4 Main Pumping	F-2
F-2	Drawdown Extent and Residuals in Response to Well ER-20-4 Main Pumping on Day 22 of the Well Development and Testing Period	F-3
F-3	Comparisons of Simulated and Observed Drawdowns in Response to Well ER-20-7 Main Pumping	F-4
F-4	Drawdown Extent and Residuals in Response to Well ER-20-7 Main Pumping on Day 10 of the Well Development and Testing Period	F-5
F-5	Comparisons of Simulated and Observed Drawdowns in Response to Well ER-20-8-2 Main Pumping	F-6
F-6	Drawdown Extent and Residuals in Response to Well ER-20-8-2 Main Pumping on Day 20 of the Well Development and Testing Period	F-7
F-7	Comparisons of Simulated and Observed Drawdowns in Response to Well ER-20-8 Main Upper and Lower Pumping	F-8
F-8	Drawdown Extent and Residuals in Response to Well ER-20-8 Main Upper and Lower Pumping on Day 82 of the Well Development and Testing Period	F-9
F-9	Comparisons of Simulated and Observed Drawdowns in Response to Well ER-20-11 Main Pumping	F-10
F-10	Drawdown Extent and Residuals in Response to Well ER-20-11 Main Pumping on Day 39 of the Well Development and Testing Period	F-11
F-11	Comparisons of Simulated and Observed Drawdowns in Response to Well ER-EC-11 Main Pumping	F-12

List of Figures *(Continued)*

Number	Title	Page
F-12	Drawdown Extent and Residuals in Response to Well ER-EC-11 Main Pumping on Day 18 of the Well Development and Testing Period	F-13
F-13	Comparisons of Simulated and Observed Drawdowns in Response to Well ER-EC-12 Main Upper and Lower Pumping	F-14
F-14	Drawdown Extent and Residuals in Response to Well ER-EC-12 Main Upper and Lower Pumping on Day 48 of the Well Development and Testing Period	F-15
F-15	Comparisons of Simulated and Observed Drawdowns in Response to Well ER-EC-13 Main Lower Zone Pumping	F-16
F-16	Drawdown Extent and Residuals in Response to Well ER-EC-13 Main Lower Zone Pumping on Day 250 of the Well Development and Testing Period	F-17
F-17	Comparisons of Simulated and Observed Drawdowns in Response to Well ER-EC-13 Main Upper Zone Pumping	F-18
F-18	Drawdown Extent and Residuals in Response to Well ER-EC-13 Main Upper Zone Pumping on Day 21 of the Well Development and Testing Period	F-19
F-19	Comparisons of Simulated and Observed Drawdowns in Response to Well ER-EC-14 Main Upper and Lower Pumping	F-20
F-20	Drawdown Extent and Residuals in Response to Well ER-EC-14 Main Upper and Lower Pumping on Day 54 of the Well Development and Testing Period	F-21
F-21	Comparisons of Simulated and Observed Drawdowns in Response to Well ER-EC-15 Main Upper, Intermediate, and Lower Pumping	F-22
F-22	Drawdown Extent and Residuals in Response to Well ER-EC-15 Main Upper, Intermediate, and Lower Pumping on Day 40 of the Well Development and Testing Period	F-24

List of Figures *(Continued)*

Number	Title	Page
H-1	Modeled and Measured ^{3}H Concentrations versus Time at ER-20-1_p1 (1,000 Years)	H-3
H-2	Modeled and Measured ^{3}H Concentrations versus Time at ER-20-2-1_p1 (1,000 Years)	H-4
H-3	Modeled and Measured ^{3}H Concentrations versus Time at ER-20-4_m1 (1,000 Years)	H-4
H-4	Modeled and Measured ^{3}H Concentrations versus Time at ER-20-4_p2 (1,000 Years)	H-5
H-5	Modeled and Measured ^{3}H Concentrations versus Time at ER-20-5-1_m1 (1,000 Years)	H-5
H-6	Modeled and Measured ^{3}H Concentrations versus Time at ER-20-5-3_m1 (1,000 Years)	H-6
H-7	Modeled and Measured ^{3}H Concentrations versus Time at ER-20-6-1_p1 (1,000 Years)	H-6
H-8	Modeled and Measured ^{3}H Concentrations versus Time at ER-20-6-2_p1 (1,000 Years)	H-7
H-9	Modeled and Measured ^{3}H Concentrations versus Time at ER-20-6-3_p1 (1,000 Years)	H-7
H-10	Modeled and Measured ^{3}H Concentrations versus Time at ER-20-7_m1 (1,000 Years)	H-8
H-11	Modeled and Measured ^{3}H Concentrations versus Time at ER-20-8_p1 (1,000 Years)	H-8
H-12	Modeled and Measured ^{3}H Concentrations versus Time at ER-20-8_m2 (1,000 Years)	H-9
H-13	Modeled and Measured ^{3}H Concentrations versus Time at ER-20-8_p3 (1,000 Years)	H-9

List of Figures *(Continued)*

Number	Title	Page
H-14	Modeled and Measured ^{3}H Concentrations versus Time at ER-20-8-2_m1 (1,000 Years)	H-10
H-15	Modeled and Measured ^{3}H Concentrations versus Time at ER-20-11_m1 (1,000 Years)	H-10
H-16	Modeled and Measured ^{3}H Concentrations versus Time at ER-20-12_m1 (1,000 Years)	H-11
H-17	Modeled and Measured ^{3}H Concentrations versus Time at ER-20-12_p1 (1,000 Years)	H-11
H-18	Modeled and Measured ^{3}H Concentrations versus Time at ER-20-12_p2 (1,000 Years)	H-12
H-19	Modeled and Measured ^{3}H Concentrations versus Time at ER-20-12_p3 (1,000 Years)	H-12
H-20	Modeled and Measured ^{3}H Concentrations versus Time at ER-20-12_p4 (1,000 Years)	H-13
H-21	Modeled and Measured ^{3}H Concentrations versus Time at ER-EC-1_m1-3 (1,000 Years)	H-13
H-22	Modeled and Measured ^{3}H Concentrations versus Time at ER-EC-2A_m3 (1,000 Years)	H-14
H-23	Modeled and Measured ^{3}H Concentrations versus Time at ER-EC-4_m2-6 (1,000 Years)	H-14
H-24	Modeled and Measured ^{3}H Concentrations versus Time at ER-EC-5_m1-3 (1,000 Years)	H-15
H-25	Modeled and Measured ^{3}H Concentrations versus Time at ER-EC-6_m1-4 (1,000 Years)	H-15
H-26	Modeled and Measured ^{3}H Concentrations versus Time at ER-EC-6_m2-4 (1,000 Years)	H-16

List of Figures *(Continued)*

Number	Title	Page
H-27	Modeled and Measured ^{3}H Concentrations versus Time at ER-EC-6_m2_a1 (1,000 Years)	H-16
H-28	Modeled and Measured ^{3}H Concentrations versus Time at ER-EC-6_m4_a3 (1,000 Years)	H-17
H-29	Modeled and Measured ^{3}H Concentrations versus Time at ER-EC-8_m1-3 (1,000 Years)	H-17
H-30	Modeled and Measured ^{3}H Concentrations versus Time at ER-EC-11_p1 (1,000 Years)	H-18
H-31	Modeled and Measured ^{3}H Concentrations versus Time at ER-EC-11_m2 (1,000 Years)	H-18
H-32	Modeled and Measured ^{3}H Concentrations versus Time at ER-EC-11_p3 (1,000 Years)	H-19
H-33	Modeled and Measured ^{3}H Concentrations versus Time at ER-EC-12_p2 (1,000 Years)	H-19
H-34	Modeled and Measured ^{3}H Concentrations versus Time at ER-EC-12_m2 (1,000 Years)	H-20
H-35	Modeled and Measured ^{3}H Concentrations versus Time at ER-EC-13_p1 (1,000 Years)	H-20
H-36	Modeled and Measured ^{3}H Concentrations versus Time at ER-EC-13_m2 (1,000 Years)	H-21
H-37	Modeled and Measured ^{3}H Concentrations versus Time at ER-EC-14_p1 (1,000 Years)	H-21
H-38	Modeled and Measured ^{3}H Concentrations versus Time at ER-EC-14_m2 (1,000 Years)	H-22
H-39	Modeled and Measured ^{3}H Concentrations versus Time at ER-EC-15_p1 (1,000 Years)	H-22

List of Figures *(Continued)*

Number	Title	Page
H-40	Modeled and Measured ^{3}H Concentrations versus Time at ER-EC-15_p2 (1,000 Years)	H-23
H-41	Modeled and Measured ^{3}H Concentrations versus Time at ER-EC-15_m3 (1,000 Years)	H-23
H-42	Modeled and Measured ^{3}H Concentrations versus Time at PM-1_o2Z (1,000 Years)	H-24
H-43	Modeled and Measured ^{3}H Concentrations versus Time at PM-2_m1-o7 (1,000 Years)	H-24
H-44	Modeled and Measured ^{3}H Concentrations versus Time at PM-3_p1 (1,000 Years)	H-25
H-45	Modeled and Measured ^{3}H Concentrations versus Time at PM-3_p2 (1,000 Years)	H-25
H-46	Modeled and Measured ^{3}H Concentrations versus Time at U-19ad_PS_1A (1,000 Years)	H-26
H-47	Modeled and Measured ^{3}H Concentrations versus Time at U-19e_PS_2D (1,000 Years)	H-26
H-48	Modeled and Measured ^{3}H Concentrations versus Time at U-19q_PS_1D (1,000 Years)	H-27
H-49	Modeled and Measured ^{3}H Concentrations versus Time at U-19v_PS_1D (1,000 Years)	H-27
H-50	Modeled and Measured ^{3}H Concentrations versus Time at U-20aa_PS_1D (1,000 Years)	H-28
H-51	Modeled and Measured ^{3}H Concentrations versus Time at U-20f_PS_1D (1,000 Years)	H-28
H-52	Modeled and Measured ^{3}H Concentrations versus Time at U-20i_PS_1D (1,000 Years)	H-29

List of Figures *(Continued)*

Number	Title	Page
H-53	Modeled and Measured ^{3}H Concentrations versus Time at U-20m_PS_1D (1,000 Years)	H-29
H-54	Modeled and Measured ^{3}H Concentrations versus Time at U-20n_PS_1D_o1Z (1,000 Years)	H-30
H-55	Modeled and Measured ^{3}H Concentrations versus Time at U-20n_PS_1D_o2 (1,000 Years)	H-30
H-56	Modeled and Measured ^{3}H Concentrations versus Time at U-20n_PS_1D_o3Z (1,000 Years)	H-31
H-57	Modeled and Measured ^{3}H Concentrations versus Time at U-20n_PS_1D_o5Z (1,000 Years)	H-31
H-58	Modeled and Measured ^{3}H Concentrations versus Time at U-20n_PS_1D_m2 (1,000 Years)	H-32
H-59	Modeled and Measured ^{3}H Concentrations versus Time at U-20_WW (1,000 Years)	H-32
H-60	Modeled and Measured ^{3}H Concentrations versus Time at UE-18r_o1 (1,000 Years)	H-33
H-61	Modeled and Measured ^{3}H Concentrations versus Time at UE-19c_WW_m1 (1,000 Years)	H-33
H-62	Modeled and Measured ^{3}H Concentrations versus Time at UE-19h_m1 (1,000 Years)	H-34
H-63	Modeled and Measured ^{3}H Concentrations versus Time at UE-20bh_1_o1 (1,000 Years)	H-34
H-64	Modeled and Measured ^{3}H Concentrations versus Time at UE-20n_1_o2 (1,000 Years)	H-35
H-65	Modeled and Measured ^{14}C Concentrations versus Time at U-19ad_PS_1A	H-36

List of Figures *(Continued)*

Number	Title	Page
H-66	Modeled and Measured ^{14}C Concentrations versus Time at U-19q_PS_1D	H-37
H-67	Modeled and Measured ^{14}C Concentrations versus Time at U-19v_PS_1D	H-37
H-68	Modeled and Measured ^{14}C Concentrations versus Time at U-20n_PS_1D_o2	H-38
H-69	Modeled and Measured ^{14}C Concentrations versus Time at U-20n_PS_1D_o3Z	H-38
H-70	Modeled and Measured ^{14}C Concentrations versus Time at U-20n_PS_1D_m2	H-39
H-71	Modeled and Measured ^{14}C Concentrations versus Time at UE-20n_1_o2	H-39
H-72	Modeled and Measured ^{14}C Concentrations versus Time at ER-20-5-1_m1	H-40
H-73	Modeled and Measured ^{14}C Concentrations versus Time at ER-20-5-3_m1	H-40
H-74	Modeled and Measured ^{14}C Concentrations versus Time at ER-20-7_m1	H-41
H-75	Modeled and Measured ^{14}C Concentrations versus Time at ER-20-8_p1	H-41
H-76	Modeled and Measured ^{14}C Concentrations versus Time at ER-20-8_m2	H-42
H-77	Modeled and Measured ^{14}C Concentrations versus Time at ER-20-8-2_m1	H-42
H-78	Modeled and Measured ^{14}C Concentrations versus Time at ER-20-11_m1	H-43

List of Figures *(Continued)*

Number	Title	Page
H-79	Modeled and Measured ^{14}C Concentrations versus Time at ER-EC-11_p3	H-43
H-80	Modeled and Measured ^{36}Cl Concentrations versus Time at U-19ad_PS_1A	H-44
H-81	Modeled and Measured ^{36}Cl Concentrations versus Time at U-19q_PS_1D	H-45
H-82	Modeled and Measured ^{36}Cl Concentrations versus Time at U-19v_PS_1D	H-45
H-83	Modeled and Measured ^{36}Cl Concentrations versus Time at U-20n_PS_1D_o2	H-46
H-84	Modeled and Measured ^{36}Cl Concentrations versus Time at U-20n_PS_1D_o3Z	H-46
H-85	Modeled and Measured ^{36}Cl Concentrations versus Time at ER-20-5-1_m1	H-47
H-86	Modeled and Measured ^{36}Cl Concentrations versus Time at ER-20-5-3_m1	H-47
H-87	Modeled and Measured ^{36}Cl Concentrations versus Time at ER-20-7_m1	H-48
H-88	Modeled and Measured ^{36}Cl Concentrations versus Time at ER-20-8_p1	H-48
H-89	Modeled and Measured ^{36}Cl Concentrations versus Time at ER-20-8_m2	H-49
H-90	Modeled and Measured ^{36}Cl Concentrations versus Time at ER-20-8-2_m1	H-49
H-91	Modeled and Measured ^{36}Cl Concentrations versus Time at ER-20-11_m1	H-50
H-92	Modeled and Measured ^{36}Cl Concentrations versus Time at ER-EC-11_p3	H-50
H-93	Modeled and Measured ^{90}Sr Concentrations versus Time at U-19ad_PS_1A	H-52
H-94	Modeled and Measured ^{90}Sr Concentrations versus Time at U-19q_PS_1D	H-52
H-95	Modeled and Measured ^{90}Sr Concentrations versus Time at U-20n_PS_1D_o1Z	H-53

List of Figures *(Continued)*

Number	Title	Page
H-96	Modeled and Measured ^{90}Sr Concentrations versus Time at U-20n_PS_1D_o5Z	H-53
H-97	Modeled and Measured ^{90}Sr Concentrations versus Time at U-20n_PS_1D_o2	H-54
H-98	Modeled and Measured ^{90}Sr Concentrations versus Time at ER-20-12_m1	H-54
H-99	Modeled and Measured ^{90}Sr Concentrations versus Time at ER-20-12_p1	H-55
H-100	Modeled and Measured ^{90}Sr Concentrations versus Time at ER-20-12_p3	H-55
H-101	Modeled and Measured ^{99}Tc Concentrations versus Time at U-19ad_PS_1A	H-57
H-102	Modeled and Measured ^{99}Tc Concentrations versus Time at U-19q_PS_1D	H-57
H-103	Modeled and Measured ^{99}Tc Concentrations versus Time at U-19v_PS_1D	H-58
H-104	Modeled and Measured ^{99}Tc Concentrations versus Time at U-20n_PS_1D_o5Z	H-58
H-105	Modeled and Measured ^{99}Tc Concentrations versus Time at U-20n_PS_1D_o2	H-59
H-106	Modeled and Measured ^{99}Tc Concentrations versus Time at U-20n_PS_1D_o3Z	H-59
H-107	Modeled and Measured ^{99}Tc Concentrations versus Time at U-20n_PS_1D_m2	H-60
H-108	Modeled and Measured ^{99}Tc Concentrations versus Time at UE-20n_1_o2	H-60

List of Figures *(Continued)*

Number	Title	Page
H-109	Modeled and Measured ^{99}Tc Concentrations versus Time at ER-20-5-1_m1	H-61
H-110	Modeled and Measured ^{99}Tc Concentrations versus Time at ER-20-5-3_m1	H-61
H-111	Modeled and Measured ^{99}Tc Concentrations versus Time at ER-20-7_m1	H-62
H-112	Modeled and Measured ^{99}Tc Concentrations versus Time at ER-20-8_p1	H-62
H-113	Modeled and Measured ^{99}Tc Concentrations versus Time at ER-20-8_m2	H-63
H-114	Modeled and Measured ^{99}Tc Concentrations versus Time at ER-20-8-2_m1	H-63
H-115	Modeled and Measured ^{99}Tc Concentrations versus Time at ER-20-11_m1	H-64
H-116	Modeled and Measured ^{99}Tc Concentrations versus Time at ER-EC-11_p3	H-64
H-117	Modeled and Measured ^{99}Tc Concentrations versus Time at ER-20-12_m1	H-65
H-118	Modeled and Measured ^{99}Tc Concentrations versus Time at ER-20-12_p1	H-65
H-119	Modeled and Measured ^{99}Tc Concentrations versus Time at ER-20-12_p3	H-66
H-120	Modeled and Measured ^{129}I Concentrations versus Time at U-19ad_PS_1A	H-68
H-121	Modeled and Measured ^{129}I Concentrations versus Time at U-19q_PS_1D	H-69
H-122	Modeled and Measured ^{129}I Concentrations versus Time at U-19v_PS_1D	H-69
H-123	Modeled and Measured ^{129}I Concentrations versus Time at U-20n_PS_1D_o5Z	H-70
H-124	Modeled and Measured ^{129}I Concentrations versus Time at U-20n_PS_1D_o2	H-70

List of Figures *(Continued)*

Number	Title	Page
H-125	Modeled and Measured ^{129}I Concentrations versus Time at U-20n_PS_1D_o3Z	H-71
H-126	Modeled and Measured ^{129}I Concentrations versus Time at UE-20n_1_o2	H-71
H-127	Modeled and Measured ^{129}I Concentrations versus Time at ER-20-5-1_m1	H-72
H-128	Modeled and Measured ^{129}I Concentrations versus Time at ER-20-5-3_m1	H-72
H-129	Modeled and Measured ^{129}I Concentrations versus Time at ER-20-7_m1	H-73
H-130	Modeled and Measured ^{129}I Concentrations versus Time at ER-20-8_p1	H-73
H-131	Modeled and Measured ^{129}I Concentrations versus Time at ER-20-8_m2	H-74
H-132	Modeled and Measured ^{129}I Concentrations versus Time at ER-20-8-2_m1	H-74
H-133	Modeled and Measured ^{129}I Concentrations versus Time at ER-20-11_m1	H-75
H-134	Modeled and Measured ^{129}I Concentrations versus Time at ER-EC-11_p3	H-75
H-135	Modeled and Measured ^{129}I Concentrations versus Time at ER-20-12_m1	H-76
H-136	Modeled and Measured ^{129}I Concentrations versus Time at ER-20-12_p1	H-76
H-137	Modeled and Measured ^{129}I Concentrations versus Time at ER-20-12_p3	H-77
H-138	Modeled and Measured ^{137}Cs Concentrations versus Time at U-19ad_PS_1A	H-79
H-139	Modeled and Measured ^{137}Cs Concentrations versus Time at U-19q_PS_1D	H-79
H-140	Modeled and Measured ^{137}Cs Concentrations versus Time at U-20n_PS_1D_o5Z	H-80
H-141	Modeled and Measured ^{137}Cs Concentrations versus Time at U-20n_PS_1D_o2	H-80

List of Figures *(Continued)*

Number	Title	Page
H-142	Modeled and Measured ^{137}Cs Concentrations versus Time at U-20n_PS_1D_o3Z	H-81
H-143	Modeled and Measured ^{137}Cs Concentrations versus Time at U-20n_PS_1D_m2	H-81
H-144	Modeled and Measured ^{137}Cs Concentrations versus Time at UE-20n_1_o2	H-82
H-145	Modeled and Measured ^{137}Cs Concentrations versus Time at ER-20-5-1_m1	H-82
H-146	Modeled and Measured ^{137}Cs Concentrations versus Time at ER-20-5-3_m1	H-83
H-147	Modeled and Measured U (Total) Concentrations versus Time at U-19ad_PS_1A	H-85
H-148	Modeled and Measured U (Total) Concentrations versus Time at U-19q_PS_1D	H-86
H-149	Modeled and Measured U (Total) Concentrations versus Time at U-19v_PS_1D	H-86
H-150	Modeled and Measured U (Total) Concentrations versus Time at U-20n_PS_1D_o2	H-87
H-151	Modeled and Measured U (Total) Concentrations versus Time at U-20n_PS_1D_o3Z	H-87
H-152	Modeled and Measured U (Total) Concentrations versus Time at U-20n_PS_1D_m2	H-88
H-153	Modeled and Measured U (Total) Concentrations versus Time at UE-20n_1_o2	H-88
H-154	Modeled and Measured U (Total) Concentrations versus Time at ER-20-5-1_m1	H-89

List of Figures *(Continued)*

Number	Title	Page
H-155	Modeled and Measured U (Total) Concentrations versus Time at ER-20-5-3_m1	H-89
H-156	Modeled and Measured U (Total) Concentrations versus Time at ER-20-7_m1	H-90
H-157	Modeled and Measured U (Total) Concentrations versus Time at ER-20-8_p1	H-90
H-158	Modeled and Measured U (Total) Concentrations versus Time at ER-20-8_m2	H-91
H-159	Modeled and Measured U (Total) Concentrations versus Time at ER-20-8-2_m1	H-91
H-160	Modeled and Measured U (Total) Concentrations versus Time at ER-20-11_m1	H-92
H-161	Modeled and Measured U (Total) Concentrations versus Time at ER-EC-11_p3	H-92
H-162	Modeled and Measured U (Total) Concentrations versus Time at ER-20-12_m1	H-93
H-163	Modeled and Measured U (Total) Concentrations versus Time at ER-20-12_p1	H-93
H-164	Modeled and Measured U (Total) Concentrations versus Time at ER-20-12_p3	H-94
H-165	Modeled and Measured U (Total) Concentrations versus Time at ER-20-12_p4	H-94
H-166	Modeled and Measured $^{239/240}$Pu Concentrations versus Time at U-19ad_PS_1A	H-97
H-167	Modeled and Measured $^{239/240}$Pu Concentrations versus Time at U-19q_PS_1D	H-97

List of Figures *(Continued)*

Number	Title	Page
H-168	Modeled and Measured $^{239/240}$Pu Concentrations versus Time at U-19v_PS_1D	H-98
H-169	Modeled and Measured $^{239/240}$Pu Concentrations versus Time at U-20n_PS_1D_o5Z	H-98
H-170	Modeled and Measured $^{239/240}$Pu Concentrations versus Time at U-20n_PS_1D_o2	H-99
H-171	Modeled and Measured $^{239/240}$Pu Concentrations versus Time at U-20n_PS_1D_o3Z	H-99
H-172	Modeled and Measured $^{239/240}$Pu Concentrations versus Time at U-20n_PS_1D_m2	H-100
H-173	Modeled and Measured $^{239/240}$Pu Concentrations versus Time at ER-20-5-1_m1	H-100
H-174	Modeled and Measured $^{239/240}$Pu Concentrations versus Time at ER-20-5-3_m1	H-101
H-175	Modeled and Measured $^{239/240}$Pu Concentrations versus Time at ER-20-7_m1	H-101
H-176	Modeled and Measured $^{239/240}$Pu Concentrations versus Time at ER-20-8_p1	H-102
H-177	Modeled and Measured $^{239/240}$Pu Concentrations versus Time at ER-20-8_m2	H-102
H-178	Modeled and Measured $^{239/240}$Pu Concentrations versus Time at ER-20-8-2_m1	H-103
H-179	Modeled and Measured $^{239/240}$Pu Concentrations versus Time at ER-20-11_m1	H-103
H-180	Modeled and Measured $^{239/240}$Pu Concentrations versus Time at ER-EC-11_p3	H-104

List of Figures *(Continued)*

Number	Title	Page
H-181	Modeled and Measured $^{239/240}$Pu Concentrations versus Time at ER-20-12_m1	H-104
H-182	Modeled and Measured $^{239/240}$Pu Concentrations versus Time at ER-20-12_p1	H-105
H-183	Modeled and Measured $^{239/240}$Pu Concentrations versus Time at ER-20-12_p3	H-105
H-184	Modeled and Measured $^{239/240}$Pu Concentrations versus Time at PM-3_p1	H-106
H-185	Modeled and Measured $^{239/240}$Pu Concentrations versus Time at PM-3_p2	H-106
H-186	Modeled $^{239/240}$Pu Concentrations versus Time at U-19e_PS_2D	H-108
H-187	Modeled $^{239/240}$Pu Concentrations versus Time at U-20aa_PS_1D	H-108
H-188	Modeled $^{239/240}$Pu Concentrations versus Time at U-20f_PS_1D	H-109
H-189	Modeled $^{239/240}$Pu Concentrations versus Time at U-20i_PS_1D	H-109
H-190	Modeled $^{239/240}$Pu Concentrations versus Time at U-20m_PS_1D	H-110
H-191	Modeled $^{239/240}$Pu Concentrations versus Time at U-20n_PS_1D_o1Z	H-110
H-192	Modeled $^{239/240}$Pu Concentrations versus Time at U-20_WW	H-111
H-193	Modeled $^{239/240}$Pu Concentrations versus Time at UE-19c_WW_m1	H-111
H-194	Modeled $^{239/240}$Pu Concentrations versus Time at UE-19h_m1	H-112
H-195	Modeled $^{239/240}$Pu Concentrations versus Time at UE-20bh_1_o1	H-112
H-196	Modeled $^{239/240}$Pu Concentrations versus Time at UE-20n_1_o2	H-113

List of Tables

Number	Title	Page
2-1	HGUs of the PM-OV HFM	28
4-1	Pump-Scale Aquifer Test Hydraulic Conductivity Data Analyzed by HSUs	84
4-2	Slug-Scale Aquifer Test Hydraulic Conductivity Data Analyzed by HSUs	84
4-3	Pump-Scale Aquifer Test Hydraulic Conductivity Data Analyzed by HGUs	85
4-4	Slug-Scale Aquifer Test Hydraulic Conductivity Data Analyzed by HGUs	86
4-5	Observation Group Contribution to the Measurement Objective Function and MAE Error	105
4-6	Calibrated HSU Hydraulic Conductivity and Specific Storage or the Base Case Model	116
4-7	Calibrated Fault Permeability and Specific Storage for the Base Case Model	118
4-8	Sensitivity Analysis Steady-State Head Objective Function Values	153
4-9	Sensitivity Analysis Flow Path Travel Distance at 200 Years	153
5-1	Mass Percentages Available for Transport in the PM CAU Model	164
5-2	Inventory and Half-Lives for RNs Included in the PM CAU Model (Decay-corrected to September 30, 2012)	177
5-3	Matrix Porosity Distributions Used in the PM CAU Transport Model	179
5-4	Effective Porosity Distributions Used for the HGUs Treated as Fractured Dual-Porosity Media in the PM CAU Transport Model	182
5-5	Bulk Rock Density (kg/m^3) Distributions Used in the PM CAU Transport Model	186
5-6	Log_{10} Fracture Aperture (m) Distributions Used in the PM CAU Transport Model	190

List of Tables *(Continued)*

Number	Title	Page
5-7	Matrix Diffusion Coefficient (m^2/s) Distributions Used in the PM CAU Transport Model	196
5-8	Source Mass Flux Start Times Used in the PM CAU Transport Model for the 82 Underground Detonations	206
5-9	^3H Observations Used in the PM CAU Transport Model Calibration	209
5-10	^3H Observation Group Contribution to the Measurement Objective Function	219
5-11	Observations of RNs Other than ^3H	261
5-12	Source Mass Flux Start Times Used in the PM CAU Transport Model for the 3 Near-Surface Cratering Detonations	288
5-13	MCLs for Each Modeled RN	289
B-1	Implementation of QAP Modeling and Software Requirements in the PM CAU Flow and Transport Model	B-2
B-2	Implementation of QAPP Data Management Requirements in the PM CAU Flow and Transport Model	B-14
C-1	HSUs of the PM-OV HFM	C-2
D-1	Central and Western PM Underground Nuclear Test Information	D-2
G-1	Assigned Chemistry Subareas and Diagenetic Zones Used for K_d Selection	G-2
G-2	Log K_d Distributions Used in the PM CAU Transport Model	G-5

List of Acronyms and Abbreviations

General Acronyms and Abbreviations

1-D	One-dimensional
2-D	Two-dimensional
3-D	Three-dimensional
ac-ft/yr	Acre feet per year
amsl	Above mean sea level
ASTM	ASTM International
bgs	Below ground surface
BLM	Bureau of Land Management
Bq/L	Becquerels per liter
°C	Degrees Celsius
CADD	Corrective action decision document
CAI	Corrective action investigation
CAIP	Corrective action investigation plan
CAP	Corrective action plan
CAS	Corrective action site
CAU	Corrective action unit
CB	Contaminant boundary
CDF	Cumulative distribution function
CEV	Cumulative exceedance volume
Ci	Curie
COTS	Commercial off-the-shelf
CR	Closure report
CY	Calendar year
DFN	Discrete fracture network
DISU	Unstructured discretization
DISV	Discretization by vertices
DoD	U.S. Department of Defense
DOE	U.S. Department of Energy
DOE/EMNV	U.S. Department of Energy Environmental Management Nevada Program
DOE/NV	U.S. Department of Energy Nevada Operations Office

List of Acronyms and Abbreviations *(Continued)*

DRI	Desert Research Institute
DVRFS3	Death Valley Regional Flow System
DZ	Diagenetic zone
EM	Environmental Management
EPA	U.S. Environmental Protection Agency
ET	Evapotranspiration
EV	Exchange volume
EZ	Exchange zone
FEHM	Finite Element Heat and Mass Transfer
FEV	Fractional exceedance volume
FFACO	*Federal Facility Agreement and Consent Order*
ft	Foot
ft/day	Feet per day
ft^2/day	Square feet per day
GW	Groundwater
GWF	Groundwater flow
HDD	Hydrologic data document
HFM	Hydrostratigraphic framework model
HGL	HydroGeoLogic, Inc.
HGU	Hydrogeologic unit
HPC	High-performance computing
HST	Hydrologic source term
HSU	Hydrostratigraphic unit
in./yr	Inches per year
K	Hydraulic conductivity
K_d	Distribution coefficient
kg/m^3	Kilograms per cubic meter
km	Kilometer
km^2	Square kilometer
km^3	Cubic kilometer
kt	Kiloton

List of Acronyms and Abbreviations *(Continued)*

LaGriT	Los Alamos Grid Toolbox
LANL	Los Alamos National Laboratory
LLNL	Lawrence Livermore National Laboratory
m	Meter
m/day	Meters per day
m^2/s	Square meters per second
m^2/yr	Square meters per year
m^3	Cubic meter
m^3/day	Cubic meters per day
m^3/yr	Cubic meters per year
Ma	Million years ago
MAE	Mean absolute error
MAW	Multi-aquifer well
MCL	Maximum contaminant level
m/day	Meters per day
mHSU	Modified hydrostratigraphic unit
mi	Mile
mi^2	Square mile
mm/yr	Millimeters per year
MNW	Multi-node, drawdown-limited well
msl	Mean sea level
Mt	Megaton
MWAT	Multiple-well aquifer test
m/yr	Meters per year
N/A	Not applicable
NAD	North American Datum
NDEP	Nevada Division of Environmental Protection
N-I	Navarro-Intera, LLC
NNSA/NFO	U.S. Department of Energy, National Nuclear Security Administration Nevada Field Office
NNSA/NSO	U.S. Department of Energy, National Nuclear Security Administration Nevada Site Office
NNSS	Nevada National Security Site

List of Acronyms and Abbreviations *(Continued)*

NOAA	National Oceanic and Atmospheric Administration
NSTec	National Security Technologies, LLC
NTS	Nevada Test Site
NTTR	Nevada Test and Training Range
NV	Nevada
NWIS	National Water Information System
pCi/L	Picocuries per liter
PER	Preemptive review
PEST	Parameter estimation
PM	Pahute Mesa
PM-OV	Pahute Mesa–Oasis Valley
QA	Quality assurance
QAP	Quality Assurance Plan
R_c	Cavity radius
ROTC	Record of Technical Change
RMS	Root mean square
RM/SM	Rainier Mesa/Shoshone Mountain
RN	Radionuclide
RST	Radiologic source term
S	Storage coefficient
SDD	Source term data document
SDWA	*Safe Drinking Water Act*
SME	Subject matter expert
Ss	Specific storage
SWNVF	Southwestern Nevada Volcanic Field
TDD	Transport data document
UCDB	UGTA Chemistry Database
UGTA	Underground Test Area
USAF	U.S. Air Force
USGS	U.S. Geological Survey
UTM	Universal Transverse Mercator

List of Acronyms and Abbreviations *(Continued)*

VOIA	Value-of-information analysis
WP	Working point
WT	Water table
YF/CM	Yucca Flat/Climax Mine
µg/L	Micrograms per liter

Stratigraphic, Geologic, Hydrostratigraphic, and Hydrogeologic Unit Abbreviations and Symbols

AA	Alluvial aquifer
ATCCU	Argillic tuff caldera confining unit
ATCU	Argillic tuff confining unit
ATICU	Ammonia Tanks intrusive confining unit
ATMLFA	Ammonia Tanks mafic lava-flow aquifer
ATWTA	Ammonia Tanks welded-tuff aquifer
BA	Benham aquifer
BFCU	Bullfrog confining unit
BMICU	Black Mountain intrusive confining unit
BRA	Belted Range aquifer
BWCU	Buttonhook Wash confining unit
BWWTA	Buttonhook Wash welded-tuff aquifer
CA	Carbonate aquifer
CCICU	Claim Canyon intrusive confining unit
CCU	Clastic confining unit
CFCM	Crater Flat composite unit
CFCU	Crater Flat confining unit
CHICU	Calico Hills intrusive confining unit
CHLFA	Calico Hills lava-flow aquifer
CHLFA1	Calico Hills lava-flow aquifer 1
CHLFA2	Calico Hills lava-flow aquifer 2
CHLFA3	Calico Hills lava-flow aquifer 3
CHLFA4	Calico Hills lava-flow aquifer 4

List of Acronyms and Abbreviations *(Continued)*

CHLFA5	Calico Hills lava-flow aquifer 5
CHVTA	Calico Hills vitric-tuff aquifer
CHZCM	Calico Hills zeolitized composite unit
CNCC	Central Nevada caldera complex
CPA	Comb Peak aquifer
CZ	Zabriskie Quartzite
CZw	Wood Canyon Formation
Dg	Guilmette Formation
Ds	Simonson Dolomite
DSs	Sevy Dolomite
DVA	Detached volcanic aquifer
DVCM	Detached volcanic composite unit
FC-BH	Fluorspar Canyon-Bullfrog Hills detachment fault
FCCM	Fortymile Canyon composite unit
FCCU	Fluorspar Canyon confining unit
FCLLFA	Fortymile Canyon lower lava-flow aquifer
FCLMLFA	Fortymile Canyon lower mafic lava-flow aquifer
FCULFA	Fortymile Canyon upper lava-flow aquifer
FCULFA1	Fortymile Canyon upper lava-flow aquifer 1
FCULFA2	Fortymile Canyon upper lava-flow aquifer 2
FCULFA3	Fortymile Canyon upper lava-flow aquifer 3
FCULFA4	Fortymile Canyon upper lava-flow aquifer 4
FCULFA5	Fortymile Canyon upper lava-flow aquifer 5
FCULFA6	Fortymile Canyon upper lava-flow aquifer 6
FCULFA7	Fortymile Canyon upper lava-flow aquifer 7
FCUMLFA	Fortymile Canyon upper mafic lava-flow aquifer
FCWTA	Fortymile Canyon welded-tuff aquifer
FCWTA1	Fortymile Canyon welded-tuff aquifer 1
GCCSMNW	Grouse Canyon caldera structural margin NW
GCU	Granitic confining unit
IA	Inlet aquifer

List of Acronyms and Abbreviations *(Continued)*

ICU	Intrusive confining unit
IICU	Intracaldera intrusive confining unit
KA	Kearsarge aquifer
LCA	Lower carbonate aquifer
LCA3	Lower carbonate aquifer-thrust plate
LCCU	Lower clastic confining unit
LCCU1	Lower clastic confining unit - thrust plate
LFA	Lava-flow aquifer
LPCU	Lower Paintbrush confining unit
LVTA2	Lower vitric-tuff aquifer 2
mBZ	Modified brecciated zone
mBRA_SW	Modified Belted Range southwest
MDc	Late Devonian through Mississippian siliciclastic rocks
MDe	Eleana Formation
MGCU	Mesozoic granite confining unit
MHMSZ	Moor Hen Meadow structural zone
mPBRCM_LFA	Modified Pre-Belted Range composite unit lava-flow aquifer
mPBRCM_SW	Modified Pre-Belted Range composite unit southwest
mPBRLFA	Modified Pre-Belted Range lava-flow aquifer
MPCU	Middle Paintbrush confining unit
mRMWTA2	Modified Rainier Mesa welded-tuff aquifer 2
mTCA	Modified Tiva Canyon aquifer
mTCA_W	Modified Tiva Canyon aquifer west
mUPCU_SW	Modified Upper Paintbrush confining unit southwest
NTMMSZ	Northern Timber Mountain moat structure
Op	Pogonip Group
PBPCU	Post-Benham Paintbrush confining unit
PBRCM	Pre-Belted Range composite unit
PCM	Paintbrush composite unit
PLFA	Paintbrush lava-flow aquifer
PMNICU	Pahute Mesa Northern Extension intrusive confining unit

List of Acronyms and Abbreviations *(Continued)*

PVTA	Paintbrush vitric-tuff aquifer
Qam	Middle alluvium
Qay	Young alluvial deposits
Qb	Quaternary Basalt
Qs	Quaternary sediments
QTa	Quaternary/Tertiary alluvium
QTc	Quaternary/Tertiary colluvium
QTu	Quaternary/Tertiary undifferentiated surficial deposit
RMICU	Rainier Mesa intrusive confining unit
RMWTA	Rainier Mesa welded-tuff aquifer
RVICU	Redrock Valley intrusive confining unit
SCCC	Silent Canyon caldera complex
SCICU	Silent Canyon intrusive confining unit
SCVCU	Subcaldera volcanic confining unit
Sl	Laketown Dolomite
SMLFA	Shoshone Mountain lava-flow aquifer
SPA	Scrugham Peak aquifer
SWA	Stockade Wash aquifer
Tac	Calico Hills Formation
Tal	Tuffs of Antelope Springs lower
Tam	Tuffs of Antelope Springs middle
Tau	Tuffs of Antelope Springs
TB	Tuff breccia
Tb	Belted Range Group
Tbg	Grouse Canyon Tuff
Tbgs	Comendite of Split Ridge
Tbq	Comendite of Quartet Dome
TC	Tuff cone
Tc	Crater Flat Group
TCA	Tiva Canyon aquifer
Tcb	Bullfrog Tuff

List of Acronyms and Abbreviations *(Continued)*

Tcbs	Bullfrog Tuff, Stockade Wash Lobe
Tcg	Latite of Grimy Gulch
Tci	Rhyolite of Inlet
TCL	Thirsty Canyon Lineament
Tcpj	Tuff of Jorum
Tcpk	Rhyolite of Kearsarge
Tcps	Rhyolite of Sled
Tcu	Tuff of Pool
TCU	Tuff confining unit
TCVA	Thirsty Canyon volcanic aquifer
Te	Volcanics of Central Nevada
Tec	Fraction Tuff and related rocks
Tem	Monotony Tuff
Tep	Pahranagat Tuff
Tes	Shingle Pass Tuff
Tf	Volcanics of Fortymile Canyon
Tf/Tfr	Fraction Tuff and related rocks
Tfb	Beatty Wash Formation
Tfbb	Basalt of Chukar Canyon
Tfbw	Rhyolite of Beatty Wash
Tfd	Lava flows of Dome Mountain
Tff	Rhyodacite of Fleur-de-lis-Ranch
Tfl	Tuff of Leadfield Road
Tfr	Rhyolite of Rainbow Mountain
Tfs	Rhyolite of Shoshone Mountain
Tft	Intermediate-age basalt
Tfu	Rhyolite of Boundary Butte
Tgc	Caldera moat-filling sediments
Tgm	Late synvolcanic sedimentary rock
Tgy	Basin-fill sediments, undivided
Tgyx	Younger landslide and sedimentary breccia

List of Acronyms and Abbreviations *(Continued)*

Th	Calico Hills Formation
THCM	Tannenbaum Hill composite unit
THCU	Tannenbaum Hill confining unit
THLFA	Tannenbaum Hill lava-flow aquifer
Ti	High-silica granodiorite, etc.
Tk	Volcanics of Kawich Valley
Tm	Timber Mountain Group
Tma	Ammonia Tanks Tuff
TMA	Timber Mountain aquifer
Tmab	Ammonia Tanks bedded tuff
Tmap	Ammonia Tanks mafic-poor
Tmat	Rhyolite of Tannenbaum Hill
Tmaw	Rhyolite of Tannenbaum Hill
Tmay	Rhyolite of Tannenbaum Hill
Tmc	Caldera-collapse breccia of Timber Mountain caldera complex
TMCC	Timber Mountain caldera complex
TMCCSM	Timber Mountain caldera complex structural margin
TMCM	Timber Mountain composite unit
TMD	Timber Mountain Dome
TMLVTA	Timber Mountain lower vitric-tuff aquifer
Tmr	Rainier Mesa Tuff
Tmrb	Rainier Mesa bedded tuff
Tmrf	Rhyolite of Fluorspar Canyon
Tmrh	Tuff of Holmes Road
TMUWTA	Timber Mountain upper welded-tuff aquifer
Tmw	Rhyolite of Windy Wash
TMWTA	Timber Mountain welded-tuff aquifer
Tn	Tunnel Formation
To	Volcanics of Oak Spring Butte
Tor	Redrock Valley Tuff
Tori	Redrock Valley intrusive

List of Acronyms and Abbreviations (Continued)

Tot	Tuff of Twin Peaks
Tp	Paintbrush Group
Tpb	Rhyolite of Benham
Tpc	Tiva Canyon Tuff
Tpd	Rhyolite of Delirium Canyon
Tpe	Rhyolite of Echo Peak
Tpk	Rhyolite of Comb Peak
Tpr	Rhyolite of Silent Canyon
Tps	Rhyolite of Scrugham Peak
Tpt	Topopah Spring Tuff
Tq	Volcanics of Quartz Mountain
Tr	Tram Ridge Group
TSA	Topopah Spring aquifer
Tsp	Spearhead Member of Stonewall Flat Tuff
Tt	Thirsty Canyon Group
Tu	Volcanics of Big Dome
Ttc	Comendite of Ribbon Cliff
Ttg	Gold Flat Tuff
Tth	Trachyte of Hidden Cliff
Ttp	Pahute Mesa and Rocket Wash Tuffs
Tts	Trachytic rocks of Pillar Spring and Yellow Cleft
UCCU	Upper clastic confining unit
UPCU	Upper Paintbrush confining unit
VCU	Volcaniclastic confining unit
VT	Vitrophyric tuff
VTA	Vitric-tuff aquifer
WTA	Welded-tuff aquifer
WWA	Windy Wash aquifer
YMCFCM	Yucca Mountain Crater Flat composite unit
YVCM	Younger volcanic composite unit
Zj	Johnnie Formation

List of Acronyms and Abbreviations *(Continued)*

Zs	Stirling Quartzite
M	Mesozoic
pC	Pre-Cambrian & Paleozoic
Q	Quaternary
T	Tertiary

Elements and Compounds

Al	Aluminum
Am	Americium
Ar	Argon
Br	Bromine
C	Carbon
Ca	Calcium
Cd	Cadmium
Cl	Chlorine
Cm	Curium
Co	Cobalt
Cs	Cesium
Eu	Europium
^{3}H	Tritium
Ho	Holmium
HTO	Hydrogen tritium oxide
I	Iodine
K	Potassium
Kr	Krypton
Nb	Niobium
Ni	Nickel
Np	Neptunium
Pd	Palladium
Pu	Plutonium
Rn	Radon

List of Acronyms and Abbreviations *(Continued)*

Sm	Samarium
Sn	Tin
Sr	Strontium
Tc	Technetium
Th	Thorium
TNT	Trinitrotoluene
U	Uranium
Zr	Zirconium
$\delta^{2}H$	Delta deuterium
$\delta^{13}C$	Delta carbon-13
$\delta^{34}S$	Delta sulfur-34

Executive Summary

The Central and Western Pahute Mesa (PM) corrective action units (CAUs), which lie in the northwestern portion of the Nevada National Security Site (NNSS) in southern Nevada (Figure ES-1), are the topic of this report. These are two of the areas at the NNSS that were historically used for underground nuclear testing. Underground nuclear tests deposit radioactive elements in the subsurface, resulting in groundwater contamination in the vicinity of the underground test locations.

There are ongoing radiologic groundwater investigation and remediation efforts at the NNSS being conducted due to concerns about potential human health and environmental risks posed by underground test-related radioactivity. These efforts are conducted under the Underground Test Area (UGTA) Activity, which is responsible for developing a more thorough and consistent understanding of radionuclide (RN) occurrence and movement in groundwater, as derived from all underground tests conducted at the NNSS.

Background

The work of UGTA is built around an integrated campaign of drilling and sampling, data aggregation and interpretation, computer modeling, and broader monitoring activities, all of which are conducted under the auspices of a joint *Federal Facility Agreement and Consent Order* (FFACO, 1996 as amended) developed between the State of Nevada, the U.S. Department of Energy (DOE), and the U.S. Department of Defense (DoD). (Note: References cited in this Executive Summary are listed at the end of this section.) This agreement includes a process for planning, investigating, and responding to both current and anticipated groundwater contamination conditions at the NNSS and surrounding areas originating from underground nuclear tests. Under the FFACO, the underground nuclear tests conducted at the NNSS were grouped into five CAUs based primarily on geographically distinct areas of underground nuclear testing. The two CAUs at Pahute Mesa, Central PM CAU 101 and Western PM CAU 102, are the topic of this report.

Eighty-five underground nuclear tests were conducted at the PM CAUs (Figure ES-2) between 1965 and 1992 (NNSA/NFO, 2015), resulting in more than $2.68 \times 10^{+07}$ curies of residual long-lived unclassified radiologic inventory of potential concern (decay-corrected to September 30, 2012)

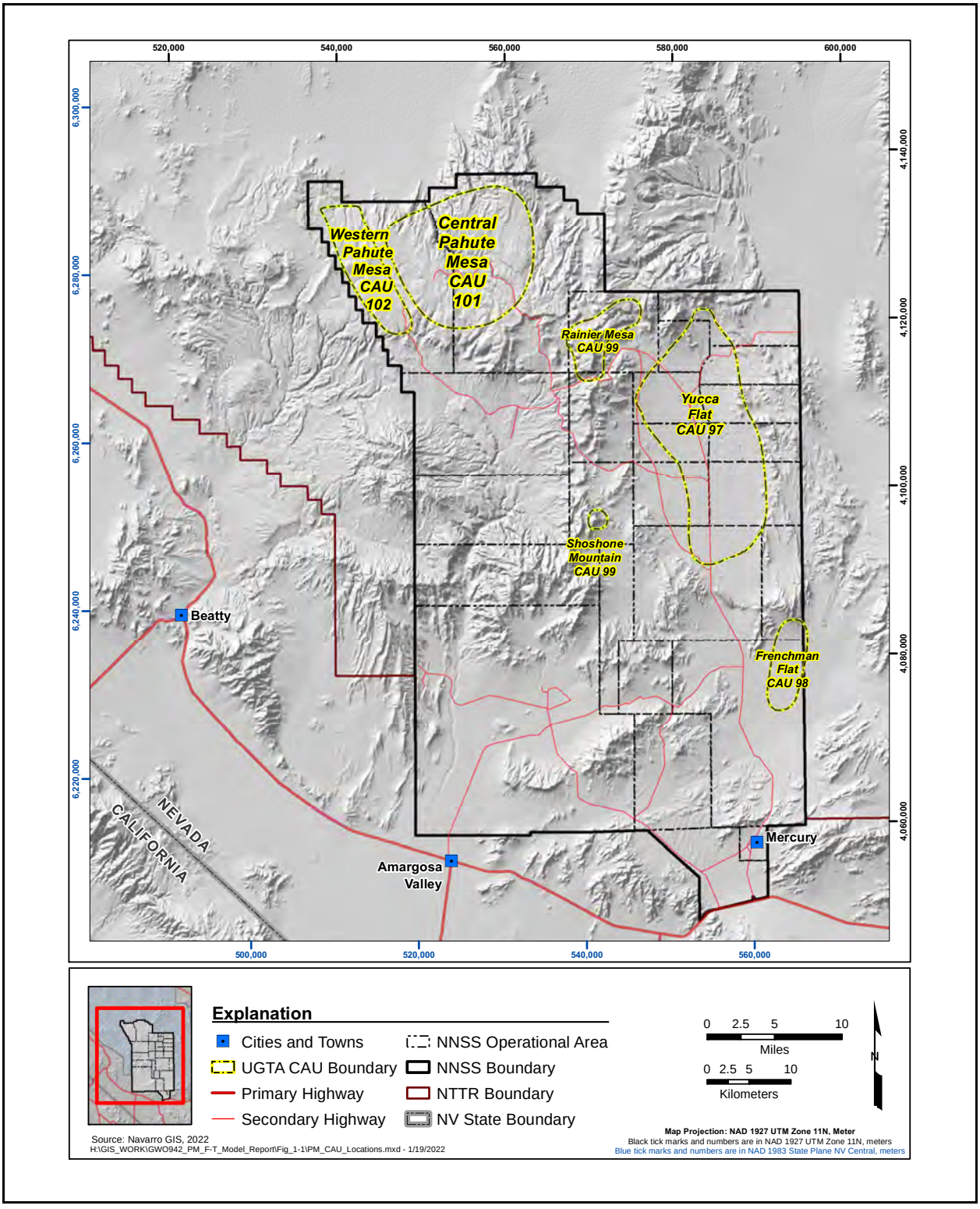

Figure ES-1
Location of the PM CAUs

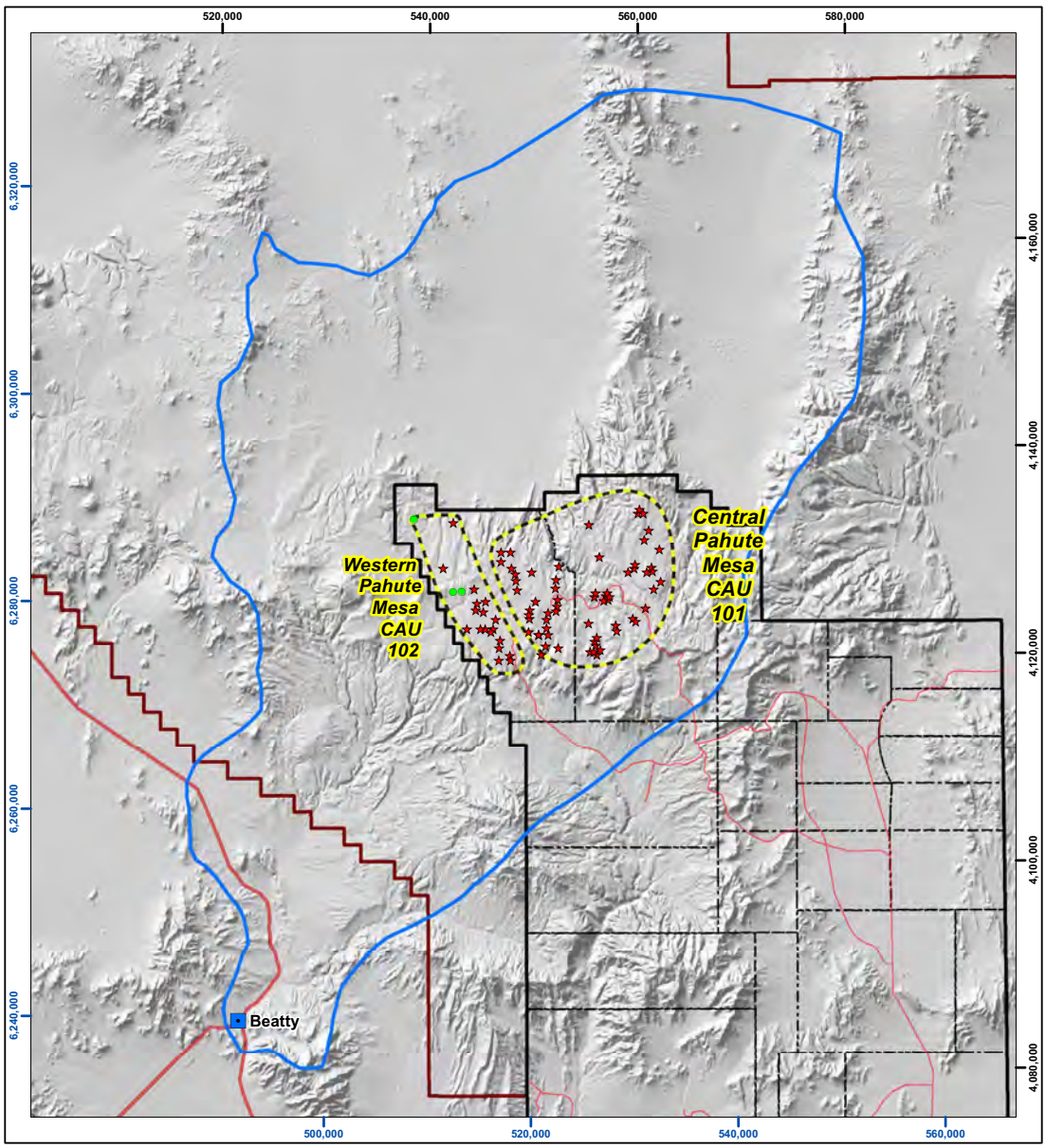

Figure ES-2
Map Showing PM Test Locations

remaining underground (Finnegan et al., 2016). Eighty-two of these tests were detonated in deep vertical shafts, comprising 60.2 percent of the radiologic inventory from the underground nuclear tests on the NNSS. The remaining three tests were shallow cratering events that are not assigned to the UGTA Activity as defined in FFACO (1996, as amended); however, they are incorporated in the work reported here for the sake of completeness.

The UGTA strategy, defined in Appendix VI of the FFACO, assumes that active remediation of underground nuclear tests is not cost-effective with current technology, and because of the high remediation costs, closure in place with monitoring and institutional controls is the only likely corrective action. The important potential risks from radiological contamination of groundwater are to workers, the public, and the environment; and exposure to these risks requires access to groundwater. The technical basis for achieving the UGTA strategy is through an evaluation of the CAU, using a combination of (1) data collection; (2) modeling of hydrological setting, radiological source term (RST), and flow and contaminant transport; (3) iterative model evaluations and monitoring; and (4) identification and documentation of land-use policies (institutional controls). This four-component approach is used to accomplish the primary objective of the UGTA strategy, which is to define perimeter boundaries over the next 1,000 years that encompass groundwater that potentially exceeds the radiological standards of the *Safe Drinking Water Act* (SDWA) (CFR, 2021). The FFACO stipulates that simulation modeling of contaminant transport will be used to forecast the location of contaminant boundaries (CBs) within 1,000 years and must show the 95th percentile of the model results boundary (outside of which only 5 percent of the simulations exceed the SDWA standards). This document presents the groundwater flow and transport models developed for this purpose along with their results.

While the third and fourth components listed above (those pertaining to iterative model evaluations and identification of land-use practices) will be conducted during the subsequent project steps, the first two components are addressed in this document and in the references cited herein. For the PM CAUs, data collection and analysis related to hydrologic data are presented in *Hydrologic Data for the Groundwater Flow and Contaminant Transport Model for Corrective Action Units 101 and 102: Central and Western Pahute Mesa, Nye County, Nevada* (Navarro 2021b); transport parameter data are presented in *Contaminant Transport Parameters for the Groundwater Flow and Contaminant Transport Model for Corrective Action Units 101 and 102: Central and Western Pahute Mesa,*

Nye County, Nevada (Navarro 2021a); and source term and RN observation data are presented in *Unclassified Source Term and Radionuclide Data for the Groundwater Flow and Contaminant Transport Model for Corrective Action Units 101 and 102: Central and Western Pahute Mesa, Nye County, Nevada* (Navarro 2021c). The hydrogeologic framework model (HFM) that forms the basis of the PM numerical flow and transport models along with the relevant data and analysis are presented in DOE/EMNV (2020). A conceptual model of flow at the PM is discussed in Jackson et al. (2021). A hydrologic source term (HST) model and screening analysis to select the RNs to be included in the PM CAU transport model are presented in Carle et al. (2020). The data collected as part of the geochemistry investigations, related analysis, and geochemical modeling to evaluate flow paths are detailed in Navarro (2020). Data, analysis, and modeling in support of the recharge input to the flow model is detailed in Fenelon et al. (2016), Halford and Jackson (2020), and Middleton et al. (2019).

The flow and transport model presented in this report evolved from and benefited from a succession of studies and models that came before it. These models were developed with the data that existed at the time, and provided insights in the where and how new data would help to reduce uncertainties. The new data that were obtained enhanced the models that followed. The current model is the beneficiary of this cycle of modeling, data collection, and model refinement that have been ongoing for more than 25 years. The models that directly inform the current work include pre-Phase I regional groundwater models (IT, 1996a, b, and c); PM Phase I flow and transport models (SNJV, 2006, 2007, and 2009); U.S. Geological Survey (USGS) Pahute Mesa-Oasis Valley (PM-OV) basin delineation model (Fenelon et al., 2016); USGS volcanic rock characterization model (Garcia et al. 2017); Los Alamos National Laboratory (LANL) AMANZI Bench area model (Lu et al., 2021); USGS Death Valley regional groundwater flow system Model (Halford and Jackson, 2020); and USGS HANDLEY flow and tritium (^{3}H) transport model (Jackson, 2021).

The forecasts of RN migration presented in this report are based on the SDWA standards for RNs (CFR, 2021) and the requirements of the FFACO (1996, as amended). The forecasts are probabilistic calculations as planning tools intended to facilitate regulatory decisions designed to protect the health and safety of the public and to provide tools to evaluate future groundwater monitoring. The modeling basis of these forecasts is biased toward overestimating the potential contaminant transport when faced with sparse data that may be subject to alternative interpretations, or when the conceptual

model is likely to lead to significant increase in computational burden. As such, the probabilistic forecasts do not represent the actual extent of contamination in groundwater. Current and future groundwater sampling to measure or evaluate concentration data will provide better understanding of actual extent of contamination.

The FFACO (1996, as amended) requires that the CAU models of the corrective action investigation (CAI) stage will be constructed and consider, at a minimum, eight modeling topics with the objective of evaluating future migration of contaminants to forecast CBs that encompass the uncertainty of current and future contaminant migration. These are listed below along with brief statements regarding how they are addressed in this work:

- **Alternative hydrological framework models of the CAU modeling domain:** The Phase I PM-OV HFM used separate, fully functioning alternative HFMs to address uncertainty associated with hydrogeologically significant non-unique interpretations incorporated into the Phase I HFM (see Section 6.0 in BN, 2002). Phase II work took a different approach to uncertainty analysis by testing techniques that exploit the functionality of EarthVision (Dynamic Graphics, 2015) to help understand and evaluate the potential hydrologic effects of uncertainty associated with certain aspects of the PM-OV HFM. A technique was used in which the team assessed the uncertainty associated with fault offsets and the juxtaposition of hydrostratigraphic units (HSUs) across certain faults at PM (DOE/EMNV, 2020). PM CAU flow model calibration evaluated several hydrologic conceptual model alternatives that included subdividing (laterally or vertically) some HSUs into smaller sub-HSUs with distinct material properties. The flow model included an alternative that identified faults as distinct flow regimes separate from the HSUs.

- **Uncertainty in the RST and HST:** The uncertainty in the HST as it applies to the PM CAU model is concisely described in Carle et al. (2020). Their sensitivity analysis showed that greatest impact to uncertainty came from the parameters regarding RN distribution within the source volume. Their results showed that with few exceptions (^{137}Cs at CHANCELLOR, $^{239/240}$Pu at CHANCELLOR and ALMENDRO, and ^{14}C at CAMEMBERT), the observations from near-field and downgradient samples fall within the range of base case model calculations or lower. The PM CAU transport model used an approach aligned with the screening model base case, yielding source concentrations that allowed calibration of ^{3}H using parameter values within the range of observations. More importantly, the base case source approach produced source concentrations for RNs other than ^{3}H that when simulated with the calibrated transport model typically produced conservative or consistent results compared with observations.

- **Alternative models of groundwater recharge:** Different alternative models of the recharge distribution were simulated as part of the uncertainty analysis of the flow model.

- **Alternative model boundary conditions and models of groundwater flow:** The Fenelon et al. (2016) evaluation determined that to a large extent the groundwater flow system in the PM-OV groundwater basin is self-contained such that the discharge observed in Oasis Valley is derived from recharge that occurred within the boundaries of the basin. The uncertainty in the boundary conditions is quite small compared with the total flow through the basin. The uncertainty in the boundary flux is shown in Fenelon et al. (2016) to be about ±150 acre-feet per year (ac-ft/yr), or 2.5 percent of the total basin flow. The total discharge is estimated to be 5,900 ac-ft/yr with about a 15 percent uncertainty. Compared with parameter uncertainty in hydraulic conductivity, porosity, diffusion and sorption parameters, and source concentration, the amount of boundary flux uncertainty is much smaller and is not likely to be a major factor in the overall uncertainty in the migration of RNs in the PM-OV groundwater basin.

- **Multiple permissive sets of calibrated flow models:** The calibration included several alternative model formulations, each of which was calibrated to the observed data. During the calibration process, it was determined that distinct alternative HFMs were not needed to achieve calibration because the observed heterogeneity of flow properties was substantial and provided a sufficient range of values for calibration. Rather than develop alternative HFMs, the approach chosen during flow calibration was to add hydraulic conductivity heterogeneity by subdividing (laterally or vertically) some HSUs into smaller sub-HSUs with distinct material properties. Several alternative hydrologic conceptual models were also investigated that included an alternative that identified faults as distinct flow regimes separate from the HSUs. The different alternative flow models yield what can be termed permissive sets of parameters that yield similar calibrations. These alternative flow cases were used to simulate RN transport during probabilistic forecast simulations used to identify the ensemble of CBs.

- **Probabilistic simulations of transport using plausible sets of alternative framework and recharge models, model boundary conditions, and models of groundwater flow from calibrated flow models:** The base case model and three alternative flow models were used to simulate RN transport and generate the probabilistic forecasts.

- **Ensembles of forecasts of CBs for the CAU:** The ensembles of forecasts of CBs were calculated including the base model and the three alternatives.

- **Sensitivity and uncertainty analysis of the model outputs:** A comprehensive parameter sensitivity is obtained from the use of the parameter estimation (PEST) optimization software (Doherty, 2018), which produces a sensitivity matrix of model responses compared with calibration targets for every adjustable parameter in the model. PEST further calculates a parameter identifiability for each parameter, which ranks the parameters in terms of their influence in the calibration. In addition to the PEST sensitivity calculations, transport from the BENHAM detonation was modeled to evaluate to show how the results are influenced by uncertainties in dispersivity and source mass of Pu.

To forecast the ensemble of CBs, the PM CAU model report documents the following:

- The development of a three-dimensional (3-D) mathematical groundwater flow and transport model that incorporates the important features of the flow and transport system and honors CAU-specific and RN-specific data and information.
- Simulation of the groundwater flow and RN transport incorporating HSTs for RN release into groundwater to determine the direction and magnitude of groundwater fluxes and RN migration based on calibration to PM hydrogeologic data and ^{3}H observation data in downgradient wells.
- Quantification of the uncertainty in the direction and magnitude of groundwater flow and RN transport due to uncertainty in parameter values and alternative conceptual models.
- Identification of pathlines from test locations and expected distances of transport to assess the monitoring network design and identify gaps in the monitoring network.

Modeling Approach

Model development was guided by the need to be as realistic as practically feasible in selecting hydrogeologic features, flow processes, transport processes, and parameter distributions for inclusion in the model, while keeping in mind the purpose of PM CAU flow and transport modeling, which is to support the UGTA corrective action strategy objective of forecasting CBs. The philosophy adopted in model development was to be conservative in the modeling assumptions when, judged on the basis of theoretical and numerical considerations, they were likely to affect the forecast extent and magnitude of RN transport, especially when data were sparse or may be subject to alternative interpretations or when the conceptual model was likely to lead to significant increase in computational burden. This philosophy led to the decision to use models or parameter values that, while reproducing many realistic features of the system (such as observed basin discharge, hydraulic heads, transmissivities, flow paths, ^{3}H concentrations at several observation wells, and transit times) tend to overestimate the potential contaminant transport. Confidence in the PM CAU flow model was established, and our understanding of the flow system was supported by calibration of the model to observed hydraulic data. Confidence in the transport model was increased by demonstrating that the model could be calibrated to observed ^{3}H data with parameter values selected within ranges of parameter uncertainty. The choice of the conservative assumptions was evaluated, when practically feasible, against the model outcomes to determine if the result was sensitive to the assumptions.The forecast contaminant transport overestimation was demonstrated by comparing modeled contaminant

transport with contaminant concentration observations at and downgradient from test cavities. For example, consider colloid-facilitated transport of plutonium (Pu). As a conservative approximation, filtration and retardation of the colloids are ignored because colloid filtration process is not well-quantified. The model conservatism could be reduced with more detailed considerations of colloid transport, but that would significantly increase the complexity and numerical demands of the model. The current PM CAU model forecasts Pu transport at levels well above observations, but rather than refining the model at this time, the conservative results are accepted as they provide an additional level of protection or buffer.

The 3-D CAU-scale model consists of two integrated but mathematically decoupled components: the CAU flow model and the CAU transport model. The approach begins with characterization of the subsurface hydrogeology and the flow system. Conceptual models of the flow as well as transport are developed based on the results of characterization and assumptions regarding system processes. The processes deemed important in the conceptual models are represented mathematically and implemented on computers in numerical codes capable of representing the temporal and spatial scales of relevance to achieve the objectives. The models use numerical 3-D flow and transport simulators that capture the complex geologic structure underlying the PM, including units of variable thickness, faults, and offsets, as well as complex transport processes associated with reactive solutes and fractured rock.

For the PM CAU flow model, groundwater flow is taken to be fully saturated, isothermal, and steady-state with recharge and discharge in balance. An equivalent continuum behavior for flow is assumed, where the hydraulic head is interpreted in an average sense for the computational cell, hydraulic conductivity is taken to be an average scaler quantity, and hydrologic features that may be present on a smaller scale are simulated using dispersion. It is conceptualized that RNs from underground nuclear tests at PM can be transported with groundwater flowing through water-saturated geologic formations. It is assumed that the RNs dissolved in the pore fluid have negligible effect on fluid motion and are carried along by the pore fluid moving at its local velocity. The advective flow paths correspond with the groundwater flow paths, and the fluid velocity determines the rate of advection of aqueous RNs along flow paths. Many of the geologic units of importance to transport at PM are fractured volcanic formations. They are conceptualized as dual porosity where flow occurs through the high-permeability fractures with stagnant fluid in the rock matrix and RNs can diffuse between

the fractures and the matrix. The migration processes relevant for evaluating RN transport at PM are radioactive decay of the species, advection in porous and fractured media, dispersion, diffusion of RNs between fracture water and matrix water, sorption onto immobile minerals in the matrix, and colloid-facilitated transport. Solute sorption onto fracture walls, and colloid filtration/retardation in the fractures is ignored in this work.

The flow model is constructed using the USGS code MODFLOW6 (Langevin et al., 2017). The calibration of the flow model is aided by the use of the PEST software (Doherty, 2018). The model is configured with brick-shaped blocks following the block-centered formulation of MODFLOW6 with refinement in areas containing a higher frequency of observational and measured data and around structural features such as faults and caldera boundaries that are believed to influence groundwater flow.

The screening model (Carle, 2020) provides an explanation of the process to evaluate the total RN inventory (Finnegan et al., 2016) as a means to identify the RNs of relevance or potentially of relevance. RNs to be included in the transport model are defined to be the subset of the RN inventory isotopes anticipated to exist in source area groundwater at concentrations that exceed one tenth of the SDWA standards (CFR, 2021) for at least 100 years, as based upon screening model calculations and historical RN measurements in groundwater. RN mass is distributed within the specific geometric volume associated with each detonation location to serve as initial conditions for the transport simulation.

Transport processes included in the PM CAU transport model for evaluating RN transport at PM are radioactive decay of the species, advection in porous and fractured media, dispersion, diffusion of RNs between fracture water and matrix water, sorption onto immobile minerals, and colloid-facilitated transport. The first part of the transport modeling approach is based on particle tracking to simulate the transport processes of advection and dispersion using the code Walkabout (Painter, 2011). Particle tracking is used to minimize numerical dispersion. RN input to the groundwater system is represented by a swarm of particles distributed over the input region, with each particle assigned a fixed fraction of the input RN mass. The particle track information generated by Walkabout was converted to solute concentrations using a method based on superposition, convolution integration, and residence time distribution function approach using a code called

PLUMECALC (Robinson and Dash, 2006; Robinson et al., 2010 and 2011). The calculations performed by PLUMECALC incorporate radioactive decay, sorption, and matrix diffusion.

Confidence was developed in the flow and transport models by calibrating to observational hydraulic and RN data. Considerable hydraulic data and analysis exist (Navarro, 2021b) regarding steady-state hydraulic heads, transient hydraulic head responses to groundwater pumping, transmissivities, and groundwater discharge in Oasis Valley. Over the past several decades, groundwater samples have been analyzed for RNs (Navarro, 2021c) and for geochemical constituents (Navarro, 2020) from numerous locations including postshot wells that sample the cavity-chimney environment, as well as downgradient wells within and beyond the NNSS boundary. These data were used for flow as well as transport model calibrations with the PEST software (Doherty, 2018).

Flow and Transport Model

The PM CAU model consists of a 3-D flow simulation of groundwater flow in the PM-OV groundwater basin, based on recharge occurring primarily in upland areas within the basin and groundwater discharge to locations in Oasis Valley, and 3-D transport simulations of RNs within the groundwater flow system defined by the flow model. It is conceptualized that RNs from underground nuclear tests at PM can be transported with groundwater flowing through water-saturated geologic formations. Groundwater flow is taken to be fully saturated, isothermal, and steady-state with recharge and discharge in balance. As a conservative approach, flow and transport through the unsaturated zone is not included in the model, and the source terms are placed directly in the water table. The areal extent and mesh of the PM CAU flow and transport model is presented in Figure ES-3. The model domain coincides with the PM-OV groundwater basin, spanning approximately100 kilometers (km) in the northeast–southwest direction and encompassing about 3,600 square kilometers (km^2). The vertical extent is from 0 meters (m) above mean sea level (amsl) at the model's base to the top of the model, which stairsteps to follow the water table. The depth varies from approximately 1,800 m in the northeast to 1,000 m in Oasis Valley. The model includes 63 HSUs and 88 faults. The hydrogeologic properties—hydraulic conductivity and specific storage—in each HSU and fault zone were assumed to be uniform. Lateral boundaries and the bottom of the model were treated as no-flow boundaries, and specified recharge was applied to the top of the model. Discharge at springs within Oasis Valley was simulated as steady-state outflows at the model's upper surface.

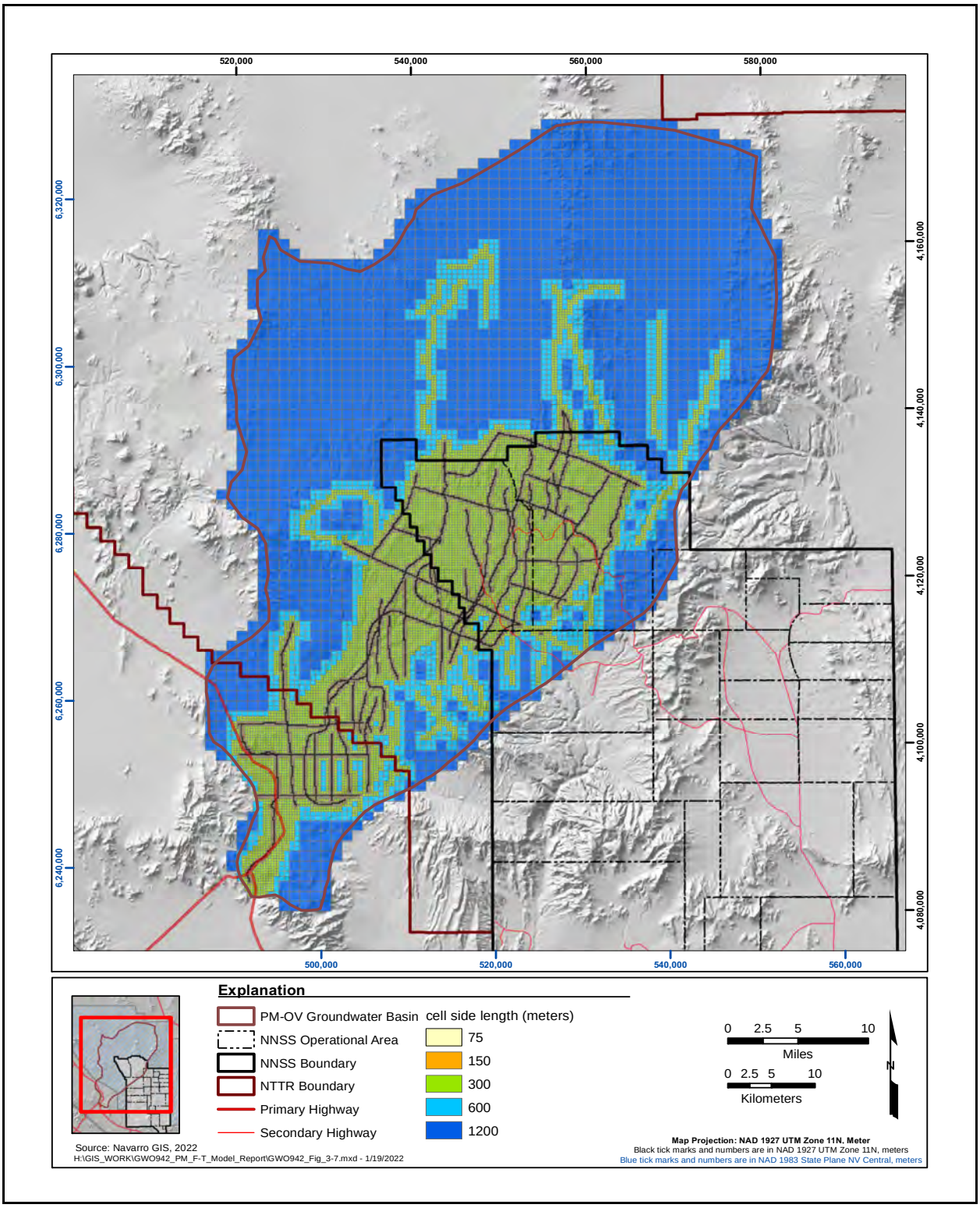

Figure ES-3
Areal Extent and Mesh of the PM CAU Flow and Transport Model

The 15 RNs determined by Carle et al. (2020) as being relevant or potentially relevant—^{3}H, ^{90}Sr, ^{129}I, ^{137}Cs, ^{232}U, ^{233}U, ^{234}U, ^{238}U, $^{239/240}$Pu, ^{14}C, ^{36}Cl, ^{99}Tc, ^{237}Np, and ^{238}Pu—were included in the transport model.

Modeling Results

The flow model was successfully calibrated to steady-state hydraulic heads, transient hydraulic head responses to groundwater pumping, measured transmissivity, groundwater discharge in Oasis Valley, and hydraulic gradients. Additionally, RN migration pathways obtained from ^{3}H observations and geochemical analysis were used as soft constraints. The many different types of observations used in the model calibration make obtaining a good agreement with all data difficult. A much better agreement could be obtained if only one type of observations were considered in the model calibration (e.g., exclusively calibrating to hydraulic heads). However, considering all data provides the basis for a better model for making CB forecasts.

Good agreement was obtained with the steady-state head and majority of the drawdown data. Fair agreement was obtained with the horizontal head gradient and transmissivity data. The simulated base case potentiometric surface with residuals (simulated-observed heads) is presented in Figure ES-4. A scatter plot of the simulated versus observed heads at the 184 well and spring locations used as observations is presented in Figure ES-5.

As expected, groundwater flow from PM is primarily south–southwest to the discharge areas in Oasis Valley. High velocities occur west of the Purse fault, in southwest Area 20 and in Oasis Valley (Figure ES-6). A high-velocity channel is present from southwest Area 20 to the Bench area and is coincident with the higher transmissivity in this area. The velocities in southern Oasis Valley are higher than the average PM-OV velocities due to narrowing of the groundwater basin and reduction in volcanic rock thickness. The model predicts that advective flow paths from Area 20 nuclear tests will extend beyond the NNSS boundary. The fastest groundwater flow occurs from the STILTON, HANDLEY, GOLDSTONE, JORUM, PEPATO, MOLBO, BENHAM, GREELEY, COLBY, KASH, PURSE, and FONTINA nuclear tests.

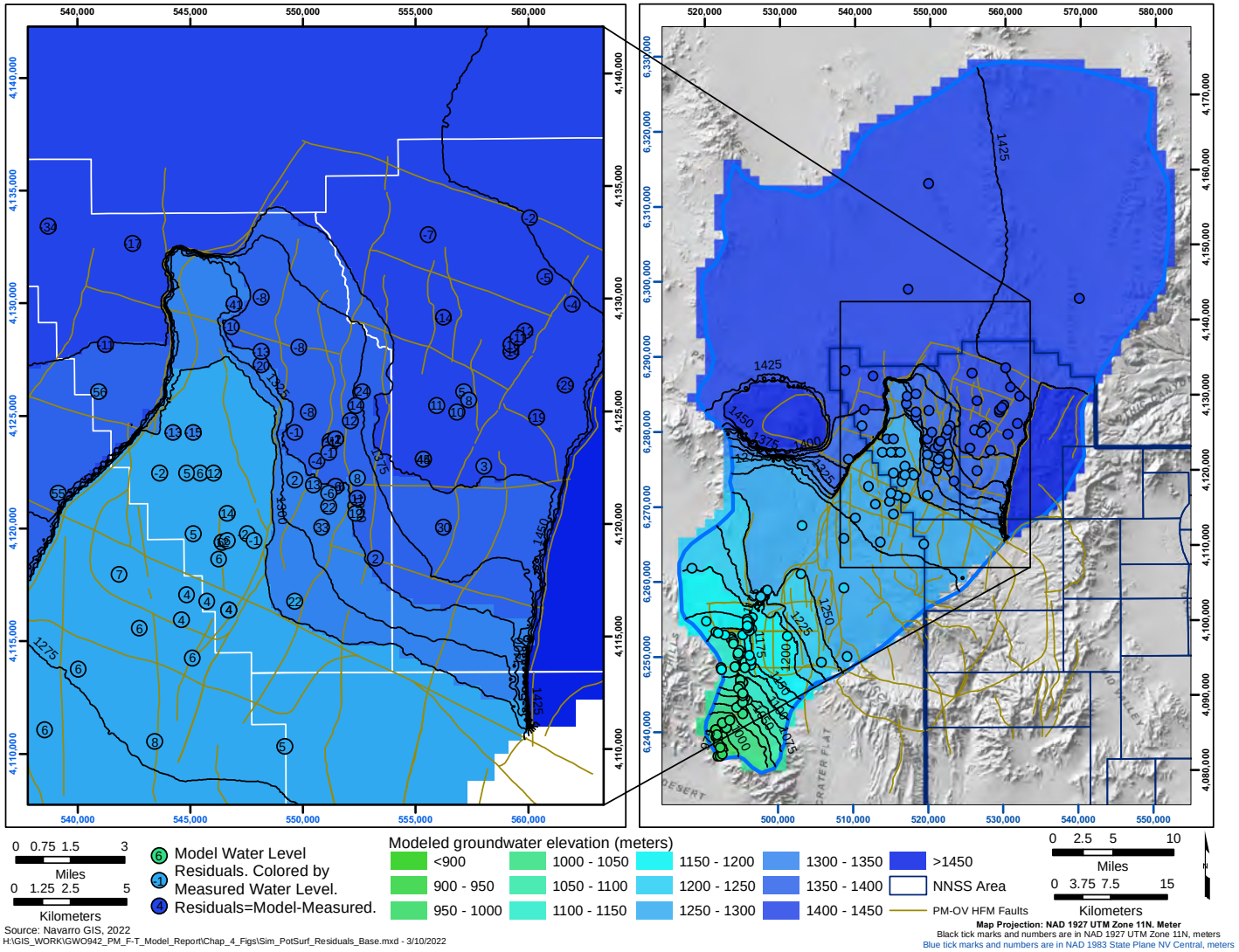

Figure ES-4
Potentiometric Surface and Residuals of the PM CAU Flow Model

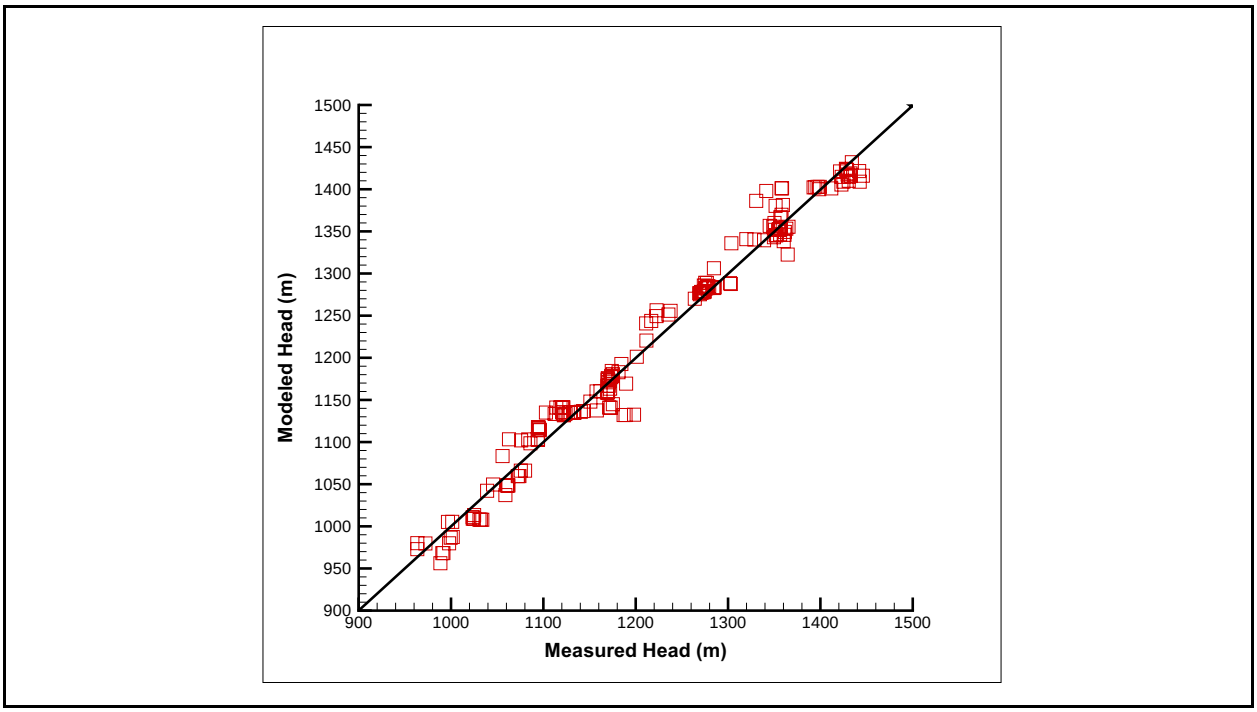

Figure ES-5
Modeled versus Measured Steady-State Heads for the PM CAU Flow Model

There are uncertainties in the flow model. The goal of the uncertainty analysis is to identify and include models that are likely to lead to more extensive transport than the base case and still have permissible fits to the calibration data. Four alternative models were constructed and calibrated, including a model with all faults defined with the HFM, two models using alternative recharge distributions (INFILv3 and DVRFS3), and a model using a water-table upper boundary condition. Calibration of the alternate model containing all faults identified in the PM-OV HFM did not result in unexpectedly fast flow paths in the fault zones. The model calibrations using alternative recharge distributions indicate that flow path directions are not particularly sensitive to the expected uncertainty in recharge. The calibration of an unconfined model indicates that approximating the unconfined system as a confined system did not introduce significant error into the PM CAU flow model. The unconfined model calibration indicates that any error introduced by approximating the PM-OV flow system as confined is conservative in that RN transport will be faster compared to an unconfined model.

The transport model using the base case flow model with transport parameter values within ranges identified in Navarro (2021a) was successfully calibrated to ^{3}H observations in groundwater samples

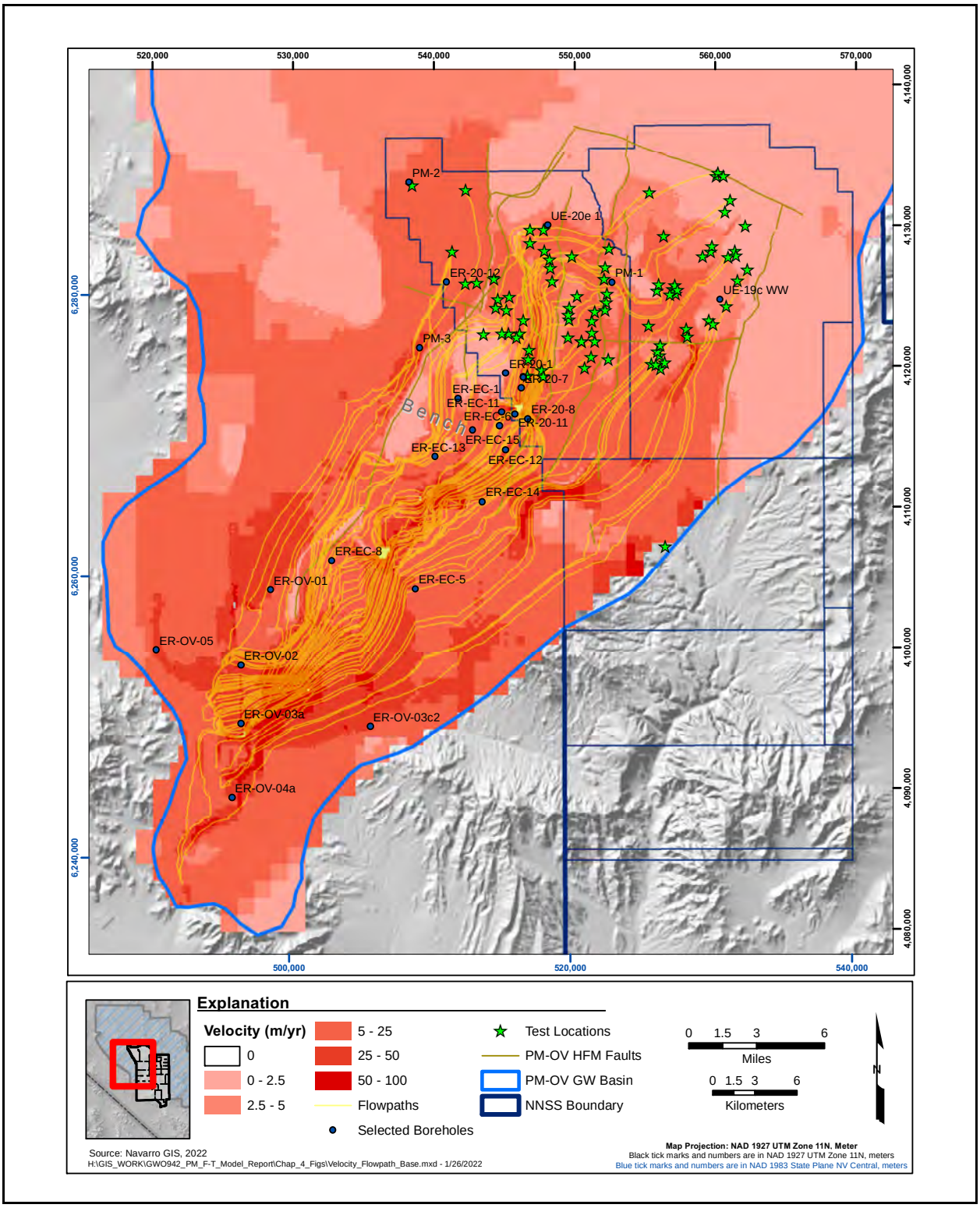

Figure ES-6
Groundwater Velocity Field and Simulated Groundwater Flow Paths from Underground Nuclear Tests in the PM CAU Flow Model

collected from open intervals in numerous wells in the model area. The following adjustable parameters for each HSU zone were used in the calibration: effective (fracture) porosity, fracture aperture, matrix porosity, and matrix diffusion coefficient. Figure ES-7 shows the modeled extent of ^{3}H at 55 years corresponding approximately to the present time. A scatter plot of the simulated versus observed concentrations at all measurements obtained from all of the observation wells is presented in Figure ES-8. Reasonable agreement is achieved at many observation locations. The exceptions to this observation can be understood and hence do not reduce the overall confidence in the model:

- At several observation points, the model overpredicts ^{3}H concentrations by several orders of magnitude; however, this is considered acceptable as a conservative approach.
- At some observation points, the model predicts no ^{3}H where ^{3}H has been observed. The most notable of these locations is ER-20-5-3_m1, where the slower, deeper flow path from BENHAM passes to the west of the chosen observation location. However, there is good agreement with ^{3}H observations at ER-20-5-1_m1, which is located just above ER-20-5-3_m1 and has observed ^{3}H values that are roughly 2 orders of magnitude higher.
- Downgradient of HANDLEY, the model predicts no ^{3}H at the two intermediate wells at ER-20-12 (ER-20-12_p2 and ER-20-12_p3). There is good agreement at the upper and lower wells at ER-20-12, which have higher ^{3}H values. Further downgradient of HANDLEY at PM-3, the model conservatively overpredicts ^{3}H at PM-3_p1 (deeper completion in the Tiva Canyon aquifer [TCA]), but predicts no ^{3}H at PM-3_p2 (shallow completion in the upper Paintbrush confining unit [UPCU]). The effect of these mismatches on the lateral extents of the CBs is negligible.

Although other RNs were not used for model calibration, comparison was made between the model results and observational data for ^{14}C, ^{36}Cl, ^{90}Sr, ^{129}I, ^{137}Cs, ^{232}U, ^{233}U, ^{234}U, ^{238}U, ^{239}Pu, and ^{240}Pu. Good agreement is achieved with ^{14}C, ^{129}I, and some ^{137}Cs observations. The model conservatively overpredicts ^{36}Cl and ^{90}Sr observations. The model also overpredicts $^{239/240}Pu$ by several orders of magnitude, suggesting that the assumptions regarding the transport of colloidal Pu (i.e., reduced matrix sorption, reduced matrix diffusion, zero colloid filtration and zero colloid retardation) may be too conservative. The model tends to underpredict U, which is not surprising because naturally occurring U is not accounted for in the model.

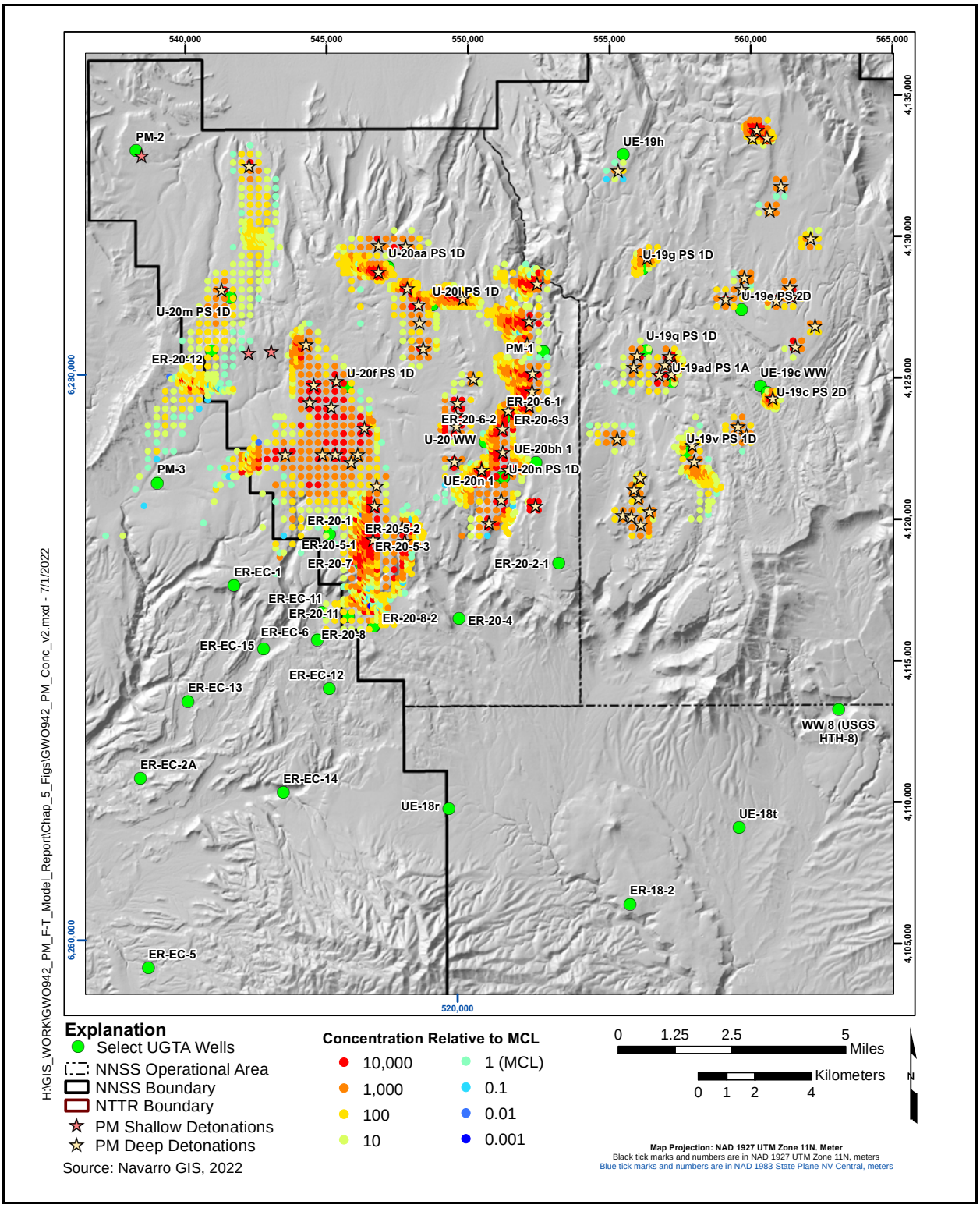

Figure ES-7
Simulated Extent of ^{3}H from Calibrated PM CAU Transport Model at 55 Years (2020)

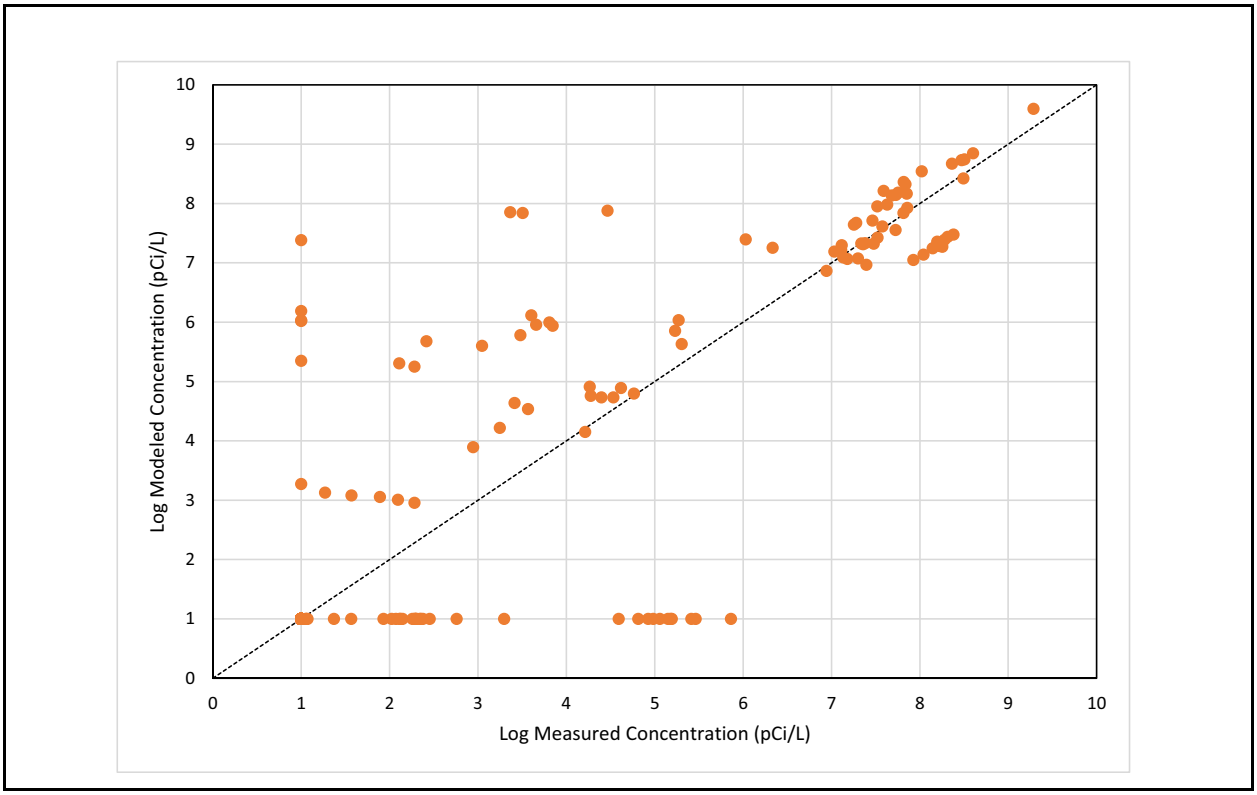

Figure ES-8
Modeled versus Measured ^{3}H Concentrations for the PM CAU Transport Model

Contaminant Boundaries

CBs used the full ranges of uncertainty for the parameter values. CBs were calculated for the PM CAU transport model using the base case PM CAU flow model, and for transport models using the two alternative flow models with alternative recharge distributions and the alternative flow model that contained all faults as defined in the PM-OV HFM. All four of these transport models employed the "base case" source term as defined in Carle et al. (2020) for the 15 selected RNs. For each of the four transport models described in the previous sentence, Monte Carlo probabilistic simulations were conducted by varying the effective porosity, fracture aperture, tortuosity, and matrix sorption coefficients over the ranges of values in the transport data document (TDD) (Navarro, 2021a). Dispersion was modeled in all of these simulations using longitudinal, horizontal transverse, and vertical transverse dispersivity values of 150 m, 15 m, and 1.5 m. The transport model using the base case flow model with transport parameter values within ranges identified in Navarro (2021a) was successfully calibrated to ^{3}H observations in groundwater samples collected from open intervals in numerous wells in the model area. The transport model was not recalibrated to the alternative flow

models. Although transport model calibration using the alternative flow models would have created additional permissive sets of transport parameters, those parameters are not used directly in the CB calculations. Rather, the CB calculations use the full range of uncertainty for each model parameter. Recalibration of the transport model using the alternative flow models would not have changed the CB forecasts. Radioactive decay was defined using a fixed half-life for each RN. The resulting CBs are shown in Figure ES-9, which presents the ensemble of 1,000-year time-cumulative 95th-percentile CB forecasts for the PM base case flow model on top, underlain by the INFILv3 recharge alternative flow model, the DVRFS3 recharge alternative flow model, and the alternative flow model including all faults, with a single color representing each alternative. The forecasted ensemble of CBs remains on federally controlled land, extending approximately 2 to 3 km past the western NNSS boundary onto the Nevada Test and Training Range (NTTR) at four locations: (1) north of PM-3, (2) east of PM-3, (3) in the Bench area near ER-EC-6, and (4) northeast of ER-EC-1. The CB ensemble is defined largely by the extent of ^{3}H contamination.

The vertical extents of the CBs making up the ensemble vary across the computational domain and vary among the alternatives. The bottoms of the CBs intersect many different HSUs. The results are plotted as the depth below the water table in Figures ES-10 through ES-13 and display each CB case colored by the saturated depth of contamination. The lowest depths of contamination (1,000 to 1,200 m below the water table) designated by the dark blue color are associated with the cavity regions of the most deeply buried tests. The plumes that appear to be moving beyond the NNSS boundary onto the NTTR are generally of the shallowest depths.

Model forecasts predict that once the ^{3}H plume has decayed (about 120 years), the extent of contaminant migration is dominated by ^{239}Pu for the remainder of 1,000 years. After ^{239}Pu is ^{240}Pu, also for 1,000 years. They are followed by ^{238}Pu (up to about 380 years), ^{90}Sr (up to about 300 years), and ^{129}I and ^{36}Cl out to 1,000 years; ^{237}Np and U are insignificant contributors to the extent of contaminant migration (Figure ES-14). Note that while the time-dependent extent of contamination is dominated by different RNs at different times, the maximum extent of contamination at any time (within 1,000 years) for other RNs does not exceed that experienced by ^{3}H at times earlier than 120 years. Hence, the CB is dominated by ^{3}H.

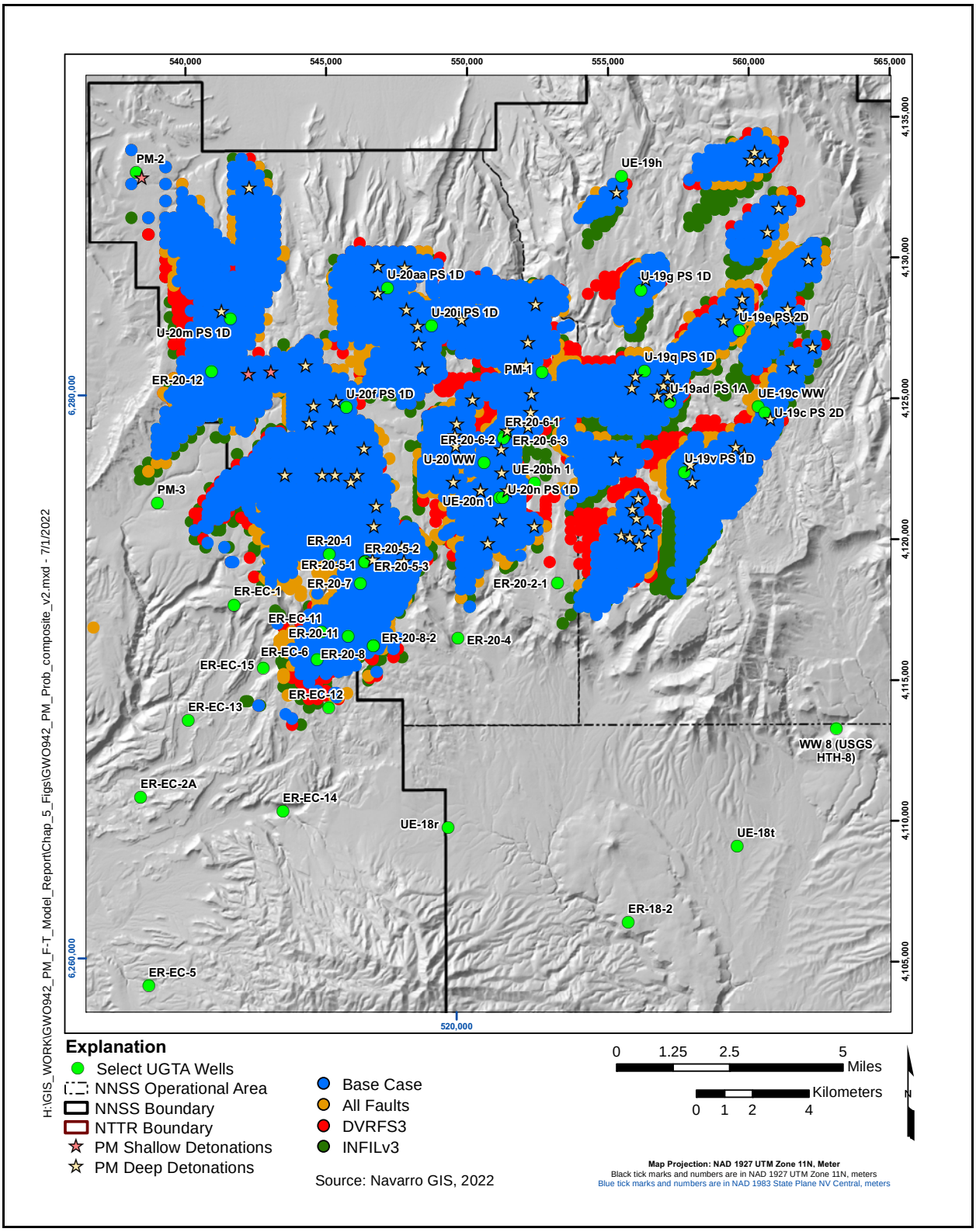

Figure ES-9
Ensemble of 1,000-Year Time-Cumulative Probability of Exceedance of MCLs CB Forecasts (Base Case on Top)

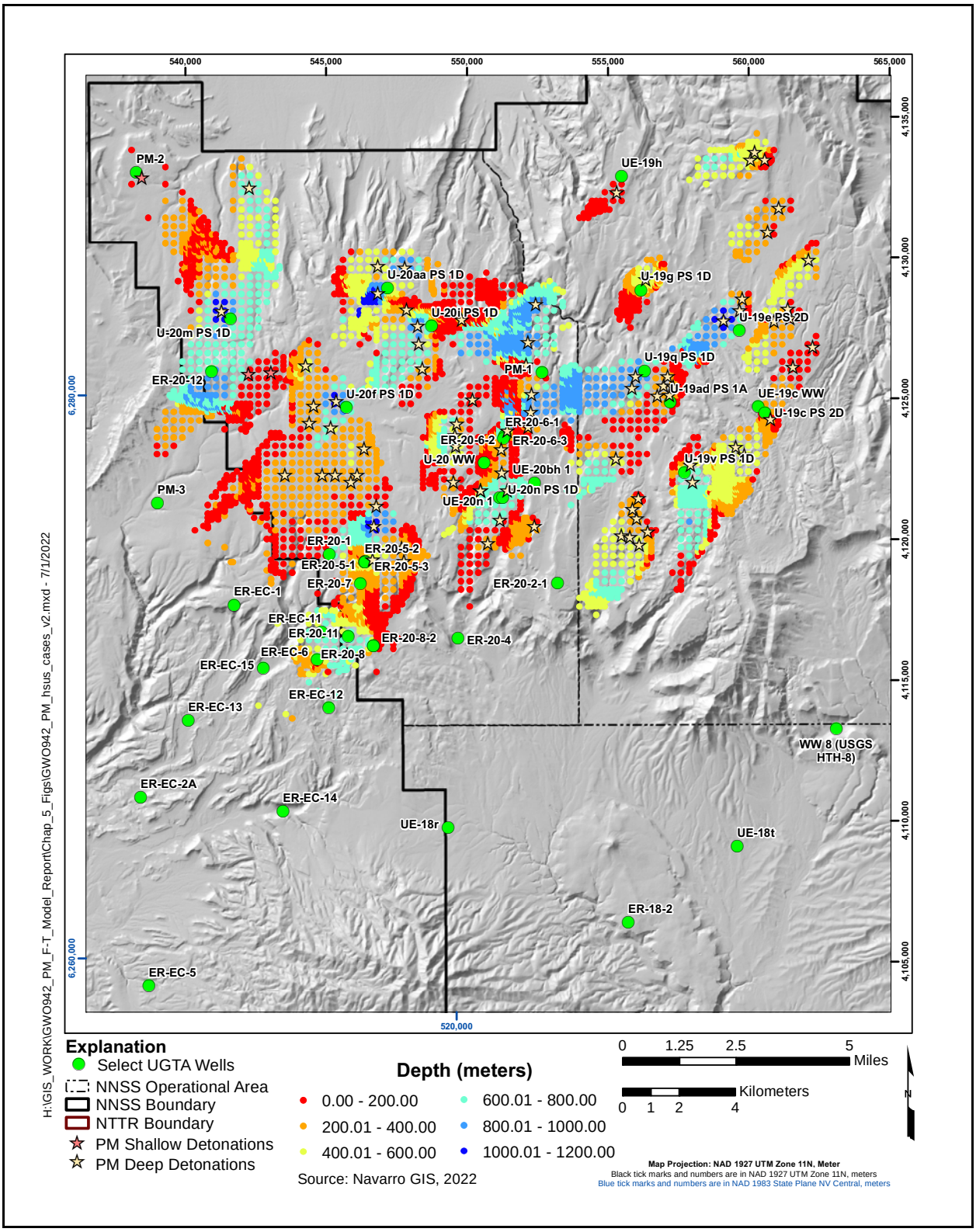

Figure ES-10
CB of Base Case Colored by Saturated Depth of Contamination (as Determined by MCL Exceedance for Relevant RNs)

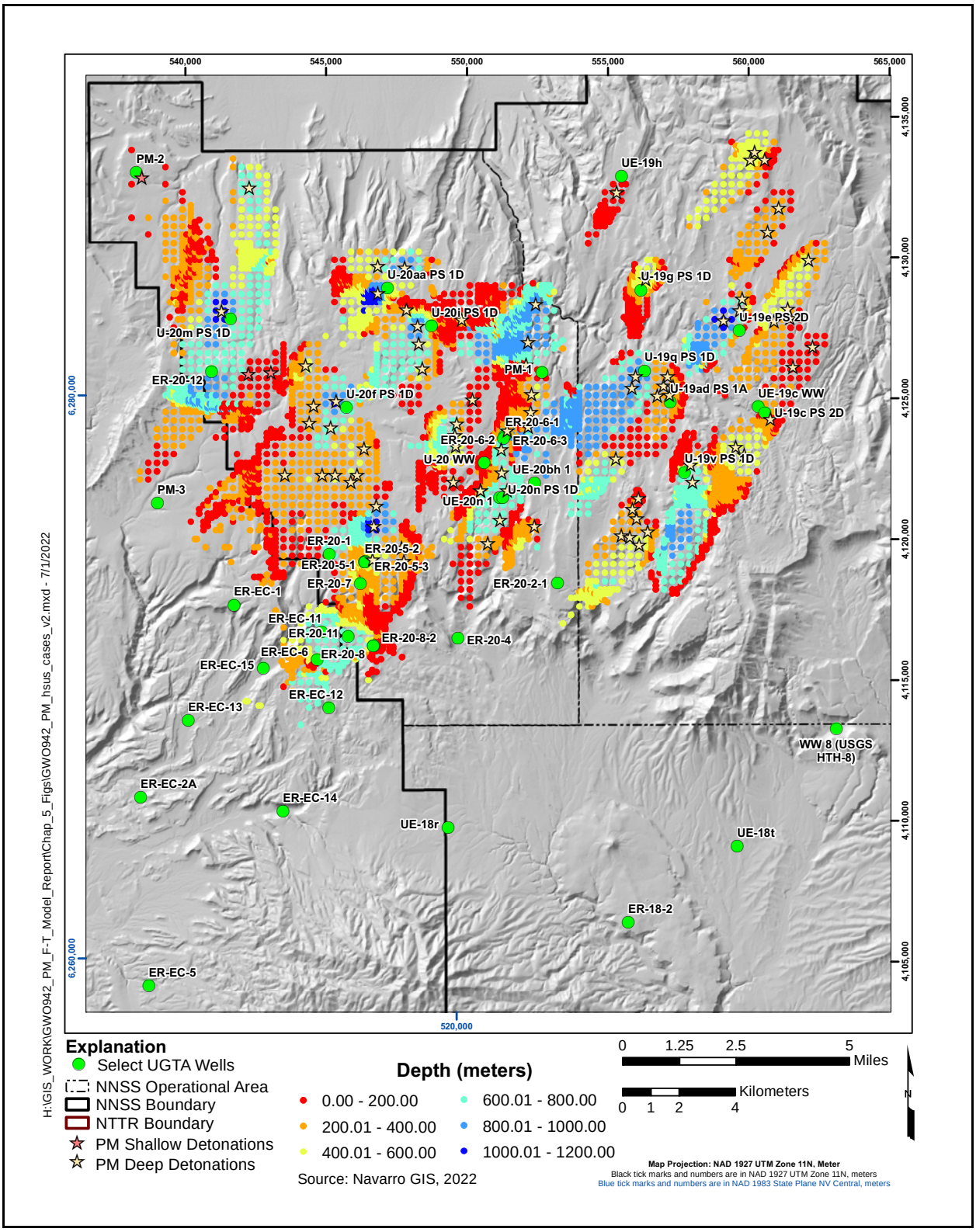

Figure ES-11
CB of INFILv3 Recharge Alternative Flow Model
Colored by Saturated Depth of Contamination
(as Determined by MCL Exceedance for Relevant RNs)

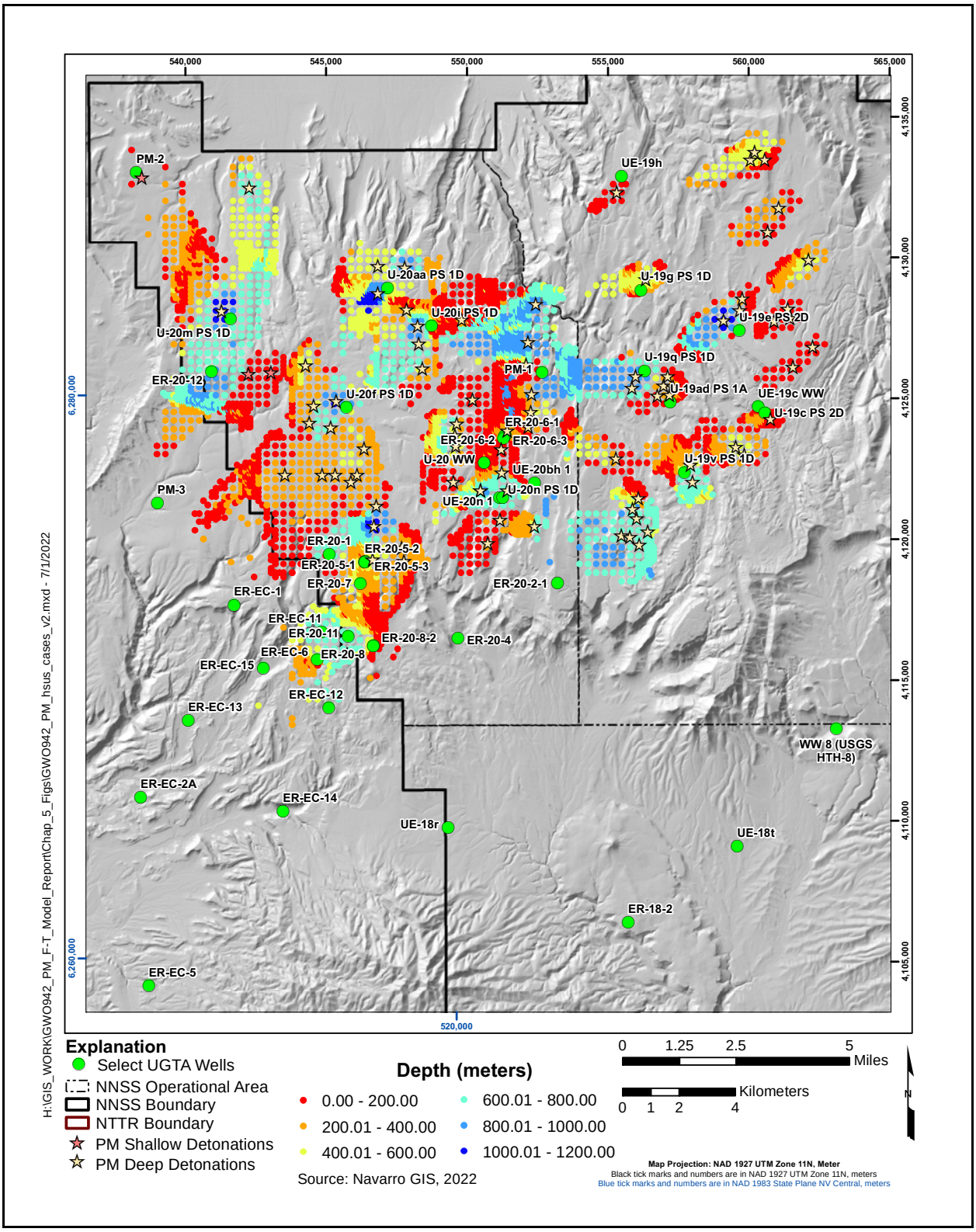

Figure ES-12
CB of DVRFS3 Recharge Alternative Flow Model
Colored by Saturated Depth of Contamination
(as Determined by MCL Exceedance for Relevant RNs)

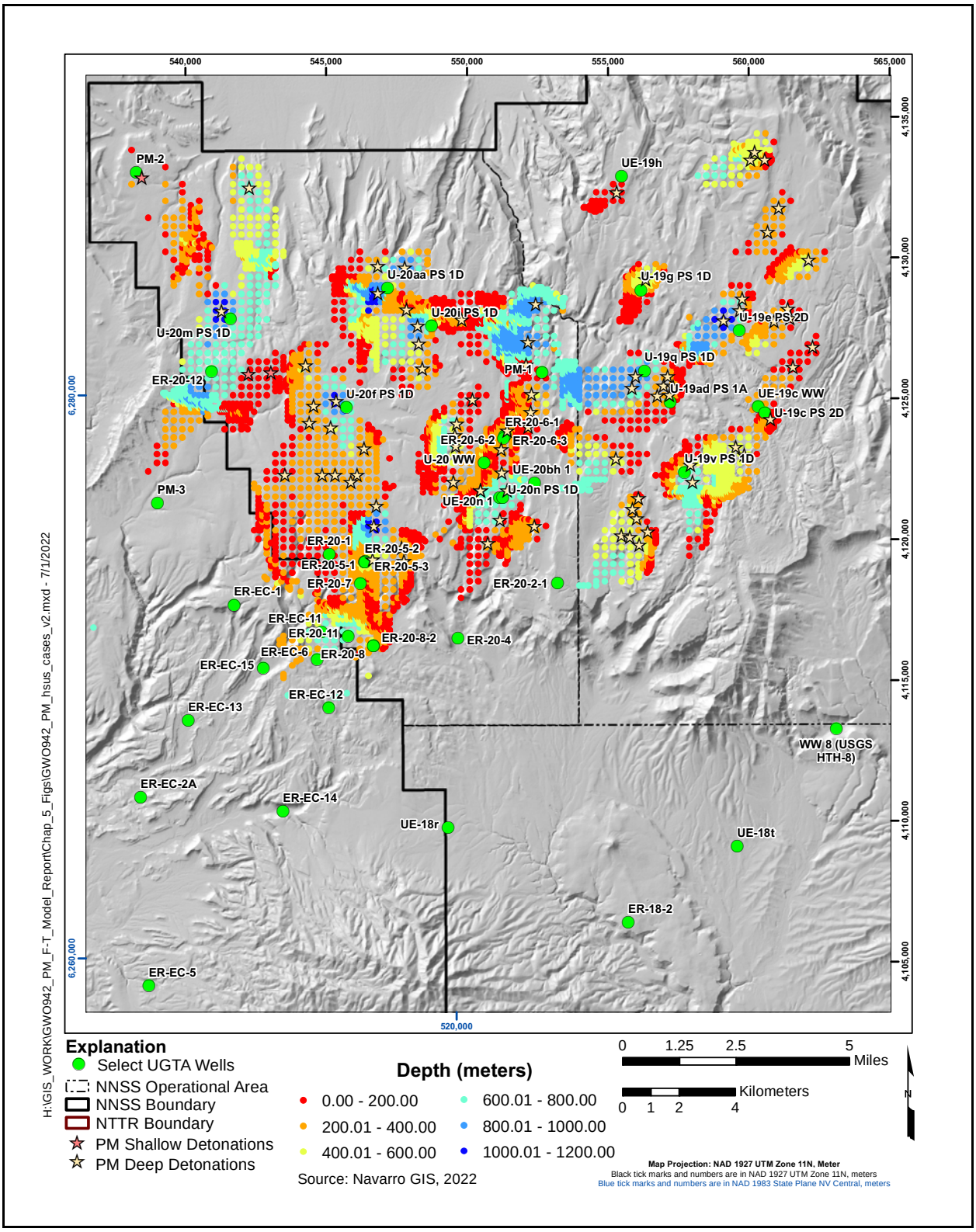

Figure ES-13
CB of Alternative Flow Model Including All Faults
Colored by Saturated Depth of Contamination
(as Determined by MCL Exceedance for Relevant RNs)

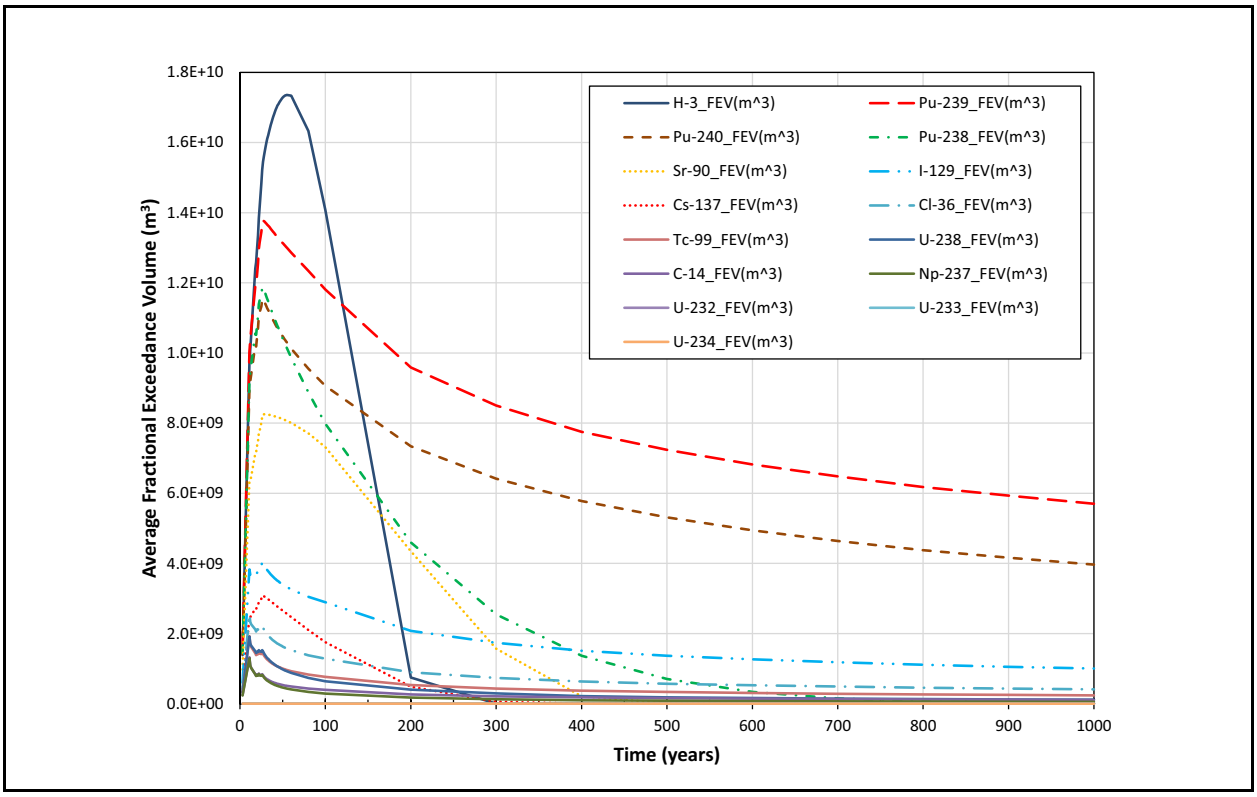

Figure ES-14
Average Fractional Exceedance Volume by RN for PM Base Case

The ensemble forecast of CBs was shown to be dominated by the ^{3}H concentration for the first approximately 120 years. After that time, ^{3}H concentrations are reduced by transport processes and radioactive decay. None of the other 14 RNs simulated were transported in concentrations above maximum contaminant level (MCL) to influence the CBs. The ensemble of CBs extends beyond the boundary of the NNSS in four places. In all cases, the distance of the CBs beyond the borders of the NNSS is less than 5 km. This suggests that RN migration will occur but is not expected to arrive at the discharge locations in Oasis Valley in concentrations exceeding the SDWA standards (CFR, 2021). Effective monitoring to track the migration of RNs will be necessary to ensure the long term safety of downgradient groundwater users.

Conclusions

More than 25 years of drilling, data collection, analysis, and modeling have culminated in the PM CAU flow and transport model. The calibration of the groundwater flow model (base case and four alternatives) provides confidence that the simulated groundwater flow paths are consistent with

observations of hydraulic head and RN migration. Further confidence was gained by calibration of the RN transport model using parameter values within ranges of parameter uncertainty to ^{3}H observations in near-field and downgradient wells. Forward calculations of RN transport for the 14 RNs (in addition to ^{3}H) further demonstrate that the PM CAU model forecasts are conservative and generally overpredict the downgradient RN concentrations in groundwater.

The probabilistic CB forecasts encompass the observations of RNs in groundwater. As demonstrated by the calibrations, the model forecasts are somewhat conservative representations of the CB ensemble within the next 1,000 years. The CB forecasts indicate that more than one plume of RNs may move beyond the boundary of the NNSS, but that the extent of the ensemble of CBs will be a few kilometers beyond the boundary of the NNSS and will remain more than 12 km upgradient of the closest public receptor in Oasis Valley. These results support the interpretation that RNs from underground nuclear testing on PM pose a small risk to the health of groundwater users in Oasis Valley.

References

CFR, see *Code of Federal Regulations.*

Carle, S.F., A.F.B. Tompson, and M. Zavarin. 2020. *Radionuclide Screening Analysis and Transport Parameters for Pahute Mesa Detonations, Nevada National Security Site*, LLNL-TR-812351, Livermore, CA: Lawrence Livermore National Laboratory.

Code of Federal Regulations. 2021. Title 40 CFR, Part 141, “National Primary Drinking Water Regulations.” Washington, DC: U.S. Government Printing Office.

DOE/EMNV, see U.S. Department of Energy Environmental Management Nevada Program.

Doherty, J. 2018. “Methodologies and Software for PEST-Based Model Predictive Uncertainty Analysis.” Brisbane, Australia: Watermark Numerical Computing. Available at Iwww.pesthomepage.org\Downloads.php?file=pest_uncert.zip. As accessed on 2 January.

FFACO, see *Federal Facility Agreement and Consent Order*.

Federal Facility Agreement and Consent Order. 1996 (as amended March 2010). Agreed to by the State of Nevada; U.S. Department of Energy, Environmental Management; U.S. Department of Defense; and U.S. Department of Energy, Legacy Management. Appendix VI, which contains the Underground Test Area Strategy, was last modified June 2014, Revision No. 5.

Fenelon, J.M., K.J. Halford, and M.T. Moreo. 2016. *Delineation of the Pahute Mesa–Oasis Valley Groundwater Basin, Nevada,* Scientific Investigations Report 2015–5175. Carson City, NV: U.S. Geological Survey.

Finnegan, D.L., S.M. Bowen, J.L. Thompson, C.M. Miller, P.L. Baca, L.F. Olivas, C.G. Geoffrion, D.K. Smith, W. Goishi, B.K. Esser, J.W. Meadows, N. Namboodiri, and J.F. Wild. 2016. *Nevada National Security Site Underground Radionuclide Inventory, 1951–1992: Accounting for Radionuclide Decay through September 30, 2012,* LA-UR-16-21749. Los Alamos, NM: Los Alamos National Laboratory.

Garcia, C.A., T.R. Jackson, K.J. Halford, D.S. Sweetkind, N.A. Damar, J.M. Fenelon, and S.R. Reiner. 2017. *Hydraulic Characterization of Volcanic Rocks in Pahute Mesa Using an Integrated Analysis of 16 Multiple-Well Aquifer Tests, Nevada National Security Site, 2009–14,* Scientific Investigations Report 2016-5151. Carson City, NV: U.S. Geological Survey.

Halford, K.J., and T.R. Jackson. 2020. *Groundwater Characterization and Effects of Pumping in the Death Valley Regional Groundwater Flow System, Nevada and California, with Special Reference to Devils Hole,* Professional Paper 1863. Reston, VA: U.S. Geological Survey.

IT Corporation. 1996a. *Groundwater Recharge and Discharge Data Documentation Package (Underground Test Area Subproject Phase I Data Analysis Documentation, Volume III*). Prepared for the U.S. Department of Energy, Nevada Operations Office. Las Vegas, NV.

IT Corporation. 1996b. *Hydrologic Parameter Data Documentation Package (Underground Test Area Subproject Phase 1 Data Analysis Documentation, Volume IV).* Prepared for the U.S. Department of Energy, Nevada Operations Office. Las Vegas, NV.

IT Corporation. 1996c. *Regional Geologic Model Data Documentation Package (Underground Test Area Subproject Phase 1 Data Analysis Documentation, Volume I).* Prepared for the U.S. Department of Energy, Nevada Operations Office. Las Vegas, NV.

Jackson, T.R. 2021. *Permeable Groundwater Pathways and Tritium Migration Patterns from the HANDLEY Underground Nuclear Test, Pahute Mesa, Nevada,* Scientific Investigations Report 2021-5032. Reston, VA: U.S. Geological Survey.

Jackson, T.R., J.M. Fenelon, and R. Paylor. 2021. *Groundwater Flow Conceptualization of the Pahute Mesa–Oasis Valley Groundwater Basin, Nevada: A Synthesis of Geologic, Hydrologic, Hydraulic Property, and Tritium Data,* Scientific Investigations Report 2020-5134. Carson City, NV: U.S. Geological Survey.

Langevin, C.D., J.D. Hughes, E.R. Banta, R.G. Niswonger, S. Panday, and A.M. Provost. 2017. *Documentation for the MODFLOW 6 Groundwater Flow Model,* Techniques and Methods 6-A55. Reston, VA: U.S. Geological Survey.

Lu, Z., E. Kwicklis, T. Miller and M. Bourret. 2021. *Development and Calibration of the Pahute Mesa Bench Area Groundwater Flow and Tritium Transport Model,* Nevada National Security *Site,* LA-UR-21-23595. Los Alamos, NM: Los Alamos National Laboratory.

Middleton, R.S., E.M. Kwicklis, K.H. Birdsell, D.G. Levitt, and J. Hevesi. 2019. *Net Infiltration Models for the Pahute Mesa Area,* LA-UR-16-27513, Rev 1. Los Alamos, NM: Los Alamos National Laboratory.

Navarro GIS, see Navarro Geographic Information Systems.

NNSA/NFO, see U.S. Department of Energy, National Nuclear Security Administration Nevada Field Office

Navarro. 2020. *Phase II Geochemical and Isotopic Evaluation of Groundwater Flow in the Pahute Mesa–Oasis Valley Flow System, Nevada*. Rev. 1, N/0002653--069. Las Vegas, NV.

Navarro. 2021a. *Contaminant Transport Parameters for the Groundwater Flow and Contaminant Transport Model of Corrective Action Units 101 and 102: Central and Western Pahute Mesa, Nye County, Nevada,* Rev. 1, N/0002653--077. Las Vegas, NV.

Navarro. 2021b. *Hydrologic Data for the Groundwater Flow and Contaminant Transport Model of Corrective Action Units 101 and 102: Central and Western Pahute Mesa, Nye County, Nevada,* Rev. 1, N/0002653--073. Las Vegas, NV.

Navarro. 2021c. *Unclassified Source Term and Radionuclide Data for the Groundwater Flow and Contaminant Transport Model for Corrective Action Units 101 and 102: Central and Western Pahute Mesa, Nye County, Nevada,* Rev 1, N/0002653--088. Las Vegas, NV.

Navarro Geographic Information Systems. 2021. ESRI ArcGIS Software.

Painter, S.L. 2011. *User's Manual for Walkabout V1.0*, LA-UR-11-01952. Los Alamos, NM: Los Alamos National Laboratory.

Robinson, B.A., and Z.V. Dash. 2006. *User's Guide for the PLUMECALC Application*, Version 2.2. Los Alamos, NM: Los Alamos National Laboratory.

Robinson, B.A., Z.V. Dash, and G. Srinivasan. 2010. "A Particle Tracking Transport Method for the Simulation of Resident and Flux-Averaged Concentration of Solute Plumes in Groundwater Models." In *Computational Geosciences*, Vol. 14(4): pp. 779–792.

Robinson, B.A., Z.V. Dash, and S.L. Painter. 2011. *User's Guide for the PLUMECALC Application with Subgridding, Version 2.3.2,* LA-UR-11-02090. Los Alamos, NM: Los Alamos National Laboratory.

Stoller-Navarro Joint Venture. 2006. *Groundwater Flow Model of Corrective Action Units 101 and 102: Central and Western Pahute Mesa, Nevada Test Site, Nye County, Nevada,* Rev. 0, S-N/99205--076. Las Vegas, NV.

Stoller-Navarro Joint Venture. 2007. *Addendum to the Groundwater Flow Model of Corrective Action Units 101 and 102: Central and Western Pahute Mesa, Nevada Test Site, Nye County, Nevada,* Rev. 0, S-N/99205--076-ADD. Las Vegas, NV.

Stoller-Navarro Joint Venture. 2009. *Phase I Transport Model of Corrective Action Units 101 and 102: Central and Western Pahute Mesa, Nevada Test Site, Nye County, Nevada,* Rev. 1, S-N/99205--111. Las Vegas, NV.

U.S. Department of Energy Environmental Management Nevada Program. 2020. *Pahute Mesa-Oasis Valley Hydrostratigraphic Framework Model for Corrective Action Units 101 and 102: Central and Western Pahute Mesa, Nye County, Nevada,* Rev. 0, DOE/EMNV--0014. Las Vegas, NV.

U.S. Department of Energy, National Nuclear Security Administration Nevada Field Office. 2015. *United States Nuclear Tests, July 1945 through September 1992,* DOE/NV-209, Rev. 16. Las Vegas, NV.

1.0 Introduction

This document, titled *Groundwater Flow and Contaminant Transport Model of Corrective Action Units 101 and 102: Central and Western Pahute Mesa, Nye County, Nevada*, presents the groundwater flow and transport models along with simulation forecasts needed for the purpose of developing the ensemble of contaminant boundaries (CBs) for the Central and Western Pahute Mesa (PM) corrective action units (CAUs) 101 and 102. The PM CAUs are areas of the Nevada National Security Site (NNSS) that were historically used for underground nuclear testing (Figure 1-1). Eighty-five underground nuclear tests were conducted at the PM CAUs between 1965 and 1992 (NNSA/NFO, 2015b). Underground nuclear tests deposit radioactive elements in the subsurface, resulting in groundwater contamination in the vicinity of the underground test locations. At the PM CAUs, the testing resulted in more than 2.68×10^7 curies of radioactivity of potential concern (decay-corrected to September 30, 2012) remaining underground (Finnegan et al., 2016). Of the 85 underground nuclear tests conducted at the PM CAUs, three were shallow tests detonated within 200 meters (m) of the surface and are referred to as the "near-surface tests" in this document; the remaining 82 were detonated deeper than 200 m below the surface and are referred to as the "deep underground tests."

Because of the existence of this underground contamination, the U.S. Department of Energy (DOE), Environmental Management (EM) Nevada Program's Underground Test Area (UGTA) Activity is conducting a corrective action investigation (CAI) of the PM CAUs. This work is performed in accordance with the *Federal Facility Agreement and Consent Order* (FFACO) (1996, as amended). A major part of the UGTA strategy, as discussed in Section 1.1, is the CAU groundwater flow and transport model. This model provides the CB forecasts required by the FFACO.

The forecasts of radionuclide (RN) migration presented in this report are based on the U.S. Environmental Protection Agency (EPA) *Safe Drinking Water Act* (SDWA) standards for RNs (CFR, 2021) and the requirements of the FFACO (1996, as amended). The forecasts are probabilistic calculations intended as planning tools to minimize health risks to downgradient water users and the environment and to provide a tool to evaluate future groundwater monitoring. These forecasts are intentionally overly conservative and overestimate the extent of groundwater contaminated by RNs. As such, the probabilistic forecasts do not represent the actual extent of contamination in

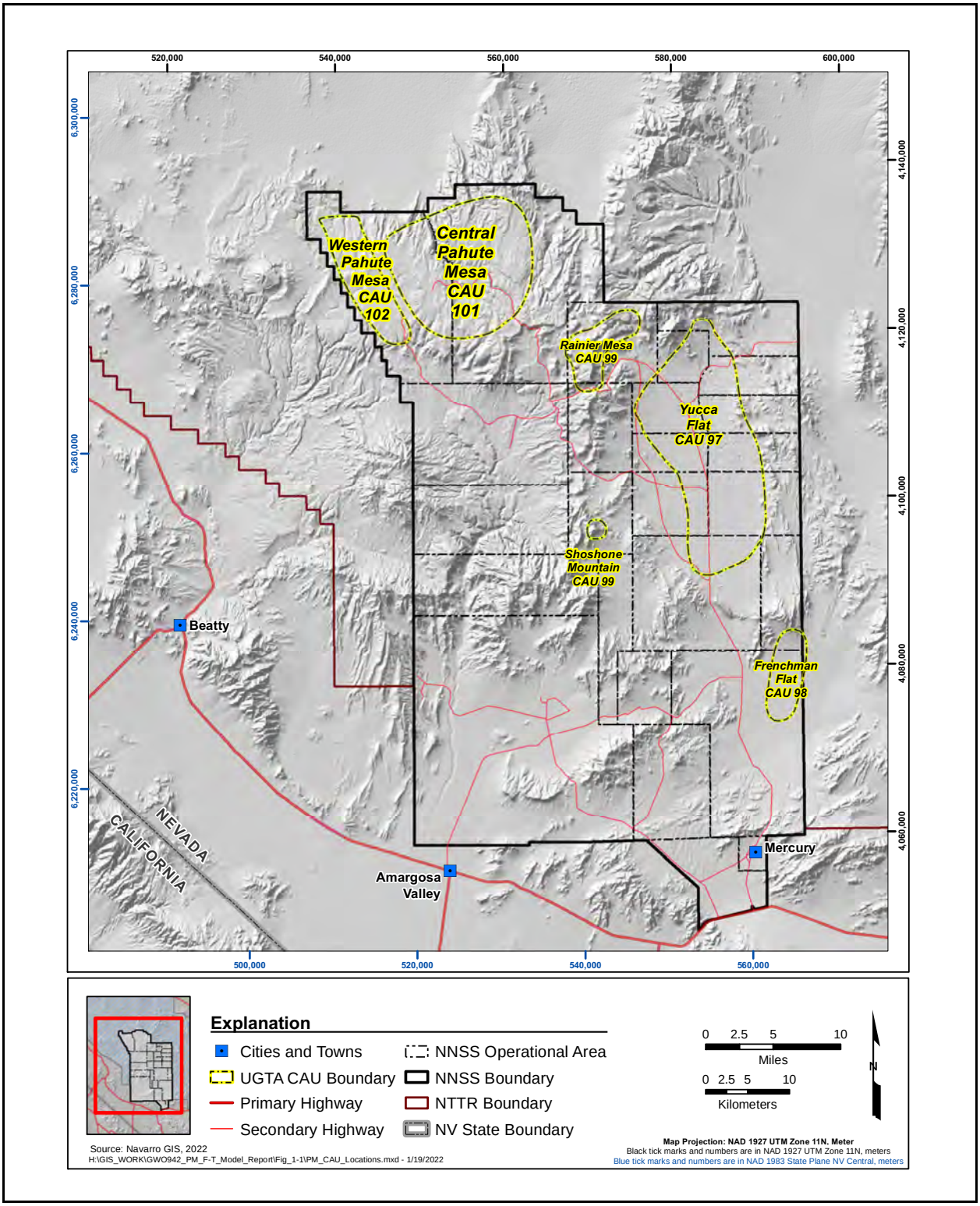

Figure 1-1
Location of the PM CAUs
Note: Other UGTA CAUs are shown for reference.

groundwater. Calibration of the PM CAU model to a range of observational data using the parameter values within ranges of parameter uncertainty and the similarity of the resulting groundwater flow paths to observed ^{3}H migration paths provided confidence that the PM CAU flow model adequately simulates observed hydraulic conditions in the PM-OV flow system and supports understanding of the flow system. The probabilistic forecasts of the CB were generated using the full range of transport parameter uncertainty rather than narrowing on the calibrated values. Hence, they are larger than would be expected on the basis of calibrated parameter values and are protective of human health.

This report is a Phase II update of the previously published groundwater flow model report (SNJV, 2006) and contaminant transport model report (SNJV, 2009b) for the PM CAUs. A revision (NNSA/NSO, 2009) to the original PM corrective action investigation plan (CAIP) (DOE/NV, 1999) identified additional data collection and analysis activities to be completed during Phase II of the PM CAI. A considerable amount of characterization activities—including well drilling, well logging, well development, geological characterization, single-well aquifer testing, multiple-well aquifer testing, sampling, laboratory testing, data analysis, groundwater flow and transport modeling, geochemical modeling, source term characterization, groundwater basin delineation, groundwater discharge studies, and infiltration analysis—have taken place since 2009 (listed in Appendix A), resulting in a large body of published work that has become available. This work was performed in compliance with the UGTA Quality Assurance Plan (QAP) (NNSA/NFO, 2015a; DOE/EMNV, 2018b), and this current document takes advantage of this work. Where appropriate, data and information documented elsewhere are briefly summarized with reference to the complete documentation.

The flow model discussed here is referred to as the “PM CAU flow model” in this document, and the contaminant transport model is referred to as the “PM CAU transport model.” Together, they are referred to as the “PM CAU flow and transport model” or simply the “PM CAU model.” Since several alternate flow models and transport models for the PM CAU are also addressed in this report, the plural terms “PM CAU flow models,” “PM CAU transport models,” and “PM CAU models” are also used.

A number of other flow models and contaminant transport models relevant to this document—such as a regional-scale flow models (Fenelon et al., 2016; Halford and Jackson, 2020), localized flow

models (Garcia et al., 2011 and 2017) and localized flow and transport models (Lu et al., 2021; Jackson 2021)—are also discussed.

On PM, each deep underground nuclear test assigned to UGTA is composed of a single detonation (NNSA/NFO, 2015b). In this document, when applied to PM, the words “detonation” and “test” are used interchangeably unless otherwise noted. The remainder of this section provides a brief summary of the UGTA Activity background and project background, describes the setting of the PM CAUs and nuclear testing at the PM CAUs, and presents the purpose and scope of the work described in this document. Brief descriptions of this document’s contents are provided at the end of the section.

1.1 UGTA Activity Background

The primary regulatory agreement governing the UGTA Activity is the FFACO (1996, as amended), which was agreed to by the State of Nevada acting by and through the Department of Conservation and Natural Resources, Nevada Division of Environmental Protection (NDEP); U.S. Department of Defense (DoD); and DOE. The FFACO has multiple purposes, including identifying sites of potential historic contamination to ensure that potential impacts of releases into state waters are thoroughly investigated and are subject to corrective actions and closure requirements under the oversight of NDEP. The purposes also include determination of whether releases of contaminants could potentially migrate, and if so, identification of the nature and extent of that migration. The FFACO also stipulates that the corrective action decisions and institutional controls are to be fully protective of human health and the environment. The NNSS and Nevada Test and Training Range (NTTR) are federally controlled lands not accessible to the general public. Public exposure to the test-derived RNs would be of concern if the contaminants were to migrate beyond the boundaries of NNSS and NTTR into the groundwater beneath public or private lands at levels that exceed the radiological standards of the SDWA (CFR, 2021).

The individual locations covered by the FFACO are known as corrective action sites (CASs) and are grouped into CAUs. The UGTA CAUs are Frenchman Flat, Central Pahute Mesa, Western Pahute Mesa, Yucca Flat/Climax Mine (YF/CM), and Rainier Mesa/Shoshone Mountain (RM/SM) (Figure 1-1). Central Pahute Mesa (CAU 101) and Western Pahute Mesa (CAU 102) are addressed together as stated in the FFACO (1996, as amended), and referred to as the PM CAU or the PM

CAUs, because of their adjacent locations, similarities in testing practices, geology, hydrology, and expected time frame for implementation of the corrective action activities.

The UGTA strategy, defined in Appendix VI of the FFACO, assumes that active remediation of underground nuclear tests is not cost-effective with current technology, and because of the high remediation costs, closure in place with monitoring and institutional controls is the only likely corrective action. The FFACO also assumes that the important potential risks from radiological contamination of groundwater are to workers, the public, and the environment; and exposure to these risks requires access to groundwater. As a result, the corrective action for each CAU is based on a combination of characterization and modeling studies, monitoring, and institutional controls.

The technical basis for achieving the UGTA strategy is through an evaluation of the CAU, using a combination of (1) data collection; (2) modeling of hydrological setting, radiological source term (RST), and flow and contaminant transport; (3) iterative model evaluations and monitoring; and (4) identification and documentation of land-use policies (institutional controls).
This four-component approach is used to accomplish the primary objective of the UGTA strategy, which is to define perimeter boundaries over the next 1,000 years that encompass groundwater that potentially exceeds the radiological standards of the SDWA (CFR, 2021). The integration and balancing of modeling studies, monitoring, and institutional controls provide the foundation of a risk-informed strategy for regulatory decision-making. The perimeter boundaries enclose areas potentially exceeding the radiological standards of the SDWA. Modeling forecasts of contaminant transport provide the fundamental basis for identifying CBs. A CB is formally defined as a probabilistic model-forecast perimeter and a lower hydrostratigraphic unit (HSU) boundary that delineates the extent of RN-contaminated groundwater from underground testing over 1,000 years. Simulation modeling of contaminant transport will be used to forecast the location of CBs within 1,000 years and must show the 95th percentile of the model results boundary (outside of which only 5 percent of the simulations exceed the SDWA standards).

The UGTA strategy is implemented individually for each CAU through a four-stage approach that comprises the following: (1) corrective action investigation plan (CAIP), (2) corrective action investigation (CAI), (3) corrective action decision document (CADD)/corrective action plan (CAP), and (4) closure report (CR). The CAU work progresses through these stages sequentially as approved

by NDEP. There are nine decision points within this strategy that require NDEP concurrence before the project can proceed to the next step. Figure 1-2 illustrates the individual steps and decision points within each strategy stage; major decisions between NDEP and DOE EM Nevada Program (formerly DOE, National Nuclear Security Administration Nevada Field Office [NNSA/NFO]) are highlighted in yellow. Three of the UGTA decision points are at the transition between stages. Nonapproval of decision points by NDEP affects the CAU progression, requiring looping back to designated previous steps to revise/addend the work, acquire and analyze new data, develop new models, and reassess whether the UGTA strategy is achievable. The work presented in this report will support two decision points within the CAI stage: Decision Point No. 2, which is a joint DOE EM and NDEP decision answering the question, “Are the model results and data adequate?”; and Decision Point No. 4, which is an NDEP decision on the question, “Is the CAU model acceptable for CADD/CAP studies?”

1.1.1 UGTA Strategy Implementation for PM CAUs

This section provides the current (calendar year [CY] 2021) status of the PM CAUs in regard to the implementation and progress of the UGTA strategy, along with a brief summary of the progress since the initiation of the strategy in 1998, (DOE/NV, 1999) and a short statement of expected future progress.

The PM CAUs are currently (in CY 2022) in Phase II of the CAI stage.

In 1998, at the beginning of the CAIP stage, a value of information analysis (VOIA) was prepared for the PM CAUs. The CAIP was prepared and revised in an iterative manner from 1998 through 2001 (Figure 1-2), and the PM CAUs progressed to the CAI stage. Work in this investigation stage led to the development of a hydrostratigraphic framework model (HFM) (BN, 2002), transport data document (TDD) (Shaw, 2003), hydrologic data document (HDD) (SNJV, 2004a), unclassified source term report (SNJV, 2004c), groundwater flow model report (SNJV, 2006) and addendum (SNJV, 2007), and Phase I transport model report (SNJV, 2009b). The modeling objective was to use flow and transport models to generate forecasts of CBs for the PM CAU. However, a preemptive review (PER) subcommittee evaluated the model results and judged that the models had incompletely constrained parameter values and that the CB forecasts could be overly conservative and/or unrealistic (NNSA/NSO, 2009). The subcommittee recommended modifying the primary goal of the

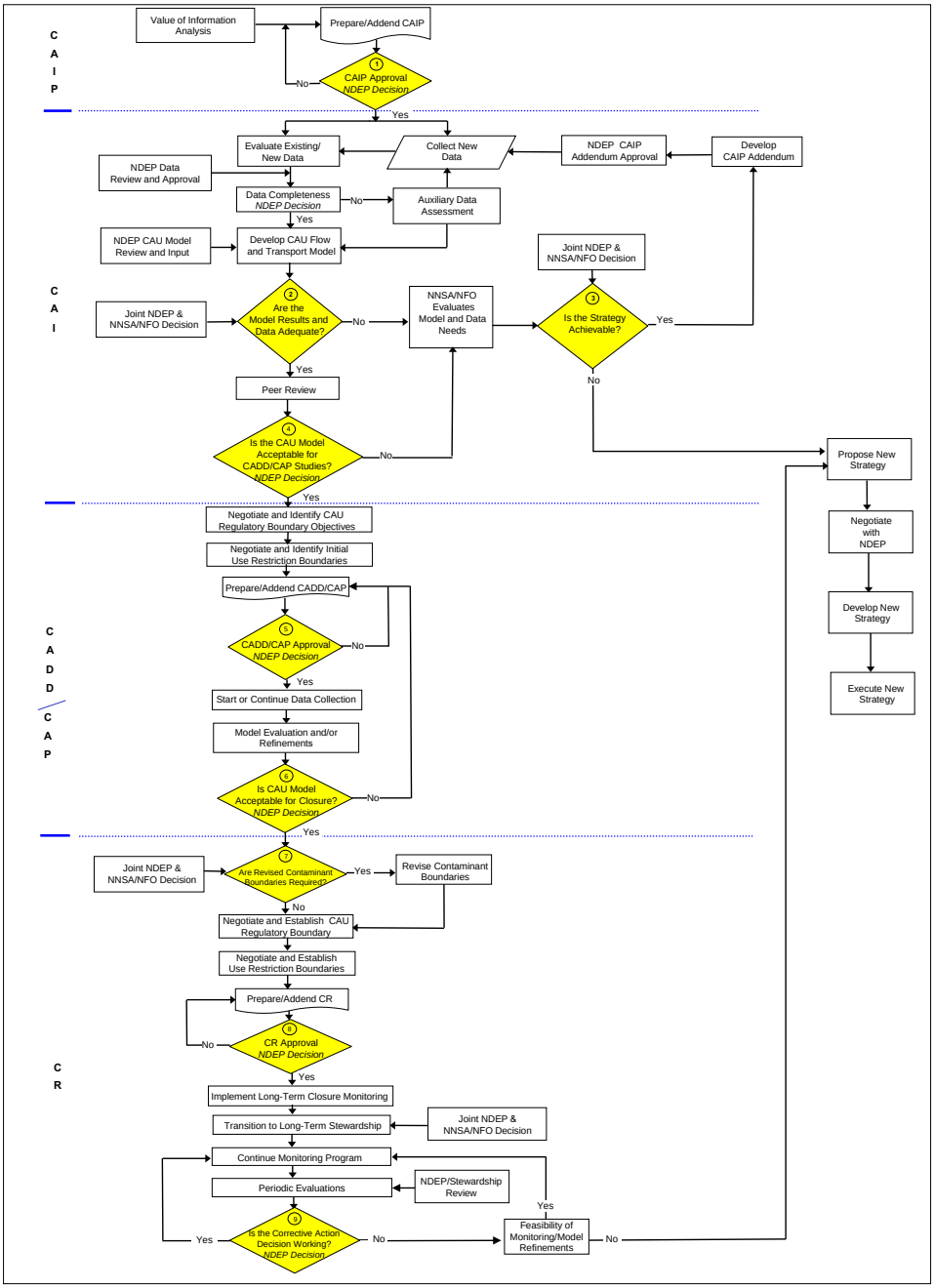

Figure 1-2
FFACO UGTA Strategy Flowchart

Phase I CAU transport model to assess the primary model components that contribute to model uncertainty. The subcommittee identified data needs, prioritized new data collection, data analysis, and modeling activities to support Phase II modeling. The DOE, National Nuclear Security Administration Nevada Site Office (NNSA/NSO) and NDEP agreed with the subcommittee recommendations, provided an answer of "No" at the second decision point (Figure 1-2), decided that the UGTA strategy for the CAU was achievable (third decision point), and initiated a second phase (Phase II) of the CAI studies.

An updated addendum, the Phase II CAIP, was developed, submitted, and reviewed, which led to revision and subsequent approval in 2009 (NNSA/NSO, 2009). Transition from Phase I to Phase II of the CAI stage for the PM CAUs was approved by NDEP in June 2010. Subsequently, a Record of Technical Change (ROTC) to the Phase II CAIP was submitted and approved (NNSA/NFO, 2014). The CAI stage includes data collection, data evaluation and analysis, and development of CAU-specific numerical models of flow and transport using CAU-specific data; analog data from appropriate HSUs of the NNSS and data from the hydrological literature to supplement site-specific data (FFACO, 1996 as amended). Drilling, completion, and testing of new Phase II wells occurred through 2016. Based on the new data and analysis, the Phase II CAIP (DOE/EMNV, 2020b) was updated and approved in 2020. Phase II follows the same progression as Phase I: a revised HFM (DOE/EMNV, 2020a), TDD (Navarro, 2021a), HDD (Navarro, 2021b), and source term data document (SDD) (Navarro, 2021c) were developed to provide the hydrogeologic framework, hydrologic data for developing the Phase II groundwater flow model, and transport data and source term specifications for developing the Phase II transport model. NDEP assessed the completeness of data collection and data evaluation, judging that significant gaps did not exist in the data that could affect the efficiency of the modeling studies (DOE/EMNV, 2021).

The FFACO (1996, as amended) requires that the CAU models of the CAI stage will be constructed and consider, at a minimum, the eight modeling topics listed below with the objective of evaluating future migration of contaminants to forecast CBs that encompass the uncertainty of current and future contaminant migration:

- Alternative hydrological framework models of the CAU modeling domain
- Uncertainty in the RST and hydrologic source term (HST)

- Alternative models of groundwater recharge
- Alternative model boundary conditions and models of groundwater flow
- Multiple permissive sets of calibrated flow models
- Probabilistic simulations of transport using plausible sets of alternative framework and recharge models, model boundary conditions, and models of groundwater flow from calibrated flow models
- Ensembles of forecasts of CBs for the CAU
- Sensitivity and uncertainty analysis of the model outputs

Section 7.0 of this report documents how each of these topics is addressed by the PM CAU model.

With the completion of this PM CAU flow and transport model document, the second decision point has been reached. If the model results and data are judged to be adequate in a joint decision by NDEP and DOE EM, a peer review will be conducted as the next step in the execution of the UGTA strategy for the PM CAUs. This will lead to the fourth decision point, which is an NDEP decision regarding "Is the CAU model acceptable for CADD/CAP studies?" If the NDEP decision is "Yes," the CAUs will progress to the CADD/CAP stage.

The technical suitability of the models used to evaluate groundwater flow and contaminant transport in the PM CAUs is supported by the implementation of the quality assurance (QA) requirements identified in the UGTA QAP (NNSA/NFO, 2015a; DOE/EMNV, 2018b). The relevant requirements are the following, with QAP section numbers in parentheses:

- Data Management (A.8)
- Computer Software and Codes (A.9)
- Nondirect Data (B.4)
- Groundwater Flow and Transport Modeling (B.5)
- Model Evaluation (B.6)
- Configuration Control (B.7)
- Document Review and Issuance (C.4)

Appendix B summarizes how each of the QA requirements has been addressed in the activities supporting the development and application of the PM CAU flow and transport models.

1.2 Purpose, Objectives, and Scope

The purpose, objectives, and scope of the PM CAU flow and transport model are presented in the following subsections.

1.2.1 Purpose and Objectives

The purpose of the PM CAU flow and transport modeling is to support the UGTA corrective action strategy objective of forecasting CBs. A CB is formally defined as a probabilistic model-forecast perimeter and a lower HSU boundary that delineates the extent of RN-contaminated groundwater from underground testing over 1,000 years. Contaminated groundwater is defined as water exceeding the radiological standards of the SDWA (CFR, 2021). Simulation modeling of contaminant transport will be used to forecast the location of CBs within 1,000 years and must show the 95th percentile of the model results (boundary outside of which only 5 percent of the simulations exceed the SDWA standards).

To forecast the CBs, the PM CAU model accomplishes the following:

- Develops a three-dimensional (3-D) mathematical groundwater flow and transport model that incorporates the important features of the flow and transport system and honors CAU-specific and RN-specific data and information (see Sections 4.0 and 5.0).
- Simulates the groundwater flow (see Section 4.0) and RN transport incorporating HSTs for RN release into groundwater (see Section 5.0) to determine the direction and magnitude of groundwater fluxes and RN migration based on calibration to PM hydrogeologic data and tritium (^{3}H) observation data in downgradient wells.
- Quantifies the uncertainty in the direction and magnitude of groundwater flow (see Section 4.0) and RN transport (see Section 5.0) due to uncertainty in parameter values and alternative component conceptual models.

Additionally, as stated in the update to the Phase II CAIP for PM CAU (DOE/EMNV, 2020b), the model results will be used to identify pathlines from test locations and expected distances of transport to assess the monitoring network design and identify gaps in the monitoring network.

In addition to forecast goals for the CBs, the specific objectives of the PM flow and transport modeling were identified in the Phase II CAIP (NNSA/NSO, 2009) as follows:

- Reevaluate role of major hydrostratigraphic and structural features.
- Refine model boundary conditions.
- Conduct simultaneous flow and transport simulation.
- Correct water table clipping.
- Develop sub-CAU scale heterogeneity model.
- Develop sub-CAU model of the Bench subdomain.
- Revise fracture parameter model.
- Develop discrete fracture models for upscaling.
- Revise the simplified source term model.
- Reduce the number of RNs modeled.

1.2.2 Scope

The area of investigation, as described in the CAIP update (DOE/EMNV, 2020b), was selected to encompass the PM CAUs and the Pahute Mesa-Oasis Valley (PM-OV) groundwater basin (Fenelon et al., 2016) to identify downgradient locations that may be impacted by contamination related to nuclear testing within these CAUs over the 1,000-year period (i.e., PM-OV area). This area encompasses the northwestern portion of the NNSS and adjacent NTTR lands to the north and west managed by the U.S. Air Force (USAF) and the Bureau of Land Management (BLM). Some of the major physiographic features included in the PM CAU model are PM, the western portion of Rainier Mesa, Timber Mountain, Thirsty Canyon, Black Mountain, Oasis Valley, Gold Flat, and Kawich Valley (Figure 1-3).

The time period for simulations was selected to start on December 19, 1968, which is the date of the first detonation tested underground that was later to be included under the UGTA Activity, and the period was extended 1,000 years beyond that to the year 2968 for all detonations.

1.3 Major Data Collection and Analysis Activities in Phase II

Major data collection and analysis activities completed for the PM CAU Phase II work are noted below.

- Installation and testing of 11 wells (as listed in Appendix A).

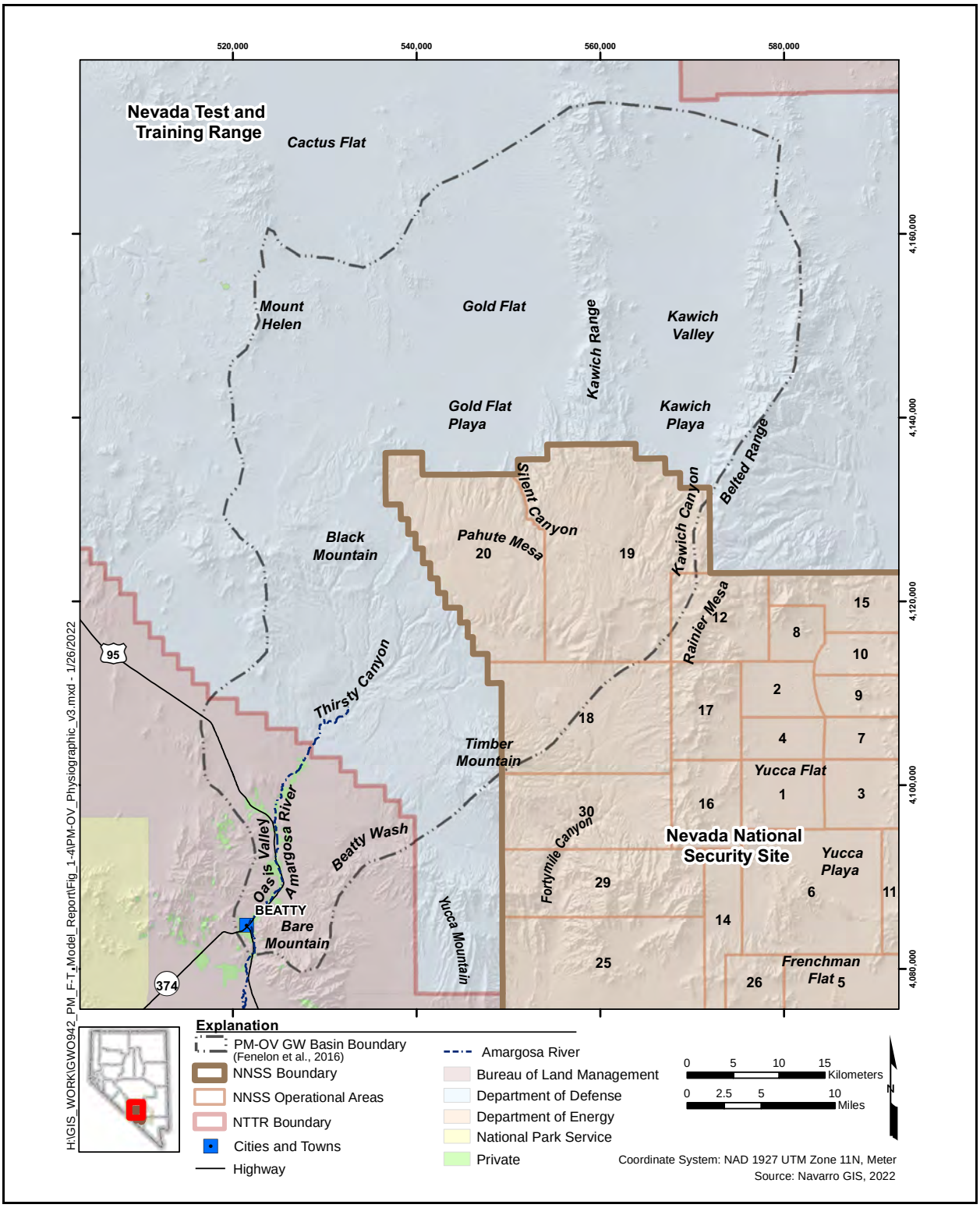

Figure 1-3
Physiographic Features of the PM CAU Model

- Additional dispersion summaries (Zhou et al., 2005; HGL, 2018).
- Assessment of hydraulic connections across a complex sequence of volcanic rocks—analysis of U-20 WW multiple-well aquifer test (MWAT) (Garcia et al., 2011).
- Additional matrix diffusion estimates (Telfeyan et al., 2018; Zavarin et al., 2013).
- Infiltration studies (Fenelon et al., 2016; Middleton et al., 2019; Hershey et al., 2020; Halford and Jackson, 2020).
- Delineation of the PM-OV groundwater basin (Fenelon et al., 2016).
- Additional studies on colloid formation and transport (Zavarin et al., 2015 and 2019; Reimus and Boukhalfa, 2014; Reimus, 2018).
- Additional studies of fracture analysis (Golder, 2016; Hoaglund, 2017; Makedonska et al., 2020; HGL, 2017).
- Analyses of 16 MWATs, yielding estimates of transmissivity, identified the hydraulic connections between wells and provided calibration data for numerical models (as listed in Appendix A of Garcia et al., 2017).
- Study of regional stress and fracture permeability (Reeves et al., 2017).
- Standardization of PM single-well aquifer test results (Frus and Halford, 2018).
- Updated matrix sorption coefficients (Carle, 2018; Carle et al., 2020).
- Discrete fracture network (DFN) modeling studies (Makedonska et al., 2020; Parashar et al., 2019).
- Development of a new yield-weighting method of estimating radiological inventories (Tompson et al., 2019).
- Estimates of porosity derived from analysis of geophysical log data (Navarro, 2019c).
- Analysis of additional groundwater samples that show where test-derived constituents are and are not found (Navarro, 2021c).
- Geochemical and isotopic evaluation of groundwater flow in the PM-OV flow system (Navarro, 2020).
- An updated regional flow model (Halford and Jackson, 2020).
- RN screening analysis and transport parameters for PM detonations (Carle et al., 2020).

- PM Area 20 subregion flow and transport model (Lu et al., 2021).
- Interpretation of mineral diagenesis for assessment of RN transport (Carle, 2020).
- Groundwater flow and ^{3}H transport simulations from the HANDLEY test (Jackson, 2021).
- PM conceptual hydrologic model framework (Jackson et al., 2021).
- Review of cavity radius (R_c) and chimney height information (Carle et al., 2021).

1.4 Supporting Documents

The documents noted above provided valuable information needed to construct and calibrate the PM CAU model. In addition, the results from a wide range of studies were integrated into several data documents to facilitate the data review:

- Revision of PM HFM based on new data (DOE/EMNV, 2020a)
- Update to the PM TDD (Navarro, 2021a)
- Update of the PM HDD (Navarro, 2021b)
- Update to the PM SDD (Navarro, 2021c)

1.5 Document Organization

This document consists of eight sections and eight appendices:

- Section 1.0 provides an introduction, FFACO background, regulatory status of the PM CAUs, a listing of recent data collection and analysis activities, purpose, and objectives.
- Section 2.0 provides a summary description of the physical and hydrogeologic setting of the PM CAUs, a summary of the underground nuclear testing, overview of flow paths based on geochemical data, and a review of previous modeling studies directly used in the current work.
- Section 3.0 provides a description of the flow and transport modeling technical approach.
- Section 4.0 discusses the PM CAU flow model development, construction, calibration, and results.
- Section 5.0 discusses the PM CAU transport model development, construction, calibration, and results.
- Section 6.0 presents the CB forecasts.

- Section 7.0 provides the summary and conclusions.
- Section 8.0 provides the references cited in the document.
- Appendix A lists major Phase II data collection and analysis activities.
- Appendix B presents the QA summary.
- Appendix C provides definitions of the HSUs.
- Appendix D contains a table of underground nuclear test information at PM.
- Appendix E provides the discussion of software selection and development.
- Appendix F presents hydrographs comparing simulated and observed drawdown from 16 MWATs at PM.
- Appendix G documents the distribution coefficients (K_ds) for various RNs by HSUs used in the PM CAU model.
- Appendix H presents detailed transport model results.
- Appendix I contains NDEP comments.

2.0 PM Background

This section presents a brief description of the physical and hydrogeologic setting of the PM CAUs and a summary of underground nuclear testing at PM. Nuclear testing at PM occurred in CAUs 101 and 102 (Figure 1-2), which are enclosed in the PM-OV groundwater basin (Fenelon et al., 2016). Hence, the geologic description encompasses the entire PM-OV area and a small region surrounding it.

2.1 Physical Setting

The area relevant to the PM CAU flow and transport model encompasses the PM-OV groundwater basin (Fenelon et al., 2016). It is approximately 160 kilometers (km) (100 miles [mi]) northwest of Las Vegas, Nevada, and includes lands managed by the U.S. Air Force (USAF) (NTTR) and the Bureau of Land Management (BLM), in addition to the northwestern portion of the NNSS. The area also includes small, scattered tracts of private land in and near the town of Beatty, Nevada.

The landforms and topography of the PM-OV area reflect the complex geology of its location in the arid Basin and Range physiographic province (DOE/EMNV, 2020a). The Basin and Range province is characterized by generally north-trending, linear mountain ranges separated by intervening valleys. Mountain ranges of the Great Basin are mostly tilted, fault-bounded blocks that are as much as 80 km (50 mi) long and 24 km (15 mi) wide. In the PM CAU model investigation area, these Basin and Range features are modified by volcanic calderas.

Dominant structural features (Figure 2-1) include the Timber Mountain (a resurgent dome of the Timber Mountain caldera complex [TMCC]) and its arcuate valley (“moat”); Black Mountain, a “classic-shaped” caldera in the northwest; PM, a high volcanic plateau covering most of the area to the northeast; Oasis Valley, a basin in the southwestern part of the model area; and the Thirsty Canyon Lineament (TCL), a north–northeast-trending, geophysically inferred feature, within the Thirsty Canyon Fault Zone, that has been identified based on regional gravity and aeromagnetic maps (Mankinen et al., 1999 and 2003). Some of these features are dissected locally by several prominent surficial drainages typically characterized by steep-sided canyons and arroyos (e.g., Fortymile Canyon, Thirsty Canyon [Figure 1-3]).

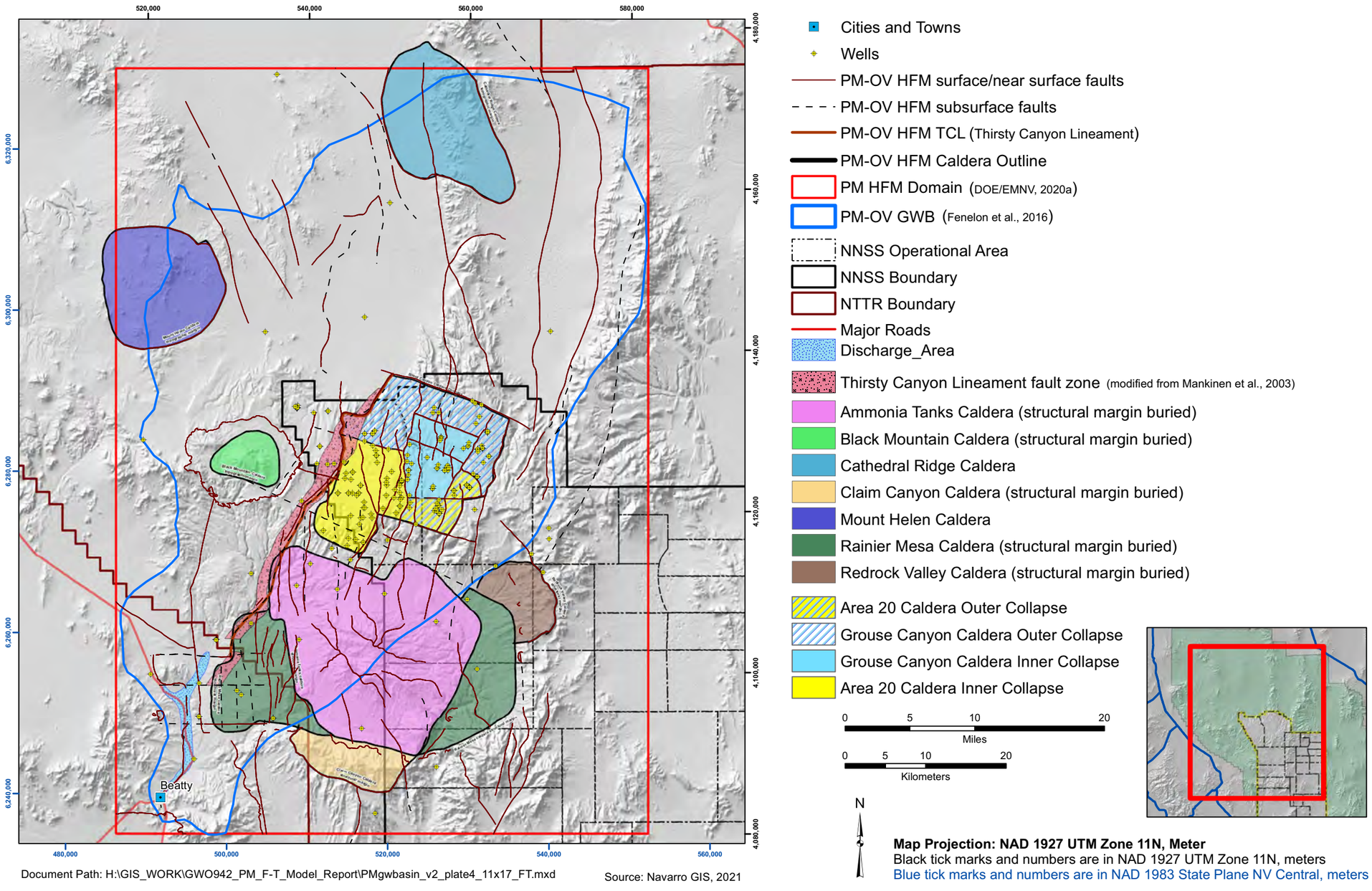

Figure 2-1
Structural Features of the PM-OV HFM
Source: DOE/EMNV 2020a

Figure 2-2 shows the location of the PM-OV groundwater basin and the major groundwater basins surrounding the NNSS area as defined in Fenelon et al. (2016). The PM-OV groundwater flow system is a nearly closed basin (with the exception of small surface and subsurface flow that moves south of Beatty into the Amargosa Desert) that encompasses all of the PM tests, and the groundwater that could be contaminated by them is expected to move toward the discharge area in Oasis Valley (Fenelon et al., 2016).

PM CAUs are in the central part of the PM-OV groundwater basin, in the northwestern part of the NNSS. The CAUs include NNSS Areas 19 and 20 (Figure 1-1). PM is an elevated plateau of about 500 square kilometers (km^2) (200 square miles [mi^2]) at an altitude that ranges from 1,676 meters (m) (5,500 feet [ft]) on the western edge to over 2,134 m (7,000 ft) above mean sea level (amsl) throughout the eastern part (Blankennagel and Weir, 1973).

PM geology is dominated by deposition of rock units from volcanic eruptions from nested calderas (DOE/EMNV, 2020a). With the exception of some deeply buried Paleozoic rocks in a few places and some shallow alluvium, all rocks known to underlie PM are volcanic with total thickness approaching 5 km (Ferguson et al., 1994; DOE/EMNV 2020a).

2.2 PM-OV Geologic Setting

The PM-OV basin area is geologically complex, encompassing at least seven of the eight Miocene-age calderas of the Southwestern Nevada Volcanic Field (SWNVF) and one caldera, Cathedral Ridge, from the Central Nevada caldera complex (CNCC), many relatively young basin-and-range-style normal faults, and Mesozoic-age thrust faults and intrusive bodies, all superimposed on a basement complex of highly deformed Proterozoic and Paleozoic sedimentary and metasedimentary rocks. A generalized geologic map of the PM-OV basin and surrounding area is shown in Figure 2-3. For a more detailed geologic map (adapted from Slate et al., 1999) that shows the surficial distribution of the predominantly Tertiary volcanic units, the younger surficial deposits, and the limited outcrops of pre-Cenozoic rocks within the study area, see DOE/EMNV (2020a, Plate 1). The following paragraphs summarize the geology of the model area. More detailed discussions of the structure and stratigraphy of the model area are provided in DOE/EMNV (2020a). The PM-OV basin area is dominated by Miocene-age volcanic rocks formed of generally rhyolitic composition that were erupted from various volcanic vents on and adjacent to the western and

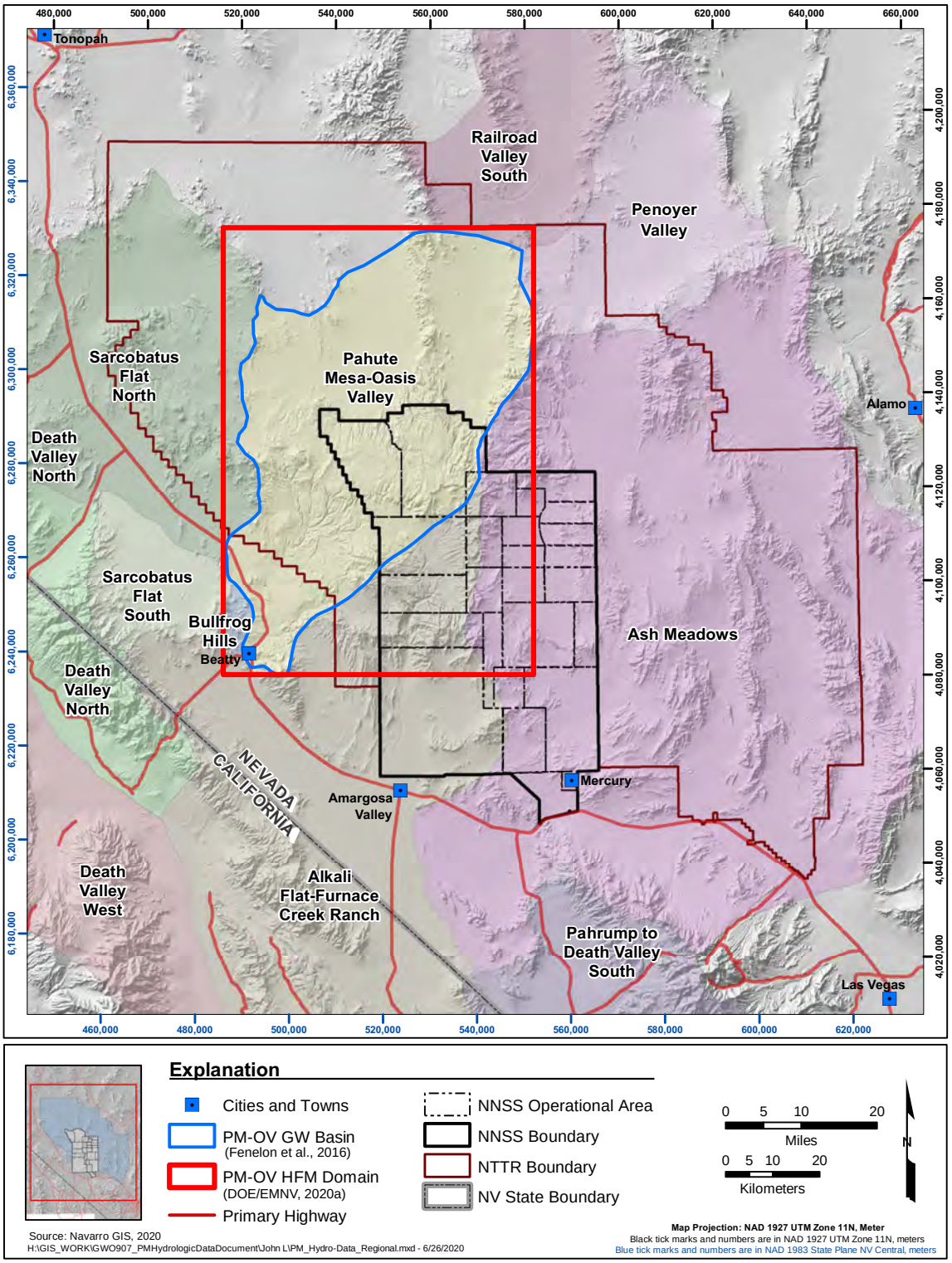

Figure 2-2
Groundwater Basins in and near the PM-OV HFM

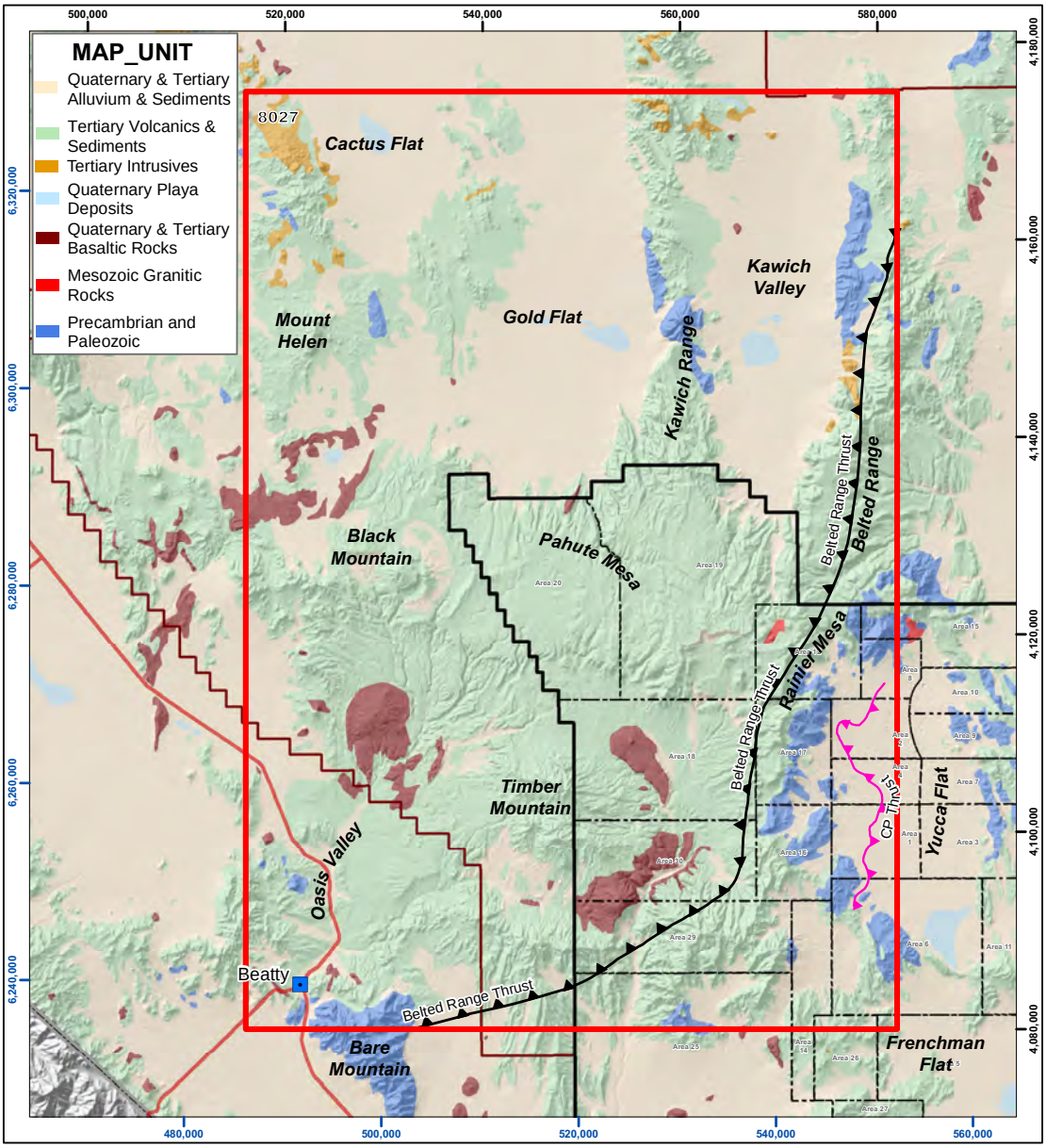

Figure 2-3
Generalized Geologic Map of the PM-OV HFM and Surrounding Area

northwestern portions of the NNSS. At least nine calderas have been identified (Figure 2-1) in this multicaldera silicic volcanic field (i.e. SWNVF) along with the Cathedral Ridge caldera from the CNCC. The calderas formed by the voluminous eruption of zoned ignimbrites between 16 million and 7.5 million years ago (Ma) (Sawyer et al., 1994). The volcanic rocks are covered in many areas by a variety of late Tertiary and Quaternary surficial deposits. These deposits consist of alluvium, colluvium, eolian deposits, spring deposits, basalt lavas, lacustrine deposits, and playa deposits. (See DOE/EMNV, 2020a, Sections 4.2.1 and 4.3.1 for more information on these deposits.) Underlying the Tertiary volcanic rocks regionally are Paleozoic and Proterozoic sedimentary rocks including dolomite, limestone, quartzite, and argillite, which form the basement of the PM-OV groundwater basin. The only surface exposure of Mesozoic-age rocks in the model area is the Gold Meadows stock, a granitic intrusion at the northeastern edge of the PM-OV basin.

2.3 PM-OV Hydrogeologic Setting

The PM-OV hydrogeologic setting is summarized in this section to support the flow and transport models presented in this report. This includes a summary of the groundwater flow system and the PM-OV HFM.

2.3.1 Surface Water and Drainage at the NNSS

The testing areas relevant to the PM CAU model are within the NNSS, which in turn is within the Great Basin, a physiographic province that comprises numerous closed hydrographic basins, which are defined by surface-water divides. Most streams in the region are ephemeral, flowing only in response to precipitation events or snowmelt. Runoff is conveyed through normally dry washes toward the lowest areas of the closed hydrographic sub-basins, such as in discharge areas or playas on valley floors. Within the PM-OV basin area, playas occur north of PM in Gold Flat and Kawich Valley. In the larger context, two more playas occur on the NNSS, both east of the PM-OV basin area (Figure 1-3): Yucca Playa, which lies in Yucca Flat; and Frenchman Playa in Frenchman Flat (this playa is not visible in Figure 1-3 because it occurs in southern Frenchman Flat beyond the southern boundary of the figure; its location is shown in DOE/EMNV, 2019). While water may stand for a few weeks on the playas before evaporating, the playas are dry most of the year. Surface water may leave the PM-OV basin in only a few places. Ephemeral flows in Fortymile Canyon exit along the southeast part of the PM-OV basin boundary, and this surface water ultimately infiltrates along

the channel or evaporates as it flows toward the Amargosa Valley floor. Beatty Wash and Thirsty Canyon Wash feed into the Amargosa River on the western and southwest margins of the NNSS. The Amargosa River dispenses occasional storm runoff from the Oasis Valley hydrographic sub-basin near Beatty, Nevada. Finally, Silent Canyon and Kawich Canyon drain northward into Gold Flat and Kawich Valley, respectively. Springs in Oasis Valley are formed by upwelling of water along natural structures or at the contacts with low-permeability rocks. The springs and seeps in the discharge area of Oasis Valley are summarized in Reiner et al. (2002), who also report spring discharge rates in Oasis Valley were measured or estimated to provide the basis for the discharge boundary condition used in the model. Most water discharged from springs travels only a short distance from the source before evapotranspiring. The springs are important sources of water for wildlife.

2.3.2 Groundwater Flow System

The PM-OV groundwater flow system, as defined in Fenelon et al. (2016) and Jackson et al. (2021) (Figure 2-4), is part of the Death Valley regional groundwater flow system. A conceptual model of the PM-OV groundwater flow system was previously developed during the regional evaluation (DOE/NV, 1997) and the area refined in subsequent investigations (BN, 2002; Fenelon et al., 2016; Jackson et al., 2021).

Regional potentiometric contours (Figure 2-5) generally mimic the topography. The highest regional potentiometric contours are found along the boundaries of the basin, coincident with elevated topographic features such as Rainier Mesa, the Kawich Range, the Belted Range, and the Cactus Range. Potentiometric contours beneath PM are intermediate to those found along the basin boundaries and those found within the discharge area. Groundwater beneath PM generally flows in a southwesterly direction, primarily through fractured lava-flow and tuff aquifers (Navarro, 2021b), discharging to the surface within the Oasis Valley discharge area in the form of springs.

Details of the groundwater flow system are presented in Jackson et al. (2021) and Fenelon et al. (2016); only a brief summary is presented here. Groundwater in the PM-OV basin encounters an alternating sequence of low- and high-transmissivity rocks as it moves across PM. Flow from all PM nuclear tests is to Oasis Valley. Flow converges along a corridor of high transmissivity between PM and Oasis Valley. The lateral PM-OV basin boundary is well defined and, with a few minor exceptions, represents a no-flow boundary. Some boundary uncertainty exists in the northeastern part

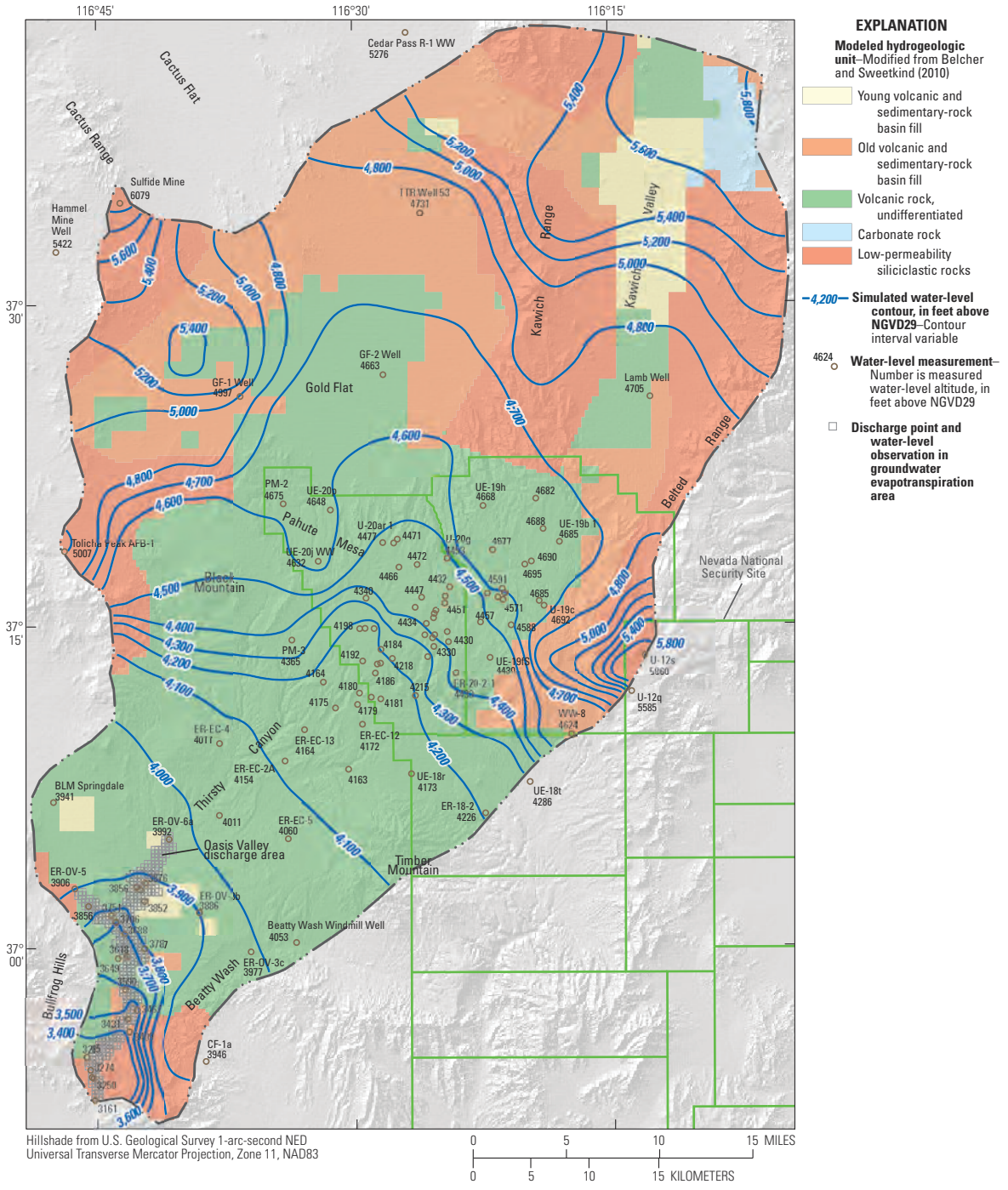

Figure 2-4
Features of the PM-OV Groundwater Basin
Source: Fenelon et al., 2016

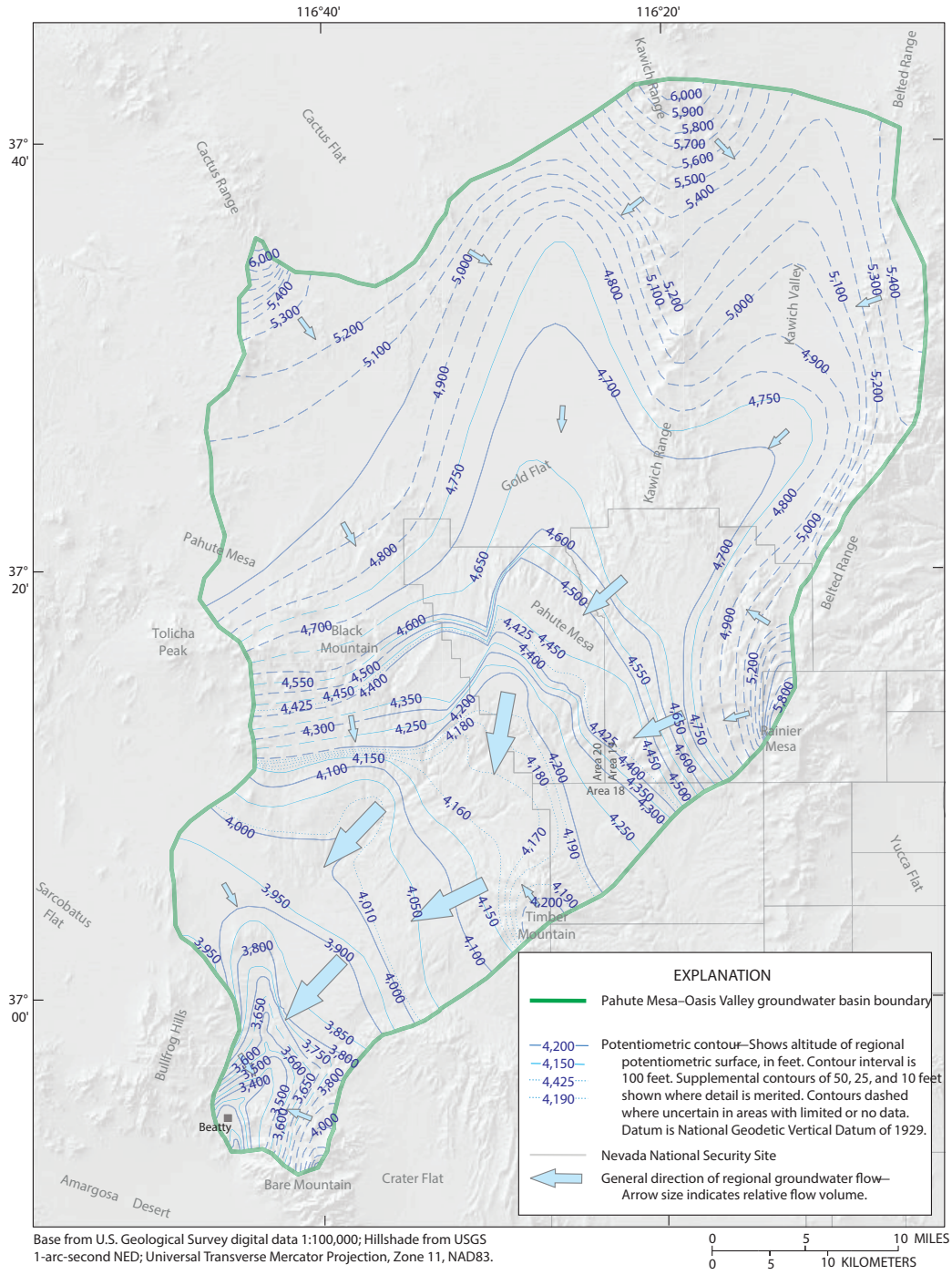

Potentiometric contours and regional groundwater-flow paths in the Pahute Mesa–Oasis Valley groundwater basin, southern Nevada (Modified from Jackson et al., 2021).

Figure 2-5
PM-OV Basin Steady-State Potentiometric Contour Map
(based on water-level data as reported in Jackson et al., 2021)

of the basin, but potential flow-rate estimates across the northeastern boundary resulting from this uncertainty are small relative to the basin groundwater budget. The dominant recharge to the PM-OV groundwater basin is slow, steady, diffuse percolation of old water through the unsaturated zone; however, episodic recharge of modern water also occurs in minor amounts following wet winters. About half the recharge in the PM-OV basin is derived from the eastern PM area. The remaining recharge is derived primarily from other highland areas including Timber Mountain, Belted and Kawich Ranges, and Black Mountain. The PM-OV groundwater system is nearly steady-state, where recharge is balanced by the 5,900 acre-feet per year (ac-ft/yr) of natural discharge at Oasis Valley. Volcanic rocks form the primary aquifers and confining units in the PM-OV basin. Volcanic hydrogeologic units (HGUs) and HSUs have transmissivity distributions that span up to eight orders of magnitude with considerable overlap between distributions.

2.3.3 Hydrogeologic Framework

The hydrogeologic framework used in the PM-OV HFM is based on the conceptual hydrologic system established for the NNSS area by Winograd and Thordarson (1975) and Blankennagel and Weir (1973). This early work was summarized and updated in Laczniak et al. (1996), the UGTA Phase I hydrostratigraphic regional model (IT, 1996c), and the UGTA Phase II PM HFM (NSTec, 2014). The PM-OV HFM (DOE/EMNV, 2020a), which supersedes the previous draft (NSTec, 2014) and published PM HFM reports, contains the relevant details, summary discussion, and supporting information regarding the history and development of the HFM.

The rocks of the NNSS have been classified using a two-level classification scheme, in which HGUs are grouped to form HSUs (Prothro et al., 2009a; DOE/EMNV, 2020a). The HSUs are used to categorize rocks according to their ability to transmit groundwater, which is mainly a function of the rocks' primary lithologic properties, degree of fracturing, and secondary mineral alteration. However, it must be mentioned that many HSUs, regardless of their general classification as an aquifer or confining unit, exhibit a wide range of transmissivity (Figure 2-6) which arises from local site to site variation. In some cases, they exhibit the characteristics of an aquifer, and in others, those of a confining unit.

At the CAU scale, a more consistent view is apparent. HGUs also have a large range in estimated transmissivity (Jackson et al., 2021). However, transmissivity distributions among HGU groupings

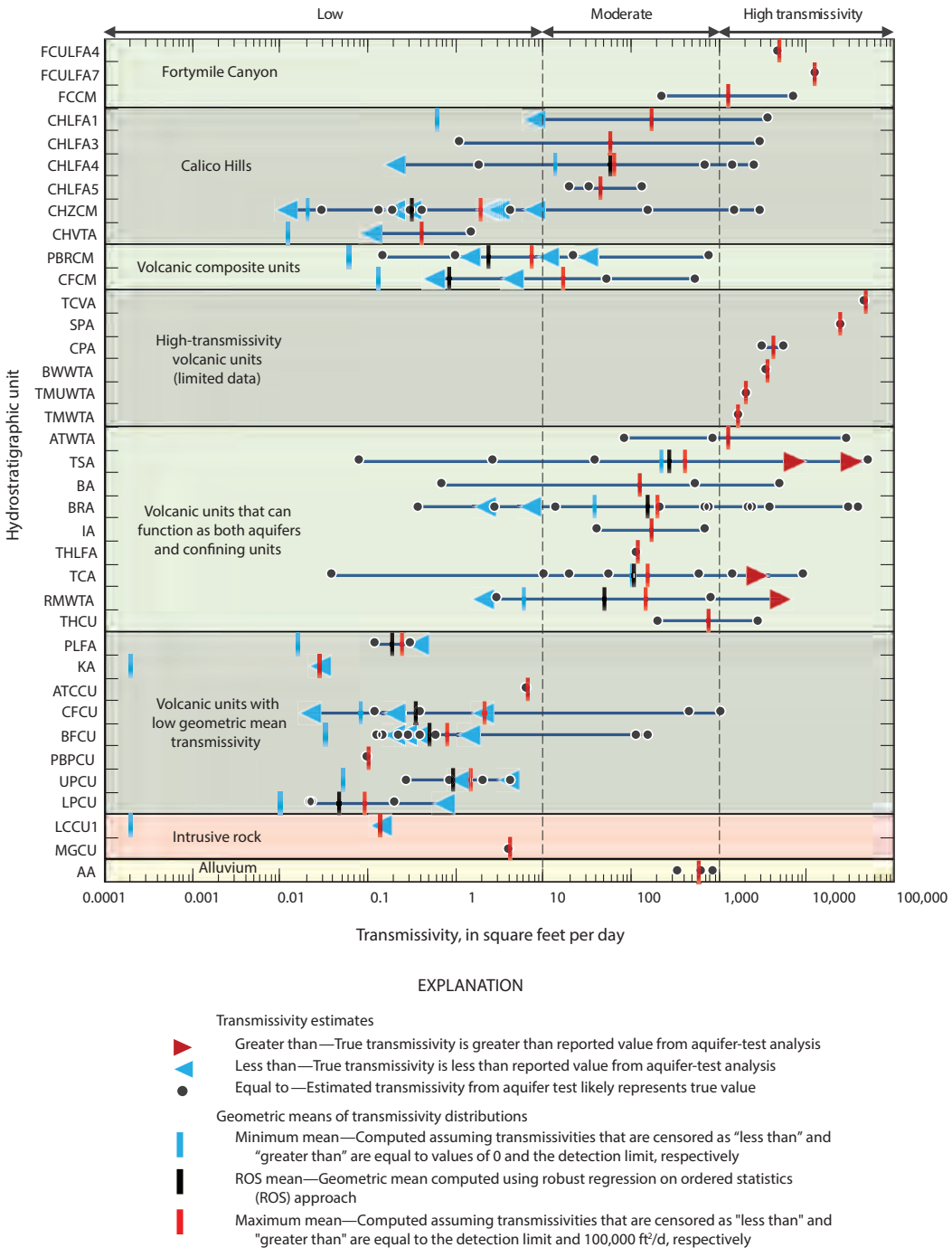

Transmissivities estimated from aquifer tests in wells within the Pahute Mesa–Oasis Valley groundwater basin, southern Nevada (Modified from Jackson et al., 2021).

Figure 2-6
PM Transmissivity Ranges

provide information regarding the general behavior of HGUs and HSUs. For example, bedded and nonwelded tuffs typically have low transmissivity, whereas welded-tuff aquifers (WTAs) and lava-flow aquifers (LFAs) generally are more transmissive, with geometric mean transmissivities in the moderate range, spanning 10 to 1,000 square feet per day (ft^2/day) (Jackson et al., 2021). Using hydraulic conceptualizations of HGUs, expected values of effective transmissivity (and hydraulic conductivity) can be defined for HSUs. A large number of HSUs were defined in the PM-OV HFM and were used in the PM CAU models to provide lateral and vertical hydraulic variability. The concept of HSUs made up of groups of similar HGUs is useful in volcanic terrains because stratigraphic units can differ greatly in hydrologic character both laterally and vertically. The HSUs serve as “layers” in the PM-OV CAU HFM and other NNSS CAU-scale HFMs.

The PM Phase II HFM (NSTec, 2014) was expanded to include the entire PM-OV groundwater basin, as defined in Fenelon et al. (2016) by adding areas to the north, south, east, and west, thereby significantly increasing the size of the HFM domain. This new PM-OV HFM domain fully incorporates the PM-OV basin which is the domain of the PM CAU model. This additional area resulted in an increase in the number of structural elements (i.e., faults and caldera margins) and HSUs in the PM-OV HFM than in the previously less extensive area. Surface mapping, geophysics, and limited borehole information provide the majority of data in the new areas. The lower data density (e.g., fewer boreholes and lower-resolution geophysics) of the northern extension results in a lower resolution of the modeled HSU distribution in this area. However, given the minimal amount of recharge (Fenelon et al., 2016) and the presence of confining and composite units under the depositional basins in the northern extension (i.e., Gold Flat and Kawich Valley), there is expected to be only a minimal impact on the PM CAU flow model regarding this uncertainty.

The following paragraphs summarize the HGUs and HSUs as well as the structural features that make up the PM-OV HFM. Detailed descriptions of the HGUs, HSUs, and structural features are given in the PM-OV HFM report (DOE/EMNV, 2020a).

2.3.3.1 Hydrogeologic Units

The rocks of the NNSS and UGTA CAUs have been classified in terms of nine HGUs, which are the alluvial aquifer, four volcanic HGUs, two intrusive HGUs, and two HGUs that represent the pre-Tertiary rocks (Table 2-1). Table 2-1 provides a definition and brief description of significant

Table 2-1
HGUs of the PM-OV HFM

HGU	Typical Lithologies	Hydrologic Significance
Alluvial aquifer (AA) [a]	Unconsolidated to partially consolidated gravelly sand, eolian sand, and colluvium; thin, basalt flows of limited extent	Has characteristics of a highly conductive aquifer, but less so where lenses of clay-rich paleocolluvium or playa deposits are present.
Welded-tuff aquifer (WTA)	Welded ash-flow tuff; vitric to devitrified	Degree of welding greatly affects interstitial porosity (less porosity as degree of welding increases) and permeability (greater fracture permeability as degree of welding increases).
Vitric-tuff aquifer (VTA)	Bedded tuff; ash-fall and reworked tuff; vitric	Constitutes a volumetrically minor HGU. Generally does not extend far below the static water level due to tendency to become zeolitized under saturated conditions.Significant interstitial porosity (20 to 40 percent) and matrix permeability. Typically insignificant fracture permeability.
Lava-flow aquifer (LFA)	Rhyolite lava flows; includes flow breccias (commonly at base) and pumiceous zones (commonly at top)	Generally a caldera-filling unit (with exceptions: e.g., ER-20-12). Hydrologically complex; wide range of transmissivities; fracture density and interstitial porosity differ with lithologic variations.
Tuff confining unit (TCU)	Zeolitized bedded tuff with interbedded, but less significant, zeolitized, nonwelded to partially welded ash-flow tuff	May be saturated but measured transmissivities are very low unless locally fractured.
Intra caldera intrusive confining unit (IICU)	Highly altered, highly injected/intruded country rock and granitic material	Assumed to be impermeable. Conceptually underlies each of the SWNVF calderas and Calico Hills. Developed for this study to designate basement beneath calderas as different from basement outside calderas.
Granite confining unit (GCU)	Granodiorite, quartz monzonite	Relatively impermeable; forms local bulbous stocks, north of Rainier Mesa.
Clastic confining unit (CCU)	Argillite, siltstone, quartzite	Clay-rich rocks are relatively impermeable; more siliceous rocks are fractured, but with fracture porosity generally sealed due to secondary mineralization.
Carbonate aquifer (CA)	Dolomite, limestone	Transmissivity values differ greatly and are directly dependent on fracture frequency.

Source: DOE/EMNV, 2020a

[a] AA is also an HSU in the PM-OV HFM.

hydrologic properties of each HGU. Jackson et al. (2021) summarizes the properties and spatial distribution of HGUs within the PM-OV flow system.

In the PM-OV basin, volcanic HGUs form the principal aquifers and confining units in the PM-OV basin because of their widespread distribution and also because these HGUs are mostly located at shallower depths. It is recognized that in the PM-OV basin HGUs at depths shallower than 500 m are more transmissive than those that are at depths greater than 500 m (Jackson et al., 2021; Navarro, 2020). The volcanic rocks within the study area can be categorized into four HGUs based on primary lithologic properties, degree of fracturing, and secondary mineral alteration. The HGUs are vitric-tuff aquifers (VTAs) (e.g. vitric, non-welded, bedded, and reworked); tuff confining units (TCUs) (zeolitic and/or argillic altered non-welded or bedded rocks); welded-tuff aquifers (WTAs) (welded vitric to devitrified ash-flows); and lava-flow aquifers (LFAs). These HGUs host some, if not most, of the important flow paths within the PM-OV HFM.

The principal aquifers are the LFAs and WTAs, which consist of rhyolitic-to-dacitic lavas and welded tuffs, respectively. LFAs can have high permeabilities where fractured, but have limited areal continuity and thickness (Prothro and Drellack, 1997). WTAs can have well-connected fracture networks and are widespread, which can provide lateral continuity for water to move through the flow system (Winograd and Thordarson, 1975). The TCUs consist of altered (zeolitic and/or argillic) nonwelded and bedded tuffs, which have limited fracture networks and, as a result, have been classified as confining units, even though locally they may exhibit moderate conductivities, especially where they are zeolitized (Blankennagel and Weir, 1973). The VTAs are composed of vitric tuffs, which have been classified as aquifers because they have high matrix porosity and moderate permeability. The TCUs primarily occur below the water, and the VTAs are primarily above the water table.

The intrusive confining unit (ICU) category includes intracaldera intrusive confining units (IICUs) and the granitic confining unit (GCU). These rocks are relatively impermeable, are considered to behave as a confining unit, and are located in the deeper sections of the PM-OV groundwater basin. The IICUs conceptually underlie the calderas of the SWNVF, as well as other calderas in the PM-OV HFM.

The pre-Tertiary rocks beneath the study area are categorized as one of two HGUs based on primary lithologic properties, degree of fracturing, and secondary mineral alteration. The two HGUs are

clastic confining units (CCUs) or carbonate aquifers (CAs). The pre-Tertiary rocks mostly occur in the deep sections of the basin and are generally beneath the groundwater model's bottom boundary.

The deposits of alluvium (alluvial aquifers [AAs]) fill the main depositional basins of the NNSS including PM-OV basin, and generally consist of an unconsolidated to partially consolidated mixture of boulders, gravel, sand, silt, and clay derived from volcanic and Paleozoic sedimentary rocks (Slate et al., 1999). Overall, the alluvium is typically thin and unsaturated over much of the PM-OV groundwater basin. The ICUs, CCUs, CAs, and AA have less importance in the CAU groundwater model because of limited abundance downgradient of the testing areas or because they are mostly below the flow model bottom.

2.3.3.2 Hydrostratigraphic Units

HSUs are groupings of contiguous stratigraphic units that have a particular hydrogeologic character, such as being either an aquifer or a confining unit. HSUs may also be differentiated by properties important to transport such as reactive minerals and matrix porosity. An HSU may contain several HGUs. An HSU can be subjected to multiple stages of mineral alteration (e.g., vitric, zeolitic, transitional, quartzofeldspathic) and diagenetic zones can transgress stratigraphic boundaries (Carle, 2020; Moncure et al., 1981). These are taken into account in the more fine-scaled modeling performed in support of the screening analysis presented in Carle et al. (2020) and summarized in Navarro (2021c). Definitions, from the PM-OV HFM (DOE/EMNV, 2020a), for the 77 HSUs are provided in Table C-1 (Appendix C). The HSU's stratigraphic position is based on volcanic stratigraphy, lithologic properties related to depositional environment, postdepositional alteration, and degree of welding. Section 4.0 of the PM-OV HFM (DOE/EMNV, 2020a) provides further discussion, formation, properties, and information regarding HGUs and HSUs.

Outside the caldera complexes, structural relationships depicted on hand-drawn cross sections, surface map data, and borehole lithostratigraphic logs were used to assist in determining the distribution of volcanic HSUs. The Warren et al. (2000b) block model was also used for additional guidance in this area. Volcanic units within the caldera complex were mapped as horizontal layers because they typically have very low dips. The PM-OV HFM report (DOE/EMNV, 2020a) provides the rationale and detailed information regarding model parameters and stratigraphy. The dominant

lithology of some units may change or pinch out laterally (e.g., LFA close to the source vents, WTA farther away, and nonwelded TCU or VTA at distal edges).

Hydrostratigraphic cross sections through the Bench area and Area 20 are illustrated in Figure 2-7. Two of the sections (A–A´ and B–B´) are oriented approximately parallel to regional flow and follow approximate flow paths from BENHAM, and HANDLEY tests, respectively. One section (C–C´) is oriented perpendicular to flow and is through the Bench area. The cross sections show that faults often juxtapose aquifers against confining units potentially creating flow-path connections or barriers. As groundwater flows from the testing areas toward Oasis Valley, groundwater encounters alternating sequences of low- and high-transmissivity rock.

The more important HSUs regarding flow and transport beneath PM are those containing LFA and WTA HGUs downgradient of nuclear tests. These HSUs include the Benham aquifer (BA), Calico Hills zeolitized composite unit (CHZCM), Tiva Canyon aquifer (TCA), Topopah Spring aquifer (TSA), Belted Range aquifer (BRA), and Pre-Belted Range composite unit (PBRCM). Tritium plumes—which serve as indicators to flow paths, associated with the BENHAM, TYBO, and possibly GOLDSTONE tests— occur in the BA, TSA, TCA, and Calico Hills lava-flow aquifer 5 (CHLFA5) HSUs. Tritium plumes possibly associated with the BELMONT and MOLBO tests occur in the TCA and TSA HSUs. The Timber Mountain welded-tuff aquifer (TMWTA), Timber Mountain lower vitric-tuff aquifer (TMLVTA), TSA, BA, PBRCM, and possibly the Upper Paintbrush confining unit (UPCU) are important to flow and transport west of the Purse fault, where shallow and deep ^{3}H transport from the HANDLEY test been observed within the ER-20-12 and PM-3 wells. The important HSUs containing LFAs and WTAs are briefly described below, and the distribution of LFAs and WTAs within the unit is discussed:

- The BA consists of a single LFA. It consists of rhyolite lava flow lithologies of the rhyolite of Benham that occur mostly west of the intersection of the Boxcar and West Boxcar faults in southwestern Area 20 (Prothro and Drellack, 1997).

- The CHZCM is present in much of Area 20. It consists of a complex 3-D distribution of lava and zeolitized bedded and nonwelded tuff of the Calico Hills Formation. The HSU consists of several LFAs separated by TCUs. The LFAs within the CHZCM are separated by thick intervals of TCUs, resulting in flow compartmentalization (Prothro and Drellack, 1997), which may limit flow and transport within the CHLFAs enveloped by the CHCZM. In the

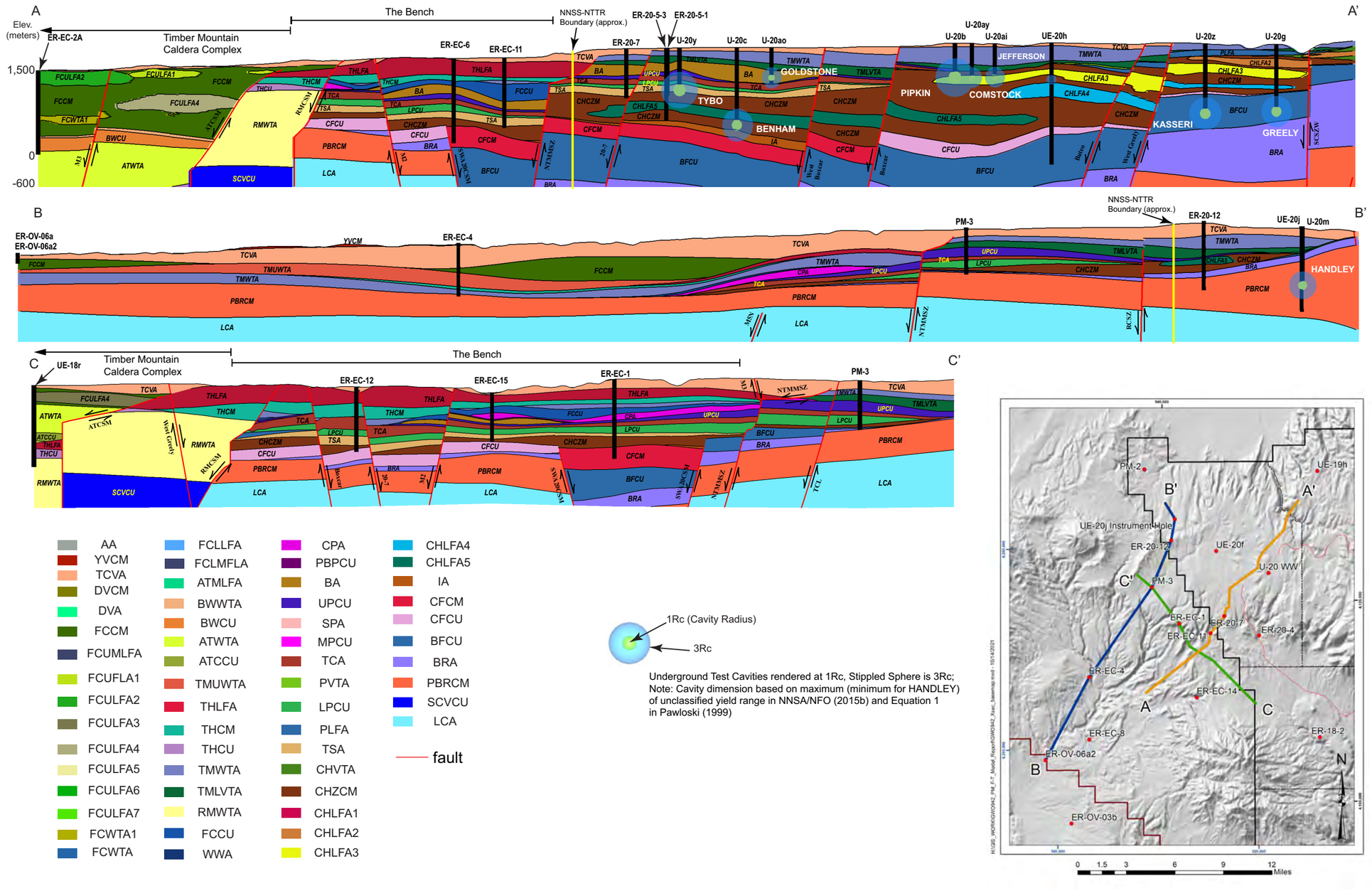

Figure 2-7
Cross Sections of HSUs through the PM-OV HFM Area
Source: DOE/EMNV 2020a

PM-OV HFM, the CHZCM is conceptualized as a TCU and CHLFA 1-5 are explicitly differentiated and removed from the CHZCM.

- The TCA is composed of welded ash-flow of the PM lobe of the Tiva Canyon Tuff beneath PM (DOE/EMNV, 2020a). The HSU occurs beneath much of PM and is present across the Bench and to the west. The unit is saturated on the Bench, partially saturated north of the Northern Timber Mountain moat structure (NTMMSZ) and west of the West Greeley fault, and unsaturated east of the West Greeley fault. The TCA is highly transmissive and is likely the primary flow pathway from HANDLEY to Well PM-3 (e.g., Jackson, 2021).

- The TSA consists of a single WTA composed of welded ash-flow tuff of the PM lobe of the Topopah Spring Tuff in southern Area 20. The TSA is highly transmissive but is limited in areal extent. The unit is saturated in Western Area 20 (DOE/EMNV, 2020a).

- The BRA is composed mainly of LFAs and WTAs consisting mostly of lava and welded ash-flow tuff of the Belted Range Group, which formed and filled the Grouse Canyon caldera. The BRA underlies most of Areas 19 and 20. It is very thick, particularly within the Grouse Canyon caldera, where it is as much as 2,000 m (6,500 ft) thick. LFA is probably the most abundant HGU within the BRA, particularly in Area 20 and the upper and lower portions of the unit in Area 19. The middle portion of the unit beneath Area 19 consists of thick WTA of the caldera-forming Grouse Canyon Tuff (Prothro and Drellack, 1997).

- The TMWTA consists mainly of welded ash-flow tuff of the Rainier Mesa Tuff, where it occurs outside the Rainier Mesa caldera (i.e., extra-caldera). Includes minor amounts of unsaturated welded ash-flow tuff and vitric bedded tuff of the overlying Ammonia Tanks Tuff outside the limit of the TMUWTA (e.g., in eastern PM). Mostly unsaturated, except for deeper portions in the extreme northwest portion of PM, southern portions of the Bench, and in the Oasis Valley basin between the western margins of the TMCC and the Hogback fault.

- The TMLVTA consists mainly of vitric nonwelded and bedded tuffs of the lower portion of the Timber Mountain Group. These include the basal nonwelded portion of the Rainier Mesa Tuff, and nonwelded and bedded tuffs of the underlying tuff of Holmes Road and tuff of Fluorspar Canyon. Locally includes minor intervals of vitric lithologies at the top the underlying Paintbrush Group. Mostly unsaturated, except for western portions on PM where the lower portion becomes saturated.

- The PBRCM is a thick accumulations of tuff and lava that predates the Belted Range Group and is believed to underlie PM. Very little is known about these deep rocks beneath PM. However, exposures of these rocks in other areas indicate that they consist of lava, welded ash-flow tuff, nonwelded tuff, and bedded tuff, forming an unknown distribution of LFAs, WTAs, and TCUs (Prothro and Drellack, 1997).

2.3.3.3 Structural Features

Geologic structural features are an important part of the hydrogeologic framework of the PM-OV groundwater flow system. They define the geometric configuration of the flow domain, including the distribution, thickness, and orientation of rock units. The depositional patterns of many of the geologic units in the area may have been strongly influenced by synvolcanic structures, including caldera faults and some normal faults. Figure 2-1 provides an overview of some of the significant structures incorporated into the PM-OV HFM and their spatial distribution within the PM-OV basin. Geologic structures on the NNSS, NTTR, and surrounding areas were identified on the basis of surface mapping, drilling activities, and geophysical data collection. Section 3.0 of the PM-OV HFM (DOE/EMNV, 2020a) provides more detailed discussion, references and information regarding structural features and their influence on hydrogeologic processes.

The PM-OV HFM includes a total of 105 structural elements that are either faults or calderas. Faulting (such as caldera-related, and basin-and-range), for example, may result in juxtaposition of units with different hydrologic properties or influence depositional thickness. Structures themselves may influence flow patterns by acting as conduits for flow or barriers to flow (Prothro et al., 2009; DOE/EMNV, 2020a).

Included in the structural features identified in the PM-OV HFM are nine calderas. These calderas reflect a variety of geometries and collapse processes. Caldera-collapse processes include the “piston,” down-sag, trap-door, and piecemeal collapse. Some of the calderas seem to have collapsed along pre-existing linear faults, resulting in polygonal boundaries (Kane et al., 1981; Ferguson et al., 1994).

The Bench area is a transitional area between the Silent Canyon Caldera Complex (SCCC) and TMCC, and is an area of high transmissivity located near the southwestern boundary of Area 20. The NTMMSZ forms the northern boundary of a structural bench designated the northwestern Timber Mountain bench by Warren et al. (2000b) but referred to as simply “the Bench” in this and other Phase II documents (SNJV, 2009a). The southern boundary of the Bench is the buried northern structural margin of the TMCC. Collapse of the Bench accounts for the thick accumulation of the rhyolite of Tannenbaum Hill. Within the Bench area, HSUs have been downdropped by more than 305 m (~1,000 ft) by the NTMMSZ. HSUs designated as confining units may leak in the Bench

area because of intense fracturing or faulting that breaches and creates hydraulic pathways through the TCUs (Jackson et al., 2021). The Bench area is the location of much of the Phase II data collection activities and, as indicated by ^{3}H plumes, zone of the flow paths moving beyond the NNSS site boundary.

2.4 Summary of Underground Nuclear Testing at PM

The PM CAUs cover the areas of PM used as underground testing areas of the Nevada Test Site (NTS), now the NNSS, for 27 years between 1965 and 1992 (NNSA/NFO, 2015b); a total of 85 underground nuclear tests were conducted. Their locations are shown in Figure 2-8. Three of these tests (SCHOONER, PALANQUIN, and CABRIOLET) were shallow cratering events and are not considered as part of the UGTA Activity. Although these three CASs are not assigned to the UGTA Activity as defined in the FFACO (1996, as amended), they will be included in the CAU contaminant transport model as sources at the water table for completeness because of known contamination associated with SCHOONER at Well PM-2. The remaining nuclear tests conducted at PM were detonated in deep vertical shafts (from 225 m to 1,452 m depth below ground surface [bgs]). A total of 82 such deep underground nuclear tests were conducted at PM; 33 were at or below the water table, and 49 were above the water table (see Appendix D). Of the tests above the water table, only three are potentially more than a 3 R_c distance (i.e., maximum exchange volume [EV] size) above the water table (based on an unclassified R_c as discussed below), implying that 79 tests had EVs that may be at least partially below the water table.

The term “yield” refers to the total effective energy released in a nuclear explosion and is expressed in terms of equivalent tonnage of trinitrotoluene (TNT) required to produce the same energy release in an explosion. A kiloton (kt) yield represents the energy of a nuclear explosion equivalent to the explosive power of one thousand tons ($1{,}000 \times 1{,}000$ kg) of TNT, and a megaton (Mt) is equivalent to one million tons of TNT. The yield associated with most tests is classified and is therefore reported as an unclassified yield range (NNSA/NFO, 2015b). Similarly, R_c is classified when the yield is classified and an unclassified R_c is estimated based on the maximum of the yield range (minimum for HANDLEY) from NNSA/NFO (2015b) and Equation 1 in Pawloski (1999). In cases where the yield is unclassified, the measured R_c is also unclassified (Zavarin, 2014; Carle et al., 2021).

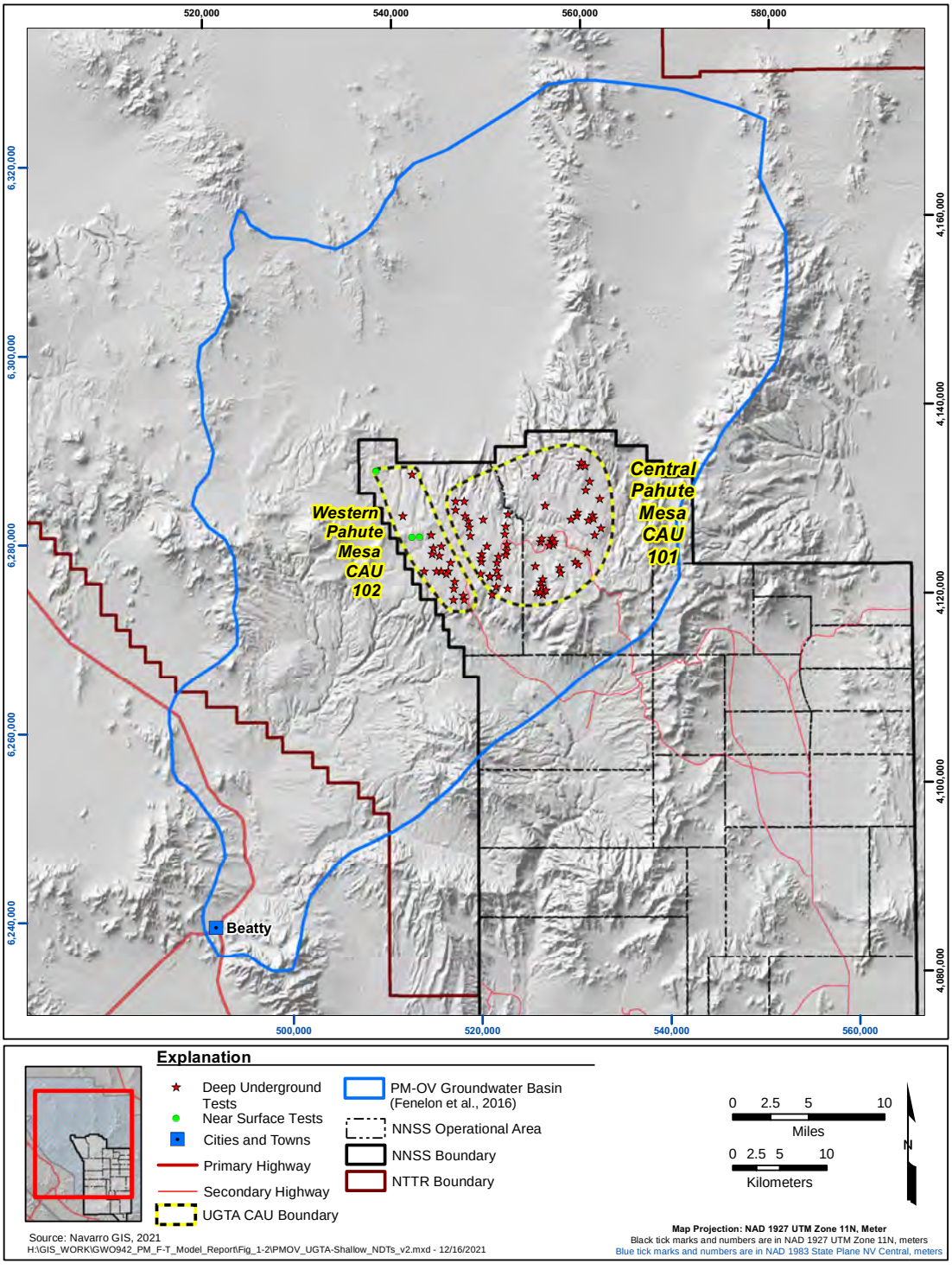

Figure 2-8
Map Showing PM Test Locations

The announced yield or yield ranges for the PM tests are between less than 20 kt to greater than 1 Mt. Three tests had announced yield or yield ranges exceeding 1 Mt (NNSA/NFO, 2015b), with HANDLEY at more than 1 Mt, BENHAM at 1.15 Mt, and BOXCAR at 1.3 Mt. The 82 deep underground tests on PM comprised 60.2 percent of the radiologic inventory from the underground nuclear tests on NNSS as of September 30, 2012, based on curies (Finnegan et al., 2016).
Media contaminated by the underground nuclear tests on PM are geologic formations within the unsaturated and saturated zones. Transport via groundwater in the saturated zone is the potential mechanism of migration for the subsurface contamination away from the PM underground nuclear tests.

Table D-1 in Appendix D identifies each of the nuclear tests in CAUs 101 and 102 along with the emplacement hole name, CAS number, test coordinates, detonation date, yield range, chimney height, land surface elevation, working point (WP) elevation, water-level elevation, and HSU at the WP.

2.5 Geochemistry and Flow Paths

Groundwater flow system evaluations consider groundwater chemistry data because they provide a means for determining the origin, pathway, and timescale of groundwater flow that is independent of estimates based on conventional hydraulic data. Groundwater chemistry and hydraulic data reflect distinct but complementary aspects of a groundwater flow system, and are therefore considered together to develop a consistent, comprehensive, and defensible flow system assessment.
A geochemical evaluation of the PM-OV flow system is presented in the Phase I HDD (SNJV, 2004a), which describes groundwater chemistry data in the western portion of the NNSS, areas upgradient of the NNSS to the north, and downgradient areas as far south as the Amargosa Desert and as far southwest as Death Valley.

A Phase II geochemistry evaluation for the PM-OV flow system was recently completed (Navarro, 2020). The Phase II evaluation focused on a smaller area within the PM-OV flow system where an additional 11 wells were drilled and additional groundwater sampling was performed in support of the NNSS Integrated Groundwater Sampling Plan (DOE/EMNV, 2019a). The overall objective of the evaluation was to reduce uncertainty for the conceptual flow model used for transport modeling.
To accomplish this objective, geochemical and isotopic parameters were examined to build an understanding of potential groundwater sources and flow paths within the vicinity of the Phase II

focus area. Groundwater flow paths identified during Phase I were revised based on the new data. The usefulness of carbon-14 (^{14}C) data for estimating travel times along the potential groundwater flow paths was also evaluated. Geochemical and isotopic data were also used to evaluate the revised groundwater flow system boundaries presented in Fenelon et al. (2016) and hydrologic conceptual model of Jackson et al. (2021).

2.5.1 Flow Path Evaluation

Potential flow paths were identified based on the spatial trends identified using the conservative tracer data. Inverse water-rock reaction geochemical models were developed to determine potential proportions of groundwater from various upgradient wells that may be present in groundwater at a downgradient well, and identify the nature and extent of water-rock interactions that may have affected the composition of the groundwater between the wells. Water-rock interactions were estimated from the reactive species (pH, cations, silica, alkalinity and delta carbon-13 [$\delta^{13}C$]) once the effects of mixing were established. The reactive components considered by these models therefore potentially limit the number of possible mixing models estimated from nonreactive species to a smaller number of models for which plausible water-rock interaction models can also be found.

Refinement to Phase I flow path interpretations resulted from new data from Phase II wells, new data for Phase I and other PM wells (including new delta sulfur-34 [$\delta^{34}S$] results), and revised delineation of PM-OV groundwater basin (Fenelon et al., 2016). The data collected as part of the Phase II geochemistry investigations were combined with data previously reported in Kwicklis et al. (2005) to produce the composite maps of groundwater chlorine (Cl) and delta deuterium ($\delta^{2}H$) shown in Figure 2-9. These flow paths are summarized below, and the locations of wells and place names used in the bulleted discussion of geochemical pathways are shown in Figure 2-10.

- Flow Path 1 represents groundwater flowing from Rainier Mesa along Fortymile Canyon into western Jackass Flats. This path was refined based on recent data to include only a Rainier Mesa source. Previously, this flow path had allowed for the possibility of groundwater flow along Fortymile Canyon from locations as far north as Well UE-19c in Area 19 of PM. This flow path was revised based on hydrologic and geochemical studies at Rainier Mesa (Hershey et al., 2008), which showed that lateral flow from perched systems at Rainier Mesa spread out radially from the high-elevation recharge areas, preventing groundwater from the Area 19 testing locations from flowing south through Fortymile Canyon.

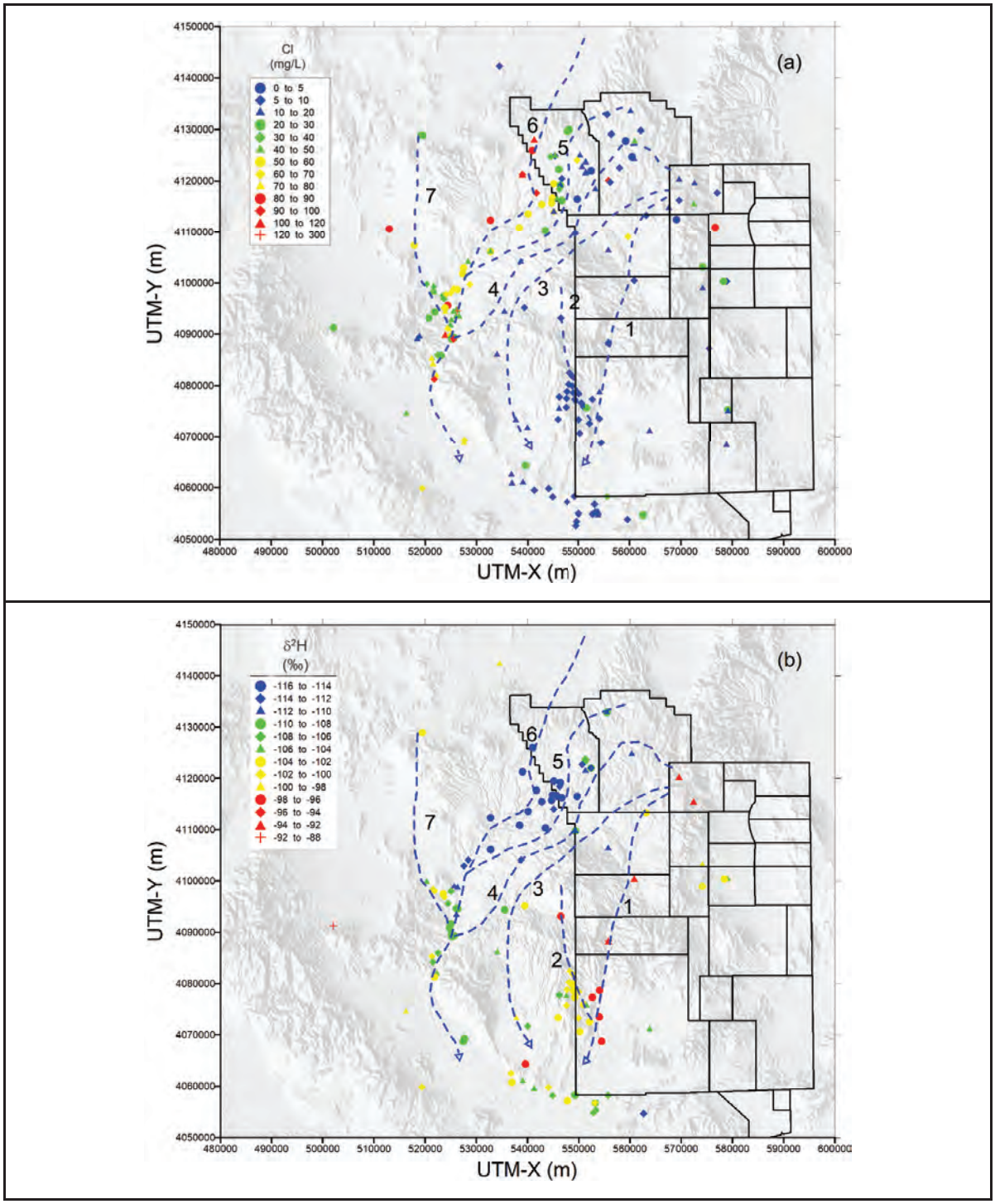

Figure 2-9
Geochemistry Flow Paths Derived Using (a) Cl and (b) δ^2H of Wells and Springs
Source: Navarro, 2020, Figure 9-1

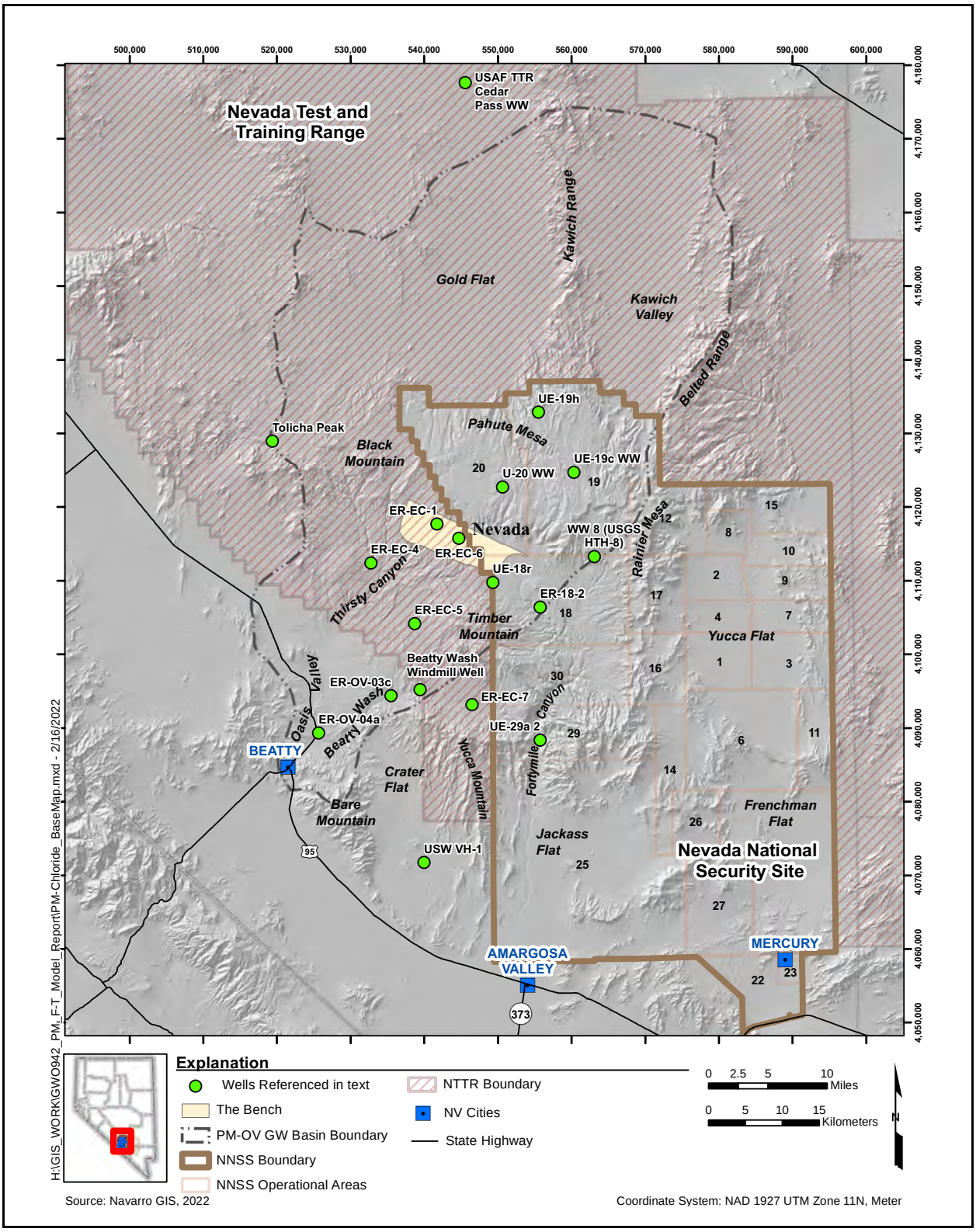

Figure 2-10
Locations of Select Wells and Places for Discussion of Geochemical Pathways

- Flow Path 2 represents an additional flow path southeasterly of groundwater flow from upper Beatty Wash across northeast Yucca Mountain toward Fortymile Wash. Upper Beatty Wash groundwater was represented by ER-EC-7.

- Flow Path 3 represents groundwater flow from the vicinity of south-eastern portion of Area 19 on PM to west-south-west beneath Timber Mountain and lower Beatty Wash and into northwest Crater Flat (represented by Well USW VH-1). Groundwater in lower Beatty Wash (represented by ER-OV-03c and Beatty Wash Windmill Well), with at most a minor fraction contributed by groundwater in upper Beatty Wash (ER-EC-7), was identified as a source of USW VH-1 groundwater. Successful models required the $\delta^{13}C$ constraint be relaxed. ER-OV-03c was previously shown to primarily represent PM groundwater that moved through the vicinity of UE-18r in northern Timber Mountain. Beatty Wash Windmill Well models indicated contribution from WW-8 (up to 84 percent) along with smaller amounts of groundwater from ER-18-2, UE-18r, and ER-EC-7. Alternatively, Beatty Wash Windmill Well can result from PM groundwater mixing with groundwater flow down Beatty Wash or from Timber Mountain recharge depending on whether ER-EC-7 groundwater is interpreted to represent recharge at Timber Mountain in general, or groundwater that is characteristic of upper Beatty Wash.

- Flow Path 4 allows for more westward and even northern flow from the Rainier Mesa area in response to the radial spread of diverted infiltration spreading radially outward from Rainier Mesa, as depicted in Hershey et al. (2008) and DOE/EMNV (2018a). Flow Path 4 also incorporates groundwater from PM flowing southwest along north-west flank of Timber Mountain and lower Beatty Wash toward the Oasis Valley discharge area (represented by groundwater from ER-OV-04a). The model results suggest that most of the groundwater at ER-OV-04a originates from lower Beatty Wash near ER-OV-03c. The sources for groundwater at ER-OV-03c were subsequently investigated and were observed to primarily be groundwater from ER-EC-5 and Timber Mountain recharge and surface runoff down Beatty Wash. Groundwater at ER-EC-5 was observed to be derived predominantly from UE-18r, with smaller amounts of groundwater from U-20 WW and ER-EC-1.

- Flow Path 5 represents groundwater flowing southwest from western PM through Thirsty Canyon to Oasis Valley. Oasis Valley groundwater is represented by ER-OV-3a in the geochemical models used to evaluate this flow path. Mixing of PM groundwater from UE-19h (14 to 65 percent) or U-20 WW (0 to 48 percent) with ER-EC-1 groundwater (29 to 47 percent) north of Thirsty Canyon was required to produce groundwater compositions consistent with ER-OV-03a. Local recharge from surface water runoff, represented by Well UE-29a#2, is a minor contributor (0 to 8 percent) to these models. Flow Path 5 marks the western limit of the unmixed dilute groundwater flowing west from eastern PM. Flow Path 5 trends north–south through southern Area 20 and the Bench, and then turns sharply west in the northwest TMCC. Between Flow Paths 5 and 6 is a mixing zone of intermediate concentration groundwater where these two groundwater systems come together in a hydraulic trough in southern Area 20 of the NNSS before flowing through the Thirsty Canyon Area toward Oasis Valley.

- Flow Path 6 represents western PM groundwater flowing toward Oasis Valley and mixing with groundwater flowing from north of the NNSS. This flow path from Gold Flat into western PM was added to explain the high Cl and chloride and sulphate groundwater observed in western PM. Oasis Valley groundwater was represented by ER-OV-01 in the geochemical models used to evaluate this flow path. Groundwater from ER-EC-6 was identified as the primary source (55 to 93 percent) of ER-OV-01 groundwater. Cedar Pass Well, representing groundwater from north of the NNSS (0 to 31 percent); USAF Tolicha Peak Well #1, representing potential groundwater flow from the northwest corner of the PM-OV basin (0 to 16 percent); local recharge represented by Well UE-29a#2 (0 to 6 percent); and Thirsty Canyon Well ER-EC-4 (0 to 20 percent) were identified as potential minor contributors. Geochemical models developed for ER-EC-6 identified ER-EC-1 and U-20 WW as roughly equal contributors, with a possible minor contribution of groundwater from the vicinity of UE-19h. This flow path is generally consistent with the CAU model beginning in the vicinity of the underground nuclear tests and downgradient. North of the NNSS, the CAU model suggests a water source to the west of the source proposed by the geochemistry in Gold Flat. This inconsistency upgradient of the testing area is not considered significant with respect to the forecasts of downgradient migration.

- Flow Path 7 represents groundwater flowing from northwest Oasis Valley (represented by Well ER-OV-05) as a minor component in some downgradient Oasis Valley groundwaters. Two model categories were developed for this flow path. The first model category required groundwater from north of the NNSS (the Cedar Pass well) and a relatively large component of local recharge (represented by groundwater from UE-29a#2). The second model category required groundwater from the Tolicha Peak area, with a smaller amount of groundwater from Thirsty Canyon (ER-EC-4). Both model categories include a significant mixing fraction of ER-EC-4 groundwater.

The flow paths identified in Navarro (2020) based on evaluation of the geochemistry of groundwater are generally consistent with flow paths identified using hydrologic data (Jackson et al., 2021) and groundwater modeling (Fenelon et al., 2016; Halford and Jackson, 2020).

2.6 Previous Modeling Studies

The flow and transport model presented in this report evolved from and benefited from a succession of studies and models that came before it. These models were developed with the data that existed at the time, and provided insights in where and how new data would help to reduce uncertainties. The new data that was obtained enhanced the models that followed. The current model is the beneficiary of this cycle of modeling, data collection, and model refinement that has been ongoing for more than 25 years.

2.6.1 Pre-Phase I Regional Groundwater Modeling

The initial RN transport calculations were presented by IT Corporation (IT, 1996a and 1996b). The work was intended to provide initial estimates of transport distances and provided an extensive sensitivity analysis to support data collection activities. With no ^{3}H observations downgradient of PM at the time, the transport calculations were probabilistic and yielded very rapid transport velocities. For example, the 50 percent travel distance for the TYBO test was about 30 km in 25 years. Nonetheless, the work of IT Corp. set several precedents that carried into future model studies. These precedents included (1) development of an HFM with HSUs to assign properties to the model grid, (2) decrease of hydraulic conductivity at greater depths in the flow system, (3) calibration to hydraulic head values and known or estimated discharge at basin scales, and (4) a dual-porosity transport conceptual model with primary flow in fractures and diffusion into the matrix.
A shortcoming of the IT Corp. simulations was a simplified HFM that showed just one HSU (a volcanic aquifer) of uniform properties between the TYBO test and the discharge at Oasis Valley. This model also showed that the direction of flow from most tests on PM was southwest to Oasis Valley with the exception of some tests in central to eastern Area 19 that followed a path to the east of Timber Mountain.

2.6.2 Phase I Modeling Study

Beginning in 1995, DOE embarked on an extensive six-year data collection program that involved drilling wells, conducting tests, and interpreting results. DOE drilled seven wells on the NNSS within what is now the PM-OV groundwater basin; these comprised three drill holes at the ER-20-5 location associated with observations of RNs downgradient of a test, three wells for Bullion Forced Gradient tracer experiment (IT, 1998), and Well ER-18-2 northeast of Timber Mountain. The drilling and sampling of the wells at ER-20-5 led to the recognition of colloid facilitated transport of plutonium (Pu) (Kersting et al., 1998) and to the continued development of the conceptual model that thermally driven convection in test cavities and chimneys could release RNs into geologic units between the test and water table. In addition to the onsite wells, DOE also drilled an additional seven wells on the NTTR downgradient of Area 20, and through the U.S. Geological Survey (USGS), drilled 12 wells in publicly accessible environment in and northeast of Oasis Valley. Aquifer testing, sampling, and other data collection activities were performed as part of this data collection program. The Phase I CAU model (SNJV, 2006, 2007, and 2009b) utilized the large amount of new data from the 26-well drilling

program to refine estimates of groundwater flow and RN transport from underground nuclear tests on PM. Several shortcomings of the Phase I modeling included a model with uncertain boundary fluxes in some areas, HFM uncertainty in the regions downgradient of the testing areas, and a general lack of ^{3}H observations in wells with the exception of the ER-20-5 well locations. The Phase I model was discussed briefly in Section 1.1.1 as it related to the reasons the Phase I data and model were not deemed adequate and the resulting decision to move forward with a Phase II data collection and model for PM. The Phase I model helped to refine uncertainties that needed to be addressed, which led to the development of the Phase II CAIP (NNSA/NSO, 2009) and an additional round of drilling and data collection.

2.6.3 Modeling Studies Performed during Phase II

The Phase I model and subsequent CAIP led to the drilling, testing, and sampling of 11 additional wells (six within the boundaries of the NNSS and five on the NTTR). These new wells provided geologic and hydrologic data as was typical of previous wells, but the relative nearness of most of these wells to each other facilitated a series of multiple-well aquifer tests (MWATs) (Garcia et al., 2017). In addition, the new wells were positioned to intercept contaminant plumes and for the first time, provided direct evidence of RN migration that could be used to calibrate a transport model. The new data provided the opportunity for numerous modeling studies that have informed the PM CAU model presented in this report.

Over the past decade, several modeling studies of the PM groundwater system have been performed by USGS and Los Alamos National Laboratory (LANL) as part of PM Phase II data collection and interpretation activities. These supporting modeling studies were performed at various scales including regional, basin, and local scales. The regional model provides the broad hydrogeologic context for the smaller CAU-scale model. The local scale models focus on small-scale (relative to the CAU) processes such as high-resolution flow and transport in the Bench area subregion that cannot be simulated at the CAU scale. Summary descriptions of the groundwater flow models are presented in this section in the order of when the studies were performed.

2.6.3.1 USGS PM-OV Basin Delineation Model

Fenelon et al. (2016) delineated the PM-OV groundwater basin area based on regional water-level contours, geologic controls, balancing of groundwater discharges in the PM-OV groundwater basin and adjacent basins against available water from precipitation, and geochemical considerations. A two-dimensional (2-D) numerical model of the PM-OV basin area was constructed to ensure that groundwater data from the PM-OV groundwater basin were internally consistent with the regionally defined basin boundary. Internal consistency was tested by calibrating the numerical model of groundwater flow to water-level, land-surface, transmissivity, and discharge observations in the PM-OV groundwater basin. Estimated recharge rates and transmissivities in the numerical model also were constrained to expected values from the conceptual model.

A single-layer, groundwater-flow model was constructed to simulate steady-state water levels within the delineated PM-OV groundwater basin boundary (Figure 2-11) using MODFLOW (Harbaugh et al., 2000). The PM-OV basin flow model was divided areally into 308 rows and 217 columns of uniform square cells that are 300 m (984 ft) on a side. The 2-D model conceptually extended from the water table to the base of the aquifer system, although the specific thickness of the aquifer was not defined. Lateral boundaries were simulated as no-flow. The only exception was a single specified head in the southernmost cell of the Oasis Valley discharge area. The boundary simulated the subsurface discharge from Oasis Valley to Amargosa Desert through a narrow section of saturated alluvium.

The 5,900 ac-ft/yr of basin flow (Reiner et al., 2002; Fenelon et al., 2016) was simulated as specified discharges at locations defined using the maps of groundwater discharge rate by ET unit created by Reiner et al. (2002). A recharge distribution was estimated for the USGS PM-OV basin delineation model based on a conceptual model that areas with higher precipitation rates have higher recharge rates and precipitation falling on low-permeability rocks moves laterally until it can infiltrate more permeable materials. The recharge and transmissivity were parameterized throughout the model using pilot points (RamaRao et al., 1995). Recharge rates and transmissivity were interpolated from pilot points to model cells with kriging (Doherty et al., 2010).

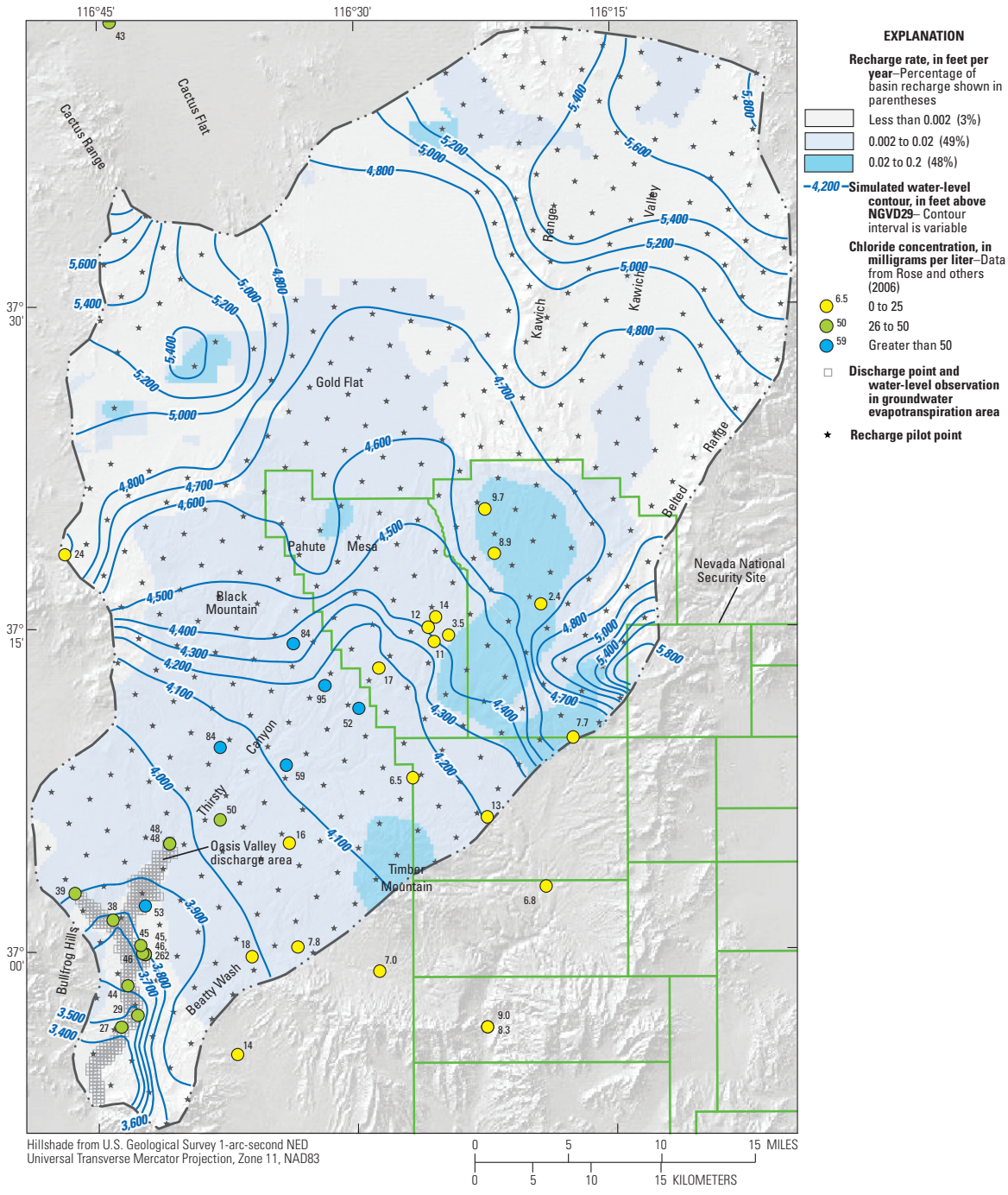

Figure 2-11
PM-OV Chloride Concentrations and Simulated Recharge Rates

Note: Simulated using calibrated flow model; also included are simulated water levels, discharge area, and recharge pilot points.

Source: Fenelon et al., 2016, Figure 9

The total recharge amount for the PM-OV groundwater basin was simulated as 6,000 ac-ft/yr (7,393,232 cubic meters per year [m^3/yr]), which includes 100 ac-ft/yr of subsurface discharge that occurs through a narrow section of saturated alluvium at the terminus of Oasis Valley (Fenelon et al., 2016). Figure 2-11 presents the distribution of recharge simulated by the numerical model. Recharge exceeds 25 millimeters per year (mm/yr) (1 inch per year [in./yr]) in the highest elevation of eastern PM and lower (typically 2 to 5 mm/yr) (0.08 to 0.3 in./yr) in the lower elevations at the western end of PM.

Groundwater chloride concentrations were consistent with the recharge as distributed in the USGS PM-OV basin delineation model (Figure 2-11). The lowest concentrations occurred on eastern PM and to the south near Timber Mountain. These areas have relatively high rates of recharge, resulting in less evapo-concentration of initial chloride in precipitation (Cooper et al., 2013). Conversely, to the west, chloride concentrations are 10 to 30 times higher and simulated recharge rates are about 10 times lower. Downgradient of the NNSS and into Oasis Valley, chloride concentrations are intermediate, suggesting mixing of the two groundwater types (Rose et al., 2006).

The USGS PM-OV basin delineation model demonstrated that the hydrologic data in the PM-OV groundwater basin are internally consistent with the delineated “nearly” no-flow basin boundary. A small amount of groundwater flows out of the basin in the alluvium south along the Amargosa River and may flow across the PM-OV model boundaries, particularly south of Timber Mountain, but the amount of the flow is small in comparison to the discharge in Oasis Valley. The simulated water levels compared well to measured water levels and the simulated flow through the PM-OV groundwater basin was consistent with the groundwater budget in the PM-OV and adjacent basins. Water generally flows from north to south–southwest, discharging at Oasis Valley. Flow is southwesterly from the NNSS to Oasis Valley and is well-constrained by data (Figure 2-12). The simulated and measured transmissivities also compared favorably. Simulated transmissivities were especially high in the Bench area, where they locally exceeded 100,000 ft^2/day. Two high-transmissivity and high-velocity areas were simulated from southwest Area 20 to and through the Bench area (Figure 2-13).

The work of Fenelon et al. (2016) provided a recharge distribution across the entire PM-OV groundwater basin determined as part of the model calibration. The delineation of the boundaries of

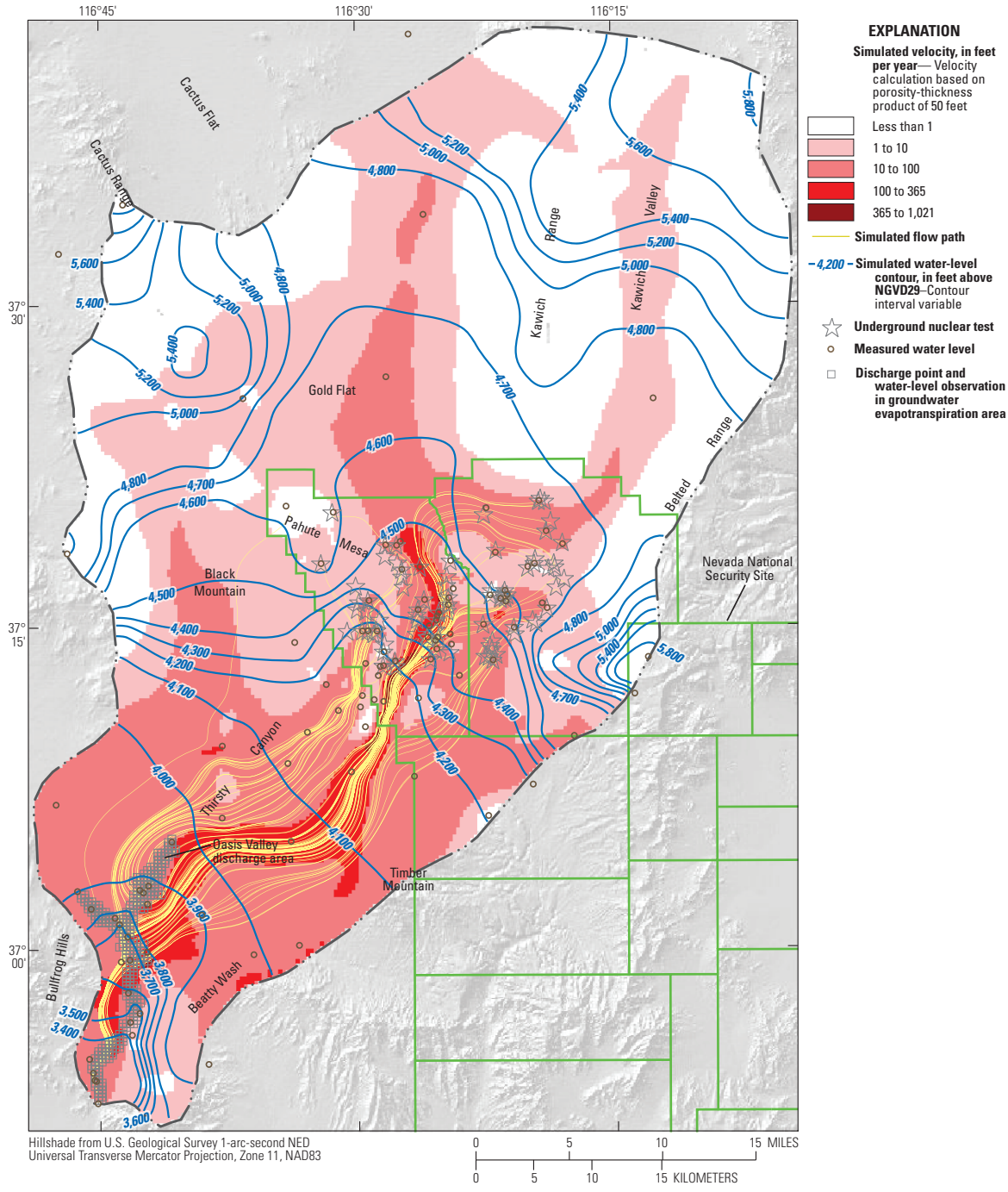

Figure 2-12
PM-OV Groundwater Flow Paths Simulated by the Basin Delineation Model
Note: Also included are the groundwater velocity field and simulated water levels.
Source: Fenelon et al., 2016, Figure 13

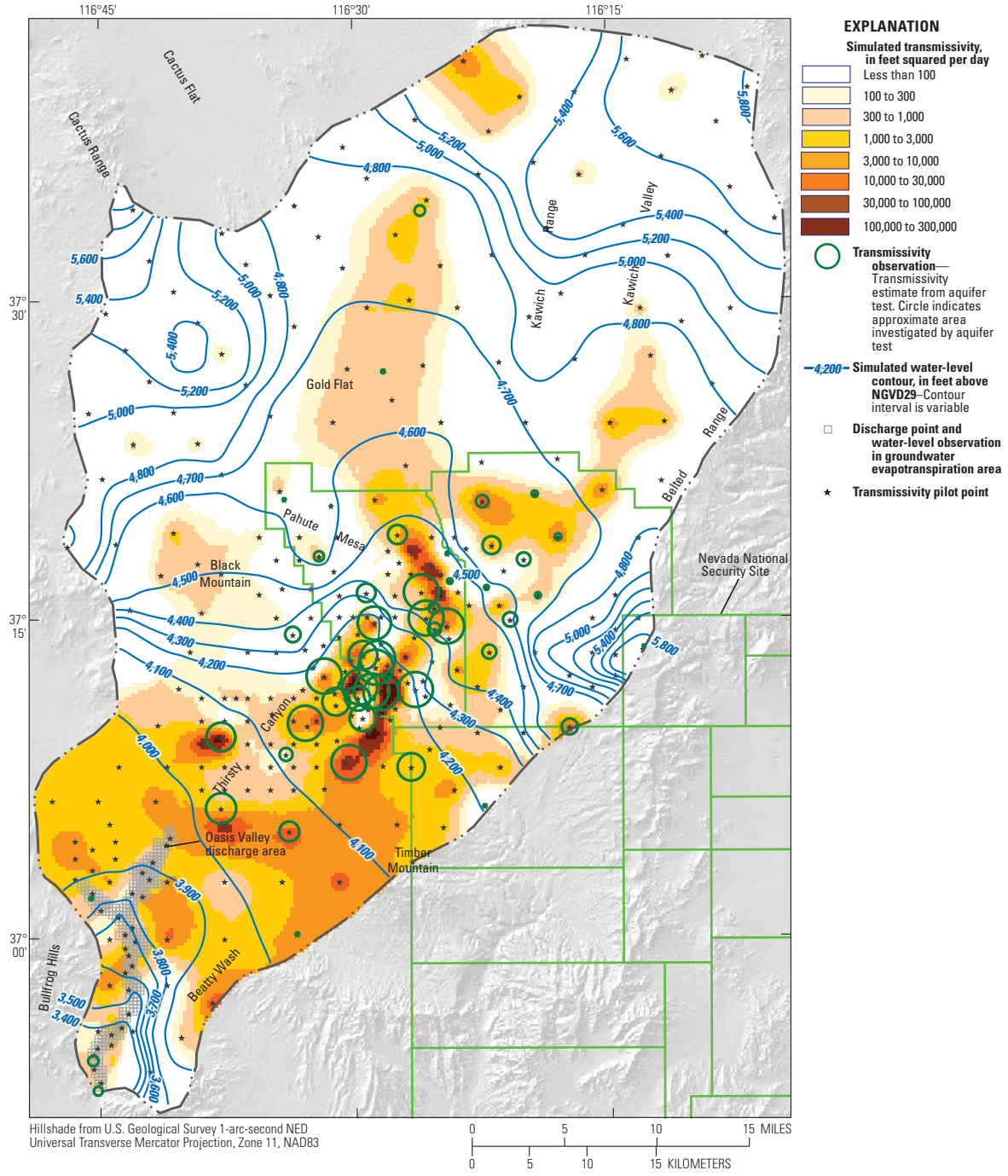

Figure 2-13
PM-OV Transmissivity Distribution Simulated by Basin Delineation Model
Note: Also included are transmissivity observations, simulated water levels, discharge area, and transmissivity points.
Source: Fenelon et al., 2016, Figure 6

what can be effectively treated as a closed basin (with the small outflow noted earlier) simplifies the definition of boundary conditions in the PM CAU model. The 2-D delineation model provides a good comparison for flow paths, although it does not provide a flow path from any underground test to the location of Well PM-3, where the presence of low levels of ^{3}H suggests a nearby plume. The flow paths from the delineation model show that previous calculations of a flow path from Area 19 along the eastern side of Timber Mountain does not exist. This was corroborated by geochemical analyses published by Navarro (2020) that evaluated the most recent groundwater sample data.

2.6.3.2 USGS Volcanic Rock Characterization Model

Garcia et al. (2017) characterized bulk hydraulic properties of volcanic rocks using an integrated analysis of 16 MWATs. Drawdowns from 16 MWATs were estimated and distinguished from natural fluctuations in more than 200 pumping and observation wells using analytical water-level models. Drawdown was detected at distances greater than 3 miles from pumping wells and propagated across HSUs and major structures. Hydraulic properties of aquifers and confining units were estimated by simulating drawdowns from multiple aquifer tests using Phase II PM HFM (NSTec, 2014) and multiple groundwater-flow models. Individual models for each MWAT were simultaneously calibrated using identical hydrologic properties.

The hydraulic properties estimated included hydraulic conductivity, specific yield, and specific storage. The properties were estimated by simulating drawdowns with 11 groundwater-flow models from pumping during the 16 MWATs. The groundwater-flow models used a single HFM to estimate identical hydraulic properties in the HSUs for each model. The multiple groundwater-flow models allowed grid refinement near each pumping well and different pumping schedules specific to each aquifer test.

The drawdowns were simulated with MODFLOW (Harbaugh et al., 2000). All 11 well-site models shared a common lateral extent of about 400,000 ft (76 mi, 122 km) on a side. All well-site models were discretized into 119 rows of 128 columns. Grids of the 11 well-site models differed because each was locally refined to a 33-ft (10-m) sided cell at each pumping well. All 11 well-site models were discretized vertically from 1,700 ft (518 m) below sea level to 4,200 ft (1,280 m) above sea level, which approximated the water table. Well-site model grids laterally extended about 160,000 ft (~49 km) beyond the Phase II HFM edge to avoid the influence of boundary effects at pumping and

observation wells. All well-site models were discretized identically into 29 layers with vertical discretization made finer between 2,300 and 3,700 ft (~701 and 1,128 m) above sea level (layers 5–20) because most wells were completed between these depths. All the external model boundaries were specified no-flow boundaries.

The existing 55 HSUs in the Phase II HFM were subdivided and grouped into 22 modified HSUs so that groundwater-flow models could replicate observed hydraulic responses between pumping and observation wells. The Phase II HFM was modified through an iterative process using observed drawdowns and hydraulic-property estimates from aquifer testing and insights from groundwater-flow model results. Hydraulic properties were distributed with pilot points.

Simulated and observed drawdowns compared well and simulated transmissivities were similar to values derived from single-well aquifer tests. Most modified hydrostratigraphic units (mHSUs) evaluated were found to be hydraulically similar in the area investigated by the 16 MWATs. Hydraulic-conductivity distributions in the mHSUs typically spanned several orders of magnitude. Ranges of hydraulic conductivity in mHSUs overlapped greatly among many mHSUs. Heterogeneous hydraulic-property distributions within mHSUs and radial signal propagation from aquifer tests indicated that hydraulic distinctions among most mHSUs are limited.

Distinct areas of lower- and higher-than-average transmissivity were identified in the area investigated. Low transmissivities of less than 1,000 ft^2/day were simulated between well sites ER-EC-6, ER-EC-12, and ER-EC-15. A relatively transmissive feature was simulated between well sites ER-EC-1 and ER-EC-13, where transmissivities generally exceeded 10,000 ft^2/day (Figure 2-14). Some structural features such as the NTMMSZ and Timber Mountain caldera complex structural margin (TMCCSM) were identified to possibly have increased transmissivity. More than 90 percent of the transmissivity in the area investigated was within 2,000 ft (~610 m) of the water table. However, at some locations, deeper transmissive intervals were identified (e.g., at the ER-EC-11 well site, where 70 percent of the transmissivity was between 1,000 and 3,000 ft (~305 and 914 m) below the water table).

The model developed by Garcia et al. (2017) highlights the 3-D heterogeneous nature of the volcanic rocks in the region immediately downgradient of the testing areas in the southern portion of Area 20. It is important to note that the HFM utilized by Garcia et al. (2017) was simplified by lumping a

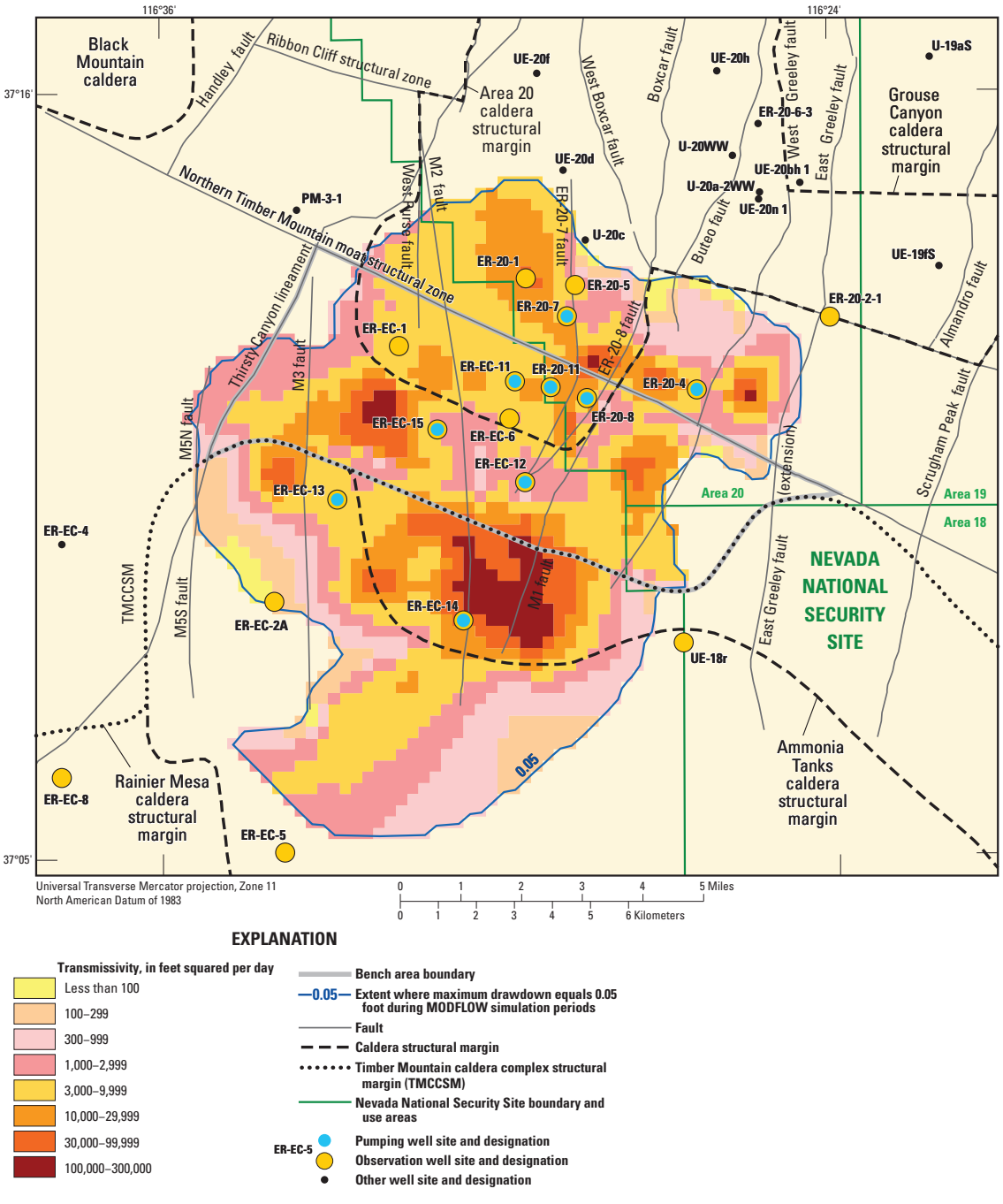

Figure 2-14
Simulated Transmissivity Distribution from the Integrated Groundwater-Flow Model in the Area Investigated by the 16 MWATs
Source: Garcia et al., 2017, Figure 25

number of similar HSUs together while adding a couple of low-permeability HSUs primarily to hydraulically separate two vertical zones near a multi-completion well. As well, their model treats faults as only offset to unit on either side and showed that calibration of the model to drawdown data was possible without treating fault zones a separate flow units within the HFM. The model calibration utilized transient responses only and did not attempt to incorporate ambient flow via steady-state heads. It will be difficult for the PM CAU model to match the resolution of Garcia et al. (2017) when simulating hydraulic responses to the MWATs.

2.6.3.3 LANL AMANZI Bench Area Model

Lu et al. (2021) created a high-resolution groundwater flow and transport model for a subregion of PM to provide insight about the possible origins of the ^{3}H at observation wells. The model domain included all the Area 20 nuclear tests in western PM; the Bench area where most of the PM CAU Phase II wells were drilled; and the northwestern part of the TMCC, which is expected to lie along RN transport paths.The model included all HSUs and structural features (faults, caldera boundaries, structural zones) contained in the HFM documented by NSTec (2014).

The groundwater flow system was modeled with AMANZI, a high-performance computing (HPC) code developed by the DOE EM division for use on legacy (Cold War-era) environmental sites. The model area was roughly 35 km in the north–south direction and 20 km in the east–west direction. The model included more than 7 million nodes, with horizontal grid spacing of 100 m and a vertical grid spacing of 25 m or less. The lateral boundaries were assigned hydrostatic head based on the estimated water table elevations surrounding the model, and the upper boundary was assigned a steady-state flux derived from infiltration modeling (Middleton et al., 2019). A no-flow condition was specified at the bottom of the model. Hydraulic properties were estimated for each HSU and structural feature within the model domain by calibrating the model to drawdowns measured during Phase II well-development and testing activities along with observations of steady-state hydraulic heads. Satisfactory matches to the steady-state heads and most of the cross-hole hydraulic responses during hydraulic testing were achieved, although the fit to some cross-hole responses was limited by the accuracy of the HFM. The groundwater trough present in Area 20 was simulated by a combination of flow barriers caused by the low-permeability Purse fault and West Purse fault on the west, and the low permeability West Boxcar fault on the east, combined with the presence of the

high-permeability ER-20-7 fault, which creates a drain for groundwater flow toward and across the Bench.

Flow pathlines from nuclear test locations indicated that RNs from all but a few tests will pass through a line of wells between ER-EC-1 on the west and ER-20-4 on the east (Figure 2-15). Tritium transport calculations were performed using particle tracking and a convolution-based transport code. The transport simulations included the effects of radioactive decay of ^{3}H and matrix diffusion. The model was calibrated to the ^{3}H observations through a combination of manual adjustments to the parameters and parameter estimation using the PEST parameter estimation code (Doherty, 2018).

The flow and transport model identified the extent of ^{3}H contamination in Area 20 exceeding the 20,000 picocuries per liter (pCi/L) MCL. The model simulated that several extensive ^{3}H plumes exist in Area 20 at the present time that have not been previously observed in monitoring wells (Figure 2-16). These plumes were distinct because of the isolated locations of the nuclear tests that created them and because of flow separation associated with faults. However, the separate plumes begin to coalesce toward the Bench because of the convergent nature of flow in Area 20 caused by the hydraulic trough, so that almost all present and future contamination associated with Area 20 nuclear tests will pass across a line of existing wells defined by ER-EC-01 on the west and ER-20-4 on the east. Another important finding was that the extent of ^{3}H contamination, as defined in a regulatory sense by the 20,000-pCi/L boundary, is likely to already be close to its furthest downgradient extent (see Lu et al., 2021, Figures 65, 66, and 67) because radioactive decay will approximately offset its further migration due to groundwater flow.

The AMANZI model demonstrated for the first time the ability to calibrate a model of the PM CAU to both groundwater flow observations and RN (^{3}H) observations. This model used a conceptual model that treated faults as unique flow zones within the HFM. This differs from the work of Garcia et al. (2017) and Fenelon et al. (2016). Lu et al. (2021) were able to use supercomputer capabilities at LANL to simulate a large number of nodes (about 7 million) at a finer resolution than is possible with PM CAU Model. However, the model domain of Lu et al. (2021) was smaller than the PM-OV groundwater basin and suffered from uncertainty related to boundary fluxes. Their work provides a

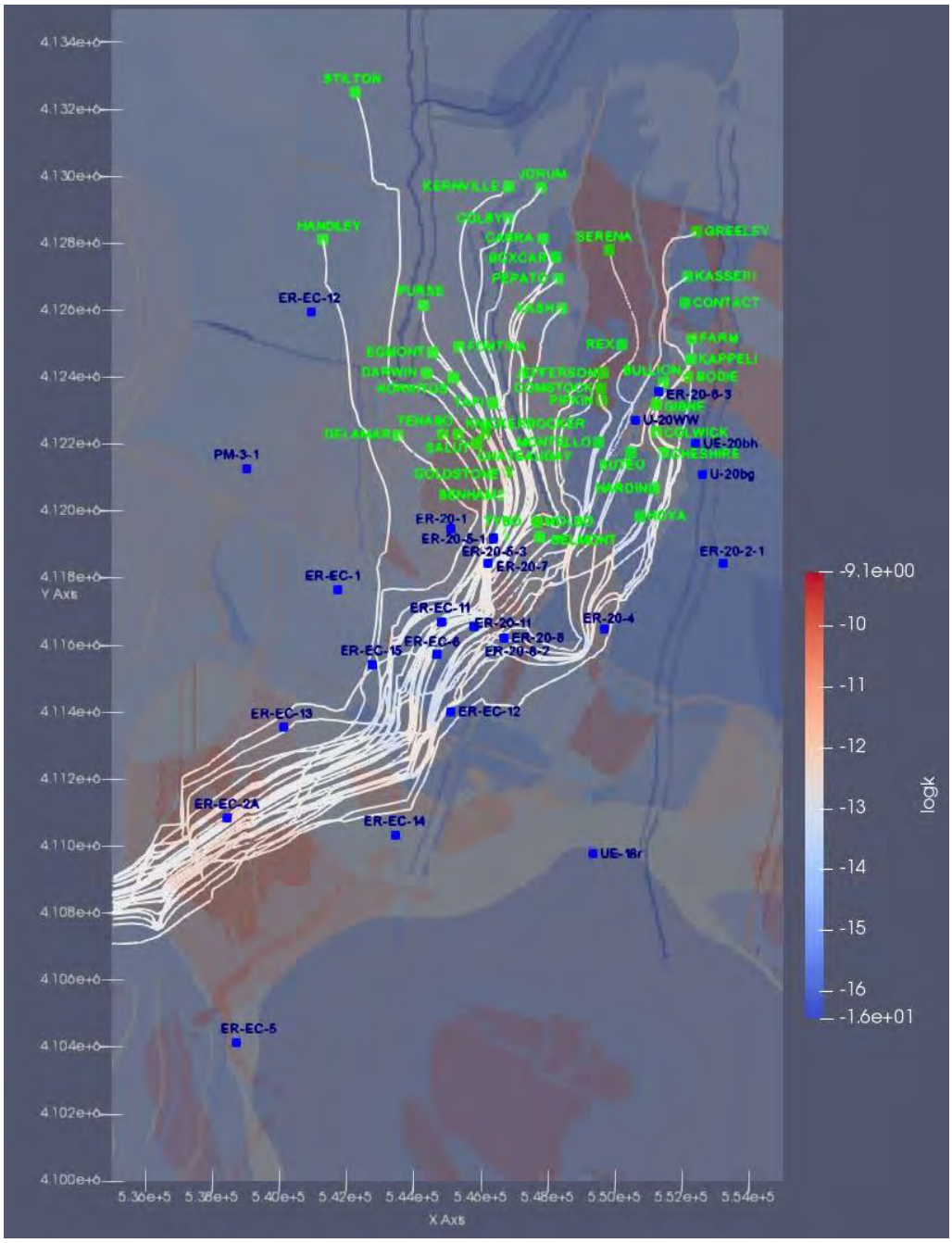

Figure 2-15
Flow Pathlines Simulated by the LANL AMANZI Bench Model
Source: Lu et al., 2021, Figure 63

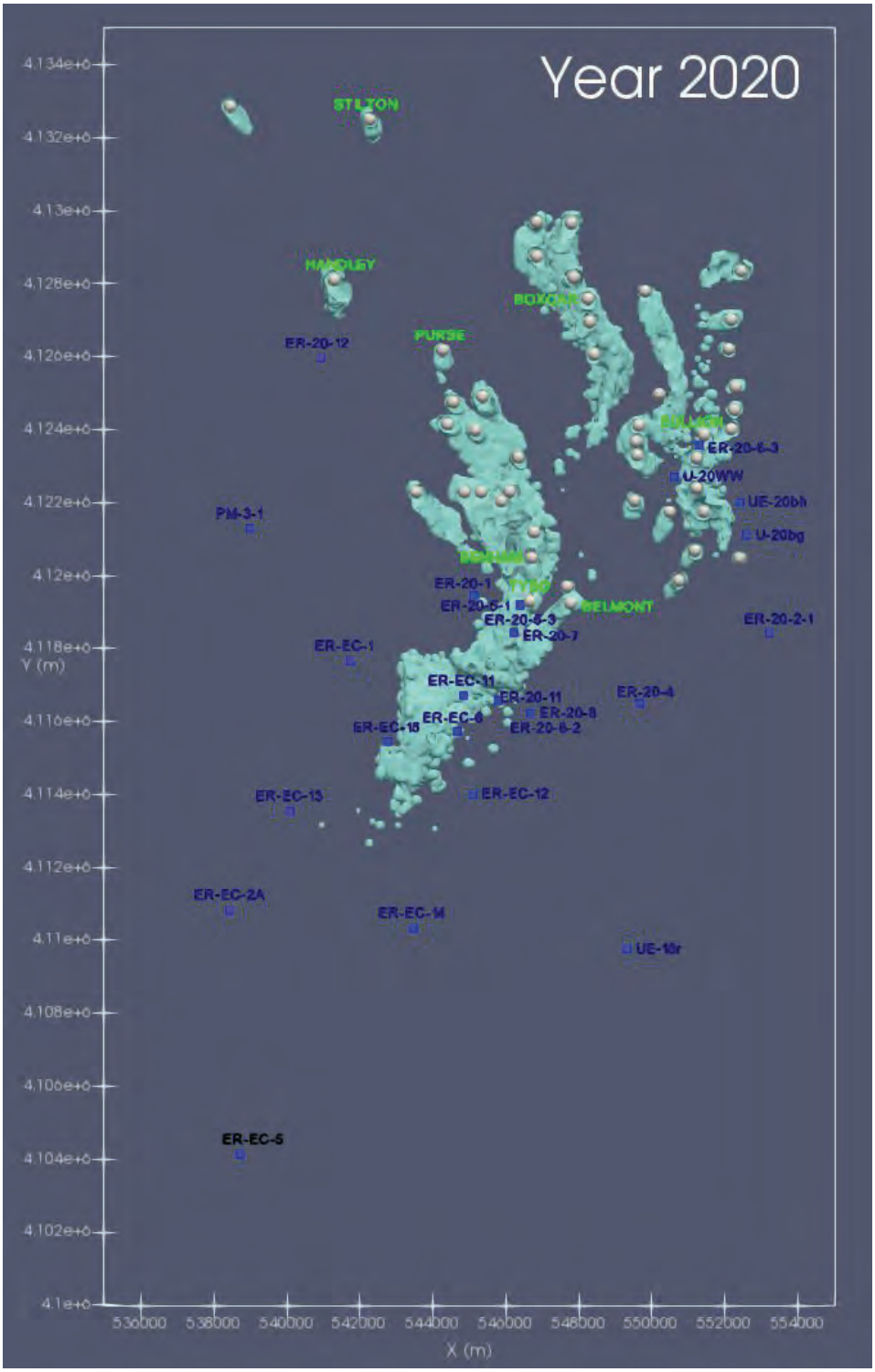

Figure 2-16
Simulated Distribution of ^{3}H above the 20,000-pCi/L MCL as of 2020
Note: White spheres are nuclear test locations, and blue squares are current observation wells.
Source: Lu et al., 2021, Figure 66

nice corroboration of the results in this report, except in the vicinity of Well PM-3 where the AMANZI model was unable to simulation RN transport to that location.

2.6.3.4 USGS Death Valley Regional Groundwater Flow System Model

Halford and Jackson (2020) characterized groundwater flow and development in four groundwater basins of the Death Valley Regional Flow System (DVRFS) using calibrated groundwater-flow models. The main purpose of the study was to characterize predevelopment groundwater flow and evaluate the effects of pumping on water levels with special reference to Devils Hole. Water levels in Devils Hole were a special focus because endangered Devils Hole pupfish (Cyprinodon diabolis) are affected by water-level declines. A simplified hydrogeologic framework was developed that consisted of four hydraulically unique HGUs: (1) basin fill; (2) carbonate rocks; (3) volcanic rocks; and (4) low-permeability granitic and siliciclastic rocks. HGUs and division of carbonate and volcanic rocks between shallow and deep were supported by aquifer tests and specific-capacity estimates. More than 90 percent of field-estimated transmissivity occurred within 1,600 ft (~487.7 m) of the water table.

Recharge and hydraulic-property distributions were estimated by simultaneously calibrating four 3-D numerical groundwater models of the study area. Multiple models with identical spatial extents were constructed to simulate and differentiate the effects of predevelopment flow; changes from groundwater development (two models); and changes from a large-scale MWAT.

All groundwater models shared a common domain, gridding, hydrogeologic framework, and hydraulic properties. Model domains extended laterally to the edges of the study area (Figure 2-17). Each model was divided areally into 268 rows of 221 columns of variably spaced, rectangular cells that ranged from 820 ft (250 m) to 4,920 ft (1,500 m) on a side. Furnace Creek area, Devils Hole area, Rainier Mesa, and Yucca Flat were areas of finer discretization. The groundwater model grids were divided into six layers and coincided with the grid of the hydrogeologic framework, which extended vertically from the water table to 3,300 ft (1,000 m) below sea level. Heterogeneous hydraulic-property (and recharge) distributions were estimated using pilot points.

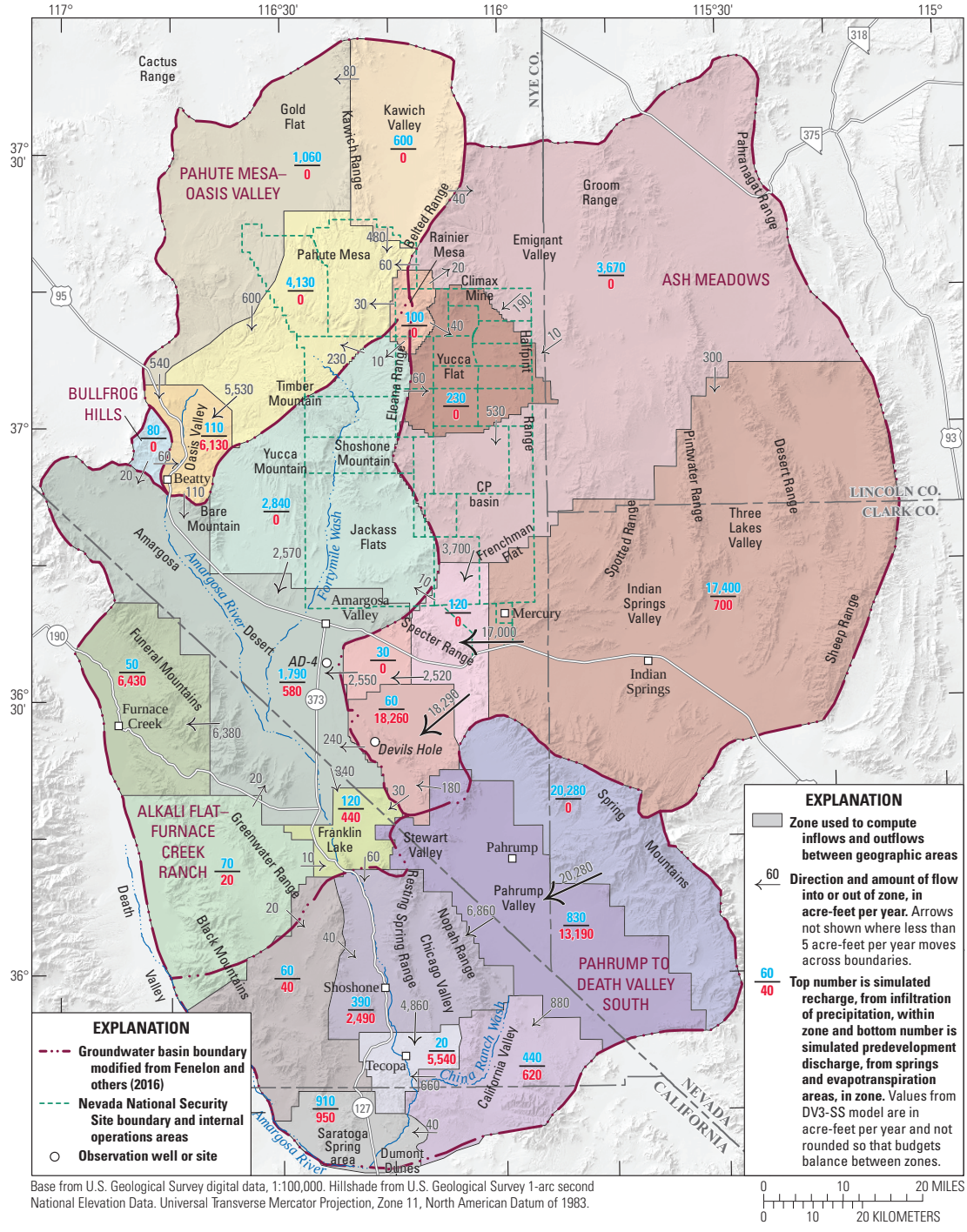

Figure 2-17
Predevelopment Water Budgets within and between Geographic Areas in the Death Valley Regional Flow System
Source: Halford and Jackson, 2020, Figure 88

The four groundwater basins were subdivided to estimate water budgets where estimated flow rates were needed. Groundwater-flow estimates were used to constrain groundwater-velocity estimates from underground nuclear tests in CAUs at the NNSS. Estimated flow rates also inform water availability in subareas. Groundwater basins were divided into subareas, where flow across subarea divides was minimal, to minimize sensitivity of flow-rate estimates to specific divides. Groundwater-flow equations were solved using the USGS finite-difference model, MODFLOW (Harbaugh, 2005). The four coupled (stress-response) groundwater models were calibrated simultaneously using the PEST code (Doherty, 2018).

The numerical modeling determined most of the recharge in the PM-OV groundwater basin is derived from the highlands of PM. Total simulated recharge in the PM-OV groundwater basin was 5,900 ac-ft/yr. More than 90 percent of the groundwater discharging in Oasis Valley is derived from recharge sourced at the highlands of PM and Timber Mountain. Total simulated discharge in Oasis Valley is 6,130 ac-ft/yr.

Flow paths were simulated for 296 of the 828 underground nuclear tests on the NNSS that were detonated below the water table or less than 328 ft (100 m) above the water table. Simulated advective-flow distances and velocities from underground nuclear tests were found to be within the range of advective transport calculations from ^{3}H data and previous RN transport investigations. Boundary conditions and flow rates from the regional model in the study were considered plausible for local-scale flow and RN transport models. Simulated 165-year groundwater flow paths (Figure 2-18) did not extend into the Oasis Valley discharge area, and effects of regional pumping on advective transport were found to be negligible.

This updated regional model provides additional corroboration for the PM CAU Model presented in this report. It corroborates the work of Fenelon et al. (2016) that it is unlikely there is a flow path from Area 19 along the eastern side of Timber Mountain. As with the previous models, the regional model was unable to identify a flow path from an underground test to the location of PM-3.

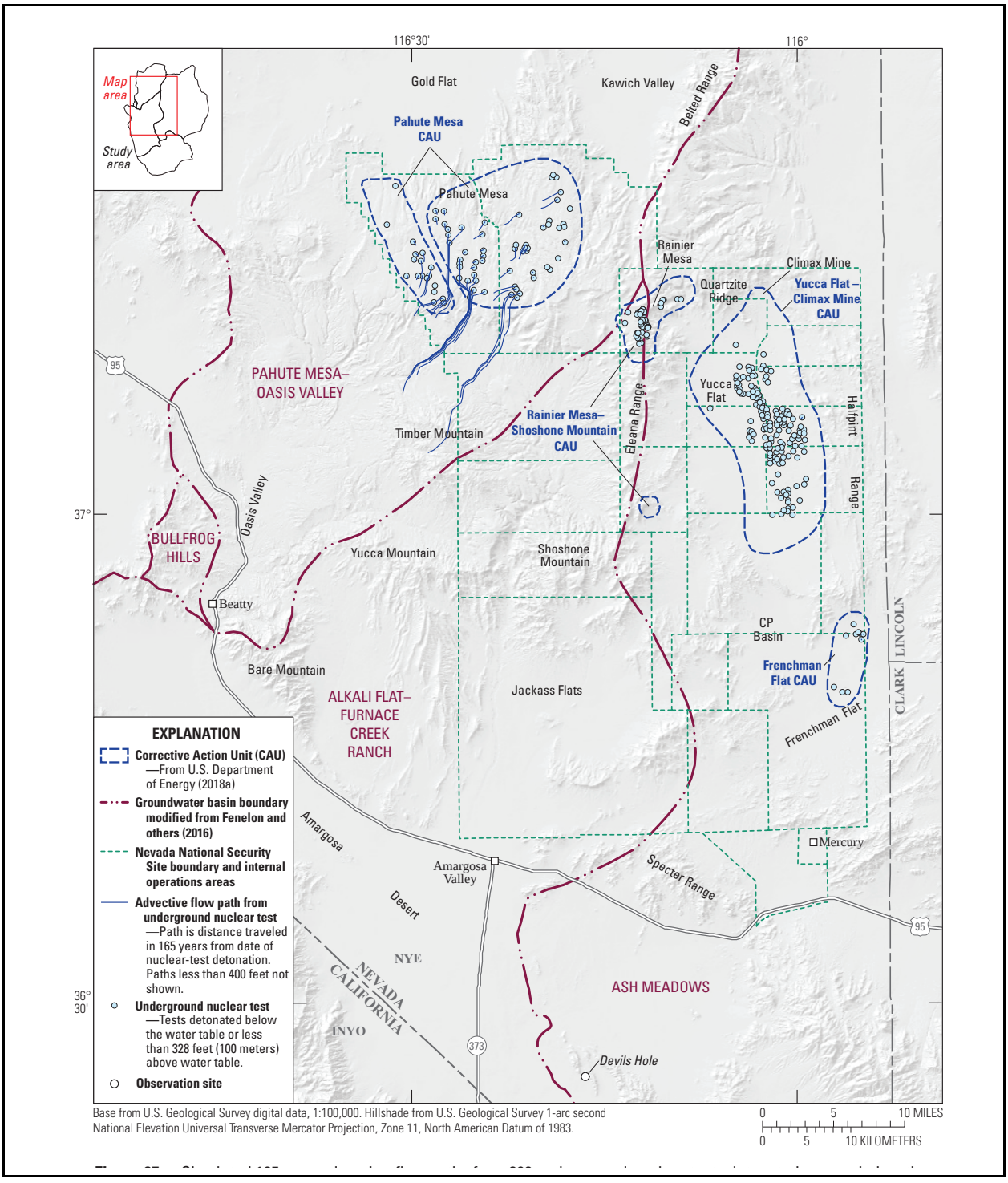

Figure 2-18
Simulated 165-Year Advective-Flow Paths by DVRFS Model from 296 Underground Nuclear Tests Detonated near or below Water Table in NNSS

Note: Simulated flow paths do not coincide with ^{3}H plumes and do not represent ^{3}H plumes.
Source: Halford and Jackson, 2020, Figure 95

2.6.3.5 USGS HANDLEY Flow and ^{3}H Transport Model

Jackson (2021) developed a quasi-3-D groundwater-flow and ^{3}H-transport model focused on a localized area to estimate hydraulic and transport properties between the HANDLEY test and boreholes ER-20-12 and PM-3, and to simulate ^{3}H migration from the HANDLEY test. Geologic, hydrologic, and ^{3}H data were used in the model to infer the location of permeable pathways near and downgradient from the HANDLEY test. Recharge, hydraulic-conductivity, specific-yield, specific-storage, and effective-porosity distributions were estimated with the numerical model by fitting simulated water-level altitudes, vertical-head differences, aquifer-test transmissivities, ^{3}H concentrations, and drawdowns in wells PM-3-1 and PM-3-2 to measured equivalents. Drawdowns were estimated in Wells PM-3-1 and PM-3-2 in response to groundwater withdrawals during the drilling of borehole ER-20-12.

The model domain is a flow path that is 2,000 ft wide, 28,400 ft long, and 2,000 ft deep; the path begins 2,000 ft upgradient from the HANDLEY test at borehole U-20m and extends 2,600 ft downgradient from borehole PM-3. The model uses a uniform horizontal discretization of 200 ft and vertical discretization of 141 ft. The model uses a modified HFM that incorporated HSUs from the PM-OV HFM. HSUs in the model were modified from the PM-OV HFM (DOE/EMNV, 2020a) by grouping HSUs that, conceptually, are hydraulically similar and splitting HSUs based on water-level, aquifer-test, and ^{3}H data. Heterogeneous hydraulic-property (hydraulic conductivity, specific yield, and specific storage) and effective-porosity distributions were estimated with the PEST code (Doherty, 2018), using pilot points (RamaRao et al., 1995).

Permeable groundwater pathways from the HANDLEY nuclear test to borehole PM-3 were discerned from model-simulated distributions of hydraulic conductivity, specific yield, and specific storage (Figure 2-19). Permeable pathways occur within modified HSUs conceptualized as aquifers. A shallow permeable pathway occurs within the semiperched TMWTA. Deeper permeable pathways occur within the BRA, TCA, and a modified unit from the PBRCM referred to as the modified Pre-Belted Range Lava-Flow Aquifer (mPBRLFA) (Figure 2-19). A vertical permeable pathway was postulated between borehole ER-20-12 and the downgradient Ribbon Cliff structural zone. This permeable feature, referred to as a modified brecciated zone (mBZ), hydraulically connects the BRA and mPBRLFA with the TCA (Figure 2-19).

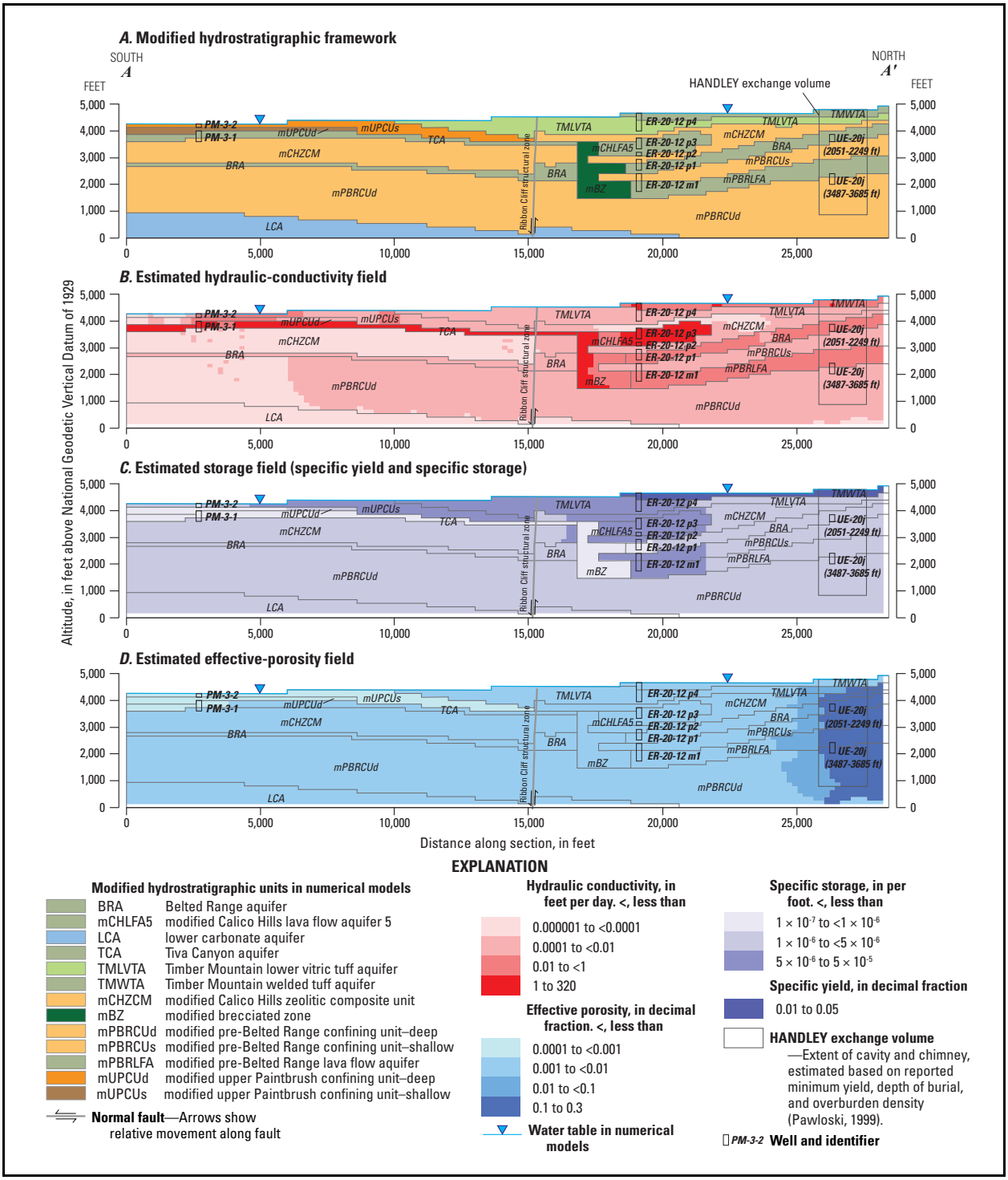

Figure 2-19
Cross Sections Showing Modified Hydrostratigraphic Framework, Hydraulic Conductivity, Combined Specific Yield and Specific Storage, and Effective Porosity
Source: Jackson (2021) Figure 14

Jackson et al. (2021) simulated the shallow ^{3}H plume moving through the semiperched TMWTA and deeper ^{3}H plumes moving predominantly through the BRA and mPBRLFA. The deeper ^{3}H plumes move upward through the permeable mBZ and then migrate toward well PM-3-1 through the TCA (Figure 2-19). Simulated ^{3}H concentrations with time indicate that the leading edge of the shallow and deeper ^{3}H plumes reached borehole ER-20-12 within about 20 years of the detonation of the HANDLEY nuclear test. The leading edge of the simulated deeper ^{3}H plumes reached Well PM-3-1 between 30 and 40 years after the detonation of the HANDLEY nuclear test. Tritium concentrations could not be matched at boreholes PM-3 and ER-20-12 when all wells are simulated along the same groundwater flow path. When borehole ER-20-12 is offset 200 ft east from the groundwater flow path connecting HANDLEY to borehole PM-3, ^{3}H concentrations could be matched, suggesting the center of the ^{3}H plume occurs west of ER-20-12.

2.6.4 Summary of Previous Modeling Studies Performed during Phase II

This section presented five groundwater flow modeling studies performed by USGS and LANL as part of PM Phase II activities. These are the USGS PM-OV Basin model, USGS volcanic rock characterization model, LANL AMANZI Bench area model, USGS Death Valley Regional Groundwater Flow System model, and the USGS HANDLEY ^{3}H transport model. These modeling studies provide datasets (e.g., the PM-OV recharge distribution and basin boundary from Fenelon et al., 2016), insights, and corroborating results that are used in the PM CAU model development. The modeling studies were performed at different scales and used various subsets of the available data specific to each model's purpose. As well, the models were constructed with different assumptions that influenced the design and construction of the models. None of these models incorporated all available data or aspects of the PM-OV groundwater basin, but each provided valuable insights into the groundwater flow and RN transport on PM.

USGS PM-OV Basin delineation model (Fenelon et al., 2016) verified groundwater data are consistent with the delineated basin boundaries. Basin boundaries and distributions of recharge and discharge within the PM-OV basin were developed during the modeling study. The model is 2-D and was calibrated to steady-state heads, transmissivity, and estimates of total basin flow. The model employed a PEST (Doherty, 2018) pilot point approach that led to a heterogeneous distribution of transmissivity across the model domain. An important feature of the model is a high-transmissivity

pathway that leads from eastern Area 20 through an area known as the Bench to Oasis Valley. The groundwater pathlines simulated by the model provided support to the concept that RNs in the groundwater of PM are expected to travel to the southwest toward the discharge areas in Oasis Valley. The model was not designed to provide an explanation for the observation of ^{3}H at Well PM-3.
The USGS PM-OV Basin delineation model provides the model domain area and boundaries, basin flow, recharge, and discharge distribution for the PM CAU model. The USGS PM-OV Basin delineation model also provides corroborating estimates of transmissivity within the PM-OV Basin. USGS PM-OV Basin delineation model was constructed with only minimal reliance on the PM HFM (Prothro et al., 2009a) yet was able to demonstrate at the CAU scale that a model based on heterogeneous but smoothly varying transmissivity provided a good match to the potentiometric surface and discharge in Oasis Valley.

USGS Bench area model (Garcia et al., 2017) estimated total transmissivity around each pumping well from well development and testing activities within the Bench area. Drawdowns from MWATs were estimated and distinguished from natural fluctuations using analytical water-level models (Halford et al., 2016; Garcia et al., 2013). The model is 3-D and was calibrated to the estimated drawdowns within the Bench area. The USGS Bench area model provides drawdown data for calibrating the PM CAU model and corroborating estimates of transmissivity within the Bench area. Garcia et al. (2017) used a modified HSU approach where several HSUs of similar hydraulic properties were combined. They accounted for structural features such as faults and caldera boundaries as vertical offsets of HSUs across structures. They used a pilot point approach to create smoothed heterogeneous hydraulic parameter fields within and between HSUs. They showed that heterogeneous hydraulic parameters was sufficient to simulate the hydraulic responses between pumped and observation wells without the need to treat structures as distinct flow zones.
The simulations of Garcia et al. (2017) were based on hydraulic response only and avoided the complexity of the superimposed effect of the regional potentiometric surface.

LANL AMANZI Bench area model (Lu et al., 2021) investigated the possible origins of the ^{3}H at observation wells. The model is 3-D and was calibrated to steady-state heads, drawdowns, flow near boundary segments, and ^{3}H concentrations. The model domain included the nuclear testing areas and the downgradient area with ^{3}H detections in observation wells, but it did not include the entire PM-OV basin. The LANL AMANZI Bench area model provides initial estimates of HSU hydraulic

conductivity and corroborating estimates of ^{3}H transport from potential sources for the PM CAU model. The LANL model was transient 3-D and calibrated to both the aquifer test hydraulic responses and the regional flow system superimposed upon it. The AMANZI model covered only a portion of the PM-OV groundwater basin and had the additional complexity of defining boundary conditions along sides of the model. Conceptually, the LANL used a very different approach than the USGS models. LANL used an HFM approach to define spatial locations of HSUs in the flow system. They assigned uniform hydraulic properties to each HSU (in contrast to the USGS pilot point approach) and included major structural features such as faults and caldera boundaries as distinct property zones different from the adjacent HSUs. This allowed LANL to account for specific faults as either low-permeability barriers or highly fractured high-permeability pathways. LANL's was the first model to attempt to match both hydraulic data and ^{3}H transport observations. Overall the LANL model was successful in simulating the general direction groundwater flow from PM to Oasis Valley consistent with known ^{3}H migration, but overestimated the rate of groundwater flow. As with earlier models, the AMANZI model was unable to explain ^{3}H observations at Well PM-3.

The USGS DVRFS model characterized groundwater flow and development in four groundwater basins of the Death Valley regional flow system. Groundwater flow prior to development was characterized using distributions and rates of groundwater recharge and discharge, and the hydraulic conductivities of saturated rocks in the study area. The model domain incorporated four basins of the Death Valley groundwater flow system, including the PM-OV basin. The model is 3-D and calibrated to steady-state heads (including head differences), transmissivity, drawdown from aquifer testing in Yucca Flat, and water-level declines from groundwater development in groundwater basins. The USGS DVRFS model provides basin flows, corroborating estimates of transmissivity within the PM-OV basin and corroborating estimates of advective-flow paths from the PM CAU underground nuclear tests.

The USGS HANDLEY nuclear test flow and transport model inferred the location of permeable pathways near and downgradient from the HANDLEY test using geologic, hydrologic, and ^{3}H data. This is a quasi-3-D model between the HANDLEY test and well PM-3 passing through Well ER-20-12. The model was calibrated to water levels, vertical-head differences, aquifer-test transmissivities, ^{3}H concentrations, and drawdowns in Wells PM-3-1 and PM-3-2 in response to groundwater withdrawals during the drilling of borehole ER-20-12. Tritium transport was simulated

using the calibrated model to better understand ^{3}H migration from the HANDLEY test. The model provides a conceptual framework for ^{3}H transport to Wells ER-20-12 and PM-3 and corroborating estimates of ^{3}H travel times from the HANDLEY test along with estimates of hydraulic and transport properties. This model demonstrated the important role of vertical flow and transport resulting from the variation in material properties.

Lessons can be drawn from the previous models. Some form of heterogeneity in hydraulic properties will be necessary. However, whether that heterogeneity needs to be inter-HSU or intra-HSU is not clear from previous models. The answer to that question may be scale-dependent. At small scales, relative to the CAU model scale, intra-HSU heterogeneity may be necessary to match many observations over distances of a few kilometers. On the other hand, for simulations of RN transport for the 1,000-year time frame of interest over large spatial scales of tens of kilometers, perhaps the inter-HSU variability and larger structural offsets are the primary controls.

As is evident, the PM CAU model benefited from and built upon the previous efforts. It represents the third iteration of models and is built upon two significant campaigns of drilling, testing, data collection, analysis and sampling. It is the culmination of 25 years of modeling, data collection, analysis, and sampling.

3.0 Flow and Transport Modeling Approach

This section presents an overview of the PM CAU modeling approach and data requirements. Details of the PM CAU flow and transport models, along with their results, are presented in Sections 4.0 and 5.0.

As described in Section 1.0, the technical basis of the UGTA FFACO (1996, as amended) strategy includes modeling of contaminant transport to provide probabilistic forecasts of areas of current and future contamination for 1,000 years. These probabilistic model forecasts provide the fundamental basis for identifying CBs. Because the FFACO specifies contaminated groundwater as a volume, developing 3-D numerical models of flow and transport on the CAU scale is a reasonable approach to meet the requirements. This is the approach being followed for the PM CAUs. Confidence in the PM CAU flow and transport model was increased by calibration of the model to observed hydraulic and RN data using the parameter values within ranges of parameter uncertainty. The philosophy adopted in model development was to be conservative in the modeling assumptions when they were likely, judged on the basis of theoretical and numerical considerations, to affect the forecast extent and magnitude of RN transport, especially when data were sparse or may be subject to alternative interpretations or when the conceptual model was likely to lead to significant increase in computational burden. This philosophy led to the decisions regarding models or parameter values that lead to a calibrated PM CAU flow and transport model that, while realistically reproducing many hydraulic and transport aspects of the system, tends to overestimate the potential contaminant transport. Since the calibrated transport model parameters represent the realistic case, the CB calculations using the full range of parameter uncertainty encompass the realistic case as well as forecasting up to a 95 percent case.

A groundwater flow model is a prerequisite for the transport model, along with the specifications of the contaminant source term. Groundwater flow and transport at PM occurs through diverse and structurally complex rocks (Section 2.2). Given the complexity of the PM-OV flow system, contamination sources, and processes controlling transport, numerical models are required to meet the objectives of the FFACO strategy. The modeling approach, therefore, integrates 3-D numerical models for flow and for transport.

For the PM CAU model, groundwater flow is taken to be fully saturated, isothermal, and steady state with recharge and discharge in balance. An equivalent continuum behavior for flow is assumed, where the hydraulic head is interpreted in an average sense for the computational cell, hydraulic conductivity is taken to be an average scaler quantity, and hydrologic features that may be present on a smaller scale are simulated using dispersion. It is conceptualized that RNs from underground nuclear tests at PM can be transported with groundwater flowing through water-saturated geologic formations. It is assumed that the RNs dissolved in the pore fluid have negligible effect on fluid motion and are carried along by the pore fluid moving at its local velocity. The advective flow paths correspond with the groundwater flow paths, and the fluid velocity determines the rate of advection of aqueous RNs along flow paths. Many of the geologic units of importance to transport at PM are fractured volcanic formations. They are conceptualized as dual porosity where flow occurs through the high permeability fractures with stagnant fluid in the rock matrix and RNs can diffuse between the fractures and the matrix. The migration processes relevant for evaluating RN transport at PM are radioactive decay of the species, advection in porous and fractured media, dispersion, diffusion of RNs between fracture water and matrix water, sorption onto immobile minerals in the matrix, and colloid-facilitated transport. Solute sorption onto fracture walls and colloid filtration/retardation in the fractures are conservatively ignored in this work.

The 3-D CAU-scale model consists of two integrated but mathematically decoupled components: the PM CAU flow model and the PM CAU transport model. The approach begins with characterization of the subsurface hydrogeology and the flow system. Conceptual models of the flow as well as transport are developed based on the results of characterization and assumptions regarding system processes. The processes deemed important in the conceptual models are represented mathematically and implemented on computers in numerical codes capable of representing the temporal and spatial scales of relevance to achieve the objectives discussed in Sections 1.0 and 2.0. The models use numerical 3-D flow and transport simulators that capture the complex geologic structure underlying the PM, including units of variable thickness, faults, and offsets, as well as complex transport processes associated with reactive solutes and fractured rock.

The hydrologic conceptual flow model is presented in Jackson et al. (2021). Navarro (2021b) presents the hydrologic data supporting the conceptual model and the PM CAU flow model. Hydrologic parameters and data types required for the groundwater flow model include permeability

(or hydraulic conductivity or transmissivity), storage parameters, precipitation recharge, lateral boundary fluxes, discharge locations and volumetric rates, and hydraulic heads. These parameters are discussed in Navarro (2021b), as well as data and analysis pertinent for each parameter giving ranges of values or distributions as appropriate. A conceptual model encompassing physical and chemical transport processes of importance for the PM CAU transport model is discussed in Navarro (2021a, Section 3.0). Major data types of relevance to transport include radioactive decay constants, effective porosity, matrix porosity, fracture spacing, fracture aperture, dispersivity, matrix diffusion coefficients, tortuosity, and sorption coefficients. These parameters are discussed in Navarro (2021a), as well as data and analysis pertinent for each parameter giving ranges of values or distributions as appropriate.

The geologic formations of importance for the PM CAU model are heterogeneous; hence, flow and transport parameters show considerable variability that can not be adequately captured by the zonation approach used by the HFM. Additionally, scales of measurements of the various parameters do not generally correspond to the scales required by the numerical representation utilized in the PM CAU models. The approach in the PM CAU model is to use the process of calibration so that the selected values of relevant flow and transport parameters lead to computations that match observed data. Observed data are numerous and of various types; hence, the comparison of computational results and observation data is conducted by minimizing an error function defined over the entire dataset. Parameter estimation software is used (see Sections 4.0 and 5.0) to optimize the values of input parameters and minimize the overall error. The computerized process of calibration is aided by manually taking into account soft information embedded in the conceptual flow and transport models. For convenience, the flow model is calibrated first; however, predicted flow pathways are compared with RN observation data and the flow parameters adjusted to lead to results consistent with transport observations and model results.

Results from a number of supporting models are directly required for formulating the PM CAU flow and transport models. These include (a) HFM (DOE/EMNV, 2020a), which provides a hydrogeologic framework for the flow and transport models; (b) PM conceptual model (Jackson et al., 2021); (c) delineation of the PM-OV groundwater basin (Fenelon et al., 2016); (d) infiltration model to specify influx of water to the groundwater flow model (Middleton et al., 2019; and Fenelon et al., 2016; Halford and Jackson, 2020); and (e) screening model to select the RNs relevant to the transport

model (Carle et al., 2020). Several of these supporting models in turn require the results of further supporting models; these are cited in the relevant sections of these documents as well as in Navarro (2021a and b).

The source term provides the origination conditions of contamination to the transport model, which then get transported away with the flowing groundwater. Contaminants to be addressed for the PM CAU transport model are the RNs that originate from underground nuclear testing. Primary source of contamination at PM is the HST, the portion of the RST that is available for aqueous transport (discussed in Section 5.3) associated with the underground nuclear tests.

The screening model (Carle, 2020) provides an explanation of the process to evaluate the total RN inventory (Finnegan et al., 2016) as a means to identify the RNs of relevance or potentially of relevance. Relevant RNs are defined to be the subset of the RN inventory isotopes anticipated to exist in source area groundwater at concentrations that exceed the SDWA standards (CFR, 2021) for at least 100 years, as based upon screening model calculations and historical RN measurements in groundwater. Potentially relevant RNs are defined to be the subset of the RN inventory isotopes anticipated to exist in source area groundwater at concentrations that exceed 10 percent of the SDWA standards (CFR, 2021) for at least 100 years, as based upon screening model calculations and historical RN measurements in groundwater. The transport models require the specification of contaminant mass for each relevant RN at each source location in the model on the specific day of each detonation. RN mass is distributed within a specific geometric volume associated with each detonation location (discussed in Section 5.3). These prescriptions serve as initial conditions for the transport simulation.

Selection of the suite of codes used in flow (MODFLOW6) and transport (Walkabout, a utility code; and PLUMCALC) modeling is discussed in Appendix E.

3.1 Flow Model Approach

The flow model is constructed using the USGS code MODFLOW6 (Langevin et al., 2017). The calibration of the flow model is aided by the use of the parameter estimation (PEST) software (Doherty, 2018). The model is configured with brick-shaped blocks following the block-centered formulation of MODFLOW6 with refinement in areas containing a higher frequency of observational

and measured data and around structural features such as faults and caldera boundaries that are believed to influence groundwater flow. The physical properties represented in the flow code are based on the conceptual HFM constructed using EarthVision geological modeling software (Dynamic Graphics, 2019). The grid file containing locations and connectivity of grid elements was constructed using the USGS FloPy Toolbox for MODFLOW6 (USGS, 2019).

The model grid has vertical and horizontal refinement to allow for parameter values to be assigned on the basis of HSUs and major structural features such as faults and caldera boundaries. Typically, the model parameters assigned to model nodes within an HSU or structural element are the same and change only across HSU or structural boundaries. However, the model also provides for the option of assigning spatially variable parameter values to nodes using a pilot point approach (Doherty, 2018) that can yield spatially variable parameters within an HSU. The model can be configured to limit the depth of the flow system as suggested by Jackson et al. (2021). The model construction is designed to provide flexibility to evaluate different modeling approaches as noted in Section 2.6.3.

MODFLOW6 solves a discretized version of the groundwater governing equation to generate hydraulic heads at cell centroids. Using these, it then constructs areal fluxes on cell faces based on the cell connectivity.

3.2 Transport Model Approach

The goal of transport modeling described here is to generate RN concentrations in the model domain as functions of space and time incorporating the transport processes listed above. The first step of the modeling approach is based on particle tracking to simulate the transport processes of advection and dispersion using the code Walkabout (Painter, 2011). Particle tracking is used to minimize numerical dispersion.

RN input to the groundwater system is represented by a swarm of particles distributed over the input region, with each particle assigned a fixed fraction of the input RN mass, given as initial RN mass divided by the number of particles assigned to the source. The number of particles does not change during the simulation. The particles are inert and move with the flowing groundwater. Walkabout then marches each particle using an interpolated velocity field at each point in space, superimposed with a random walk model to include dispersion, generating a sequence of positions with time to develop a

particle track. This process is repeated for each particle to develop a suite of particle tracks for each source. It is assumed that the spatial and temporal distribution of the HST for any given test is the same for all RNs of importance to the PM CAU transport model. Since advection and dispersion are independent of the RN specification, the same set of particle tracks is used for all RNs from a given source, and RN-specific properties are handled in PLUMCALC as discussed in the text.

A utility code developed by the project was used to map the flow results from the MODFLOW6 rectangular grid to a tetrahedral mesh required by Walkabout. The areal fluxes on the cell faces provided by MODFLOW6 on the rectangular grid are mapped to provide fluid velocities at the tetrahedral vertices needed by Walkabout. Information about the development and testing of the utility code is provided in Appendix E.

The particle track information generated by Walkabout was converted to solute concentrations using a method based on superposition, convolution integration, and residence time distribution function approach using a code called PLUMECALC (Robinson and Dash, 2006; Robinson et al., 2010 and 2011). The calculations performed by PLUMECALC incorporate radioactive decay, sorption, and matrix diffusion.

4.0 Flow Model

This section presents the hydrogeologic background information and the technical basis for the development of PM CAU flow models. As discussed in Section 1.2.1, the purpose of the PM CAU models is to support the UGTA corrective action strategy objective of forecasting CBs. The key objective is to develop the conceptual flow model and transform the conceptual model into computational models that form the basis of the transport models (see Section 5.0) for use in forecasting CBs presented in Section 6.0. The model development process includes data collection and analysis, development of the conceptual and computational models, model parameterization, model calibration to observational data through parameter adjustment, assessment of calibration results, model uncertainty analysis and model sensitivity analysis.

The organization and content of this section are as follows:

- Section 4.1, "Hydrogeologic Data and Flow Model Conceptualization," presents the hydrogeologic data used to develop the conceptual model and calibrate the groundwater flow model. The flow model conceptualization describes the integrated understanding of the hydrogeologic data and defines the important elements of the flow system, along with the significant assumptions made during the development and calibration of the groundwater flow model. Flow path information derived from geochemical data is summarized in Section 2.5.

- Section 4.2, "Flow Model Development and Calibration," presents the development and calibration of the groundwater flow model, including the discretization of the PM-OV groundwater basin, parameterization of HSUs and known faults based on the HFM, identification of the type and extent of appropriate boundary conditions, model calibration data, and calibration results.

- Section 4.3, "Flow Model Uncertainty Analysis," presents the development and calibration of alternative conceptual models that may lead to more extensive transport.

- Section 4.4, "Flow Model Sensitivity Analysis," presents an assessment of parameter sensitivity to observational data and model sensitivity to barrier faults located on the boundaries of the SCCC and increased recharge near Black Mountain,

- Section 4.5, "Flow Modeling Summary and Conclusions," presents a summary and the major conclusions of PM CAU flow modeling.

4.1 Hydrogeologic Data and Flow Model Conceptualization

The PM CAU HDD (Navarro, 2021b) contains much of the hydrogeologic data necessary for construction of the PM CAU flow model. The key data required for construction and calibration of the flow model are summarized in this section. For further details of the data and accompanying analysis/interpretation, the reader is referred to the PM CAU HDD (Navarro, 2021b). Flow path information derived form geochemical data is summarized in Section 2.5. RN observational data are presented in the PM CAU SDD (Navarro, 2021c).

4.1.1 Groundwater Basin Area

Fenelon et al. (2016) delineated the lateral PM-OV groundwater basin area based on regional water-level contours, geologic controls, balancing of groundwater discharges within the PM-OV groundwater basin and adjacent basins against available water from precipitation (Section 2.6.3.1), and geochemical considerations. The PM-OV groundwater basin encompasses approximately 3,600 km^2 and extends from Gold Flat and Kawich Valley in the north to the terminus in Oasis Valley in the southwest (Figure 4-1). The basin's eastward extent is to the Belted Range and incorporates all underground nuclear testing areas on PM. The basin's western boundary is poorly defined, but it is thought to be the region from Sarcobatus Flat in the south to the Cactus Range in the north.
The lateral basin boundary of the PM-OV basin represents a no-flow boundary, although minor amounts of water may cross into or out of the basin in several places.

Jackson et al. (2021) defined two lower boundaries of the PM-OV groundwater basin. The first lower boundary defined the active part of the flow system where nearly all flow occurs, and the second lower boundary defined the depth that encompassed all nuclear tests and ^3H plumes. The lower flow system boundary was determined from detailed analyses of hydraulic conductivity and transmissivity with depth. The depth-analysis results indicated that greater than 90 percent of the total transmissivity contributing to groundwater flow and RN transport occurs within 1,600 ft of the water table.
The extent of initial radioactive contamination following an underground nuclear test is dependent on the nature of the RN, subsurface conditions and the yield of the nuclear test. Tritium has the largest extent of initial contamination below the water table and is typically a factor of 3 greater than radius of the cavity created by the nuclear test (Pawloski et al., 2001; Tompson et al., 2011).

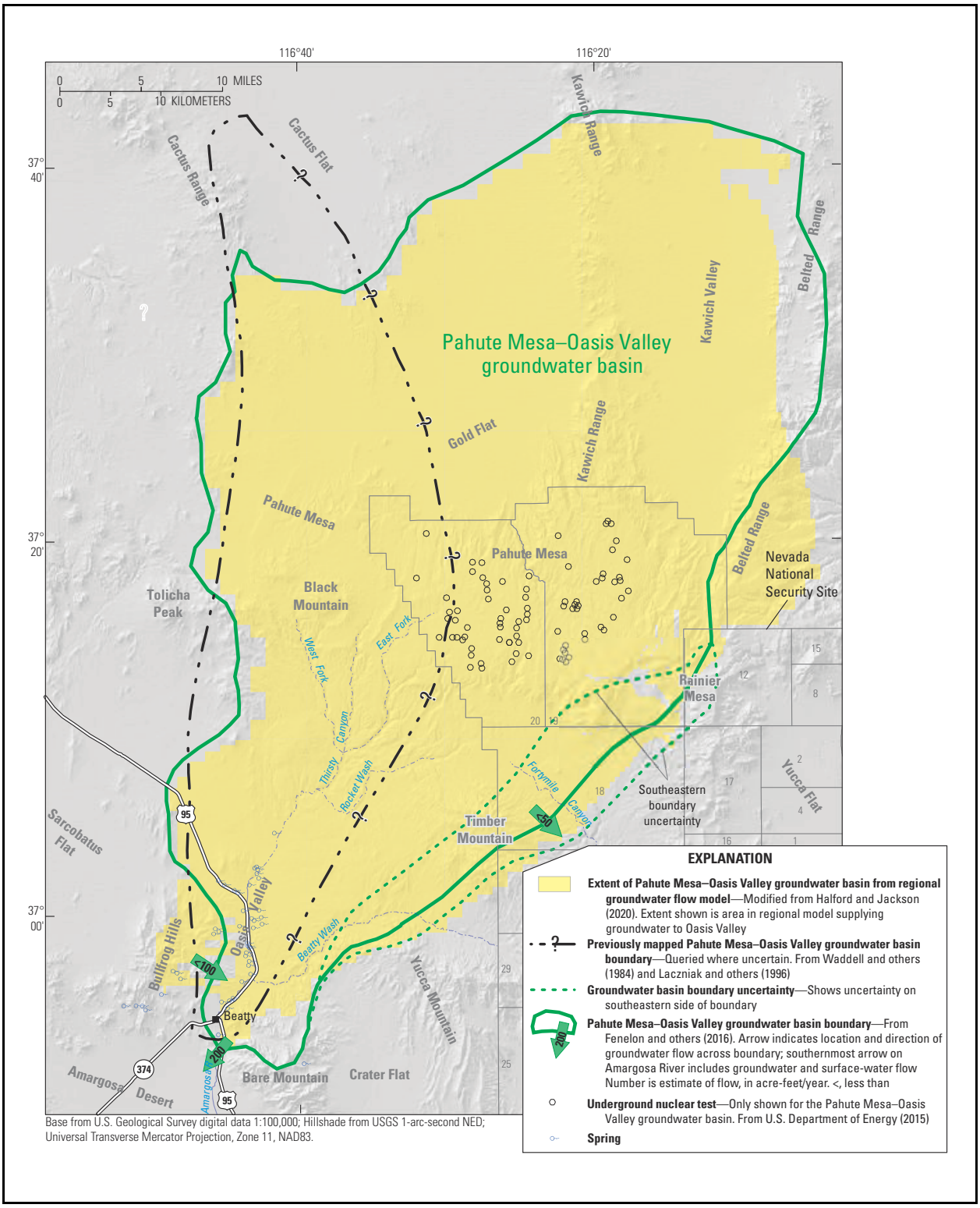

Figure 4-1
PM-OV Groundwater Basin Boundary and Boundary Flows
Source: Jackson et al. (2021) Figure 21

The HANDLEY test has the deepest extent of initial ^{3}H contamination and was used to estimate a lower basin boundary at 4,000 ft below the water table.

4.1.2 Recharge and Discharge

Altitudes in the PM-OV groundwater basin range from about 3,300 ft amsl (1,000 m) near Beatty, Nevada, to about 8,300 ft amsl (2,500 m) in the Kawich and Belted ranges in the northernmost areas. The basic pattern of recharge reflects the topographic influences on precipitation and the estimated distribution of soil and rock properties. The groundwater flow system of the PM-OV area is replenished by recharge from precipitation on the volcanic highlands such as PM. Recharge beneath alluvium on the valley floors is negligibly small compared with most upland areas except beneath ephemeral washes (Middleton et al., 2019). Overall, interbasin flow between the PM-OV groundwater basin and adjacent basins is insignificant compared with recharge, and the recharge is in equilibrium with discharge (Jackson et al., 2021).

Natural discharge to the surface from the PM-OV groundwater basin occurs in the form of springs and evapotranspiration (ET) in the Oasis Valley discharge area. In Oasis Valley, most groundwater discharged from springs does not leave the valley by surface flow. Surface water flow out of the valley occurs mostly through the Amargosa River. Spring water either re-infiltrates into the flow system or evaporates. A small portion of the spring water may enter the Amargosa River. Thus, the majority of the groundwater discharged by springs is effectively lost from the groundwater system through ET within the discharge area.

A best estimate for groundwater discharges to springs and seeps in Oasis Valley is 5,900 ac-ft/yr (7,268,800 m^3/yr) and may range from 5,000 to 6,800 ac-ft/yr (Fenelon et al., 2016). Laczniak et al. (2001) performed a Monte Carlo uncertainty analysis of groundwater discharge for DVRFS3 and estimated a discharge range of approximately 4,200 to 8,900 ac-ft/yr within the PM-OV groundwater basin. Both studies cite the source of the discharge data as Reiner et al. (2002). However, the lower- and upper-end values estimated by Laczniak et al. (2001) are unlikely because these estimates represent the low-probability input parameters on the tails of the parameter distributions used in the analysis. Subsurface discharge from Oasis Valley to the Amargosa Desert through alluvium in southern Oasis Valley is estimated at about another 100 ac-ft/yr (123,200 m^3/yr), and an additional estimated 300 ac-ft/yr (369,600 m^3/yr) of surface water in the Amargosa River

flows southward out of Oasis Valley (Fenelon et al., 2016). The best estimate of total recharge generated within the PM-OV groundwater basin from precipitation-derived recharge infiltration is 6,300 ac-ft/yr (7,761,600 m^3/yr), assuming the groundwater system is in steady state and recharge equals discharge. Current water well production rates estimated from 2010 pumping records are approximately 100 acre-ft/yr and represents less than 2 percent of the ET estimate.

4.1.3 Hydraulic Heads

Hydraulic head is a key hydrogeologic measurement used to constrain groundwater flow modeling. Hydraulic head information for the groundwater flow system in PM CAU and vicinity was compiled to determine representative steady-state hydraulic head values for the flow system that can serve as model calibration targets. Jackson et al. (2021) developed contour maps to represent the predevelopment hydraulic-head distribution within the PM-OV aquifer systems. Developing the contour maps included performing a transient-effects analysis to identify which water-level measurements collected during periods of onsite groundwater activity (pumping and underground nuclear testing) actually represent predevelopment conditions. Jackson et al. (2021) compiled and analyzed more than 17,000 depth-to-water records representing 577 well completions in 227 boreholes from the USGS National Water Information System (NWIS) database. The period of record spans from 1941 to 2016. In addition, Jackson et al. (2021) included 75 springs to supplement the available water-level data (Figure 4-2).

As part of the water-level analysis by Jackson et al. (2021), each water level was evaluated to be representative of one of the following three hydrologic conditions: (1) natural predevelopment conditions, (2) transient conditions resulting from nearby nuclear testing, and (3) transient conditions resulting from pumping. Assignment of a water level as a predevelopment condition assumed that human activity has not affected or has minimally affected the water level. Of the 577 well completions analyzed for this study, 387 had at least one water level identified as representative of predevelopment conditions. The predevelopment water levels identified by Jackson et al. (2021) are selected as possible target heads for the steady-state CAU flow model. In addition to the steady-state water levels, the land surface elevation at spring locations provides additional target heads. Figure 4-2 illustrates the steady-state and spring water-level sites.

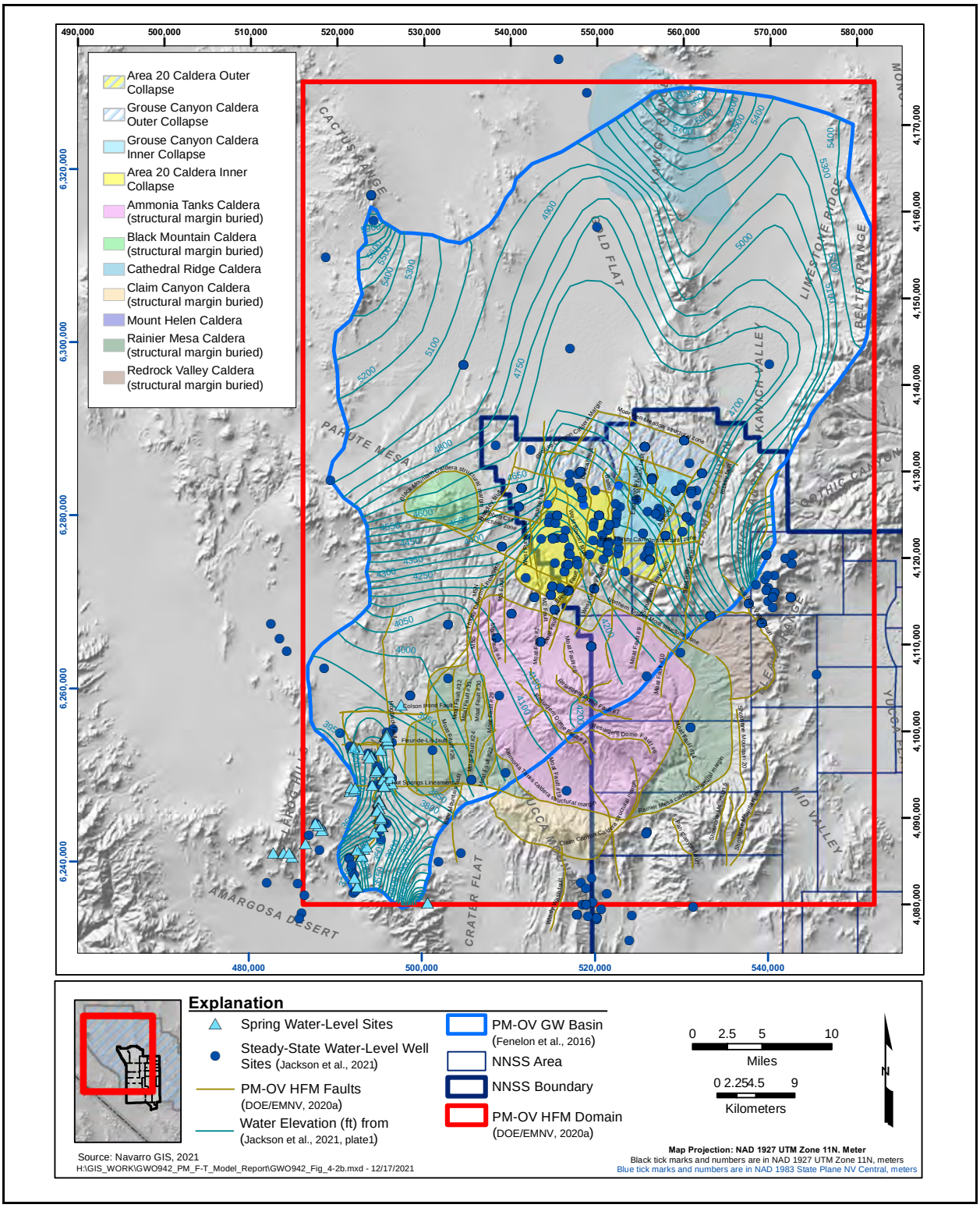

Figure 4-2
Potentiometric Surface, Steady-State Water-Level Sites from Wells, Spring Locations, and Structural Features within the PM Groundwater Basin

The hydraulic gradient is related to the geologic structures, hydraulic properties of the rock, and location of recharge areas; and can be used to inform model development and calibration.

The following areas of distinct geologic structure that influence the hydraulic gradient are identified.

Eastern Silent Canyon Caldera Complex

The SCCC is a deeply buried feature that consists of at least two nested calderas: the Grouse Canyon caldera and the younger Area 20 caldera (DOE/EMNV, 2020a). The eastern SCCC is the area is between the East Greeley and Rickey faults, within the SCCC (Figures 4-2 and 4-3). The area includes the majority of tests in Area 19. The hydraulic gradient is generally low in the northern half of this area because of the presence of the extensive and productive BRA near the water table. The hydraulic gradient in the south is generally medium to high because of the presence of the thick Bullfrog confining unit (BFCU) near the water table.

Western Silent Canyon Caldera Complex

This area includes the northern area between the West Greeley and West Boxcar faults where the dominant HSU in which testing was conducted is the CHZCM (Figures 4-2, 4-3, and 2-7 [Section A–A´]). Within the northern area, the hydraulic gradient is generally low due to several high-permeability rhyolitic lava flows. The groundwater flow in this area is likely controlled by the distribution of rhyolite lavas in the CHZCM. The steepening of the hydraulic gradient near West Boxcar fault corresponds to an increase in the percentage of low-permeability zeolitized tuff (CHZCM) in the saturated zone (Blankennagel and Weir, 1973). It is also possible that groundwater is redirected more southward by the Boxcar and West Boxcar faults. The groundwater flow in the area between the Boxcar and Purse faults is likely controlled by the distribution and continuity of the Paintbrush welded tuffs (TCA and TSA) and rhyolitic LFAs (Benham aquifer [BA], Comb Peak aquifer [CPA], and Scrugham Peak aquifer [SPA]).

West of the Purse Fault

The Thirsty Canyon Lineament (TCL) is a north–northeast-trending, geophysically inferred feature associated with the Purse and West Purse faults and is characterized by a zone of en echelon faults 2 to 3 km wide (Mankinen et al., 1999 and 2003). The TCL and Purse fault may behave as a

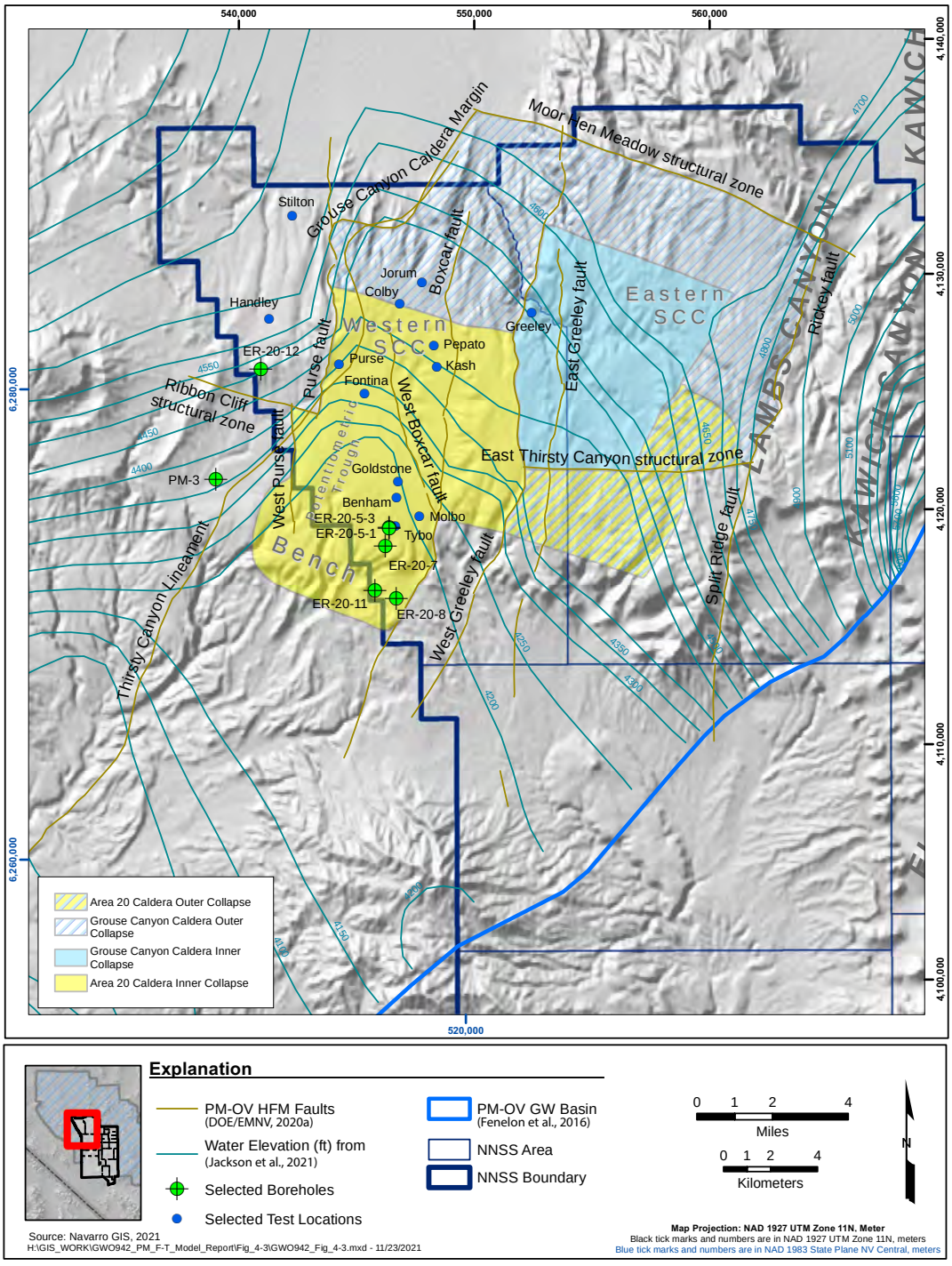

Figure 4-3
Structural Features near the Nuclear Testing Areas of PM

structural barrier to groundwater flow across the axis of the feature, providing a discontinuity between flow paths in the aquifers to the east and to the west of the features (Figures 4-2, 4-3, and 2-7 [Section B–B´]). The discontinuity results in heads that are several hundred feet higher west of the features and groundwater flow that is predominantly parallel to the discontinuity (SNJV, 2006). The Purse fault coincides with the northwestern boundary of the SCCC and separates two groundwater systems with distinct chemical compositions. The groundwater chemistry in the upper Thirsty Canyon, west of the Purse fault, is distinct from PM groundwater immediately to the east (Navarro, 2020).

Southwest Area 20 and the Bench Area

The Bench area is a transitional area between the SCCC and TMCC (Figures 4-2, 4-3, and 2-7 [Section C–C´]). A southwest-trending trough in the potentiometric surface begins in Area 20 and extends through the Bench area to the southwest and down through Thirsty Canyon. The trough may be attributed to a zone of higher transmissivity due to fracturing associated with the caldera margin or a thick accumulation of intra-caldera tuffs in the Area 20 caldera. Transmissivities are especially high just southwest of the NNSS in the Bench area as a result of thick rhyolite lava flows near the water table (Fenelon et al., 2016). The Purse and West Purse faults on the western margin of the trough and the Boxcar and West Boxcar faults on the eastern part of the trough may also contribute to the trough by restricting flow into the structural block, creating the higher gradients seen on the margins.

West Side of the Ammonia Tanks and Rainier Mesa Calderas

In the northwestern portion of the Timber Mountain caldera between the Bench area and the Timber Mountain, flow will transition in a complicated way through the caldera moat into the Fortymile Canyon composite unit (FCCM) and Timber Mountain composite unit (TMCM) around the northwest flank of the Timber Mountain resurgent dome. The gradient begins to increase in the central area of the western Timber Mountain moat, possibly because of constriction of the flow paths due to the Timber Mountain resurgent dome or transition to lower-permeability rock in this area. The gradient increases near the entrance to Oasis Valley in part because of narrowing of the groundwater basin, the presence of low-permeability rock, and reduction in volcanic rock thickness.

Oasis Valley Discharge Area

Outflow from Oasis Valley is controlled by a deep confining unit of siliciclastic rocks, which underlies the southern part of the PM-OV flow system and crops out near Oasis Valley. The confining unit may force water upward through faults in the area. The potentiometric contours surrounding this valley exhibit a prominent “V” shape along the valley near the terminus of the PM-OV groundwater basin (Figure 4-2). Most of the water that flows through the PM area of the NNSS is assumed to be discharged by springs and seeps in Oasis Valley (Fenelon et al., 2016). The gradient in the Oasis Valley discharge area is much higher than the average PM-OV gradient because of further narrowing of the groundwater basin and reduction in volcanic rock thickness.

4.1.4 Subsurface Hydraulic Properties

The values used for the hydraulic properties of HSUs in the simulation of groundwater flow and transport should be consistent with available information to provide confidence in the simulation results. Specifically, hydraulic conductivity is a basic parameter for groundwater flow modeling that determines the volumetric flow rate. Representative hydraulic conductivities for the formations to be modeled at the scale over which the model is discretized are integral to producing defensible model predictions. Storage properties of the formations also are of interest as a basic hydraulic parameter needed for transient simulations of groundwater flow. The available hydraulic properties are summarized in this section.

4.1.4.1 Hydraulic Conductivity

The compilation of hydraulic conductivity data included separate evaluations of aquifer-pumping and slug-testing data to determine statistics for hydraulic conductivity at both scales. The pumping-scale aquifer tests are conducted in situ on short to long well completion intervals (typically in the range of 100 to 1,000 ft or more [30 to 300 m or more]), moving relatively large volumes of water to induce pressure change in the test formation over relatively long periods of time (typically several hours to several days). The slug- and packer-test scale tests are conducted in situ on fairly short test intervals (typically in the range of about 50 to 500 ft in PM wells) using small volumes of water (less than 100 gallons up to several hundred gallons) to induce pressure pulses that equilibrate in a relatively short period (ranging from several seconds to several days).

Pumping-scale tests provide the most appropriate information for use in large-scale modeling because they provide results representative of the greatest aquifer volume and are more likely to reflect high hydraulic conductivity structure in tested formations. Slug-scale aquifer tests provide less representative information because they test smaller volumes of the formation and are more affected by local variability and effects related to drilling, construction, and test methods.

The hydraulic conductivity dataset was derived from single-well aquifer tests, including pump- and slug-scale aquifer tests performed on PM wells (Frus and Halford, 2018). The single-well test dataset consists of 360 individual well completions and 1,468 analyses of transmissivity or hydraulic conductivity. The majority of the single-well data are slug-scale aquifer tests, which include 310 of the 360 aquifer tests. The remainder of the tests are constant or variable rate pump-scale aquifer tests. The number of aquifer tests analyzed was much greater than the number of actual tests because some responses to a water-level displacement were interpreted multiple times using different analytical models by different investigators. Frus and Halford (2018) standardized the aquifer test results and identified the best transmissivity estimate for each well. Furthermore, the majority of the PM wells are screened across multiple HSUs or HGUs; hence, the amount of data that is primarily representative of a single type of rock from pump-scale aquifer testing is very limited. (Navarro, 2021b).

Table 4-1 summarizes the hydraulic conductivity data grouped by HSU from the pump-scale aquifer tests. Pump-scale aquifer test data are available for only 11 HSUs, and only for aquifer or composite unit HSUs. Table 4-2 summarizes the hydraulic conductivity data grouped by HSU from the slug-scale aquifer tests. An adequate amount of data is available to characterize only the BRA, PBRCM, BFCU, Calico Hills lava-flow aquifer (CHLFA), CHZCM, and Inlet aquifer (IA) HSUs. Data are limited to a few data points each for the other HSUs.

Tables 4-3 and 4-4 summarize the pump- and slug-scale aquifer test hydraulic conductivity data grouped by HGU, respectively. The amount of slug-scale aquifer test hydraulic conductivity data is considerably larger than pump-scale aquifer test data. The LFA mean hydraulic conductivity is slightly higher than the WTA, but the two HSUs are hydraulically similar based on the variability seen in the data. The average hydraulic conductivity of the TCU is moderately lower than the LFA and WTA HGUs.

Table 4-1
Pump-Scale Aquifer Test Hydraulic Conductivity Data Analyzed by HSUs

HSU	Mean of Log10 K (ft/day)	Number of Data Points
TSA	1.71E+00	1
ATWTA	1.32E+00	1
FCULFA	1.04E+00	1
BA	1.04E+00	1
CPA	7.29E-01	1
CHLFA	4.69E-01	2
BRA	2.08E-01	7
LCA3	5.93E-02	1
TCA	-3.81E-01	3
RMWTA	-4.88E-01	3
PBRCM	-1.23E+00	2

ATWTA = Ammonia Tanks welded-tuff aquifer
FCULFA = Fortymile Canyon upper lava-flow aquifer
LCA3 = Lower carbonate aquifer-thrust plate
RMWTA = Rainier Mesa welded-tuff aquifer
ft/day = Feet per day
K = Hydraulic conductivity

Table 4-2
Slug-Scale Aquifer Test Hydraulic Conductivity Data Analyzed by HSUs
(Page 1 of 2)

HSU	Mean of Log10 K (ft/day)	Standard Deviation of Log10 K (ft/day)	Number of Data Points	Log Normal [a]
ATWTA	-8.60E-01	NA	7	NA
TCA	-1.18E+00	NA	1	NA
CHVTA	-1.27E+00	NA	1	NA
THCU	-1.30E+00	NA	3	NA
CHLFA	-1.36E+00	5.56E-01	24	Yes
IA	-1.65E+00	7.76E-01	13	Yes
RMWTA	-1.84E+00	NA	3	NA
CHZCM	-1.87E+00	7.29E-01	24	Yes
CFCM	-1.87E+00	6.60E-01	9	NA

Table 4-2
Slug-Scale Aquifer Test Hydraulic Conductivity Data Analyzed by HSUs
(Page 2 of 2)

HSU	Mean of Log10 K (ft/day)	Standard Deviation of Log10 K (ft/day)	Number of Data Points	Log Normal [a]
PLFA	-1.88E+00	NA	3	NA
UPCU	-1.96E+00	NA	4	NA
ATCU	-1.98E+00	NA	2	NA
BRA	-2.00E+00	9.20E-01	107	Yes
PBPCU	-2.00E+00	NA	1	NA
CFCU	-2.05E+00	NA	3	NA
LPCU	-2.18E+00	NA	1	NA
PBRCM	-2.19E+00	1.21E+00	27	Yes
BFCU	-2.30E+00	9.10E-01	25	Yes
KA	-2.34E+00	NA	2	NA
THLFA	-2.82E+00	NA	1	NA
TSA	-3.86E+00	NA	1	NA

[a] Log normality is evaluated for distributions with 10 points or greater.

ATCU = Argillic tuff-confining unit
CFCM = Crater Flat composite unit
CFCU = Crater Flat confining unit
CHVTA = Calico Hills vitric-tuff aquifer
KA = Kearsarge aquifer
LPCU = Lower Paintbrush confining unit
PLFA = Paintbrush lava-flow aquifer
PBPCU = Post-Benham Paintbrush confining unit
THCU = Tannenbaum Hill confining unit
THLFA = Tannenbaum Hill lava-flow aquifer
NA = Not applicable

Table 4-3
Pump-Scale Aquifer Test Hydraulic Conductivity Data Analyzed by HGUs

HGU	Mean of Log10 K (ft/day)	Standard Deviation of Log10 K (ft/day)	Number of Data Points	Log Normal [a]
LFA	6.54E-01	7.73E-01	10	Yes
WTA	9.78E-02	NA	8	NA
CA	0.087	NA	1	NA
TCU	-1.38E-02	NA	3	NA

[a] Log normality is evaluated for distributions with 10 points or greater.

Table 4-4
Slug-Scale Aquifer Test Hydraulic Conductivity Data Analyzed by HGUs

HGU	Mean of Log10 K (ft/day)	Standard Deviation of Log10 K (ft/day)	Number of Data Points	Log Normal [a]
VTA	-1.48E+00	NA	2	NA
LFA	-1.68E+00	8.88E-01	102	Yes
ICU	-1.86	NA	1	NA
WTA	-1.96E+00	1.03E+00	47	Yes
TCU	-2.23E+00	8.40E-01	86	Yes

[a] Log normality is evaluated for distributions with 10 points or greater.

Generally, the variability of hydraulic conductivity within an HSU or HGU group is larger than the variability across groups. This suggests that the HSU or HGU groups do not identify unique hydraulic conductivity values in most cases. This further suggests that other factors such as degree of fracturing and alteration dominate the hydraulic conductivity of most tested intervals. These findings are consistent with Garcia et al. (2017) and Oberlander et al. (2007) in that most HSUs in the Bench area are heterogeneous, and the aquifer and confining unit HSUs can have similar hydraulic behaviors.

Depth Decay of Hydraulic Conductivity

The hydraulic conductivity is expected to decrease with depth in many situations because the pore spaces or fractures through which water flows are expected to close under the increasing overburden pressure at greater depths. Additionally, deeper units are generally older and may have greater mineral precipitation or alteration that obstructs pore space.

Figure 4-4 presents the hydraulic conductivity versus depth from pump- and slug-scale aquifer testing. Very low hydraulic conductivity occurs at all tested depths, but the highest hydraulic conductivity values (in excess of 10 ft/day [~3 meters per day (m/day)]) generally occur within 2,000 ft (~600 m) of the water table, but a few values indicate deeper highly conductive rock is present. These findings are consistent with Jackson et al. (2021) who state that the largest transmissivity occurs in the first 1,600 ft (~488 m) below the water table because of a decreasing abundance of high-transmissivity devitrified rock at depth and an increasing abundance of low-transmissivity rock with argillic and mineralized alteration.

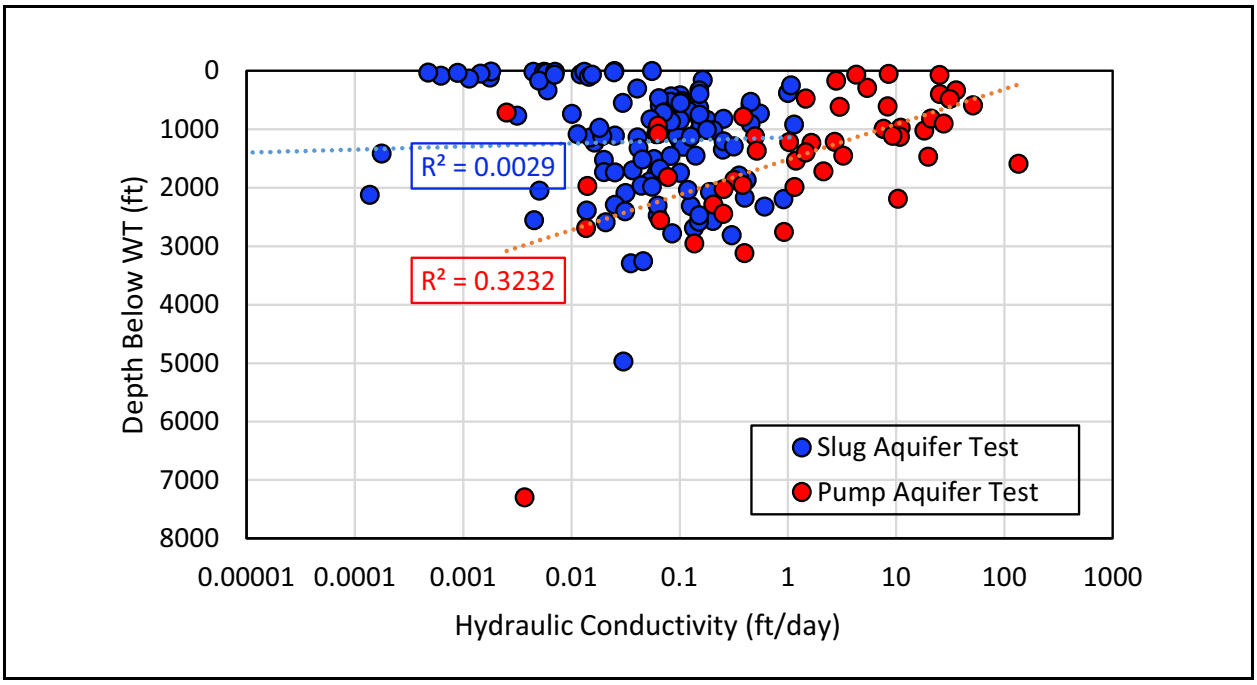

Figure 4-4
Pump- and Slug-Scale Aquifer Test Hydraulic Conductivity versus Depth

A trend of decreasing hydraulic conductivity with depth is seen only in the pump-test data. No trend is seen in the slug-test hydraulic conductivity. Slug tests beneath PM were primarily intended to locate low-permeability rocks suitable for the testing of nuclear devices, and much of the slug-scale aquifer testing consisted of multiple tests in each borehole using packers over short adjacent intervals throughout the borehole (Blankennagel, 1967; Blankennagel and Weir, 1973). The pump-test hydraulic conductivity is also notably higher than the slug-test data, likely due to bias of completing wells in productive intervals rather than unproductive intervals to facilitate water production for water supply or sampling volume.

Fault Hydraulic Conductivity

Faults at the NNSS tend to form relatively narrow (less than ~300 ft [~100 m]) fault zones with flow properties that vary from fault to fault as well as along individual faults. Fault zones resulting from the most recent tectonic activity may form permeable fault zones, but only where they cut the stronger and more consolidated HGUs such as WTA, LFA, and CA. Where these faults intersect TCU, they likely form zones of enhanced fracture permeability, but the permeability may be less than that for the fault zones in the stronger HGUs (Prothro et al., 2009b).

Faults may act as either conduits of groundwater flow, if characterized by open fractures, or barriers to flow, if associated with fine-grained gouge or increased alteration of nearby rocks (Protho et al., 2009b). The hydraulic conductivity data from PM pumping-scale aquifer tests suggest a correlation of increasing hydraulic conductivity is present with proximity to faults at a distance of less than 1,000 ft, but the amount of data is very limited (Navarro, 2020). An enhanced permeability zone of 1,000-ft width is consistent with the observations of fault zones at the NNSS by Prothro et al. (2009b). However, faults may not be hydraulically distinct from adjacent host rocks and have no direct hydraulic significance. During aquifer testing in Southwest Area 20 and the Bench area, drawdowns were seen across structural blocks and faults (Garcia et al., 2017) suggesting faults in the Bench area do not have a strong hydraulic influence in this area.

The hydraulic influence of faults on groundwater in the PM-OV groundwater basin is uncertain but has been inferred from hydraulic gradients. Jackson et al. (2021) identified a limited number of faults, and caldera margins have been hypothesized to function as flow barriers or conduits based on hydraulic gradient and other data:

- The southern part of the Boxcar fault has been identified as a transverse barrier to groundwater flow based on hydraulic-head differences on each side of the fault. In this area, flow is directed southward, nearly paralleling the Boxcar fault.

- ER-20-8 fault has been identified as a vertical hydraulic connection between three aquifers separated by confining units in the ER-20-8 well. During pumping from either the TCA or TSA completions, similar drawdowns were seen in the SPA, TCA, and TSA completions that are separated by the Middle Paintbrush confining unit (MPCU) and LPCU. However, hydraulic conductivity data indicate aquifer and confining-unit HSUs can have similar hydraulic behaviors (Section 4.1.4.1) and may not hydraulically separate the aquifer HSUs in Well ER-20-8.

- The TCL and Purse fault are likely barriers to groundwater flow on its northern end, and the TCL a conduit farther south. The steep gradient across the northern TCL and Purse fault indicates a hydraulic barrier formed because of structural features associated with these structures. High transmissivity near Wells ER-EC-8 and ER-EC-4 coincident with southern TCL suggest the conduit behavior along the TCL axis.

- High transmissivity and low hydraulic gradients in the region near the northern margin of the Ammonia Tanks caldera margin between Wells ER-EC-12 and ER-EC-14 indicate the caldera margin behaves as a conduit.

- Faults in Oasis Valley are thought to control springs by acting as conduits or barriers through juxtaposition of permeable and impermeable rocks, termination of aquifer against low-permeability rocks, or abrupt thinning of aquifers (Figure 2-4).

Hydraulic Conductivity Anisotropy

Anisotropy is a concept that provides for a directional dependency of hydraulic conductivity. For example, hydraulic conductivity may be preferably aligned with a dominant fracture orientation or bedding orientations. The effect of horizontal anisotropy on groundwater flow is an apparent departure of flow direction from the horizontal gradient direction. At the basin scale, effect of anisotropy on groundwater flow likely is minor within the PM-OV basin because flow paths derived from geochemistry data (Figure 2-11) are generally consistent with the gradient direction seen in the potentiometric surface (Figure 4-2). Regional-scale anisotropy could occur on PM because of a regional stress field that conceptually allows preferentially oriented faults and fracture to have a higher hydraulic conductivity. However, this preferential orientation for faults and fractures to have higher conductivity would be about N15°E to N30°E (Reeves et al., 2017), which is similar to the average regional flow direction estimated from geochemistry flow paths and hydraulic gradients; and would not significantly change flow directions within the areas of expected RN transport.

4.1.4.2 Aquifer Storage

The storage coefficient (S) is defined as the volume of water an aquifer releases from or takes into storage per unit surface area of the aquifer per unit change in head (Freeze and Cherry, 1979). It is a dimensionless variable generally smaller than 0.005 in confined aquifers. In unconfined aquifers, it is called the specific yield and is a measure of the drainable porosity. Specific storage (Ss) is the amount of water an aquifer releases from or takes into storage per unit volume per unit change in head. It is calculated by dividing the storage coefficient by the saturated thickness.

The two main sources for estimated values of Ss are the analyses based on the use of earth tides (N-I, 2012; Navarro, 2018) and those estimated through the use of numerical modeling to estimate hydraulic parameters by matching simulated and observed drawdowns from hydraulic testing in the PM area (Garcia et al., 2017). The values of Ss estimated using earth tides range from a low of 9.9E-07 to a high of 6.62E-05 1/m. The analyses performed for Garcia et al. (2017) range from approximately 6.1E-09 to 3.1E-07 1/m. The values of Ss estimated by Garcia et al. (2017) are

generally one to two orders of magnitude lower than the values estimated using earth-tide analyses (N-I, 2012; Navarro, 2018). The underestimation of model-estimated specific storage values was attributed to overestimation of the aquifer thicknesses contributing to flow within the model.

4.1.5 Conceptual Flow Model Summary

The conceptual model is the integrated understanding of the hydrogeologic and geochemical data and provides the context to develop the mathematical model. The conceptual model defines the important elements of the flow system, including the components of the water balance (recharge, discharge, and changes in storage) and hydrogeologic controls on groundwater flow. Jackson et al. (2021) present a comprehensive synthesis of hydrogeologic data and conceptualization of the PM-OV groundwater basin. Much of the PM CAU groundwater conceptual model is based on this work. The key components of the groundwater conceptual model are summarized as follows:

- The PM-OV groundwater basin extends from Gold Flat and Kawich Valley in the north to the terminus in Oasis Valley in the southwest. The basin's western boundary is the region from Sarcobatus Flats in the south to the Cactus Range in the north. The basin's eastward extent is to the Belted Range and incorporates all underground nuclear testing areas on PM (Figure 4-1). A number of cross sections are included with the PM-OV HFM report (Navarro, 2019a) that present the modeled hydrostratigraphy over the full HFM domain, north to south, east to west, and over a series of transects through the areas that are the focus of the current report. Although the outlying areas contribute to and are affected by the PM-OV groundwater flow system, the supplemental sections provided in the current report have been configured to show the hydrostratigraphic details more clearly than would be possible with sections the full length and width of the HFM.

- The lateral basin boundary of the PM-OV basin represents a no-flow boundary, although minor amounts of water may flow into or out of the basin as underflow or surface flow (Jackson et al., 2021).

- Generally, the majority of the flow through the PM-OV basin occurs in the shallower aquifers. Jackson et al. (2021) showed that the largest transmissivity occurs in the first 1,600 ft (~490 m) below the water table due to a decreasing abundance of high-transmissivity devitrified rock at depth and an increasing abundance of low-transmissivity rock with argillic and mineralized alteration. However, areas of deeper conductive aquifer are present in the PM subsurface in some areas.

- Groundwater in the PM-OV basin generally flows south-southwesterly and discharges at Oasis Valley. An estimated 5,900 ac-ft/yr of groundwater discharges in Oasis Valley. Subsurface discharge from Oasis Valley to the Amargosa Desert through alluvium in

southern Oasis Valley is estimated at about another 100 ac-ft/yr, and an additional estimated 300 ac-ft/yr surface water in the Amargosa River flows southward out of Oasis Valley (Fenelon et al., 2016).

- The basic spatial pattern of recharge reflects the topographic influences on precipitation and the estimated spatial distribution of soil and rock properties. Recharge occurs primarily in upland areas. Recharge on the valley floors is negligibly small compared with most upland areas except beneath ephemeral washes.

- The groundwater flow system is considered to be in steady state based on observations of temporal trends in water levels in wells and balanced recharge with discharge. Although the PM-OV groundwater system is not in true steady state, groundwater underlying most of the PM-OV basin reflects steady-state conditions, where short-term changes in recharge and ET cause water levels to naturally oscillate around long-term (century-scale) average conditions (Jackson et al., 2021). The amount of groundwater discharged through wells is small compared to that of natural discharge. The 2010 well discharge of approximately 100 ac-ft/yr (125,850 m^3/yr) represents less than 2 percent of the total basin flow (Navarro, 2021b). Water production is assumed to be negligible compared to total basin flow and is not included in the flow models.

- Aquifer and confining HSUs can have similar hydraulic behavior, and HSUs can be very heterogeneous. The mean hydraulic conductivity of data grouped by HSU and HGU are very similar regardless of hydraulic character (e.g., aquifer or confining unit). However on average, aquifer HSUs have moderately higher hydraulic conductivity than confining unit HSUs (Section 4.1.4.1).

- The presence of regional-scale (basin-scale) hydraulic conductivity anisotropy on groundwater flow is unknown but likely is minor within the PM-OV basin (Jackson et al., 2021). As demonstrated by the work of Garcia et al. (2017) and Lu et al. (2021), flow models can be calibrated to PM hydraulic data conductivity without invoking grid-block scale anisotropy.

- Faults are narrow zones in the PM-OV groundwater basin generally less than 300 ft (~100 m) wide. Fault zones may behave as conduits along the fault axis due to high fracturing in the damage zone, or faults behave as barriers due to the presence of the fine-grained material in a fault or by displacing permeable units against low-permeability confining units. Most faults cannot be differentiated hydraulically from adjacent host rocks, and only a limited number of faults and caldera margins may have hydraulic significance on the flow field.

4.2 PM CAU Flow Model Development and Calibration

This section describes the technical approach and methods implemented to construct the PM CAU flow model. The key objective is to transform the conceptual model described in Section 4.1.5 into computational models that can simulate the PM-OV groundwater flow system. The model construction process includes domain definition, spatial discretization, definition of boundary conditions, and assignment of model parameters and model calibration.

The model was constructed with the MODFLOW 6 groundwater flow modeling code, Version 6.1.0 (Langevin et al., 2017). The MODFLOW 6 code uses a generalized control-volume finite-difference approach in which a cell can be hydraulically connected to any number of surrounding cells allowing for the resolution of the grid to vary spatially to capture source areas and complex structures, such as faults with higher resolution than other areas where coarser discretization is sufficient.

4.2.1 Model Area and Numerical Grid

The numerical flow model is based on the PM CAU HFM (DOE/EMNV, 2020a). The lateral model boundaries were selected to encompass the lateral extent of the PM-OV groundwater basin, which includes all areas that can potentially capture and transport RN contamination emanating from the underground nuclear detonation sites along with the basin recharge and discharge areas.

The areal extent and mesh of the PM CAU flow and transport model is presented in Figure 4-5. The PM-OV groundwater basin spans approximately 62 mi (100 km) in the northeast–southwest direction and encompasses about 1,400 sq. mi (3,600 km^2). The vertical extent is from 0 m amsl at the model's base to the top of the model, which stairsteps to follow the water table. The depth varies from approximately 5,900 ft (1,800 m) in the northeast to 3,200 ft (980 m) in Oasis Valley. Cell dimensions range from 3,937 ft (1,200 m) on a side to 246 ft (75 m) on a side in the horizontal direction. The model is refined to 984 ft (300 m) within the main flow corridor from the testing areas to Oasis Valley. Fine mesh refinement along faults is used along the main flow corridor, and course fault refinement is used outside the main flow corridor. The model is discretized into 33 layers and contains 1,328,019 total model cells. Vertical discretization was made finer between 2,297 ft (700 m) and the water table to capture the many HSUs within the Bench area and the depth at which most wells with responses to well development and testing activities are completed.

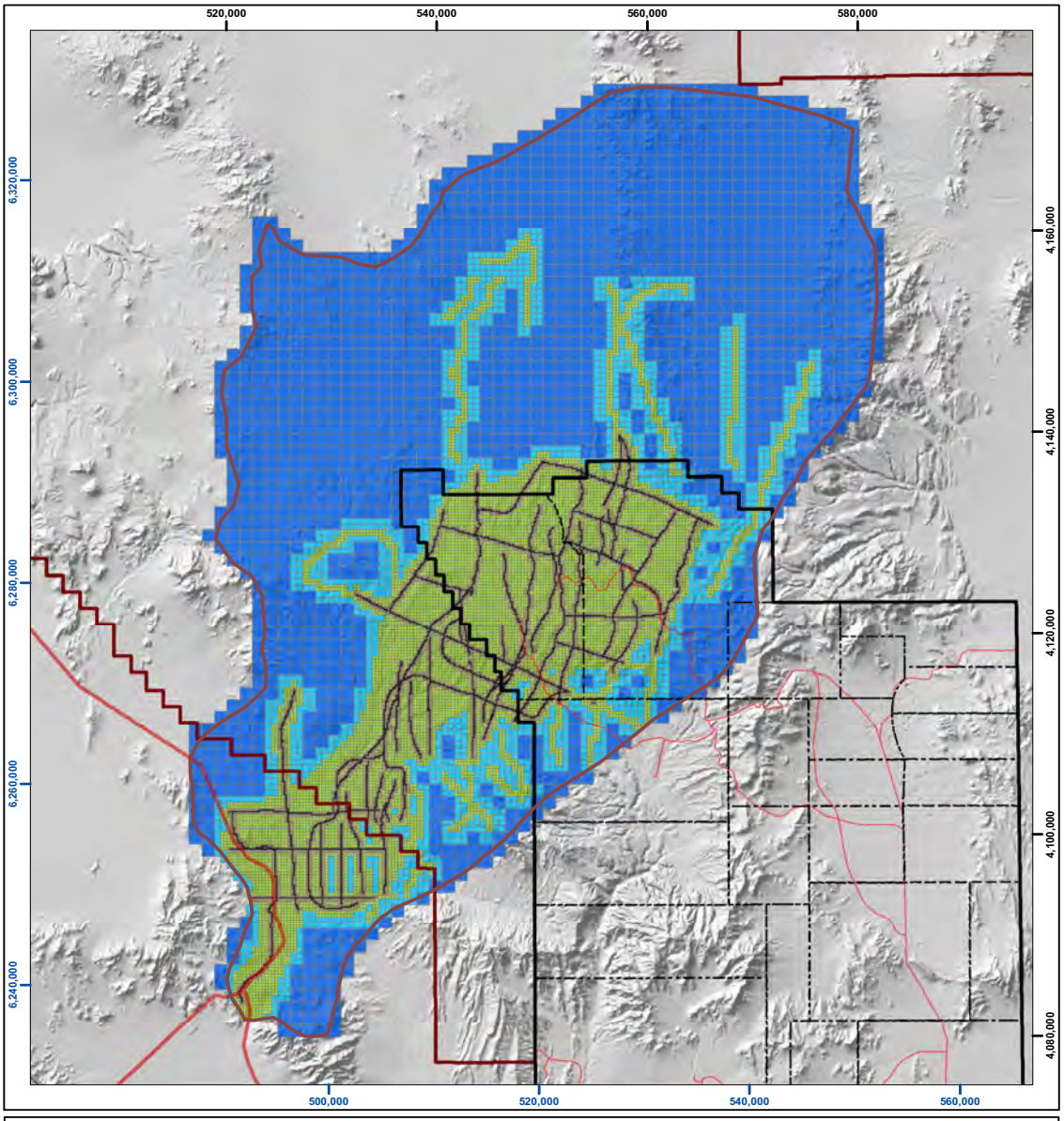

Figure 4-5
Areal Extent and Mesh of the PM CAU Flow Model

4.2.2 Material Parameter Assignment

The PM subsurface is primarily composed of volcanic rock originating from multiple Miocene-age calderas. The PM-OV HFM (Section 4.1.2) classified the subsurface of PM into spatially continuous HSUs that have a particular hydrogeologic character, such as being either an aquifer or a confining unit. The PM-OV HFM also included the basin faults and calderas as structural features.

For modeling purposes, the entire study domain was divided into many regions based on the HSUs and fault zones defined in the HFM. This enabled a discrete specification of hydraulic properties in each of these regions. A model cell, therefore, represented either rock associated with the particular HSU or a fault. The model domain only includes the saturated HSUs and faults in the PM groundwater basin; it includes 63 HSUs and 88 faults. Because of the large scale of the PM CAU flow model, nuclear test cavity and chimney structures are not included as discrete features within the model. The vertical movement of RNs within the chimneys is approximated by distributing the source term throughout cavity and chimney zones during transport modeling (Section 5.4).

The largest transmissivity and majority of flow generally occurs in the first 1,600 ft (488 m) below the water table (Jackson et al., 2021). However, areas of deep conductive aquifer are present in the PM subsurface. Garcia et al. (2017) estimated that 70 percent of the transmissivity at Well ER-EC-11 occurs between 1,000 and 3,000 ft (305 to 914 m) below the water table, and ^{3}H has been measured within the lower completion Well ER-20-12 at a depth of approximately 2,500 ft (762 m) below the water table due to an apparently permeable pathway from the HANDLEY test (Jackson, 2021). A low hydraulic conductivity deep aquifer zone was defined at depths greater than 2,500 ft (762 m) below the water table, which allows areas of transmissive aquifer within 2,500 ft of the water table where needed to match observed drawdowns from aquifer testing and deep ^{3}H measurements. The vertically extensive RMWTA HSU was divided into three zones by depth below the water table to allow better agreement with the ER-EC-14 aquifer test results. The zones include a shallow zone above 820 ft (250 m) depth, a middle zone between 820 and 1,969 ft (250 and 600 m), and a deep zone below 1,969 ft (600 m) beneath the water table.

Creating flow paths to Wells ER-20-12 and PM-3 consistent with ^{3}H observations in these wells required defining separate zones for the UPCU, LPCU, TCA, BRA, and PBRCM HSUs located west of the Purse fault. The UPCU, LPCU, BRA, and PBRCM HSUs west of the Purse were further

divided into north and south subzones at the location of the Ribbon Cliff fault. The top 656 ft (200 m) of the PBRCM west of the Purse fault and north of the Ribbon Cliff fault was defined as a separate zone to allow a permeable flow path from the HANDLEY chimney to the lowest completion in Well ER-20-12. Jackson et al. (2021) identified LFAs in the upper PBRCM of borehole UE-20j and Well ER-20-12 that may have facilitated ^{3}H transport from the HANDLEY detonation to the PBRCM in Well ER-20-12. The hydrogeologic properties in each HSU and fault zone were assumed to be uniform. Material parameters include hydraulic conductivity and specific storage for HSU and fault zones.

4.2.3 Boundary Conditions

Interbasin flow between the PM-OV groundwater basin and adjacent basins is thought to be insignificant, and including the entire PM-OV groundwater basin in the PM CAU flow model allows use of no-flow lateral model boundaries that do not require estimating uncertain boundary fluxes. One model parameter specifies the outflow head in Oasis Valley, which accounts for the estimated 400 ac-ft/yr of subsurface and surface flow out of the model (Section 4.1.5).

Recharge in the PM CAU Flow model domain primarily occurs in upland areas as a result of spring snowmelt during years of above-normal winter precipitation, and discharge occurs at springs and seeps within Oasis Valley. The recharge and discharge distribution from USGS PM-OV basin delineation model (Section 2.6.3.1) provides the model's upper boundary condition (Figure 2-11). The recharge distribution from the USGS basin model did not include the upland area of Black Mountain as an area of significant recharge. The recharge beneath Black Mountain was increased to account for the higher recharge that likely occurs due to the high elevation in this area. The elevation of Black Mountain exceeds 7,000 ft and is comparable to the elevation of Rainier Mesa, a known area of recharge as seen in water-level responses from wet winter events (Jackson and Fenelon, 2018). A factor of 10 increase in the amount of recharge near Black Mountain was estimated by matching the travel times of ^{3}H from HANDLEY to Wells ER-20-12 and PM-3. Travel time calculations used an effective porosity of 0.01, which resulted in flow path velocities consistent with ^{3}H migration distances downgradient of the BENHAM and TYBO nuclear tests measured in Wells ER-20-5, ER-20-7, ER-20-11, and ER-EC-11. A value of 0.01 for porosity is relatively large compared to data from tracer tests and fracture data, and represents an effective transport porosity that uses a larger

value to approximate the retarding effects of matrix diffusion. A factor of 10 increase of recharge near Black Mountain increased the total basin flow by approximately 12 percent. Fenelon et al. (2016) estimated the uncertainty of total basin flow to be approximately 15 percent.

The recharge is simulated as a steady-state flux at the model's upper surface using the MODFLOW Recharge Package and the discharge at springs within Oasis valley is simulated as steady-state outflows at the model's upper surface using the MODFLOW Well Package (Figure 4-6). Steady-state water production is assumed to be negligible compare to total basin flow and is not included in the flow model (Section 4.1.2). The model's lower boundary condition is no-flow.

4.2.4 Base Case Flow Model Calibration

The PM CAU flow model hydraulic properties are estimated by simultaneously calibrating twelve 3-D groundwater models using identical parameterization. The 12 models include a steady-state model of predevelopment flow conditions and 11 transient stress response models of well development and testing activities. The steady-state model provides initial conditions for the transient stress response models. All models share the same boundary conditions, hydraulic conductivity, and specific storage values. The temporal separation of the well development and testing activities allows for independent simulation of these events. The model calibrations were performed with the parameter estimation software PEST (Doherty, 2018).

During model development and calibration, several fault parameterization approaches were evaluated including models with all faults, a limited number of known hydraulically significant faults or no faults. A model with a limited number of faults generally behaving as hydraulic barriers provided the best overall agreement with calibration data and flow paths inferred from ^{3}H observations in wells. This model is considered the base case model. An alternative model containing all faults is included in the uncertainty analysis (Section 4.3.1).

The faults included in the base case model are located near the margins of SCCC and one fault is within the SCCC. The faults include (Figure 4-2) the Purse, Grouse Canyon caldera structural margin NW (GCCSMNW), and TCL, located near the western boundary of the SCCC; Moor Hen Meadow structural zone (MHMSZ), Split Ridge, and Rickey, located near the northern and eastern boundary of SCCC; and the Ribbon Cliff, located west of the Purse fault near Well ER-20-12. The barrier faults on

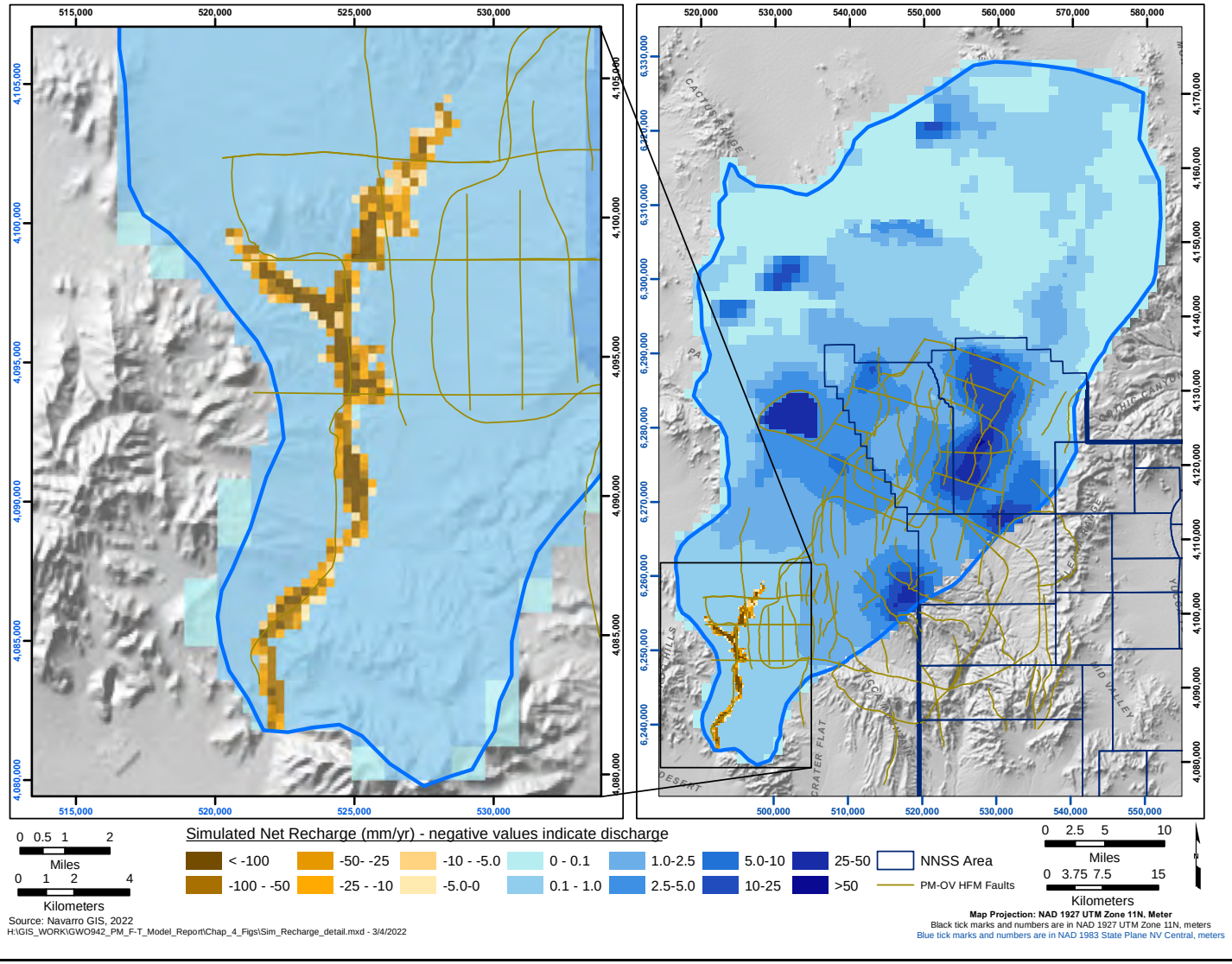

Figure 4-6
Recharge and Discharge Rates from the PM CAU Flow Model

the western boundary are needed to simulate the steep west-to-east hydraulic gradient observed across the Purse fault and TCL. The steep gradient indicates the presence of a hydraulic barrier that may be related to the considerable vertical offset of HSUs across the Purse fault. The barrier faults near the northern and eastern boundary of the SCCC are model artifacts needed to prevent flow paths toward Rainier Mesa as a result of the highest recharge occurring in western Area 19. The PBRCM HSU is the dominant HSU north and east of the SCCC and may have a lower hydraulic conductivity in these areas, thereby limiting flow toward Rainier Mesa. However, the PBRCM is an extensive HSU present in many areas of the PM-OV HFM and requires moderate hydraulic conductivity to achieve a good calibration to steady-state heads elsewhere. The barrier faults may be acting as a surrogate for lower PBRCM hydraulic conductivity outside of the SCCC.

4.2.4.1 Observations Used for Model Calibration

Hydraulic conductivity, specific storage and basin flow were estimated by minimizing a weighted composite sum-of-squares objective function. The objective function was informed by steady-state heads, aquifer stress responses (drawdowns), transmissivity measurements, and rate of groundwater flow moving through the PM-OV groundwater basin. Steady-state heads, aquifer stress responses from aquifer testing, or transmissivity measurements are available for nearly 400 well completions and spring locations in the PM CAU flow model domain. This section describes the observation data used in the model calibration and formulation of the objective function.

Steady-State Water Levels and Gradients

Hydraulic head is the most available hydrogeologic measurement used to constrain the PM CAU flow model. Jackson et al. (2021) analyzed water-level trends and hydraulic gradients of aquifer systems in the PM-OV groundwater basin from a detailed evaluation and assessment of available water-level measurements. A total of 184 hydraulic heads in PM-OV well completions or spring elevations considered to be representative of predevelopment conditions were used as water-level observations in the steady-state model calibration. For wells with multiple completions, the heads from completions considered most representative of the regional aquifer system were used. These were the completions identified by Jackson et al. (2021) as open to transmissive intervals or having long open intervals, heads with low uncertainty, and heads consistent with surrounding wells.

The steady-state head data are described in detail in Section 4.1.3. The most prominent features of the hydraulic head dataset that affect the model calibration are a steep west-to-east gradient across the Purse fault, and a potentiometric surface trough in southwest Area 20 and the Bench area. The steep gradient across the Purse fault may be attributed to the large vertical offset of HSUs that juxtapose permeable rock on the east against impermeable rock on the west or low permeability of the fault. The potentiometric surface trough in southwest Area 20 coincides with a zone of higher transmissivity. The high transmissivity may be due to fracturing associated with the caldera margin, or a thick accumulation of intra-caldera tuffs that are often welded and thick rhyolite lava flows in the area (Fenelon et al., 2016).

A total of 80 hydraulic gradients between well pairs (Table C-4 of Navarro, 2021b) were used as observations in the steady-state model calibration. The hydraulic gradients were calculated from the water-level data of Jackson et al. (2021) using the straight-line distance between wells. The well pairs selected for gradient observations are aligned with the general direction of flow toward Oasis Valley and are within 4 to 20 km of one another. Water-level uncertainty imparts excessive uncertainty on flow directions and horizontal gradients at distances of less than 4 km between wells due to water-level uncertainty being of the same magnitude as the head difference between wells (Navarro, 2021b).

MWAT Pumping Responses

Phase II data collection activities between November 2009 and September 2016 included well development and testing of 10 wells in the Bench area (SNJV, 2009a), and one additional well northwest of the Bench (Well ER-20-12). The wells contain single or multiple completions and, for the wells with multiple completions, the individual completions were hydraulically isolated during pump-scale aquifer testing using packers. The pumping along with the drawdowns seen in the observation well network associated with each tested interval can be considered individual aquifer tests, thereby providing a total of 16 MWATs (Figure 4-7). The distal location of ER-20-12 from observation wells prohibits the well development and testing data from this well being interpreted as an MWAT.

Garcia et al. (2017) performed simultaneous interpretation of the 16 MWATs to estimate hydraulic properties on PM (Section 2.6.3.2). The data compiled by Garcia et al. (2017) represent the available

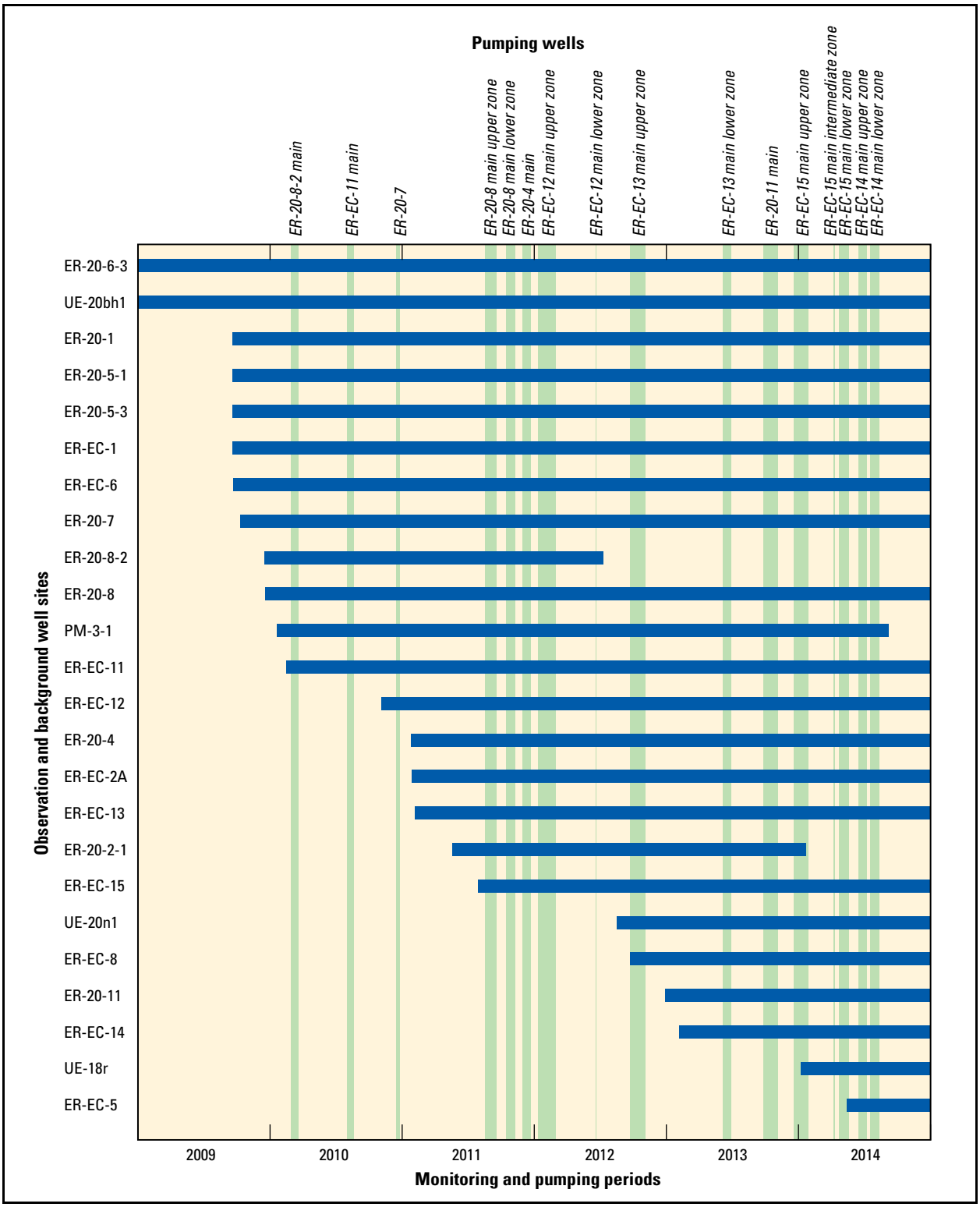

Figure 4-7
Monitoring and Pumping Periods for the PM MWATs
Source: Garcia et al., 2017, Figure 6

stress-responses used to calibrate the CAU groundwater flow model. Data collected during the 16 MWATs included pumping schedules and continuous water-level, temperature, and barometric-pressure measurements. Water levels and temperatures were measured continuously or intermittently in the observation wells, background wells, and pumping wells from November 2009 to October 2014. A total of 38 completions at 26 well locations have aquifer stress responses to groundwater withdrawals were used along with wells not having aquifer stress responses in calibration of the CAU groundwater flow model.

Transmissivity Measurements

Transmissivities have been estimated from aquifer tests in 50 wells within the PM-OV groundwater basin and were used as observations in the model calibration. Observation weights considered volume of water extracted during aquifer testing and magnitude of the measured transmissivity value. The use of transmissivity data from aquifer testing during model calibration requires conversion of model hydraulic conductivity to transmissivity. Hydraulic conductivity equals transmissivity divided by the thickness of rock contributing water to the well, which can vary from a fraction of the well open-interval length to the entire aquifer thickness. The aquifer thickness contributing to an aquifer test is related to the pumping rate, transmissivity distribution near the well, and volume of water extracted during the aquifer test. During aquifer testing, high transmissivity wells are typically pumped at higher rates, larger volumes of water are extracted, and a greater thickness of the aquifer contributes to the pumped volume of water. For aquifer tests where transmissivity was less than 100 square meters per day (m^2/day) or small volumes of water were pumped, the contributing thickness was limited to the well screen length. For aquifer tests where transmissivity exceeded 100 m^2/day or more than 400 cubic meters (m^3) of water were pumped, the contributing thickness was the entire model thickness. Halford and Jackson (2020) used a similar approach when calculating model transmissivity for comparison to transmissivity estimates from aquifer-test results. The approximate threshold of 100 m^2/day to determine whether the well screen thickness or entire model thickness is used to calculate model transmissivity from model hydraulic conductivity was taken from the approach used by Halford and Jackson (2020) for the DVRFS3 modeling and simple reasoning that larger pumping rates draw water from a thicker section of the aquifer. Halford and Jackson (2020) state: “For aquifer tests where transmissivity was less than 1,000 ft^2/d or small volumes of water were pumped, the contributing thickness was limited to the well screen length. For aquifer tests

where transmissivity exceeded 1,000 ft²/d or large volumes (more than 100,000 gal) of water were pumped (Halford and others, 2006), the contributing thickness was the aquifer thickness from the DV3 hydrogeologic framework model."

The highest transmissivities in the PM-OV groundwater basin mostly occur in southwest Area 20 and the Bench area (Figure 4-8). This area of higher transmissivity coincides with a southwest-trending potentiometric surface trough. Groundwater flow converges in the potentiometric trough and moves downgradient into Thirsty Canyon and Oasis Valley. Transmissivities in northern Area 20 and Area 19 are generally lower except in Well UE-19h.

Objective Function Formulation

During model calibration, the PEST software minimizes a least-squares objective function, which is the sum of squared weighted differences between observations (e.g., measured values of water levels) and corresponding model outputs (Doherty, 2018). The PM CAU flow model objective function included the following observations groups: (1) steady-state heads, (2) steady-state gradients aligned along the general flow direction, (3) aquifer stress responses to well development and aquifer testing, (4) total basin flow, and (5) transmissivity measurements. The calibration observation weights were selected such that each observation group is visible in the objective function. More emphasis was placed on the most certain and informative observations to transport. The objective function observation weights consider the number and magnitude of observations, observation uncertainty, and value of information provided to transport calculations.

Most emphasis was placed on the steady-state heads and aquifer stress responses. Both of these observation groups are considered highly reliable and informative to the CAU model. The hydraulic heads along with hydraulic conductivity values calibrated to the aquifer stress responses drive the rate of RN migration away from the source areas. Tritium has been observed at concentrations above the MCL within wells in southwest Area 20 and the Bench area. The nuclear tests in this area likely pose the highest risk to groundwater in Oasis Valley due to the close proximity of the NNSS boundary and presence of high transmissivity. Steady-state heads in southwest Area 20 and the Bench area were given more emphasis than heads outside of this area.

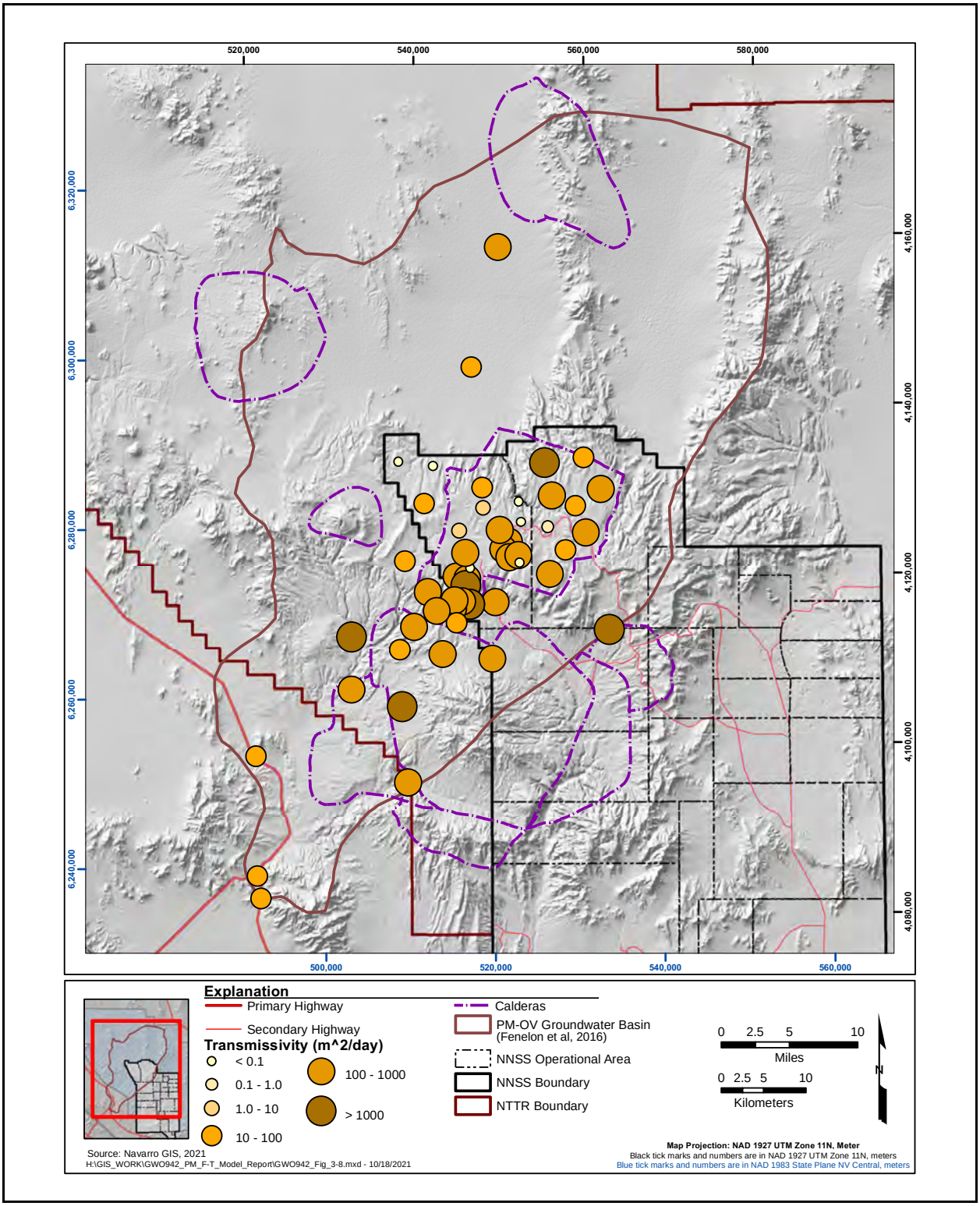

Figure 4-8
Transmissivity Measurements within the PM CAU Flow Model Domain

Less emphasis was placed on the hydraulic head gradients, transmissivities, and the total basin flow. The gradient observations are less certain than the steady-state heads because water-level uncertainty can be a large fraction of the head difference between wells, especially in areas of low gradient. The transmissivity data are also considered to be less certain compared to other types of observations because of the unknown aquifer thickness contributing to production during aquifer tests. Total basin flow is well-constrained in the PM CAU flow model and does not require a large weight because both the recharge distribution and Oasis Valley discharges to springs and seeps are fixed values. Only a relatively small underflow occurring near Beatty, Nevada, as a result of the specified head boundary condition in this area can vary the total basin flow amount.

4.2.4.2 Calibration Results

The goal of the model calibration was to obtain a model that is consistent with the conceptual model and has good agreement with the most certain and informative observation data. The many different types observations used in the model calibration make obtaining a good agreement with all data difficult. A much better agreement could be obtained if only one type observation were considered in the model calibration (e.g. exclusively calibrating to hydraulic heads). However, considering all data provides the basis for a better model for making CB forecasts.

The criteria for deciding whether or not a model is deemed to be “calibrated” is subjective and the decision should also consider the insight of the investigators and the appropriateness of the conceptual model rather than only the exact values of the measures of goodness of fit. The following criteria was used to support the assessment of calibration adequacy:

- Good agreement with steady-state head data. Steady-state heads are the most informative, certain, and abundant data for calibrating the model. Agreement is considered good when the vast majority of steady-state head residuals are less than 10 percent of the range of water levels within the basin, which is approximately 50 m.

- Fair agreement with horizontal head gradient data. Gradient data is less certain than hydraulic head data due to water-level uncertainty often being large compared to head differences between wells. Agreement is considered good when the majority of simulated gradients are within a factor of 2 the measured gradients.

- Good agreement with the majority of the drawdown data. Agreement is considered good when both timing and magnitude of the drawdown were matched.

- Acceptable agreement with the majority of the transmissivity data. The uncertainty of transmissivity data is higher than other data types because the aquifer thickness contributing to production during aquifer tests is unknown. Furthermore, the homogeneous treatment of HSUs does not allow the model to match the transmissivity from different wells located within the same HSU. Agreement is considered acceptable when the majority of simulated transmissivity values are with a factor of 10 of the measured value.

Agreement with observation data was evaluated with scatterplots, maps of residuals (simulated minus measured), water-level profiles, hydrographs, and maps of transmissivity. Good agreement was achieved with most observations. The results of the model calibration are measured by the objective function, which is defined as the weighted sum of squared errors between the observed and simulated values. Table 4-5 lists each observation group's contributions to the objective function and the mean absolute error (MAE).

Table 4-5
Observation Group Contribution to the Measurement Objective Function and MAE Error

Observation Group	Objective Function	MAE	MAE Units
Steady-State Heads	2.6E+07	14	m
Steady-State Head Gradients	4.0E+06	2.1E-03	m/m
MWAT Drawdowns	6.7E+06	4.0E-02*	m
Transmissivity	4.4E+05	0.96	Log10 m^2/day
Basin Flow	7.3E+05	17	m^3/day
Total	3.8E+07	N/A	N/A

*Drawdown MAE excludes the pumped wells
m^3/day = Cubic meters per day
N/A = Not applicable

MAE is the average of the absolute values of the errors. MAE is fundamentally easier to understand than the square root of the average of squared errors (root mean square [RMS]) because each error influences MAE in direct proportion to the absolute value of the error. The RMS error is scale-dependent and will overemphasize the largest data (e.g., drawdown in the pumped well compared with the smaller drawdown in observations wells).

The MAE is calculated as follows:

$$MAE = \frac{\sum_{i=1}^{n} \left|(y_i - x_i)\right|}{n} \qquad (4\text{-}1)$$

The relative contributions of each observation group to the overall objective function mostly reflect the relative observation group weights.

Steady-State Head and Gradient

The simulated base case potentiometric surface with residuals (simulated-observed heads) is presented in Figure 4-9. A scatterplot of the simulated versus observed heads at the 184 well and spring locations used as observations is presented in Figure 4-10. A scatter-plot of the simulated versus observed gradients between the 80 well pairs used as observations is presented in Figure 4-11. The potentiometric trough observed in central Area 20 and extending into Oasis Valley along with the steep west-to-east gradient across the Purse fault is reproduced by the model. The model's potentiometric surface is generally similar to the conceptual model's potentiometric surface (Figure 2-5) of Jackson et al. (2021), especially within and downgradient of the nuclear testing areas. The model's agreement between simulated and observed steady-state heads is good. However, the heads are generally underpredicted in northern Areas 19 and 20 and overpredicted in southern Area 19 and 20. Among the measured and simulated steady-state heads, 179 of 184 have residuals that are less than 50.

Simulated and measured water levels have good agreement along profiles generally aligned with the general direction flow toward Oasis Valley (Figure 4-12). Some of the largest head residuals are west of the Purse fault, where heads are overestimated at wells ER-20-12 and PM-3-1. The head observation at Well ER-20-12 used to calibrate the model is from the lower completion, located in the PBRCM HSU. The observed water level in the upper TMLVTA completion of the well is within a semi-perched aquifer that is ~240 ft (~74 m) higher than the lower completion. The upper completion water level is underestimated by the model. Simulating water levels west of the Purse fault is more difficult due to semiperched conditions occurring in the area and due to the need to create permeable flow paths consistent with observed ^{3}H transport from the HANDLEY test to Wells ER-20-12 and PM-3 while maintaining agreement with basin flow estimates in this area.

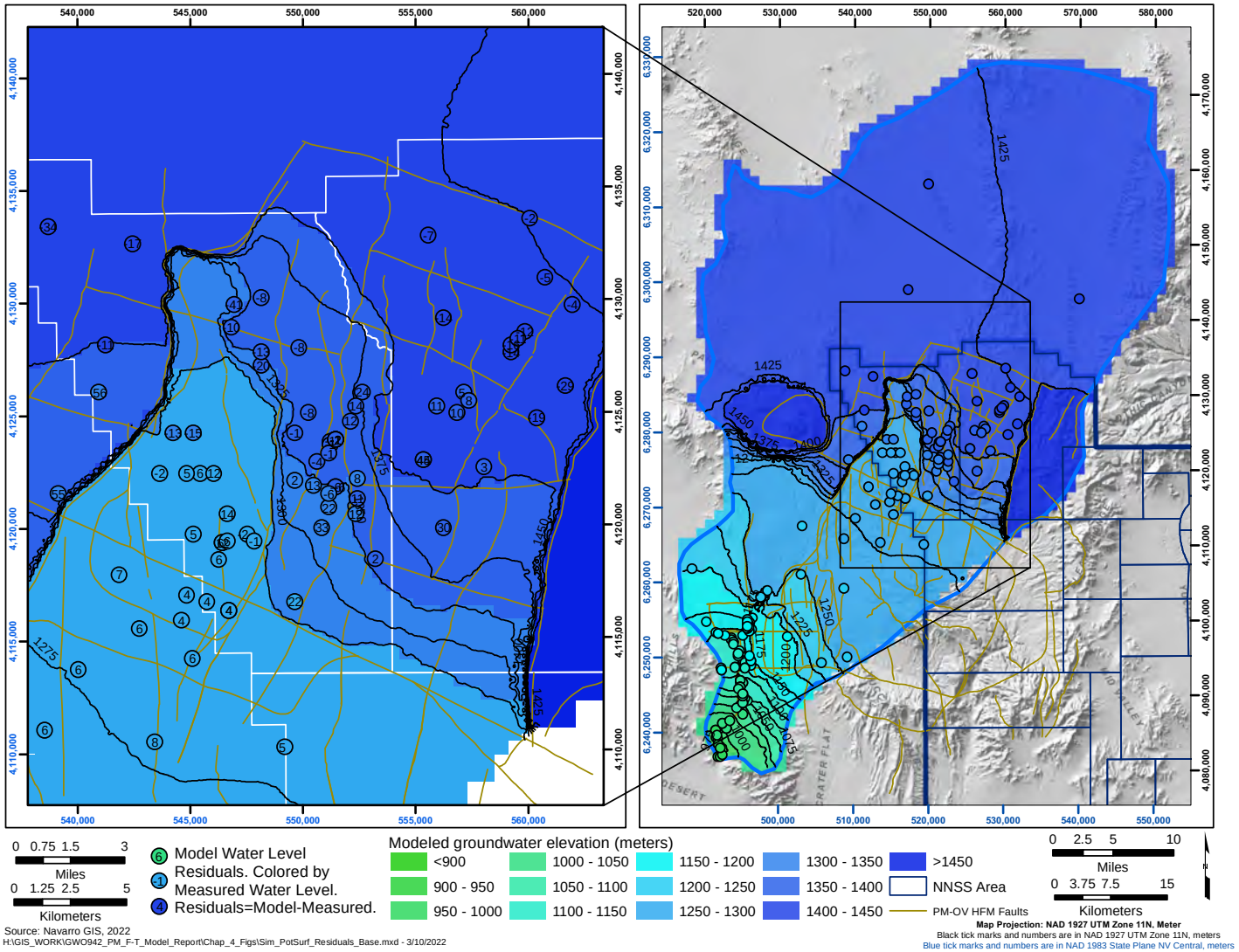

Figure 4-9
Potentiometric Surface and Residuals of the PM CAU Flow Model

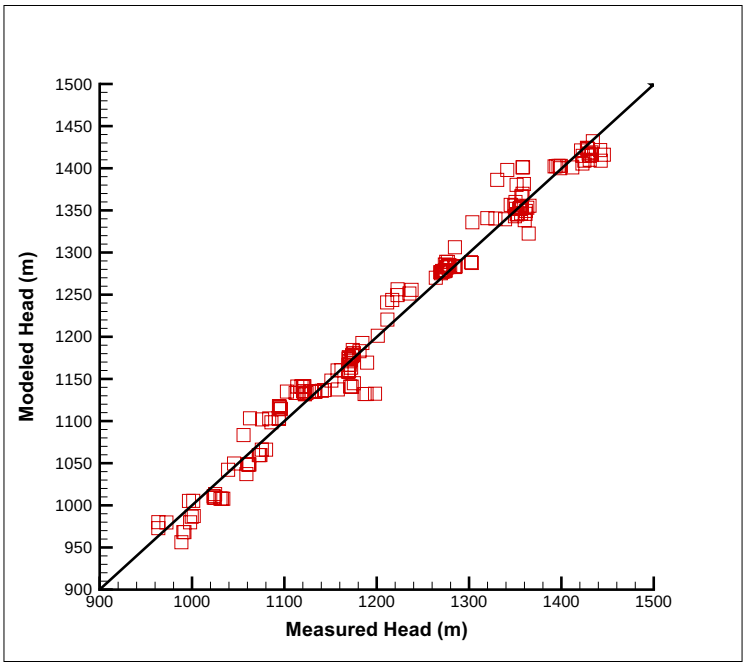

Figure 4-10
Modeled versus Measured Steady-State Heads for the PM CAU Flow Model

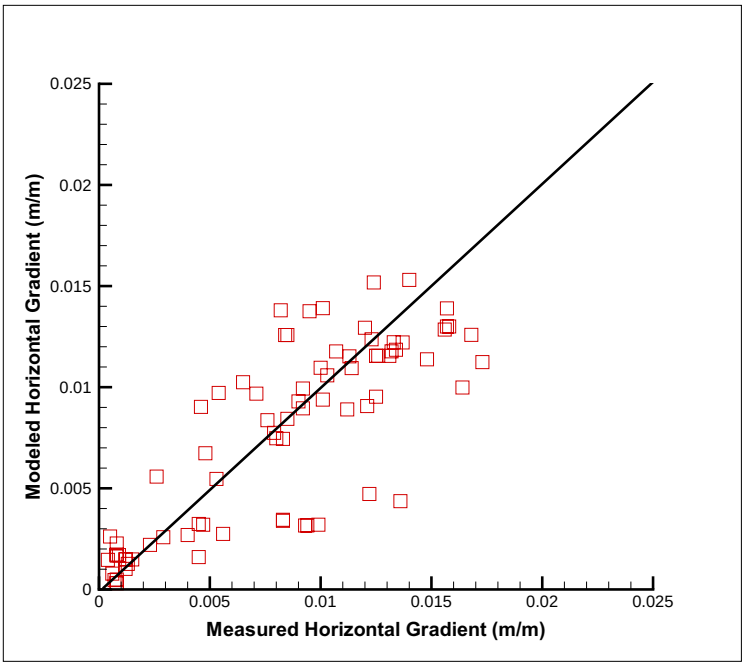

Figure 4-11
Modeled versus Measured Gradients for the PM CAU Flow Model

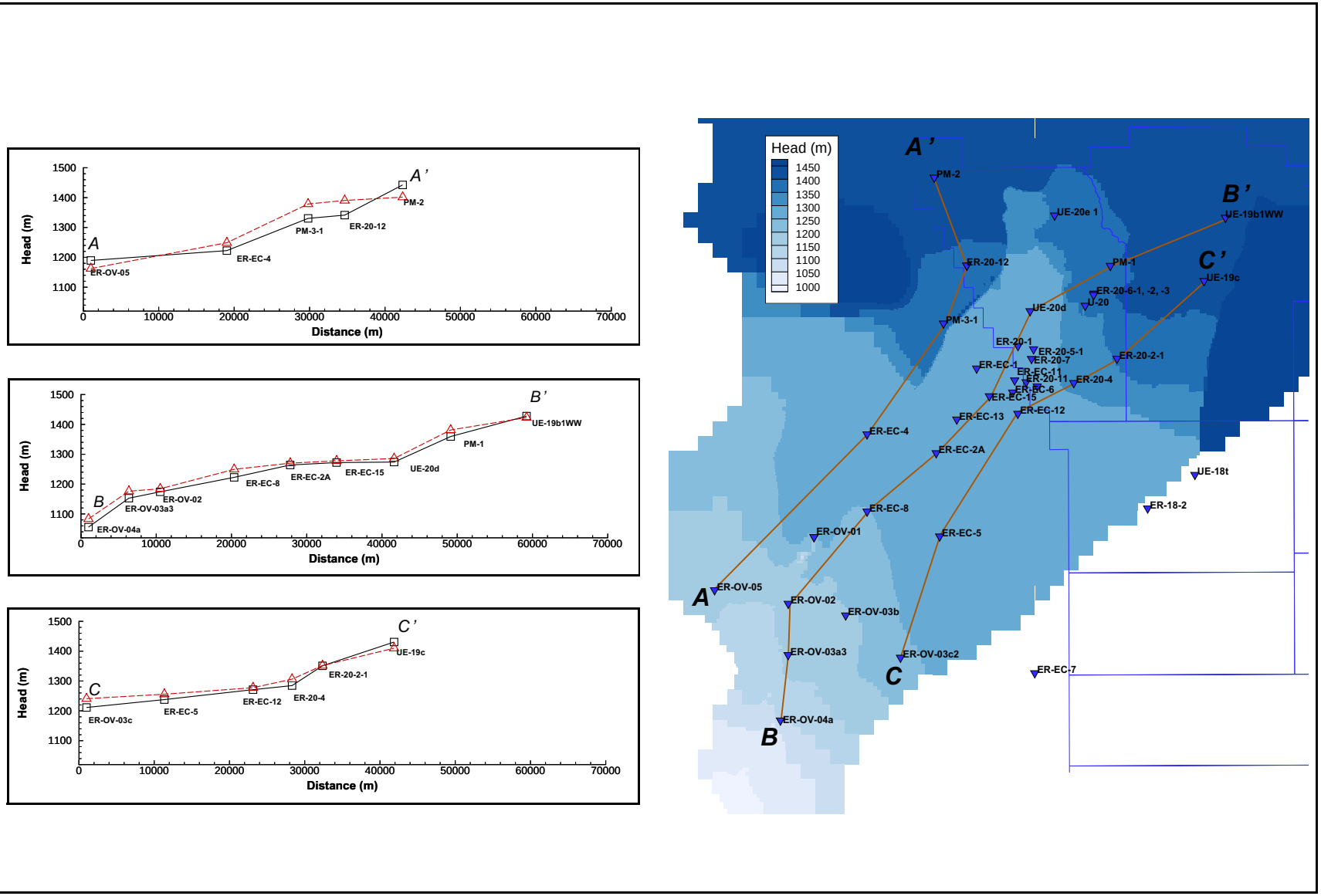

Figure 4-12
Measured and Simulated Water-Level Profiles Coincident with Flow Paths (red dashed lines are simulated heads)

Achieving an extremely good calibration to steady-state heads throughout the entire model domain is difficult because of the zonation approach used for model parameterization. The simulated HSUs are distinct zones with a single representative hydraulic conductivity. The heterogeneous nature of HSUs results in variability of hydraulic conductivity estimates within HSUs that is often larger than the variability of average hydraulic conductivity across all HSUs (Section 4.1.4.1). The model's homogeneous treatment of HSU hydraulic properties is likely responsible for the pattern of bias seen in the steady-state head residuals. The calibrated HSU hydraulic conductivity represents an average of sub-HSU scale areas of low and high hydraulic conductivity within the HSUs, which introduces the bias where small scale hydraulic conductivity is overestimated or underestimated.

The model's overall agreement with gradient observations is acceptable, considering the uncertainty in water-level estimates. The magnitude of the water-level uncertainty can approach that of the head difference between wells, especially in areas with a low gradient. Among the measured and simulated gradients, 61 of 80 have agreement within a factor of 2. Gradients are underpredicted from northern to southern Area 20 and in the area west of the Purse fault. The model's underprediction of gradients between northern and southern Area 20 and in the area west of the Purse fault will likely result in overpredicting transport. Simply using the lower than observed gradients would imply the model is underpredicting transport. However, the higher observed gradient implies a lower than simulated permeability area exists in this region of the model, which would slow transport. Steady-state head residuals are the highest and gradients are underpredicted in the area west of the Purse fault, yet this area has the fastest flow paths within model (see the following subsection, "Simulated Groundwater Velocity and Flow Paths").

MWAT Responses

Simulated and observed drawdowns compared well. The MAE for drawdown estimates excluding the pumped well is 0.040 m. Garcia et al. (2017) considered drawdowns reliable when confounding factors, such as frictional well loss or thermal effects, are not present. The MAE is similar in magnitude to the detection threshold of 0.015 m reported by Garcia et al. (2017).Good agreement between simulated and observed drawdowns was achieved in 152 of the pumping-well and observation-well pairs. Fair agreement was achieved in 32 of the pumping-well and observation-well pairs, and poor agreement was achieved in 22 well pairs. Agreement was considered good when both

timing and magnitude of the drawdown were matched. Agreement was considered fair when either magnitude or timing of the drawdown was matched. Simulated drawdowns with poor agreement in both timing and magnitude were considered poor. The majority of the observed drawdowns are in the Bench area. Well ER-EC-11 is located centrally in the Bench area and was monitored during 9 of the 11 MWATs. Good matches between simulated observed drawdown were achieved from most of the MWATs at this location (Figure 4-13). Appendix F presents the simulated and observed drawdowns for all monitored pumping- and observation-well pairs.

Transmissivity

The highest transmissivity measurements in the PM-OV groundwater basin (Figure 4-8) occur in southwest Area 20 and the Bench area; and high simulated transmissivities occur in the same area (Figure 4-14). A high-transmissivity corridor extends through southwest Area 20 into the Bench area due to high hydraulic conductivity in the TSA, TCA, SPA, and BA HSUs, creating fast groundwater velocities from test locations with known fast ^{3}H transport. High simulated transmissivity also occurs in northeast Area 20 due to high hydraulic conductivity in the TSA, TCA, Calico Hills lava-flow aquifer 3 (CHLFA3), and Calico Hills lava-flow aquifer 1 (CHLFA1) HSUs.

Simulated transmissivity generally agrees with the measurements. The MAE between simulated and observed transmissivity values is approximately an order of magnitude. Among the measured and simulated transmissivity values, 27 of 50 have agreement within a factor of 10. The large MAE for the transmissivity observation group compared to other observation groups reflects the low weights assigned to transmissivity observations and higher uncertainty of transmissivity data compared to steady-state heads and drawdown data. The uncertainty is higher because of the unknown aquifer thickness contributing to production during aquifer tests.

Model Parameters

The flow model calibration parameters are hydraulic conductivity and specific storage for the HSUs and faults in the HFM. The PM model is a highly parameterized groundwater model and has more parameters than can be estimated uniquely on the basis of the calibration dataset. A parameter identifiability index can be calculated by the PEST software, which identifies the parameters that can be estimated during the inverse modeling process. Identifiability ranges between 0 and 1; parameters

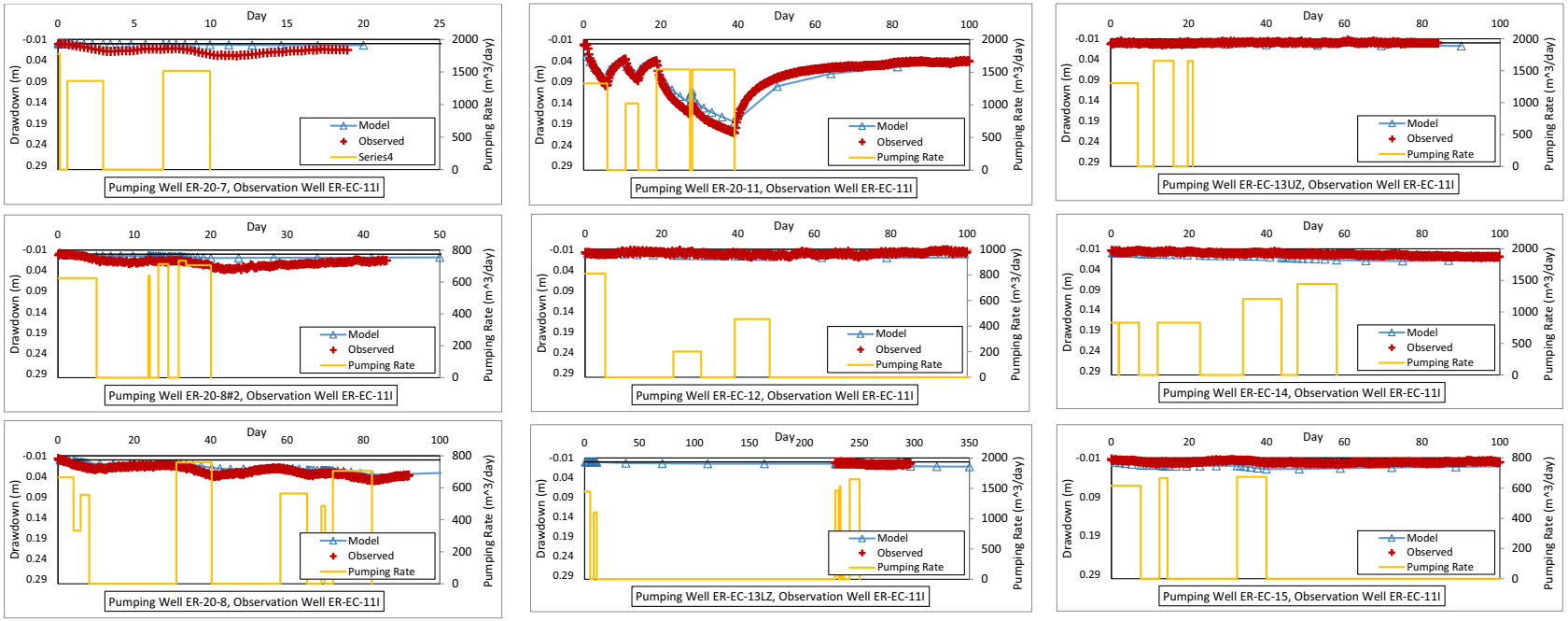

Figure 4-13
Comparisons of Simulated and Observed Drawdowns in ER-EC-11 Intermediate

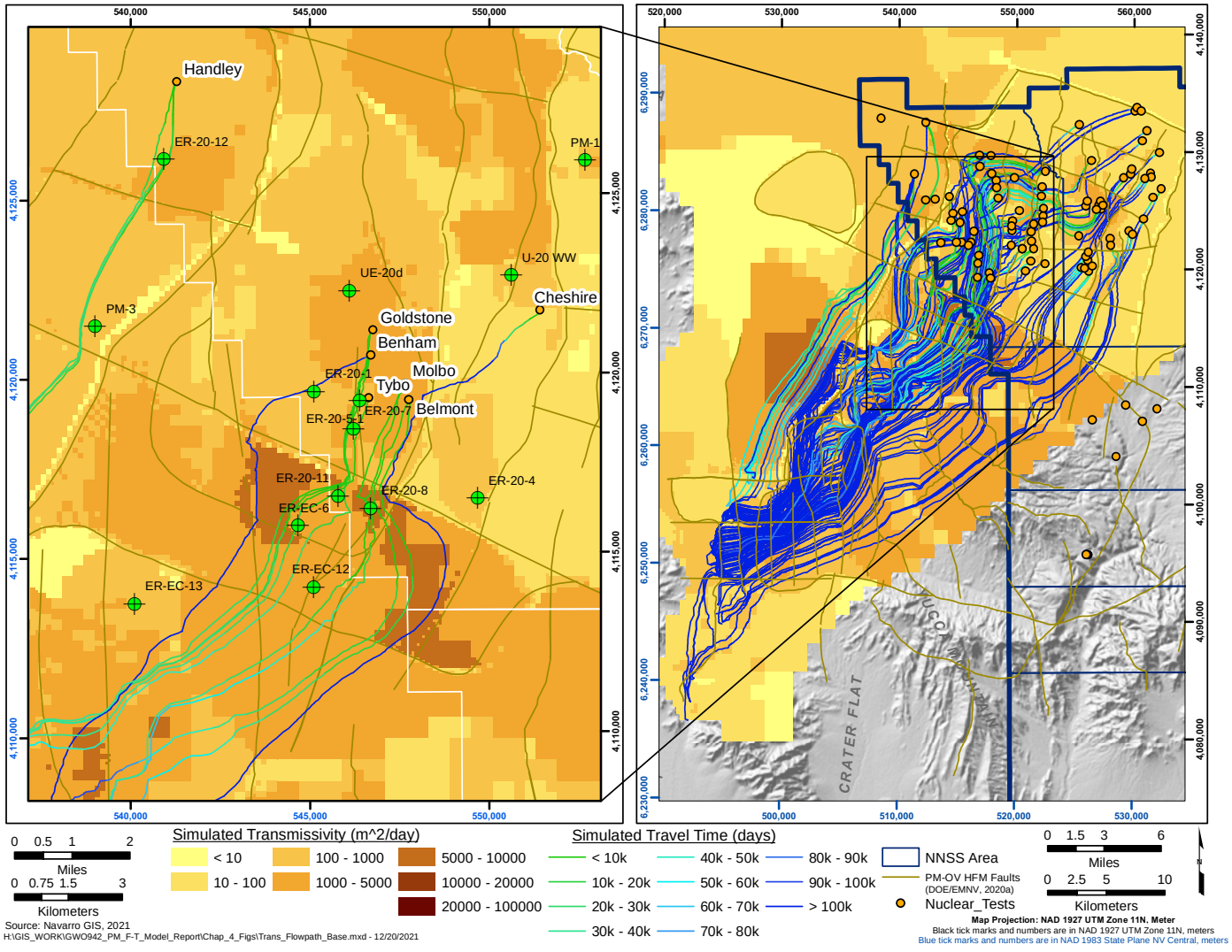

Figure 4-14
Simulated Transmissivity and Groundwater Flow Paths from Underground Nuclear Tests in the PM CAU Flow Model

having an identifiability index of 1 are fully identifiable, and parameters having an identifiability index of 0 are totally unidentifiable.

A total of 47 parameters have an identifiability index greater than 0.5 (Figure 4-15). The following parameters and their identifiability values are notable:

- The deep confining HSUs (Ammonia Tanks intrusive confining unit [ATICU], Pahute Mesa Northern Extension intrusive confining unit [PMNICU], Rainier Mesa intrusive confining unit [RMICU]), UCCU, ATCCU and LCA are highly identifiable as having a very low hydraulic conductivity, consistent with the conceptual model of hydraulic conductivity being low deep in the model.

- The UPCU and LPCU are highly identifiable as not behaving as confining units, which suggests these HSUs may be fractured.

- The LCCU, LCCU1, and BRA HSUs are highly identifiable as having moderate hydraulic conductivity. The LCCU, LCCU1, and BRA extend into the deep area of the model, which is consistent with high hydraulic conductivity not being present in the deep aquifer.

- The TSA HSU is highly identifiable as being extremely conductive, which is consistent with the fast ^{3}H transport measured at wells in the TSA downgradient of the BENHAM test.

The volume of the PM groundwater model is 5,570 km^3, and the volume-averaged hydraulic conductivity is 0.5 m/day, which reflects a large volume of low hydraulic conductivity in the deep aquifer. Hydraulic conductivity among the HSUs is highly variable and ranged between 4.4E-05 and 40 m/day (Table 4-6). Of the 15 HSUs that have a volume greater than 5 km^3 and hydraulic conductivities greater than 1 m/day (Table 4-6), the most permeable were the TMUWTA, RMWTA between 250 and 600 below the water table (mRMWTA2), TCA, TSA, and the top 200 m of the PBRCM located west of the Purse fault (mPBRCM_lfa). Extensive low-permeability HSUs include the ATICU, UCCU, PMNICU, CHZCM, FCCM, CFCM, and LCA. Many of the low-permeability HSUs are located deep in the model. The low permeability of the CHZCM and FCCM HSUs is a result of the high-permeability regions in the HSUs being included in the CHLFA, FCULFA, and FCLFA HSUs. Over 90 percent of the rock volume has a hydraulic conductivity of less than 1 m/day and can be considered semipervious to impervious (Bear, 1972). The limited number of faults included in the model behaved as hydraulic barriers to cross flow across except the Ribbon Cliff fault, which behaves as a conduit connecting the conductive mPBRCM_lfa and TCA HSUs west of the Purse fault (Table 4-7). The Ribbon Cliff fault acting as a permeable feature is needed to facilitate a

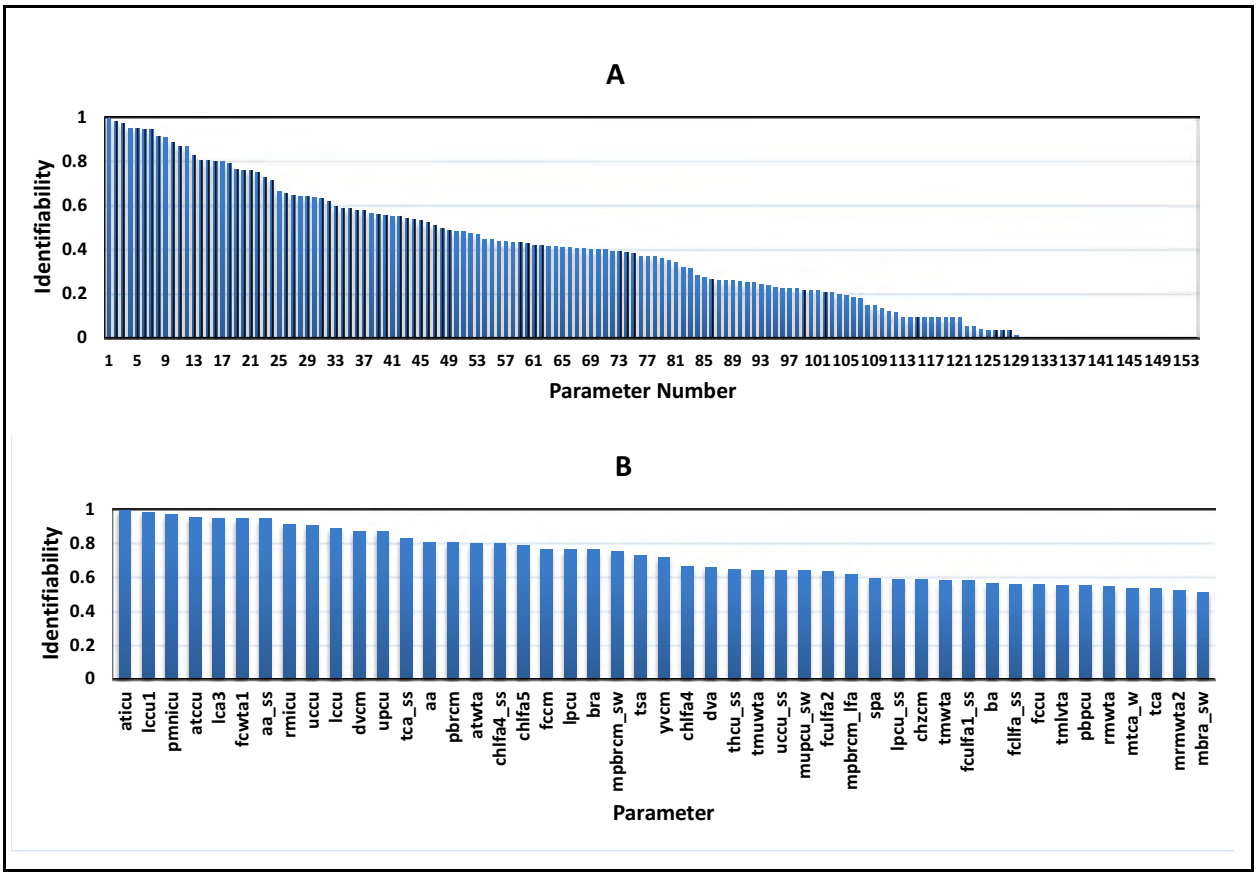

Figure 4-15
Identifiability Index for Independent Parameters: (A) All Parameters and (B) Parameters with Identifiability Index Greater than or Equal to 0.5

Notes: Identifiability Index is depicted for each of the units listed below.
ATCCU = Argillic tuff caldera confining unit
DVA = Detached volcanic aquifer
DVCM = Detached volcanic composite unit
FCCU = Fluorspar Canyon confining unit
FCLLFA = Fortymile Canyon lower lava-flow aquifer
FCWTA1 = Fortymile Canyon welded-tuff aquifer
LCCU1 = Lower clastic confining unit-thrust plate
mBRA_sw = Modified Belted Range southwest
mPBRCM_lfa = Modified Pre-Belted Range composite unit lava-flow aquifer
mPBRCM_sw = Modified Pre-Belted Range composite unit southwest
mRMWTA2 = Modified Rainier Mesa welded-tuff aquifer 2
mTCA_w = Modified Tiva Canyon aquifer west
mUPCU_sw = Modified Upper Paintbrush confining unit southwest
TMLVTA = Timber Mountain lower vitric-tuff aquifer
TMUWTA = Timber Mountain upper welded-tuff aquifer
UCCU = Upper clastic confining unit
YVCM = Younger volcanic composite unit

Table 4-6
Calibrated HSU Hydraulic Conductivity and Specific Storage for the Base Case Model
(Page 1 of 2)

HSU [a]	Hydraulic Conductivity (m/day) [b]	Specific Storage (1/m)	Hydraulic Conductivity Identifiability	Volume (km^3)	HSU [a]	Hydraulic Conductivity (m/day) [b]	Specific Storage (1/m)	Hydraulic Conductivity Identifiability	Volume (km^3)
YVCM	2.70E-03	2.29E-05	0.713	2.53E-01	FCLLFA	4.64E-01	3.95E-07	0.402	6.60E+00
AA	4.00E+00	1.09E-06	0.805	1.36E+02	FCULFA1	9.31E-02	5.47E-07	0.497	8.76E-03
CHZCM	4.71E-04	2.07E-05	0.585	9.89E+01	FCULFA4	1.96E+00	4.56E-08	0.418	2.76E+00
CHZCM_w	3.27E-04	4.24E-05	0.221	6.53E+00	PLFA	1.04E-02	1.97E-06	0.272	2.67E+00
FCWTA	2.99E-01	2.45E-07	0.414	1.27E+01	CHLFA4	4.26E-02	1.18E-08	0.663	6.62E+00
DVCM	1.37E-02	2.61E-05	0.868	9.96E+01	CHLFA5	4.23E-02	1.05E-07	0.789	1.37E+01
DVA	3.14E-02	3.98E-07	0.654	4.00E+01	CHLFA5_w	3.07E-01	1.09E-07	0.468	1.24E+00
FCULFA5	1.13E+00	4.61E-07	0.472	1.79E+00	IA_	9.00E-03	1.31E-06	0.370	1.70E+01
KA	2.28E-01	5.75E-07	0.486	3.31E-01	CHLFA2	1.55E-02	8.57E-07	0.392	1.52E+00
PCM	6.50E-03	8.27E-05	0.120	7.74E-01	CHLFA3	1.27E+01	4.34E-06	0.409	4.54E+00
YMCFCM	3.38E-03	4.57E-05	0.437	1.13E+01	CHLFA1	3.51E+00	8.71E-09	0.391	8.16E-01
MGCU	4.08E-02	8.75E-07	0.401	3.79E+01	PBRCM	2.80E-02	1.56E-05	0.803	1.43E+03
LCCU1	2.63E-02	1.12E-06	0.981	2.95E+02	PBRCM_sw	2.16E-03	5.81E-05	0.749	1.77E+02
LCCU	6.31E-02	2.19E-06	0.886	2.51E+02	PBRCM_nw	2.52E-03	9.44E-05	0.444	6.57E+02
PMNICU	9.34E-05	4.32E-06	0.969	1.08E+02	mPBRCM_lfa	1.68E+00	1.26E-04	0.618	1.66E+02
TMLVTA	3.74E+00	4.08E-07	0.551	3.87E+01	FCCM	2.91E-03	6.89E-05	0.764	8.41E+01
TCVA	2.04E-03	3.81E-07	0.370	2.24E+02	THCM	6.70E-04	7.51E-07	0.143	4.78E+00
PVTA	4.72E-02	8.42E-07	0.389	1.04E-01	CFCM	4.40E-05	1.28E-06	0.405	2.75E+01
CHVTA	6.04E+00	9.39E-07	0.433	5.53E+00	BWCU	1.38E+00	2.46E-06	0.483	9.73E+00
TMUWTA	2.29E+01	8.81E-07	0.641	2.16E+01	THCU	3.44E-02	1.39E-06	0.417	1.91E+01
TMWTA	1.48E-01	5.01E-07	0.578	5.67E+01	UPCU	1.39E-01	1.49E-07	0.867	5.24E+00
RMWTA	8.15E-04	8.87E-06	0.543	1.53E+02	UPCU_nw	3.27E+00	1.36E-07	0.445	8.82E-01
mRMWTA1	2.20E-01	8.96E-07	0.399	2.68E+01	SCVCU	1.25E-02	1.62E-07	0.433	8.61E+00

Table 4-6
Calibrated HSU Hydraulic Conductivity and Specific Storage for the Base Case Model
(Page 2 of 2)

HSU [a]	Hydraulic Conductivity (m/day) [b]	Specific Storage (1/m)	Hydraulic Conductivity Identifiability	Volume (km^3)	HSU [a]	Hydraulic Conductivity (m/day) [b]	Specific Storage (1/m)	Hydraulic Conductivity Identifiability	Volume (km^3)
mRMWTA2	9.50E+00	1.55E-06	0.520	6.56E+01	UPCU_sw	2.67E+00	1.84E-07	0.638	2.83E+00
WWA	3.79E+00	4.02E-07	0.349	1.57E-02	FCCU	4.98E-03	9.23E-07	0.555	3.28E+00
TCA	8.04E+00	1.35E-07	0.530	7.02E+00	PBPCU	8.29E+00	6.15E-07	0.548	1.31E-01
TCA_w	4.12E+00	1.03E-07	0.536	1.91E+00	MPCU	3.09E-03	2.91E-08	0.480	9.10E-01
TSA	6.25E+00	2.79E-05	0.727	5.37E+00	LPCU	2.85E-01	1.90E-04	0.759	1.14E+01
FCWTA1	2.90E+00	1.07E-06	0.946	1.86E+00	LPCU_nw	2.10E-02	6.66E-05	0.367	1.04E+00
BWWTA	1.76E+01	9.20E-07	0.383	3.82E+00	LPCU_sw	2.13E-02	2.90E-05	0.339	1.78E+00
ATWTA	1.75E-01	7.25E-05	0.801	1.09E+02	BFCU	9.54E-03	7.74E-05	0.414	6.45E+01
CPA	2.00E-03	3.05E-07	0.050	4.03E+00	CFCU	1.03E-02	3.25E-08	0.405	2.83E+01
BRA	3.42E-02	1.38E-05	0.759	2.49E+02	LCA	8.00E-05	3.58E-07	0.035	3.71E+02
BRA_nw	9.06E-02	1.62E-05	0.426	2.30E+01	ATCCU	9.06E-04	4.66E-07	0.950	1.75E+00
BRA_sw	6.95E-02	8.42E-06	0.509	4.15E+00	LCA3	5.44E-03	3.24E-07	0.949	1.62E+02
BA	2.10E+01	1.95E-07	0.563	1.95E+00	UCCU	8.10E-04	1.72E-06	0.907	1.64E+02
THLFA	4.42E-02	7.45E-07	0.361	2.73E+00	RMICU	4.94E-04	9.65E-07	0.912	7.92E-01
SPA	4.00E+01	4.42E-08	0.594	1.60E+00	ATICU	1.21E-04	5.24E-06	0.995	8.98E+00
FCULFA2	2.47E+01	1.55E-06	0.633	9.07E-01					

[a] For HSU definitions, please refer to Acronym List.
[b] Hydraulic conductivity below 2,500 ft of the water table is limited to 1E-04 m/day.

Table 4-7
Calibrated Fault Permeability and Specific Storage for the Base Case Model

Fault	Hydraulic Conductivity (m/day)	Specific Storage (1/m)
Grouse Canyon Caldera Structural Margin NW	3.72E-05	9.21E-07
Purse	7.50E-05	2.88E-07
Thirsty Canyon Lineament	3.73E-05	8.97E-07
Rickey	7.55E-05	7.88E-07
Split Ridge	7.54E-05	5.11E-07
Moor Hen Meadow Structural Zone	4.82E-04	8.11E-07
Ribbon Cliff	1.10E+00	9.21E-07

fast flow from the HANDLEY chimney to the deep completion of Well ER-20-12. Jackson (2021) identified a similar feature near the Ribbon Cliff fault that was inferred from the propagation of the pumping (well drilling) signal from borehole ER-20-12 to borehole PM-3.

The calibrated hydraulic conductivities of all HSUs in the model displayed as the dominant HGU with each HSU are illustrated in Figure 4-16. The TCU, WTA, and LFA HGUs are highly heterogeneous with respect to hydraulic conductivity. Estimated hydraulic conductivity of each of these three HGUs varies by five to six orders of magnitude. The range of transmissivities estimated for TCU, WTA, and LFA indicates that these HGUs can function spatially as either aquifers or confining units. However, the higher hydraulic conductivity values (>1 m/day) are more often associated with HGUs typically considered to be aquifers (VTA, WTA, and LFA), and some of the lowest hydraulic conductivity values (<0.01 m/day) are more often associated with HGUs typically considered to be confining units (TCU, CCU, and ICU). The dominant HGUs associated with composite units HSUs (CHZCM, PBRCM, and FCCM) tend to have lower hydraulic conductivity values.

Hydraulic conductivity is more important than specific storage because it defines the direction and relative magnitude of groundwater flow that will affect the transport of RNs. Specific storage is secondary to hydraulic conductivity in importance because it must be estimated to simulate transient water-level responses that help inform hydraulic conductivity estimates. Specific storage estimates are not used directly in the steady-state transport calculations. The specific storage values ranged

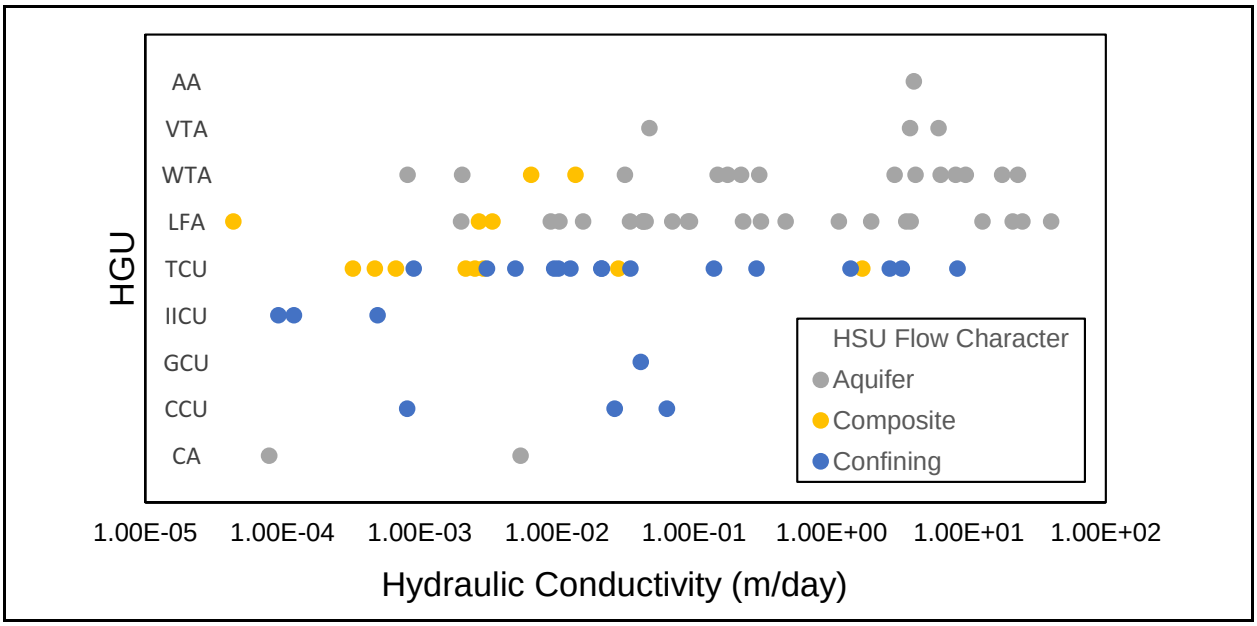

Figure 4-16
Calibrated Hydraulic Conductivity as a Function of HGU

from 8.7E-09 to 7.7E-04 1/m. The vast majority of the HSU specific storage values are within the expected range for fractured rock and are within the range of values estimated from earth tide data (Section 4.1.4.2).

Simulated Groundwater Velocity and Flow Paths

The groundwater velocity is controlled by the model's transmissivity and recharge distribution. As expected, groundwater flow from PM is primarily south-southwest to the discharge areas in Oasis Valley. High velocities occur west of the Purse fault, in southwest Area 20 and in Oasis Valley (Figure 4-17). A high-velocity channel is present from southwest Area 20 to the Bench area within the TSA and TCA HSUs. The velocities in southern Oasis Valley are higher than the average PM-OV velocities due to narrowing of the groundwater basin and reduction in volcanic rock thickness. Groundwater velocities are generally low north of the NNSS, where transmissivity and recharge are conceptualized as being low.

Tritium has been observed (see Figure 5-1) downgradient of BENHAM/TYBO, CHESHIRE, and HANDLEY detonations. The simulated flow paths indicate the GOLDSTONE, MOLBO, and BELMONT detonations may also contribute to the ^{3}H observations in southwest Area 20 and the Bench area (Figure 4-18). The model's Darcy velocity field was used to evaluate flow paths and

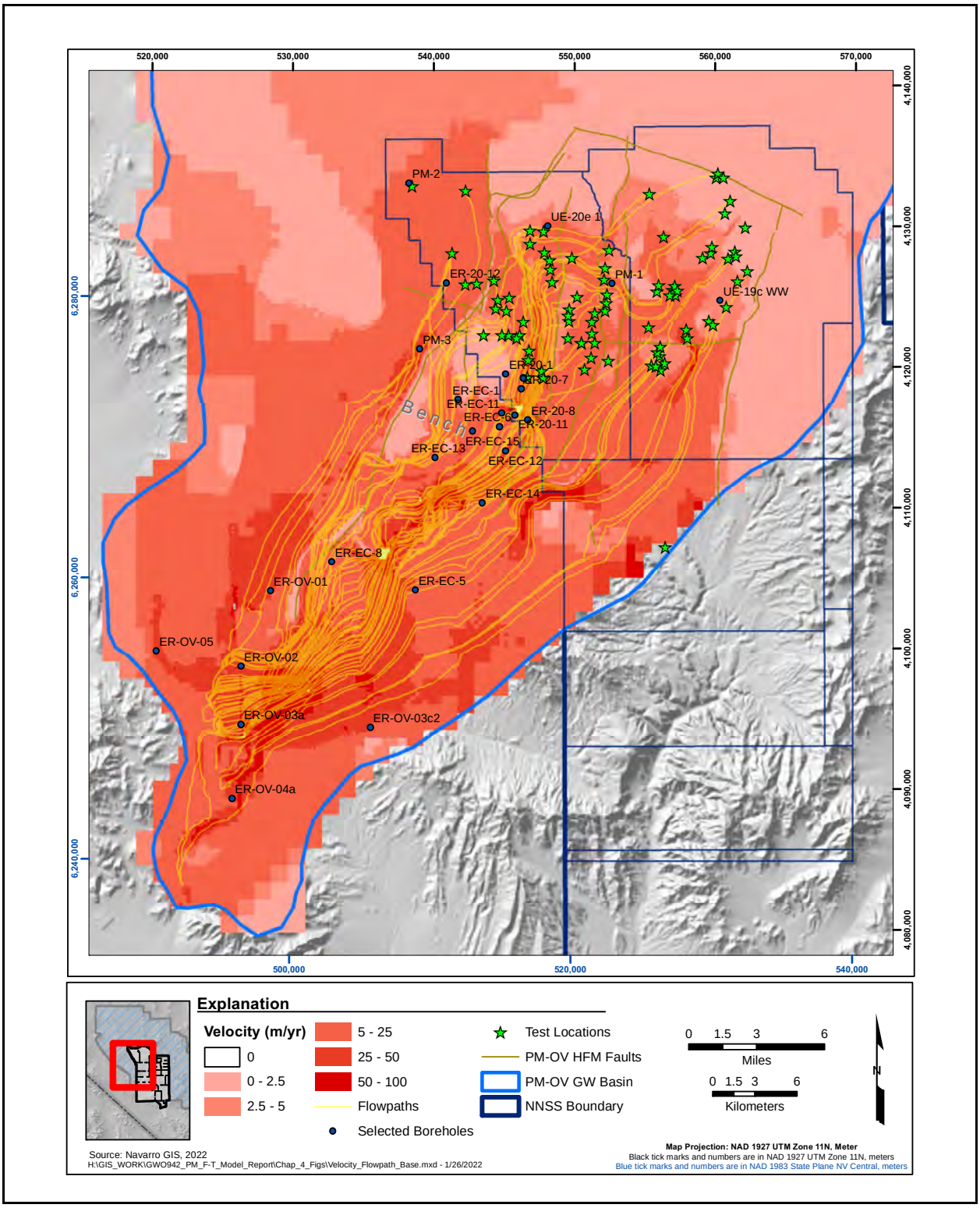

Figure 4-17
Groundwater Velocity Field and Simulated Groundwater Flow Paths from Underground Nuclear Tests in the PM CAU Flow Model

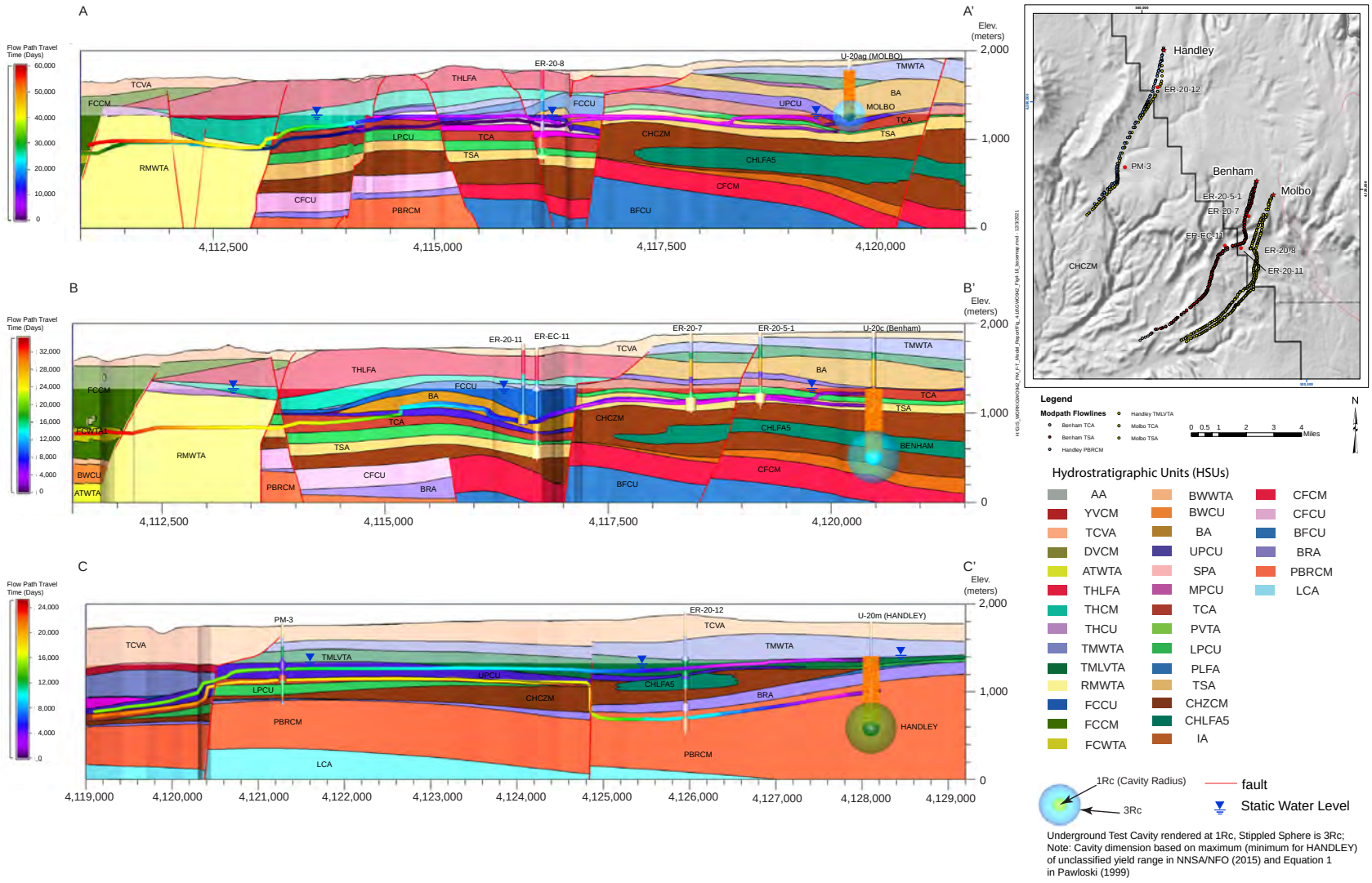

Figure 4-18
Cross Sections Showing HSUs and Flow Paths Originating from the HANDLEY, BENHAM, and MOLBO Detonations

linear velocity from the PM underground detonation locations using a porosity of 0.01. The resulting simulated advective-flow distances were within the range of observed advective transport from the ^{3}H data. This relatively large porosity compared to those from tracer test data and cubic law-based estimates from fracture data (Navarro, 2021a) represent an effective transport porosity that uses a larger porosity to approximate the retarding effects of matrix diffusion.

Figure 4-14 illustrates the simulated transmissivity field and flow paths color-coded for travel time from all detonations. Flow path starting locations are from the cavity center for detonations with saturated working points and from the water table for detonations with unsaturated working points. Additional flow path starting locations were placed in the high-hydraulic conductivity HSUs in the rubblized chimney zones. Tritium from these detonations likely moved vertically upward within the rubblized chimney due to thermal convection before moving laterally downgradient from these detonations.

Simulated fast flow paths occur from the detonations in southwest Area 20 and from the HANDLEY detonation. The fastest flow paths occur through the TSA and TCA from the BENHAM chimney and TYBO cavity, through the TSA and TCA from the MOLBO cavity, and through the TMLVTA then UPCU and PBRCM then TCA from the chimney of HANDLEY (Figure 4-18 inset and Figure 4-18). The advective travel time, without explicitly accounting for transport mechanisms discussed in Section 5.0, from the chimney of BENHAM and cavity of TYBO to Wells ER-20-11 and ER-EC-11 is approximately 30 years, which is consistent with the ^{3}H observations. The flow path from the BENHAM cavity located in the CHZCM is extremely slow. Flow paths from the HANDLEY detonation pass near Well ER-20-12, and the advective travel times from the TMLVTA within the chimney are approximately 20 years to Well ER-20-12 and approximately 40 years to a location near Well PM-3.

Tritium dominates the other RNs in the HST (see Section 5.2) with respect to the extent of RN migration at concentrations above the regulatory limits (see Section 5.3). However, the short half-life of ^{3}H will likely result in concentrations falling below regulatory limits within 200 years. The average flow path length at 200 years provides an integrated metric for evaluating advective velocity and comparing flow fields from the alternative models (Section 4.3). Additionally, the distance from flow path endpoints at 200 years to Springdale Lower well provide a metric for evaluating the potential of

groundwater from test areas arriving at the discharge areas in Oasis Valley from different models. The Springdale Lower well is near the center of the groundwater ET areas in Oasis Valley.

The average flow path travel distance from all detonations at 200 years is 10 km, and the minimum distance from any detonation flow path endpoint to the Springdale Lower well is 2.1 km. The fastest groundwater flow occurs from the STILTON, HANDLEY, GOLDSTONE, JORUM, PEPATO, MOLBO, BENHAM, GREELEY, COLBY, TYBO, KASH, PURSE, and FONTINA sites, all of which are located in Area 20 and have 200-year groundwater travel distances greater than 20 km (Figure 4-19).

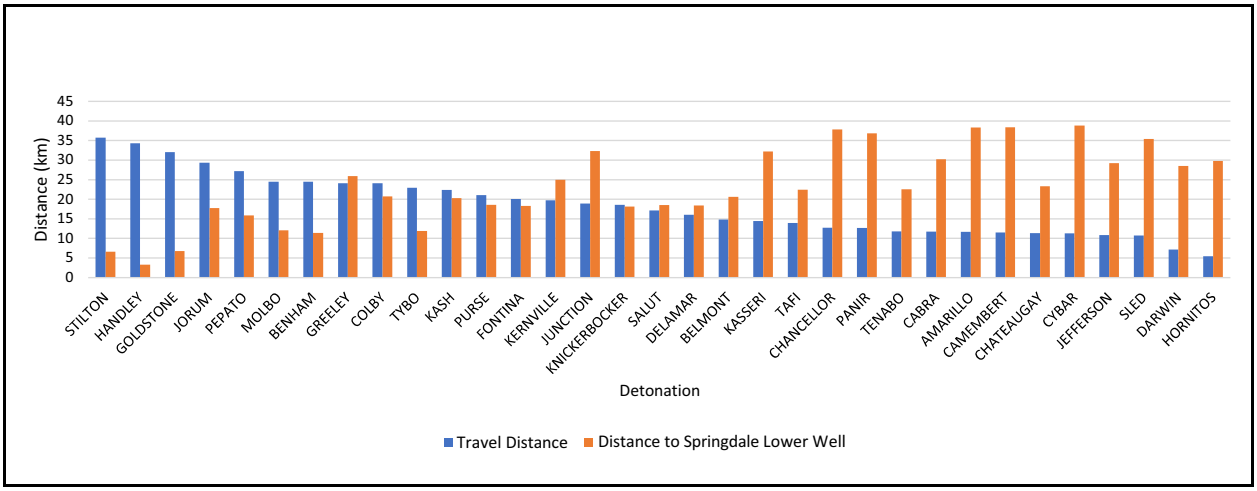

Figure 4-19
Tests and Base Case Advective Travel Distances in Excess of 5 km after 200 Years

The test with groundwater travel endpoint nearest to the discharge areas after 200 years is HANDLEY, followed by STILTON and GOLDSTONE, which all are within 5 km of the Springdale Lower well. Measurements of ^{3}H in Well PM-3 support the model's fast groundwater velocities occurring west of the Purse fault. Tritium, at concentrations below the MCL, has apparently migrated approximately 7.1 km in 41 years from HANDLEY to Well PM-3, which is a velocity of approximately 163 meters per year (m/yr). In comparison, ^{3}H has migrated approximately 4.1 km in 43 years from BENHAM to Well ER-EC-11, which is a velocity of approximately 98 m/yr. The fast flow paths west of Purse fault simulated by the model are more uncertain compared to other areas because of high steady-state head residuals in this area and because flow in this area is not well characterized. However, the model's uncertainty associated with the area west of the Purse fault is likely biased toward overestimating rather than underestimating flow and transport.

4.3 Flow Model Uncertainty Analysis

Identifying unexpected and more extensive RN transport due to model uncertainty is the primary concern for the uncertainty analysis. Therefore, the goal of the uncertainty analysis is to identify and include models that are likely to lead to more extensive transport than the base case and still have permissible fits to the calibration data. Four alternative models were constructed and calibrated, including a model with all faults defined with the HFM, two models using alternative recharge distributions and a model using a water table upper boundary condition. These alternative models and calibration results are described in this section.

4.3.1 Model Including All Faults

Faults are narrow zones in the PM-OV groundwater basin generally less than 100 m wide; the PM-OV HFM includes 105 structural fault features (DOE/EMNV, 2020a). Fault zones are thought to behave as conduits along the fault axis due to high fracturing in the damage zone on either side of the fault plane. Faults may also behave as barriers due to the presence of the fine-grained material in the fault plane or by displacing permeable units against low-permeable confining units, effectively creating barriers to flow (Section 4.1.4.1).

The hydraulic behavior of faults in the PM-OV groundwater basin is uncertain and various analyses have different findings. Garcia et al. (2017) performed an analysis of aquifer testing data from southwest Area 20 and the Bench area and identified drawdowns propagating across structural blocks and faults, suggesting faults in the Bench area do not have a strong hydraulic influence (Section 2.6.3.2). However, (Lu et al., 2021) performed an analysis using the same aquifer testing data along with steady-state head and ^{3}H observations and identified faults behaving as both barriers and conduits (Section 2.6.3.3). Jackson et al. (2021) performed a conceptualization of the groundwater flow in the PM-OV basin and concluded most faults cannot be differentiated hydraulically from adjacent host rocks, but a limited number of faults and caldera margins may be considered flow barriers or conduits based on hydraulic information. A regression analysis between log-transformed hydraulic conductivities in wells and distance to the nearest fault indicated a correlation of increasing hydraulic conductivity is present with proximity to faults at a distances of less than 1,000 ft (Section 4.1.4.1).

An alternative model containing all faults identified in the HFM was calibrated to evaluate the likelihood that faults may be hydraulically significant and create fast flow pathways. Boundary conditions for the all-faults alternative model are the same as for the base case model, which includes increased recharge near Black Mountain. The calibration of the model including all faults achieved an objective function value of 4.2E+07, which is similar to the base case objective function of 3.8E+07. Figures 4-20 through 4-22 present the potentiometric surface with residuals, MWAT responses at Well ER-EC-11 intermediate, and the transmissivity field with flow paths. Hydraulic heads and residuals are higher in southern Area 20 and the Bench area compared to the base case model. The drawdown in Well ER-EC-11 intermediate resulting from pumping Well ER-20-11 during well development, and testing is overpredicted. Faults provide moderate hydraulic connections through regions of low hydraulic conductivity and moderate barriers to cross-flow in regions of very high hydraulic conductivity. Within the high-permeability Bench area, faults do not provide fast pathways for transport and are more disposed to function as barriers resulting in flow paths from the BENHAM detonation passing west of Wells ER-20-5-1, ER-20-7, and ER-20-8. North of the Bench area, faster transport is seen from several tests located northwest of the BENHAM test. The average flow path travel distance from all detonations at 200 years is 9.9 km, and the minimum distance from any detonation flow path endpoint to the Springdale Lower well is 4.0 km, which are both similar to the base case.

4.3.2 Models with Alternative Recharge Distributions

The total estimated recharge generated in the PM-OV groundwater basin from precipitation-derived infiltration is 6,300 ac-ft/yr (7,761,600 m^3/yr), assuming the groundwater system is in steady state and recharge equals discharge (Section 4.1.2). Navarro (2021b) reviewed three different studies that estimate recharge in the PM-OV groundwater basin and concluded that, with consideration of mass-balance constraints from discharge volumes, uncertainty in the total recharge occurring in the PM-OV groundwater basin is likely less than a factor of 2. However, on a local scale within the basin, the uncertainty associated with spatial variability of recharge is higher. Furthermore, calibrating the base case model to heads west of the Purse fault along with simulating fast ^{3}H transport observed from the HANDLEY test required increasing recharge occurring in the vicinity of Black Mountain beyond that used by the USGS basin delineation model (Fenelon et al., 2016), indicating that the USGS basin model may underestimate recharge in western PM. A factor of 10 increase of recharge

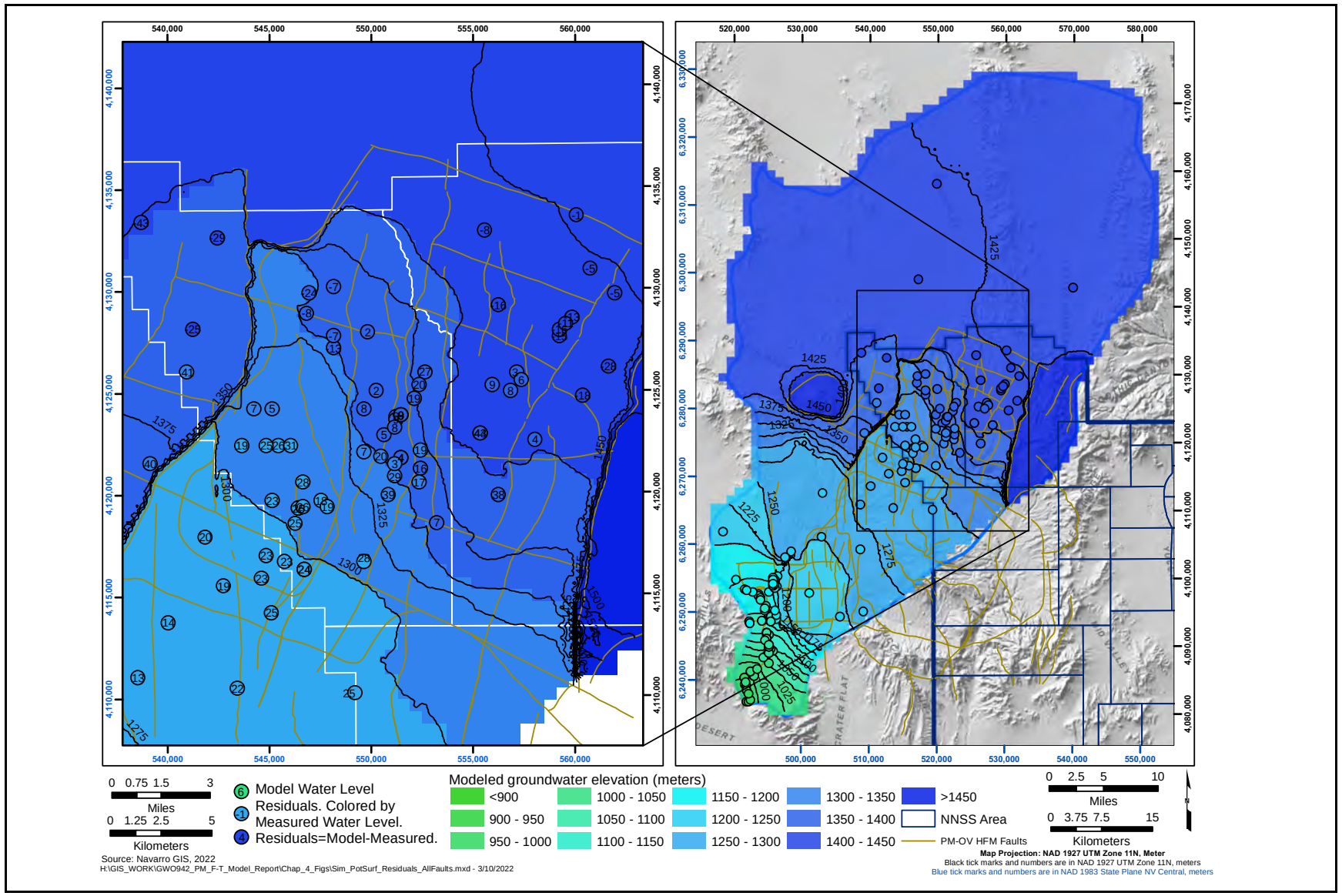

Figure 4-20
Potentiometric Surface and Residuals for the PM CAU Flow Model with All Faults Identified in the HFM

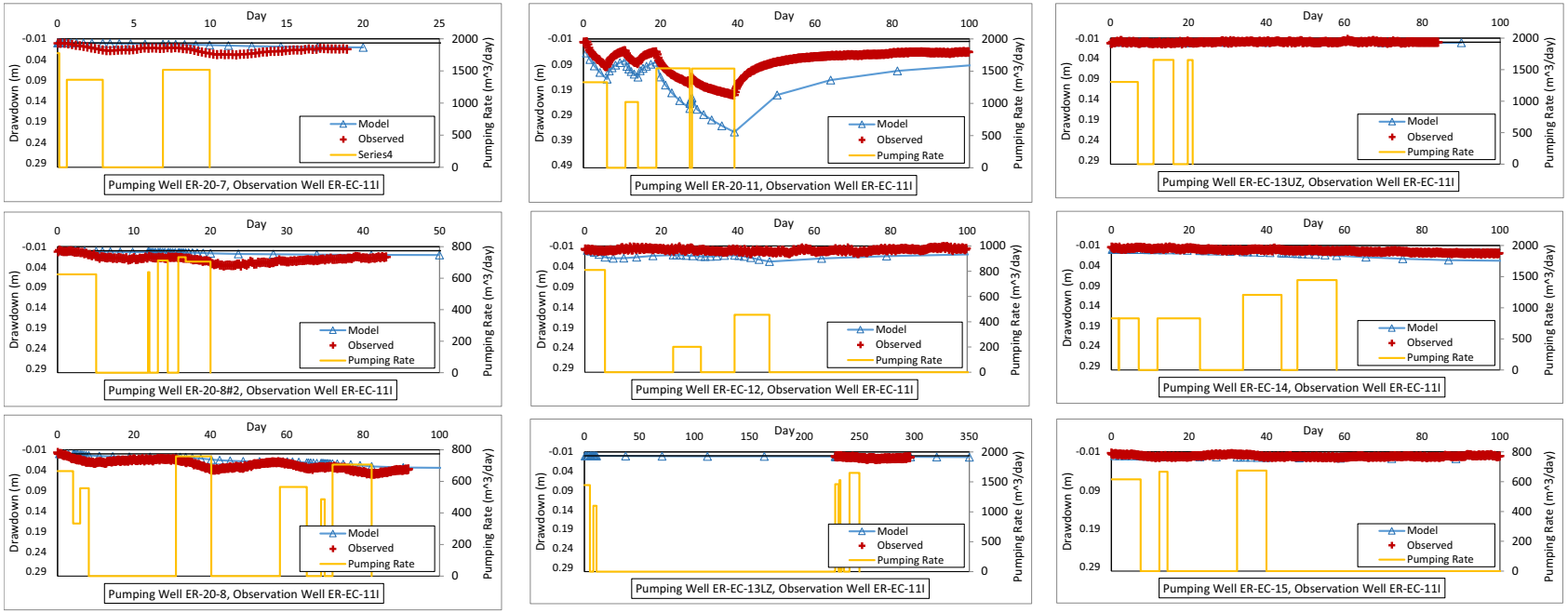

Figure 4-21
Comparisons of Simulated and Observed Drawdowns in ER-EC-11 Intermediate for a Model with All Faults Identified in the HFM

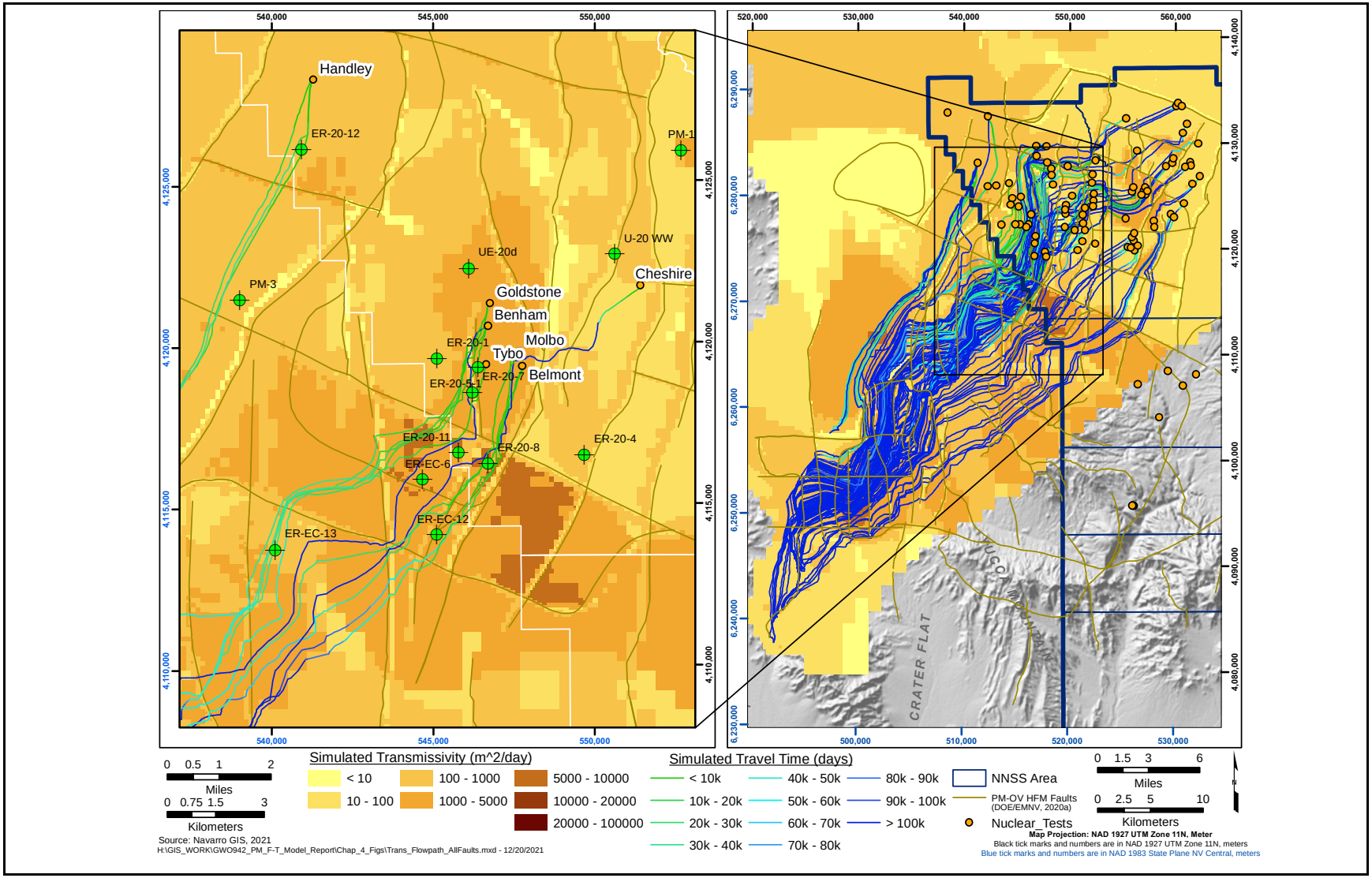

Figure 4-22
Simulated Transmissivity and Groundwater Flow Paths from Underground Nuclear Tests for a Model with All Faults Identified in the HFM

near Black Mountain increased the total basin flow by approximately 12 percent, which is within the estimated uncertainty of total basin flow of approximately 15 percent given by Fenelon et al. (2016). Two alternative recharge distributions were considered to assess the impacts of recharge uncertainty, the first being the recharge in the PM-OV basin used by the DVRFS3 model (Halford and Jackson, 2020) and the second being recharge estimated from infiltration modeling (Middleton et al., 2019). The recharge near Black Mountain was not increased in the INFILv3 and DVRFS3 alternative recharge models; both have higher recharge in the Black Mountain area compared to the original recharge distribution from Fenelon et al. (2016) used in the base case model before the increase.

4.3.2.1 DVRFS3 Recharge Model

Halford and Jackson (2020) estimated the recharge distribution by calibrating numerical models using pilot points (RamaRao et al., 1995) to distribute recharge within the DVRFS3 study area. The initial recharge distribution was based on a conceptual model of water availability and permeability of rocks in recharge areas. The conceptual model of total annual recharge to the study area consisted of a modified Maxey-Eakin (Maxey and Eakin, 1951) approach that distributed recharge is a piecewise linear function of total annual precipitation. The water available for recharge was estimated from precipitation, where proportions of recharge increase from 0 to 0.9, 0.9 to 4.6, and 4.6 to 41 percent of annual precipitation in the ranges 0.3–1.0, 1.0–1.5, and 1.5–2.5 ft/yr of precipitation. The total recharge within the PM-OV basin estimated by the DVRFS3 models is approximately 21,000 m^3/day (6,200 ac-ft/year). The highest recharge estimated by the USGS DVRFS3 model occurs in a relatively small area in southwest Area 19 and southeast Area 20 compared to the other recharge distributions. The recharge in the of region of Black Mountain is higher than the recharge estimated by the USGS basin delineation model (Figure 4-23).

The model calibration achieved an objective function value of 1.2E+08, approximately 3 times higher than the base case objective function of 3.8E+07. Figures 4-24 through 4-26 present the potentiometric surface with residuals, MWAT responses at Well ER-EC-11, and transmissivity field with flow paths. High localized recharge occurring in southwest Area 19 and southeast Area 20 result in higher simulated heads and higher residuals in this area. The drawdown in Well ER-EC-11 intermediate from pumping Well ER-EC-13LZ during well development, and testing is overpredicted compared with the base case model. Transmissivity is similar to the base case model; however, flow

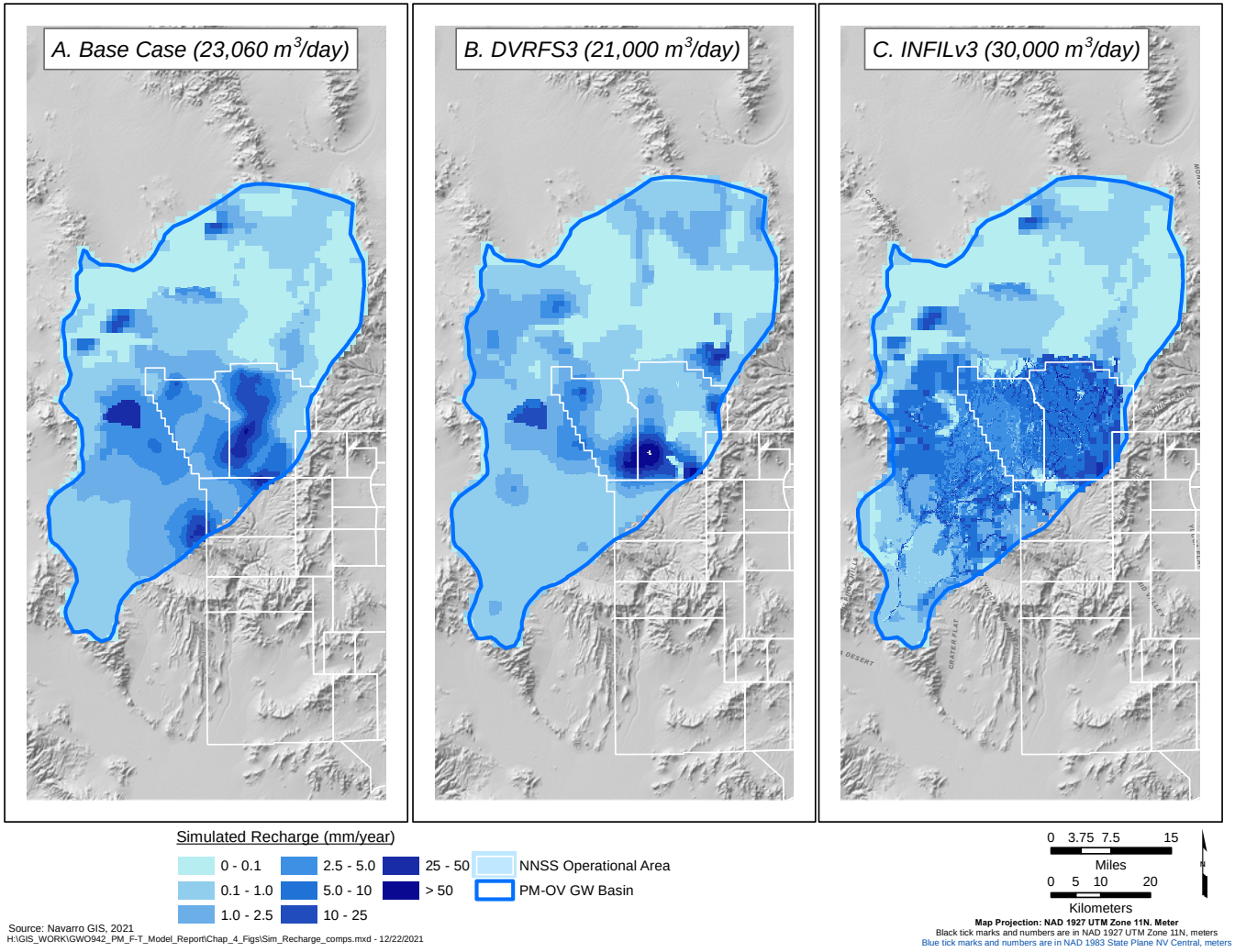

Figure 4-23
Base Case and Alternative Recharge Distributions: (A) Base Case, (B) DVRFS3, and (C) INFILv3

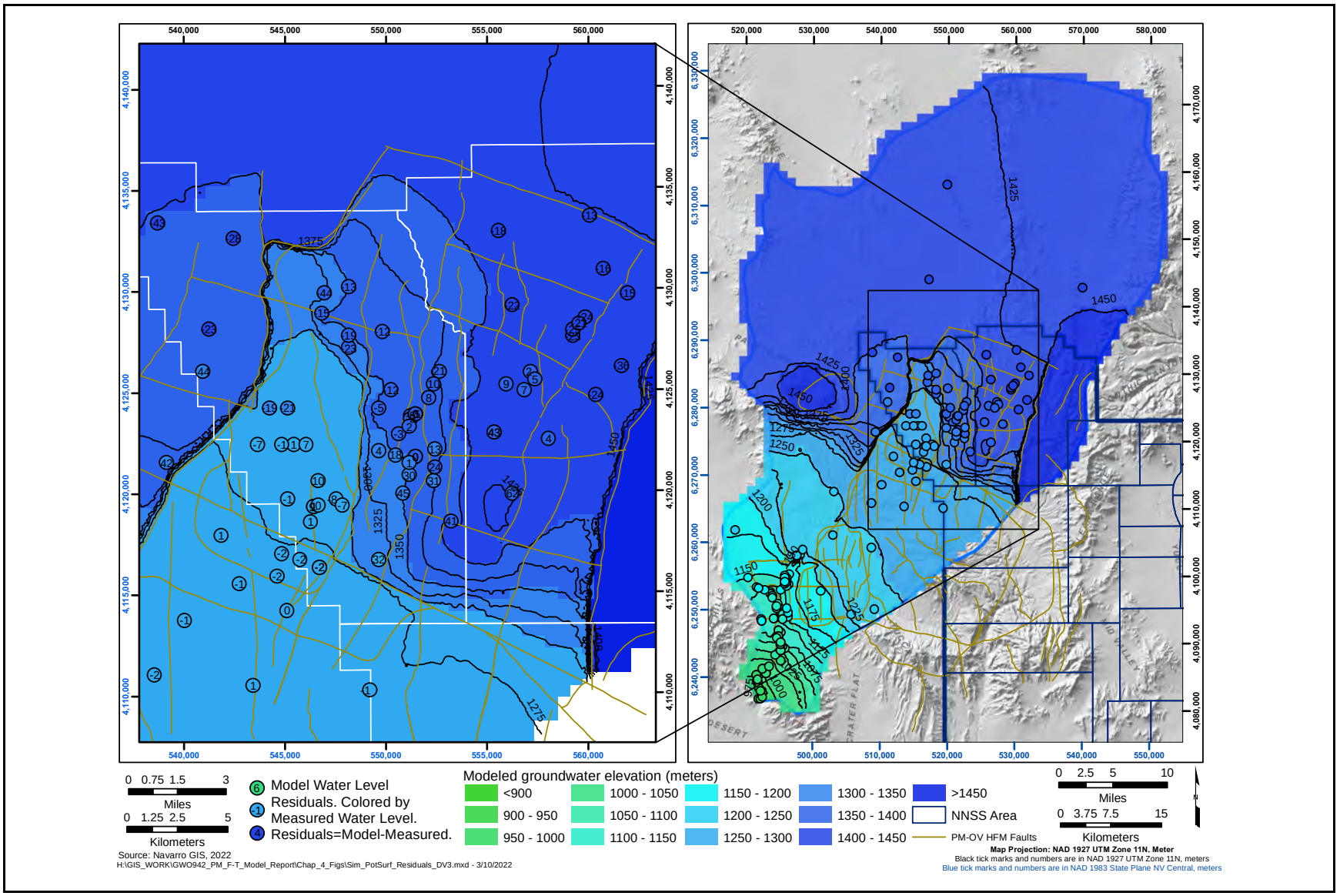

Figure 4-24
Potentiometric Surface and Residuals in a Model with Recharge from the USGS DVRFS3 Model

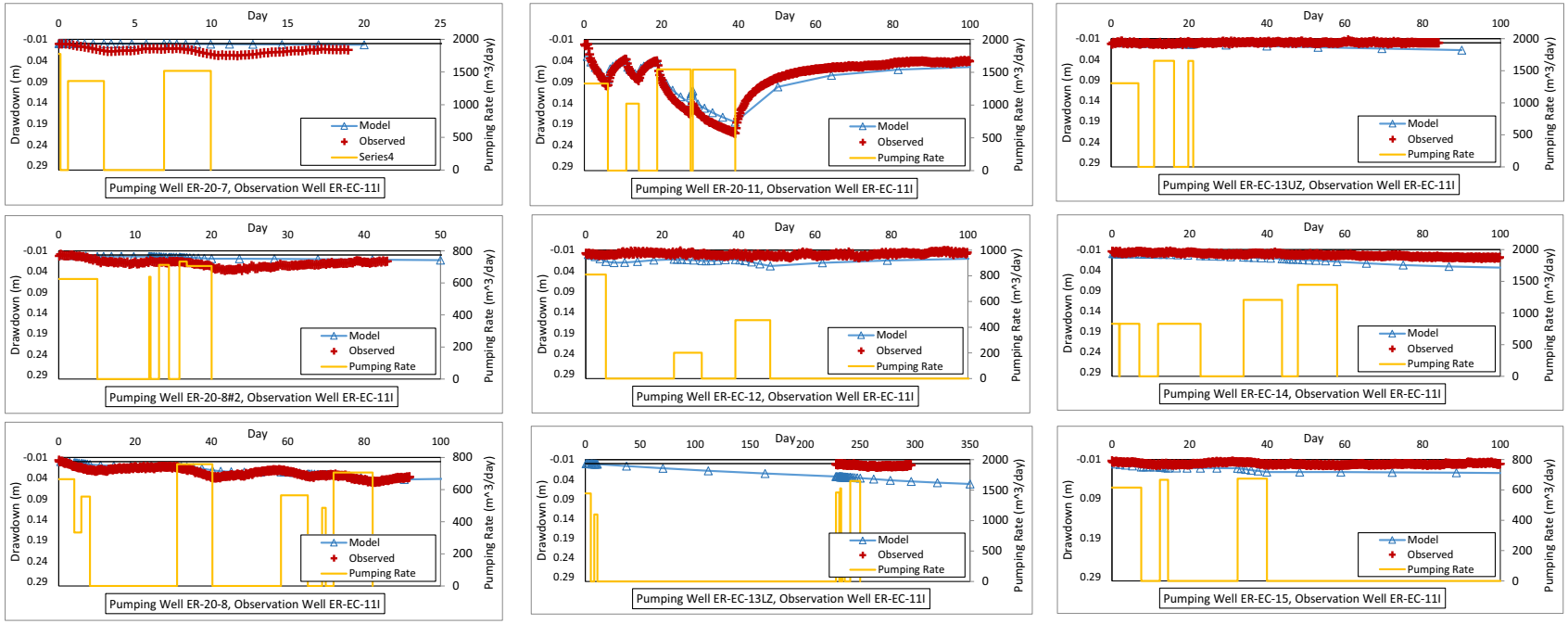

Figure 4-25
Comparisons of Simulated and Observed Drawdowns in ER-EC-11 Intermediate for a Model with Recharge from the USGS DVRFS3 Model

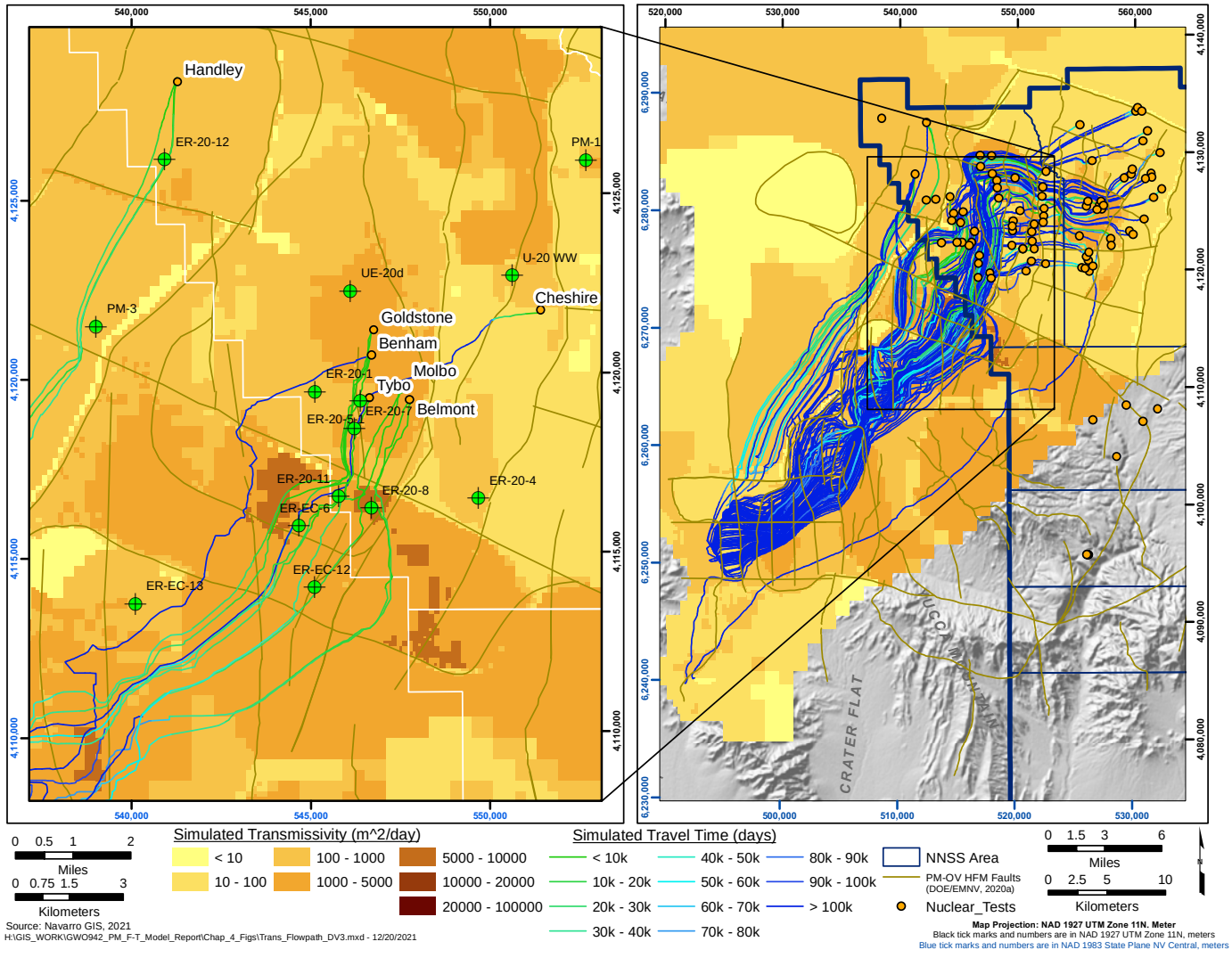

Figure 4-26
Simulated Transmissivity and Groundwater Flow Paths from Underground Nuclear Tests for a Model with Recharge from the USGS DVRFS3 Model

paths originating from tests in southwest Area 19 and southeast Area 20 are more westerly compared with the base case flow paths due to the groundwater mounding in this area from the higher recharge. Flow paths originating from the MOLBO, BENHAM, and HANDLEY are similar to the base case. The average flow path travel distance from all detonations at 200 years is 9.7 km, and the minimum distance from any detonation flow path endpoint to the Springdale Lower well is 3.5 km, similar to the base case.

4.3.2.2 INFILv3 Recharge Model

Middleton et al. (2019) estimated net infiltration rates within the PM-OV area using the INFILv3 code (USGS, 2008b) and daily data from 26 meteorological stations in the NNSS area to constrain the water balance for groundwater flow models being developed for the PM-OV flow system. Daily water balances were calculated for each model cell using a 50-by-50-m resolution digital elevation model, which allowed surface topographic features, geology, and soil and vegetation characteristics to be defined with greater precision than could be represented in previous infiltration studies. Middleton et al. (2019) also used shallow water-table fluctuations to evaluate model estimates of deep net infiltration beneath canyons and performed comparisons between estimates of modeled net infiltration with infiltration estimates based on the chloride mass balance method.

The area for the estimated recharge corresponds to the Phase I transport model area (SNJV, 2009b) and does not cover the entire PM-OV groundwater basin as defined by Fenelon et al. (2016). The INFILv3 infiltration rates were augmented with the USGS basin model infiltration located outside of the INFILv3 area to complete the coverage of the PM-OV basin. Infiltration rates are higher in the high-elevation areas of PM, along north-facing slopes, and along drainages. The recharge is more distributed across the PM highlands and near Black Mountain compared with the base case and DVRFS3 models estimates (Figure 4-23). The total recharge occurring in the PM-OV groundwater basin is notably higher than the other models and the total recharge estimated by Jackson et al. (2021). The total recharge is approximately 30,000 m^3/day (8,900 ac-ft/year) and likely represents an extreme upper bound of the total possible recharge occurring in the PM-OV groundwater basin. Fenelon et al. (2016) estimated the discharge to springs and seeps to range from approximately 5,000 to 6,800 ac-ft/yr. Laczniak et al. (2001) performed a Monte Carlo uncertainty analysis of groundwater discharge for DVRFS3 and estimated a discharge range of approximately

4,200 to 8,900 ac-ft/yr within the PM-OV groundwater basin. Both studies cite the source of the discharge data as Reiner et al. (2002). The upper end values estimated by Laczniak et al. (2001) are unlikely because these estimates represent the low probability input parameters on the tails of the parameter distributions used in the analysis.

The model calibration achieved an objective function value of 1.1E+08, approximately 3 times higher than the base case objective function of 3.8E+07. The calibration to steady-state heads was slightly better than the base case, but higher drawdown and total basin flow residuals increased the total objective function compared to the base case. Figures 4-27 through 4-29 present the potentiometric surface with residuals, MWAT responses at Well ER-EC-11, and transmissivity field with flow paths. The steady-state heads are lower within western Area 19 compared to the base case model. Western Area 19 is the location of the highest recharge in the base case model and the more dispersed recharge estimated by the INFILv3 model results in moderately lower heads in this area. The drawdown in Well ER-EC-11 intermediate from pumping Well ER-20-11 during well development, and testing is underpredicted compared with the base case model. The pattern of flow paths is similar to the base case. As expected, the higher total basin flow produced by the INFILv3 recharge distribution results in moderately faster advective velocity. The average flow path travel distance from all detonations at 200 years is 12 km, and the minimum distance from any detonation flow path endpoint to the Springdale Lower well is 0.3 km.

4.3.3 Unconfined Model

The base case, all faults and alternative recharge models utilize a confined aquifer approximation in which the water table defines the top of confined aquifer. Simulating groundwater flow in a water-table aquifer, also known as an unconfined aquifer, can be difficult because the saturated thickness available for flow depends on model-calculated hydraulic head, which results in a non-linear problem. Using a confined approximation for an unconfined aquifer can reduce execution time and increase model stability, which can be especially useful when many model runs are required such as during inverse model calibration. Faunt et al. (2010) compared confined and unconfined models of the DVRFS3 model and concluded that approximating the unconfined system as a confined system performed very well when the head-limit capabilities of the MODFLOW Multi-Node, Drawdown-Limited Well (MNW) Package are applied. The MNW package was used to

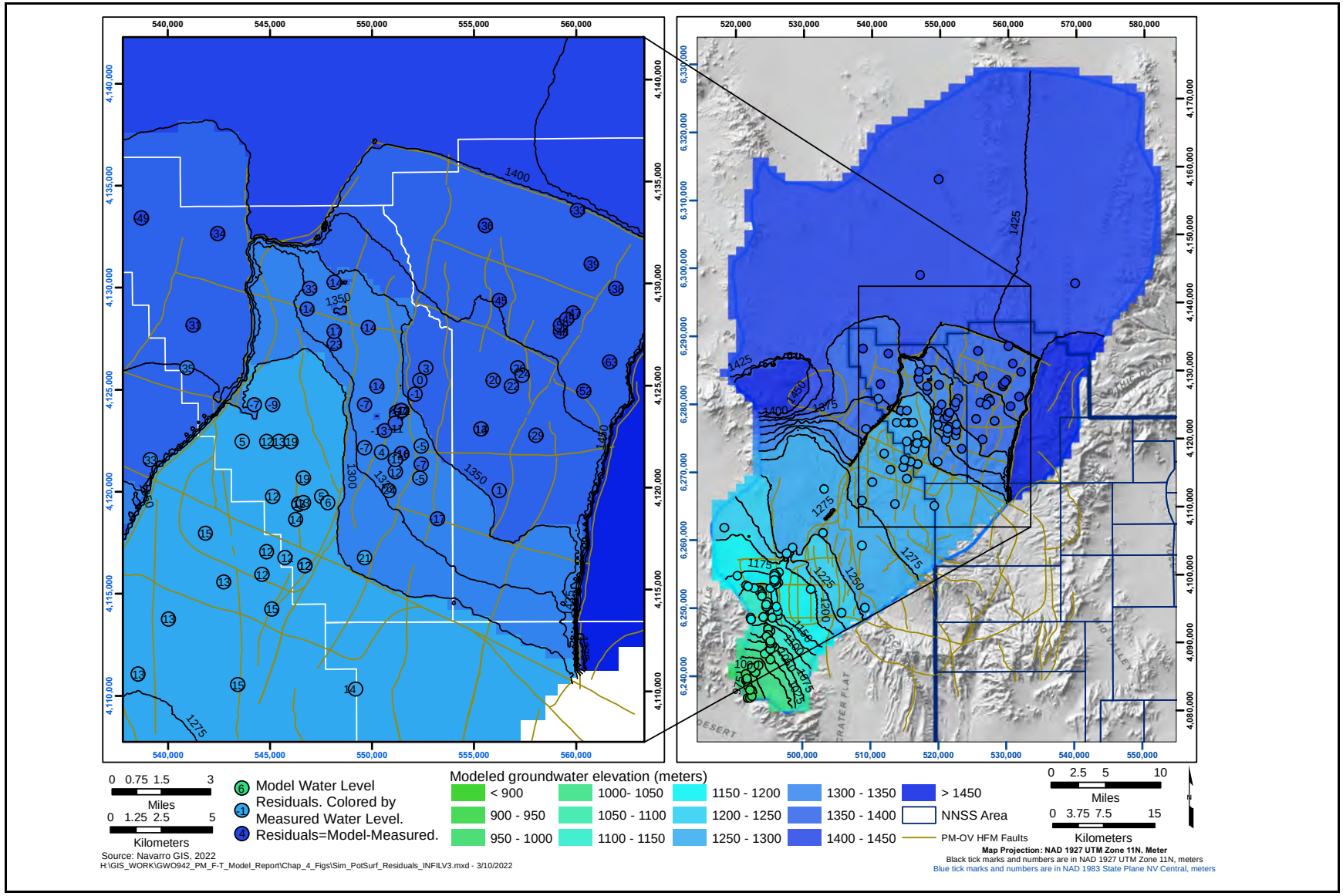

Figure 4-27
Potentiometric Surface and Residuals of a Model with Recharge from the INFILv3 Model

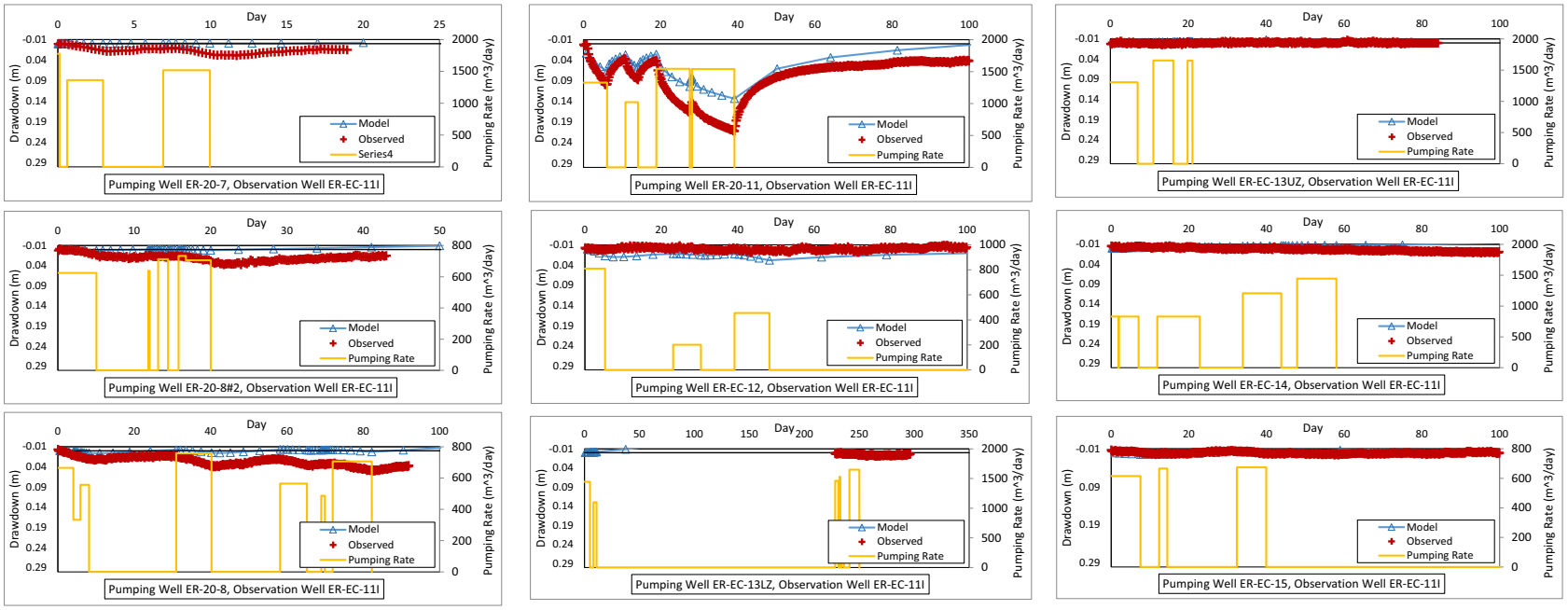

Figure 4-28
Comparisons of Simulated and Observed Drawdowns in ER-EC-11 Intermediate for a Model with Recharge from the INFILV3 Model

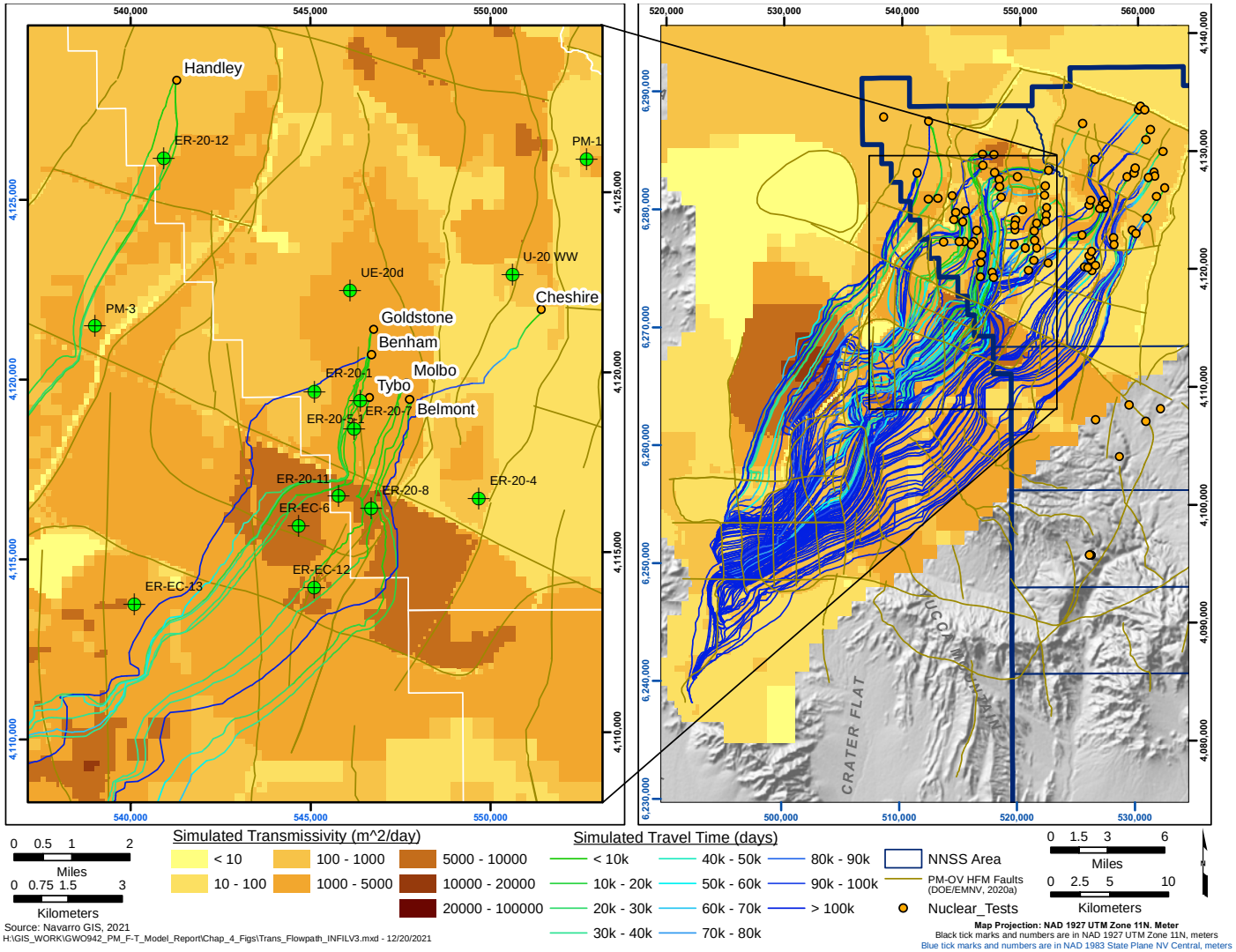

Figure 4-29
Simulated Transmissivity and Groundwater Flow Paths from Underground Nuclear Tests for a Model with Recharge from the INFILv3 Model

simulate wells that extend over several layers. The head-limit option allows flow into or out of a cell to be constrained, when heads fall below or exceed a specified limit. The Multi-Aquifer Well (MAW) Package replaced the MNW package from MODFLOW 2005 in MODFLOW 6 and was used to define pumping wells within the PM CAU flow model.

An unconfined version of the CAU groundwater model was calibrated to evaluate uncertainty associated with assuming confined conditions for the base case model. The model's upper surface was placed 50 m above the water table and the saturated thickness in model cells was allowed to vary with the computed head to allow an increased or decreased water table elevation compared to the base case model. The calibration of the unconfined model achieved an objective function value of 4.5E+07, which is moderately higher than the base case objective function of 3.8E+07. Figures 4-30 through 4-32 present the potentiometric surface with residuals, MWAT responses at Well ER-EC-11 intermediate, and the transmissivity field with flow paths. Hydraulic heads are lower and residuals are larger in Area 19 compared to the base case model, yet the potentiometric surface is very similar to the base case model. The drawdown in Well ER-EC-11 intermediate resulting from pumping Well ER-20-11 during well development and testing is overpredicted. Within the unconfined model, the hydraulic conductivity of HSUs within the Bench area, Area 20 and the area located west of the Purse fault were moderately reduced compared to the base case resulting in moderately slower flow paths in these areas, yet the overall spatial pattern of flow paths is very similar to the base case model. The average flow path travel distance from all detonations at 200 years is 8.7 km, and the minimum distance from any detonation flow path endpoint to the Springdale Lower well is 3.3 km. The similar model behavior and objective function value achieved during calibration of the unconfined model compared to the base case model, indicate that approximating the unconfined system as a confined system did not introduce significant error into the PM CAU flow model.

4.4 Flow Model Sensitivity Analysis

Two approaches were used to evaluate model parameter sensitivity of the PM CAU flow model. In the first approach, local parameter sensitivity is evaluated using the PEST code (Doherty, 2004). During parameter optimization, the PEST code calculates a sensitivity coefficient for each parameter with respect to all weighted observations. This analysis is termed "local" because parameter values near the calibrated value are investigated using only slight changes to parameter values. The second

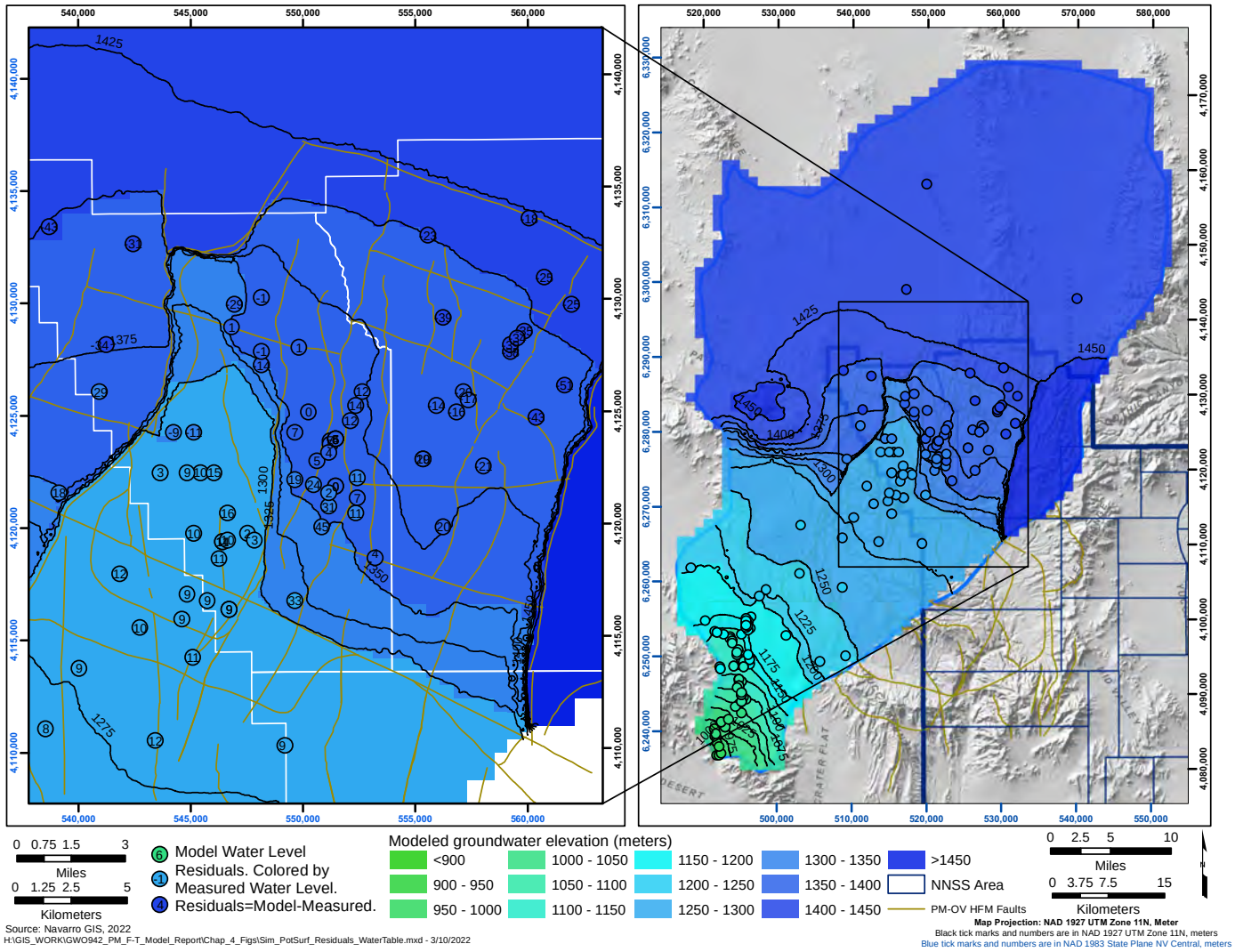

Figure 4-30
Potentiometric Surface, Residuals, and Mesh for a PM CAU Flow Model Using a Water Table Boundary Condition

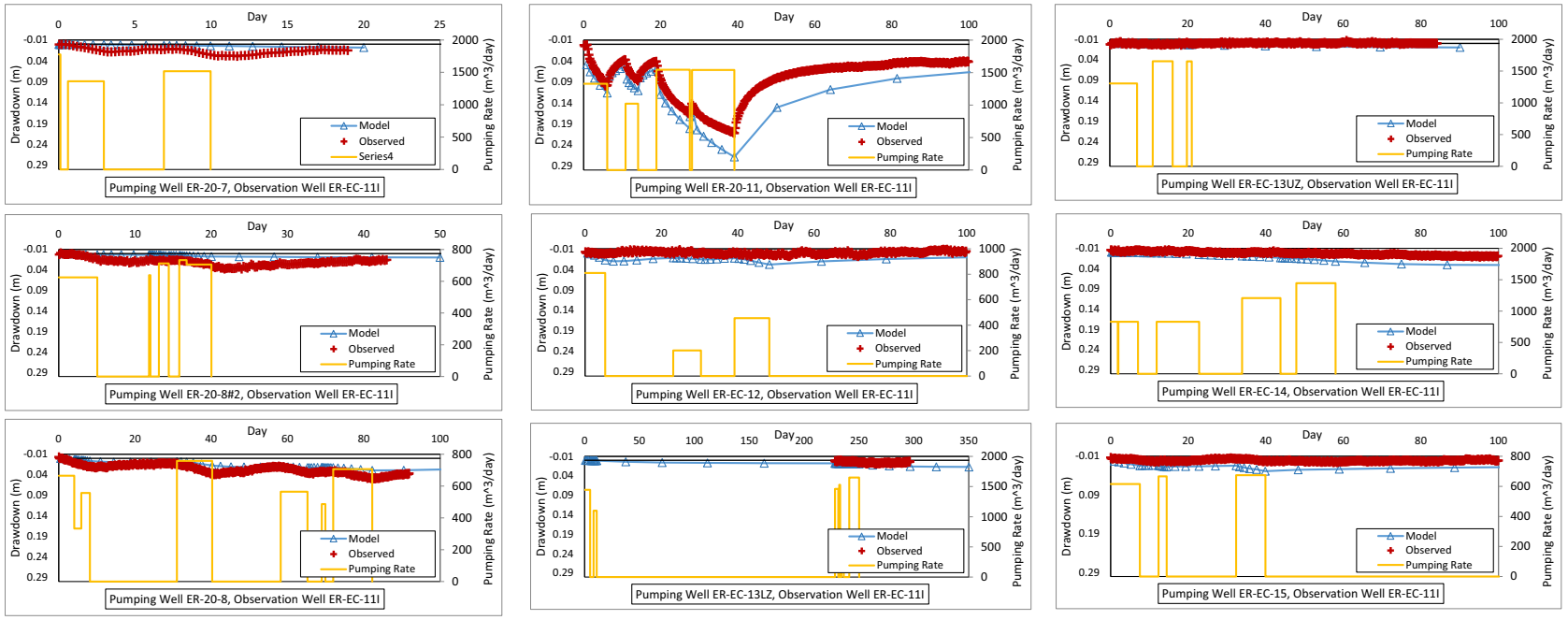

Figure 4-31
Comparisons of Simulated and Observed Drawdowns in ER-EC-11 Intermediate for a Model Using a Water Table Boundary Condition

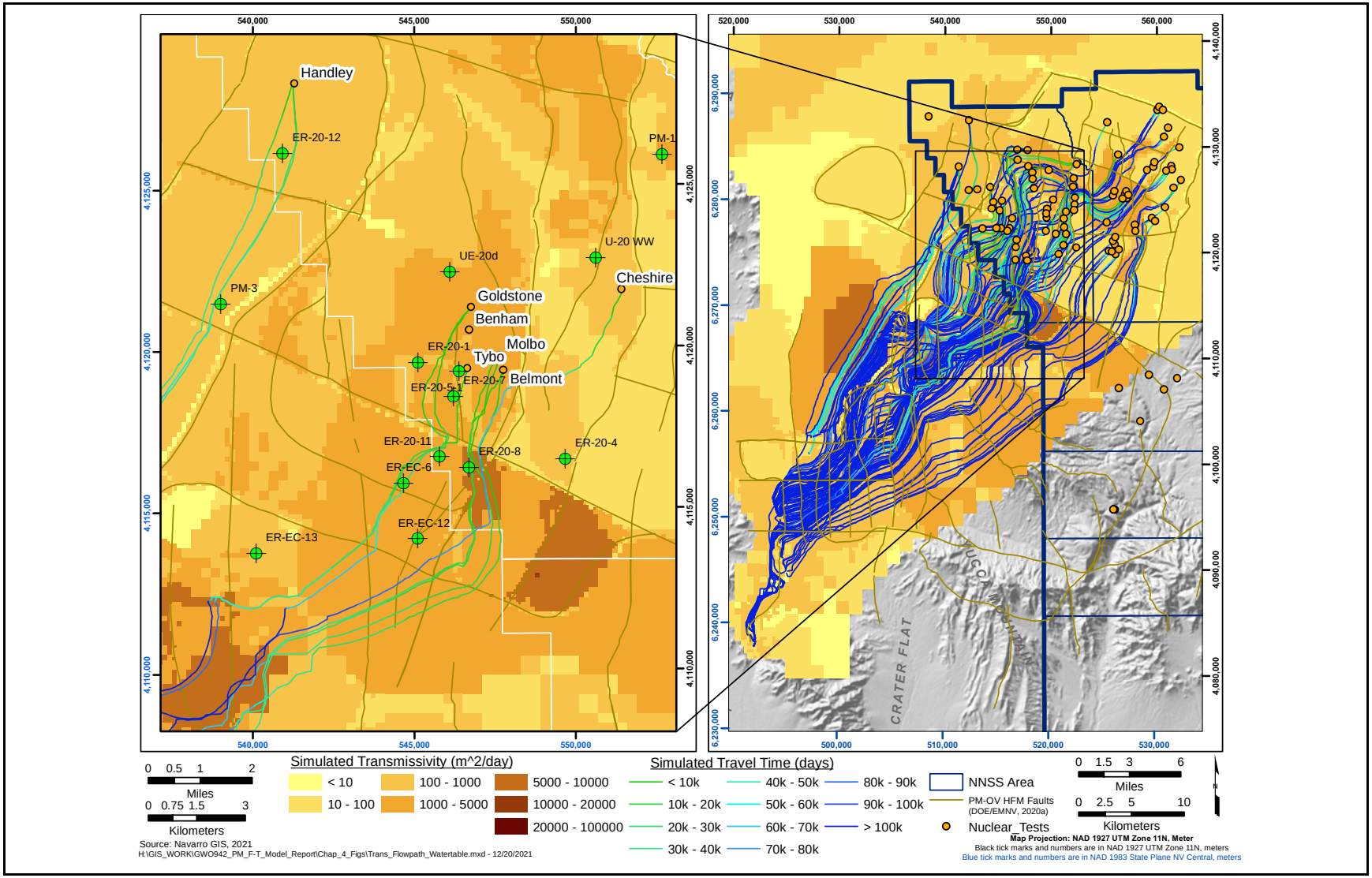

Figure 4-32
Simulated Transmissivity and Groundwater Flow Paths from Underground Nuclear Tests for a Model Using a Water Table Boundary Condition

approach involves perturbing two uncertain aspects of the model that give rise to discussion and may affect flow and transport. The sensitivity of barrier faults located on the northern and eastern boundary of the SCCC and increased recharge near Black Mountain were evaluated.

4.4.1 Local Parameter Sensitivity Analysis

Sensitivity coefficients, computed by PEST, are the change in output divided by the change in input and reflect the slope of the input-output relationship at a reference point. The reference point used by the sensitivity analysis is the calibrated parameter values and is indicative of the parameter sensitivity in the vicinity of the calibration point. The sensitivity only applies only to the parameter range over which the input-output relationship is linear. During parameter optimization, PEST calculates the Jacobian matrix. The Jacobian matrix relates the model-calculated observations to the model input parameters where any element of the Jacobian matrix, J_{ij}, describes the derivative of the *i'*th observation with respect to the *j'*th parameter. Based on the Jacobian matrix, PEST calculates the composite sensitivity of each parameter with respect to all weighted observations.

The composite sensitivity of parameter *i* (s_i) is defined as follows (Doherty, 2004):

$$s_i = \frac{\sqrt{[J^t Q J]_{jj}}}{m} \qquad (4\text{-}2)$$

where

- J = Jacobian matrix
- J^t = Transpose of the Jacobian matrix
- $Q\ i$ = Cofactor matrix, an m-dimensional, square, diagonal matrix composed of the squared observation weights
- m = Number of observations of non-zero weight

In other words, the sensitivity coefficient for a given parameter is the weighted average of the derivatives of all the observations with respect to that parameter.

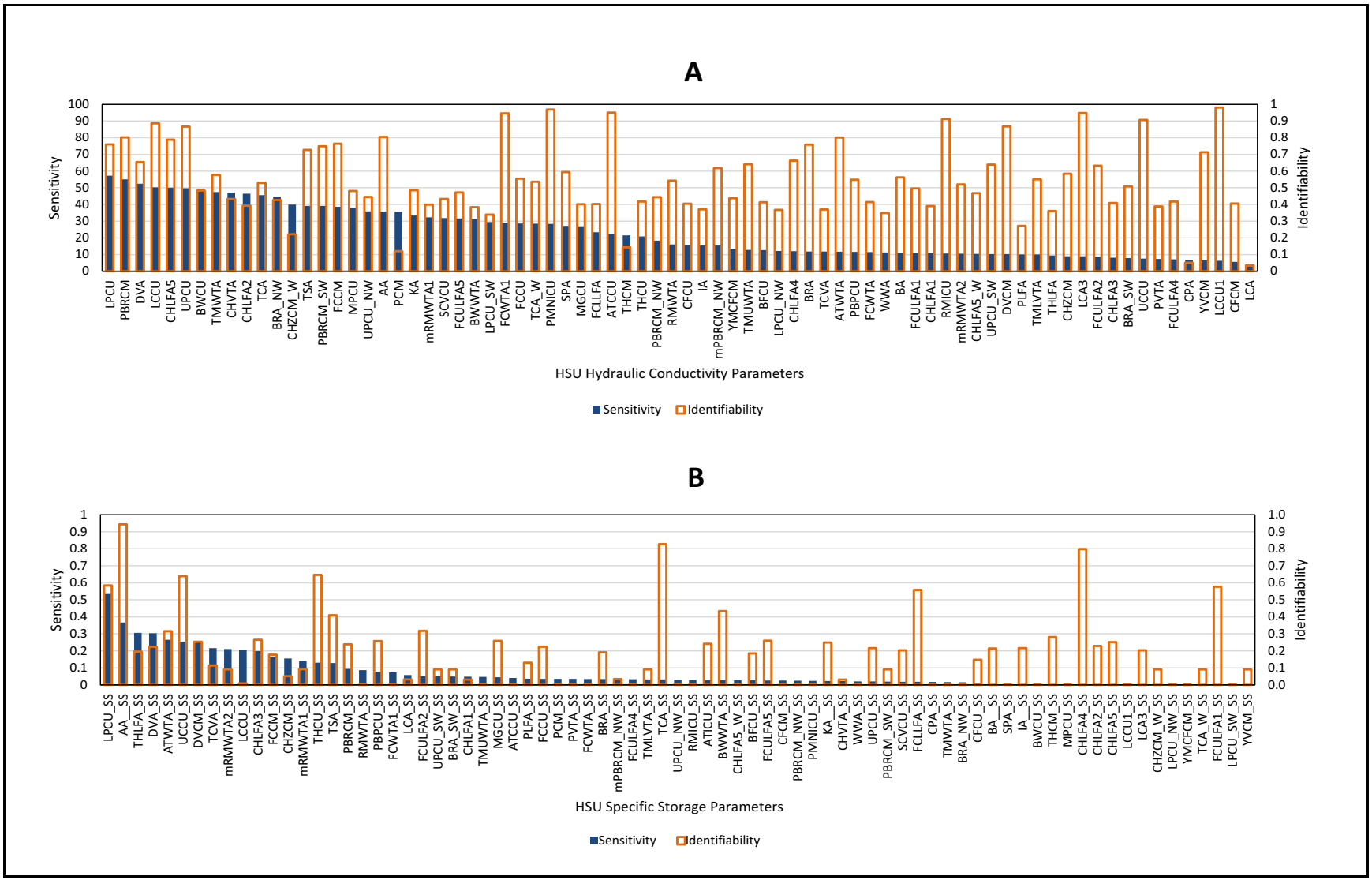

Figure 4-33
Sensitivity and Identifiability for Model Parameters: (A) Hydraulic Conductivity and (B) Specific Storage

The base case model parameter sensitivity and identifiability values calculated by PEST are presented in Figure 4-33. A model with a limited number of faults generally behaving as hydraulic barriers near the SCCC margins provided the best overall agreement with calibration data and flow paths inferred from ^{3}H observations in wells. The hydraulic conductivity of these faults was manually calibrated and fixed to the calibrated value during the PEST parameter optimizations. As a result, the PEST parameter sensitivity and identifiability were calculated only for the HSU hydraulic conductivity and specific storage parameters.

The observations used during the CAU model calibration included steady-state heads, aquifer stress responses, transmissivity measurements, and rate of groundwater flow moving through the PM-OV groundwater basin. The most sensitive parameters are HSU hydraulic conductivity values because all observations have input to the composite sensitivity value. Whereas, specific storage values are primarily informed by the drawdown observations. Of the hydraulic conductivity parameters, the base case model is most sensitive to the LPCU. Many other hydraulic conductivity parameters are highly sensitive, and 27 parameters have sensitivity values within a factor of 2 of the LPCU value. The LPCU also has the most identifiable specific storage parameter. Four other specific storage parameters have sensitivity values within a factor of 2 of the LPCU value. Highly sensitive parameters tend to be those representing HSUs with a large volumes or HSUs located in the Bench area. It is notable that parameter sensitivity is not correlated to identifiability, but hydraulic conductivity parameters are more sensitive and identifiable than specific storage parameters. Because the sensitivities of some of the HSUs located west of Purse are lower than those of HSUs in the Bench area, the predicted contaminant transport may be less certain in the area west of the Purse fault compared with the Bench area.

4.4.2 Model Sensitivity Analysis of the SCCC Barrier Faults and Increased Black Mountain Recharge

The sensitivity of barrier faults located on the northern and eastern boundary of the SCCC and increased recharge near Black Mountain were evaluated. The objective function value along with the spatial pattern head residuals and flow paths are used to evaluate the affect of including or removing these two aspects of the PM CAU flow model. The objective function is a common metric of goodness-of-fit for model calibration.

The objective function is the sum of the squares of the weighted residuals:

$$\Phi = \sum_{i=1}^{m} (w_i r_i)^2 \qquad (4\text{-}3)$$

where

Φ = Objective function
w = Observation weight
r = Residual or difference between the simulated and measured values
m = Number of observations of non-zero weight

For the PM CAU flow model, Φ can be divided into various components representing different types of calibration target data and the steady-state head objective function was used for the sensitivity analysis. The other components of the objective function were not greatly affected by the sensitivity analysis. As was done for the base case and uncertainty analysis models, the average flow path length at 200 years provides an integrated metric for evaluating advective velocity and comparing flow fields from the alternative models (Section 4.3). Additionally, the minimum distance of any flow path endpoint to the Springdale Lower Well, at 200 years, provides a metric for evaluating the potential of groundwater from test areas arriving at the discharge areas in Oasis Valley from the different models. Distance to the Springdale Lower Well is a convenient metric for nearness of contamination to the receptors, and it can be used regardless of source locations. Focusing on the various flow models under discussion, only INFILv3 recharge model using a recharge boundary condition from Middleton et al. (2019) is possibly overly conservative by having a total basin flow at the upper bounds of possible basin flows. However, the INFILv3 modeling of Middleton et al. (2019) used daily data from 26 meteorological stations in the NNSS area to constrain the water balance. The INFILv3 modeling also used shallow water-table fluctuations to evaluate model estimates of deep net infiltration beneath canyons and performed comparisons between estimates of modeled net infiltration with infiltration estimates based on the chloride mass balance method. All flow models, including the INFILv3 recharge model, have good agreement with steady-state heads, drawdowns from well development and testing, total basin flow, hydraulic gradients, and interpreted flow path directions from geochemistry data and RN concentrations. A discussion of the possible range in total basin flow is presented in Section 4.1.2, and the Middleton et al. (2019) modeling is discussed in Section 4.4.2.2.

4.4.2.1 Model Sensitivity of SCCC Barrier Faults

A model with a limited number of faults generally behaving as hydraulic barriers provided the best overall agreement with calibration data and flow paths inferred from ^{3}H observations in wells. Barrier faults on the Western boundary of the SCCC include the Purse, Grouse Canyon caldera structural margin NW, and TCL. Barrier faults on the SCCC northern and eastern boundaries include the Moor Hen Meadow structural zone, Rickey, and Split Ridge. Compelling evidence supports a barrier behavior of faults on the western boundary of SCCC either through the faults having a low transverse hydraulic conductivity or juxtaposition of aquifer HSUs against confining unit HSUs (Section 4.1.4.1). Hydraulic heads are several hundred feet higher west of the Purse fault (Figure 4-3), and two groundwater systems with distinct geochemistry groundwater compositions are seen across the Purse fault (Navarro, 2020). The presence of barrier faults on the northern and eastern boundary is less certain. The hydraulic properties of the northern and eastern faults were simply estimated from model calibration to hydraulic heads and flow path directions.

The barrier faults direct groundwater resulting from recharge occurring north of the SCCC west of the Purse fault, thereby increasing the water levels west of the Purse fault, and limit groundwater from high recharge occurring within eastern PM from flowing north or east, thereby increasing water levels within the SCCC. Removing the barrier faults from the base case and various alternative models lowers the water levels by approximately 10 m within northern Areas 19 and 20, except for the INFILv3 alternative recharge model, which has water levels that are approximately 20 m lower in northern Area 20 and approximately 2 m lower in northern Area 19 (Figures 4-34 through 4-38). Removing the barrier faults increases the steady-state head objective function by 20 to 90 percent among the different models (Table 4-8).

For the base case model, removing the barrier faults results in flow paths from a few tests in northern Area 19 having an initially northward direction due to groundwater mounding in Area 19. Conversely, removing the barrier faults from the various alternative models does not result in northerly flow paths from tests in northern Area 19 because the alternative models generally have higher transmissivity in Area 19, which prevents groundwater mounds from occurring in Area 19. Removing the barrier faults moderately decreased flow path velocities for the base case, the all-faults alternative, and the DVRFS3 alternative models. The average 200-year flow path travel distance from all tests was increased, and the minimum distance to the Springdale Lower Well from any test for the

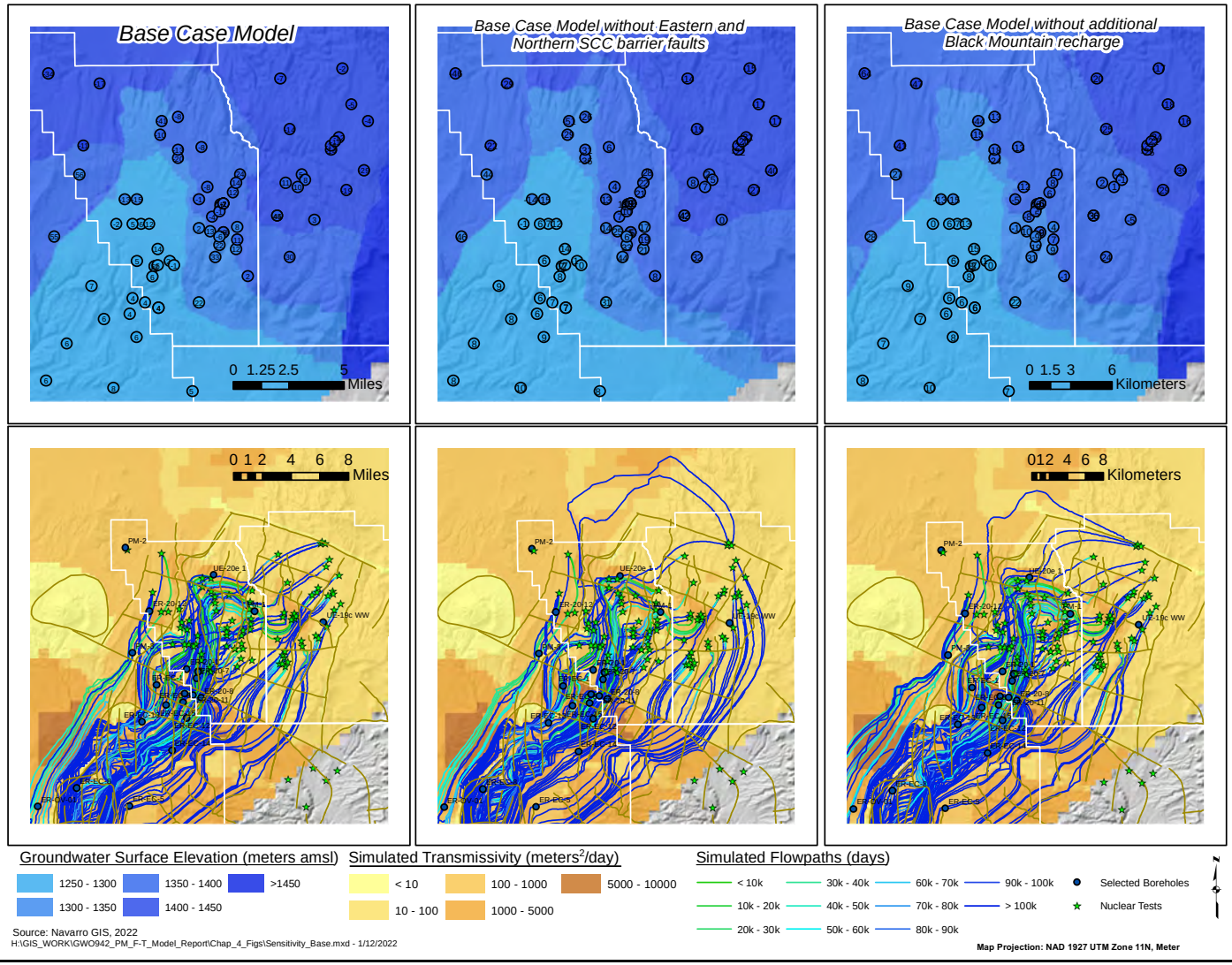

Figure 4-34
Head Residuals and Flow Path Sensitivity of the Base Case Model

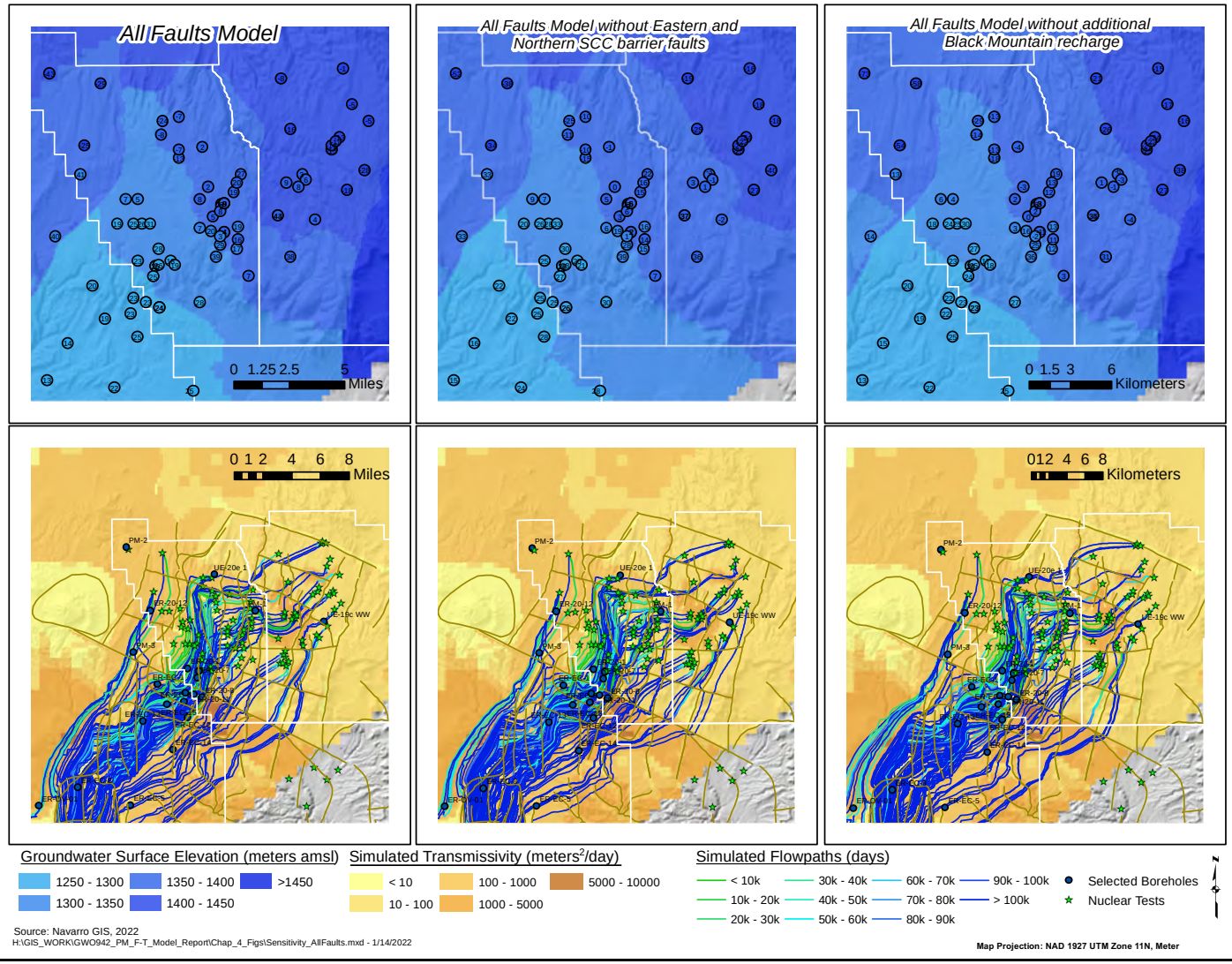

Figure 4-35
Head Residuals and Flow Path Sensitivity of the All Faults Alternative Model

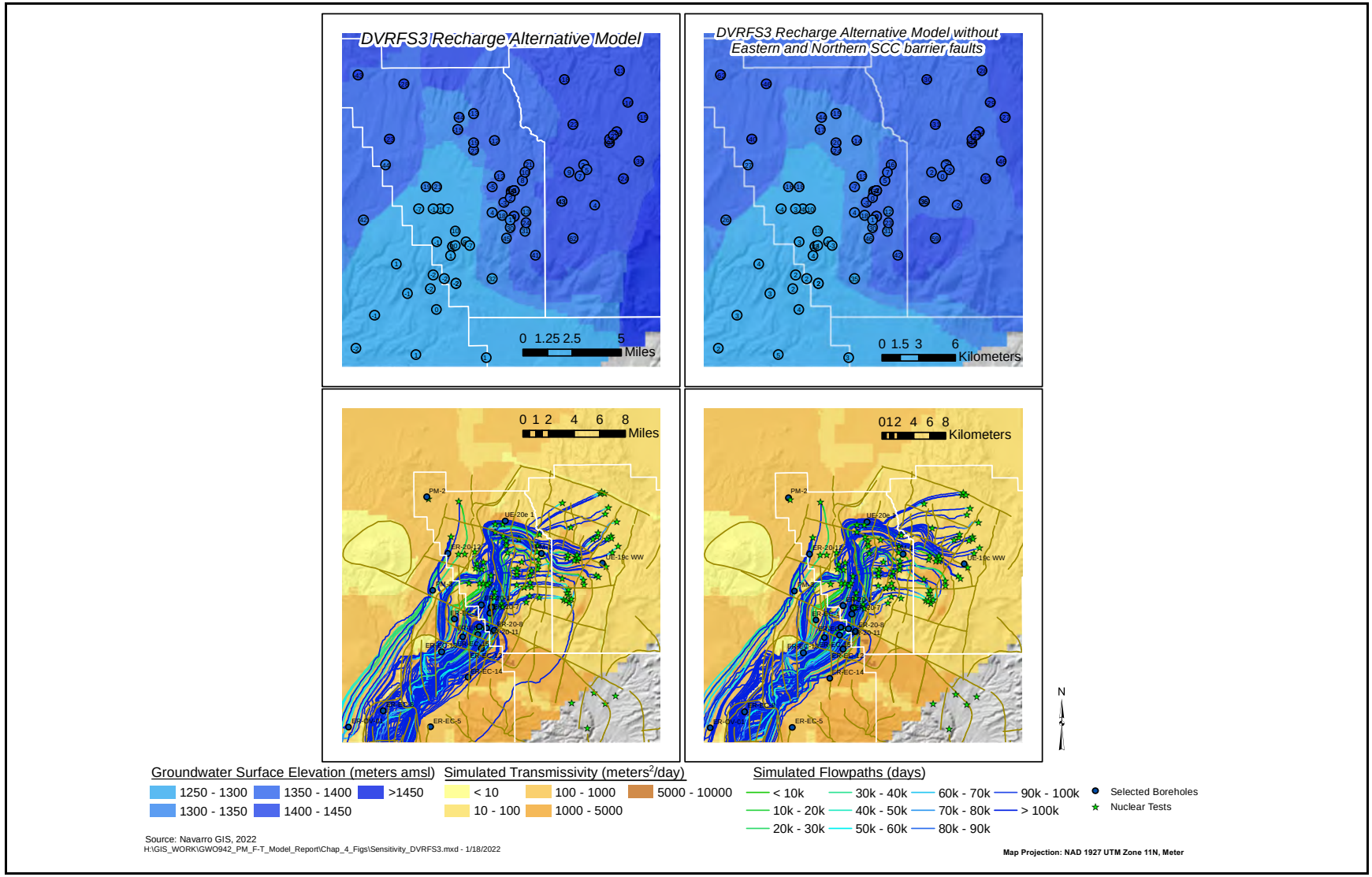

Figure 4-36
Head Residuals and Flow Path Sensitivity of the DVRFS3 Alternative Recharge Model

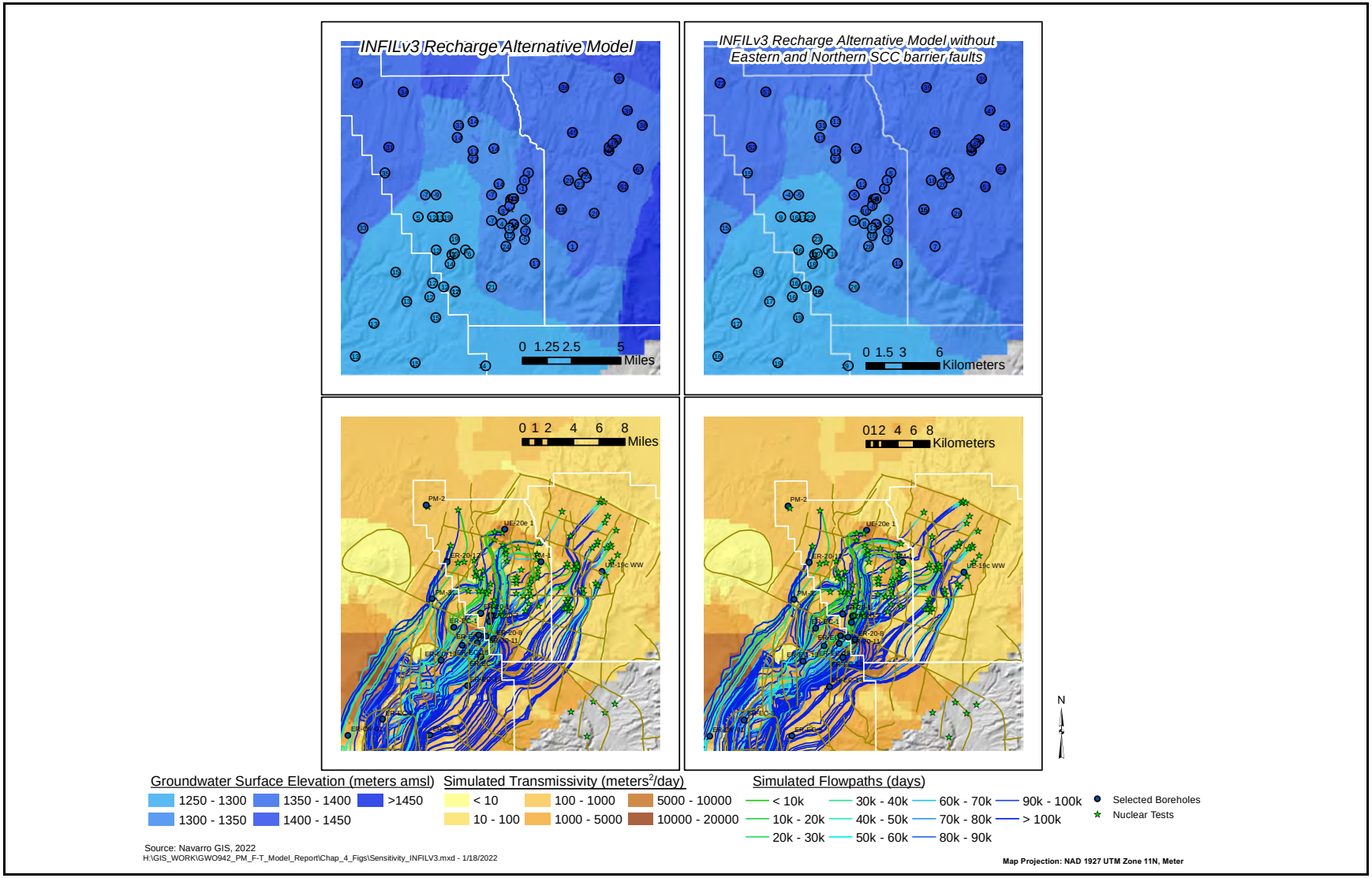

Figure 4-37
Head Residuals and Flow Path Sensitivity of the INFILv3 Alternative Recharge Model

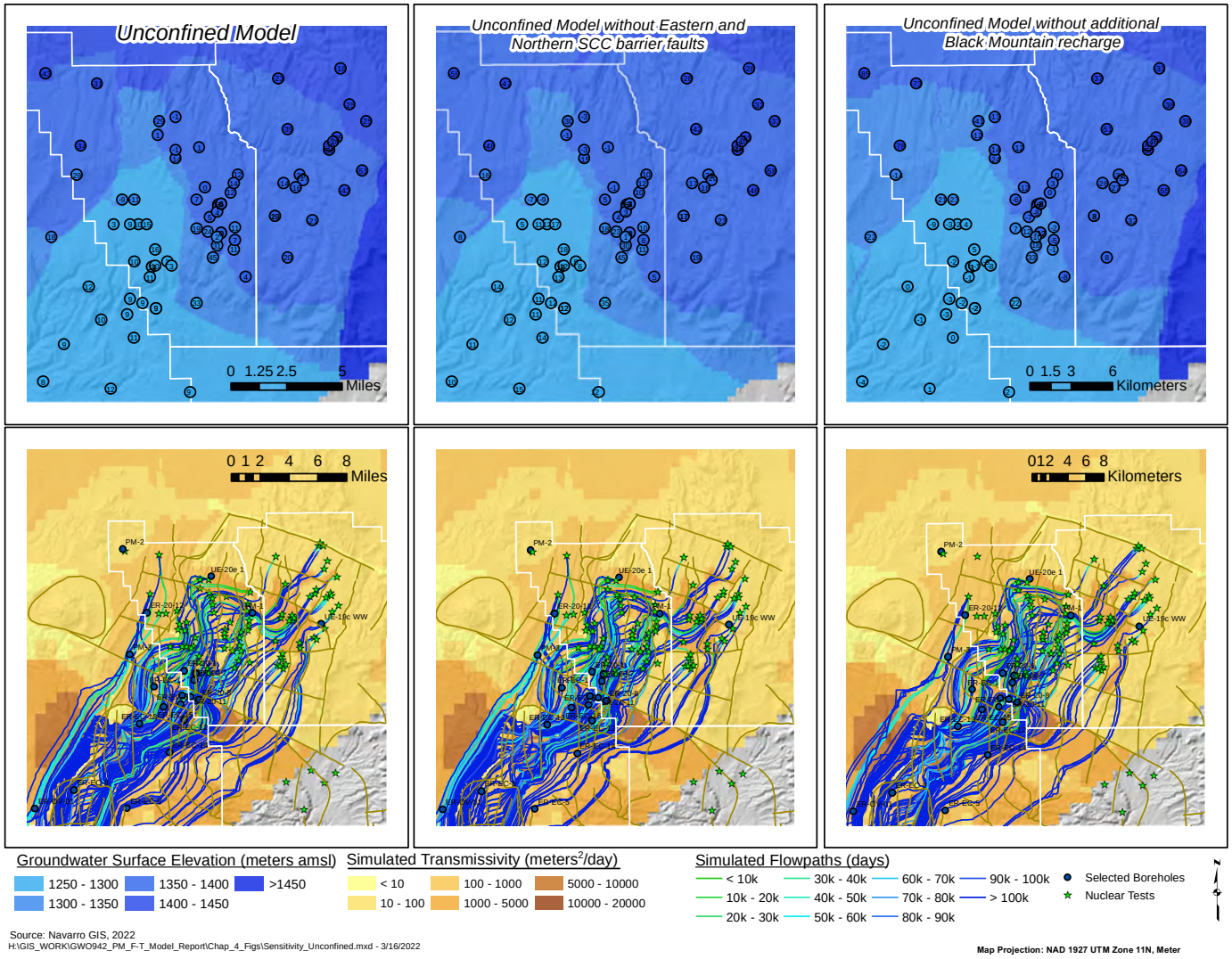

Figure 4-38
Head Residuals and Flow Path Sensitivity of the Unconfined Alternative Model

base case was decreased (Table 4-9). Removing the barrier faults had the opposite effect on the INFILv3 and unconfined alternative models, as flow path velocities were moderately increased.

Table 4-8
Sensitivity Analysis Steady-State Head Objective Function Values

Model	Steady State Head Objective Function Values		
	Calibrated Model	No Northern and Eastern SCCC Barrier Faults	No Increased Black Mountain Recharge
Base Case	2.57E+07	3.13E+07	3.57E+07
All Faults Alternative	2.72E+07	3.28E+07	4.26E+07
DVRF3 Recharge Alternative	2.43E+07	3.48E+07	NA
Infilv3 Recharge Alternative	2.45E+07	4.72E+07	NA
Unconfined Alternative	1.84E+07	2.88E+07	4.60E+07

Table 4-9
Sensitivity Analysis Flow Path Travel Distance at 200 Years

Model	Average Flow Travel Distance from All Tests (Minimum Distance to Springdale Lower Well from Any Test)		
	Calibrated Model	No Northern and Eastern SCCC Barrier Faults	No Increased Black Mountain Recharge
Base Case	1.03E+04 (2.14E+03)	9.10E+03 (2.39E+03)	9.74E+03 (3.75E+03)
All Faults Alternative	9.90E+03 (3.98E+02)	9.47E+03 (3.80E+02)	9.35E+03 (4.65E+03)
DVRF3 Recharge Alternative	9.74E+03 (3.53E+03)	9.55E+03 (4.51E+03)	NA
Infilv3 Recharge Alternative	1.16E+03 (2.84E+02)	1.22E+04 (2.73E+02)	NA
Unconfined Alternative	8.66E+03 (3.32E+03)	8.69E+03 (3.12E+03)	8.47E+03 (4.56+03)

4.4.2.2 Model Sensitivity of Increased Black Mountain Recharge

The recharge distribution from USGS PM-OV basin delineation model provides the upper boundary condition for the base case, all faults alternative, and unconfined alternative models. The recharge distribution from the USGS PM-OV basin delineation model did not include the upland area of Black

Mountain as an area of significant recharge, and during model calibration, the recharge near Black Mountain was increased by a factor of 10 to provide better agreement to steady-state heads and fast ^{3}H transport observed from the HANDLEY test. The increase in recharge near Black Mountain may have overestimated the amount of groundwater flow that occurs in Western PM. Jackson et al. (2021) conceptualized groundwater flow through the Western PM–Black Mountain area as being relatively minor, comprising less than 15 percent of the PM-OV basin budget. A perturbation analysis of removing the increased Black Mountain recharge was performed on the base case, all faults alternative, and unconfined alternative models to investigate the models' sensitivity to the increased recharge. The recharge near Black Mountain was not increased in the DVRFS3 and INFILv3 recharge alternative models, and these models are not included in the perturbation analysis.

Removing the increased Black Mountain recharge decreased water levels by approximately 30 m in the area west of the Purse fault and approximately 10 m in Area 19. Water levels within Area 20 east of the Purse fault and the Bench area were not markedly changed by removing the increased Black Mountain recharge in all models, except within the unconfined model. Removing the increased Black Mountain recharge uniformly lowered heads by approximately 10 m throughout Areas 19 and 20 in the unconfined model.

Removing the increased recharge near Black Mountain had a larger effect on the steady-state head objective function than removing the northern SCCC barrier faults, and the steady-state head objective function increased by 40 to 150 percent among the different models (Table 4-8).

Removing the increased recharge near Black Mountain moderately decreased average flow path velocities for all models (Table 4-9). The flow path directions were not markedly changed except for the base case model, which has more westward flow paths in northern Area 19 after removal of the increased recharge (Figure 4-34).

4.5 Flow Modeling Summary and Conclusions

The PM CAU flow model calibration incorporates the large amount of new data gathered during the Phase II data-collection activities with the goal to produce flow and transport models that are more certain than the Phase I models. The PM CAU flow model calibration is the first attempt to simultaneously incorporate all available data for the PM-OV flow system. Several earlier flow

models have been developed but use only a subset of the available data or represent a portion of PM-OV basin (Section 2.6).

The Phase II data collection activities included drilling 11 new wells, most with multiple completion intervals. The wells have been hydraulically tested and sampled for RNs on a regular basis, which provided MWAT data for flow model calibration and radionuclide concentration data for transport model calibration (see Section 5.0). In addition, the PM HFM has been revised to incorporate the geologic and hydrologic detail available from Phase II well drilling, include high-permeability lava flows in otherwise confining composite HSUs, and expand the domain to encompass the entire groundwater basin delineated by Fenelon et al. (2016). Phase II collection activities have reduced model uncertainty, but uncertainties still persist in all aspects of the PM CAU flow model, and it is not possible to conclusively identify a single representative flow field during model development. However, a calibration-constrained base case and three alternative flow fields have been developed that are expected to bound RN transport.

Based on the flow modeling presented in this section, it is concluded that the flow models developed and calibrated are a reasonable representation of the range of possible flow conditions that could potentially affect the extent of RN transport from the PM UGTA areas, and the flow models are expected to result in transport models that realistically bound RN transport. The key findings that support this conclusion are summarized below:

- A base case flow model and four conceptual uncertainty models have been developed that have good agreement with steady-state heads, drawdowns, total basin flow, hydraulic gradients, and interpreted flow path directions from geochemistry data and RN concentrations. The agreement with transmissivity data is reasonable, considering the uncertainty of transmissivity data and the zonation parameterization approach used for HSUs. The conceptual uncertainty models include models having an alternative conceptualization of faults, two alternative recharge distributions, and an unconfined alternative conceptualization of the model’s upper boundary condition.

- Calibration of a model containing all faults identified in the PM-OV HFM did not result in unexpectedly fast flow paths in the fault zones. Fault hydraulic properties tended to moderate HSU hydraulic behavior by providing moderate hydraulic connections through regions of low hydraulic conductivity and moderate barriers to cross-flow in regions of very high hydraulic conductivity.

- The model calibrations using alternative recharge distributions indicate that flow path directions are not particularly sensitive to the expected uncertainty in recharge. This is because all recharge distributions considered respect the conceptual model of higher recharge occurring in areas of higher elevation and higher permeability at land surface and the possible range in total basin flow. The alternative recharge distribution from the INFILv3 model likely represents an extreme upper bound of the total possible recharge occurring in the PM-OV groundwater basin and results in a model with an upper bound in advective velocity.

- The calibration of an unconfined model indicates that error introduced into the PM-OV CAU flow model by approximating the unconfined system as a confined system is acceptable. Hydraulic conductivity of the HSUs within the testing areas and flow path velocities originating from nuclear tests were moderately reduced compared to the base case model. The unconfined model calibration indicates that any error introduced by approximating the PM CAU flow system as confined is conservative in that RN transport will be faster compared to an unconfined model.

- Inconsistencies exist between the hydraulic data and the Phase II HFM. The Phase II HFM generally reproduces a flow field consistent with observations, but modifications were required, especially within the larger HSUs (RMWTA, PBRCM, UPCU, LPCU, TCA, and BRA). The vertically extensive RMWTA HSU was divided into three zones by depth below the water table to obtain good agreement with the hydraulic responses from aquifer testing. Separate zones for the UPCU, LPCU, TCA, BRA, and PBRCM HSUs west of the Purse fault were defined to obtain better agreement with interpreted flow paths from the HANDLEY test.

- Calibrated HSU hydraulic conductivity did not always agree with the HSU designation as aquifer or confining units. This tendency was also seen in the hydraulic conductivity data estimated from aquifer testing (Section 4.1.4.1). The calibrated values for aquifer and confining unit HSUs often reflect similar hydraulic behaviors. This suggests that factors other than the rock's primary lithology, such as degree of fracturing and alteration, greatly influence the hydraulic conductivity of HSUs and that HSUs are heterogeneous.

- Flow paths from the nuclear tests in eastern Area 20 and western Area 19 converge in the Bench area between Wells ER-EC-1 and ER-20-4 due to a hydraulic trough beginning in central Area 20 and continuing to the southwest toward Oasis Valley. The hydraulic trough is caused by the low-permeability barrier Purse fault structure to the west of the trough, high transmissivity in the trough area, and lower transmissivity east of the trough due to increasing thickness of the low-permeability CHZCM HSU.

- Flow paths from the GOLDSTONE, BENHAM, and TYBO nuclear tests all likely contribute to the ^{3}H observed in Wells ER-20-5, ER-20-7, ER-20-11 and ER-EC-11. Flow paths indicate the ^{3}H observed in Wells ER-20-8 and ER-20-2 is from the MOLBO and BELMONT tests, and ^{3}H in Wells ER-20-12 and PM-3 is from the HANDLEY test.

- The fastest groundwater flow occurs from the STILTON, HANDLEY, GOLDSTONE, JORUM, PEPATO, MOLBO, BENHAM, GREELEY, COLBY, KASH, PURSE, and

FONTINA nuclear tests, which all have 200-year groundwater travel distances greater than ~12 mi (20 km) using an effective porosity of 0.01. All models predict that advective flow paths from Area 20 nuclear tests will extend beyond the NNSS boundary, and that flow paths from the HANDLEY and STILTON nuclear tests will arrive at the discharge areas within 200 years. However, radioactive decay, matrix diffusion, and sorption are expected to reduce RN concentrations to levels below the SDWA standards (CFR, 2021) before arriving at the discharge areas as demonstrated in Section 5.0.

- An analysis of parameter sensitivity to observations found that highly sensitive model parameters tend to be those representing HSUs with large volumes or HSUs in the Bench area because these parameters are informed by the large number of steady-state head and drawdown observations in this area.

- A sensitivity analysis of removing the barrier faults on the northern and eastern boundary of the SCCC and increased recharge near Black Mountain did not significantly change hydraulic heads or flow path directions from tests in southwest Area 20, which is the primary area of concern due to the observed ^{3}H migrating beyond the NNSS boundaries in this area. The average flow path velocity from all tests was moderately decreased when these two aspects were removed from the models except for the INFILv3 and unconfined alternative model, which have moderately increased average flow path velocities after removing the northern SCCC barrier faults.

5.0 PM CAU Transport Model

This section presents the background information and the technical basis for developing the PM CAU transport model, model calibration to observed ^{3}H data along with the model results, and development of the ensemble of CBs. RNs starting at the source areas are transported downgradient with flowing groundwater subject to the processes of radioactive decay, advection, dispersion, diffusion between fracture water and rock matrix water, and matrix sorption. This is reflected in the structure of this section, which is organized as follows:

- Section 5.1 presents the development of the unclassified HST, uncertainty in the HST, the screening analysis that was used to define the RNs of interest in the PM CAU transport model, and implementation of the HST in the PM CAU transport model.
- Section 5.2 summarizes the conceptual transport, transport processes being modeled, and transport parameters and distributions required by the model.
- Section 5.3 summarizes relevant RN observation data.
- Section 5.4 presents a summary of the numerical approach and software used in the transport model.
- Section 5.5 describes the PM CAU transport model, calibration process and results, as well as the Monte Carlo process and results.
- Section 5.6 discusses sensitivity analysis.
- Section 5.7 presents the ensemble of CBs.
- Section 5.8 presents a summary of PM CAU transport model results.

5.1 Unclassified HST

The total amount of residual radioactivity remaining underground after an underground nuclear test is defined as its RST (Finnegan et al., 2016), regardless of its physical form and spatial distribution. Following detonation, portions of the RST are partitioned into gaseous, water-based, rubble-based, and melt-glass physical forms, as a function of their elemental properties and phenomenological effects associated with the detonation (Navarro, 2021c; and references therein). A comprehensive unclassified inventory providing an estimate of long-lived radioactive material from nuclear testing

for the NNSS is found in the total underground RN inventory (Finnegan et al., 2016). The inventory includes 43 radiological contaminants that have half-lives greater than 10 years (with the exception of europium-154 [^{154}Eu], which has a half-life of 8.593 years).

Not all of the RNs comprising the RST are equally available for transport in groundwater in any given time frame. The HST is defined as the portion of the RST that is released over time following the explosion of an underground nuclear test into the groundwater occupying saturated rock or into subsurface gases and moisture occupying partially saturated rock, and consequently available for near- and far-field transport (Kersting, 1996; Finnegan et al., 2016). The post-detonation phenomenology relevant to RST and HST formation is summarized in Navarro (2021c) along with references to more detailed publications. In this work, the HST represents specific fractions of each isotope that make up the RST that are available for transport in groundwater after a detonation. Initially, it excludes other fractions that are bound up in solidified melt glass or released as gaseous constituents. However, portions of the melt glass constituents may later be released into groundwater as dissolved aqueous or colloidal forms, often over long periods of time, as a function of melt glass dissolution processes. Dissolution rates will vary and be influenced by temperature histories in the subsurface after a detonation. What is released may be in the form of immediately soluble species or colloidally bound species that emanate from melt glass alteration products. In addition, many HST constituents may undergo water-rock sorption reactions.

The exchange volume (EV) is commonly defined as a spherical volume of rock centered at the working point (WP) of the detonation that envelops the test cavity and the immediate extent of radioactive contamination following the detonation of an underground nuclear test (Carle et al., 2020; Tompson et al., 2011). EV is conceptualized to be sufficiently large to encompass the majority of detonation effects (Navarro, 2021c) affecting the distribution of the RNs in the near-field. These effects were addressed for RM/SM (Tompson et al., 2011; DOE/EMNV, 2019b) and YF/CM (N-I, 2013; Navarro, 2019c; Pawloski et al., 2008; Tompson et al., 2008) by selecting EV radii that ranged from 1 to 3 times R_c for specific RNs. EV radial limits are specific to each RN and are given as a range. It is expected that an EV with a radius of $3R_c$ is sufficiently large to encompass the majority of detonation effects at PM (Navarro, 2021c; Carle et al., 2021) affecting the distribution of the RNs in the near-field. The value of $3R_c$ is used in the current work. After the development of a chimney,

RNs are distributed in the chimney as well, and an exchange zone (EZ) can be defined that includes the saturated portion of the EV and the saturated portion (if any) of the chimney (Carle et al., 2020).

As discussed in Navarro (2021c), three underground detonations have their EV completely above the local water table. As a conservative approximation, RNs available for aqueous transport from these three tests, as well as those for the three shallow cratering tests, are included in the PM CAU transport model by placing them near the top of the water table. There are 65 detonations that have EVs partially intersecting the water table. For these detonations, the saturated portion is treated as a source of RNs to the groundwater flow system. It should be noted that the estimated R_c are upper bounds for the classified tests. This is a conservative approach for estimating which tests have EVs intersecting the water table. The remaining 14 of the detonations at PM have EVs fully below the water table and are accompanied by vertical chimneys extending from the top of the cavity. The portions of the chimneys below the water table are included in the source term volume, defined above as the EZ. As a conservative approach, it is assumed that the portions of the cavity and EV as well as the chimney below the water table are fully water saturated and are in direct hydrological communication with the HSUs that intersect the EZ, allowing the RNs in the aqueous phase to be transported with the groundwater flux through the volume.

The near-field environment generally encompasses a region within several cavity radii of the test (SNJV, 2004c). HST evolves through processes that take place after the more dynamic processes have already transpired within initial fractions of a second after detonation (Tompson et al., 1999; SNJV, 2004c). These processes include decay and ingrowth of RNs; partitioning of the RNs between the melt glass, rubble, gas, and water fractions of the cavity/chimney region; release of RNs as a function of melt-glass dissolution; chemical reactions including aqueous complexation, surface complexation, ion exchange, precipitation, and dissolution; diffusion of aqueous RNs into mobile/immobile pore spaces in the rock; and sorption of RNs onto solid surfaces and colloids. Glass dissolution is a function of temperature, and the dependence of glass dissolution rates on temperature is exponential (Zavarin et al., 2019). Therefore, RN release from melt glass is expected to be greatest soon after the detonation and decrease exponentially as the glass cools. Glass dissolution can play a role in transport of actinides and other refractory minerals because of their high levels in the melt glass (Tompson et al., 2011) and colloid formation contributing to enhanced mobilization (Zavarin et al., 2019).

Melt glass dissolution was reported not to play a major role in determining CBs for the YF/CM CAU (N-I, 2013; SNJV, 2009c; Pohlmann et al., 2007) and the RM/SM CAU (Tompson et al., 2011). At PM, higher water temperatures occur in the test EVs in comparison to other CAUs at NNSS (e.g., Carle et al., 2003) due to greater yield ranges, greater depths of burial, and post-test permeability reduction in some tests that limit circulation and cooling rates, which can be expected to result in greater melt glass dissolution rates. Formation of secondary alteration minerals on the melt glass surfaces (Zavarin et al., 2004 and 2019; Rose et al., 2011) is another process that has the competing effects of slowing the release of entrained RNs by sorption and by blocking access to the surface, while on the other hand increasing the transport of RNs via aqueous colloid movement. For detonations performed within high-permeability rock, flowing water is available to transport the RNs into the groundwater flow system; however, flow of groundwater cools the cavity and melt glass, thus limiting the dissolution of melt glass. For detonations performed in low-permeability rock or due to post-test permeability reduction of permeability in some tests, higher temperatures persist for longer durations because cooling must occur primarily by heat conduction (Pawloski et al., 2001), thus permitting higher melt glass dissolution; however, transport of the RNs into the groundwater flow system is limited due to low permeability and occurrence of sorbing clays in the rock formations. Either prolonged elevated temperatures promote significant melt-glass dissolution in a low-permeability setting with limited transport, or shorter lived elevated temperatures inhibit melt-glass dissolution in settings characterized by higher permeability that allows for convective-based cooling. An example of this is obtained by comparing the results of Carle et al. (2003), summarized in Navarro (2021c), for CHESHIRE and ALMENDRO.

This discussion points out that while an application of melt glass dissolution rate equation (such as the Eq. B11 of Tompson et al., 2011) would suggest higher rates of dissolution over time, impact of these rates on the RN transport would be moderated by other processes. The RN observation data discussed in Navarro (2012c) and summarized in Section 5.3 show that ^{3}H is the only test-derived RN transported to the far-field at concentrations exceeding the maximum contaminant level (MCL) and out of the actinides Pu is the only one observed at concentrations near 0.1 MCL while all others are well below even 0.1 MCL. Hence, melt glass dissolution over time is not expected to play a major role in determining CBs at PM.

5.1.1 Uncertainty in HST

There is uncertainty in the HST that results from uncertainties in the RST itself (Finnegan et al., 2016); uncertainties in partitioning among melt glass, water, rubble and gas; and uncertainties in the physical distribution of the materials within the cavity and chimney (Carle et al. 2020; Tompson et al., 2011). Additionally, the mass of RNs in the aqueous phase is subjected to transport processes within the source region, in particular matrix diffusion and sorption (Carle et al., 2020), before it becomes available for aqueous transport away from the source region. The uncertainties in the parameters governing these transport processes get propagated into the estimates of mass/concentrations of RNs available as inputs to the PM CAU transport model. The spatial extent and distribution of the RNs in the source term also have associated uncertainties. The source geometry consists of an EV with radius of $3R_c$ around the detonation point, and a chimney with a radius of $1R_c$ extending from the cavity vertically upward to some height. At PM, 11 detonations have announced yield and measured R_c that are unclassified (see Appendix D). The remaining 71 detonations have announced yield ranges and classified R_c. As a result, their R_c is estimated from the maximum of the announced yield range (or minimum, in the case of HANDLEY) from NNSA/NFO (2015b) and Equation 1 of Pawloski (1999). In this work, the EV is assumed to be spherical and centered on the detonation location. The radius of the EV is uncertain; work on other CAUs has reported the use of triangular distributions with ranges from $1.5R_c$ to $3R_c$ for volatile/gaseous RNs and $1R_c$ to $1.5R_c$ for refractory RNs (N-I, 2013; Navarro, 2019c; Carle et al., 2021; Tompson et al., 2019). Flow and RN transport within the cavity-chimney system feeding into intersecting geological units is complex, as summarized from published literature for three known cases (Navarro, 2021c). The total RN mass available for aqueous transport for any given source will get distributed over time to various intersecting aquifer units depending on the hydrologic and thermal conditions within and in the vicinity of the source. The degree of hydraulic communication between the cavity/EV and the surrounding formations is uncertain as well. Hence, the fraction of RN mass available to flow out of the EV versus chimney has uncertainties associated with it.

The time dependence of the HST also has uncertainties associated with it. RST formation associated with the detonation and subsequent cavity and EV formation occurs quickly, over a time frame of seconds to hours. Chimney formation can occur within minutes to days. The formation of the HST is affected by additional processes of radioactive decay, melt glass dissolution, advection, hydrothermal

convection, and colloid-assisted transport and diffusion, which take place over longer durations. There are uncertainties associated with the quantification of these processes.

5.1.2 Screening Analysis

The PM CAU transport model focuses on a subset of RNs in the HST, selected on the basis of a screening analysis (Carle et al., 2020).Determination of relevance is primarily based on data and/or model results indicating source concentration exceeding MCL (CFR, 2021) out to 100 years since the time of detonation. Carle et al. (2020) performed a screening analysis by combining results of a screening model and groundwater radiochemistry data to estimate plausible aqueous concentrations of RNs dissolved in groundwater at the source of contamination for the 82 PM underground tests. The screening model takes into account RST inventory; partitioning of the RST into melt glass, water, gas, and rubble fractions; accessible pore volume within the cavity, melt glass, EV, and chimney; diffusion between flowing (fractures) and stagnant (matrix) pore space; sorption onto solid surfaces within the matrix rock volume; and variable levels of water saturation that may be present in the EZ. Uncertainties in the parameters related to these processes were taken into account to forecast ranges of concentrations.

Carle et al. (2020) present three families of plots of concentration versus time along with the available data for various RNs. They state, *"The 'min' and 'max' cases use parameters that minimize and maximize source activity or concentration, respectively. The 'base' case uses mean parameters. Most of the available data for source locations (open symbols) tend to fall within model results for 'min' and 'base' parameters. This indicates the 'max' parameters are unrealistically conservative, which is the case for nearly every RN in the inventory for the reasons discussed in Section 4.1 of Carle et al. (2020). Accordingly, model-based determination of RN relevance to the HST will rely on model results for 'base' parameters."* They also state, *"The 'base' case uses mean parameters."* In this document, mass of various RNs assigned for transport is based on the average of values given by Carle et al. (2020) for melt-glass and gas percentage, as reported in Table 5-1.

The analysis resulted in a reduction of the list of 43 RNs in the inventory of Finnegan et al. (2016) to a smaller list of RNs that are relevant (for which either groundwater sampling or the screening model indicate 100-year persistence above 1 MCL) or potentially relevant (for which either groundwater sampling or the screening model indicate 100-year persistence above 0.1 MCL) to the HST.

Table 5-1
Mass Percentages Available for Transport in the PM CAU Model

RN	Average Melt Glass Percentage calculated from Carle et al. (2020)	Average Gas Percentage calculated from Carle et al. (2020)	Mass Percentage Available for Transport
^{3}H	0	2	100
^{14}C	0	80	20
^{36}Cl	30	0	70
^{137}Cs	32.5	0	67.5
^{129}I	30	0	70
^{237}Np	95	0	5
^{238}Pu	97.5	0	2.5
^{239}Pu	97.5	0	2.5
^{240}Pu	97.5	0	2.5
^{90}Sr	60	0	40
^{99}Tc	60	0	40
^{232}U	80	0	20
^{233}U	80	0	20
^{234}U	80	0	20
^{238}U	80	0	20

Carle et al. (2020) identified ^{3}H, ^{90}Sr, ^{129}I, ^{137}Cs, ^{232}U, ^{233}U, ^{234}U, ^{238}U, and $^{239/240}Pu$ as relevant and ^{14}C, ^{36}Cl, ^{99}Tc, ^{237}Np, and ^{238}Pu as potentially relevant to the PM CAU transport model HST. In this work it is assumed that this selection can be applied to the three shallow cratering tests as well.

Although identified as a potentially relevant RN by Carle et al. (2020), ^{232}Th was not included in the HST. The ^{232}Th is not expected to contribute to groundwater contamination because of its very low solubility (Carle et al., 2020). In fact, the screening model results of Carle et al. (2020) were consistently below 0.1 MCL, and ^{232}Th has been reported as a nondetect (detection limits below the MCL) in samples collected from the cavity environment and from RN plumes within PM. Carle et al. (2020) included ^{232}Th as an RN of potential relevance because of the radioactive daughters in its decay chain and the possibility of near-secular equilibrium of these daughters in the rock. Secular equilibrium would result in equal activity of daughter products within the decay chain and could

potentially result in high gross alpha value and ^{226}Ra (^{238}U decay) / ^{228}Ra (^{232}Th decay) activities. The decision to exclude these daughter products follows the guidance documented in the *RN Decay and In-growth Technical Basis* document (Kersting et al., 2003). Kersting et al. (2003) based this on the fact that the groundwater interacts with a much larger volume of rock containing significant parent and daughter RNs along the flow path, which decreases the relative contribution of the device component of these RNs downgradient from the test. A recent evaluation of RN observational data was found to be consistent with Kersting et al. (2003). Gross alpha, U, and ^{226}Ra data for NNSS groundwaters shows that in many cases even the unadjusted gross alpha (including contributions from U) was below the MCL. Additionally, even in cases where the unadjusted gross alpha exceeded the MCL, since the gross alpha was dominated by U, adjusted gross alpha (gross alpha - U activity) values do not exceed the 15-pCi/L MCL (Navarro, 2021c). Also, ^{226}Ra ranged from below 0.5 to 7 pCi/L in the ALMENDRO and CHESHIRE postshot wells, respectively. These concentrations were consistent with the ^{226}Ra distribution of groundwaters from within the study area (ranging from to <0.1 to 6.5 pCi/L in clean wells). These results are consistent with Kersting et al. (2003) and therefore support continued use of this historical guidance.

5.1.3 Implementation of HST

The available mass of RNs at each detonation location is calculated from the yield-weighted fraction of the inventory in Finnegan et al. (2016), using the maximum of the announced yield range given in DOE/NV 209--Rev. 16 (NNSA/NFO, 2015b) (except for HANDLEY, for which the minimum of the yield range is used), and decay corrected using the method described in Tompson et al. (2019).

Average melt-glass percentages (representing the range of partitioning of the RN inventory into melt glass) and gas percentages (representing the fraction of the inventory partitioned into the unsaturated zone by gas-phase redistribution) for the RNs of interest were calculated from information presented in Table 4 of Carle et al. (2020). With the exception of ^{3}H, these percentages were removed from the total mass to determine the mass of each RN available for transport. Mass percentages available for transport are shown in Table 5-1. The processes leading to the creation of the disturbed zone (EV consisting of a sphere with $3R_c$ and saturated portion, if any, of the chimney represented by a cylinder of radius R_c) and the distribution of the RNs within the disturbed zone were assumed to be rapid compared to the timescale of interest to the PM CAU transport model. For the 79 deep tests with

some portion of EZ below the water table, the available mass of each RN for each test was assumed to be uniformly distributed initially over the saturated portion of the EZ. The RN mass for the three tests with EZ fully above the water table was distributed in a thin disk at the water table (top of model) with the same diameter as the EZ, and RN mass for the three near-surface cratering tests was distributed in a thin disk at the water table (top of model) with the same diameter as the crater.

Note that according to the screening analysis by Carle et al. (2020), the RN mass available for aqueous transport decreases with time due to matrix diffusion and sorption (in addition to fractionation in the melt glass), and significant fractions of the RN mass are retained within the cavities for years after detonation. In the PM CAU transport model, as a conservative approach, all available mass is released in one day on the day of detonation.

5.2 Conceptual Model

RNs from underground nuclear tests at PM can be transported with groundwater flowing through water-saturated geologic formations toward areas of natural or anthropogenic discharge. Evaluation of RN transport at PM requires the knowledge of flow velocities within the domain, which are obtained from the PM CAU flow model. All tests conducted at PM were within the PM-OV groundwater basin. The flow model domain is chosen so that lateral boundaries coincide with the no-flow boundaries of the PM-OV groundwater basin except for the discharge area in the southwest portion of the model (Section 4.2.4). Important HSUs and structural features, discussed in Section 2.0, are explicitly represented in the PM CAU flow model. The flow model is calibrated by optimizing hydraulic conductivities and storativities to match hydrologic data, including steady-state pressure heads measured at monitoring wells, cross-hole responses to pumping at wells, head gradients, transmissivity measurements, and discharge estimates. Flow model calibrations are also informed by flow paths and transport times indicated by RN measurements (Section 2.5, and Rehfeldt and Wilborn, 2020) and geochemical data (Navarro, 2020).

Transport of RNs through the geologic formations at PM is affected by multiple physical and chemical processes that depend both on the hydrogeologic system and its properties, and the specific properties of the RNs. It is assumed that the RNs dissolved in the pore fluid have negligible effect on fluid motion and are carried along by the pore fluid moving at its local velocity. The advective flow paths correspond with the groundwater flow paths, and the fluid velocity determines the rate of

advection of aqueous RNs along flow paths. The migration processes relevant for evaluating RN transport at PM, summarized in this section, include radioactive decay of the species, advection in porous and fractured media, dispersion, diffusion of RNs between fracture water and matrix water, sorption onto immobile minerals, and colloid-facilitated transport. These processes are included in the PM CAU transport model. Detailed discussions of the data and distributions of parameters required as inputs to the PM CAU transport model are presented in Navarro (2021a) and summarized in Section 5.2.2. Transport parameters in general can show variability depending on HSU, HGU, scale, depth, diagenetic zone (DZ), and water chemistry. These variabilities are specific to each parameter, and are discussed in subsections of Section 5.2.2 for each transport parameter of importance to the PM CAU transport model.

5.2.1 Transport Processes

5.2.1.1 Radioactive Decay

Radioactive decay is the process by which a nucleus of an unstable element or isotope (radioisotope) loses energy by radiation and converts to another element or isotope. The rate at which a radioisotope decays is given by the equation:

$$\frac{dN}{dt} = -\lambda \cdot N \qquad (5\text{-}1)$$

where

N = Number of nuclei of the radioisotope at a given time t
dN = Number of nuclei that decay in a small time increment dt
λ = Decay constant, related to the half-life ($T_{1/2}$) as: $\lambda = ln(2)/T_{1/2}$
$T_{1/2}$ = Half life of the radioisotope

Decay constants (or half-lives) of RNs are fixed properties of the specific isotopes (determined by the mass number and atomic number of the isotopic nucleus) and are not dependent on environmental factors such as the geological media, fluid composition, pressures, or temperatures. Kersting et al. (2003) examined potential decay chains associated with RNs included in the NNSS RST that are not produced naturally (i.e., ^{232}Th and ^{238}U decay chains were not included). The most important chain was identified as ^{241}Pu ($T_{1/2}$ ~ 14.3 y) → ^{241}Am ($T_{1/2}$ ~432.6 y) → ^{237}Np ($T_{1/2}$ ~ 2.14E+06 y). As part of Phase I modeling, field-scale streamtube simulations from the TYBO detonation were conducted to, among other things, address assumptions regarding radioactive decay daughter products

(see Appendix C of SNJV, 2009c). Atoms of Np present near the front of a plume arise either by transport of Np in the aqueous phase, or via the decay of Pu or Am that arrive there via colloid-assisted transport. Area 20 inventory has (Finnegan et al., 2016) 6.43 x 10^{+23} atoms of ^{241}Pu, 3.54 x 10^{+24} atoms of ^{241}Am and 9.03 x 10^{+25} atoms of ^{237}Np. Even if it is assumed that the initial atoms of Pu and Am present in PM are instantaneously converted to atoms of Np, there will be an increase of only about 4 percent in the Np inventory (atom- or curie [Ci]-wise), which is not expected to make a significant difference to the ensemble of CBs. Therefore, decay chains and their daughter products are not included in the radioactive decay simulated in the PM CAU transport model.

5.2.1.2 Advective Transport of Dissolved RNs

Dissolved, aqueous RNs are able to advect with the groundwater moving through porous and fractured media in the flow system (colloid-facilitated transport is addressed in Section 5.2.1.7). It is assumed that the RNs dissolved in the pore fluid have negligible effect on fluid motion and are carried along by the pore fluid moving at its local velocity. The advective flow paths correspond with the groundwater flow paths and the fluid velocity determines the rate of advection of aqueous RNs along flow paths. (Matrix diffusion is addressed in Section 5.2.1.5, and sorption is addressed in Section 5.2.1.6.)

For saturated flow, the fluid velocity, v, is related to the Darcy flux, q, of the groundwater via flowing porosity, ϕ_{eff}, by:

$$v = \frac{q}{\phi_{eff}} \qquad (5\text{-}2)$$

The Darcy flux, q, required by this equation is obtained from the flow model. The PM CAU flow model is a numerical model that represents the flow system on a discretized mesh yielding values of hydraulic heads and fluxes averaged over the computational blocks, which range from tens to hundreds of meters in size. Generally, the flux can vary with position, and it can vary with time if time-dependent scenarios are considered. The flowing porosity, ϕ_{eff}, is a property of the geological medium. ϕ_{eff} is supplied to the PM CAU transport model on the scale of computational blocks, and it can vary with position due to the heterogeneities of the geological media. For modeling purposes, within a geologic unit, the porosity is assumed to be spatially constant but uncertain.

In the single-porosity model of geologic media, the flowing porosity is a large fraction of the entire porosity of the medium, typically assumed to be equal to the matrix porosity; and stagnant portions of the porosity, if any, do not play a significant role in the flow and transport considerations.
Units modeled as single-porosity media include VTAs, AAs, and unfractured confining units. TCUs are also generally modeled as single-porosity media unless otherwise indicated by available transport data. This is because, as noted in Section 2.3.3.1, while generally acting as competent confining units, there are instances where TCUs are fractured and transmissivity is much greater (Jackson et al., 2021). The transport parameter required by the PM CAU transport model is the effective porosity, discussed in Section 5.2.2.3.

5.2.1.3 Dual-Porosity Conceptualization of Fracture Transport

In fractured media such as welded tuffs, some bedded tuffs, and lava flows at PM that can sustain open fractures, the hydraulic conductivity of the fractures is many orders of magnitude greater than that in the rock matrix surrounding the fractures. Hence, fluid flow occurs preferentially in the fractures, and the flow through the rock matrix can be neglected. Thus, the flowing porosity used for advection is the fracture volume divided by the bulk volume, which is typically much smaller than the matrix porosity. Thus, for the same flux, simulated fluid velocities are much higher in fractured rock than they are for porous media. This representation of a geological media is called an equivalent continuum approach, where the groundwater flow is described with the use of average values of hydraulic conductivities and porosities; the influence of heterogeneities within a member is incorporated into the model via dispersion and matrix diffusion (discussed in Sections 5.2.1.4 and 5.2.1.5). This treatment represents a considerable simplification of the complex fracture network observed in volcanic rocks. The use of an abstracted dual-porosity model is acceptable because the model is intended to be used in large-scale simulations. However, the material properties for use in the abstracted model are scale-dependent and difficult to estimate. In numerical modeling studies, such uncertainties are commonly addressed by sampling parameter distributions with broad ranges of values. Permissible range of values for uncertain parameters is constrained by available field-scale data, such as the RN measurements at multiple wells at PM as well as fine scaled models using a DFN approach.

DFN approaches explicitly capture the high degree of heterogeneity that fractures impart to a flow system. DFN models typically start with measured/estimated fracture statistics, generate a large number of system realizations, and solve flow and transport equations at scales finer than fracture spacing to evaluate upscaled average material properties (Parashar et al., 2019; Makedonska et al., 2020). By solving for flow and transport in individual elements of a fracture network, DFN approaches can (while computationally intensive and impractical for large scales required by the PM CAU model) evaluate upscaled equivalent conductivity tensors, porosities, fracture spacing and aperture, dispersivities, and diffusivities for equivalent continuum approach. For example, Makedonska et al. (2020) estimated ranges for equivalent effective porosities, dispersivities, fracture apertures, and spacing for use in continuum transport models using DFN models for the TSA, LFA, and TCA at PM.

For fracture-dominated systems, the matrix is conceptualized as stagnant, and effective porosity is approximately the fracture porosity. The transport parameter required by the PM CAU transport model for advective flow is the effective porosity, ϕ_{eff}, discussed in Section 5.2.2.3.

5.2.1.4 Dispersion

Hydrodynamic dispersion of solutes in groundwater describes the spreading phenomenon at a macroscopic level by the combined action of mechanical dispersion and molecular diffusion (EPA, 1988). Dispersion is caused by velocity variations at scales less than the scale of observation (SNJV, 2004b). At typical scales of observation, dispersion is a mixing process, which causes dilution of the solute within the plume while spreading nonzero concentration over a greater spatial extent (Freeze and Cherry, 1979). Dispersion is represented in the transport equations as a mass flux term expressed in terms of concentration gradient premultiplied by a dispersion coefficient tensor (Bear, 1972). The dispersion tensor includes a modified coefficient of molecular diffusion and terms that are products of the velocity vector and the dispersivity tensor (or dispersivity). It is common practice in groundwater modeling (Freeze and Cherry, 1979) to represent the effects of dispersion with the use of three independent dispersivities: the longitudinal dispersivity along the direction of the bulk fluid velocity, and two transverse dispersivities orthogonal to the flow direction. This is the approach used in the PM CAU transport model.

As noted in Section 5.2.1.2 describing advection, the fluid velocity used by the PM CAU transport model is an average over the computational blocks, which can range in size from tens of meters to 1,200 m. The PM CAU transport model includes zones representing the HSUs and major structural features such as faults identified in the HFM. However, these zones are coarse, and it is recognized that material heterogeneities and features exist that are not included explicitly in the HFM. These heterogeneities can cause divergence and/or convergence of flow paths within the zones assumed to have single material properties. For example, not every fault in the model domain may be represented explicitly. The presence of faults in an otherwise homogeneous zone could affect the tortuous nature of flow in that zone over the scale of hundreds of meters to kilometers. Likewise, lava beds in a zeolitic confining unit can change the local nature of flow paths. At the very small scale, velocities differ along flow paths between the grains or within fractures. None of these processes are accounted for explicitly in the PM CAU transport model. Rather, dispersion terms and coefficients are used to represent spreading and molecular diffusion along and transverse to the advective flow paths computed in the flow model.

Field data have shown the dispersivities to be dependent on the scale of the problem (Gelhar et al., 1992; Neuman, 1990; Zhou et al., 2005; Schulze-Makuch, 2005). Makedonska et al. (2020) present insights obtained in scaling dispersivities up to 250-m scale using detailed DFN simulations based on fracture statistics. Dispersivity values at field scale are typically obtained by calibrating flow and transport models to contaminant measurements. Identification of a single optimal model is not possible in data-limited situations, and multiple conceptual models could acceptably reproduce observed data; and the dispersivity values estimated by each model may be quite different (SNJV, 2004a). This makes it difficult to definitively determine the appropriate dispersivity at large scales from current data.

As employed in the PM CAU transport model, the parameters required to represent dispersion are longitudinal and transverse dispersivities. They are documented in Section 5.2.2.7.

5.2.1.5 Matrix Diffusion

In fractured rock zones (e.g., WTAs and LFAs), the permeability of fractures is many orders of magnitude greater than that of the rock matrix. Hence, it is assumed that fluid flow occurs only in fractures and that stagnant fluid resides in the saturated rock matrix. This is the dual-porosity model

of the rock formation where solutes advect with the fluid flowing in the fractures, and diffuse in and out of the fluid within the rock matrix. Within the matrix, due to low permeability, the velocity for the bulk movement of the groundwater is effectively zero. Subsequently, the advection of the solute while in the matrix is effectively zero. The Brownian motion of the solute molecules becomes dominant, and the effect of advection resumes when the solute diffuses back into the fracture. The result is a delay; bulk solute movement through the fractures is thus retarded due to matrix diffusion. Numerous theoretical, laboratory, and field studies support the validity of the matrix diffusion conceptual and numerical model, showing that single effective material properties cannot adequately capture the complex transport behavior of a solute that advects in fractures (e.g., Sudicky and Frind, 1981; Maloszewski and Zuber, 1985; and Reimus and Callahan, 2007). For fractured rock zones represented by the dual-porosity approach in the PM CAU transport model, matrix diffusion is idealized by a model of uniform flow and transport within a system of equally spaced parallel plate fractures. Solutes diffuse between fractures and the matrix according to concentration gradients and the surface area-to-volume ratio of the fractures from which they diffuse. Diffusion is limited by the volume of matrix material into which diffusion occurs, which is determined by the spacing between fractures. In a situation where solutes enter the flowing fractures first with the matrix devoid of solute, over time the solute concentration in the matrix can increase due to diffusion, thus reducing the concentration gradient driving diffusion out of the fractures. For limited-duration source releases, the fractures are flushed of solute first and then the concentration gradient is reversed, causing diffusion back into the fractures from matrix storage. This behavior is often seen in laboratory and field experiments in long concentration tails of breakthrough curves, well after peak arrival times. The effect is to slow the rate of RN advection in fractures and to reduce peak concentrations in the mobile phase. Near-source locations diffusion into and later out of matrix blocks can lead to prolonged elevated concentrations in the groundwater sweeping past the zones with high concentrations. This can lead to source concentrations that decrease over time only by radioactive decay.

This conceptual model is a considerable simplification of the actual processes that occur in complex fracture networks. In reality, fractures intersect and are of variable length and aperture. Diffusion out of some fractures can actually lead to interference of diffusion or enhancement of concentrations in other fractures. However, at the CAU scale, an abstraction is appropriate and designed to capture the net effect of fracture-matrix interactions with CAU gridblock-scale parameters. The parameters are uncertain, which is addressed by stochastic sampling of fracture and matrix properties. Some

guidance on the likely ranges of equivalent parallel-plate fracture spacing and apertures is available from DFN models (Makedonska et al., 2020; Parashar et al., 2019; Pham et al., 2020). The transport parameters required for representing matrix diffusion in the PM CAU transport model are matrix porosity (see Section 5.2.2.2), effective porosity (see Section 5.2.2.3), fracture spacing (see Section 5.2.2.5), fracture aperture (see Section 5.2.2.6), and matrix diffusion coefficient (or free water diffusion coefficient and matrix tortuosity) (see Section 5.2.2.8).

5.2.1.6 Matrix and Fracture Sorption

Sorption reactions occur between the rock surfaces in contact with the pore fluid and some of the RNs, tending to retard the transport of these RNs. The reactive minerals known to occur in PM rocks include zeolite, smectite, mica, hematite, and calcite (Zavarin et al., 2004; Carle, 2020; Carle et al., 2020). Sorption reactions are chemical reactions that involve the distribution of chemical constituents between water and solid surfaces. In single-porosity media, the reactions occur as the solute comes into contact with the immobile minerals along the flow paths between the grains. In double-porosity media, the solute can react with rock surfaces bounding the fractures and also diffuse into the rock matrix and react with the pore walls within the matrix.

Sorption reactions between the aqueous RNs and minerals on the rock surfaces can result in reduced mobility for the reactive RNs. Although the RN-rock reactions can be complex, they are represented in the PM CAU transport model by a constant called the sorption coefficient, K_d (Freeze and Cherry, 1979). The use of the K_d approach requires that the reactions must be in equilibrium, instantaneous (kinetics), linear, and reversible. The sorption coefficient K_d is RN-specific, and also depends on the mineralogy and specific surface area of the rock matrix surfaces exposed to the pore water, chemical composition of the pore water, and temperature. Some RNs such as ^{3}H, ^{36}Cl, and ^{129}I are considered to be nonreactive and do not sorb. Some RNs are moderately adsorbing, such as U and Np; or strongly sorbing such as ^{238}Pu, $^{239/240}$Pu, ^{137}Cs, and ^{90}Sr (Carle, 2018).

The transport parameters required for representing matrix sorption in the PM CAU transport model are RN-specific K_ds for each HSU/HGU, presented in Section 5.2.2.9, matrix porosity presented in Section 5.2.2.2, and bulk rock density presented in Section 5.2.2.4. In fractured media, sorption reactions occur between surfaces of fractures and some of the RNs, tending to retard the transport of

these RNs. As a simplification in the PM CAU transport model, sorption reactions on fracture surfaces are neglected. This is a conservative assumption.

5.2.1.7 Colloid-Facilitated Transport

Sorption mechanisms can cause certain RNs to bond to small mobile particles (i.e., colloids). “Small” here means submicrometer size, small in comparison to average fracture aperture, but larger than the solute molecules. These particles can move with the groundwater within fractures, but they are not able to diffuse into the matrix pores. This reduces the retardation of RNs due to molecular diffusion into stagnant matrix, potentially increasing the mobility of these RNs. For example, data from Well ER-20-5-1 suggest that Pu (as well as europium [Eu], cobalt [Co], and cesium [Cs]) migrated downgradient via colloid transport (Kersting et al., 1999; Zavarin, 2012). However, those data also suggest that the activity of RNs that do transport downgradient from the cavities via colloids is very small at PM, well below the MCL. Kersting et al. (1999) identified Pu concentrations ~0.03 becquerels per liter (Bq/L) (~0.8 pCi/L compared to Pu-MCL of 15 pCi/L) 1.3 km downgradient from the BENHAM test and determined that the migration was facilitated by colloids. Kersting et al. (1999) also suggest that other RNs including isotopes of Eu, Co, and Cs are transported with colloidal material in groundwaters at PM. For colloid-facilitated transport of RNs to have a significant impact on the CB estimates, the RN must exist in the source region in sufficient quantities, colloids must exist in sufficient quantities in the water, RNs must be able to access and bind to the colloids in sufficient concentrations, and the colloids must transport downgradient with groundwater.

Zavarin et al. (2015) and Zavarin et al. (2019) document long-term (~3-year) laboratory experiments on nuclear melt-glass alteration that were conducted under conditions that “represent the range of hydrothermal conditions in underground nuclear test cavities when nuclear melt glass is in contact with groundwater” (e.g., at temperatures ranging from 25 degrees Celsius [°C] to 200 °C) to identify the mechanisms controlling Pu mobilization. It was found that colloid concentrations in water are temperature-dependent, with higher temperatures producing higher colloid concentrations. Thus, it was concluded that, based on the median colloid concentration reported for NNSS groundwater, “Colloid concentrations (and associated Pu concentrations) measured in 140 and 200 °C samples are about 2 orders of magnitude higher than the median colloid concentrations observed at the NNSS.” It was also concluded that “the early-time elevated temperatures expected at underground nuclear

tests are likely to yield maximum Pu fluxes to groundwater (and maximum Pu concentrations) and that release rates under long-term ambient conditions will be substantially reduced."

Reimus (2018) addressed the question of whether Pu should continue to be considered as an RN that could potentially define the CBs. He concluded that, unless some unlikely combination of circumstances occurs, it is unlikely that Pu concentrations would ever exceed the MCL at offsite locations and that Pu would never surpass ^{3}H in radiological significance unless it is at some distant time in the future when ^{3}H has decayed to a level below the MCL. (Specifically, he said, "It would have to be a relatively high-yield test with Pu concentrations at least as high as measured in the CHANCELLOR cavity, with high initial glass temperatures at the time of water immersion, with an aquifer unit intersecting the chimney near the top of the cavity, and probably relatively close to the NNSS boundary [or with a very low-volume, channel-like pathway to the boundary] so that there is limited opportunity for mixing and dilution of the plume.' Furthermore, colloid filtration and Pu desorption from colloids would have to be very limited in both the cavity/chimney system and in the downgradient aquifer.")

Given these conclusions, it is likely that the influence of colloid-facilitated transport on the extent of the forecast CBs is minor, in large part because of the lateral extent of contamination associated with more mobile and dose-significant RNs (e.g., ^{3}H, ^{129}I) over the time period of interest. However, as a conservative approach, colloid-facilitated transport is included in the PM CAU model using a simplified approach that includes the following assumptions (DOE/EMNV, 2019b):

- All Pu isotopes present in groundwater are associated with a generic colloidal material (either inorganic mineral colloids or large organic macromolecules).
- The majority (99 percent) of aqueous Pu is (reversibly) associated with the generic colloidal material, with the remaining fraction (1 percent) in a noncolloidal (aqueous) form. This level of fractionation is roughly consistent with measured data (Zhao et al., 2011; Kersting et al., 1999).
- The migration of colloidally bound Pu in the fracture flow system is not inhibited by colloid filtration or any other colloid retardation processes.
- The diffusion of colloidally bound Pu into the matrix is inhibited because of physical or molecular size limitations. However, because of the reversibility assumption, Pu is considered able to disassociate from the colloids in solution, and the (small 1 percent) noncolloidal fraction is itself considered able to diffuse into the matrix.

- The noncolloidal fraction of Pu that is allowed to diffuse into the matrix is considered able to sorb to matrix surfaces.

- Only the total concentration (total = 99 percent colloidal + 1 percent noncolloidal) is used as a variable in the model to represent the abundance of any given Pu isotope. The specific colloidal or noncolloidal subfractions are not explicitly evaluated.

There are two important consequences of this conceptualization. First, because most Pu will be colloidally bound, each Pu species incorporated into the model will retain (conservatively) a great deal of mobility. Because matrix diffusion will be experienced only by the noncolloidal fraction of Pu, a reduced effective matrix diffusivity (D_{eff}) by a factor of 100 is assigned to the total concentration of each Pu species as a way to account for this fractionation effect. Additionally, as a conservative approximation, a reduced matrix sorption coefficient ($K_{d,eff}$) is assigned to the total concentration for each Pu species where K_d for Pu is reduced by a factor of 100. Thus

$$D_{eff} = 0.01 D_m \qquad (5\text{-}3a)$$

$$K_{d,\,eff} = 0.01 K_d \qquad (5\text{-}3b)$$

5.2.2 Transport Parameters and Distributions

Major data types of relevance include radioactive decay constants, effective porosity, matrix porosity, fracture spacing, fracture aperture, dispersivity, matrix diffusion coefficients, and sorption coefficients. Details for these parameters are presented in Navarro (2021a) and summarized in this subsection. Note that the HSU assignments in the PM CAU transport model are identical to those in the PM CAU flow model, and transport parameters are sampled on the basis of HSUs.

5.2.2.1 Radioactive Decay Constants

The radioactive decay constants are well-defined properties of the specific RNs, independent of the geologic medium and the ambient underground conditions. Decay constants (λ) are related to the half-life ($T_{1/2}$) as $\lambda = \ln(2)/T_{1/2}$. For the RNs included in the PM CAU model, half-lives are obtained from Finnegan et al. (2016) and are presented in Table 5-2.

Table 5-2
Inventory and Half-Lives for RNs Included in the PM CAU Model
(Decay-corrected to September 30, 2012)

RN	Category	Half-Life (Years)	Curies	
			PM Area 19	PM Area 20
^{3}H	Tritium	12.32	5.76E+06	1.91E+07
^{14}C	Activation	5,715	2.19E+02	4.68E+02
^{36}Cl	Activation	3.01E+05	9.11E+01	1.57E+02
^{90}Sr	Fission	28.78	3.58E+05	4.22E+05
^{99}Tc	Fission	2.13E+05	1.34E+02	1.78E+02
^{129}I	Fission	1.57E+07	4.15E-01	5.60E-01
^{137}Cs	Fission	30.07	4.39E+05	5.65E+05
^{232}U	Actinide (device)	69.8	7.16E+01	1.42E+02
^{233}U	Actinide (device)	1.592E+05	6.51E+01	1.18E+02
^{234}U	Actinide (device+natural)	2.46E+05	7.70E+01	7.03E+01
^{238}U	Actinide (device+natural)	4.47E+09	6.83E+00	1.25E+01
^{237}Np	Actinide (device)	2.14E+06	1.21E+01	2.50E+01
^{238}Pu	Actinide (device)	87.7	2.44E+03	4.07E+03
^{239}Pu	Actinide (device)	2.410E+04	7.68E+03	1.26E+04
^{240}Pu	Actinide (device)	6.56E+03	2.04E+03	4.40E+03

Source: Finnegan et al. (2016)

Note: Data are decay-corrected to September 30, 2012.

5.2.2.2 Matrix Porosity

There are several types of porosity. Of particular interest are matrix and effective porosities. For fractured geologic units these two types of porosity are distinct, while for porous geologic units the two overlap. In fact, matrix porosity measurements may be used to approximate the effective porosity of porous geologic units. Thus, following a discussion of the role of matrix porosity in RN transport in groundwater, this section includes the distributions of the matrix porosity used for HSUs in the PM CAU model.

5.2.2.2.1 Role of Matrix Porosity in Contaminant Transport

The role of matrix porosity depends on whether the host geologic media are porous or fractured. In porous geologic media, water movement occurs through the rock matrix, through the connected pores measured as effective porosity. In fractured rock material, the portion of the rock that is not fractured is considered the matrix. It is generally accepted that water movement is primarily through the fractures in the rock, but not all fractures transmit measurable quantities of water. Therefore, the volume of rock through which the majority of water flows is a small percentage of the total rock volume. The matrix represents the majority of the rock volume. In fractured saturated geologic units, the volume of water in the matrix porosity may be greater by factors of up to 100 or more than the volume in the fractures. This large reservoir of water in the matrix may be extremely important to the simulation of RN migration. If RN migration occurs between the fractures and matrix via a process called matrix diffusion (Section 5.2.2.8), the rate of RN migration will be reduced relative to the bulk water flow rate in the fractures. The matrix porosity, coupled with the matrix diffusion coefficient, govern the movement of the RNs into and out of the matrix. Thus, matrix porosity is expected to be an important parameter in the simulation of RN migration in the groundwater system of PM.

5.2.2.2.2 Distributions Used in the PM CAU Transport Model

Statistics describing the matrix porosity distributions used in the PM CAU transport model are provided in Table 5-3 for each HSU/fault zone in the model, taken from Table 5-4 of Navarro (2021a). Distributions are either log-normal or triangular. For the log-normal distributions, minimum and maximum values are calculated as the mean value plus or minus 2 standard deviations.

5.2.2.3 Effective Porosity

This section includes descriptions of the role of effective porosity in RN transport in groundwater and the distributions of the effective porosity used in the PM CAU model. For porous media, the effective porosity (with some caveats) is represented by the matrix porosity discussed in Section 5.2.2.2.

Table 5-3
Matrix Porosity Distributions Used in the PM CAU Transport Model
(Page 1 of 3)

HSU	Mean/Likely	Standard Deviation	Minimum	Maximum	Distribution Type
ATICU	1.80E-02	N/A	2.00E-03	1.03E-01	Triangular
RMICU	1.80E-02	N/A	2.00E-03	1.03E-01	Triangular
UCCU	3.00E-05	N/A	5.00E-06	5.00E-04	Triangular
ATCCU	2.83E-01	1.11E-01	6.10E-02	5.05E-01	Log-Normal
LCA	5.00E-02	N/A	1.00E-02	9.70E-02	Triangular
CFCU	2.19E-01	N/A	1.41E-01	3.65E-01	Triangular
BFCU	2.83E-01	1.03E-01	7.70E-02	4.89E-01	Log-Normal
LPCU	2.73E-01	N/A	7.60E-02	5.45E-01	Triangular
MPCU	3.73E-01	N/A	1.92E-01	5.19E-01	Triangular
PBPCU	3.22E-01	N/A	1.27E-01	4.34E-01	Triangular
FCCU	3.76E-01	N/A	1.88E-01	5.44E-01	Triangular
SCVCU	4.00E-03	N/A	1.00E-03	6.00E-03	Triangular
UPCU	3.15E-01	N/A	8.00E-02	5.39E-01	Triangular
THCU	3.57E-01	N/A	2.52E-01	5.01E-01	Triangular
BWCU	2.83E-01	1.11E-01	6.10E-02	5.05E-01	Log-Normal
CFCM	1.72E-01	N/A	5.00E-02	4.98E-01	Triangular
THCM	3.15E-01	N/A	1.38E-01	5.53E-01	Triangular
FCCM	3.13E-01	N/A	7.90E-02	5.25E-01	Triangular
PBRCM	2.16E-01	N/A	1.02E-01	4.26E-01	Triangular
CHLFA1	1.89E-01	N/A	3.80E-02	5.49E-01	Triangular
CHLFA3	1.89E-01	N/A	3.80E-02	5.49E-01	Triangular
CHLFA2	1.89E-01	N/A	3.80E-02	5.49E-01	Triangular
IA	1.93E-01	7.10E-02	5.10E-02	3.35E-01	Log-Normal
CHLFA5	1.89E-01	N/A	3.80E-02	5.49E-01	Triangular
CHLFA4	1.89E-01	N/A	3.80E-02	5.49E-01	Triangular
PLFA	2.07E-01	7.70E-02	5.30E-02	3.61E-01	Log-Normal
FCULFA4	1.93E-01	N/A	5.70E-02	4.00E-01	Triangular
FCULFA1	1.93E-01	N/A	5.70E-02	4.00E-01	Triangular
FCLLFA	2.19E-01	9.60E-02	2.70E-02	4.11E-01	Log-Normal

Table 5-3
Matrix Porosity Distributions Used in the PM CAU Transport Model
(Page 2 of 3)

HSU	Mean/Likely	Standard Deviation	Minimum	Maximum	Distribution Type
FCULFA2	1.93E-01	N/A	5.70E-02	4.00E-01	Triangular
SPA	1.63E-01	N/A	2.80E-02	3.64E-01	Triangular
THLFA	2.08E-01	7.60E-02	5.60E-02	3.60E-01	Log-Normal
BA	2.09E-01	N/A	6.70E-02	5.46E-01	Triangular
BRA	2.19E-01	N/A	3.50E-02	4.72E-01	Triangular
CPA	2.27E-01	N/A	4.20E-02	5.48E-01	Triangular
ATWTA	1.77E-01	6.00E-02	5.70E-02	2.97E-01	Log-Normal
BWWTA	2.86E-01	N/A	4.40E-02	6.84E-01	Triangular
FCWTA1	2.38E-01	9.10E-02	5.60E-02	4.20E-01	Log-Normal
TSA	1.68E-01	N/A	5.10E-02	4.21E-01	Triangular
TCA	1.86E-01	N/A	5.20E-02	4.98E-01	Triangular
WWA	2.02E-01	7.50E-02	5.20E-02	3.52E-01	Log-Normal
RMWTA	1.27E-01	N/A	2.20E-02	4.44E-01	Triangular
TMWTA	1.35E-01	N/A	6.50E-02	2.31E-01	Triangular
TMUWTA	1.85E-01	6.90E-02	4.70E-02	3.23E-01	Log-Normal
CHVTA	2.82E-01	1.01E-01	8.00E-02	4.84E-01	Log-Normal
PVTA	2.95E-01	9.80E-02	9.90E-02	4.91E-01	Log-Normal
TCVA	2.33E-01	8.10E-02	7.10E-02	3.95E-01	Log-Normal
TMLVTA	3.63E-01	N/A	5.30E-02	4.83E-01	Triangular
PMNICU	1.80E-02	N/A	2.00E-03	1.03E-01	Triangular
LCCU	3.30E-02	N/A	2.00E-03	1.00E-01	Triangular
LCCU1	3.30E-02	N/A	2.00E-03	1.00E-01	Triangular
MGCU	1.80E-02	N/A	2.00E-03	1.03E-01	Triangular
YMCFCM	2.43E-01	9.10E-02	6.10E-02	4.25E-01	Log-Normal
PCM	1.74E-01	6.70E-02	4.00E-02	3.08E-01	Log-Normal
KA	2.06E-01	7.60E-02	5.40E-02	3.58E-01	Log-Normal
FCULFA5	1.93E-01	N/A	5.70E-02	4.00E-01	Triangular
DVA	2.64E-01	9.20E-02	8.00E-02	4.48E-01	Log-Normal
DVCM	3.41E-01	N/A	6.00E-02	7.50E-01	Triangular

Table 5-3
Matrix Porosity Distributions Used in the PM CAU Transport Model
(Page 3 of 3)

HSU	Mean/Likely	Standard Deviation	Minimum	Maximum	Distribution Type
FCWTA	2.38E-01	9.10E-02	5.60E-02	4.20E-01	Log-Normal
CHZCM	2.81E-01	N/A	6.50E-02	5.50E-01	Triangular
AA	3.20E-01	N/A	2.38E-01	4.02E-01	Triangular
YVCM	3.41E-01	N/A	6.00E-02	7.50E-01	Triangular
LCA3	5.00E-02	N/A	1.00E-02	9.70E-02	Triangular
PBRCM_sw	2.16E-01	N/A	1.02E-01	4.26E-01	Triangular
BRA_sw	2.19E-01	N/A	3.50E-02	4.72E-01	Triangular
TCA_w	1.86E-01	N/A	5.20E-02	4.98E-01	Triangular
CHZCM_w	2.81E-01	N/A	6.50E-02	5.50E-01	Triangular
UPCU_sw	3.15E-01	N/A	8.00E-02	5.39E-01	Triangular
LPCU_sw	2.73E-01	N/A	7.60E-02	5.45E-01	Triangular
CHLFA5_w	1.89E-01	N/A	3.80E-02	5.49E-01	Triangular
UPCU_nw	3.15E-01	N/A	8.00E-02	5.39E-01	Triangular
LPCU_nw	2.73E-01	N/A	7.60E-02	5.45E-01	Triangular
PBRCM_nw	2.16E-01	N/A	1.02E-01	4.26E-01	Triangular
BRA_nw	2.19E-01	N/A	3.50E-02	4.72E-01	Triangular
mRMWTA1	1.27E-01	N/A	2.20E-02	4.44E-01	Triangular
mRMWTA2	1.27E-01	N/A	2.20E-02	4.44E-01	Triangular
mPBRCM_lfa	2.16E-01	N/A	1.02E-01	4.26E-01	Triangular
Faults (Barrier)	1.80E-02	N/A	2.00E-03	1.03E-01	Triangular
Faults (Conduit)	1.89E-01	N/A	3.80E-02	5.49E-01	Triangular

Source: Table 5-4 of Navarro (2021a)

5.2.2.3.1 Role of Effective Porosity in Contaminant Transport

Effective porosity affects the movement of contaminants in groundwater because it is an important factor in determining the magnitudes of groundwater velocity and matrix diffusion. The flux of groundwater is calculated as the volumetric flow rate per cross-sectional open area. The space open to

flow is the interconnected pore space/fractures through which water flows and is generally characterized by the effective porosity. Effective porosity can be related to the groundwater flux and velocity via Equation 5-2.

In fractured media, as previously noted, two components of the porosity can be identified: a fracture porosity and a matrix porosity. Water primarily flows through the more permeable fracture openings. Thus, the fracture porosity generally controls the velocity of groundwater. The range of effective porosity in porous media (typically 15 to 40 percent) can result in a factor of 2 or 3 variation in groundwater velocity; but for fractured systems, the effective porosity variation (<0.01 to 10 percent [Freeze and Cherry, 1979]) can produce several orders of magnitude variation in pore velocity.

In the PM CAU model, the HSUs that are confining units or vitric tuffs—i.e., those dominated by the HGUs ICU, CCU, GCU, and VTA as well as faults that act as barriers to flow—were treated as single-porosity media. On the other hand, the HSUs dominated by the LFA and WTA HGUs and designated as aquifers, as well as TCUs, were treated as fractured dual-porosity media.

5.2.2.3.2 Distributions Used in the PM CAU Transport Model

Statistics describing the effective porosity distributions used for the HGUs treated as fractured dual-porosity media in the PM CAU model are provided in Table 5-4, taken from Section 5.3 of Navarro (2021a).

Table 5-4
Effective Porosity Distributions Used for the HGUs Treated as Fractured Dual-Porosity Media in the PM CAU Transport Model
(Page 1 of 4)

HSU	Mean/Likely	Minimum	Maximum	Distribution Type
ATCCU	9.35E-05	8.00E-06	2.36E-04	Log-Triangular
LCA	5.00E-03	2.00E-04	2.00E-02	Log-Triangular
CFCU	9.35E-05	8.00E-06	2.36E-04	Log-Triangular
BFCU	9.35E-05	8.00E-06	2.36E-04	Log-Triangular
LPCU	9.35E-05	8.00E-06	2.36E-04	Log-Triangular
MPCU	9.35E-05	8.00E-06	2.36E-04	Log-Triangular
PBPCU	9.35E-05	8.00E-06	2.36E-04	Log-Triangular

Table 5-4
Effective Porosity Distributions Used for the HGUs Treated as Fractured Dual-Porosity Media in the PM CAU Transport Model
(Page 2 of 4)

HSU	Mean/Likely	Minimum	Maximum	Distribution Type
FCCU	9.35E-05	8.00E-06	2.36E-04	Log-Triangular
SCVCU	9.35E-05	8.00E-06	2.36E-04	Log-Triangular
UPCU	9.35E-05	8.00E-06	2.36E-04	Log-Triangular
THCU	9.35E-05	8.00E-06	2.36E-04	Log-Triangular
BWCU	9.35E-05	8.00E-06	2.36E-04	Log-Triangular
CFCM	3.70E-03	1.00E-04	2.30E-02	Log-Triangular
THCM	9.35E-05	8.00E-06	2.36E-04	Log-Triangular
FCCM	9.35E-05	8.00E-06	2.36E-04	Log-Triangular
PBRCM	9.35E-05	8.00E-06	2.36E-04	Log-Triangular
CHLFA1	3.70E-03	1.00E-04	2.30E-02	Log-Triangular
CHLFA3	3.70E-03	1.00E-04	2.30E-02	Log-Triangular
CHLFA2	3.70E-03	1.00E-04	2.30E-02	Log-Triangular
IA	3.70E-03	1.00E-04	2.30E-02	Log-Triangular
CHLFA5	3.70E-03	1.00E-04	2.30E-02	Log-Triangular
CHLFA4	3.70E-03	1.00E-04	2.30E-02	Log-Triangular
PLFA	3.70E-03	1.00E-04	2.30E-02	Log-Triangular
FCULFA4	3.70E-03	1.00E-04	2.30E-02	Log-Triangular
FCULFA1	3.70E-03	1.00E-04	2.30E-02	Log-Triangular
FCLLFA	3.70E-03	1.00E-04	2.30E-02	Log-Triangular
FCULFA2	3.70E-03	1.00E-04	2.30E-02	Log-Triangular
SPA	3.70E-03	1.00E-04	2.30E-02	Log-Triangular
THLFA	3.70E-03	1.00E-04	2.30E-02	Log-Triangular
BA	3.70E-03	1.00E-04	2.30E-02	Log-Triangular
BRA	9.89E-04	1.10E-04	6.00E-03	Log-Triangular
CPA	3.70E-03	1.00E-04	2.30E-02	Log-Triangular
ATWTA	9.89E-04	1.10E-04	6.00E-03	Log-Triangular
BWWTA	9.89E-04	1.10E-04	6.00E-03	Log-Triangular
FCWTA1	9.89E-04	1.10E-04	6.00E-03	Log-Triangular

Table 5-4
Effective Porosity Distributions Used for the HGUs Treated as Fractured Dual-Porosity Media in the PM CAU Transport Model
(Page 3 of 4)

HSU	Mean/Likely	Minimum	Maximum	Distribution Type
TSA	9.89E-04	1.10E-04	6.00E-03	Log-Triangular
TCA	9.89E-04	1.10E-04	6.00E-03	Log-Triangular
WWA	3.70E-03	1.00E-04	2.30E-02	Log-Triangular
RMWTA	9.89E-04	1.10E-04	6.00E-03	Log-Triangular
TMWTA	9.89E-04	1.10E-04	6.00E-03	Log-Triangular
TMUWTA	9.89E-04	1.10E-04	6.00E-03	Log-Triangular
TCVA	9.89E-04	1.10E-04	6.00E-03	Log-Triangular
YMCFCM	3.70E-03	1.00E-04	2.30E-02	Log-Triangular
PCM	9.89E-04	1.10E-04	6.00E-03	Log-Triangular
KA	3.70E-03	1.00E-04	2.30E-02	Log-Triangular
FCULFA5	3.70E-03	1.00E-04	2.30E-02	Log-Triangular
DVA	9.89E-04	1.10E-04	6.00E-03	Log-Triangular
DVCM	9.89E-04	1.10E-04	6.00E-03	Log-Triangular
FCWTA	9.89E-04	1.10E-04	6.00E-03	Log-Triangular
CHZCM	9.35E-05	8.00E-06	2.36E-04	Log-Triangular
YVCM	3.70E-03	1.00E-04	2.30E-02	Log-Triangular
LCA3	5.00E-03	2.00E-04	2.00E-02	Log-Triangular
PBRCM_sw	9.35E-05	8.00E-06	2.36E-04	Log-Triangular
BRA_sw	9.89E-04	1.10E-04	6.00E-03	Log-Triangular
TCA_w	9.89E-04	1.10E-04	6.00E-03	Log-Triangular
CHZCM_w	9.35E-05	8.00E-06	2.36E-04	Log-Triangular
UPCU_sw	9.35E-05	8.00E-06	2.36E-04	Log-Triangular
LPCU_sw	9.35E-05	8.00E-06	2.36E-04	Log-Triangular
CHLFA5_w	3.70E-03	1.00E-04	2.30E-02	Log-Triangular
UPCU_nw	9.35E-05	8.00E-06	2.36E-04	Log-Triangular
LPCU_nw	9.35E-05	8.00E-06	2.36E-04	Log-Triangular
PBRCM_nw	9.35E-05	8.00E-06	2.36E-04	Log-Triangular
BRA_nw	9.89E-04	1.10E-04	6.00E-03	Log-Triangular

Table 5-4
Effective Porosity Distributions Used for the HGUs Treated as Fractured Dual-Porosity Media in the PM CAU Transport Model
(Page 4 of 4)

HSU	Mean/Likely	Minimum	Maximum	Distribution Type
mRMWTA1	9.89E-04	1.10E-04	6.00E-03	Log-Triangular
mRMWTA2	9.89E-04	1.10E-04	6.00E-03	Log-Triangular
mPBRCM_lfa	9.35E-05	8.00E-06	2.36E-04	Log-Triangular
Faults (Conduit)	3.70E-03	1.00E-04	2.30E-02	Log-Triangular

Source: Section 5.3 of Navarro (2021a)

5.2.2.4 Bulk Rock Density

Bulk rock density is the mass per unit volume of a rock. It is used to determine the matrix retardation coefficient and is a necessary parameter for the transport calculations. The density logs provide an estimate of bulk rock density (Navarro, 2021a).

5.2.2.4.1 Distributions Used in the PM CAU Transport Model

Statistics describing the bulk rock density distributions used in the PM CAU transport model are provided in Table 5-5 for each HSU/fault zone in the model, taken from Tables 5-9 through 5-11 of Navarro (2021a). Distributions are either uniform (constant values) or normal. For the normal distributions, minimum and maximum values are calculated as the mean value plus or minus 2 standard deviations.

5.2.2.5 Fracture Spacing

Considering contaminant transport through dual-porosity media, the fracture spacing affects (1) the estimation of mass transfer from the fractures to the matrix by defining the volume of storage for solutes diffusing into the matrix and the surface area across which diffusion occurs, and (2) velocity of the fluid flowing through the fractures.

Table 5-5
Bulk Rock Density (kg/m^3) Distributions Used in the PM CAU Transport Model
(Page 1 of 3)

HSU	Mean/Likely	Standard Deviation	Minimum	Maximum	Distribution Type
ATICU	2455	N/A	2455	2455	Uniform
RMICU	2455	N/A	2455	2455	Uniform
UCCU	2455	N/A	2455	2455	Uniform
ATCCU	2090	160	1770	2410	Normal
LCA	2455	181.4	2092	2818	Normal
CFCU	2220	50	2120	2320	Normal
BFCU	2090	160	1770	2410	Normal
LPCU	2130	120	1890	2370	Normal
MPCU	1940	80	1780	2100	Normal
PBPCU	2030	80	1870	2190	Normal
FCCU	1960	130	1700	2220	Normal
SCVCU	2090	160	1770	2410	Normal
UPCU	2060	140	1780	2340	Normal
THCU	1970	70	1830	2110	Normal
BWCU	2090	160	1770	2410	Normal
CFCM	2300	90	2120	2480	Normal
THCM	2080	110	1860	2300	Normal
FCCM	2060	150	1760	2360	Normal
PBRCM	2240	70	2100	2380	Normal
CHLFA1	2250	150	1950	2550	Normal
CHLFA3	2250	150	1950	2550	Normal
CHLFA2	2250	150	1950	2550	Normal
IA	2240	120	2000	2480	Normal
CHLFA5	2250	150	1950	2550	Normal
CHLFA4	2250	150	1950	2550	Normal
PLFA	2240	120	2000	2480	Normal
FCULFA4	2220	80	2060	2380	Normal
FCULFA1	2220	80	2060	2380	Normal
FCLLFA	2240	120	2000	2480	Normal

Table 5-5
Bulk Rock Density (kg/m^3) Distributions Used in the PM CAU Transport Model
(Page 2 of 3)

HSU	Mean/Likely	Standard Deviation	Minimum	Maximum	Distribution Type
FCULFA2	2220	80	2060	2380	Normal
SPA	2220	80	2060	2380	Normal
THLFA	2240	120	2000	2480	Normal
BA	2230	100	2030	2430	Normal
BRA	2220	160	1900	2540	Normal
CPA	2170	130	1910	2430	Normal
ATWTA	2310	120	2070	2550	Normal
BWWTA	2310	120	2070	2550	Normal
FCWTA1	2310	120	2070	2550	Normal
TSA	2300	120	2060	2540	Normal
TCA	2270	90	2090	2450	Normal
WWA	2240	120	2000	2480	Normal
RMWTA	2380	100	2180	2580	Normal
TMWTA	2350	40	2270	2430	Normal
TMUWTA	2310	120	2070	2550	Normal
CHVTA	1970	120	1730	2210	Normal
PVTA	1970	120	1730	2210	Normal
TCVA	2310	120	2070	2550	Normal
TMLVTA	1960	130	1700	2220	Normal
PMNICU	2455	N/A	2455	2455	Uniform
LCCU	2455	N/A	2455	2455	Uniform
LCCU1	2455	N/A	2455	2455	Uniform
MGCU	2455	N/A	2455	2455	Uniform
YMCFCM	2240	120	2000	2480	Normal
PCM	2310	120	2070	2550	Normal
KA	2240	120	2000	2480	Normal
FCULFA5	2220	80	2060	2380	Normal
DVA	2310	120	2070	2550	Normal
DVCM	2310	120	2070	2550	Normal

Table 5-5
Bulk Rock Density (kg/m^3) Distributions Used in the PM CAU Transport Model
(Page 3 of 3)

HSU	Mean/Likely	Standard Deviation	Minimum	Maximum	Distribution Type
FCWTA	2310	120	2070	2550	Normal
CHZCM	2110	200	1710	2510	Normal
AA	1787	78.4	1630	1944	Normal
YVCM	2240	120	2000	2480	Normal
LCA3	2455	181.4	2092	2818	Normal
PBRCM_sw	2240	70	2100	2380	Normal
BRA_sw	2220	160	1900	2540	Normal
TCA_w	2270	90	2090	2450	Normal
CHZCM_w	2110	200	1710	2510	Normal
UPCU_sw	2060	140	1780	2340	Normal
LPCU_sw	2130	120	1890	2370	Normal
CHLFA5_w	2250	150	1950	2550	Normal
UPCU_nw	2060	140	1780	2340	Normal
LPCU_nw	2130	120	1890	2370	Normal
PBRCM_nw	2240	70	2100	2380	Normal
BRA_nw	2220	160	1900	2540	Normal
mRMWTA1	2380	100	2180	2580	Normal
mRMWTA2	2380	100	2180	2580	Normal
mPBRCM_lfa	2240	70	2100	2380	Normal
Faults (Barrier)	2455	N/A	2455	2455	Uniform
Faults (Conduit)	2250	150	1950	2550	Normal

Source: Tables 5-9 through 5-11 of Navarro (2021a)

kg/m^3 = Kilograms per cubic meter

Fracture spacing is not an input to PLUMECALC. PLUMECALC calculates fracture spacing from fracture aperture and fracture porosity as:

$$B = \frac{b}{\phi_f} \qquad (5\text{-}4)$$

where

ϕ_f = Fracture porosity [L/L]
b = Fracture aperture [L]
B = Fracture spacing [L]

5.2.2.6 Fracture Aperture

Fracture aperture is a key factor determining the rate of groundwater flow and RN migration through fractured rock. The width of the apertures determines the cross-sectional area available for flow through fractured rock, which in turn controls the velocity and quantity of groundwater flow. Additionally, it influences matrix diffusion calculations through its relationship to fracture porosity and spacing.

5.2.2.6.1 Role of Fracture Aperture in the PM CAU Transport Model

In the dual-porosity conceptualization, fracture aperture affects the estimation of mass transfer between the flowing fluid in the fractures and the stagnant fluid in the matrix by defining the volume of storage for diffusion of solutes and the surface area across which diffusion occurs; as well as velocity of the fluid flowing through the fractures via the cubic law for hydraulic conductivity using the parallel plate conceptualization (Navarro, 2021a). Fracture aperture, fracture porosity, and fracture spacing are related through Equation 5-4. Fracture aperture is a direct input to the code PLUMECALC.

5.2.2.6.2 Distributions Used in the PM CAU Transport Model

Statistics describing the log fracture aperture distributions used in the PM CAU transport model are derived from Table 5-16 of Navarro (2021a) and are provided in Table 5-6 for each HSU/fault zone in the model. The minimum and maximum fracture aperture values used in the transport model were calculated as the mean value plus or minus 2 standard deviations, and were not taken from Table 5-16 of Navarro (2021a). Due to roundoff errors in these calculations, some of the minimum and maximum

values listed in Table 5-6 are not identical to those listed in Table 5-16 of Navarro (2021a). Specifically, the following differences are noted:

- For WTA, the minimum value used in the transport model was -4.98, not -4.97 as noted in Table 5-16 of Navarro (2021a).
- For WTA, the maximum value used in the transport model was -2.22, not -2.23 as noted in Table 5-16 of Navarro (2021a).
- For TCU, the maximum value used in the transport model was -2.46, not -2.45 as noted in Table 5-16 of Navarro (2021a).
- For CA, the minimum value used in the transport model was -4.48, not -4.47 as noted in Table 5-16 of Navarro (2021a).

These differences are very small, and the impact of these differences on the developed fracture aperture distributions, and hence to the calculated CB, is negligible.

Table 5-6
Log_{10} Fracture Aperture (m) Distributions Used in the PM CAU Transport Model
(Page 1 of 3)

HSU	Mean/Likely	Standard Deviation	Minimum	Maximum	Distribution Type
ATCCU	-3.56	0.55	-4.66	-2.46	Normal
LCA	-3.58	0.45	-4.48	-2.68	Normal
CFCU	-3.56	0.55	-4.66	-2.46	Normal
BFCU	-3.56	0.55	-4.66	-2.46	Normal
LPCU	-3.56	0.55	-4.66	-2.46	Normal
MPCU	-3.56	0.55	-4.66	-2.46	Normal
PBPCU	-3.56	0.55	-4.66	-2.46	Normal
FCCU	-3.56	0.55	-4.66	-2.46	Normal
SCVCU	-3.56	0.55	-4.66	-2.46	Normal
UPCU	-3.56	0.55	-4.66	-2.46	Normal
THCU	-3.56	0.55	-4.66	-2.46	Normal
BWCU	-3.56	0.55	-4.66	-2.46	Normal
CFCM	-3.32	0.44	-4.2	-2.44	Normal
THCM	-3.56	0.55	-4.66	-2.46	Normal

Table 5-6
Log_{10} Fracture Aperture (m) Distributions Used in the PM CAU Transport Model
(Page 2 of 3)

HSU	Mean/Likely	Standard Deviation	Minimum	Maximum	Distribution Type
FCCM	-3.56	0.55	-4.66	-2.46	Normal
PBRCM	-3.56	0.55	-4.66	-2.46	Normal
CHLFA1	-3.32	0.44	-4.2	-2.44	Normal
CHLFA3	-3.32	0.44	-4.2	-2.44	Normal
CHLFA2	-3.32	0.44	-4.2	-2.44	Normal
IA	-3.32	0.44	-4.2	-2.44	Normal
CHLFA5	-3.32	0.44	-4.2	-2.44	Normal
CHLFA4	-3.32	0.44	-4.2	-2.44	Normal
PLFA	-3.32	0.44	-4.2	-2.44	Normal
FCULFA4	-3.32	0.44	-4.2	-2.44	Normal
FCULFA1	-3.32	0.44	-4.2	-2.44	Normal
FCLLFA	-3.32	0.44	-4.2	-2.44	Normal
FCULFA2	-3.32	0.44	-4.2	-2.44	Normal
SPA	-3.32	0.44	-4.2	-2.44	Normal
THLFA	-3.32	0.44	-4.2	-2.44	Normal
BA	-3.32	0.44	-4.2	-2.44	Normal
BRA	-3.60	0.69	-4.98	-2.22	Normal
CPA	-3.32	0.44	-4.2	-2.44	Normal
ATWTA	-3.60	0.69	-4.98	-2.22	Normal
BWWTA	-3.60	0.69	-4.98	-2.22	Normal
FCWTA1	-3.60	0.69	-4.98	-2.22	Normal
TSA	-3.60	0.69	-4.98	-2.22	Normal
TCA	-3.60	0.69	-4.98	-2.22	Normal
WWA	-3.32	0.44	-4.2	-2.44	Normal
RMWTA	-3.60	0.69	-4.98	-2.22	Normal
TMWTA	-3.60	0.69	-4.98	-2.22	Normal
TMUWTA	-3.60	0.69	-4.98	-2.22	Normal
TCVA	-3.60	0.69	-4.98	-2.22	Normal
YMCFCM	-3.32	0.44	-4.2	-2.44	Normal

Table 5-6
Log_{10} Fracture Aperture (m) Distributions Used in the PM CAU Transport Model
(Page 3 of 3)

HSU	Mean/Likely	Standard Deviation	Minimum	Maximum	Distribution Type
PCM	-3.60	0.69	-4.98	-2.22	Normal
KA	-3.32	0.44	-4.2	-2.44	Normal
FCULFA5	-3.32	0.44	-4.2	-2.44	Normal
DVA	-3.60	0.69	-4.98	-2.22	Normal
DVCM	-3.60	0.69	-4.98	-2.22	Normal
FCWTA	-3.60	0.69	-4.98	-2.22	Normal
CHZCM	-3.56	0.55	-4.66	-2.46	Normal
YVCM	-3.32	0.44	-4.2	-2.44	Normal
LCA3	-3.58	0.45	-4.48	-2.68	Normal
PBRCM_sw	-3.56	0.55	-4.66	-2.46	Normal
BRA_sw	-3.60	0.69	-4.98	-2.22	Normal
TCA_w	-3.60	0.69	-4.98	-2.22	Normal
CHZCM_w	-3.56	0.55	-4.66	-2.46	Normal
UPCU_sw	-3.56	0.55	-4.66	-2.46	Normal
LPCU_sw	-3.56	0.55	-4.66	-2.46	Normal
CHLFA5_w	-3.32	0.44	-4.2	-2.44	Normal
UPCU_nw	-3.56	0.55	-4.66	-2.46	Normal
LPCU_nw	-3.56	0.55	-4.66	-2.46	Normal
PBRCM_nw	-3.56	0.55	-4.66	-2.46	Normal
BRA_nw	-3.60	0.69	-4.98	-2.22	Normal
mRMWTA1	-3.60	0.69	-4.98	-2.22	Normal
mRMWTA2	-3.60	0.69	-4.98	-2.22	Normal
mPBRCM_lfa	-3.56	0.55	-4.66	-2.46	Normal
Faults (Conduit)	-3.32	0.44	-4.2	-2.44	Normal

Source: Table 5-16 of Navarro (2021a)

5.2.2.7 Dispersivity

This section describes the role of dispersion in contaminant transport in groundwater and the range of dispersivity values used in the PM CAU model.

5.2.2.7.1 Role of Dispersivity

Dispersion is the process of spreading a solute over a volume that is larger than would be predicted based on estimates of the mean groundwater velocity. Hydrodynamic dispersion, often shortened to simply dispersion, is the term used to represent the combined impacts of mechanical dispersion and molecular diffusion. Mechanical dispersion arises from the complex and heterogeneous movement of water and solute particles through an intricate network of pores and fractures. It is common practice in groundwater modeling (Freeze and Cherry, 1979) to represent the effects of dispersion with the use of three independent dispersivities: the longitudinal dispersivity along the direction of the bulk fluid flow, and two transverse dispersivities orthogonal to the flow direction. This is the approach used in the PM CAU transport model.

Conceptually, dispersivity is a modeling parameter to describe plume spreading that accounts for the unmeasured and/or unspecified variability in the hydraulic properties within the flow and transport model domain. Dispersivity is often observed to be scale-dependent (i.e., a function of a representative scale of the problem). Reported dispersivity values (at specific transport scales) are typically derived from data collected during tracer tests, and from model calibration of contaminant plumes and geochemical or environmental isotope distributions in regional flow systems.

5.2.2.7.2 Dispersivity Values Used in the PM CAU Transport Model

Section 5.7 of Navarro (2021a) provides an acceptable range of longitudinal dispersivity at PM between ~3.28 and 656 ft (1 and 200 m). For the PM CAU transport model, a longitudinal dispersivity value of ~492 ft (150 m) was used, which is consistent with the value of 500 ft (~152 m) used by Jackson (2021). Following recommendation in the TDD, the transverse horizontal dispersivity is selected to be one--tenth of the longitudinal dispersivity (15 m), and the transverse vertical dispersivity is selected to be one-hundredth of the longitudinal dispersivity (1.5 m).

5.2.2.8 Matrix Diffusion

This section describes the role of matrix diffusion and tortuosity in contaminant transport in groundwater and the distribution of tortuosity used in the PM CAU model.

5.2.2.8.1 Role of Matrix Diffusion

Matrix diffusion is typically associated with systems in which flow is predominantly in high-conductivity features such as fractures, while the porous rock matrix surrounding the fractures contains significant quantities of stagnant fluid in diffusive communication with the flowing features. Transport of RNs and other contaminants in saturated fractured rock can be strongly retarded by matrix diffusion. Diffusive mass transfer occurs also in media not dominated by fracture flow, such as alluvium or nonwelded tuffs, by diffusion between the more permeable zones and lower-permeability zones. Diffusion, however, is expected to be less important in such media because the ratio of stagnant to flowing water volume is usually much smaller and the permeability contrast is less severe than in fracture-dominated media.

The importance of the diffusion of solutes between fractures and the adjacent matrix has been studied and reported extensively in the literature and has been established as an important process for retarding the transport of solutes introduced into fractured geologic systems; see Navarro (2021c) for a listing of references.

5.2.2.8.2 Diffusion Process and Tortuosity

The molecular diffusion conceptualization is based on Fick's second law of diffusion (Crank, 1975) which, for a one-dimensional (1-D) system in a porous medium, may be expressed as:

$$\frac{\partial C}{\partial t} = D_m \frac{\partial^2 C}{\partial z^2} \qquad (5\text{-}5)$$

where

C = Species concentration (M/L^3)
D_m = Effective matrix diffusion coefficient for solutes in the pores (L^2/T)
z = Coordinate position (L)
t = Time (T)

This form of Fick's second law is seen in many standard hydrogeology texts, including Bear (1972) and Freeze and Cherry (1979). The diffusion in the porous medium is restricted compared to free water because of the presence of the solid phase. The ratio of matrix diffusion coefficient in porous media (D_m) to the free water diffusion coefficient of the solute (D_o) is defined as the tortuosity (τ).

Several definitions of tortuosity can be found in literature; this work uses the definition given in Bear (1972):

$$D_m = \tau \cdot D_0 \qquad (5\text{-}6)$$

Tortuosity can be defined as a bulk measure of the constrictivity and tortuous nature of the interconnected pore space through which diffusion is occurring. Tortuosity ranges from zero for material with zero porosity (zero pore space) to 1 for material with porosity of 1 (i.e., free water). Smaller tortuosities are indicative of longer diffusional path lengths and greater resistance to diffusion through the medium.

Freeze and Cherry (1979) state typical laboratory values for tortuosity range up to 0.5. De Marsily (1986) provides an upper limit of 0.7 for sands. Bear (1972) provides a review and gives an upper bounding value of the ratio of actual tortuous length of travel by a molecule between two points in the porous medium to the distance between those points as 0.8, which would correspond to τ equal to 0.64.

5.2.2.8.3 Distributions Used in the PM CAU Transport Model

The tortuosity statistics for the normal distribution used for all HSUs in the PM CAU transport model, independently sampled for each HSU, were as follows (Navarro, 2021a):

- Mean of ln(tortuosity) = -2.5043
- Standard deviation of ln(tortuosity) = 1.1224
- Minimum of ln(tortuosity) = -4.7491
- Maximum of ln(tortuosity) = -0.2595

The free-water diffusion coefficient is a function of fluid temperature and the ionic radius of the solute. As discussed in Navarro (2021a), free water diffusion coefficient increases by about a factor of 2.5 for a temperature increase from 25°C to 60°C. Since the range of tortuosity given above is nearly

two orders of magnitude, the free water diffusion coefficient at 25°C is conservatively used in this work. While it is possible to use a discrete value for each RN, doing so would introduce a large number of additional stochastic variables that may have a marginal impact on the results. Therefore, the approach taken here is to split matrix diffusion into two classes representing either lighter or heavier RNs.

Tritium, as hydrogen tritium oxide (HTO), is the RN with the largest free-water diffusion coefficient (2.236×10E-09 square meters per second [m^2/s] at 25 °C [Mills, 1973]). The RN with the lowest free-water diffusion coefficient is Am (3×10E-10 m^2/s [DOE/WIPP, 2004]). Thus, these two values bound the range for free water diffusion coefficients for species relevant to the NNSS. In the PM CAU transport model, RNs with an atomic mass greater than 137 were assigned a free-water diffusion coefficient of 3.0E-10 m^2/s, and those with an atomic mass less than or equal to 137 were assigned a free-water diffusion coefficient of 2.24E-09 m^2/s.

Using Equation 5-6, the statistics describing the matrix diffusion coefficients used in the PM CAU transport model (independently sampled for each HSU) were obtained as shown in Table 5-7.

Table 5-7
Matrix Diffusion Coefficient (m^2/s) Distributions Used in the PM CAU Transport Model

	Median	Minimum	Maximum	Distribution Type
Light RNs	1.83E-10	1.94E-11	1.72E-09	Lognormal
Heavy RNs	2.45E-11	2.60E-12	2.31E-10	Lognormal

As discussed in Section 5.2.1.7, matrix diffusivity for each Pu species is reduced by a factor of 100 as shown in Equation 5-3 to account for colloid-assisted transport.

5.2.2.9 Matrix Sorption Parameters

This section includes a description of the matrix sorption process and the distributions used in the PM CAU model. Matrix K_ds are needed to simulate source-term RNs that enter the natural hydrologic systems and react with immobile minerals. The RNs of interest are the sorbing RNs of relevance (Sr, Cs, U and Pu) or potential relevance (Np) to the PM HST as specified in Section 5.1.2.

5.2.2.9.1 Role of Matrix Sorption in Contaminant Transport Models

Matrix sorption is the physiochemical process at mineral-water interfaces that controls solute retardation within the pore spaces of the immobile rock matrix. Similar physiochemical processes may occur on minerals coating fractures. However, the surface area of the fractures is small compared to that of the matrix. For that reason, and as a conservative approximation, sorption to fracture surfaces is not included in the PM CAU transport model.

The method for mathematically representing the matrix sorption process in the PM CAU transport model is to use isotherms to describe the concentration-dependent partitioning of chemical species between the solute and liquid phases. The isotherm approach seeks to describe or abstract on a large scale the integrated behavior of the smaller-scale mechanistic processes (Navarro, 2021a). For solutes and materials in which this relation is linear, the ratio is a constant known as the linear distribution coefficient, or K_d (Freeze and Cherry, 1979). Modeling solute transport using K_ds is attractive due to the simplicity with which they are implemented and because the K_ds represent an average behavior over the large volumes likely to be represented in the PM CAU transport model. The distribution coefficient K_d provides a relatively simple method for simulating retardation due to equilibrium sorption with immobile minerals. The K_d value is defined as (Freeze and Cherry, 1979).

$$K_d = \frac{\textit{Moles of solute per gram of solid phase}}{\textit{Moles of solute per milliliter of solution}} \qquad (5\text{-}7)$$

Assumptions implicit with the use of K_d include (1) only trace amounts of contaminants exist in the aqueous and solid phases, (2) the relationship between the RN activity in the solid and liquid phases is linear, (3) equilibrium conditions exist, (4) equally rapid adsorption and desorption kinetics exist, (5) it describes contaminant partitioning between one RN and one sorbent, and (6) all adsorption sites are accessible and have equal strength (EPA, 1999). The K_d parameter may be developed by direct measurement on aquifer material samples, or it can be computed by upscaling mechanistic processes.

5.2.2.9.2 Distributions Used in the PM CAU Transport Model

Various sources of data relevant to the K_d distributions appropriate for PM were discussed in Navarro (2021a). Mean log K_d and standard deviation of log K_d were taken from Tables 12 and 13 of Carle et al. (2020). Carle et al. (2020) consider five broad areal subdivisions of PM, termed chemistry subareas, on the basis of groundwater chemistry. Area 20 is broadly segmented into three chemistry

subareas, and Area 19 into two chemistry subareas. They also consider vertical zonation of PM on the basis of minerologic diagenesis, termed diagenetic zones (DZs). The DZs are formed by hydration and hydrothermal processes that transform the mineralogical composition of the rock. Carle et al. (2020) classify all rock formations at PM into four DZs. They assign K_d distributions for each RN of interest on the basis of HGU, DZ, and chemistry subarea.

The HSUs in the PM CAU transport model have constant transport properties, and many HSU zones in the PM CAU transport model extend throughout Areas 19 and 20. As such, the transport model does not have enough complexity to support the subdivisions of K_d by DZ and chemistry subarea as defined in Carle et al. (2020). Because the general direction of flow in the PM flow model is to the southwest, and that the leading edges of the plumes are observed to be in the west and southwest of Area 20, these chemistry subareas were assigned to the HSUs in the PM CAU model, as listed in Table G-1 (see Appendix G).

Information on DZ assignment for each HSU in the PM CAU transport model was taken from Carle (2020). For many HSUs, a single DZ is defined in Carle (2020). For some HSUs, more than one DZ is defined in Carle (2020), and in these cases, a single DZ that led to the lowest (most conservative) value of K_d was assumed to represent the entire HSU. For a few HSUs, no DZ is defined in Carle (2020), due to lack of well data for those HSUs. These few HSUs tend to be located away from the central transport area in the PM CAU transport model, and a DZ is assumed. The DZs assigned to the HSUs in the PM CAU model are listed in Table G-1 (see Appendix G).

The K_d distributions used in the PM CAU transport model, selected on the basis of chemistry subareas and DZs listed in Table G-1 are listed in Table G-2 (see Appendix G).

5.3 Summary of RN Observation Data

A brief summary of the RN observation data for the PM is presented in this section, a detailed evaluation is presented in Navarro (2021c). Over the past several decades, groundwater samples have been collected from numerous wells within the PM CAUs and analyzed for RNs. The RN data used for this evaluation are stored in the UGTA Chemistry Database (UCDB) (Navarro, 2021e) and represent a compilation of new and historical data. Sampling locations included in the evaluation are

shown in Figure 5-1. Figure 5-1 also shows the most recent ^{3}H activity relative to the 20,000-pCi/L MCL in the shallowest well completions. The highest ^{3}H levels are generally associated with the shallowest completion.

The evaluation included nine postshot wells that sample the cavity-chimney environment. Four of these wells—accessing the ALMENDRO, CAMEMBERT, CHANCELLOR, and CHESHIRE environments—have been sampled multiple times for a large suite of RNs. The other wells—accessing the BOXCAR, COLBY, FONTINA, HANDLEY, and MUENSTER environments—have been sampled a single time for ^{3}H, and for gross-alpha, gross-beta, and gamma-emitting RNs in three of these locations (FONTINA, HANDLEY, and MUENSTER). While ^{3}H exceeds its 20,000-pCi/L MCL in all these wells, the other measured RNs were reported at levels well below their MCL with the following exceptions: (1) ^{90}Sr at CHANCELLOR and CHESHIRE; (2) ^{129}I at ALMENDRO and CHANCELLOR; (3) ^{137}Cs at CHANCELLOR and CHESHIRE; (4) $^{239/240}$Pu at the CHANCELLOR; and (5) gross alpha at CAMEMBERT, CHANCELLOR, and FONTINA postshot wells. At the CHANCELLOR postshot well, the gross-alpha activity is largely attributed to $^{239/240}$Pu; the total activity of measured U isotopes (^{234}U, ^{235}U, ^{236}U, ^{238}U) was quite low (2.3 pCi/L) for these samples. Because U isotopic data are not available, adjusted gross alpha (gross alpha minus U isotopes) could not be calculated for the other postshot well samples.

RN data from seven locations that access groundwater near underground (BULLION, TYBO/BENHAM, CHESHIRE) and near-surface (SCHOONER) nuclear tests were also evaluated. These wells include the following:

1. UE-20n 1, located approximately 300 m downgradient of CHESHIRE

2. ER-20-5-1, located approximately 280 m west of TYBO and screened at the approximate depth of TYBO; and ER-20-5-3, located about 30 m from ER-20-5-1, screened in a deeper aquifer at the approximate depth of BENHAM. The ER-20-5 cluster is approximately 1,300 m south of BENHAM.

3. ER-20-6-1, ER-20-6-2, and ER-20-6-3, located 166 m, 207 m, and 296 m southwest of BULLION, respectively, in the approximate direction of natural groundwater flow

4. PM-2, located 70 m northwest of SCHOONER, a near-surface test that created a large crater (~129.8 m radius and 63.4 m depth)

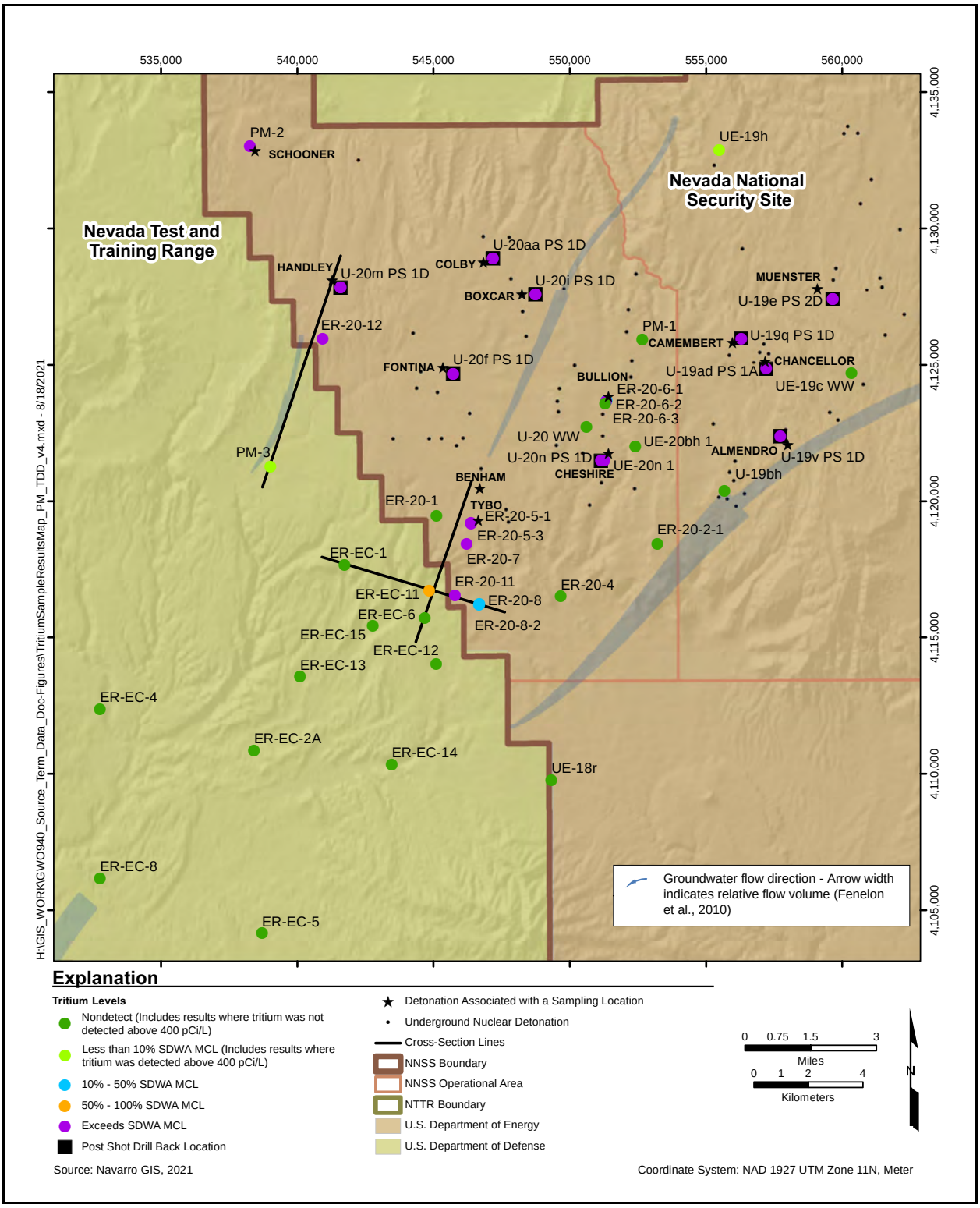

Figure 5-1
^{3}H Relative to SDWA MCL in PM and Downgradient Groundwaters
Source: Navarro, 2021c
Note: ^{3}H associated with the most recent sample from the most shallow well completion is shown.

Additional locations within the NNSS and outside the NNSS boundary but within the NTTR were included in the evaluation (Table 3-11 from Navarro, 2021c). Many of these wells have multiple completions at different depths, increasing the number of sampled locations to more than 50. The data show that ^{3}H is the only RN migrating away from the testing areas at concentrations exceeding the MCL. Although gross alpha was reported above 15 pCi/L in some locations, the adjusted gross alpha was below the 15-pCi/L MCL at all but one location (ER-20-5-3). This indicates that most of the gross-alpha activity is attributed to the U. The RNs contributing the elevated gross alpha at ER-20-5-3 are unknown. While no RNs except ^{3}H exceed their MCL in wells other than postshot wells, 0.1 MCL has been exceeded at ER-20-5-1 (^{129}I and ^{137}Cs), ER-20-5-3 (^{90}Sr), ER-20-6-1 (^{90}Sr and ^{137}Cs), ER-20-7 (^{90}Sr), and UE-20n 1 (^{129}I). However, the ^{90}Sr results are suspect because the results were not reproduced in duplicate samples and/or in subsequent samples collected from the well.

Two distinct ^{3}H transport plumes edging near the NNSS boundary appear to exist within the PM CAUs, as seen in Figure 5-1: one in the region of ER-20-5-3, ER-20-5-1, ER-20-7, ER-20-11, ER-EC-11, ER-EC-6 (likely associated with the BENHAM/TYBO tests, other tests in the region may contribute as well) in Area 20, and the second one in the region of U-20m, ER-20-12, and PM-3 (which is likely associated with the HANDLEY test). Two additional locations on the NNSS, PM-1 and UE-19h, have shown a consistent presence of ^{3}H. These ^{3}H data are used as transport model calibration targets, as discussed in detail in Section 5.5.1.1.

5.4 Numerical Approach

Three numerical codes are used to simulate transport processes in the 3-D PM CAU transport models. The first is a utility code developed by the project (see Appendix E) to map the flow results from the MODFLOW6 hexahedral grid to a tetrahedral grid required by the second code. The second code is a particle-tracking code named Walkabout (Painter, 2011) that, given the flow field calculated by the groundwater flow code, simulates the transport processes of advection and dispersion. The third code is PLUMECALC (Robinson et al., 2011), which, given the particle trajectories calculated by Walkabout, uses a convolution integral and residence time distribution function approach to calculate solute concentrations as functions of position and time incorporating the transport processes of radioactive decay, matrix diffusion, and matrix sorption.

Walkabout performs random walk particle tracking to determine flow paths and particle trajectories from the velocity field of the flow model. Walkabout incorporates the process of advection by linearly interpolating fluid velocities within each computational cell and performing first order forward time (Eulerian) integration. The process of dispersion is modeled using a random walk technique to calculate the positions of each particle evolving in time. The particle-tracking algorithm defines the temporal and spatial distribution of advective-dispersive particle trajectories along the forecast travel paths derived from the velocity fields developed from MODFLOW6. Walkabout requires that the domain of interest be discretized with tetrahedral elements.

In order to use Walkabout, a tetrahedral grid was constructed from the hexahedral MODFLOW6 grid. It is a requirement in MODFLOW6 that the top and bottom surfaces of each cell must be horizontal. As such, curved surfaces such as the top surface of an HSU, as represented in the HFM, may have a stairstepped appearance in the MODFLOW6 grid. Thus, the vertices of a common face between two adjacent cells in the same layer may not be coincident. For example, the vertices on the top face of one cell will have the same x- and y-coordinates of the adjacent cell on the common face between cells but may have different z coordinates. In order to construct a continuous tetrahedral grid from the MODFLOW grid, the z-coordinates of the common vertices of adjacent cells were averaged so that adjacent vertices also share the same z-coordinate. The flow model is an approximation of the HFM, and the transport model is a slightly different approximation of the HFM. The flow model uses artificial stairstepping, as necessitated by MODFLOW, to approximate the water table surface and HSU horizons. The transport model uses sloping planes to approximate the same water table surface and HSU horizons, as necessitated by WALKABOUT. Both approximations are necessitated by the computational methods used in the codes. At a vertical interface between two adjacent cells, the z-coordinates of cell interface vertices are the averages of respective common vertices. Velocities at respective common vertices are calculated by averaging the vertices' velocities from all adjacent cells with the same common vertices. This type of averaging is valid whether or not the grid layer is stairstepping or completely horizontal. This methodology is different from what is used in the USGS MODPATH 7 code, which was developed by USGS specifically to perform particle tracking based on MODFLOW 6 simulations. MODPATH 7 can be used to simulate advection; however, it does not have the capability to perform all the necessary transport process simulation (e.g., dispersion, matrix diffusion, radioactive decay) and was not selected. The adopted methodology yields excellent results when material properties are homogeneous.

The PM CAU model has a high degree of heterogeneity. Because of vertices averaging, heterogeneity can give rise to slightly different local velocity distribution. The combined effects of the heterogeneity and z-coordinate averaging at the site scale were investigated and documented in Appendix E of the report by comparing results based on MODPATH 7 and WALKABOUT. As indicated in Appendix E, it was found that flow patterns and directions based on WALKABOUT and MODPATH 7 were similar, with some differences noted between the flow paths calculated by the two codes due to the high degree of heterogeneity in the PM CAU model.

The resulting distribution of vertices was then connected with tetrahedral elements using the Los Alamos Grid Toolbox (LaGriT) meshing software (LANL, 2011). PLUMECALC is a convolution-based transport code that uses the particle-track information generated by Walkabout to calculate the mobile resident solute concentration (i.e., volume-averaged concentrations of RNs dissolved in mobile fluid) by superposition of solute flux over the particles. Note that the concentrations thus calculated include only the RN mass associated with the mobile fluid and not that associated with stagnant fluid in the matrix or that sorbed onto the immobile solid surfaces. PLUMECALC utilizes the concept of residence time distribution (Robinson et al. 2011) to convert particle track information to concentrations and incorporate the effects of first order radioactive decay, diffusion and matrix sorption.

PLUMECALC requires the following inputs:

- Particle trajectories and transport times (i.e., particle tracks) from each source location, developed from each flow model
- Source contaminant mass flux distributions for each modeled RN as a function of time at each source location
- Transport parameter distributions

Particle tracks were created using each of the flow models. The saturated portion of the $3R_c$ EV for each test was simulated with 10,000 particles and the saturated portion of the chimney (if applicable) was simulated with another 10,000 particles in Walkabout to create the particle track information for input to PLUMECALC. For the 79 deep underground tests with EZ intersecting the water table, the initial particle locations were randomly distributed within the saturated portions of a region defined by a cylinder with a radius of R_c for the chimney and a sphere with a radius of $3R_c$ for the EV. Either

the spherical EV or the cylindrical chimney was truncated by the regional water-table surface, with particles distributed in only the saturated volumes of the sphere and cylinder (Section 5.1). For the three tests with EZ fully in the unsaturated zone, 10,000 particles were randomly distributed within a region defined by a thin disk at the water table surface with radius equal to the $3R_c$. For the three near-surface cratering tests, 10,000 particles were randomly distributed within a region defined by a thin disk at the water table surface with a diameter equal to the crater diameter. The same particle tracks generated by Walkabout were used for different RNs for each source, and different PLUMECALC runs were made for each RN using appropriate transport parameter values. Available mass for each RN for each run was distributed equally among all the particles for each source.

5.5 PM CAU Transport Model

The PM CAU transport model was calibrated to historical ^{3}H observations. Details and results of the calibration are discussed in Section 5.5.1. The purpose of the calibration is to demonstrate that using the base case flow model (i.e., flow paths and flow velocities) in combination with transport parameter values (i.e., porosities, dispersivities, diffusivities, and fracture characteristics) selected within realistic ranges produced results that compared well with the observational data, thus increasing confidence in the model. It is recognized that the values of transport parameters required for calibration will change if a different set of flow paths and flow velocities are supplied by the flow model. Hence, the resulting set of transport parameter values should be viewed as one of a number of permissible datasets. The CB forecasts (see Section 5.5.2) did not use the specific calibrated parameter values; they used the full parameter ranges from accepted distributions for the Monte Carlo realizations.

Following the PM CAU transport model calibration, a stochastic approach (Monte Carlo) was used for simulating transport to explore the range of parametric uncertainty and to provide probabilistic forecasts of areas of contamination over 1,000 years. Details and results of the Monte Carlo simulations are discussed in Section 5.5.2.

5.5.1 Calibration

The PM CAU transport model calibration is performed using PEST (Doherty, 2018) to run PLUMECALC, supplemented with a series of manual PLUMECALC runs with parameter adjustments.

Using the calibrated base case flow model, particle tracks from each of the 82 underground detonations (the three near-surface cratering detonations were not included) were calculated with Walkabout using the following dispersivity values (Section 5.2.2.7.2):

- Longitudinal dispersivity = 150 m
- Transverse horizontal dispersivity = 15 m
- Transverse vertical dispersivity = 1.5 m

The developed particle tracks and the source masses described in Section 5.1.3 were inputs to PLUMECALC. The start time of the PLUMECALC simulations is the date of the first underground test at PM, BUTEO, on May 12, 1965 (NNSA/NFO, 2015b). For all detonations, the source contaminant mass flux was applied in one day on the day of detonation (see Table 5-8). The source contaminant mass flux for each detonation was divided equally among the number of particles representing that detonation. Discrete PLUMECALC output times are specified by year, corresponding to the observation dates given in Table 5-9 (see Section 5.5.1.1).

The following adjustable parameters for each HSU zone were used in the calibration: effective (fracture) porosity, fracture aperture, matrix porosity, and matrix diffusion coefficient. Parameter ranges are provided in Tables 5-4, 5-6, 5-3, and 5-7. Note that fracture spacing was calculated by PLUMECALC from fracture porosity and aperture; the results were compared with the ranges given in Navarro (2021a). The PM CAU transport model uses the same HSU/fault zonation as the flow model, and it is assumed that transport parameters are uniform in each HSU/fault zone.

Table 5-8
Source Mass Flux Start Times Used in the PM CAU Transport Model for the 82 Underground Detonations
(Page 1 of 3)

Detonation	Date	Source Mass Flux Start Day
BUTEO	05/12/1965	1
REX	02/24/1966	289
DURYEA	04/14/1966	338
CHARTREUSE	05/06/1966	360
HALFBEAK	06/30/1966	415
GREELEY	12/20/1966	588
SCOTCH	05/23/1967	742
KNICKERBOCKER	05/26/1967	745
STINGER	03/22/1968	1,046
SCROLL	04/23/1968	1,078
BOXCAR	04/26/1968	1,081
RICKEY	06/15/1968	1,131
CHATEAUGAY	06/28/1968	1,144
SLED	08/29/1968	1,206
BENHAM	12/19/1968	1,318
PURSE	05/07/1969	1,457
JORUM	09/16/1969	1,589
PIPKIN	10/08/1969	1,611
HANDLEY	03/26/1970	1,780
ALMENDRO	06/06/1973	2,948
TYBO	05/14/1975	3,655
STILTON	06/03/1975	3,675
MAST	06/19/1975	3,691
CAMEMBERT	06/26/1975	3,698
KASSERI	10/28/1975	3,822
INLET	11/20/1975	3,845
MUENSTER	01/03/1976	3,889
FONTINA	02/12/1976	3,929

Table 5-8
Source Mass Flux Start Times Used in the PM CAU Transport Model for the 82 Underground Detonations
(Page 2 of 3)

Detonation	Date	Source Mass Flux Start Day
CHESHIRE	02/14/1976	3,931
ESTUARY	03/09/1976	3,955
COLBY	03/14/1976	3,960
POOL	03/17/1976	3,963
BACKBEACH	04/11/1978	4,718
FONDUTTA	04/11/1978	4,718
PANIR	08/31/1978	4,860
EMMENTHAL	11/02/1978	4,923
FARM	12/16/1978	4,967
PEPATO	06/11/1979	5,144
SHEEPSHEAD	09/26/1979	5,251
COLWICK	04/26/1980	5,464
KASH	06/12/1980	5,511
TAFI	07/25/1980	5,554
SERPA	12/17/1980	5,699
HARZER	06/06/1981	5,870
HOSTA	02/12/1982	6,121
MOLBO	02/12/1982	6,121
GIBNE	04/25/1982	6,193
NEBBIOLO	06/24/1982	6,253
CABRA	03/26/1983	6,528
CHANCELLOR	09/01/1983	6,687
KAPPELI	07/25/1984	7,015
EGMONT	12/09/1984	7,152
TIERRA	12/15/1984	7,158
TOWANDA	05/02/1985	7,296
SALUT	06/12/1985	7,337
SERENA	07/25/1985	7,380

Table 5-8
Source Mass Flux Start Times Used in the PM CAU Transport Model for the 82 Underground Detonations
(Page 3 of 3)

Detonation	Date	Source Mass Flux Start Day
GOLDSTONE	12/28/1985	7,536
JEFFERSON	04/22/1986	7,651
DARWIN	06/25/1986	7,715
CYBAR	07/17/1986	7,737
GALVESTON	09/04/1986	7,786
LABQUARK	09/30/1986	7,812
BELMONT	10/16/1986	7,828
BODIE	12/13/1986	7,886
DELAMAR	04/18/1987	8,012
HARDIN	04/30/1987	8,024
LOCKNEY	09/24/1987	8,171
KERNVILLE	02/15/1988	8,315
COMSTOCK	06/02/1988	8,423
ALAMO	07/07/1988	8,458
KEARSARGE	08/17/1988	8,499
CONTACT	06/22/1989	8,808
AMARILLO	06/27/1989	8,813
HORNITOS	10/31/1989	8,939
BARNWELL	12/08/1989	8,977
BULLION	06/13/1990	9,164
TENABO	10/12/1990	9,285
HOUSTON	11/14/1990	9,318
BEXAR	04/04/1991	9,459
MONTELLO	04/16/1991	9,471
HOYA	09/14/1991	9,622
JUNCTION	03/26/1992	9,816

Table 5-9
^{3}H Observations Used in the PM CAU Transport Model Calibration
(Page 1 of 8)

Well Name	Observation Date	Log Observed ^{3}H Concentration (pCi/L)
ER-20-1_p1	02/24/2015	1.00
	05/23/2017	1.00
	05/21/2019	1.00
ER-20-2-1_p1	07/06/2000	1.00
	07/25/2001	1.00
	06/19/2002	1.00
	07/20/2005	1.00
	06/13/2007	1.00
	05/14/2008	1.00
	05/20/2009	1.00
	05/11/2010	1.00
	06/14/2011	1.00
	07/02/2012	1.00
	05/23/2017	1.00
	09/10/2018	1.00
ER-20-4_m1	09/20/2011	1.00
	06/21/2018	1.00
ER-20-4_p2	05/30/2018	1.00
ER-20-5-1_m1	06/03/1996	7.86
	04/22/1997	7.84
	07/09/1998	7.81
	11/30/2004	7.58
	04/26/2011	7.48
	04/02/2015	7.39
	09/24/2019	7.30

Table 5-9
^{3}H Observations Used in the PM CAU Transport Model Calibration
(Page 2 of 8)

Well Name	Observation Date	Log Observed ^{3}H Concentration (pCi/L)
ER-20-5-3_m1	07/31/1996	5.18
	04/22/1997	5.46
	04/30/1998	5.19
	11/15/2001	5.15
	11/29/2004	5.06
	04/26/2011	4.98
	03/13/2015	4.92
	09/17/2019	4.81
ER-20-6-1_p1	12/17/1996	4.47
	08/27/1997	3.36
	05/14/1998	3.51
	06/23/2017	1.00
ER-20-6-2_p1	11/27/1996	5.23
	07/17/1997	3.85
	06/16/2017	1.00
ER-20-6-3_p1	12/16/1996	1.00
	07/17/1997	3.60
	05/13/1998	3.05
	06/09/2017	1.00
ER-20-7_m1	07/01/2009	7.25
	09/24/2010	7.28
	11/21/2014	7.18
	08/31/2017	7.13
ER-20-8_p1	08/08/2011	2.41
	09/03/2014	2.11
	09/27/2017	2.28
ER-20-8_m2	06/27/2011	3.48
	03/07/2015	3.66
	09/14/2017	3.81
ER-20-8_p3	09/10/2014	3.25

Table 5-9
^{3}H Observations Used in the PM CAU Transport Model Calibration
(Page 3 of 8)

Well Name	Observation Date	Log Observed ^{3}H Concentration (pCi/L)
ER-20-8-2_m1	12/18/2009	2.94
	10/16/2014	3.41
	09/19/2017	3.56
ER-20-11_m1	08/04/2013	5.27
	10/18/2017	5.31
ER-20-12_m1	08/19/2016	4.53
	07/12/2017	4.62
ER-20-12_p1	07/06/2016	4.28
	07/17/2017	4.40
ER-20-12_p2	08/30/2016	4.59
ER-20-12_p3	06/10/2016	1.00
	07/24/2017	2.45
ER-20-12_p4	07/06/2017	4.76
ER-EC-1_m1-3	04/23/1999	1.00
	02/01/2000	1.00
	06/03/2003	1.00
	04/02/2009	1.00
	07/15/2016	1.00
ER-EC-2A_m3	07/27/2000	1.00
	07/08/2003	1.00
	05/20/2010	1.00
	10/11/2016	1.00
	06/11/2019	1.00
ER-EC-4_m2-3	06/15/1999	1.00
	08/17/2000	1.00
	06/24/2003	1.00
	07/19/2018	1.00
ER-EC-5_m1-3	05/25/2000	1.00
	07/15/2003	1.00
	06/26/2019	1.00
ER-EC-6_m1-4	02/10/2000	1.00

Table 5-9
^{3}H Observations Used in the PM CAU Transport Model Calibration
(Page 4 of 8)

Well Name	Observation Date	Log Observed ^{3}H Concentration (pCi/L)
ER-EC-6_m2-4	06/10/2003	1.00
	04/09/2009	1.00
ER-EC-6_m4_a3	01/12/2015	1.00
	08/17/2017	1.00
	08/22/2018	1.00
ER-EC-8_m1-3	07/23/1999	1.00
	07/12/2000	1.00
	07/01/2003	1.00
	09/27/2010	1.00
	09/29/2016	1.00
ER-EC-11_p1	05/02/2010	1.00
	07/25/2014	1.00
	10/02/2017	1.07
ER-EC-11_p2	08/12/2014	1.05
	09/26/2017	1.05
ER-EC-11_p3	08/25/2014	4.21
	10/12/2017	4.26
ER-EC-12_m1	03/26/2012	1.00
	10/04/2018	1.00
ER-EC-12_m2	11/27/2011	1.00
	07/20/2016	1.00
ER-EC-13_m1	03/28/2013	1.00
	06/05/2019	1.00
ER-EC-13_m2	07/13/2012	1.00
	06/04/2019	1.00
ER-EC-14_m1	05/12/2014	1.00
	06/19/2019	1.00
ER-EC-14_m2	04/06/2014	1.00
	06/18/2019	1.00
ER-EC-15_m1	02/16/2014	1.00
	05/15/2019	1.00

Table 5-9
^{3}H Observations Used in the PM CAU Transport Model Calibration
(Page 5 of 8)

Well Name	Observation Date	Log Observed ^{3}H Concentration (pCi/L)
ER-EC-15_m2	01/10/2014	1.00
	05/16/2019	1.00
ER-EC-15_m3	11/06/2013	1.00
	05/21/2019	1.00
PM-1_o2Z	01/01/1994	2.30
	01/01/1995	2.34
	06/23/1998	2.26
	06/29/2000	2.28
	06/25/2002	2.30
	06/13/2007	2.12
	04/23/2008	2.11
	04/28/2009	1.93
	05/19/2010	2.15
	03/15/2011	2.07
	03/13/2012	2.02
PM-2_m1-o7	05/04/1994	5.86
	10/26/2005	5.41
PM-3_p1	07/22/2011	1.27
	08/11/2013	1.57
	06/11/2014	1.89
	09/13/2016	2.09
	06/07/2018	2.28
PM-3_p2	07/22/2011	1.57
	08/22/2013	2.35
	06/11/2014	2.37
	09/13/2016	2.29
	06/14/2018	2.76
U-19ad_PS_1A	09/27/2004	7.34
	05/01/2008	7.11
U-19e_PS_2D	08/27/2015	6.33

Table 5-9
^{3}H Observations Used in the PM CAU Transport Model Calibration
(Page 6 of 8)

Well Name	Observation Date	Log Observed ^{3}H Concentration (pCi/L)
U-19q_PS_1D	10/20/1998	7.38
	07/16/2003	7.03
U-19v_PS_1D	09/28/1993	8.38
	06/20/1996	8.31
	09/22/1998	8.28
	08/18/1999	8.22
	09/27/2000	8.20
	05/31/2001	8.26
	07/23/2003	8.15
	04/18/2006	8.04
	09/16/2009	7.93
U-20aa_PS_1D	10/05/2016	7.46
U-20f_PS_1D	08/20/2015	7.36
U-20i_PS_1D	05/23/2017	6.03
U-20m_PS_1D	07/22/2015	6.94
U-20n_PS_1D_o1Z	09/13/1976	9.29
U-20n_PS_1D_o5Z	09/09/1983	8.60
	10/23/1984	8.51
	05/29/1985	8.47
U-20n_PS_1D_o2	11/07/1985	8.36
	07/19/1988	8.02
	09/14/1994	7.82
	06/18/1996	7.75
	07/22/1997	7.68
	07/28/1998	7.59
U-20n_PS_1D_o3Z	09/21/1998	7.85
	10/12/1999	7.73
	07/09/2003	7.63
	11/15/2005	7.52
U-20n_PS_1D_m2	11/19/2019	7.12

Table 5-9
^{3}H Observations Used in the PM CAU Transport Model Calibration
(Page 7 of 8)

Well Name	Observation Date	Log Observed ^{3}H Concentration (pCi/L)
U-20_WW	12/08/1985	1.00
	12/03/1986	1.00
	12/08/1987	1.00
	12/12/1989	1.00
	04/11/1991	1.00
	07/12/1993	1.00
	10/05/1994	1.00
	08/07/1995	1.00
	01/29/1996	1.00
	11/05/1997	1.00
	10/15/1998	1.00
	01/20/1999	1.00
	05/01/2018	1.00
UE-18r_o1	02/02/1968	1.00
	08/01/1976	1.00
	06/07/1977	1.00
	02/01/1978	1.00
	05/08/1986	1.37
	12/08/1987	1.00
	01/01/1994	1.00
	01/01/1995	1.00
	07/13/2000	1.00
	05/01/2001	1.00
	05/22/2002	1.00
	04/22/2003	1.00
	03/23/2004	1.00
	03/16/2005	1.00
	04/17/2007	1.00
	10/11/2017	1.00

Table 5-9
^{3}H Observations Used in the PM CAU Transport Model Calibration
(Page 8 of 8)

Well Name	Observation Date	Log Observed ^{3}H Concentration (pCi/L)
UE-19c_WW_m1	10/30/1984	1.00
	12/08/1985	1.00
	12/03/1986	1.00
	12/08/1987	1.00
	12/12/1989	1.00
	12/10/1990	1.00
	12/09/1991	1.00
	12/02/1992	1.00
	05/24/1999	1.00
UE-19h_m1	12/11/1999	3.29
UE-20bh_1_o1	12/08/1999	1.00
UE-20n_1_o2	08/06/1987	8.49
	05/24/2012	7.72
	11/06/2019	7.52

A nondetect limit of 10 pCi/L was assumed; thus, any concentrations less than or equal to 10 pCi/L have a log value of 1.

5.5.1.1 Observations Used for Model Calibration

The extents of the CBs are expected to be defined largely by ^{3}H contamination. Compared to the other RNs of interest, observations of ^{3}H are more abundant throughout PM. For these reasons, the PM CAU transport model was calibrated to ^{3}H observations only. Tritium observations in PM are described in Section 3.2 of Navarro (2021c). The ^{3}H observations used in the calibration are listed in Table 5-9 and locations shown in Figure 5-1. The observed ^{3}H values throughout PM span several orders of magnitude, ranging from 0 pCi/L to 1.93E+09 pCi/L.

During model calibration, the PEST software minimizes a least-squares objective function, which is the sum of squared weighted differences between observations (i.e., measured ^{3}H concentrations) and corresponding model outputs (Doherty, 2018). In the calibration, the log of concentration was used to compare modeled and measured (observed) values, and a ^{3}H non-detect limit of 10 pCi/L was assumed; thus, any concentrations less than or equal to 10 pCi/L had a log value of 1. Hence, using

the log-transformed ^{3}H values, as well as the non-detect assumption, the range of observed values spanned a range from 1 to about 10. Doing this reduced the likelihood that extreme residuals would overwhelm the total objective function.

Observation locations were defined in several ways. For each observation at a post shot hole, the x,y coordinates of the observation location in the grid were chosen to be those closest to the x,y coordinates of the detonation WP. At the selected x,y location in the grid, only those nodes with elevations between the top and bottom elevations of the open interval of the observation well were selected to be the observation nodes in the model. At each output time, modeled concentrations at the selected column of nodes were averaged, and it was the average concentration that was compared to observed concentration. For many observation wells, the same method was used to define a column of observation nodes at an x,y location in the grid closest to the x,y coordinates of the observation well.

For some observation wells, instead of a single column of nodes, several columns of nodes were used to represent the observation location. These columns were defined by picking the closest x,y locations surrounding the x,y coordinates of the observation well. This was done at well locations further away from the detonations. For comparison to observed values, the average concentration was computed for each column, and the maximum average value from all columns was chosen to compare to observed values. This was done for observations at ER-20-1_p1, ER-20-5-1_m1, ER-20-5-3_m1, and ER-20-7_m1.

For observation wells further downgradient, fence lines were defined passing through the observation wells roughly perpendicular to the flow direction, extending for some reasonable distance on either side of the wells. Columns of nodes along each fence line were selected by choosing those with x,y coordinates closest to the fence line. For comparison to observed values, the average concentration was computed for each column of nodes within the open interval along the fence line, and the maximum average value from the columns along the fence was chosen to compare to observed values. This was done for observations at ER-20-8_p1, ER-20-8_m2, ER-20-8_p3, ER-20-8-2_m1, ER-20-11_m1, ER-20-12_m1, ER-20-12_p1, ER-20-12_p2, ER-20-12_p3, ER-20-12_p4, ER-EC-11_p1, ER-EC-11_m2, ER-EC-11_p3, PM-3_p1, and PM-3_p2.

5.5.1.2 Objective Function Formulation

The PM CAU transport model objective function included observation groups specific to each observation well. All observations obtained from each well belong to the observation group for that well. The calibration observation weights were selected such that each observation group is visible in the objective function. The PEST utility PWTADJ1 was used to adjust weights so that each observation group initially contributed a value of 1 to the objective function. All observations within each observation group were given equal weight (summing to 1).

Initial calibration attempts with all observation groups equally weighted resulted in very good agreement at the observations associated with postshot holes, but very poor agreement (often underpredicting ^{3}H concentrations) in downgradient areas of concern, such as observation locations near the Bench and downgradient of HANDLEY (in other words, in areas near the leading edges of observed ^{3}H plumes). Recognizing that this model is not perfect, the guiding philosophy behind the transport calibration was that it would be better to conservatively overpredict ^{3}H concentrations at observation locations rather than underpredict ^{3}H concentrations at observation locations where ^{3}H is observed, especially in areas of concern. With this in mind, several adjustments were made in order to improve agreement in areas near the leading edges of observed ^{3}H plumes:

- It was decided to reduce the calibration weights for observation groups associated with the postshot holes to 1 percent of their previous values, thus reducing the influence of these observations on the total objective function. This was deemed acceptable, because in the PM CAU transport model, the observation locations at the postshot holes are coincident with nodes where the contaminant source mass is introduced, and very little transport occurs between these source locations and observation locations.

- In cases where a single HSU intersects multiple observation wells in relatively close proximity, observation weights were adjusted so that the observation well in the area of interest with the highest observed ^{3}H concentrations was given more influence in the objective function. For example, the TCA intersects ER-20-1, ER-20-8_p1, ER-20-8_m2, ER-EC-11_m2, ER-EC-12_m2, and ER-EC-15_m2. Of these wells, ER-20-8_p1, ER-20-8_m2, and ER-EC-11_m2 are closest to the observed ^{3}H plume in the Bench; and of these three wells, ER-20-8_m2 has the highest observed ^{3}H. Therefore, the observation weights for ER-20-8_m2 were left as is, and the observation weights of the others were set to zero.

- It was decided to reduce the calibration weights for observation groups associated with far-field observation locations with no observed ^{3}H to 1 percent of their previous values, thus

reducing the influence of these observations on the total objective function. This included the following observation locations: ER-20-2-1, ER-20-4, ER-EC-1, ER-EC-2a, ER-EC-4, ER-EC-6, ER-EC-8, ER-EC-12, ER-EC-13, ER-EC-14, ER-EC-15, U-20_ww, and UE-18r. The same was done for UE-19c_ww and UE-20bh_1.

5.5.1.3 Calibration Results

Ideally, the calibrated PM CAU transport model would match ^{3}H observations at all observation locations and times. Uncertainty in the ^{3}H source mass fluxes at each detonation location and simplifications in the model, such as grid resolution at detonation and observation locations, as well as uniform-property zones in each HSU, make this impossible. Thus, because the log of modeled and measured ^{3}H concentrations are compared, agreement with observed ^{3}H concentrations is considered "good" when modeled concentrations are within 1 order of magnitude of observed values.

Table 5-10 lists each observation group's contributions to the objective function.

Table 5-10
^{3}H Observation Group Contribution to the Measurement Objective Function
(Page 1 of 2)

Observation Group	Objective Function
ER-20-1	1.0263
ER-20-2-1	0
ER-20-4	0
ER-20-5-1_m1	0.24097
ER-20-5-3_m1	0.99997
ER-20-6	1.0054
ER-20-7	1.1536
ER-20-8_p1	0.76499
ER-20-8_m2	0.82191
ER-20-8_p3	0.16212
ER-20-8-2_m1	0.22266
ER-20-11	0.17593
ER-20-12_m1	0.20629
ER-20-12_p1	0.57009
ER-20-12_p2	0.99998
ER-20-12_p3	0.99998
ER-20-12_p4	0.86391

Table 5-10
^{3}H Observation Group Contribution to the Measurement Objective Function
(Page 2 of 2)

Observation Group	Objective Function
ER-EC-1	0
ER-EC-2a	0
ER-EC-4	0
ER-EC-5	0
ER-EC-6	0
ER-EC-8	0
ER-EC-11_p1	5.19E-04
ER-EC-11_m2	1
ER-EC-11_p3	2.72E-02
ER-EC-12	0
ER-EC-13	0
ER-EC-14	0
ER-EC-15	0
PM-1	0.99997
PM-2	1
PM-3_p1	2.0787
PM-3_p2	1
U-19ad_ps_1a	0.56072
U-19e_ps_2d	1
U-19q_ps_1d	0.20776
U-19v_ps_1d	1.2509
U-20aa_ps_1d	1.5526
U-20f_ps_1d	0.52185
U-20i_ps_1d	0.9817
U-20m_ps_1d	5.3714
U-20n_ps_1d	1.1969
U-20_ww	0
UE-18r	1
UE-19c_ww	0
UE-19h	1
UE-20bh_1	0
UE-20n_1	1.94E-02

Agreement with observation data was evaluated with scatter-plots, specifically plots of modeled concentration versus measured concentration and plots of modeled and measured concentrations versus time.

A scatterplot of the simulated versus observed concentrations at all measurements obtained from all of the observation wells (listed in Table 5-9) is presented in Figure 5-2. Reasonable agreement is achieved at many observation locations, but there are several observation points where the model overpredicts by several orders of magnitude, as well as several observation points where the model predicts no ^{3}H (showing a log value of 1). Data points corresponding to all 221 observations listed in Table 5-9 are displayed in Figure 5-2 but are not apparent because many of these points overlap at (1,1).

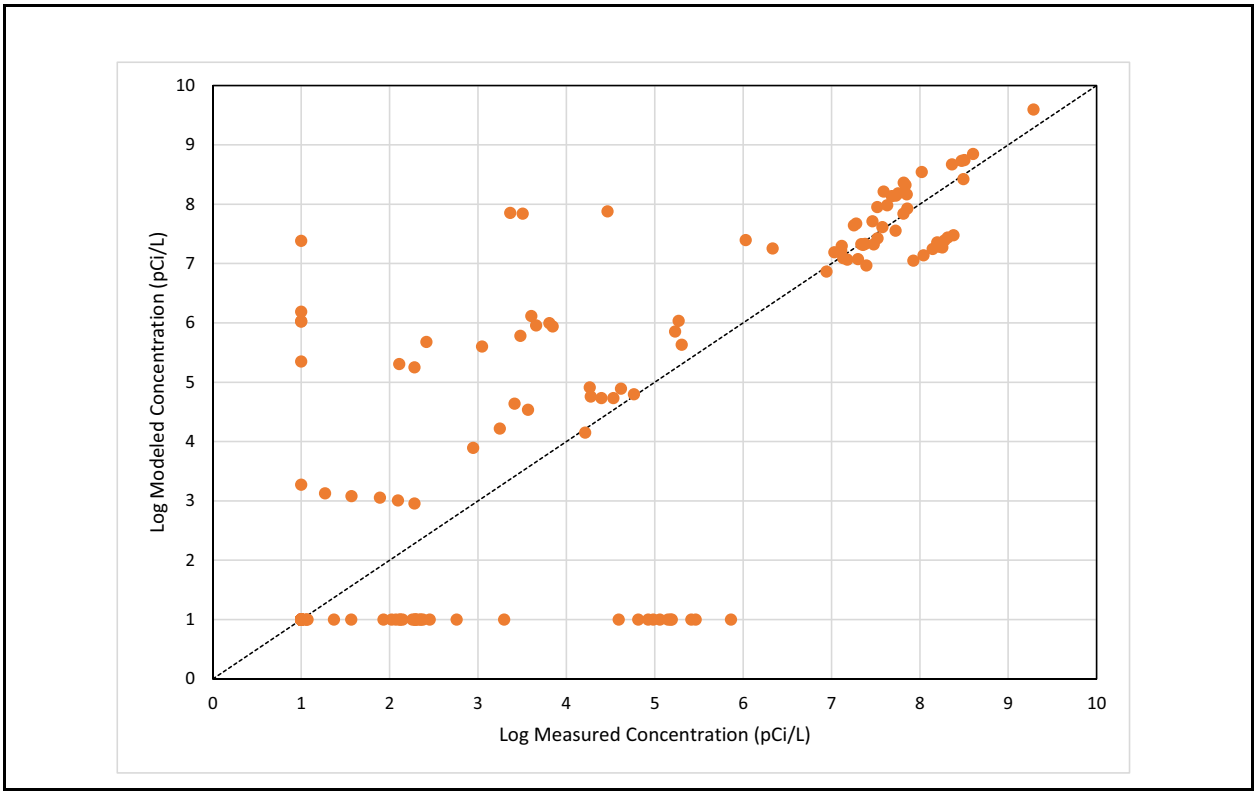

Figure 5-2
Modeled versus Measured ^{3}H Concentrations for the PM CAU Transport Model

Figure 5-3 shows the subset of the points shown in Figure 5-2 representing the observation locations at postshot holes in the PM CAU transport model. Good agreement between measured and modeled values is achieved with the model either overpredicting or underpredicting within 1 order of

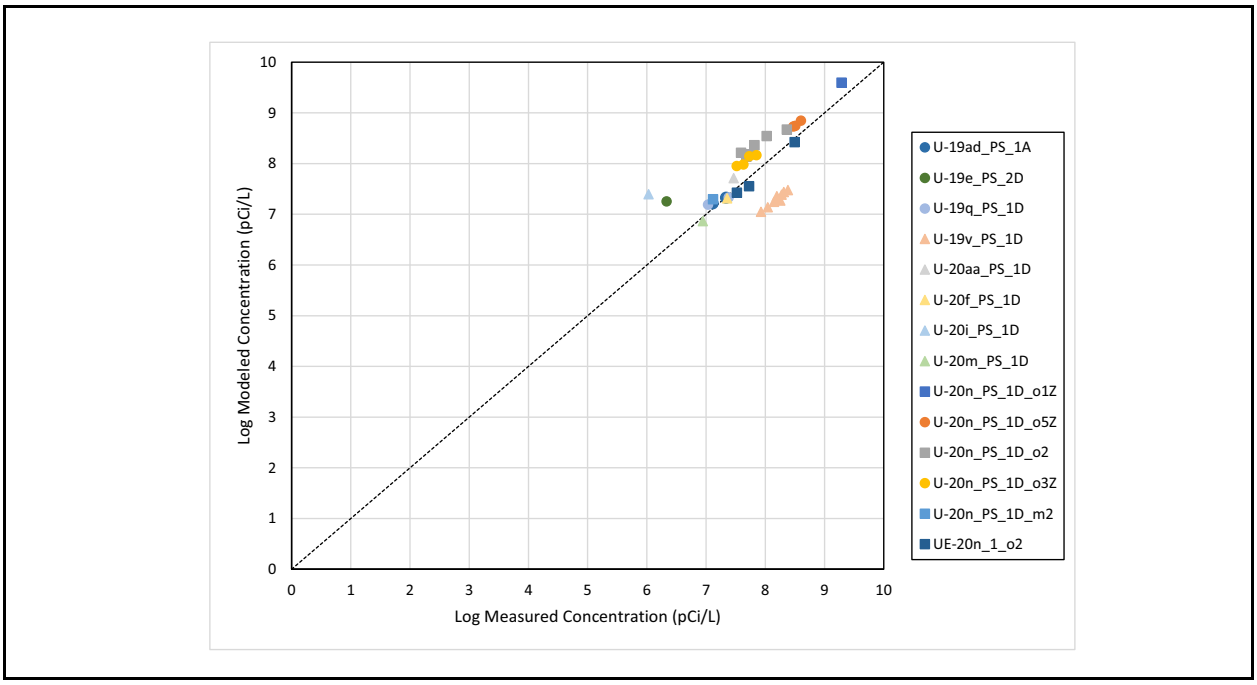

Figure 5-3
Modeled versus Measured ^{3}H Concentrations for the Postshot Holes in the PM CAU Transport Model
Note: While not a postshot hole, UE-20n_1_o2 is included here for convenience.

magnitude at most of these locations. This is likely due to the fact that the observation locations at the postshot holes are coincident with nodes where the source particles are located, meaning that very little transport has occurred between source location and measurement location. Plots of modeled and measured ^{3}H concentrations over time at these observation locations are shown in Figures 5-4 through 5-17. These figures show model outputs over the first 60 years, which encompasses all observation times. Corresponding plots spanning the entire 1,000-year simulation time can be found in Appendix H in Figures H-46 through H-58 and Figure H-64.

Each of these figures exhibits a sudden increase in concentrations at early times in the simulation, first showing no modeled concentration (indicated by a log value of 1) at one output time, then showing very high concentration at the next output time. This behavior is expected at the postshot observation locations because (1) the source contaminant mass flux was applied in one day on the day of detonation (i.e., not introduced over a long period of time), and (2) the observation locations at the postshot holes are coincident with nodes where the particle tracks originate. For example, Figure 5-4 shows modeled and measured ^{3}H concentrations versus time at U-19ad_PS_1A, the postshot hole

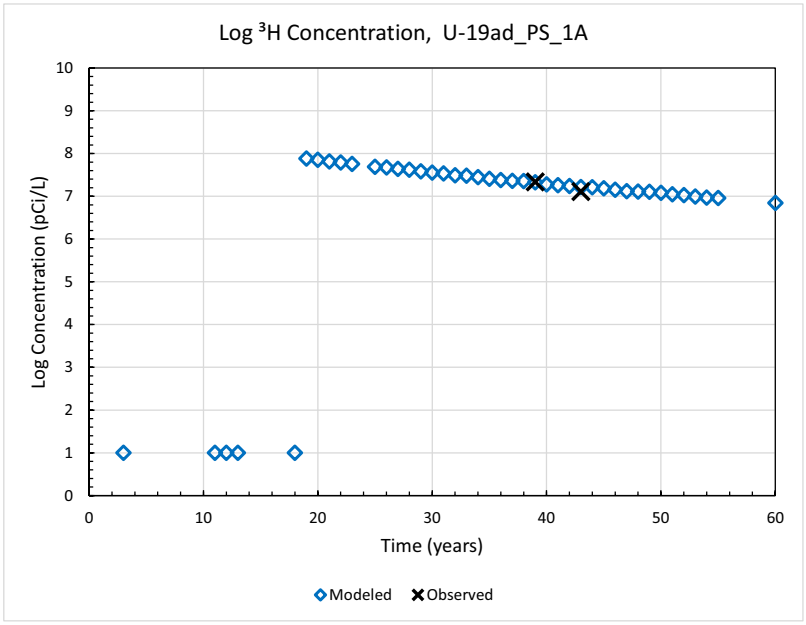

Figure 5-4
Modeled and Measured ^{3}H Concentrations versus Time at U-19ad_PS_1A

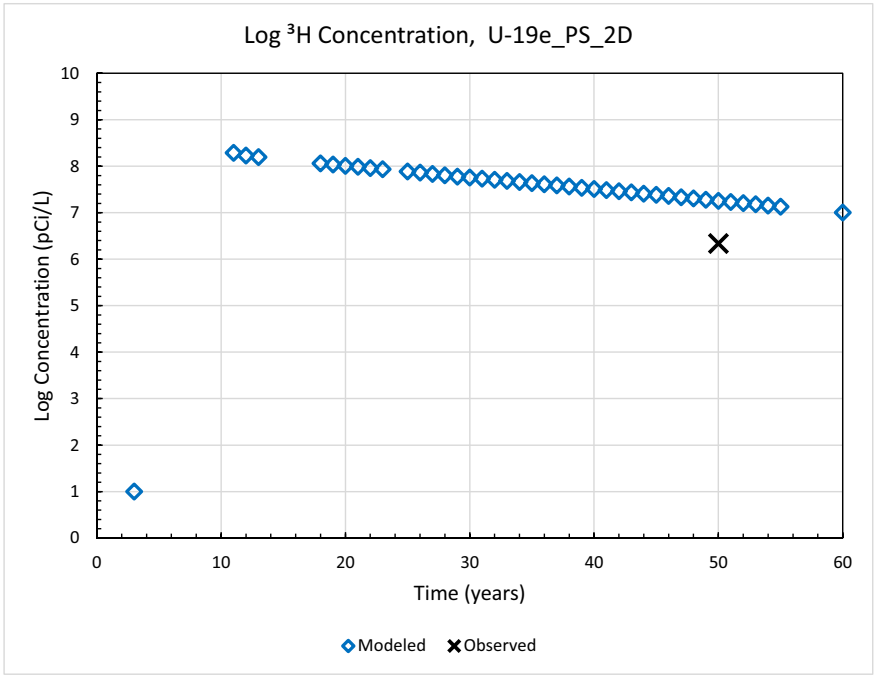

Figure 5-5
Modeled and Measured ^{3}H Concentrations versus Time at U-19e_PS_2D

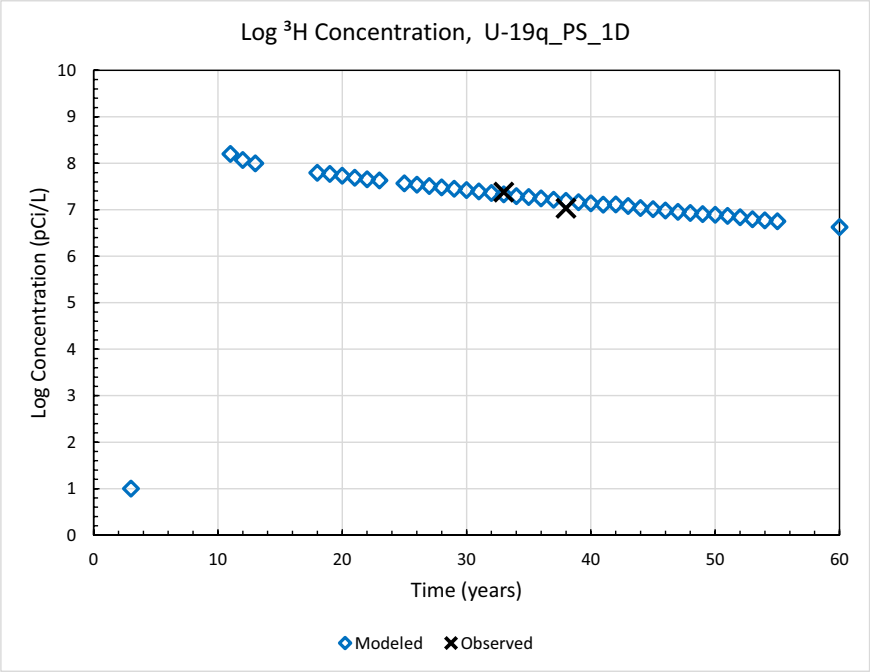

Figure 5-6
Modeled and Measured ^{3}H Concentrations versus Time at U-19q_PS_1D

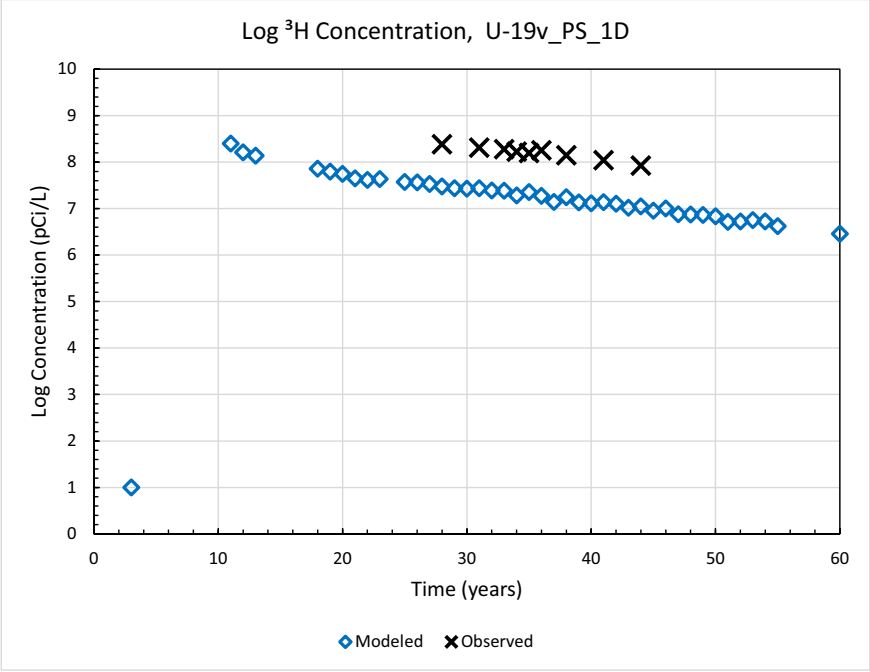

Figure 5-7
Modeled and Measured ^{3}H Concentrations versus Time at U-19v_PS_1D

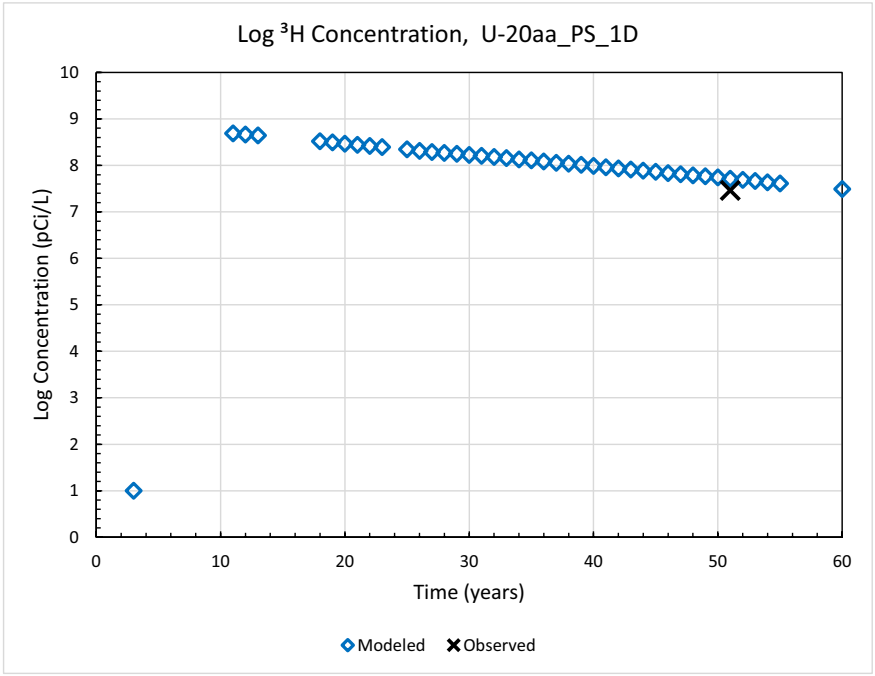

Figure 5-8
Modeled and Measured ^{3}H Concentrations versus Time at U-20aa_PS_1D

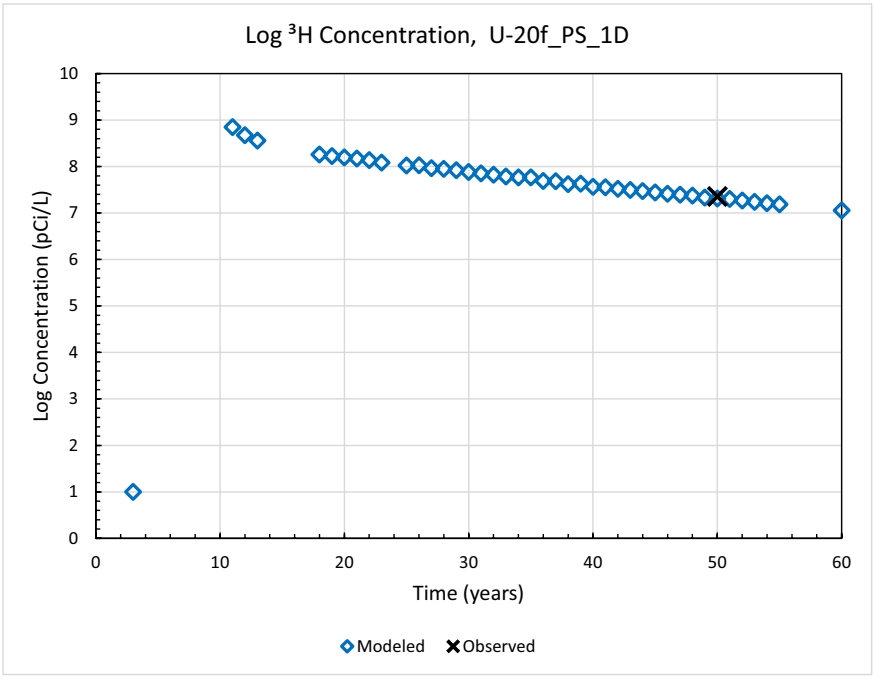

Figure 5-9
Modeled and Measured ^{3}H Concentrations versus Time at U-20f_PS_1D

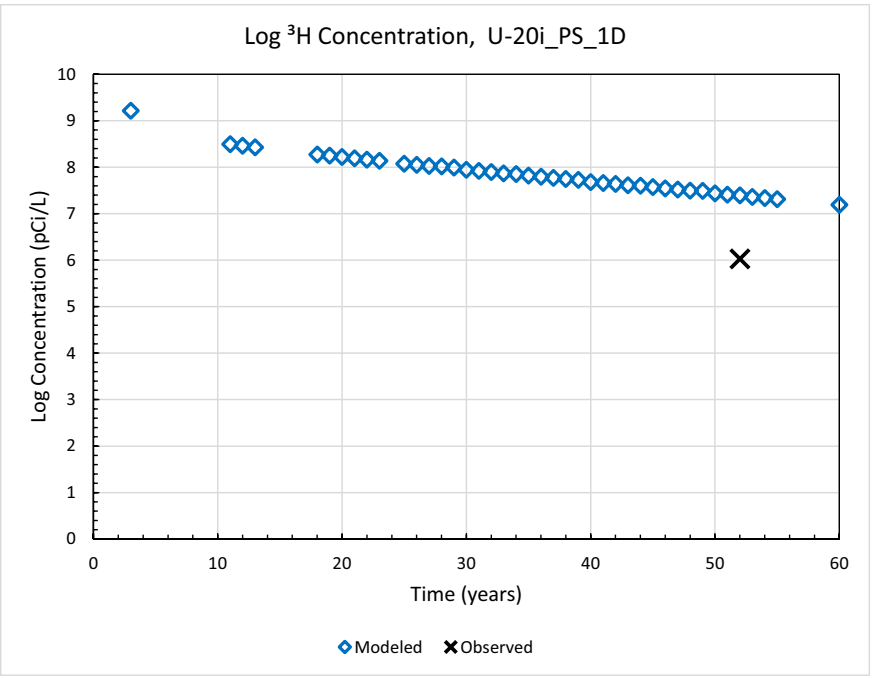

Figure 5-10
Modeled and Measured ^{3}H Concentrations versus Time at U-20i_PS_1D

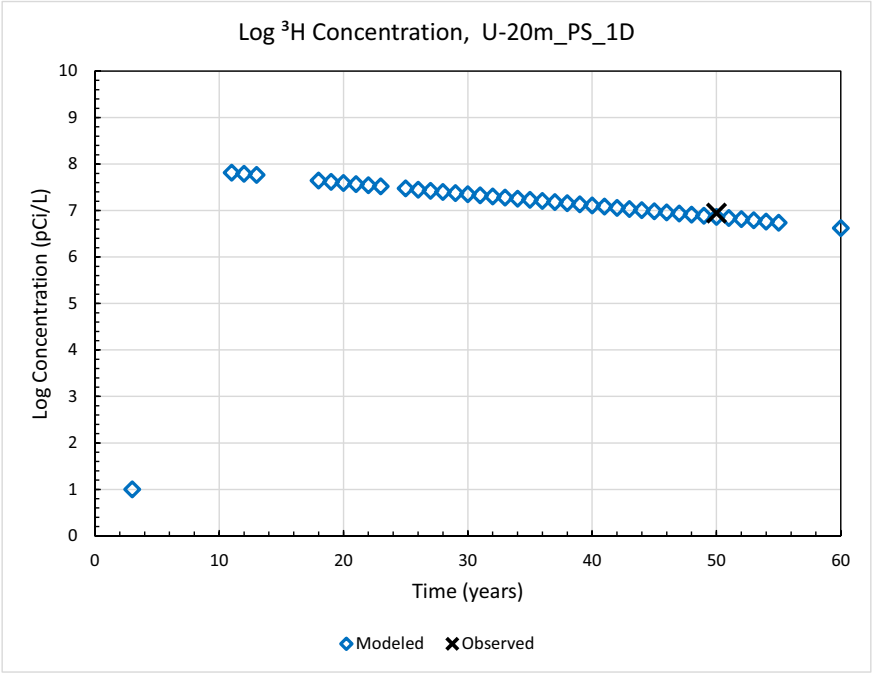

Figure 5-11
Modeled and Measured ^{3}H Concentrations versus Time at U-20m_PS_1D

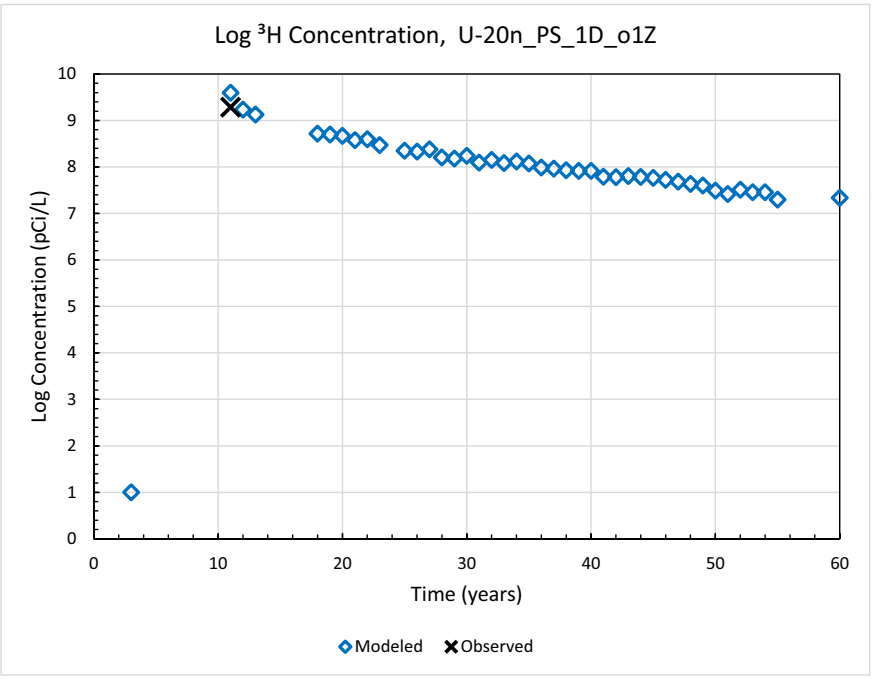

Figure 5-12
Modeled and Measured ^{3}H Concentrations vs Time at U-20n_PS_1D_o1Z

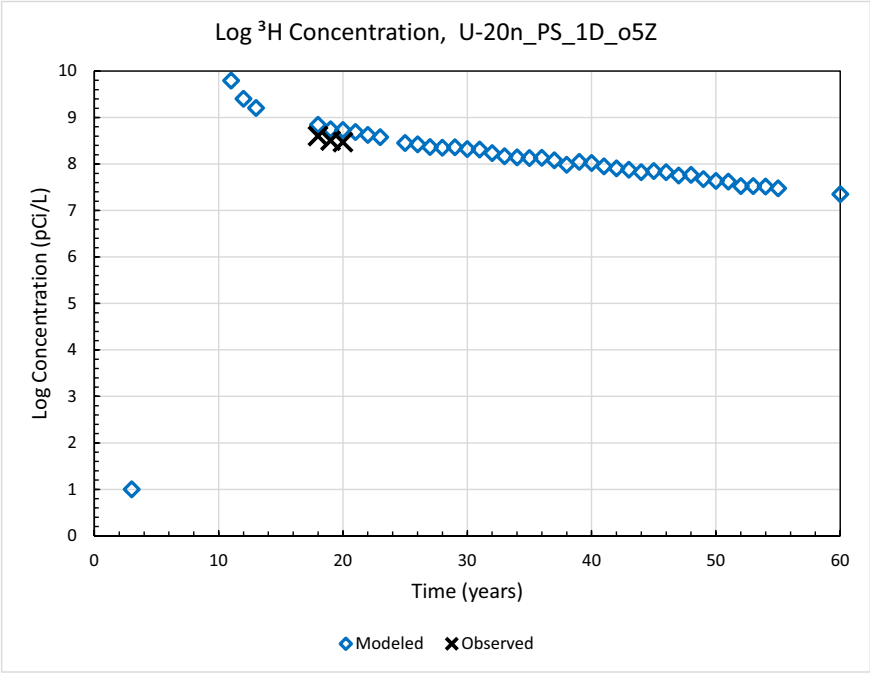

Figure 5-13
Modeled and Measured ^{3}H Concentrations versus Time at U-20n_PS_1D_o5Z

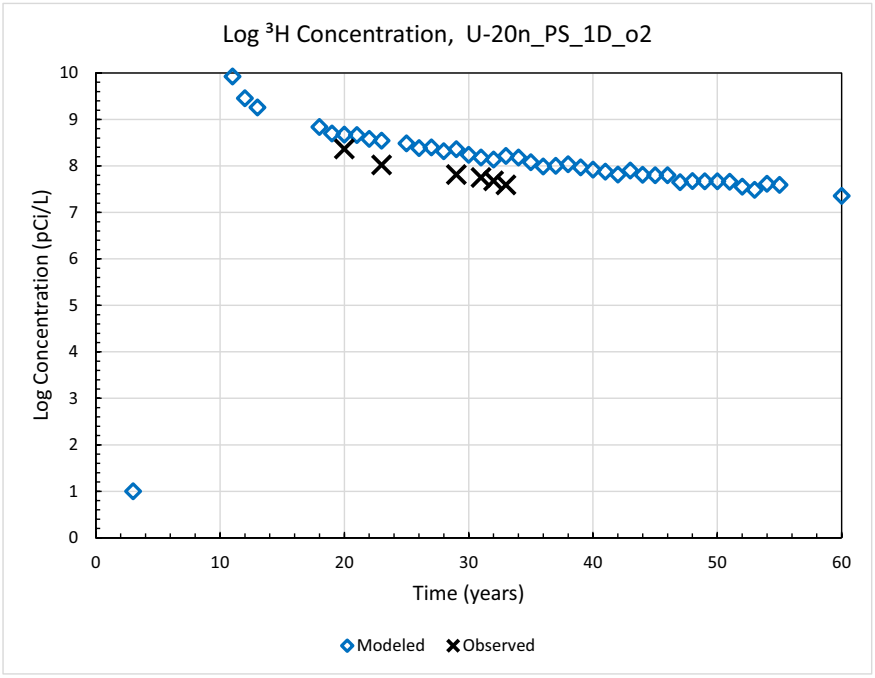

Figure 5-14
Modeled and Measured ^{3}H Concentrations versus Time at U-20n_PS_1D_o2

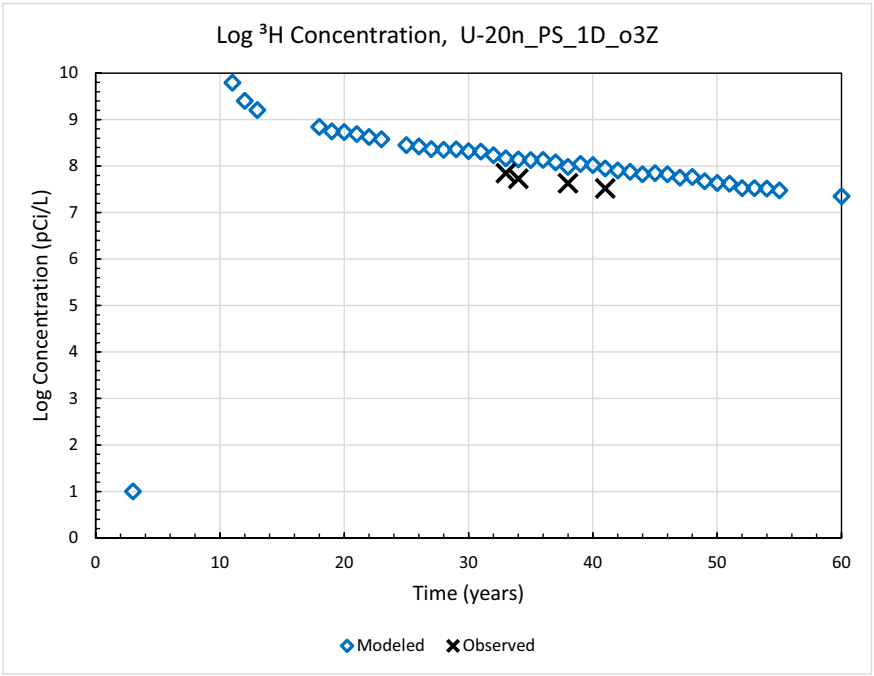

Figure 5-15
Modeled and Measured ^{3}H Concentrations versus Time at U-20n_PS_1D_o3Z

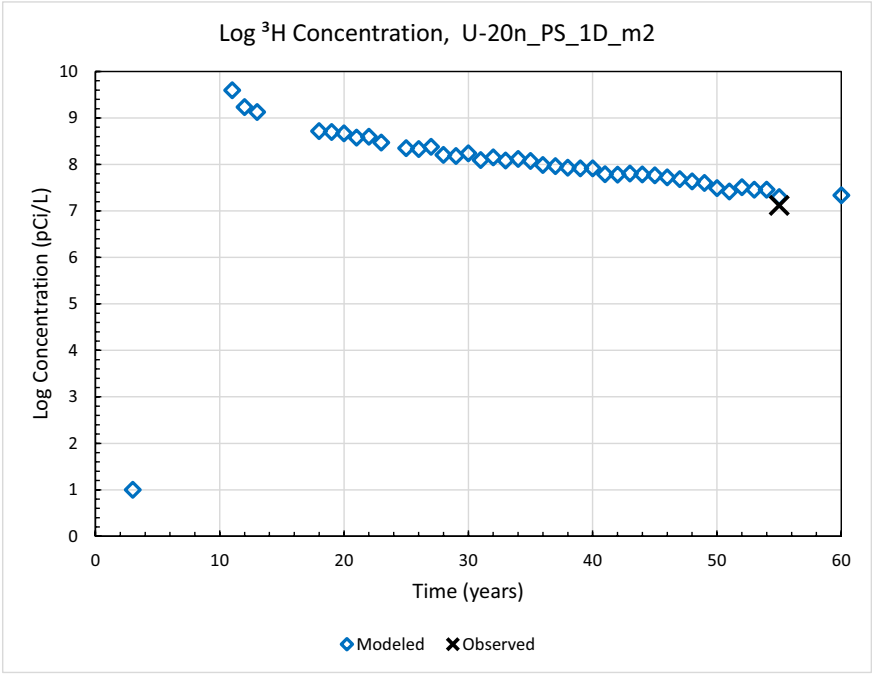

Figure 5-16
Modeled and Measured ^{3}H Concentrations versus Time at U-20n_PS_1D_m2

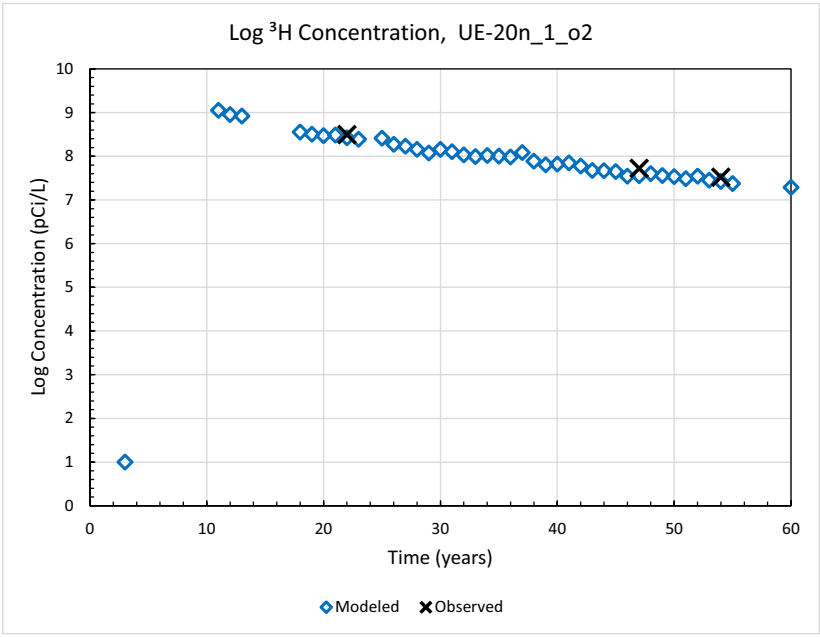

Figure 5-17
Modeled and Measured ^{3}H Concentrations versus Time at UE-20n_1_o2

for CHANCELLOR, which was detonated on September 1, 1983. The source mass flux pulse (lasting one day) for CHANCELLOR was introduced to the transport simulation on day 6,687 (see Table 5-8), 18.3 years after the start of the simulation. Examination of Figure 5-4 indicates no concentration (indicated by a log value of 1) at 18 years, followed by a concentration of 7.60E+07 pCi/L (log value of 7.88) at 19 years (the next output time), indicating the introduction of contaminant mass that occurred at 18.3 years.

Figure 5-18 shows the subset of the points shown in Figure 5-2 representing the observation locations near TYBO and BENHAM in the PM CAU transport model. Plots of modeled and measured ^{3}H concentrations over time at these observation locations are shown in Figures 5-19 through 5-21. These figures show model outputs over the first 60 years, which encompasses all observation times. Corresponding plots spanning the entire 1,000-year simulation time can be found in Appendix H in Figures H-5, H-6, and H-10.

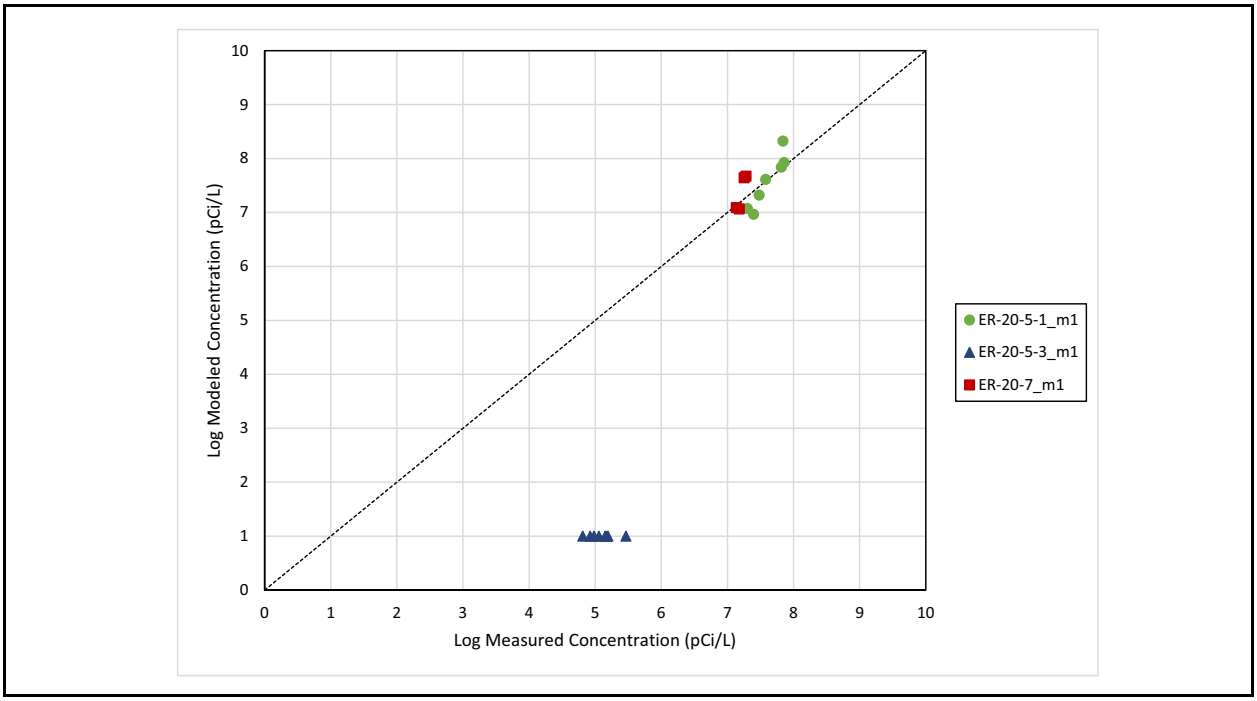

Figure 5-18
Modeled versus Measured ^{3}H Concentrations for the Observation Locations near TYBO and BENHAM in the PM CAU Transport Model

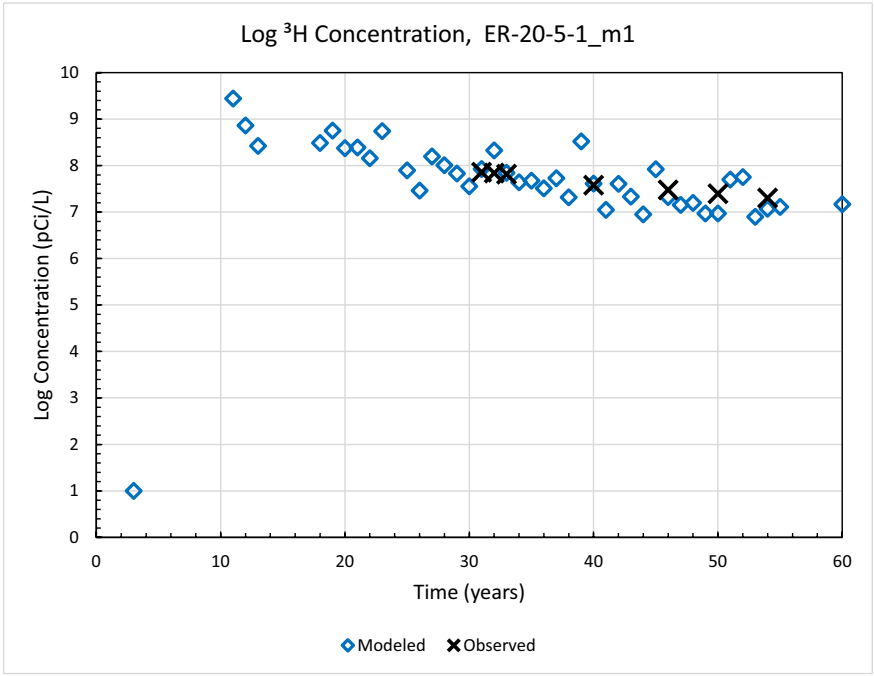

Figure 5-19
Modeled and Measured ^{3}H Concentrations versus Time at ER-20-5-1_m1

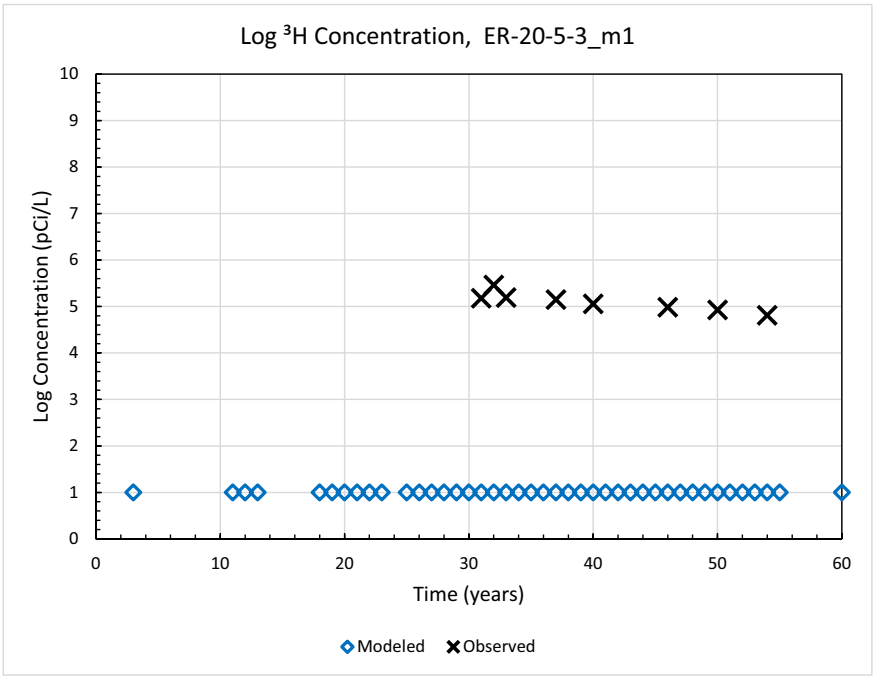

Figure 5-20
Modeled and Measured ^{3}H Concentrations versus Time at ER-20-5-3_m1

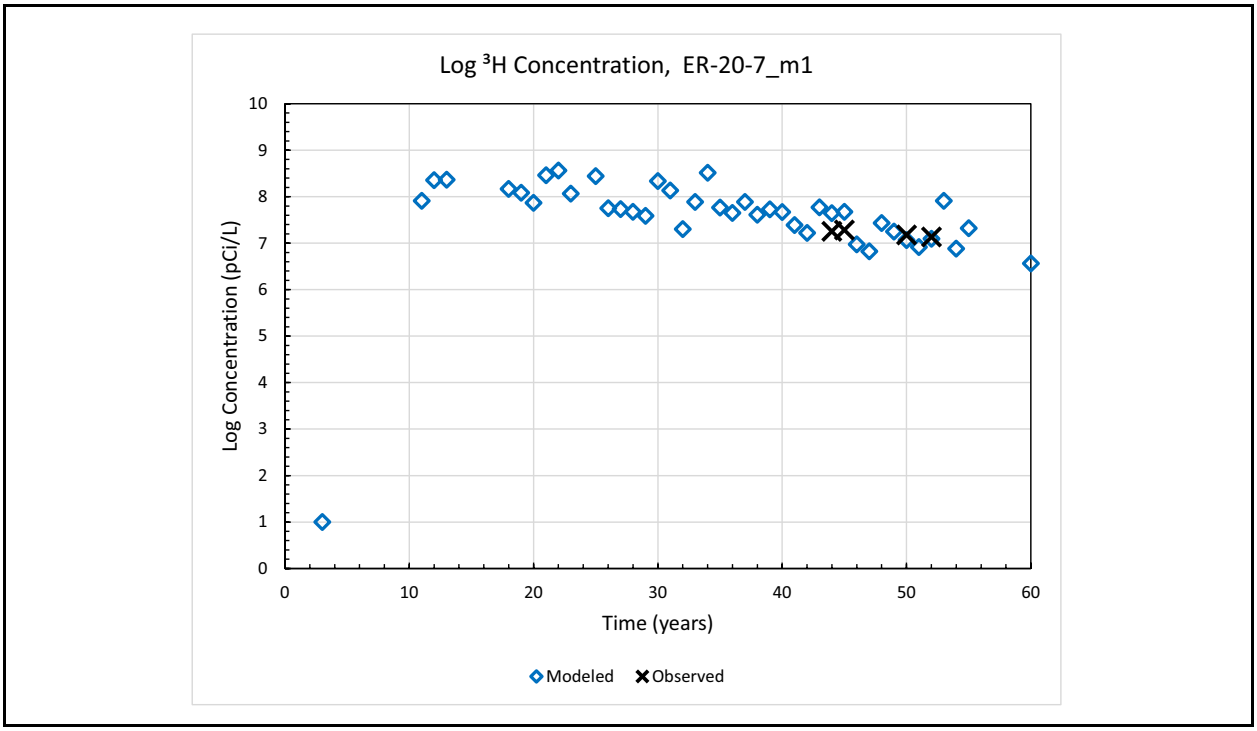

Figure 5-21
Modeled and Measured ^{3}H Concentrations versus Time at ER-20-7_m1

Good agreement between measured and modeled values is achieved at ER-20-5-1_m1 and ER-20-7_m1. There is poor agreement at ER-20-5-3_m1, where the model predicts no ^{3}H over the first 60 years, as shown in Figure 5-20. However, as shown in Figure H-6, the model predicts ^{3}H at 200 years, so flow through the observation locations associated with ER-20-5-3_m1 appears to be slower. Examination of the 20,000 particle tracks from BENHAM indicated that there are two distinct flow paths from BENHAM: a faster, shallow flow path from the chimney that heads south through ER-20-5-1_m1 in the TSA; and a slower, deeper flow path from the cavity that also heads south but passes to the east of ER-20-5-3_m1 in the CHLFA5 (while CHLFA5 is a fairly permeable lava-flow aquifer, it is enveloped by the less permeable CHZCM, which effectively limits flow and transport through the CHLFA5). The chosen observation locations in the model for both ER-20-5-1_m1 and ER-20-5-3_m1 share the same x,y location. If, during the calibration, the observation location of ER-20-5-3_m1 were shifted to the next closest x,y location to the east (150 m away), then modeled ^{3}H would have been recorded, and the calibrated transport parameters for the CHLFA5 would likely be different.

Using the calibrated transport results, Figure 5-22 shows a scatterplot of the simulated versus observed concentrations, representing the observation locations near TYBO and BENHAM in the PM CAU transport model with the observation location of ER-20-5-3_m1 shifted to the next closest x,y location to the east (150 m away). At the adjusted observation location for ER-20-5-3_m1, which was not used in the calibration, the model overpredicts ^{3}H by about an order of magnitude. This suggests that the best match to observed ^{3}H at ER-20-5-3_m1 is likely located between the original x,y location and the adjusted x,y location.

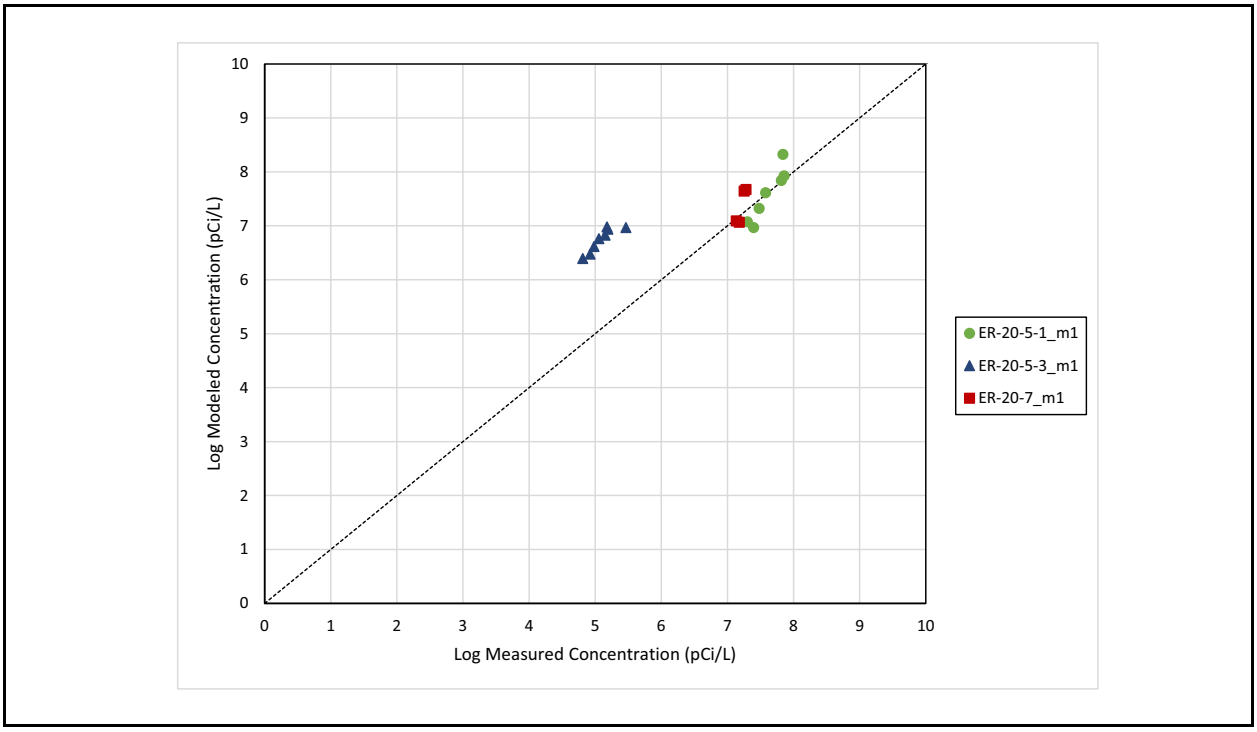

Figure 5-22
Modeled versus Measured ^{3}H Concentrations for the Observation Locations near TYBO and BENHAM in the PM CAU Transport Model with Adjusted Observation Location for ER-20-5-3

Figure 5-23 shows the subset of the points shown in Figure 5-2 representing the observation locations near the Bench in the PM CAU transport model. Good agreement between measured and modeled values is achieved at ER-20-11_m1, ER-EC-11_p1, ER-EC-11_m2, ER-EC-11_p3, ER-20-8-2_m1, and ER-20-8_p3. The model overpredicts ^{3}H concentrations at ER-20-8_p1 and ER-20-8_m2. Plots of modeled and measured ^{3}H concentrations over time at these observation locations are shown in Figures 5-24 through 5-31. These figures show model outputs over the first 60 years, which encompasses all observation times. Corresponding plots spanning the entire 1,000-year simulation time can be found in Appendix H in Figures H-11 through H-15 and Figures H-30 through H-32.

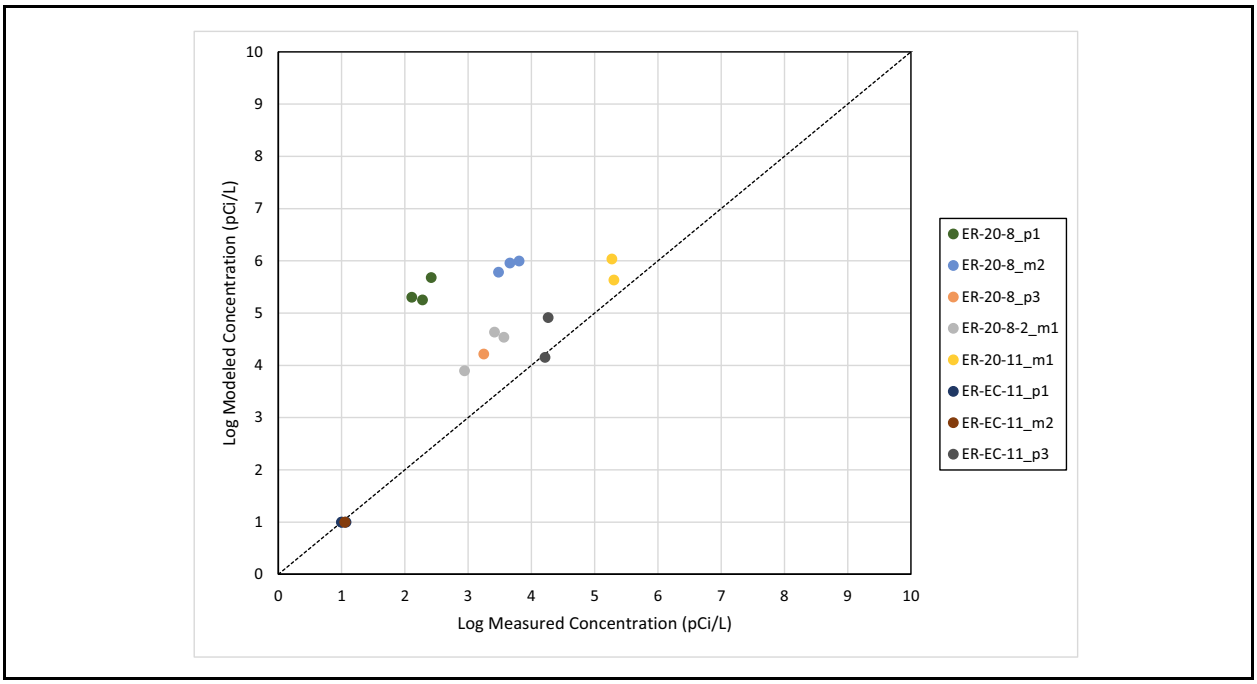

Figure 5-23
Modeled versus Measured ^{3}H Concentrations for the Observation Locations near the Bench in the PM CAU Transport Model

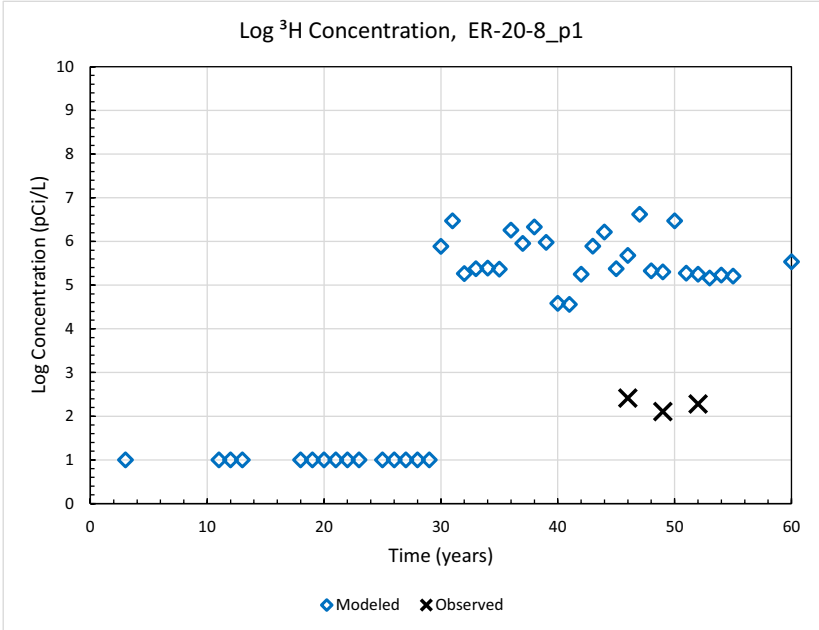

Figure 5-24
Modeled and Measured ^{3}H Concentrations versus Time at ER-20-8_p1

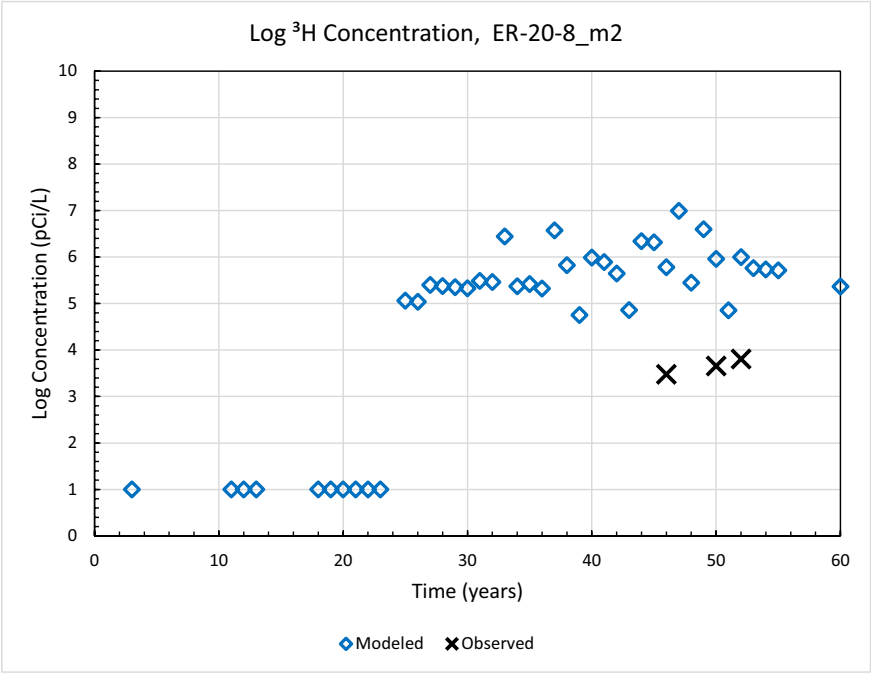

Figure 5-25
Modeled and Measured ^{3}H Concentrations versus Time at ER-20-8_m2

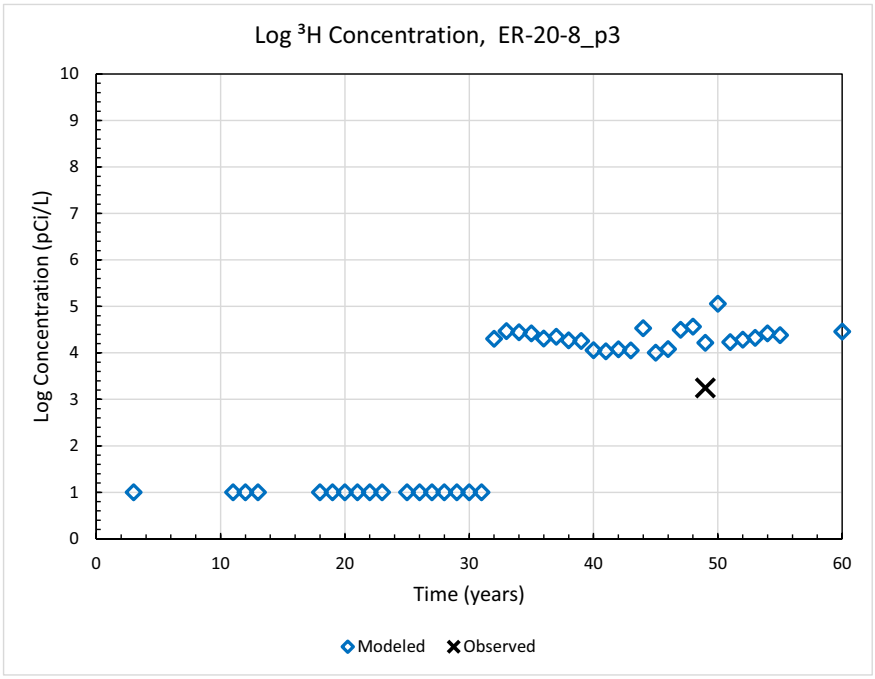

Figure 5-26
Modeled and Measured ^{3}H Concentrations versus Time at ER-20-8_p3

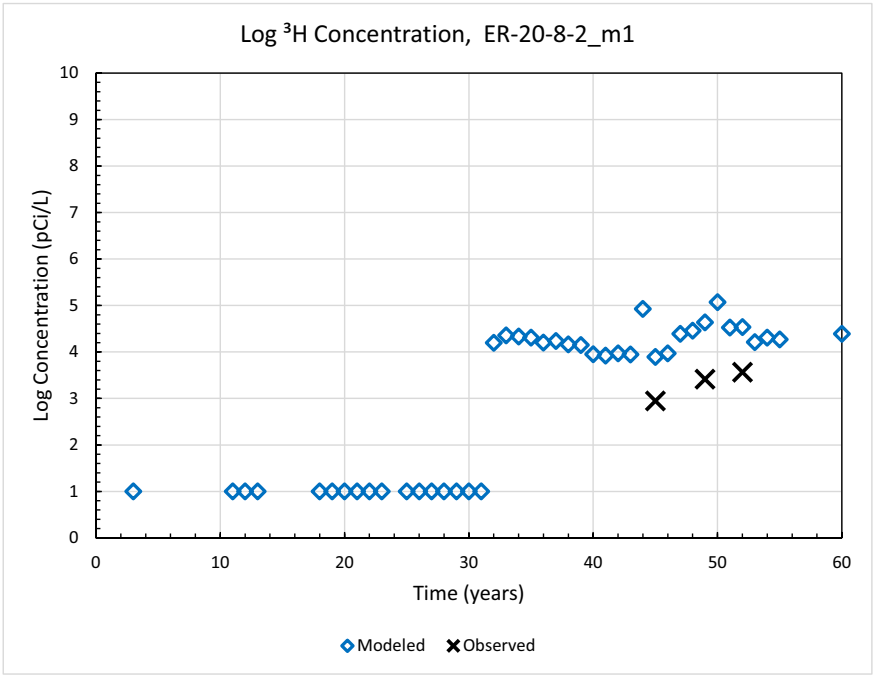

Figure 5-27
Modeled and Measured ^{3}H Concentrations versus Time at ER-20-8-2_m1

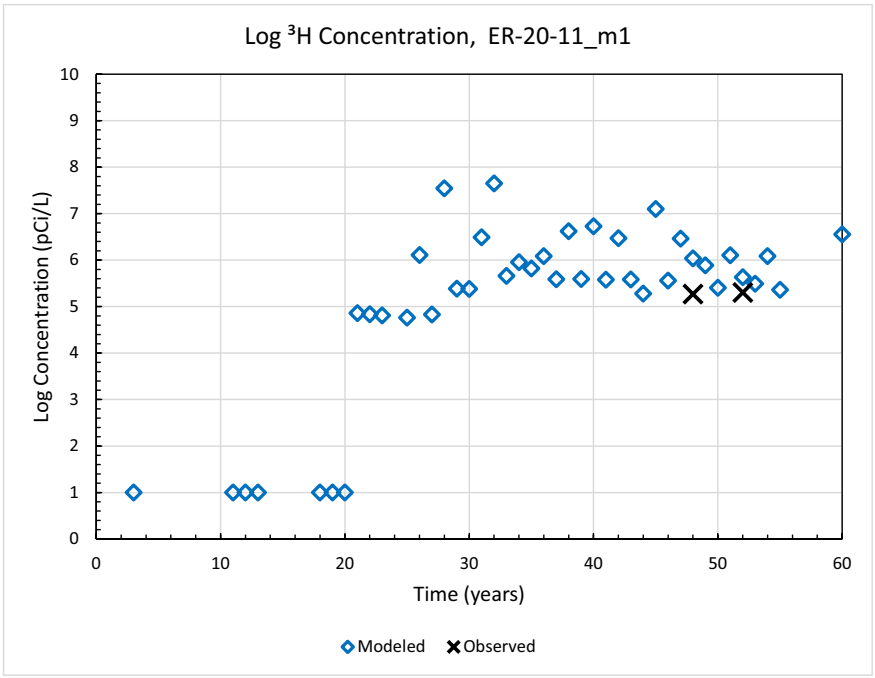

Figure 5-28
Modeled and Measured ^{3}H Concentrations versus Time at ER-20-11_m1

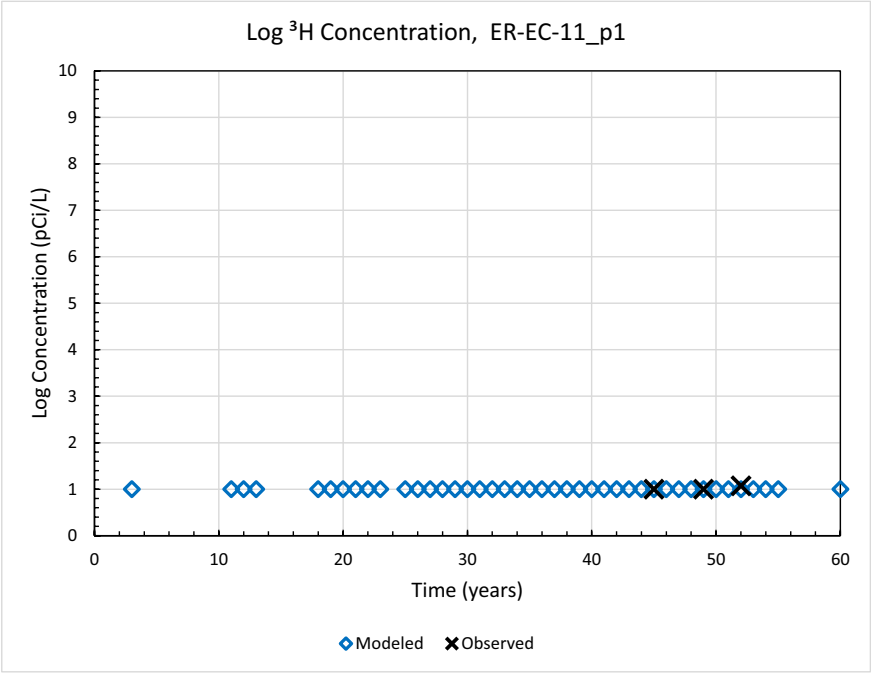

Figure 5-29
Modeled and Measured ^{3}H Concentrations versus Time at ER-EC-11_p1

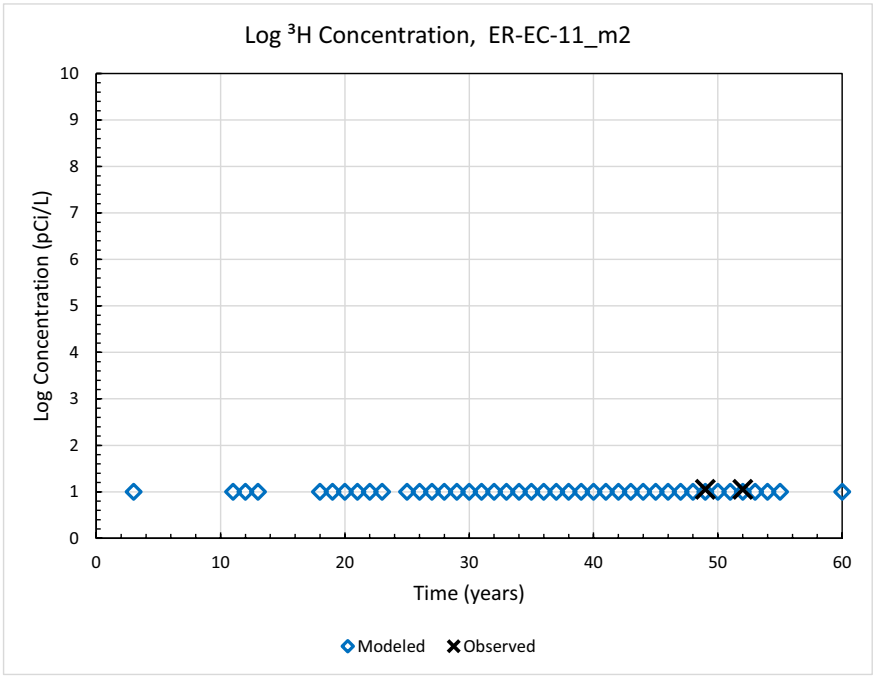

Figure 5-30
Modeled and Measured ^{3}H Concentrations versus Time at ER-EC-11_m2

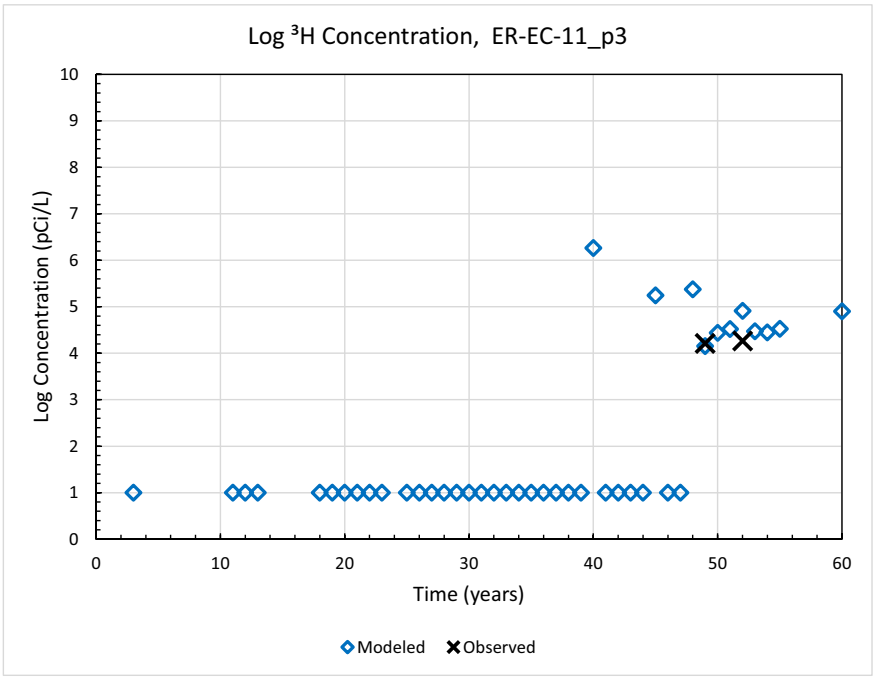

Figure 5-31
Modeled and Measured ^{3}H Concentrations versus Time at ER-EC-11_p3

Figure 5-32 shows the subset of the points shown in Figure 5-2 representing the observation locations near HANDLEY in the PM CAU transport model. Good agreement between measured and modeled values is achieved at ER-20-12_m1 (deep path from HANDLEY in PBRCM), ER-20-12_p1 (deep path from HANDLEY in BRA), and ER-20-12_p4 (shallow path from HANDLEY in TMLVTA). The model predicts no ^{3}H at the two intermediate wells at ER-20-12_p2 and ER-20-12_p3. Flow paths to these two locations appears to be very slow. At PM-3, farther downgradient from HANDLEY, the model overpredicts ^{3}H at PM-3_p1 (deeper completion in the TCA), but predicts no ^{3}H at PM-3_p2 (shallow completion in the UPCU). The head gradient at PM-3 is downward, suggesting that flow should go from the UPCU at PM-3_p2 down to the TCA at PM-3_p1; however, the flow model has the flow path proceeding through the TCA to PM-3. Plots of modeled and measured ^{3}H concentrations over time at these observation locations are shown in Figures 5-33 through 5-39. These figures show model outputs over the first 60 years, which encompasses all observation times. Corresponding plots spanning the entire 1,000-year simulation time can be found in Appendix H in Figures H-16 through H-20 and Figures H-44 and H-45.

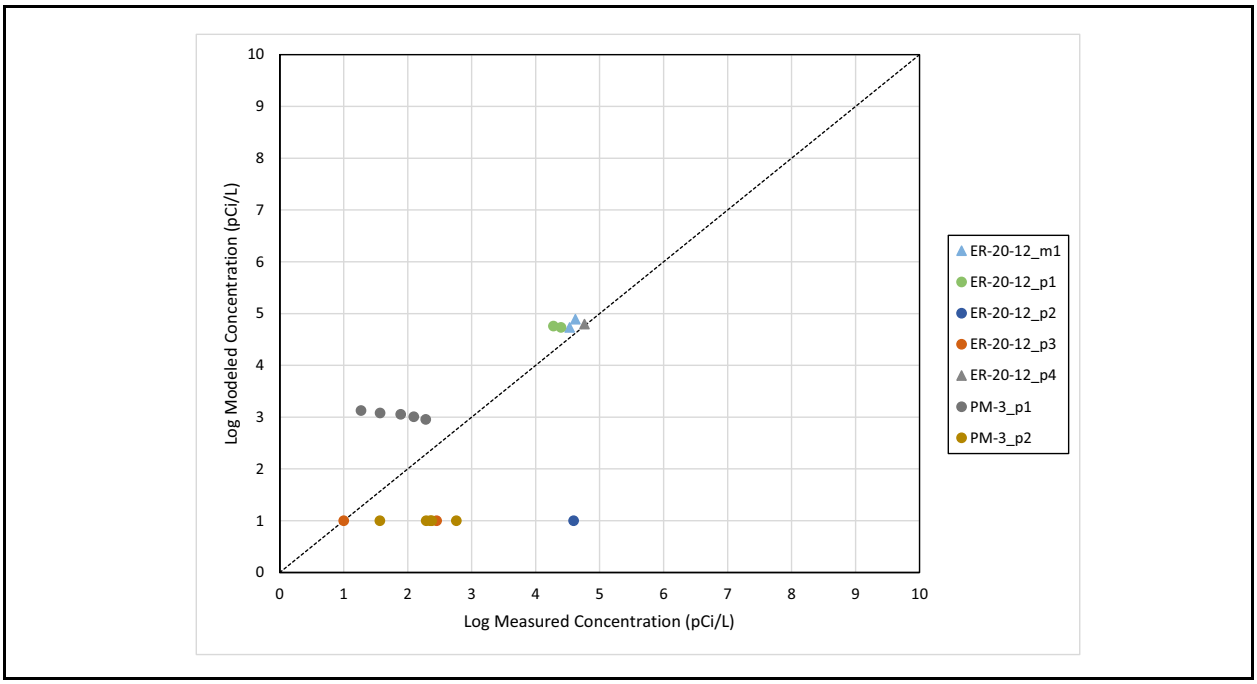

Figure 5-32
Modeled versus Measured ^{3}H Concentrations for Observation Locations near HANDLEY in the PM CAU Transport Model

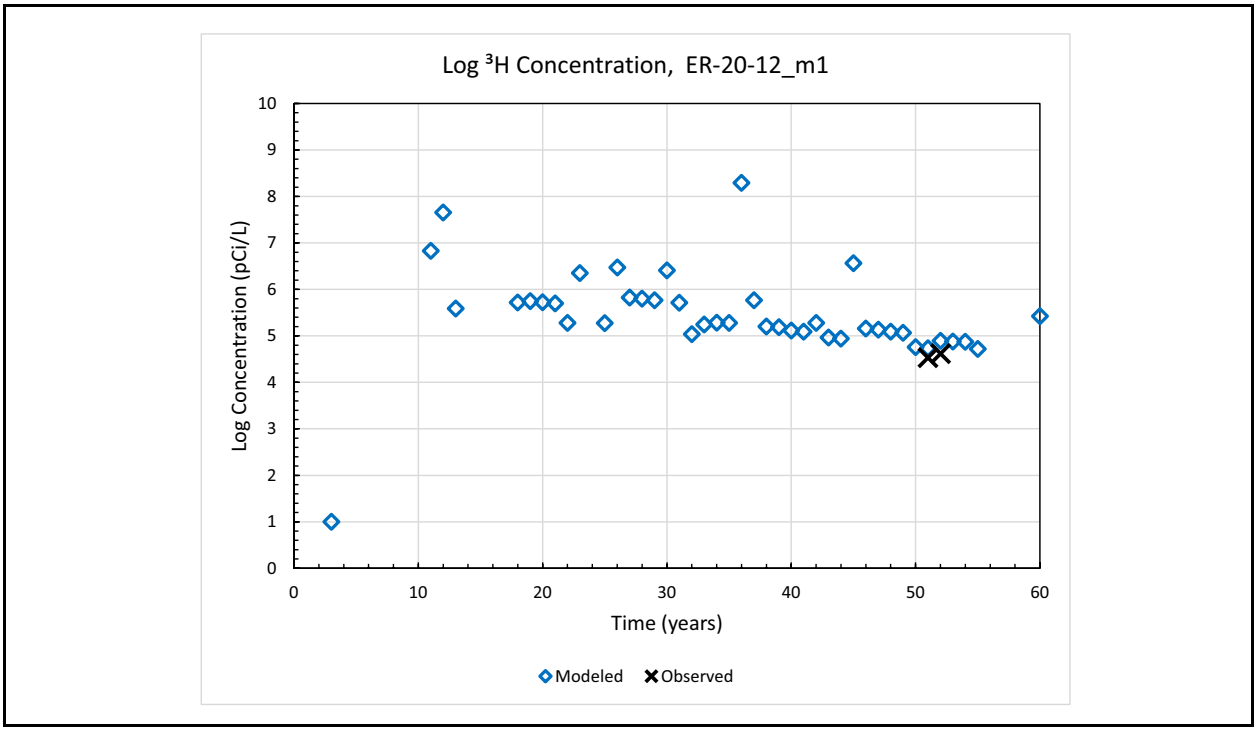

Figure 5-33
Modeled and Measured ^{3}H Concentrations versus Time at ER-20-12_m1

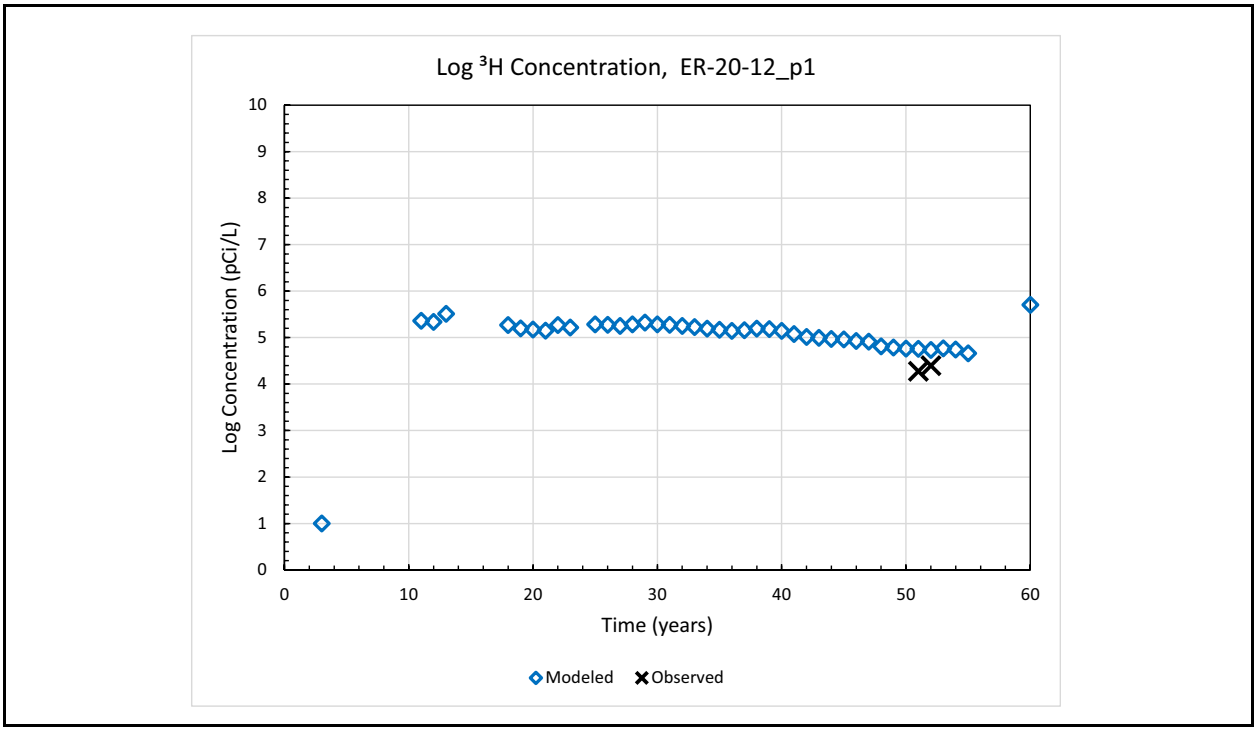

Figure 5-34
Modeled and Measured ^{3}H Concentrations versus Time at ER-20-12_p1

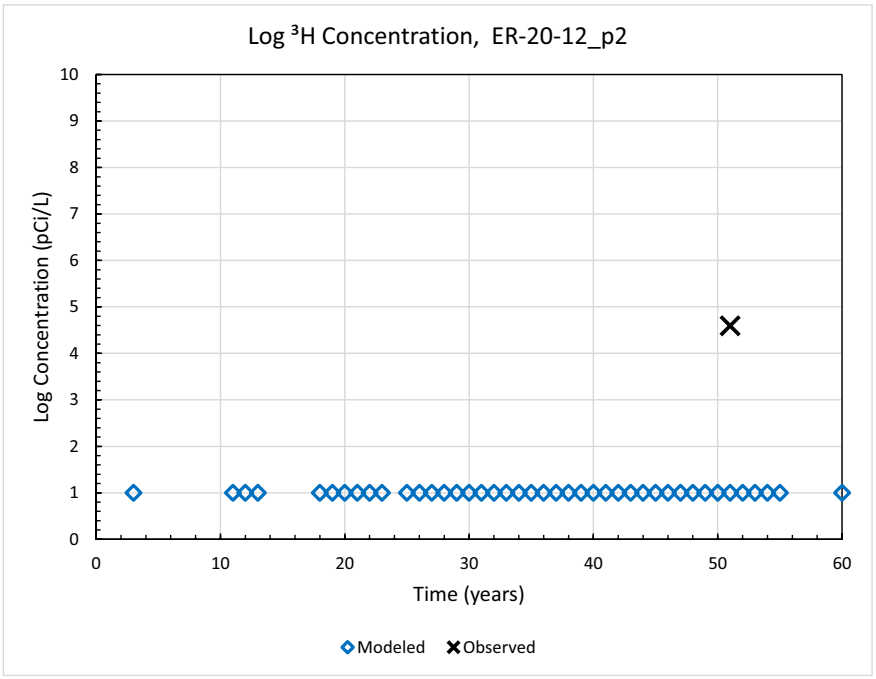

Figure 5-35
Modeled and Measured ^{3}H Concentrations versus Time at ER-20-12_p2

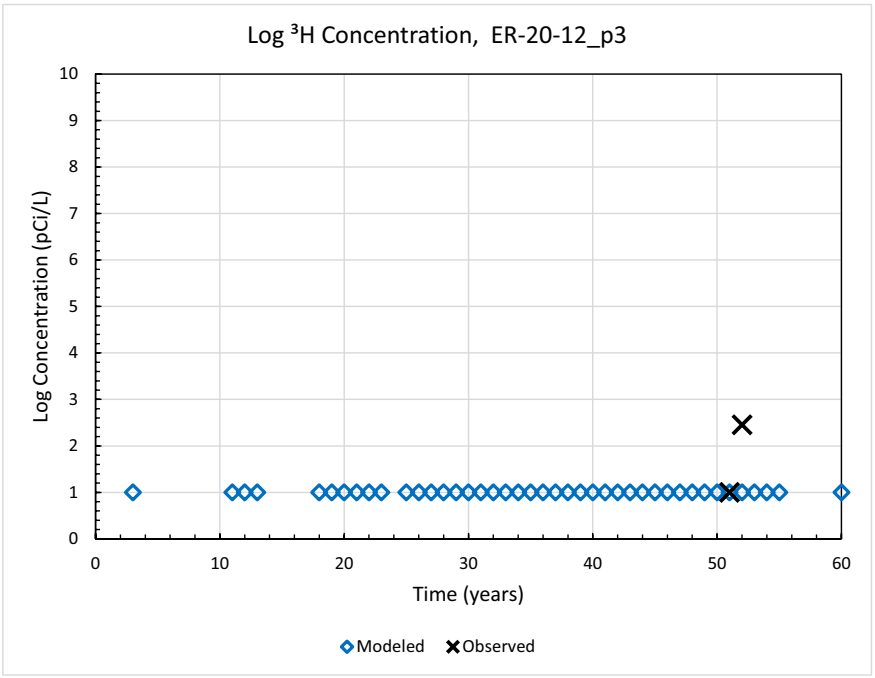

Figure 5-36
Modeled and Measured ^{3}H Concentrations versus Time at ER-20-12_p3

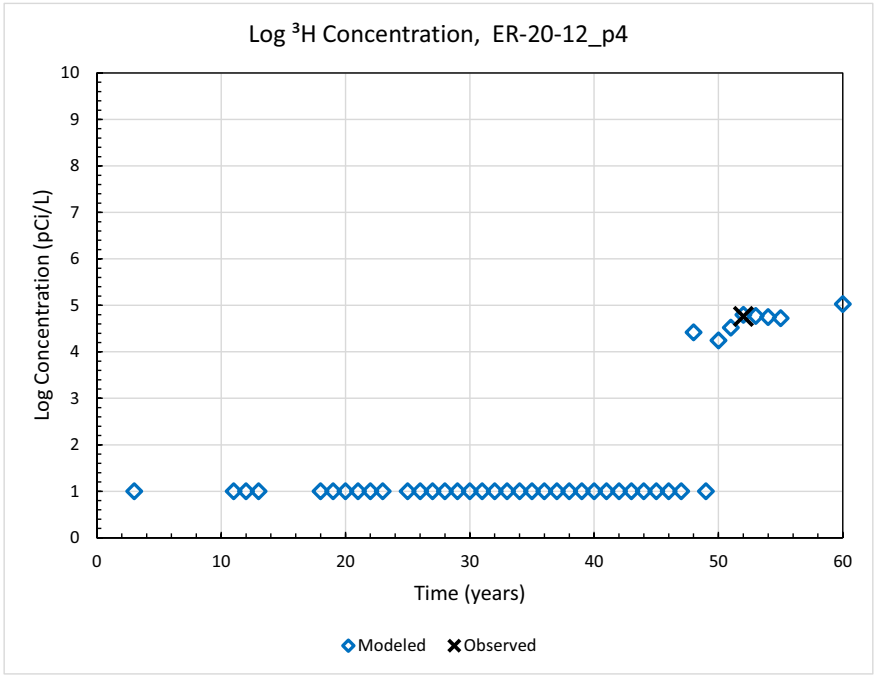

Figure 5-37
Modeled and Measured ^{3}H Concentrations versus Time at ER-20-12_p4

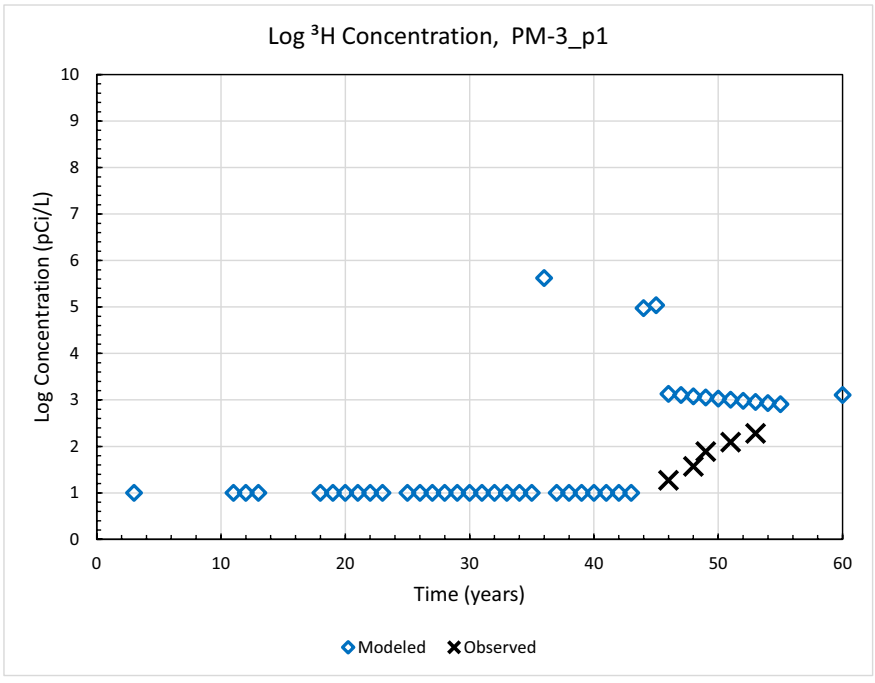

Figure 5-38
Modeled and Measured ^{3}H Concentrations versus Time at PM-3_p1

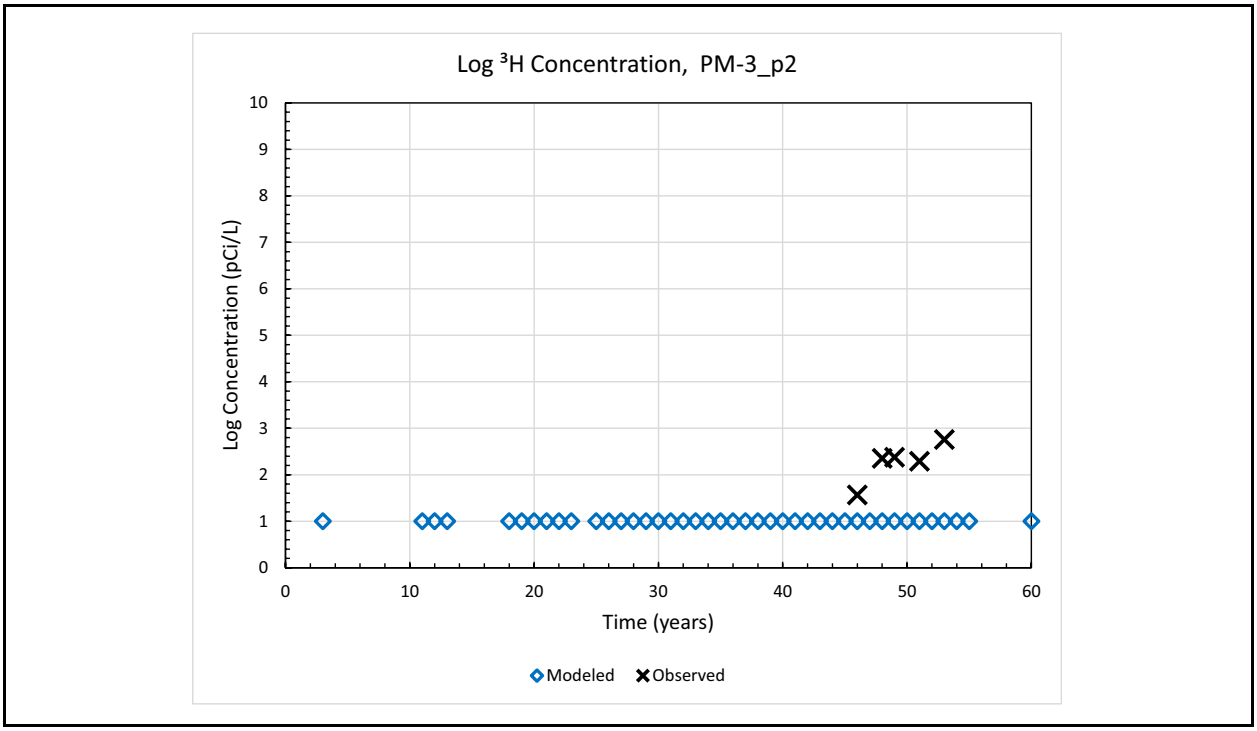

Figure 5-39
Modeled and Measured ^{3}H Concentrations versus Time at PM-3_p2

Figure 5-40 shows the subset of the points shown in Figure 5-2 representing the observation locations at the ER-20-6 wells. The model greatly overpredicts ^{3}H at these locations. Plots of modeled and measured ^{3}H concentrations over time at these observation locations are shown in Figures 5-41 through 5-43. These figures show model outputs over the first 60 years, which encompasses all observation times. Corresponding plots spanning the entire 1,000-year simulation time can be found in Appendix H in Figures H-7 through H-9. The ER-20-6 wells are south–southwest of BULLION. The simulated results may be showing breakthrough from BULLION or BODIE. The pulse in observed concentrations at the ER-20-6 wells was due to pumping ER-20-6 #3 and drawing BULLION contaminants toward them (IT, 1998). The model, because it is steady-state and does not include transient pumping on PM, cannot replicate this result.

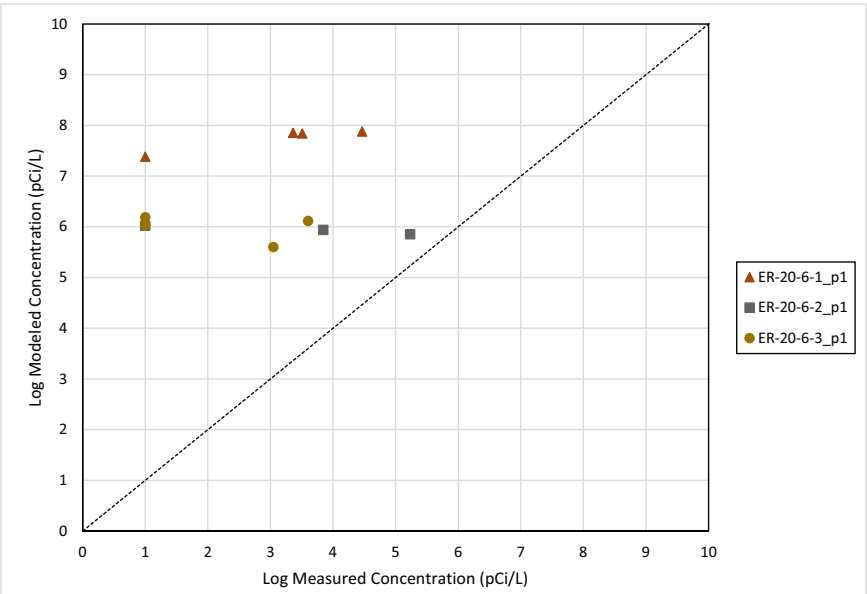

Figure 5-40
Modeled versus Measured ^{3}H Concentrations for Observation Locations near BULLION in the PM CAU Transport Model

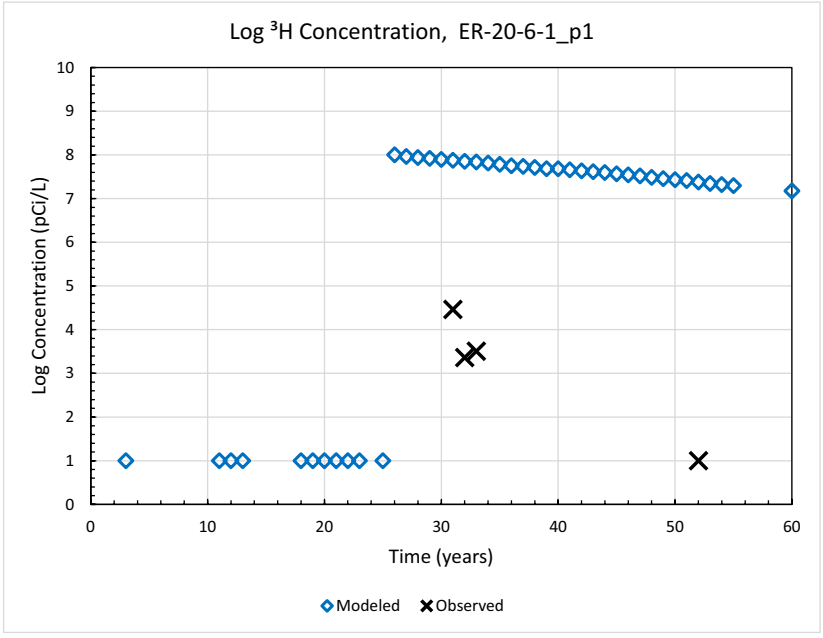

Figure 5-41
Modeled and Measured ^{3}H Concentrations versus Time at ER-20-6-1_p1

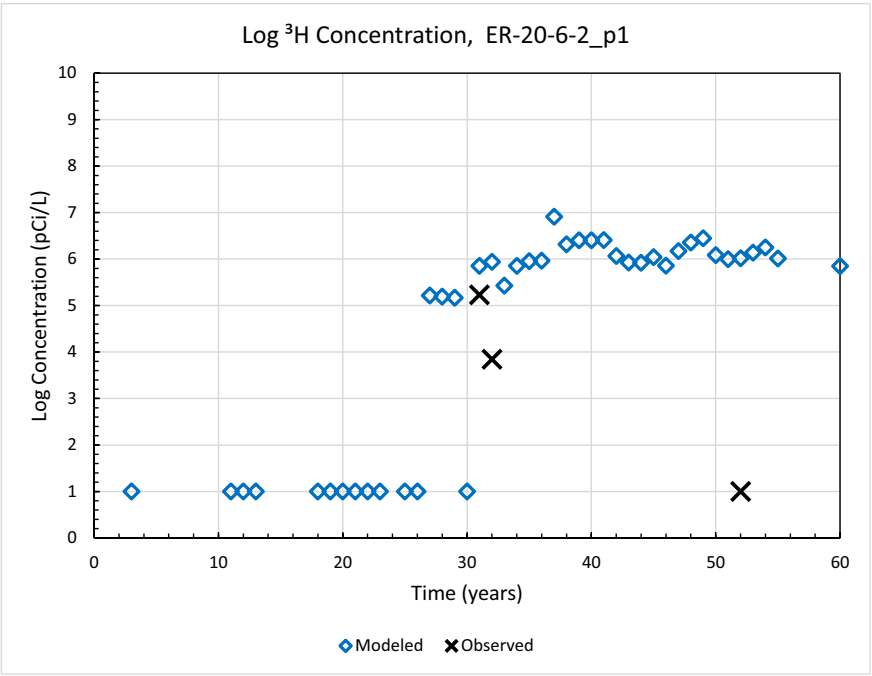

Figure 5-42
Modeled and Measured ^{3}H Concentrations versus Time at ER-20-6-2_p1

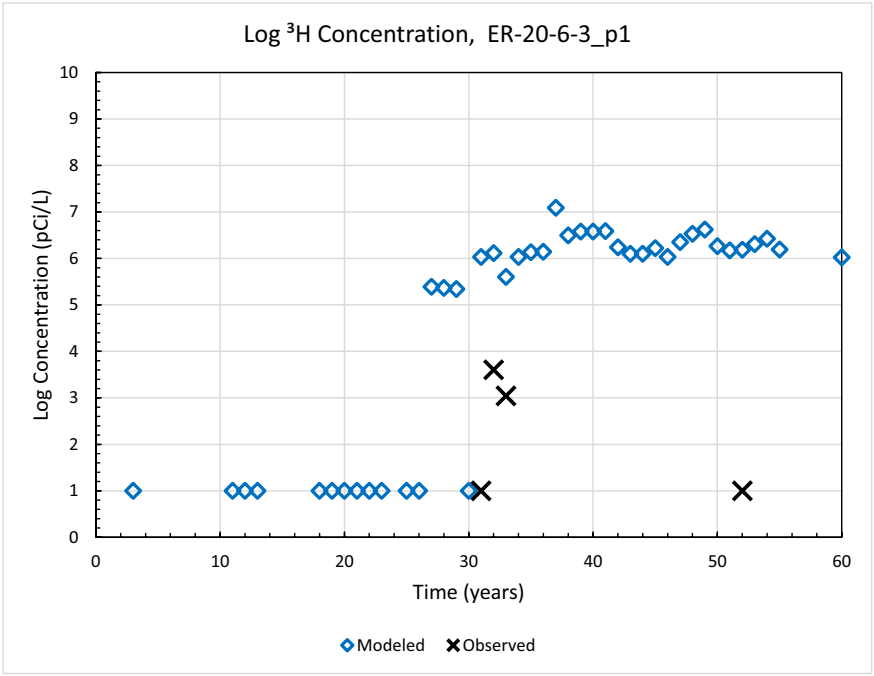

Figure 5-43
Modeled and Measured ^{3}H Concentrations versus Time at ER-20-6-3_p1

Figure 5-44 shows the subset of the points shown in Figure 5-2 representing the remaining observation locations with no modeled ^{3}H in the PM CAU transport model. Plots of modeled and measured ^{3}H concentrations over time at these observation locations spanning the entire 1,000-year simulation time can be found in Appendix H in Figures H-42, H-43, H-60, and H-62. Three of these locations—PM-2, UE-18r, and UE-19h—do not have ^{3}H carried to them (flow paths do not head toward these locations). PM-1 is adjacent to a plume, but the chosen observation node closest to the well shows no ^{3}H.

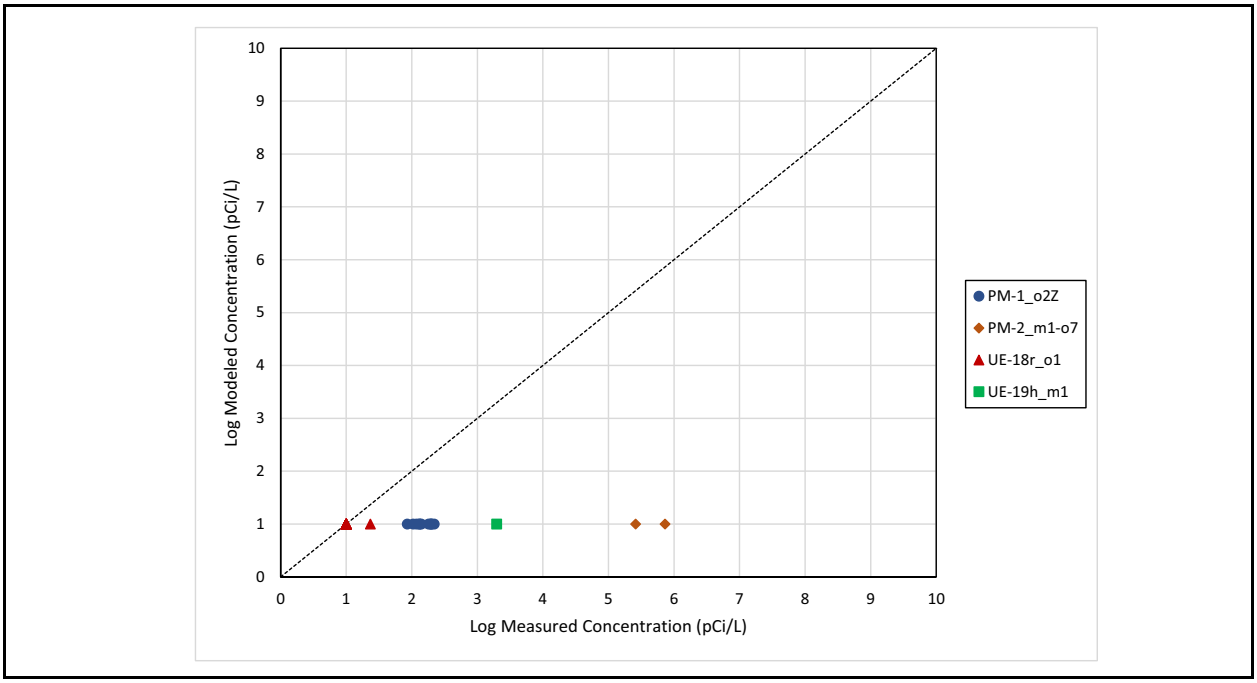

Figure 5-44
Modeled versus Measured ^{3}H Concentrations at Remaining Observation Locations with No Modeled ^{3}H in the PM CAU Transport Model

Figure 5-45 shows the subset of the points shown in Figure 5-2 representing the remaining observation locations with no measured ^{3}H in the PM CAU transport model. Plots of modeled and measured ^{3}H concentrations over time at these observation locations spanning the entire 1,000-year simulation time can be found in Appendix H in Figures H-1 through H-4, H-21 through H-29, H-33 through H-41, H-59, H-61, and H-63. Out of all of these locations, only ER-20-1_p1 shows modeled ^{3}H from the calibration. The remaining wells indicated in the figure have no modeled ^{3}H, so all of the points for those wells are overlapped in the figure at (1,1). ER-20-1_p1 is located near the edge of a plume, but due to grid spacing, the observation location in the model associated with ER-20-1_p1

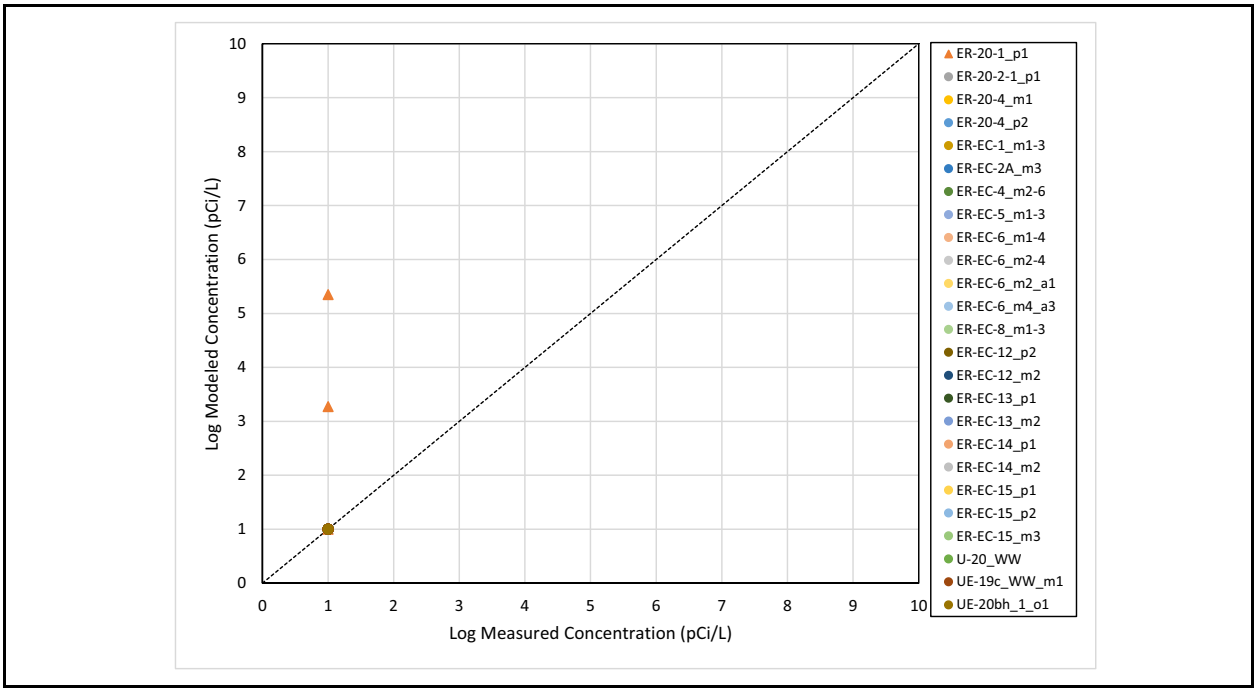

Figure 5-45
Modeled versus Measured ^{3}H Concentrations at Remaining Observation Locations with No Measured ^{3}H in the PM CAU Transport Model

intersects the plume. The closest chosen observation location for ER-20-1_p1 is approximately 113 m west of ER-20-1. If, during the calibration, the observation location of ER-20-1_p1 were shifted to the next closest node to the east (300 m away from the original observation node), then modeled ^{3}H would not have been recorded.

Using the calibrated transport results, Figure 5-46 shows a scatterplot of the simulated versus observed concentrations, representing the remaining observation locations with no measured ^{3}H in the PM CAU transport model with the observation location of ER-20-1_p1 shifted to the next closest x,y location to the east (300 m away). At the adjusted observation location for ER-20-1_p1, which was not used in the calibration, the model predicts no ^{3}H, agreeing with observations.

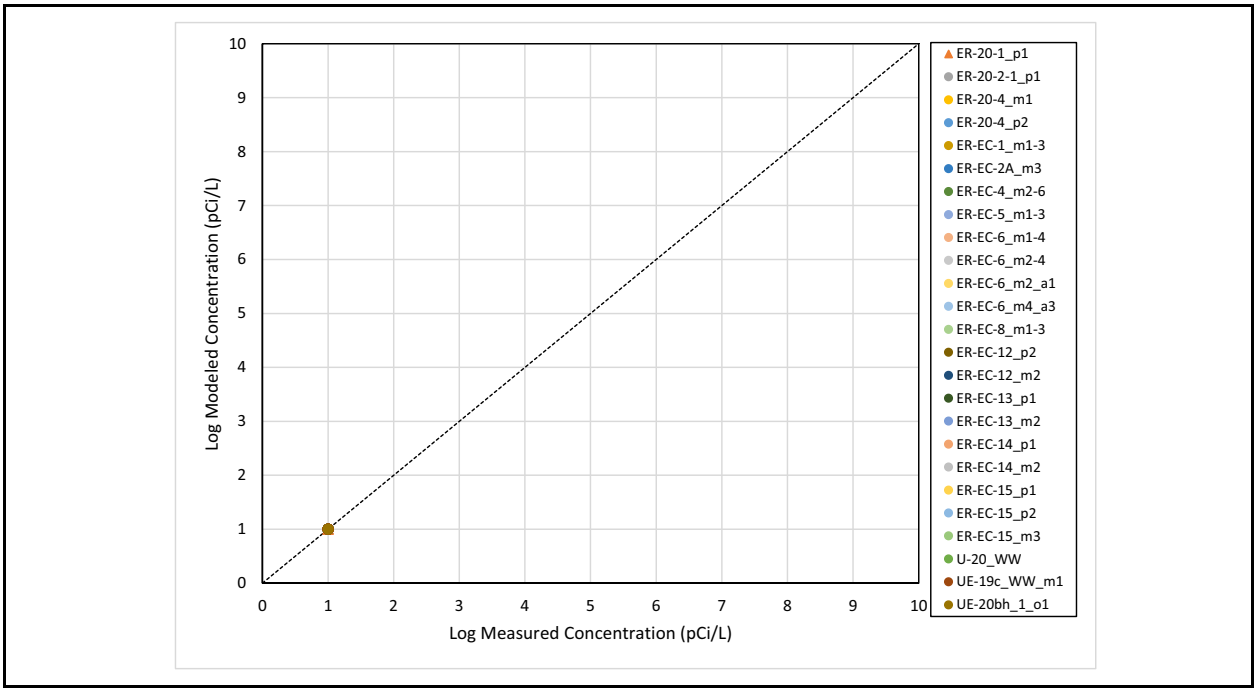

Figure 5-46
Modeled versus Measured ^{3}H Concentrations at Remaining Observation Locations with No Measured ^{3}H in the PM CAU Transport Model with Adjusted Observation Location for ER-20-1

5.5.1.3.1 Transport Parameter Estimates

The PM CAU transport model calibration parameters are effective porosity, matrix porosity, matrix diffusion coefficient, and fracture aperture for the HSUs and faults in the HFM. The PM CAU transport model is highly parameterized and has more parameters than can be estimated uniquely on the basis of the calibration dataset. A parameter identifiability index can be calculated by the PEST software, which identifies the parameters that can be estimated during the inverse modeling process. Identifiability ranges between 0 and 1; parameters having an identifiability index of 1 are fully identifiable, and parameters having an identifiability index of 0 are totally unidentifiable.

Calculated parameter identifiability indices for effective porosity, matrix porosity, matrix diffusion coefficient, and fracture aperture are shown in Figures 5-47 through 5-50. Considering parameters with an identifiability index greater than 0.5, the following parameters/HSUs are identifiable as being important to transport:

- Effective porosity in the CHLFA4, CHZCM, TSA, TCA, BFCU, BA and CHLFA3.
- Matrix porosity in the TMLVTA, BRA_nw, TCA, BA, SPA, CHLFA4, PBRCM_nw, CHLFA3, CHZCM, CHLFA1, TSA, BFCU, CFCM, CHVTA, PLFA, BRA, LPCU, and CHLFA5.
- Matrix diffusion coefficient in the CHLFA4, TSA, CHZCM, BFCU, TCA, BA, and LPCU.
- Fracture aperture in the CHLFA3, BRA_nw, TSA, BFCU, CHLFA4, PBRCM_nw, TCA, CHZCM, UPCU, BA, CFCU, and LPCU.

It is noteworthy that the HSUs identified above intersect observation locations, for example:

- The TSA intersects ER-20-5-1_m1 (near BENHAM) and ER-20-7_m1 (near BENHAM), ER-EC-11_p1 (in the Bench).
- The TCA intersects ER-20-8_m2 (in the Bench) and ER-EC-11_m2 (in the Bench).
- The CHZCM intersects ER-20-8_p1 (in the Bench).
- The BA intersects ER-20-11_m1 (in the Bench) and ER-EC-11_p3 (in the Bench).
- The PBRCM_nw intersects ER-20-12_m1 (near HANDLEY).
- The BRA_nw intersects ER-20-12_p1 (near HANDLEY).
- The TMLVTA intersects ER-20-12_p4 (near HANDLEY).
- The CHLFA4 intersects UE-20n_1_o2 (CHESHIRE) and U-20n_PS_1D (CHESHIRE).
- The CHLFA3 intersects U-20i_PS_1D (BOXCAR) and ER-20-6 (western Area 20).
- The BFCU intersects U-19q_PS_1D (CAMEMBERT), U-20i_PS_1D (BOXCAR), and U-20aa_PS_1D (COLBY).
- The BRA intersects U-19e_PS_2D (MUENSTER), U-19q_PS_1D (CAMEMBERT), U-19v_PS_1D (ALMENDRO).

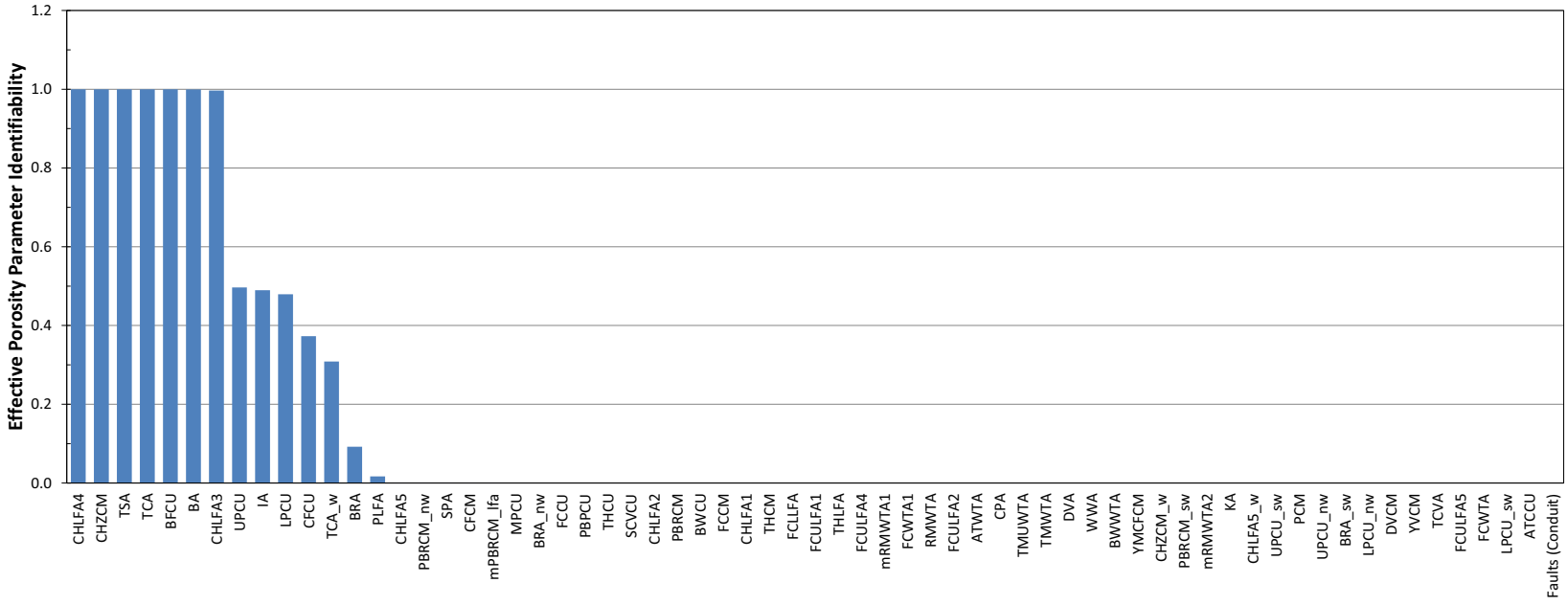

Figure 5-47
Identifiability Index for Effective Porosity Parameters

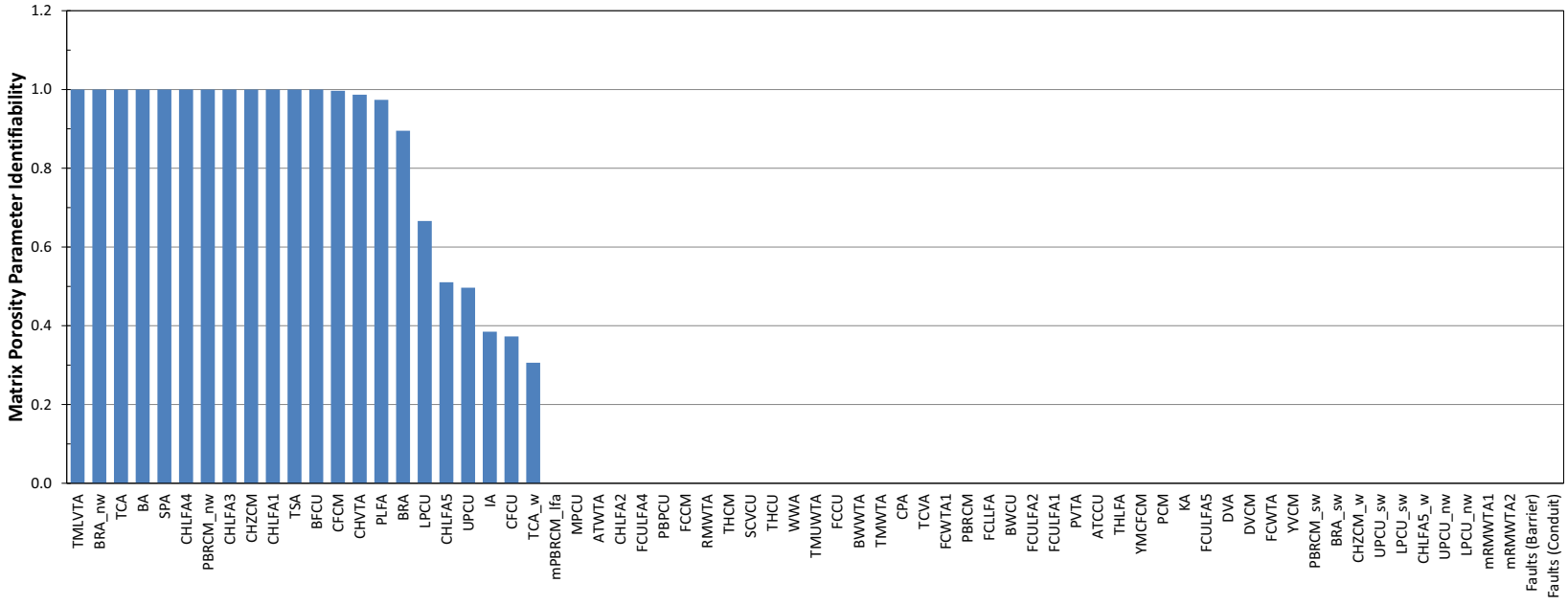

Figure 5-48
Identifiability Index for Matrix Porosity Parameters

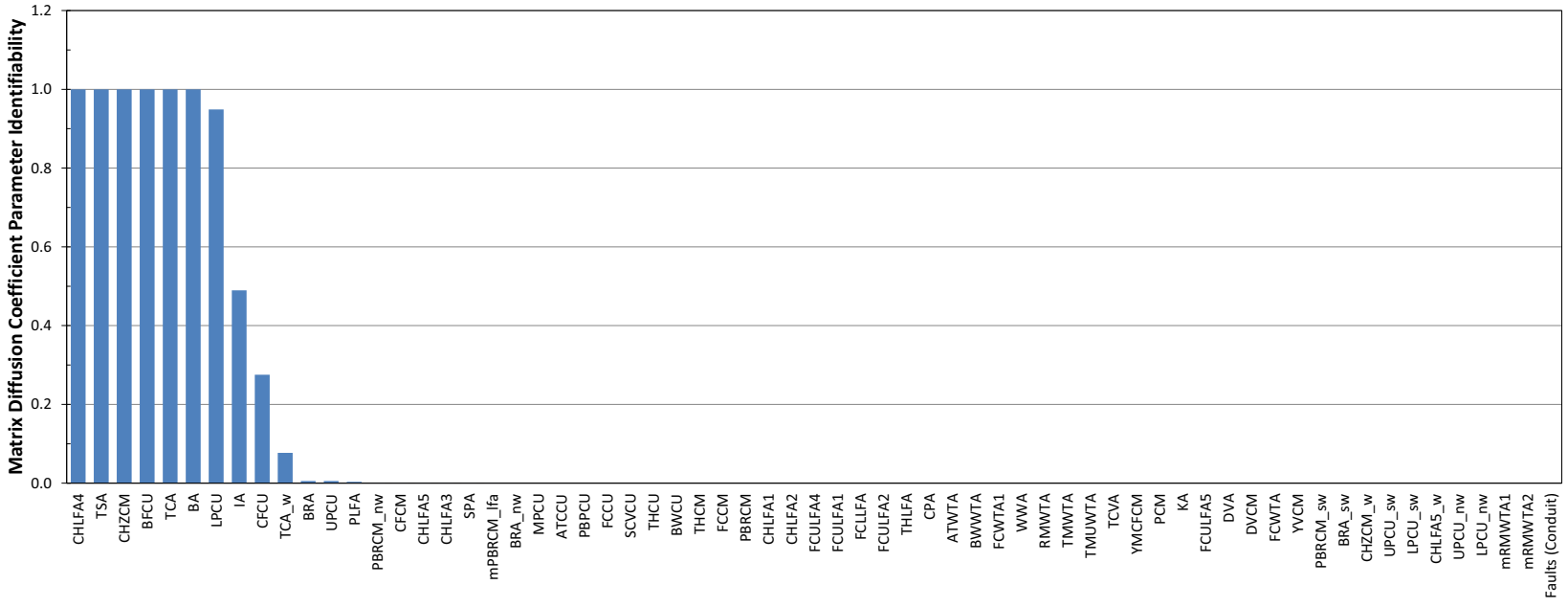

Figure 5-49
Identifiability Index for Matrix Diffusion Coefficient Parameters

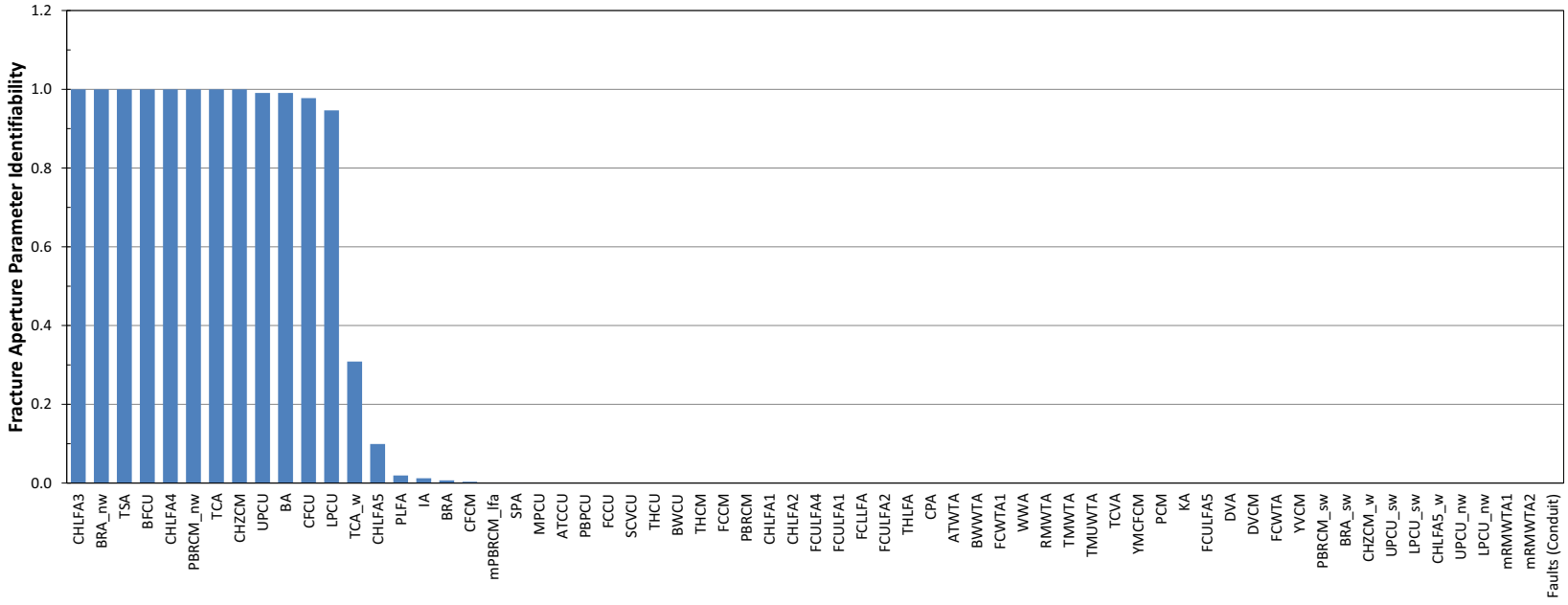

Figure 5-50
Identifiability Index for Fracture Aperture Parameters

Final values for adjustable transport parameters, namely effective porosity, matrix porosity, matrix diffusion coefficient, and fracture aperture, obtained from the calibration are shown in Figures 5-51 through 5-54. Each figure shows upper and lower limits, initial value (i.e., the mean value), and final value for each parameter in each HSU zone. Figure 5-55 shows fracture spacing values that were estimated from final values of effective porosity and fracture aperture using Equation 5-4.

5.5.1.3.2 Extent of ^{3}H Contamination from Model Calibration

Figure 5-56 shows the extent of ^{3}H contamination obtained from the model calibration at 55 years (year 2020). Each colored dot represents the ^{3}H concentration in moles/L (as output from PLUMECALC) at a model node. The spacing between colored dots reflects the model grid spacing, so the dots are spaced close together (overlapping in places) in areas with smaller nodal spacing, and farther apart in areas with larger nodal spacing. Values displayed are concentrations relative to the MCL of ^{3}H; thus, any value greater than 1 is above the MCL. Figure 5-56 is displayed such that at each x,y location, the maximum concentration (relative to MCL) at any depth is shown.

Looking at Figure 5-56, a couple of observation locations with no observed ^{3}H appear to show ^{3}H contamination, namely ER-20-1_p1 and U-20 WW. As discussed in Section 5.5.1.3, ER-20-1_p1 is located near the edge of a plume, but due to grid spacing (300 m in this area), the observation location in the model associated with ER-20-1_p1 intersects the plume. A lateral adjustment of the observation location for ER-20-1_p1 by one node would eliminate this (see Figure 5-46). There is no modeled ^{3}H at U-20 WW during the period of observations spanning the first 60 years of simulation time (see Figure H-59). U-20 WW is located adjacent to a plume, but the symbol sizes used on Figure 5-56 may make it appear that there is ^{3}H at this location.

5.5.1.4 Comparison of Other RNs to Observed Values

The ability of the calibrated PM CAU transport model to replicate other RN measurements was examined with a series of forward transport model runs using the calibrated transport parameters with source contaminant mass fluxes from RNs other than ^{3}H, namely, ^{14}C, ^{36}Cl, ^{90}Sr, ^{129}I, ^{137}Cs, ^{232}U, ^{233}U, ^{234}U, ^{238}U, ^{239}Pu, and ^{240}Pu. No recalibration of the model was performed using these sources. Observations of these RNs in PM are described in Section 3.2 of Navarro (2021c) and summarized in Table 5-11. Observation locations are shown in Figure 5-1.

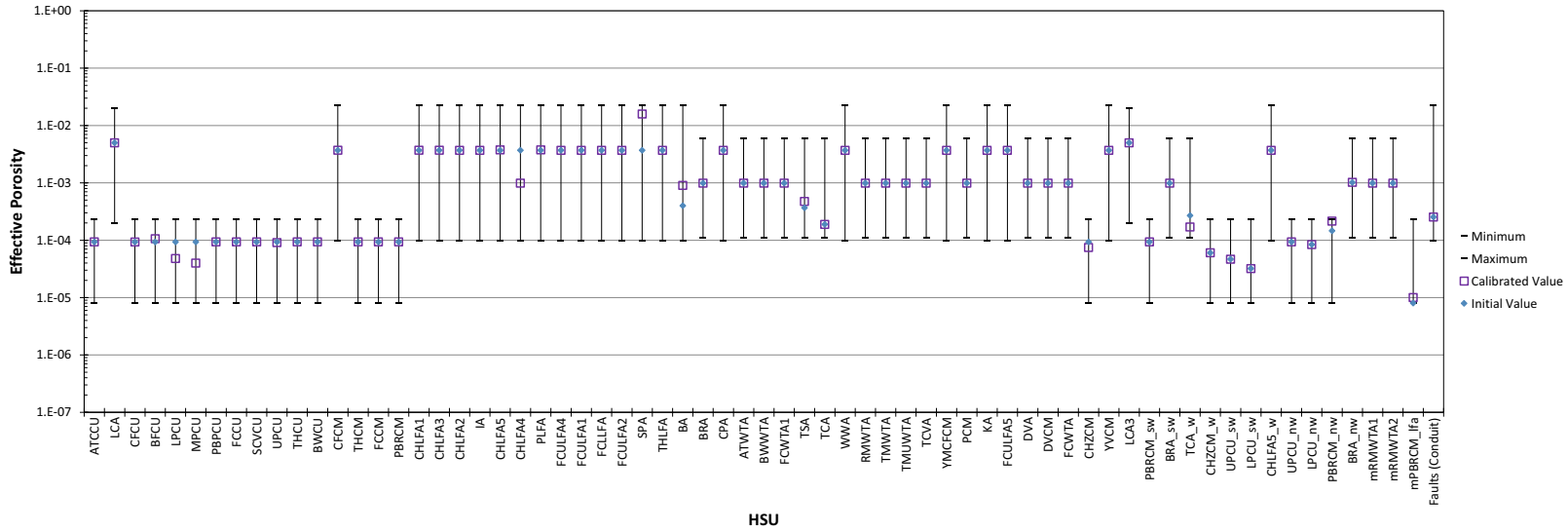

Figure 5-51
Calibrated Effective Porosity Values

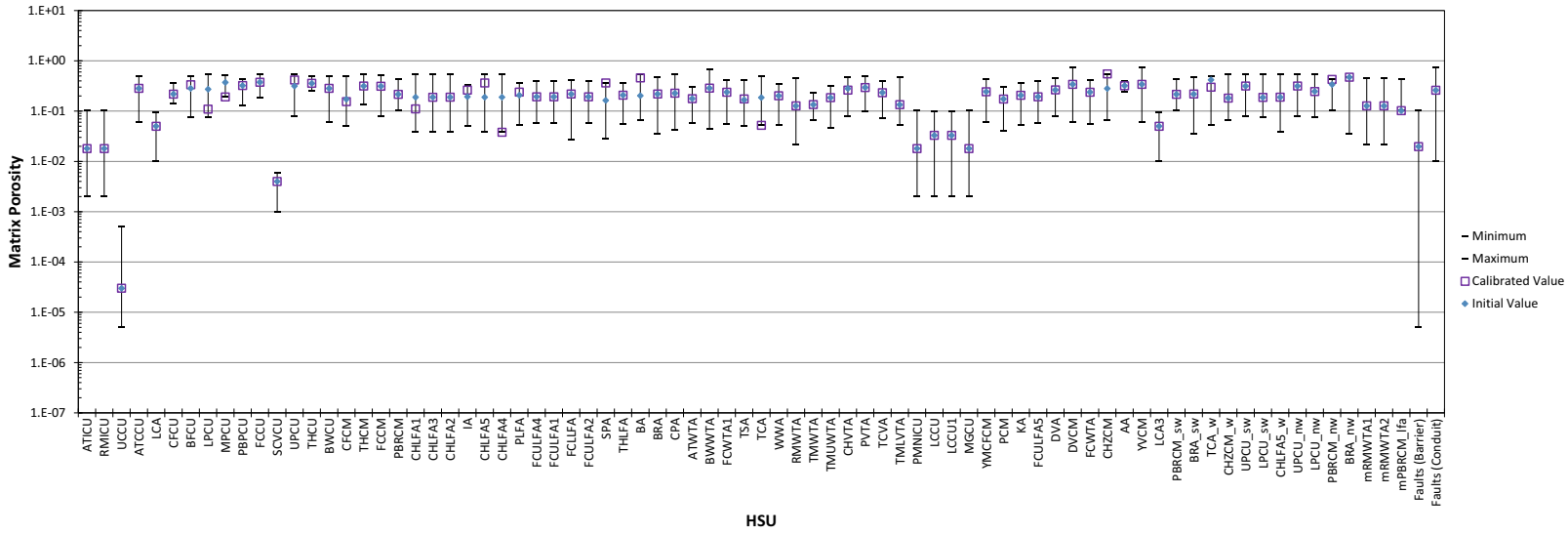

Figure 5-52
Calibrated Matrix Porosity Values

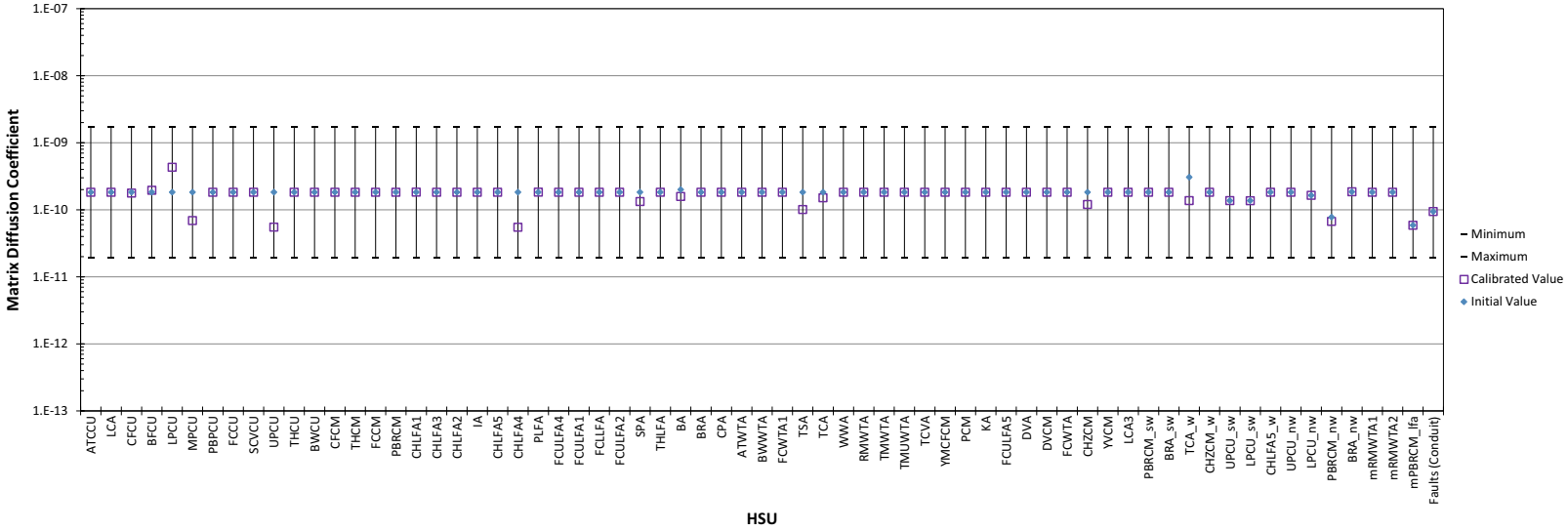

Figure 5-53
Calibrated Matrix Diffusion Coefficient Values

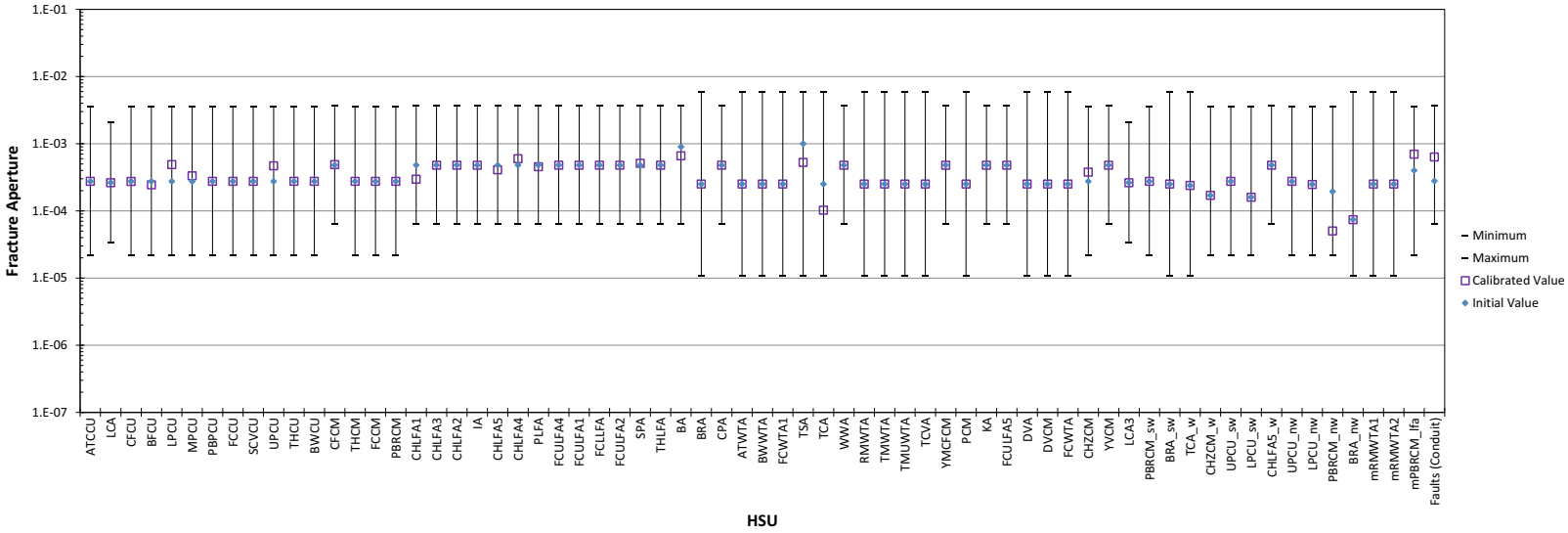

Figure 5-54
Calibrated Fracture Aperture Values

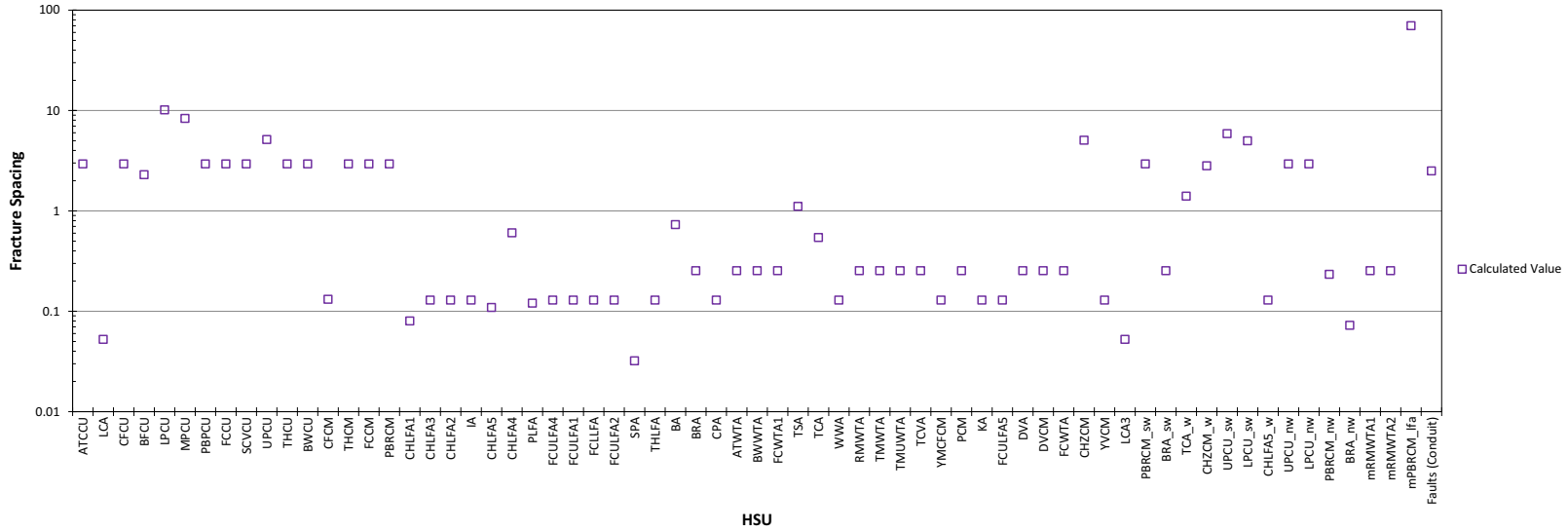

Figure 5-55
Calculated Fracture Spacing Values

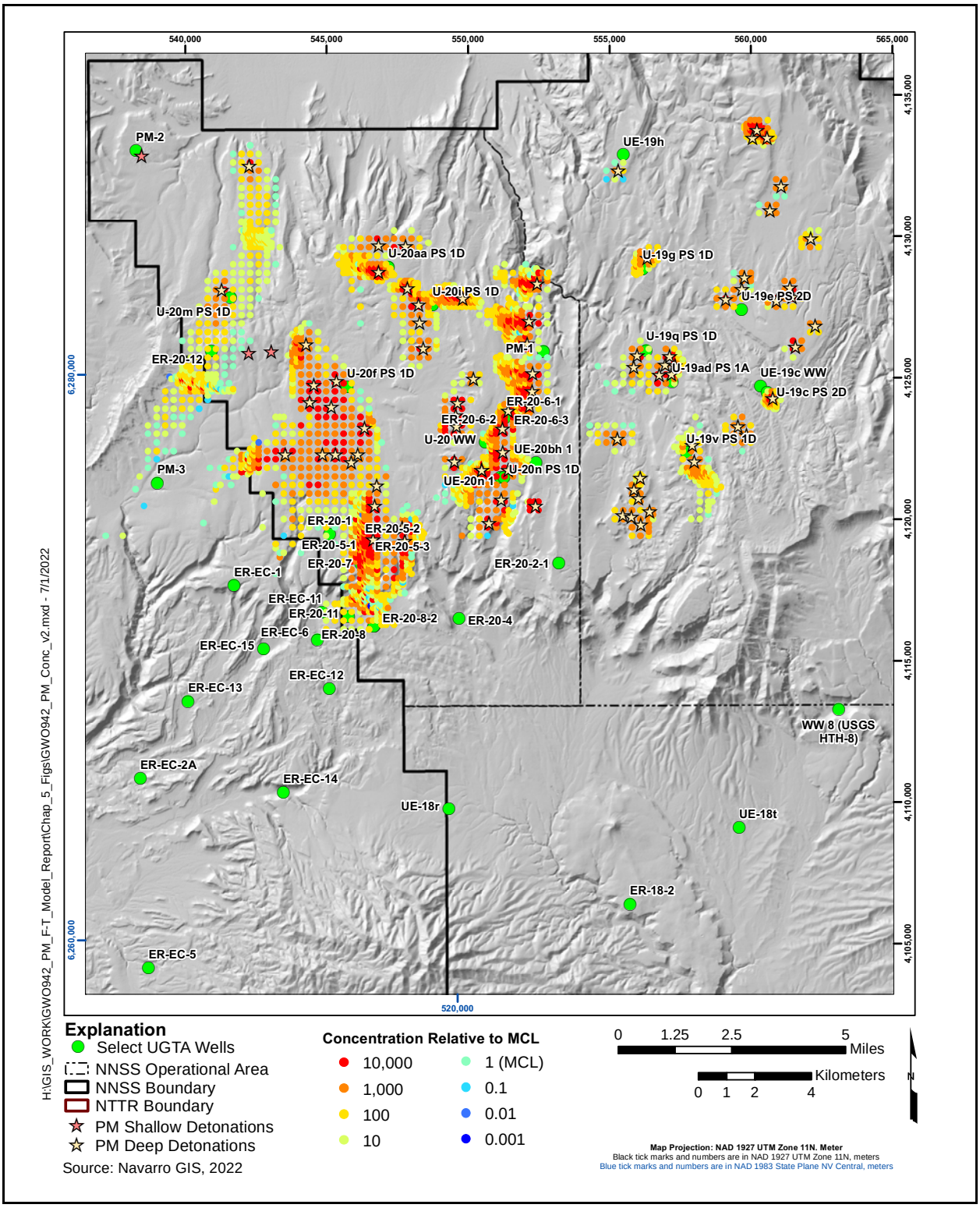

Figure 5-56
Simulated Extent of ^{3}H Contamination from Calibrated PM CAU Transport Model at 55 Years (2020)

Table 5-11
Observations of RNs Other than ^{3}H

(Page 1 of 5)

Well Name	Observation Date	Observed Concentration (pCi/L, unless otherwise noted)							
		^{14}C	^{36}Cl	^{90}Sr	^{99}Tc	^{129}I	^{137}Cs	$^{239/240}Pu$	U (μg/L)
ER-20-5-1_m1	06/03/1996	63.2	3.43	--	--	--	15.4	0.262	15
	04/22/1997	75.1	2.89	--	--	--	15.7	0.621	14.4
	07/09/1998	179	3.32	--	0.27	0.268	16.3	0.59	16.9
	11/30/2004	224	3.57	--	0.345	0.192	--	0.424	14.1
	04/26/2011	472	3.6	--	0.38	0.193	9.2	0.2912	12.9
	04/02/2015	164.66	5.7	--	0.428	0.195	--	0.4	--
	09/24/2019	--	6.6	--	--	--	--	--	14
ER-20-5-3_m1	07/31/1996	1.89	0.0102	--	--	--	0.143	0.03	500
	04/22/1997	1.89	0.00942	--	--	--	0.054	0.088	5.5
	04/30/1998	1.73	0.011	--	--	--	--	--	80.7
	11/15/2001	2.08	0.0218	--	--	0.0012	--	--	12.8
	11/29/2004	2.73	0.0131	--	0.017	0.0014	--	--	5.64
	04/26/2011	2.72	0.0126	--	0.004	0.000442	0.4	--	4.6
	03/13/2015	2.74	0.0142	--	0.00871	0.000404	--	0.0055	--
	09/17/2019	13.1	5.8	--	12.79	--	--	--	6.6
ER-20-7_m1	07/01/2009	--	--	--	--	--	--	0.068	6.3
	09/24/2010	165	2.41	--	16.4	0.132	--	0.1	8.23
	11/21/2014	118.37	2.52	--	3.06	0.135	--	0.0449	8.66
	08/31/2017	130	2.62	--	8.9	0.125	--	0.053	7.9

Table 5-11
Observations of RNs Other than ^{3}H
(Page 2 of 5)

Well Name	Observation Date	Observed Concentration (pCi/L, unless otherwise noted)							
		^{14}C	^{36}Cl	^{90}Sr	^{99}Tc	^{129}I	^{137}Cs	$^{239/240}Pu$	U (μg/L)
ER-20-8_p1	08/08/2011	0.064	0.00092	--	0	0.0000353	--	0	2.6
	09/27/2017	--	--	--	--	--	--	--	3.5
ER-20-8_m2	06/27/2011	0.197	0.00336	--	--	0.000206	--	0	2.85
	03/07/2015	0.3369	0.00549	--	0.13	0.000376	--	0	2.71
	09/14/2017	0.44	0.00699	--	0.248234	0.000479	--	0	2.6
ER-20-8-2_m1	12/18/2009	0.134	0.00209	--	0	0.0000927	--	0	2.6
	10/16/2014	0.2171	0.00339	--	0.0000747	0.000237	--	0	2.47
	09/19/2017	0.282	0.00468	--	0.0000955	0.000291	--	0	2.4
ER-20-11_m1	08/04/2013	3.8362	0.072572	--	0.953	0.00443	--	0	4.01
	10/18/2017	7.26	0.0895	--	0.97924	0.00663	--	0	3.8
ER-20-12_m1	08/19/2016	--	--	0	0.00536	0.0000464	--	0	6.4
	07/12/2017	--	--	0	0.0260218	--	--	0	6.3
ER-20-12_p1	07/06/2016	--	--	--	0	0.0000331	--	0	0.06
	07/17/2017	--	--	0	0.0631712	0.0000395	--	0	0.81
ER-20-12_p3	07/24/2017	--	--	0	0.0292745	0.00000594	--	0	0.33
ER-20-12_p4	07/06/2017	--	--	--	--	--	--	--	12
ER-EC-11_p3	08/25/2014	0.6265	0.00785	--	0.00045	0.000375	--	0	4.9
	10/12/2017	0.768	0.00973	--	0.0342391	0.000405	--	0	2.7

Table 5-11
Observations of RNs Other than ^{3}H
(Page 3 of 5)

Well Name	Observation Date	Observed Concentration (pCi/L, unless otherwise noted)							
		^{14}C	^{36}Cl	^{90}Sr	^{99}Tc	^{129}I	^{137}Cs	$^{239/240}Pu$	U (μg/L)
PM-3_p1	07/22/2011	--	--	--	--	--	--	0	--
	08/11/2013	--	--	--	--	--	--	0	--
	06/07/2018	--	--	--	--	--	--	0	--
PM-3_p2	07/22/2011	--	--	--	--	--	--	0	--
	09/13/2016	--	--	--	--	--	--	0	--
	06/14/2018	--	--	--	--	--	--	0	--
U-19ad_PS_1A	09/27/2004	404	9.18	1,780	378	1.94	28,900	15 and 53	2.2 and 3.32
	05/01/2008	158	7.17	--	25.4	1.32	12,100	7 and 47	1.36 and 2.71
U-19q_PS_1D	10/20/1998	1310	0.018	0	0.084	0.00407	7.9	0.21	--
	07/16/2003	293	0.0184	--	--	0.00198	11.9	--	2.61
U-19v_PS_1D	09/28/1993	--	--	--	--	--	--	0	0
	09/22/1998	94.2	--	--	0.2	--	--	0	0
	08/18/1999	35.6	2.1	--	--	1.39	--	9.45	0
	09/27/2000	101	3.7	--	--	2.76	--	0	0.02
	05/31/2001	93.3	3.6	--	--	2.33	--	0.183	0.03
	07/23/2003	74.4	5.62	--	--	2.54	--	0	0.11
	04/18/2006	76.2	4.68	--	0.1	2.58	--	0	0.03
	09/16/2009	76.4	32.6	--	2.89	2.73	--	--	0.13
U-20n_PS_1D_o1Z	09/13/1976	--	--	0	--	--	--	--	--

Table 5-11
Observations of RNs Other than ^{3}H
(Page 4 of 5)

Well Name	Observation Date	Observed Concentration (pCi/L, unless otherwise noted)							
		^{14}C	^{36}Cl	^{90}Sr	^{99}Tc	^{129}I	^{137}Cs	$^{239/240}Pu$	U (μg/L)
U-20n_PS_1D_o5Z	09/09/1983	--	--	126	67	--	2,940	0.22	--
	10/23/1984	--	--	90	51	0.32	3,750	0.216	--
	05/29/1985	--	--	121	38.3	--	2,750	--	--
U-20n_PS_1D_o2	05/25/1985	--	--	--	49	--	440	--	--
	05/28/1985	--	--	--	--	--	599	--	--
	06/18/1985	--	--	4.1	--	--	591	0.108	--
	09/11/1985	--	--	--	--	--	181	--	--
	10/01/1985	--	--	--	--	--	513	--	--
	11/07/1985	--	--	--	--	0.24	--	--	--
	07/19/1988	--	--	--	--	--	8.1	--	--
	09/14/1994	--	--	--	--	--	23.4	0.0853	--
	06/18/1996	--	--	--	--	--	25.1	--	--
	07/22/1997	37.8	--	23.2	--	--	23.5	0	4
	07/28/1998	111	0.246	0	31	--	4.2	0	3.1
	09/21/1998	--	--	--	--	--	1644.24	0.61	0
U-20n_PS_1D_o3Z	09/21/1998	211	0.497	--	20	--	1540	0.468	2.64
	10/12/1999	200	0.42	--	22.3	0.11	1570	0.6	2.3
	07/09/2003	183	0.8	--	12.3	0.15	1970	0.31	2.07
	11/15/2005	--	0.48	--	0.93	0.14	--	0.46	0.36

Table 5-11
Observations of RNs Other than ^{3}H
(Page 5 of 5)

Well Name	Observation Date	Observed Concentration (pCi/L, unless otherwise noted)							
		^{14}C	^{36}Cl	^{90}Sr	^{99}Tc	^{129}I	^{137}Cs	$^{239/240}Pu$	U (μg/L)
U-20n_PS_1D_m2	11/19/2019	135.8	--	--	33.89	--	745	0.385	2.39
UE-20n_1_o2	07/20/1987	--	--	--	--	--	3.17	--	--
	10/27/1987	--	--	--	--	--	0.33	--	--
	02/09/1988	--	--	--	--	--	1.35	--	--
	05/10/1988	--	--	--	--	--	0.11	--	--
	07/19/1988	--	--	--	--	--	0.1	--	--
	05/24/2012	218	--	--	--	--	0.003	--	2.88
	11/06/2019	279.33	--	--	0	0	--	--	2.6

-- = Not analyzed

Note: Observed values below the analytical detection level are reported as zero.

Sr, Cs, U, and Pu are sorbing RNs, and as such, require a matrix sorption coefficient (K_d) to be specified in the PLUMECALC inputs. Two forward runs were made with each sorbing RN, one using the minimum K_d for all zones and one using the maximum K_d for all zones. This was done to establish a range of possible outcomes for each sorbing RN. K_d ranges for each HSU zone for each RN are provided in Appendix G. Like the other transport parameters that were used in the calibration, it is assumed that K_d values are uniform in each zone.

Observations of Pu are reported as $^{239/240}$Pu; thus, forward runs of ^{239}Pu and ^{240}Pu were made independently, and the resulting concentrations were summed for comparison to observed values. Likewise, observations of U are reported as total U; thus, forward runs of ^{232}U, ^{233}U, ^{234}U, and ^{238}U were made independently, and the resulting concentrations were summed for comparison to observed values.

Agreement with observation data was evaluated with scatter-plots, specifically plots of modeled versus measured values of concentration and plots of modeled and measured concentrations versus time.

5.5.1.4.1 ^{14}C Results

Figure 5-57 shows a plot of the simulated versus observed ^{14}C concentrations in log space for observation locations near postshot holes in the PM CAU transport model. Good agreement between measured and modeled values is achieved with the model either overpredicting or underpredicting within approximately 1 order of magnitude at these locations.

Figure 5-58 shows a plot of the simulated versus observed ^{14}C concentrations in log space for observation locations near the Bench in the PM CAU transport model. Zero values were approximated with a value of 1E-06, resulting in a log value of -6. With the exception of ER-20-5-3_m1, good agreement between measured and modeled values is achieved with the model either overpredicting or underpredicting within approximately 1 order of magnitude at these locations. As discussed in Section 5.5.1.3, the poor agreement at ER-20-5-3_m1 is likely due to the deeper flow path from BENHAM passing to the east of the defined observation nodes.

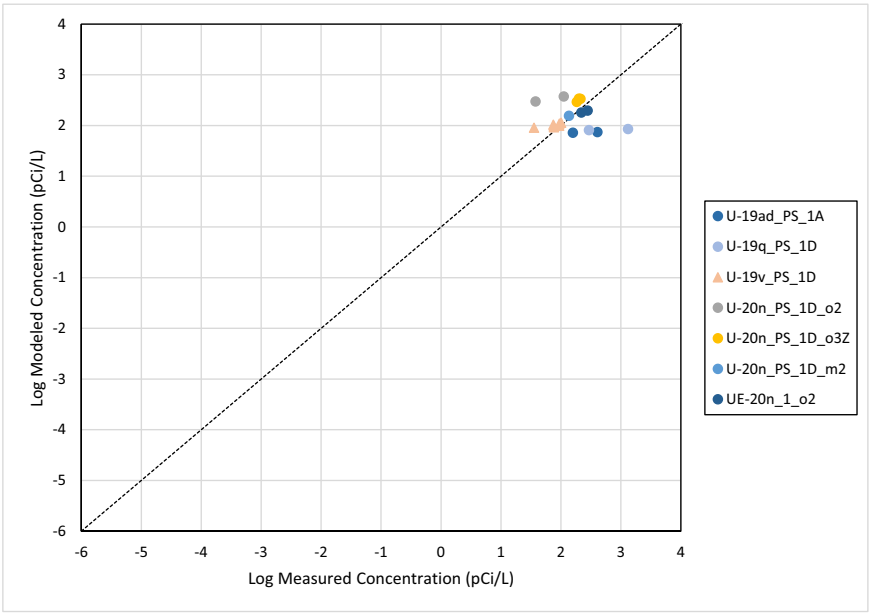

Figure 5-57
Modeled versus Measured ^{14}C Concentrations for the Postshot Holes in the PM CAU Transport Model

Note: While not a postshot hole, UE-20n_1_o2 is included here for convenience.

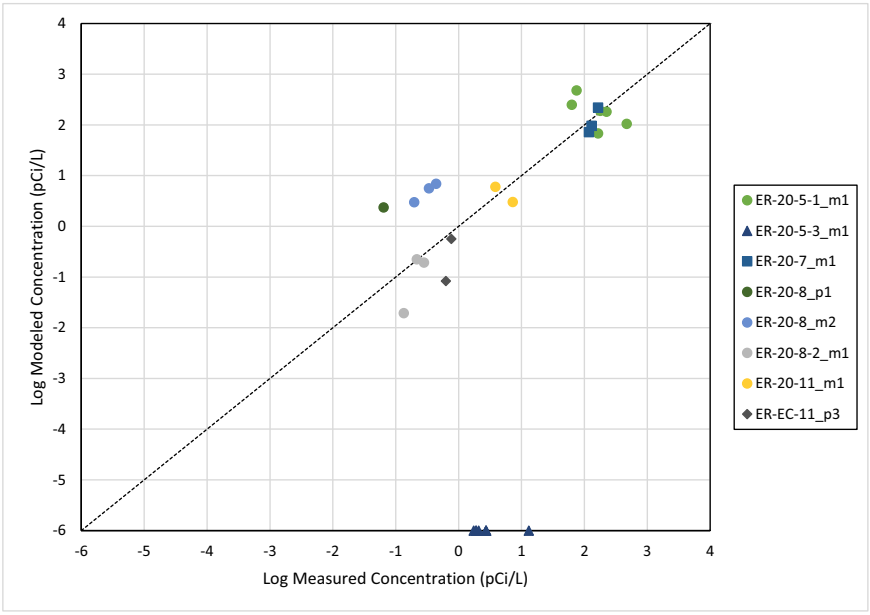

Figure 5-58
Modeled versus Measured ^{14}C Concentrations near the Bench in the PM CAU Transport Model

Plots of modeled and measured ^{14}C concentrations over time at these observation locations are shown in Appendix H in Figures H-65 through H-79.

5.5.1.4.2 ^{36}Cl Results

Figure 5-59 shows a plot of the simulated versus observed ^{36}Cl concentrations in log space for observation locations near postshot holes in the PM CAU transport model. The model overpredicts ^{36}Cl at these locations by approximately 1 to 3 orders of magnitude. In the discussion of calibrated ^{3}H results in Section 5.5.1.3, it is stated that the observation locations at the postshot holes are coincident with nodes where the source particles are located, meaning that very little transport has occurred between the source locations and measurement locations. Because of this and because ^{36}Cl is nonsorbing, the only feasible explanation for the overprediction of ^{36}Cl at some postshot locations is that the source mass input to the model at these locations is high. This suggests that ^{36}Cl source mass input to the PM CAU transport model may be conservatively high at the sources near these observation locations (CHANCELLOR, CAMEMBERT, ALMENDRO, and CHESHIRE).

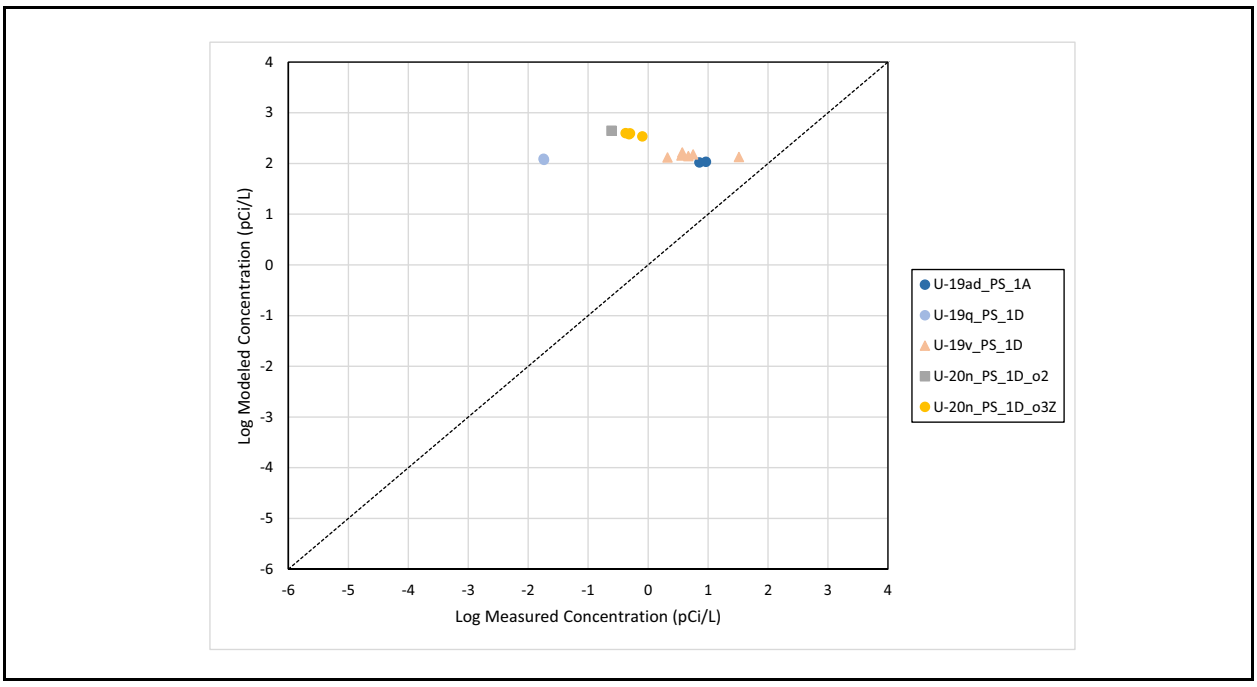

Figure 5-59
Modeled versus Measured ^{36}Cl Concentrations for the Postshot Holes in the PM CAU Transport Model

Figure 5-60 shows a plot of the simulated versus observed ^{36}Cl concentrations in log space for observation locations near the Bench in the PM CAU transport model. Zero values were approximated with a value of 1E-06, resulting in a log value of -6. With the exception of ER-20-5-3_m1, the model overpredicts ^{36}Cl at these locations by approximately 1 to 3 orders of magnitude. Again, this suggests that ^{36}Cl source mass input to the PM CAU transport model may be conservatively high at the sources that contribute RNs at these observation locations. As discussed in Section 5.5.1.3, the poor agreement at ER-20-5-3_m1 is likely due to the deeper flow path from BENHAM passing to the east of the defined observation nodes.

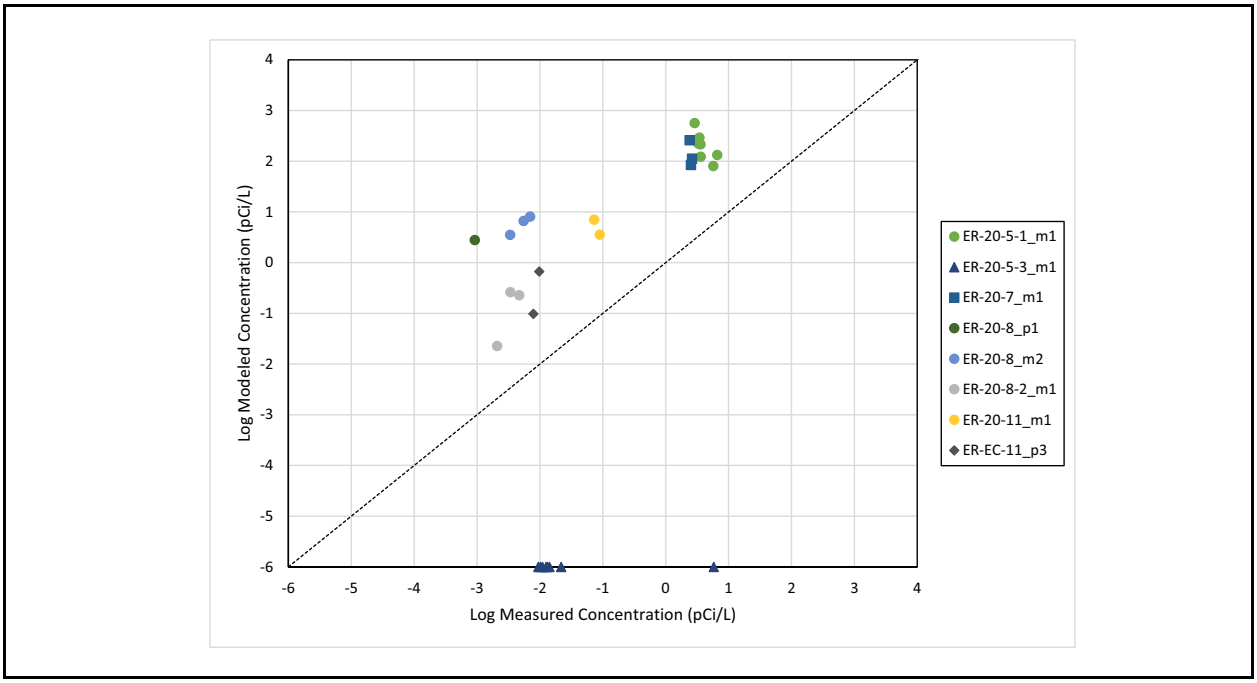

Figure 5-60
Modeled versus Measured ^{36}Cl Concentrations near the Bench in the PM CAU Transport Model

Plots of modeled and measured ^{36}Cl concentrations over time at these observation locations are shown in Appendix H in Figures H-80 through H-92.

5.5.1.4.3 ^{90}Sr Results

Figure 5-61 shows a plot of the simulated versus observed ^{90}Sr concentrations in log space for observation locations near postshot holes in the PM CAU transport model. Modeled concentrations at each observation location are represented by two end points connected by a bar. The two end points

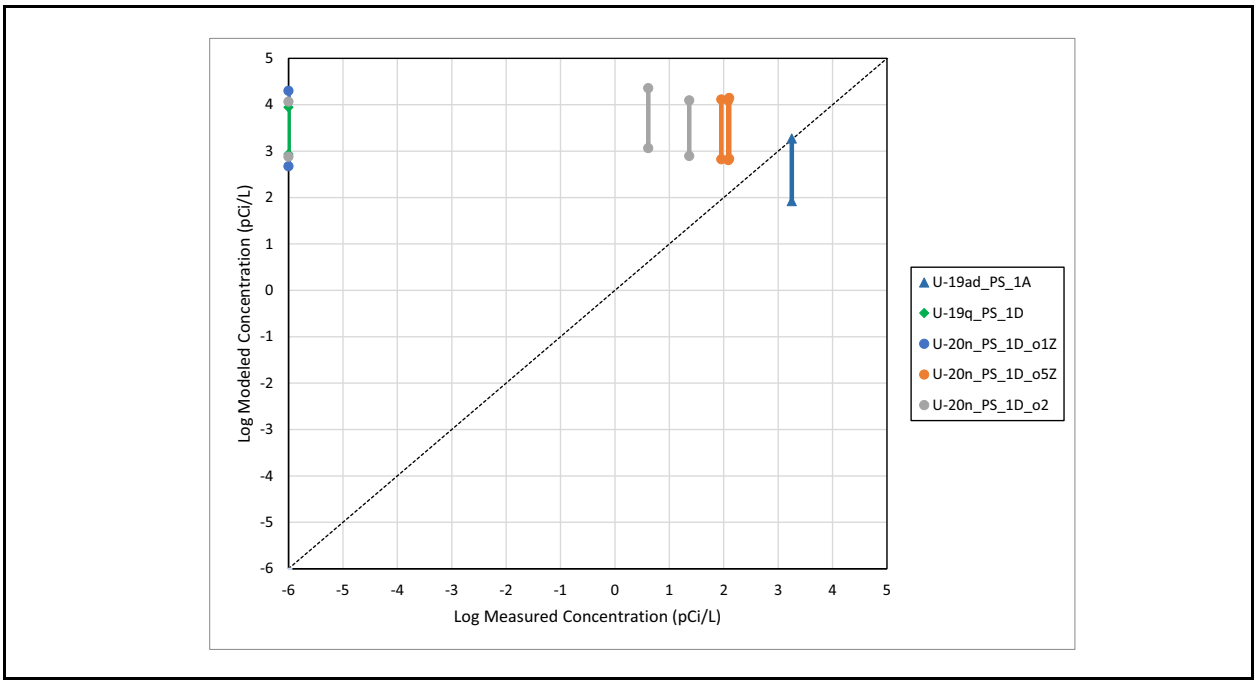

Figure 5-61
Modeled versus Measured ^{90}Sr Concentrations for the Postshot Holes in the PM CAU Transport Model

represent concentrations calculated using either minimum K_d for all zones or maximum K_d for all zones, and the bar represents the range of possible calculated concentrations when K_ds are varied. There is good agreement at U-19ad PS 1A (CHANCELLOR), where the modeled concentration range spans a range of values that is near the measured value at the upper end to a value that underpredicts by approximately 1 order of magnitude. At the other postshot locations, the modeled concentration range overpredicts measured values by a range of 1 to several orders of magnitude. This suggests that ^{90}Sr source mass input to the PM CAU transport model may be conservatively high at the sources that contribute RNs at these observation locations (CAMEMBERT and CHESHIRE).

Figure 5-62 shows a plot of the simulated versus observed ^{90}Sr concentrations in log space for observation locations at ER-20-12, downgradient of HANDLEY. Zero values were approximated with a value of 1E-06, resulting in a log value of -6. All ^{90}Sr observations are zero (or below detection limit), but the model shows high concentrations, indicating poor agreement at this location. This suggests that ^{90}Sr source mass input to the PM CAU transport model at HANDLEY may be conservatively high.

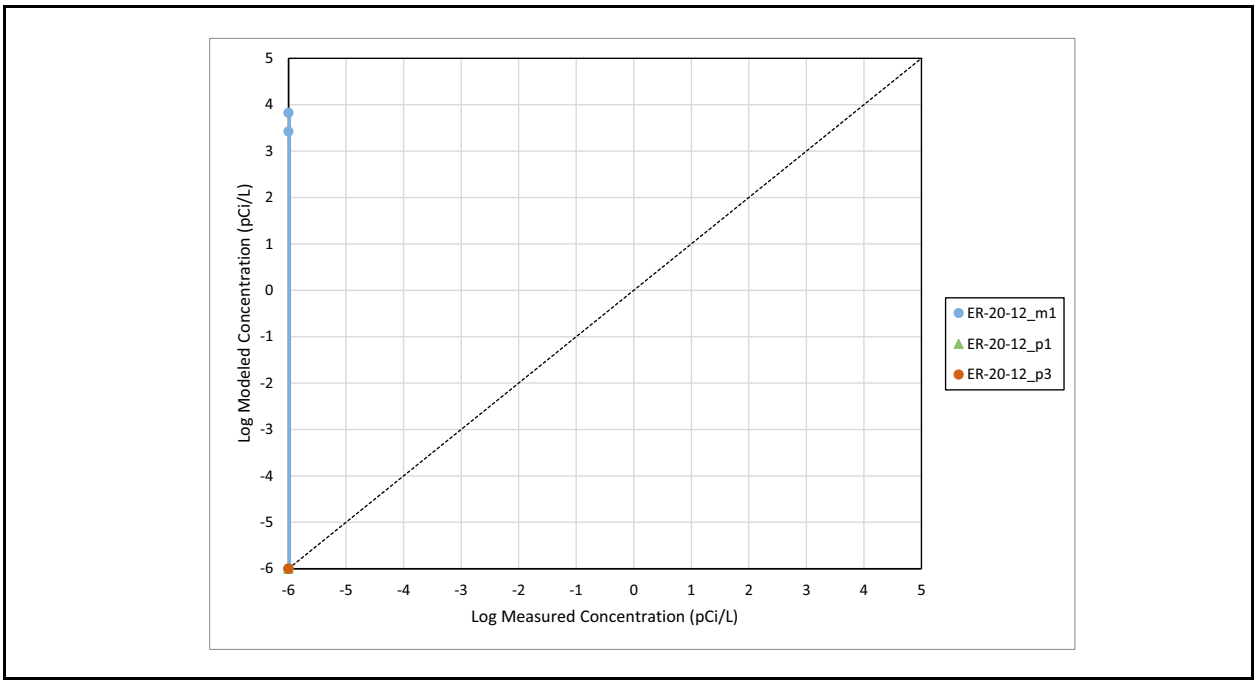

Figure 5-62
Modeled versus Measured ^{90}Sr Concentrations near HANDLEY in the PM CAU Transport Model

Plots of modeled and measured ^{90}Sr concentrations over time at these observation locations are shown in Appendix H in Figures H-93 through H-100.

5.5.1.4.4 ^{99}Tc Results

Figure 5-63 shows a plot of the simulated versus observed ^{99}Tc concentrations in log space for observation locations near postshot holes in the PM CAU transport model. Zero values were approximated with a value of 1E-06, resulting in a log value of -6. Good agreement between measured and modeled values is achieved at U-19ad PS 1A (CHANCELLOR). The model overpredicts ^{99}Tc concentrations by 3 orders of magnitude at U-19q PS 1D (CAMEMBERT) and by 2 to 3 orders of magnitude at U-19v PS 1D (ALMENDRO). At CHESHIRE, fairly good agreement is achieved at U-20n PS 1D_o5Z, U-20n PS 1D_o2, and U-20n PS 1D_m2, with the model overpredicting ^{99}Tc concentrations by less than an order of magnitude. However, the model overpredicts at the remaining CHESHIRE locations by up to several orders of magnitude. These results suggest that ^{99}Tc source mass input to the PM CAU transport model at CHESHIRE may be conservatively high.

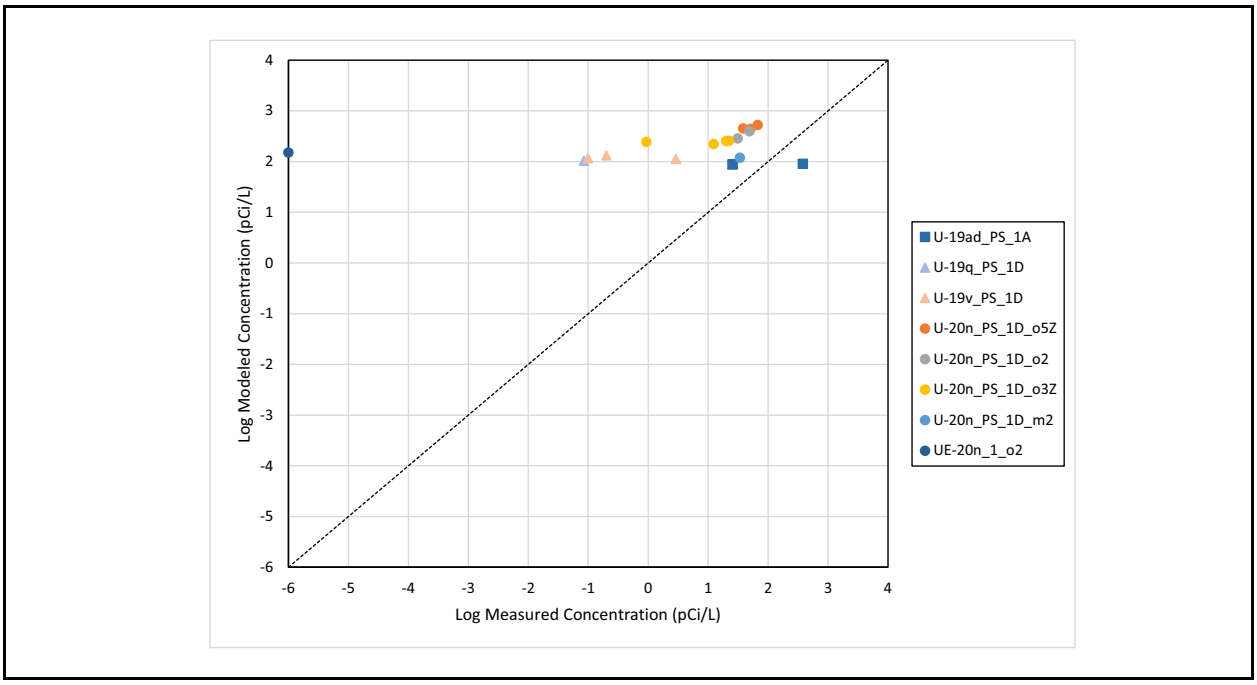

Figure 5-63
Modeled versus Measured ^{99}Tc Concentrations for the Postshot Holes in the PM CAU Transport Model
Note: While not a postshot hole, UE-20n_1_o2 is included here for convenience.

Figure 5-64 shows a plot of the simulated versus observed ^{99}Tc concentrations in log space for observation locations near the Bench in the PM CAU transport model. Zero values were approximated with a value of 1E-06, resulting in a log value of -6. The model overpredicts ^{99}Tc concentrations at these locations by up to several orders of magnitude. Good agreement is achieved at ER-20-11_m1. These results suggest that ^{99}Tc source mass input to the PM CAU transport model may be conservatively high at the sources that contribute RNs at these observation locations. The model predicts no ^{99}Tc at ER-20-5-3_m1. As discussed in Section 5.5.1.3, the poor agreement at ER-20-5-3_m1 is likely due to the deeper flow path from BENHAM passing to the east of the defined observation nodes.

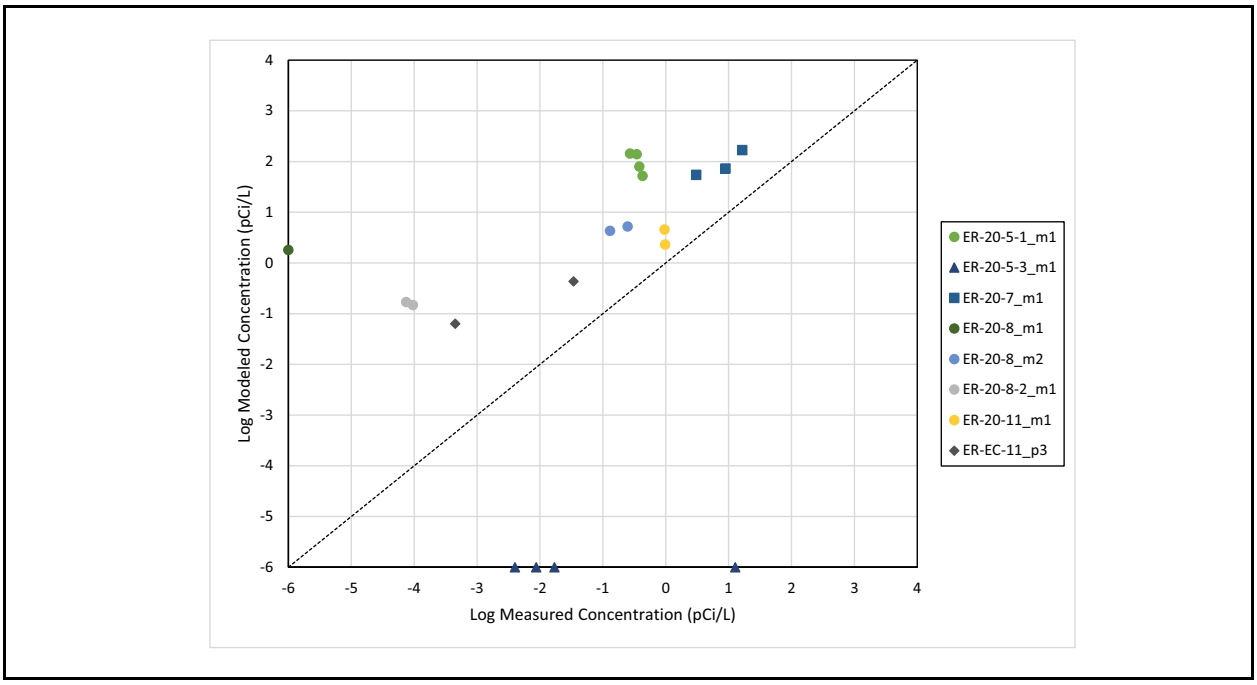

Figure 5-64
Modeled versus Measured ^{99}Tc Concentrations near the Bench in the PM CAU Transport Model

Figure 5-65 shows a plot of the simulated versus observed ^{99}Tc concentrations in log space for observation locations near HANDLEY in the PM CAU transport model. Zero values were approximated with a value of 1E-06, resulting in a log value of -6. The model overpredicts ^{99}Tc concentrations at ER-20-12_m1 (in the PBRCM) and ER-20-12_p1 (in the BRA), although fairly good agreement is achieved for one observation at ER-20-12_p1. However, the model shows no ^{99}Tc at ER-20-12_p3 (in the CHLFA5). These results are somewhat consistent with the modeled ^{3}H concentrations at ER-20-12 (see Figure 5-32), except that modeled ^{3}H values at ER-20-12_m1 and ER-20-12_p1 were much closer to observed values. This suggests that ^{99}Tc source mass input to the PM CAU transport model at HANDLEY may be conservatively high.

Plots of modeled and measured ^{99}Tc concentrations over time at these observation locations are shown in Appendix H in Figures H-101 through H-119.

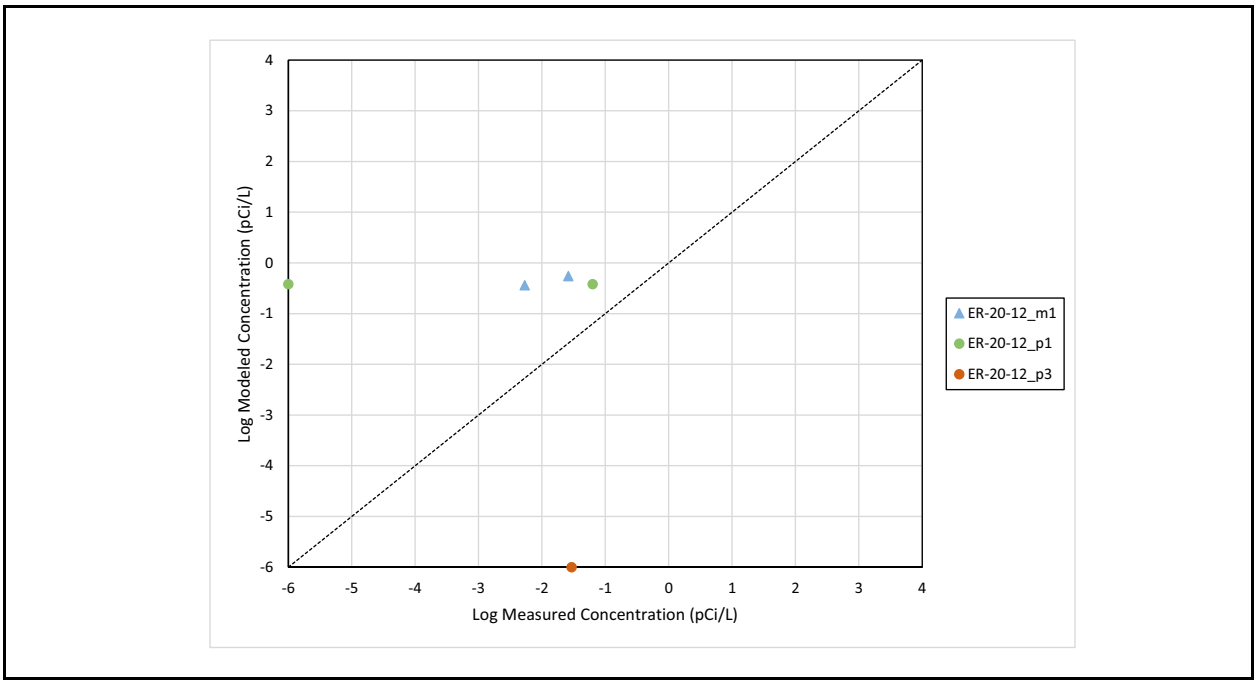

Figure 5-65
Modeled versus Measured ^{99}Tc Concentrations near HANDLEY in the PM CAU Transport Model

5.5.1.4.5 ^{129}I Results

Figure 5-66 shows a plot of the simulated versus observed ^{129}I concentrations in log space for observation locations near postshot holes in the PM CAU transport model. Zero values were approximated with a value of 1E-06, resulting in a log value of -6. Good agreement between measured and modeled values is achieved at U-19ad PS 1A (CHANCELLOR) and U-19v PS 1D (ALMENDRO), with the model underpredicting ^{129}I concentrations by less than 1 order of magnitude at these locations. At U-20n PS 1D (CHESHIRE), the model overpredicts ^{129}I concentrations by approximately 1 order of magnitude. The observed values of ^{129}I at UE-20n_1 (CHESHIRE) is zero (or below detection limit), but the model calculates a concentration of 0.829 pCi/L (log value of -0.0814) at this location. The model also overpredicts ^{129}I concentrations at U-19q PS 1D (CAMEMBERT) by 2 to 3 orders of magnitude. These results suggest that ^{129}I source mass input to the PM CAU transport model at CHESHIRE and CAMEMBERT may be conservatively high.

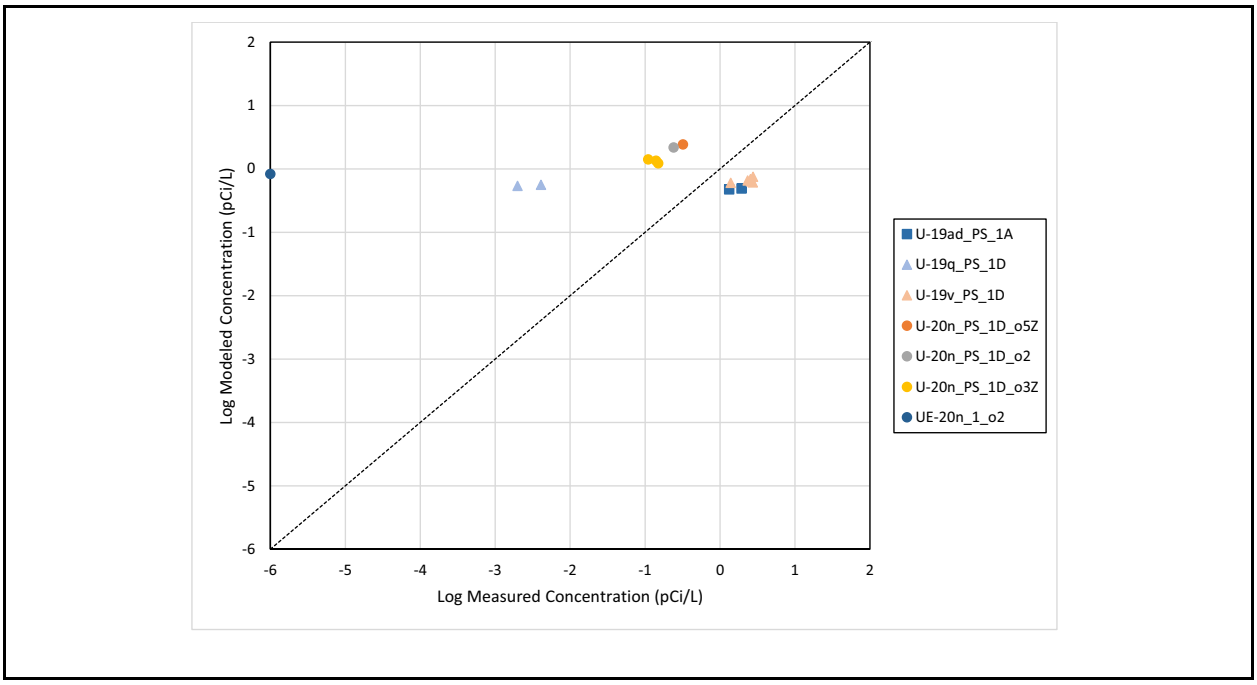

Figure 5-66
Modeled versus Measured ^{129}I Concentrations for the Postshot Holes in the PM CAU Transport Model
Note: While not a postshot hole, UE-20n_1_o2 is included here for convenience.

Figure 5-67 shows a plot of the simulated versus observed ^{129}I concentrations in log space for observation locations near the Bench in the PM CAU transport model. Zero values were approximated with a value of 1E-06, resulting in a log value of -6. At ER-20-5-1 (in the TSA), ER-20-7 (in the TSA), ER-20-11 (in the BA), ER-EC-11_p3 (in the BA), and ER-20-8-2 (in the SPA) good agreement between measured and modeled values is achieved with the model overpredicting ^{129}I concentrations within 1 order of magnitude at these locations. At ER-20-8_p1 (in the CHZCM) and ER-20-8_m2 (in the TCA) the model overpredicts ^{129}I concentrations by 2 to 3 orders of magnitude. The model predicts no ^{129}I at ER-20-5-3_m1 (in the CHLFA5). As discussed in Section 5.5.1.3, the poor agreement at ER-20-5-3_m1 is likely due to the deeper flow path from BENHAM passing to the east of the defined observation nodes.

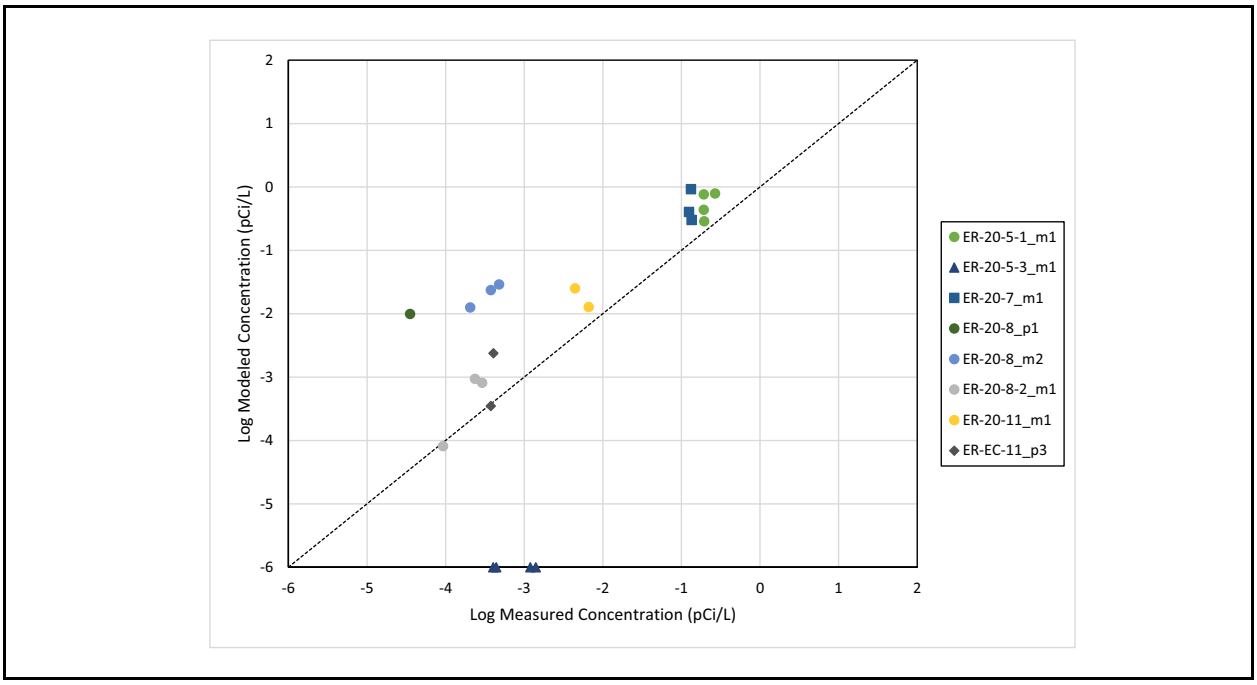

Figure 5-67
Modeled versus Measured ^{129}I Concentrations near the Bench in the PM CAU Transport Model

Figure 5-68 shows a plot of the simulated versus observed ^{129}I concentrations in log space for observation locations near HANDLEY in the PM CAU transport model. Zero values were approximated with a value of 1E-06, resulting in a log value of -6. The model overpredicts ^{129}I concentrations at ER-20-12_m1 (in the PBRCM) and ER-20-12_p1 (in the BRA) by approximately 2 orders of magnitude. However, the model shows no ^{129}I at ER-20-12_p3 (in the CHLFA5). These results are somewhat consistent with the modeled ^{3}H concentrations at ER-20-12 (see Figure 5-32), except that modeled ^{3}H values at ER-20-12_m1 and ER-20-12_p1 were much closer to observed values. This suggests that ^{129}I source mass input to the PM CAU transport model at HANDLEY may be conservatively high.

Plots of modeled and measured ^{129}I concentrations over time at these observation locations are shown in Appendix H in Figures H-120 through H-137.

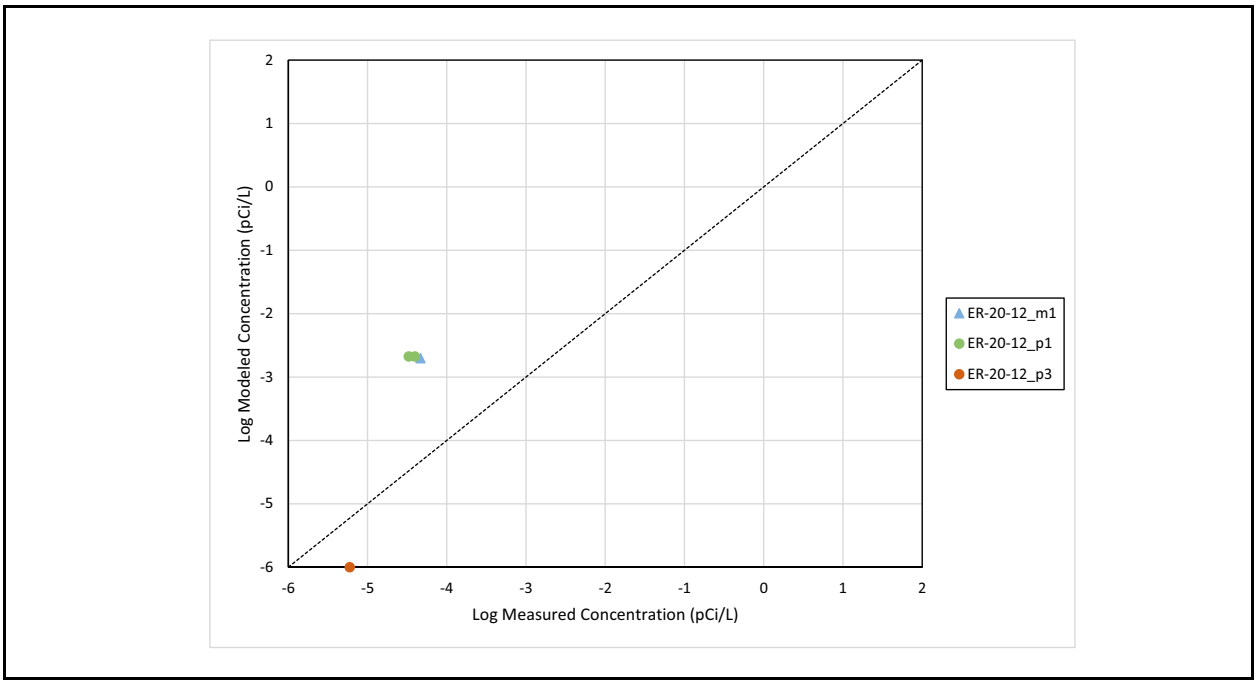

Figure 5-68
Modeled versus Measured ^{129}I Concentrations near HANDLEY in the PM CAU Transport Model

5.5.1.4.6 ^{137}Cs Results

Figure 5-69 shows a plot of the simulated versus observed ^{137}Cs concentrations in log space for observation locations near postshot holes in the PM CAU transport model. Modeled concentrations at each observation location are represented by two end points connected by a bar. The two end points represent concentrations calculated using either minimum K_d for all zones or maximum K_d for all zones, and the bar represents the range of possible calculated concentrations when K_ds are varied. Zero values were approximated with a value of 1E-06, resulting in a log value of -6.

There is good agreement at U-19q PS 1D (CAMEMBERT) where the observed ^{137}Cs concentrations are bracketed by the range of modeled ^{137}Cs concentrations. Modeled results at CHESHIRE (U-20n PS 1D and UE-20n_1) are varied. There is good agreement at U-20n PS 1D_o5Z and U-20n PS 1D_o3Z where the observed ^{137}Cs concentrations are bracketed by the range of modeled ^{137}Cs concentrations. There is also fairly good agreement at U-20n PS 1D_m2, where the range of modeled ^{137}Cs concentrations is less than observed value by approximately 1 order of magnitude. At U-20n PS 1D_o2, 5 of the 11 observations are bracketed by the range of modeled ^{137}Cs concentrations, and the

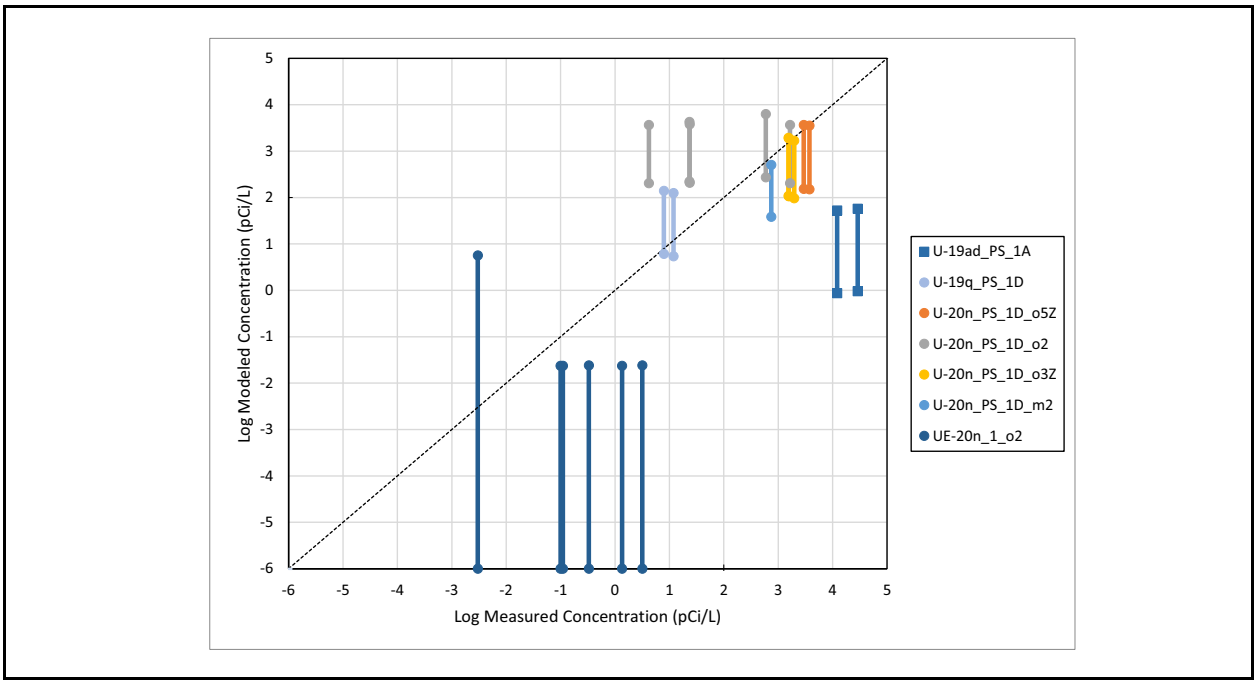

Figure 5-69
Modeled versus Measured ^{137}Cs Concentrations for the Postshot Holes in the PM CAU Transport Model
Note: While not a postshot hole, UE-20n_1_o2 is included here for convenience.

remaining observations are overpredicted by 2 to 3 orders of magnitude. At UE-20n_1 (CHESHIRE) only one observation is bracketed by the range of modeled ^{137}Cs concentrations, with the remaining observations being underpredicted by the range of modeled ^{137}Cs concentrations.

Figure 5-70 shows a plot of the simulated versus observed ^{137}Cs concentrations in log space for observation locations at ER-20-5-1 (in the TSA) and ER-20-5-3 (in the CHLFA5), near the Bench. Zero values were approximated with a value of 1E-06, resulting in a log value of -6. The model overpredicts ^{137}Cs concentrations at ER-20-5-1 by 2 to 3 orders of magnitude. The model predicts no ^{137}Cs at ER-20-5-3_m1. As discussed in Section 5.5.1.3, the poor agreement at ER-20-5-3_m1 is likely due to the deeper flow path from BENHAM passing to the east of the defined observation nodes.

Plots of modeled and measured ^{137}Cs concentrations over time at these observation locations are shown in Appendix H in Figures H-138 through H-146.

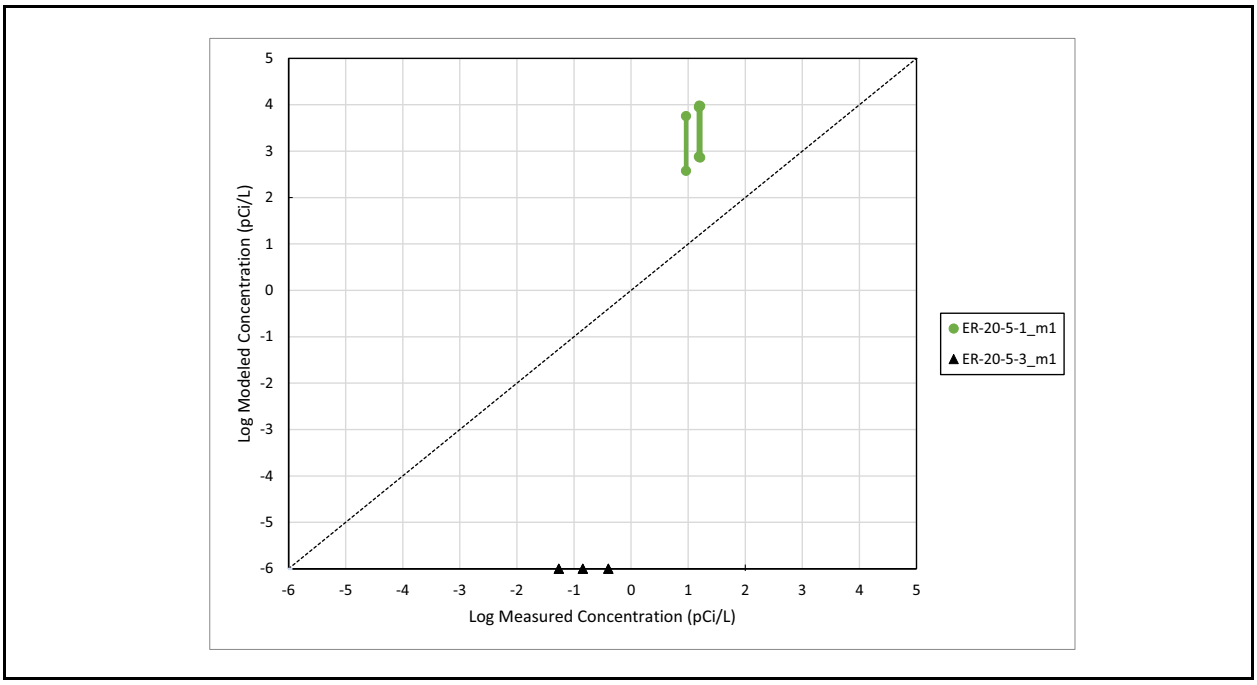

Figure 5-70
Modeled versus Measured ^{137}Cs Concentrations near the Bench in the PM CAU Transport Model

5.5.1.4.7 U (Total) Results

Figure 5-71 shows a plot of the simulated versus observed U (total) concentrations in log space for observation locations near postshot holes in the PM CAU transport model. Modeled concentrations at each observation location are represented by two end points connected by a bar. The two end points represent concentrations calculated using either minimum K_d for all zones or maximum K_d for all zones, and the bar represents the range of possible calculated concentrations when K_ds are varied. Zero values were approximated with a value of 1E-06, resulting in a log value of -6.

There is good agreement at U-19q PS 1D (CAMEMBERT) where the observed U (total) concentrations are bracketed by the range of modeled U (total) concentrations. At CHESHIRE, there is good agreement at UE-20n_1 and U-20n PS 1D_m2, where the observed U (total) concentrations are bracketed by the range of modeled U (total) concentrations. There is fairly good agreement at U-20n PS 1D_o2 and U-20n PS 1D_o3Z, where the range of modeled U (total) concentrations overpredicts observed U (total) concentrations by up to 2 orders of magnitude. The most recent observation at U-20n PS 1D_o2 shows no U (or below detection limit) where the modeled

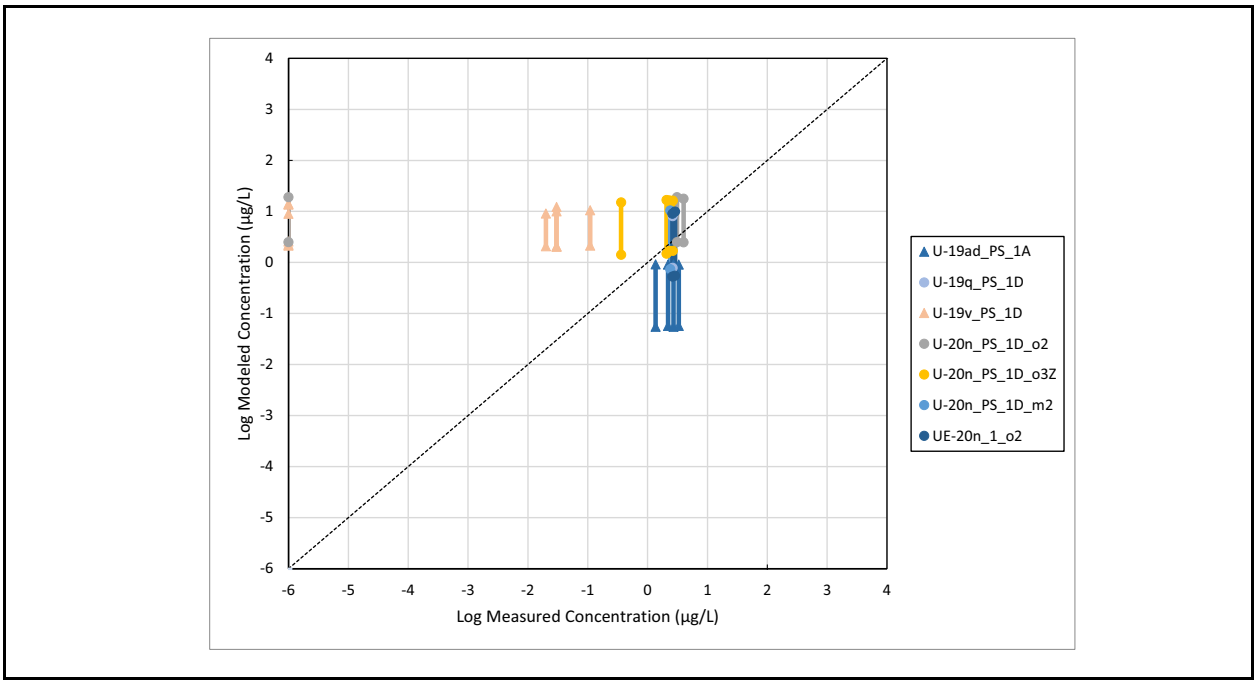

Figure 5-71
Modeled versus Measured U Concentrations for the Postshot Holes in the PM CAU Transport Model
Note: While not a postshot hole, UE-20n_1_o2 is included here for convenience.

concentration ranges from 2.51 µg/L to 19.1 µg/L (0.399 to 1.28 in log space). At most of the observations at U-19v PS 1D (ALMENDRO) the model overpredicts by up to 3 orders of magnitude. The earliest observations at U-19v PS 1D show no U (or below detection limit) where the modeled concentration ranges from 2.14 µg/L to 14.0 µg/L (0.33 to 1.15 in log space). At U-19ad PS 1A (CHANCELLOR) the model underpredicts by up to 2 orders of magnitude.

Figure 5-72 shows a plot of the simulated versus observed U (total) concentrations in log space for observation locations near the Bench in the PM CAU transport model. Modeled concentrations at each observation location are represented by two end points connected by a bar. The two end points represent concentrations calculated using either minimum K_d for all zones or maximum K_d for all zones, and the bar represents the range of possible calculated concentrations when K_ds are varied. Zero values were approximated with a value of 1E-06, resulting in a log value of -6. At ER-20-5-1 (in the TSA) and ER-20-7 (in the TSA), good agreement between measured and modeled U (total) concentrations is achieved with the ranges of modeled concentrations bracketing observations on the higher sides of the ranges. The model predicts no U at ER-20-5-3_m1 (in the CHLFA5). As discussed

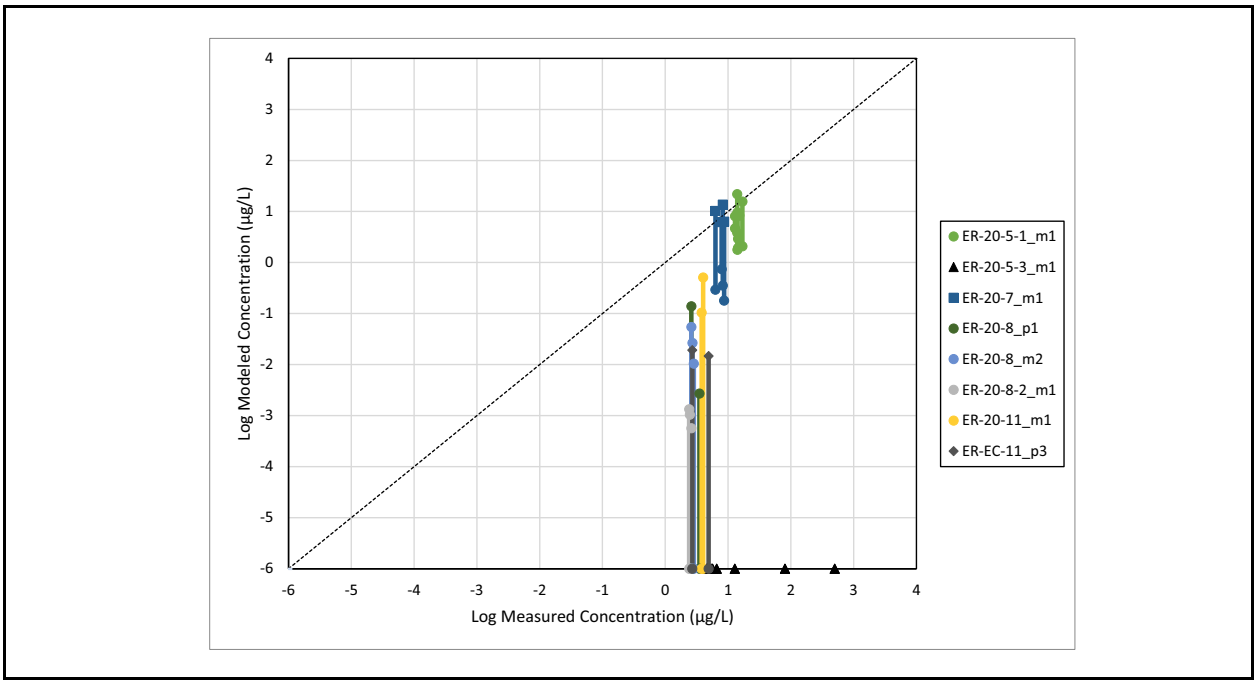

Figure 5-72
Modeled versus Measured U Concentrations near the Bench in the PM CAU Transport Model

in Section 5.5.1.3, the poor agreement at ER-20-5-3_m1 is likely due to the deeper flow path from BENHAM passing to the east of the defined observation nodes. At locations further downgradient, ER-20-8_p1 (in the CHZCM), ER-20-8_m2 (in the TCA), ER-20-8-2 (in the SPA), ER-20-11 (in the BA), and ER-EC-11_p3 (in the BA), the model generally underpredicts U (total) concentrations by up to several orders of magnitude.

Figure 5-73 shows a plot of the simulated versus observed U (total) concentrations in log space for observation locations near HANDLEY in the PM CAU transport model. Modeled concentrations at each observation location are represented by two end points connected by a bar. The two end points represent concentrations calculated using either minimum K_d for all zones or maximum K_d for all zones, and the bar represents the range of possible calculated concentrations when K_ds are varied. Zero values were approximated with a value of 1E-06, resulting in a log value of -6. The model underpredicts U (total) concentrations at ER-20-12_m1 (in the PBRCM) and ER-20-12_p1 (in the BRA) by 2 to 3 orders of magnitude. There is poor agreement at ER-20-12_p3 (in the CHLFA5), where the model shows no U although it has been observed. The poor agreement at ER-20-12_p3 is similar to poor agreement with ^{3}H results (see Figure 5-32).

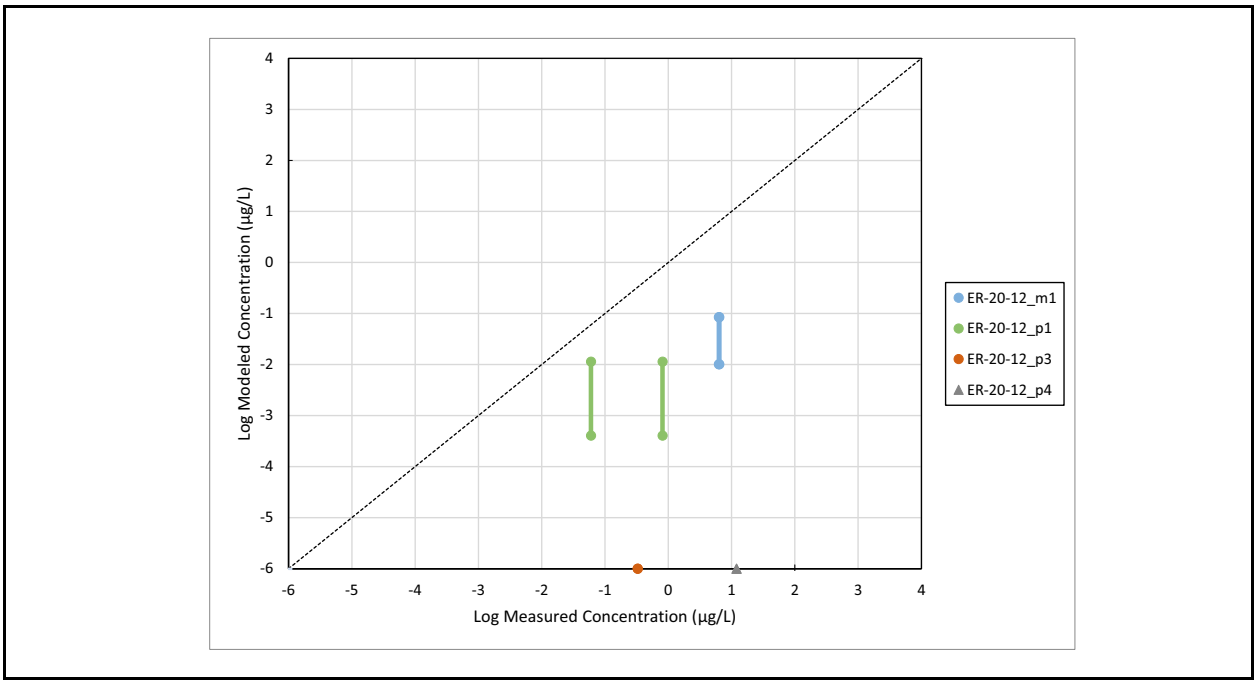

Figure 5-73
Modeled versus Measured U Concentrations near HANDLEY in the PM CAU Transport Model

Naturally occurring U is known to be present in PM; thus, field measurements of U would contain both naturally occurring as well as U from nuclear detonations. Because naturally occurring U is not modeled, underprediction of U by the model is not surprising.

Plots of modeled and measured U (total) concentrations over time at these observation locations are shown in Appendix H in Figures H-147 through H-165.

5.5.1.4.8 $^{239/240}$Pu Results

Figure 5-74 shows a plot of the simulated versus observed $^{239/240}$Pu concentrations in log space for observation locations near postshot holes in the PM CAU transport model. Modeled concentrations at each observation location are represented by two end points connected by a bar. The two end points represent concentrations calculated using either minimum K_d for all zones or maximum K_d for all zones, and the bar represents the range of possible calculated concentrations when K_ds are varied. Zero values were approximated with a value of 1E-06, resulting in a log value of -6.

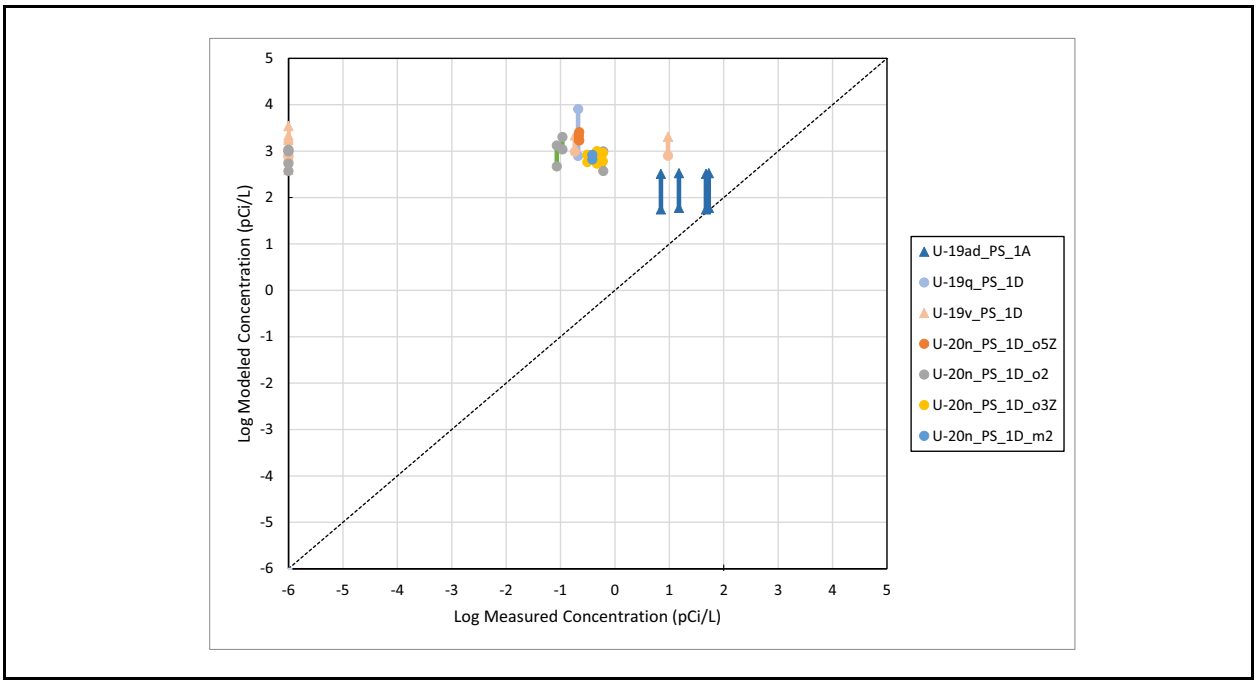

Figure 5-74
Modeled versus Measured $^{239/240}$Pu Concentrations for the Postshot Holes in the PM CAU Transport Model

The model overpredicts $^{239/240}$Pu concentrations at all postshot observation locations. At U-19ad PS 1A (CHANCELLOR) the range of modeled values overpredicts $^{239/240}$Pu concentrations by 1 to 2 orders of magnitude. At U-19q PS 1D (CAMEMBERT), the range of modeled values overpredicts $^{239/240}$Pu concentrations by 3 to 4 orders of magnitude. At U-19v PS 1D (ALMENDRO), the range of modeled $^{239/240}$Pu concentrations in log space is typically between 2.8 and 3.3, even for the observations where there is no Pu. Non-zero observations are overpredicted by 2 to 4 orders of magnitude. At U-20n PS 1D (CHESHIRE), the range of modeled $^{239/240}$Pu concentrations in log space is typically between 2.6 and 3.3, even for the observations where there is no Pu. Non-zero observations are overpredicted by 3 to 4 orders of magnitude. The large overprediction of $^{239/240}$Pu concentrations at the postshot observation locations suggests that the ^{239}Pu and ^{240}Pu source masses input to the PM CAU transport model at these locations may be conservatively high.

Figure 5-75 shows a plot of the simulated versus observed $^{239/240}$Pu concentrations in log space for observation locations near the Bench in the PM CAU transport model. Modeled concentrations at each observation location are represented by two end points connected by a bar. The two end points represent concentrations calculated using either minimum K_d for all zones or maximum K_d for all

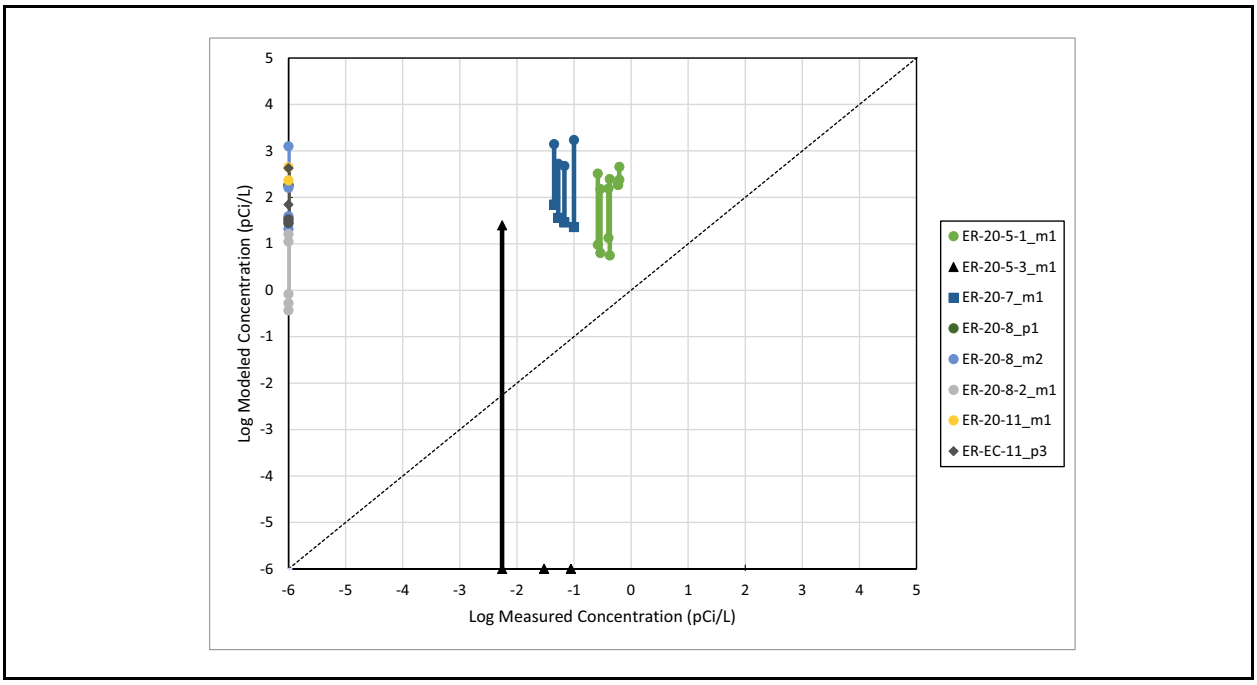

Figure 5-75
Modeled versus Measured $^{239/240}$Pu Concentrations near the Bench in the PM CAU Transport Model

zones, and the bar represents the range of possible calculated concentrations when K_ds are varied. Zero values were approximated with a value of 1E-06, resulting in a log value of -6.

At ER-20-5-1 (in the TSA), the model overpredicts $^{239/240}$Pu concentrations by approximately 1 to 3 orders of magnitude. At ER-20-7 (further downgradient in the TSA), the model overpredicts $^{239/240}$Pu concentrations by approximately 2 to 5 orders of magnitude. The fact that modeled $^{239/240}$Pu concentrations in the TSA increase further downgradient indicates that not enough attenuation of Pu is occurring in the modeled fractured TSA, suggesting that the assumptions regarding the transport of colloidal Pu (i.e., reduced matrix sorption and reduced matrix diffusion coefficient) may be too conservative.

At two observation times at ER-20-5-3_m1 (in the CHLFA5), the model predicts no $^{239/240}$Pu. As discussed in Section 5.5.1.3, the poor agreement at ER-20-5-3_m1 is likely due to the deeper flow path from BENHAM passing to the east of the defined observation nodes. This is consistent with modeled concentrations of other RNs. However, at the remaining observation time at ER-20-5-3_m1,

the model predicts $^{239/240}$Pu for the case with minimum K_d. This result is inconsistent with results for other RNs.

At locations further downgradient, ER-20-8_p1 (in the CHZCM), ER-20-8_m2 (in the TCA), ER-20-8-2 (in the SPA), ER-20-11 (in the BA), and ER-EC-11_p3 (in the BA), there is no observed Pu, but the model predicts $^{239/240}$Pu concentrations similar to what is observed at ER-20-5-1 and ER-20-7. These results also suggest that not enough attenuation of Pu is occurring in the model and that the assumptions regarding the transport of colloidal Pu (i.e., reduced matrix sorption and reduced matrix diffusion coefficient) may be too conservative.

Figure 5-76 shows a plot of the simulated versus observed $^{239/240}$Pu concentrations in log space for observation locations near HANDLEY in the PM CAU transport model. Modeled concentrations at each observation location are represented by two end points connected by a bar. The two end points represent concentrations calculated using either minimum K_d for all zones or maximum K_d for all zones, and the bar represents the range of possible calculated concentrations when K_ds are varied. Zero values were approximated with a value of 1E-06, resulting in a log value of -6. At both ER-20-12_p3 and PM-3_p2, the model predicts no Pu, which agrees with observations at this location. These results are consistent with results from other RNs at ER-20-12_p3 and PM-3_p2. At ER-20-12_m1, ER-20-12_p1, and PM-3_p1, there is no observed Pu. However, the model predicts $^{239/240}$Pu concentrations up to 7.5 pCi/L at ER-20-12_m1, $^{239/240}$Pu concentrations up to 2.2 pCi/L at ER-20-12_p1, and $^{239/240}$Pu concentrations up to 3.4 pCi/L at PM-3_p1. These results suggest that (1) the ^{239}Pu and ^{240}Pu source masses input to the PM CAU transport model at HANDLEY may be conservatively high, and/or (2) not enough attenuation of Pu is occurring in the model and that the assumptions regarding the transport of colloidal Pu (i.e., reduced matrix sorption and reduced matrix diffusion coefficient) may be too conservative.

Plots of modeled and measured $^{239/240}$Pu concentrations over time at these observation locations are shown in Appendix H in Figures H-166 through H-185.

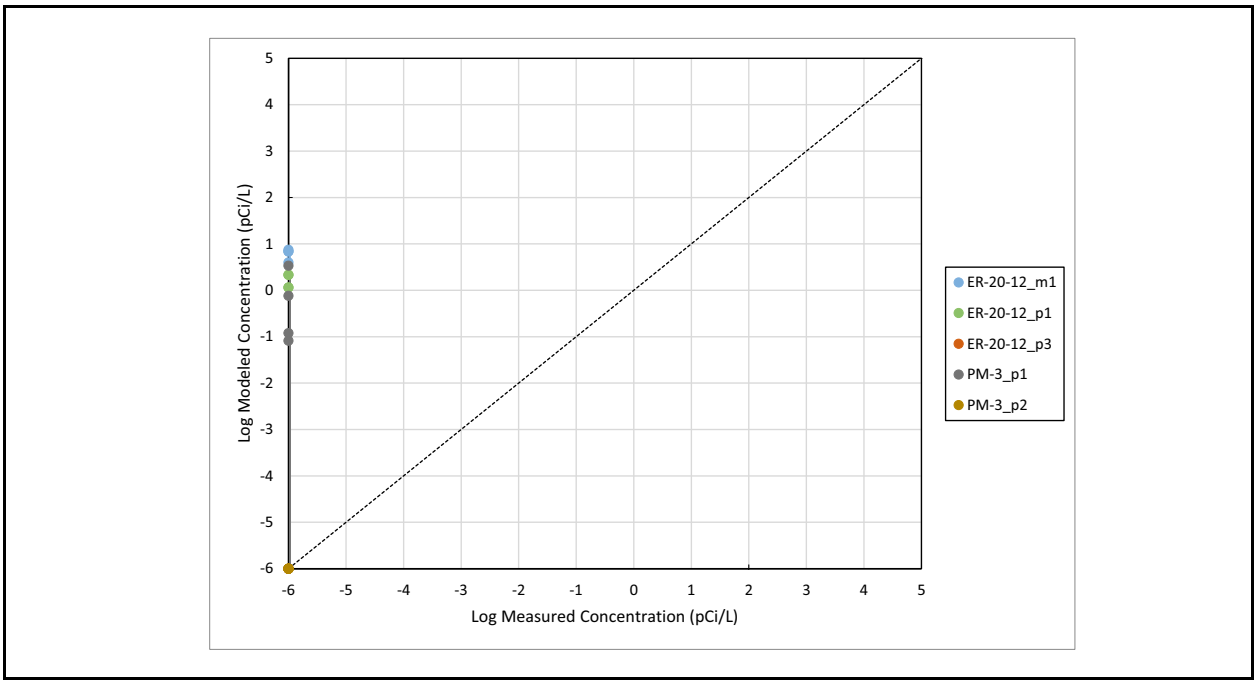

Figure 5-76
Modeled versus Measured $^{239/240}$Pu Concentrations near HANDLEY in the PM CAU Transport Model

5.5.2 Monte Carlo Transport Simulations

A stochastic (i.e., Monte Carlo) approach was used for simulating transport for 1,000 years to explore the range of parametric uncertainty. In this Monte Carlo approach, for a given calibrated groundwater flow field and particle trajectories that are calculated for the given advective flow field with a given dispersivity, 400 transport realizations are performed, with each realization sampling the uncertain transport parameter values from parameter distributions, using the source mass flux for each RN. The RNs modeled are ^{3}H, ^{90}Sr, ^{129}I, ^{137}Cs, ^{232}U, ^{233}U, ^{234}U, ^{238}U, ^{239}Pu, ^{240}Pu, ^{14}C, ^{36}Cl, ^{99}Tc, ^{237}Np, and ^{238}Pu (Section 5.1.2). The base case flow model and three alternative flow models described in Section 4.0 (i.e., the INFILv3 recharge alternative flow model, the DVRFS3 recharge alternative flow model, and the alternative flow model including all faults) were considered.

The base case and all-faults alternative flow models use the same recharge boundary condition, which includes increased recharge near Black Mountain. The recharge near Black Mountain was not increased in the INFILv3 and DVRFS3 alternative recharge models, which both have higher recharge

in the Black Mountain area compared to the original recharge distribution from Fenelon et al. (2016) used in the base case model before modification.

For a given flow model, particle tracks from each of the 85 detonations (82 underground detonations and three near-surface cratering detonations), were calculated with Walkabout using the following dispersivity values (Section 5.2.2.7.2):

- Longitudinal dispersivity = 150 m
- Transverse horizontal dispersivity = 15 m
- Transverse vertical dispersivity = 1.5 m

Dispersivity values were not varied in the Monte Carlo calculations. Dispersivity is specified when creating the particle tracks using Walkabout. In order to vary the dispersivity for the Monte Carlo calculations, Walkabout would need to be run 400 times, which would be a large computational and storage burden.

The developed particle tracks and the source masses described in Section 5.1.3 were inputs to PLUMECALC. For all detonations, the source contaminant mass flux (moles/day) was applied in one day on the day of detonation. The source contaminant mass flux for each detonation was divided equally among the number of particles representing that detonation.

The following uncertain transport parameter values were sampled for each HSU/fault zone using Latin Hypercube sampling:

- Effective (fracture) porosity (Table 5-4)
- Fracture aperture (Table 5-6)
- Matrix porosity (Table 5-3)
- Matrix diffusion coefficient (Table 5-7)
- Bulk rock density (Table 5-5)
- Matrix sorption coefficients (Table 5-11)

Given the particle trajectories and transport times developed from the flow model, input mass fluxes, and transport parameter values, PLUMECALC calculates the contaminant concentration in each control-volume cell at specified times from the date of the first deep underground test in PM, BUTEO, on May 12, 1965. For all detonations, the source contaminant mass flux was applied in one day on the day of detonation (see Table 5-8 for the 82 underground tests and Table 5-12 for the three

Table 5-12
Source Mass Flux Start Times Used in the PM CAU Transport Model for the 3 Near-Surface Cratering Detonations

Detonation	Date	Source Mass Flux Start Day
PALANQUIN	04/14/1965	1 [a]
CABRIOLET	01/26/1968	990
SCHOONER	12/08/1968	1,307

[a] Source mass flux start time for Palanquin is assumed to start on simulation day 1.

near-surface cratering detonations). The transport model was set up with the initial start time of May 12, 1965. Since PALANQUIN was detonated approximately one month earlier on April 14, 1965, the source mass flux for PALANQUIN was introduced on day 1 of the transport simulation. Given that PALANQUIN has a smaller announced yield (4.3 kt, NNSA/NFO, 2015b) than nearby detonations, the approximate one-month delay in the introduction of source mass from PALANQUIN will not have a large impact on the overall CB.

The discrete PLUMECALC output times chosen for analysis are specified by year, corresponding to the observation dates given in Table 5-9, as well as specified future times up to 1,000 years as follows: 3, 11, 12, 13, 18, 19, 20, 21, 22, 23, 25, 26, 27, 28, 29, 30, 31, 32, 33, 34, 35, 36, 37, 38, 39, 40, 41, 42, 43, 44, 45, 46, 47, 48, 49, 50, 51, 52, 53, 54, 55, 60, 80, 100, 200, 300, 400, 500, 600, 700, 800, 900, and 1,000 years.

The approach taken to forecast the extent of contaminant migration is to perform transport simulations for all sources and all significant RNs over a range of uncertain transport parameter values and to evaluate the probability of exceeding the SDWA MCLs (from Section 3.0 of Navarro, 2021c), defined as the number of realizations exceeding the criteria divided by the total number of realizations (400), for each modeled RN within each grid cell. These fractional exceedance values are summed over all modeled RNs to determine a probability of exceeding the MCL within each grid cell. The MCLs used are listed in Table 5-13.

Table 5-13
MCLs for Each Modeled RN

RN	Category	MCL
^{3}H	Beta	20,000 pCi/L
^{14}C	Beta	2,000 pCi/L
^{36}Cl	Beta	700 pCi/L
^{90}Sr	Beta	8 pCi/L
^{99}Tc	Beta	900 pCi/L
^{129}I	Beta	1 pCi/L
^{137}Cs	Beta	200 pCi/L
^{237}Np	Alpha	15 pCi/L
^{238}Pu	Alpha	15 pCi/L
^{239}Pu	Alpha	15 pCi/L
^{240}Pu	Alpha	15 pCi/L
^{232}U	U	30 µg/L
^{233}U	U	30 µg/L
^{234}U	U	30 µg/L
^{238}U	U	30 µg/L

Source: Tables 3-1 and 3-2 of Navarro (2021c)

The principal performance metric used in the contaminant transport analyses is the probability that any grid cell is likely to exceed the SDWA MCL concentration (CFR, 2021). Probabilities are calculated for the alpha emitters (considering contributions from all modeled alpha emitters, excluding U); for the beta emitters (considering contributions from all modeled beta emitters); for U; and for all RNs (i.e., the probability that the sum of concentrations from all RNs relative to their respective MCLs will exceed a value of 1 at that model cell).

The exceedance volume is calculated for each category of RN (i.e., alpha emitters, beta emitters, and U), as well as for all three categories combined. The exceedance volume is defined as the total (summed) volume of all cells with a 5 percent or greater probability of exceeding the SDWA standard (CFR, 2021). If a model cell exceeds the standard, that cell’s volume is added to the exceedance volume. The time-cumulative exceedance volume (CEV) is defined as the total volume

of all model cells equal to or exceeding the SDWA standard at any time up to 1,000 years for a specific realization.

The average fractional exceedance volume (FEV) is also calculated for each RN, each category of RN (i.e., alpha emitters, beta emitters, U), as well as for all three categories combined. The FEV is a time-specific measure, averaged across all 400 realizations, that ranks the RNs in terms of their importance to the exceedance volume.

The results of the CB forecasts based on multiple realizations are presented in Section 5.5.2.1.

5.5.2.1 Monte Carlo Results

Using the numerical approach described in Section 5.4, along with the transport parameter distributions described in Section 5.2.2, and source mass fluxes described in Section 5.1.3, a range of uncertainty analyses were performed to evaluate the extent of possible contamination in PM. As defined in the FFACO, the ultimate goal of the PM CAU transport modeling is to define the CBs or a composite range of possible CBs that can then be used by the EM Nevada Program and NDEP to negotiate the use restriction and regulatory boundaries. The determination of the CBs requires quantifying the probability that the volume of rock downgradient of the contamination sources exceeds the maximum permissible contaminant levels (i.e., MCLs) of the SDWA (CFR, 2021). Determining this probability for the PM CAU transport model requires multiple simulations of contaminant transport incorporating the uncertainty in alternative flow models and alternative transport parameters.

The PM CAU transport model results addressing the above uncertainties are presented in this section for the following:

- The base case flow model in Section 5.5.2.1.1
- The INFILv3 recharge alternative flow model in Section 5.5.2.1.2
- The DVRFS3 recharge alternative flow model in Section 5.5.2.1.3
- The alternative flow model including all faults in Section 5.5.2.1.4

5.5.2.1.1 Results for Base Case Flow Model

Figure 5-77 shows the forecasted 1,000-year time-cumulative probability of exceedance of alpha-emitter, beta-emitter, and U MCLs for the PM base case flow model. The time-cumulative probability of exceedance uses the probability of exceeding the MCL at each node for each individual modeled time step and identifies the maximum probability of MCL exceedance at each node regardless of the time that maximum occurs. Each colored dot represents the probability that the sum of concentrations from all RNs relative to their respective MCLs will exceed a value of 1 at that model cell. Only probabilities greater than 5 percent (i.e., the 95th percentile) are displayed. The spacing between colored dots reflects the model grid spacing, so the dots are spaced a little farther apart in areas with larger model cells. Figure 5-77 is displayed such that at each x,y location, the maximum probability of MCL exceedance at any depth is shown.

Similarly, Figure 5-78 shows the forecasted 1,000-year time-cumulative probability of exceedance of MCL for only the beta emitters, Figure 5-79 shows the forecasted 1,000-year time-cumulative probability of exceedance of MCL for only the alpha emitters, and Figure 5-80 shows the forecasted 1,000-year time-cumulative probability of exceedance of MCL for only U.

The forecasted time-varying probability of exceedance of alpha-emitter, beta-emitter, and U MCLs for the PM base case flow model is shown in Figures 5-81 through 5-88 at discrete times. As was done for Figure 5-77, Figures 5-81 through 5-88 are displayed such that at each x,y location, the maximum probability of MCL exceedance at any depth is shown. These figures illustrate the largest extent of MCL exceedance occurs between 80 and 100 years, after which the extent of contamination begins to shrink because of radioactive decay of the short-lived RNs.

For the base case, the 2-D CB perimeter is defined by the ground surface area that is obscured in Figure 5-77 by the collection of colored dots. The CB extends approximately 2 to 3 km past the western NNSS boundary onto the NTTR at four locations: (1) north of PM-3, (2) east of PM-3, (3) in the Bench area near ER-EC-6, and (4) northeast of ER-EC-1.

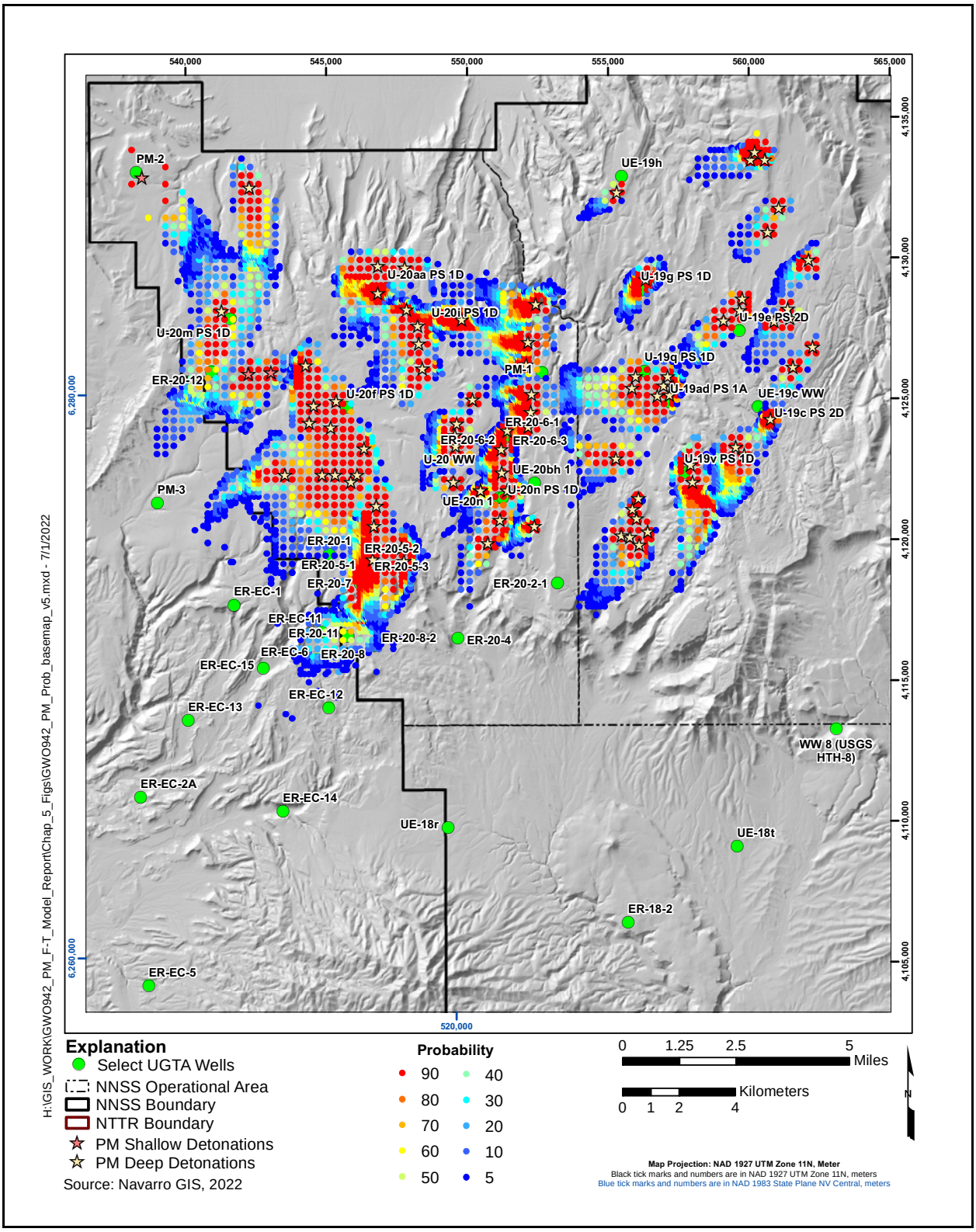

Figure 5-77
1,000-Year Time-Cumulative Probability of Exceedance of MCLs for PM Base Case

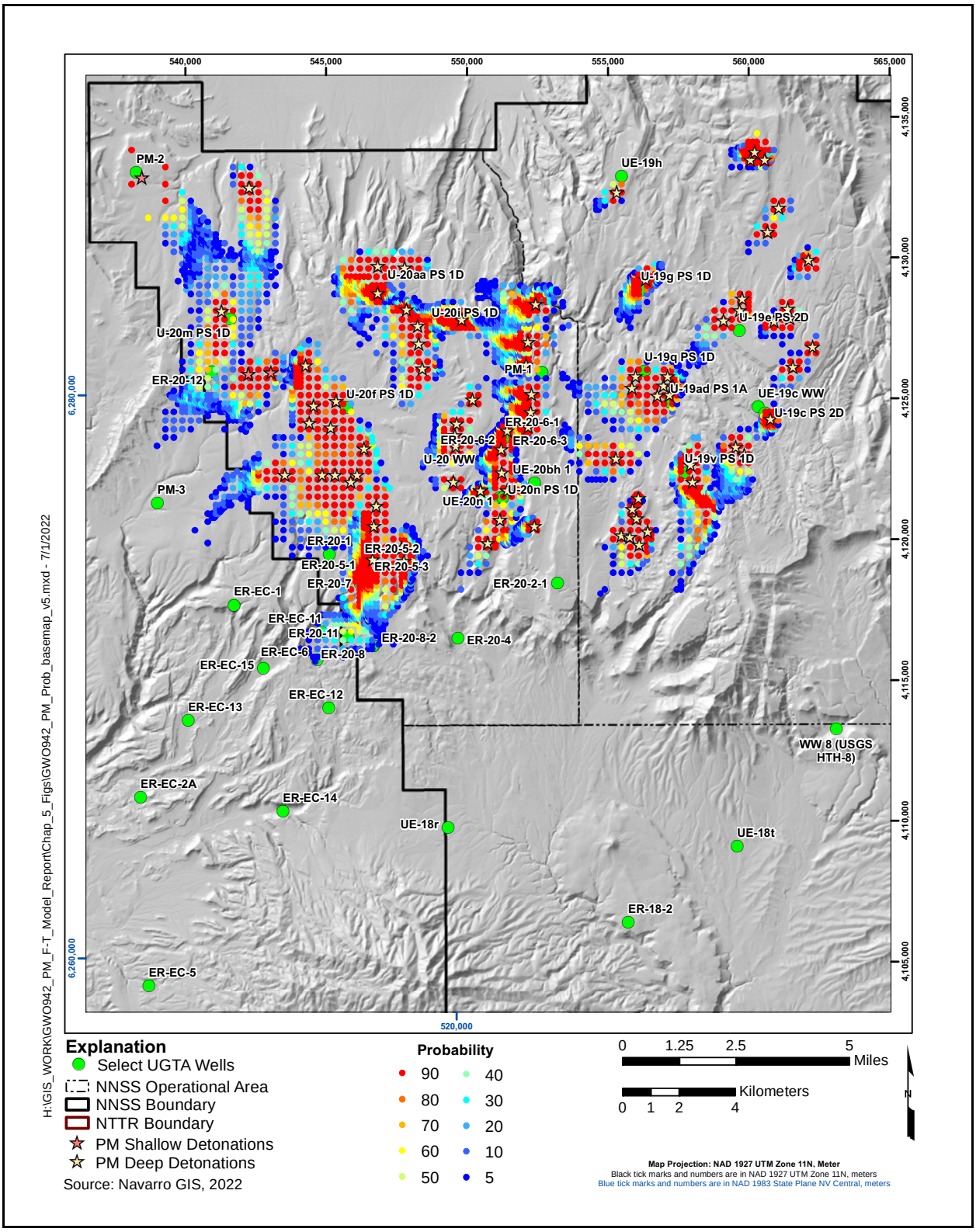

Figure 5-78
1,000-Year Time-Cumulative Probability of Exceedance of MCLs for PM Base Case (Beta Emitters)

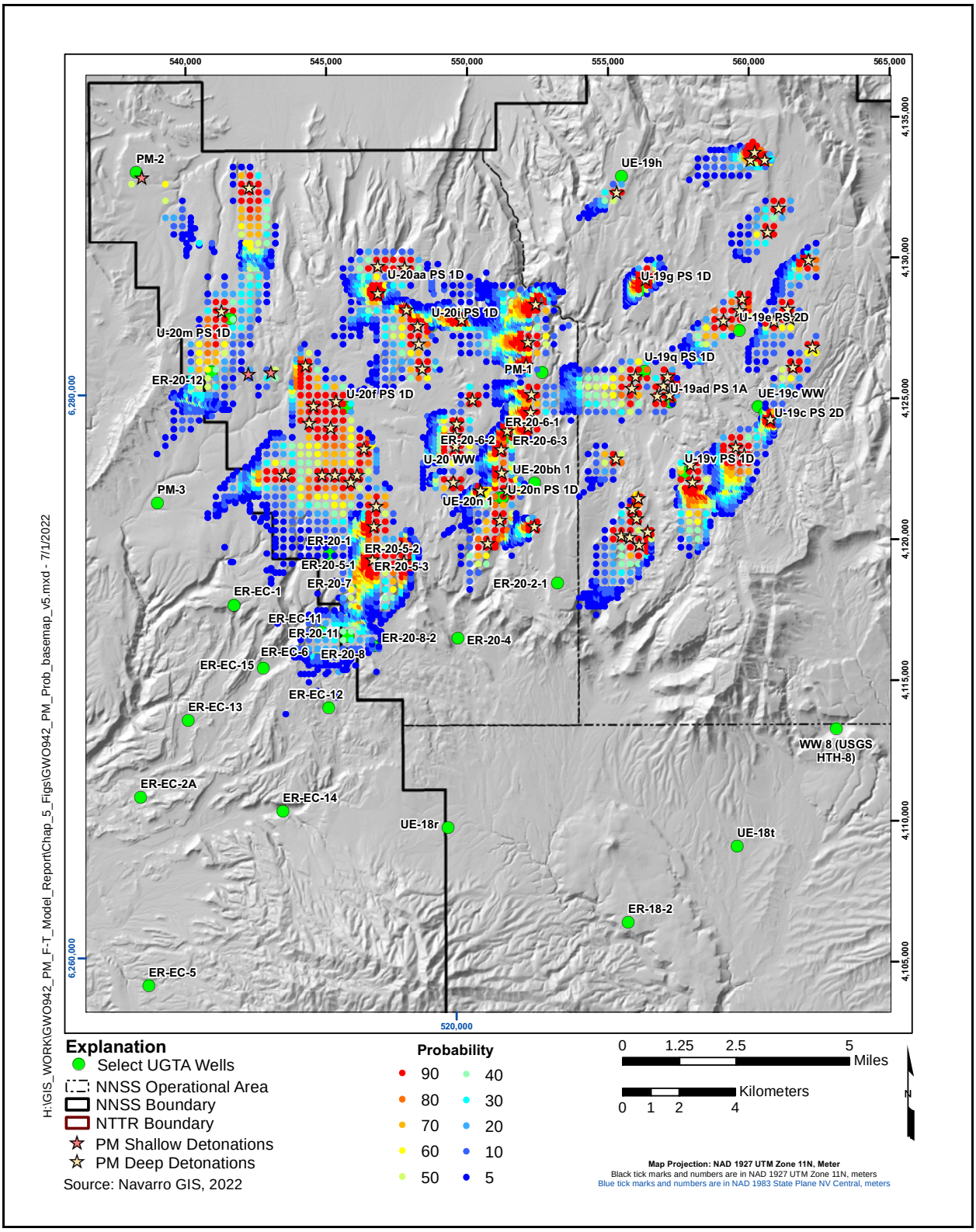

Figure 5-79
1,000-Year Time-Cumulative Probability of Exceedance of MCLs for PM Base Case (Alpha Emitters)

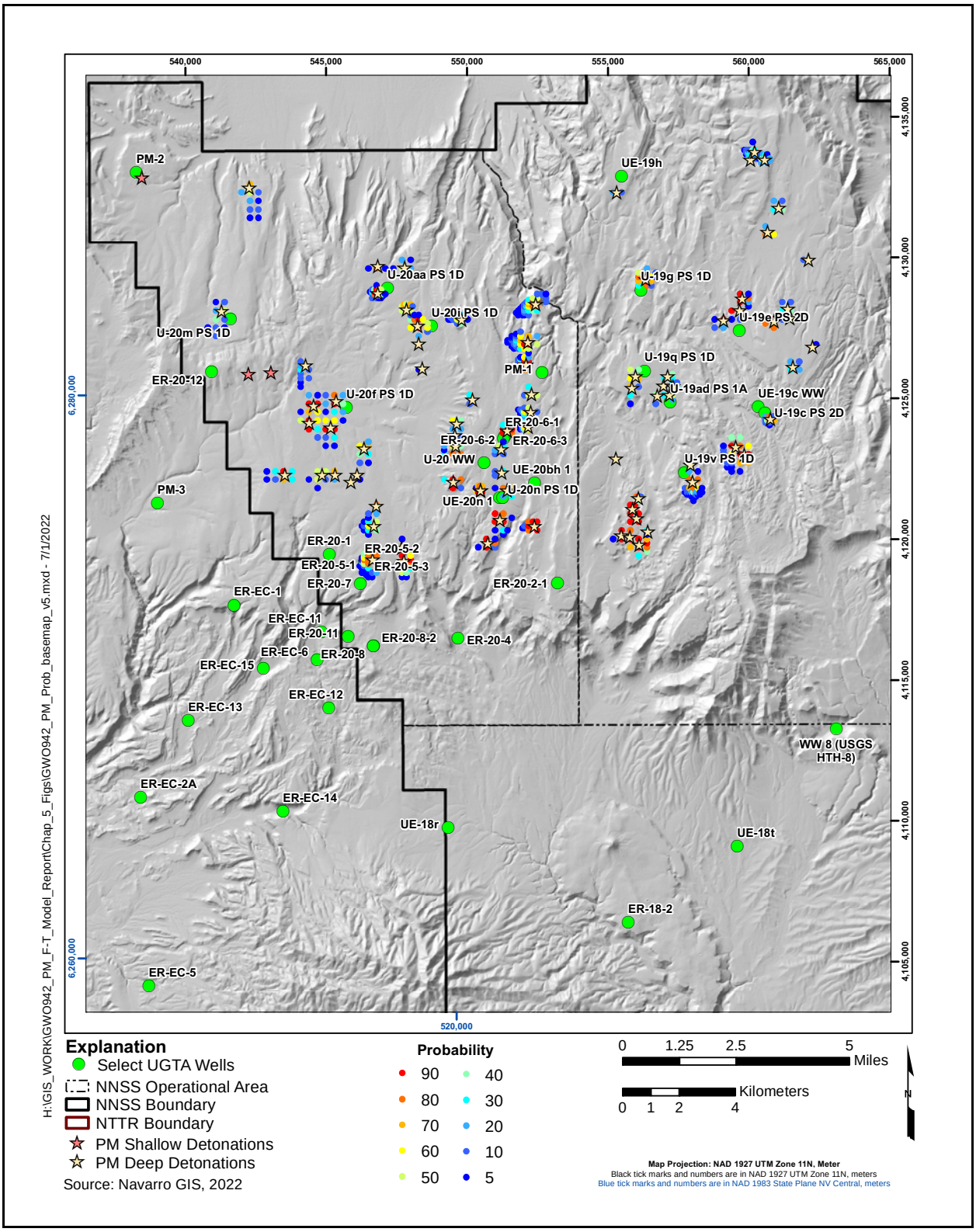

Figure 5-80
1,000-Year Time-Cumulative Probability of Exceedance of MCLs for PM Base Case (U)

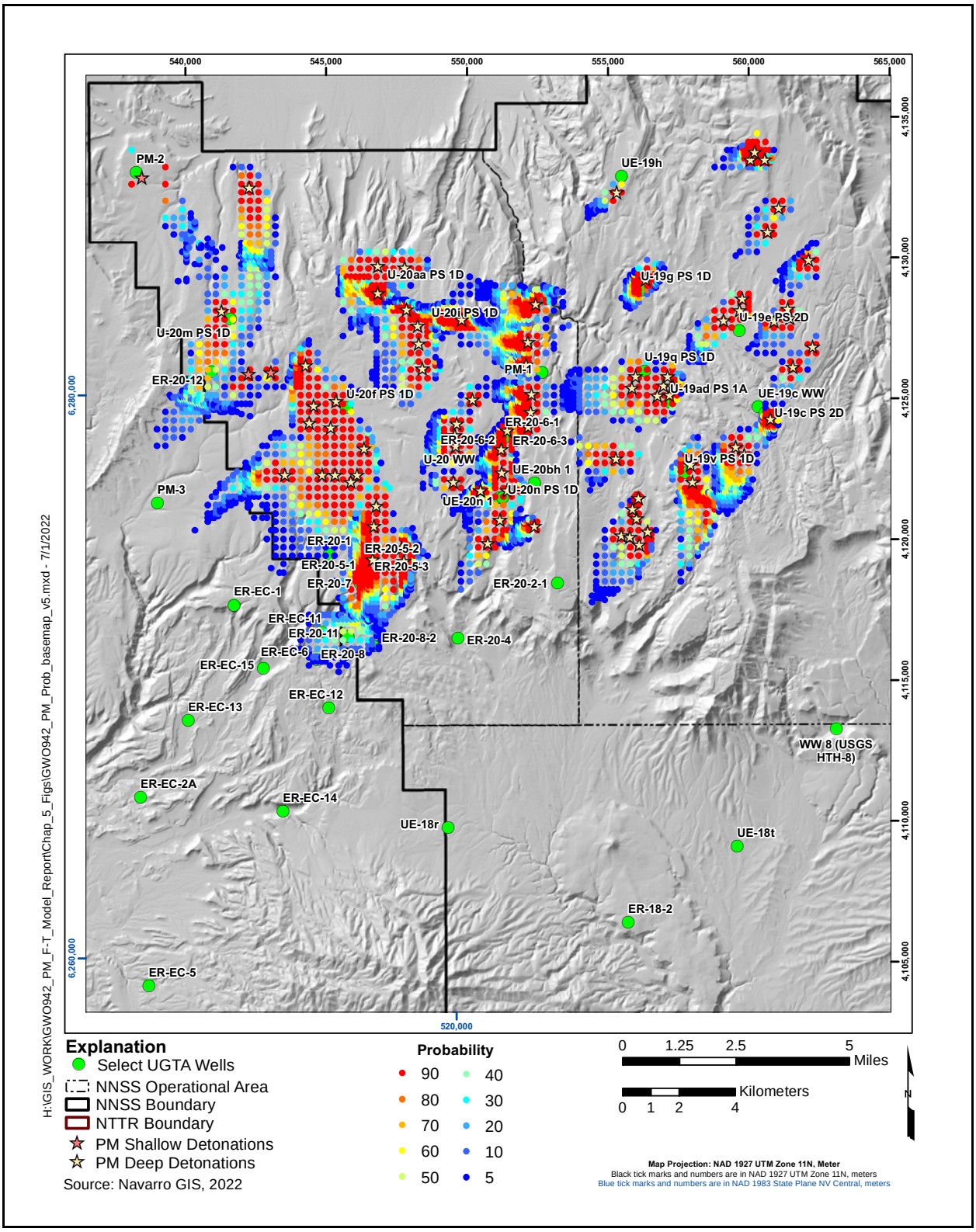

Figure 5-81
Probability of Exceedance of MCLs for the PM Flow Model Base Case (55 years)

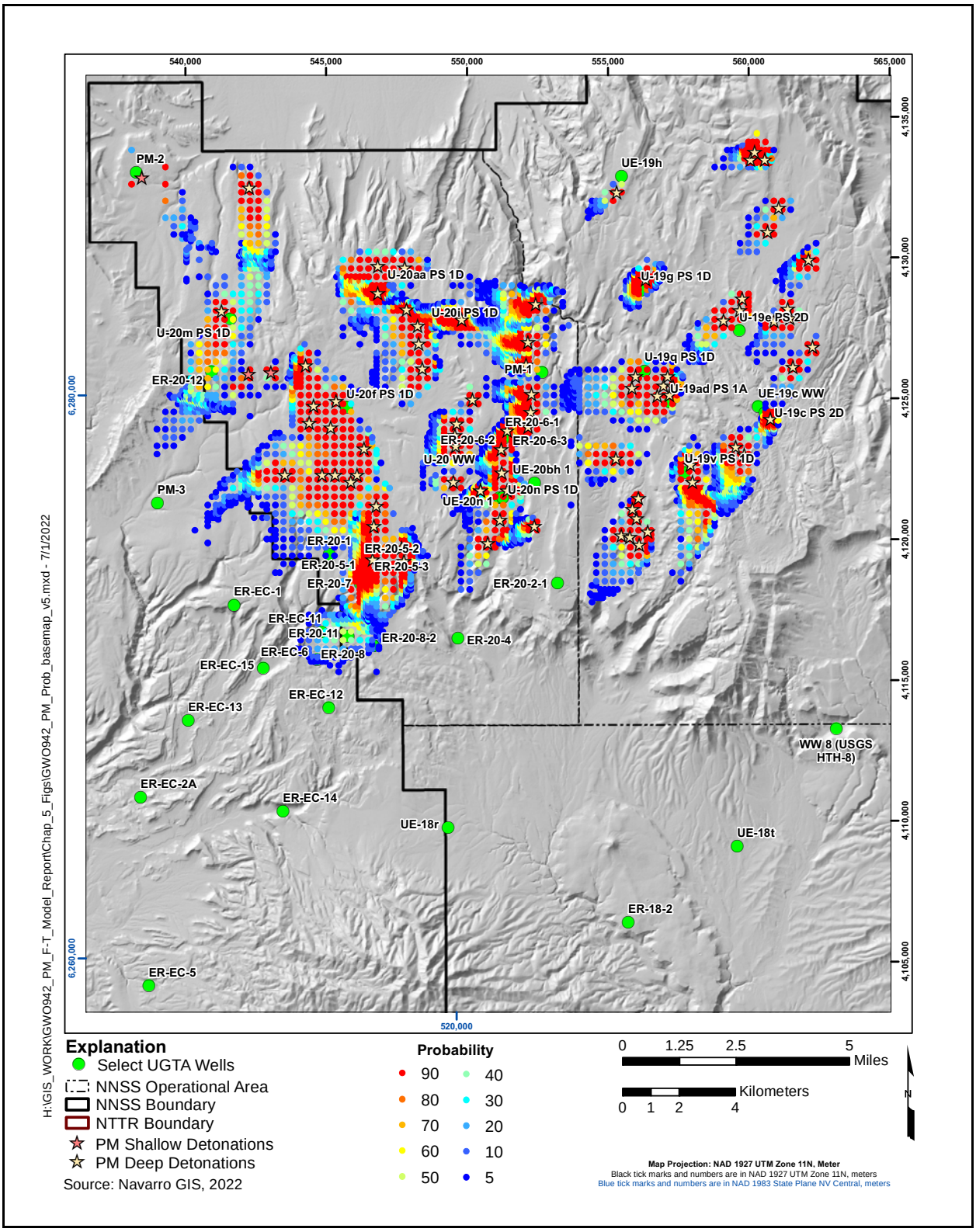

Figure 5-82
Probability of Exceedance of MCLs for the PM Flow Model Base Case (60 years)

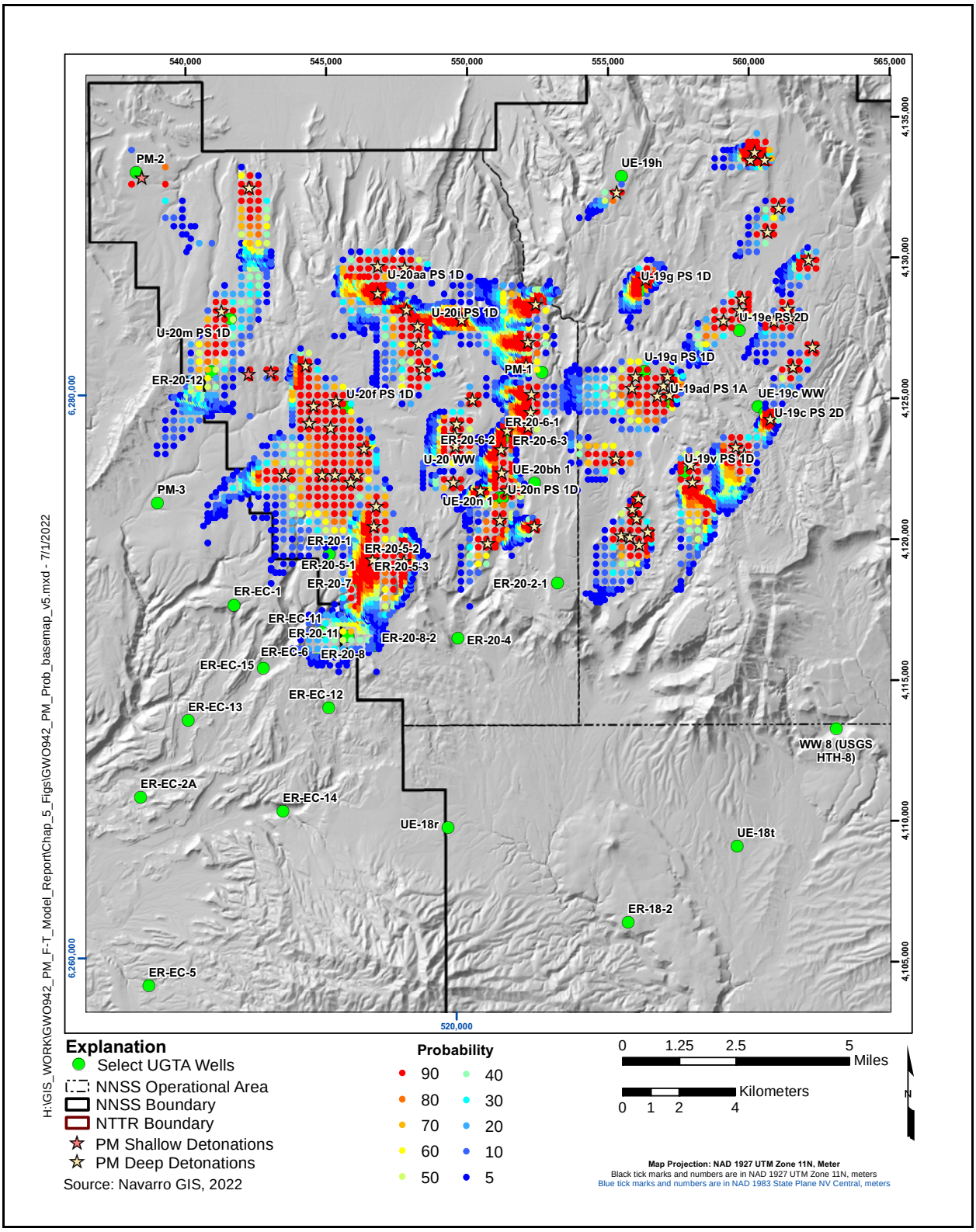

Figure 5-83
Probability of Exceedance of MCLs for the PM Flow Model Base Case (80 years)

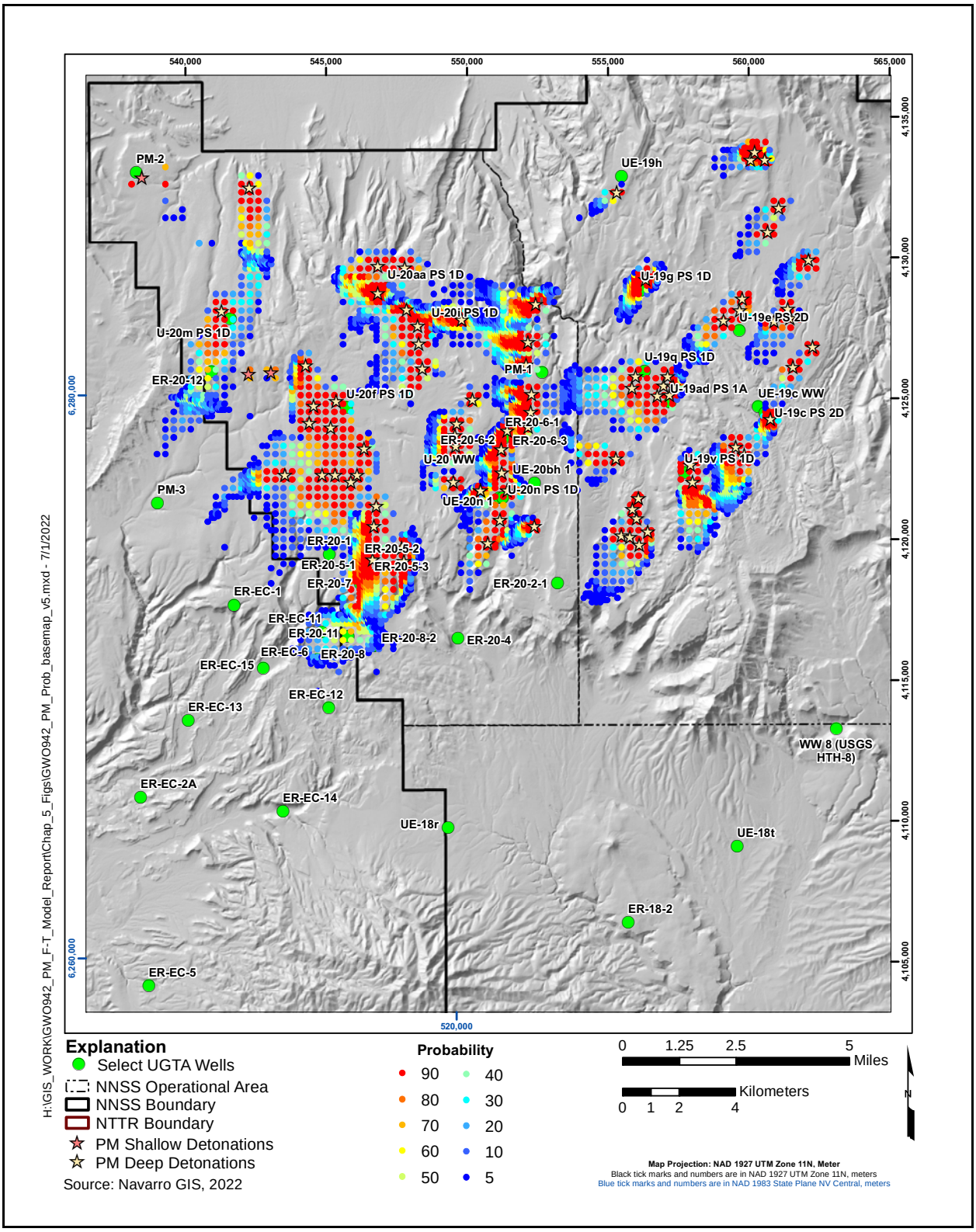

Figure 5-84
Probability of Exceedance of MCLs for the PM Flow Model Base Case (100 years)

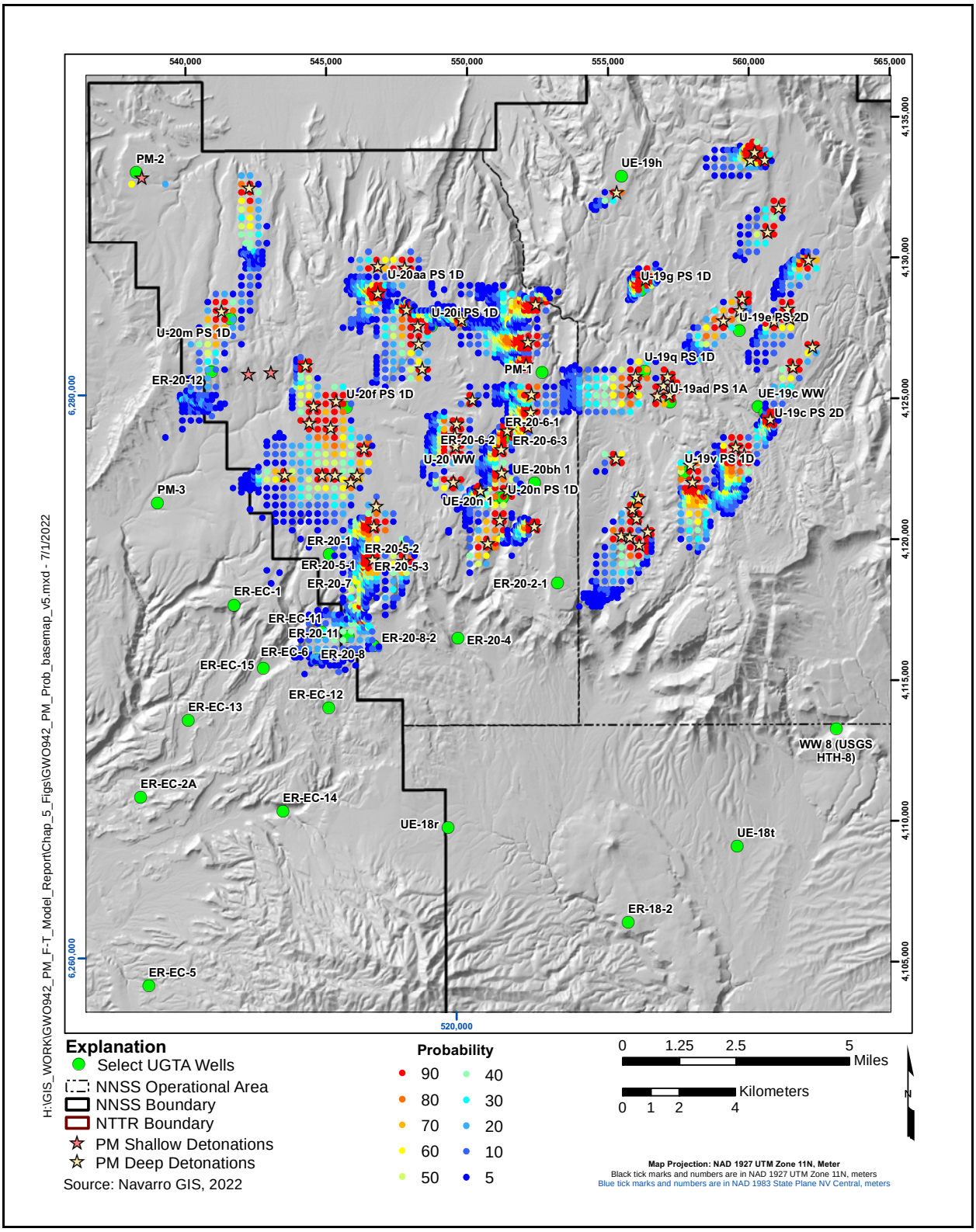

Figure 5-85
Probability of Exceedance of MCLs for the PM Flow Model Base Case (200 years)

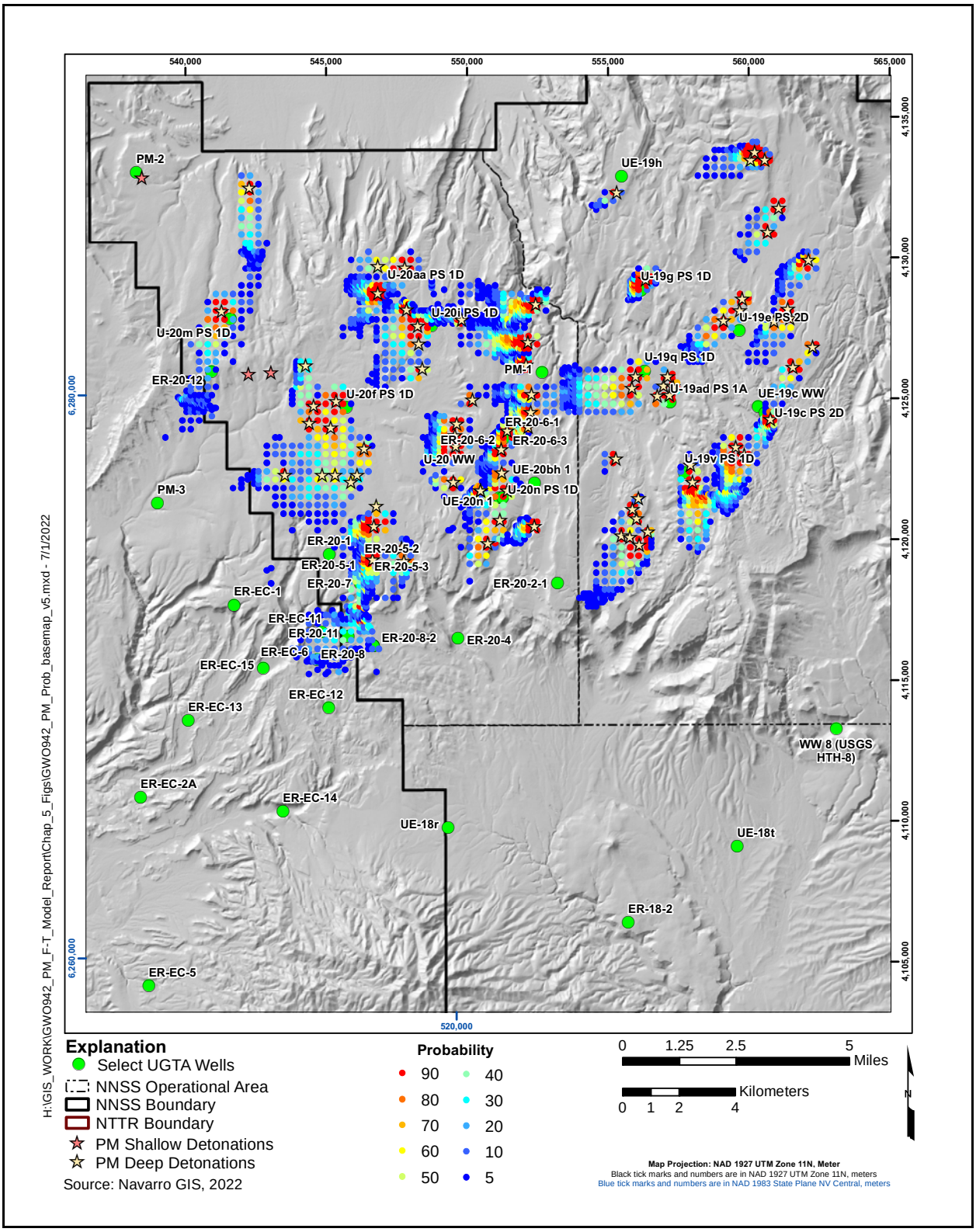

Figure 5-86
Probability of Exceedance of MCLs for the PM Flow Model Base Case (300 years)

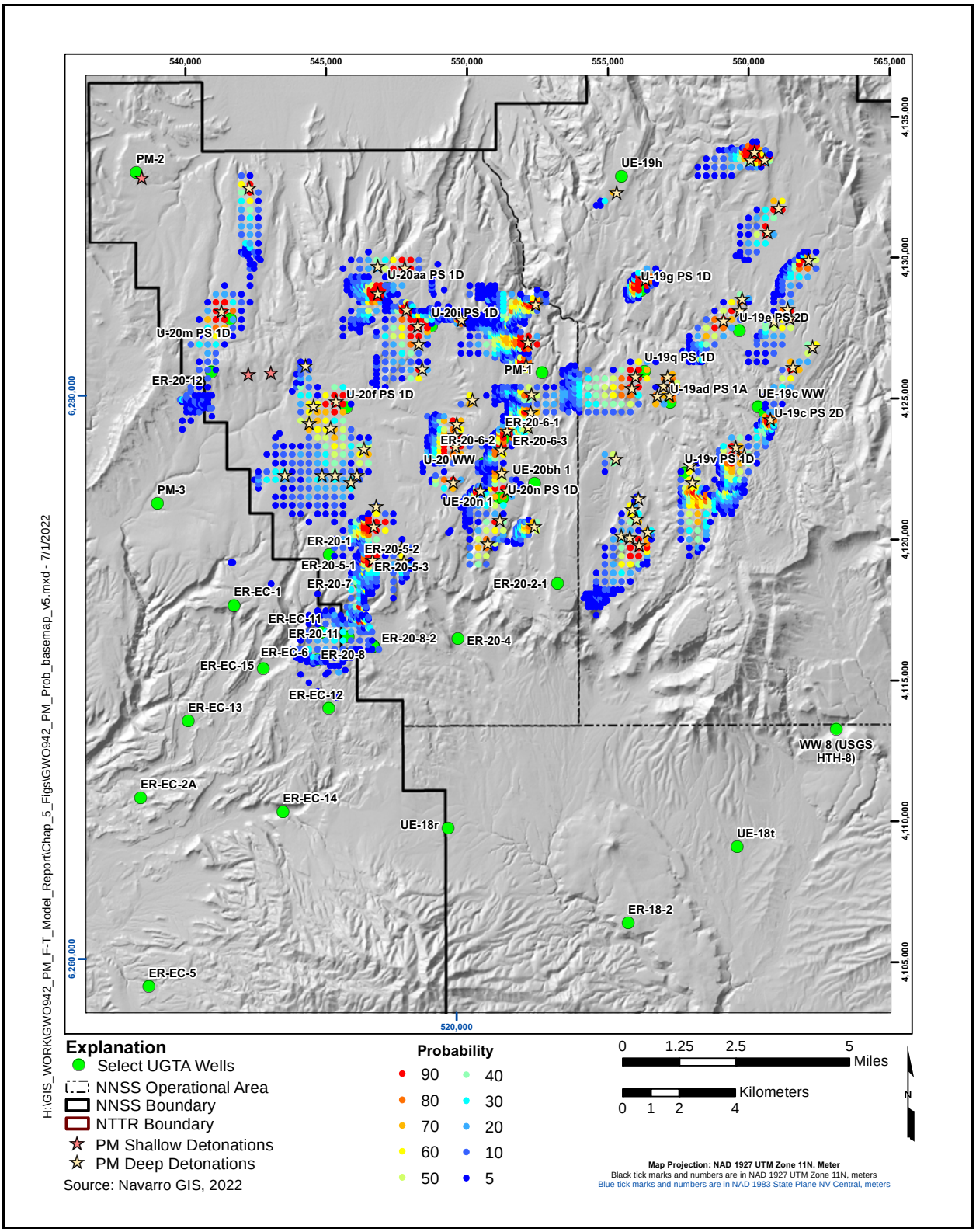

Figure 5-87
Probability of Exceedance of MCLs for the PM Flow Model Base Case (500 years)

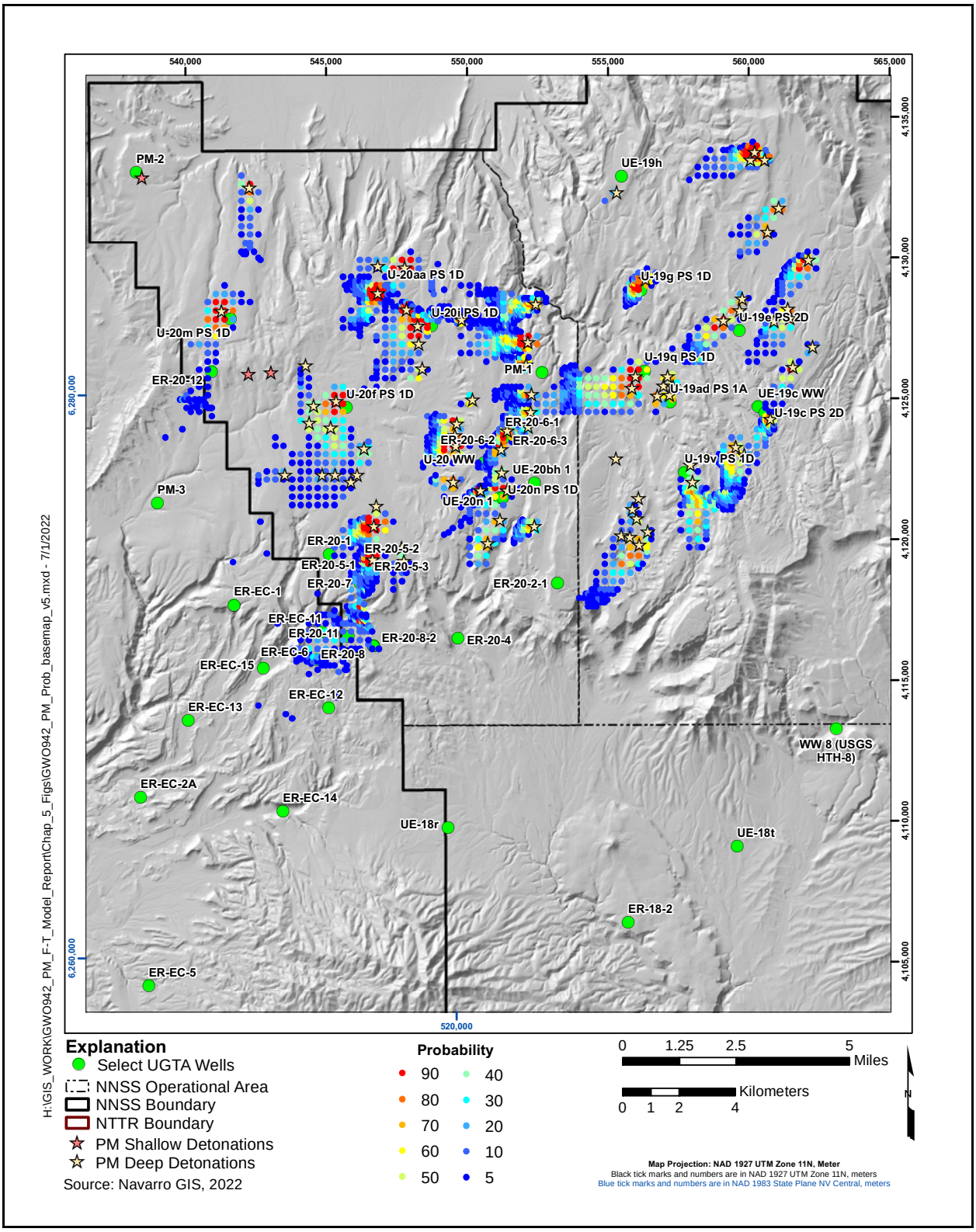

Figure 5-88
Probability of Exceedance of MCLs for the PM Flow Model Base Case (1,000 years)

Due to the complex faulted geology in PM, the vertical extent of the CB varies across the computational domain. The bottom of the CB intersects 24 HSUs, which are displayed in Figure 5-89 and listed in Figure 5-90. Figure 5-90 is not a list of all contaminated HSUs in the CB. Figure 5-91 displays the CB of the base case colored by the saturated depth of contamination.

Outside the NNSS boundary, the CB extends through the locations occupied by ER-EC-11 and ER-EC-6 but does not reach ER-EC-15 or ER-EC-12.

Nearest to the location of ER-EC-11, the saturated depth of the CB (i.e., the depth below the modeled water table surface, which represents the top of the model) is approximately 673 m (as shown in Figure 5-91). The water table at ER-EC-11 is at a depth (bgs) of approximately 450 m. Thus, the total depth of the bottom of the CB near ER-EC-11 is approximately 1,123 m bgs in the TSA (Figure 5-89), which is intersected by ER-EC-11_p1.

Just upgradient of ER-EC-6, the saturated depth of the CB is approximately 547 m (as shown in Figure 5-91). The water table at ER-EC-6 is at a depth (bgs) of approximately 434 m. Thus, the total depth of the bottom of the CB just upgradient of ER-EC-6 is approximately 981 m bgs in the TSA (Figure 5-89), which is intersected by ER-EC-6_m2.

Just downgradient of ER-EC-6, the saturated depth of the CB is approximately 290 m (as shown in Figure 5-91). The water table at ER-EC-6 is at a depth (bgs) of approximately 434 m. Thus, the total depth of the bottom of the CB just downgradient of ER-EC-6 is approximately 724 m bgs in the TCA (Figure 5-84). Upgradient of this location, the TCA is intersected by ER-EC-6_m3.

5.5.2.1.2 Results for INFILv3 Recharge Alternative Flow Model

Figure 5-92 shows the forecasted 1,000-year time-cumulative probability of exceedance of alpha-emitter, beta-emitter, and U MCLs for the INFILv3 recharge alternative flow model. The time-cumulative probability of exceedance uses the probability of exceeding the MCL at each node for each individual modeled time step and identifies the maximum probability of MCL exceedance at each node regardless of the time that maximum occurs. Each colored dot represents the probability that the sum of concentrations from all RNs relative to their respective MCLs will exceed a value of 1 at that model cell. Only probabilities greater than 5 percent (i.e., the 95th percentile) are

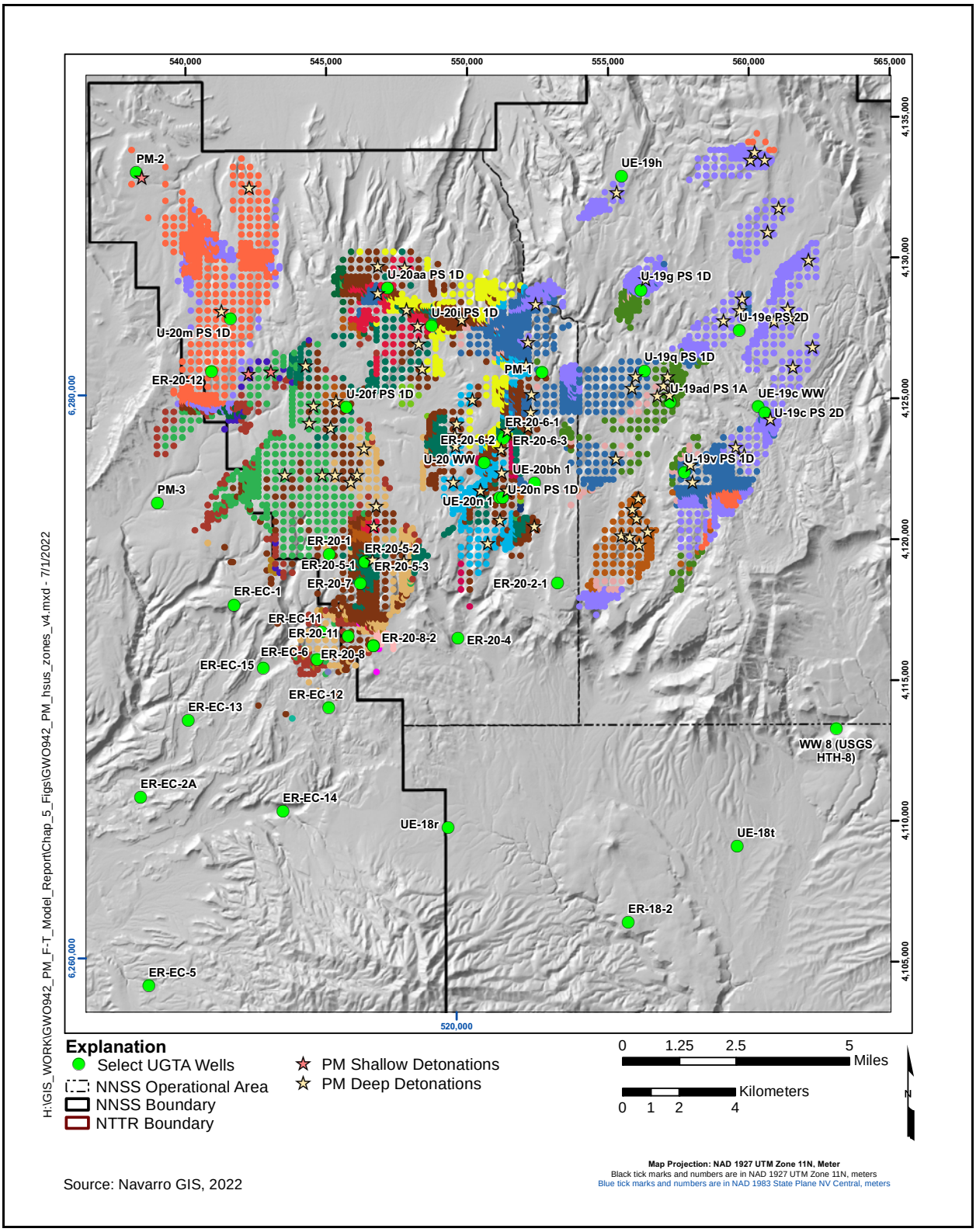

Figure 5-89
CB of Base Case Colored by Lowest Contaminated HSU

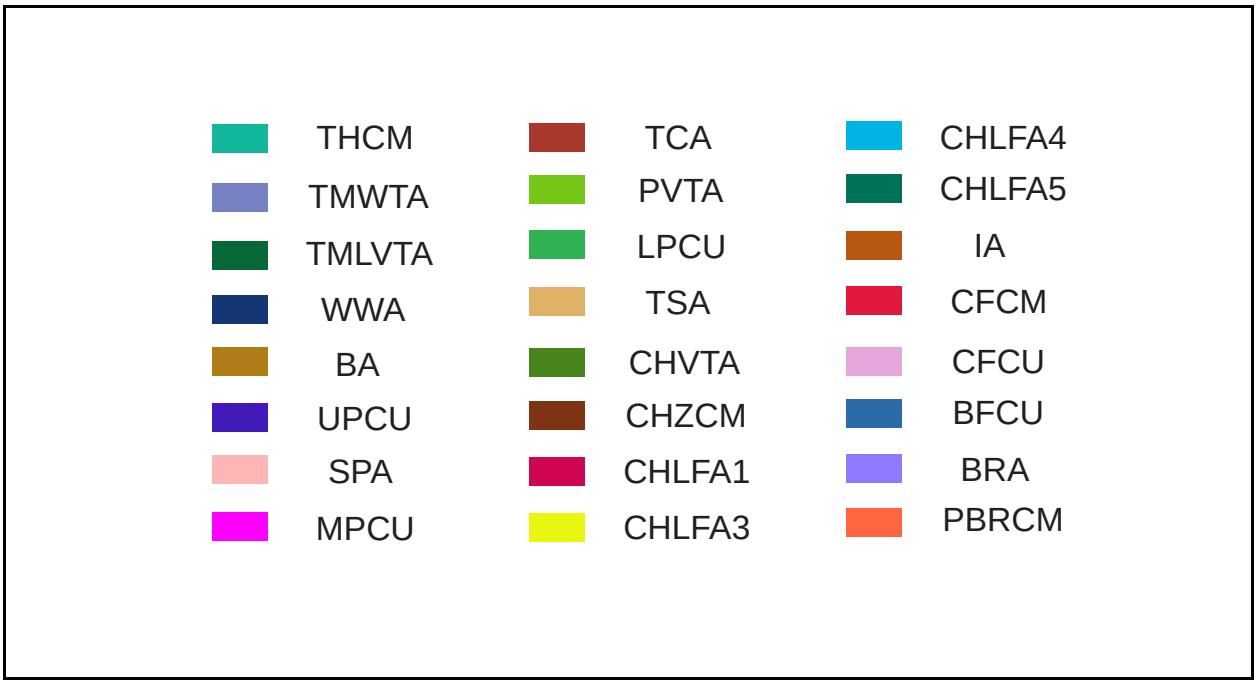

Figure 5-90
Lowest Contaminated HSUs in CB for Base Case Flow Model with Color Key for Figure 5-89

displayed. Figure 5-92 is displayed such that at each x,y location, the maximum probability of MCL exceedance at any depth is shown.

For the INFILv3 recharge alternative flow model, the 2-D CB perimeter is defined by the ground surface area that is obscured in Figure 5-92 by the collection of colored dots. The CB extends approximately 2 to 3 km past the western NNSS boundary onto the NTTR at four locations: (1) north of PM-3, (2) east of PM-3, (3) in the Bench area near ER-EC-6, and (4) northeast of ER-EC-1.

Due to the complex faulted geology in PM, the vertical extent of the CB varies across the computational domain. The bottom of the CB intersects 23 HSUs, which are displayed in Figure 5-93 and listed in Figure 5-94. Figure 5-94 is not a list of all contaminated HSUs in the CB. Figure 5-95 displays the CB of the base case colored by the saturated depth of contamination.

Outside the NNSS boundary, the CB extends through the locations occupied by ER-EC-11 and ER-EC-6. The CB further extends just past ER-EC-15 and ER-EC-12 between these two wells but does not intersect them.

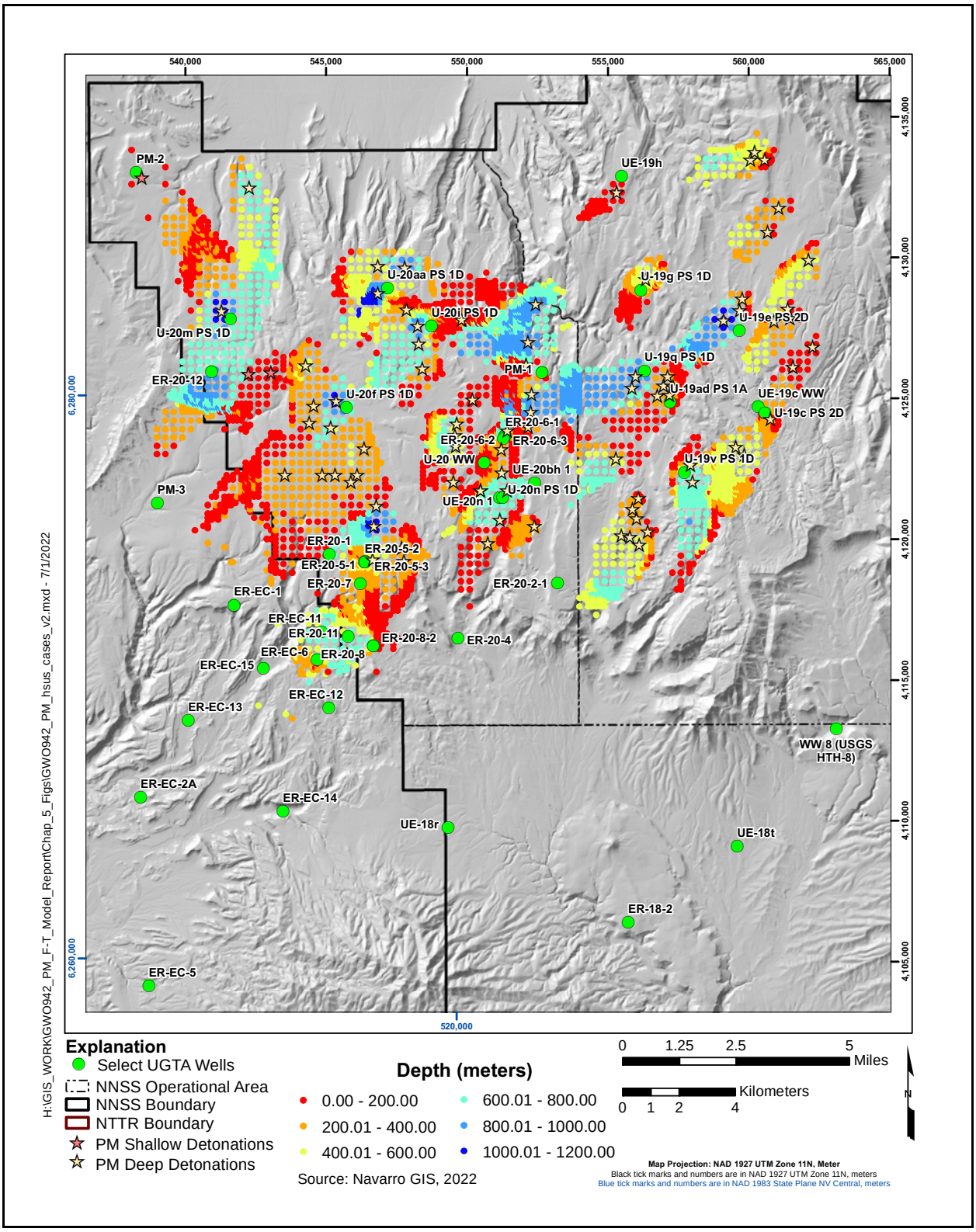

Figure 5-91
CB of Base Case Colored by Saturated Depth of Contamination

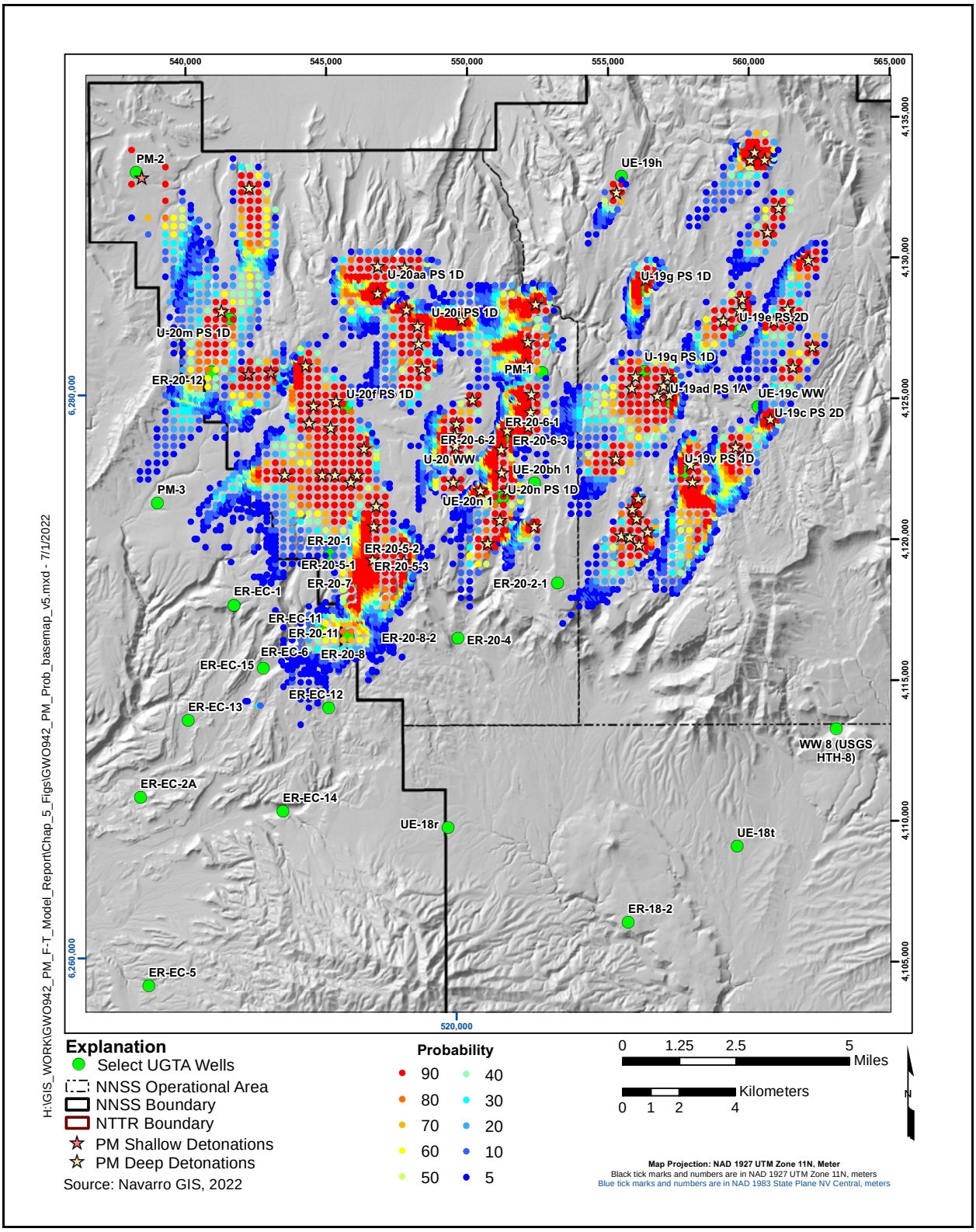

Figure 5-92
1,000-Year Time-Cumulative Probability of Exceedance of MCLs for PM INFILv3 Recharge Alternative Flow Model

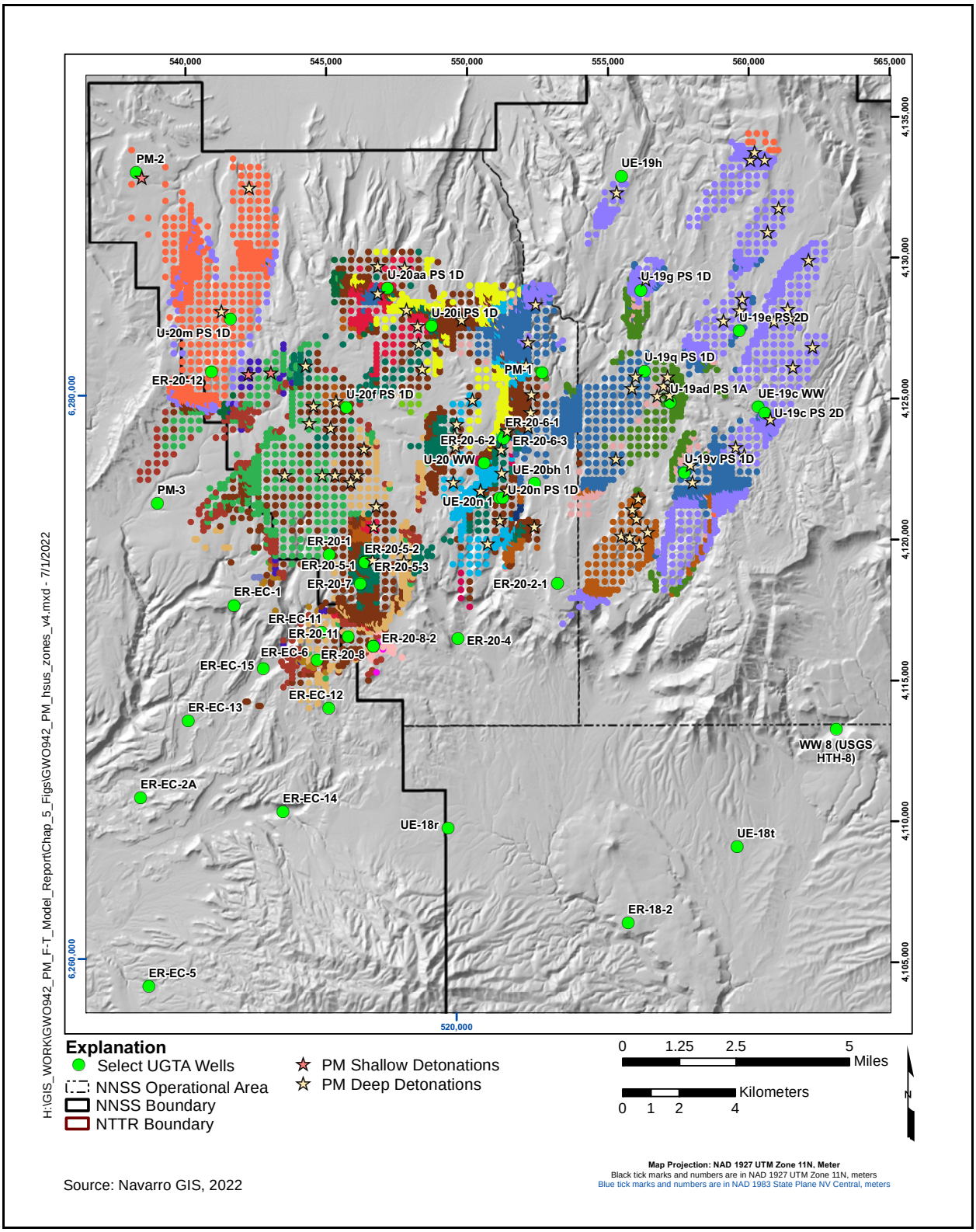

Figure 5-93
CB of INFILv3 Recharge Alternative Flow Model
Colored by Lowest Contaminated HSU

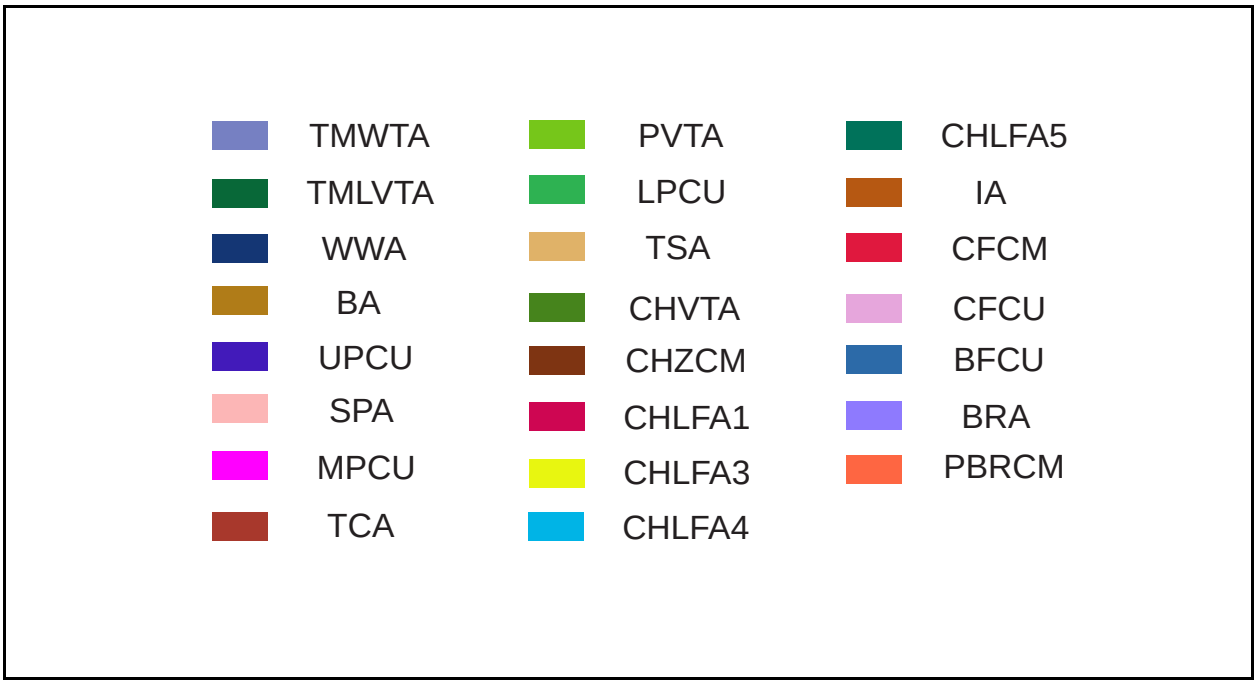

Figure 5-94
Lowest Contaminated HSUs in CB for INFILv3 Recharge Alternative Flow Model with Color Key for Figure 5-93

Nearest to the location of ER-EC-11, the saturated depth of the CB (i.e., the depth below the modeled water table surface, which represents the top of the model) is approximately 673 m (as shown in Figure 5-95). The water table at ER-EC-11 is at a depth (bgs) of approximately 450 m. Thus, the total depth of the bottom of the CB near ER-EC-11 is approximately 1,123 m bgs in the TSA (Figure 5-93), which is intersected by ER-EC-11_p1.

Just upgradient of ER-EC-6, the saturated depth of the CB is approximately 622 m (as shown in Figure 5-95). The water table at ER-EC-6 is at a depth (bgs) of approximately 434 m. Thus, the total depth of the bottom of the CB just upgradient of ER-EC-6 is approximately 1,056 m bgs in the TSA (Figure 5-93), which is intersected by ER-EC-6_m2.

Just downgradient of ER-EC-6, the saturated depth of the CB is approximately 290 m (as shown in Figure 5-95). The water table at ER-EC-6 is at a depth (bgs) of approximately 434 m. Thus, the total depth of the bottom of the CB just downgradient of ER-EC-6 is approximately 724 m bgs in the TCA (Figure 5-93). Upgradient of this location, the TCA is intersected by ER-EC-6_m3.

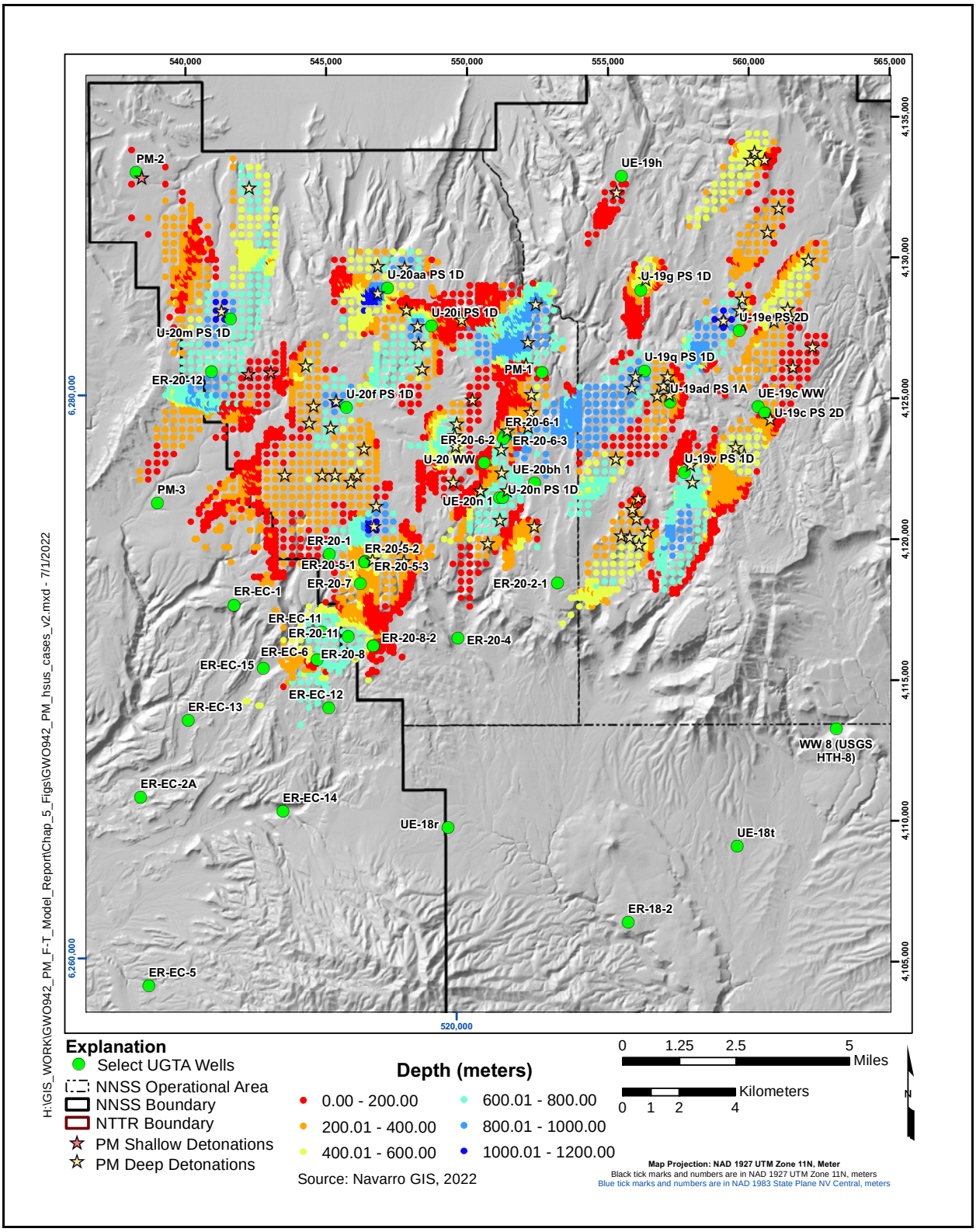

Figure 5-95
CB of INFILv3 Recharge Alternative Flow Model
Colored by Saturated Depth of Contamination

The CB exists approximately 422 m west–northwest of ER-EC-12. At this location, the saturated depth of the CB (Figure 5-95) is approximately 770 m in the TSA (Figure 5-93). The TSA is intersected by ER-EC-12_p2.

The CB exists approximately 734 m east of ER-EC-15. At this location, the saturated depth of the CB (Figure 5-95) is approximately 379 m in the TCA (Figure 5-93). The TCA is intersected by ER-EC-15_p2.

5.5.2.1.3 Results for DVRFS3 Recharge Alternative Flow Model

Figure 5-96 shows the forecasted 1,000-year time-cumulative probability of exceedance of alpha-emitter, beta-emitter, and U MCLs for the DVRFS3 recharge alternative flow model. The time-cumulative probability of exceedance uses the probability of exceeding the MCL at each node for each individual modeled time step and identifies the maximum probability of MCL exceedance at each node regardless of the time that maximum occurs. Each colored dot represents the probability that the sum of concentrations from all RNs relative to their respective MCLs will exceed a value of 1 at that model cell. Only probabilities greater than 5 percent (i.e., the 95th percentile) are displayed. Figure 5-96 is displayed such that at each x,y location, the maximum probability of MCL exceedance at any depth is shown.

For the DVRFS3 recharge alternative flow model, the 2-D CB perimeter is defined by the ground surface area that is obscured in Figure 5-96 by the collection of colored dots. The CB extends approximately 2 to 3 km past the western NNSS boundary onto the NTTR at four locations: (1) north of PM-3, (2) east of PM-3, (3) in the Bench area near ER-EC-6, and (4) northeast of ER-EC-1.

Due to the complex faulted geology in PM, the vertical extent of the CB varies across the computational domain. The bottom of the CB intersects 24 HSUs, which are displayed in Figure 5-97 and listed in Figure 5-98. Figure 5-98 is not a list of all contaminated HSUs in the CB. Figure 5-99 displays the CB of the base case colored by the saturated depth of contamination.

Outside the NNSS boundary, the CB extends through the locations occupied by ER-EC-11 and ER-EC-6. The CB further extends between ER-EC-15 and ER-EC-12 but does not intersect them.

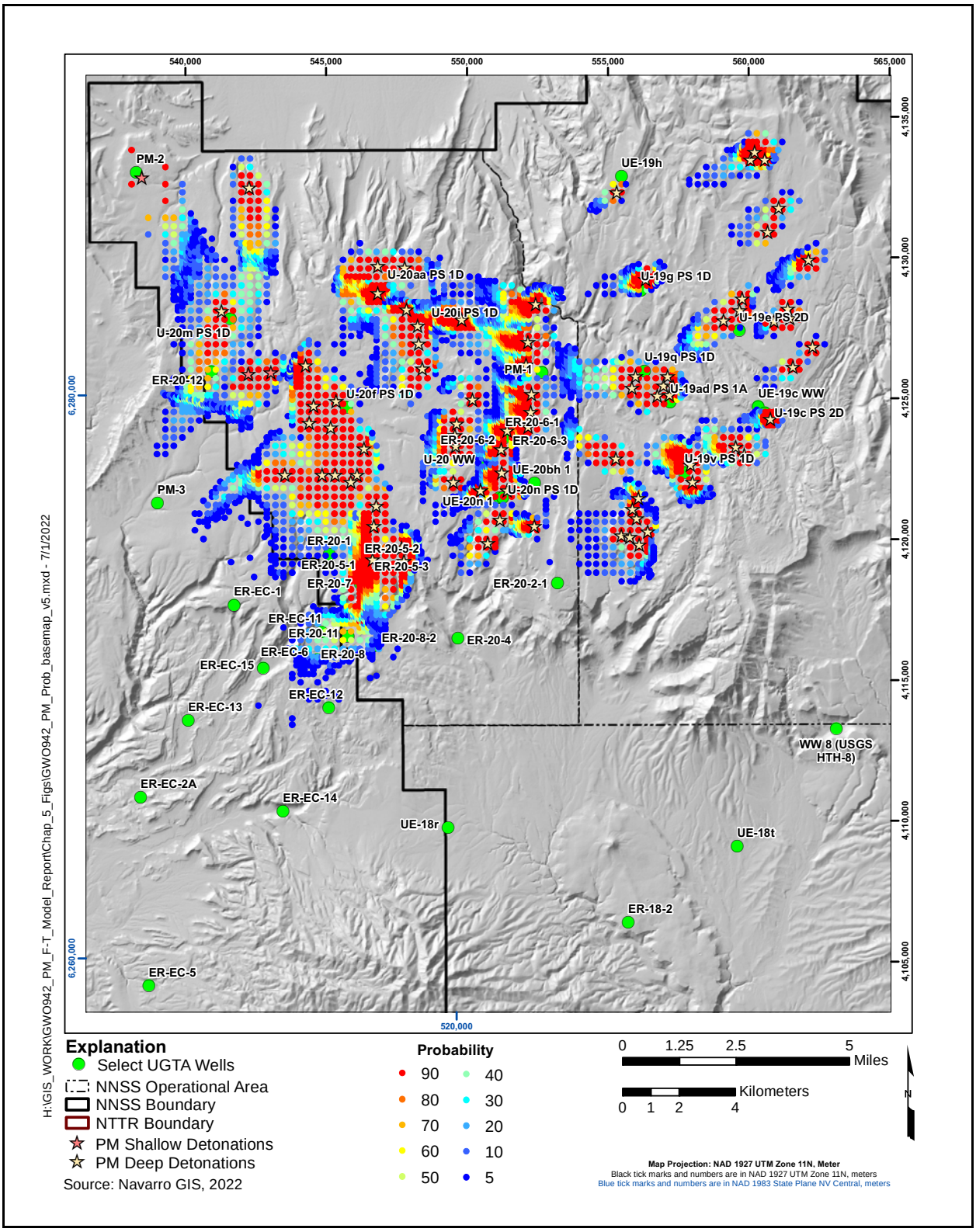

Figure 5-96
1,000-Year Time-Cumulative Probability of Exceedance of MCLs for PM DVRFS3 Recharge Alternative Flow Model

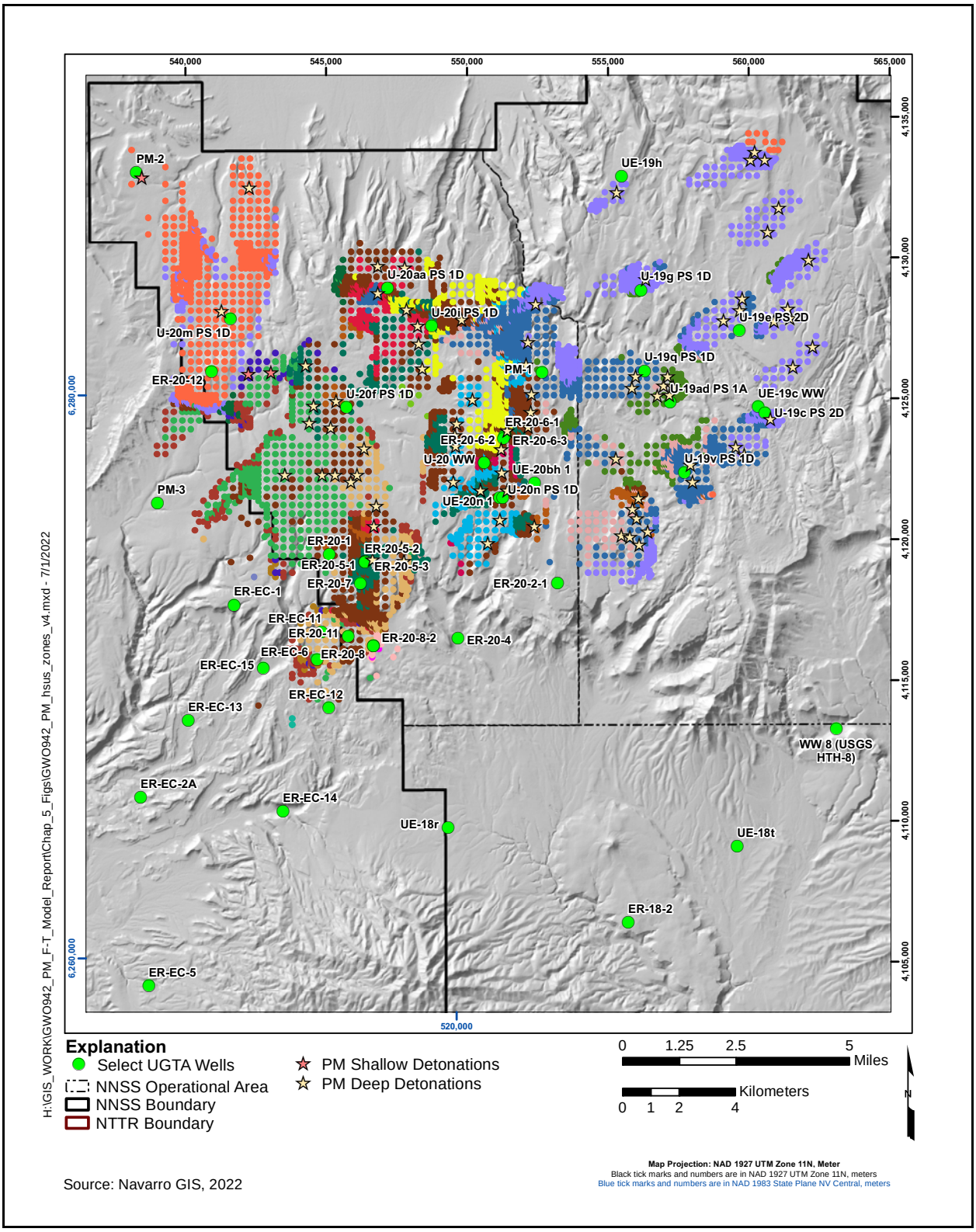

Figure 5-97
CB of DVRFS3 Recharge Alternative Flow Model
Colored by Lowest Contaminated HSU

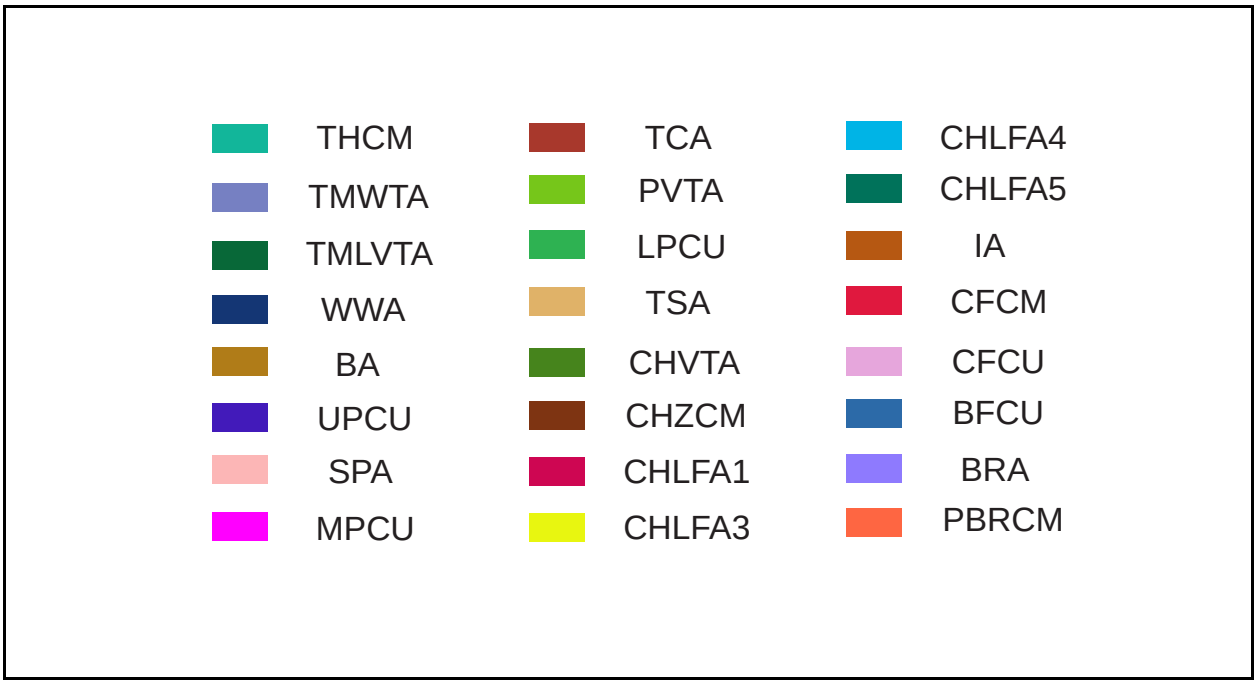

Figure 5-98
Lowest Contaminated HSUs in CB for DVRFS3 Recharge Alternative Flow Model with Color Key for Figure 5-97

Nearest to the location of ER-EC-11, the saturated depth of the CB (i.e., the depth below the modeled water table surface, which represents the top of the model) is approximately 673 m (as shown in Figure 5-99). The water table at ER-EC-11 is at a depth (bgs) of approximately 450 m. Thus, the total depth of the bottom of the CB near ER-EC-11 is approximately 1,123 m bgs in the TSA, which is intersected by ER-EC-11_p1.

Just upgradient of ER-EC-6, the saturated depth of the CB is approximately 547 m (as shown in Figure 5-99). The water table at ER-EC-6 is at a depth (bgs) of approximately 434 m. Thus, the total depth of the bottom of the CB just upgradient of ER-EC-6 is approximately 981 m bgs in the TSA (Figure 5-97), which is intersected by ER-EC-6_m2.

Just downgradient of ER-EC-6, the saturated depth of the CB is approximately 290 m (as shown in Figure 5-99). The water table at ER-EC-6 is at a depth (bgs) of approximately 434 m. Thus, the total depth of the bottom of the CB just downgradient of ER-EC-6 is approximately 724 m bgs in the TCA (Figure 5-97). Upgradient of this location, the TCA is intersected by ER-EC-6_m3.

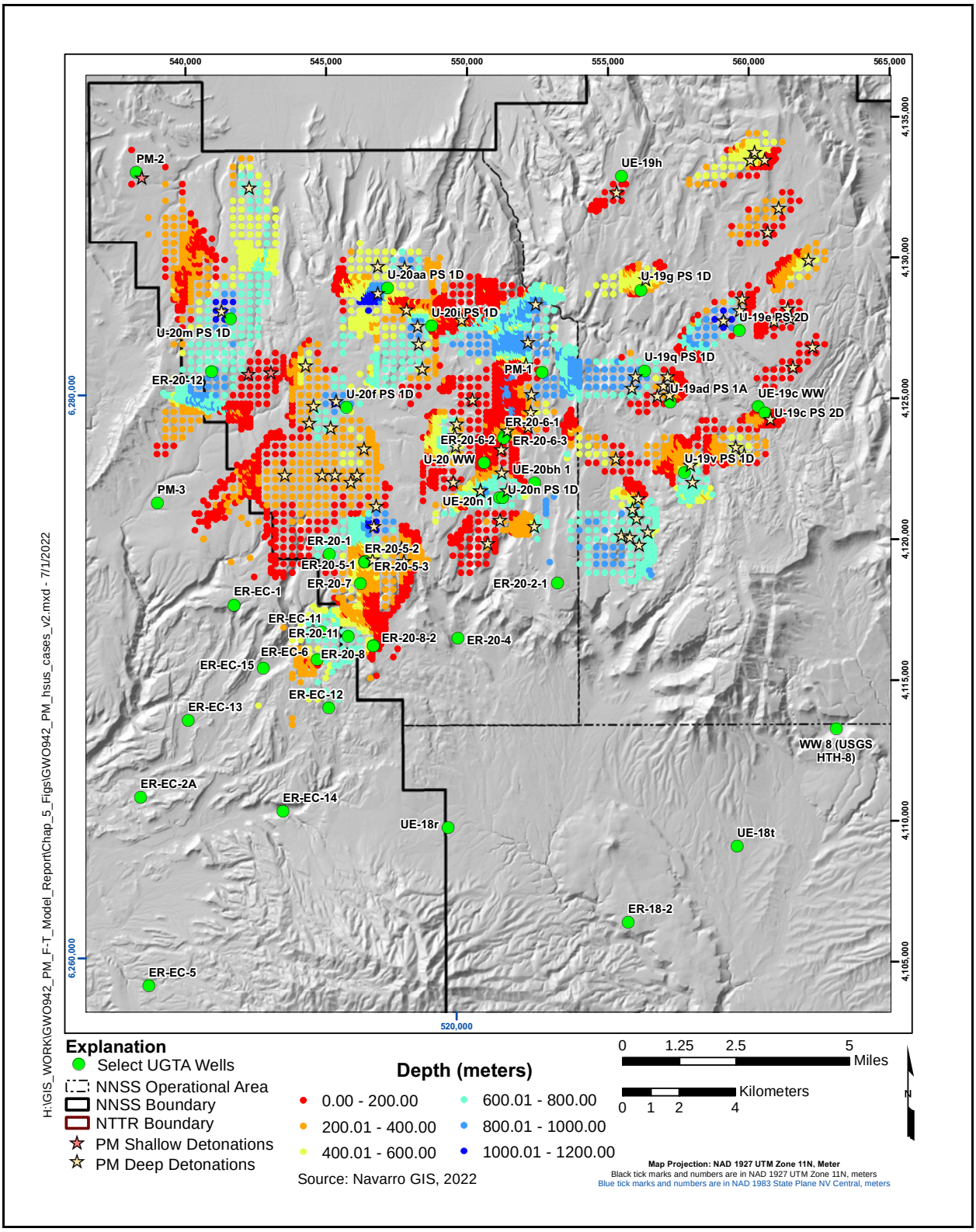

Figure 5-99
CB of DVRFS3 Recharge Alternative Flow Model
Colored by Saturated Depth of Contamination

The CB exists approximately 755 m northwest of ER-EC-12. At this location, the saturated depth of the CB (Figure 5-99) is approximately 521 m in the TCA (Figure 5-97). The TCA is intersected by ER-EC-12_p3.

The CB exists approximately 1,055 m east–southeast of ER-EC-15. At this location, the saturated depth of the CB (Figure 5-99) is approximately 312 m in the TCA (Figure 5-97). The TCA is intersected by ER-EC-15_p2.

5.5.2.1.4 Results for Alternative Flow Model Including All Faults

Figure 5-100 shows the forecasted 1,000-year time-cumulative probability of exceedance of alpha-emitter, beta-emitter, and U MCLs for the alternative flow model including all faults. The time-cumulative probability of exceedance uses the probability of exceeding the MCL at each node for each individual modeled time step and identifies the maximum probability of MCL exceedance at each node regardless of the time that maximum occurs. Each colored dot represents the probability that the sum of concentrations from all RNs relative to their respective MCLs will exceed a value of 1 at that model cell. Only probabilities greater than 5 percent (i.e., the 95th percentile) are displayed. Figure 5-100 is displayed such that at each x,y location, the maximum probability of MCL exceedance at any depth is shown.

In Figure 5-100, there is one point southwest of PM-3 that appears disconnected from the continuous collection of points approximately 6 km to the northeast. The isolated point is a cell that has lower velocities than the neighboring upgradient cells. As such, the particle track residence times are higher in this cell, resulting in higher calculated concentrations in this cell, which in turn results in a higher probability of exceeding MCL in this cell in some realizations. This point appears disconnected because only probabilities greater than 5 percent are displayed. If the figure were displayed with probabilities greater than 1 percent (i.e., the 99th percentile) the point would not appear disconnected from the other points to the northeast.

For the alternative flow model including all faults, the 2-D CB perimeter is defined by the ground surface area that is obscured in Figure 5-100 by the collection of colored dots. The CB extends approximately 2 to 3 km past the western NNSS boundary onto the NTTR at three locations: (1) north of PM-3, (2) in the Bench area near ER-EC-6, and (3) northeast of ER-EC-1.

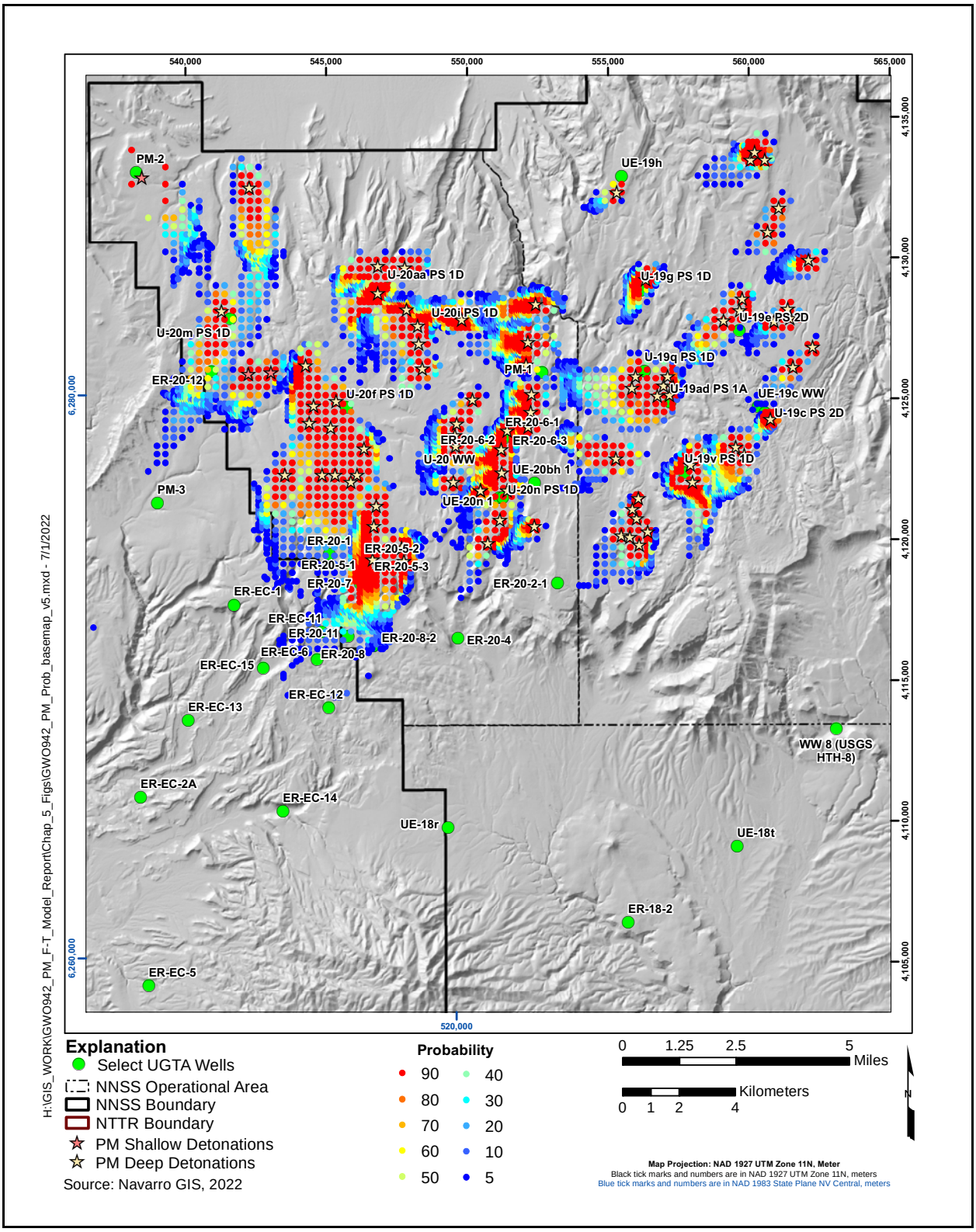

Figure 5-100
1,000-Year Time-Cumulative Probability of Exceedance of MCLs for PM Alternative Flow Model Including All Faults

Due to the complex faulted geology in PM, the vertical extent of the CB varies across the computational domain. The bottom of the CB intersects 23 HSUs, which are displayed in Figure 5-101 and listed in Figure 5-102. Figure 5-102 is not a list of all contaminated HSUs in the CB. Figure 5-103 displays the CB of the base case colored by the saturated depth of contamination.

Outside the NNSS boundary, the CB extends through the locations occupied by ER-EC-11 and just north of ER-EC-6, nearly extending to the location occupied by ER-EC-15. Another leg of the CB extends from ER-20-8 outside the NNSS boundary to a location just northeast of ER-EC-12.

Nearest to the location of ER-EC-11, the saturated depth of the CB (i.e., the depth below the modeled water table surface, which represents the top of the model) is approximately 673 m (as shown in Figure 5-103). The water table at ER-EC-11 is at a depth (bgs) of approximately 450 m. Thus, the total depth of the bottom of the CB near ER-EC-11 is approximately 1,123 m bgs in the TSA (Figure 5-101), which is intersected by ER-EC-11_p1.

The CB exists approximately 351 m northwest of ER-EC-6. At this location, the saturated depth of the CB (Figure 5-103) is approximately 223 m in the BA (Figure 5-101). The BA is intersected by ER-EC-6_m4_a3.

The CB exists approximately 1,000 m east of ER-EC-15. At this location, the saturated depth of the CB (Figure 5-103) is approximately 335 m in the TCA (Figure 5-101). The TCA is intersected by ER-EC-15_p2.

The CB exists approximately 413 m northeast of ER-EC-12. At this location, the saturated depth of the CB (Figure 5-103) is approximately 721 m in the CHZCM (Figure 5-101). The CHZCM is intersected by ER-EC-12_p2.

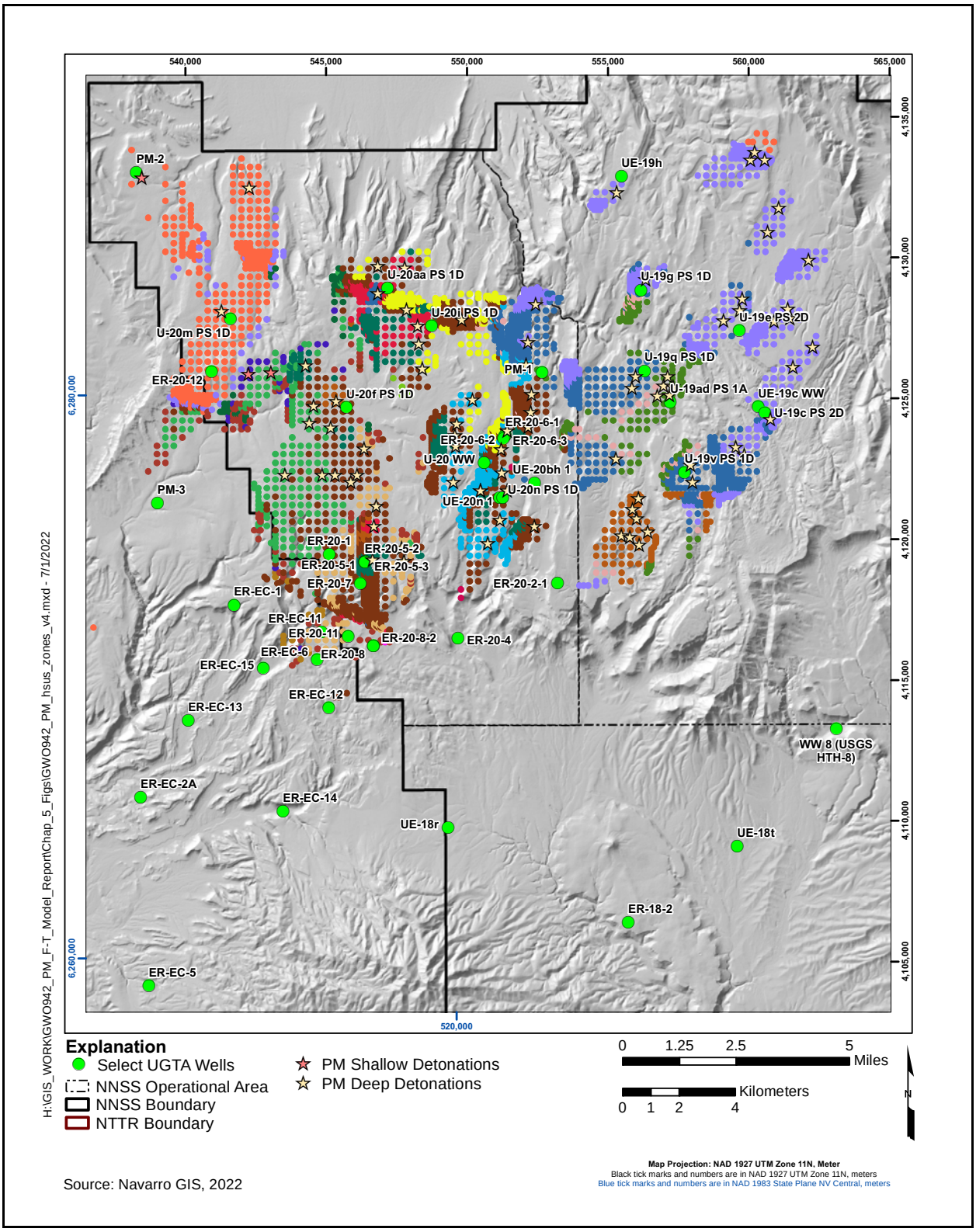

Figure 5-101
CB of Alternative Flow Model Including All Faults
Colored by Lowest Contaminated HSU

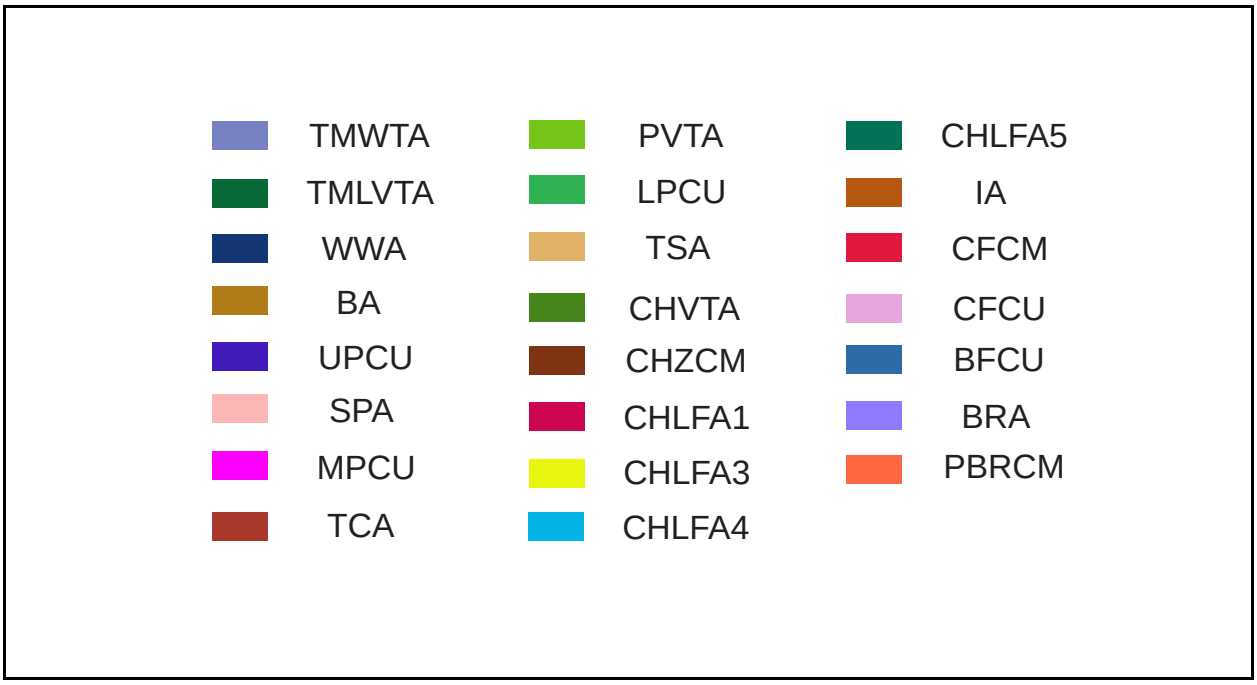

Figure 5-102
Lowest Contaminated HSUs in CB for Alternative Flow Model Including All Faults with Color Key for Figure 5-101

5.6 Sensitivity Analysis

5.6.1 Qualitative Analysis

The CB is largely defined by the CEV (see Section 5.5.2), which represents the total volume of all model cells equal to or exceeding the SDWA standard (CFR, 2021) at any time up to 1,000 years for a specific realization. For the base case PM CAU transport model, a qualitative sensitivity analysis was performed in which scatter-plots were generated that simply plotted CEV against each transport parameter for all 400 realizations. Examination of these plots did not yield any conclusive results that would indicate any parameters were more or less sensitive than any parameters as related to the CEV. A second attempt was made by generating scatter-plots that plotted a reduced CEV comprising only the portion of the CEV at the leading edge in western Area 20 against each transport parameter for all 400 realizations. The resulting plots were different from the first attempt in that some parameters began to stand out, but correlations were poor. The results (or lack thereof) of the qualitative analysis suggest that parameter sensitivity is scale dependent. At the CAU scale, the region affected by transport spans many HSUs. While some HSUs span large areas of the CAU, many HSUs exist in

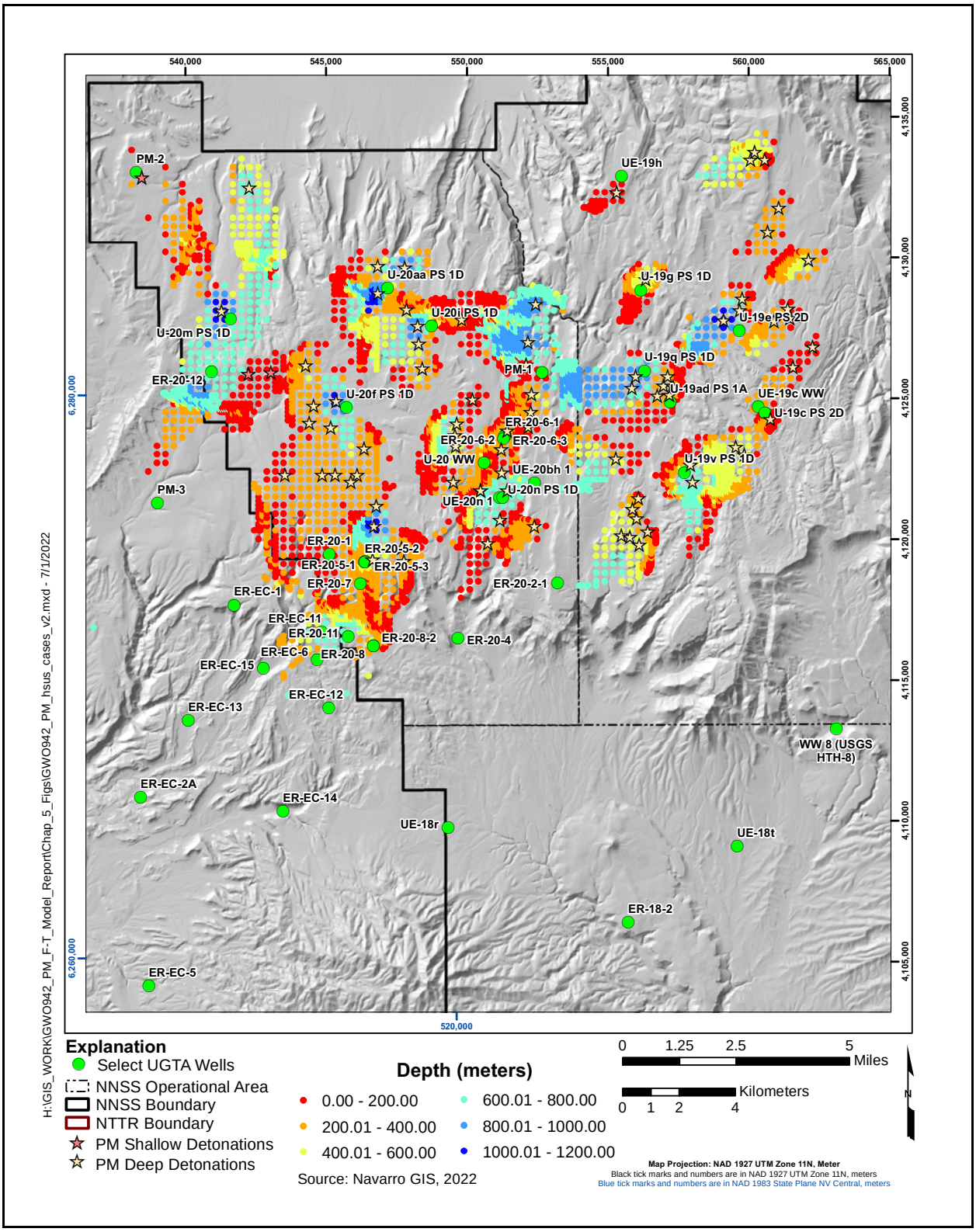

Figure 5-103
CB of Alternative Flow Model Including All Faults
Colored by Saturated Depth of Contamination

relatively small localized areas. Thus, no one HSU and its associated transport parameters will have a large effect on the CEV.

5.6.2 Local Parameter Sensitivity Analysis

As discussed in Section 4.4.1, local parameter sensitivity is evaluated using the PEST code (Doherty, 2004). During parameter optimization, the PEST code calculates a sensitivity coefficient for each parameter with respect to all weighted observations. This analysis is termed “local” because parameter values near the calibrated value are investigated using only slight changes to parameter values. Sensitivity coefficients, computed by PEST are the change in output divided by the change in input and reflect the slope of the input-output relationship at a reference point. The reference used by the sensitivity analysis is given by the calibrated parameter values and is indicative of the parameter sensitivity in the vicinity of the calibration point.

The base case model parameter sensitivity and identifiability values calculated by PEST are presented in Figure 5-104 for only the parameters with calculated sensitivity greater than zero.The most sensitive transport parameters tend to have the highest identifiability, although not every highly identifiable parameter is highly sensitive. The most sensitive transport parameters are those in the TMLVTA, BRA_nw, PBRCM_nw, TSA, CHZCM, TCA, and BA. These are the HSUs through which transport occurs in the Bench area and downgradient from HANDLEY. In the Bench area, observation locations in these HSUs include ER-20-5-1_m1 in the TSA, ER-20-7_m1 in the TSA, ER-20-8_p1 in the CHZCM, ER-20-8_m2 in the TCA, ER-20-11_m1 in the BA, ER-EC-11_p1 in the TSA, ER-EC-11_m2 in the TCA, and ER-EC-11_p3 in the BA. Observation locations downgradient from HANDLEY in these HSUs include ER-20-12_m1 in the PBRCM_nw, ER-20-12_p1 in the BRA_nw, ER-20-12_p4 in the TMLVTA, and PM-3_p1 in the TCA_w. It is not surprising that the above observation locations were highly weighted in the PM CAU transport model calibration, and the calibration results at these locations showed good matches to or overpredictions of observed ^{3}H concentrations.

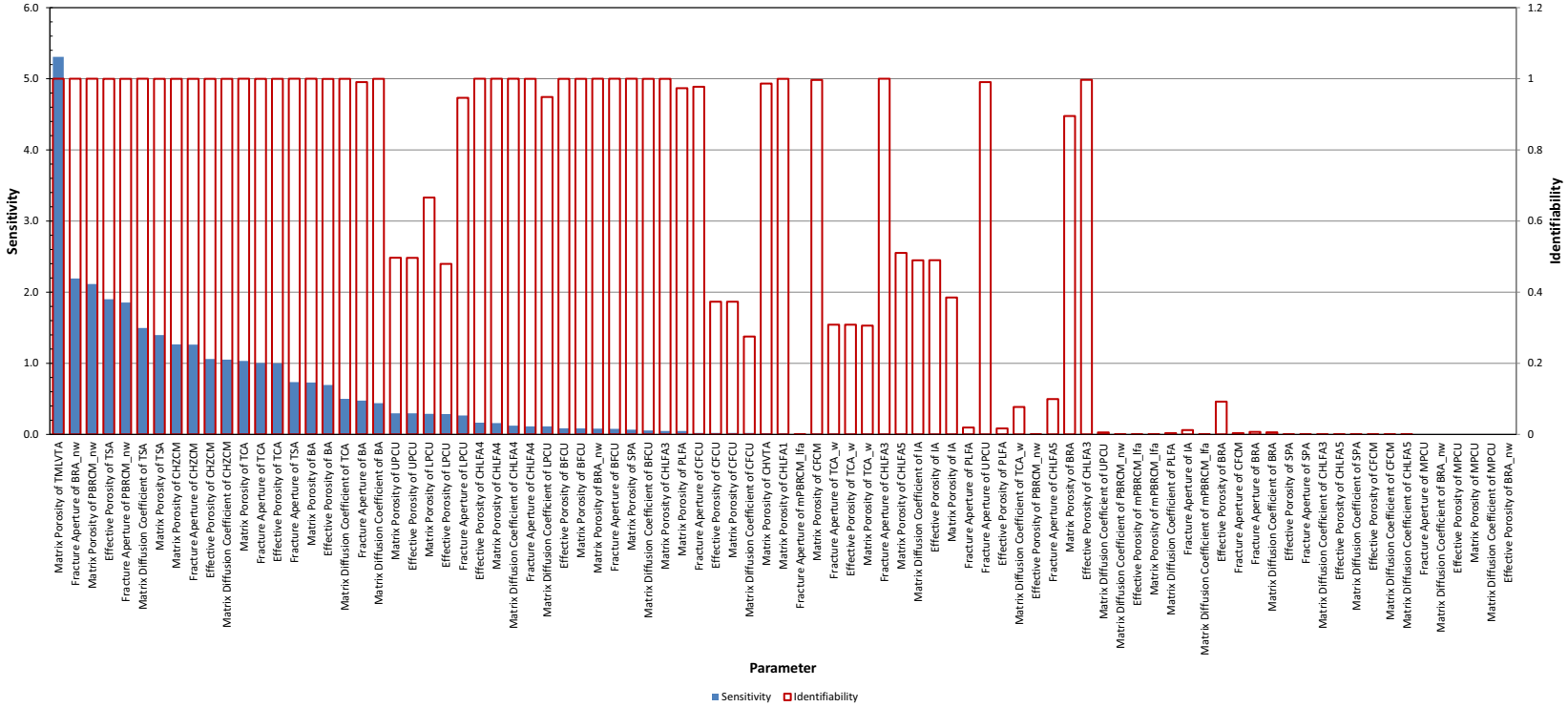

Figure 5-104
Sensitivity and Identifiability for Transport Parameters

5.6.3 Sensitivity to Dispersion

As discussed in Section 5.2.2.7.2, the calibration and Monte Carlo simulations used a longitudinal dispersivity of 150 m, a transverse horizontal dispersivity of 15 m, and a transverse vertical dispersivity of 1.5 m. The effect of using different values of dispersion was investigated by running PLUMECALC for ^{3}H using calibrated transport parameters for the BENHAM detonation using the following values for dispersion (longitudinal, transverse horizontal, transverse vertical):

- 150 m, 15 m, 1.5 m
- 100 m, 10 m, 1 m
- 50 m, 5 m, 0.5 m
- 15 m, 1.5 m, 0.15 m
- 1 m, 0.1 m, 0.01 m
- 0 m, 0 m, 0 m (i.e., no dispersion)

Figures 5-105 and 5-106 show ^{3}H concentration plumes (showing concentrations above MCL) from BENHAM at 55 years for the six cases of dispersivity. As expected, as the length and width of the ^{3}H plumes decrease due to decreased dispersion the concentrations in the plume tend to increase. Upgradient ^{3}H migration is only modeled in the case with highest dispersivities (i.e., 150 m, 15 m, 1.5 m) as seen in Figure 5-105. Dispersion is scale dependent, so it is not expected that the highest dispersivity values would occur so close to the source locations resulting in upgradient migration. Therefore, modeled values of upgradient migration near sources shown in the CBs (which use dispersivities of 150 m, 15 m, 1.5 m) may be disregarded.

Figure 5-107 shows the peak straight-line distance of ^{3}H above the MCL from BENHAM at 55 years for varying dispersivity values. The straight-line distance is computed as the lateral distance from the x,y location of the BENHAM WP to the x,y location of the furthest node away where ^{3}H is above the MCL. As expected, as the dispersivity values decrease, distance traveled downgradient decreases as forward spread of ^{3}H is reduced. The distances range from a maximum of 4,417 m for dispersivities of 150 m, 15 m, 1.5 m, asymptotically approaching a minimum value of 3,538 m that occurs for the case of no dispersion, which represents a total decrease of about 25 percent.

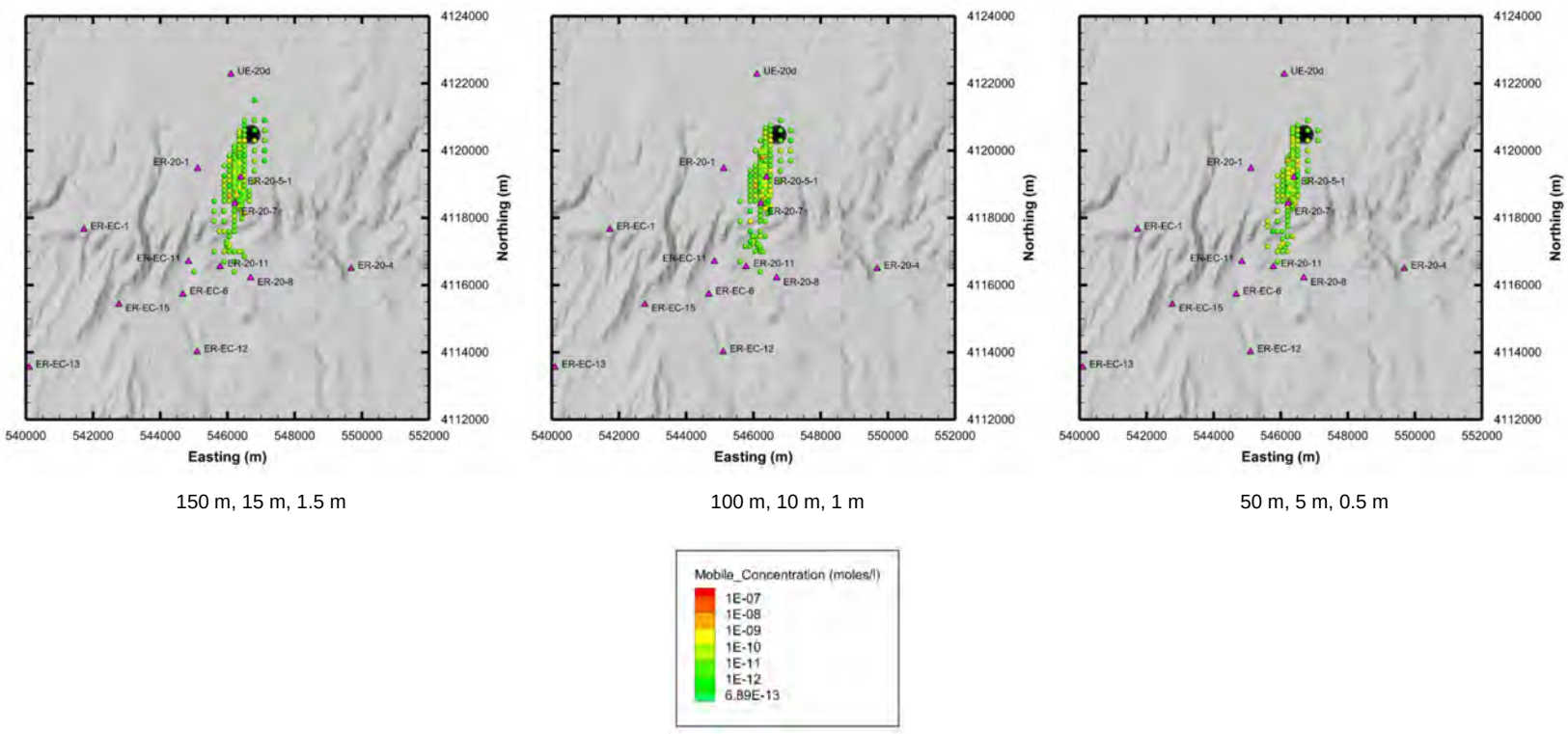

Cavity dimension based on maximum announced yield identified in DOE/NV--209 Rev. 16 (NNSA/NFO, 2015) and Equation 1 in UCRL-ID-136003 (Pawloski, 1999).

Figure 5-105
^{3}H Plumes above MCL from BENHAM at 55 Years for Varying Dispersivity Values
Note: Left: longitudinal dispersivity = 150 m, center: longitudinal dispersivity = 100 m, right: longitudinal dispersivity = 50 m.

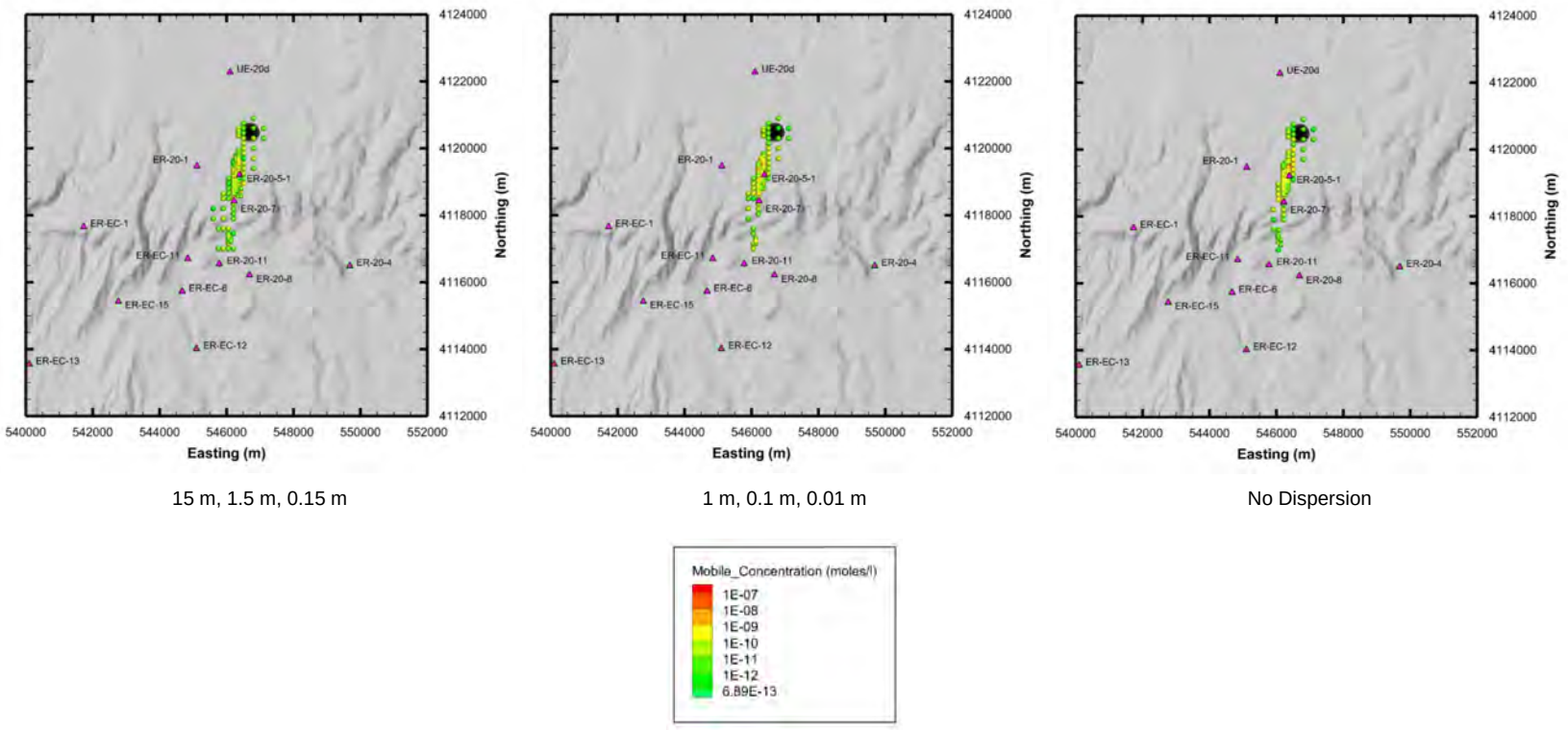

Cavity dimension based on maximum announced yield identified in DOE/NV--209 Rev. 16 (NNSA/NFO, 2015) and Equation 1 in UCRL-ID-136003 (Pawloski, 1999).

Figure 5-106
^{3}H Plumes above MCL from BENHAM at 55 Years for Varying Dispersivity Values
Note: Left: longitudinal dispersivity = 150 m, center: longitudinal dispersivity = 100 m, right: longitudinal dispersivity = 50 m.

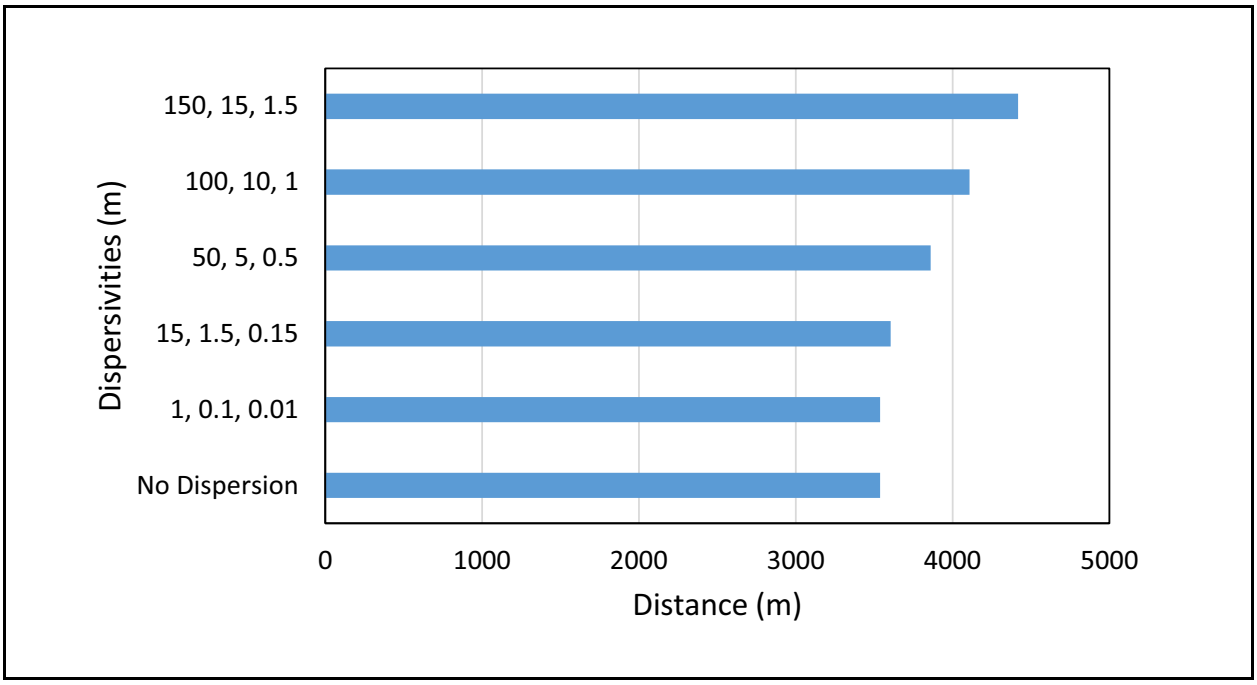

Figure 5-107
Peak Straight-Line Distance of ^{3}H above MCL from BENHAM at 55 Years for Varying Dispersivity Values
Note: Longitudinal, transverse horizontal, transverse vertical.

5.6.4 Sensitivity to Initial Pu Source Mass

As discussed in Section 5.1.2, the calibration and Monte Carlo simulations used the average melt glass percentage for Pu from Carle et al. (2020). The effect of doubling the initial source mass on transport distance was investigated by running PLUMECALC for $^{239/240}$Pu using calibrated transport parameters for the BENHAM detonation using the following melt glass percentages:

- The average melt glass percentage for Pu from Carle et al. (2020), 97.5 percent, resulting in 2.5 percent of available Pu mass being input to the PM CAU transport model
- The minimum melt glass percentage for Pu from Carle et al. (2020), 95 percent, resulting in 5 percent of available Pu mass being input to the PM CAU transport model, effectively doubling the initial mass of Pu over the average case

Figure 5-108 shows ^{239}Pu plumes (showing concentrations above MCL) from BENHAM at 55 years for the two melt glass fractions using minimum K_ds for all zones. Figure 5-109 shows ^{239}Pu plumes (showing concentrations above MCL) from BENHAM at 55 years for the two melt glass fractions using maximum K_ds for all zones. As expected the plumes with minimum K_ds are more extensive than

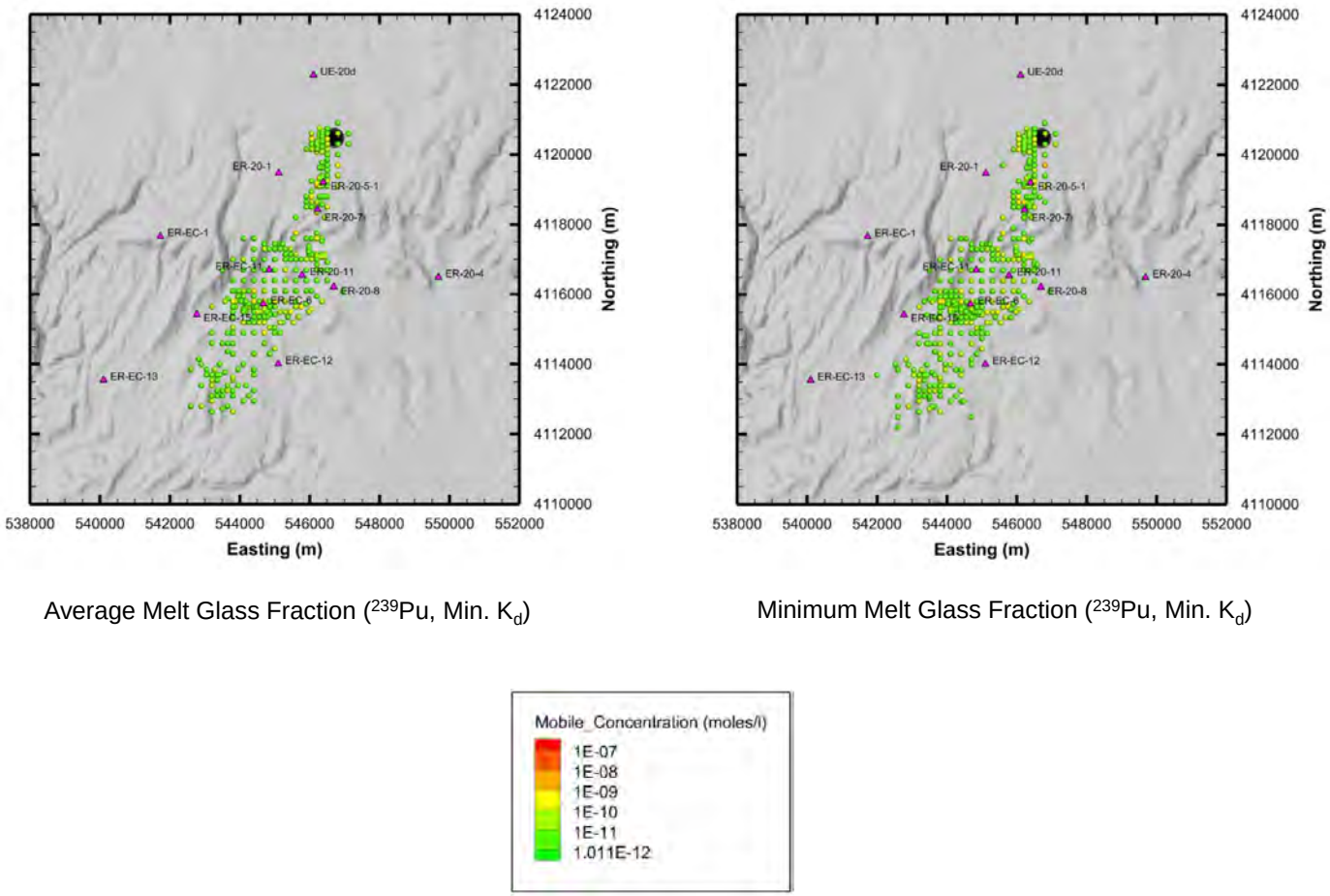

Average Melt Glass Fraction (^{239}Pu, Min. K_d)

Minimum Melt Glass Fraction (^{239}Pu, Min. K_d)

Cavity dimension based on maximum announced yield identified in DOE/NV--209 Rev. 16 (NNSA/NFO, 2015) and Equation 1 in UCRL-ID-136003 (Pawloski, 1999).

Figure 5-108
^{239}Pu Plumes above MCL from BENHAM at 55 Years with Minimum K_ds for Different Melt Glass Fractions

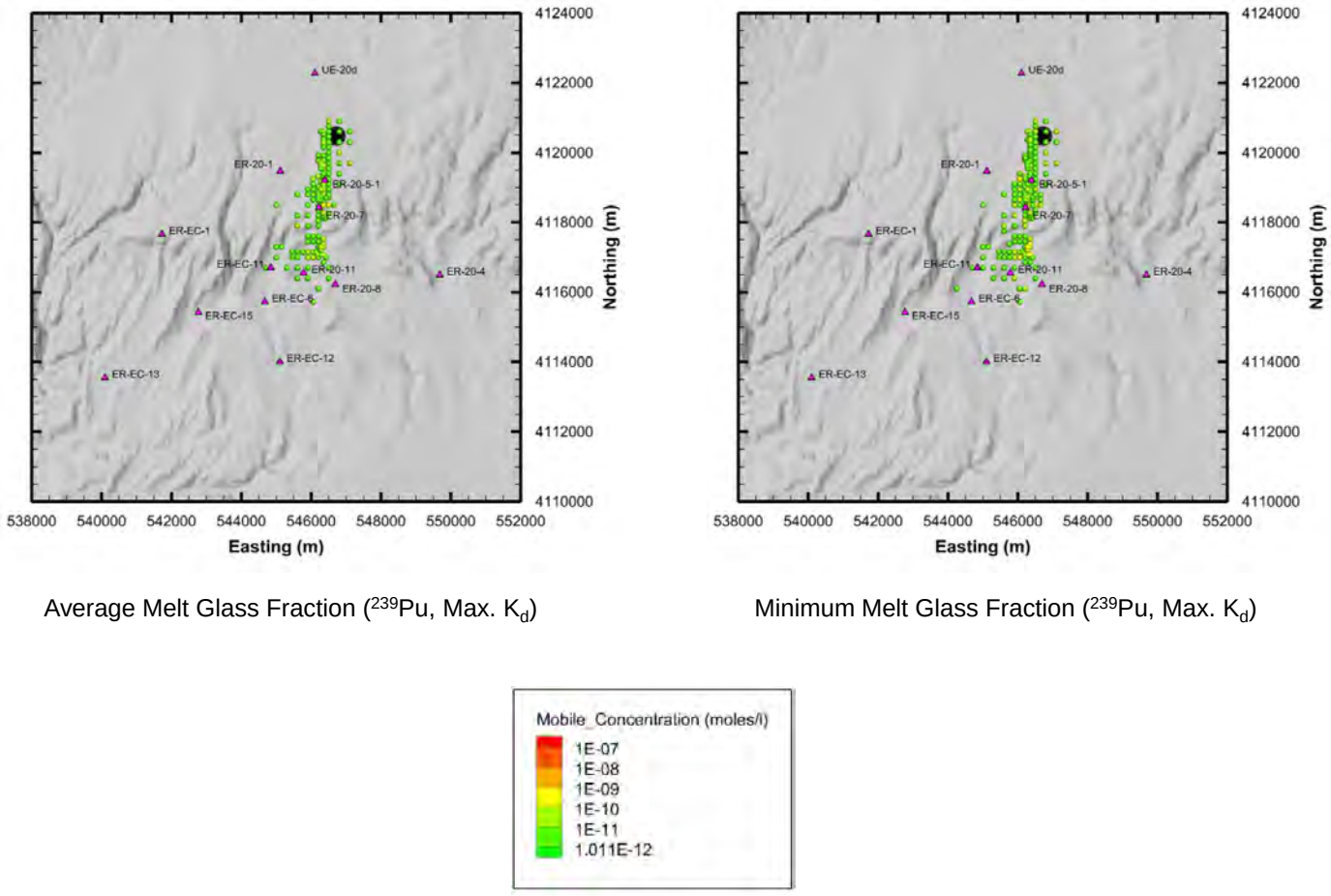

Average Melt Glass Fraction (^{239}Pu, Max. K_d)

Minimum Melt Glass Fraction (^{239}Pu, Max. K_d)

Cavity dimension based on maximum announced yield identified in DOE/NV--209 Rev. 16 (NNSA/NFO, 2015) and Equation 1 in UCRL-ID-136003 (Pawloski, 1999).

Figure 5-109
^{239}Pu Plumes above MCL from BENHAM at 55 Years with Maximum K_ds for Different Melt Glass Fractions

those with maximum K_ds. Also as expected, the modeled plumes using the minimum glass fraction for Pu are slightly more extensive than those using the average glass fraction.

Figure 5-110 shows the peak straight-line distance of ^{239}Pu above the MCL from BENHAM at 55 years for the two melt glass fractions. The straight-line distance is computed as the lateral distance from the x,y location of the BENHAM WP to the x,y location of the furthest node away where ^{239}Pu is above the MCL. For the minimum K_d results, the distances are 8,703 m with the average melt glass fraction and 9,237 m with the minimum melt glass fraction, which represents an increase of approximately 6 percent. It is noteworthy that doubling the source mass of Pu only resulted in a relatively small increase in transport distance at 55 years.

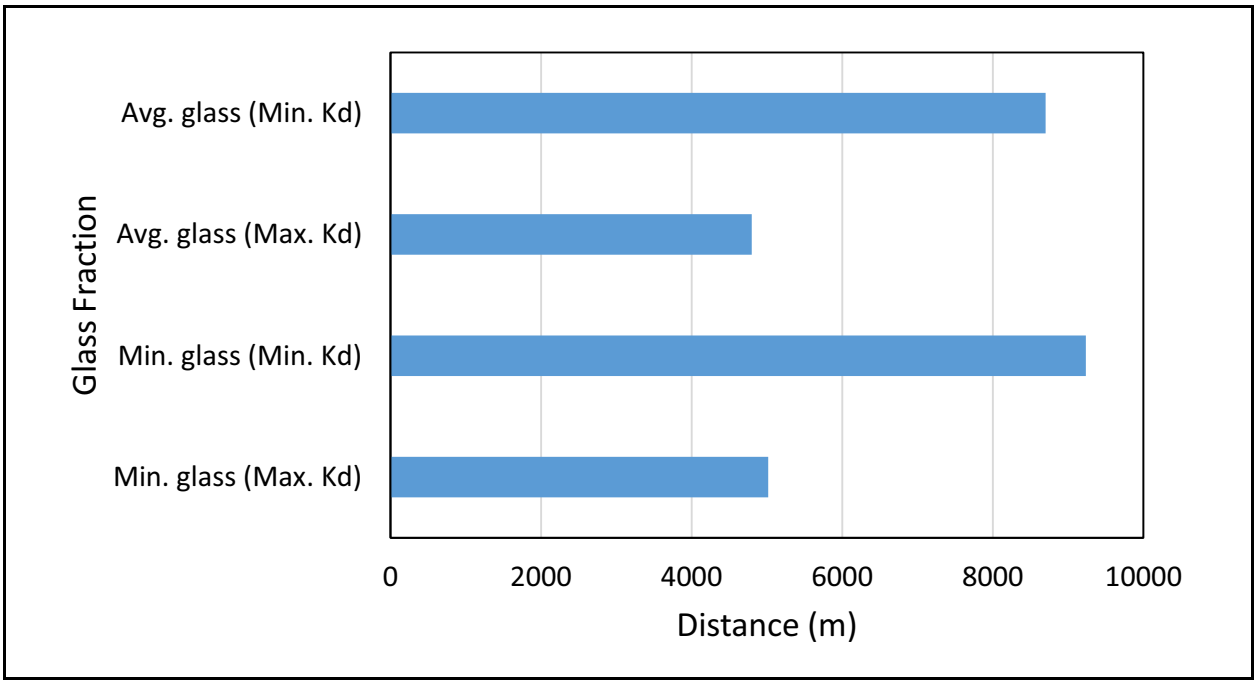

Figure 5-110
Peak Straight-Line Distance of ^{239}Pu above MCL from BENHAM at 55 Years for Different Melt Glass Fractions

5.6.5 Sensitivity to Number of Particles

As discussed in Section 5.4, the calibration and Monte Carlo simulations used up to 20,000 particles at each source location (10,000 particles distributed in the saturated portion of the exchange zone, and 10,000 particles distributed in the saturated portion of the chimney, if present). The effect of using a different number of particles was investigated by running PLUMECALC for ^{3}H using calibrated transport parameters for the BENHAM detonation using particle tracks created with 20,000, 100,000, and 200,000 particles.

Figure 5-111 shows ^{3}H concentration plumes (showing concentrations above MCL) from BENHAM at 55 years for the three cases. The three plumes are similar with respect to concentration levels. The plume with 20,000 particles shows more discontinuity downgradient (i.e., more nodes below MCL between nodes above MCL). Figure 5-112 shows the peak straight-line distance of ^{3}H above the MCL from BENHAM at 55 years for varying numbers of particles. The straight-line distance is computed as the lateral distance from the x,y location of the BENHAM WP to the x,y location of the furthest node away where ^{3}H is above the MCL. The distances are 4,417 m for 20,000 particles, 4,223 m for

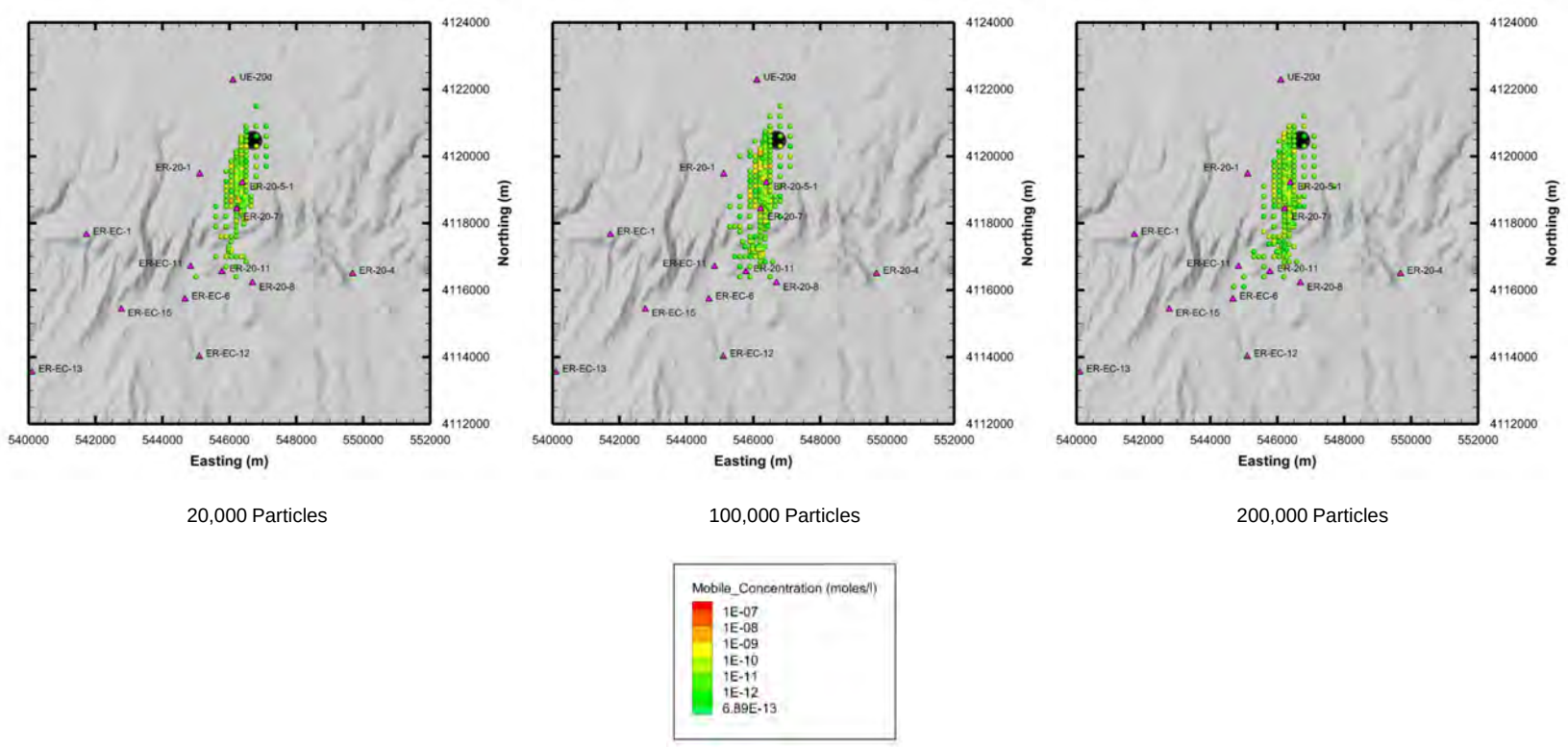

Cavity dimension based on maximum announced yield identified in DOE/NV--209 Rev. 16 (NNSA/NFO, 2015) and Equation 1 in UCRL-ID-136003 (Pawloski, 1999).

Figure 5-111
^{3}H Plumes above MCL from BENHAM at 55 Years for Varying Numbers of Particles

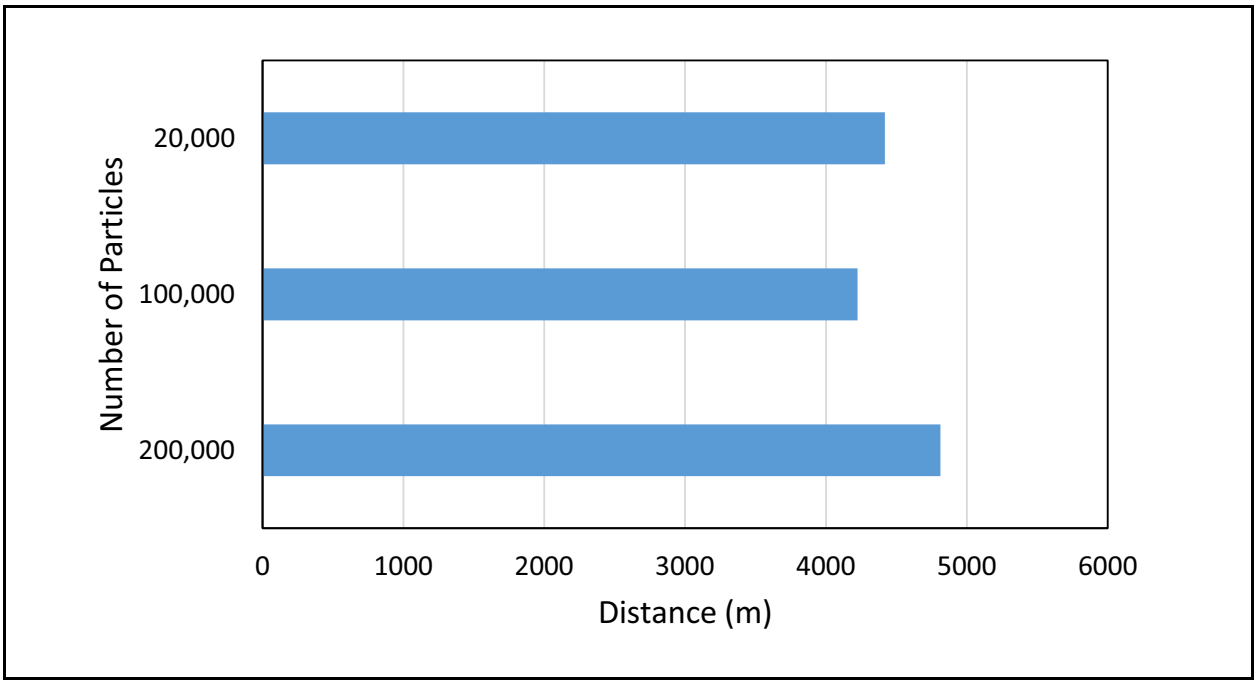

Figure 5-112
Peak Straight-Line Distance of ^{3}H above MCL from BENHAM at 55 Years for Varying Numbers of Particles

100,000 particles, and 4,812 m for 200,000 particles. The distance with 100,000 particles is approximately 5 percent shorter than the distance with 20,000 particles. However, the distance with 200,000 particles is approximately 8 percent longer than the distance with 20,000 particles.

Figure 5-113 shows modeled and measured ^{3}H concentrations (in log space) at ER-20-5-1_m1 (near BENHAM) as a function of time for the three cases. Figure 5-114 shows modeled and measured ^{3}H concentrations (in log space) at ER-20-7_m1 (further downgradient from ER-20-5-1_m1) as a function of time for the three cases. Figure 5-115 shows modeled and measured ^{3}H concentrations (in log space) at ER-20-11_m1 (further downgradient from ER-20-7_m1) as a function of time for the three cases. As the number of particles increases, the concentration levels over time appear less noisy. but observations are still matched fairly well for all three cases. The differences between the three cases is most noticeable further downgradient as attenuating transport processes cause the ^{3}H concentrations to decrease. The noisiness observed using 20,000 particles may explain why the straight-line distance with 20,000 particles is more than the straight line distance with 100,000 particles.

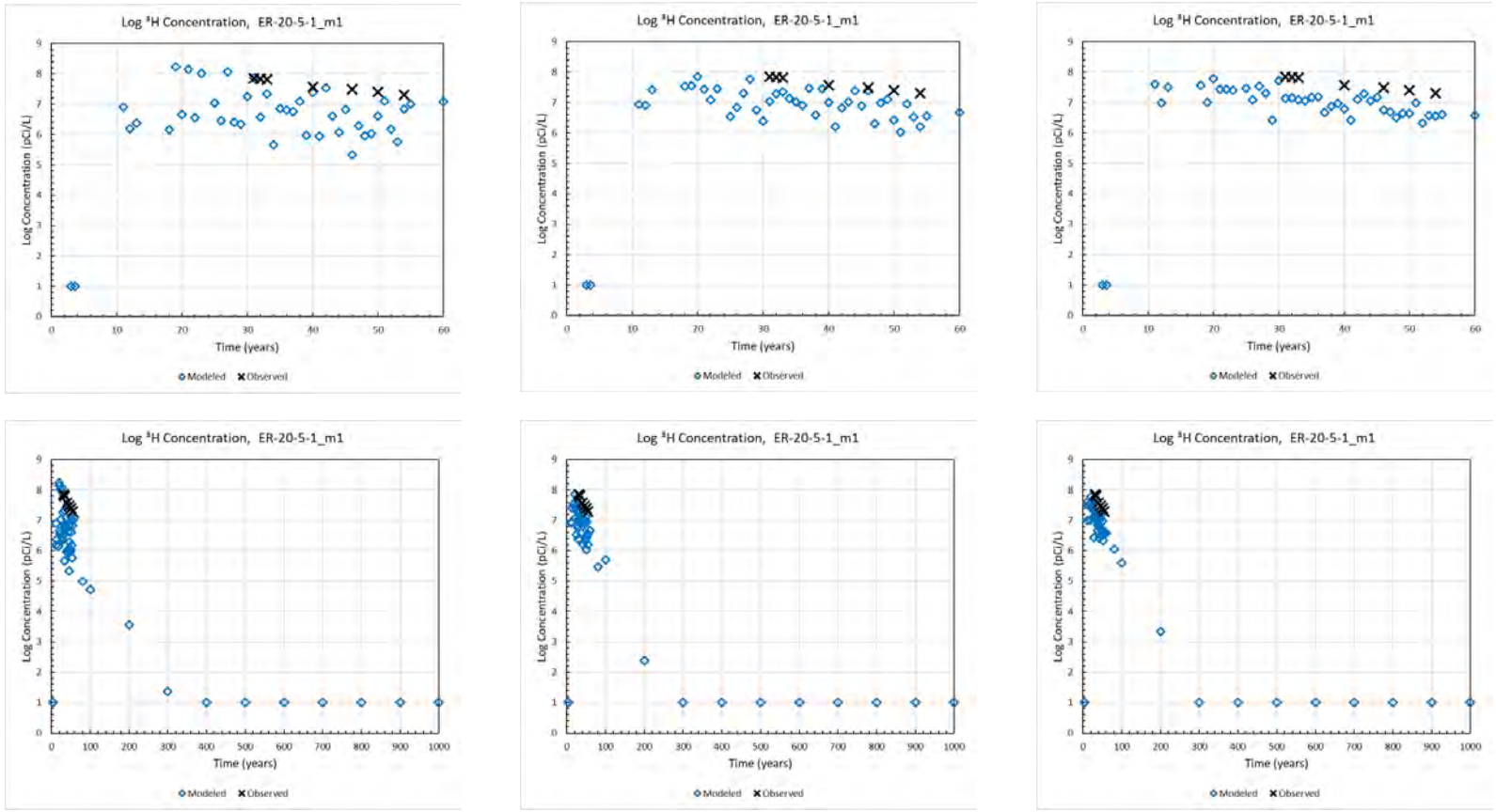

20,000 Particles | 100,000 Particles | 200,000 Particles

Figure 5-113
Modeled and Measured ^{3}H Concentrations at ER-20-5-1_m1 for Varying Numbers of Particles
Note: Top row for 60 years, bottom row for 1,000 years.

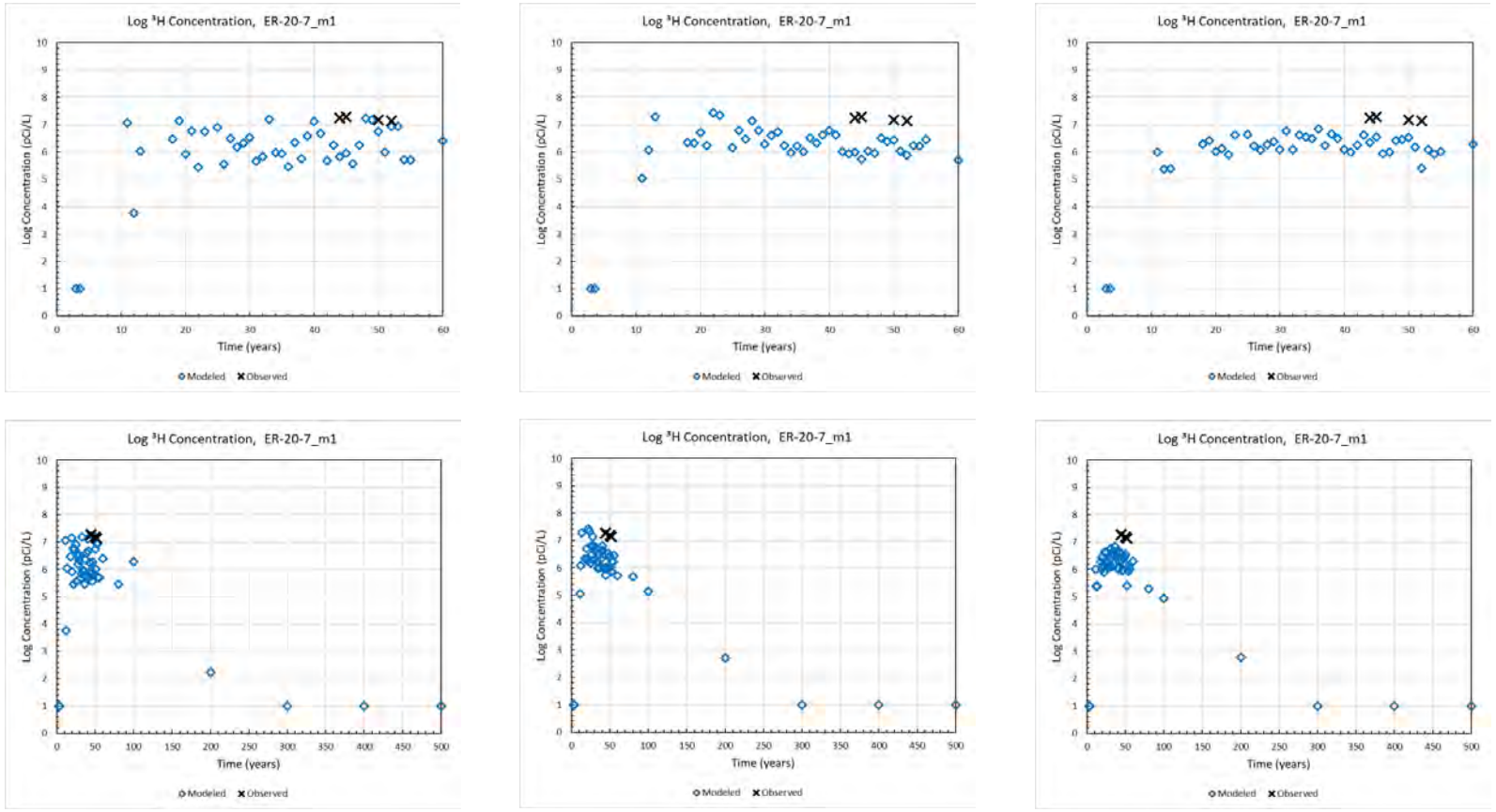

Figure 5-114
Modeled and Measured ^{3}H Concentrations at ER-20-7_m1 for Varying Numbers of Particles
Note: Top row for 60 years, bottom row for 1,000 years.

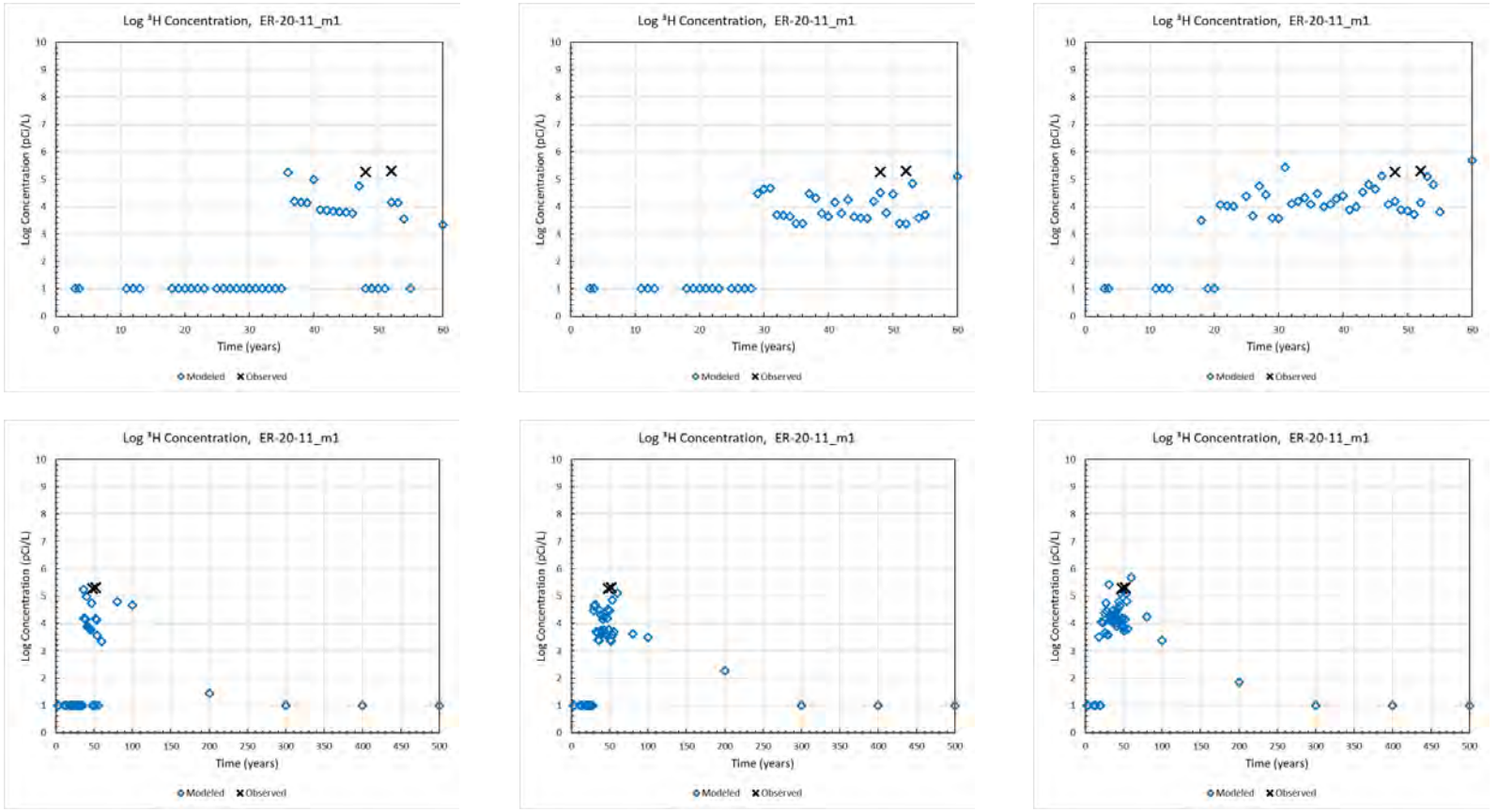

20,000 Particles | 100,000 Particles | 200,000 Particles

Figure 5-115
Modeled and Measured ^{3}H Concentrations at ER-20-11_m1 for Varying Numbers of Particles
Note: Top row for 60 years, bottom row for 1,000 years.

Using 10 times the number of particles used in the Monte Carlo simulations would undoubtedly provide more accurate forecasts. However, doing so would come at the expense of greater data storage needs and much longer run times. Based on these results, it is expected that a smaller number of particles results in an error in contaminant transport distances by around 10 percent.

5.7 CB Ensemble

Figures 5-116 through 5-119 show the 1,000-year time-cumulative 95th-percentile 1,000-year, CB forecasts for the PM base case flow model, the INFILv3 recharge alternative flow model, the DVRFS3 recharge alternative flow model, and the alternative flow model including all faults, with a single color representing each alternative. Because the four alternatives are so similar in area covered, the ensemble is presented in four figures, with each figure showing a different alternative CB on top.

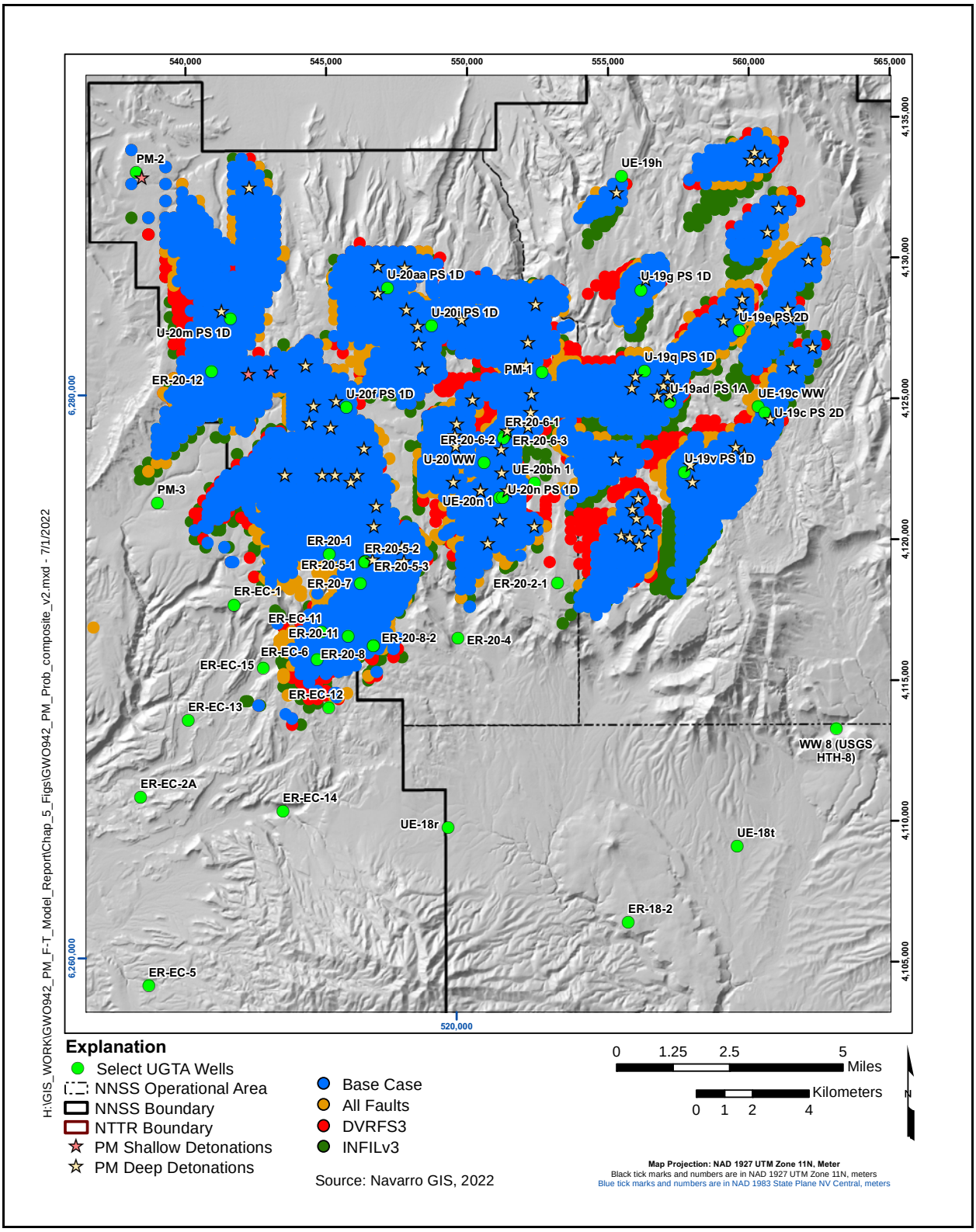

Figure 5-116
1,000-Year Time-Cumulative Probability of Exceedance of MCLs CB Forecasts
Note: Base case on top.

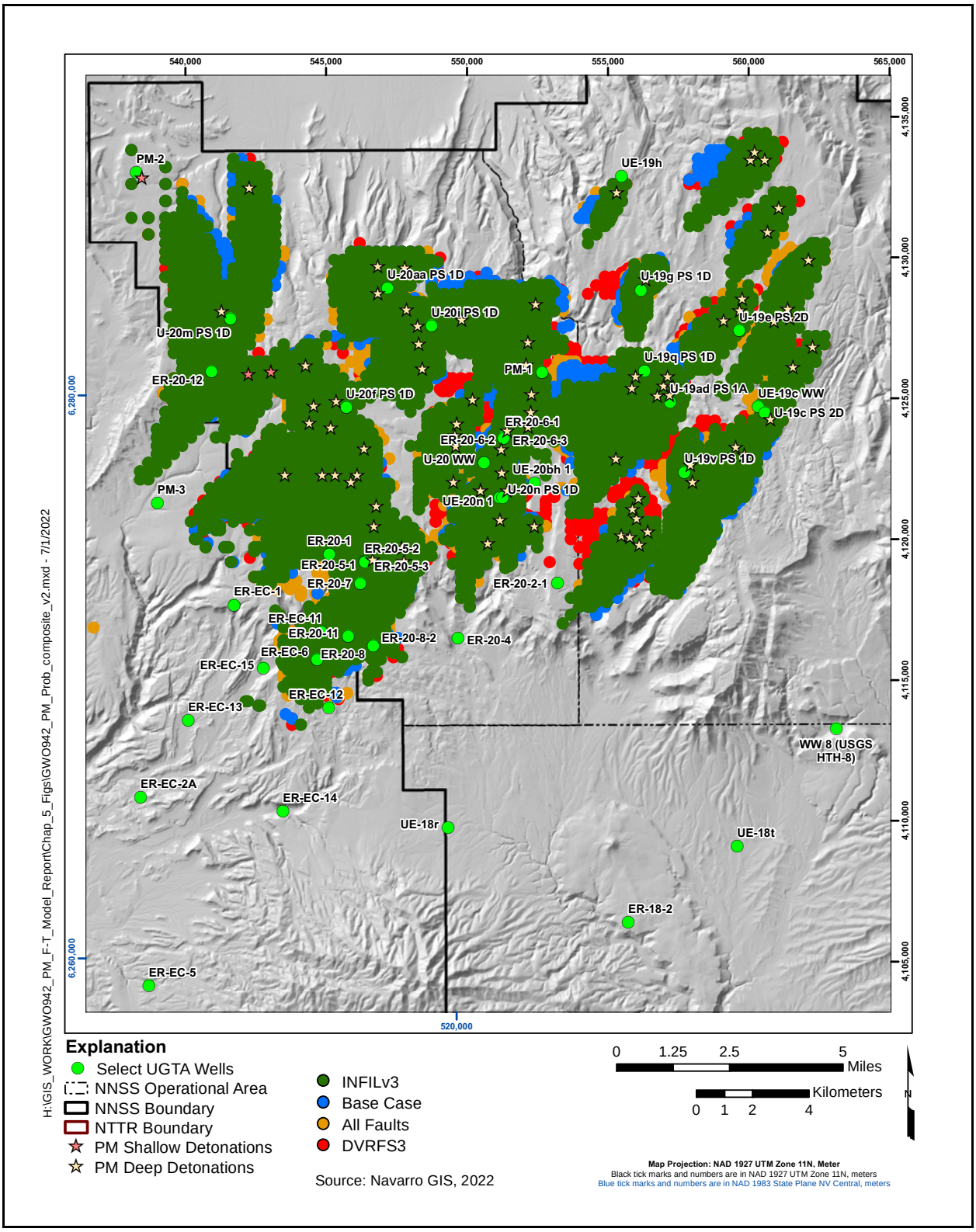

Figure 5-117
1,000-Year Time-Cumulative Probability of Exceedance of MCLs CB Forecasts
Note: INFILv3 recharge alternative flow model on top.

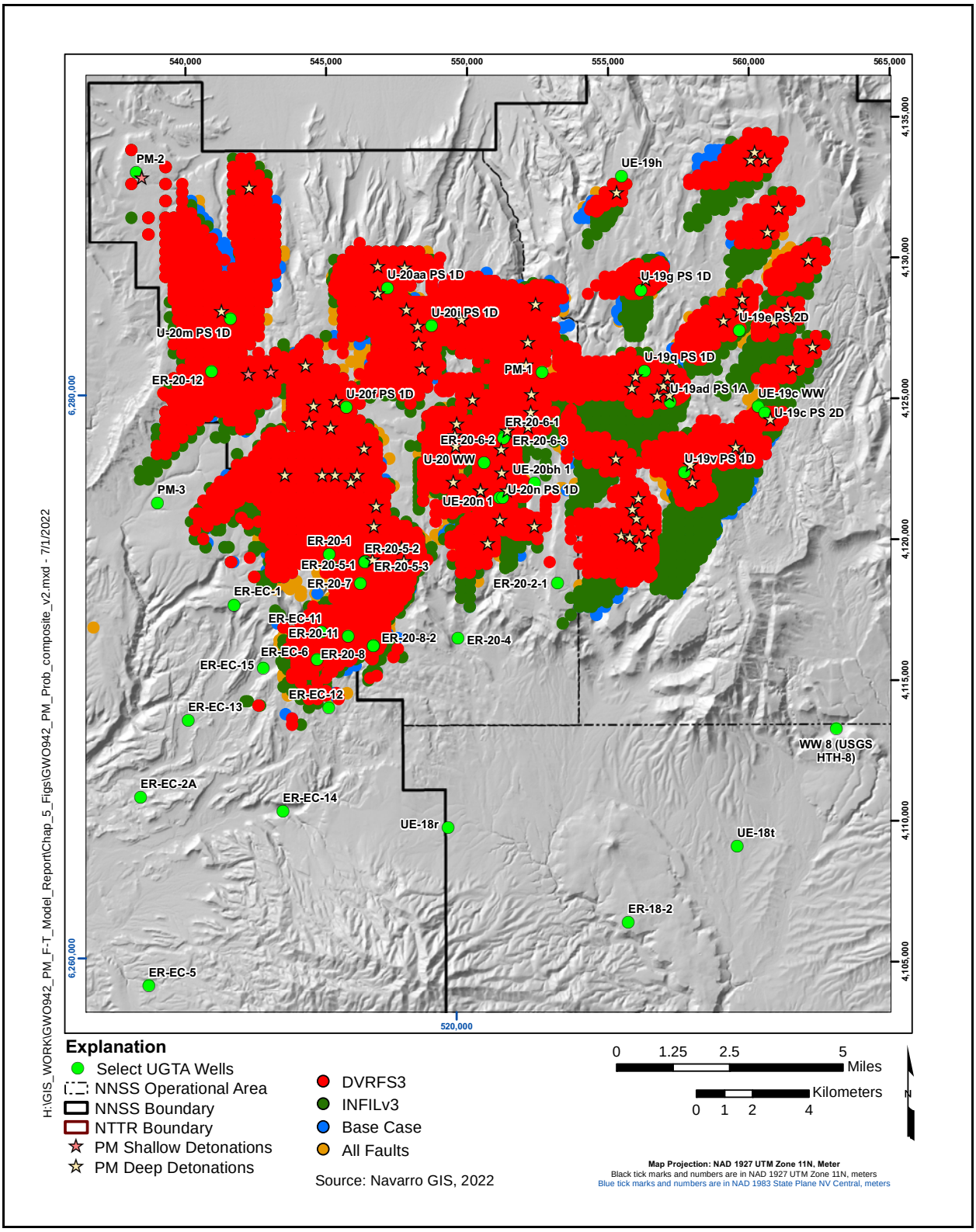

Figure 5-118
1,000-Year Time-Cumulative Probability of Exceedance of MCLs CB Forecasts
Note: DVRFS3 recharge alternative flow model on top.

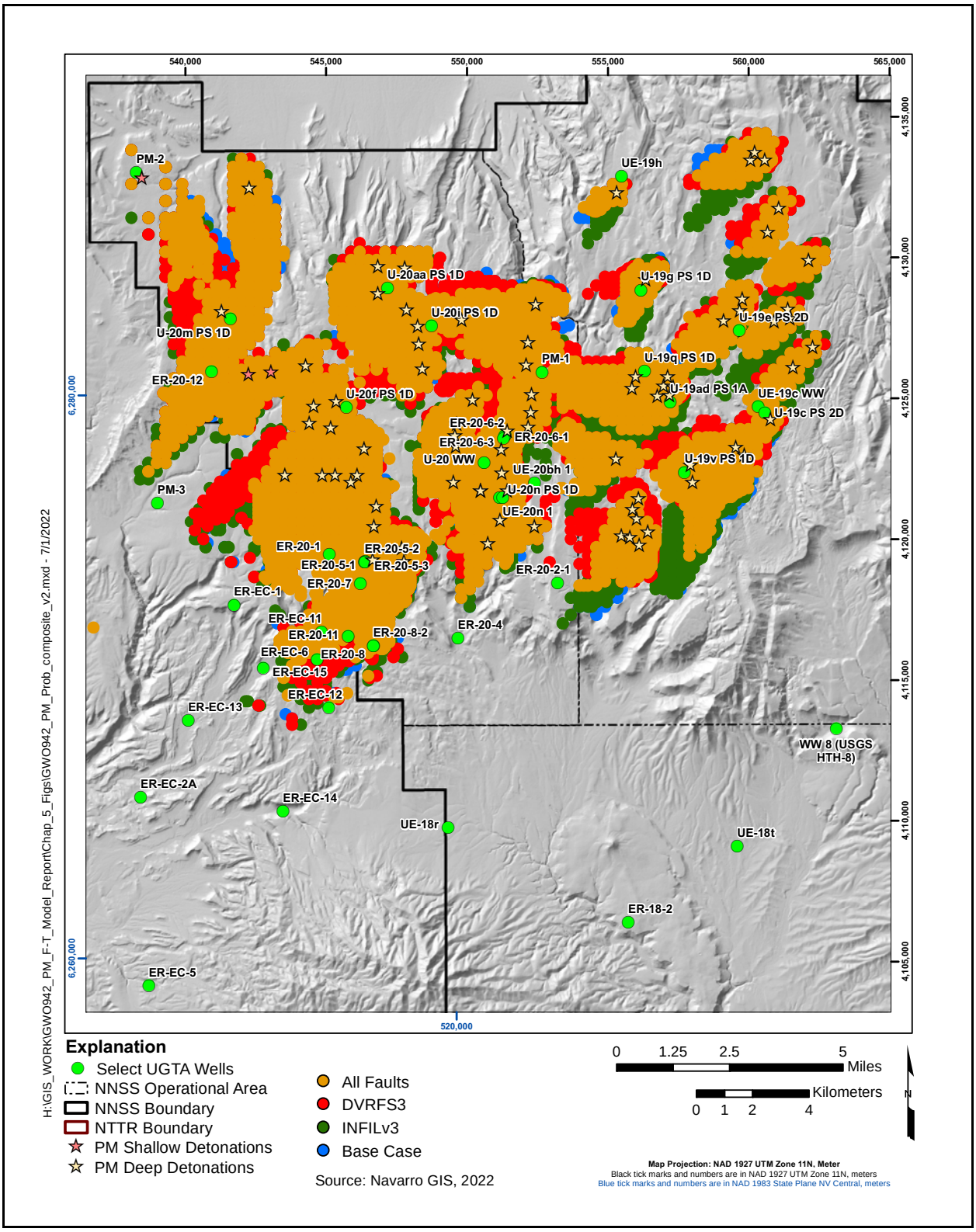

Figure 5-119
1,000-Year Time-Cumulative Probability of Exceedance of MCLs CB Forecasts
Note: Alternative flow model including all faults on top.

The CEV is defined as the total volume of all model cells equal to or exceeding the SDWA standard (CFR, 2021) at any time up to 1,000 years for a specific realization. The cumulative distribution functions (CDFs) of CEV for the four alternatives is shown in Figure 5-120. The CEV distributions for the four cases are quite similar. The INFILv3 recharge alternative has the highest distribution of CEVs, indicating that this case has the largest volume of model cells that exceed the SDWA standard.

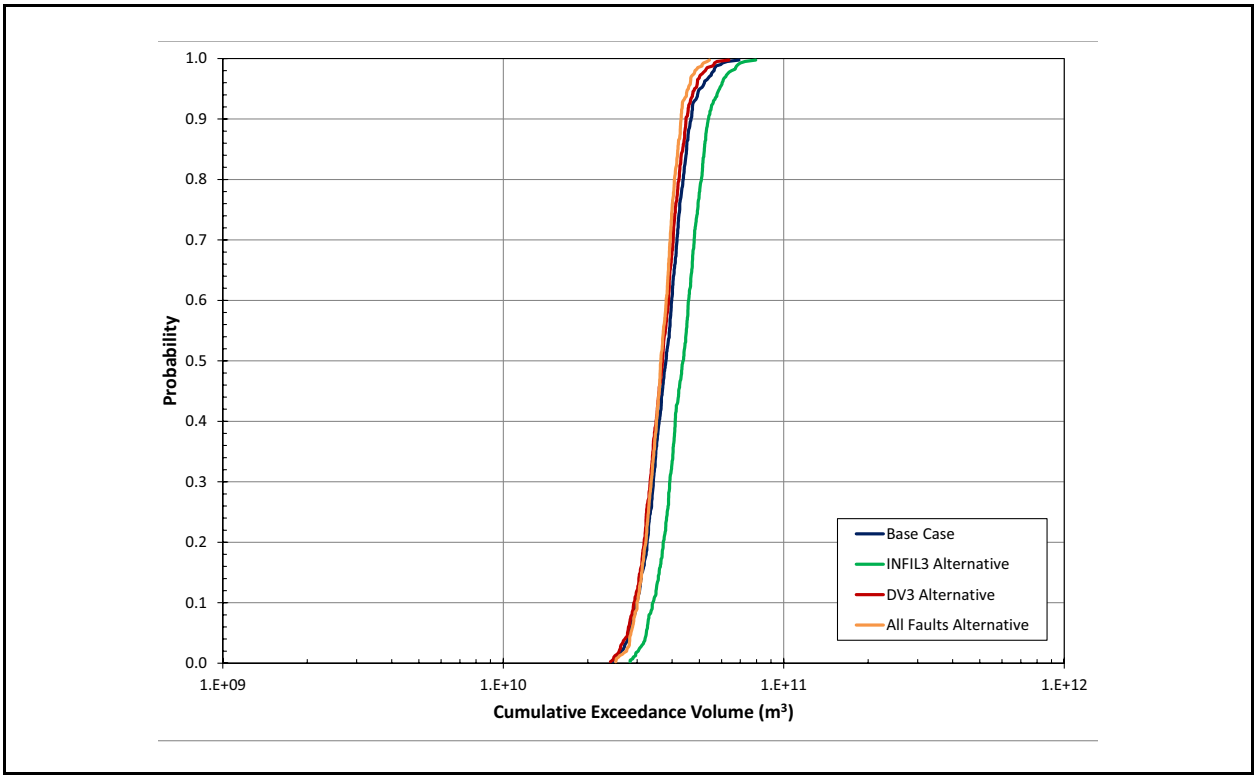

Figure 5-120
Distributions of Cumulative MCL Exceedance Volume for PM Base Case and Alternative Flow Models

For a single realization, the FEV is defined as the total volume of all model cells equal to or exceeding the SDWA standard (CFR, 2021) for a particular RN (or alternatively a class of RNs) at any time up to 1,000 years divided by the CEV. The FEV is a time-specific measure that ranks the RNs in terms of their importance to the CEV. Average FEV plots (averaged across all 400 realizations) for the PM base case flow model are shown in Figure 5-121 for each RN and in Figure 5-122 for each RN class. Because all alternative models use the same source terms as input, it is expected that the FEV plots for each alternative will be nearly identical. Tritium contributes most to

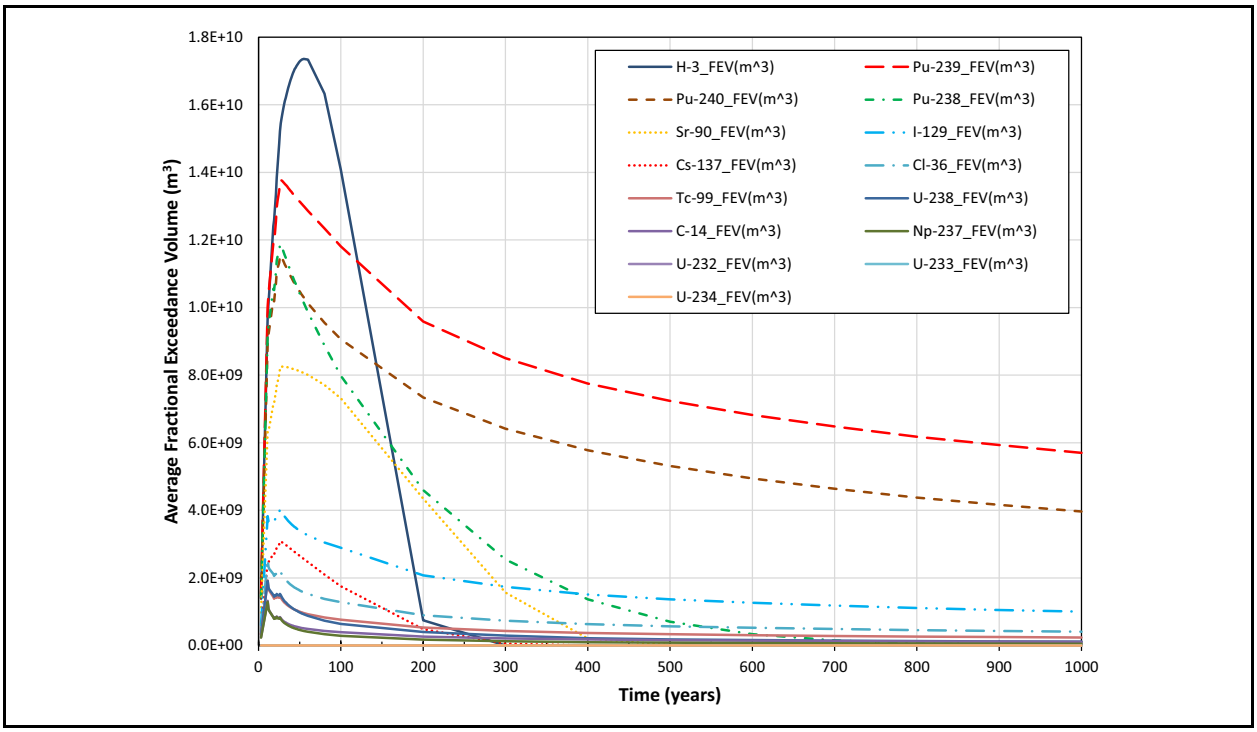

Figure 5-121
Average Fractional Exceedance Volume by RN for PM Base Case

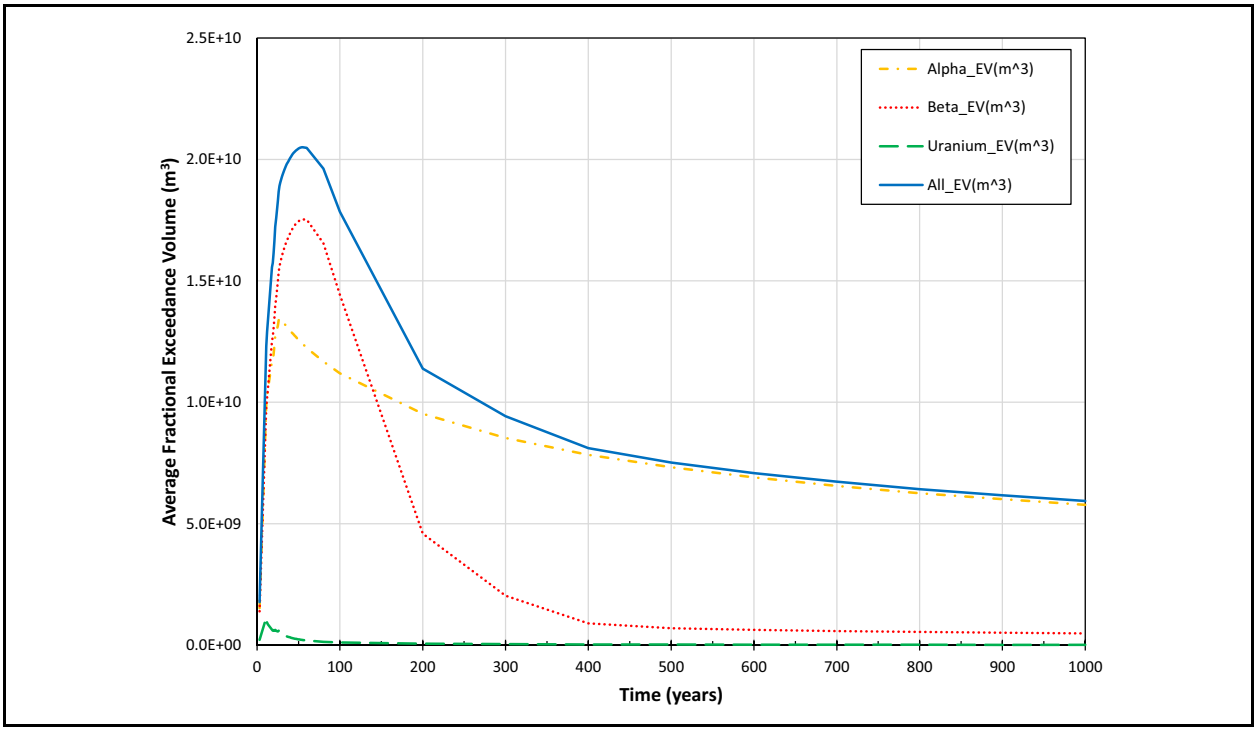

Figure 5-122
Average Fractional Exceedance Volume by RN Class for PM Base Case

the exceedance volume up to approximately 120 years, after which ^{239}Pu contributes most, followed by ^{240}Pu, ^{238}Pu (up to about 380 years), ^{90}Sr (up to about 300 years), ^{129}I, and ^{36}Cl out to 1,000 years. A single model cell can exceed the MCLs for multiple RNs at the same time and, as a result, that model cell will contribute to the FEVs of multiple RNs. This condition occurs in many places throughout the volume of the CB. Therefore, the FEV curves displayed in the figures should not be added together.

5.8 Summary

The following observations can be made from the PM CAU transport model results:

- Tritium dominates the extent of contaminant migration, but due to the short half-life, the maximum extent of contamination peaks between 60 and 80 years.
- Model forecasts predict that once the ^{3}H plume has decayed, the extent of contaminant migration is dominated by ^{239}Pu, followed by ^{240}Pu, ^{238}Pu (up to about 380 years), ^{90}Sr (up to about 300 years), ^{129}I, and ^{36}Cl out to 1,000 years.^{237}Np and U are insignificant contributors to the extent of contaminant migration (Figure 5-121).
- The forecasted CB ensemble (Figures 5-116 through 5-119) remains on federally controlled land, extending approximately 2 to 3 km past the western NNSS boundary onto the NTTR at four locations: (1) north of PM-3, (2) east of PM-3, (3) in the Bench area near ER-EC-6, and (4) northeast of ER-EC-1.

6.0 CB Forecasts

Figure 6-1 shows the ensemble of 1,000-year time-cumulative 95th-percentile 1,000-year CB forecasts for the PM CAU base case flow model on top, underlain by the INFILv3 recharge alternative flow model, the DVRFS3 recharge alternative flow model, and the alternative flow model including all faults, with a single color representing each alternative. The 2-D CB perimeter is defined by the ground surface area that is covered in Figure 6-1 by the collections of colored dots.
The forecasted CB ensemble remains on federally controlled land, extending approximately 2 to 3 km past the western NNSS boundary onto the NTTR at four locations: (1) north of PM-3, (2) east of PM-3, (3) in the Bench area near ER-EC-6, and (4) northeast of ER-EC-1. The CB ensemble is defined largely by the extent of ^{3}H contamination.

The vertical extents of the CBs making up the ensemble vary across the computational domain and vary among the alternatives. The bottoms of the CBs intersect many different HSUs, as follows:

- 24 HSUs for the base case (Figure 6-3)
- 23 HSUs for the INFILv3 recharge alternative flow model (Figure 6-6)
- 24 HSUs for the DVRFS3 recharge alternative flow model (Figure 6-9)
- 23 HSUs for the alternative model including all faults (Figure 6-12)

The HSUs, listed in Figures 6-3, 6-6, 6-9, and 6-12, are displayed graphically in Figures 6-2, 6-5, 6-8, and 6-11, in which each CB is colored by the lowest contaminated HSU. The designation of the lowest contaminated HSU is a requirement of the FFACO (1996, as amended). The number and complexity of the HSUs are demonstrated by the wide range of HSUs that form the designation of the deepest contaminated HSUs. As an aid to interpreting the lowest contaminated HSU, the result was plotted as the depth below the water table. Figures 6-4, 6-7, 6-10, and 6-13 display each CB case colored by the saturated depth of contamination. This method of depicting the depth of contamination is easier to interpret and leads to the following observations. The lowest depths of contamination (1,000 to 1,200 m below the water table) designated by the dark blue color are associated with the cavity regions of the most deeply buried tests. The light blue regions (800 to 1,000 m depth) are limited to a few areas immediately downgradient of several of the deeper tests. The intermediate depth is prominent in the area of the STILTON and HANDLEY tests. Much of the other portions of the testing area show shallow depths of 0 to 400 m (orange and red). The plumes that appear to be

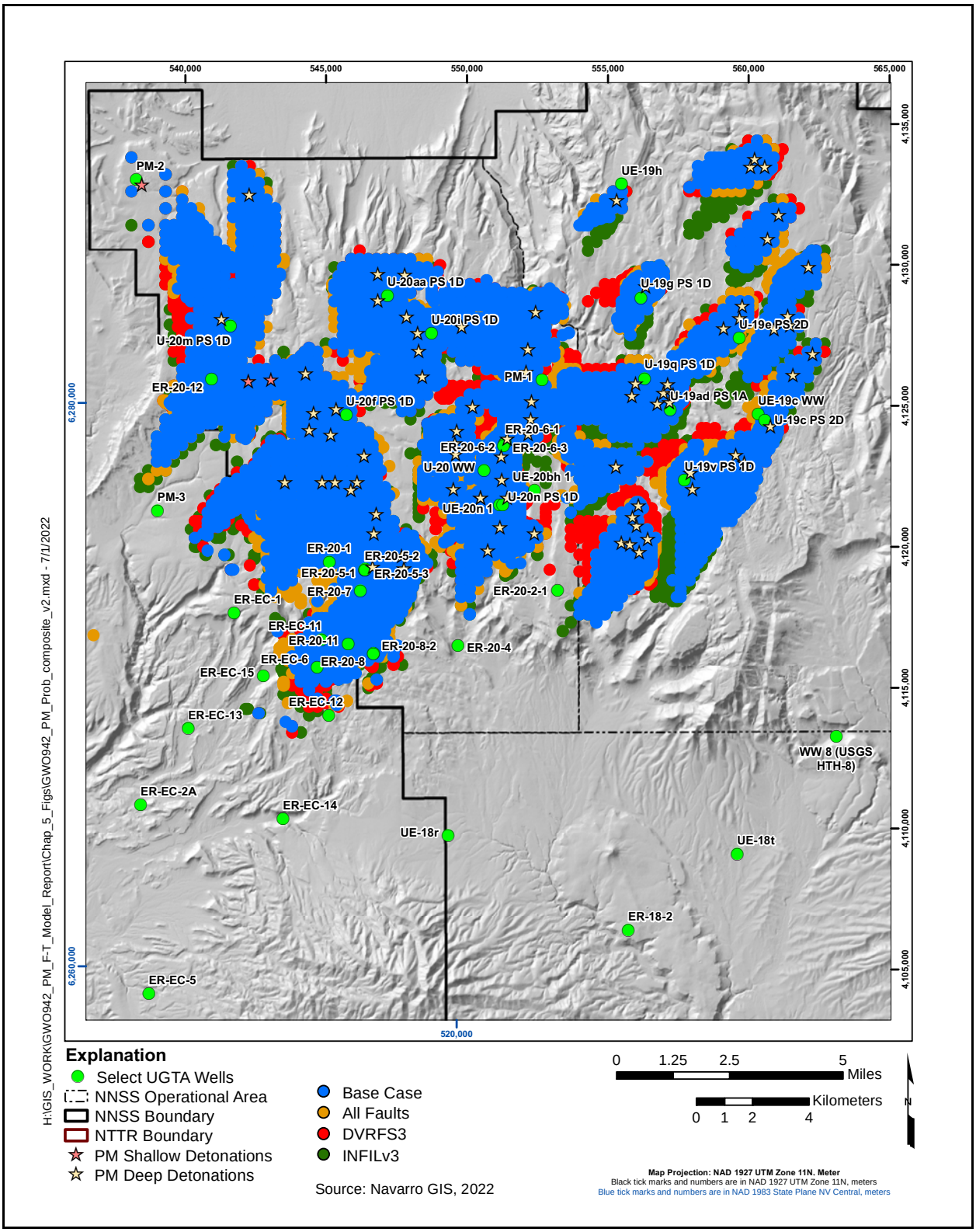

Figure 6-1
1,000-Year Time-Cumulative Probability of Exceedance of MCLs CB Forecasts (Base Case on Top)

moving beyond the NNSS boundary onto the NTTR are generally of the shallowest depths. These results suggest that as the plumes migrate downgradient, the zones most likely to contain contamination are more likely to be shallower (generally, within the upper 600 m of the saturated zone, but may extend as deep as 800 m). An interesting feature is visible in the vicinity of the Bench, where shallow depths of contamination are visible upgradient of the NTMMSZ, but as the flow crosses that structure, the flow moves deeper in the flow system to find permeable pathways and the depth of contamination as shown by the yellow and light green color are more common south of the NTMMSZ. This information will be beneficial to help guide the potential depth of future groundwater monitoring wells.

Tritium dominates the extent of contaminant migration, but due to the short half-life, the maximum extent of contamination peaks between 60 and 80 years.

PM CAU model forecasts predict that once the ^{3}H plume has decayed (about 120 years), the extent of contaminant migration is dominated by ^{239}Pu for the remainder of 1,000 years. Following ^{239}Pu is ^{240}Pu, also for 1,000 years. Next are ^{237}Np and U, which are insignificant contributors to the extent of contaminant migration (Figure 5-121).

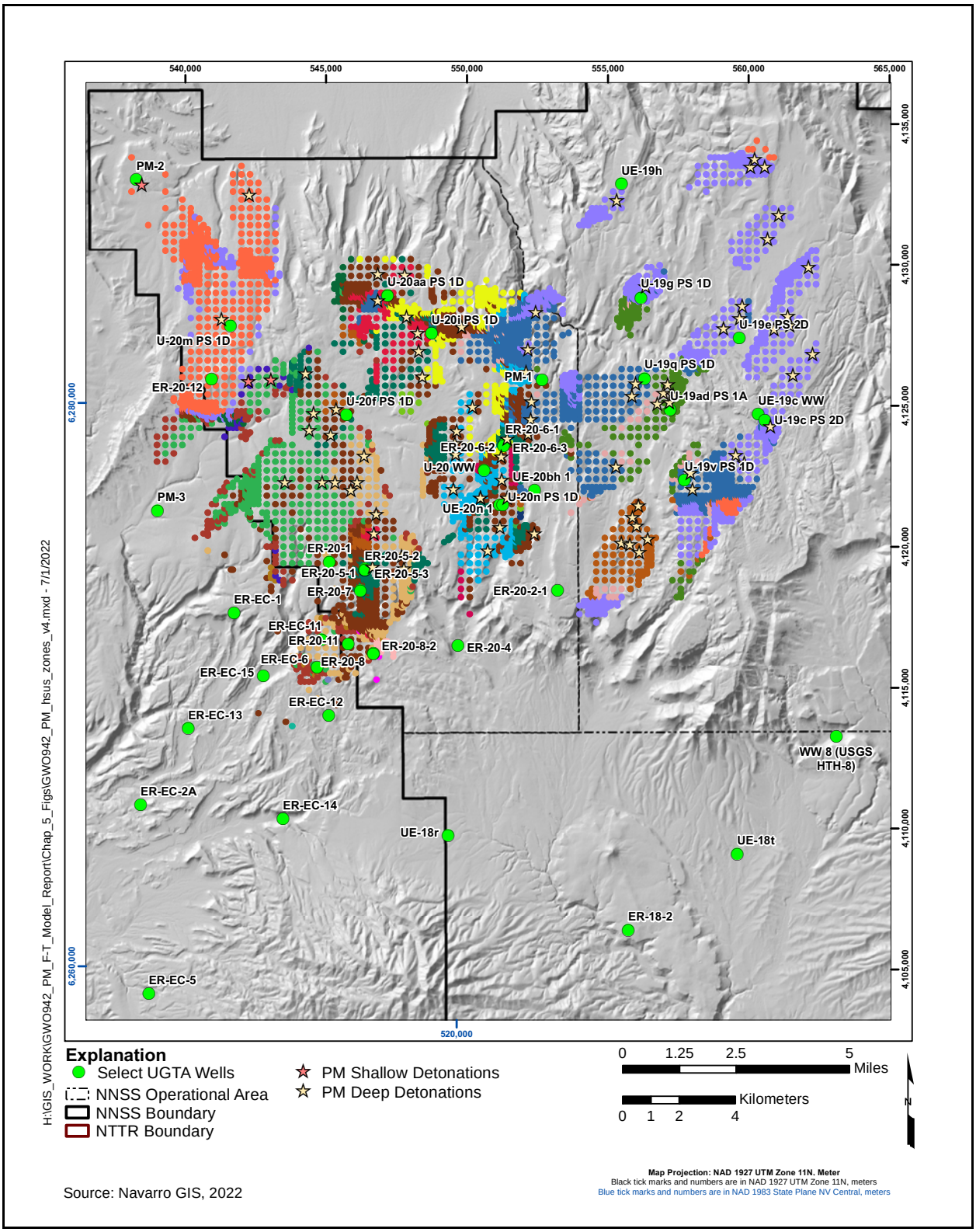

Figure 6-2
CB of Base Case Colored by Lowest Contaminated HSU

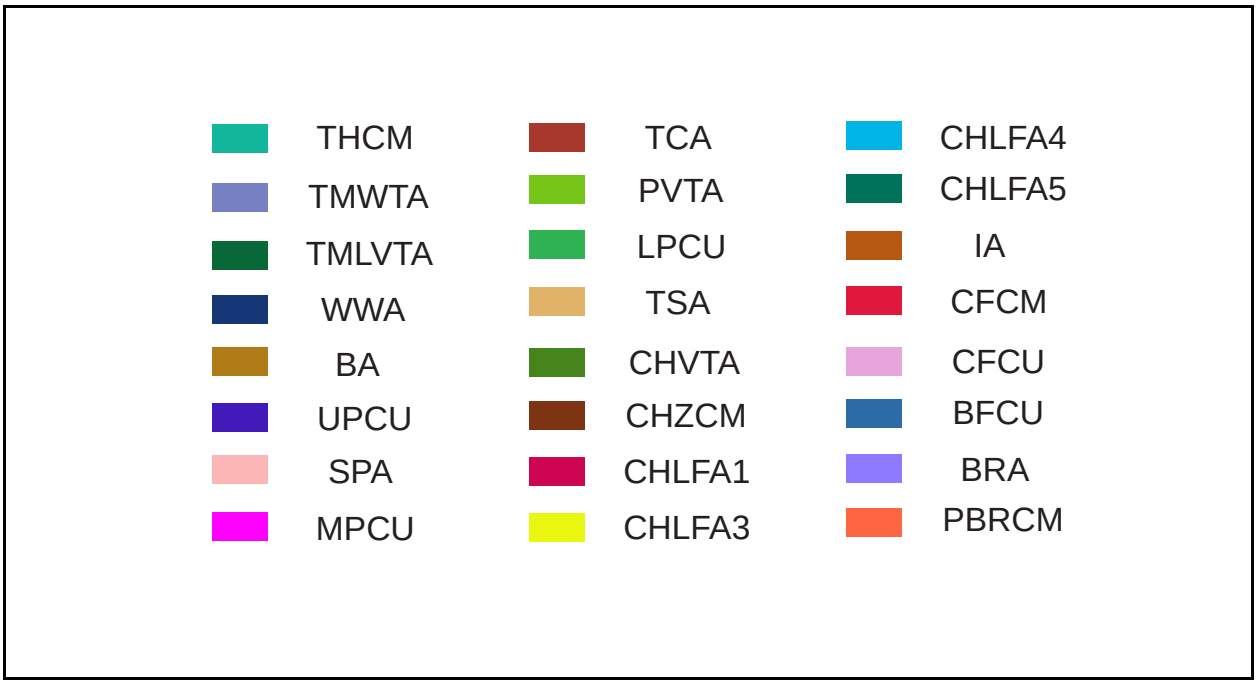

Figure 6-3
Lowest Contaminated HSUs in CB for Base Case Flow Model with Color Key for Figure 6-2

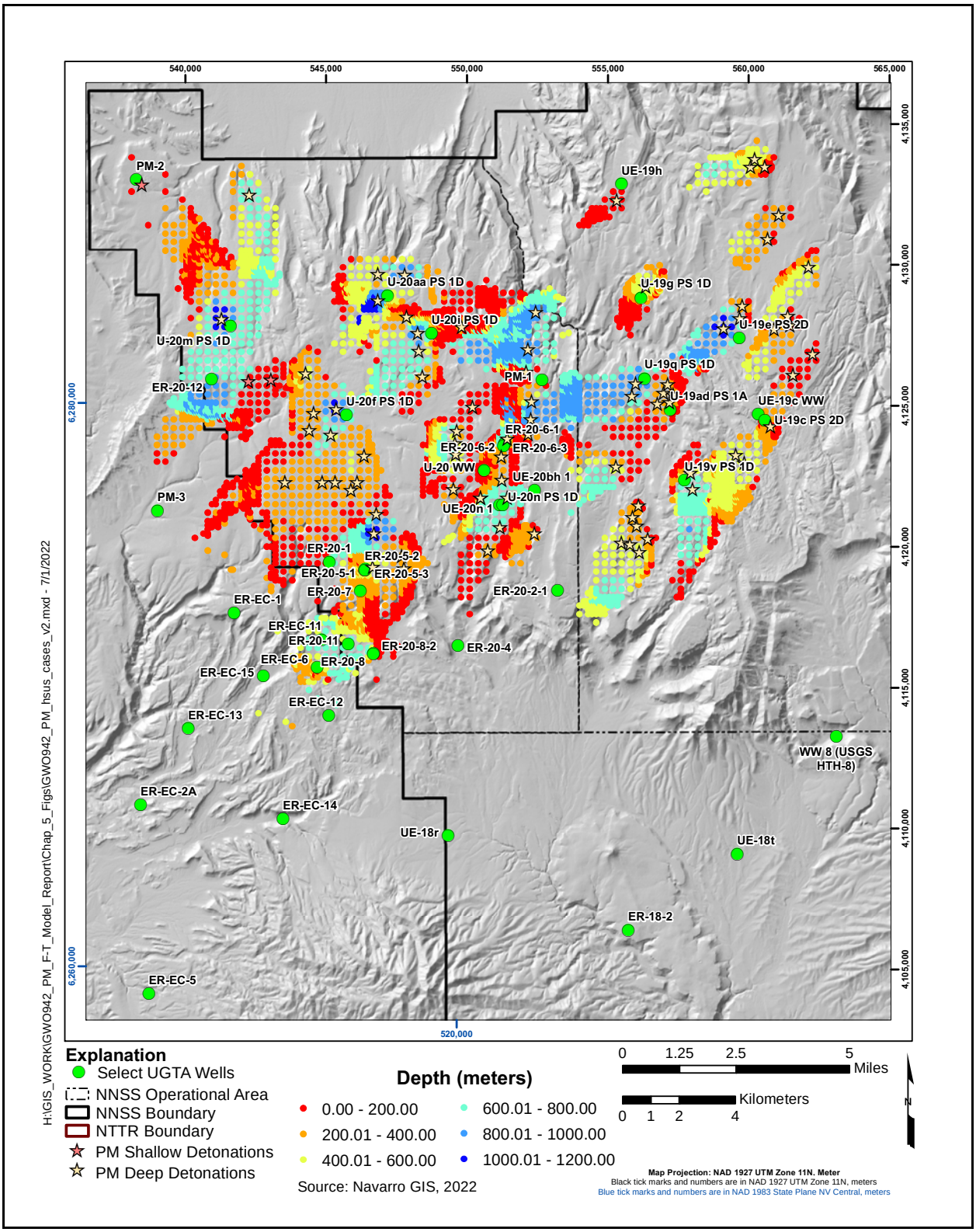

Figure 6-4
CB of Base Case Colored by Saturated Depth of Contamination

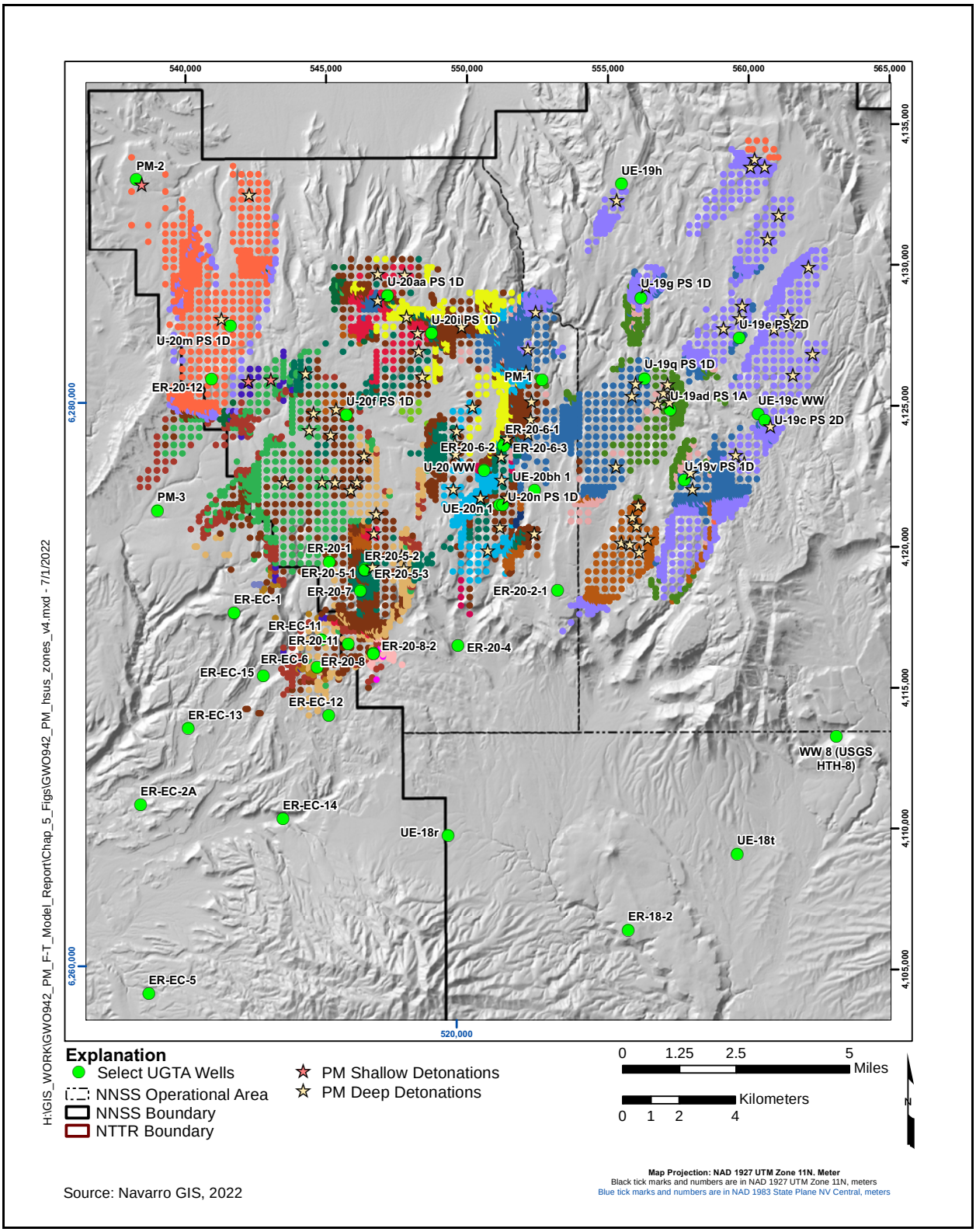

Figure 6-5
CB of INFILv3 Recharge Alternative Flow Model
Colored by Lowest Contaminated HSU

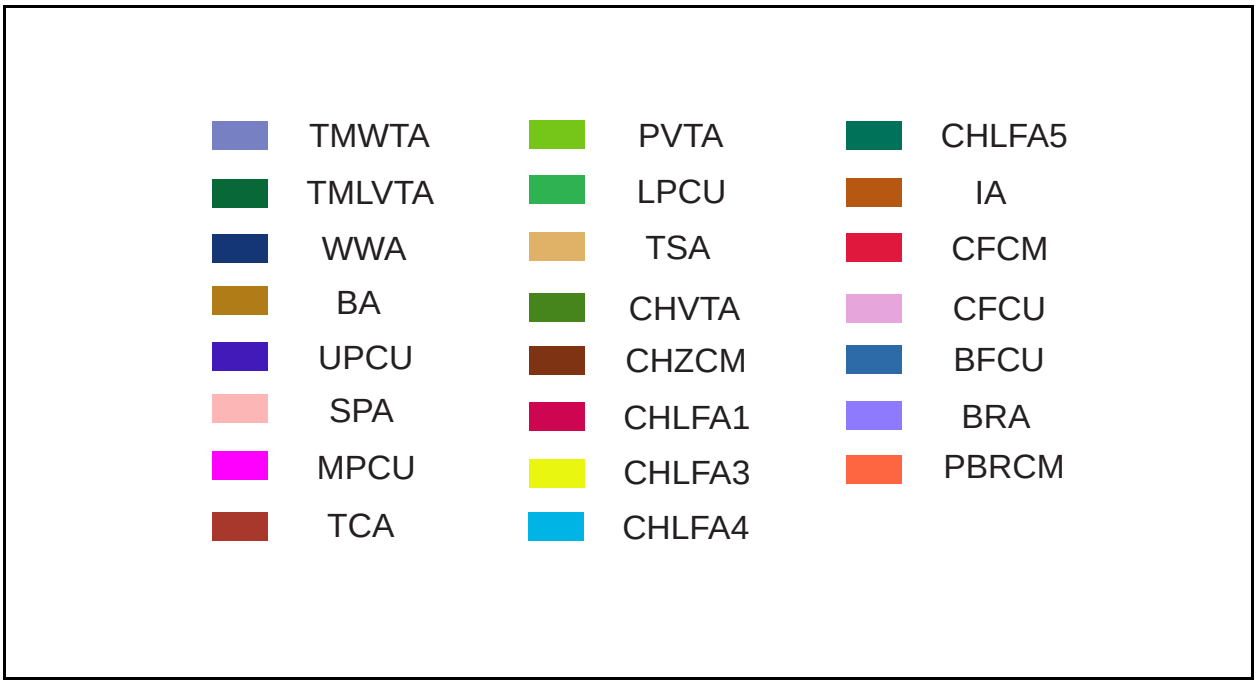

Figure 6-6
Lowest Contaminated HSUs in CB for INFILv3 Recharge Alternative Flow Model with Color Key for Figure 6-5

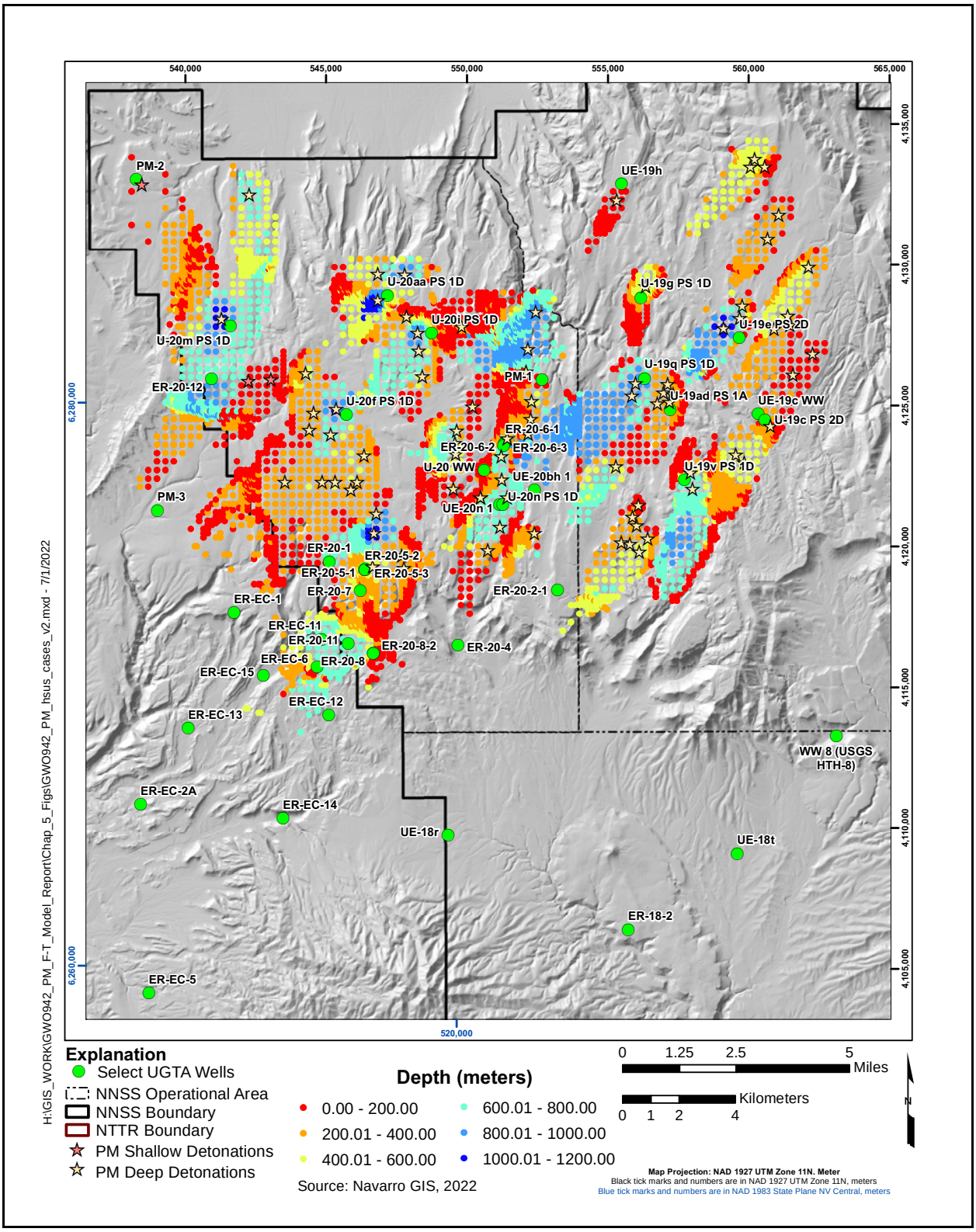

Figure 6-7
CB of INFILv3 Recharge Alternative Flow Model
Colored by Saturated Depth of Contamination

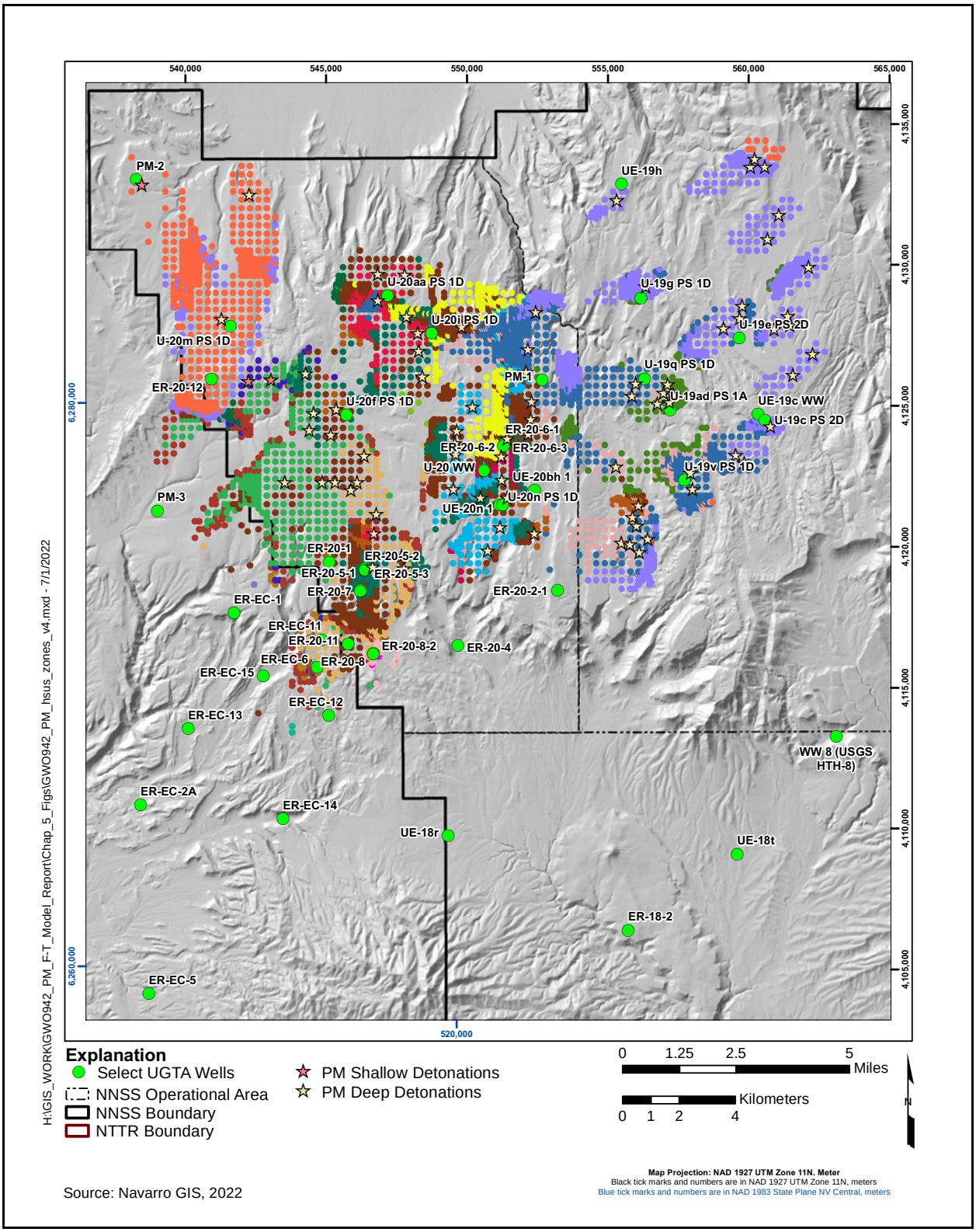

Figure 6-8
CB of DVRFS3 Recharge Alternative Flow Model
Colored by Lowest Contaminated HSU

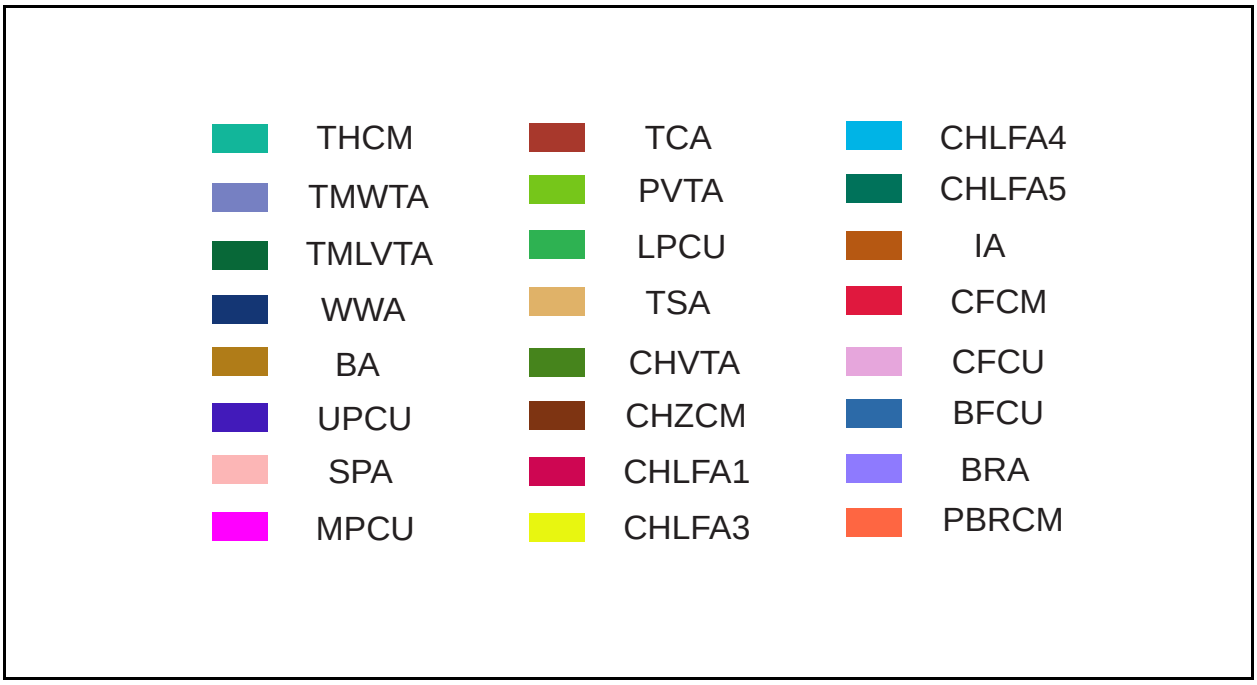

Figure 6-9
Lowest Contaminated HSUs in CB for DVRFS3 Recharge Alternative Flow Model with Color Key for Figure 6-8

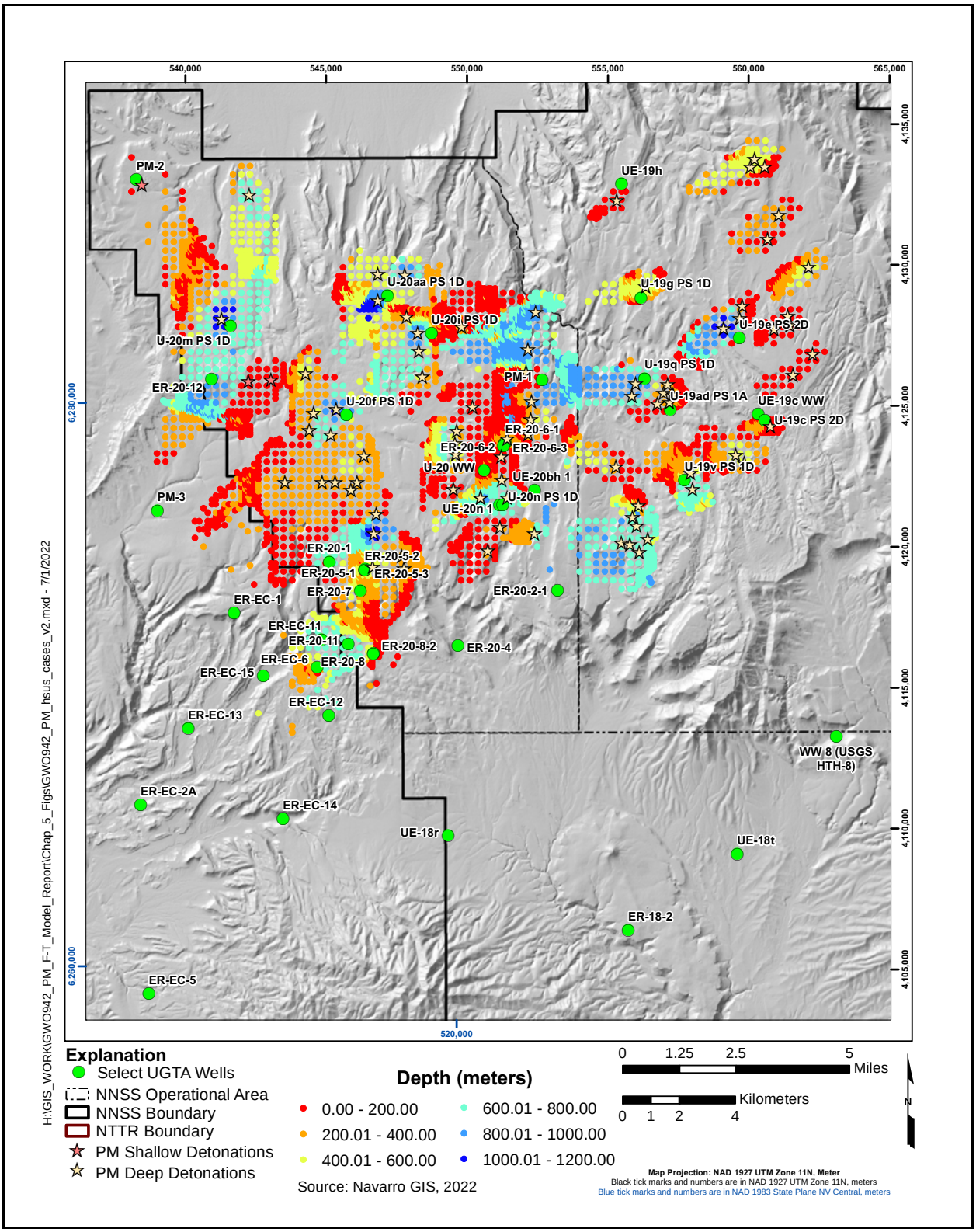

Figure 6-10
CB of DVRFS3 Recharge Alternative Flow Model
Colored by Saturated Depth of Contamination

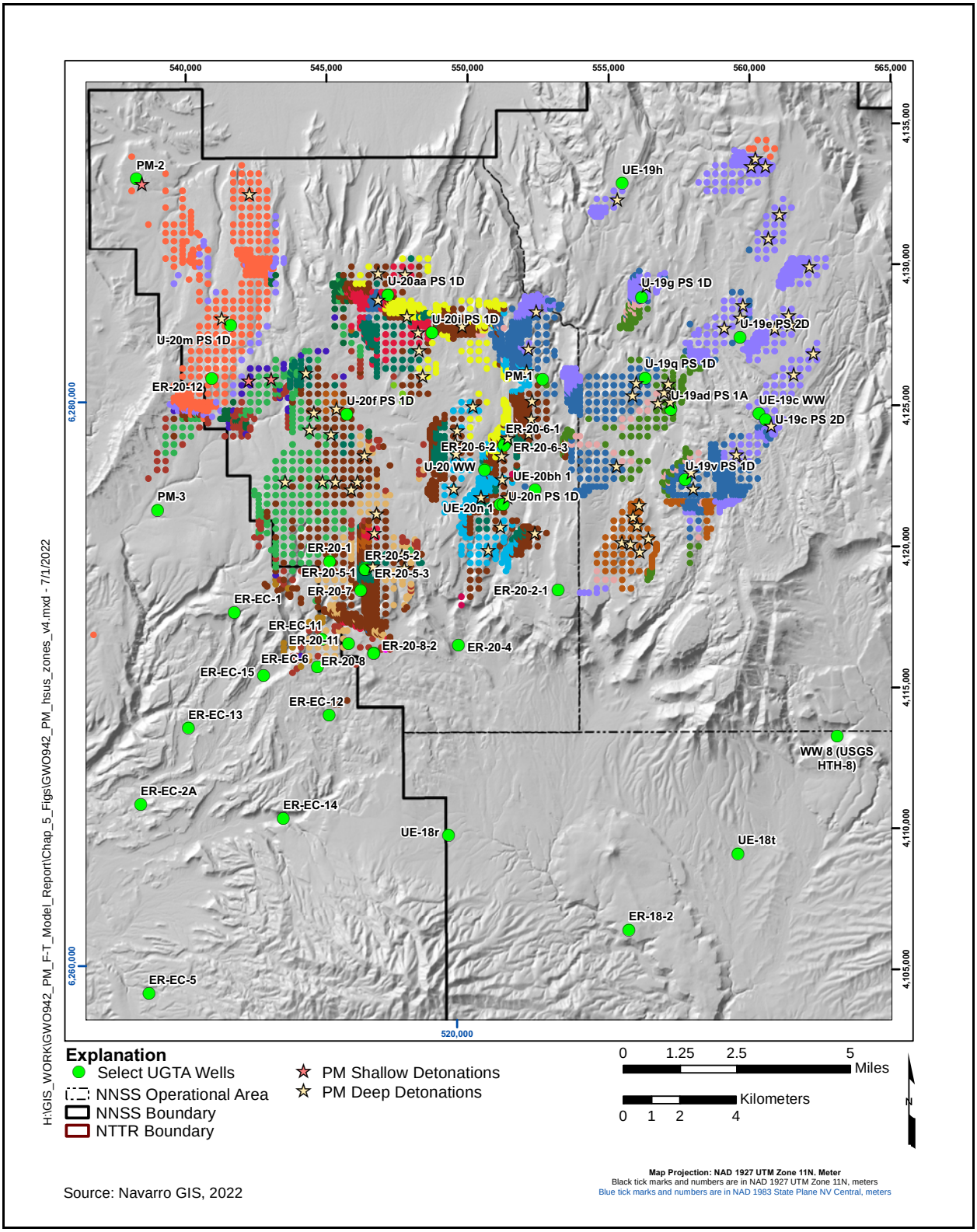

Figure 6-11
CB of Alternative Flow Model Including All Faults
Colored by Lowest Contaminated HSU

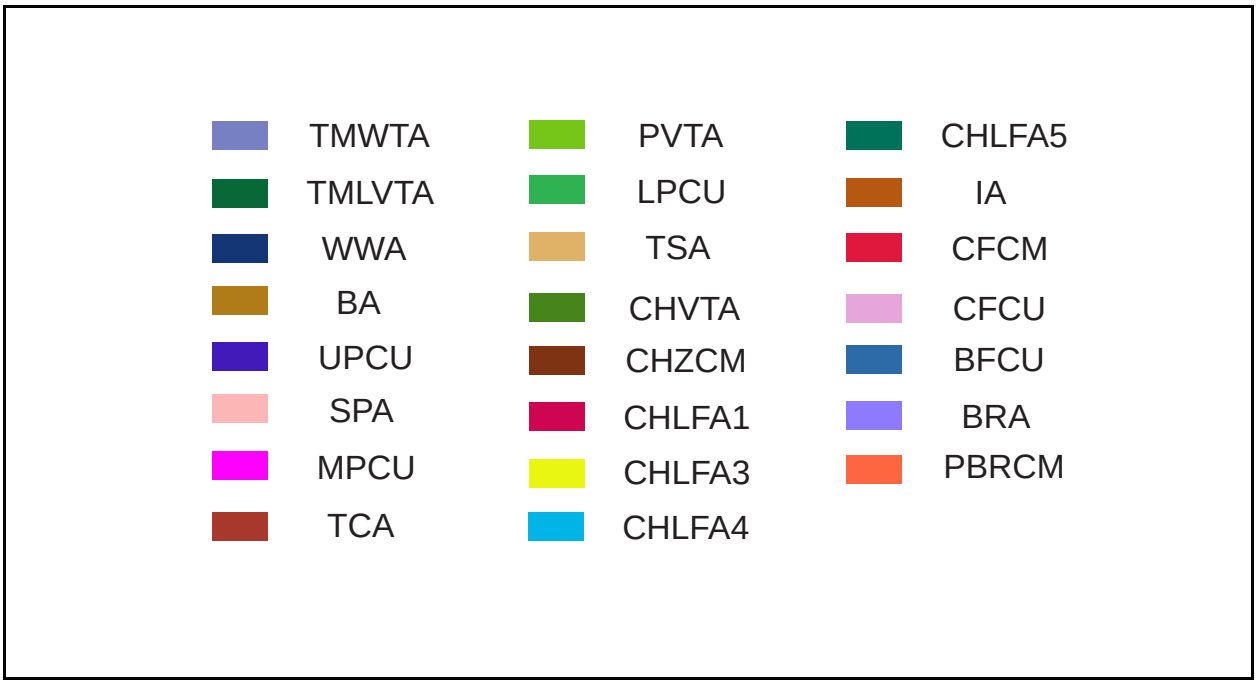

Figure 6-12
Lowest Contaminated HSUs in CB for Alternative Flow Model Including All Faults with Color Key for Figure 6-11

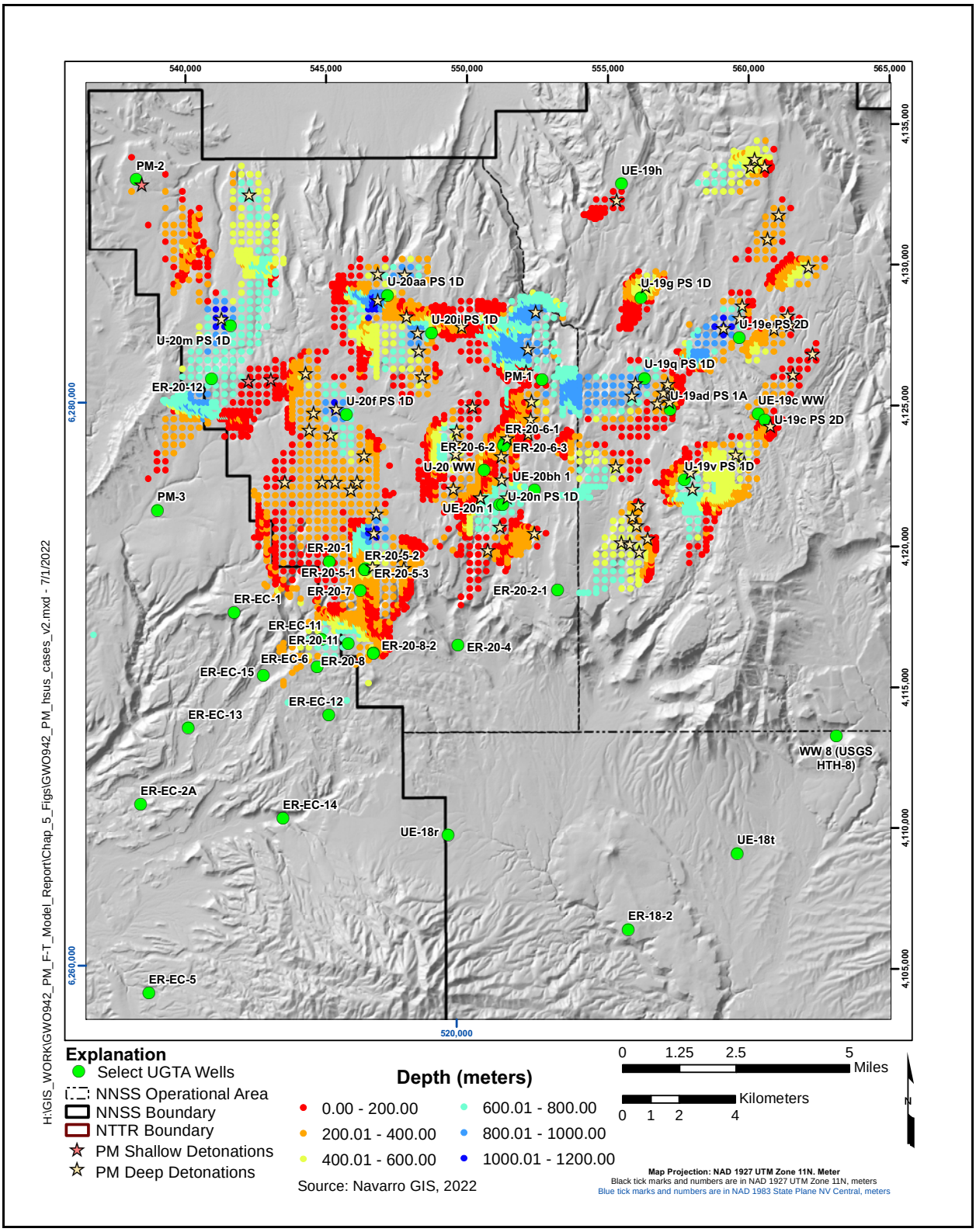

Figure 6-13
CB of Alternative Flow Model Including All Faults
Colored by Saturated Depth of Contamination

7.0 Summary and Conclusions

The FFACO UGTA strategy (FFACO, 1996 as amended) defines the process governing the characterization, analysis, evaluation, and closure of UGTA CAUs. For PM CAUs 101 and 102, the flow and transport model presented in this report is a key element to be used by DOE and NDEP to decide whether the strategy is achievable. The primary purpose of the PM CAU flow and transport model is to forecast 3-D CBs using a probabilistic approach. As stated in Section 1.0, a CB is formally defined as a probabilistic model-forecast perimeter and a lower HSU boundary that delineates the extent of RN-contaminated groundwater from underground testing over 1,000 years. Contaminated groundwater is defined as water exceeding the radiological standards of the SDWA (CFR, 2021).

Simulation modeling of contaminant transport was used to forecast the location of CBs within 1,000 years and shows the 95th percentile of the model results (boundary outside of which only 5 percent of the simulations exceed the SDWA standards). The ensemble of CBs was presented in Section 6.0 based on the base case flow model and three alternative flow models using the base case hydrologic source term for 15 RNs of concern or potentially of concern and uncertain transport parameter ranges that encompass the parameter values of the transport model calibration. The ensemble of CBs shown in Section 6.0 is defined primarily by the concentrations of ^{3}H and Pu in groundwater. This suggests that other RNs, while observed in groundwater in the immediate vicinity of nuclear tests, are not likely to be present in downgradient groundwater at concentrations above the SDWA standard either individually or in combination. The PM CAU model results (e.g., Figures 5-77 and 5-91) forecast spread of RNs over a wide area of PM and are generally consistent with observations along the leading edge of migration, but they overestimate some RN concentrations, indicating that the model is conservative. Tritium is the only RN present in concentrations well above the SDWA standard, and it is ^{3}H concentrations that define the location of the CB ensemble. The Pu influence is the result of conservative assumptions about colloid facilitated transport that, based on comparisons to measure Pu in groundwater, is likely an overestimate of the influence of Pu on the CBs.

7.1 Building Confidence in the PM CAU Flow and Transport Model

Calibration is one way to build confidence in the PM CAU flow and transport model. Calibration refers to demonstration that a model adequately simulates observed hydraulic and contaminant conditions (calibration values consisting mostly of field-measured hydraulic heads, hydraulic properties, estimated boundary flows, and RN observations) within an acceptable range of error throughout a model domain. For PM, sufficient RN ^{3}H observations were available to allow for calibration of the transport model to measured RN data in groundwater samples. As presented in Section 5.0, the calibrated transport model was used to simulate the transport of the other 14 RNs in the source for comparison to measurements of those RNs in groundwater. The other RNs were not calibrated, but used upper and lower bound values for sorption (K_d) values to show the range of simulations. For nonsorbing RNs (I, Cl, Tc, C) the simulations typically overestimate the concentration. For sorbing RNs (Cs, Sr), K_d values may be estimated that would allow simulations to match observations within the restrictions imposed by the assumption of homogeneity within each HSU. The Pu results suggest an overestimation by the model. This may be due to the conservative approach taken to simulate the Pu transport as colloid-facilitated. This approach was deemed conservative and appears to overestimate transport of Pu compared with measured values. The results for U are different from the other RNs in that the model typically underpredicts the concentration. While there may be small to zero U K_d values that could be used to match observed values, a more likely explanation for the underprediction is the fact that U is present in the background waters at PM at concentrations similar (Rose et al., 2006) to those reported here (Navarro, 2021c). The model simulates only the U from the source cavity and does not account for U already present in the ambient groundwater. An analysis of measured U data presented in Navarro (2021c) shows that except for a few locations, the background and test influenced ^{3}H concentrations are nearly indistinguishable. The similarity of values indicates that the test derived U is a small component to the overall total U present in the groundwater. This suggests that the small U concentration value simulated by the model (representing the test derived component) may be a reasonable estimate of the test introduced U.

The PM groundwater flow model was presented in Section 4.0. The flow model was designed to account for the important flow processes and structural controls on groundwater flow. The model was calibrated (Section 4.2) using steady-state hydraulic heads, transient hydraulic head responses to pumping from MWATs, measured transmissivity values, groundwater hydraulic gradient, total basin

discharge at Oasis Valley, and groundwater flow paths identified from observed geochemistry data and ^{3}H migration. The calibration used a range of observational data, and the similarity of the resulting groundwater flow paths to observed ^{3}H migration paths increased confidence in the ability of the PM CAU flow model to simulate observed hydraulic conditions in the PM-OV flow system.

A significant aspect of the PM transport simulations was the ability to compare simulated ^{3}H and other RN concentrations to observations in groundwater sampled from numerous sampling intervals in wells across the model area. This comparison of simulations to observations was not possible in the other UGTA CAUs (Frenchman Flat, YF/CM, RM/SM) because there were few observations of RN migration in the other UGTA CAUs. In the PM CAUs, at least three ^{3}H plumes have been observed: (1) in the Bench area downgradient of the tests BENHAM, TYBO, MOLBO, BELMONT, and GOLDSTONE; (2) along the western portion of Area 20 downgradient of tests HANDLEY and STILTON; and (3) in eastern Area 20 downgradient of the test CHESHIRE. RN observations at multiple sampling times from wells in the aforementioned three areas allow for calibration of the transport simulations. In addition, RN observations were compared at postshot well locations.
The transport simulations are primarily dependent on the flow model for providing a pathway from a source to a particular observation location. No amount of transport parameter adjustment can make up for the lack of a path from source to observation. A significant part of the flow as well as transport model calibration was ensuring that the calibrated flow model provided the necessary paths.
The transport model was calibrated to ^{3}H observations because, as stated in Section 5.5.1.1, the CBs are dominated by ^{3}H and observations of ^{3}H are more abundant than other RNs at PM. Calibration of ^{3}H observations was obtained using the base-case ^{3}H mass at test locations as sources (distributed between cavity; EV; and chimney, where a chimney was present below the water table) and varying the transport parameters to obtain an acceptable match within an acceptable range of error. As presented in Section 5.0 (Section 5.5.1), the transport model was able to simulate ^{3}H observations, primarily in the Bench area but also in western Area 20. In a few locations such as downgradient of BULLION test, the forecasts are much larger than observations and in some locations the model forecasts ^{3}H at 55 years where none is observed, suggesting that the model may be overpredicting transport in those locations. In several locations, the model fails to forecast ^{3}H where ^{3}H is observed. In most cases, this occurs near the margins of larger plumes and is likely due to the uncertainty in the precise location of a model simulated path that may be laterally displaced a few hundred meters due to local heterogeneities. In the case of the ^{3}H observations at the ER-20-5-3 well,

the flow model does not provide a pathway (direction and groundwater flux) sufficient to simulate the observed ^{3}H at that location. As the primary pathway for RN migration in the vicinity of the Bench is through the shallower HSUs that calibrated well to observations, the lack of calibration at ER-20-5-3 does not impact the extent of the CBs. Nonetheless, the ability to calibrate the transport model to the larger observed ^{3}H plumes provides confidence that the flow and transport model adequately simulate ^{3}H migration from underground nuclear tests on PM.

7.1.1 CAIP Specific Objectives

In addition to confidence gained via calibration of the flow and transport model to observations, several specific objectives of the PM CAU flow and transport modeling were identified in the Phase II CAIP (DOE/NV, 2009) as follows:

- Reevaluate role of major hydrostratigraphic and structural features.
- Refine model boundary conditions.
- Conduct simultaneous flow and transport simulation.
- Correct water-table clipping.
- Develop sub-CAU scale heterogeneity model.
- Develop sub-CAU model of the Bench subdomain.
- Revise fracture parameter model.
- Develop discrete fracture models for upscaling.
- Revise the simplified source model.
- Reduce the number of RNs modeled.

These objectives were also noted in the update to the CAIP (DOE/EMNV, 2020b). The specific actions taken to address these objectives are outlined below.

Reevaluate role of major hydrostratigraphic and structural features: The PM-OV HFM (DOE/EMNV, 2020a) updated the hydrostratigraphy to be consistent with the latest drilling data and included numerous faults considered to potentially have an influence on the flow system. The TCL was added as a potentially significant structural feature. These changes were made to allow flexibility in the development of the model. Comparison of the results of flow models that included (a) limited number of faults, (b) no faults, and (c) all faults led to the conclusion that inclusion of the faults did not improve the flow model calibration, and that the CB ensemble was not significantly impacted

Refine model boundary conditions: Based on an evaluation of the PM-OV groundwater flow system (Fenelon et al., 2016), the boundaries of the flow and transport model were implemented to coincide with the PM-OV groundwater basin boundaries. This allowed the model to use natural hydraulic boundaries and reduced uncertainty regarding the boundary flux definitions compared with the Phase I model (SNJV, 2006 and 2007).

Conduct simultaneous flow and transport simulation: As represented in Sections 4.0 and 5.0, both the groundwater flow model and the RN transport model were calibrated to observed data. RN migration information (flow path and general rate of transport) and flow paths derived from geochemical data were used as soft information in flow model calibration. The calibration was not simultaneous because it is computationally burdensome and practically unnecessary; however, calibration was achieved to both hydrologic and transport data.

Correct water-table clipping: The concern expressed regarding water-table clipping of the Phase I model was a maximum elevation for the top of the model that clipped a portion of the water table in areas of higher water-table elevation. The current model was constructed for the model top to coincide with the water table across the model area.

Develop sub-CAU scale heterogeneity model: Within large composite units, embedded lava-flow aquifers have been delineated and mapped as separate units in the HFM (DOE, 2020a). This provides for large-scale heterogeneity in formerly undifferentiated composite units.

Develop sub-CAU model of the Bench subdomain: The Bench model developed by LANL (Lu et al., 2021) included most of Area 20 and the flow system downgradient to Oasis Valley. There was a focus on the region of the Bench in southern Area 20. The Bench model provided insights into the flow and transport processes that were helpful in the development of the PM CAU flow and transport model.

Revise fracture parameter model and develop discrete fracture models for upscaling: These two items are listed together because they were developed in parallel. Scientists at LANL (Makedonska et al., 2020) and the Desert Research Institute (DRI) (Parashar et al., 2019) utilized detailed fracture characterization data and DFN models to simulate groundwater flow and RN transport processes at the scale of individual fractures. The DFN models are too complex and detailed to be used for

CAU-scale simulations; instead, they were used to simulate processes at the individual fracture scale to evaluate the appropriate CAU-scale parameters. The “upscaled” parameters from the DFN models were included in the analysis of transport parameter data (Navarro, 2021a).

Revise the simplified source model and reduce the number of RNs modeled: These two items were developed in parallel. The source model was reevaluated and published as a Lawrence Livermore National Laboratory (LLNL) report (Carle et al., 2020). The number of RNs was not reduced but rather was based on the screening analysis of Carle et al. (2020) to identify RNs potentially important to the CB calculations on the basis of concentrations likely to be present in the test cavities or near the vicinity.

The development of the PM CAU flow and transport model presented in this document addressed the specific objectives identified in the Phase II CAIP (NNSA/NSO, 2009).

7.1.2 FFACO Modeling Topics

In addition to the specific objectives noted above, the FFACO (1996, as amended) defines requirements for the CAU flow and transport model that are intended to provide confidence that the model is acceptable for forecasting the ensemble of CBs needed to progress in the implementation of the FFACO UGTA strategy. The FFACO requires that the CAU models of the CAI stage will be constructed and consider, at a minimum, the eight modeling topics listed below with the objective of evaluating future migration of contaminants to forecast CBs that encompass the uncertainty of current and future contaminant migration:

- Alternative HFMs of the CAU modeling domain
- Uncertainty in the RST and HST
- Alternative models of groundwater recharge
- Alternative model boundary conditions and models of groundwater flow
- Multiple permissive sets of calibrated flow models
- Probabilistic simulations of transport using plausible sets of alternative framework and recharge models, model boundary conditions, and models of groundwater flow from calibrated flow models

- Ensembles of forecasts of CBs for the CAU
- Sensitivity and uncertainty analysis of the model outputs

The model presented in this report was constructed with consideration of these eight modeling topics as described below.

Alternative hydrological framework models of the CAU modeling domain: The HFM (DOE/EMNV, 2020a) was constructed as a single model that best represented the distribution and arrangement of HGUs in the PM-OV basin. This differs from previous approaches where multiple HFM models were created. The approach for the PM CAU model was to take the HFM as developed and simulate with it to calibrate the model. If the flow model could not be calibrated with the HFM as published, then alternative HFMs would be considered and developed. During the calibration process, it was determined that distinct alternative HFMs were not needed to achieve calibration because the observed heterogeneity of flow properties within and between HSUs (Jackson et al., 2020; Navarro 2021b) was substantial and provided a sufficient range of values for calibration.

Rather than develop alternative HFM models, the flow calibration evaluated several hydrologic conceptual model alternatives (Section 4.3) that included subdividing (laterally or vertically) some HSUs into smaller sub-HSUs with distinct material properties. The flow model included an alternative that identified faults as distinct flow regimes separate from the HSUs. This alternative differs substantially from the base case where the faults represent zones of displacement, but where material properties in the fault zone are consistent with material properties of the HSUs adjacent to the fault. In the base model, faults displace HSUs and allow two different HSUs, often with different hydraulic properties to abut one another. This creates flow paths that often move vertically or laterally around zones of low hydraulic conductivity. In the alternative case, faults were treated as zones of differing material properties from the surrounding rock. In the alternative, a fault could be a barrier over a majority of its surface or a fault could be a flow conduit. This fault conceptual alternative allowed for an assessment of two very different conceptual models.

Alternatives were developed during the flow model calibration process to address regions where calibration based on parameter adjustments alone proved unsatisfactory. Transport simulations were conducted using the base and alternative flow models during the probabilistic transport forecasts. In

this way, alternative conceptualizations were used to improve the model and provide increased confidence in the model forecasts.

Uncertainty in the RST and HST: The uncertainty in the source term as it applies to the PM CAU model is concisely described in Carle et al. (2020). While the RST is largely defined by Finnegan et al. (2016), there are a number of assumptions regarding the distribution of RNs in the cavity environment as well as hydrologic and geochemical factors that influence the HST. Carle et al. (2020) incorporated all the above factors into a probabilistic analysis to generate a range of source concentrations for the RNs of concern.

The impact of uncertainty in the source was broadly evaluated in the development of the screening model (Carle et al., 2020). The screening model was developed to estimate a range of possible source concentrations in groundwater that accounts for uncertainty in partitioning into melt glass and sorption into surrounding rock of the EZ. The model also accounts for the varied hydrogeochemical settings. The screening model evaluated transport parameters from databases of hydrogeologic units, chemistry, mineralogy, fracture spacing, fracture aperture, fracture openness, matrix porosity, bulk density saturation and alteration. Uncertainties included in the screening analysis include (1) RN distribution parameters (EV radius, source concentration, and fraction in melt glass); (2) fracture parameters (area per unit volume; openness, which represents the portion of the fracture that is open to flow; aperture); and (3) matrix diffusion parameters (free-water diffusivity, sorption coefficient, matrix porosity, and bulk density). The sensitivity analyses in the screening model using the three parameter groups above suggest the greatest impact to uncertainty comes from the first group, the RN distribution parameters.

The screening model was created to evaluate the minimum and maximum concentrations that may be expected to be observed at the source locations. A base model case was obtained using mean parameters. Where available, measurements of RN concentrations from near-field and in some cases downgradient water samples were obtained and compared with the screening model results to provide confidence in the results.

Carle et al. (2020) note that the concentrations identified in the screening model tend to be conservative (i.e., high relative to the observations) for two main reasons: (1) source dispersal processes (i.e., advection and dispersion) of downstream transport are not included in the screening

analysis, and (2) partitioning into the melt glass is likely underestimated because the fractionation of RNs into melt glass within the rubble fraction defined in radiochemistry studies is not considered (Rose et al., 2011). The screening model includes the following processes:

- RN decay
- Partitioning into melt glass
- Fracture-matrix interactions
- Temporal effects of matrix diffusion and sorption onto rock material
- Unsaturated conditions above the water table
- Variable lithology, mineralogy, and alteration of rock properties
- Water chemistry effects of pH and major ion composition

The screening model used a batch reactor approach to calculate the aqueous concentration after initial placement of RNs into the mobile pore space and allowing for the processes noted above to evolve and produce the mobile phase concentration available for groundwater transport.

Comparison of screening model results with observations is provided by Carle et al. (2020) where observational data are available. The results showed that with few exceptions (^{137}Cs at CHANCELLOR, $^{239/240}$Pu at CHANCELLOR and ALMENDRO, and ^{14}C at CAMEMBERT) the observations from near-field and downgradient samples fall within the base and minimum range. This provides additional confidence that the maximum range values should not be used for forecast simulations because they consistently overestimate the observed values.

Based on the uncertainty provided in the screening analysis, the PM CAU transport model used an approach aligned with the screening model base case. The transport model requires as input the RN mass available for aqueous transport rather than the concentrations; this was estimated using the mean values of source term parameters as described in Section 5.0. This approach yielded source concentrations that allowed calibration of ^{3}H data using parameter values within the range of observations. More importantly, the base case source approach produced source concentrations for RNs other than ^{3}H that, when simulated with the calibrated transport model, typically produced conservative or consistent results compared with observations (Section 5.5.1.4).

Alternative models of groundwater recharge: Different alternative models of the recharge distribution were simulated as part of the uncertainty analysis of the flow model (Section 4.3.2). The recharge distributions come from different approaches to estimate recharge. The calibrated PM

CAU flow model used an initial recharge distribution from the work of Fenelon et al. (2016) which was developed from calibration of a PM-OV basin delineation model. During calibration of the PM CAU flow model, the recharge distribution from Fenelon et al (2016) was adjusted to allow for greater flow west of the Purse fault. Two additional alternative recharge distributions were examined.

The first alternative used the recharge from the regional scale flow model of Halford and Jackson (2020). The recharge from the regional scale model provided the same total recharge consistent with measurements of discharge in Oasis Valley (Reiner et al., 2002), but differed in the spatial distribution. The second alternative recharge model used the work of Middleton et al. (2019) who provided recharge estimates based on a model of net infiltration beneath the root zone. The net infiltration estimate was not calibrated to total basin discharge and provided an estimate of total recharge about 25 percent greater. Nonetheless, this alternative evaluates a somewhat conservative case of increased flow through the PM CAU model. The uncertainty in the distribution of recharge is addressed in the PM CAU model using the alternative recharge cases.

Alternative model boundary conditions and models of groundwater flow: The work of Fenelon et al. (2016) evaluated the boundary conditions of the PM-OV groundwater basin. The Fenelon et al. (2016) evaluation determined that to a large extent the groundwater flow system in the PM-OV groundwater basin is self-contained such that the discharge observed in Oasis Valley is derived from recharge that occurred within the boundaries of the basin. The uncertainty in the boundary conditions is quite small compared with the total flow through the basin, and is not likely to be a major factor in the overall uncertainty in the migration of RNs in the PM-OV groundwater basin.

Multiple permissive sets of calibrated flow models: As presented in Section 4.3, the calibration included several alternative model formulations, each of which was calibrated to the observed data. The different alternative models yield what can be termed permissive sets of parameters that yield similar calibrations. These alternative flow cases were used to simulate RN transport during probabilistic forecast simulations used to identify the CB ensemble.

Probabilistic simulations of transport using plausible sets of alternative framework and recharge models, model boundary conditions, and models of groundwater flow from calibrated flow models: The current base case model and three alternative flow models were used to simulate RN transport. The source term used for the probabilistic simulations is the base case as presented by

Carle et al. (2020). The base case was considered sufficient because as the results of Carle et al. (2020) demonstrate, the observed RN data generally fall within the minimum and base case ranges and rarely in the maximum case range. By using the base case, it avoids an overly conservative maximum case and provides greater overall transport than a case that included both the minimum and base case in the probabilistic forecast. The combined use of observations for both the flow and transport calibrations results in parameter values for some HSUs that are constrained relative to the initial range of possible values identified in the HDD (Navarro, 2021b) and TDD (Navarro, 2021a). These constrained parameter ranges would likely result in reduced forecast uncertainty, but this approach was not used for the probabilistic forecasts. Instead the probabilistic simulations used the full range of parameter uncertainty for the transport parameters, which may have slightly overestimated the forecast uncertainty. Overall, the probabilistic forecasts are a reasonable measure of uncertainty in CB forecasts.

Ensembles of forecasts of CBs for the CAU: The ensembles of forecasts of CBs were calculated for the base model and the three alternatives. As presented in Section 6.0, the transport simulations using the alternative flow models yielded an ensemble of CB forecasts. The ability to calibrate the alternative flow simulations to observations helped to constrain the range of outcomes from the alternative flow model cases.

Sensitivity and uncertainty analysis of the model outputs: The sensitivity of model results for the PM simulations was presented in Sections 4.0 and 5.0. A comprehensive parameter by parameter sensitivity is obtained from the use of the PEST optimization software (Doherty, 2018), which produces a sensitivity matrix of model responses compared with calibration targets for every adjustable parameter in the model (Sections 4.2 and 5.5). Using the sensitivity matrix, the PEST software adjusts the values of parameters that most influence the desired outcome. In this way a full set of sensitivity calculations is performed as part of flow and transport model calibration. PEST further calculates a parameter identifiability for each parameter, which ranks the parameters in terms of their influence in the calibration.

In addition to the PEST sensitivity calculations, Sections 4.2, 4.4, and 5.6 evaluate specific parameters such as dispersion and source strength to show how the model results are influenced by uncertainties in the input parameters. As noted in the paragraphs above, the approach of performing

the probabilistic forecasts is believed to provide a slightly conservative range of uncertainty when considering the potential impact of parameters that are unconstrained by the calibration.

7.2 Summary of Results

The PM CAU model consists of a 3-D flow simulation of groundwater flow in the PM-OV groundwater basin, based on recharge occurring primarily in upland areas within the basin and groundwater discharge to locations in Oasis Valley, and 3-D transport simulations of RNs within the groundwater flow system defined by the flow model. The flow model was successfully calibrated to steady-state hydraulic heads, transient hydraulic head responses to groundwater pumping, measured transmissivity, groundwater discharge in Oasis Valley, hydraulic gradients, and RN migration pathways obtained from ^{3}H observations. Four alternative flow models were simulated: two cases using alternative recharge (one representing the upper bound of plausible total basin recharge), a case with all faults identified in the HFM modeled as distinct flow zones independent of the adjacent HSUs, and a model using a water-table upper boundary condition. The base case model and alternatives were able to simulate groundwater flow paths consistent with ^{3}H observations (direction and velocity).

The transport model was developed using the base case flow model and was successfully calibrated to ^{3}H observations in groundwater samples collected from open intervals in numerous wells in the model area.

Using the base case flow model, three of the alternative flow models, and the base case source term, Monte Carlo probabilistic simulations for 15 RNs were conducted using the transport model with longitudinal, horizontal transverse, and vertical transverse dispersion values of 150 m, 15 m, and 1.5 m. The fourth alternative flow model of a water-table simulation consistently yielded lower groundwater flux than the other three alternatives. As the water-table case is less conservative, it was not included in the probabilistic transport forecast simulations. The effective porosity, fracture aperture, tortuosity, and matrix sorption coefficients were varied per ranges of values in the TDD (Navarro, 2021a). Radioactive decay was defined using a fixed half-life for each RN. Sensitivity of the transport results to lower dispersivity values was assessed by simulating BENHAM as the source term (Section 5.6.4); it was found that the peak straight-line distance of ^{3}H travel above the MCL (20,000 pCi/L) from BENHAM at 55 years decreased by about 25 percent for zero dispersivity.

This shows that the base case considered in the CB evaluations may be somewhat conservative. Sensitivity of the transport results to double the source mass values was assessed by simulating Pu transport from BENHAM as the source; it was found that the peak straight-line distance of ^{239}Pu travel above the MCL (15 pCi/L) from BENHAM at 55 years increased by only about 6 percent. It is noteworthy that doubling the source mass of Pu resulted in only a relatively small increase in transport distance at 55 years.

The ensemble forecast of CBs was shown to be dominated by the ^{3}H concentration for the first approximately 150 years. After that time, ^{3}H concentrations are reduced by transport processes and radioactive decay. None of the other 14 RNs simulated were transported far enough in concentrations above MCL to influence the CB. The ensemble CB extends beyond the boundary of the NNSS in four places. In all cases, the distance of the CB beyond the borders of the NNSS is less than 5 km. The CB remains more than 12 km upgradient of the nearest potential public receptors located on the NTTR boundary in Oasis Valley. This suggests that RN migration will occur but is not expected to arrive at the discharge locations in Oasis Valley in concentrations exceeding the SDWA standards. Effective monitoring to track the migration of RNs will be necessary to ensure the long-term safety of downgradient groundwater users.

8.0 References

BN, see Bechtel Nevada.

Bear, J. 1972. *Dynamics of Fluids in Porous Media*. New York, NY: Elsevier Publishing Co.

Bechtel Nevada. 2002. *Hydrostratigraphic Model and Alternatives for the Groundwater Flow and Contaminant Transport Model of Corrective Action Units 101 and 102: Central and Western Pahute Mesa, Nye County, Nevada,* DOE/NV/11718-646. Prepared for U.S. Department of Energy, National Nuclear Security Administration Nevada Operations Office. Las Vegas, NV.

Blankennagel, R.K. 1967. *Hydraulic Testing Techniques of Deep Drill Holes at Pahute Mesa, Nevada Test Site,* Open-File Report 67-18. Prepared in cooperation with the U.S. Atomic Energy Commission. Washington, DC: U.S. Geological Survey.

Blankennagel, R.K., and J.E. Weir, Jr. 1973. *Geohydrology of the Eastern Part of Pahute Mesa, Nevada Test Site, Nye County, Nevada*, Professional Paper 712-B. Denver, CO: U.S. Geological Survey.

CFR, see *Code of Federal Regulations.*

Carle, S.F. 2018. *Updated K_d Estimates for Modeling Sorption of Cs, Sr, and Pu Isotopes in Hydrostratigraphic Units of Rainier Mesa and Shoshone Mountain,* LLNL-TR-751397. Livermore, CA: Lawrence Livermore National Laboratory.

Carle, S.F. 2020. *Interpretation of Mineralogical Diagenesis for Assessment of Radionuclide Transport at Pahute Mesa, Nevada National Security Site,* LLNL-TR-810225. Livermore, CA: Lawrence Livermore National Laboratory.

Carle, S.F., R. M. Maxwell, and G.A. Pawloski. 2003. *Impact of Heat on Groundwater Flow at Pahute Mesa, Nevada Test Site,* UCRL-ID-152599. Livermore, CA: Lawrence Livermore National Laboratory.

Carle, S.F., A.F.B. Tompson, and M. Zavarin. 2020. *Radionuclide Screening Analysis and Transport Parameters for Pahute Mesa Detonations, Nevada National Security Site,* LLNL-TR-812351, Livermore, CA: Lawrence Livermore National Laboratory.

Carle, S.F., A.F.B. Tompson, and M. Zavarin. 2021. *Review of Cavity Radius and Chimney Height Information for Underground Nuclear Tests at Nevada National Security Site,* LLNL-TR-818725. Livermore, CA: Lawrence Livermore National Laboratory.

Cooper, C.A., R.L. Hershey, J.M. Healey, and B.F. Lyles. 2013. *Estimation of Groundwater Recharge at Pahute Mesa Using the Chloride Mass-Balance Method,* DOE/NV/0000939-09; Publication No. 45251. Reno, NV: Desert Research Institute, Water Resources Center.

Crank, J. 1975. *The Mathematics of Diffusion.* Oxford, UK: Clarendon Press.

Code of Federal Regulations. 2021. Title 40 CFR, Part 141, "National Primary Drinking Water Regulations." Washington, DC: U.S. Government Printing Office.

DOE, see U.S. Department of Energy.

DOE/EMNV, see U.S. Department of Energy Environmental Management Nevada Program.

DOE/NV, see U.S. Department of Energy, Nevada Operations Office.

DOE/WIPP, see U.S. Department of Energy, Waste Isolation Pilot Plant.

Dynamic Graphics, see Dynamic Graphics, Inc.

de Marsily, G. 1986. *Quantitative Hydrogeology: Groundwater Hydrology for Engineers*. San Diego, CA: Academic Press, Inc.

Doherty, J. 2004. *PEST: Model-Independent Parameter Estimation, User Manual*, Fifth Edition, Brisbane, Australia: Watermark Numerical Computing.

Doherty, J. 2018. "Methodologies and Software for PEST-Based Model Predictive Uncertainty Analysis." Brisbane, Australia: Watermark Numerical Computing. Available at Iwww.pesthomepage.org\Downloads.php?file=pest_uncert.zip. As accessed on 2 January.

Doherty, J., R.J. Hunt, and M.J. Tonkin. 2010. *Approaches to Highly Parameterized Inversion: A Guide to Using PEST for Model-Parameter and Predictive-Uncertainty Analysis,* Scientific Investigations Report 2010-5211. Reston, VA: U.S. Geological Survey.

Dynamic Graphics, Inc. 2019. *EarthVision 10: Software for 3D Modeling & Visualization*. Alameda, CA.

EPA, see U.S. Environmental Protection Agency.

FFACO, see *Federal Facility Agreement and Consent Order*.

Faunt, C.C., A.M. Provost, M.C. Hill, and W.R. Belcher. 2010. "Comment on 'An unconfined groundwater model of the Death Valley Regional Flow System and a comparison to its confined predecessor' by R.W.H. Carroll, G.M. Pohll and R.L. Hershey." In *Journal of Hydrology,* Vol. 373(3–4): pp. 316–328.

Federal Facility Agreement and Consent Order. 1996 (as amended March 2010). Agreed to by the State of Nevada; U.S. Department of Energy, Environmental Management; U.S. Department of Defense; and U.S. Department of Energy, Legacy Management. Appendix VI, which contains the Underground Test Area Strategy, was last modified June 2014, Revision No. 5.

Fenelon, J.M., K.J. Halford, and M.T. Moreo. 2016. *Delineation of the Pahute Mesa–Oasis Valley Groundwater Basin, Nevada,* Scientific Investigations Report 2015–5175. Carson City, NV: U.S. Geological Survey.

Ferguson, J.F., A.H. Cogbill, and R.G. Warren. 1994. "A Geophysical-Geological Transect of the Silent Canyon Caldera Complex, Pahute Mesa, Nevada." In *Journal of Geophysical Research: Solid Earth,* Vol. 99(B3): pp. 4323–4339.

Finnegan, D.L., S.M. Bowen, J.L. Thompson, C.M. Miller, P.L. Baca, L.F. Olivas, C.G. Geoffrion, D.K. Smith, W. Goishi, B.K. Esser, J.W. Meadows, N. Namboodiri, and J.F. Wild. 2016. *Nevada National Security Site Underground Radionuclide Inventory, 1951–1992: Accounting for Radionuclide Decay through September 30, 2012,* LA-UR-16-21749. Los Alamos, NM: Los Alamos National Laboratory.

Freeze, R.A., and J.A. Cherry. 1979. *Groundwater.* Englewood Cliffs, NJ: Prentice Hall.

Frus, R.J., and K.J. Halford. 2018. *Documentation of Single-Well Aquifer Tests and Integrated Borehole Analyses, Pahute Mesa and Vicinity, Nevada,* Scientific Investigations Report 2018-5096. Reston, VA: U.S. Geological Survey.

Golder, see Golder Associates, Ltd.

Garcia, C.A., J.M. Fenelon, K.J. Halford, S.R. Reiner, and R.J. Laczniak. 2011. *Assessing Hydraulic Connections Across a Complex Sequence of Volcanic Rocks—Analysis of U-20 WW Multiple-Well Aquifer Test, Pahute Mesa, Nevada National Security Site, Nevada*, Scientific Investigations Report 2011–5173, 24 pp. Reston, VA: U.S. Geological Survey.

Garcia, C.A., K.J. Halford, and J.M. Fenelon. 2013. "Detecting Drawdowns Masked by Environmental Stresses with Water-Level Models." In *Groundwater,* Vol. 51(3): pp. 322–332.

Garcia, C.A., T.R. Jackson, K.J. Halford, D.S. Sweetkind, N.A. Damar, J.M. Fenelon, and S.R. Reiner. 2017. *Hydraulic Characterization of Volcanic Rocks in Pahute Mesa Using an Integrated Analysis of 16 Multiple-Well Aquifer Tests, Nevada National Security Site, 2009–14,* Scientific Investigations Report 2016-5151. Carson City, NV: U.S. Geological Survey.

Gelhar, L.W., W. Welty, and K.R. Rehfeldt. 1992. "A Critical Review of Data on Field Scale Dispersion in Aquifers." In *Water Resources Research,* Vol. 28(7): pp. 1955–1974. Washington, DC: American Geophysical Union.

Golder Associates, Ltd. 2016. Written communication to K. Rehfeldt (Navarro). Subject: “1.0 Fractures and Groundwater Flow at Pahute Mesa.”

HGL, see HydroGeologic, Inc.

Halford, K., C.A. Garcia, J. Fenelon, and B. Mirus. 2016. A*dvanced Methods for Modeling Water-Levels and Estimating Drawdowns with SeriesSEE, an Excel Add-In,* Techniques and Methods Report 4-F4, Version 1.1. Reston, VA: U.S. Geological Survey.

Halford, K.J., and T.R. Jackson. 2020. *Groundwater Characterization and Effects of Pumping in the Death Valley Regional Groundwater Flow System, Nevada and California, with Special Reference to Devils Hole,* Professional Paper 1863. Reston, VA: U.S. Geological Survey.

Harbaugh, A.W., E.R. Banta, M.C. Hill, and M.G. McDonald. 2000. *MODFLOW-2000, The U.S. Geological Survey Modular Ground-water Model User Guide to Modularization Concepts and the Ground-water Flow Process.* Open-File Report 00-92. Denver, CO: U.S. Geological Survey.

Harbaugh, A.W. 2005. *MODFLOW-2005: The U.S. Geological Survey Modular Ground-water Model-The Ground-water Flow Process,* Techniques and Methods 6-A16. Reston, VA: U.S. Geological Survey.

Hershey, R.L., J.B. Paces, M.J. Singleton, E.M. Kwicklis, D.L. Decker, W.M. Fryer, and S. Earman. 2008. *Geochemical and Isotopic Evaluation of Groundwater Movement in Corrective Action Unit 99: Rainier Mesa and Shoshone Mountain, Nevada Test Site,* DOE/NV/26383-10; Publication No. 45229. Las Vegas, NV: Desert Research Institute.

Hershey, R.L., R. Parashar, C.A. Cooper, K.M. Heintz, H.V. Pham, and B.F. Lyles. 2020. *Evaluation of Timber Mountain Recharge and Groundwater Flow in Relation to Pahute Mesa-Oasis Valley Flow System,* DOE/NV/0003590-56; Publication No. 45294. Las Vegas, NV: Desert Research Institute.

Hess, K.H., Davis, J.A., Kent, D.B., and Coston, J.A. 2002. *Multispecies reactive tracer test in an aquifer with spatially variable chemical conditions, Cape Cod, Massachusetts: Dispersive transport of bromide and nickel*, In Water Resources Research, Vol. 38(8): pp. 1161. 10.1029/2001WR000945, Washington, DC: American Geophysical Union.

Hoaglund, J., 2017. Written communication to K. Rehfeldt (Navarro). Subject: *Effect of Fault Proximity on Large-Scale Hydraulic Conductivity.* Las Vegas, NV.

HydroGeoLogic, Inc. 2017. Written communication to K. Rehfeldt (Navarro). Subject: “Task Order 3: Fracture Analysis,” Technical Data Repository No. UGTA-4-1808, 29 September. Reston, VA.

HydroGeoLogic, Inc. 2018. Written communication to K. Rehfeldt (Navarro). Subject: “Task Order 5: Transport Parameters (Dispersivity, Matrix Diffusion, and Mass Transfer Coefficient),” Technical Data Repository No. UGTA-4-2099, 22 August. Reston, VA.

IT, see IT Corporation.

IT Corporation. 1996a. *Groundwater Recharge and Discharge Data Documentation Package (Underground Test Area Subproject Phase I Data Analysis Documentation, Volume III*). Prepared for the U.S. Department of Energy, Nevada Operations Office. Las Vegas, NV.

IT Corporation. 1996b. *Hydrologic Parameter Data Documentation Package (Underground Test Area Subproject Phase 1 Data Analysis Documentation, Volume IV).* Prepared for the U.S. Department of Energy, Nevada Operations Office. Las Vegas, NV.

IT Corporation. 1996c. *Regional Geologic Model Data Documentation Package (Underground Test Area Subproject Phase 1 Data Analysis Documentation, Volume I).* Prepared for the U.S. Department of Energy, Nevada Operations Office. Las Vegas, NV.

IT Corporation. 1998. *Report and Analysis of the BULLION Forced-Gradient Experiment,* Rev. 0, DOE/NV/13052-042; ITLV/13052-042; UC-700. Las Vegas, NV.

Jackson, T.R. 2021. *Permeable Groundwater Pathways and Tritium Migration Patterns from the HANDLEY Underground Nuclear Test, Pahute Mesa, Nevada*, Scientific Investigations Report 2021-5032. Reston, VA: U.S. Geological Survey.

Jackson, T.R., and J.M. Fenelon. 2018. *Conceptual Framework and Trend Analysis of Water-Level Responses to Hydrologic Stresses, Pahute Mesa–Oasis Valley Groundwater Basin, Nevada, 1966–2016,* Scientific Investigation Report 2018-5064. Reston, VA: U.S. Geological Survey.

Jackson, T.R., J.M. Fenelon, and R. Paylor. 2021. *Groundwater Flow Conceptualization of the Pahute Mesa–Oasis Valley Groundwater Basin, Nevada: A Synthesis of Geologic, Hydrologic, HydraulicProperty, and Tritium Data*, Scientific Investigations Report 2020-5134. Carson City, NV: U.S. Geological Survey.

Kane, M.F., M.W. Webring, and B.K. Bhattacharyya. 1981. *A Preliminary Analysis of Gravity and Aeromagnetic Surveys of the Timber Mountain Area, Southern Nevada,* Open-File Report 81-189. Denver, CO: U.S. Geological Survey.

Kersting, A.B. 1996. *The State of the Hydrologic Source Term.* UCRL-ID-126557. Livermore, CA: Lawrence Livermore National Laboratory.

Kersting, A.B., D.W. Efurd, D.L. Finnegan, D.J. Rokop, D.K. Smith, and J.L. Thompson. 1999. “Migration of Plutonium in Ground Water at the Nevada Test Site.” In *Nature,* Vol. 397: pp. 56–59.

Kersting, A.B., D.L. Finnegan, A.F.B. Tompson, B.K. Esser, D.K. Smith, M. Zavarin, C.J. Bruton, and G.A. Pawloski. 2003. *Radionuclide Decay and In-growth Technical Basis Document,* UCRL-ID-153798. Livermore, CA: Lawrence Livermore National Laboratory.

Kwicklis, E.M., T.P. Rose, and F.C. Benedict, Jr. 2005. *Evaluation of Groundwater Flow in the Pahute Mesa–Oasis Valley Flow System Using Groundwater Chemical and Isotopic Data*, LA-UR-05-4344. Los Alamos, NM: Los Alamos National Laboratory.

LANL, see Los Alamos National Laboratory.

Laczniak, R.J., J.C. Cole, D.A. Sawyer, and D.A. Trudeau. 1996. *Summary of Hydrogeologic Controls on Ground-Water Flow at the Nevada Test Site, Nye County, Nevada*, Water-Resources Investigations Report 96-4109. Carson City, NV: U.S. Geological Survey.

Laczniak, R.J., J.L. Smith, P.E. Elliott, G.A. DeMeo, M.A. Chatigny, and G. Roemer. 2001. *Ground-Water Discharge Determined from Estimates of Evapotranspiration, Death Valley Regional Flow System, Nevada and California*, Water-Resources Investigations Report 01-4195. Carson City, NV: U.S. Geological Survey.

Langevin, C.D., J.D. Hughes, E.R. Banta, R.G. Niswonger, S. Panday, and A.M. Provost. 2017. *Documentation for the MODFLOW 6 Groundwater Flow Model*, Techniques and Methods 6-A55. Reston, VA: U.S. Geological Survey.

Los Alamos National Laboratory. 2011. *LaGriT Los Alamos Grid Toolbox* website. As accessed at http://lagrit.lanl.gov/.

Lu, Z., E. Kwicklis, T. Miller and M. Bourret. 2021. *Development and Calibration of the Pahute Mesa Bench Area Groundwater Flow and Tritium Transport Model,* Nevada National Security *Site*, LA-UR-21-23595. Los Alamos, NM: Los Alamos National Laboratory.

Makedonska, N., E.M. Kwicklis, J.D. Hyman, and S.M. Bourret. 2020. *Discrete Fracture Network Modeling to Estimate Upscaled Parameters for the Topopah Spring, Lava Flow, and Tiva Canyon Aquifers at Pahute Mesa, Nevada National Security Site*, LA-UR-20-22665. Los Alamos, NM: Los Alamos National Laboratory.

Maloszewski, P., and A. Zuber. 1985. “On the Theory of Tracer Experiments in Fissured Rocks with a Porous Matrix.” In *Journal of Hydrology*, Vol. 79(3–4): p. 333–358.

Mankinen, E.A., T.G. Hildenbrand, G.L. Dixon, E.H. McKee, C.J. Fridrich, and R.J. Laczniak. 1999. *Gravity and Magnetic Study of the Pahute Mesa and Oasis Valley Region, Nye County, Nevada*, Open-File Report 99-303, Version 1.0. Reston, VA: U.S. Geological Survey.

Mankinen, E.A., T.G. Hildenbrand, C.J. Fridrich, E.H. McKee, and C.J. Schenkel. 2003. *Geophysical Setting of the Pahute Mesa-Oasis Valley Region, Southern Nevada*, Report 50. Reno, NV: Nevada Bureau of Mines and Geology.

Maxey, G.B., and T.E. Eakin. 1951. “Ground Water in Railroad, Hot Creek, Reveille, Kawich, and Penoyer Valleys, Nye, Lincoln, and White Pine Counties, Nevada.” In *Contributions to the Hydrology of Eastern Nevada,* Water Resources Bulletin No. 12. pp. 127–171. Carson City, NV: State of Nevada, Office of the State Engineer/U.S. Geological Survey.

Middleton, R.S., E.M. Kwicklis, K.H. Birdsell, D.G. Levitt, and J. Hevesi. 2019. *Net Infiltration Models for the Pahute Mesa Area,* LA-UR-16-27513, Rev 1. Los Alamos, NM: Los Alamos National Laboratory.

Mills, R. 1973. “Self-Diffusion in Normal and Heavy Water in the Range 1-45°.” In *The Journal of Physical Chemistry,* Vol. 77(5): pp. 685–688.

Moncure, G.K., R.C. Surdam, and H.L. McKague. 1981. “Zeolite Diagenesis below Pahute Mesa.” In *Clays and Clay Minerals*, Vol. 29(5): pp. 385–396.

Navarro GIS, see Navarro Geographic Information Systems.

N-I, see Navarro-Intera, LLC.

NNSA/NFO, see U.S. Department of Energy, National Nuclear Security Administration Nevada Field Office.

NSTec, see National Security Technologies, LLC.

National Security Technologies, LLC. 2014. Written communication. Subject: *Phase II Hydrostratigraphic Framework Model for Corrective Action Units 101 and 102 Central and Western Pahute Mesa, Nye County Nevada*. November. Las Vegas, NV.

Navarro. 2018. *Pahute Mesa Well Development and Testing Analyses for Wells ER-EC-12 and ER-EC-13, Nevada National Security Site, Nye County, Nevada*, Rev. 0, N/0002653--051. Las Vegas, NV.

Navarro. 2019c. Written communication. Subject: *Pahute Mesa Geophysical Log Data Evaluation for Matrix Porosity*, UGTA Technical Data Repository No. UGTA-4-2037. Las Vegas, NV.

Navarro. 2020. *Phase II Geochemical and Isotopic Evaluation of Groundwater Flow in the Pahute Mesa–Oasis Valley Flow System, Nevada*. Rev. 1, N/0002653--069. Las Vegas, NV.

Navarro. 2021a. *Contaminant Transport Parameters for the Groundwater Flow and Contaminant Transport Model of Corrective Action Units 101 and 102: Central and Western Pahute Mesa, Nye County, Nevada,* Rev. 1, N/0002653--077. Las Vegas, NV.

Navarro. 2021b. *Hydrologic Data for the Groundwater Flow and Contaminant Transport Model of Corrective Action Units 101 and 102: Central and Western Pahute Mesa, Nye County, Nevada,* Rev. 1, N/0002653--073. Las Vegas, NV.

Navarro. 2021c. *Unclassified Source Term and Radionuclide Data for the Groundwater Flow and Contaminant Transport Model for Corrective Action Units 101 and 102: Central and Western Pahute Mesa, Nye County, Nevada*, Rev 1, N/0002653--088. Las Vegas, NV.

Navarro. 2021d. Written communication. Subject: *UGTA Chemistry Database (UCDB)*, UGTA Technical Data Repository Database Identification Number UGTA-4-1197. Las Vegas, NV. As accessed on 14 June.

Navarro Geographic Information Systems. 2020–2021. ESRI ArcGIS Software.

Navarro-Intera, LLC. 2012. *Pahute Mesa Well Development and Testing Analyses for Wells ER-20-8 and ER-20-4, Nevada National Security Site, Nye County, Nevada*, Rev. 0, N-I/28091--061. Las Vegas, NV.

Navarro-Intera, LLC. 2013. *Phase I Flow and Transport Model Document for Corrective Action Unit 97: Yucca Flat/Climax Mine, Nevada National Security Site, Nye County, Nevada*, Rev. 1, N-I/ 28091--080. Las Vegas, NV.

Neuman, S.P. 1990. "Universal Scaling of Hydraulic Conductivities and Dispersivities in Geologic Media." In *Water Resources Research*, Vol. 26(8): pp. 1749–1758. Washington, DC: American Geophysical Union.

Oberlander, P.L., D. McGraw, and C. E. Russell. 2007. *Hydraulic Conductivity With Depth for Underground Test Area (UGTA) Wells*, DOE/NV/26383-08; Publication No. 45228. Las Vegas, NV: Desert Research Institute, Water Resources Center.

Painter, S.L. 2011. *User's Manual for Walkabout V1.0*, LA-UR-11-01952. Los Alamos, NM: Los Alamos National Laboratory.

Parashar, R., H.V. Pham, and N.L. Sund. 2019. *Development of Upscaling Techniques and Construction of Calibrated Models for Fractured Rocks Using Discrete Fracture Network Approaches*, DOE/NV/0003590-43; Publication No. 45289. Las Vegas, NV: Desert Research Institute.

Pawloski, G.A. 1999. *Development of Phenomenological Models of Underground Nuclear Tests on Pahute Mesa, Nevada Test Site—BENHAM and TYBO*, UCRL-ID-136003. Livermore, CA: Lawrence Livermore National Laboratory.

Pawloski, G.A., A.F.B. Tompson, and S.F. Carle eds. 2001. *Evaluation of the Hydrologic Source Term from Underground Nuclear Tests on Pahute Mesa at the Nevada National Security Site: The CHESHIRE Test*, UCRL-ID-147023 Livermore, CA: Lawrence Livermore National Laboratory.

Pham, H.V., R. Parashar, N.L. Sund, and K.F. Pohlmann. 2020. "Determination of Fracture Apertures Via Calibration of Three-Dimensional Discrete-Fracture-Network Models: Application to Pahute Mesa, Nevada National Security Site, USA." In *Hydrogeology Journal*, Vol. 29(4): pp. 841–857.

Pohlmann, K., M. Ye, D. Reeves, D. Decker, J. Chapman, and M. Zavarin. 2007. *Modeling of Groundwater Flow and Radionuclide Transport at the Climax Mine Sub-CAU, Nevada Test Site*, DOE/NV/26383-06; Publication No. 45226. Las Vegas, NV: Desert Research Institute.

Prothro, L.B., and S.L. Drellack, Jr. 1997. *Nature and Extent of Lava-Flow Aquifers Beneath Pahute Mesa, Nevada Test Site,* DOE/NV-11718-156. Las Vegas, NV: Bechtel Nevada.

Prothro, L.B., S.L. Drellack, and J.M. Mercadante. 2009a. *A Hydrostratigraphic System for Modeling Groundwater Flow and Radionuclide Migration at the Corrective Action Unit Scale, Nevada Test Site and Surrounding Areas, Clark, Lincoln, and Nye Counties, Nevada*, DOE/NV/25946--630. Las Vegas, NV: National Security Technologies, LLC.

Prothro, L.B., S.L. Drellack, D.N. Haugstad, H.E. Huckins-Gang, and M.J. Townsend. 2009b. *Observations on Faults and Associated Permeability Structures in Hydrogeologic Units at the Nevada Test Site*, DOE/NV/25946--690. Las Vegas, NV: National Security Technologies, LLC.

RamaRao, B.S., A.M. Lavenue, G. de Marsily, and M.G. Marietta. 1995. "Pilot Point Methodology for Automated Calibration of an Ensemble of Conditionally Simulated Transmissivity Fields 1. Theory and Computational Experiments." In *Water Resources Research*, Vol. 31(3): pp. 475–493.

Reeves, D.M., K.D. Smith, R. Parashar, C. Collins, and K.M. Heintz. 2017. *Investigating the Influence of Regional Stress on Fault and Fracture Permeability at Pahute Mesa, Nevada National Security Site*, DOE/NV/0000939-41; Publication No. 45275. Las Vegas, NV: Desert Research Institute.

Rehfeldt, K., and B. Wilborn. 2020. "Achieving the End State for the Pahute Mesa Corrective Action Units at the Nevada National Security Site – Paper 20355." WM2020 Conference, 8–12 March. Phoenix, AZ.

Reimus, P.W. 2018. *Evaluation of the Need to Consider Colloid-Facilitated Plutonium Transport in Contaminant Boundary Calculations for Pahute Mesa at the Nevada National Security Site*, LAUR-18-29291. Los Alamos, NM: Los Alamos National Laboratory.

Reimus, P.W., and T.J. Callahan. 2007. "Matrix Diffusion Rates in Fractured Volcanic Rocks at the Nevada Test Site: Evidence for a Dominant Influence of Effective Fracture Apertures." In *Water Resources Research*, Vol. 43, W07421. Washington, DC: American Geophysical Union.

Reimus, P.W., and H. Boukhalfa. 2014. *Chancellor Water Colloids: Characterization and Radionuclide Associated Transport*, LA-UR-14-27538. N. Wasserman, B. Erdmann, A.I. Abdel-Fattah, S.D. Ware, P. He, S. Tarimala, and B. Martinez, contributors. Los Alamos, NM: Los Alamos National Laboratory.

Reimus, P.W., and M.J. Haga. 1999. *Analysis of Tracer Responses in the BULLION Forced-Gradient Experiment at Pahute Mesa, Nevada*, LA-13615-MS. Los Alamos, NM: Los Alamos National Laboratory.

Reiner, S.R., R.J. Laczniak, G.A. DeMeo, J. LaRue Smith, P.E. Elliott, W.E. Nylund, and C.J. Fridrich. 2002. *Ground-Water Discharge Determined from Measurements of Evapotranspiration, Other Available Hydrologic Components, and Shallow Water-Level Changes, Oasis Valley, Nye County, Nevada*, Water-Resources Investigations Report 01-4239. Carson City, NV: U.S. Geological Survey.

Robinson, B.A., and Z.V. Dash. 2006. *User's Guide for the PLUMECALC Application*, Version 2.2. Los Alamos, NM: Los Alamos National Laboratory.

Robinson, B.A., Z.V. Dash, and G. Srinivasan. 2010. "A Particle Tracking Transport Method for the Simulation of Resident and Flux-Averaged Concentration of Solute Plumes in Groundwater Models." In *Computational Geosciences*, Vol. 14(4): pp. 779–792.

Robinson, B.A., Z.V. Dash, and S.L. Painter. 2011. *User's Guide for the PLUMECALC Application with Subgridding, Version 2.3.2*, LA-UR-11-02090. Los Alamos, NM: Los Alamos National Laboratory.

Rose, T.P., F.C. Benedict, Jr., J.M. Thomas, W.S. Sicke, R.L. Hershey, J.B. Paces, I.M. Farnham, and Z.E. Peterman. 2006. *Geochemical Data Analysis and Interpretation of the Pahute Mesa–Oasis Valley Groundwater Flow System, Nye County, Nevada, August 2002*, UCRL-TR-224559. Livermore, CA: Lawrence Livermore National Laboratory.

Rose, T.P., Q. Hu, P. Zhao, C.L. Conrado, R. Dickerson, G.F. Eaton, A.B. Kersting, J.E. Moran, G. Nimz, B.A. Powell, E.C. Ramon, F.J. Ryerson, R.W. Williams, P.T. Wooddy, and M. Zavarin. 2011. *Radionuclide Partitioning in an Underground Nuclear Test Cavity*, LLNL-TR-409817. Livermore, CA: Lawrence Livermore National Laboratory.

Shaw, see Shaw Environmental, Inc.

SNJV, see Stoller-Navarro Joint Venture.

Sawyer, D.A., R.J. Fleck, M.A. Lanphere, R.G. Warren, D.E. Broxton, and M.R. Hudson. 1994. "Episodic Caldera Volcanism in the Miocene Southwestern Nevada Volcanic Field: Revised Stratigraphic Caldera Framework, $^{40}Ar/^{39}Ar$ Geochronology, and Implications for Magmatism and Extension." In *Geological Society of America Bulletin*, Vol. 106(10): pp. 1304–1318.

Schulze-Makuch, D. 2005. "Longitudinal Dispersivity Data and Implications for Scaling Behavior." In Ground Water, Vol. 43(3): pp. 443–456.

Shaw Environmental, Inc. 2003. *Contaminant Transport Parameters for the Groundwater Flow and Contaminant Transport Model of Corrective Action Units 101 and 102: Central and Western Pahute Mesa, Nye County, Nevada*, Rev. 0, Shaw/13052-201-CD. Las Vegas, NV.

Slate, J.L., M.E. Berry, P.D. Rowley, C.J. Fridrich, K.S. Morgan, J.B. Workman, O.D. Young, G.L. Dixon, V.S. Williams, E.H. McKee, D.A. Ponce, T.G. Hildenbrand, W.C. Swadley, S.C. Lundstrom, E.B. Ekren, R.G. Warren, J.C. Cole, R.J. Fleck, M.A. Lanphere, D.A. Sawyer, S.A. Minor, D.J. Grunwald, R.J. Laczniak, C.M. Menges, J.C. Yount, and A.S. Jayko. 1999. *Part A. Digital Geologic Map of the Nevada Test Site and Vicinity, Nye, Lincoln, and Clark Counties, Nevada, and Inyo County, California, Revision 4*, Open-File Report 99-554-A, scale 1:120,000. Denver, CO: U.S. Geological Survey.

Stoller-Navarro Joint Venture. 2004a. *Hydrologic Data for the Groundwater Flow and Contaminant Transport Model of Corrective Action Units 101 and 102: Central and Western Pahute Mesa, Nye County, Nevada*, Rev. 0, S-N/99205--002, Shaw/13052-204. Las Vegas, NV.

Stoller-Navarro Joint Venture. 2004b. *The Role of Dispersion in Radionuclide Transport - Data and Modeling Requirements,* Rev. 1, S-N/99205-003. Las Vegas, NV.

Stoller-Navarro Joint Venture. 2004c. *Unclassified Source Term and Radionuclide Data for the Groundwater Flow and Contaminant Transport Model of Corrective Action Units 101 and 102: Central and Western Pahute Mesa, Nye County, Nevada*, Rev. 0, S-N/99205--022. Las Vegas, NV.

Stoller-Navarro Joint Venture. 2006. *Groundwater Flow Model of Corrective Action Units 101 and 102: Central and Western Pahute Mesa, Nevada Test Site, Nye County, Nevada,* Rev. 0, S-N/99205--076. Las Vegas, NV.

Stoller-Navarro Joint Venture. 2007. *Addendum to the Groundwater Flow Model of Corrective Action Units 101 and 102: Central and Western Pahute Mesa, Nevada Test Site, Nye County, Nevada*, Rev. 0, S-N/99205--076-ADD. Las Vegas, NV.

Stoller-Navarro Joint Venture. 2009a. *Central and Western Pahute Mesa Phase II Hydrogeologic Investigation Wells Drilling and Completion Criteria,* Rev. 0, S-N/99205--120. Las Vegas, NV.

Stoller-Navarro Joint Venture. 2009b. *Phase I Transport Model of Corrective Action Units 101 and 102: Central and Western Pahute Mesa, Nevada Test Site, Nye County, Nevada*, Rev. 1, S-N/99205--111. Las Vegas, NV.

Stoller-Navarro Joint Venture. 2009c. *Unclassified Source Term and Radionuclide Data for Corrective Action Unit 97: Yucca Flat/Climax Mine, Nevada Test Site, Nevada,* Rev. 2, S-N/99205--114. Las Vegas, NV.

Sudicky, E.A., and E.O. Frind. 1981. “Carbon 14 Dating of Groundwater in Confined Aquifers: Implications of Aquitard Diffusion.” In *Water Resources Research,* Vol. 17(4): pp. 1060–1064. Washington, DC: American Geophysical Union.

Telfeyan, K., S.D. Ware, P.W. Reimus, and K.H. Birdsell. 2018, “Comparison of Experimental Methods for Estimating Matrix Diffusion Coefficients for Contaminant Transport Modeling.” In *Journal of Contaminant Hydrology*, Vol. 209: pp. 51–60.

Tompson, A.F.B., C.J. Bruton, and G.A. Pawloski eds. 1999. *Evaluation of the Hydrologic Source Term from Underground Nuclear Tests in Frenchman Flat at the Nevada Test Site: The CAMBRIC Test*, UCRL-ID-132300. Livermore, CA: Lawrence Livermore National Laboratory.

Tompson, A.F.B., M. Zavarin, W.W. McNab, S.F. Carle, D.E. Shumaker, C. Lu, Y. Sun, G.A. Pawloski, Q. Hu, and S.K. Roberts. 2011. *Hydrologic Source Term Processes and Models for Underground Nuclear Tests at Rainier Mesa and Shoshone Mountain, Nevada National Security Site*, LLNL-TR-483852-REV1. Livermore, CA: Lawrence Livermore National Laboratory.

Tompson, A., M. Zavarin, and D. Shumaker. 2019. *Yield-Weighting Approaches for Calculating Radiologic Inventories for Individual Underground Nuclear Tests at the Nevada National Security Site,* LLNL-TR-773562, Lawrence Livermore National Laboratory, Livermore, CA.

U.S. Department of Energy Environmental Management Nevada Program. 2018a. *Rainier Mesa/Shoshone Mountain Flow and Transport Model Report Nevada National Security Site, Nevada*, Rev. 1, DOE/NV--1588, Las Vegas, NV.

U.S. Department of Energy, Environmental Management Nevada Program. 2018b. *Record of Technical Change to Underground Test Area Activity Quality Assurance Plan, Nevada National Security Site, Nevada*, Rev. 2, DOE/NV--1450-REV.2; Technical Change No. DOE/NV--1450-REV.2-ROTC-1, 5 February. Las Vegas, NV.

U.S. Department of Energy Environmental Management Nevada Program. 2019a. *Record of Technical Change to Nevada National Security Site Integrated Groundwater Sampling Plan*, Rev. 1, DOE/NV--1525-REV. 1; ROTC No. DOE/NV--1525-REV.1-ROTC 1, 5 February. Las Vegas, NV.

U.S. Department of Energy Environmental Management Nevada Program. 2019b. *Addendum to the Rainier Mesa/Shoshone Mountain Flow and Transport Model Report, Nevada National Security Site, Nevada*. Rev. 1, DOE/EMNV--0002. Las Vegas, NV.

U.S. Department of Energy, Environmental Management Nevada Program. 2020a. *Pahute Mesa-Oasis Valley Hydrostratigraphic Framework Model for Corrective Action Units 101 and 102: Central and Western Pahute Mesa, Nye County, Nevada*, Rev. 0, DOE/EMNV--0014. Las Vegas, NV.

U.S. Department of Energy Environmental Management Nevada Program. 2020b. *Update to the Phase II Corrective Action Investigation Plan for Corrective Action Units 101 and 102, Central and Western Pahute Mesa, Nevada National Security Site, Nye County, Nevada,* Rev. 1, DOE/EMNV--0018. Las Vegas, NV.

U.S. Department of Energy Environmental Management Nevada Program. 2021. *Pahute Mesa Data Completeness Analysis*, Rev 1, DOE/EMNV--0032. Las Vegas, NV.

U.S. Department of Energy, National Nuclear Security Administration Nevada Field Office. 2014. *Record of Technical Change to Phase II Corrective Action Investigation Plan for Corrective Action Units 101 and 102: Central and Western Pahute Mesa, Nevada Test Site, Nye County, Nevada*, DOE/NV--1312-Rev. 2; Technical Change No. DOE/NV--1312-Rev. 2 ROTC 2, 25 November. Las Vegas, NV.

U.S. Department of Energy, National Nuclear Security Administration Nevada Field Office. 2015a. *Underground Test Area Activity Quality Assurance Plan, Nevada National Security Site, Nevada*, Rev. 2, DOE/NV--1450-REV.2. Las Vegas, NV.

U.S. Department of Energy, National Nuclear Security Administration Nevada Field Office. 2015b. *United States Nuclear Tests, July 1945 through September 1992,* DOE/NV-209, Rev. 16.

U.S. Department of Energy, National Nuclear Security Administration Nevada Field Office. 2016. *Underground Test Area (UGTA) Closure Report for Corrective Action Unit 98: Frenchman Flat Nevada National Security Site, Nevada*, Rev. 1, DOE/NV--1538. Las Vegas, NV.

U.S. Department of Energy, National Nuclear Security Administration Nevada Site Office. 2009. *Phase II Corrective Action Investigation Plan for Corrective Action Units 101 and 102, Central and Western Pahute Mesa, Nevada Test Site, Nye County, Nevada*, Rev. 2, DOE/NV--1312. Las Vegas, NV.

U.S. Department of Energy, Nevada Operations Office. 1997. *Regional Groundwater Flow and Tritium Transport Modeling and Risk Assessment of the Underground Test Area, Nevada Test Site, Nevada,* DOE/NV--477, UC-700. Las Vegas, NV.

U.S. Department of Energy, Nevada Operations Office. 1999. *Corrective Action Investigation Plan for Corrective Action Units 101 and 102, Central and Western Pahute Mesa, Nevada Test Site, Nevada*, Rev. 1, DOE/NV--516. Las Vegas, NV.

U.S. Department of Energy, Waste Isolation Pilot Plant. 2004. Title 40 CFR Part 191 “Compliance Certification Application for the Waste Isolation Pilot Plant,” DOE/WIPP 2004-3231. March. Carlsbad, NM: Carlsbad Field Office.

U.S. Environmental Protection Agency. 1988. *Groundwater Modeling: An Overview and Status Report.* EPA/600/2-89/028 Ada, OK: Robert S. Kerr Environmental Research Laboratory.

U.S. Environmental Protection Agency. 1999. *Understanding Variation in Partition Coefficient, K_d, Values Volume II: Review of Geochemistry and Available K_d Values for Cadmium, Cesium, Chromium, Lead, Plutonium, Radon, Strontium, Thorium, Tritium (^3H), and Uranium*, EPA 402-R-99-004B. Washington, DC: Office of Air and Radiation.

U.S. Geological Survey. 2008. USGS Groundwater Software INFIL3.0 – *A Grid-Based, Distributed-Parameter Watershed Model to Estimate Net Infiltration Below the Root Zone*. As accessed at https://water.usgs.gov/nrp/gwsoftware/Infil/Infil.html.

U.S. Geological Survey. 2019. "FloPy: Python Package for Creating, Running, and Post-Processing MODFLOW-Based Models." Accessed at http://https://www.usgs.gov/software/flopy-python-package-creating-running-and-post-processing-modflow-based-models on 8 August.

Waddell, R.K., Robison, J.H., and Blankennagel, R.K., 1984. *Hydrology of Yucca Mountain and Vicinity, Nevada–California—Investigative Results through Mid-1983,* Water-Resources Investigations Report 84–4267. Denver, CO: U.S. Geological Survey.

Warren, R.G., G.L. Cole, and D. Walther. 2000b. *A Structural Block Model for the Three-Dimensional Geology of the Southwestern Nevada Volcanic Field,* LA-UR-00-5866. Los Alamos, NM: Los Alamos National Laboratory Report.

Winograd, I.J., and W. Thordarson. 1975. *Hydrogeologic and Hydrochemical Framework, South-Central Great Basin, Nevada-California, with Special Reference to the Nevada Test Site,* Professional Paper 712-C. Washington, DC: U.S. Geological Survey.

Zavarin, M. 2014. *Yields and Cavity Radii of Underground Nuclear Tests with Specified Yields Reported in DOE/NV--209-Rev 15 (2000)*, LLNL-TR-664664. Livermore, CA: Lawrence Livermore National Laboratory.

Zavarin, M., Lawrence Livermore National Laboratory. 2012. Memorandum to B. Wilborn (NNSA/NSO) titled "Isotopic Analyses: Environmental Monitoring Well ER-20-7," 3 October. Livermore, CA.

Zavarin, M., S.K. Roberts, B.E. Viani, G.A. Pawloski, and T.P. Rose. 2004. *Nuclear Melt Glass Dissolution and Secondary Mineral Precipitation at 40 to 200 °C,* UCRL-TR-204870. Livermore, CA: Lawrence Livermore National Laboratory.

Zavarin, M., S.K. Roberts, M.R. Johnson, Q. Hu, B.A. Powell, P. Zhao, A.B. Kersting, R.E. Lindvall, and R. Pletcher. 2013. *Colloid-Facilitated Radionuclide Transport in Fractured Carbonate Rock fromYucca Flat, Nevada National Security Site*, LLNL-TR-6119352. Livermore, CA: Lawrence Livermore National Laboratory.

Zavarin, M., P. Zhao, C. Joseph, J. Begg, M. Boggs, Z. Dai, and A.B. Kersting. 2015. *Hydrothermal Alteration of Glass from Underground Nuclear Tests: Formation and Transport of Pu-clay Colloids at the Nevada National Security Site*, LLNL-TR-671402.Livermore, CA: Lawrence Livermore National Laboratory.

Zavarin, M., P. Zhao, C. Joseph, J.D. Begg, M.A. Boggs, Z. Dai, and A.B. Kersting. 2019. "Hydrothermal Alteration of Nuclear Melt Glass, Colloid Formation, and Plutonium Mobilization at the Nevada National Security Site, U.S.A." In *Environmental Science and Technology*, Vol. 53: pp. 7363–7370.

Zhao, P., M. Zavarin, R.N. Leif, B.A. Powell, M.J. Singleton, R.E. Lindvall, and A.B. Kersting. 2011. a"Mobilization of Actinides by Dissolved Organic Compounds at the Nevada Test Site." In *Applied Geochemistry*, Vol. 26(3): pp. 308–318.

Zhou, Q., H.-H. Liu, F.J. Molz, Y. Zhang, and G.S. Bodvarsson, 2005. "Field-Scale Effective Matrix Diffusion Coefficient for Fractured Rock: Results From Literature Survey." In *Journal of Contaminated Hydrology*, Vol. 93(1–4).

Appendix A

Bibliography of Selected Phase II Investigations

A.1.0 Major Data Collection and Analysis Activities

Major data collection and analysis activities completed as a part of Phase II of CAI for PM CAU are noted below. This list is not comprehensive but provides representative recent analyses of data in support of the PM CAU model. Many of the references are cited elsewhere in this document where appropriate. New data analysis activities directly relevant to flow and transport modeling are listed below.

Activities relevant to the development of the PM CAU model:

- Revision of PM HFM based on new data (DOE/EMNV, 2020)
- Description of the HST and compilation of RN analyses of groundwater samples collected to show where test-derived constituents are and are not found (Navarro, 2021c)
- Compilation of the hydrologic data used to support development of the PM groundwater flow model (Navarro, 2021b)
- Compilation of the RN transport data used to support development of the PM groundwater RN transport model (Navarro, 2021a)
- Phase II geochemical and isotopic evaluation of groundwater flow in the PM-OV flow system (Navarro, 2020)
- Development of a new yield-weighting method of estimating radiological inventories (Tompson et al., 2019)
- Additional studies on colloid formation and transport (Zavarin et al., 2015 and 2019; Reimus and Boukhalfa, 2014; Reimus, 2018)
- Interpretation of mineral diagenesis for assessment of RN transport (Carle, 2020)
- Updated matrix sorption coefficients (Carle et al., 2020)
- RN screening analysis and transport parameters for PM detonations (Carle et al., 2020)
- Installation and testing of 11 wells (references cited in Section A.2.0 of this report)
- Analyses of 16 MWATs, yielding estimates of transmissivity, identified the hydraulic connections between wells, and provided calibration data for numerical models (as listed in Appendix A of Garcia et al., 2017)

- Estimates of porosity derived from analysis of geophysical log data (Navarro, 2021a)
- Additional studies of fracture analysis (HGL, 2017)
- Additional matrix diffusion estimates (Telfeyan et al., 2018; Zavarin et al., 2013)
- Additional dispersion studies (Zhou et al., 2005; HGL, 2018)
- DFN modeling studies (Makedonska et al., 2020; Parashar et al., 2019)
- Study of regional stress and fracture permeability (Reeves et al., 2017)
- Delineation of the PM-OV groundwater basin incorporating water budget from Reiner et al., 2002 (Fenelon et al., 2016)
- PM conceptual hydrologic model framework (Jackson et al., 2021)
- Standardization of PM single-well aquifer test results (Frus and Halford, 2018)
- Groundwater characterization and effects of pumping in the Death Valley Regional Groundwater Flow System incorporating water budget from Reiner et al., 2002 (Halford and Jackson, 2020)
- Assessing hydraulic connections across a complex sequence of volcanic rocks—analysis of U-20 WW MWAT (Garcia et al., 2011)
- Infiltration studies (Fenelon et al., 2016; Middleton et al., 2019; Hershey et al., 2020; Halford and Jackson, 2020)
- Interpretation of mineral diagenesis for assessment of RN transport (Carle, 2020)
- PM Area 20 subregion flow and transport model (Lu et al., 2021)
- Groundwater flow and ^{3}H transport simulations from the HANDLEY test (Jackson, 2021)
- Review of R_c and chimney height information (Carle et al., 2021)

A.2.0 Bibliography of Well-Specific Phase II Investigations

ER-20-4

Navarro-Intera, LLC. 2011. Written communication. Subject: *Pahute Mesa ER-20-4 Well Data Report,* Rev. 0. Las Vegas, NV.

U.S. Department of Energy, National Nuclear Security Administration Nevada Site Office. 2011. *Completion Report for Well ER-20-4, Corrective Action Units 101 and 102: Central and Western Pahute Mesa*, DOE/NV--1447. Prepared by National Security Technologies, LLC. Las Vegas, NV.

Navarro-Intera, LLC. 2012. Written communication. Subject: *Pahute Mesa Phase II ER-20-4 Well Development, Testing, and Sampling Data Report,* Rev. 0. Las Vegas, NV.

Navarro-Intera, LLC. 2012. *Pahute Mesa Well Development and Testing Analyses for Wells ER-20-8 and ER-20-4, Nevada National Security Site, Nye County, Nevada,* Rev. 0, N-I/28091--061. Las Vegas, NV.

ER-20-7

Navarro-Intera, LLC. 2010. Written communication. Subject: *Pahute Mesa ER-20-7 Well Data Report,* Rev. 0. Las Vegas, NV.

U.S. Department of Energy, National Nuclear Security Administration Nevada Site Office. 2010. *Completion Report for Well ER-20-7, Corrective Action Units 101 and 102: Central and Western Pahute Mesa*, DOE/NV--1386. Prepared by National Security Technologies, LLC. Las Vegas, NV.

Navarro-Intera, LLC. 2011. Written communication. Subject: *Pahute Mesa Phase II ER-20-7 Well Development, Testing, and Sampling Data Report,* Rev. 0. Las Vegas, NV.

Navarro-Intera, LLC. 2011. *Pahute Mesa Well Development and Testing Analyses for Wells ER-20-7, ER-20-8 #2, and ER-EC-11,* Rev. 1, N-I/28091-037. Las Vegas, NV.

ER-20-8

Navarro-Intera, LLC. 2010b. Written communication. Subject: *Pahute Mesa ER-20-8 Well Data Report,* Rev. 0. Las Vegas, NV.

U.S. Department of Energy, National Nuclear Security Administration Nevada Site Office. 2011. *Completion Report for Wells ER-20-8 and ER-20-8#2, Corrective Action Units 101 and 102: Central and Western Pahute Mesa,* DOE/NV--1440. Prepared by National Security Technologies, LLC. Las Vegas, NV.

Navarro-Intera, LLC. 2012b. Written communication. Subject: *Pahute Mesa Phase II ER-20-8 Well Development, Testing, and Sampling Data Report,* Rev. 0. Las Vegas, NV.

Navarro-Intera, LLC. 2012. *Pahute Mesa Well Development and Testing Analyses for Wells ER-20-8 and ER-20-4, Nevada National Security Site, Nye County, Nevada,* Rev. 0, N-I/28091--061. Las Vegas, NV.

ER-20-8#2

Navarro-Intera, LLC. 2010. Written communication. Subject: *Pahute Mesa ER-20-8#2 Well Data Report,* Rev. 0. Las Vegas, NV.

U.S. Department of Energy, National Nuclear Security Administration Nevada Site Office. 2011. *Completion Report for Wells ER-20-8 and ER-20-8#2, Corrective Action Units 101 and 102: Central and Western Pahute Mesa,* DOE/NV--1440. Prepared by National Security Technologies, LLC. Las Vegas, NV.

Navarro-Intera, LLC. 2010. Written communication. Subject: *Pahute Mesa Phase II ER-20-8#2 Well Development, Testing, and Sampling Data Report,* Rev. 0. Las Vegas, NV.

Navarro-Intera, LLC. 2011. *Pahute Mesa Well Development and Testing Analyses for Wells ER-20-7, ER-20-8#2, and ER-EC-11,* Rev. 1, N-I/28091-037. Las Vegas, NV.

ER-20-11

Navarro-Intera, LLC. 2013. Written communication. Subject: *Pahute Mesa ER-20-11 Well Data Package,* Rev. 0. Las Vegas, NV.

U.S. Department of Energy, National Nuclear Security Administration, Nevada Site Office. 2013. *Completion Report for Well ER-20-11 Corrective Action Units 101 and 102: Central and Western Pahute Mesa*, DOE/NV--1498. Las Vegas, NV.

Navarro-Intera, LLC. 2014. Written communication. Subject: *Pahute Mesa Phase II Well ER-20-11 Well Development, Testing, and Sampling Data Report,* Rev. 0. Las Vegas, NV.

Navarro. 2016. *Pahute Mesa Well Development and Testing Analyses for Well ER-20-11, Nevada National Security Site, Nye County, Nevada,* Rev. 0, N/0002653--028. Las Vegas, NV.

ER-20-12

Navarro. 2016. Written communication. Subject: *Pahute Mesa ER-20-12 Well Data Package,* Rev. 0. Las Vegas, NV.

U.S. Department of Energy, National Nuclear Security Administration Nevada Field Office. 2016. *Completion Report for Well ER-20-12, Corrective Action Units 101 and 102: Central and Western Pahute Mesa*, DOE/NV--1549. Las Vegas, NV.

Navarro. 2018. *Pahute Mesa Phase II Well ER-20-12 Well Development, Testing, and Sampling Data and Analysis Report*. Rev. 0, N/0002653--046. Las Vegas, NV.

ER-EC-11

Navarro-Intera, LLC. 2010. Written communication. Subject: *Pahute Mesa ER-EC-11 Well Data Report,* Rev. 0. Las Vegas, NV.

U.S. Department of Energy, National Nuclear Security Administration Nevada Field Office. 2013. *Completion Report for Well ER-20-11, Corrective Action Units 101 and 102: Central and Western Pahute Mesa,* DOE/NV--1498. Prepared by National Security Technologies, LLC. Las Vegas, NV.

Navarro-Intera, LLC. 2010. Written communication. Subject: *Pahute Mesa Phase II ER-EC-11 Well Development, Testing, and Sampling Data Report,* Rev. 0. Las Vegas, NV.

Navarro-Intera, LLC. 2011. *Pahute Mesa Well Development and Testing Analyses for Wells ER-20-7, ER-20-8 #2, and ER-EC-11,* Rev. 1, N-I/28091-037. Las Vegas, NV.

ER-EC-12

Navarro-Intera, LLC. 2011. Written communication. Subject: *Pahute Mesa ER-EC-12 Well Data Report,* Rev. 0. Las Vegas, NV.

U.S. Department of Energy, National Nuclear Security Administration Nevada Field Office. 2011. *Completion Report for Well ER-20-12, Corrective Action Units 101 and 102: Central and Western Pahute Mesa,* DOE/NV--1446. Prepared by National Security Technologies, LLC. Las Vegas, NV.

Navarro-Intera, LLC. 2012. Written communication. Subject: *Pahute Mesa Phase II Well ER-EC-12 Well Development, Testing, and Sampling Data Report,* Rev. 0. Las Vegas, NV.

Navarro 2018. *Pahute Mesa Well Development and Testing Analyses for Wells ER-EC-12 and ER-EC-13, Nevada National Security Site, Nye County, Nevada*. Rev 0. N/0002653--051. Las Vegas, NV.

ER-EC-13

Navarro-Intera, LLC. 2011. Written communication. Subject: *Pahute Mesa ER-EC-13 Well Data Report,* Rev. 0. Las Vegas, NV.

U.S. Department of Energy, National Nuclear Security Administration Nevada Site Office. 2011. *Completion Report for Well ER-EC-13, Corrective Action Units 101 and 102: Central and Western Pahute Mesa*, DOE/NV--1448. Prepared by National Security Technologies, LLC. Las Vegas, NV.

Navarro-Intera, LLC. 2013. Written communication. Subject: *Pahute Mesa Phase II Well ER-EC-13 Well Development, Testing, and Sampling Data Report,* Rev. 0. Las Vegas, NV.

Navarro 2018. *Pahute Mesa Well Development and Testing Analyses for Wells ER-EC-12 and ER-EC-13, Nevada National Security Site, Nye County, Nevada*, Rev 0. N/0002653--051. Las Vegas, NV.

ER-EC-14

Navarro-Intera, LLC. 2013. Written communication. Subject: *Pahute Mesa ER-EC-14 Well Data Package,* Rev. 0. Las Vegas, NV.

U.S. Department of Energy, National Nuclear Security Administration Nevada Field Office. 2013. *Completion Report for Well ER-EC-14, Corrective Action Units 101 and 102: Central and Western Pahute Mesa*, DOE/NV--1499. Prepared by National Security Technologies, LLC. Las Vegas, NV.

Navarro-Intera, LLC. 2015. Written communication. Subject: *Pahute Mesa Phase II Well ER-EC-14 Well Development, Testing, and Sampling Data Report,* Rev. 0. Las Vegas, NV.

Navarro. 2015. *Pahute Mesa Well Development and Testing Analyses for Wells ER-EC-14 and ER-EC-15, Nevada National Security Site, Nye County, Nevada*, Rev. 0, N/0002653--006. Las Vegas, NV.

ER-EC-15

Navarro-Intera, LLC. 2011. Written communication. Subject: *Pahute Mesa ER-EC-15 Well Data Report,* Rev. 0. Las Vegas, NV.

U.S. Department of Energy, National Nuclear Security Administration Nevada Site Office. 2011. *Completion Report for the Well ER-EC-15, Corrective Action Units 101 and 102: Central and Western Pahute Mesa*, DOE/NV--1449. Prepared by National Security Technologies, LLC. Las Vegas, NV.

Navarro-Intera, LLC. 2014. Written communication. Subject: *Pahute Mesa Phase II Well ER-EC-15 Well Development, Testing, and Sampling Data Report*, Rev. 0. Las Vegas, NV.

Navarro. 2015. *Pahute Mesa Well Development and Testing Analyses for Wells ER-EC-14 and ER-EC-15, Nevada National Security Site, Nye County, Nevada*, Rev. 0, N/0002653--006. Las Vegas, NV.

A.3.0 References Cited in Section A.1.0

Carle, S.F. 2020. *Interpretation of Mineralogical Diagenesis for Assessment of Radionuclide Transport at Pahute Mesa, Nevada National Security Site*, LLNL-TR-810225. Livermore, CA: Lawrence Livermore National Laboratory.

Carle, S.F., A.F.B. Tompson, and M. Zavarin. 2020. *Radionuclide Screening Analysis and Transport Parameters for Pahute Mesa Detonations, Nevada National Security Site*, LLNL-TR-812351, Livermore, CA: Lawrence Livermore National Laboratory.

DOE/EMNV, see U.S. Department of Energy, Environmental Management Nevada Program

Fenelon, J.M., K.J. Halford, and M.T. Moreo. 2016. *Delineation of the Pahute Mesa–Oasis Valley Groundwater Basin, Nevada*, Version 1.1, Scientific Investigations Report 2015-5175. Carson City, NV: U.S. Geological Survey.

Frus, R.J., and K.J. Halford. 2018. *Documentation of Single-Well Aquifer Tests and Integrated Borehole Analyses, Pahute Mesa and Vicinity, Nevada,* Scientific Investigations Report 2018-5096. Reston, VA: U.S. Geological Survey.

Garcia, C.A., J.M. Fenelon, K.J. Halford, S.R. Reiner, and R.J. Laczniak. 2011. *Assessing Hydraulic Connections Across a Complex Sequence of Volcanic Rocks-Analysis of U-20 WW Multiple-Well Aquifer Test, Pahute Mesa, Nevada National Security Site, Nevada*, Scientific Investigations Report 2011-5173. 24 pp. Reston, VA: U.S. Geological Survey.

Garcia, C.A., T.R. Jackson, K.J. Halford, D.S. Sweetkind, N.A. Damar, J.M. Fenelon, and S.R. Reiner. 2017. *Hydraulic Characterization of Volcanic Rocks in Pahute Mesa Using an Integrated Analysis of 16 Multiple-Well Aquifer Tests, Nevada National Security Site, 2009–14,* Scientific Investigations Report 2016-5151. Carson City, NV: U.S. Geological Survey.

HGL, see HydroGeoLogic, Inc.

Halford, K.J., and T.R. Jackson. 2020. *Groundwater Characterization and Effects of Pumping in the Death Valley Regional Groundwater Flow System, Nevada and California, with Special Reference to Devils Hole,* Professional Paper 1863. Reston, VA: U.S. Geological Survey.

Hershey, R.L., R. Parashar, C.A. Cooper, K.M. Heintz, H.V. Pham, and B.F. Lyles. 2020. *Evaluation of Timber Mountain Recharge and Groundwater Flow in Relation to Pahute Mesa-Oasis Valley Flow System,* DOE/NV/0003590-56; Publication No. 45294. Las Vegas, NV: Desert Research Institute.

HydroGeoLogic, Inc. 2017. Written communication to K. Rehfeldt (Navarro). Subject: "Technical Memorandum: Task Order 3: Fracture Analysis," Technical Data Repository No. UGTA-4-1808, 29 September. Reston, VA.

HydroGeoLogic, Inc. 2018. Written communication to K. Rehfeldt (Navarro). Subject: "Technical Memorandum: Task Order 5: Transport Parameters (Dispersivity and Matrix Diffusion)," Technical Data Repository No. UGTA-4-2099, 22 August. Reston, VA.

Jackson, T.R. 2021. *Permeable Groundwater Pathways and Tritium Migration Patterns from the HANDLEY Underground Nuclear Test, Pahute Mesa, Nevada*, Scientific Investigations Report 2021-5032. Reston, VA: U.S. Geological Survey.

Jackson, T.R., J.M. Fenelon, and R. Paylor. 2021. *Groundwater Flow Conceptualization of the Pahute Mesa-Oasis Valley Groundwater Basin, Nevada: A Synthesis of Geologic, Hydrologic, Hydraulic-Property, and Tritium Data,* Scientific Investigations Report 2020-5134. Carson City, NV: U.S. Geological Survey.

Lu, Z., E. Kwicklis, T. Miller and M. Bourret. 2021. *Development and Calibration of the Pahute Mesa Bench Area Groundwater Flow and Tritium Transport Model*, Nevada National Security *Site*, LA-UR-21-23595. Los Alamos, NM: Los Alamos National Laboratory.

Makedonska, N., E.M. Kwicklis, J.D. Hyman, and S.M. Bourret. 2020. *Discrete Fracture Network Modeling to Estimate Upscaled Parameters for the Topopah Spring, Lava Flow, and Tiva Canyon Aquifers at Pahute Mesa, Nevada National Security Site*, LA-UR-20-22665. Los Alamos, NM: Los Alamos National Laboratory.

Middleton, R.S., E.M. Kwicklis, K.H. Birdsell, D.G. Levitt, and J. Hevesi. 2019. *Net Infiltration Models for the Pahute Mesa Area,* LA-UR-16-27513, Rev 1. Los Alamos, NM: Los Alamos National Laboratory.

NNSA/NSO, see U.S. Department of Energy, National Nuclear Security Administration Nevada Site Office.

Navarro. 2020. *Phase II Geochemical and Isotopic Evaluation of Groundwater Flow in the Pahute Mesa–Oasis Valley Flow System, Nevada*, Rev. 1, N/0002653--069. Las Vegas, NV.

Navarro. 2021a. *Contaminant Transport Parameters for the Groundwater Flow and Contaminant Transport Model of Corrective Action Units 101 and 102: Central and Western Pahute Mesa, Nye County, Nevada,* Rev. 1; N/0002653--077. Las Vegas, NV.

Navarro. 2021b. *Hydrologic Data for the Groundwater Flow and Contaminant Transport Model of Corrective Action Units 101 and 102: Central and Western Pahute Mesa, Nye County, Nevada,* Rev. 1, N/0002653--073. Las Vegas, NV.

Navarro. 2021c. *Unclassified Source Term and Radionuclide Data for the Groundwater Flow and Contaminant Transport Model for Corrective Action Units 101 and 102: Central and Western Pahute Mesa, Nye County, Nevada*, Rev 1, N/0002653--088. Las Vegas, NV.

Parashar, R., H.V. Pham, and N.L. Sund. 2019. *Development of Upscaling Techniques and Construction of Calibrated Models for Fractured Rocks Using Discrete Fracture Network Approaches*, DOE/NV/0003590-43; Publication No. 45289. Las Vegas, NV: Desert Research Institute.

Reeves, D.M., K.D. Smith, R. Parashar, C. Collins, and K.M. Heintz. 2017. *Investigating the Influence of Regional Stress on Fault and Fracture Permeability at Pahute Mesa, Nevada National Security Site*, DOE/NV/0000939-41; Publication No. 45275. Las Vegas, NV: Desert Research Institute.

Reimus, P.W. 2018. *Evaluation of the Need to Consider Colloid-Facilitated Plutonium Transport in Contaminant Boundary Calculations for Pahute Mesa at the Nevada National Security Site*, LA-UR-18-29291. Los Alamos, NM: Los Alamos National Laboratory.

Reimus, P.W., and H. Boukhalfa. 2014. *Chancellor Water Colloids: Characterization and Radionuclide Associated Transport*, LA-UR-14-27538. N. Wasserman, B. Erdmann, A.I. Abdel-Fattah, S.D. Ware, P. He, S. Tarimala, and B. Martinez, contributors. Los Alamos, NM: Los Alamos National Laboratory.

Telfeyan, K., S.D. Ware, P.W. Reimus, and K.H. Birdsell. 2018. "Comparison of Experimental Methods for Estimating Matrix Diffusion Coefficients for Contaminant Transport Modeling." In *Journal of Contaminant Hydrology*, Vol. 209: pp. 51-60.

Tompson, A., M. Zavarin, and D. Shumaker. 2019. *Yield-Weighting Approaches for Calculating Radiologic Inventories for Individual Underground Nuclear Tests at the Nevada National Security Site*, LLNL-TR-773562. Livermore, CA: Lawrence Livermore National Laboratory.

U.S. Department of Energy, Environmental Management Nevada Program. 2020. *Pahute Mesa-Oasis Valley Hydrostratigraphic Framework Model for Corrective Action Units 101 and 102: Central and Western Pahute Mesa, Nye County, Nevada*, Rev. 0, DOE/EMNV--0014. Las Vegas, NV.

U.S. Department of Energy, National Nuclear Security Administration Nevada Site Office. 2009. *Phase II Corrective Action Investigation Plan for Corrective Action Units 101 and 102, Central and Western Pahute Mesa, Nevada Test Site, Nye County, Nevada*, Rev. 2, DOE/NV--1312. Las Vegas, NV.

Zavarin, M., S.K. Roberts, M.R. Johnson, Q. Hu, B.A. Powell, P. Zhao, A.B. Kersting, R.E. Lindvall, and R.J. Pletcher. 2013. *Colloid-Facilitated Radionuclide Transport in Fractured Carbonate Rock from Yucca Flat, Nevada National Security Site*, LLNL-TR-619352. Livermore, CA: Lawrence Livermore National Laboratory.

Zavarin, M., P. Zhao, C. Joseph, J. Begg, M. Boggs, Z. Dai, and A.B. Kersting. 2015. *Hydrothermal Alteration of Glass from Underground Nuclear Tests: Formation and Transport of Pu-Clay Colloids at the Nevada National Security Site*, LLNL-TR-671402. Livermore, CA: Lawrence Livermore National Laboratory.

Zavarin, M., P. Zhao, C. Joseph, J.D. Begg, M.A. Boggs, Z. Dai, and A.B. Kersting. 2019. "Hydrothermal Alteration of Nuclear Melt Glass, Colloid Formation, and Plutonium Mobilization at the Nevada National Security Site, U.S.A." In *Environmental Science & Technology*, Vol. 53(13): pp. 7363–7370.

Zhou, Q., H.-H. Liu, F.J. Molz, Y. Zhang, and G.S. Bodvarsson. 2005. "Field-Scale Effective Matrix Diffusion Coefficient for Fractured Rock: Results From Literature Survey." In *Journal of Contaminated Hydrology*, Vol. 93(1–4).

Appendix B

QAP Implementation

B.1.0 Implementation of QAP Requirements in the PM CAU Flow and Transport Model

The UGTA QAP was revised in June 2015 (NNSA/NFO, 2015) and includes a subsequent ROTC (DOE/EMNV, 2018).

The PM CAU flow and transport model is meant to be compliant with the QAP and associated FFACO requirements (FFACO, 1996 as amended). This appendix summarizes how the QAP modeling and software requirements and the data management requirements have been addressed in the activities supporting the development of the PM CAU flow and transport model. To ease the presentation and to provide a uniform means of comparing how the requirements have been addressed, the material in this appendix is presented in a tabular format referenced to sections in the QAP (NNSA/NFO, 2015).

As indicated in Tables B-1 and B-2, all QAP requirements have been met either in this document or in products and activities supporting this product.

Table B-1
Implementation of QAP Modeling and Software Requirements in the PM CAU Flow and Transport Model
(Page 1 of 12)

QAP Requirement	How the QAP Requirement Is Addressed for the PM CAU	Where QAP Requirement Is Addressed
QAP (2015) Section 1.5 Quality Objectives and Criteria		
The QA requirements associated with sampling parameter distributions, multiple realizations of the models, model evaluations, PERs, and peer reviews establish the confidence needed in the model results.	The requirements are discussed in the data documents and in this report	Navarro 2021a, b, c and other participant reports
The FFACO (1996, Appendix VI, Section 3.2.1) also requires CAU models to consider the following, at a minimum: • Alternative HFMs, recharge models, boundary conditions, and groundwater flows • Uncertainty in the RST and HST • Multiple permissive sets of calibrated flow models • Probabilistic simulations of transport from calibrated flow models • Ensembles of forecasts of contaminant boundaries for the CAU • Sensitivity and uncertainty analyses of the model outputs	Model simulations were designed and conducted to address these FFACO model needs. Alternative recharge and fault conceptualization models were evaluated. Impact of source uncertainty was evaluated via a sensitivity calculation with a higher Pu source concentration and in the screening report (Carle et al., 2020). The alternative flow models were calibrated, but the alternative transport models were not because the transport forecasts used full ranges of values and were not impacted by the transport calibration. Model output sensitivity to alternative models, source concentration, and dispersion were evaluated.	Sections 4.0 and 5.0. Carle et al. (2020)
QAP (2015) Section 1.9 Computer Software and Codes		
Organizations must develop and implement procedures and/or forms for the development (if necessary), revision, verification, and control of computer software codes.	The software and codes used in the calculation of contaminant transport from the contaminant sources in the PM CAU have been verified and controlled using project participants' procedures. These softwares include MODFLOW6, PLUMECALC, LaGriT, MF6-Walkabout preprocessor, and Walkabout.	Records packages developed and maintained by each participant document the participant procedures related to development, modification, verification, and control of computer software.
Acquisition of commercial off-the-shelf (COTS) software must be controlled through the procurement process. Commercial software should be evaluated for proper installation.	Off-the-shelf software (e.g., Microsoft Excel, TecPlot, MODFLOW6, and other data processing software) were acquired through the software acquisition process at each UGTA participant organization.	Records packages developed and maintained by each participant document the participant procedures related to COTS software acquisition.

Table B-1
Implementation of QAP Modeling and Software Requirements in the PM CAU Flow and Transport Model
(Page 2 of 12)

QAP Requirement	How the QAP Requirement Is Addressed for the PM CAU	Where QAP Requirement Is Addressed
QAP (2015) Section 1.9 Computer Software and Codes (continued)		
The code developer is responsible for "internally developed" code requirements. If a participant receives software from another participant (noncommercial entity), the "acquired" requirements must be followed.	The MODFLOW6/Walkabout preprocessor development followed project procedures. Walkabout, LaGriT and PlumeCalc were previously obtained from and verified by LANL.	Records packages developed and maintained by each participant document the participant procedures related to codes developed.
QAP (2015) Section 1.9.1 Selection		
Participants must identify the required and desirable attributes of a code in procurement, installation, or technical review documents.	The required attributes of codes were identified in the corrective action planning process, including the CAIP.	CAIP (DOE/NV, 2009) and CAIP update (DOE/EMNV, 2020b). See also Appendix E of this document.
Participants must evaluate codes based on the identified attributes.	Code evaluation of Walkabout and LaGriT conducted by Navarro-Intera, LLC (N-I) using N-I software installation and checkout procedure.	Records packages developed and maintained by each participant. The code evaluation was conducted during Yucca Flat investigations and deemed sufficient for PM needs.
Participants must document the code and selection criteria for groundwater flow and transport models in the CAIP.	Codes selected for groundwater flow and RN transport were identified in the CAIP Update. Codes selected included MODFLOW6 (a commercial off-the-shelf code) and codes Walkabout and PlumeCalc from LANL.	CAIP (DOE/NV, 2009) and CAIP update (DOE/EMNV, 2020b). Code selection is discussed in Appendix E of this document.
If no available code performs to the required attributes, the participant may develop the needed code after consultation with the UGTA Activity Lead.	A preprocessor code was created to allow MODFLOW6 output to be used with Walkabout. An additional code, LaGriT, was required as a step in this process. This code was acquired from LANL and was evaluated by N-I using N-I software installation and checkout procedures.	The development and testing of the preprocessor is documented in data packages and summarized in Appendix E of this document.
If a code change is required after publication of the CAIP, justification for the change and identification of the potential codes must be submitted to the Activity Lead for approval.	Changes to the software chosen were presented to the federal Activity Lead as part of annual task planning and during annual data completeness presentations to DOE and NDEP.	Records packages developed and maintained by each participant. The change in codes from the CAIP (DOE/NV, 2009) are presented in the CAIP update (DOE/EMNV, 2020b).

Table B-1
Implementation of QAP Modeling and Software Requirements in the PM CAU Flow and Transport Model
(Page 3 of 12)

QAP Requirement	How the QAP Requirement Is Addressed for the PM CAU	Where QAP Requirement Is Addressed
QAP (2015) Section 1.9.1 Selection (continued)		
Justification must incorporate, at the minimum, a justification for the change, code attributes, testing results against the above criteria, and a comparison between available codes.	The justification for the proposed change from FEHM_sptr to MODFLOW6-Walkabout for particle tracking was to facilitate migration to a fully supported COTS flow model while maintaining access to PLUMECALC as the preferred transport model code.	Justification is provided in Appendix E of this document.
Upon approval, either a CAIP addendum or ROTC must be submitted to NDEP for approval.	New data and analyses led to the update to the CAIP for PM to incorporate the new information gained from the Phase II data collection and analysis activities.	CAIP (NNSA/NSO, 2009) and CAIP update (DOE/EMNV, 2020b)
Participants must document other code selection within a records package or with the procurement documentation.	Other codes have been documented in participant data packages.	Records packages developed and maintained by each participant.
QAP (2015) Section 1.9.2 Development		
Participants developing code or software must ensure that code purpose, requirements, and Activity Lead consultation are documented before development.	One preprocessor code development was necessary to use MODFLOW6 output with Walkabout. MODFLOW6 is COTS software. Walkabout was developed by LANL following LANL procedures.	Records packages developed and maintained by each participant. The development of the MF6-Walkabout processor is documented in a data package. A summary of the preprocessor is provided in Appendix E.
Developed software must be uniquely identified, and documentation must include the following, at a minimum: • Input and output requirements (including the range of acceptable inputs) • Functional requirements including the operating system(s) • Assumptions • Identification of any limitations on applications • Compiler and its version • Instructions adequate for installation and execution of the software • Description and equations, algorithms, and numerical solution techniques, as applicable	Input and output requirements were defined. Software was designed to work with project computers, compilers, and operating systems. Instructions for use and verification tests were provided. A description of equations, algorithms, and solution techniques were provided. Walkabout and LaGriT were developed by LANL following LANL procedures.	Records packages developed and maintained by each participant. Additional documentation of Walkabout in Painter (2011). Summary of the preprocessor development is provided in Appendix E of this report.

Table B-1
Implementation of QAP Modeling and Software Requirements in the PM CAU Flow and Transport Model
(Page 4 of 12)

QAP Requirement	How the QAP Requirement Is Addressed for the PM CAU	Where QAP Requirement Is Addressed
QAP (2015) Section 1.9.2 Development (continued)		
The developer shall develop a test case for software intended for multiple users.	The code development was intended for the single PM CAU model user. Walkabout and LaGriT were developed and tested by LANL following LANL procedures. Additional testing was performed by N-I for the YF/CM CAU as documented in the YF/CM model report (N-I, 2013). The code to allow MODFLOW 6 output to be used by Walkabout was tested by Navarro.	Records packages developed and maintained by each participant. See Appendix E for the documentation of the testing of the MODFLOW6 to Walkabout code.
The test case must be provided for installation testing (see Section 1.9.4 of this table) to ensure the software is functioning as intended and results are consistent with those observed by the code developer.	A test case was provided to verify proper functioning of the code. Walkabout and LaGriT were developed by LANL following LANL procedures and installation testing was performed as documented in YF/CM Model report (N-I, 2013). The code to allow MODFLOW 6 output to be used by Walkabout was tested by Navarro.	Records packages developed and maintained by each participant. See Appendix E for the documentation of the testing of the MODFLOW6 to Walkabout code.
The test case must exercise key features of the code used for UGTA models. The test case must be provided to the users and must include acceptance criteria for the results.	A test case was provided to verify proper functioning of the code. Walkabout and LaGriT were developed by LANL following LANL procedures and installation testing performed as documented in the YF/CM model report (N-I, 2013). The code to allow MODFLOW 6 output to be used by Walkabout was tested by Navarro.	Records packages developed and maintained by each participant. See Appendix E for the documentation of the testing of the MODFLOW6 to Walkabout code.
Test case documentation must include any necessary instructions and input data to execute (clearly identifying the specific application[s] tested).	A test case was provided to verify proper functioning of the code. Walkabout was developed by LANL following LANL procedures and installation testing performed. The testing of the code to allow MODFLOW 6 output to be used by Walkabout was documented.	Records packages developed and maintained by each participant. Summaries of the testing results and references to documentation are included in Appendix E.

Table B-1
Implementation of QAP Modeling and Software Requirements in the PM CAU Flow and Transport Model
(Page 5 of 12)

QAP Requirement	How the QAP Requirement Is Addressed for the PM CAU	Where QAP Requirement Is Addressed
QAP (2015) Section 1.9.3 Verification		
Once code development is complete, the code developer or designee must verify and document that the code performs the intended functions correctly and that the documentation identified in Section 1.9.2 of this table is complete.	Verification testing performed by developer and CAU modeler.	Records packages developed and maintained by each participant. Summary of verification provided in Appendix E.
The verification required will depend on the complexity, risk, and uniqueness of the code.	Verification testing performed on Walkabout and LaGriT was commensurate with complexity, risk, and uniqueness of the code.	Records packages developed and maintained by each participant.
Code modifications must be verified in accordance with the same requirements as the original code. Verification of changes may be limited to the scope of the modification if the rest of the code is not affected. Verifiers may use ASTM International (ASTM) D6025, Section 7.6: "Code Testing Evaluation Criteria" (ASTM, 2008), for determining appropriate measures for the evaluation.	Code modifications to Walkabout verified by LANL. No modifications were required to the MF6-Walkabout preprocessor once the final version was implemented.	Records packages developed and maintained by each participant.
Verification documentation must describe the testing and results.	Verification testing results are documented.	Records packages developed and maintained by each participant. Additional documentation is provided in Appendix E.
QAP (2015) Section 1.9.4 Installation Testing		
Upon installation of software or code on a computer, operational checks (i.e., test cases provided by code developer) must be performed to verify that the software is functioning as intended.	Installation testing performed by Navarro.	Records packages developed and maintained by each participant.
Installation testing results must agree within the test-specified acceptance criteria before code application proceeds.	Installation testing results compared to acceptance criteria.	Records packages developed and maintained by each participant.
Installation testing must be conducted when operation and hardware system configurations change.	Installation testing conducted when changes are made in operating and hardware system.	Records packages developed and maintained by each participant.

Table B-1
Implementation of QAP Modeling and Software Requirements in the PM CAU Flow and Transport Model
(Page 6 of 12)

QAP Requirement	How the QAP Requirement Is Addressed for the PM CAU	Where QAP Requirement Is Addressed
QAP (2015) Section 1.9.5 Code Review		
Code reviews must be performed and documented to ensure that codes and code applications are technically adequate and properly documented, and satisfy established technical and quality requirements.	Code reviews occur during the development and testing of the codes and are conducted by each participant responsible for code development.	Records packages are developed and maintained by each participant.
Reviewers must possess the appropriate technical expertise and must not have participated in the development or installation testing of the code.	Independent reviewers are responsible for code reviews.	Records packages indicating the independent reviewers are developed and maintained by each participant.
The reviewer(s) must address the following elements, as applicable: • Is the code appropriate for its intended application? Is it properly applied? • Are the assumptions reasonable and valid? • Are the mathematical model and mathematical operations correct? • Do the methods conform to accepted and published concepts? • Are results consistent with known data using either visual or quantitative measures? • Is documentation sufficient to reproduce development or testing, as applicable? • Is verification adequate to ensure confidence in the software/code?	These criteria are embodied in procedures of the participants responsible for code development. Code development may be single-use routines and codes intended for multiple applications.	Records package with review criteria, and review comments and comment resolutions are maintained as records by each participant.
QAP (2015) Section 1.9.6 Configuration Control		
Participants must maintain an inventory of computer software and codes. A system for identifying, revising, and controlling hardware/software configurations must be developed and implemented in accordance with DOE Order 200.1A, *Information Technology Management* (DOE, 2008).	Software configuration control is maintained by each participant developing and using software.	Records packages containing configuration control hardware and software are maintained by each participant.
The configuration of software must be controlled and documented so traceability is maintained until software retirement.	Software configuration control is maintained by each participant developing and using software.	Records packages containing software configuration are maintained by each participant.

Table B-1
Implementation of QAP Modeling and Software Requirements in the PM CAU Flow and Transport Model
(Page 7 of 12)

QAP Requirement	How the QAP Requirement Is Addressed for the PM CAU	Where QAP Requirement Is Addressed
QAP (2015) Section 1.9.6 Configuration Control (continued)		
The participant responsible for code development and/or configuration control must perform maintenance, verification, and instruction manual updates as necessary	Code maintenance, verification, and manual updates are controlled by each participant.	Records packages containing maintenance, verification, and instruction manuals are maintained by each participant.
Participants must obtain documentation for commercially available or acquired software.	Code documentation is controlled by each participant.	Records packages containing documentation for commercial or acquired software are maintained by each participant.
This documentation should contain reference material, operational test records, and user-oriented information, as available, and must be maintained as records.	Code reference materials are controlled by each participant.	Records packages containing reference materials are maintained by each participant.
Configuration items include, but are not limited to, the following: • Operating system components • Software executables • Source code files, if available • Users documentation, including software requirements and designs	Software configuration items are controlled by each participant.	Records packages containing software configuration items are maintained by each participant.
QAP (2015) Section 2.6 Groundwater Flow and Transport Modeling		
Construction of numerical flow and transport models is based on the conceptual model.	The elements of the conceptual model incorporated in the PM CAU model and described in this report.	This document contains the documentation of the flow and transport modeling. Additional records packages are maintained by each participant.
QAP (2015) Section 2.6.1 Model Parameters		
The documentation of processing, calculating, characterizing, or applying data shall be included in the documents described in the following subsections.	Sections 4.0 and 5.0.	N/A
QAP (2015) Section 2.6.1 Hydrostratigraphic Framework Model		
CAU-specific documents describe how the HFM and alternatives were developed, describe the models, and document the data sources.	Addressed in the HFM document.	DOE/EMNV, 2020a

Table B-1
Implementation of QAP Modeling and Software Requirements in the PM CAU Flow and Transport Model
(Page 8 of 12)

QAP Requirement	How the QAP Requirement Is Addressed for the PM CAU	Where QAP Requirement Is Addressed
QAP (2015) Section 2.6.1 Hydrologic Data		
A CAU-specific HDD presents hydrologic data and the supporting information used to develop the groundwater flow and transport model; data quality assessments; data analyses to derive expected values or probability distributions; and hydrologic-parameter uncertainty estimates.	Addressed in the PM HDD.	Navarro, 2021b
QAP (2015) Section 2.6.1 Transport Parameters		
A CAU-specific transport parameter document describes transport parameters and the supporting information used to develop the groundwater flow and transport model; data quality assessments; data analyses to derive expected values or probability distributions; and transport-parameter uncertainty estimates.	Addressed in the PM TDD.	Navarro, 2021a
QAP (2015) Section 2.6.1 Source Term Data		
A source term document is prepared for each CAU that describes development of simplified models or the conceptual models used for implementing source terms for the flow and transport models.	Addressed in HST documents and unclassified HST report.	Carle et al., 2020 and 2021; Tompson et al., 2019; Navarro, 2021c
QAP (2015) Section 2.6.2 Model Calibration		
The calibration process is documented in the groundwater flow and transport model document in the CAI stage, and or subsequent modeling report developed during the CADD/CAP or CR stage.	Flow model calibration for the PM CAU model steady-state and transient water level data. Total basin discharge, measured transmissivity, observed groundwater flow direction also influenced the calibration. The PM CAU transport model was calibrated to ^{3}H observations in wells.	Sections 4.0 and 5.0

Table B-1
Implementation of QAP Modeling and Software Requirements in the PM CAU Flow and Transport Model
(Page 9 of 12)

QAP Requirement	How the QAP Requirement Is Addressed for the PM CAU	Where QAP Requirement Is Addressed
QAP (2015) Section 2.6.2 Model Calibration (continued)		
Documentation shall include the following: • Specific approaches used for model calibration • Rationale for selecting particular model calibration approaches • Calibration results • Comparison of initial versus final unit properties (e.g., porosity, permeability) • How the final properties relate to the conceptual model	Approaches and results of model calibration for PM CAU flow and transport model are documented in the this report.	Sections 4.0 and 5.0
In addition, the model developer shall document why the model is a reasonable approximation of the in situ conditions.	Documentation of reasonableness of models includes comparison to alternative lines of evidence, multiple different measurements and alignment with the conceptual model (Jackson et al., 2021). Uncertainty in calibration is addressed using selected alternative calibrations and sensitivity calculations.	Sections 4.0 and 5.0
B.5.4 Sensitivity Analysis		
Sensitivity analysis will consider the purpose of the analysis and focus on the hypothesis to be tested.	Sensitivity analyses have been performed to identify the impact of key parameters on radionuclide migration forecasts. Alternative flow models have been developed to investigate a reasonable range of calibrated models. Range of alternative contaminant boundary forecasts are developed to evaluate model uncertainty.	Sections 3.0 through 6.0
The sensitivity analysis approach selected by the modeler shall be described and justified with respect to the model purpose in the flow and transport model document (or subsequent modeling documents).	The sensitivity analysis approach is described and justified.	Sections 3.0 through 6.0
B.5.5 Uncertainty Analysis		
The method applicability to the uncertainty type shall be described and justified by the modeler with respect to the model purpose.	Uncertainty analyses have been performed to evaluate the effect of uncertainty in recharge, fault properties, and transport parameters. The impact of selected source term assumptions was evaluated.	Sections 3.0 through 6.0

Table B-1
Implementation of QAP Modeling and Software Requirements in the PM CAU Flow and Transport Model
(Page 10 of 12)

QAP Requirement	How the QAP Requirement Is Addressed for the PM CAU	Where QAP Requirement Is Addressed
B.5.6 Contaminant Boundary Calculations		
The contaminant boundary calculation procedure involves the following steps:		
Selecting a groundwater flow model (which may include HFM and/or parameterization alternatives).	Groundwater flow models in the saturated groundwater system have been developed considering selected HFM alternatives and parameter uncertainty.	Section 4.0
Assigning the HST(s) using consistent groundwater flow rates observed in the selected flow model—if the test is not completely in the unsaturated zone.	Uncertainties in HST parameters (e.g., size of exchange volume, properties of altered zones, inventory) have been evaluated in the screening analysis (Carle et al, 2020). Comparison with observation data suggests the mid-range estimates best present the expected source term for simulation.	Implementation is presented in Sections 4.0 and 5.0
Executing RN transport calculations for flow model results, including consideration of source term and transport uncertainties.	Transport calculations have been conducted. Source term uncertainties were evaluated in the screening analysis (Carle et al, 2020) and compared with measured data. Source concentrations, consistent with observations were carried forward into the CAU transport simulations.	Sections 4.0 and 5.0
Collecting contaminant concentration distributions (in space) at regular, specified output times over a 1,000-year period, for all simulations of the transport model.	Transport calculations are provided at 10, 50, 100, 150, 200, 300, 400, 500, 600, 700, 800, 900, and 1,000 years.	Section 6.0
Converting contaminant concentration distributions to the radiological standards of the SDWA (CFR, 2021) for each transport model result.	Contaminant concentrations are normalized to SDWA MCLs (CFR, 2021), and fractional exceedances of MCLs are added to determine the probability the MCL will be exceeded from all RNs considered.	Section 6.0

Table B-1
Implementation of QAP Modeling and Software Requirements in the PM CAU Flow and Transport Model
(Page 11 of 12)

QAP Requirement	How the QAP Requirement Is Addressed for the PM CAU	Where QAP Requirement Is Addressed
QAP (2015) Section 2.6.5 Contaminant Boundary Calculations		
Determining spatial locations and times where radiological standards are exceeded for each transport model result.	Spatial locations where MCL is forecast to be exceeded are determined.	Section 6.0
Logging the frequency that radiological standards are exceeded at each model element location, regardless of time, over the entire series of transport model simulations.	Time cumulative probabilities of exceeding the MCL have been determined for each modeling case simulated.	Section 6.0
Identifying model element locations where the frequency that radiological standards are exceeded is greater than 5% of the total number of transport simulations. Elements meeting this criterion are then considered within the contaminant boundary at 95th percentile; elements not meeting this criterion are considered outside the boundary.	Time cumulative probabilities of exceeding the MCL have been determined for each modeling case, allowing for determining the frequency that radiological standards are exceeded in at least 5% of the realizations.	Section 6.0
Repeating the described procedural steps for multiple alternative models.	Alternative flow models using alternative recharge and fault properties were conducted. Transport calculations were performed on the alternative flow models. Representations of PM transport parameter distributions have been repeated in Monte Carlo simulations to develop the probability of areas exceeding the MCL for each alternative flow model.	Sections 5.0 and 6.0
QAP (2015) Section 2.7 Model Evaluation		
During this stage, additional data will be gathered to increase confidence in the conceptual model and flow and transport model results reliability.	Model evaluation occurs during the CADD/CAP stage of the UGTA strategy. As such, this requirement is not explicitly addressed in this document.	Additional data will be collected during the CADD/CAP stage of the UGTA strategy to evaluate the representativeness of key processes likely to affect contaminant transport from underground nuclear detonations conducted in the PM CAU. These data collection activities will be identified in the CADD/CAP.

Table B-1
Implementation of QAP Modeling and Software Requirements in the PM CAU Flow and Transport Model
(Page 12 of 12)

QAP Requirement	How the QAP Requirement Is Addressed for the PM CAU	Where QAP Requirement Is Addressed
QAP (2015) Section 2.7 Model Evaluation (continued)		
Refinements to the model will be documented as addenda to the CADD/CAP or in a summary report.	N/A at this stage of implementing the UGTA strategy.	N/A
These evaluations will be documented as addenda to the CR or in a summary report.	N/A at this stage of implementing the UGTA strategy.	N/A
QAP (2015) Section 2.8 Configuration Control		
Models accepted by NDEP (before the CADD/CAP and CR stages) will be archived and placed under configuration control. The model documentation must be sufficient to ensure traceability and reproducibility.	N/A at this stage of implementing the UGTA strategy. Model documentation is traceable and reproducible.	Model documentation data packages are retained as records by the participants.
Documentation must include the following: • Input data and source identification • Identification of model assumptions and limitations • Model executable codes, including pre- and post-processors • Computer calculations, and basis to permit traceability of inputs and outputs • Final results and output data files • Identification of the originator(s) and reviewer(s)	This documentation is included in data packages prepared by the participants supporting the modeling of the PM CAU in accordance with their applicable procedures.	This documentation is retained as records by the individual participants.

Table B-2
Implementation of QAPP Data Management Requirements in the PM CAU Flow and Transport Model
(Page 1 of 6)

QAP Requirement	How the QAP Requirement Is Addressed for the PM CAU	Where QAP Requirement Is Addressed
QAP (2015) Section 1.8 Information/Data Management		
Organizations must ensure processes are in place for the management, control, and transfer of information/data.	Data management, control, and transfer are addressed by individual participant procedures.	Project procedures for data management, control, and transfer are maintained by each participant.
The processes must include provisions for gathering, manipulating, and distributing data, and must address the following:	Processes for gathering, manipulating, and distributing data are addressed by individual participant procedures.	Project procedures for gathering, manipulating, and distributing data are maintained by each participant.
Participants must verify that transcription and transfer of data are performed correctly by doing the following: • Reviewing a representative sample of sufficient data points to provide confidence that data have been transcribed or transferred properly. • Documenting the method of verification and verification results. • Documenting the transfer of data to software applications, including software application name and version number.	Processes for verifying transcription and transfer of data are addressed by individual participant procedures.	Project procedures and records packages containing processes for verifying transcription and transfer of data are maintained by each participant.
Data used in reports, analyses, models, or interpretive works are traceable to their source.	Processes for evaluating data traceability are addressed by individual participant procedures.	Procedures and records packages containing processes for data traceability are maintained by each participant. Data used in this document are traceable to their source.
Data that have been manipulated are checked to ensure the manipulation process was performed as intended.	Processes for checking data manipulation are addressed by individual participant procedures.	Procedures and records packages containing processes for checking data manipulation are maintained by each participant.
Data are maintained during the lifetime of the project using backup and archival processes.	Data are maintained using backup and archival processes.	Procedures and records packages containing processes for maintaining data during the project lifetime are maintained by each participant.
Data used in reports, analyses, models, or interpretive works are maintained as records in accordance with Section 1.7 of the QAP.	Data are maintained using processes addressed in individual participant procedures.	Procedures and records packages containing data used in reports, analyses, and models are maintained by each participant.

Table B-2
Implementation of QAPP Data Management Requirements in the PM CAU Flow and Transport Model
(Page 2 of 6)

QAP Requirement	How the QAP Requirement Is Addressed for the PM CAU	Where QAP Requirement Is Addressed
QAP (2015) Section 1.8 Information/Data Management (continued)		
Access to databases, datasets, and files is controlled so that unauthorized modifications or deletions are not allowed.	Database access is controlled.	Access to databases is controlled by Navarro database procedures.
Data source(s), extraction criteria, and data quality are documented or referenced, and maintained with the dataset extracted from a database.	Databases identify data sources and data quality.	Databases maintained and controlled by Navarro identify data sources and data quality.
When transmitting information, professional judgment, data, code, models, or inputs to another participant, the originating participant must ensure the source(s) of the transmittal is identified and traceable.	Input provided by LANL, LLNL, DRI, and USGS identified the source of the material.	Material sources for all inputs are identified in the document. Additional documentation of inputs is retained as records by individual participants.
The originating participant must also identify any limitations or qualifiers for the data or information to the receiving entity.	Originating participant has identified limitations and qualifiers on information provided.	Documentation of limitations and qualifiers is retained as records by sending and receiving participants.
QAP (2015) Section 2.5 Non-direct Data		
Nondirect data must be reviewed and accepted in accordance with this section.	Data used in this analysis have been generally acquired in accordance with the requirements of the QAP.	Most data are summarized in the PM HDD (Navarro, 2021b) and TDD (Navarro, 2021a). Additional data, also developed in compliance with the QAP, are presented in the SDD (Navarro, 2021c). Data acquired by recognized national organizations such as the National Oceanic and Atmospheric Administration (NOAA) and USGS have been determined to be acceptable.

Table B-2
Implementation of QAPP Data Management Requirements in the PM CAU Flow and Transport Model
(Page 3 of 6)

QAP Requirement	How the QAP Requirement Is Addressed for the PM CAU	Where QAP Requirement Is Addressed
QAP (2015) Section 2.5.1 Approach		
A subject matter expert (SME) or topical committee shall evaluate nondirect data sources (e.g., defense projects, Yucca Mountain Project, databases) to determine the appropriateness of the methods and the correctness of the resulting dataset or data source.	Nondirect data are generally used in a corroborative sense and are not directly relied upon for the saturated zone flow and transport models.	Data appropriateness for most datasets is evaluated in the PM HDD (Navarro, 2021b) and TDD (Navarro, 2021a). Records packages associated with the appropriateness of additional data sources are maintained by each participant.
The SME or committee must develop a data acceptance report and address the following, as applicable: • Description of data, its source, rationale for its selection, and its intended uses • Extent and reliability of the documentation associated with the data • Conditions under which the data were obtained, if germane to the data, are acceptable • Prior uses of the data and associated verification processes • Dataset(s) used for corroboration, rationale for selection, and justification of inferences drawn • Data acquisition, collection, or development records (includes procedures) • Data flags to be assigned to the data • Data quality indicators (i.e., accuracy, precision, representativeness, completeness, and comparability) • Impact of use or nonuse of data • Uncertainties and restrictions, if any • Assumptions, constraints, bounds, or limits on the data or source	Because other nondirect data are generally used in a corroborative sense and are not directly relied upon for the flow and transport model, these requirements are not applicable. Other datasets are determined to be appropriate by the participant.	Data appropriateness for most datasets is evaluated in the PM HDD (Navarro, 2021b) and TDD (Navarro, 2021a). Records packages associated with the appropriateness of additional data sources are maintained by each participant.

Table B-2
Implementation of QAPP Data Management Requirements in the PM CAU Flow and Transport Model
(Page 4 of 6)

QAP Requirement	How the QAP Requirement Is Addressed for the PM CAU	Where QAP Requirement Is Addressed
QAP (2015) Section 2.5.1 Documentation Review		
If a committee does not perform the acceptance evaluation, an independent reviewer must review the document for the following items: • The content of the report is technically adequate, complete, and correct. • Uncertainties and restrictions are discussed. • The assumptions, constraints, bounds, or limits on the data are identified.	Because nondirect data are only used in a corroborative sense and are not directly relied upon for the flow and transport model, there is no need to develop a data acceptance report.	Data appropriateness for most datasets is evaluated in the PM HDD (Navarro, 2021b) and TDD (Navarro, 2021a). Records packages associated with the appropriateness of additional data sources are maintained by each participant.
QAP (2015) Section 2.6.1.1 Data Quality Evaluation		
Participants must evaluate and document the quality of data used in reports, analyses, interpretive works, or models.	Data quality is evaluated by each participant responsible for collecting or developing data before their use in models, analyses, interpretive works, or reports.	Records packages containing processes for data quality evaluations are maintained by each participant. Principal data quality evaluations are contained in the PM HDD (Navarro, 2021b) and TDD (Navarro, 2021a). Data acquired by recognized national organizations such as NOAA and USGS have been determined to be acceptable.
Reports, models, or interpretive works shall indicate the quality of the data being used.	The data used in this report, other than those used in corroborative analyses, are direct data and have been generated using processes compliant with the Qp or have been qualified in other project documents.	Records packages containing processes for indicating the quality of data are maintained by each participant. The PM HDD (Navarro, 2021b) and TDD (Navarro, 2021a) document the quality of data used in the flow and transport models.

Table B-2
Implementation of QAPP Data Management Requirements in the PM CAU Flow and Transport Model
(Page 5 of 6)

QAP Requirement	How the QAP Requirement Is Addressed for the PM CAU	Where QAP Requirement Is Addressed
QAP (2015) Section 2.6.1.2 Data Transferability		
Participants shall determine the transferability of data using the following steps:		
Establish acceptance criteria based on the use of the parameter and its importance. These criteria are established before the modeling simulations and the uncertainty and parameter sensitivity evaluations are performed. Changes in the criteria might be expected as the CAU investigations and modeling progress. Thus, if it is determined that more restrictive criteria are needed for a particular parameter, it will be necessary to repeat the transferability evaluation. If the previously used criteria are restrictive enough, it will not be necessary to reevaluate.	Acceptance criteria for most data used in the PM CAU models have been used in the data reports. Additional data transferability is evaluated with applicable participant procedures.	Data transferability for most datasets is evaluated in the PM HDD (Navarro, 2021b) and TDD (Navarro, 2021a). Records packages associated with the transferability of additional data sources are maintained by each participant.
Evaluate whether geologic, geochemical, hydrologic, or other factors would disqualify the measurement for use.	Factors potentially affecting the transferability of data are addressed in the data documents.	The effect of identified factors on data transferability for most datasets is evaluated in the PM HDD (Navarro, 2021b) and TDD (Navarro, 2021a).Records packages associated with the transferability of additional data sources are maintained by each participant.
Document the process and data used in sufficient detail that others can understand and repeat the process. This information should be incorporated either directly or by reference.	Data used in the models and analyses have been documented in this document or supporting documents.	The principal data evaluation documents supporting the models in the current document are the PM HDD (Navarro, 2021b) and TDD (Navarro, 2021a).

Table B-2
Implementation of QAPP Data Management Requirements in the PM CAU Flow and Transport Model
(Page 6 of 6)

QAP Requirement	How the QAP Requirement Is Addressed for the PM CAU	Where QAP Requirement Is Addressed
QAP (2015) Section 2.6.1.2 Data Transferability (continued)		
Participants shall determine the transferability of data using the following steps:		
The approach for implementing the data transfer process must be parameter-specific and must consider the following, if applicable: • Parameter characteristics, including underlying dependencies on other parameters • Similarity of geologic setting and other relevant characteristics • Type of measurement and/or interpretative technique, including measurement scale • Modeling approach, including conceptual models and model scale • Heterogeneity • Range in values • Sensitivity of contaminant boundary to parameter value • Reports, models, or interpretive works shall describe the transferability of the data being used.	Data transferability approach is described in the data documents. Additional data transferability is addressed in this document and related participant procedures.	Data transferability is documented in the PM HDD (Navarro, 2021b) and TDD (Navarro, 2021a), as applicable.

B.2.0 References

ASTM, see ASTM International.

ASTM International. 2008 (withdrawn 2017). *Standard Guide for Developing and Evaluating Groundwater Modeling Codes,* ASTM D6025-96(2008). West Conshohocken, PA.

CFR, see *Code of Federal Regulations.*

Carle, S.F., A.F.B. Tompson, and M. Zavarin. 2020. *Radionuclide Screening Analysis and Transport Parameters for Pahute Mesa Detonations, Nevada National Security Site,* LLNL-TR-812351, Livermore, CA: Lawrence Livermore National Laboratory.

Carle, S.F., A.F.B. Tompson, and M. Zavarin. 2021. *Review of Cavity Radius and Chimney Height Information for Underground Nuclear Tests at Nevada National Security Site,* LLNL-TR-818725. Livermore, CA: Lawrence Livermore National Laboratory.

Code of Federal Regulations. 2021. Title 40 CFR, Part 141, "National Primary Drinking Water Regulations." Washington, DC: U.S. Government Printing Office.

DOE, see U.S. Department of Energy.

DOE/NV, see U.S. Department of Energy, Nevada Operations Office.

FFACO, see *Federal Facility Agreement and Consent Order*.

Federal Facility Agreement and Consent Order. 1996 (as amended March 2010). Agreed to by the State of Nevada; U.S. Department of Energy, Environmental Management; U.S. Department of Defense; and U.S. Department of Energy, Legacy Management. Appendix VI, which contains the Underground Test Area Strategy, was last modified June 2014, Revision No. 5.

Jackson, T.R., J.M. Fenelon, and R. Paylor. 2021. *Groundwater Flow Conceptualization of the Pahute Mesa–Oasis Valley Groundwater Basin, Nevada: A Synthesis of Geologic, Hydrologic, Hydraulic Property, and Tritium Data,* Scientific Investigations Report 2020–5134. Carson City, NV: U.S. Geological Survey.

N-I, see Navarro-Intera, LLC.

NNSA/NSO, see U.S. Department of Energy, National Nuclear Security Administration Nevada Site Office.

Navarro-Intera, LLC. 2013. *Yucca Flat/Climax Mine CAU Flow and Transport Model, Nevada National Security Site, Nye County, Nevada,* Rev. 0, N-I/28091--065. Las Vegas, NV.

Navarro. 2021a. *Contaminant Transport Parameters for the Groundwater Flow and Contaminant Transport Model of Corrective Action Units 101 and 102: Central and Western Pahute Mesa, Nye County, Nevada,* Rev. 1, N/0002653--077. Las Vegas, NV.

Navarro. 2021b. *Hydrologic Data for the Groundwater Flow and Contaminant Transport Model of Corrective Action Units 101 and 102: Central and Western Pahute Mesa, Nye County, Nevada,* Rev. 1, N/0002653--073. Las Vegas, NV.

Navarro. 2021c. *Unclassified Source Term and Radionuclide Data for the Groundwater Flow and Contaminant Transport Model for Corrective Action Units 101 and 102: Central and Western Pahute Mesa, Nye County, Nevada,* Rev 1, N/0002653--088. Las Vegas, NV.

Painter, S.L. 2011. *User's Manual for Walkabout V1.0*, LA-UR-11-01952. Los Alamos, NM: Los Alamos National Laboratory.

Tompson, A., M. Zavarin, and D. Shumaker. 2019. *Yield-Weighting Approaches for Calculating Radiologic Inventories for Individual Underground Nuclear Tests at the Nevada National Security Site,* LLNL-TR-773562, Lawrence Livermore National Laboratory, Livermore, CA.

U.S. Department of Energy. 2008. *Information Technology Management*, DOE Order 200.1A. Washington, DC.

U.S. Department of Energy Environmental Management Nevada Program. 2018. *Record of Technical Change to Underground Test Area Activity Quality Assurance Plan, Nevada National Security Site, Nevada,* Rev. 2, DOE/NV--1450-REV. 2; Technical Change No. DOE/NV--1450-REV. 2-ROTC-1, 5 February. Las Vegas, NV

U.S. Department of Energy, Environmental Management Nevada Program. 2020a. *Pahute Mesa-Oasis Valley Hydrostratigraphic Framework Model for Corrective Action Units 101 and 102: Central and Western Pahute Mesa, Nye County, Nevada*, Rev. 0, DOE/EMNV--0014. Las Vegas, NV.

U.S. Department of Energy Environmental Management Nevada Program. 2020b. *Update to the Phase II Corrective Action Investigation Plan for Corrective Action Units 101 and 102, Central and Western Pahute Mesa, Nevada National Security Site, Nye County, Nevada,* Rev. 1, DOE/EMNV--0018. Las Vegas, NV.

U.S. Department of Energy, National Nuclear Security Administration Nevada Field Office. 2015. *Underground Test Area Activity Quality Assurance Plan, Nevada National Security Site, Nevada,* Rev. 2, DOE/NV--1450-REV.2. Las Vegas, NV.

U.S. Department of Energy, Nevada Operations Office. 2009. Phase II *Corrective Action Investigation Plan for Corrective Action Units 101 and 102, Central and Western Pahute Mesa, Nevada Test Site, Nye County, Nevada*, Rev. 2, DOE/NV--1312. Las Vegas, NV.

Appendix C

Hydrostratigraphic Model Supporting Information

C.1.0 Description of the PM-OV Model Layers

Brief descriptions of the HSUs used to construct the PM-OV model are provided in Table C-1. They are listed in approximate order from surface to basement, although some are laterally rather than vertically contiguous, and not all units are present in all parts of the model area. These HSUs, their structure, and their association with other HSUs are described in detail in the PM HFM report (DOE/EMNV, 2020).

Table C-1
HSUs of the PM-OV HFM
(Page 1 of 17)

HFM Model Layer Number	HSU (Symbol)	Dominant HGU(s) [a]	Stratigraphic Unit Map Symbols [b]	General Description
77	alluvial aquifer (AA) (this term is also used to designate an HGU)	AA	Qay, QTc, Qs, Qam, QTa, QTu, Qb, Tgy, Tgc, Tgm, Tgyx, Tt	Consists mainly of alluvium that fills extensional basins such as Gold Flat, Crater Flat, Kawich Valley, and Sarcobatus Flat. Also includes generally older Tertiary gravels, tuffaceous sediments, and nonwelded tuffs (where thin) that partially fill other basins such as Oasis Valley and the moat of the TMCC. In the eastern moat area of the TMCC, it includes intercalated, partially welded ash-flow tuff of the Thirsty Canyon Group.
76	younger volcanic composite unit (YVCM)	LFA, WTA, VTA	Typ	A minor unsaturated HSU that consists of Pliocene to late Miocene basaltic rocks at Thirsty Mountain and Buckboard Mesa.
75	Thirsty Canyon volcanic aquifer (TCVA)	WTA, LFA, lesser VTA	Ttg, Tth, Tts, Ttt, Ttp, Ttc	Consists mainly of welded ash-flow tuff and lava of the Thirsty Canyon Group. Unit is very thick within the Black Mountain caldera. Also is present east and south of the caldera, including the northwestern moat area of the TMCC and the northern portion of the Oasis Valley basin.
74	detached volcanics composite unit (DVCM)	WTA, LFA, TCU	Tf through Tq	Consists of a very complex distribution of lavas and tuffs that form a relatively thin, highly extended interval above the FC-BH detachment fault in the southwestern portion of the model area. Unit is locally hydrothermally altered.
73	detached volcanics aquifer (DVA)	WTA, LFA	Tgyx, Tf, Tma, Tmr	Consists of welded ash-flow tuff and lava assigned to the Ammonia Tanks Tuff and units of the Volcanics of Fortymile Canyon. Although, like the DVCM, the DVA also overlies the FC-BH detachment fault, it is considered a separate HSU because of the preponderance of WTAs and LFAs that compose the HSU and much smaller degree of hydrothermal alteration present.
72	Shoshone Mountain lava-flow aquifer (SMLFA)	LFA	Tfs	Rhyolitic lava and related dikes, plugs, tuff, and tuff breccias of the rhyolite of Shoshone Mountain. According to Slate et al. (1999): “Forms a volcanic dome straddling the southeastern topographic margin of the Rainier Mesa caldera.” A topographically prominent but unsaturated HSU.

Table C-1
HSUs of the PM-OV HFM
(Page 2 of 17)

HFM Model Layer Number	HSU (Symbol)	Dominant HGU(s) [a]	Stratigraphic Unit Map Symbols [b]	General Description
71	Fortymile Canyon composite unit (FCCM)	TCU	Tfu, Tfs, Tfd, Tfr, Tfb, Tfl, Tff	Consists mainly of zeolitic to quartzofeldspathic nonwelded and bedded tuffs of the Volcanics of Fortymile Canyon that encapsulate intercalated rhyolite lava flows and welded tuffs, which are assigned to different and separate HSUs. The FCCM is generally confined within the moat of the TMCC, where the unit forms a “depositional” ring around the Timber Mountain resurgent dome. Unit is thickest within the northwestern moat of the TMCC where measured thicknesses are 917 m (3,008 ft) at Well ER-EC-2a and greater than 500 m (1,640 ft) at Well ER-EC-13.
70	Fortymile Canyon upper mafic lava-flow aquifer (FCUMLFA)	LFA	Tfd, Tft, Tfb	Consists of as many as 12 individual flows of dense to scoriaceous trachybasalt, basaltic trachyandesite, and trachyandesite assigned to the lavas of Dome Mountain. Exposed extensively in the southeastern Timber Mountain moat (Tfd in Slate et al., 1999) where it forms a high volcanic edifice (i.e., Dome Mountain). Encountered in Well ER-30-1 (116.4–217.3-m [382–713-ft] depth interval). Saturated only in its northernmost extent in the eastern Timber Mountain moat. Modeled as a property model within the FCCM.
69	Fortymile Canyon upper lava-flow aquifer 1 (FCULFA1)	LFA, lesser VTA	Tfbw	Consists of a single buried, but shallow, rhyolitic lava flow of the rhyolite of Beatty Wash. Modeled as having limited extent beneath the northwestern Timber Mountain moat. Known only from a single occurrence in Well ER-EC-13 (6.1–147.8-m [20–485-ft] depth interval). Mostly unsaturated, but very basal portions may be saturated in places. Modeled as a property model within the FCCM.
68	Fortymile Canyon upper lava-flow aquifer 2 (FCULFA2)	LFA	Tfbw	Consists of a single rhyolitic lava flow of the rhyolite of Beatty Wash exposed in the northwestern Timber Mountain moat. Also encountered in Well ER-EC-2a (0–227.4-m [0–746-ft] depth interval). Conceptualized and modeled as an isolated LFA but could possibly correlate to, and connect with, FCULFA1. Mostly unsaturated, but basal portion is likely saturated in most places. Modeled as a property model within the FCCM.

Table C-1
HSUs of the PM-OV HFM
(Page 3 of 17)

HFM Model Layer Number	HSU (Symbol)	Dominant HGU(s) [a]	Stratigraphic Unit Map Symbols [b]	General Description
67	Fortymile Canyon upper lava-flow aquifer 3 (FCULFA3)	LFA	Tfbw	Consists of a single buried rhyolitic lava flow of the rhyolite of Beatty Wash. Known only from a single occurrence in UE-18r (137.2–286.5-m [450–940-ft] depth interval). Conceptualized and modeled as an isolated LFA of limited extent beneath the northern Timber Mountain moat. Unsaturated. Modeled as a property model within the FCCM.
66	Fortymile Canyon upper lava-flow aquifer 4 (FCULFA4)	LFA, lesser TCU	Tfb	Consists of a buried sequence of rhyolitic lava-flow lithologies of the Beatty Wash Formation that likely represent two stacked individual flow units beneath the northwestern Timber Mountain moat. Known only from a single occurrence in Well ER-EC-13 (505.4–771.1-m [1,658–2,530-ft] depth interval). Conceptualized and modeled as having limited extent. Saturated. Modeled as a property model within the FCCM.
65	Fortymile Canyon upper lava-flow aquifer 5 (FCULFA5)	LFA	Tfbw	Consists of a single buried rhyolitic lava flow of the rhyolite of Beatty Wash occurring beneath the southwestern Timber Mountain moat. Known only from a single occurrence in the MYJO Coffer well (387.1–433.4-m [1,270–1,422-ft] depth interval). Conceptualized and modeled as an isolated LFA of limited extent. Saturated. Modeled as a property model within the FCCM.
64	Fortymile Canyon upper lava-flow aquifer 6 (FCULFA6)	LFA, lesser TCU	Tfb	Consists of a thick and extensive sequence of rhyolitic lava flows of the Beatty Wash Formation, and that outcrop along Beatty Wash in the southern Timber Mountain moat. Encountered in Well ER-EC-7 (12.5–422.5-m [41–1,386-ft] depth interval). Lower portions saturated. Modeled as a property model within the FCCM.
63	Fortymile Canyon upper lava-flow aquifer 7 (FCULFA7)	LFA, lesser TCU	Tf	Consists of a buried sequence of rhyolitic lava flows of the Volcanics of Fortymile Canyon, and those that occur beneath the southern Timber Mountain moat. Known only from a single occurrence in the lower portion of Well ER-EC-7 (352.0–422.5-m [1,155–1,386-ft] depth interval). Conceptualized and modeled as an isolated LFA with limited extent. Modeled as a property model within the FCCM.

Table C-1
HSUs of the PM-OV HFM
(Page 4 of 17)

HFM Model Layer Number	HSU (Symbol)	Dominant HGU(s) [a]	Stratigraphic Unit Map Symbols [b]	General Description
62	Fortymile Canyon welded-tuff aquifer 1 (FCWTA1)	WTA	Tfb	Consists of a buried interval welded ash-flow tuff of the Beatty Wash Formation that occurs in the northwestern portion of the Timber Mountain moat. Known only from a single occurrence in Well ER-EC-2a (830.9–867.5-m [2,726–2,846-ft] depth interval). Conceptualized and modeled as an isolated WTA of limited extent. Modeled as a property model within the FCCM.
61	Fortymile Canyon welded-tuff aquifer (FCWTA)	WTA, lesser VTA and TCU	Tfb	Consists mostly of partially to moderately welded ash-flow tuff that occurs in the lower portion of the Volcanics of Fortymile Canyon in the southwestern portion of the TMCC. Exposed along the west side of the Transvaal Hills, where it is 30 to 60 m (100–200 ft) thick and consists of moderately welded tuff in upper part grading to nonwelded vitric tuff (i.e., VTA) at base (Lipman et al., 1966). West of the Transvaal Hills the unit is deeply buried and much thicker, and consists of at least two separate welded ash-flow tuff units with the upper unit described as moderately welded and the lower unit as partially welded. The buried portion is known only from a single occurrence in the MYJO Coffer well (529.4–776.3-m [1,737–2,547-ft] depth interval). Zeolitic or quartzofeldspathic bedded tuff of unknown thickness likely occurs between the two buried ash-flow tuff intervals. Mostly saturated except for portions of near-surface exposures in the Transvaal Hills.
60	Fortymile Canyon lower lava-flow aquifer (FCLLFA)	LFA, lesser TCU	Tff	Consists of rhyolitic to trachytic lava flows that likely straddle the stratigraphic contact between the Fortymile Canyon and Timber Mountain Groups. The HSU includes two geographically separate occurrences. Between the Transvaal Hills and Timber Mountain, the HSU correlates to the rhyodacite of Fleur-de-lis Ranch where it has a maximum exposed thickness of approximately 300 m (1,000 ft) along the west side of Timber Mountain (Slate et al., 1999). Farther west in Oasis Valley basin the lava flows correlate to the rhyodacite of Fleur-de-Lis Ranch and trachyte of East Cat Canyon. This buried occurrence is known only from a single occurrence in the MYJO Coffer well (776.3–855.0-m [2,547–2,805-ft] depth interval). Zeolitic or quartzofeldspathic bedded tuff of unknown thickness likely occurs between these two units in Oasis Valley basin. Saturated within the Oasis Valley basin, but portions of near-surface exposures along the west side of Timber Mountain are unsaturated.

Table C-1
HSUs of the PM-OV HFM
(Page 5 of 17)

HFM Model Layer Number	HSU (Symbol)	Dominant HGU(s) [a]	Stratigraphic Unit Map Symbols [b]	General Description
59	Fortymile Canyon lower mafic lava-flow aquifer (FCLMLFA)	LFA	Tfbb	Consists of basaltic lava that occurs at the base of the Volcanics of Fortymile Canyon in the eastern Timber Mountain moat. Modeled as having no surface exposure, but may correlate to exposures of older basalt mapped by Byers et al. (1966) in Fortymile Canyon. HSU penetrated in Well ER-30-1 from the depths 289.6–365.2 m (950–1,198 ft) where it directly overlies welded Ammonia Tanks Tuff. Saturated.
58	Ammonia Tanks mafic lava-flow aquifer (ATMLFA)	LFA	Tmay	Consists of trachytic lava flows exposed along the eastern flank of Timber Mountain, and modeled as extending into the subsurface of the southeastern Timber Mountain moat. Maximum exposed thickness is 150 m (490 ft) (Slate et al., 1999). Includes a small isolated rhyolite dome on the northern flank of Timber Mountain. Deeper portions are saturated.
57	Buttonhook Wash welded-tuff aquifer (BWWTA)	WTA	Tmaw	Consists of welded ash-flow tuff assigned to the tuff of Crooked Canyon and tuff of Buttonhook Wash. Exposed along the base of Timber Mountain (Tmb and Tmc in Byers et al., 1976). Unit is not exposed or encountered outside the margins of the TMCC. Interpreted to be in the subsurface of the southern and northwestern moat area (1,400.3–1,410.0 m [4,594–4,626-ft] depth in Well ER-EC-2a), and between Timber Mountain and the Transvaal Hills. A relatively thin subsurface occurrence is present in Well ER-EC-8 (439.5–448.7-m [1,442–1,472-ft] depth interval), indicating that a portion of the unit flowed over or around the northern end of the Transvaal Hills. Unit is not present in MYJO Coffer #1, and thus its presence west of the Transvaal Hills is limited to the area around ER-EC-8. Consists of landslide breccia in Well ER-EC-5 (246.9–305.4-m [810–1,002-ft] depth) that is sourced from Timber Mountain during resurgent doming (NNSA/NSO, 2004), and thus may be a poor aquifer in this area. An isolated occurrence is also located in the northeastern Timber Mountain moat (262.7–328.0-m [862–1,076-ft] depth in Well ER-18-2). Becomes saturated at deeper levels away from exposures along Timber Mountain. Maximum exposed thickness is 250 m (820 ft) (Slate et al., 1999). Note: Surface exposures in model are mainly from Byers et al. (1976).

Table C-1
HSUs of the PM-OV HFM
(Page 6 of 17)

HFM Model Layer Number	HSU (Symbol)	Dominant HGU(s) [a]	Stratigraphic Unit Map Symbols [b]	General Description
56	Buttonhook Wash confining unit (BWCU)	TCU	Tmaw	Zeolitic nonwelded tuff that occurs between the welded ash-flow tuffs of the Tuff of Buttonhook Wash and Ammonia Tanks Tuff. BWCU has a distribution similar to the BWWTA. Exposures of BWCU are probably present along the western base of Timber Mountain underlying BWWTA (e.g., Tmfu and Tmfl in Lipman et al. [1966]), but are not demarcated/mapped in the model. Maximum cumulative thickness of Tmfu and Tmfl in Lipman et al. (1966) is 83.8 m (275 ft).
55	Ammonia Tanks welded-tuff aquifer (ATWTA)	WTA	Tma	Welded ash-flow tuff assigned to the Ammonia Tanks Tuff. Very thick within the structural margins of the Ammonia Tanks caldera. Thinner, but still thick and extensive within the topographic low formed by the Rainier Mesa caldera. Exposed in the Transvaal Hills and on Timber Mountain. Includes nonwelded zones in the eastern portion of the Ammonia Tanks caldera (Tmb, Tmd, Tmf in Carr and Quinlivan [1966]). This heterogeneity is addressed with the inclusion of ATCCU as a property model within the ATWTA HSU. All units assigned as Tma in Slate et al. (1999) that occur within the margins of the TMCC represent ATWTA surface exposures (with the exception of those units at the base of Timber Mountain that may be assigned to BWWTA after Byers et al. [1976]).
54	Ammonia Tanks caldera confining unit (ATCCU)	TCU	Tma	Mostly nonwelded tuff exposed on the eastern portion of Timber Mountain (Tmb in Carr and Quinlivan [1966]). Expected to be altered where saturated. Modeled only in the subsurface beneath the northeastern and southeastern portions of the Ammonia Tanks caldera. This unit provides a conceptualization of the known heterogeneity in the upper and middle portions of the intra-caldera Ammonia Tanks Tuff in the eastern portion of the Ammonia Tanks caldera. It is addressed through the use of a property model within the ATWT HSU. Exposed along the eastern side of Timber Mountain where it is unsaturated and grouped within the ATWT aquifer due to the complex fault-controlled exposures on Timber Mountain. Grouped with Tma and Tml in Slate et al. (1999) and Byers et al. (1976), respectively. Present in UE-18r (897.6–1,027.2 m [2,945–3,370 ft]) as 129.5 m (425 ft) of potassic nonwelded tuff.

Table C-1
HSUs of the PM-OV HFM
(Page 7 of 17)

HFM Model Layer Number	HSU (Symbol)	Dominant HGU(s) [a]	Stratigraphic Unit Map Symbols [b]	General Description
53	Timber Mountain upper welded-tuff aquifer (TMUWTA)	WTA, lesser LFA and TCU	Tmap	Unit consists predominately of extra-caldera welded ash-flow tuff of the mafic-poor member of the Ammonia Tanks Tuff. Known only from a single occurrence in Well ER-EC-4 where it is 265.8-m (872-ft) thick. The top of the unit at Well ER-EC-4 consists of 3.7 m (12 ft) of mafic lava (i.e., LFA) overlying 15.8 m (52 ft) of zeolitic to quartzofeldspathic bedded and nonwelded tuff (i.e., TCU). The remaining 89% of the HSU consists of welded ash-flow tuff (i.e., WTA). The HSU is conceptualized as occurring within the northern portion of the Oasis Valley basin of Fridrich et al. (2007) south of the Black Mountain caldera, and between the Hogback fault on the west and the TMCC on the east. Although poorly constrained, this conceptualization is based on the thick extra-caldera occurrence in Well ER-EC-4, which suggests deposition within a structural basin. Mostly saturated except for westernmost portion.
52	Tannenbaum Hill lava-flow aquifer (THLFA)	LFA, minor VTA and TCU	Tmat	Composed entirely of rhyolitic lava of the rhyolite of Tannenbaum Hill. Main occurrence is on the Bench, and just outside the northwestern structural boundary of the TMCC. Mostly unsaturated, but very basal portions become saturated locally.
51	Tannenbaum Hill composite unit (THCM)	Mostly TCU, lesser WTA	Tmat	Zeolitic tuff and lesser welded ash-flow tuff of the rhyolite of Tannenbaum Hill that occurs stratigraphically below Tannenbaum Hill lava and above the rhyolite of Fluorspar Canyon. Distribution is similar to the THLFA. Lower portions to end to be saturated.

Table C-1
HSUs of the PM-OV HFM
(Page 8 of 17)

HFM Model Layer Number	HSU (Symbol)	Dominant HGU(s) [a]	Stratigraphic Unit Map Symbols [b]	General Description
50	Tannenbaum Hill confining unit (THCU)	TCU	Tmat, Tmab, Tmrb	Nonwelded tuff and tuff breccia occurring between the Tannenbaum Hill lava and Rainier Mesa Tuff (1,184.5–1,367.0-m [3,886–4,485-ft] depth in well UE-18r). Also includes nonwelded, bedded tuffs assigned to the bedded Ammonia Tanks Tuff (Tmab) and bedded Rainier Mesa Tuff (Tmrb) of Ferguson et al. (1994). Nonwelded tuffs are assumed to be zeolitic because of the unit's deep intra-caldera location below the water table. It is also assumed that thin nonwelded and bedded tuffs are always present between the Ammonia Tanks and Rainier Mesa Tuffs within the TMCC as observed in numerous drills holes on PM. As a result, the unit is present in an intervening position everywhere the Ammonia Tanks Tuff overlies the Rainier Mesa Tuff within the TMCC. Thin unmapped exposures of THCU are assumed to be present in the Transvaal Hills. Mostly saturated, except for elevated occurrences such as Timber Mountain, Transvaal Hills, and portions of the Bench.
49	Timber Mountain welded-tuff aquifer (TMWTA)	WTA, minor VTA	Tmr, Tma	Consists mainly of welded ash-flow tuff of the Rainier Mesa Tuff where it occurs outside the Rainier Mesa caldera (i.e., extra-caldera). Includes minor amounts of unsaturated welded ash-flow tuff and vitric bedded tuff of the overlying Ammonia Tanks Tuff outside the limit of the TMUWTA (e.g., in eastern PM). Mostly unsaturated except for deeper portions in the extreme northwest portion of PM, southern portions of the Bench, and in the Oasis Valley basin between the western margins of the TMCC and the Hogback fault.
48	Timber Mountain lower vitric-tuff aquifer (TMLVTA)	VTA	Tmr, Tmrh, Tmrf, Tp	Consists mainly of vitric (i.e., unaltered) nonwelded and bedded tuffs of the lower portion of the Timber Mountain Group. These include the basal nonwelded portion of the Rainier Mesa Tuff, and nonwelded and bedded tuffs of the underlying tuff of Holmes Road and tuff of Fluorspar Canyon. Locally includes minor intervals of vitric lithologies at the top the underlying Paintbrush Group. Mostly unsaturated except for western portions on PM where the lower portion becomes saturated.

Table C-1
HSUs of the PM-OV HFM
(Page 9 of 17)

HFM Model Layer Number	HSU (Symbol)	Dominant HGU(s) [a]	Stratigraphic Unit Map Symbols [b]	General Description
47	Rainier Mesa welded-tuff aquifer (RMWTA)	WTA	Tmr, Tmc	Thick and extensive intra-caldera welded ash-flow tuff assigned to the Rainier Mesa Tuff. Exposed only in the Transvaal Hills, where it also includes debris-flow breccia (Tmc in Slate et al. [1999]) for this study. Present everywhere within the structural margins of the Rainier Mesa caldera. Includes both the mafic-rich and mafic-poor members of Ferguson et al. (1994). Modeled thickness is approximately 1,200 m (4,000 ft). Fridrich et al. (2007) shows intra-caldera Rainier Mesa Tuff up to 2,500 m (8,000 ft) thick. Maximum exposed intra-caldera thickness is 500 m (1,640 ft) but base is not exposed (Slate et al., 1999). Mostly saturated, except for elevated occurrences such as Timber Mountain, Transvaal Hills, and portions of the Bench where the uppermost portions are unsaturated.
46	Fluorspar Canyon confining unit (FCCU)	TCU	Tmrf	Consists of zeolitic, nonwelded tuff of the rhyolite of Fluorspar Canyon. Locally, includes minor zeolitic lithologies (e.g., pumiceous lava) of the underlying topmost portion of the Paintbrush Group. HSU is confined to the Bench, where it has been structurally down-dropped below the water table, resulting in zeolitic alteration of the unit. On PM to the north, the rhyolite of Fluorspar Canyon is structurally higher, occurring mostly above the water table, and thus is vitric, and assigned to the TMLVTA. Mostly saturated except uppermost portions that are locally unsaturated.
45	Windy Wash aquifer (WWA)	LFA	Tmw	Minor unsaturated HSU consisting of the lava-flow lithofacies of the rhyolite of Windy Wash. Occurs locally along the western (down-thrown) side of the West Greeley fault in Area 20.
44	Paintbrush composite unit (PCM)	WTA, LFA, TCU	Tpc, Tp	Consists mostly of units of the Paintbrush Group that occur in the southern portion of the model area in the vicinity of the Claim Canyon caldera. Unit is dominated by thick, strongly welded Tiva Canyon Tuff within the Claim Canyon caldera. Outside the caldera, this unit is more variable, consisting of welded and nonwelded tuff and rhyolitic lava assigned to various formations of the Paintbrush Group. Stratigraphically equivalent units of the Paintbrush Group that occur in the northern portion of the model area beneath PM have been grouped into seven separate HSUs.

Table C-1
HSUs of the PM-OV HFM
(Page 10 of 17)

HFM Model Layer Number	HSU (Symbol)	Dominant HGU(s) [a]	Stratigraphic Unit Map Symbols [b]	General Description
43	Comb Peak aquifer (CPA)	LFA	Tpk	Consists of the LFA lithofacies of the rhyolite of Comb Peak at PM. HSU known from only two subsurface occurrences in Wells ER-EC-1 and ER-EC-15, where it is interpreted to consist of a single rhyolite lava flow. TCU-like lithofacies (e.g., zeolitic pumiceous lava) that occur at the top and base of the flow are grouped with the hydrostrigraphically adjacent FCCU and UPCU. Mostly saturated on the Bench. Unsaturated north of the Bench on PM.
42	Post-Benham Paintbrush confining unit (PBPCU)	TCU	Tp	Zeolitic nonwelded tuff, bedded tuff, and pumiceous lava that locally separates the BA from the CPA. Saturated on the Bench. Unsaturated north of the Bench on PM.
41	Benham aquifer (BA)	LFA	Tpb	Lava-flow lithofacies of the rhyolite of Benham. Occurs north of the TMCC and beneath the southwestern portion of PM.
40	upper Paintbrush confining unit (UPCU)	TCU	Tp	Zeolitic nonwelded tuff, bedded tuff, and pumiceous lava that separate the SPA and TCA from overlying aquifers (e.g., BA and CPA).
39	Scrugham Peak aquifer (SPA)	LFA	Tps	Consists of the LFA lithofacies of the rhyolite of Scrugham Peak. HSU is exposed along the south face of PM, and was encountered in Wells ER-20-8 and ER-20-8-2. Zeolitic pumiceous lava that occurs at the top and of the flow in these wells are group with the overlying UPCU.
38	Middle Paintbrush confining unit (MPCU)	TCU	Tp	Zeolitic nonwelded and bedded tuff that separate the TCA and the overlying SPA.
37	Tiva Canyon aquifer (TCA)	WTA	Tpc	The welded ash-flow lithofacies of the PM lobe of the Tiva Canyon Tuff beneath PM. Only saturated west of the Boxcar fault.

Table C-1
HSUs of the PM-OV HFM
(Page 11 of 17)

HFM Model Layer Number	HSU (Symbol)	Dominant HGU(s) [a]	Stratigraphic Unit Map Symbols [b]	General Description
36	Paintbrush vitric-tuff aquifer (PVTA)	VTA	Pre-Tmr tuffs, Tp	Typically includes all vitric, nonwelded and bedded tuff units below the Rainier Mesa Tuff to the top of a Paintbrush lava (e.g., Tpb or Tpe) but may extend to base of Paintbrush Tuff in eastern Area 19 where Tpe or Tpr lavas are not present. May also include the vitric pumiceous top of the Tpe lava. Unit occurs in the northern portion of the model area beneath PM.
35	lower Paintbrush confining unit (LPCU)	TCU	Tpe, Tpd, Tpt	Consists of zeolitic bedded and nonwelded tuffs that occur stratigraphically between the Tiva Canyon Tuff and the welded Topopah Spring Tuff. This mainly includes the rhyolite of Delirium Canyon and the bedded and nonwelded Topopah Spring Tuff.
34	Paintbrush lava-flow aquifer (PLFA)	LFA	Tpd, Tpe, Tpr	Lava-flow lithofacies of the rhyolite of Delirium Canyon (Tpd), rhyolite of Echo Peak (Tpe), and rhyolite of Silent Canyon (Tpr). Also includes moderately to densely welded ash-flow tuff of Tpe. Unit occurs in the northern portion of the model area beneath PM.
33	Topopah Spring aquifer (TSA)	WTA	Tpt	The welded ash-flow lithofacies of the Topopah Spring Tuff in southern Area 20.
32	Yucca Mountain Crater Flat composite unit (YMCFCM)	LFA, WTA, TCU	Tc, Th	Includes all units of the Crater Flat Group and Calico Hills Formation that occur in the southern portion of the model area in the vicinity of Yucca Mountain. Stratigraphically equivalent units that occur in the northern portion of the model area beneath PM have been grouped into nine separate HSUs.
31	Calico Hills vitric-tuff aquifer (CHVTA)	VTA	Th (Tac)	Structurally high, vitric, nonwelded tuffs of the Calico Hills Formation. Present in the northern portion of the model area beneath the eastern portion of Area 19. May become partly zeolitic in the lower portions.

Table C-1
HSUs of the PM-OV HFM
(Page 12 of 17)

HFM Model Layer Number	HSU (Symbol)	Dominant HGU(s) [a]	Stratigraphic Unit Map Symbols [b]	General Description
30	Calico Hills zeolitic composite unit (CHZCM)	TCU	Th	Formerly in the Phase I HFM, the CHZCM consisted of a complex distribution of rhyolite lava flows (i.e., LFAs) intercalated within thick and extensive mostly zeolitic and quartzofeldspathic nonwelded and bedded tuffs (i.e., TCUs) of the Calico Hills Formation. In the Phase II model, the LFAs have been demarcated and modeled as separate property models within the CHZCM. Although the composite unit designation for the CHZCM is retained in the Phase II HFM, the unit is conceptualized in the Phase II HFM as consisting entirely of TCU. In addition, the Phase I CHCU HSU has been merged with the CHZCM in the Phase II HFM. The CHZCM is present in the northern portion of the model area beneath most of eastern and central Area 20, west of the West Greeley fault. The CHZCM is mostly saturated, particularly west of the Boxcar fault. East of the Boxcar fault, the upper portion of the HSU is above the water table.
29	Calico Hills lava-flow aquifer 1 (CHLFA1)	LFA	Th	The uppermost LFA property model within the CHZCM. Conceptualized as a single rhyolite lava flow of the Calico Hills Formation. Mainly occurs as a north–south-elongated flow between the West Greeley and Boxcar faults. Only the lower portion saturated west of the West Greeley fault.
28	Calico Hills lava-flow aquifer 2 (CHLFA2)	LFA, very minor TCU	Th	An LFA property model within the CHZCM. Although modeled as a single flow, very thin zeolitic bedded tuff observed within the CHLFA2 interval in U-20aj suggests that the property model may consist locally of two separate flows. Occurs in the northern portion of PM, mostly west of the West Greeley fault. Mostly unsaturated. Lower portion saturated in some places.
27	Calico Hills lava-flow aquifer 3 (CHLFA3)	LFA, minor TCU	Th	An LFA property model within the CHZCM. Although modeled as a single flow, the lithofacies distribution within drill holes penetrating the unit suggests that the property model may consist of more than one flow. Some of the lithofacies are described as zeolitic which likely imparts TCU-like properties to portions of the flow, although these TCU-like portions appear to thin and thus minor in occurrence. Similar in size and occurrence to CHLFA2. Fully saturated only west of the Boxcar fault. Lower portion saturated between the West Greeley and Boxcar faults. Mostly unsaturated east of the West Greeley fault.

Table C-1
HSUs of the PM-OV HFM
(Page 13 of 17)

HFM Model Layer Number	HSU (Symbol)	Dominant HGU(s) [a]	Stratigraphic Unit Map Symbols [b]	General Description
26	Calico Hills lava-flow aquifer 4 (CHLFA4)	LFA	Th	An LFA property model within the CHZCM. Modeled as a single flow. Occurs as a north–south-elongated flow straddling the West Greeley fault. Mostly fully saturated west of the West Greeley fault. Portions become unsaturated east of the West Greeley fault.
25	Calico Hills lava-flow aquifer 5 (CHLFA5)	LFA	Th	The lowermost and most extensive LFA property model within the CHZCM. Modeled as a single flow. Occurs mainly west of the West Greeley fault. Saturated.
24	Inlet aquifer (IA)	LFA	Tci	Lava-flow lithofacies of the rhyolite of Inlet. Occurs as two thick isolated deposits beneath PM in the northern portion of the model area.
23	Crater Flat composite unit (CFCM)	Mostly LFA, intercalated with TCU	Tc, Tcpj, Tcps, Tcg	Includes welded tuff and lava flow lithofacies of the tuff of Jorum (Tcpj), the rhyolite of Sled (Tcps), and the andesite of Grimy Gulch (Tcg). Occurs in central Area 20 in the northern portion of the model area.
22	Crater Flat confining unit (CFCU)	TCU	Tc	Includes all zeolitic, nonwelded and bedded units below the Calico Hills Formation (Th) to the top of the Bullfrog Tuff (Tcb). Occurs mainly in Area 19 in the northern portion of the model area.
21	Kearsarge aquifer (KA)	LFA	Tcpk	Minor HSU that consists of the lava-flow lithofacies of rhyolite of Kearsarge. Unit is present as a small isolated occurrence in the northeastern portion of the model area.
20	Stockade Wash aquifer (SWA)	WTA	Tcbs	Consists of partially welded ash-flow tuff of the Stockade Wash lobe of the Bullfrog Tuff. Occurs along the eastern margin of the model area where it is extensively exposed. Mostly unsaturated.
19	Lower vitric-tuff aquifer 2 (LVTA2)	VTA	Tc	Two very small, unsaturated occurrences of vitric bedded tuff below the SWA in the extreme eastern portion of the model area.

Table C-1
HSUs of the PM-OV HFM
(Page 14 of 17)

HFM Model Layer Number	HSU (Symbol)	Dominant HGU(s) [a]	Stratigraphic Unit Map Symbols [b]	General Description
18	Bullfrog confining unit (BFCU)	TCU	Tcb	Major confining unit in the northern portion of the model area. Unit consists of thick intra-caldera, zeolitic, mostly nonwelded tuff of the Bullfrog Formation.
17	Belted Range aquifer (BRA)	LFA and WTA, with lesser TCU	Tb, Tbg, Tbgs, Tbq	Consists of welded ash-flow tuff and lava of the Belted Range Group (Tb) above the Grouse Canyon Tuff (Tbg), but may also include the lava flow lithofacies of the comendite of Split Ridge (Tbgs) and the comendite of Quartet Dome (Tbq) where present. Occurs in the northern portion of the model area.
16	Pre-Belted Range composite unit (PBRCM)	TCU, WTA, LFA	Tr, Tn, Tq, Tu, To, Tk, Te	Laterally extensive and locally very thick HSU that includes all the volcanic rocks older than the Belted Range Group.
15	subcaldera volcanic confining unit (SCVCU)	TCU	Tm, Tp, Tc, and older, undifferentiated tuffs	A highly conjectural unit that is modeled as consisting of highly altered volcanic rocks that occur stratigraphically between the Rainier Mesa Tuff and basement rocks (ATICU and RMICU) within the deeper portions of the TMCC.
14	lower clastic confining unit - thrust plate (LCCU1)	CCU	Cc, Cz, Czw, Zs	Late Proterozoic to Early Cambrian siliciclastic rocks that occur within the hanging wall of the Belted Range thrust fault.
13	lower carbonate aquifer - thrust plate (LCA3)	CA	Dg through Cc	Cambrian through Devonian, mostly limestone and dolomite, rocks that occur in the hanging wall of the Belted Range thrust fault.
12	upper clastic confining unit (UCCU)	CCU	MDc, MDe	Late Devonian through Mississippian siliciclastic rocks. Present in the eastern third of the model area.

Table C-1
HSUs of the PM-OV HFM
(Page 15 of 17)

HFM Model Layer Number	HSU (Symbol)	Dominant HGU(s) [a]	Stratigraphic Unit Map Symbols [b]	General Description
11	lower carbonate aquifer (LCA)	CA	Dg through Cc	Cambrian through Devonian mostly limestone and dolomite. Widespread throughout the model area.
10	lower clastic confining unit (LCCU)	CCU	Cc, Cz, Czw, Zs, Zj	Late Proterozoic through Early Cambrian siliciclastic rocks. Widespread throughout the model area.
9	Silent Canyon intrusive confining unit (SCICU)	IICU	Tc, Tb	Although modeled as single intrusive masses beneath the Silent Canyon and Redrock Valley calderas, the actual nature of these units is unknown. They may consist exclusively of igneous intrusive rocks, or older volcanic and pre-Tertiary sedimentary rocks that are intruded to varying degrees by igneous rocks ranging in composition from granite to basalt.
8	Redrock Valley intrusive confining unit (RVICU)	IICU	Tori	
7	Mesozoic granite confining unit (MGCU)	GCU	Kg	Consists of granitic rocks that comprise the Gold Meadows stock along the northeastern margin of the model area.

Table C-1
HSUs of the PM-OV HFM
(Page 16 of 17)

HFM Model Layer Number	HSU (Symbol)	Dominant HGU(s) [a]	Stratigraphic Unit Map Symbols [b]	General Description
6	Black Mountain intrusive confining unit (BMICU)	IICU	Not Defined	Although modeled as single intrusive masses beneath each of the Black Mountain, Ammonia Tanks, Rainier Mesa, and Claim Canyon calderas, and the Calico Hills area, the actual nature of these units is unknown. They may consist exclusively of igneous intrusive rocks, or older volcanic and pre-Tertiary sedimentary rocks that are intruded to varying degrees by igneous rocks ranging in composition from granite to basalt.
5	Calico Hills intrusive confining unit (CHICU)	IICU	Not Defined	
4	Claim Canyon intrusive confining unit (CCICU)	IICU	Not Defined	
3	Rainier Mesa intrusive confining unit (RMICU)	IICU	Not Defined	

Table C-1
HSUs of the PM-OV HFM
(Page 17 of 17)

HFM Model Layer Number	HSU (Symbol)	Dominant HGU(s) [a]	Stratigraphic Unit Map Symbols [b]	General Description
2	Ammonia Tanks intrusive confining unit (ATICU)	IICU	Not Defined	Although modeled as single intrusive masses beneath each of the Black Mountain, Ammonia Tanks, Rainier Mesa, and Claim Canyon calderas, and the Calico Hills area, the actual nature of these units is unknown. They may consist exclusively of igneous intrusive rocks, or older volcanic and pre-Tertiary sedimentary rocks that are intruded to varying degrees by igneous rocks ranging in composition from granite to basalt.
1	Pahute Mesa Northern Extension intrusive confining unit (PMNICU)	IICU	Not Defined	Modeled as individual intrusive confining units for the Mount Helen Caldera and Cathedral Ridge Calderas.

[a] See Table 2-1 of PM TDD (Navarro, 2021) for definitions of HGUs.
[b] See Tables 4-1 and 4-2 of the PM-OV HFM (DOE/EMNV, 2020) for definitions of stratigraphic units.

C.2.0 References

Byers, F.M., Jr., C.L. Rogers, W.J. Carr, and S.J. Luft. 1966. *Geologic Map of the Buckboard Mesa Quadrangle, Nye County, Nevada,* Map GQ-552, scale 1:24,000. Washington, DC: U.S. Geological Survey.

Byers, F.M., Jr., W.J. Carr, R.L. Christiansen, P.W. Lipman, P.P. Orkild, and W.D. Quinlivan. 1976. *Geologic Map of the Timber Mountain Caldera Area, Nye County, Nevada,* Map, I-891, scale 1:48,000. Reston, VA: U.S. Geological Survey.

Carr, W.J., and W.D. Quinlivan. 1966. *Geologic Map of the Timber Mountain Quadrangle, Nye County, Nevada,* Map GQ-503, scale 1:24,000. Washington, DC: U.S. Geological Survey.

Carr, W.J., and W.D. Quinlivan. 1966. *Geologic Map of the Timber Mountain Quadrangle, Nye County, Nevada,* Map GQ-503, scale 1:24,000. Washington, DC: U.S. Geological Survey.

DOE/EMNV, see U.S. Department of Energy Environmental Management Nevada Program.

Ferguson, J.F., A.H. Cogbill, and R.G. Warren. 1994. "A Geophysical-Geological Transect of the Silent Canyon Caldera Complex, Pahute Mesa, Nevada." In *Journal of Geophysical Research: Solid Earth,* Vol. 99(B3): pp. 4323–4339.

Fridrich, C.J., S.A. Minor, J.L. Slate, and P.L. Ryder. 2007. *Geologic Map of Oasis Valley Spring-Discharge Area and Vicinity, Nye County, Nevada,* Scientific Investigations Map 2957, 25 p., scale 1:50,000. Denver, CO: U.S. Geological Survey.

Lipman, P. W., W. D. Quinlivan, W. J. Carr, and R. E. Anderson, 1966. *Geologic Map of the Thirsty Canyon SE Quadrangle, Nye County, Nevada,* Map GQ-489, scale, 1:24,000. Washington, DC: U.S. Geological Survey.

NNSA/NSO, see U.S. Department of Energy, National Nuclear Security Administration Nevada Site Office.

Navarro. 2021. *Contaminant Transport Parameters for the Groundwater Flow and Contaminant Transport Model of Corrective Action Units 101 and 102: Central and Western Pahute Mesa, Nye County, Nevada,* Rev. 1, N/0002653--077. Las Vegas, NV.

Slate, J.L., M.E. Berry, P.D. Rowley, C.J. Fridrich, K.S. Morgan, J.B. Workman, O.D. Young, G.L. Dixon, V.S. Williams, E.H. McKee, D.A. Ponce, T.G. Hildenbrand, W.C. Swadley, S.C. Lundstrom, E.B. Ekren, R.G. Warren, J.C. Cole, R.J. Fleck, M.A. Lanphere, D.A. Sawyer, S.A. Minor, D.J. Grunwald, R.J. Laczniak, C.M. Menges, J.C. Yount, and A.S. Jayko. 1999. *Part A. Digital Geologic Map of the Nevada Test Site and Vicinity, Nye, Lincoln, and Clark Counties, Nevada, and Inyo County, California, Revision 4*, Open-File Report 99-554-A, scale 1:120,000. Denver, CO: U.S. Geological Survey.

U.S. Department of Energy Environmental Management Nevada Program. 2020. *Pahute Mesa-Oasis Valley Hydrostratigraphic Framework Model for Corrective Action Units 101 and 102: Central and Western Pahute Mesa, Nye County, Nevada*, Rev. 0, DOE/EMNV--014. Las Vegas, NV.

U.S. Department of Energy, National Nuclear Security Administration Nevada Site Office. 2004. *Completion Report for Well ER-EC-8*, DOE/NV/11718--435, UC-700. Prepared by Bechtel Nevada. Las Vegas, NV.

Appendix D

PM CAU Underground Nuclear Testing

D.1.0 Underground Nuclear Test Information

This section presents nuclear test information for CAUs 101 and 102. This information, provided in Table D-1, "Central and Western PM Underground Nuclear Test Information," includes for each test the detonation name, emplacement hole name, CAS number, test coordinates, detonation date, yield range, R_e, chimney height, land surface elevation, WP elevation, water-level elevation, and HSU at the WP. The sources of this information include NNSA/NFO (2015), Carle et al. (2021), FFACO (1996, as amended), and Fenelon et al. (2016).

A review of R_e and chimney height information for NNSS underground nuclear tests is provided in Carle et al. (2021). The R_e is calculated based on the maximum of the unclassified yield range (minimum for HANDLEY) in NNSA/NFO (2015) and Equation 1 in Pawloski (1999); or measured when yield is specified in NNSA/NFO (2015). The chimney height for an underground detonation is defined as the vertical distance between the WP and the top of the column of collapsed material, which may include open void space (Carle et al., 2021). The chimney height reported by Carle et al. (2021) was determined based on the presence of a subsurface or surface collapse, as follows:

- If a subsurface collapse exists, the chimney height may be measured or calculated. Calculated values are derived from an average ratio of chimney height to R_e provided for specific NNSS testing areas.
- If a surface collapse exists, the chimney height is the vertical distance between the WP and the predetonation ground surface.

Table D-1 reports the measured R_e and chimney height when available.

Table D-1
Central and Western PM Underground Nuclear Test Information
(Page 1 of 4)

Test Name [a]	Hole Name [a]	CAS No. [b]	Easting (m) [c]	Northing (m) [c]	Date [a]	Yield Range (kt) [a]	R_c (m) [d]	Chimney Height (m) [e]	Surface Elevation (m amsl) [c]	WP Elevation (m amsl) [a]	WT Elevation (m amsl) [f]	HSU at WP [g]
Central Pahute Mesa (CAU 101)												
ALAMO	U-19au	19-57-014	555278.5	4122855.8	07/07/1988	<150	62.8	345.4	1,992	1,369	1,358	CHVTA
ALMENDRO	U-19v	19-57-033	558003.1	4122055.1	06/06/1973	200-1,000	103.3	568.1	2,096	1,029	1,393	BFCU
AMARILLO	U-19ay	19-57-016	557311.4	4125422.6	06/27/1989	20-150	62.4	343.0	2,046	1,406	1,397	PLFA
BACKBEACH	U-19x	19-57-034	556020.6	4120757.9	04/11/1978	20-150	61.6	338.8	2,067	1,395	1,351	CHZCM
BARNWELL	U-20az	20-57-026	552392.4	4120468.5	12/08/1989	20-150	63.4	348.4	2,003	1,403	1,347	CHZCM
BEXAR	U-19ba	19-57-019	560899.2	4127735.5	04/04/1991	20-150	62.6	344.4	2,145	1,515	1,428	KA
BODIE	U-20ap	20-57-018	552166.9	4124002.4	12/13/1986	20-150	62.5	343.7	2,018	1,383	1,356	CHZCM
BOXCAR	U-20i	20-57-039	548242.9	4127580.9	04/26/1968	1,300	94.50 [h]	1,165.9 [h]	1,942	776	1,358	CFCM
BULLION	U-20bd	20-57-030	551420.3	4123847.4	06/13/1990	20-150	61.6	338.6	1,977	1,303	1,354	CHZCM
CABRA	U-20aj	20-57-012	547855.4	4128161.9	03/26/1983	20-150	65.0	357.4	1,934	1,391	1,357	CHLFA2
CAMEMBERT	U-19q	19-57-030	555976.6	4125798.5	06/26/1975	200-1,000	98.1	539.5	2,060	748	1,393	BFCU
CHANCELLOR	U-19ad	19-57-004	557182.9	4125122.6	09/01/1983	143	61.26 [h]	336.9	2,040	1,416	1,396	PLFA
CHARTREUSE	U-19d	19-57-022	560056.5	4133488.8	05/06/1966	73	40.23 [h]	221.3	2,091	1,424	1,418	BRA
CHESHIRE	U-20n	20-57-041	551424.4	4121743.1	02/14/1976	200-500	80.2	440.9	1,974	807	1,351	CHLFA4
COLBY	U-20aa	20-57-003	546837.4	4128745.2	03/14/1976	500-1,000	98.8	1,272.2 [h]	1,932	659	1,354	CFCM
COLWICK	U-20ac	20-57-005	551226.5	4122384.4	04/26/1980	20-150	62.5	343.9	1,973	1,340	1,348	CHLFA1
COMSTOCK	U-20ay	20-57-025	549562.4	4123673.3	06/02/1988	<150	62.8	620.3 [h]	1,988	1,367	1,351	CHLFA3
CONTACT	U-20aw	20-57-024	552097.9	4126211.4	06/22/1989	20-150	64.9	357.2	2,007	1,463	1,361	CHLFA3
CYBAR	U-19ar	19-57-012	557127.3	4125777.8	07/17/1986	119	47.90 [h]	399 [h]	2,044	1,417	1,398	PLFA
DURYEA	U-20a-1	20-57-002	550480.6	4121740.0	04/14/1966	70	52.50 [h]	288.8	1,987	1,444	1,334	CHLFA1
EGMONT	U-20aL	20-57-014	544546.0	4124748.0	12/09/1984	20-150	64.9	356.8	1,867	1,320	1,310	UPCU
EMMENTHAL	U-19t	19-57-031	562271.5	4126843.3	11/02/1978	<20	32.7	179.9	2,131	1,554	1,452	KA

Table D-1
Central and Western PM Underground Nuclear Test Information
(Page 2 of 4)

Test Name [a]	Hole Name [a]	CAS No. [b]	Easting (m) [c]	Northing (m) [c]	Date [a]	Yield Range (kt) [a]	R_c (m) [d]	Chimney Height (m) [e]	Surface Elevation (m amsl) [c]	WP Elevation (m amsl) [a]	WT Elevation (m amsl) [f]	HSU at WP [g]
ESTUARY	U-19g	19-57-025	556340.5	4129244.0	03/09/1976	200-500	86.6	856.8 [h]	2,053	1,196	1,425	BRA
FARM	U-20ab	20-57-004	552284.4	4125160.5	12/16/1978	20-150	61.2	336.7	2,006	1,317	1,359	CHZCM
FONDUTTA	U-19zs	19-57-036	559673.5	4128120.4	04/11/1978	20-150	62.5	343.9	2,099	1,466	1,424	BFCU
GALVESTON	U-19af	19-57-006	556079.1	4121450.5	09/04/1986	<20	34.1	187.6	2,045	1,558	1,353	PLFA
GIBNE	U-20ah	20-57-010	551224.8	4123206.5	04/25/1982	20-150	64.2	353.1	1,964	1,395	1,351	CHZCM
GREELEY	U-20g	20-57-037	552440.2	4128343.5	12/20/1966	870	76.50 [h]	1,216.5 [h]	1,972	756	1,370	BFCU
HALFBEAK	U-19b	19-57-018	562117.4	4129932.9	06/30/1966	365	80.77 [h]	819.3 [h]	2,070	1,251	1,428	BRA
HARDIN	U-20av	20-57-023	551172.7	4120677.8	04/30/1987	20-150	62.7	345.0	1,970	1,345	1,315	LPCU
HARZER	U-19aj	19-57-008	559768.3	4128539.1	06/06/1981	20-150	62.4	343.4	2,100	1,463	1,424	BFCU
HOSTA	U-19ak	19-57-009	560573.9	4133490.6	02/12/1982	20-150	62.4	343.0	2,103	1,463	1,416	BRA
HOUSTON	U-19az	19-57-017	555779.2	4120082.4	11/14/1990	20-150	63.5	349.4	2,058	1,464	1,351	PLFA
HOYA	U-20be	20-57-031	550733.5	4119853.2	09/14/1991	20-150	61.9	340.6	1,979	1,321	1,304	CHZCM
INLET	U-19f	19-57-024	556107.4	4119811.5	11/20/1975	200-1,000	110.4	607.0	2,053	1,234	1,351	CHZCM
JEFFERSON	U-20ai	20-57-011	549637.4	4124115.4	04/22/1986	20-150	63.2	347.5	1,982	1,375	1,353	CHLFA3
JORUM	U-20e	20-57-035	547789.2	4129655.1	09/16/1969	<1,000	101.2	1,158.8 [h]	1,925	766	1,352	CHZCM
JUNCTION	U-19bg	19-57-020	556762.5	4125085.1	03/26/1992	20-150	62.8	345.4	2,040	1,418	1,394	PLFA
KAPPELI	U-20am	20-57-015	552255.8	4124536.0	07/25/1984	20-150	62.4	343.0	2,010	1,369	1,358	CHLFA4
KASH	U-20af	20-57-008	548415.6	4126054.3	06/12/1980	20-150	62.2	645 [h]	1,939	1,294	1,355	CHLFA2
KASSERI	U-20z	20-57-046	552160.3	4127007.8	10/28/1975	200-1,000	99.0	544.4	1,984	719	1,363	BFCU
KEARSARGE	U-19ax	19-57-015	561462.5	4127859.1	08/17/1988	100-150	63.0	615.7 [h]	2,129	1,514	1,433	KA
KERNVILLE	U-20ar	20-57-020	546832.3	4129681.9	02/15/1988	20-150	65.0	541.6 [h]	1,926	1,384	1,345	TMLVTA
LABQUARK	U-19an	19-57-010	561381.3	4128183.1	09/30/1986	20-150	63.0	346.3	2,127	1,511	1,430	KA
LOCKNEY	U-19aq	19-57-011	555471.5	4120144.1	09/24/1987	20-150	63.0	614.2 [h]	2,072	1,458	1,351	PLFA

Table D-1
Central and Western PM Underground Nuclear Test Information
(Page 3 of 4)

Test Name [a]	Hole Name [a]	CAS No. [b]	Easting (m) [c]	Northing (m) [c]	Date [a]	Yield Range (kt) [a]	R_c (m) [d]	Chimney Height (m) [e]	Surface Elevation (m amsl) [c]	WP Elevation (m amsl) [a]	WT Elevation (m amsl) [f]	HSU at WP [g]
MAST	U-19u	19-57-032	560207.3	4133751.4	06/19/1975	200-1,000	107.5	591.3	2,095	1,184	1,417	BRA
MONTELLO	U-20bf	20-57-032	549522.5	4122042.6	04/16/1991	20-150	62.3	342.8	1,988	1,346	1,336	CHZCM
MUENSTER	U-19e	19-57-023	559100.9	4127774.9	01/03/1976	200-1,000	95.6	525.9	2,109	657	1,423	BRA
NEBBIOLO	U-19ae	19-57-005	555867.1	4121059.1	06/24/1982	20-150	62.4	343.0	2,065	1,426	1,351	PLFA
PANIR	U-19yS	19-57-035	556975.7	4125472.6	08/31/1978	20-150	61.4	337.7	2,040	1,359	1,396	PLFA
PEPATO	U-20ad	20-57-006	548286.3	4126944.5	06/11/1979	20-150	61.4	337.5	1,940	1,258	1,358	CHZCM
PIPKIN	U-20b	20-57-027	549594.5	4123294.0	10/08/1969	200-1,000	118.1	623.6 [h]	1,992	1,368	1,349	CHLFA3
POOL	U-19p	19-57-029	559541.6	4123266.9	03/17/1976	200-500	86.0	473.0	2,103	1,222	1,416	BFCU
REX	U-20h	20-57-038	550196.5	4124975.2	02/24/1966	19	30.30 [h]	166.7	1,999	1,327	1,356	CHZCM
RICKEY	U-19c	19-57-021	560769.4	4124276.5	06/15/1968	20-200	67.5	683.4 [h]	2,143	1,460	1,431	CFCU
SCOTCH	U-19as	19-57-013	555856.8	4125370.8	05/23/1967	155	56.39 [h]	310.1	2,061	1,083	1,390	CFCU
SCROLL	U-19n	19-57-028	555314.0	4132315.3	04/23/1968	<20	41.3	<225.6	2,059	1,833	1,427	CHVTA
SERENA	U-20an	20-57-016	549804.2	4127791.8	07/25/1985	20-150	63.4	348.9	1,970	1,372	1,360	CHLFA3
SERPA	U-19ai	19-57-007	560675.0	4130919.1	12/17/1980	20-150	64.1	352.6	2,055	1,482	1,420	BFCU
SHEEPSHEAD	U-19aa	19-57-001	556415.7	4120269.6	09/26/1979	20-150	62.4	343.0	2,060	1,420	1,353	CHZCM
SLED	U-19i	19-57-026	557922.1	4122637.7	08/29/1968	20-200	66.4	365.4	2,084	1,355	1,394	CHVTA
STINGER	U-19l	19-57-027	561067.8	4131788.3	03/22/1968	20-200	67.9	667.8 [h]	2,062	1,394	1,418	BRA
TIERRA	U-19ac	19-57-003	561575.1	4126107.7	12/15/1984	20-150	62.4	343.0	2,145	1,505	1,442	KA
TOWANDA	U-19ab	19-57-002	559842.4	4122993.4	05/02/1985	20-150	61.9	340.3	2,112	1,451	1,419	BFCU
Western Pahute Mesa (CAU 102)												
BELMONT	U-20as	20-57-021	547764.7	4119233.6	10/16/1986	20-150	63.2	347.8	1,898	1,293	1,281	UPCU
BENHAM	U-20c	20-57-033	546698.7	4120477.7	12/19/1968	1,150	99.00 [h]	544.5	1,914	512	1,272	CHZCM
BUTEO	U-20a	20-57-001	550480.6	4121740.0	05/12/1965	<20	31.2	171.6	1,987	1,292	1,334	CHZCM

Table D-1
Central and Western PM Underground Nuclear Test Information
(Page 4 of 4)

Test Name [a]	Hole Name [a]	CAS No. [b]	Easting (m) [c]	Northing (m) [c]	Date [a]	Yield Range (kt) [a]	R_c (m) [d]	Chimney Height (m) [e]	Surface Elevation (m amsl) [c]	WP Elevation (m amsl) [a]	WT Elevation (m amsl) [f]	HSU at WP [g]
CHATEAUGAY	U-20t	20-57-043	545866.2	4122030.0	06/28/1968	20-200	69.5	382.5	1,903	1,296	1,267	BA
DARWIN	U-20aq	20-57-019	544396.1	4124138.1	06/25/1986	20-150	64.8	548.9 [h]	1,876	1,327	1,299	UPCU
DELAMAR	U-20at	20-57-022	543533.9	4122280.8	04/18/1987	20-150	64.9	544.1 [h]	1,902	1,358	1,282	UPCU
FONTINA	U-20f	20-57-036	545355.1	4124900.2	02/12/1976	200-1,000	99.9	1,218.3 [h]	1,864	646	1,318	CHZCM
GOLDSTONE	U-20ao	20-57-017	546767.8	4121180.0	12/28/1985	20-150	64.8	356.4	1,914	1,365	1,270	BA
HANDLEY	U-20m	20-57-040	541289.6	4128104.3	03/26/1970	>1,000	100.1	1,209.1 [h]	1,799	590	1,408	PBRCM
HORNITOS	U-20bc	20-57-029	545158.2	4123977.7	10/31/1989	20-150	64.4	563.9 [h]	1,873	1,309	1,301	UPCU
KNICKERBOCKER	U-20d	20-57-034	546102.6	4122300.8	05/26/1967	76	46.20 [g]	254.1	1,906	1,273	1,270	BA
MOLBO	U-20ag	20-57-009	547672.0	4119690.1	02/12/1982	20-150	62.4	343.2	1,900	1,262	1,281	BA
PURSE	U-20v	20-57-044	544266.8	4126168.6	05/07/1969	20-200	69.8	598.6 [h]	1,856	1,257	1,350	UPCU
SALUT	U-20ak	20-57-013	545315.3	4122286.8	06/12/1985	20-150	63.2	347.4	1,900	1,292	1,270	BA
STILTON	U-20p	20-57-042	542263.8	4132499.9	06/03/1975	20-200	66.4	365.1	1,695	963	1,421	PBRCM
TAFI	U-20ae	20-57-007	546343.1	4123232.0	07/25/1980	20-150	61.4	680.3 [h]	1,886	1,206	1,291	UPCU
TENABO	U-20bb	20-57-028	544857.9	4122285.2	10/12/1990	20-150	63.4	348.5	1,898	1,298	1,273	PBPCU
TYBO	U-20y	20-57-045	546651.3	4119290.9	05/14/1975	200-1,000	112.2	765 [h]	1,907	1,142	1,277	TSA

[a] NNSA/NFO, 2015
[b] FFACO (1996, as amended)
[c] Navarro, 2021 (UTM, Zone 11, NAD 27)
[d] Calculated based on the maximum of the unclassified yield range (minimum for HANDLEY) in NNSA/NFO (2015) and Equation 1 in Pawloski (1999); or measured when yield is specified in NNSA/NFO (2015) as reported in Carle et al. (2021).
[e] Carle et al. (2021)
[f] Fenelon et al. (2016)
[g] DOE/EMNV (2020)
[h] Measured result reported in Carle et al. (2021).

D.2.0 References

Carle, S.F., A.F.B. Tompson, and M. Zavarin. 2021. *Review of Cavity Radius and Chimney Height Information for Underground Nuclear Tests at Nevada National Security Site*, LLNL-TR-818725. Livermore, CA: Lawrence Livermore National Laboratory.

DOE/EMNV, see U.S. Department of Energy Environmental Management Nevada Program.

FFACO, see *Federal Facility Agreement and Consent Order.*

Federal Facility Agreement and Consent Order. 1996 (as amended March 2010). Agreed to by the State of Nevada; U.S. Department of Energy, Environmental Management; U.S. Department of Defense; and U.S. Department of Energy, Legacy Management. Appendix VI, which contains the Underground Test Area Strategy, was last modified June 2014, Revision No. 5.

Fenelon, J.M., K.J. Halford, and M.T. Moreo. 2016. *Delineation of the Pahute Mesa-Oasis Valley Groundwater Basin, Nevada*, Version 1.1, Scientific Investigations Report 2015-5175. Carson City, NV: U.S. Geological Survey.

NNSA/NFO, see U.S. Department of Energy, National Nuclear Security Administration Nevada Field Office.

Navarro. 2021. Written communication. Subject: "UGTA Borehole Index Database," UGTA Technical Data Repository Database Identification Number UGTA-4-127. Las Vegas, NV. As accessed on 14 June.

Pawloski, G.A. 1999. *Development of Phenomenological Models of Underground Nuclear Tests on Pahute Mesa, Nevada Test Site-BENHAM and TYBO*, UCRL-ID-136003. Livermore, CA: Lawrence Livermore National Laboratory.

U.S. Department of Energy, Environmental Management Nevada Program. 2020. *Pahute Mesa-Oasis Valley Hydrostratigraphic Framework Model for Corrective Action Units 101 and 102: Central and Western Pahute Mesa, Nye County, Nevada*, Rev. 0, DOE/EMNV--0014.

U.S. Department of Energy, National Nuclear Security Administration Nevada Field Office. 2015. *United States Nuclear Tests, July 1945 through September 1992,* DOE/NV-209, Rev. 16. Las Vegas, NV.

Appendix E

PM CAU Flow and Transport Model Code Selection and Preprocessor Development

E.1.0 Code Selection

The code selection process and final selection of the codes are presented in this appendix. The choice of codes to perform the CAU modeling for Phase II PM was based on previous experience and a desire to move some of the modeling into COTS codes with the expectation of long-term code maintenance.

A preprocessor code was written as part of this work. The development and testing of the preprocessor is presented in this appendix.

E.1.1 Flow Model Code Selection

The attributes and capabilities of the CAU model were defined to satisfy the modeling objectives (DOE/NV, 1999, Section 5.1.2). The Phase II CAIP (NNSA/NSO, 2009, Section 5.2) stated that the Phase II modeling would use the same codes as were selected for Phase I. In the update to the CAIP (DOE/EMNV, 2020, Table A-1) a desire was expressed to replace the Phase I flow simulator with a more modern COTS code.

The CAU model is expected to have the ability to represent the important physical and chemical features of the CAU groundwater flow system. The features include faulting, stratigraphy, sources and sinks of water, the distribution of contaminants and their rates of introduction into the groundwater flow system, and other physical or chemical features unique to the CAU. The second objective requires the CAU model to simulate the movement of a variety of contaminants whose distribution and abundance serve to define the CB. The third objective requires flexibility in the CAU model to allow grid changes, placement of additional wells, and boundary condition variations. Each of these attributes will be described and assessed with respect to importance for the CAU modeling. In addition, six nonessential but desirable attributes were identified. These include finite-element formulation, steady-state capability, double-porosity/double-permeability formulation, the ability to simulate the transport of multiple solutes and daughter products, and established preprocessors and postprocessors.

E.1.1.1 General Attributes

E.1.1.1.1 Fully 3-D

The groundwater flow system is controlled by the distribution of geologic units as well as the location of sources and sinks of water. Additionally, transport properties including source location and strength, porosity, and diffusion may vary in space. The 3-D nature of the groundwater flow system means that the CAU model will need to be 3-D to adequately simulate migration of the potential contaminants within the CAU-model area.

E.1.1.1.2 Large Numbers of Nodes Capability

For a given formulation, the greater the number of nodes in the CAU model, the greater the detail that can be included. Given the large geographic area of the PM CAU model, the ability of the CAU model to simulate many nodes will control the amount of detail that can be included. In general, each of the selected codes will be limited only by the capacity of the hardware, not by the software used.

E.1.1.1.3 Multiple Boundary Condition Options

Options for specified pressure and specified flux boundary conditions for fluids may be required in implementing the CAU model. While there was initial interest in modeling both flow and temperature, subsequent experience has shown that modeling of temperature is not required at the CAU scale. Non-isothermal simulations have proven useful at small scales, including for simulating the cavity/chimney and near-field environment, but those temperature dependencies are not significant at the CAU scale where transport is forecast over distances of tens of kilometers under ambient groundwater flow conditions.

E.1.1.1.4 Transient Capability

The initial flow simulations for the CAU model will be steady-state with possible transient runs to follow. The CAU modeling has used transient simulation to calibrate to transient water-level responses observed during MWATs. The ability to simulate transient responses is important for building model confidence. Transient contaminant transport simulations are performed using the calibrated steady-state flow fields.

E.1.1.1.5 Efficient Solver

To simulate in sufficient detail, the CAU model will require a large number of nodes as mentioned above. To make a large model practical, the codes must run efficiently. Generally, a code has a selection of solvers available. The process of model calibration and Monte Carlo analysis for CB forecasts can require thousands or even tens of thousands of runs. The solvers must be efficient enough to allow for reasonable simulation times.

E.1.1.1.6 Acceptable Numerical Accuracy

The numerical solution of the transport equation is typically more difficult than the solution of the flow equation. This attribute requires the results of the code for a given test problem to have been checked against analytical solutions and results of other numerical codes for the same problem. Documentation of this QA checking must be available.

E.1.1.1.7 Minimal Numerical Dispersion

Under certain circumstances, the error in the numerical approximation of a value can become as large as the value being approximated. When this occurs, the numerical solution combines an exclusively numerical dispersion with the real hydrodynamic dispersion, producing an overestimate of the actual dispersion. Solution techniques that minimize numerical dispersion are required.

E.1.1.1.8 Acceptable Verification and Validation

The degree of computer code verification and validation varies widely depending on the code being considered. The extent to which this process has been documented for a particular code varies even more. Thoroughly documented testing is required to ensure that the code satisfies requirements specified for its options and features.

E.1.1.1.9 Access to Source Code

Computer codes are initially written by humans in a high-level language such as FORTRAN and then translated into machine language for execution on the computer. The high-level version of the code is called the “source code” and can be read and modified by humans. The machine-language version is called the “executable code” and can be deciphered only by the computer. Many distributors of

computer codes provide only the executable version of the code to the user. During the course of the development or application of the CAU model, it may be necessary to examine or modify the step-by-step procedure implemented.

E.1.1.2 Groundwater Flow Model Attributes

E.1.1.2.1 Saturated Groundwater Flow

The codes must be able to simulate saturated groundwater flow. Heterogeneous and anisotropic hydraulic conductivity aquifer heterogeneity reflects the natural variability in the subsurface. The CAU model must be capable of simulating flow through aquifers in which the hydraulic conductivity may vary from location to location. Anisotropy is a directional dependence of the hydraulic conductivity. In fractured aquifers, it is common for hydraulic conductivity to be larger in a direction parallel to fracturing and smaller perpendicular to fracturing.

E.1.1.2.2 Point and Distributed Sources and Sinks of Water

Recharge may occur over a large spatial area due to precipitation or may be concentrated into washes or craters. Discharge may occur at wells or individual springs or may occur over larger areas such as playas. The CAU model should have the capability to simulate these various cases.

E.1.1.2.3 Temperature Dependence

The flow of groundwater may be influenced by water temperature variations. Warm water is more buoyant than colder water and tends to rise. Additionally, warm water is less viscous and tends to move more easily than cold water. These processes may be important in some portions of the CAU where naturally occurring sources of heat have caused elevated groundwater temperatures. It does not appear necessary to simulate temperature-dependent flow at the CAU scale, and temperature dependent simulation was not considered an important attribute.

E.1.1.2.4 Simulate Complex Geology

The geology of the PM area is complex. It consists of multiple stratigraphic units, some of which are truncated by faults and other structural features. Even within units, changes in facies result in spatial variations in material properties. The flow of groundwater (amount and direction) is governed in large

part by the distribution of geologic units. The code must be able to include important features of the geology such as lateral and vertical changes in material properties. Much of this attribute is similar to earlier general attributes related to the number of grid nodes and simulation speed. The greater the number of nodes, the more detail can be incorporated into the CAU model.

E.1.1.3 Transport Model Attributes

E.1.1.3.1 Advection, Dispersion, Sorption, and Matrix Diffusion

It is expected that advection (via the groundwater flux) and matrix diffusion (via dual porosity) will be the primary factors influencing ^{3}H and other RN transport. It is expected that sorption will also be important for reactive contaminants. Dispersion, both longitudinal and transverse, is included because it can modify the concentrations within, and the spatial extent of, a contaminant plume.

E.1.1.3.2 Radioactive Decay

The potential contaminants of interest are RNs that transform identity according to the laws of radioactivity decay; the SDWA regulations apply to the specific identity of the RNs.

E.1.1.3.3 Daughter Products

An RN may decay into another RN (called a daughter product) or into a stable isotope. More accurate estimates of dose can be obtained if the code is capable of simulating the ingrowth and transport of an RN and daughter product(s). Kersting et al. (2003) evaluated the impact of radioactive decay daughter products and concluded that, over the 1,000-year time frame of interest and for RNs that are of interest to the PM CAU model, RN daughter products do not need to be included as additional members of the RN inventory.

E.1.1.4 Desirable Attributes

These are attributes of the computer codes that were considered valuable but not essential to satisfying the CAU-modeling objectives.

E.1.1.4.1 Finite-Element Formulation

A finite-element formulation was not used for the CAU modeling because the selected flow code, MODFLOW6, uses a finite-difference formulation. However, MODFLOW6 allows variable grid resolution, so complex structures such as faults and finite extent of HSU can reasonably be accommodated. For the PM model, successful models have been developed that are based on finite-difference formulations.

E.1.1.4.2 Steady-State Capability

Some of the codes simulate the time-dependent flow equations and reach steady state by performing transient simulations over large periods of time until steady state is reached, while some codes directly simulate the steady-state flow equations.

E.1.1.4.3 Double-Porosity/Double-Permeability Formulation

The double-porosity/double-permeability method is similar to the double-porosity method in that it allows for communication between fractures and matrix material. The term “dual porosity/dual permeability” is often used in the literature. In this report, “dual” is used interchangeably with “double,” depending on the usage in the model documentation. This feature allows for the modeling of matrix diffusion. The double-porosity/double-permeability method differs in that it allows matrix cells that communicate with fractures to also communicate with other matrix cells. While this method provides a more realistic simulation, its use is more important for unsaturated flow problems, which are not included in the PM CAU model. Of more importance for the PM CAU model is the ability to simulate matrix diffusion using a dual-porosity approach.

E.1.1.4.4 Multiple Solutes

Many codes are designed to provide a simulation of the migration of a single solute in a given run. Using a code with the ability to model transport for multiple solutes in a single run may be more efficient.

E.1.1.4.5 Established Preprocessors and Postprocessors

For complex models such as the PM CAU model, the task of input/output can consume significant resources. The task of creating the input datasets for any model is simplified by having preprocessors that take data and put it into a form that is required by the model. Postprocessors are essential as they provide ways to have meaningful evaluation and visualization of the output of the model. Postprocessors take model output and typically create graphic images of some simulated parameter such as water level or solute concentration. Pre- and postprocessors generally speed up the modeling task.

E.1.1.5 History of Code Selection for the PM CAU

Through the Phase I modeling process, the code selection process was followed and resulted in the selection of the following three codes for the Phase I PM CAU model. The Phase I flow model was based on LANL's Finite Element Heat and Mass Transfer (FEHM) code FEHM (Zyvoloski, 2007) with SPTR as the particle tracking option and selected transport models included the COTS code GoldSim (2018) and the LANL convolution integral code PLUMECALC (Robinson et al., 2011). These codes have been applied successfully to the Frenchman Flat, Rainier Mesa, and YF/CM CAU models. The modeling process as implemented used the transient flow capability of FEHM to evaluate transient well responses and then ran the model to a steady-state solution for particle tracking. The particle tracking was implemented on a tetrahedral mesh to produce pathlines from any number of starting locations. The pathlines were calculated internal to FEHM using the subroutine SPTR. The pathline process used by FEHM-sptr is unique in that the pathlines add a random walk component to account for 3-D dispersion. For transport, a cloud of particles are assigned starting locations at the source, and their future positions are forecast using the advection from its current location with a random walk dispersive displacement. This process is repeated for all particles throughout the flow system. The particle paths are passed to PLUMECALC, where mass is assigned to each particle; and the processes of radioactive decay, matrix diffusion, and sorption to solids are allowed to change the mass of each particle over time. At any location and time, the mass in a cell volume is the sum of the particle masses, and concentrations are obtained by dividing by the mobile or fracture water volume of the cell. The combination of codes identified in Phase I met the code selection criteria for Frenchman Flat, YF/CM, and Phase I of PM.

E.1.1.6 Code Selection for the Phase II PM CAU Modeling

During planning for the Phase II PM CAU model, and as noted in the update to the CAIP (DOE/EMNV, 2020) the decision was made to select the USGS MODFLOW6 code as the flow simulation code for the PM CAU model. MODFLOW6 was chosen because it is the most recent version of MODFLOW and the only version USGS plans to support into the future. MODFLOW6 provides the transient and steady-state flow simulation capability as well as the ability to simulate with heterogeneous and anisotropic hydraulic conductivity.

PM transport modeling requires codes that have low numerical dispersion, so the particle-tracking approach was selected. The MODFLOW suite of codes lacks a particle-tracking simulator capable of incorporating dispersion. For this reason, the code Walkabout was selected for simulating the advection and dispersion processes. The convolution integral based transport model PLUMECALC was retained because it has been well-received by both DOE and NDEP for the Frenchman Flat, YF/CM, and PM Phase I modeling. It was felt that continuity of the transport modeling approach and presentation was important for the last of the UGTA CAUs.

The choice of model codes, however, presented a challenge. MODFLOW6 was implemented using a grid configuration that allows for grid refinement in a rectangular mesh. This still retains the block-centered mesh and solution scheme in MODFLOW6. However, Walkabout works from a tetrahedral node-centered solution approach. To allow Walkabout to simulate transport along pathlines from MODFLOW6, one existing code and a new utility code were introduced. To produce a continuous tetrahedral grid from the MODFLOW grid, vertices were connected with tetrahedral elements using the Los Alamos Grid Toolbox (LaGriT) meshing software.

To replace the particle tracking and random walk dispersion provided by the SPTR subroutine in FEHM, the LANL code Walkabout (Painter, 2011) was introduced. Walkabout is a particle-tracking code also based on a tetrahedral node-centered approach. Pathlines from Walkabout provide the same downgradient advection and dispersion particle positions as obtained previously through FEHM-sptr. LANL provided the most recent version of Walkabout, a version that was used to support the recent AMANZI modeling reported in Lu et al. (2021).

The new code developed as part of this work was a preprocessor utility code, named MF6-Walkabout, to process the output of flow simulations from MODFLOW6 and create the input files required for Walkabout.

E.2.0 MF6-Walkabout Development and Testing

E.2.1 Summary

A methodology to process the MODFLOW6 output for simulations with Walkabout was developed. A preprocessor based on the methodology was also developed along with a correction algorithm to enhance the accuracy of velocity estimates near the domain boundary. The preprocessor is intended to be used to generate input files for Walkabout using output from MODFLOW6. The preprocessor was verified by using an output from a MODFLOW6 run to generate input files for Walkabout.
A Walkabout run based on the generated input files yielded results that agree favorably with a known solution. The developed methodology is general and applicable to all MODFLOW cell types.

E.2.2 Overview and Objectives

As noted in the previous section, one of the challenges for the utilization of output from MODFLOW6 for transport simulations using PLUMECALC was calculating particle paths. including dispersion. A possible candidate particle path simulator that includes dispersion is Walkabout (Painter, 2011). Because the current output from MODFLOW6 is not compatible with input requirements for Walkabout, a methodology to translate the output from MODFLOW was developed. A preprocessor based on the methodology was subsequently developed. Both are documented in this appendix.

MODFLOW6 and Walkabout are briefly described in Section E.3.0. The methodology is presented in Section E.4.0. Input file configurations for the preprocessor are described in Section E.5.0. References are presented in Section E.6.0.

E.3.0 MODFLOW and Walkabout

Brief descriptions of the two codes are given below.

E.3.1 MODFLOW

MODFLOW is a modular groundwater flow model developed by the USGS (Harbaugh et al., 2000) and has been used and improved over time. A new version of MODFLOW, called MODFLOW6, has recently been released (Langevin et al., 2017). The Groundwater Flow (GWF) Model for MODFLOW6 is based on a generalized control-volume finite-difference approach in which a cell can be hydraulically connected to any number of surrounding cells. Users can define the model grid using one of three discretization packages: (1) a structured discretization package for defining regular MODFLOW grids consisting of layers, rows, and columns; (2) a discretization by vertices package for defining layered unstructured grids consisting of layers and cells; and (3) a general unstructured discretization package for defining flexible grids comprising cells and their connection properties. For layered grids, a new capability is available for removing thin cells and vertically connecting cells overlying and underlying the thin cells. The GWF model is divided into “packages,” as was done in previous MODFLOW versions. A package is the part of the model that deals with a single aspect of simulation. Packages with the GWF model include those related to internal calculations of groundwater flow (discretization, initial conditions, hydraulic conductance, and storage), stress packages (constant heads, wells, recharge, rivers, general head boundaries, drains, and ET), and advanced stress packages (streamflow routing, lakes, multiple-aquifer wells, and unsaturated zone flow). An additional package is also available for moving water available in one package into the individual features of the advanced stress packages. A newly developed particle tracking code, MODPATH7 (Pollock, 2016), is compatible with MODFLOW6 with quad tree refinement; however, the current version of MODPATH7 does not deal with dispersion.

E.3.2 Walkabout

Walkabout Version 1.2 (Painter, 2011) is a computer code that performs random walk particle-tracking simulations of solute transport including advection and dispersion based on groundwater flow solutions that use fully unstructured control volume grids. Walkabout 1.2 is designed to work within the FEHM (Zyvoloski, 2007) code system, and accepts groundwater flow solutions from

FEHM and computational mesh descriptions from LaGriT (LANL, 2011). Walkabout also provides input to the PLUMECALC (Robinson et al., 2011) particle-tracking postprocessor. Although designed to work within the FEHM system, other control-volume flow codes and mesh generators could, with appropriate reformatting of the output, provide the flow fields and mesh descriptions. A typical workflow for Walkabout within the FEHM system would use LaGriT to generate unstructured grids. FEHM then provides a discretized representation of the steady-state flow field to Walkabout. Given this discrete solution, Walkabout then reconstructs a groundwater flow field, and performs the random walk particle-tracking calculation. Output is provided in a form compatible with the PLUMECALC software. PLUMECALC may be used to efficiently postprocess the particle-tracking results from Walkabout to add effects of retention/retardation and arbitrary source histories. An option exists to also record particle positions versus time, thus allowing other postprocessing codes or visualization systems to be used.

E.3.3 Incompatibility between MODFLOW6 and Walkabout

MODFLOW6 simulation is based on connectivity between cell centroids. Examples of MODFLOW cells are given in Figures E-1a, E-1b, and E-1c. There are three types of MODFLOW cells: a basic cell with eight vertices (Figure E-1a), a cell with identical vertices in the upper and lower cell surfaces (Figure E-1b), and an unstructured discretization (DISU) cell with irregular vertices (Figure E-1c). Simulation results are associated with hydraulic heads at cell centroids. Based on the heads and connectivity, areal fluxes on cell faces are determined by MODFLOW6. However, Walkabout requires velocities at cell vertices (see vertices in Figures E-1a, E-1b, and E-1c). In addition, Walkabout requires that the domain of interest be discretized with tetrahedral elements (Figure E-2). Therefore, a given MODFLOW cell must be subdivided into contiguous tetrahedral elements (see example in Figure E-3). A methodology presented in Sections E.4.0 and E.5.0 addresses the transformation of information from MODFLOW cells to vertex velocities or nodal velocities. The methodology is general and applicable to all MODFLOW cell types.

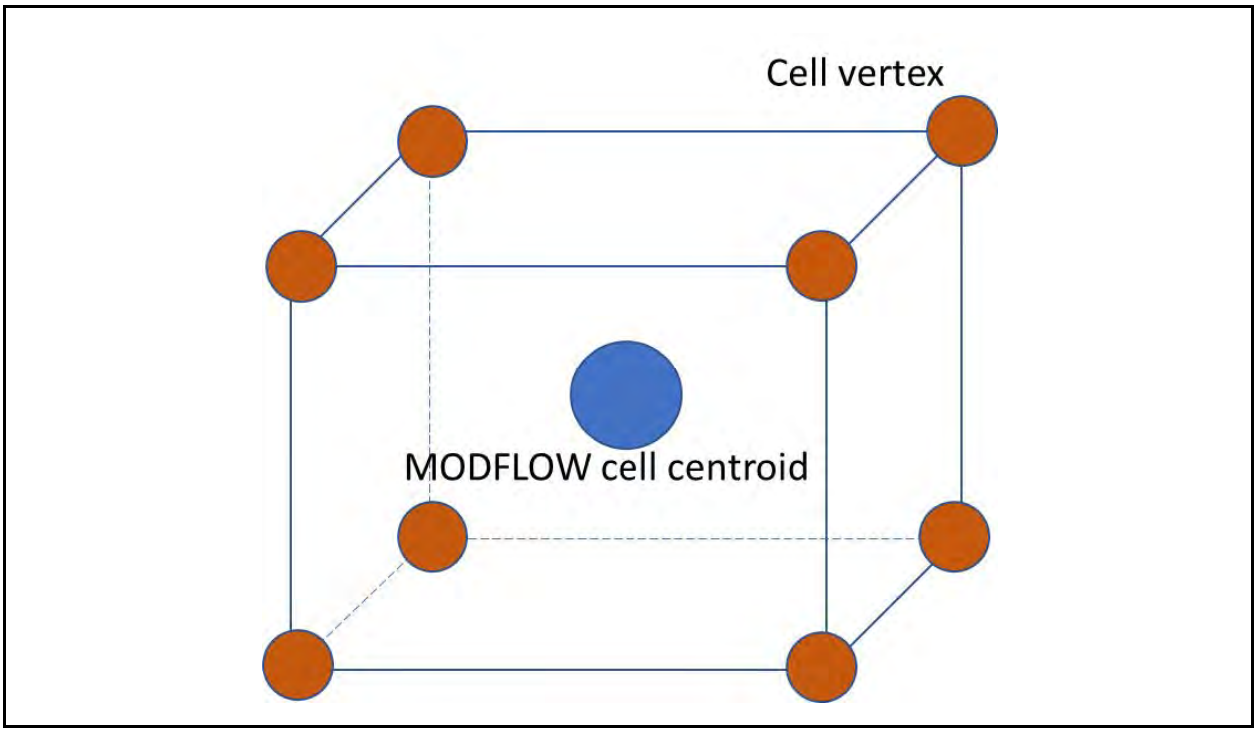

Figure E-1a
MODFLOW Cell (basic cell)

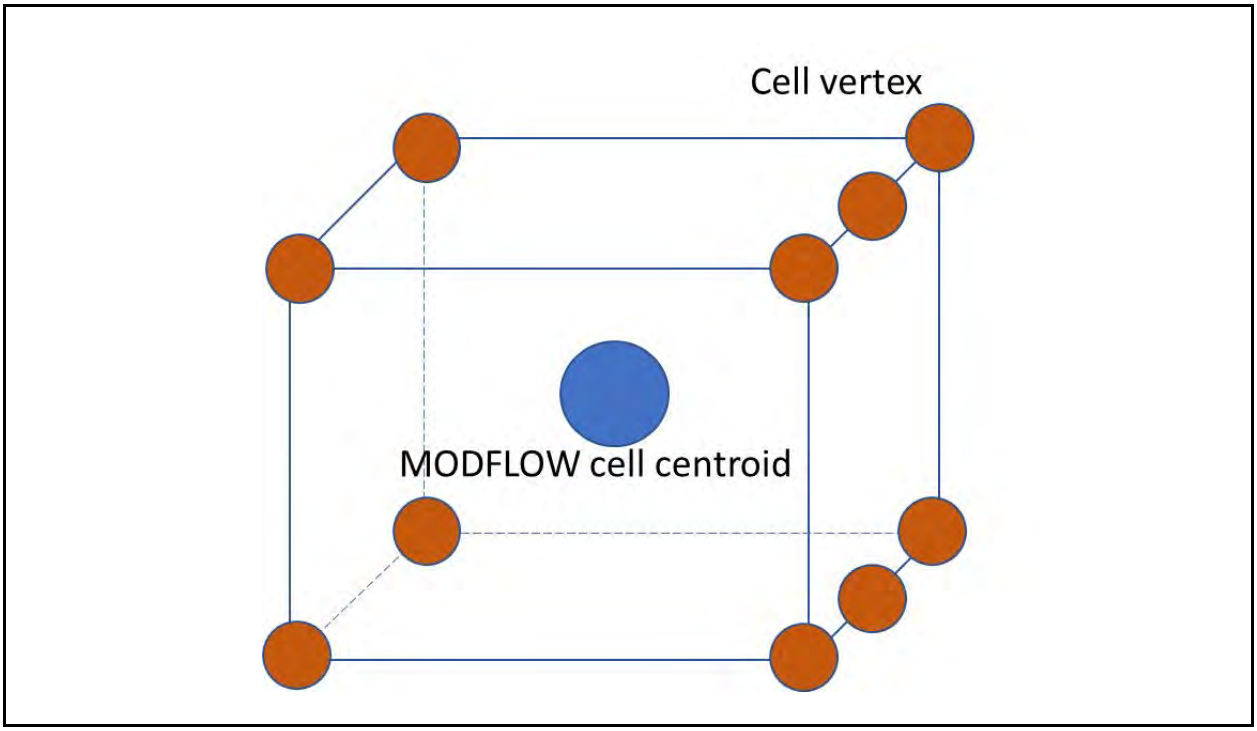

Figure E-1b
MODFLOW Cell

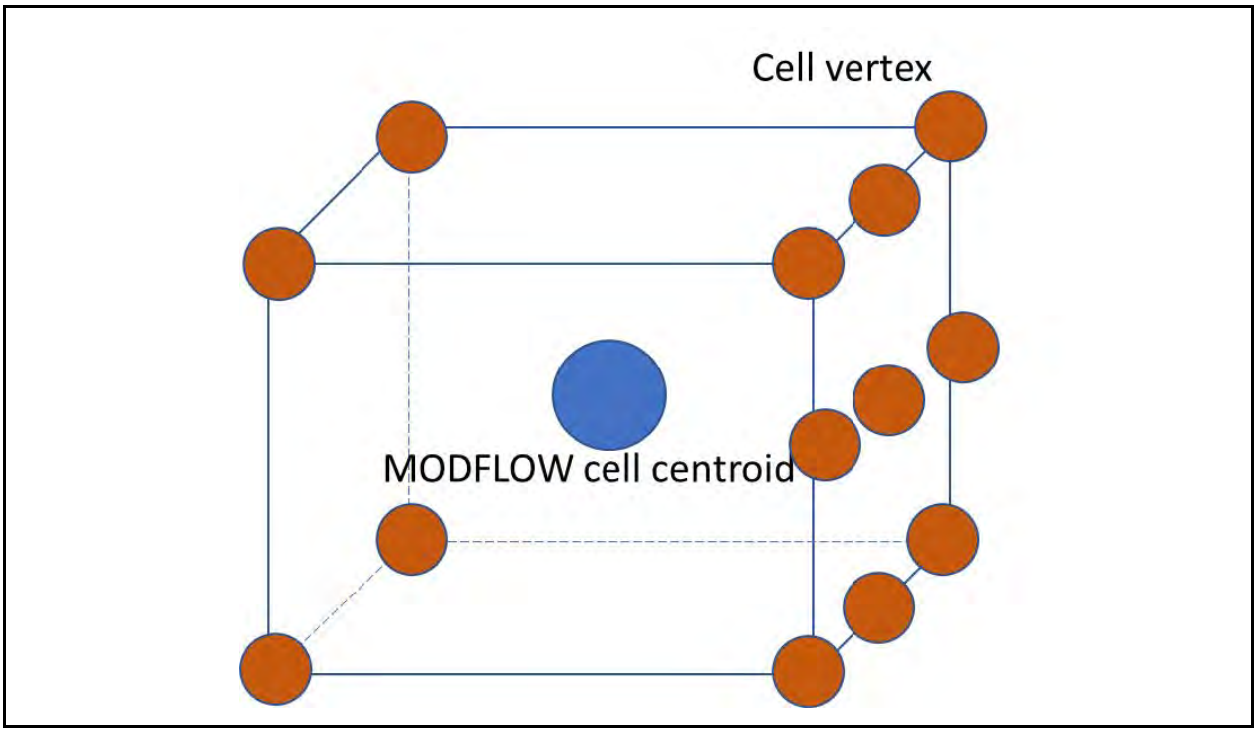

Figure E-1c
MODFLOW Cell (DISU cell)

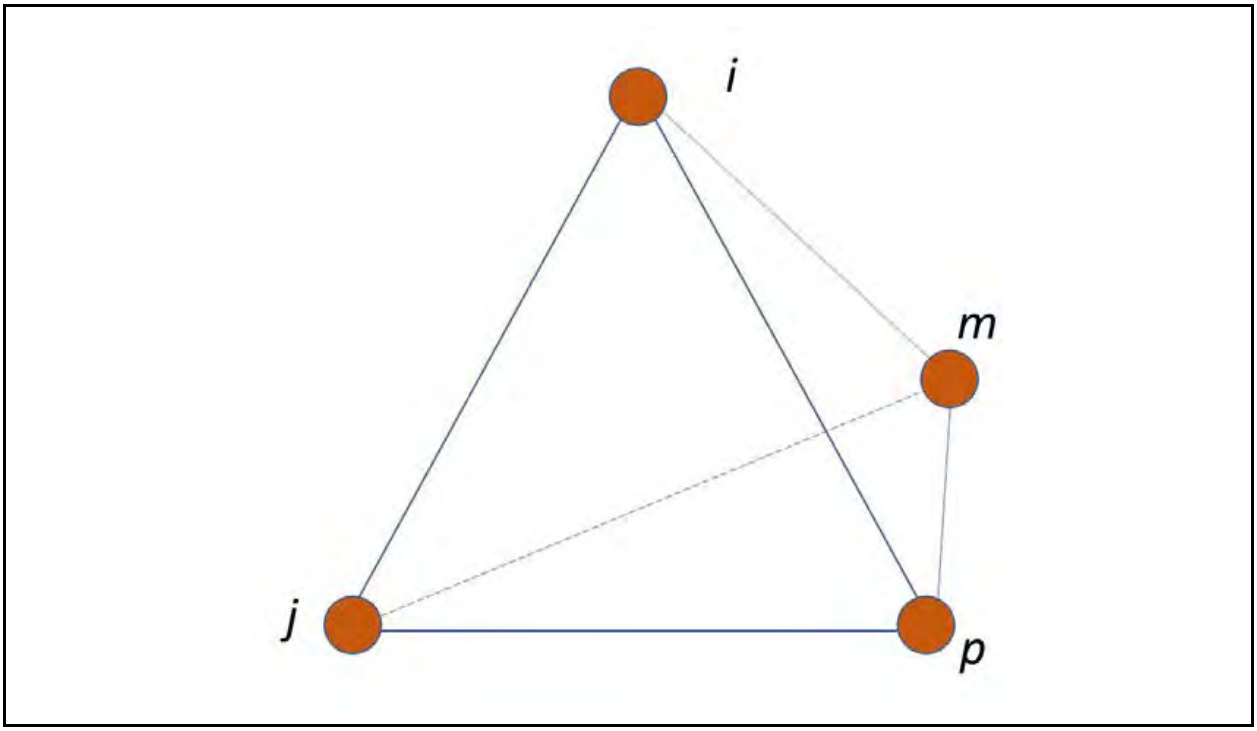

Figure E-2
Tetrahedral Element

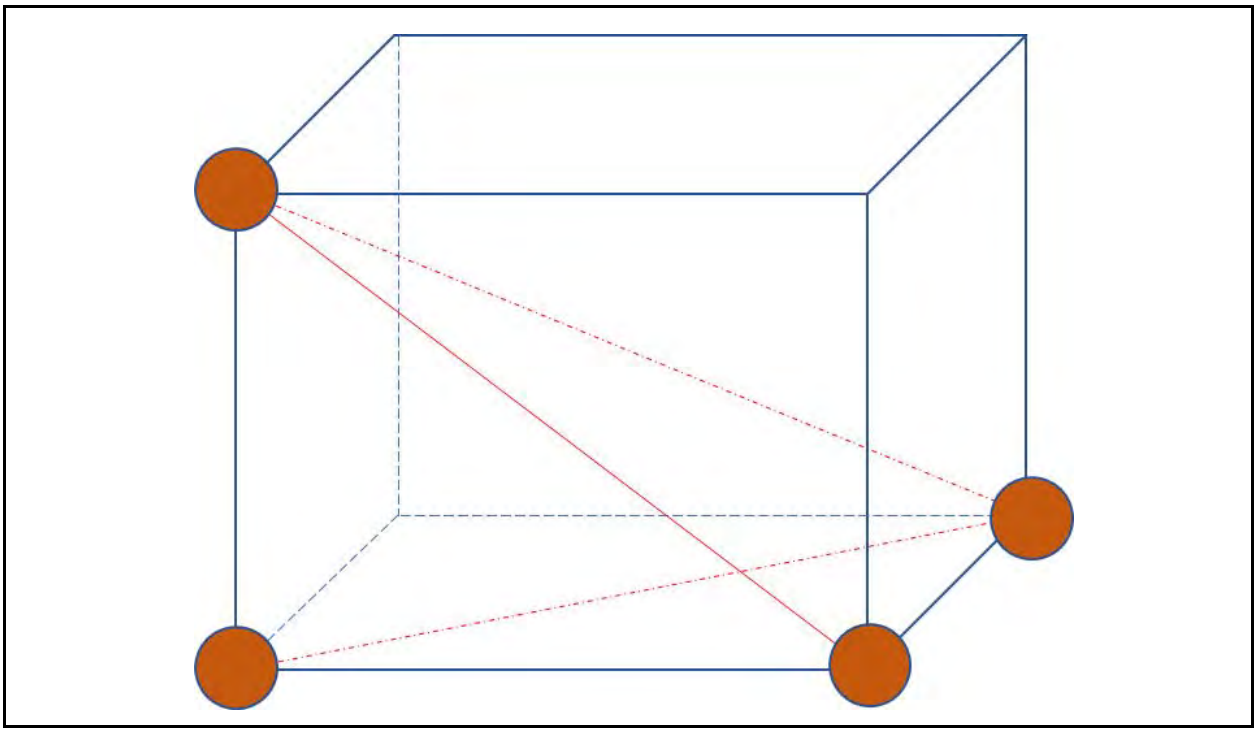

Figure E-3
Subdivision of Hexahedral Element into Tetrahedral Elements
(only one tetrahedral element is shown)

E.4.0 Transfer of Information from Cell Centroids to Cell Vertices

MODFLOW6 calculates hydraulic heads and intercell fluxes at respective cell centroids and across respective cell common faces. To use Walkabout for particle tracking, it is essential that all the information be transferred to the cell vertices. This requirement can be achieved by connecting all the vertices of each MODFLOW cell through tetrahedral subdivision (Figure E-3), thereby transforming the MODFLOW cells into a finite-element mesh with tetrahedral elements.

For each node 'i' of the finite-element mesh, a nodal head (head at a vertex) may be calculated as an average over the cell centroids of the MODFLOW6 cells connected to the node by the equation:

$$H_i = \frac{1}{n_i}\left(\sum_{j=1}^{n_i} H_{ij}\right) \qquad (E\text{-}1)$$

where

H_i = Average head at node *i*
H_{ij} = Head at node *i* due to cell *j*
n_i = Number of cells with node *i* as one of the connected nodes

E.4.1 Calculations of Hydraulic Gradients and Velocities

In each tetrahedral finite element, the variation of head is governed by the equation, using the upper case 'I' to denote the local number of the node with the global number 'i':

$$\widehat{H} = \left(\sum_{I=1}^{4} N_I H_I\right) \qquad (E\text{-}2)$$

where

$\widehat{H}$ = Head at any point (x,y,z) within a tetrahedral element
H_I = Head at node *I*. Here the index uppercase 'I' is being used with respect to the specific finite element under consideration, to corresponding to the global node number 'i' given in Eq. E-1
N_I = Basis function within the element associated with node I of a tetrahedral element

The linear basis function associated with the node I in Equation E-2 is given by Zienkiewicz and Cheung (1967):

$$N_I = a_I + b_I x + c_I y + d_I z$$
$$\sum_{I=1}^{4} N_I = 1 \qquad (E\text{-}3)$$

where

a_I, b_I, c_I, d_I = Constants
x, y, z = Cartesian coordinates

The constants in Equation E-3 in a tetrahedral element defined by nodes with global numbers i, j, m, and p (corresponding to local numbers I, J, M, and P)
(see Figure E-2) are defined by the following:

$$a_I = \frac{1}{6V} det \begin{bmatrix} x_j & y_j & z_j \\ x_m & y_m & z_m \\ x_p & y_p & z_p \end{bmatrix} \quad (E\text{-}4a)$$

$$b_I = \frac{1}{6V} det \begin{bmatrix} 1 & y_j & z_j \\ 1 & y_m & z_m \\ 1 & y_p & z_p \end{bmatrix} \quad (E\text{-}4b)$$

$$c_I = \frac{1}{6V} det \begin{bmatrix} x_j & 1 & z_j \\ x_m & 1 & z_m \\ x_p & 1 & z_p \end{bmatrix} \quad (E\text{-}4c)$$

$$d_I = \frac{1}{6V} det \begin{bmatrix} x_j & y_j & 1 \\ x_m & y_m & 1 \\ x_p & y_p & 1 \end{bmatrix} \quad (E\text{-}4d)$$

$$V = \frac{1}{6} det \begin{bmatrix} 1 & x_i & y_i & z_i \\ 1 & x_j & y_j & z_j \\ 1 & x_m & y_m & z_m \\ 1 & x_p & y_p & z_p \end{bmatrix} \quad (E\text{-}4e)$$

where

det = Determinant
V = Volume of the tetrahedral element

Velocities in the x, y, and z directions, v_{xe}, v_{ye}, and v_{ze}, in tetrahedral element e, defined by nodes i, j, m, and p, with Kx, Ky, Kz hydraulic conductivity in x,y,z directions, are given by

$$v_{xe} = -\frac{K_X}{\theta}\frac{\partial H}{\partial x} \approx -\frac{K_X}{\theta}\frac{\partial \widehat{H}}{\partial x} = -\frac{K_X}{\theta}\sum_{I=1}^{4} b_I H_I \quad (E\text{-}5a)$$

$$v_{ye} = -\frac{K_Y}{\theta}\frac{\partial H}{\partial y} \approx -\frac{K_Y}{\theta}\frac{\partial \widehat{H}}{\partial y} = -\frac{K_Y}{\theta}\sum_{I=1}^{4} c_I H_I \qquad \textit{(E-5b)}$$

$$v_{ze} = -\frac{K_Z}{\theta}\frac{\partial H}{\partial z} \approx -\frac{K_Z}{\theta}\frac{\partial \widehat{H}}{\partial z} = -\frac{K_Z}{\theta}\sum_{I=1}^{4} d_I H_I \qquad \textit{(E-5c)}$$

Velocities at each Node I, v_{xI}, v_{yI}, and v_{zI}, may be obtained by averaging velocities from all tetrahedral elements with Node I.

$$V_{xI} = \frac{1}{n_e}\sum_{e=1}^{n_e} V_{xe} \qquad \textit{(E-6a)}$$

$$V_{yI} = \frac{1}{n_e}\sum_{e=1}^{n_e} V_{ye} \qquad \textit{(E-6b)}$$

$$V_{zI} = \frac{1}{n_e}\sum_{e=1}^{n_e} V_{ze} \qquad \textit{(E-6c)}$$

It is anticipated that velocities in elements along flux boundaries may be inaccurate. This can be circumvented by simply eliminating the boundary elements (see Figure E-4). In the event that the boundary elements are to be retained, the nodal velocities at boundary nodes may be approximated from the immediately interior adjacent nodes, thus:

$$V_{xI}^{Bound} = f_v V_{xI}^{IntAdj} \qquad \textit{(E-7a)}$$

$$V_{yI}^{Bound} = f_v V_{yI}^{IntAdj} \qquad \textit{(E-7b)}$$

$$V_{zI}^{Bound} = f_v V_{zI}^{IntAdj} \qquad \textit{(E-7c)}$$

where:

V^{Bound}_{iI} = Velocity along the i-th direction at the boundary
V^{IntAdj}_{iI} = Velocity along the i-th direction in the adjacent interior node

f_v = Factor applied to velocity components at an immediately adjacent interior node. However, in most cases f_v is equal to 1.

Nodal velocities at boundary nodes in the above equations may be found by extrapolating from interior nodes. Alternatively, they can be determined using known flow conditions along the boundaries.

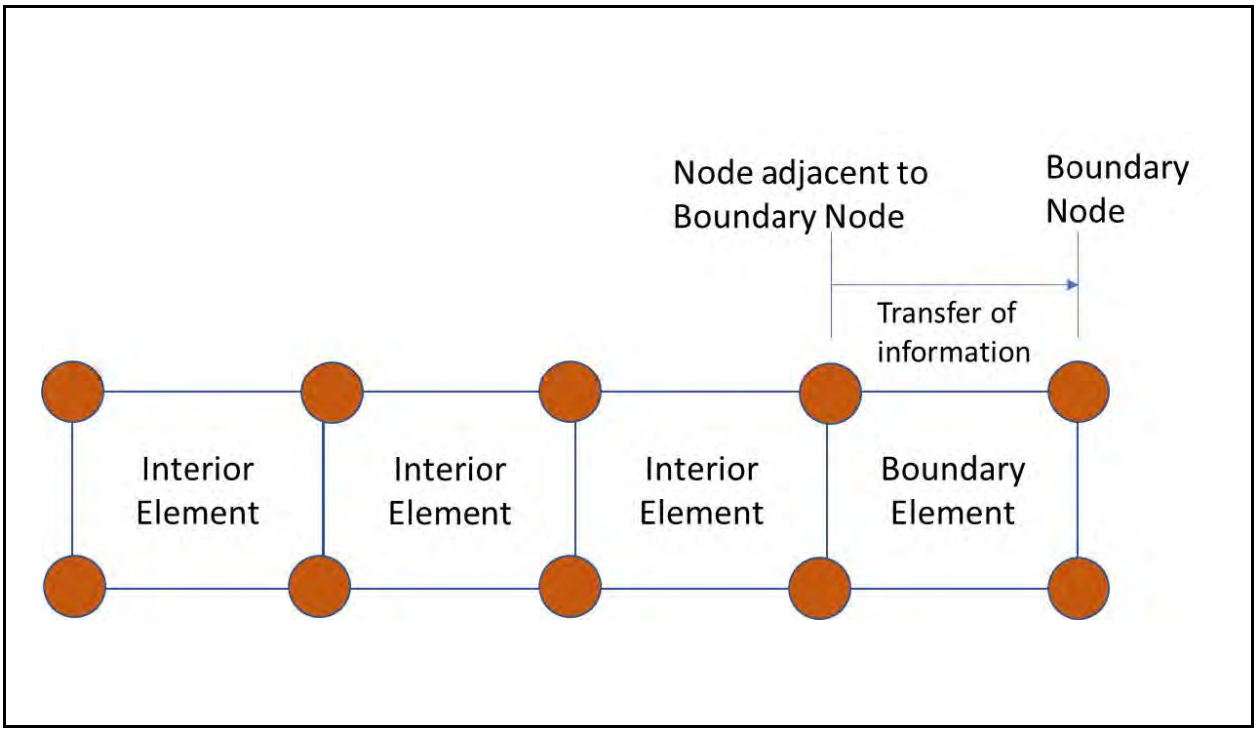

Figure E-4
Treatment of Boundary Nodes and Elements

E.4.2 Transfer of Information from Cell Interface Centroids to Cell Vertices

MODFLOW6 calculates hydraulic heads and intercell fluxes at respective cell centroids and across respective cell common faces. Velocities are calculated using intercell flow across the interface given in the *cbb* file from MODFLOW6. Velocities in x, y, and z directions at each vertex are averaged from velocities from cells connected to the vertex.

An example is shown in Figure E-5. A one-layer system with 4 cells and 10 vertices. Constant head boundaries are prescribed at the centroids of cells 1 and 4. For cells 1 and 4, interface flow rates are

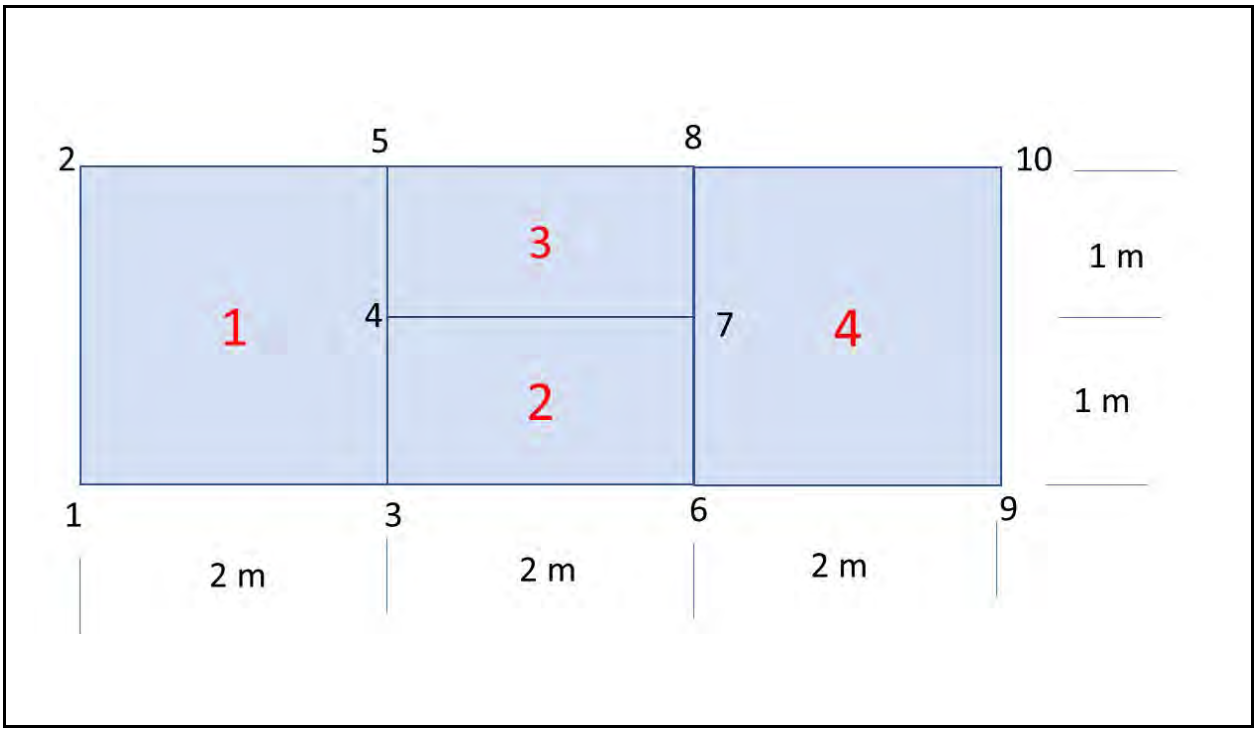

Figure E-5
Typical DISV Cells

provided for only interfaces between cells 1 and 2, 1 and 3, 4 and 2, and 4 and 3. Velocities at vertices 1, 2, 9, and 10 are not known.

E.4.3 Application Example

The preprocessor was verified using a verification example. The domain is of the following dimensions: 12m length, 10m width, and 4m height (see Figure E-6). The domain was discretized with 2m × 2m × 2m cells. Hydraulic and transport properties assigned were a uniform hydraulic conductivity of 10 m/day and a uniform porosity of 0.1. Constant heads of 13m and 12m were assigned to the boundaries at x = 1m and 11m (boundary cell centroids). With this configuration, head varies linearly from left to right (in Figure E-6) with a uniform velocity of 10 m/day.

MODFLOW6 was used to generate fluxes between cells. Flux output from MODFLOW6 was processed by the code to generate the *ama* and *avs* files for Walkabout. A comparison between fluid velocity profiles along the length of the flow domain generated by MODFLOW6 and the code with boundary element correction in Equation E-7 is shown in Figure E-7 with the velocities accurate up to the boundary nodes.

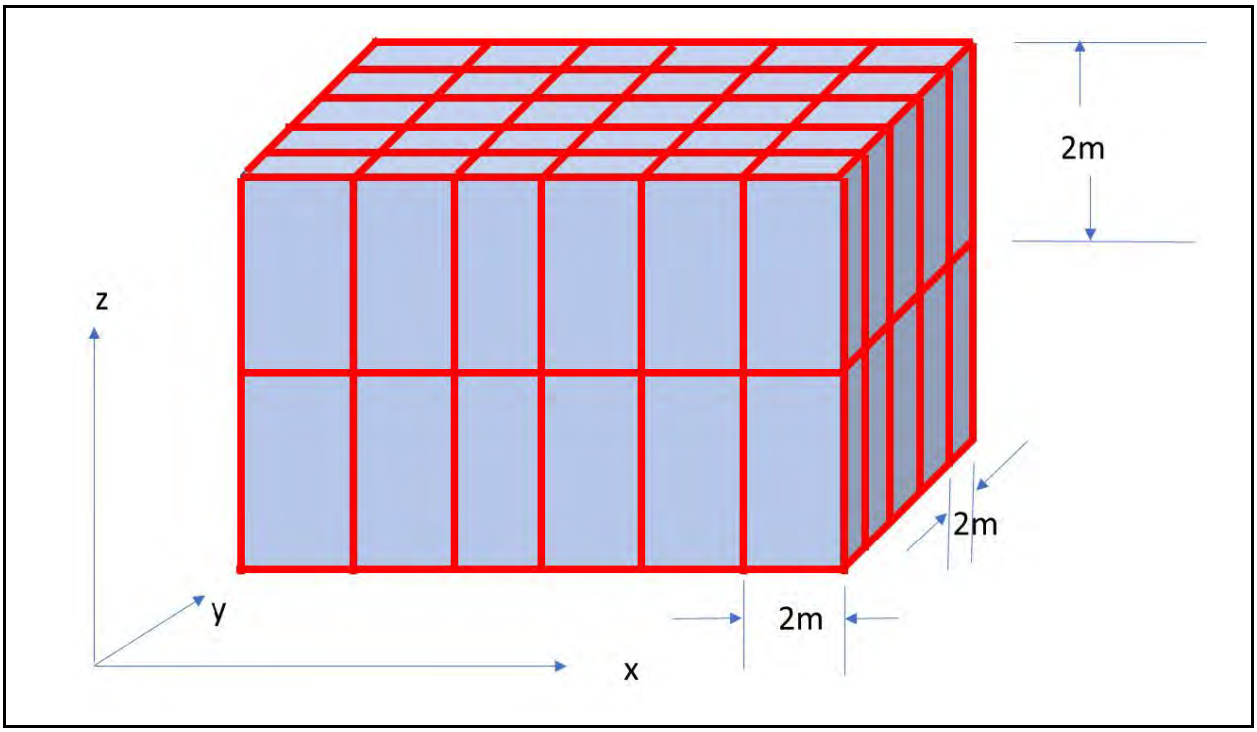

Figure E-6
Flow Domain Discretization: Application Example

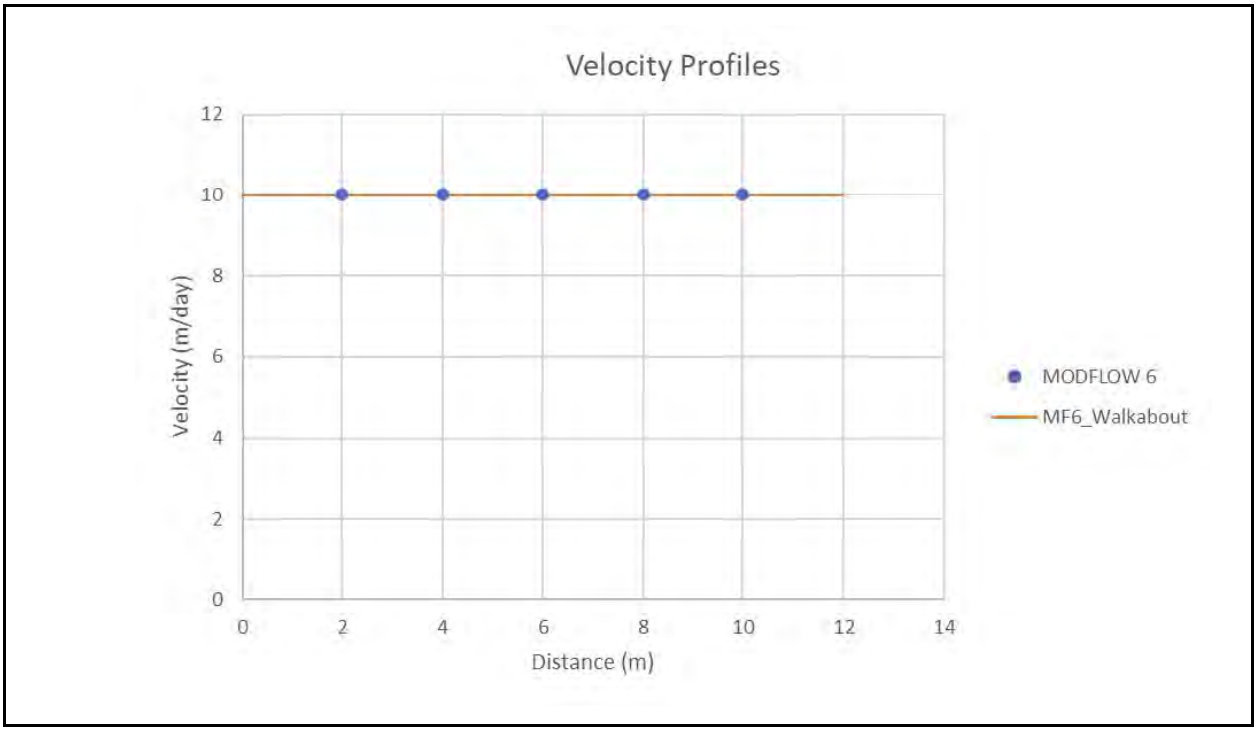

Figure E-7
Comparison of Velocity Profiles

A Walkabout run was performed with six particles. These particles were initially located at (3m, 3m, 1m), (3m, 5m, 1m), (3m, 7m, 1m), (3m, 3m, 3m), (3m, 5m, 3m), and (3m, 7m, 3m). All particles traveled as a straight line in the *x* direction from their respective initial positions. A comparison between the results from Walkabout and a simple analytical is shown in Figure E-8. The analytical solution is given as Equation E-9. As shown in Figure E-8, the particle travel distance simulated by Walkabout agrees favorably with the analytical solution.

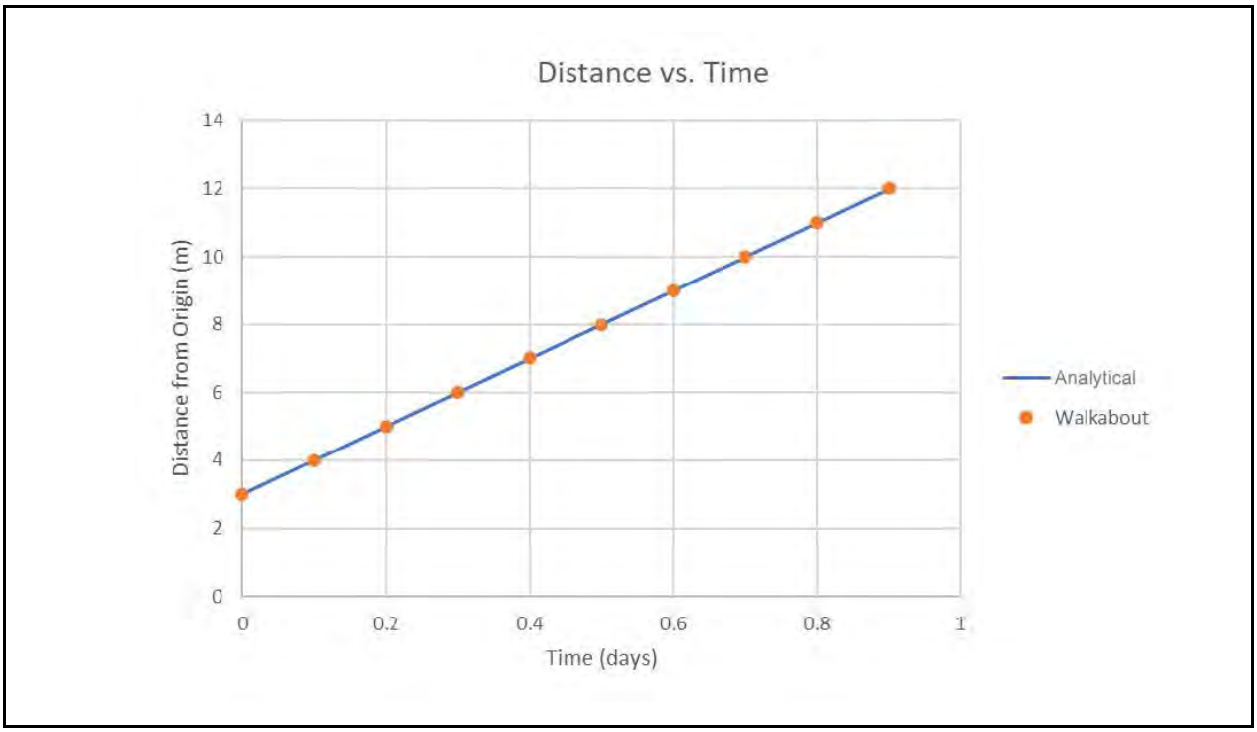

Figure E-8
Comparison of Travel Distances

The analytical solution is given as:

$$x = x0 + vt \qquad (E\text{-}8)$$

where:

- x = Distance from the origin (m)
- $x0$ = Initial distance from the origin (m)
- v = Velocity (10 m/day
- t = Time (days)

E.5.0 Preprocessor

A preprocessor was developed based on the methodology outlined in Sections 3.0 and 4.0. Section E.5.1 provides an overview of the structure of the preprocessor and steps used in data processing. Verification examples are provided in Section E.5.2.

E.5.1 Structure

A flowchart showing steps in data processing is presented in Figure E-9. In the figure, the process follows the following steps:

1. Geometric data from MODFLOW are read. Typical data consist of vertex coordinates, connectivity of vertices in a cell, top and bottom elevations of all cells. Information may be obtained from the MODFLOW *.*dis* file (or *.*disv* file or *.*disu* file).

2. Head output in a binary file from MODFLOW is read. Information is obtained from the MODFLOW *.*hds* file.

3. Material properties are read. Typical properties include hydraulic conductivity and porosity. Information relating to hydraulic properties may be extracted from MODFLOW *.*npf* file.

4. Tetrahedral element geometry is read. These tetrahedral elements should be generated using all vertices from the MODFLOW cells. The elements can be generated by the LaGriT code. FEHM's *.*fehmn* may be used.

5. Equivalent hexahedral elements are generated from MODFLOW cells. Each cell's geometry is based on the eight corner vertices. All other interior nodes are kept in the data base for data processing and velocity generation.

6. In the case that the MODFLOW cells and equivalent tetrahedral elements are generated based on two different references (e.g., from top to bottom for MODFLOW, and bottom to top for LaGriT), arrays with the information obtained in Steps 1, 2, and 3 are inverted to be compatible with information from Step 4. This step is provided as an option.

7. Heads from cell centroids are transferred to vertices using Equation E-1.

8. Tetrahedral elements are mapped to corresponding hexahedral elements.

9. Hydraulic gradients and velocities in respective tetrahedral elements are calculated using Equations E-2 to E-6.

10. If elements along flux boundaries are not eliminated, velocities are transferred to vertices using Equation E-7.

11. If the elements along the flux boundaries are to be eliminated to improve the accuracy of the velocity estimates, a list of boundary elements and associated nodes are read from an input file. After boundary element elimination, velocities are transferred to vertices using Equations E-7 and E-9.

12. The *.*fin* and *.*avs* files are generated.

The current version is limited to the MODFLOW cells.

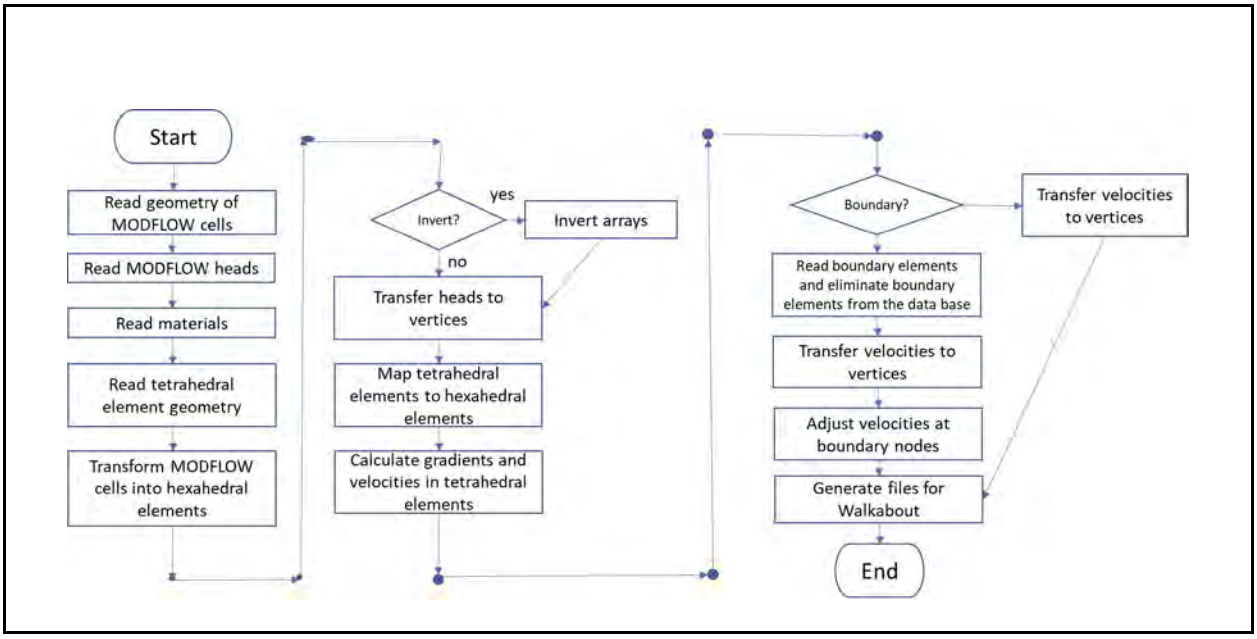

Figure E-9
Flowchart of the Preprocessor

E.5.2 Verifications

E.5.2.1 Testing on a Uniform Grid – Boundary Corrections

The preprocessor was verified using a verification example. The domain is of the following dimensions: 12m length, 10m width, and 4m height (see Figure E-6). The domain was discretized with 2m × 2m × 2m cells. Hydraulic and transport properties assigned were a uniform hydraulic conductivity of 10 m/day and a uniform porosity of 0.1. Constant heads of 13m and 12m were

assigned to the boundaries at x = 1m and 11m (boundary cell centroids). With this configuration, head varies linearly from left to right (in Figure E-6) with a uniform velocity of 10 m/day.

MODFLOW6 was used to generate heads. Head output from MODFLOW6 was processed by the preprocessor to generate files for Walkabout. A comparison between the head profiles along the length of the flow domain generated by MODFLOW and the preprocessor is shown in Figure E-10. The preprocessor proves to be accurate for the range within which head information is available. As heads are defined at cell centroids, heads at the boundary tetrahedral nodes are not well-defined. In the figure, heads at the boundary nodes are not accurately estimated. A comparison between fluid velocity profiles along the length of the flow domain generated by MODFLOW and the preprocessor without boundary element elimination is shown in Figure E-11. As shown, velocities are not accurately estimated two elements from the boundary. With the correction in Equation E-9, the velocities are accurate up to the boundary nodes (Figure E-12). Note that Equation (E-9) is an analytical solution that operates between x = 3 m and 12 m, and does not include any of the aforementioned corrections.

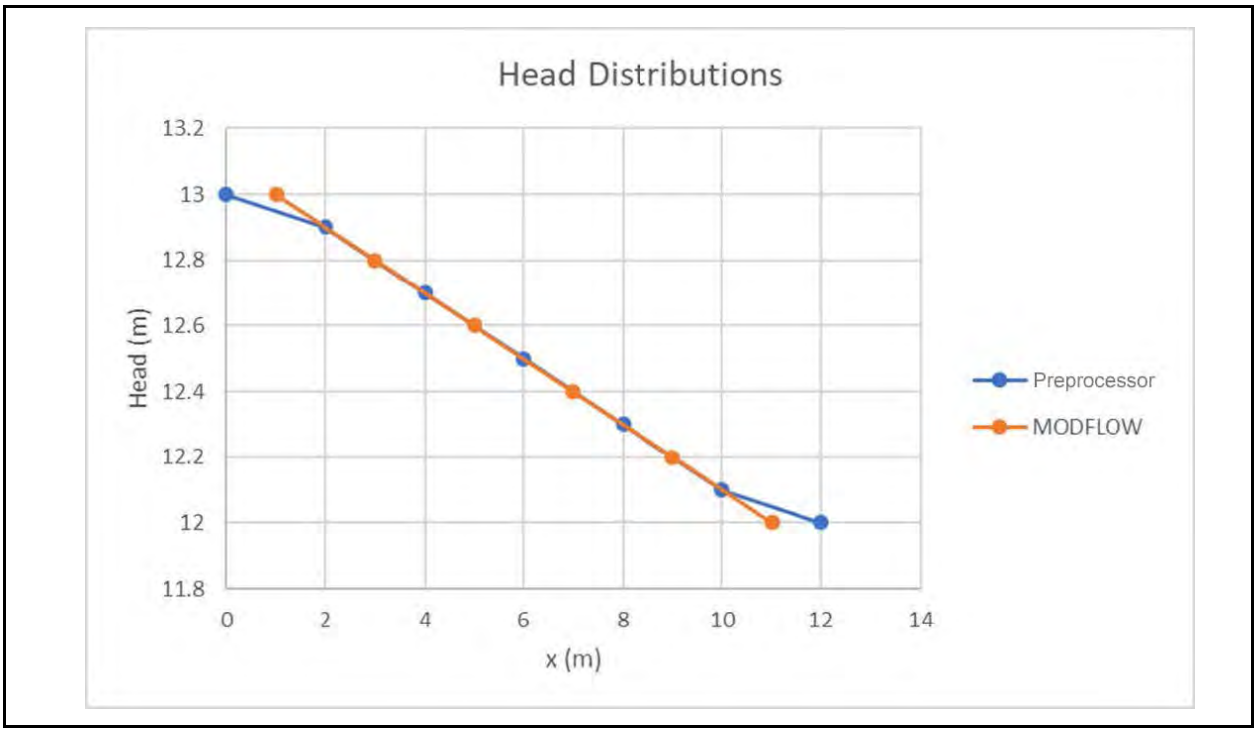

Figure E-10
Comparison of Head Profiles

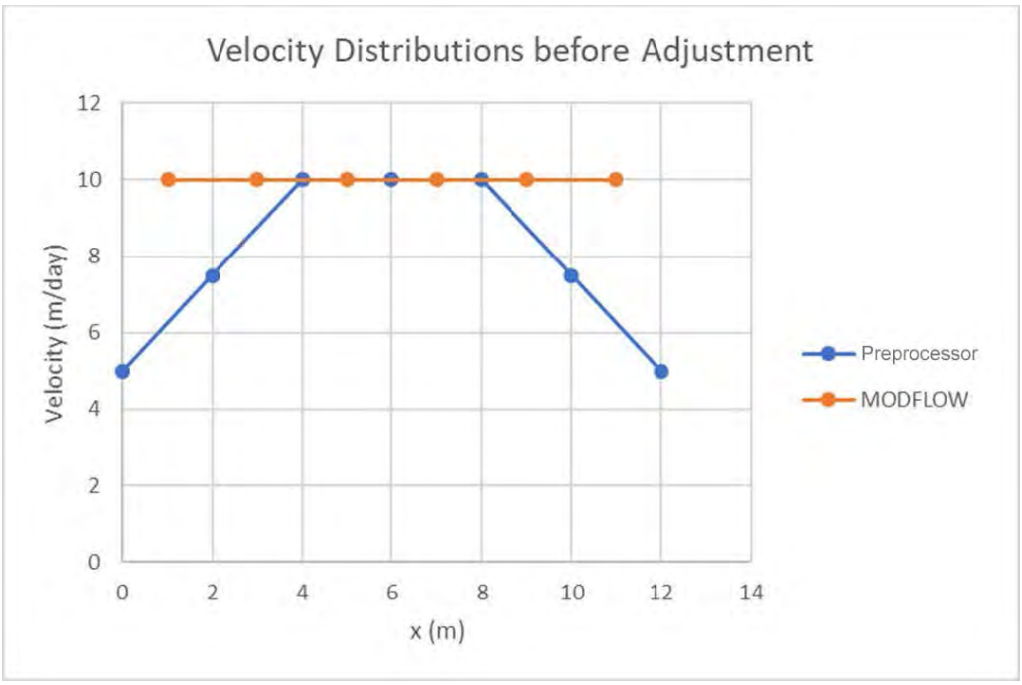

Figure E-11
Comparison of Velocity Distribution before Adjustment

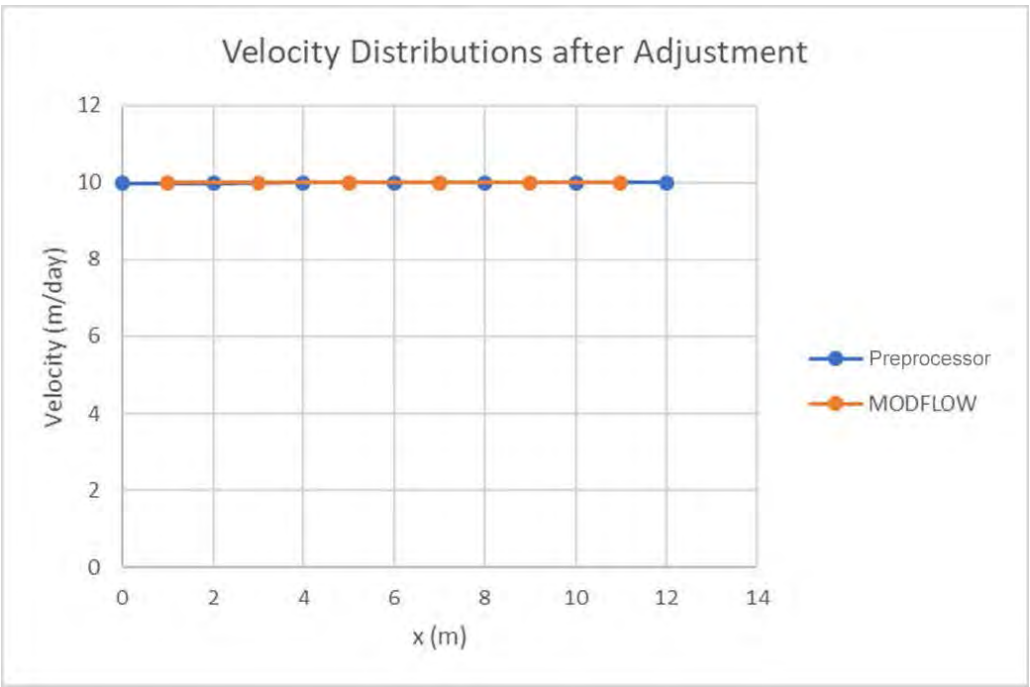

Figure E-12
Velocity Distributions after Adjustment

Two files were generated by the preprocessor for Walkabout (the *fin* and *avs* files). A Walkabout run was performed with six particles. These particles were initially located at (3m, 3m, 1m), (3m, 5m, 1m), (3m, 7m, 1m), (3m, 3m, 3m), (3m, 5m, 3m), and (3m, 7m, 1m). All particles traveled as a straight line in the *x* direction from their respective initial positions. A comparison between the results from Walkabout and a simple analytical is shown in Figure E-13.

Figure E-13
Comparison between Particle Paths Generated by Walkabout and an Analytical Solution

The analytical is given below:

$$x = x_o + vt \qquad (E\text{-}9)$$

where

x = Distance from origin (m)
x_o = Initial distance from origin = 3m
v = Velocity = 10 m/day
t = Time (days)

As shown in Figure E-13, the particle travel distance simulated by Walkabout agrees favorably with the analytical solution.

E.5.2.2 Testing on a Heterogeneous CAU Scale Grid

The preprocessor was tested using a heterogeneous CAU-scale grid, specifically the calibrated base case flow model described in Section 4.2, using a uniform porosity of 0.01 and no dispersion. Output from MODFLOW6 was processed by the preprocessor to generate files for Walkabout. With the two files generated by the preprocessor (the FIN and AVS files), a Walkabout run was performed from 117 particle starting locations distributed across the 82 underground detonations in Pahute Mesa. These 117 particle starting locations were identical to those used to calculate flow paths using MODPATH7, displayed in Figure 4-14. A comparison between the flow paths from MODPATH7 and the particle tracks from Walkabout is shown in Figures E-14 and E-15.

As shown in Figures E-14 and E-15, overall flow patterns and directions are similar, although some differences are noted between the flow paths calculated by MODPATH7 and Walkabout. This is to be expected, especially in a highly heterogeneous model like the PM CAU model, because of the different methodologies employed by the two codes. MODPATH7 uses an analytical approximation to the flow path within each hexahedral computational block with linearly interpolated velocities for cell-interior points. Our approach breaks the original MODFLOW6 hexahedrons into tetrahedrons using all the MODFLOW6 cell vertices as required by Walkabout. The fluxes at vertices (nodes) are found by combining contributing fluxes from all MODFLOW6 cell faces with respective common cell vertices and transforming them into velocities at the vertices. These velocities are then input to Walkabout, which linearly interpolates them to provide values at points within each tetrahedron for computing particle trajectories time-stepwise using Euler integration in time. The two methods give identical results for the simple homogeneous model illustrated in Figure E-6. In the heterogeneous PM CAU model where high velocity contrasts exist, particle paths computed by the two methods differ locally; however, they yield similar overall results in the model region.

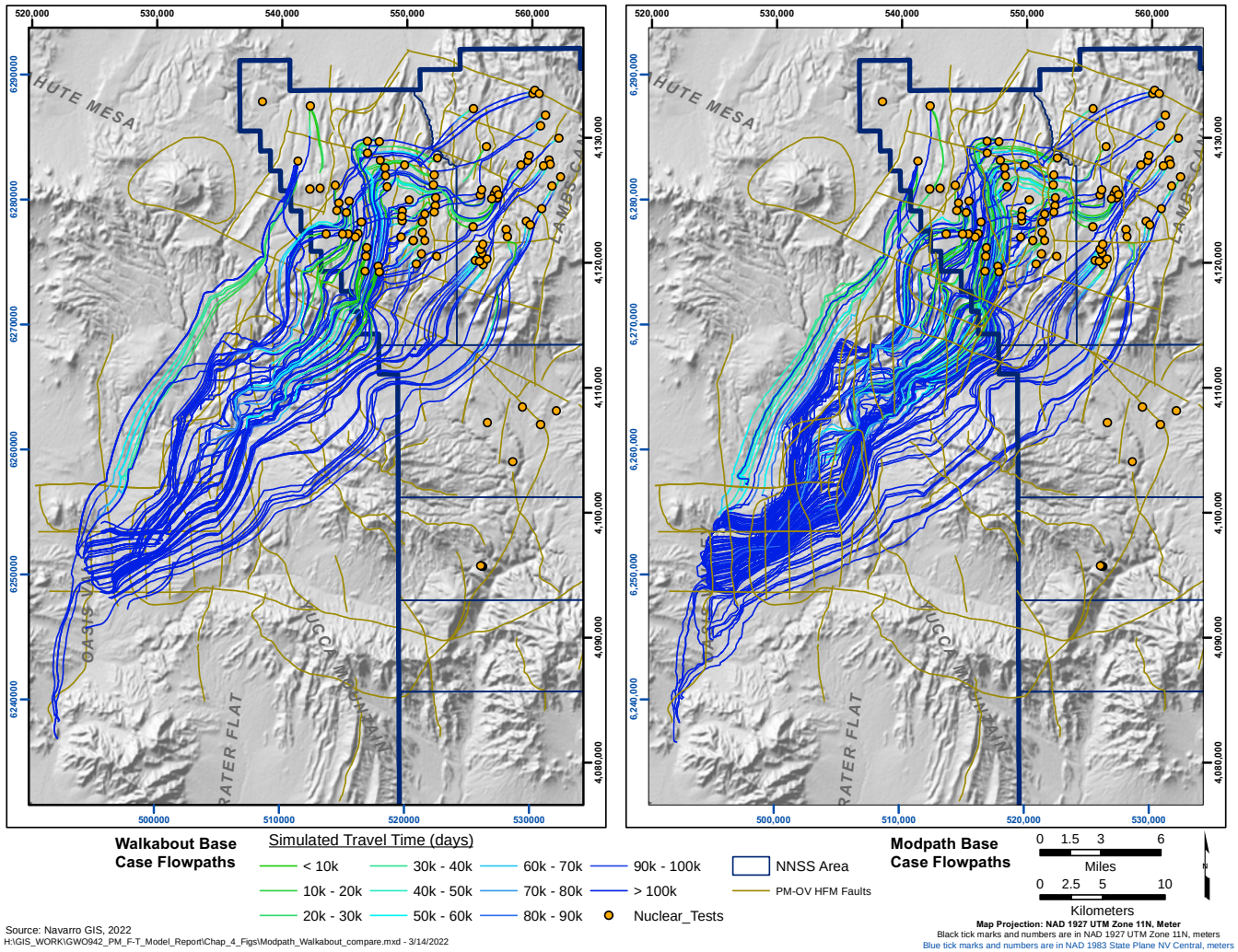

Figure E-14
Comparison of Calculated Flow Paths from MODPATH7 and Walkabout
Note: Left: Walkabout; Right: MODPATH7

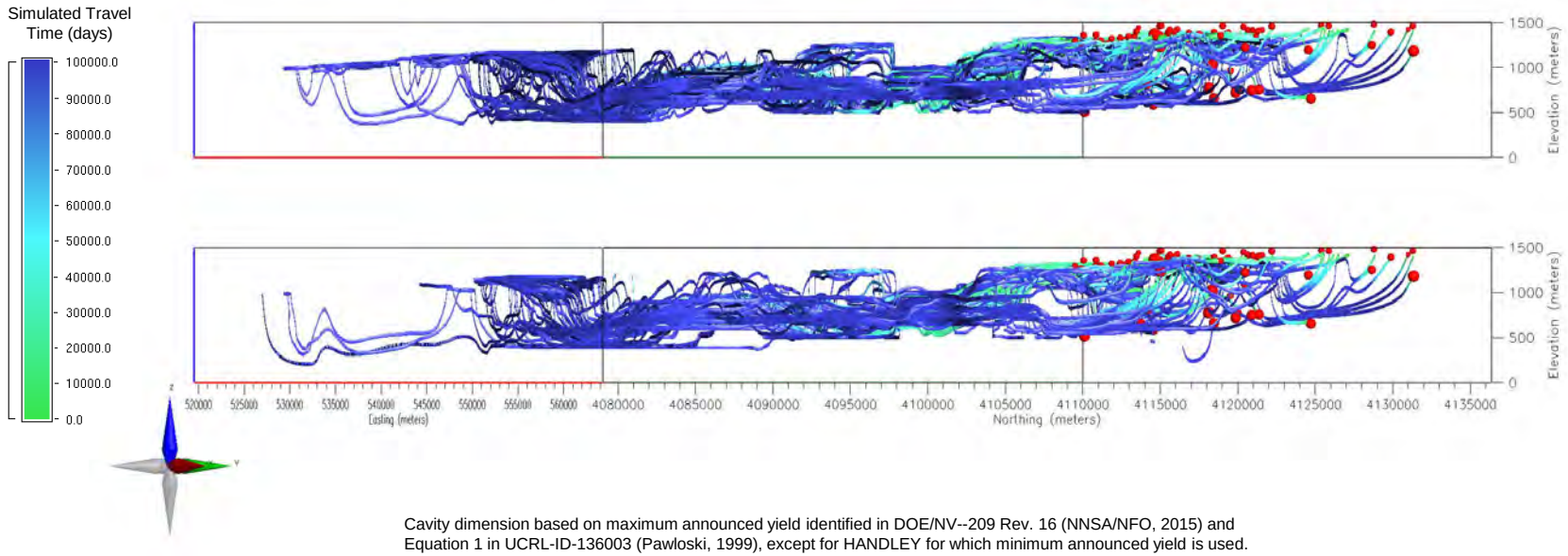

Cavity dimension based on maximum announced yield identified in DOE/NV--209 Rev. 16 (NNSA/NFO, 2015) and Equation 1 in UCRL-ID-136003 (Pawloski, 1999), except for HANDLEY for which minimum announced yield is used.

Figure E-15
Comparison of Calculated Flow Paths from MODPATH7 and Walkabout
Note: Top: MODPATH7; Bottom: Walkabout

E.6.0 References

DOE/EMNV, see U.S. Department of Energy Environmental Management Nevada Program.

DOE/NV, see U.S. Department of Energy, Nevada Operations Office.

GoldSim, see GoldSim Technology Group, LLC.

GoldSim Technology Group, LLC. 2018. *User's Guide: GoldSim Contaminant Transport Module*, Version 7.1. Issaquah, WA.

Harbaugh, A.W., E.R. Banta, M.C. Hill, and M.G. McDonald. 2000. *MODFLOW-2000, The U.S. Geological Survey Modular Ground-water Model User Guide to Modularization Concepts and the Ground-water Flow Process.* Open-File Report 00-92. Denver, CO: U.S. Geological Survey.

Kersting, A. B., D.L. Finnegan, B.K. Esser, A.F.B. Tompson, D.K. Smith, M. Zavarin, C.J. Bruton, G.A. Pawloski. 2003. *Radionuclide Decay and In-growth Technical Basis Document*, UCRL-ID-153798. Livermore, CA: Lawrence Livermore National Laboratory.

LANL, see Los Alamos National Laboratory.

Langevin, C.D., J.D. Hughes, E.R. Banta, R.G. Niswonger, S. Panday, and A.M. Provost. 2017. *Documentation for the MODFLOW 6 Groundwater Flow Model*, Techniques and Methods 6-A55. Reston, VA: U.S. Geological Survey.

Los Alamos National Laboratory. 2011. *LaGriT Los Alamos Grid Toolbox* website. Available at https://lagrit.lanl.gov/index.shtml

Lu, Z., E. Kwicklis, T. Miller and M. Bourret. 2021. *Development and Calibration of the Pahute Mesa Bench Area Groundwater Flow and Tritium Transport Model*, Nevada National Security *Site*, LA-UR-21-23595. Los Alamos, NM: Los Alamos National Laboratory.

NNSA/NSO, see U.S. Department of Energy, National Nuclear Security Administration Nevada Site Office.

Painter, S.L. 2011. *User's Manual for Walkabout V1.0*, LA-UR-11-01952. Los Alamos, NM: Los Alamos National Laboratory.

Pollock, D.W. 2016. "Extending the MODPATH Algorithm to Rectangular Unstructured Grids." In *Groundwater*, Vol. 54(1): pp. 121-125.

Robinson, B.A., Z.V. Dash, and S.L. Painter. 2011. *User's Guide for the PLUMECALC Application with Subgridding, Version 2.3.2,* LA-UR-11-02090. Los Alamos, NM: Los Alamos National Laboratory.

U.S. Department of Energy Environmental Management Nevada Program. 2020. *Update to the Phase II Corrective Action Investigation Plan for Corrective Action Units 101 and 102: Central and Western Pahute Mesa, Nevada National Security Site, Nye County, Nevada*, Rev. 1, DOE/EMNV--0018. Las Vegas, NV.

U.S. Department of Energy, National Nuclear Security Administration Nevada Site Office. 2009. *Phase II Corrective Action Investigation Plan for Corrective Action Units 101 and 102: Central and Western Pahute Mesa, Nevada Test Site, Nye County, Nevada,* DOE/NV--1312-Rev. 2. Las Vegas, NV.

U.S. Department of Energy, Nevada Operations Office. 1999. *Corrective Action Investigation Plan for Corrective Action Units 101 and 102, Central and Western Pahute Mesa, Nevada Test Site, Nevada*, Rev. 1, DOE/NV--516. Las Vegas, NV.

Zienkiewicz, O.C., and Y.K. Cheung. 1967. *Finite Element Method in Structural & Continuum Mechanics.* 1st ed. London: McGraw-Hill.

Zyvoloski, G.A. 2007. *FEHM: A Control Volume Finite Element Code for Simulating Subsurface Multi-phase Multi-fluid Heat and Mass Transfer*, LA-UR-07-3359. Los Alamos, NM: Los Alamos National Laboratory.

Appendix F

Hydrographs Comparing Simulated and Observed Drawdown from 16 MWATs at PM

F.1.0 Simulated and Observed Drawdown from 16 MWATs at PM

This appendix presents a comparison of simulated and observed drawdown hydrographs in response to MWATs performed at PM. A total of 38 completions at 26 well locations have aquifer stress responses to groundwater withdrawals that were used in calibration of the CAU groundwater flow model. Several wells have multiple completions, which are typically included in the well name such as “main upper zone” or “main lower zone for the pumped wells and “shallow,” “intermediate,” or “deep” for the observation wells. The plots use abbreviations to identify the completions such as “U” for “main upper_zone” or “S” for shallow. If drawdowns were not recorded separately from pumping multiple completions, only the well name is used and the combined pumping responses are included in the plots. The simulated pumping schedules are included in the figures using the right axis. To reduce the computational burden, the simulated pumping schedules were simplified using various step functions. Drawdown weights were adjusted to allow all pumping signals have the same effect on the objective function, regardless of magnitude, and both the observation wells with positive and negative responses to pumping were used in the model calibration.

F.1.1 Comparisons of Simulated and Observed Drawdowns in Response to Well ER-20-4 Main Pumping

The primary HSU within well completion ER-20-4 main is the CHLFA4. Garcia et al. (2017) did not identify unambiguous responses in distal observation wells monitored during the ER-20-4 MWAT and, consequently, definitive drawdowns are only observed in the pumped wellbore within the ER-20-4S and ER-20-4D completions (Figure F-1). The model has good agreement within the drawdown in ER-20-4D, but the simulated drawdown lags behind the observation within ER-20-4S, indicating the specific storage of the CHZCM HSU separating CHLFA1 within ER-20-4S and CHLFA4 within ER-20-4D is overestimated. Figure F-2 illustrates the largest drawdown in any model layer and model drawdown residuals corresponding to Day 22 of the well development and testing period. The pumped CHLFA4 HSU has limited connections to other aquifers and the extent of drawdown is limited to the area surrounding the pumping well.

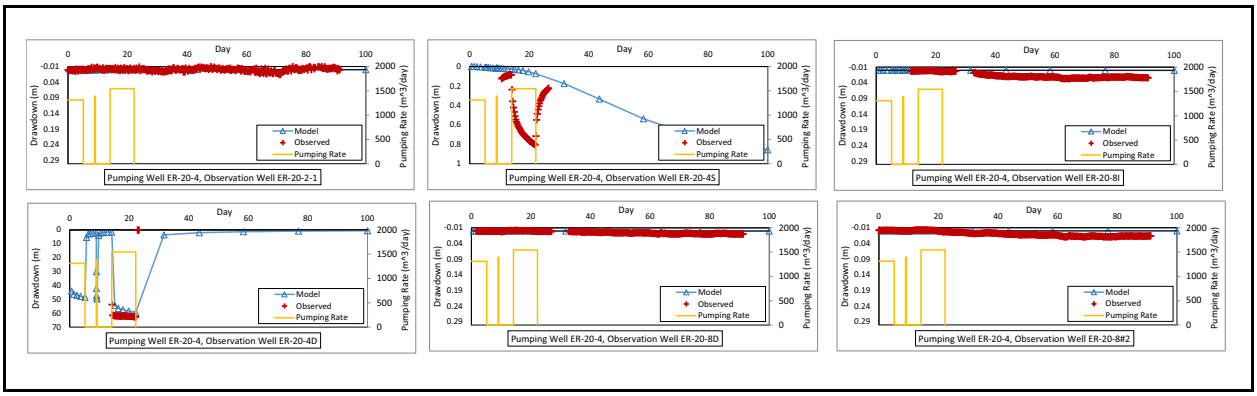

Figure F-1
Comparisons of Simulated and Observed Drawdowns in Response to Well ER-20-4 Main Pumping

F.1.2 Comparisons of Simulated and Observed Drawdowns in Response to Well ER-20-7 Main Pumping

The primary HSU within the ER-20-7 main completion is the TSA. Garcia et al. (2017) identified unambiguous responses in the ER-20-1, ER-20-5-1, ER-20-5-3, ER-20-7, ER-20-8S, ER-20-8D, ER-EC-11S, ER-EC-11I, and ER-EC-11D well completions. However, drawdowns were limited to several one hundredths of a meter in wells other than the ER-20-7 pumped completion. The model underpredicted the drawdown in the pumped completion indicating the simulated hydraulic conductivity of the TSA is overestimated at the ER-20-7 well location (Figure F-3). The small drawdown identified in several observation wells is underpredicted by the model, except for the drawdown in ER-20-5-1, which had good agreement with the observation. The underpredicted drawdowns within the pumped well and in TSA completions many of the observation wells indicate the model is overestimating the hydraulic conductivity of the TSA within the area responding to the ER-20-7 MWAT. Figure F-4 illustrates the largest drawdown in any model layer and model drawdown residuals corresponding to Day 10 of the well development and testing period.

The drawdown south of the NTMMSZ fault is underpredicted due to juxtaposition of the TSA HSU north of the fault against the FCCU south of the fault (Figure 2-7), thereby limiting drawdown propagation southward.

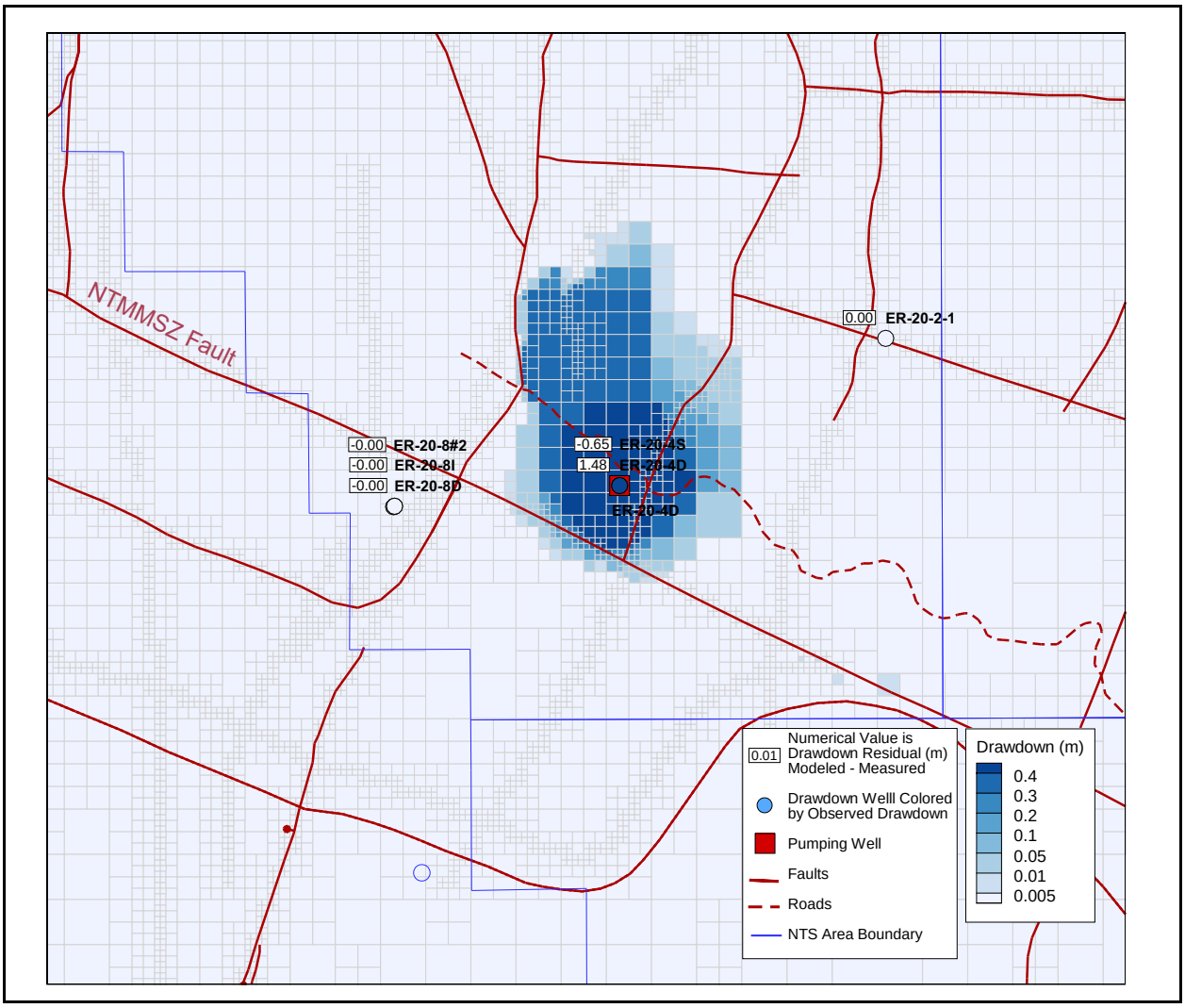

Figure F-2
Drawdown Extent and Residuals in Response to Well ER-20-4 Main Pumping on Day 22 of the Well Development and Testing Period

F.1.3 Comparisons of Simulated and Observed Drawdowns in Response to Well ER-20-8-2 Main Pumping

The primary HSU within ER-20-8-2 main completion is the SPA. Garcia et al. (2017) identified unambiguous responses in the ER-20-8D, ER-20-8I, ER-20-8S,ER-20-8-2, ER-EC-6I, ER-EC-6S, ER-EC-11S, and ER-EC-11I well completions. The model underpredicted the drawdown in the ER-20-8-2 pumped well and within the intermediate and deep completions of the nearby ER-20-8 well, indicating that the simulated hydraulic conductivity of the SPA and possibly the TCA and TSA HSUs was overestimated in the vicinity of the pumped well (Figure F-5). Figure F-6 illustrates the largest

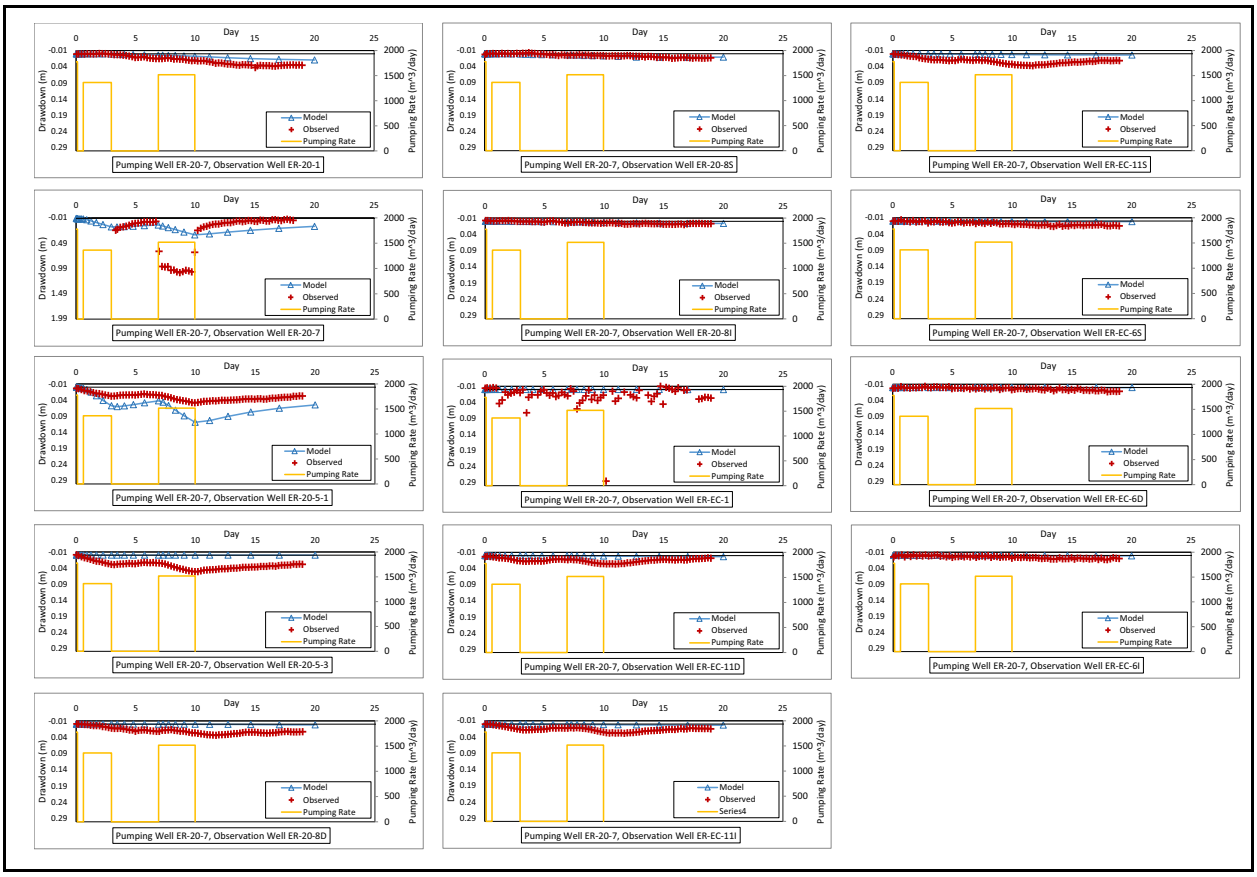

Figure F-3
Comparisons of Simulated and Observed Drawdowns in Response to Well ER-20-7 Main Pumping

drawdown in any model layer and model drawdown residuals corresponding to Day 20 of the well development and testing period.

F.1.4 Comparisons of Simulated and Observed Drawdowns in Response to Well ER-20-8 Main Upper and Lower Pumping

The primary HSUs within ER-20-8 main upper and lower completions are the TCA and TSA HSUs, respectively. Garcia et al. (2017) identified unambiguous responses in the ER-20-7, ER-20-8-2, ER-20-8S, ER-20-8I, ER-20-8D, ER-EC-6D, ER-EC-6I, ER-EC-6S, ER-EC-11S, ER-EC-11I, ER-EC-11D, ER-EC-12D, and ER-EC-12I well completions. The model underpredicted the drawdown in the pumped Well ER-20-8S, ER-20-8I, ER-20-8D completions and into the nearby ER-20-8-2 well (Figure F-7). The underpredicted drawdowns indicate that the simulated hydraulic conductivity of the TCA and TSA and possibly the SPA was overestimated in the vicinity of the

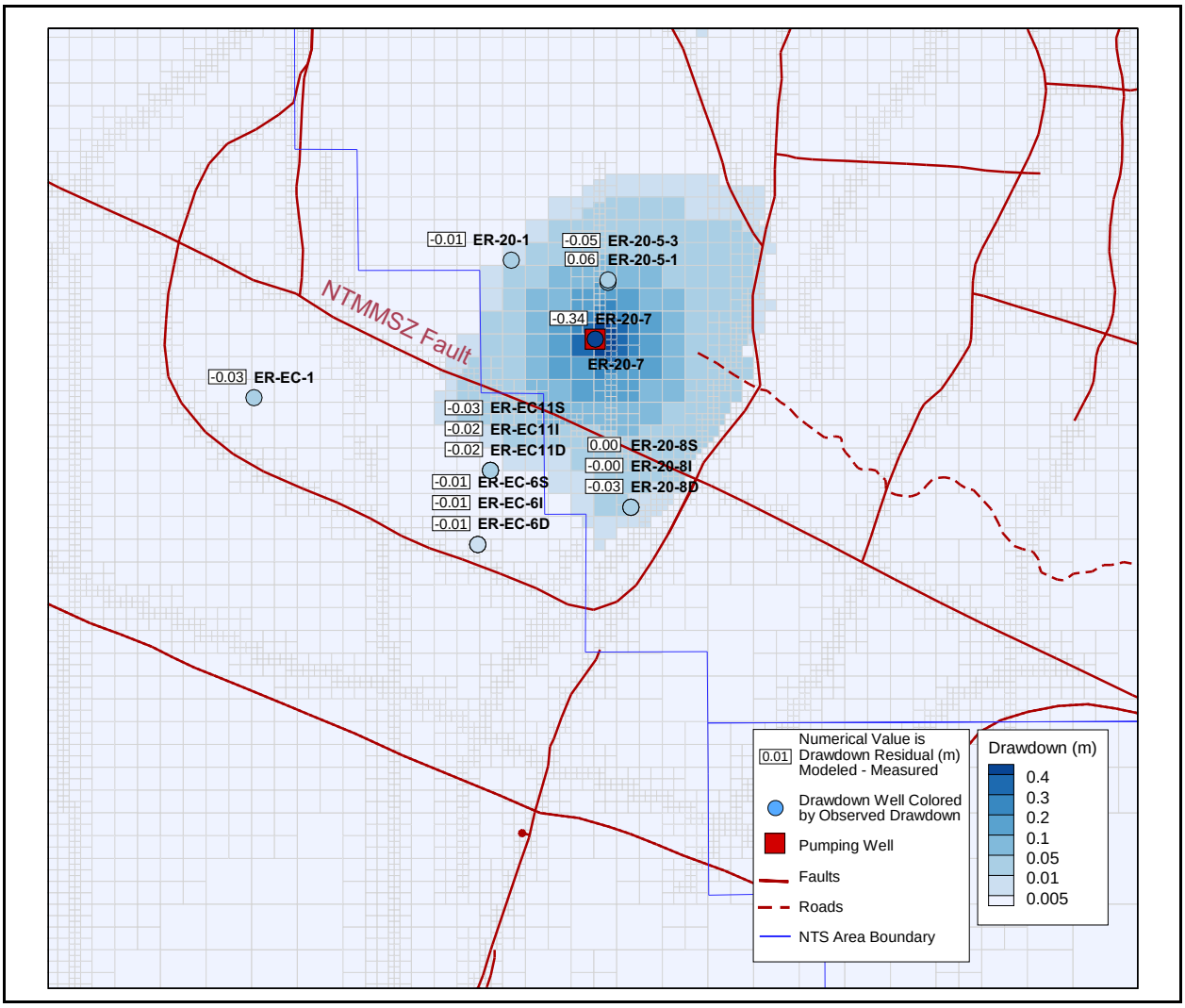

Figure F-4
Drawdown Extent and Residuals in Response to Well ER-20-7 Main Pumping on Day 10 of the Well Development and Testing Period

pumped well. Figure F-8 illustrates the largest drawdown in any model layer and model drawdown residuals corresponding to Day 82 of the well development and testing period.

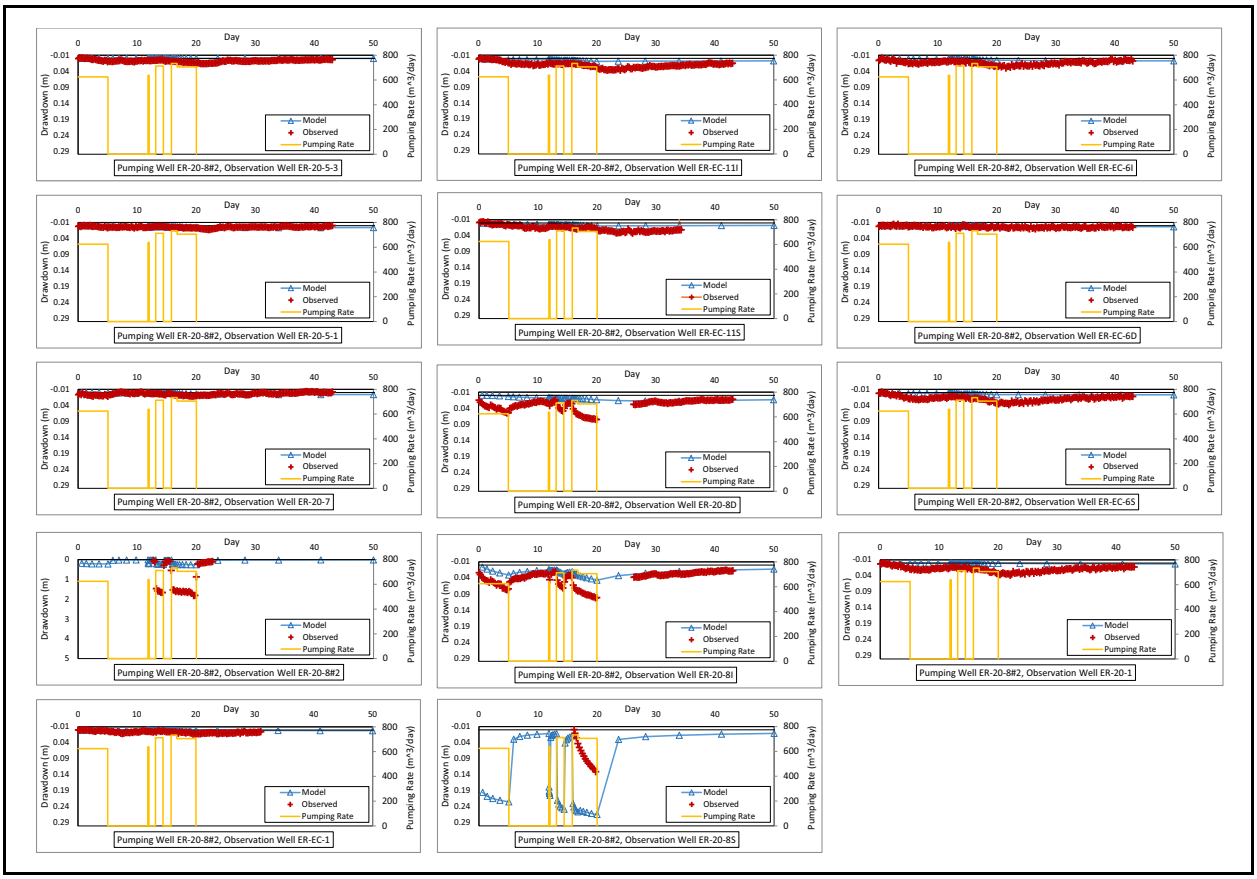

Figure F-5
Comparisons of Simulated and Observed Drawdowns in Response to Well ER-20-8-2 Main Pumping

F.1.5 Comparisons of Simulated and Observed Drawdowns in Response to Well ER-20-11 Main Pumping

The primary HSU within ER-20-11 main completion is the BA HSU. Garcia et al. (2017) identified unambiguous responses in Wells ER-20-5-1, ER-20-5-3, ER-20-7, ER-20-8S, ER-20-8I, ER-20-8D, ER-20-11, ER-EC-6S, ER-EC-6I, ER-EC-6D, ER-EC-11S, ER-EC-11I, ER-EC-11D, ER-EC-12S, ER-EC-12I, and ER-EC-12D well completions. The drawdown in the pumped Well ER-20-11 completion is underestimated, indicating the hydraulic conductivity of the BA HSU is overestimated in the vicinity of the pumped well (Figure F-9). Drawdowns are underestimated in all completions of Wells ER-20-7, ER-20-8, and ER-EC-6, and in the ER-EC-12D completion. The underprediction of drawdown in the ER-EC-6S (BA) well completion indicates the BA hydraulic conductivity between Wells ER-20-11 and ER-EC-6 is overestimated. Drawdowns are overestimated in the ER-EC-15S, ER-EC-15I, and ER-EC-12I well completions. The model has good agreement

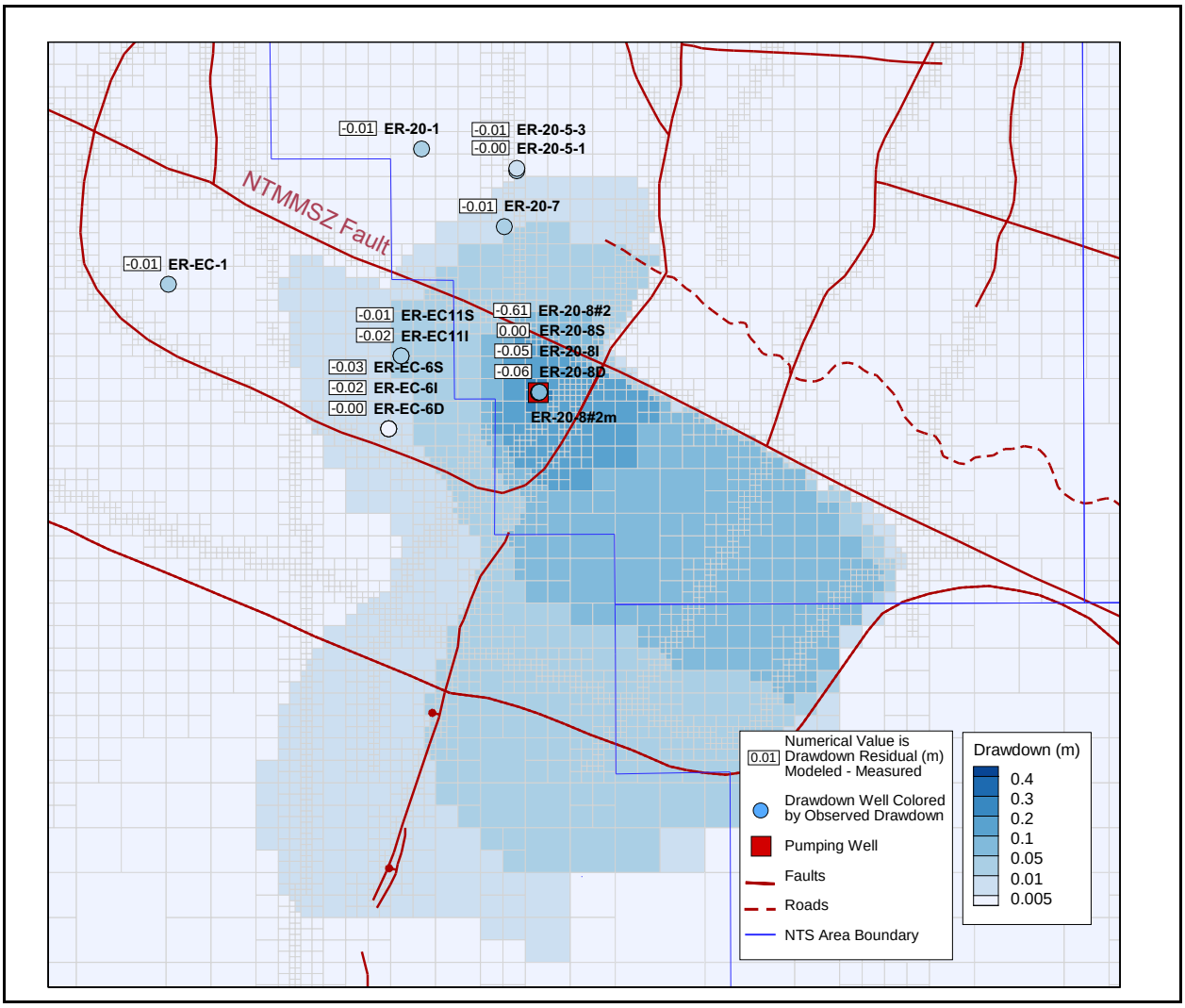

Figure F-6
Drawdown Extent and Residuals in Response to Well ER-20-8-2 Main Pumping on Day 20 of the Well Development and Testing Period

with the observed drawdowns of Well ER-EC-11. Figure F-10 illustrates the largest drawdown in any model layer and model drawdown residuals corresponding to Day 39 of the well development and testing period.

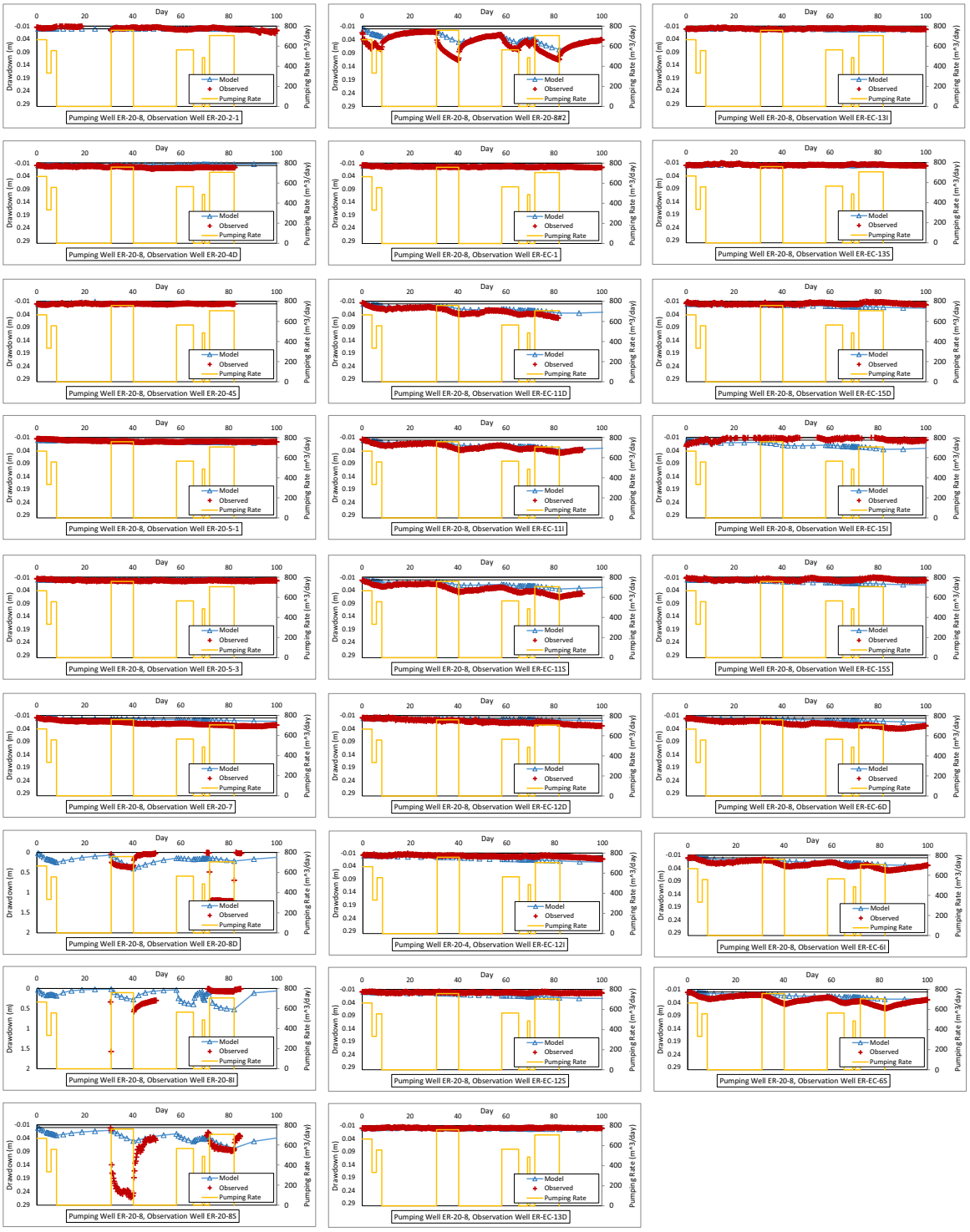

Figure F-7
Comparisons of Simulated and Observed Drawdowns in Response to Well ER-20-8 Main Upper and Lower Pumping

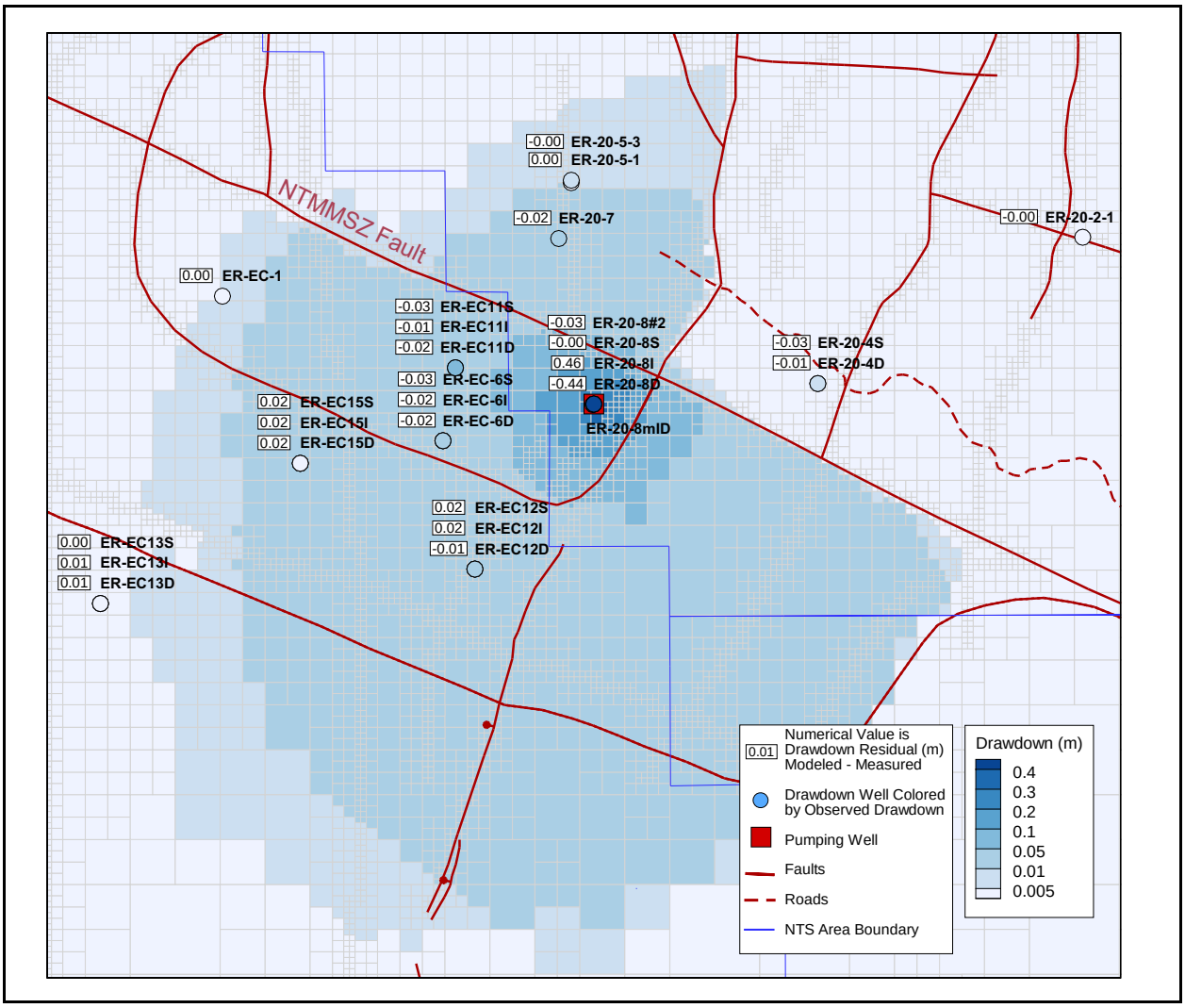

Figure F-8
Drawdown Extent and Residuals in Response to Well ER-20-8 Main Upper and Lower Pumping on Day 82 of the Well Development and Testing Period

F.1.6 Comparisons of Simulated and Observed Drawdowns in Response to Well ER-EC-11 Main Pumping

The primary HSUs within ER-EC-11 main completion are the TCA and TSA. Garcia et al. (2017) identified unambiguous responses in the ER-20-1, ER-20-5-1, ER-20-5-3, ER-20-7, ER-20-8D, ER-EC-1, ER-EC-6S, ER-EC-6I, ER-EC-6D, and ER-EC-11S well completions. The drawdown in the pumped well is underestimated, indicating the hydraulic conductivity of the TCA and TSA HSUs are overestimated in the vicinity of the pumped well. Drawdowns are underestimated in all completions of the ER-20-5, ER-20-7, and ER-EC-6 wells. Drawdown is moderately overestimated

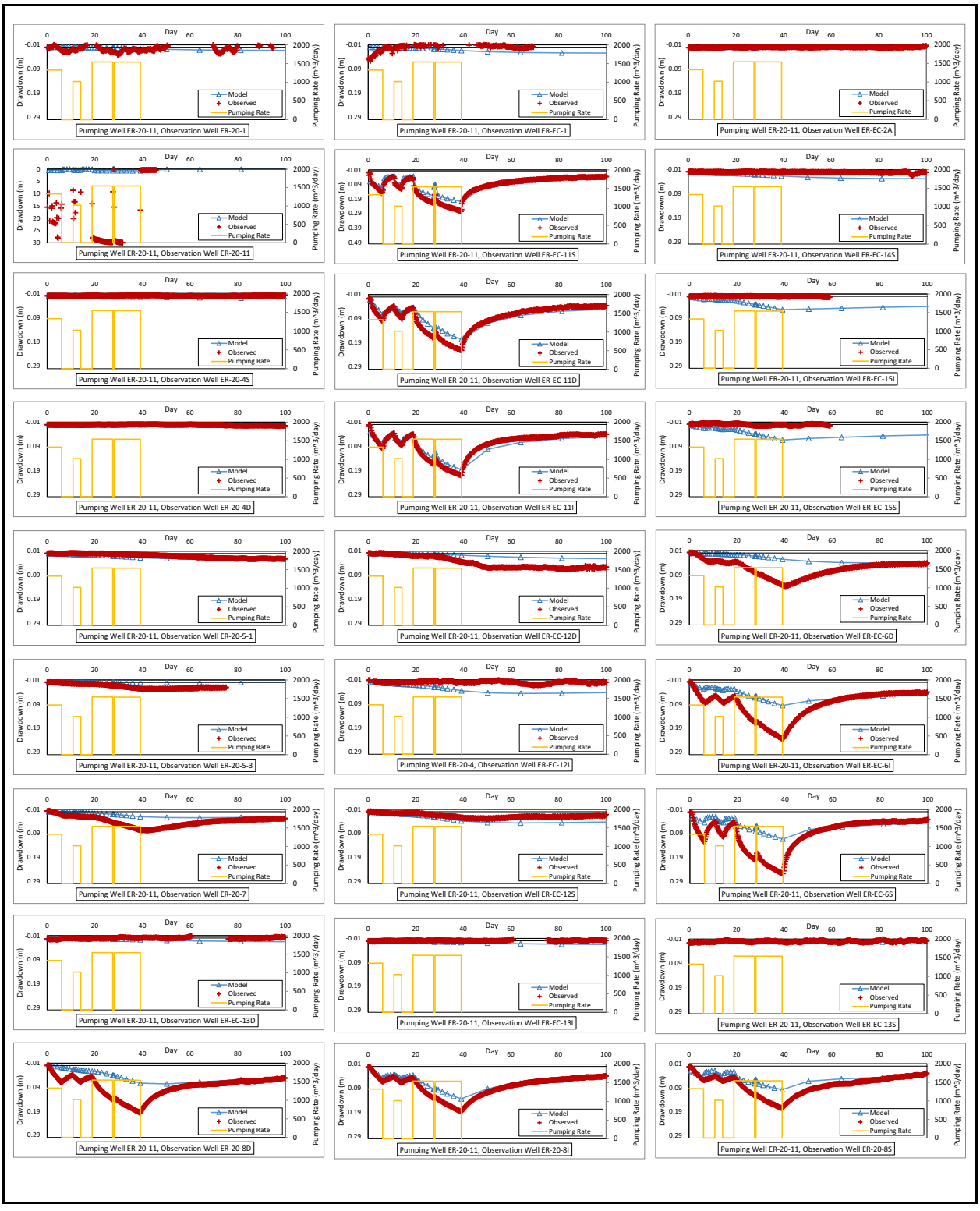

Figure F-9
Comparisons of Simulated and Observed Drawdowns in Response to Well ER-20-11 Main Pumping

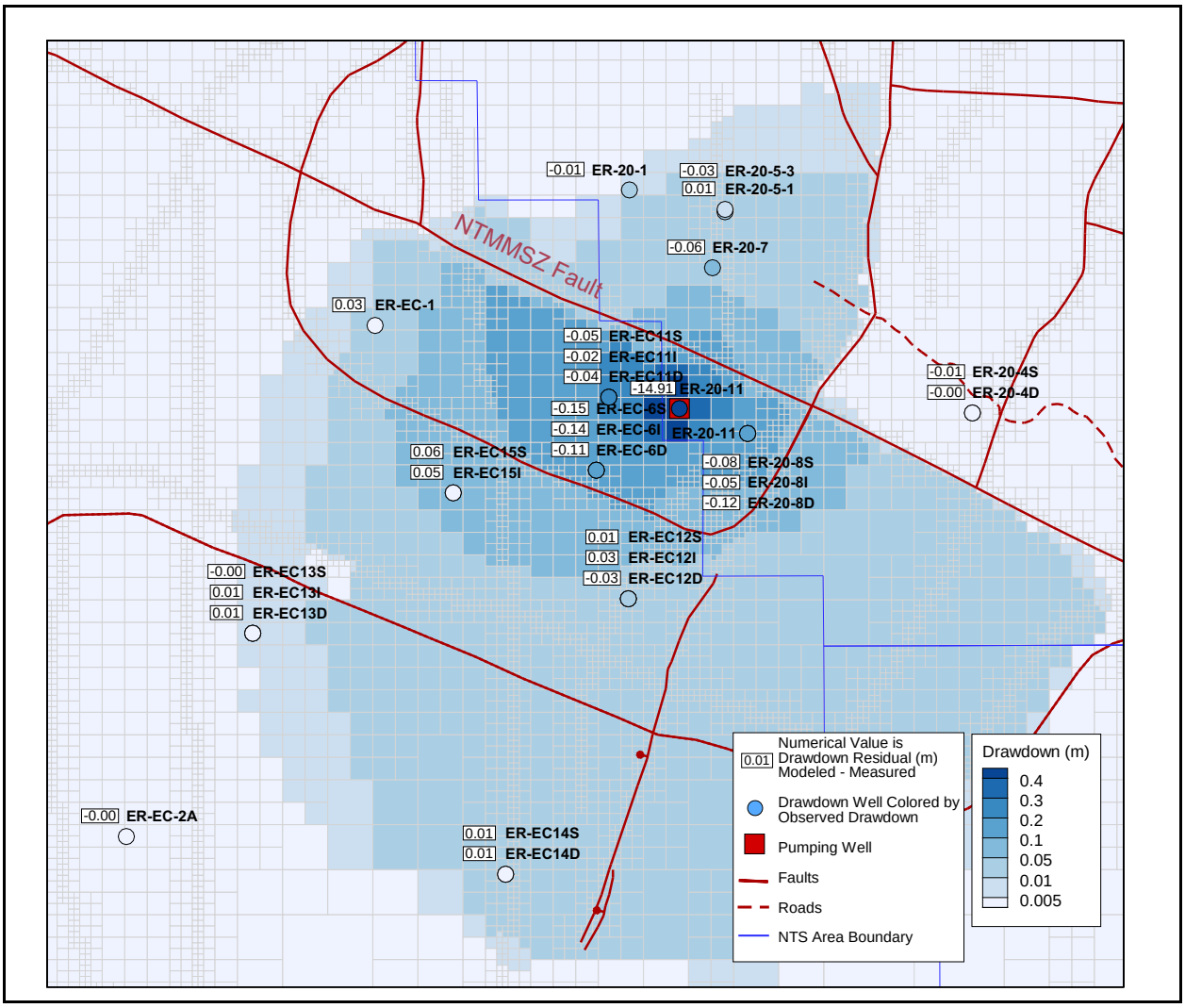

Figure F-10
Drawdown Extent and Residuals in Response to Well ER-20-11 Main Pumping on Day 39 of the Well Development and Testing Period

in the ER-20-8I well completion (Figure F-11). Figure F-12 illustrates the largest drawdown in any model layer and model drawdown residuals corresponding to Day 18 of the well development and testing period. The drawdown north of the NTMMSZ fault is underpredicted due to juxtaposition of the TSA and TCA HSUs south of the fault against the low- permeability CFCM and CHZCM composite units north of the fault (Figure 2-7), thereby limiting drawdown propagation northward.

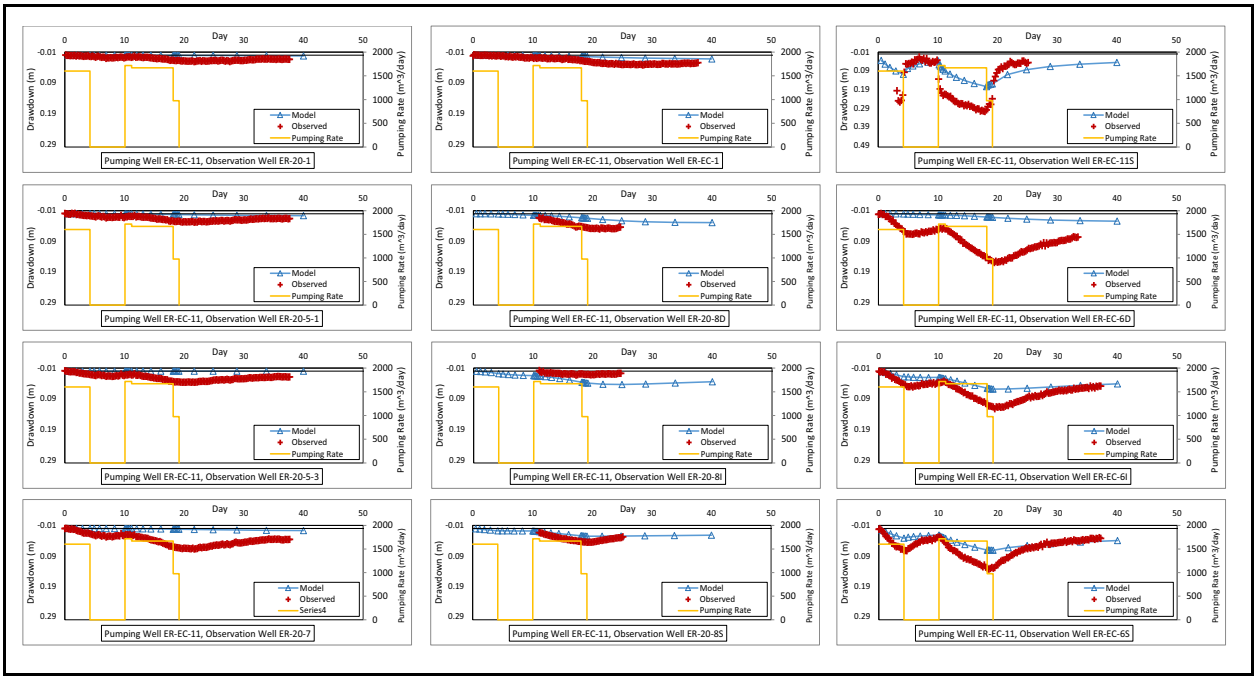

Figure F-11
Comparisons of Simulated and Observed Drawdowns in Response to Well ER-EC-11 Main Pumping

F.1.7 Comparisons of Simulated and Observed Drawdowns in Response to Well ER-EC-12 Main Upper and Lower Pumping

The primary HSUs within ER-EC-12 main upper and lower completions are the TCA and TSA, respectively. Garcia et al. (2017) did not identify any unambiguous responses in distal observation wells monitored during the ER-EC-12 MWAT. Consequently, definitive drawdowns are observed only in the pumped wellbore within the ER-EC-12S and ER-EC-12I completions. The drawdown within both completions are underestimated indicating the hydraulic conductivity of the TCA and TSA are overestimated in the vicinity of Well ER-EC-12 (Figure F-13). Figure F-14 illustrates the largest drawdown in any model layer and model drawdown residuals corresponding to Day 48 of the well development and testing period.

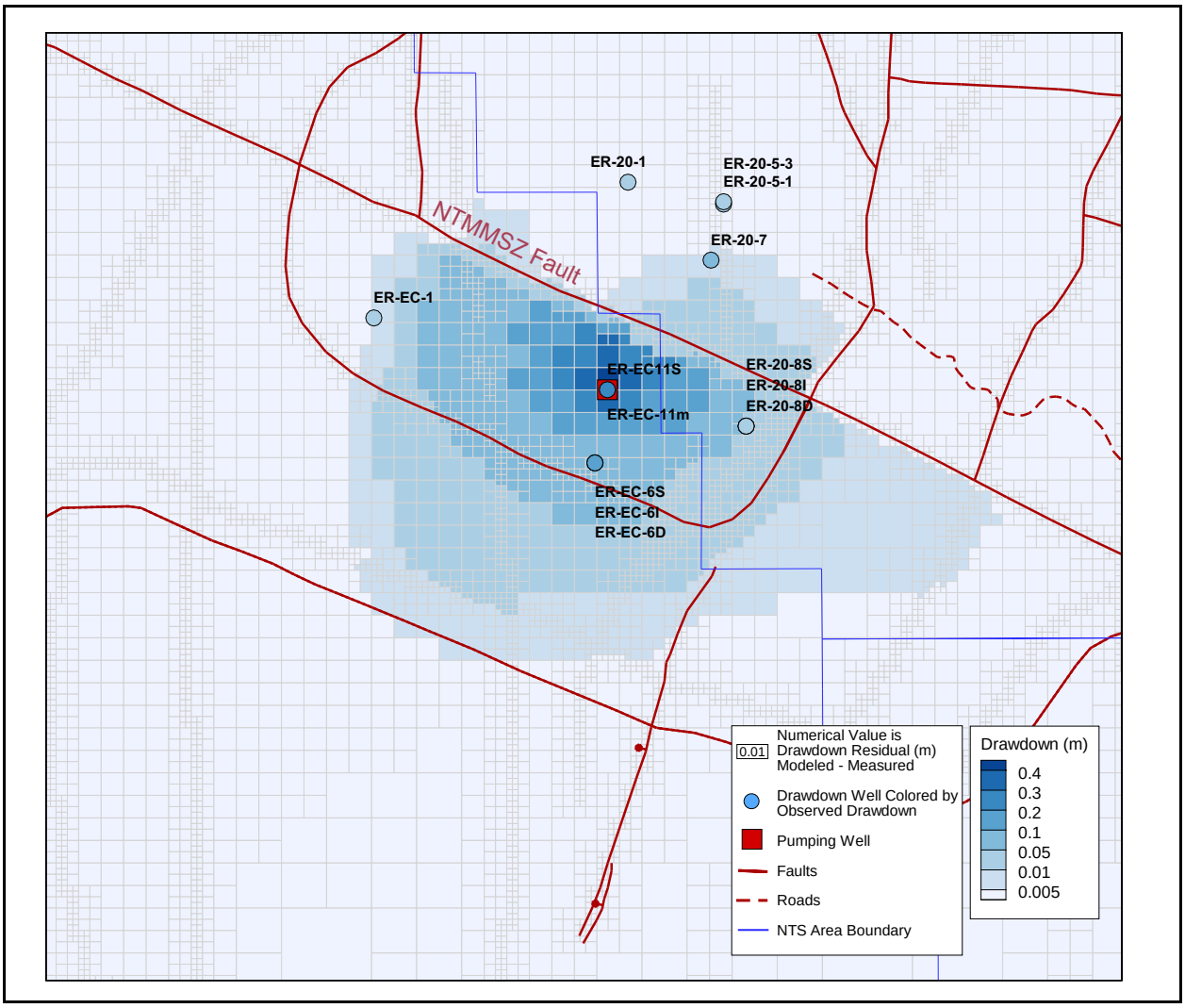

Figure F-12
Drawdown Extent and Residuals in Response to Well ER-EC-11 Main Pumping on Day 18 of the Well Development and Testing Period

F.1.8 Comparisons of Simulated and Observed Drawdowns in Response to Well ER-EC-13LZ Main Pumping

The primary HSU within ER-EC-13 main lower zone completion is the FCULFA4. Garcia et al. (2017) identified unambiguous responses in the ER-EC-1, ER-EC-2A, ER-EC-12S, ER-EC-13S, ER-EC-13I, ER-EC-13D, ER-EC-14D, ER-EC-14S, and ER-EC-15S well completions; however, drawdowns are limited to a few one-hundredths of a meter within wells other than ER-EC-13. The model has good agreement with drawdown in ER-EC-13S, underpredicts the drawdown in

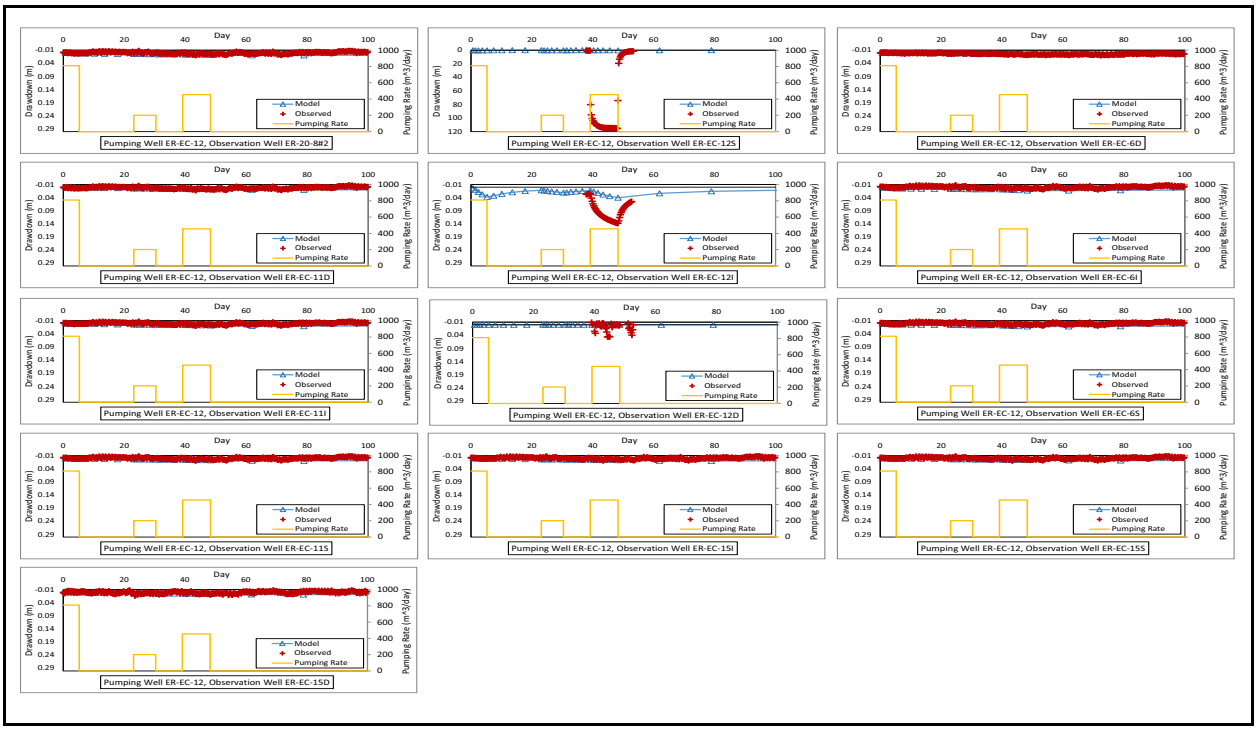

Figure F-13
Comparisons of Simulated and Observed Drawdowns in Response to Well ER-EC-12 Main Upper and Lower Pumping

ER-EC-13D, and overpredicts the drawdown in ER-EC-13I (Figure F-15). The large underprediction of drawdown in ER-EC-13D indicates the FCULFA4 hydraulic conductivity is overestimated by model in the vicinity of Well ER-EC-13. The close proximity of the lower and intermediate completions, yet very different observed drawdowns suggest vertical heterogeneity or anisotropy within the FCULFA4 is present near the well. The small drawdowns identified in most other well completions have good agreement with the simulated drawdowns. Figure F-16 illustrates the largest drawdown in any model layer and model drawdown residuals corresponding to Day 250 of the well development and testing period.

F.1.9 Comparisons of Simulated and Observed Drawdowns in Response to Well ER-EC-13 Main Upper Pumping

The primary HSU within ER-EC-13 main lower zone completion is the FCULFA4. Garcia et al. (2017) identified unambiguous responses in the ER-EC-1, ER-EC-12S, ER-EC-13S, ER-EC-13I, ER-EC-13D, ER-EC-15S, and ER-EC-15I well completions. However, drawdowns are limited to a few one hundredths of a meter in wells other than ER-EC-13. The model underpredicts the drawdown

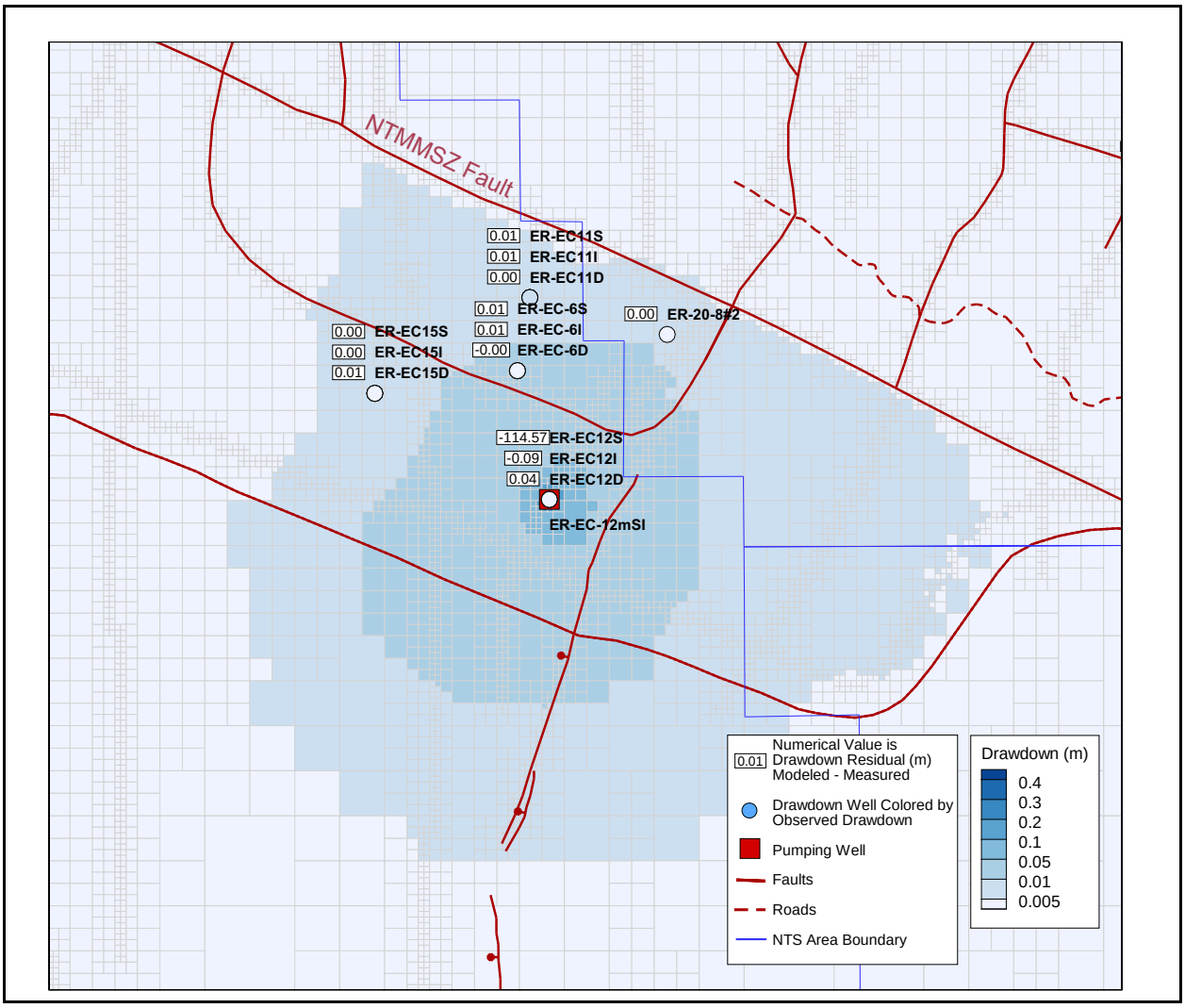

Figure F-14
Drawdown Extent and Residuals in Response to Well ER-EC-12 Main Upper and Lower Pumping on Day 48 of the Well Development and Testing Period

in the ER-EC-13I and overpredicts the drawdown in the ER-EC-13D (Figure F-17). The large underprediction of drawdown in ER-EC-13I indicates the FCULFA4 hydraulic conductivity is overestimated by the model. Similar to the ER-EC-13 main lower pumping, very different observed drawdowns were identified in deep, intermediate, and shallow completions, suggesting vertical heterogeneity or anisotropy within the FCULFA4 is present near the well. The small drawdowns identified in most other well completions have good agreement with the simulated drawdowns. Figure F-18 illustrates the largest drawdown in any model layer and model drawdown residuals corresponding to Day 32 of the well development and testing period.

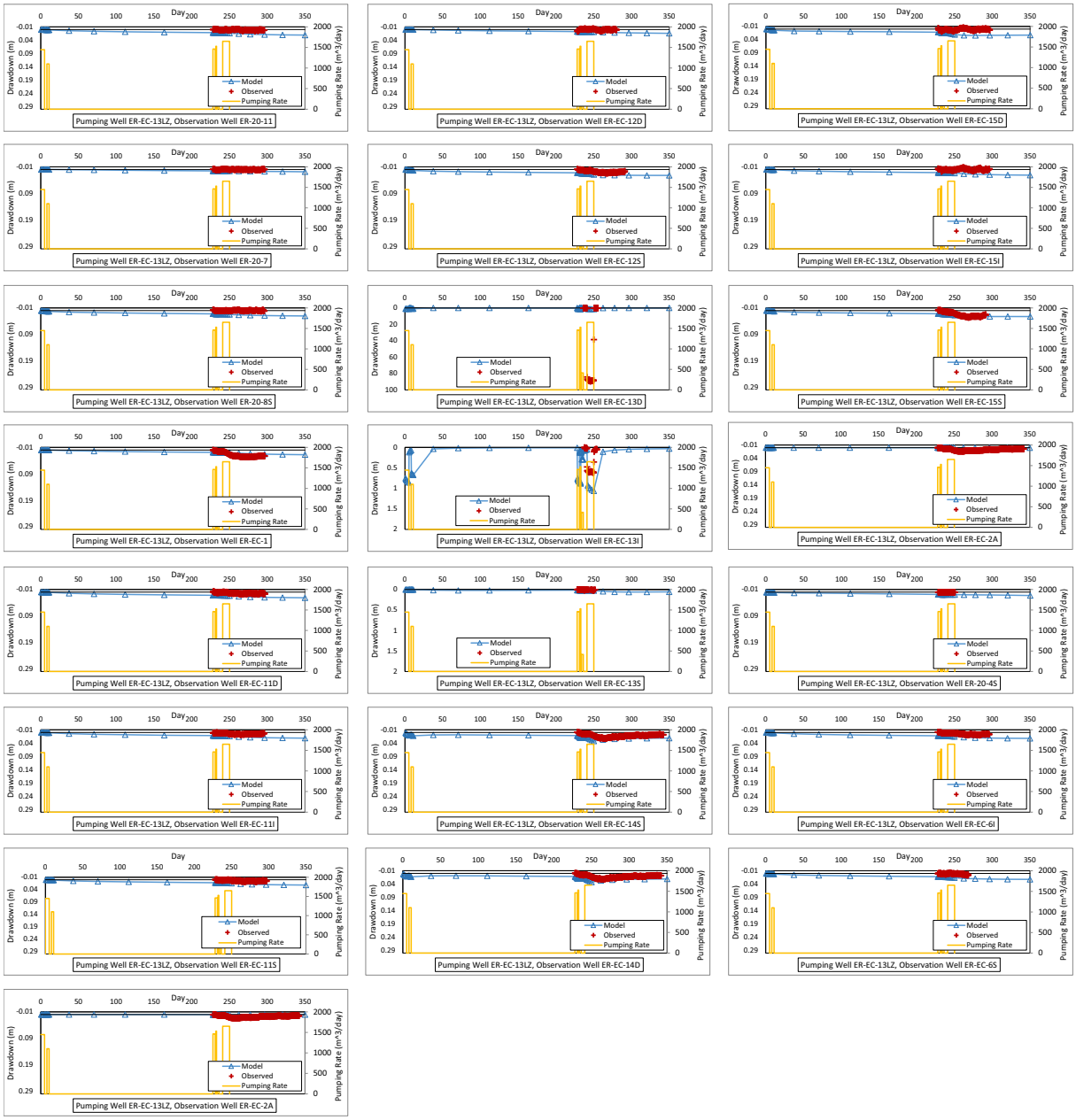

Figure F-15
Comparisons of Simulated and Observed Drawdowns in Response to Well ER-EC-13 Main Lower Zone Pumping

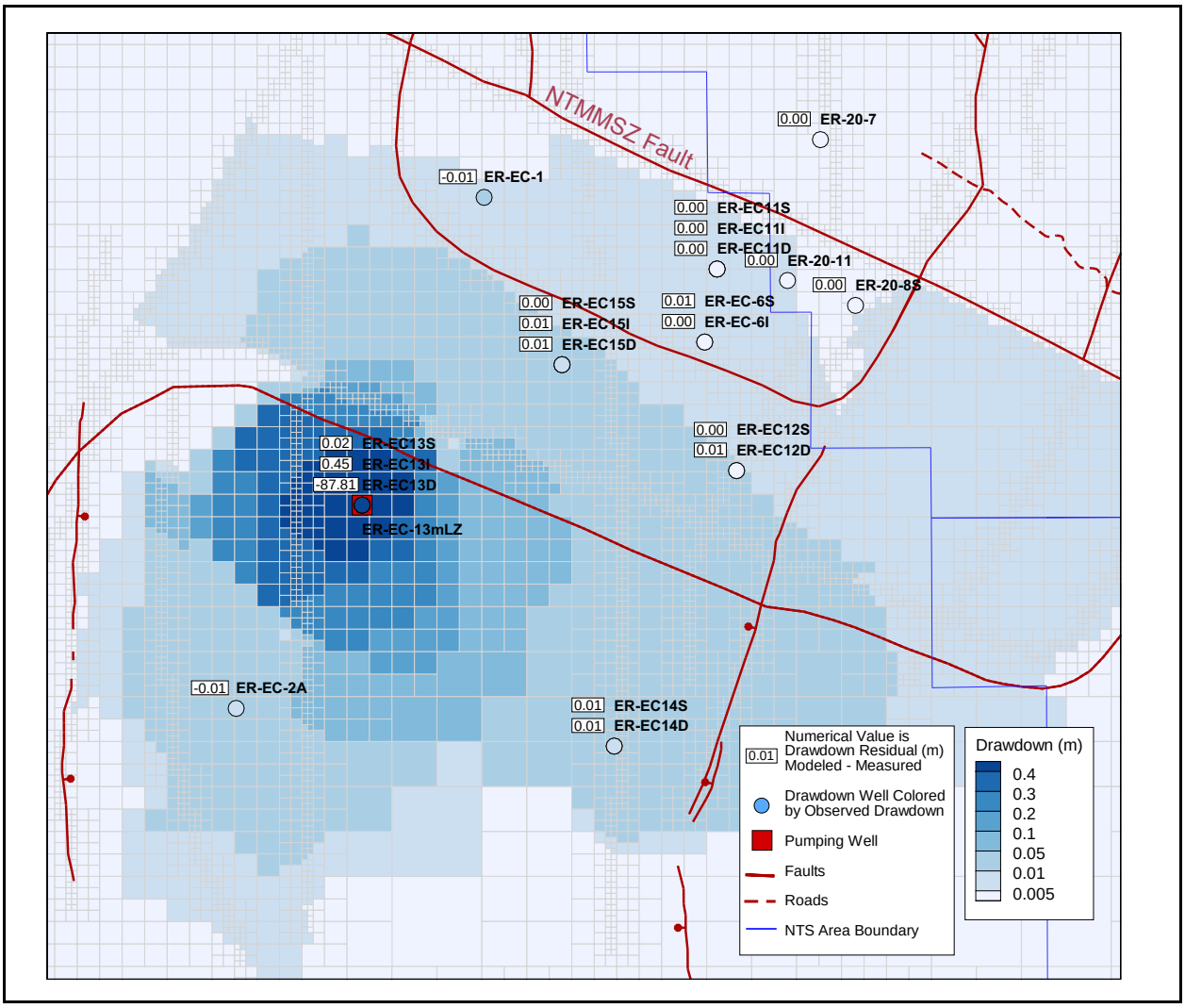

Figure F-16
Drawdown Extent and Residuals in Response to Well ER-EC-13 Main Lower Zone Pumping on Day 250 of the Well Development and Testing Period

F.1.10 Comparisons of Simulated and Observed Drawdowns in Response to Well ER-EC-14 Main Upper and Lower Pumping

The primary HSU within the ER-14 main upper and lower completion is the RMWTA HSU. Garcia et al. (2017) identified unambiguous responses in the ER-EC-12S, ER-EC-13S, ER-EC-13I, ER-EC-13D, ER-EC-14S, ER-EC-14D, ER-EC-15S, ER-EC-15I, and ER-EC-15D well completions. The drawdown in the ER-EC-14S and ER-EC-14D pumped completions is underestimated by the model, indicating the hydraulic conductivity of the RMWTA HSU is overestimated near the pumped

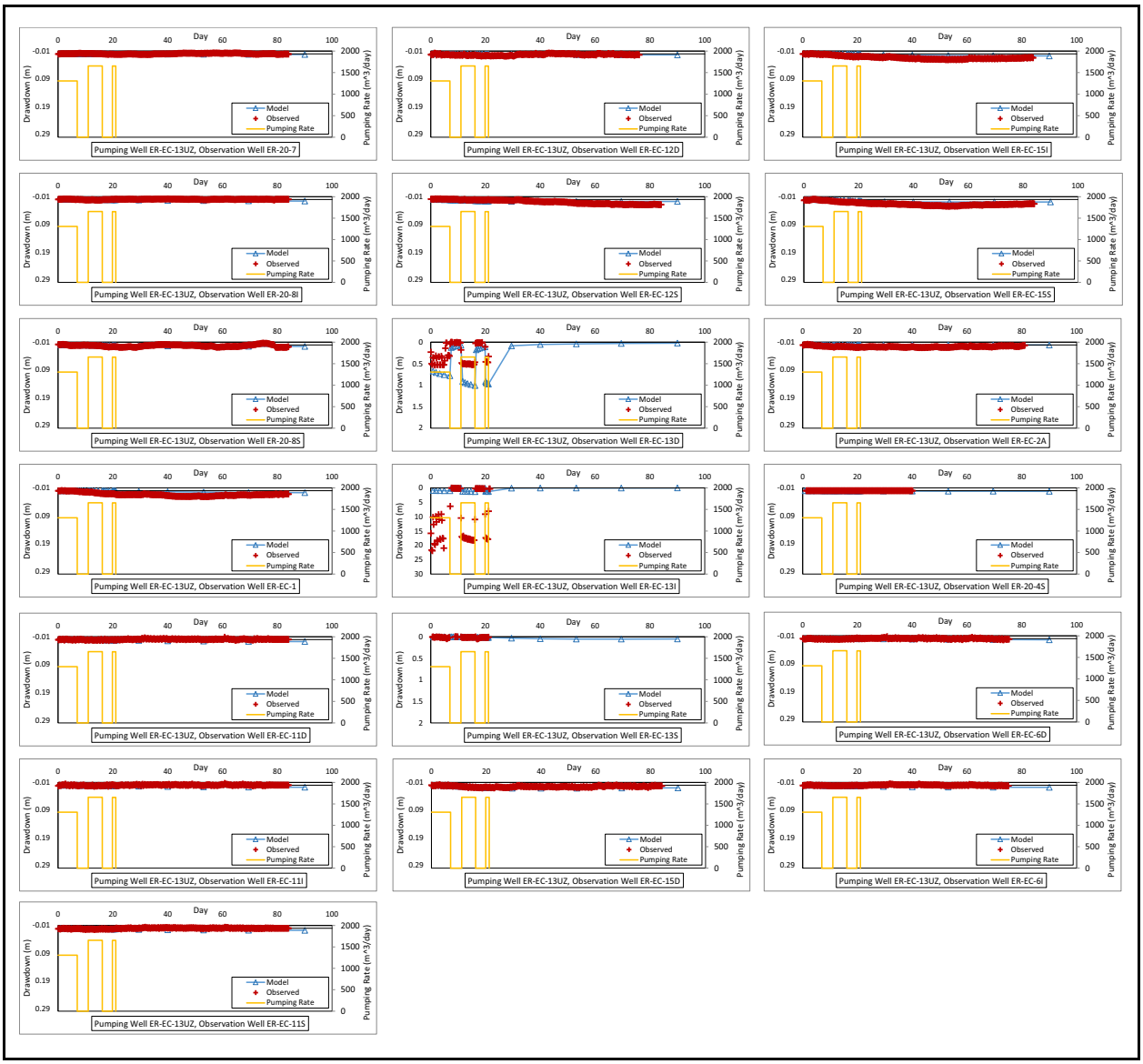

Figure F-17
Comparisons of Simulated and Observed Drawdowns in Response to Well ER-EC-13 Main Upper Zone Pumping

well (Figure F-19). Simulated drawdowns in ER-EC-15S, ER-EC-15I, and ER-EC-15D are underpredicted. The simulated drawdowns in other wells have good agreement with the observations. Figure F-20 illustrates the largest drawdown in any model layer and model drawdown residuals corresponding to Day 54 of the well development and testing period.

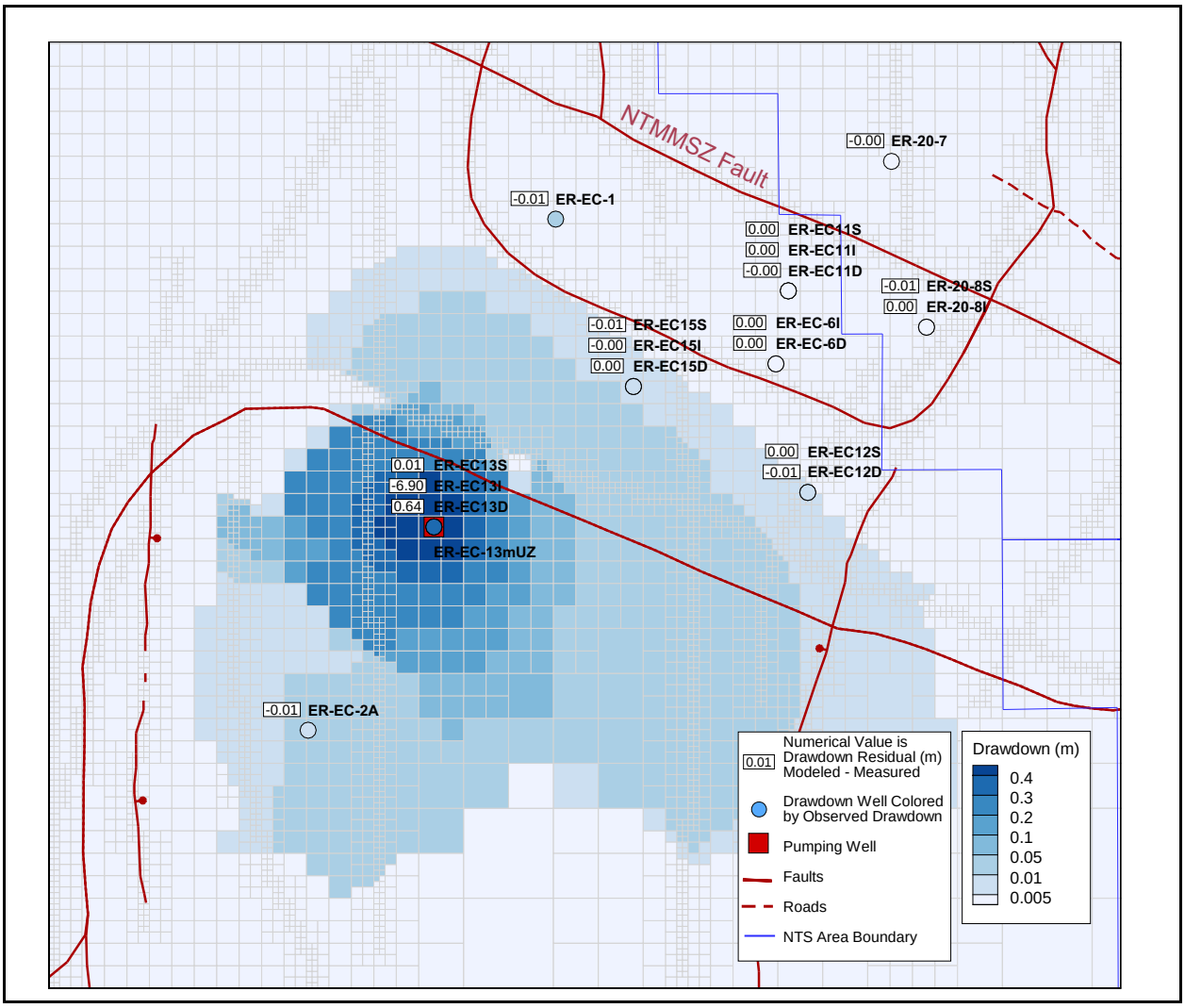

Figure F-18
Drawdown Extent and Residuals in Response to Well ER-EC-13 Main Upper Zone Pumping on Day 21 of the Well Development and Testing Period

F.1.11 Comparisons of Simulated and Observed Drawdowns in Response to Well ER-EC-15 Main Upper, Intermediate, and Lower Pumping

The primary HSUs within the ER-15 main upper, intermediate, and lower completion are the CPA, TCA, and TSA HSUs, respectively. During the ER-EC-15 MWAT, Garcia et al. (2017) identified unambiguous responses only in the ER-EC-12S distal observation well. Drawdowns were also observed in the pumped wellbore within ER-EC-15S, ER-EC-15I, and ER-EC-15D completions. The drawdown in ER-EC-15S~~,~~ is overestimated and the drawdowns in ER-EC-15I and ER-EC-15D

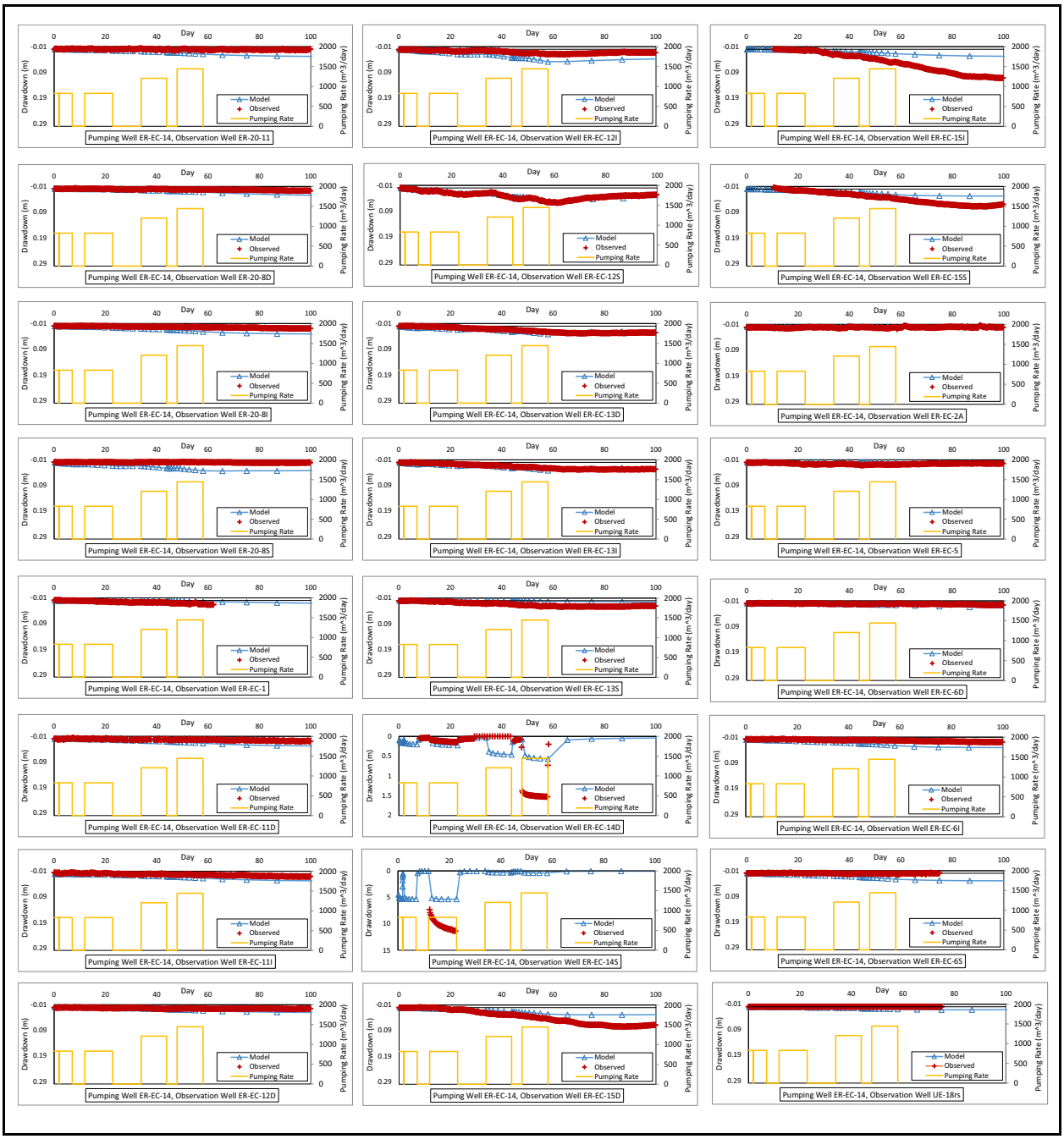

Figure F-19
Comparisons of Simulated and Observed Drawdowns in Response to Well ER-EC-14 Main Upper and Lower Pumping

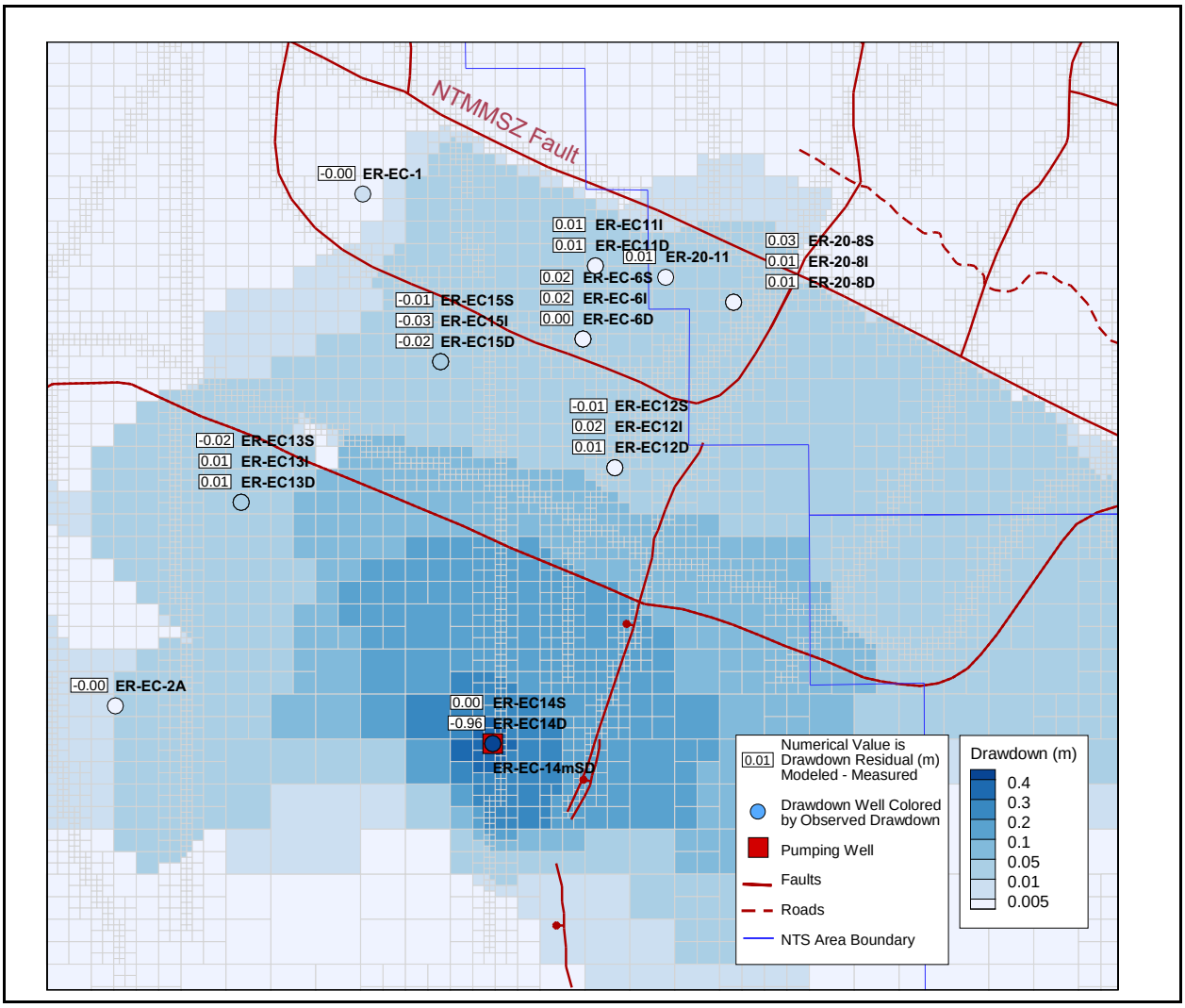

Figure F-20
Drawdown Extent and Residuals in Response to Well ER-EC-14 Main Upper and Lower Pumping on Day 54 of the Well Development and Testing Period

were underestimated, indicating the hydraulic conductivity of the CPA is underestimated, while the hydraulic conductivity of the TCA and TSA HSUs is overestimated by the model (Figure F-21). Figure F-22 illustrates the largest drawdown in any model layer and model drawdown residuals corresponding to Day 39 of the well development and testing period.

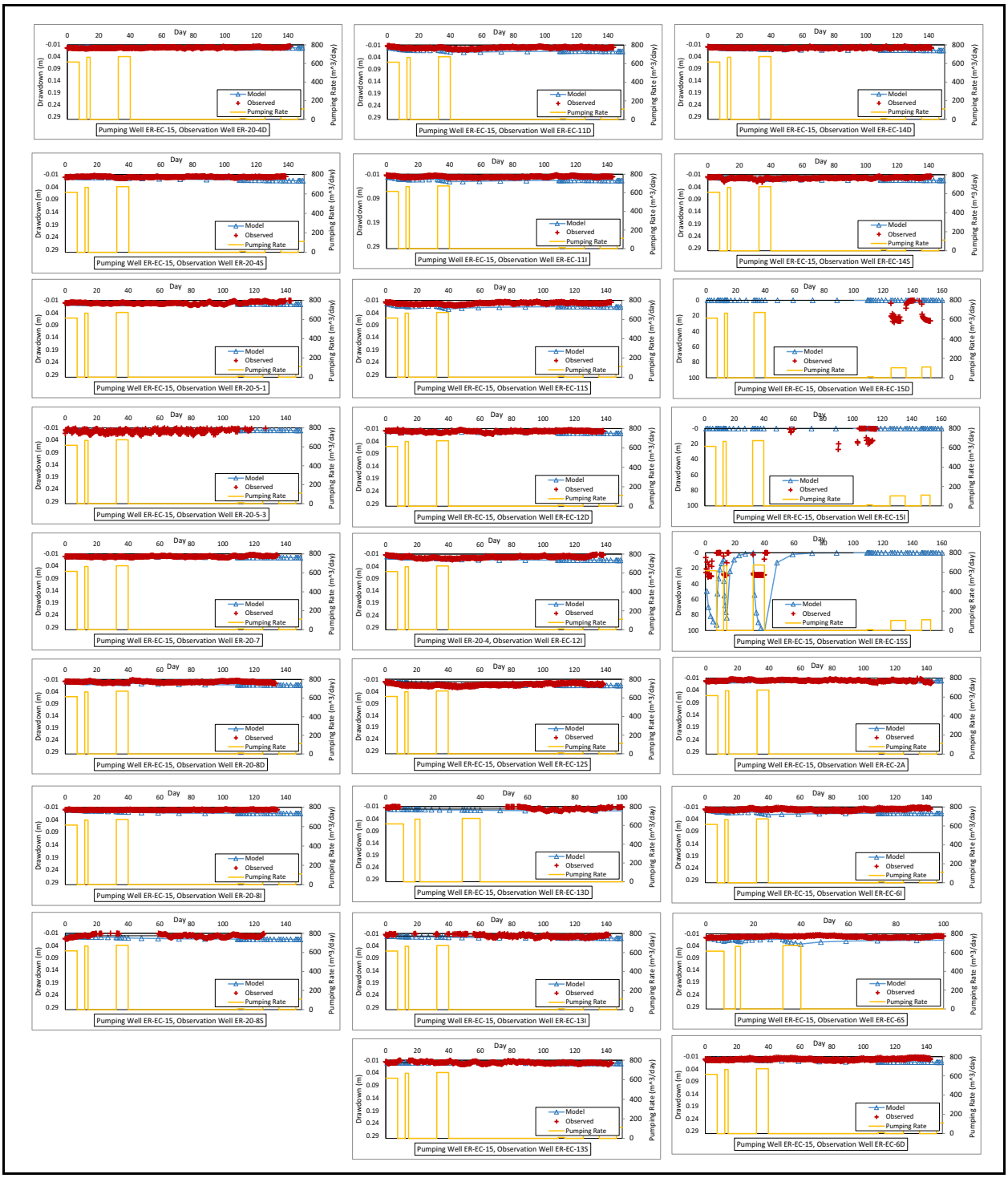

Figure F-21
Comparisons of Simulated and Observed Drawdowns in Response to Well ER-EC-15 Main Upper, Intermediate, and Lower Pumping

F.1.12 Drawdown Response Conclusions

The interpretation of the underlying cause for the model underpredicting or overpredicting drawdowns at the pumped well is evident. An underprediction of drawdown indicates hydraulic conductivity is overestimated, while an overprediction of drawdown indicates the hydraulic conductivity is underestimated by the model. However, in a complex hydrogeolic setting such as PM, the interpretation of the drawdown mismatches in distal observation wells can be difficult. Areas of underpredicted or overpredicted hydraulic conductivity between the pumped and observation well may contribute to the model underpredicting or overpredicting drawdowns. For example, an area of underpredicted hydraulic conductivity may not allow the drawdown signal to propagate to the observation well, resulting in an underprediction of drawdown. Conversely, an overprediction of hydraulic conductivity may produce an overly strong hydraulic connection resulting in the model overpredicting drawdown at the observation well. For these reasons, the areas of simulated underpredicted or overpredicted HSU hydraulic conductivity can only be definitively identified at the pumped well location.

Nonetheless, within the pumped well and observation wells, simulated drawdowns are more often underpredicted than overpredicted, suggesting the model has bias in overestimating hydraulic conductivity, which will result in overestimating groundwater flow rates and transport velocities within the area influenced by the MWATs. For a given set of transport parameters, this will lead to overpredicting the transport, and the resulting PM CAU model and the CB forecasts will be conservatively overestimating RN migration. If transport parameters are being calibrated to RN observation, overestimating transport velocities will lead to a different set of transport parameter values chosen as the calibrated set. The CBs reported in the Executive Summary, Section 5.7, and Section 6.0 are insensitive to this issue because they are computed using the entire permissible range of values for transport parameters as described in Section 5.5.2.

Nearly all simulated drawdowns within the pumped wells are underestimated. Two factors likely contribute to the model's systematic underestimation the drawdown within the pumped wells. The first is the discrete cell size used in the MODFLOW 6 mesh. Cell dimensions range from 1,200 m on a side to 75 m on a side in the horizontal direction and the model's mesh is refined to 300 m within the main flow corridor from the testing areas to Oasis Valley. Fine mesh refinement of 75 m only occurs near faults within the main flow corridor (Section 4.2.1). Most of the cells containing pumping

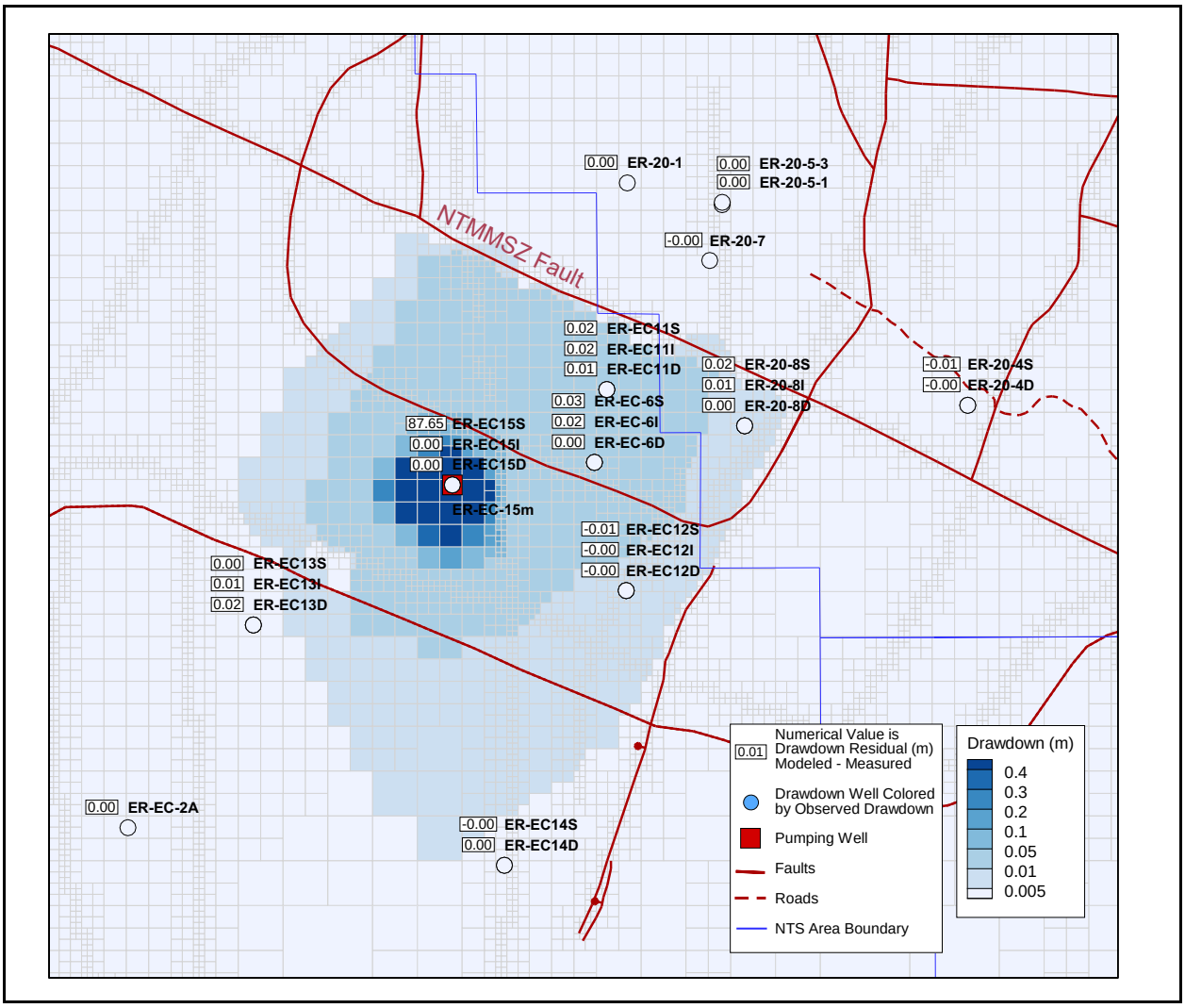

Figure F-22
Drawdown Extent and Residuals in Response to Well ER-EC-15 Main Upper, Intermediate, and Lower Pumping on Day 40 of the Well Development and Testing Period

wells have a 300-m resolution and the drawdown within the cell represents a 300 m average of the drawdown within the cone of depression surrounding the well. The underprediction of simulated drawdowns due to cell resolution will be the greatest at wells with low transmissivity and low pumping rates. The second factor is non-linear well losses often contribute to the measured drawdown within the pumped well. Navarro (2016) estimated nonlinear well losses comprise approximately 65 to 74 percent of the total drawdown observed in Well ER-20-11 during well during development and testing. Nonlinear well losses increase when transmissivity is high and pumping rates are large.

F.2.0 References

Garcia, C.A., T.R. Jackson, K.J. Halford, D.S. Sweetkind, N.A. Damar, J.M. Fenelon, and S.R. Reiner. 2017. *Hydraulic Characterization of Volcanic Rocks in Pahute Mesa Using an Integrated Analysis of 16 Multiple-Well Aquifer Tests, Nevada National Security Site, 2009–14,* Scientific Investigations Report 2016-5151. Carson City, NV: U.S. Geological Survey.

Navarro. 2016. *Pahute Mesa Well Development and Testing Analyses for Well ER-20-11, Nevada National Security Site, Nye County, Nevada,* Rev. 0, N/0002653--028. Las Vegas, NV.

Appendix G

Log K_d Distributions Used in the PM CAU Transport Model

G.1.0 Log K_d Distributions Used in the PM CAU Transport Model

Mean log K_d and standard deviation of log K_d were taken from Tables 12 and 13 of Carle et al. (2020), where K_d was taken in the units of mL/gm. Carle et al. (2020) assign K_d distributions for each RN of interest on the basis of HGU, DZ, and chemistry subarea.

The five chemistry subareas defined on the basis of groundwater geochemistry in Carle et al. (2020) are 20-NW (northwest Area 20), 20-S (south Area 20), 20-NE (northeast Area 20), 19-W (west Area 19, also identified as 19-SW), and 19-E (east Area 19, also identified as 19-NE).

Carle et al. (2020) also assign four vertical zones (DZs) to rock formations at PM on the basis of minerologic diagenesis. The DZs are formed by hydration and hydrothermal processes that transform the mineralogical composition of the rock. The upper Zone 1 corresponds to the upper volcanic section with unaltered or incipiently altered rhyolitic glass (e.g., where vitric tuffs are present). Zone 2 is zeolitic with a predominance of clinoptilolite and increasing mordenite with depth. Zone 3 is transitional from zeolite to quartz, with the zeolite predominantly analcime and mordenite with lesser or no clinoptilolite. This study adds a deeper “quartzofeldspathic” Zone 4 characterized by absence of zeolite and abundant quartz and feldspar.

The chemistry subareas and DZs assigned to each HSU in the PM transport model, except the LCA and LCA3 (which are not addressed in Carle at al., 2020), are listed in Table G-1. The LCA and LCA3 are not significant aquifers in the PM-OV flow and transport model. Nevertheless, K_d values for LCA and LCA3 are taken from Table 5-37 of Navarro (2021). The K_d statistics used in the PM transport model are defined in Table G-2, which presents the sorption coefficient values, including mean value and range or standard deviation for each RN and HSU. The minimum and maximum values presented in Table G-2 were estimated as mean - 2*(standard deviation) and mean + 2*(standard deviation).

Table G-1
Assigned Chemistry Subareas and Diagenetic Zones Used for K_d Selection
(Source: Carle et al. 2020)
(Page 1 of 3)

HSU	Chemistry Subarea	Diagenetic Zone
ATICU	20-S	4
RMICU	20-S	4
UCCU	20-S	4
ATCCU	20-S	4
LCA	20-S	N/A
CFCU	20-S	4
BFCU	20-S	4
LPCU	20-S	2
MPCU	20-S	3
PBPCU	20-S	2
FCCU	20-S	2
SCVCU	20-S	4
UPCU	20-S	2
THCU	20-S	4
BWCU	20-S	2
CFCM	20-S	4
THCM	20-S	2
FCCM	20-S	2
PBRCM	20-S	4
CHLFA1	20-S	2
CHLFA3	20-S	2
CHLFA2	20-S	2
IA	20-S	3
CHLFA5	20-S	3
CHLFA4	20-S	2
PLFA	20-S	1
FCULFA4	20-S	2
FCULFA1	20-S	1

Table G-1
Assigned Chemistry Subareas and Diagenetic Zones Used for K_d Selection
(Source: Carle et al. 2020)
(Page 2 of 3)

HSU	Chemistry Subarea	Diagenetic Zone
FCLLFA	20-S	3
FCULFA2	20-S	2
SPA	20-S	2
THLFA	20-S	1
BA	20-S	2
BRA	20-S	4
CPA	20-S	2
ATWTA	20-S	3
BWWTA	20-S	2
FCWTA1	20-S	3
TSA	20-S	3
TCA	20-S	2
WWA	20-S	1
RMWTA	20-S	4
TMWTA	20-S	2
TMUWTA	20-S	2
CHVTA	20-S	1
PVTA	20-S	1
TCVA	20-S	1
TMLVTA	20-S	1
PMNICU	20-S	4
LCCU	20-S	4
LCCU1	20-S	4
MGCU	20-S	4
YMCFCM	20-S	3
PCM	20-S	3
KA	20-S	2
FCULFA5	20-S	2

Table G-1
Assigned Chemistry Subareas and Diagenetic Zones Used for K_d Selection
(Source: Carle et al. 2020)
(Page 3 of 3)

HSU	Chemistry Subarea	Diagenetic Zone
DVA	20-S	3
DVCM	20-S	3
FCWTA	20-S	3
CHZCM	20-S	3
AA	20-S	1
YVCM	20-S	1
LCA3	20-S	N/A
PBRCMsw	20-NW	3
BRA_sw	20-NW	2
TCA_w	20-NW	2
CHZCM_w	20-NW	2
UPCU_sw	20-NW	2
LPCU_sw	20-NW	2
CHLFA5w	20-NW	2
UPCU_nw	20-NW	2
LPCU_nw	20-NW	2
PBRCMnw	20-NW	3
BRA_nw	20-NW	2
mRMWTA1	20-S	4
mRMWTA2	20-S	4
mPBRCMnw	20-NW	2
Faults (barrier)	20-S	4
Faults (conduit)	20-NW	2

Table G-2
Log K_d Distributions Used in the PM CAU Transport Model (Source: Carle et al., 2020)
(Page 1 of 16)

HSU	Distribution Type	Statistic	Cs	Sr	Np	Pu	U
ATICU	Normal	Mean	3.78	1.39	0.44	2.44	0.01
		Std. Dev.	0.22	0.23	0.22	0.22	0.21
		Minimum	3.34	0.93	0.00	2.00	-0.41
		Maximum	4.22	1.85	0.88	2.88	0.43
RMICU	Normal	Mean	3.78	1.39	0.44	2.44	0.01
		Std. Dev.	0.22	0.23	0.22	0.22	0.21
		Minimum	3.34	0.93	0.00	2.00	-0.41
		Maximum	4.22	1.85	0.88	2.88	0.43
UCCU	Normal	Mean	3.78	1.39	0.44	2.44	0.01
		Std. Dev.	0.22	0.23	0.22	0.22	0.21
		Minimum	3.34	0.93	0.00	2.00	-0.41
		Maximum	4.22	1.85	0.88	2.88	0.43
ATCCU	Normal	Mean	4.69	1.98	0.22	2.39	0.40
		Std. Dev.	0.34	0.33	0.40	0.52	0.40
		Minimum	4.01	1.32	-0.58	1.35	-0.40
		Maximum	5.37	2.64	1.02	3.43	1.20
LCA	Triangular	Mode	-1.35	-1.02	--	2.74	1.18
		Minimum	-1.70	-1.30	--	-0.12	-1.52
		Maximum	-1.15	-0.85	--	3.04	1.48

Table G-2
Log K_d Distributions Used in the PM CAU Transport Model (Source: Carle et al., 2020)
(Page 2 of 16)

HSU	Distribution Type	Statistic	Cs	Sr	Np	Pu	U
CFCU	Normal	Mean	4.69	1.98	0.22	2.39	0.40
		Std. Dev.	0.34	0.33	0.40	0.52	0.40
		Minimum	4.01	1.32	-0.58	1.35	-0.40
		Maximum	5.37	2.64	1.02	3.43	1.20
BFCU	Normal	Mean	4.69	1.98	0.22	2.39	0.40
		Std. Dev.	0.34	0.33	0.40	0.52	0.40
		Minimum	4.01	1.32	-0.58	1.35	-0.40
		Maximum	5.37	2.64	1.02	3.43	1.20
LPCU	Normal	Mean	4.25	3.55	0.09	2.59	0.36
		Std. Dev.	0.39	0.26	0.50	0.58	0.53
		Minimum	3.47	3.03	-0.91	1.43	-0.70
		Maximum	5.03	4.07	1.09	3.75	1.42
MPCU	Normal	Mean	4.46	3.15	0.28	2.53	0.47
		Std. Dev.	0.39	0.30	0.56	0.42	0.35
		Minimum	3.68	2.55	-0.84	1.69	-0.23
		Maximum	5.24	3.75	1.40	3.37	1.17
PBPCU	Normal	Mean	4.25	3.55	0.09	2.59	0.36
		Std. Dev.	0.39	0.26	0.50	0.58	0.53
		Minimum	3.47	3.03	-0.91	1.43	-0.70
		Maximum	5.03	4.07	1.09	3.75	1.42

Table G-2
Log K_d Distributions Used in the PM CAU Transport Model (Source: Carle et al., 2020)
(Page 3 of 16)

HSU	Distribution Type	Statistic	Cs	Sr	Np	Pu	U
FCCU	Normal	Mean	4.25	3.55	0.09	2.59	0.36
		Std. Dev.	0.39	0.26	0.50	0.58	0.53
		Minimum	3.47	3.03	-0.91	1.43	-0.70
		Maximum	5.03	4.07	1.09	3.75	1.42
SCVCU	Normal	Mean	4.69	1.98	0.22	2.39	0.40
		Std. Dev.	0.34	0.33	0.40	0.52	0.40
		Minimum	4.01	1.32	-0.58	1.35	-0.40
		Maximum	5.37	2.64	1.02	3.43	1.20
UPCU	Normal	Mean	4.25	3.55	0.09	2.59	0.36
		Std. Dev.	0.39	0.26	0.50	0.58	0.53
		Minimum	3.47	3.03	-0.91	1.43	-0.70
		Maximum	5.03	4.07	1.09	3.75	1.42
THCU	Normal	Mean	4.69	1.98	0.22	2.39	0.40
		Std. Dev.	0.34	0.33	0.40	0.52	0.40
		Minimum	4.01	1.32	-0.58	1.35	-0.40
		Maximum	5.37	2.64	1.02	3.43	1.20
BWCU	Normal	Mean	4.25	3.55	0.09	2.59	0.36
		Std. Dev.	0.39	0.26	0.50	0.58	0.53
		Minimum	3.47	3.03	-0.91	1.43	-0.70
		Maximum	5.03	4.07	1.09	3.75	1.42

Table G-2
Log K_d Distributions Used in the PM CAU Transport Model (Source: Carle et al., 2020)
(Page 4 of 16)

HSU	Distribution Type	Statistic	Cs	Sr	Np	Pu	U
CFCM	Normal	Mean	4.58	1.78	0.02	1.99	0.49
		Std. Dev.	0.39	0.36	0.41	0.45	0.38
		Minimum	3.80	1.06	-0.80	1.09	-0.27
		Maximum	5.36	2.50	0.84	2.89	1.25
THCM	Normal	Mean	4.25	3.55	0.09	2.59	0.36
		Std. Dev.	0.39	0.26	0.50	0.58	0.53
		Minimum	3.47	3.03	-0.91	1.43	-0.70
		Maximum	5.03	4.07	1.09	3.75	1.42
FCCM	Normal	Mean	4.25	3.55	0.09	2.59	0.36
		Std. Dev.	0.39	0.26	0.50	0.58	0.53
		Minimum	3.47	3.03	-0.91	1.43	-0.70
		Maximum	5.03	4.07	1.09	3.75	1.42
PBRCM	Normal	Mean	4.69	1.98	0.22	2.39	0.40
		Std. Dev.	0.34	0.33	0.40	0.52	0.40
		Minimum	4.01	1.32	-0.58	1.35	-0.40
		Maximum	5.37	2.64	1.02	3.43	1.20
CHLFA1	Normal	Mean	4.26	3.15	0.33	2.66	0.65
		Std. Dev.	0.36	0.42	0.55	0.47	0.57
		Minimum	3.54	2.31	-0.77	1.72	-0.49
		Maximum	4.98	3.99	1.43	3.60	1.79

Table G-2
Log K_d Distributions Used in the PM CAU Transport Model (Source: Carle et al., 2020)
(Page 5 of 16)

HSU	Distribution Type	Statistic	Cs	Sr	Np	Pu	U
CHLFA3	Normal	Mean	4.26	3.15	0.33	2.66	0.65
		Std. Dev.	0.36	0.42	0.55	0.47	0.57
		Minimum	3.54	2.31	-0.77	1.72	-0.49
		Maximum	4.98	3.99	1.43	3.60	1.79
CHLFA2	Normal	Mean	4.26	3.15	0.33	2.66	0.65
		Std. Dev.	0.36	0.42	0.55	0.47	0.57
		Minimum	3.54	2.31	-0.77	1.72	-0.49
		Maximum	4.98	3.99	1.43	3.60	1.79
IA	Normal	Mean	4.21	2.74	0.35	2.36	0.49
		Std. Dev.	0.34	0.47	0.51	0.46	0.42
		Minimum	3.53	1.80	-0.67	1.44	-0.35
		Maximum	4.89	3.68	1.37	3.28	1.33
CHLFA5	Normal	Mean	4.21	2.74	0.35	2.36	0.49
		Std. Dev.	0.34	0.47	0.51	0.46	0.42
		Minimum	3.53	1.80	-0.67	1.44	-0.35
		Maximum	4.89	3.68	1.37	3.28	1.33
CHLFA4	Normal	Mean	4.26	3.15	0.33	2.66	0.65
		Std. Dev.	0.36	0.42	0.55	0.47	0.57
		Minimum	3.54	2.31	-0.77	1.72	-0.49
		Maximum	4.98	3.99	1.43	3.60	1.79

Table G-2
Log K_d Distributions Used in the PM CAU Transport Model (Source: Carle et al., 2020)
(Page 6 of 16)

HSU	Distribution Type	Statistic	Cs	Sr	Np	Pu	U
PLFA	Normal	Mean	4.20	2.04	-0.02	1.95	0.67
		Std. Dev.	0.39	0.34	0.53	0.45	0.40
		Minimum	3.42	1.36	-1.08	1.05	-0.13
		Maximum	4.98	2.72	1.04	2.85	1.47
FCULFA4	Normal	Mean	4.26	3.15	0.33	2.66	0.65
		Std. Dev.	0.36	0.42	0.55	0.47	0.57
		Minimum	3.54	2.31	-0.77	1.72	-0.49
		Maximum	4.98	3.99	1.43	3.60	1.79
FCULFA1	Normal	Mean	4.20	2.04	-0.02	1.95	0.67
		Std. Dev.	0.39	0.34	0.53	0.45	0.40
		Minimum	3.42	1.36	-1.08	1.05	-0.13
		Maximum	4.98	2.72	1.04	2.85	1.47
FCLLFA	Normal	Mean	4.21	2.74	0.35	2.36	0.49
		Std. Dev.	0.34	0.47	0.51	0.46	0.42
		Minimum	3.53	1.80	-0.67	1.44	-0.35
		Maximum	4.89	3.68	1.37	3.28	1.33
FCULFA2	Normal	Mean	4.26	3.15	0.33	2.66	0.65
		Std. Dev.	0.36	0.42	0.55	0.47	0.57
		Minimum	3.54	2.31	-0.77	1.72	-0.49
		Maximum	4.98	3.99	1.43	3.60	1.79

Table G-2
Log K_d Distributions Used in the PM CAU Transport Model (Source: Carle et al., 2020)
(Page 7 of 16)

HSU	Distribution Type	Statistic	Cs	Sr	Np	Pu	U
SPA	Normal	Mean	4.26	3.15	0.33	2.66	0.65
		Std. Dev.	0.36	0.42	0.55	0.47	0.57
		Minimum	3.54	2.31	-0.77	1.72	-0.49
		Maximum	4.98	3.99	1.43	3.60	1.79
THLFA	Normal	Mean	4.20	2.04	-0.02	1.95	0.67
		Std. Dev.	0.39	0.34	0.53	0.45	0.40
		Minimum	3.42	1.36	-1.08	1.05	-0.13
		Maximum	4.98	2.72	1.04	2.85	1.47
BA	Normal	Mean	4.26	3.15	0.33	2.66	0.65
		Std. Dev.	0.36	0.42	0.55	0.47	0.57
		Minimum	3.54	2.31	-0.77	1.72	-0.49
		Maximum	4.98	3.99	1.43	3.60	1.79
BRA	Normal	Mean	4.68	1.98	0.43	2.59	0.63
		Std. Dev.	0.30	0.32	0.42	0.58	0.40
		Minimum	4.08	1.34	-0.41	1.43	-0.17
		Maximum	5.28	2.62	1.27	3.75	1.43
CPA	Normal	Mean	4.26	3.15	0.33	2.66	0.65
		Std. Dev.	0.36	0.42	0.55	0.47	0.57
		Minimum	3.54	2.31	-0.77	1.72	-0.49
		Maximum	4.98	3.99	1.43	3.60	1.79

Table G-2
Log K_d Distributions Used in the PM CAU Transport Model (Source: Carle et al., 2020)
(Page 8 of 16)

HSU	Distribution Type	Statistic	Cs	Sr	Np	Pu	U
ATWTA	Normal	Mean	4.30	2.54	-0.13	2.05	0.49
		Std. Dev.	0.35	0.47	0.39	0.38	0.30
		Minimum	3.60	1.60	-0.91	1.29	-0.11
		Maximum	5.00	3.48	0.65	2.81	1.09
BWWTA	Normal	Mean	4.25	2.98	-0.16	2.24	0.50
		Std. Dev.	0.40	0.43	0.40	0.40	0.31
		Minimum	3.45	2.12	-0.96	1.44	-0.12
		Maximum	5.05	3.84	0.64	3.04	1.12
FCWTA1	Normal	Mean	4.30	2.54	-0.13	2.05	0.49
		Std. Dev.	0.35	0.47	0.39	0.38	0.30
		Minimum	3.60	1.60	-0.91	1.29	-0.11
		Maximum	5.00	3.48	0.65	2.81	1.09
TSA	Normal	Mean	4.30	2.54	-0.13	2.05	0.49
		Std. Dev.	0.35	0.47	0.39	0.38	0.30
		Minimum	3.60	1.60	-0.91	1.29	-0.11
		Maximum	5.00	3.48	0.65	2.81	1.09
TCA	Normal	Mean	4.25	2.98	-0.16	2.24	0.50
		Std. Dev.	0.40	0.43	0.40	0.40	0.31
		Minimum	3.45	2.12	-0.96	1.44	-0.12
		Maximum	5.05	3.84	0.64	3.04	1.12

Table G-2
Log K_d Distributions Used in the PM CAU Transport Model (Source: Carle et al., 2020)
(Page 9 of 16)

HSU	Distribution Type	Statistic	Cs	Sr	Np	Pu	U
WWA	Normal	Mean	4.20	2.04	-0.02	1.95	0.67
		Std. Dev.	0.39	0.34	0.53	0.45	0.40
		Minimum	3.42	1.36	-1.08	1.05	-0.13
		Maximum	4.98	2.72	1.04	2.85	1.47
RMWTA	Normal	Mean	4.68	1.98	0.43	2.59	0.63
		Std. Dev.	0.30	0.32	0.42	0.58	0.40
		Minimum	4.08	1.34	-0.41	1.43	-0.17
		Maximum	5.28	2.62	1.27	3.75	1.43
TMWTA	Normal	Mean	4.25	2.98	-0.16	2.24	0.50
		Std. Dev.	0.40	0.43	0.40	0.40	0.31
		Minimum	3.45	2.12	-0.96	1.44	-0.12
		Maximum	5.05	3.84	0.64	3.04	1.12
TMUWTA	Normal	Mean	4.25	2.98	-0.16	2.24	0.50
		Std. Dev.	0.40	0.43	0.40	0.40	0.31
		Minimum	3.45	2.12	-0.96	1.44	-0.12
		Maximum	5.05	3.84	0.64	3.04	1.12
CHVTA	Normal	Mean	4.16	2.26	0.26	2.64	0.72
		Std. Dev.	0.51	0.34	0.35	0.42	0.30
		Minimum	3.14	1.58	-0.44	1.80	0.12
		Maximum	5.18	2.94	0.96	3.48	1.32

Table G-2
Log K_d Distributions Used in the PM CAU Transport Model (Source: Carle et al., 2020)
(Page 10 of 16)

HSU	Distribution Type	Statistic	Cs	Sr	Np	Pu	U
PVTA	Normal	Mean	4.16	2.26	0.26	2.64	0.72
		Std. Dev.	0.51	0.34	0.35	0.42	0.30
		Minimum	3.14	1.58	-0.44	1.80	0.12
		Maximum	5.18	2.94	0.96	3.48	1.32
TCVA	Normal	Mean	4.14	1.55	0.20	2.20	0.71
		Std. Dev.	0.36	0.26	0.34	0.27	0.29
		Minimum	3.42	1.03	-0.48	1.66	0.13
		Maximum	4.86	2.07	0.88	2.74	1.29
TMLVTA	Normal	Mean	4.16	2.26	0.26	2.64	0.72
		Std. Dev.	0.51	0.34	0.35	0.42	0.30
		Minimum	3.14	1.58	-0.44	1.80	0.12
		Maximum	5.18	2.94	0.96	3.48	1.32
PMNICU	Normal	Mean	3.78	1.39	0.44	2.44	0.01
		Std. Dev.	0.22	0.23	0.22	0.22	0.21
		Minimum	3.34	0.93	0.00	2.00	-0.41
		Maximum	4.22	1.85	0.88	2.88	0.43
LCCU	Normal	Mean	3.78	1.39	0.44	2.44	0.01
		Std. Dev.	0.22	0.23	0.22	0.22	0.21
		Minimum	3.34	0.93	0.00	2.00	-0.41
		Maximum	4.22	1.85	0.88	2.88	0.43

Table G-2
Log K_d Distributions Used in the PM CAU Transport Model (Source: Carle et al., 2020)
(Page 11 of 16)

HSU	Distribution Type	Statistic	Cs	Sr	Np	Pu	U
LCCU1	Normal	Mean	3.78	1.39	0.44	2.44	0.01
		Std. Dev.	0.22	0.23	0.22	0.22	0.21
		Minimum	3.34	0.93	0.00	2.00	-0.41
		Maximum	4.22	1.85	0.88	2.88	0.43
MGCU	Normal	Mean	3.78	1.39	0.44	2.44	0.01
		Std. Dev.	0.22	0.23	0.22	0.22	0.21
		Minimum	3.34	0.93	0.00	2.00	-0.41
		Maximum	4.22	1.85	0.88	2.88	0.43
YMCFCM	Normal	Mean	4.21	2.74	0.35	2.36	0.49
		Std. Dev.	0.34	0.47	0.51	0.46	0.42
		Minimum	3.53	1.80	-0.67	1.44	-0.35
		Maximum	4.89	3.68	1.37	3.28	1.33
PCM	Normal	Mean	4.30	2.54	-0.13	2.05	0.49
		Std. Dev.	0.35	0.47	0.39	0.38	0.30
		Minimum	3.60	1.60	-0.91	1.29	-0.11
		Maximum	5.00	3.48	0.65	2.81	1.09
KA	Normal	Mean	4.26	3.15	0.33	2.66	0.65
		Std. Dev.	0.36	0.42	0.55	0.47	0.57
		Minimum	3.54	2.31	-0.77	1.72	-0.49
		Maximum	4.98	3.99	1.43	3.60	1.79

Table G-2
Log K_d Distributions Used in the PM CAU Transport Model (Source: Carle et al., 2020)
(Page 12 of 16)

HSU	Distribution Type	Statistic	Cs	Sr	Np	Pu	U
FCULFA5	Normal	Mean	4.26	3.15	0.33	2.66	0.65
		Std. Dev.	0.36	0.42	0.55	0.47	0.57
		Minimum	3.54	2.31	-0.77	1.72	-0.49
		Maximum	4.98	3.99	1.43	3.60	1.79
DVA	Normal	Mean	4.30	2.54	-0.13	2.05	0.49
		Std. Dev.	0.35	0.47	0.39	0.38	0.30
		Minimum	3.60	1.60	-0.91	1.29	-0.11
		Maximum	5.00	3.48	0.65	2.81	1.09
DVCM	Normal	Mean	4.30	2.54	-0.13	2.05	0.49
		Std. Dev.	0.35	0.47	0.39	0.38	0.30
		Minimum	3.60	1.60	-0.91	1.29	-0.11
		Maximum	5.00	3.48	0.65	2.81	1.09
FCWTA	Normal	Mean	4.30	2.54	-0.13	2.05	0.49
		Std. Dev.	0.35	0.47	0.39	0.38	0.30
		Minimum	3.60	1.60	-0.91	1.29	-0.11
		Maximum	5.00	3.48	0.65	2.81	1.09
CHZCM	Normal	Mean	4.46	3.15	0.28	2.53	0.47
		Std. Dev.	0.39	0.30	0.56	0.42	0.35
		Minimum	3.68	2.55	-0.84	1.69	-0.23
		Maximum	5.24	3.75	1.40	3.37	1.17

Table G-2
Log K_d Distributions Used in the PM CAU Transport Model (Source: Carle et al., 2020)
(Page 13 of 16)

HSU	Distribution Type	Statistic	Cs	Sr	Np	Pu	U
AA	Normal	Mean	3.72	3.17	0.67	2.70	0.61
		Std. Dev.	0.22	0.23	0.21	0.23	0.23
		Minimum	3.28	2.71	0.25	2.24	0.15
		Maximum	4.16	3.63	1.09	3.16	1.07
YVCM	Normal	Mean	4.20	2.04	-0.02	1.95	0.67
		Std. Dev.	0.39	0.34	0.53	0.45	0.40
		Minimum	3.42	1.36	-1.08	1.05	-0.13
		Maximum	4.98	2.72	1.04	2.85	1.47
LCA3	Triangular	Mode	-1.35	-1.02	--	2.74	1.18
		Minimum	-1.70	-1.30	--	-0.12	-1.52
		Maximum	-1.15	-0.85	--	3.04	1.48
PBRCMsw	Normal	Mean	4.12	2.38	-0.10	2.36	0.32
		Std. Dev.	0.41	0.33	0.40	0.39	0.35
		Minimum	3.30	1.72	-0.90	1.58	-0.38
		Maximum	4.94	3.04	0.70	3.14	1.02
BRA_sw	Normal	Mean	3.90	2.21	-0.36	2.15	0.38
		Std. Dev.	0.42	0.45	0.30	0.36	0.31
		Minimum	3.06	1.31	-0.96	1.43	-0.24
		Maximum	4.74	3.11	0.24	2.87	1.00

Table G-2
Log K_d Distributions Used in the PM CAU Transport Model (Source: Carle et al., 2020)
(Page 14 of 16)

HSU	Distribution Type	Statistic	Cs	Sr	Np	Pu	U
TCA_w	Normal	Mean	3.90	2.21	-0.36	2.15	0.38
		Std. Dev.	0.42	0.45	0.30	0.36	0.31
		Minimum	3.06	1.31	-0.96	1.43	-0.24
		Maximum	4.74	3.11	0.24	2.87	1.00
CHZCM_w	Normal	Mean	3.91	2.78	-0.10	2.47	0.20
		Std. Dev.	0.40	0.29	0.49	0.56	0.52
		Minimum	3.11	2.20	-1.08	1.35	-0.84
		Maximum	4.71	3.36	0.88	3.59	1.24
UPCU_sw	Normal	Mean	3.91	2.78	-0.10	2.47	0.20
		Std. Dev.	0.40	0.29	0.49	0.56	0.52
		Minimum	3.11	2.20	-1.08	1.35	-0.84
		Maximum	4.71	3.36	0.88	3.59	1.24
LPCU_sw	Normal	Mean	3.91	2.78	-0.10	2.47	0.20
		Std. Dev.	0.40	0.29	0.49	0.56	0.52
		Minimum	3.11	2.20	-1.08	1.35	-0.84
		Maximum	4.71	3.36	0.88	3.59	1.24
CHLFA5w	Normal	Mean	3.92	2.38	0.06	2.54	0.54
		Std. Dev.	0.37	0.44	0.46	0.44	0.57
		Minimum	3.18	1.50	-0.86	1.66	-0.60
		Maximum	4.66	3.26	0.98	3.42	1.68

Table G-2
Log K_d Distributions Used in the PM CAU Transport Model (Source: Carle et al., 2020)
(Page 15 of 16)

HSU	Distribution Type	Statistic	Cs	Sr	Np	Pu	U
UPCU_nw	Normal	Mean	3.91	2.78	-0.10	2.47	0.20
		Std. Dev.	0.40	0.29	0.49	0.56	0.52
		Minimum	3.11	2.20	-1.08	1.35	-0.84
		Maximum	4.71	3.36	0.88	3.59	1.24
LPCU_nw	Normal	Mean	3.91	2.78	-0.10	2.47	0.20
		Std. Dev.	0.40	0.29	0.49	0.56	0.52
		Minimum	3.11	2.20	-1.08	1.35	-0.84
		Maximum	4.71	3.36	0.88	3.59	1.24
PBRCMnw	Normal	Mean	4.12	2.38	-0.10	2.36	0.32
		Std. Dev.	0.41	0.33	0.40	0.39	0.35
		Minimum	3.30	1.72	-0.90	1.58	-0.38
		Maximum	4.94	3.04	0.70	3.14	1.02
BRA_nw	Normal	Mean	3.90	2.21	-0.36	2.15	0.38
		Std. Dev.	0.42	0.45	0.30	0.36	0.31
		Minimum	3.06	1.31	-0.96	1.43	-0.24
		Maximum	4.74	3.11	0.24	2.87	1.00
mRMWTA1	Normal	Mean	4.68	1.98	0.43	2.59	0.63
		Std. Dev.	0.30	0.32	0.42	0.58	0.40
		Minimum	4.08	1.34	-0.41	1.43	-0.17
		Maximum	5.28	2.62	1.27	3.75	1.43

Table G-2
Log K_d Distributions Used in the PM CAU Transport Model (Source: Carle et al., 2020)
(Page 16 of 16)

HSU	Distribution Type	Statistic	Cs	Sr	Np	Pu	U
mRMWTA2	Normal	Mean	4.68	1.98	0.43	2.59	0.63
		Std. Dev.	0.30	0.32	0.42	0.58	0.40
		Minimum	4.08	1.34	-0.41	1.43	-0.17
		Maximum	5.28	2.62	1.27	3.75	1.43
mPBRCMnw	Normal	Mean	3.91	2.78	-0.10	2.47	0.20
		Std. Dev.	0.40	0.29	0.49	0.56	0.52
		Minimum	3.11	2.20	-1.08	1.35	-0.84
		Maximum	4.71	3.36	0.88	3.59	1.24
Faults (barrier)	Normal	Mean	3.78	1.39	0.44	2.44	0.01
		Std. Dev.	0.22	0.23	0.22	0.22	0.21
		Minimum	3.34	0.93	0.00	2.00	-0.41
		Maximum	4.22	1.85	0.88	2.88	0.43
Faults (conduit)	Normal	Mean	3.92	2.38	0.06	2.54	0.54
		Std. Dev.	0.37	0.44	0.46	0.44	0.57
		Minimum	3.18	1.50	-0.86	1.66	-0.60
		Maximum	4.66	3.26	0.98	3.42	1.68

G.2.0 References

Carle, S.F., A.F.B. Tompson, and M. Zavarin. 2020. *Radionuclide Screening Analysis and Transport Parameters for Pahute Mesa Detonations, Nevada National Security Site*, LLNL-TR-812351, Livermore, CA: Lawrence Livermore National Laboratory.

Navarro. 2021. *Contaminant Transport Parameters for the Groundwater Flow and Contaminant Transport Model of Corrective Action Units 101 and 102: Central and Western Pahute Mesa, Nye County, Nevada*, Rev. 1, N/0002653--077. Las Vegas, NV.

Appendix H

Detailed Transport Results

H.1.0 Detailed Transport Results

Detailed PM CAU transport model results for the calibrated base case are presented in this appendix, specifically as follows:

- Section H.1.1 presents plots of modeled and measured ^{3}H concentrations versus time, over the 1,000-year simulation period from the calibrated base case transport model.
- Section H.1.2 presents plots of modeled and measured ^{14}C concentrations versus time, over the first 60 years of simulation from the calibrated base case transport model.
- Section H.1.3 presents plots of modeled and measured ^{36}Cl concentrations versus time, over the first 60 years of simulation from the calibrated base case transport model.
- Section H.1.4 presents plots of modeled and measured ^{90}Sr concentrations versus time, over the first 60 years of simulation from the calibrated base case transport model.
- Section H.1.5 presents plots of modeled and measured ^{129}I concentrations versus time, over the first 60 years of simulation from the calibrated base case transport model.
- Section H.1.7 presents plots of modeled and measured ^{137}Cs concentrations versus time, over the first 60 years of simulation from the calibrated base case transport model.
- Section H.1.8 presents plots of modeled and measured U (total) concentrations versus time, over the first 60 years of simulation from the calibrated base case transport model.
- Section H.1.9 presents plots of modeled and measured $^{239/240}Pu$ concentrations versus time, over the first 60 years of simulation from the calibrated base case transport model.
- Section H.1.10 presents plots of modeled $^{239/240}Pu$ concentrations versus time at locations unobserved for Pu, over the first 60 years of simulation from the calibrated base case transport model.

The discrete PLUMECALC output times chosen for analysis are specified by year, corresponding to the observation dates given in Table 5-9, as well as specified future times up to 1,000 years as follows: 3, 11, 12, 13, 18, 19, 20, 21, 22, 23, 25, 26, 27, 28, 29, 30, 31, 32, 33, 34, 35, 36, 37, 38, 39, 40, 41, 42, 43, 44, 45, 46, 47, 48, 49, 50, 51, 52, 53, 54, 55, 60, 80, 100, 200, 300, 400, 500, 600, 700, 800, 900, and 1,000 years. This was done to keep output file sizes to a minimum. As a result, outputs are sparse during the first 20 years of the simulation.

H.1.1 Modeled and Measured ^{3}H Concentrations versus Time from Calibrated PM CAU Transport Model

Figures H-1 through H-64 present plots of modeled and measured ^{3}H concentrations versus time, over the 1,000-year simulation period from the calibrated PM CAU transport model at the observation locations. The log of concentration is used to compare modeled and measured (observed) values. A ^{3}H non-detect limit of 10 pCi/L is assumed; thus, any concentrations less than or equal to 10 pCi/L have a log value of 1.

As noted in Section 5.1.3, as a conservative approach in the PM CAU transport model, all available mass from each test is released in one day on the day of detonation, resulting in a pulse lasting one day. Considering single-day pulse of source masses and the sparse output times during the first 20 years of simulation, depending on observation location, the exact timing of the peak of the pulse may not be apparent by inspection of the outputs displayed in Figures H-1 through H-64.

At the source locations (i.e., the postshot holes), as seen in Figures H-46 through H-58, a sudden increase in concentrations at early times in the simulation is observed, first showing no modeled concentration (indicated by a log value of 1) at one output time, then showing very high concentration at the next output time. This behavior is expected at the postshot observation locations because (1) the source contaminant mass flux was applied in one day on the day of detonation (i.e., not introduced over a long period of time), and (2) the observation locations at the postshot holes are coincident with nodes where the particle tracks originate. For example, Figure H-65 shows modeled and measured ^{3}H concentrations versus time at U-19ad_PS_1A, the postshot hole for CHANCELLOR, which was detonated on September 1, 1983. The source mass flux pulse (lasting one day) for CHANCELLOR was introduced to the transport simulation on Day 6,687 (see Table 5-8), 18.3 years after the start of the simulation. Examination of Figure H-65 indicates no concentration (indicated by a log value of 1) at 18 years, followed by a concentration of 7.60E+07 pCi/L (log value of 7.88) at 19 years (the next output time), indicating the introduction of contaminant mass that occurred at 18.3 years.

Further away from the sources, as the source concentrations have been subjected to the attenuating transport processes over time and distance, the pulse is spread out over time as seen at ER-20-12_p4 (Figure H-20). Even further away from the sources, the source pulses are spread out more over time, but due to the output time resolution, the exact timing of the peak may not be represented, as seen at

ER-EC-6 in Figures H-25, H-26, and H-28, where the peak concentration is represented at 200 years, but may actually occur between 100 and 200 years.

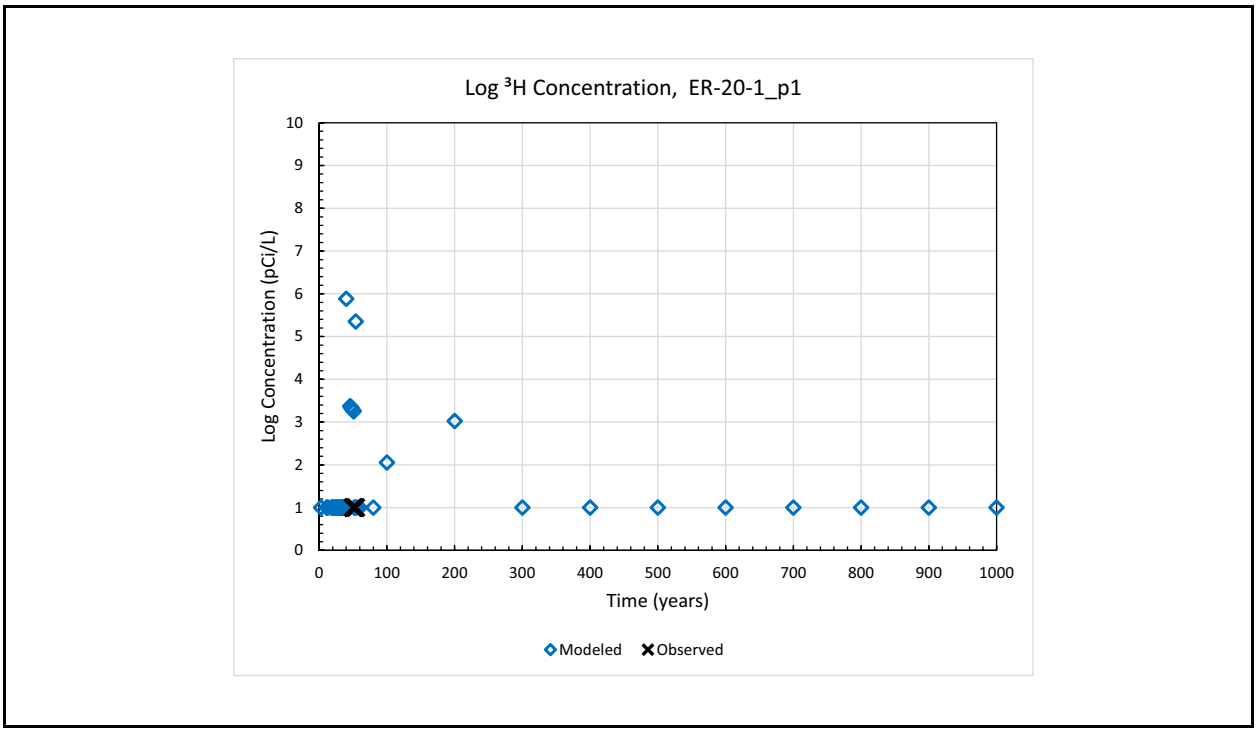

Figure H-1
Modeled and Measured ^{3}H Concentrations versus Time at ER-20-1_p1 (1,000 Years)

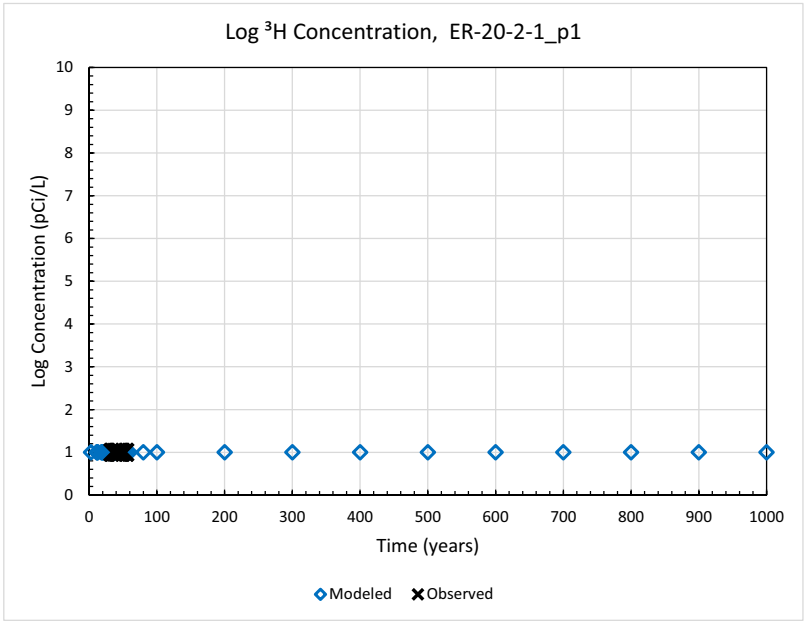

Figure H-2
Modeled and Measured ^{3}H Concentrations versus Time at ER-20-2-1_p1 (1,000 Years)

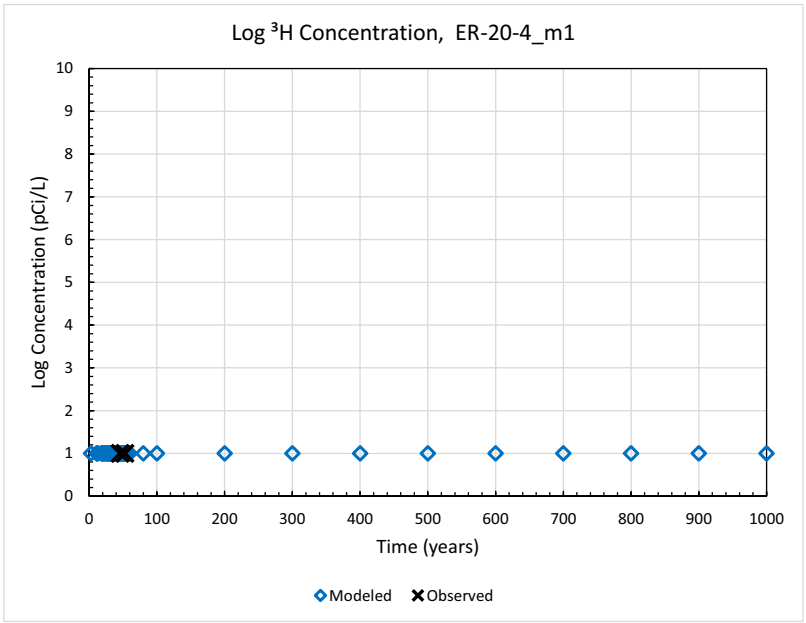

Figure H-3
Modeled and Measured ^{3}H Concentrations versus Time at ER-20-4_m1 (1,000 Years)

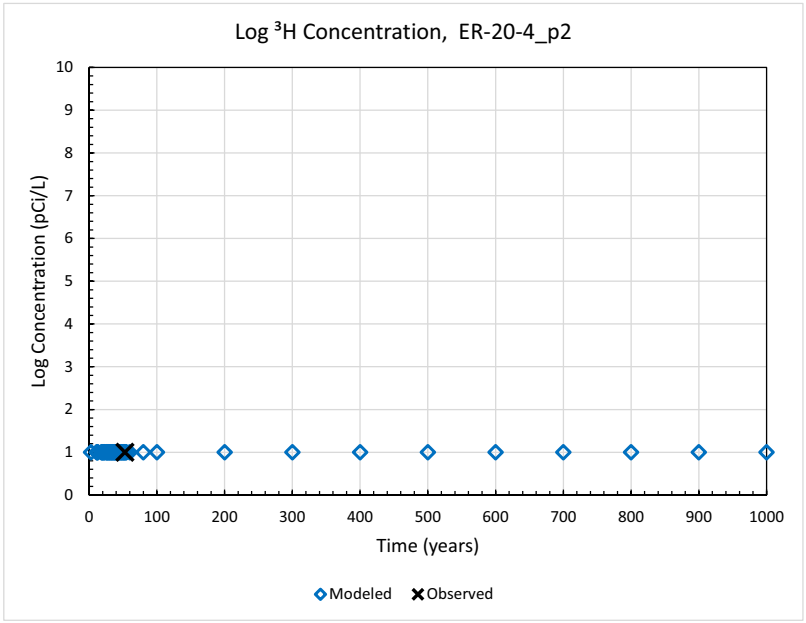

Figure H-4
Modeled and Measured ^{3}H Concentrations versus Time at ER-20-4_p2 (1,000 Years)

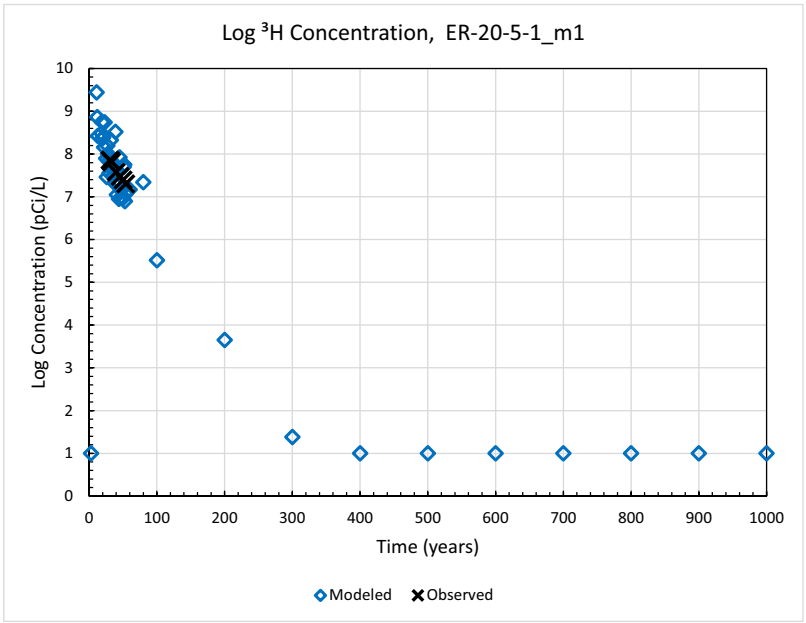

Figure H-5
Modeled and Measured ^{3}H Concentrations versus Time at ER-20-5-1_m1 (1,000 Years)

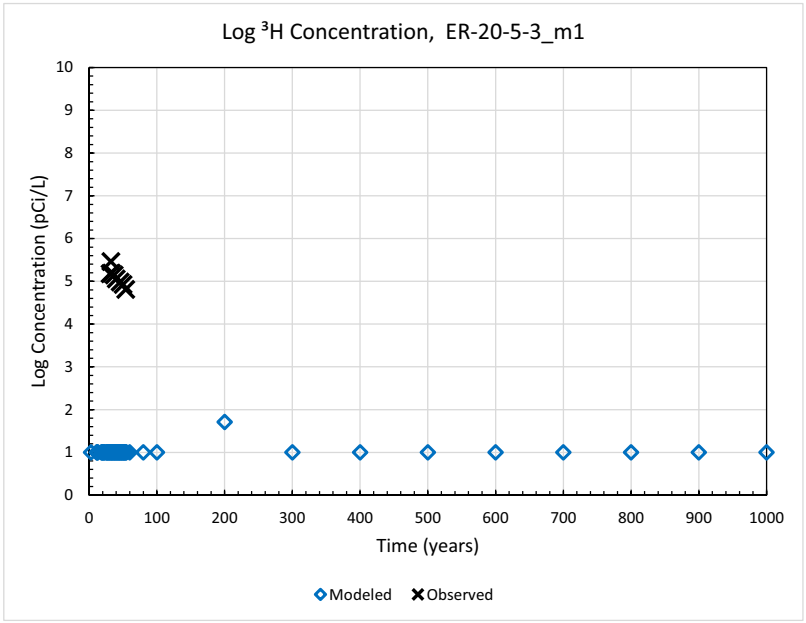

Figure H-6
Modeled and Measured ^{3}H Concentrations versus Time at ER-20-5-3_m1 (1,000 Years)

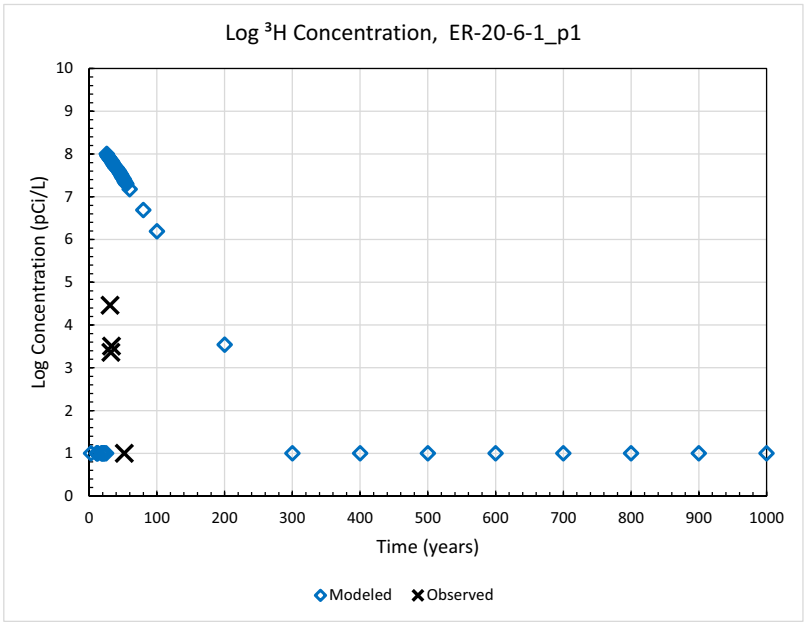

Figure H-7
Modeled and Measured ^{3}H Concentrations versus Time at ER-20-6-1_p1 (1,000 Years)

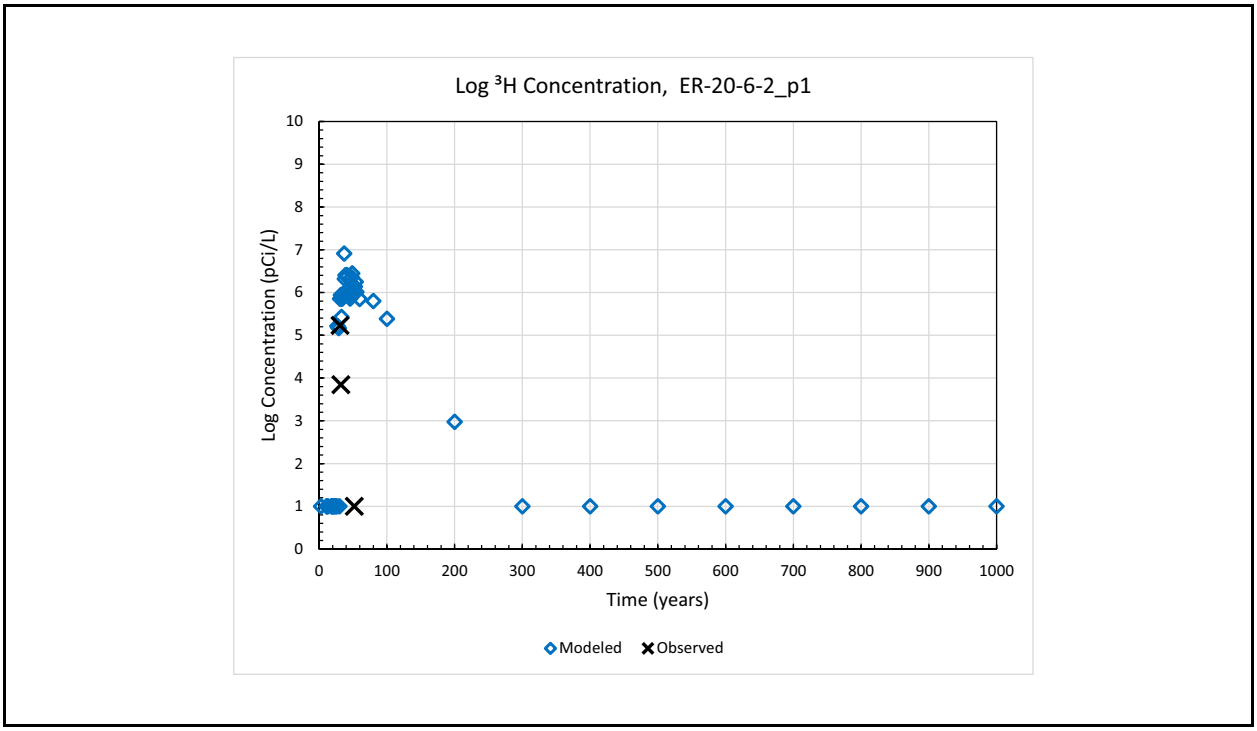

Figure H-8
Modeled and Measured ^{3}H Concentrations versus Time at ER-20-6-2_p1 (1,000 Years)

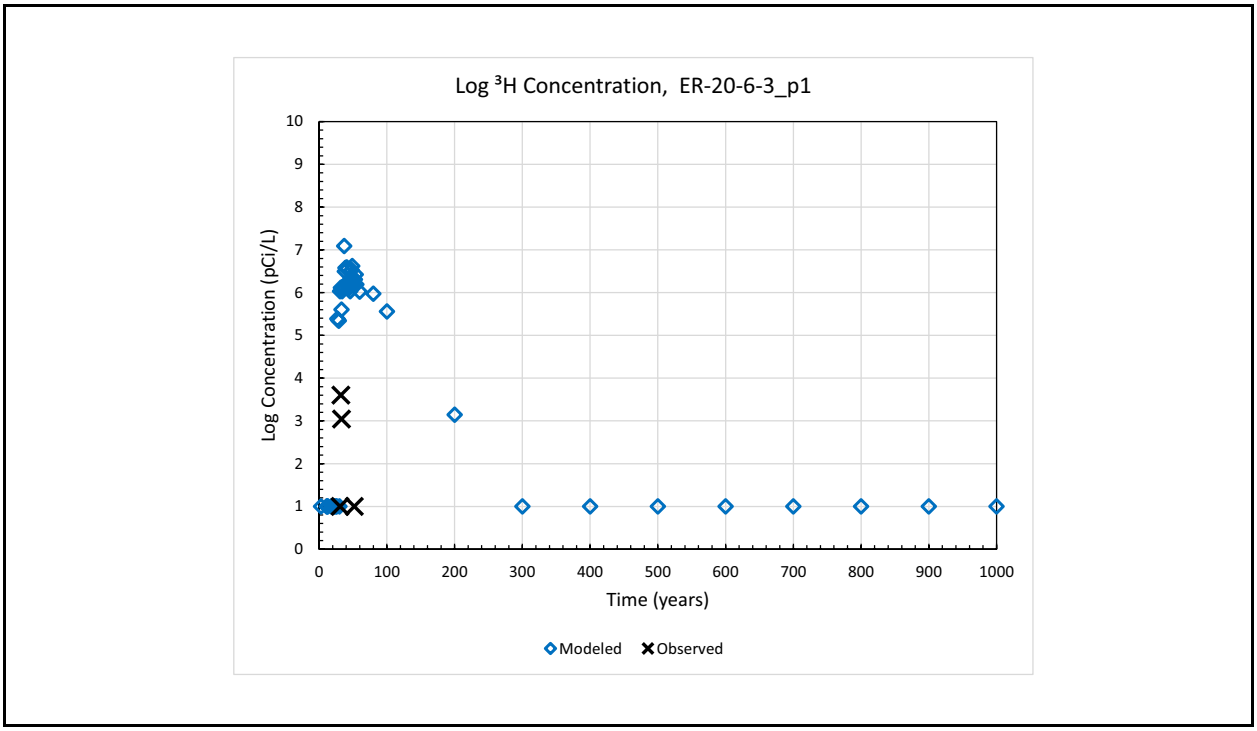

Figure H-9
Modeled and Measured ^{3}H Concentrations versus Time at ER-20-6-3_p1 (1,000 Years)

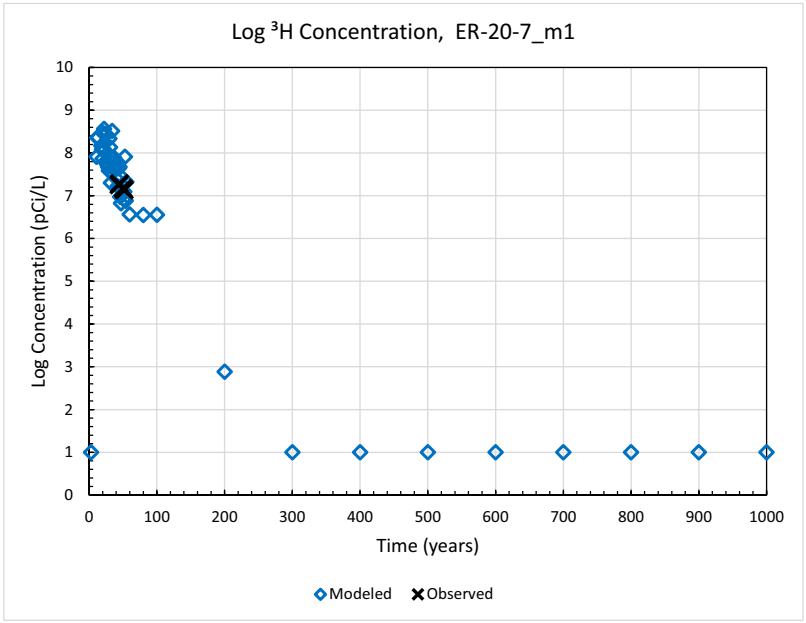

Figure H-10
Modeled and Measured ^{3}H Concentrations versus Time at ER-20-7_m1 (1,000 Years)

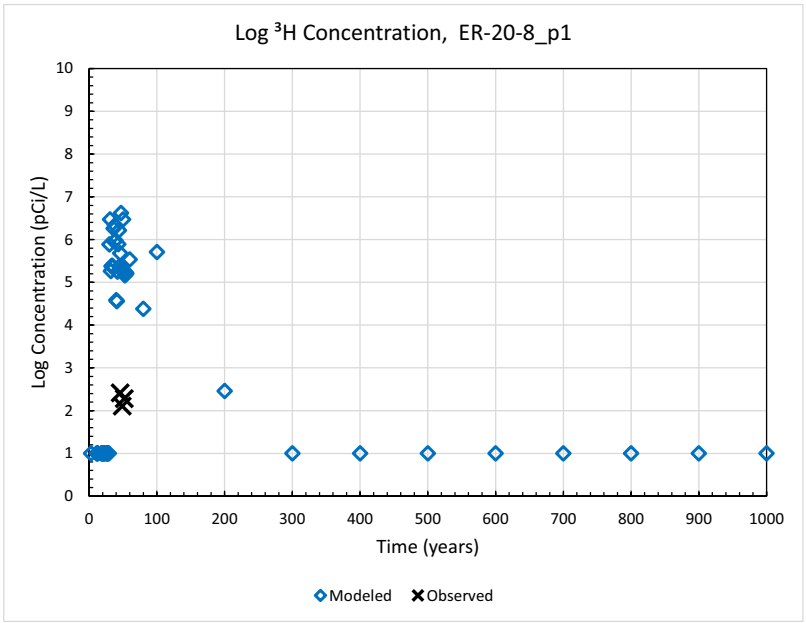

Figure H-11
Modeled and Measured ^{3}H Concentrations versus Time at ER-20-8_p1 (1,000 Years)

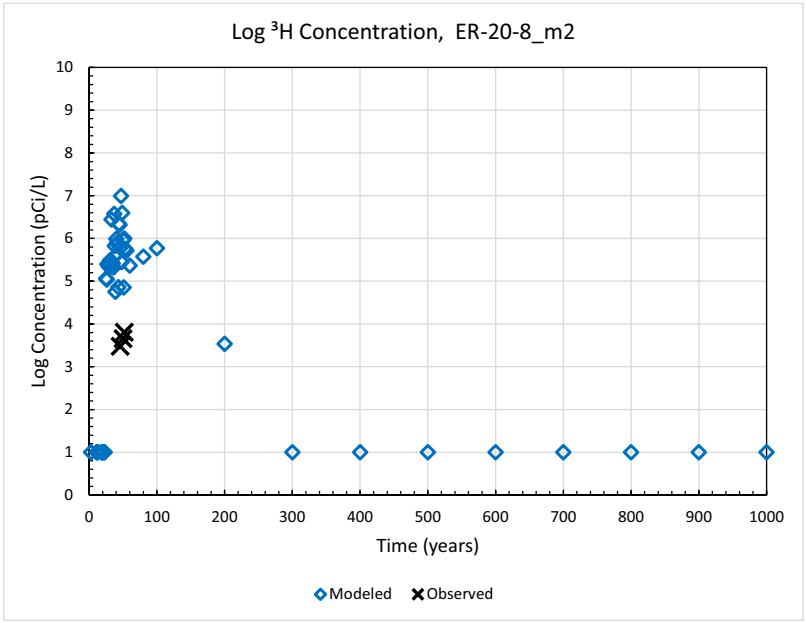

Figure H-12
Modeled and Measured ^{3}H Concentrations versus Time at ER-20-8_m2 (1,000 Years)

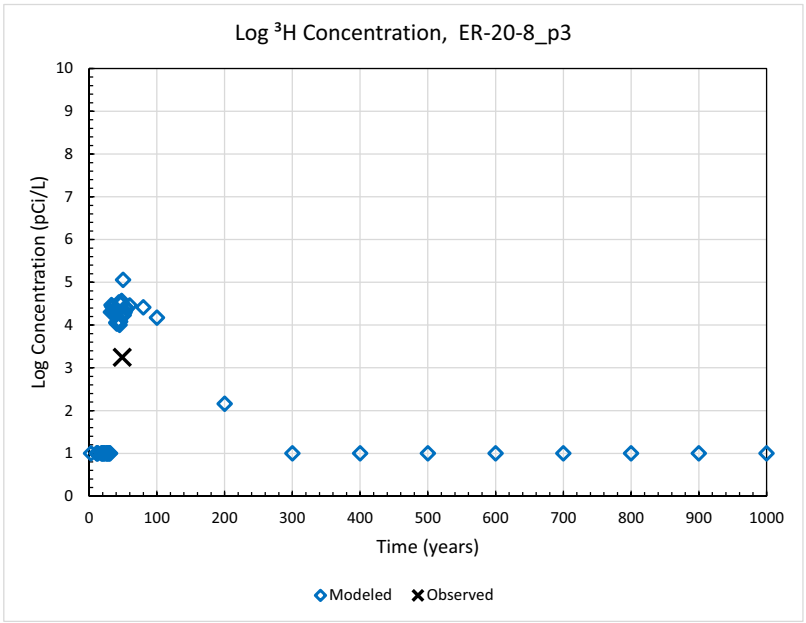

Figure H-13
Modeled and Measured ^{3}H Concentrations versus Time at ER-20-8_p3 (1,000 Years)

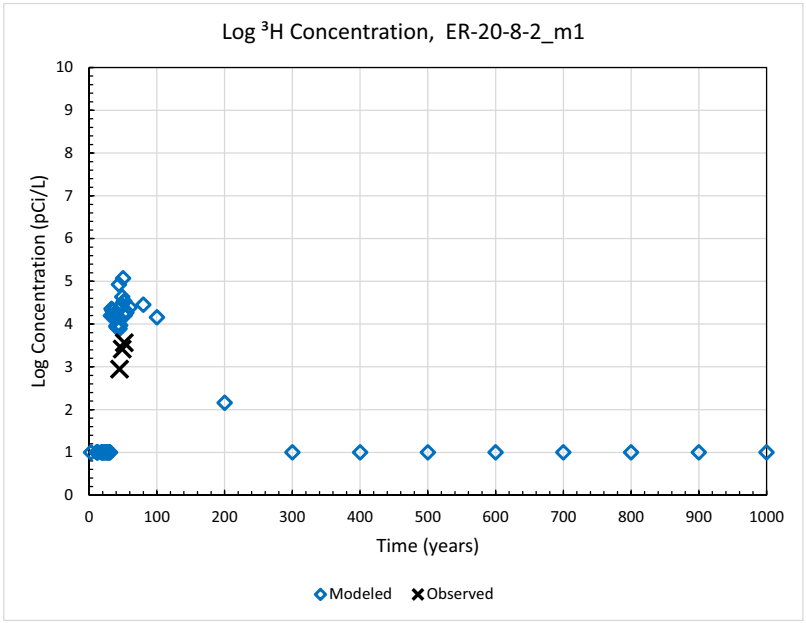

Figure H-14
Modeled and Measured ^{3}H Concentrations versus Time at ER-20-8-2_m1 (1,000 Years)

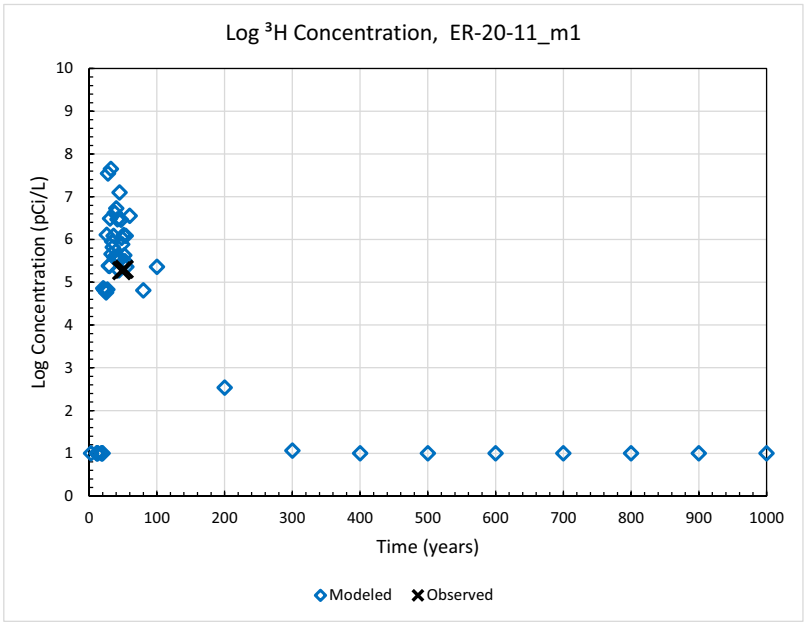

Figure H-15
Modeled and Measured ^{3}H Concentrations versus Time at ER-20-11_m1 (1,000 Years)

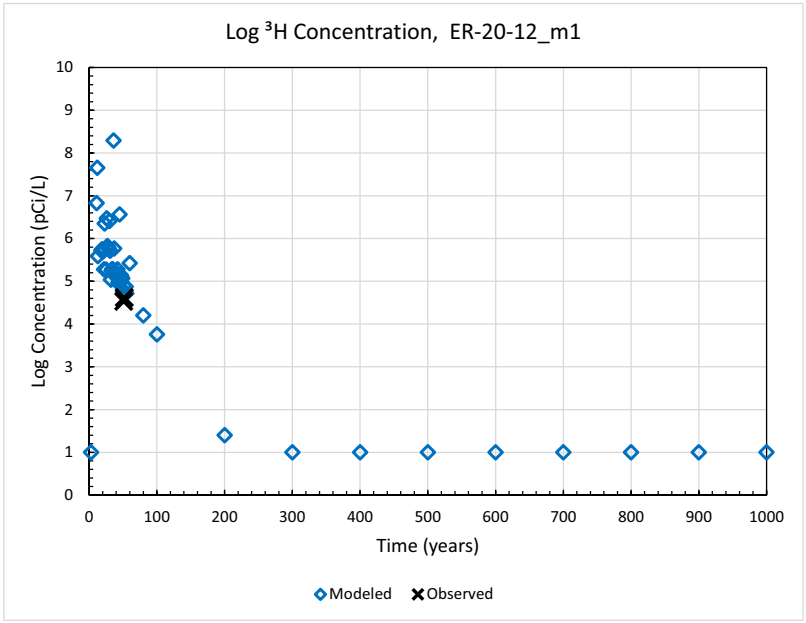

Figure H-16
Modeled and Measured ^{3}H Concentrations versus Time at ER-20-12_m1 (1,000 Years)

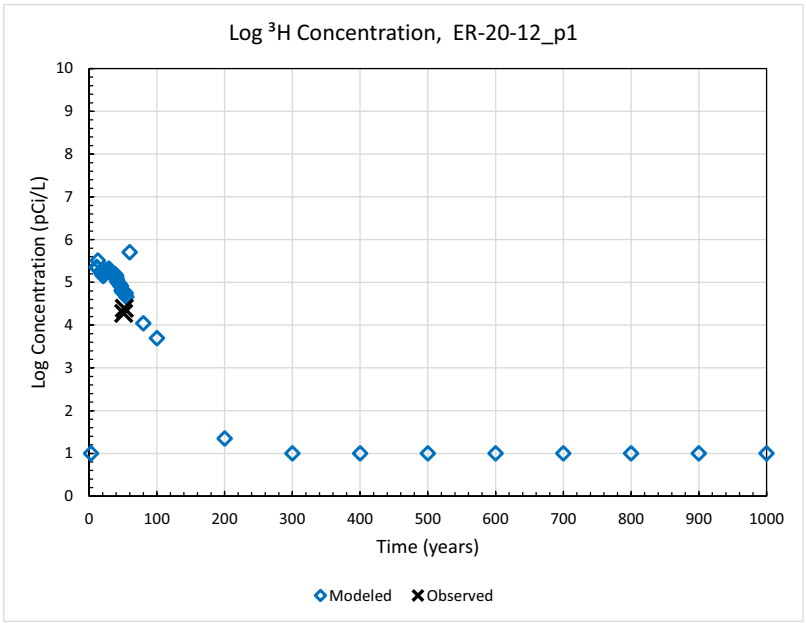

Figure H-17
Modeled and Measured ^{3}H Concentrations versus Time at ER-20-12_p1 (1,000 Years)

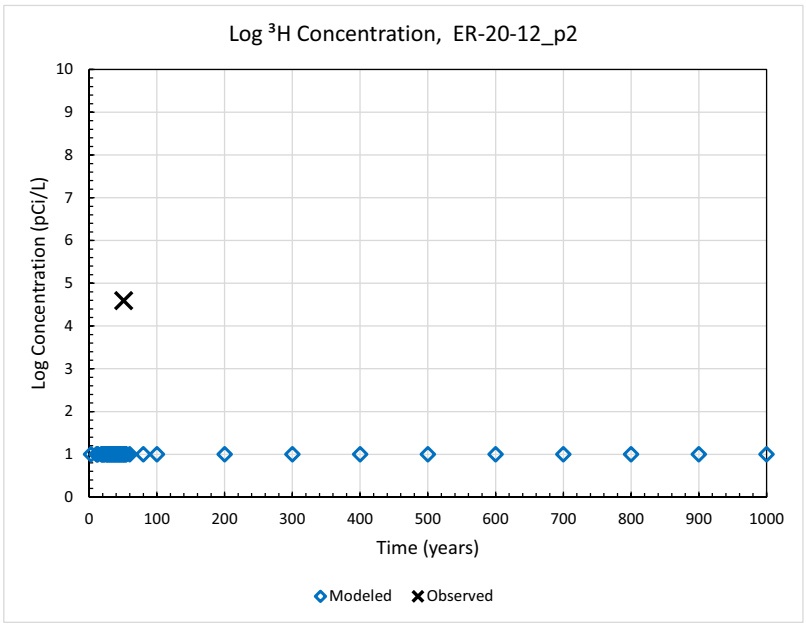

Figure H-18
Modeled and Measured ^{3}H Concentrations versus Time at ER-20-12_p2 (1,000 Years)

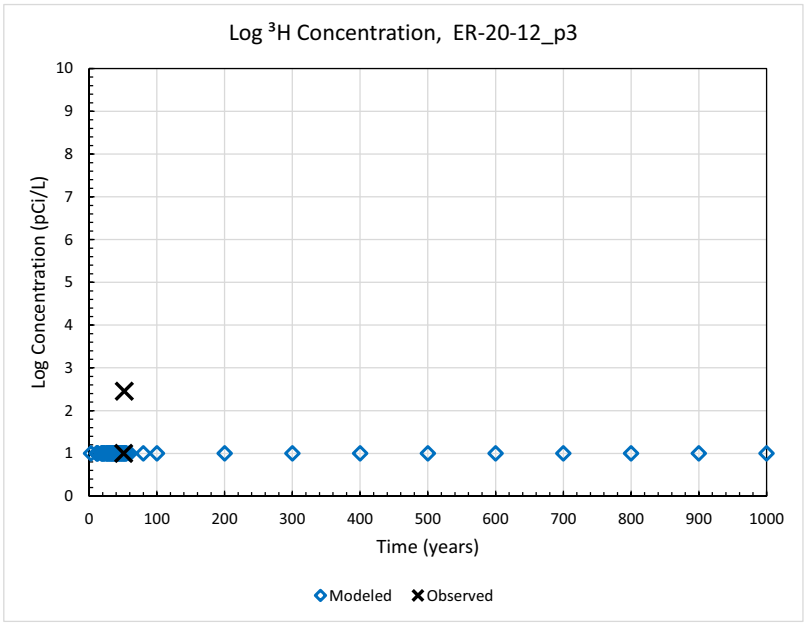

Figure H-19
Modeled and Measured ^{3}H Concentrations versus Time at ER-20-12_p3 (1,000 Years)

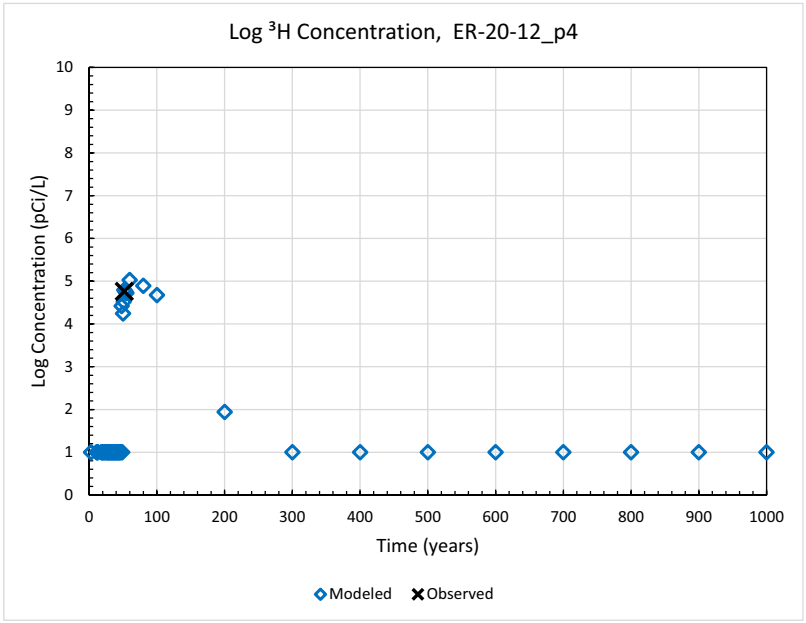

Figure H-20
Modeled and Measured ^{3}H Concentrations versus Time at ER-20-12_p4 (1,000 Years)

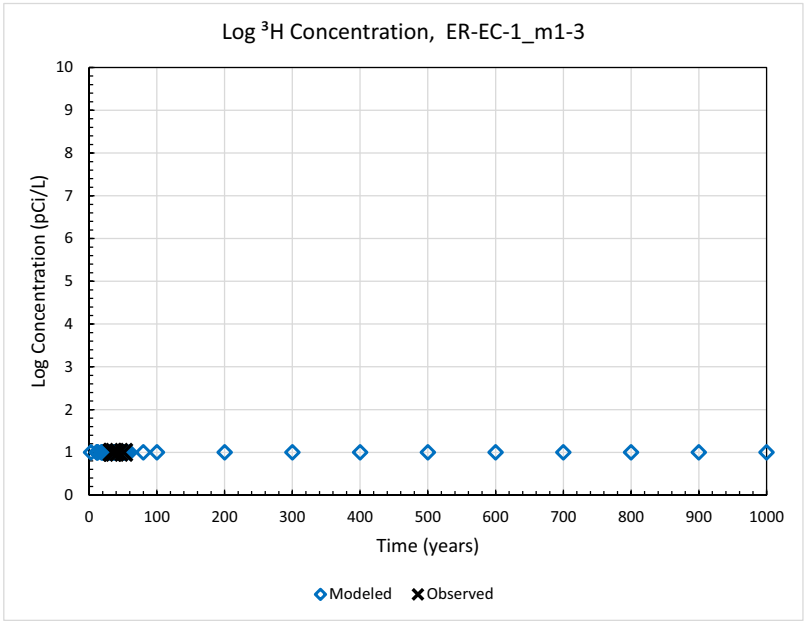

Figure H-21
Modeled and Measured ^{3}H Concentrations versus Time at ER-EC-1_m1-3 (1,000 Years)

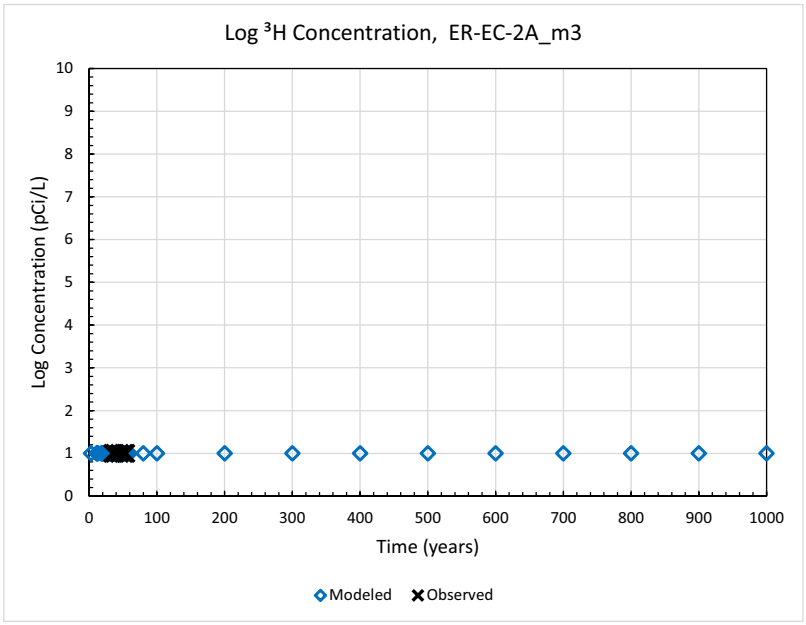

Figure H-22
Modeled and Measured ^{3}H Concentrations versus Time at ER-EC-2A_m3 (1,000 Years)

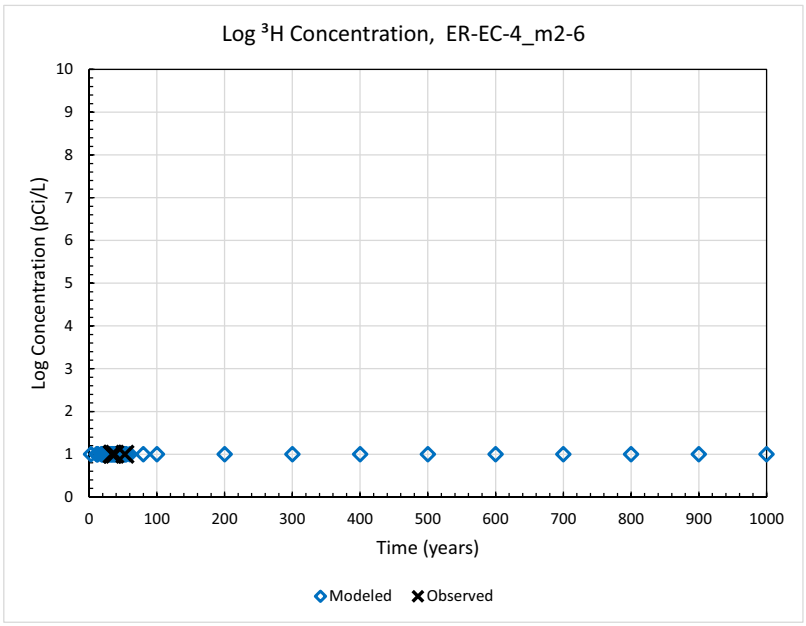

Figure H-23
Modeled and Measured ^{3}H Concentrations versus Time at ER-EC-4_m2-6 (1,000 Years)

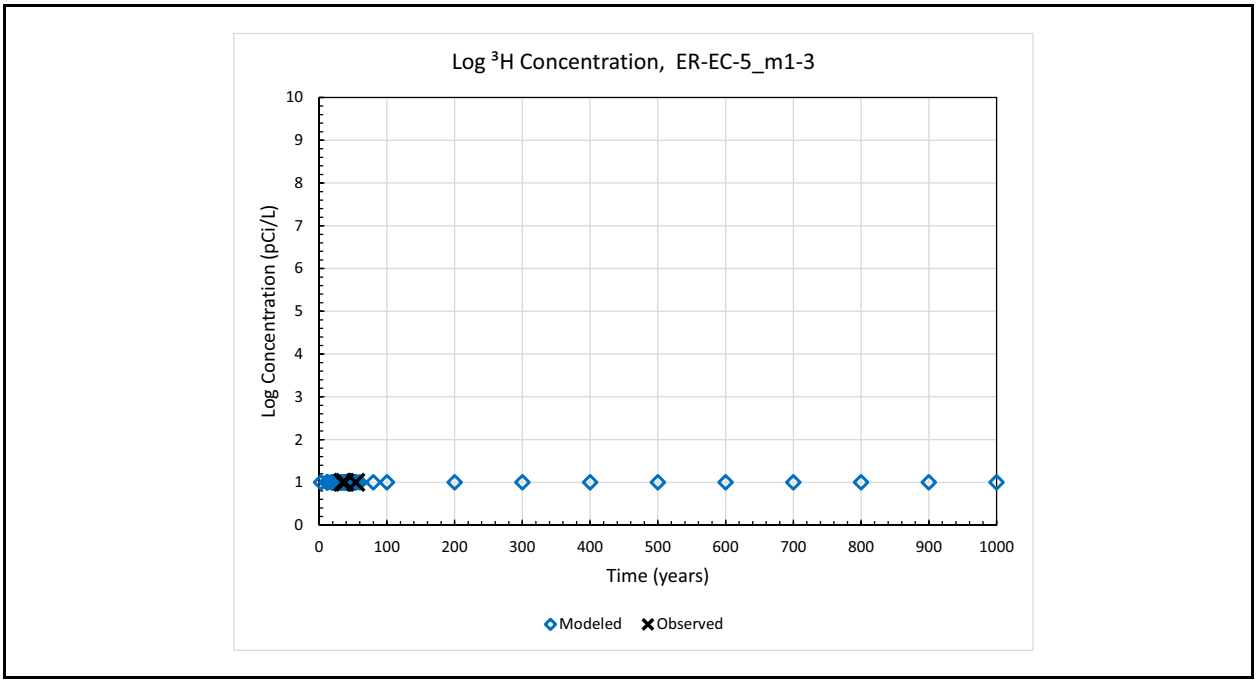

Figure H-24
Modeled and Measured ^{3}H Concentrations versus Time at ER-EC-5_m1-3 (1,000 Years)

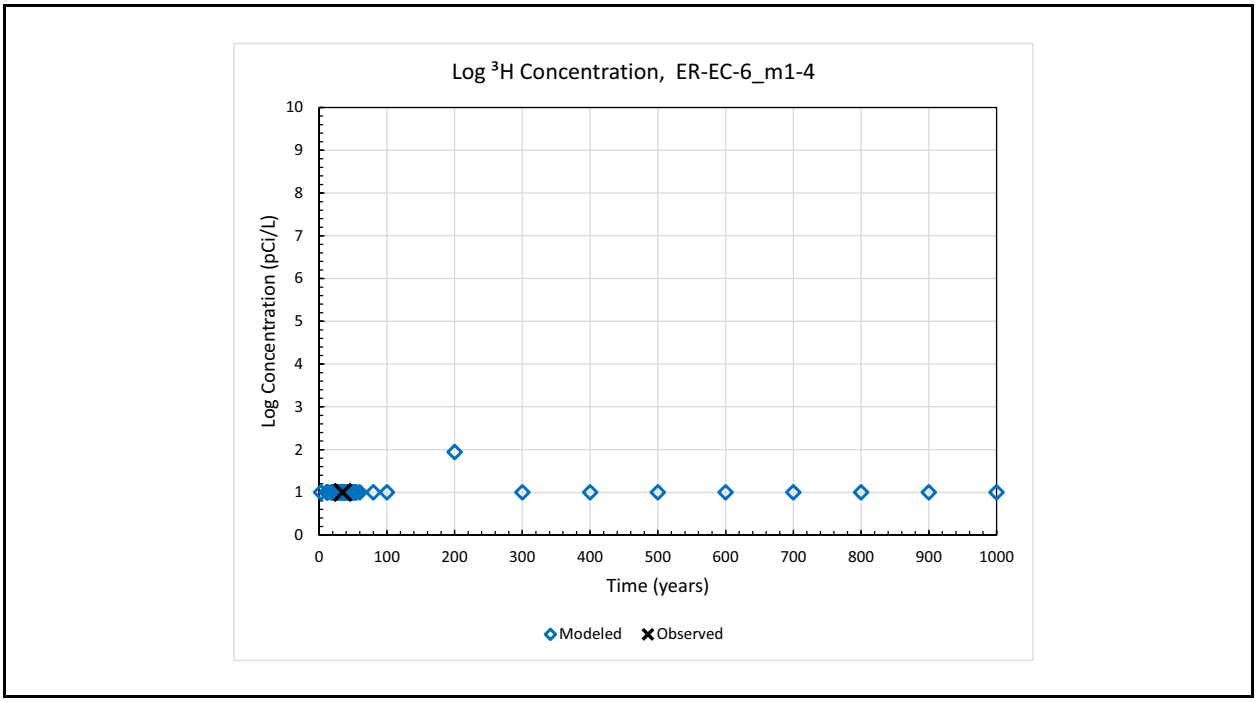

Figure H-25
Modeled and Measured ^{3}H Concentrations versus Time at ER-EC-6_m1-4 (1,000 Years)

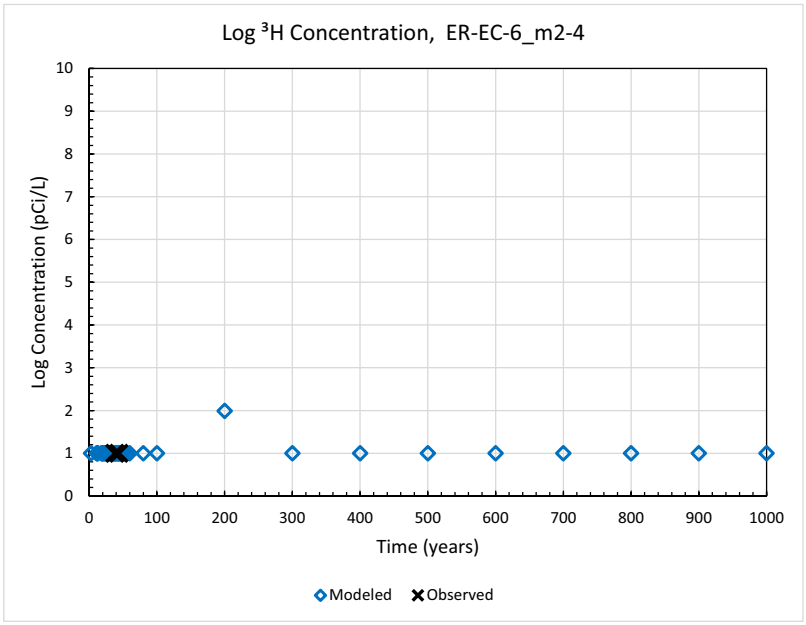

Figure H-26
Modeled and Measured ^{3}H Concentrations versus Time at ER-EC-6_m2-4 (1,000 Years)

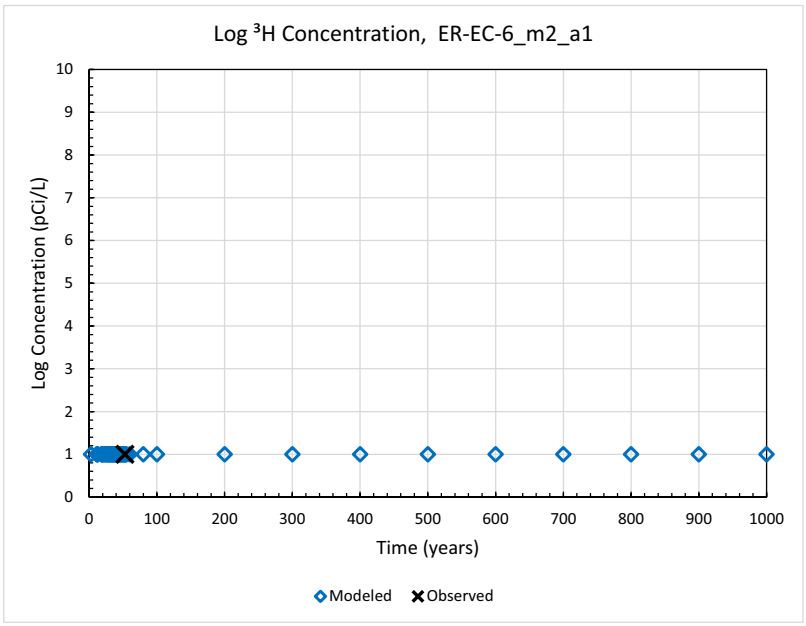

Figure H-27
Modeled and Measured ^{3}H Concentrations versus Time at ER-EC-6_m2_a1 (1,000 Years)

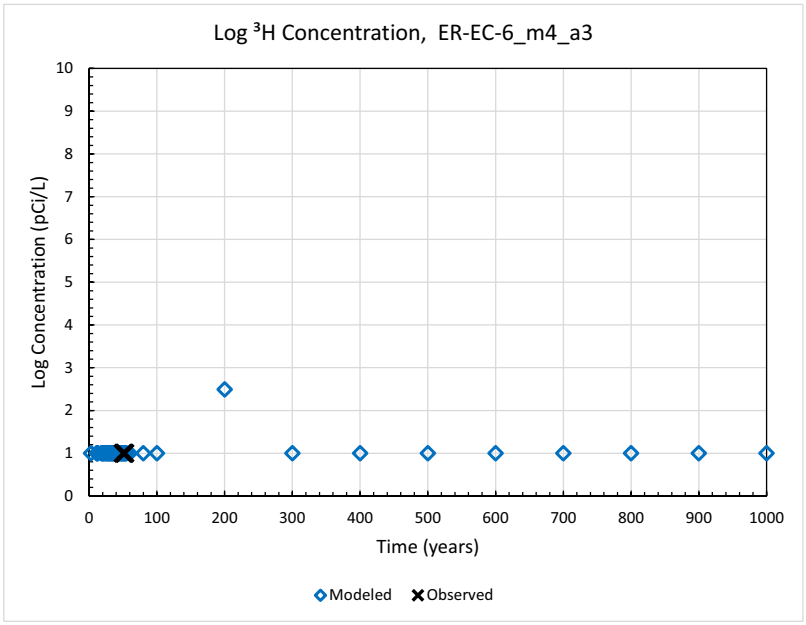

Figure H-28
Modeled and Measured ^{3}H Concentrations versus Time at ER-EC-6_m4_a3 (1,000 Years)

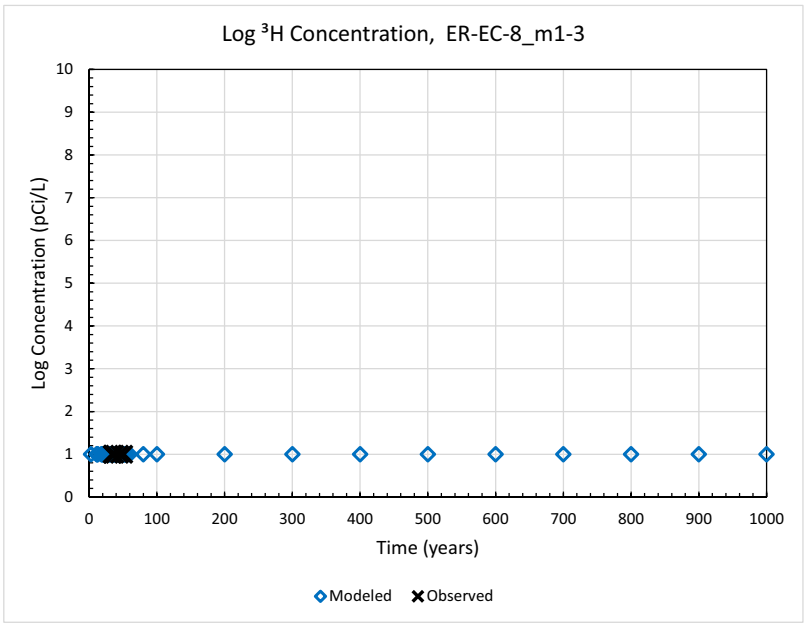

Figure H-29
Modeled and Measured ^{3}H Concentrations versus Time at ER-EC-8_m1-3 (1,000 Years)

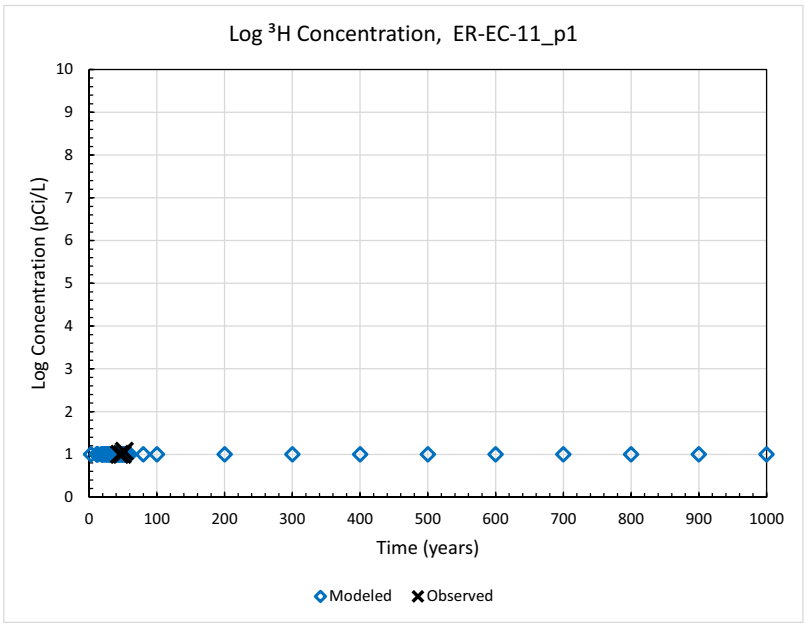

Figure H-30
Modeled and Measured ^{3}H Concentrations versus Time at ER-EC-11_p1 (1,000 Years)

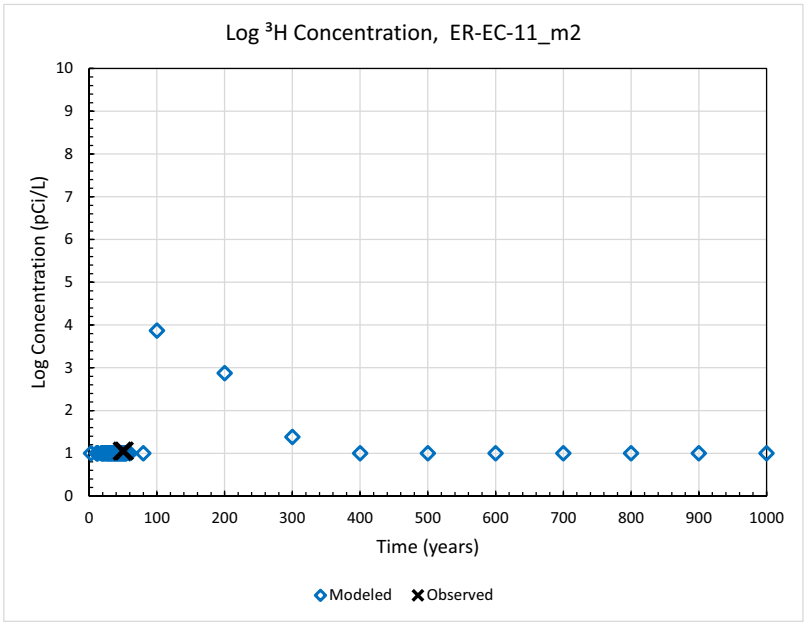

Figure H-31
Modeled and Measured ^{3}H Concentrations versus Time at ER-EC-11_m2 (1,000 Years)

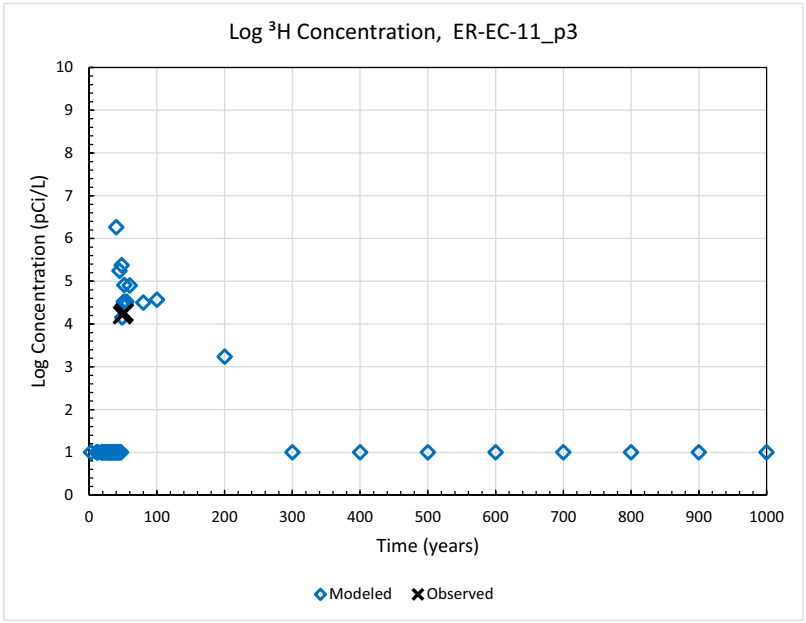

Figure H-32
Modeled and Measured ^{3}H Concentrations versus Time at ER-EC-11_p3 (1,000 Years)

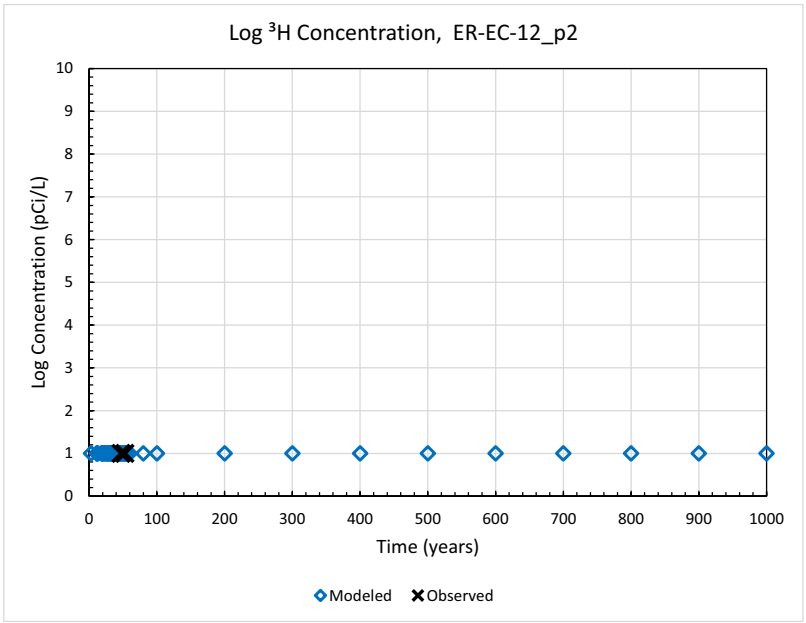

Figure H-33
Modeled and Measured ^{3}H Concentrations versus Time at ER-EC-12_p2 (1,000 Years)

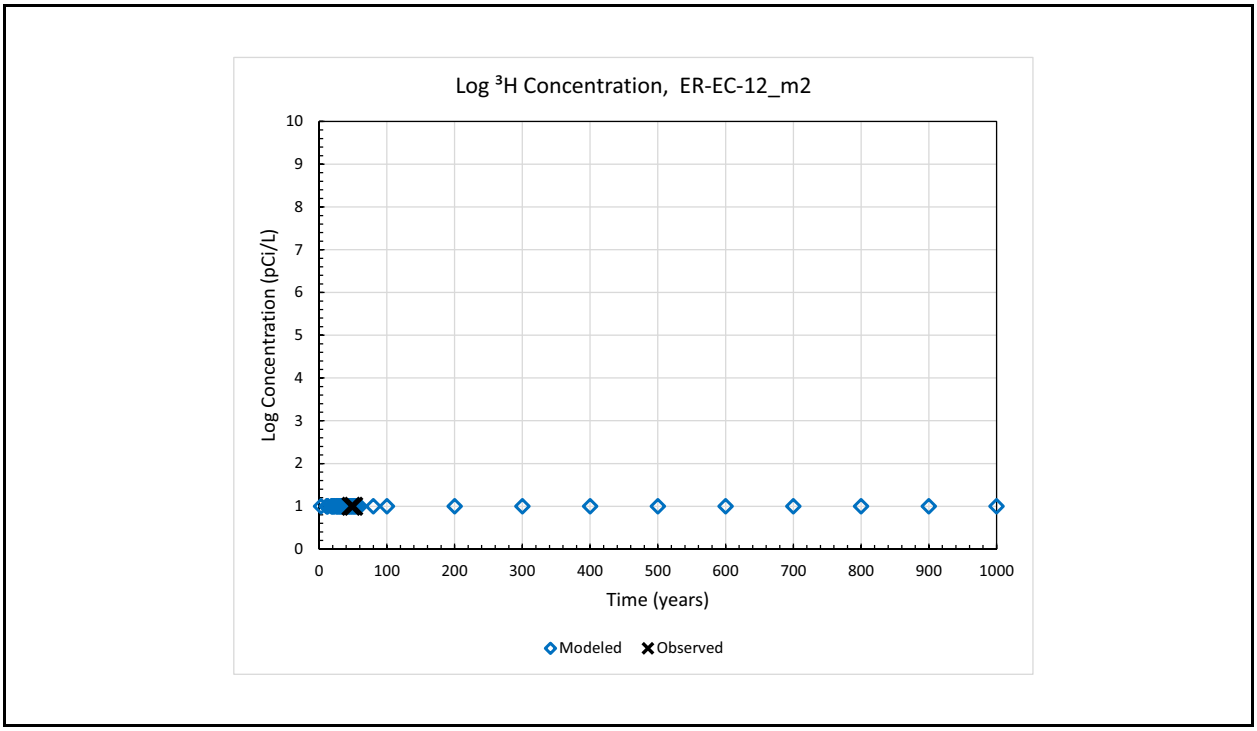

Figure H-34
Modeled and Measured ^{3}H Concentrations versus Time at ER-EC-12_m2 (1,000 Years)

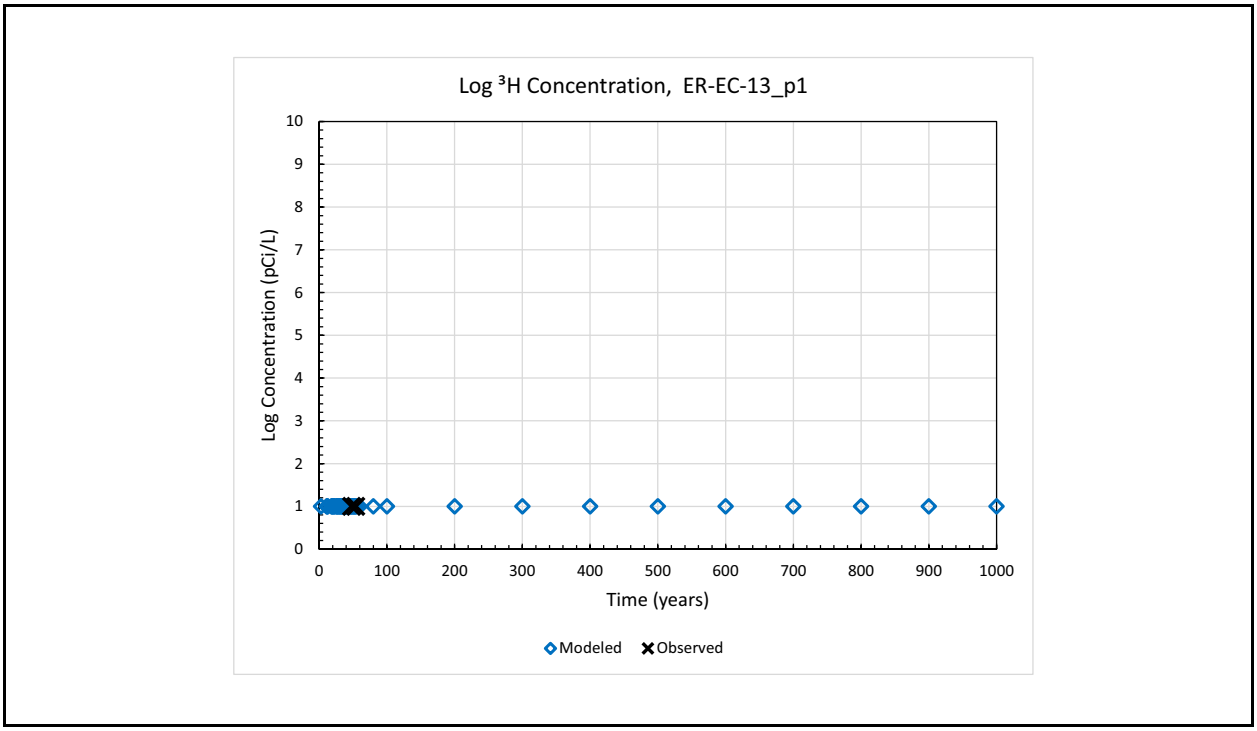

Figure H-35
Modeled and Measured ^{3}H Concentrations versus Time at ER-EC-13_p1 (1,000 Years)

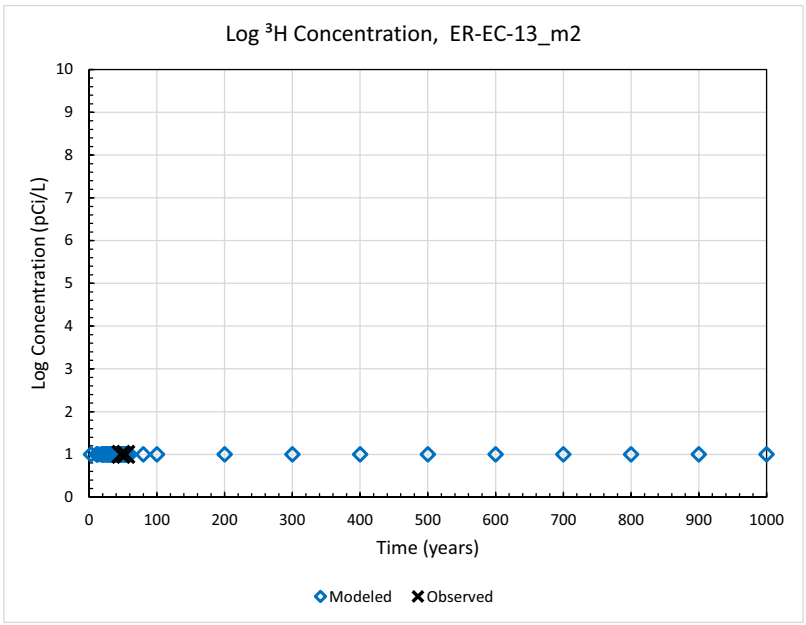

Figure H-36
Modeled and Measured ^{3}H Concentrations versus Time at ER-EC-13_m2 (1,000 Years)

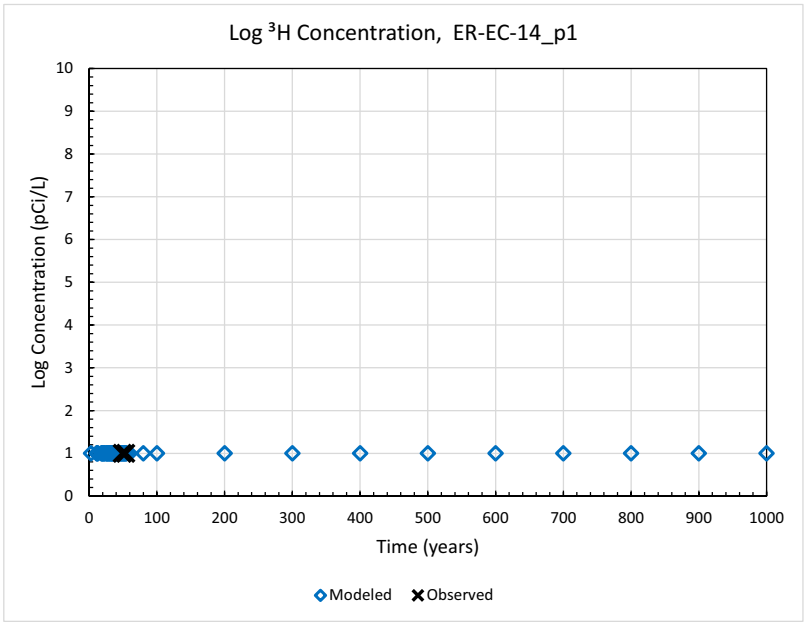

Figure H-37
Modeled and Measured ^{3}H Concentrations versus Time at ER-EC-14_p1 (1,000 Years)

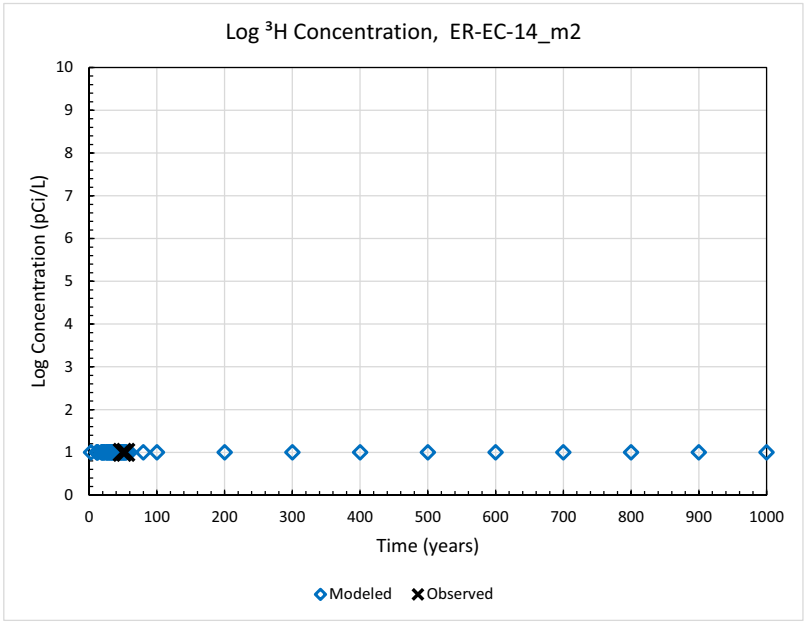

Figure H-38
Modeled and Measured ^{3}H Concentrations versus Time at ER-EC-14_m2 (1,000 Years)

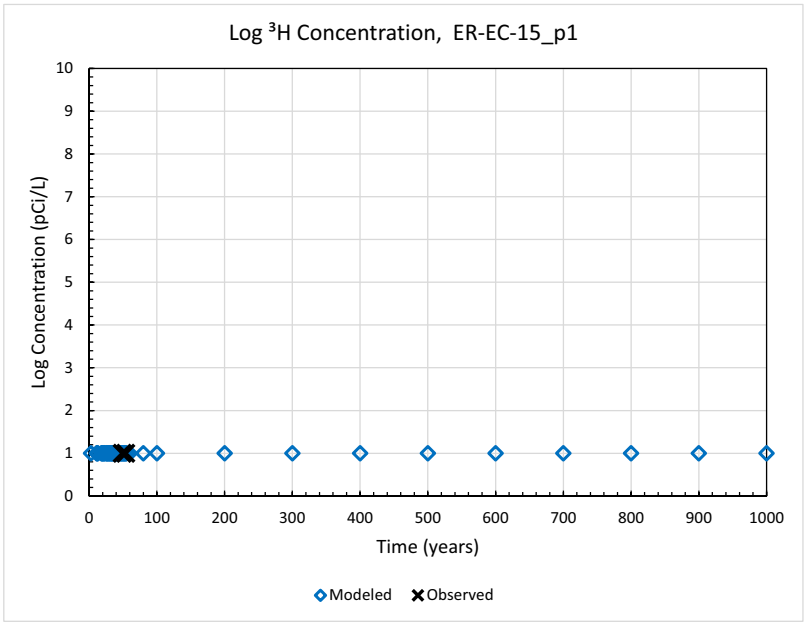

Figure H-39
Modeled and Measured ^{3}H Concentrations versus Time at ER-EC-15_p1 (1,000 Years)

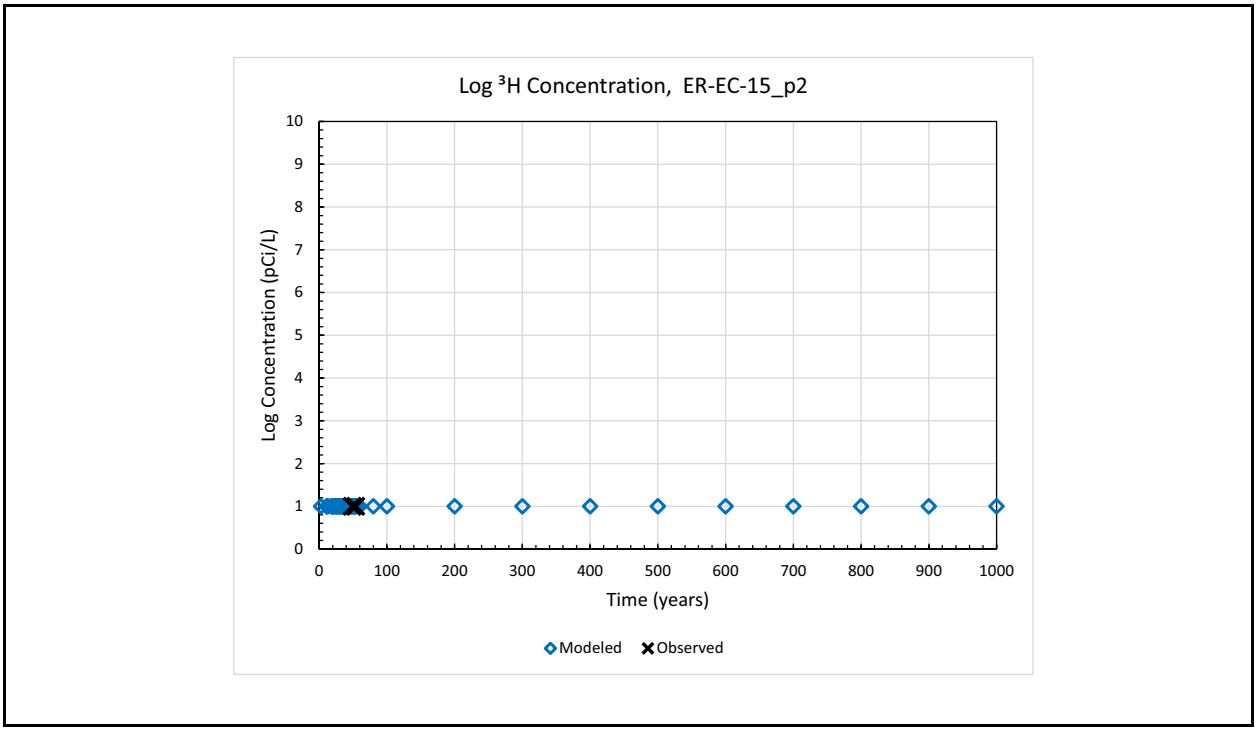

Figure H-40
Modeled and Measured ^{3}H Concentrations versus Time at ER-EC-15_p2 (1,000 Years)

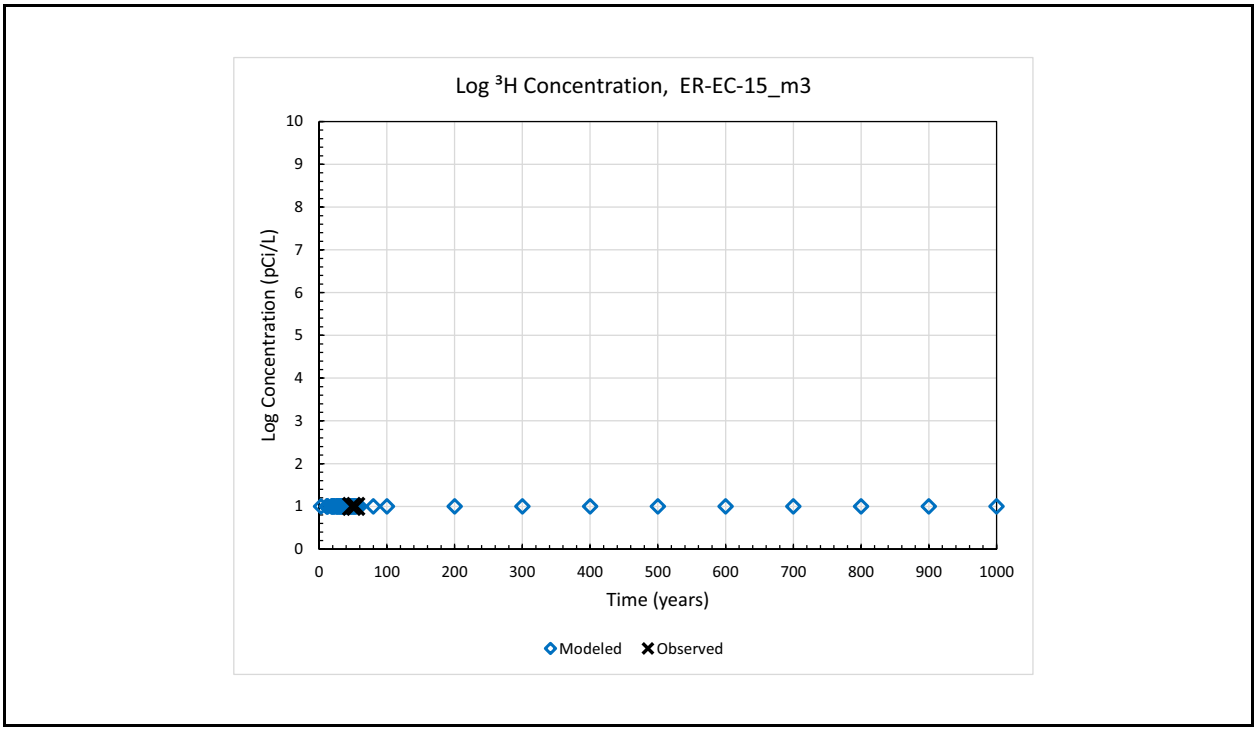

Figure H-41
Modeled and Measured ^{3}H Concentrations versus Time at ER-EC-15_m3 (1,000 Years)

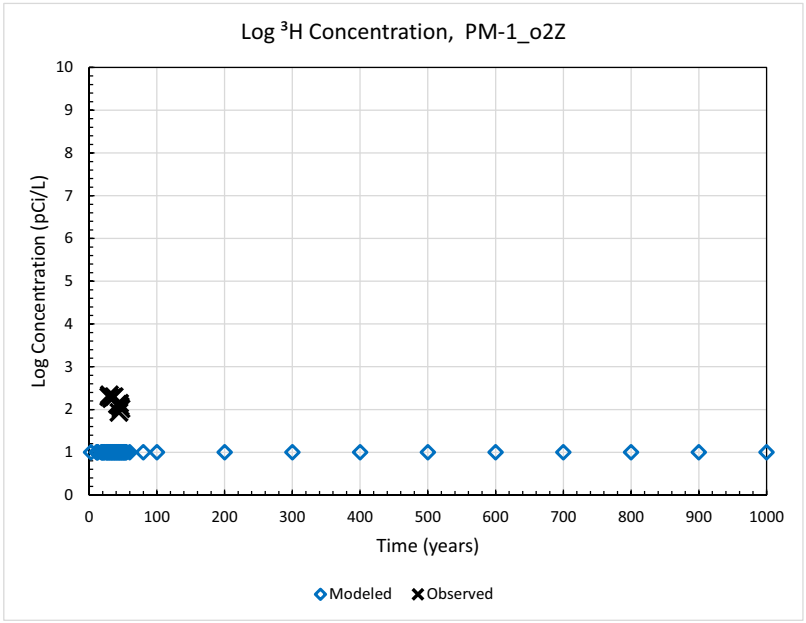

Figure H-42
Modeled and Measured ^{3}H Concentrations versus Time at PM-1_o2Z (1,000 Years)

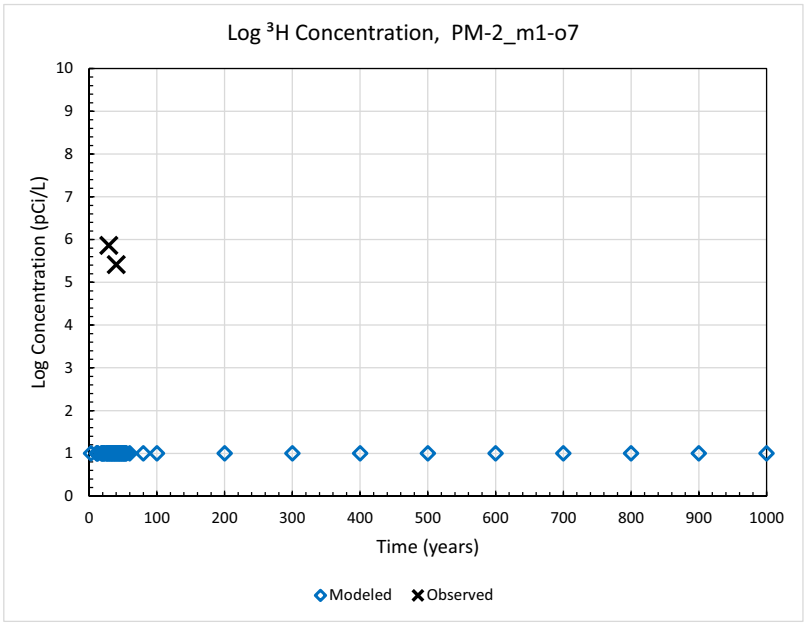

Figure H-43
Modeled and Measured ^{3}H Concentrations versus Time at PM-2_m1-o7 (1,000 Years)

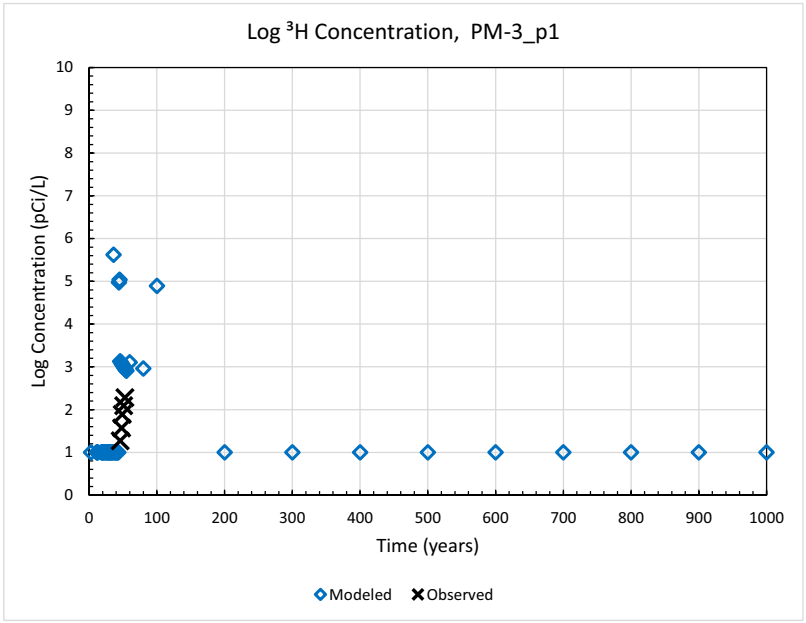

Figure H-44
Modeled and Measured ^{3}H Concentrations versus Time at PM-3_p1 (1,000 Years)

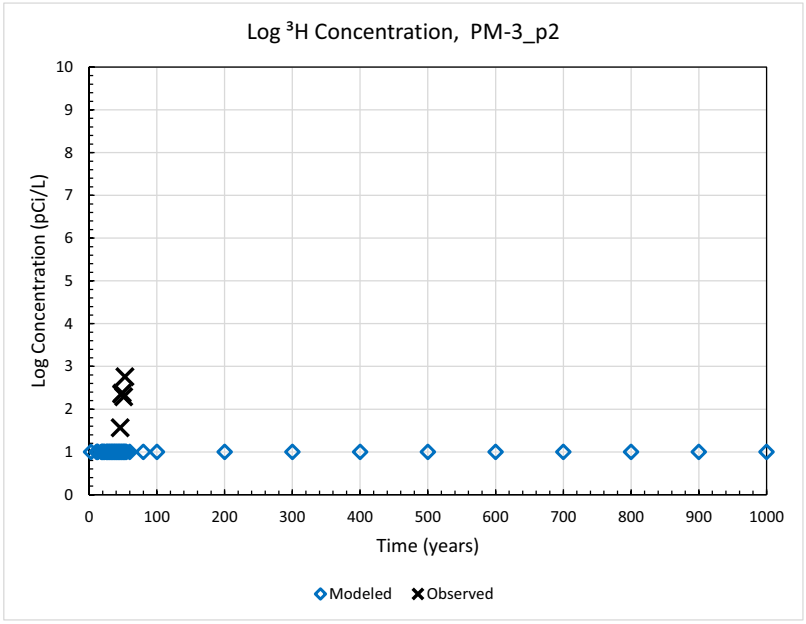

Figure H-45
Modeled and Measured ^{3}H Concentrations versus Time at PM-3_p2 (1,000 Years)

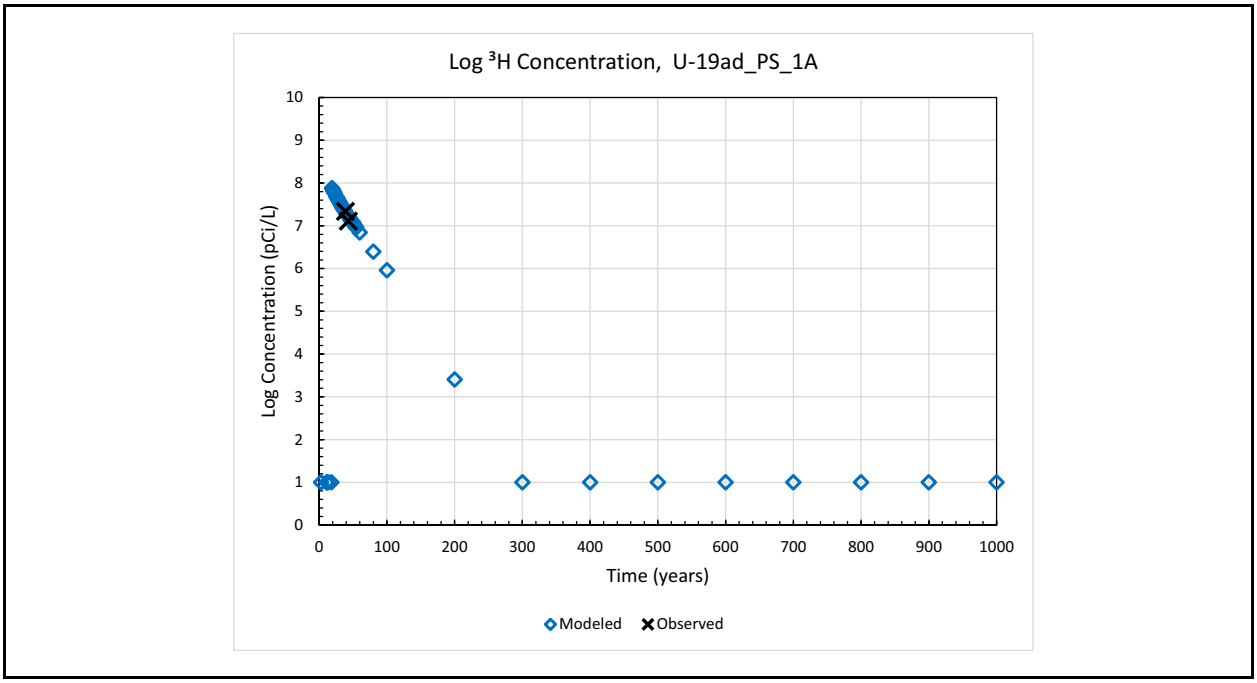

Figure H-46
Modeled and Measured ^{3}H Concentrations versus Time at U-19ad_PS_1A (1,000 Years)

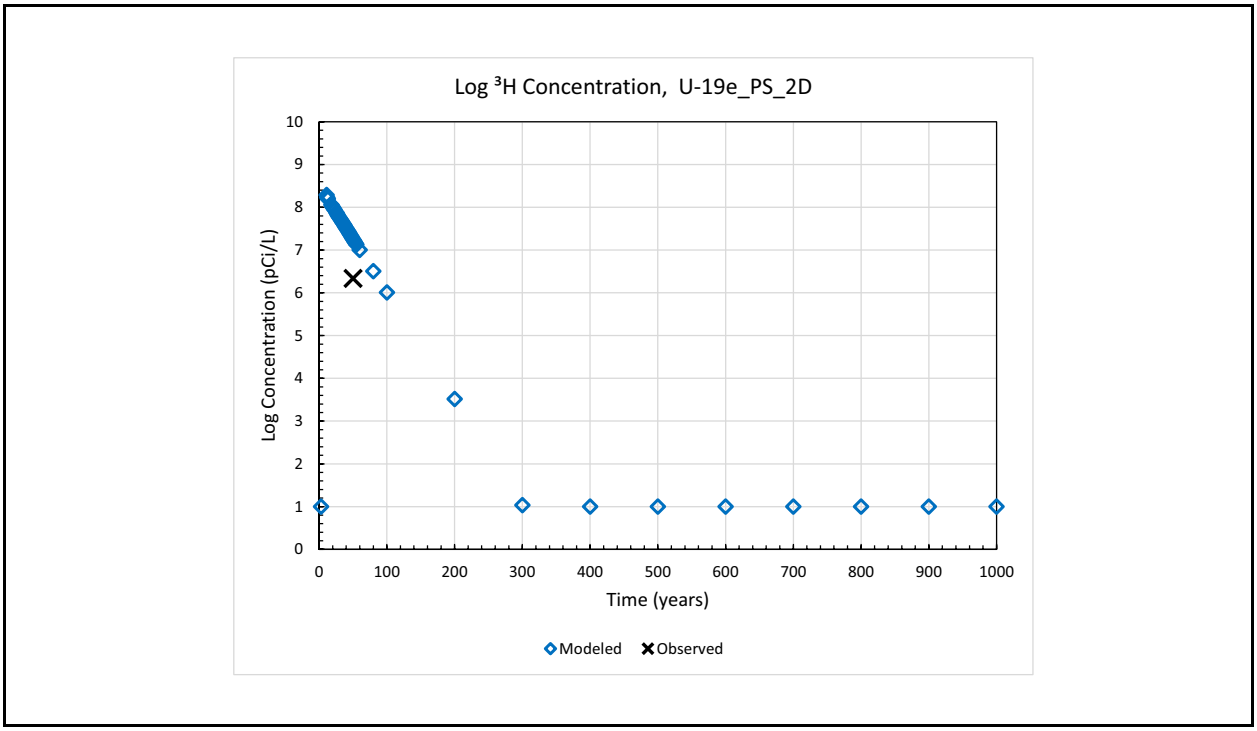

Figure H-47
Modeled and Measured ^{3}H Concentrations versus Time at U-19e_PS_2D (1,000 Years)

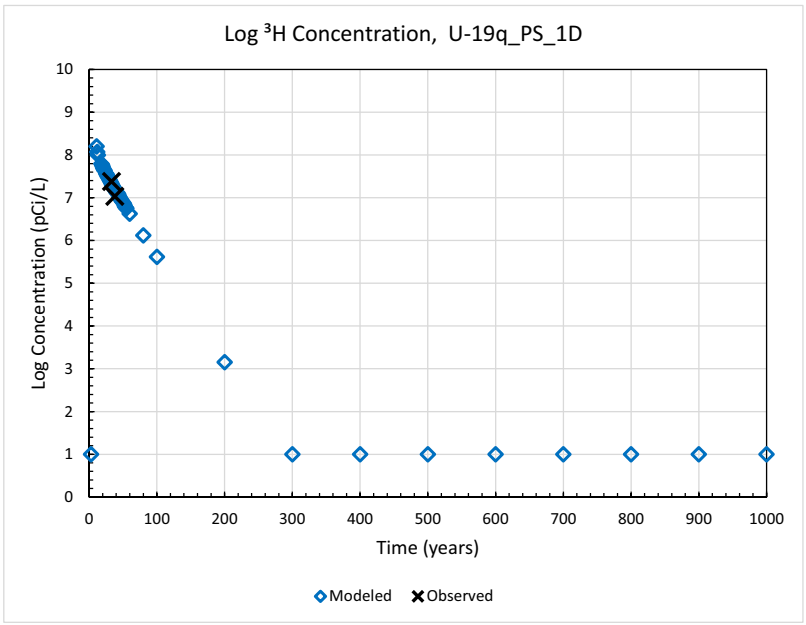

Figure H-48
Modeled and Measured ^{3}H Concentrations versus Time at U-19q_PS_1D (1,000 Years)

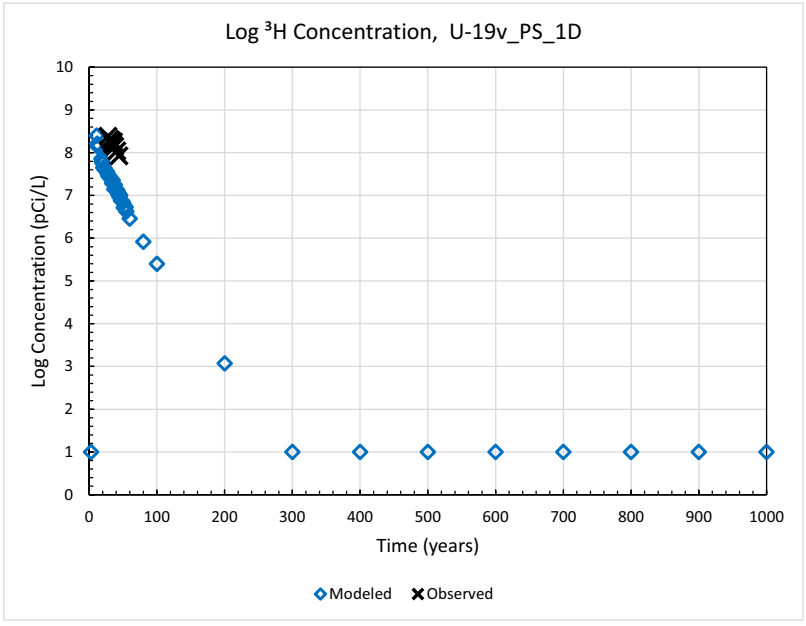

Figure H-49
Modeled and Measured ^{3}H Concentrations versus Time at U-19v_PS_1D (1,000 Years)

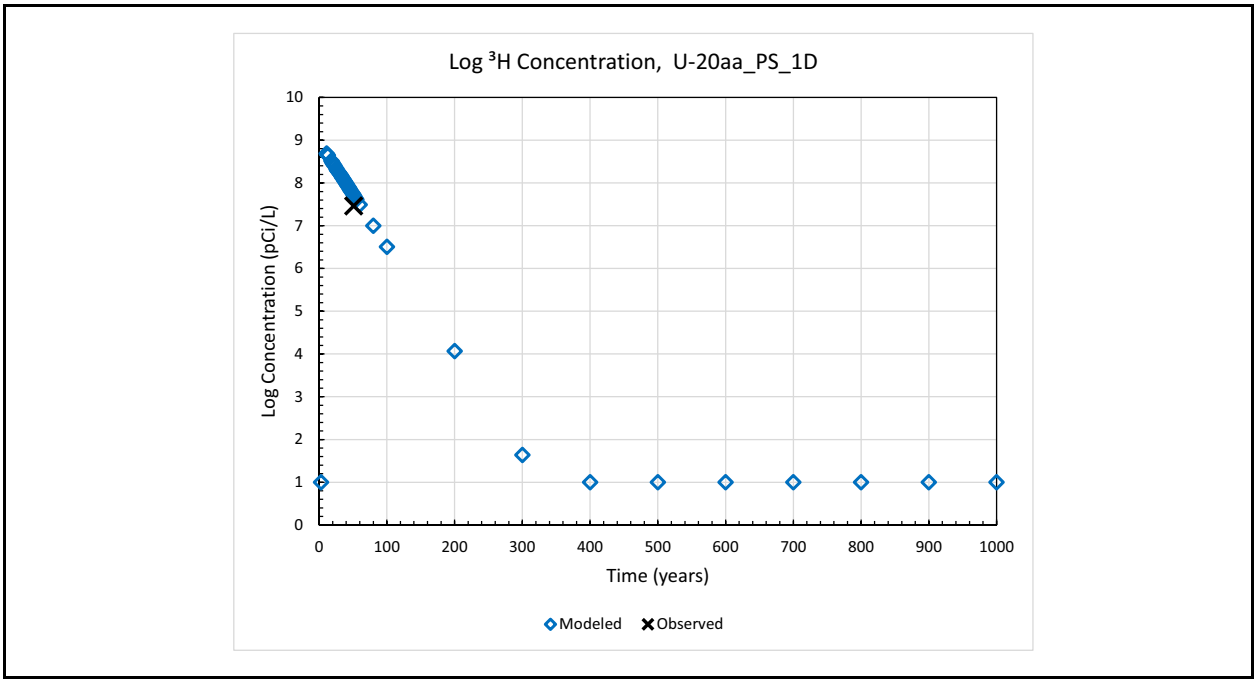

Figure H-50
Modeled and Measured ^{3}H Concentrations versus Time at U-20aa_PS_1D (1,000 Years)

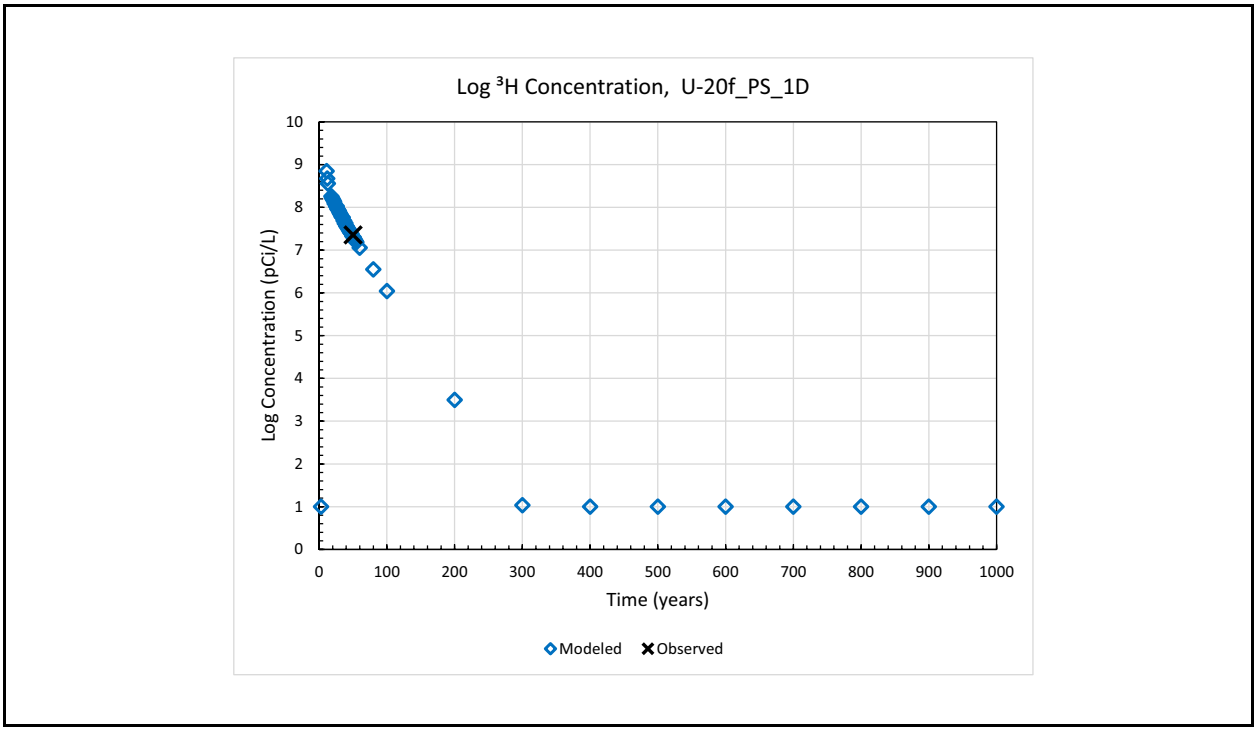

Figure H-51
Modeled and Measured ^{3}H Concentrations versus Time at U-20f_PS_1D (1,000 Years)

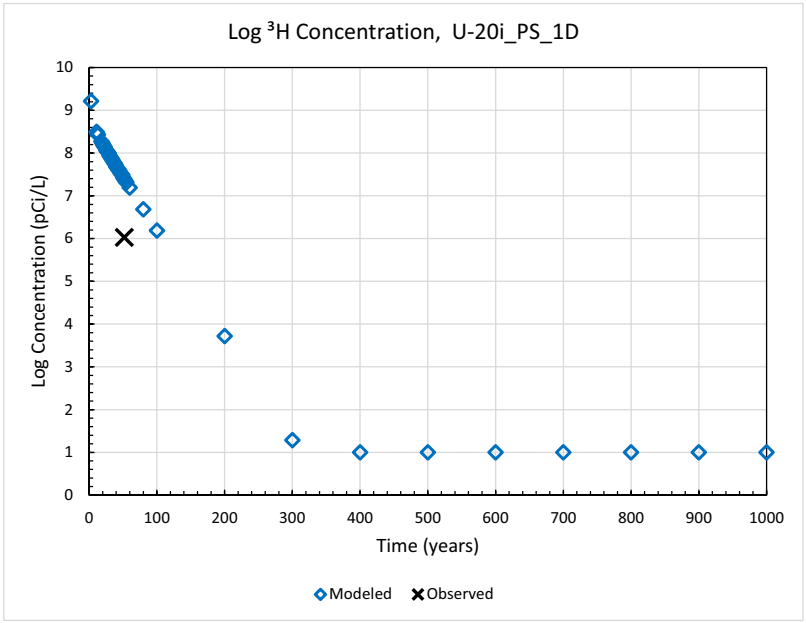

Figure H-52
Modeled and Measured ^{3}H Concentrations versus Time at U-20i_PS_1D (1,000 Years)

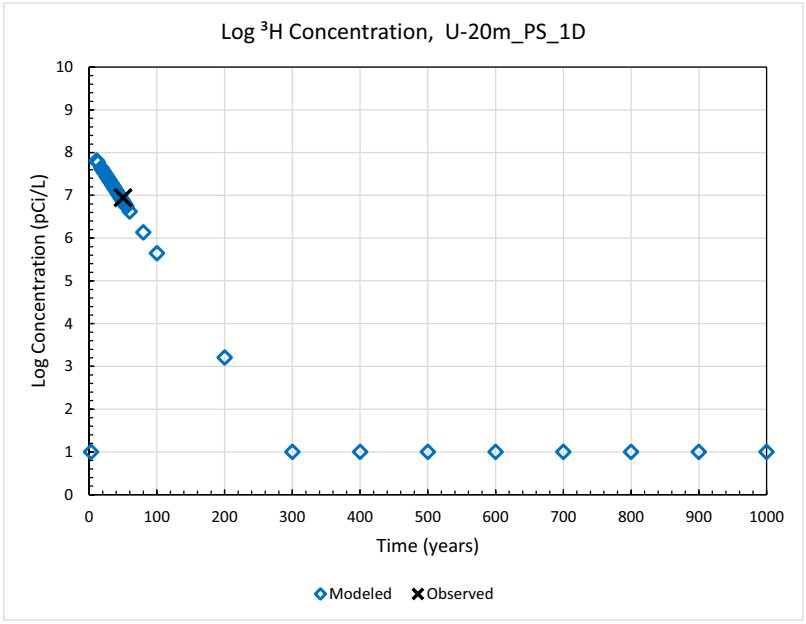

Figure H-53
Modeled and Measured ^{3}H Concentrations versus Time at U-20m_PS_1D (1,000 Years)

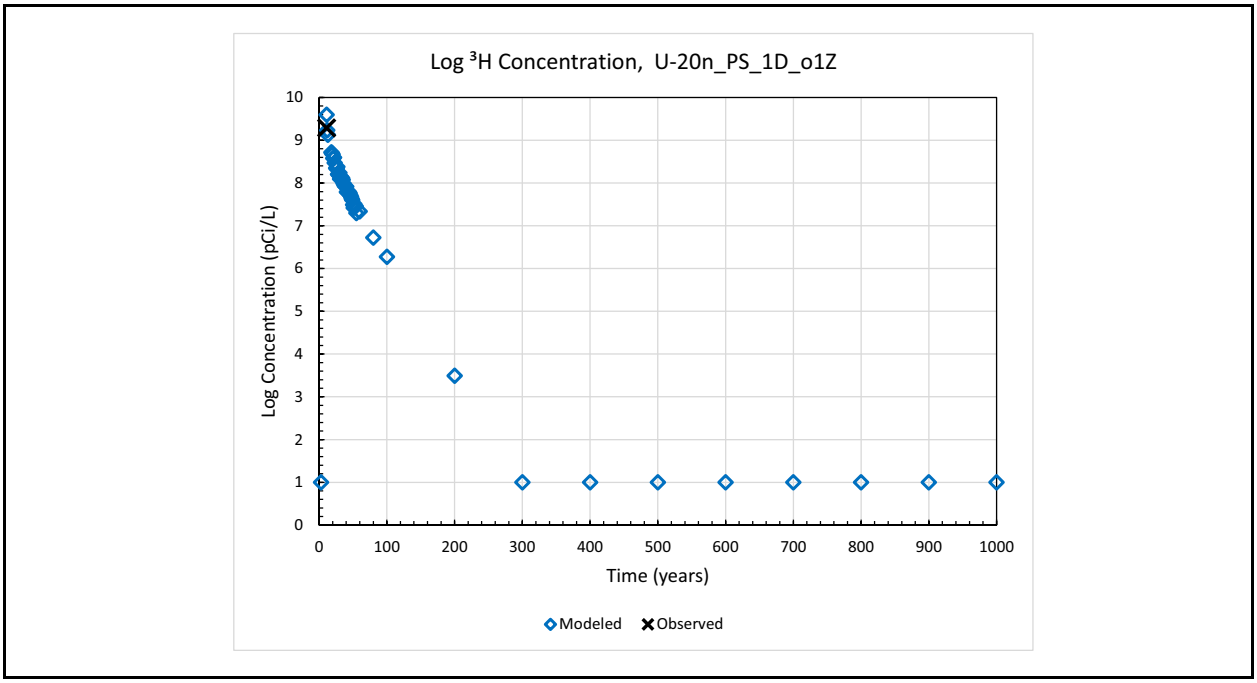

Figure H-54
Modeled and Measured ^{3}H Concentrations versus Time at U-20n_PS_1D_o1Z (1,000 Years)

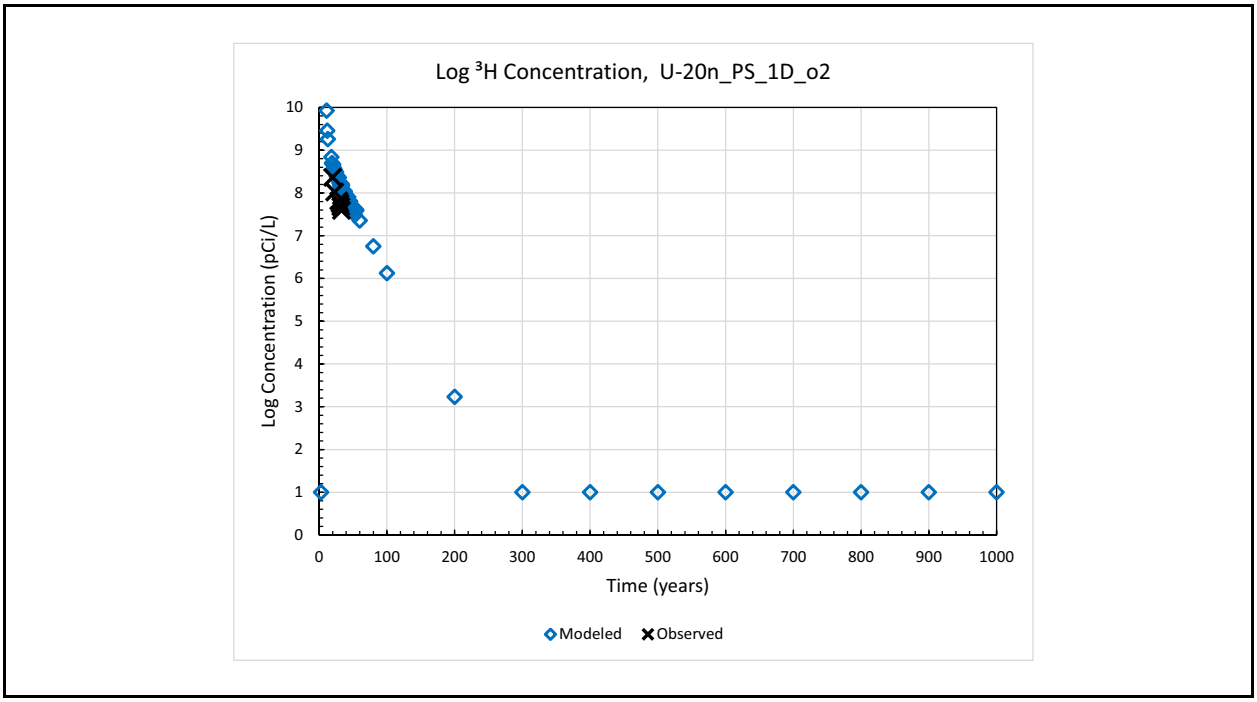

Figure H-55
Modeled and Measured ^{3}H Concentrations versus Time at U-20n_PS_1D_o2 (1,000 Years)

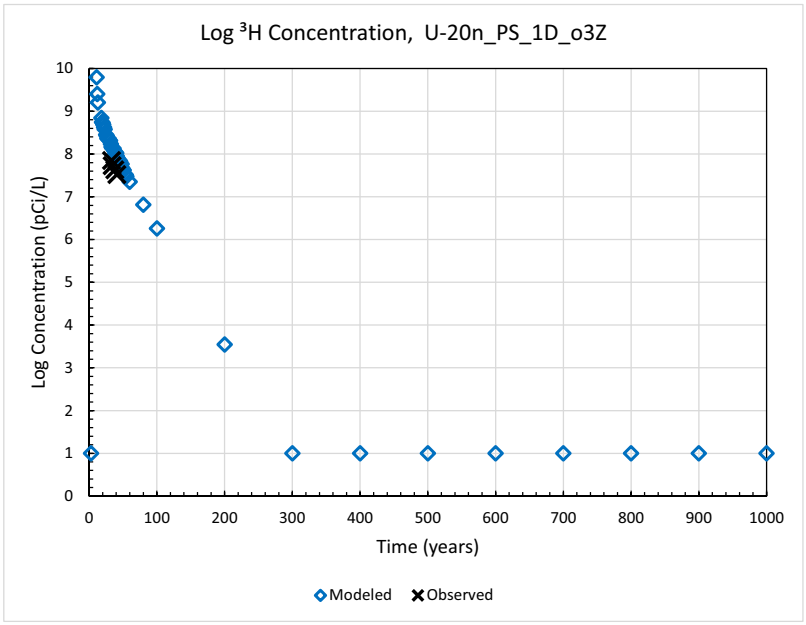

Figure H-56
Modeled and Measured ^{3}H Concentrations versus Time at U-20n_PS_1D_o3Z (1,000 Years)

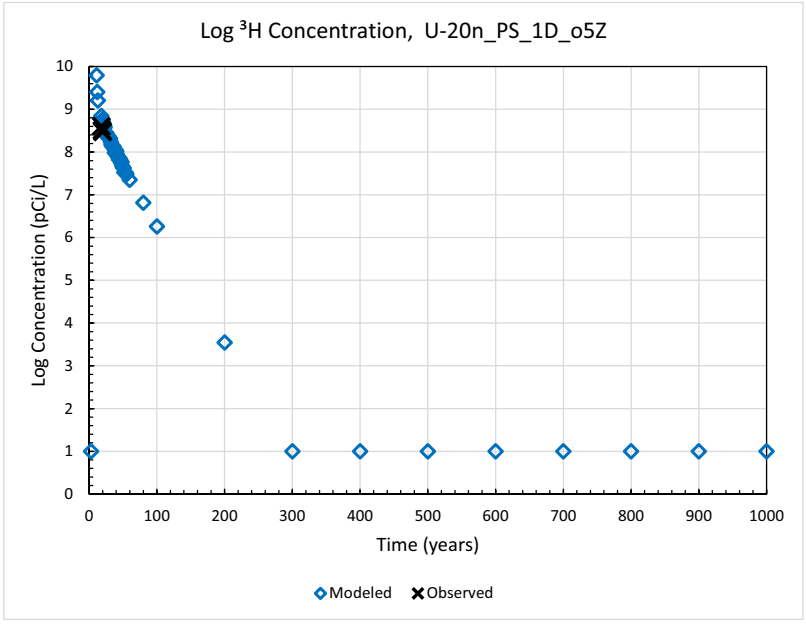

Figure H-57
Modeled and Measured ^{3}H Concentrations versus Time at U-20n_PS_1D_o5Z (1,000 Years)

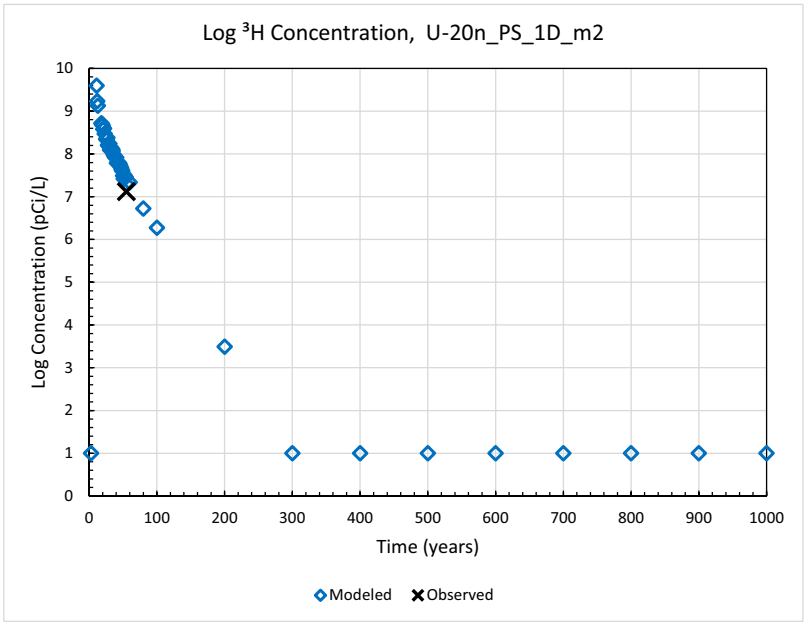

Figure H-58
Modeled and Measured ^{3}H Concentrations versus Time at U-20n_PS_1D_m2 (1,000 Years)

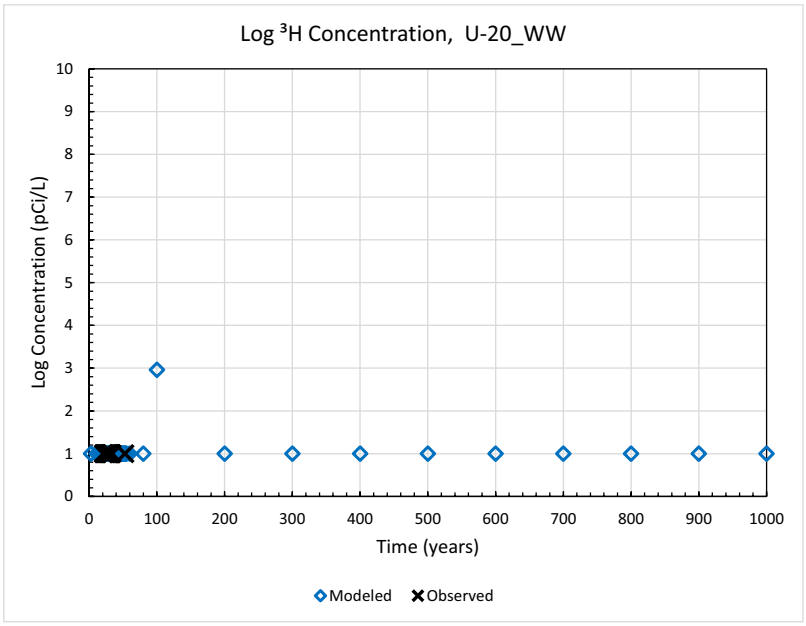

Figure H-59
Modeled and Measured ^{3}H Concentrations versus Time at U-20_WW (1,000 Years)

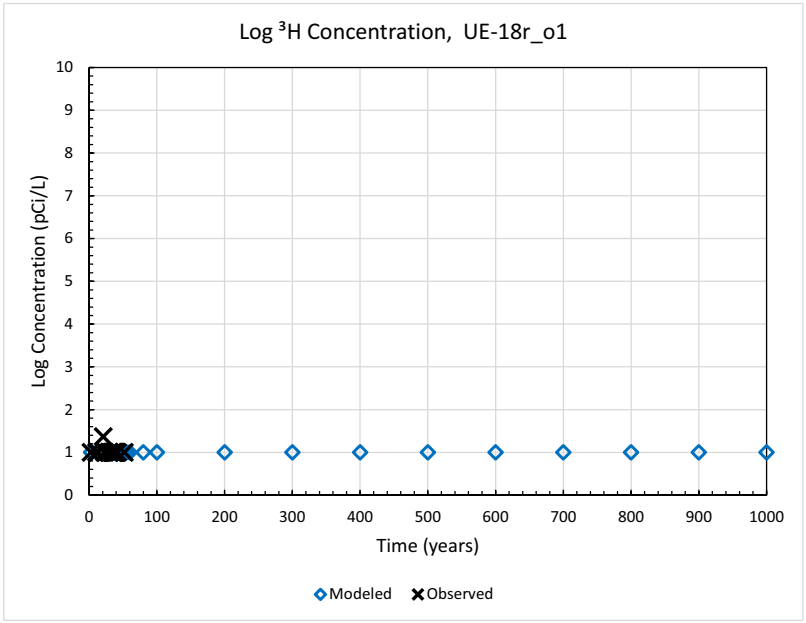

Figure H-60
Modeled and Measured ^{3}H Concentrations versus Time at UE-18r_o1 (1,000 Years)

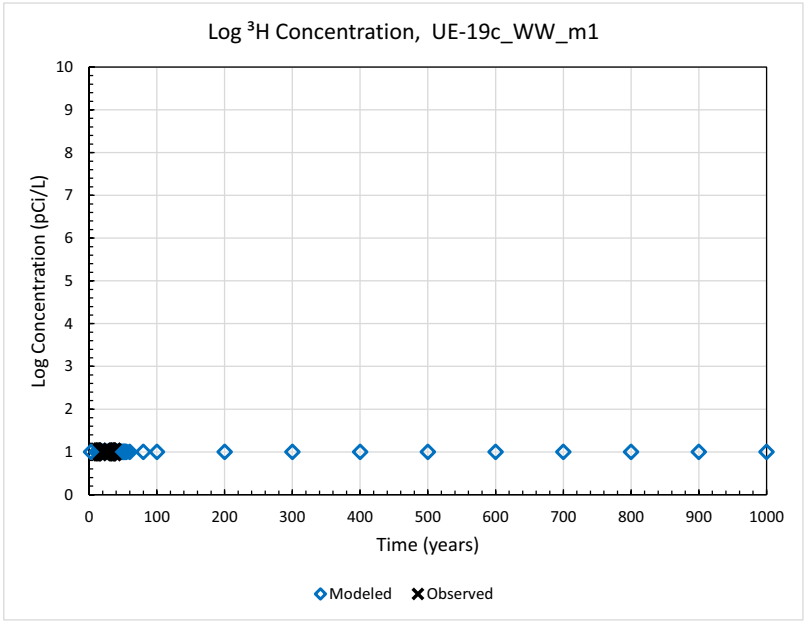

Figure H-61
Modeled and Measured ^{3}H Concentrations versus Time at UE-19c_WW_m1 (1,000 Years)

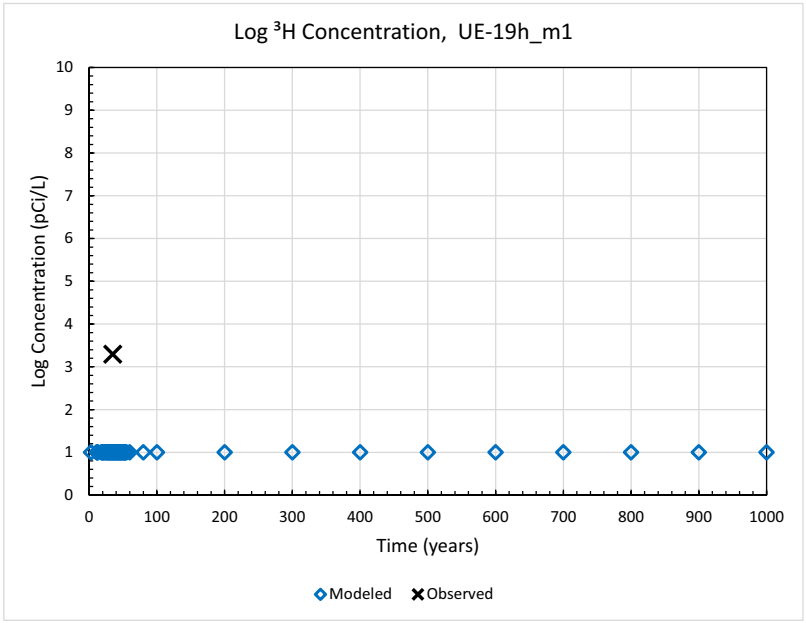

Figure H-62
Modeled and Measured ^{3}H Concentrations versus Time at UE-19h_m1 (1,000 Years)

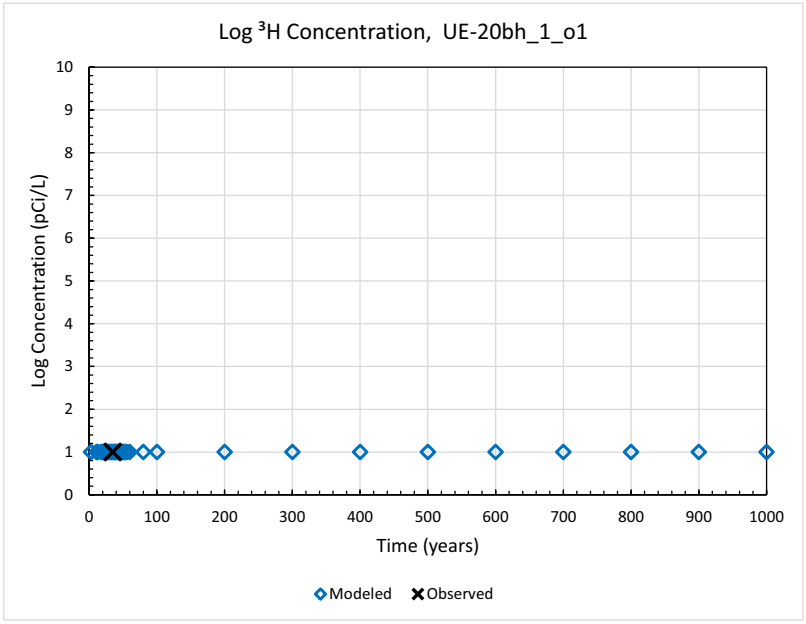

Figure H-63
Modeled and Measured ^{3}H Concentrations versus Time at UE-20bh_1_o1 (1,000 Years)

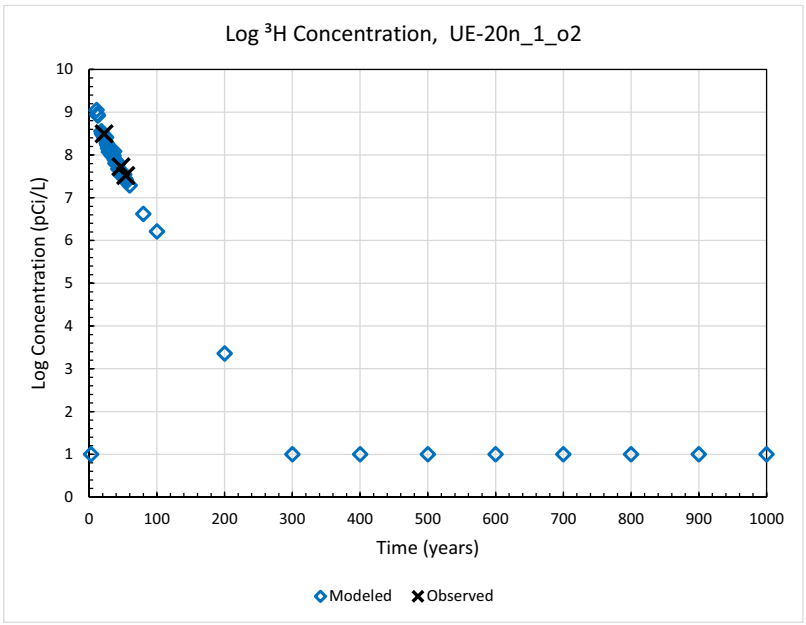

Figure H-64
Modeled and Measured ^{3}H Concentrations versus Time at UE-20n_1_o2 (1,000 Years)

H.1.2 Modeled and Measured ^{14}C Concentrations versus Time from Calibrated PM CAU Transport Model

Figures H-65 through H-79 present plots of modeled and measured ^{14}C concentrations versus time, over the first 60 years (encompassing all observation times), from the calibrated PM CAU transport model at locations with observed ^{14}C. The log of concentration is used to compare modeled and measured (observed) values. Zero values were approximated with a value of 1E-06, resulting in a log value of -6. Good agreement between measured and modeled values is achieved with the model either overpredicting or underpredicting within approximately 1 order of magnitude at these locations, except at ER-20-5-3_m1. As discussed in Section 5.5.1.3, the poor agreement at ER-20-5-3_m1 is likely due to the deeper flow path from BENHAM passing to the east of the defined observation nodes.

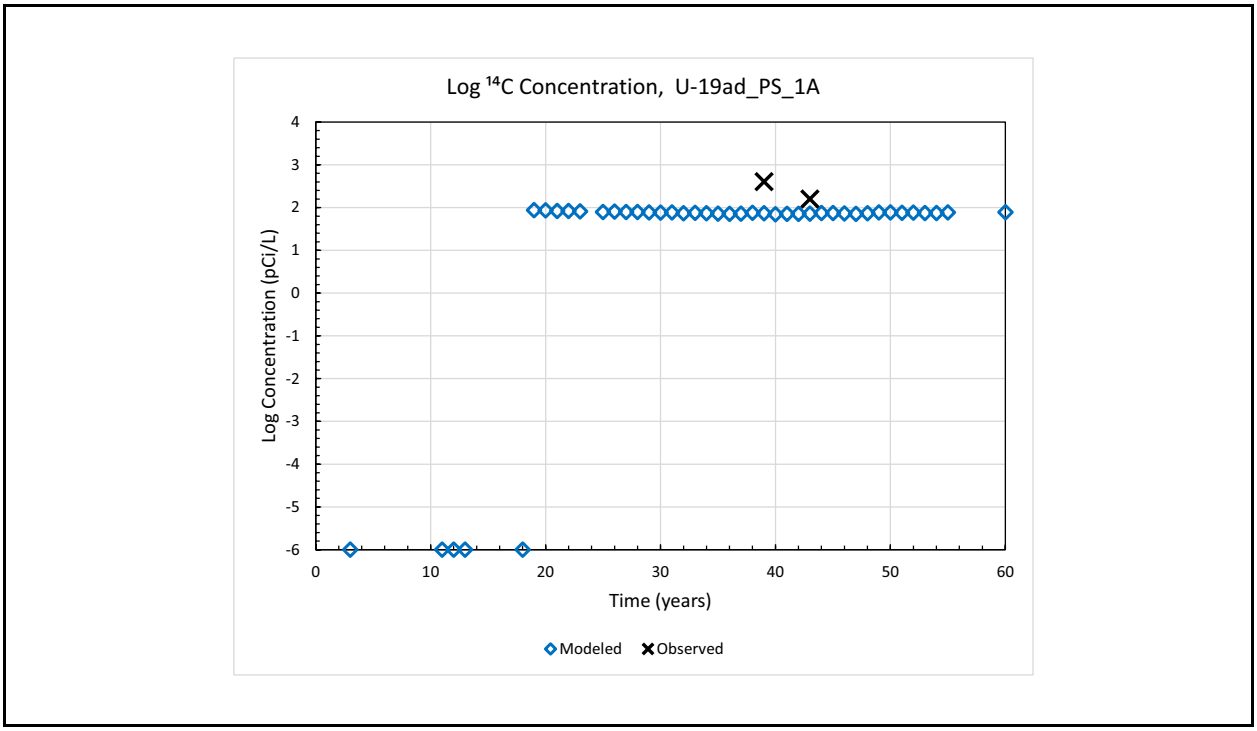

Figure H-65
Modeled and Measured ^{14}C Concentrations versus Time at U-19ad_PS_1A

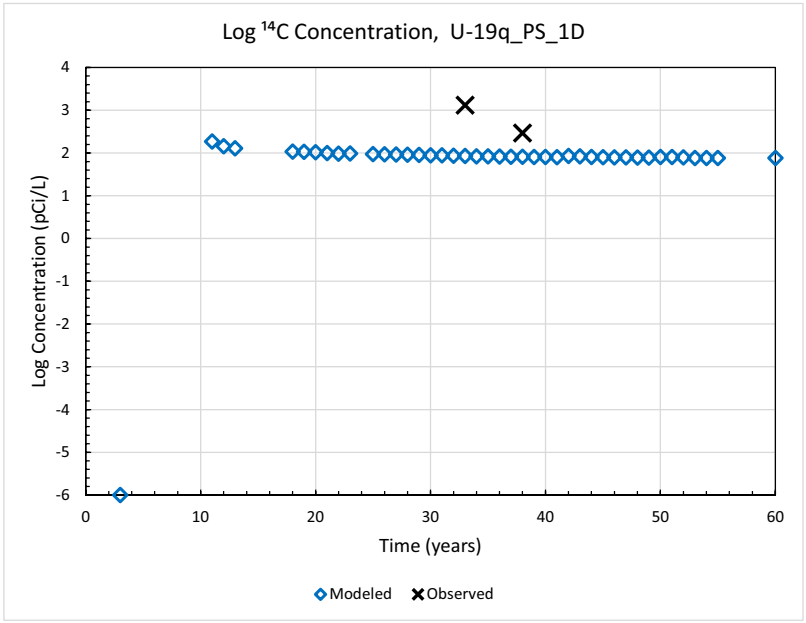

Figure H-66
Modeled and Measured ^{14}C Concentrations versus Time at U-19q_PS_1D

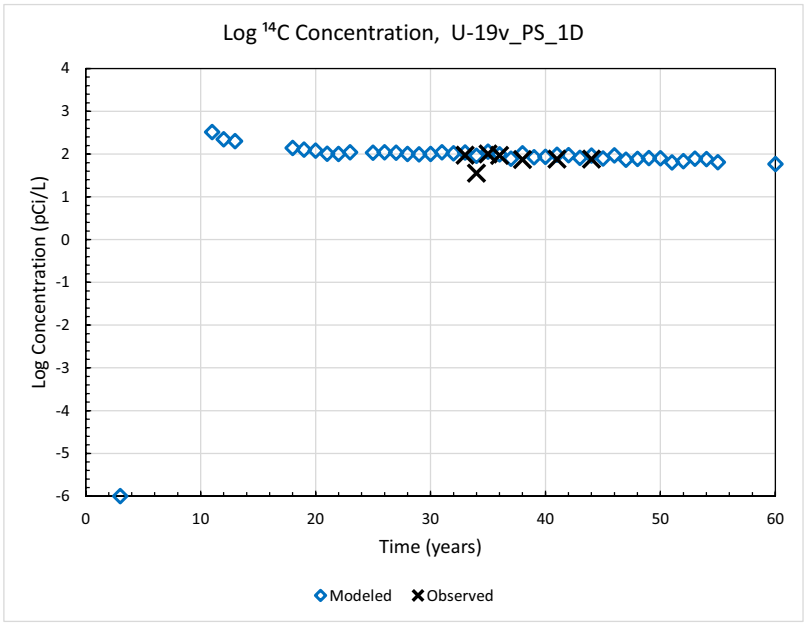

Figure H-67
Modeled and Measured ^{14}C Concentrations versus Time at U-19v_PS_1D

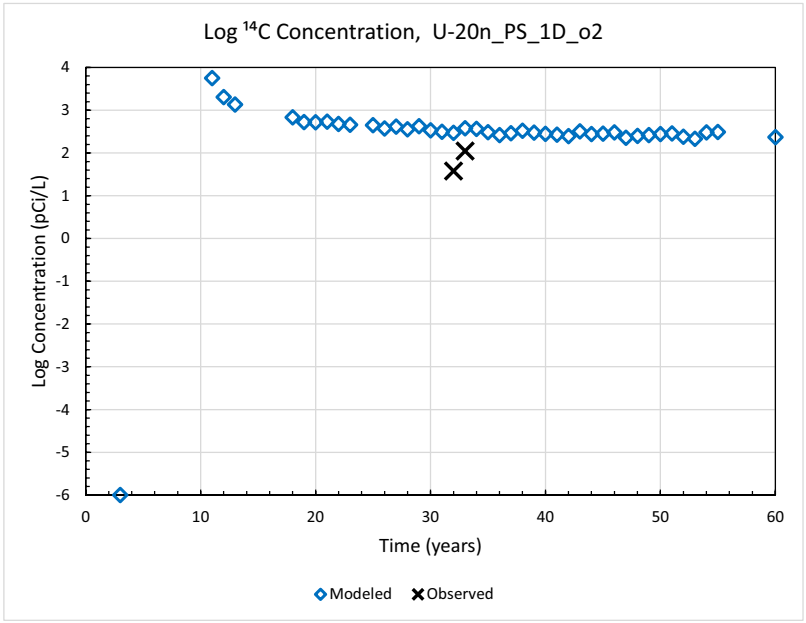

Figure H-68
Modeled and Measured ^{14}C Concentrations versus Time at U-20n_PS_1D_o2

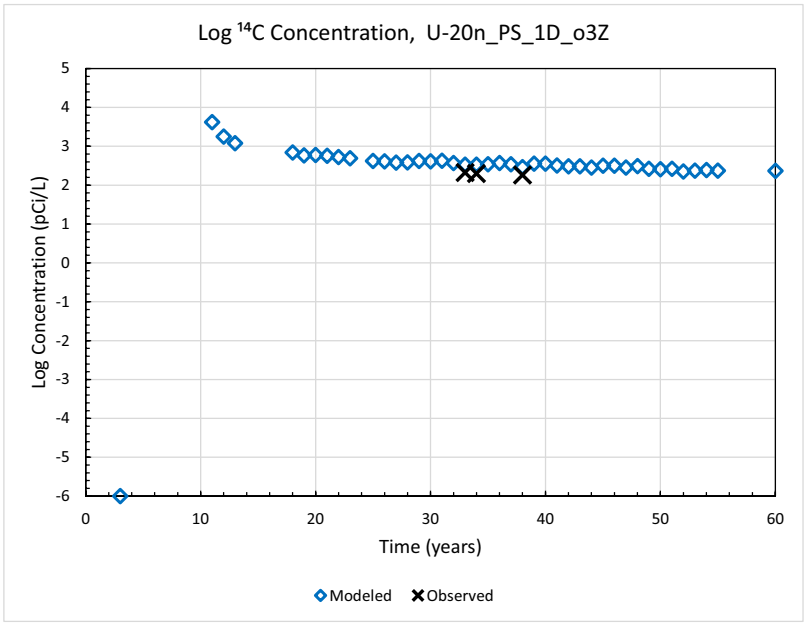

Figure H-69
Modeled and Measured ^{14}C Concentrations versus Time at U-20n_PS_1D_o3Z

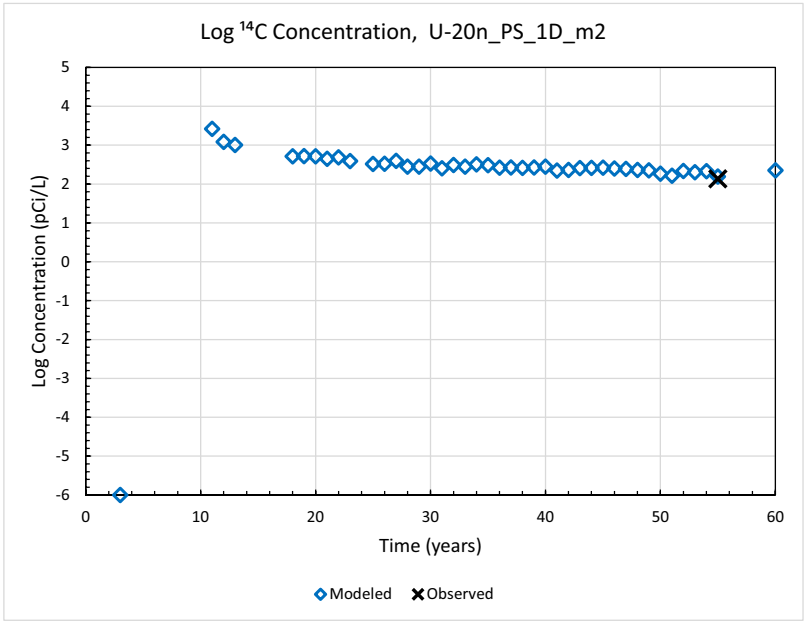

Figure H-70
Modeled and Measured ^{14}C Concentrations versus Time at U-20n_PS_1D_m2

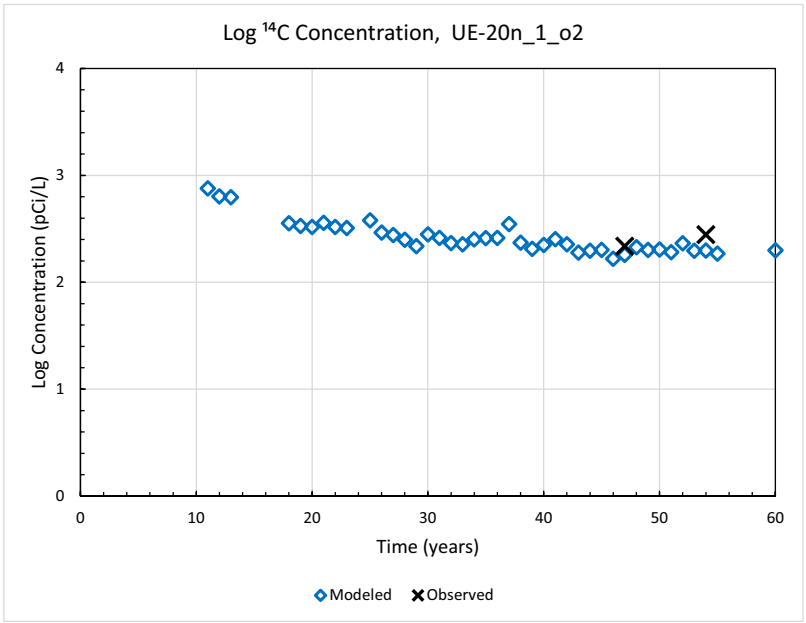

Figure H-71
Modeled and Measured ^{14}C Concentrations versus Time at UE-20n_1_o2

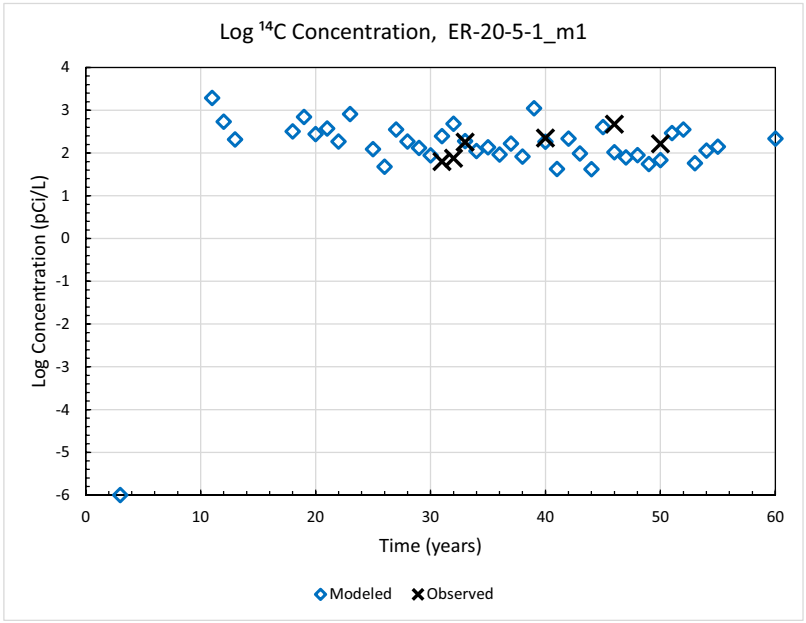

Figure H-72
Modeled and Measured ^{14}C Concentrations versus Time at ER-20-5-1_m1

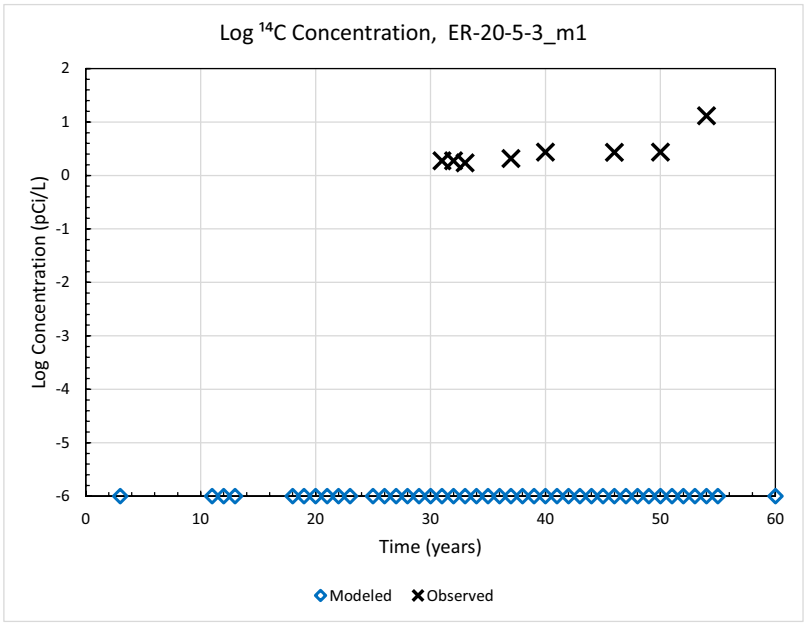

Figure H-73
Modeled and Measured ^{14}C Concentrations versus Time at ER-20-5-3_m1

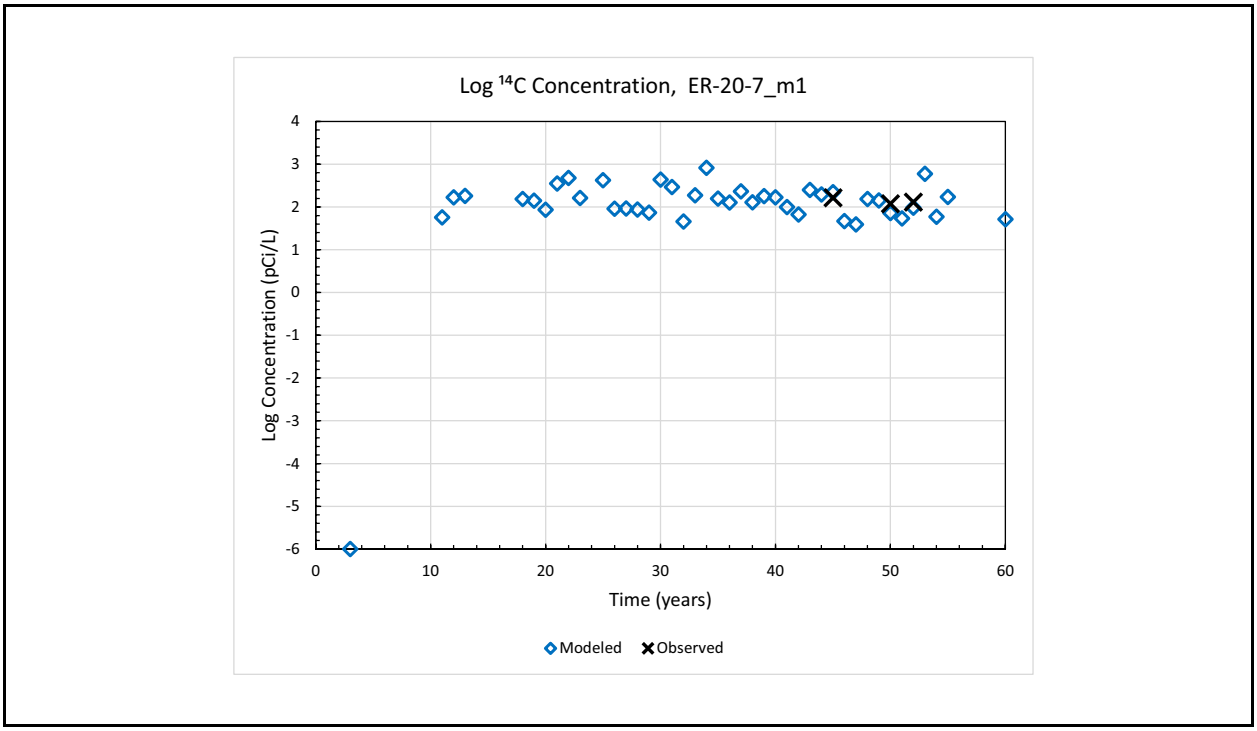

Figure H-74
Modeled and Measured ^{14}C Concentrations versus Time at ER-20-7_m1

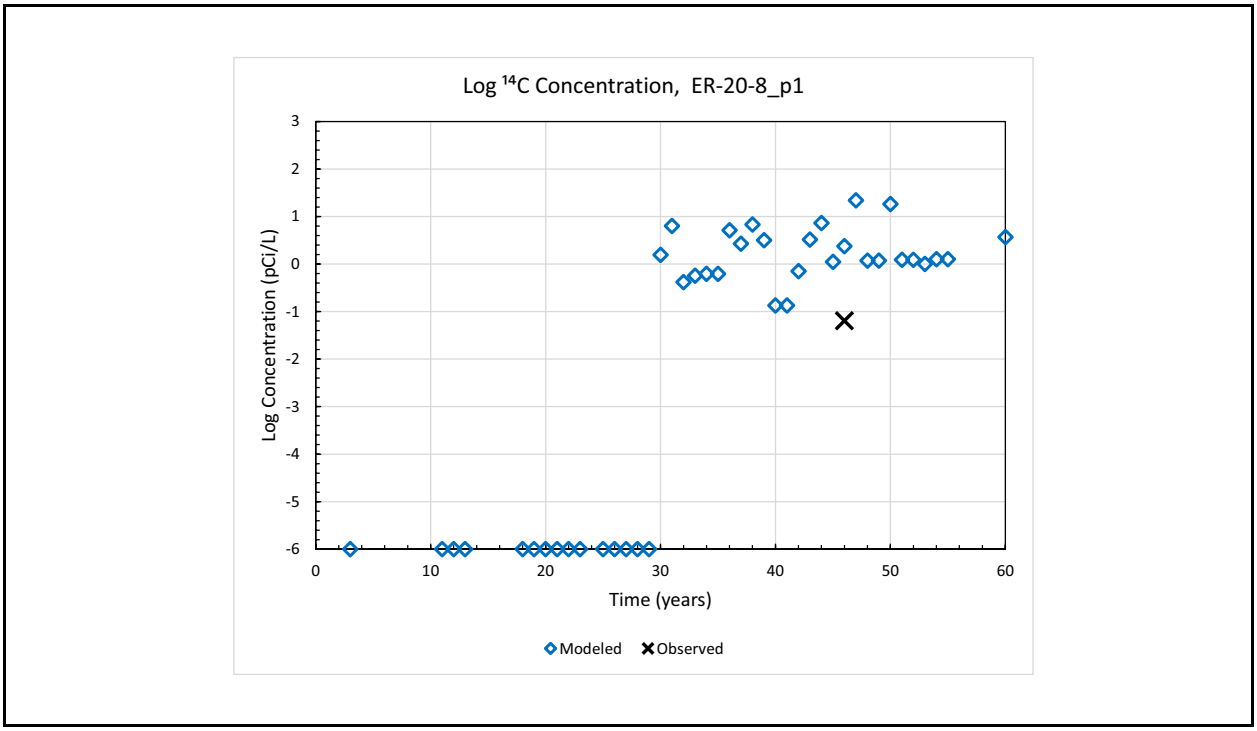

Figure H-75
Modeled and Measured ^{14}C Concentrations versus Time at ER-20-8_p1

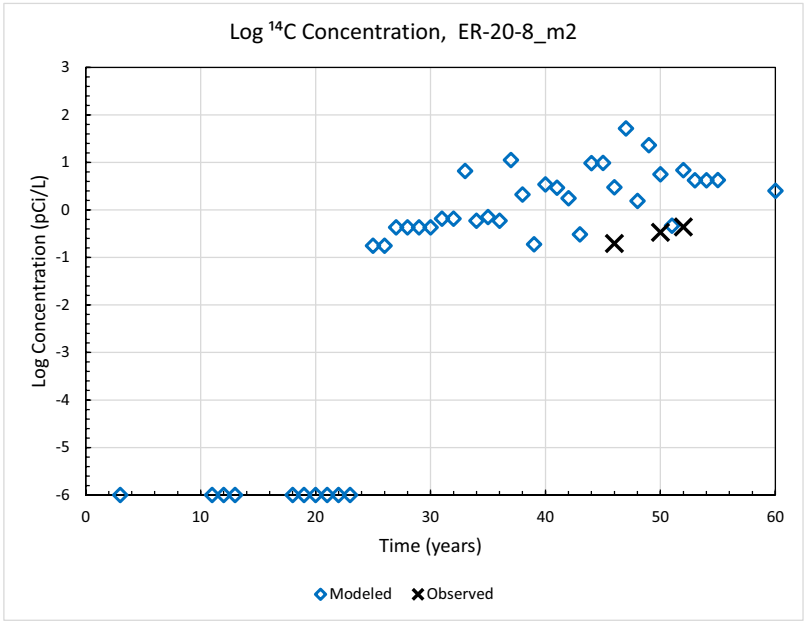

Figure H-76
Modeled and Measured ^{14}C Concentrations versus Time at ER-20-8_m2

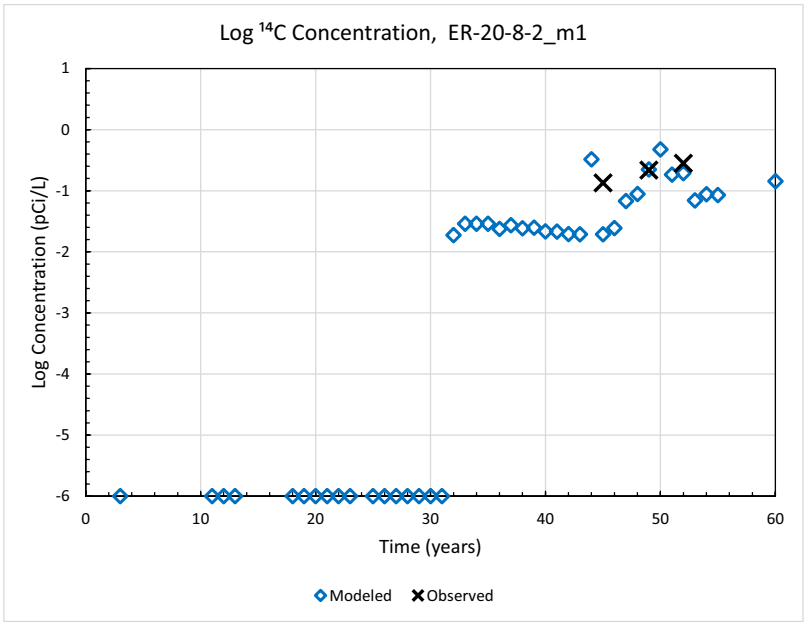

Figure H-77
Modeled and Measured ^{14}C Concentrations versus Time at ER-20-8-2_m1

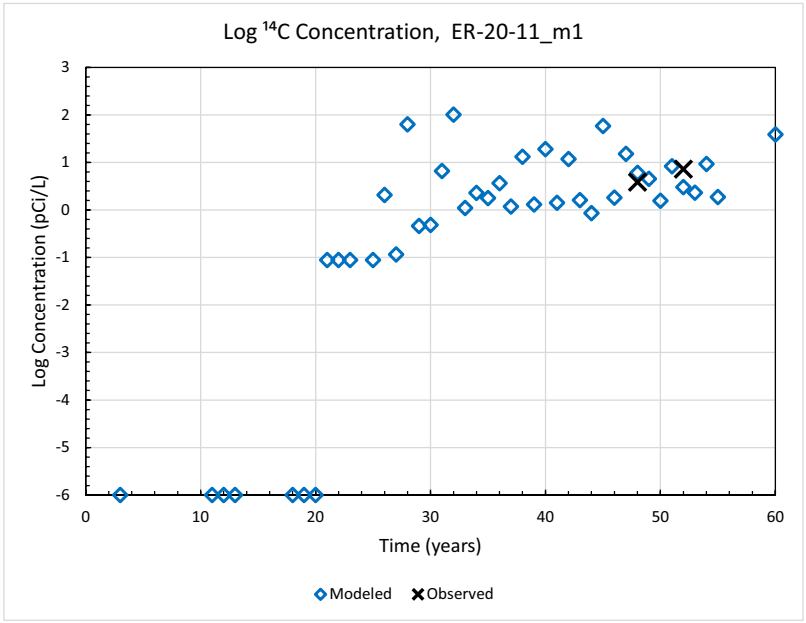

Figure H-78
Modeled and Measured ^{14}C Concentrations versus Time at ER-20-11_m1

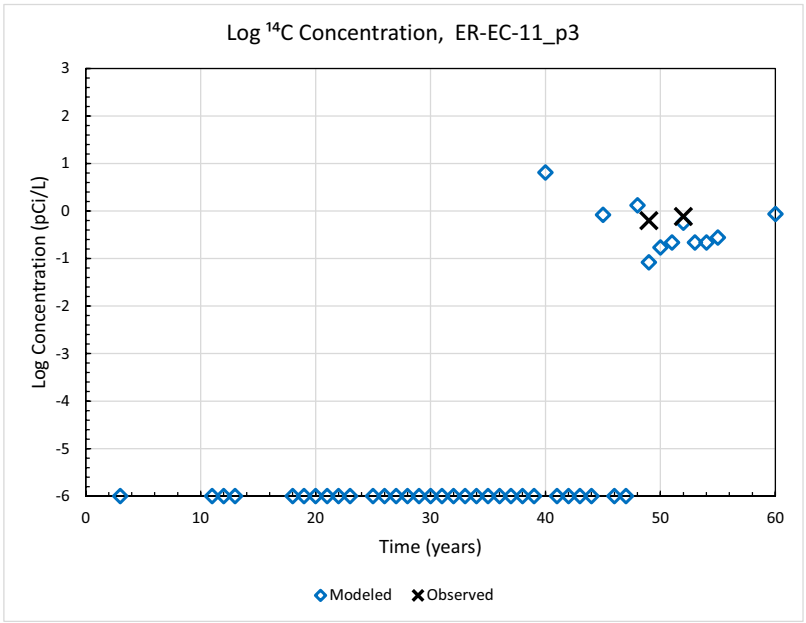

Figure H-79
Modeled and Measured ^{14}C Concentrations versus Time at ER-EC-11_p3

H.1.3 Modeled and Measured ^{36}Cl Concentrations versus Time from Calibrated PM CAU Transport Model

Figures H-80 through H-92 present plots of modeled and measured ^{36}Cl concentrations versus time, over the first 60 years (encompassing all observation times), from the calibrated PM CAU transport model at locations with observed ^{36}Cl. The log of concentration is used to compare modeled and measured (observed) values. Zero values were approximated with a value of 1E-06, resulting in a log value of -6. At the postshot holes, the model overpredicts ^{36}Cl at these locations by approximately 1 to 3 orders of magnitude. This suggests that ^{36}Cl source mass input to the PM CAU transport model may be conservatively high at the sources near these observation locations (CHANCELLOR, CAMEMBERT, ALMENDRO, and CHESHIRE). Near the bench area, with the exception of ER-20-5-3_m1, the model overpredicts ^{36}Cl at these locations by approximately 1 to 3 orders of magnitude. Again, this suggests that ^{36}Cl source mass input to the PM CAU transport model may be conservatively high at the sources that contribute RNs at these observation locations. As discussed in Section 5.5.1.3, the poor agreement at ER-20-5-3_m1 is likely due to the deeper flow path from BENHAM passing to the east of the defined observation nodes.

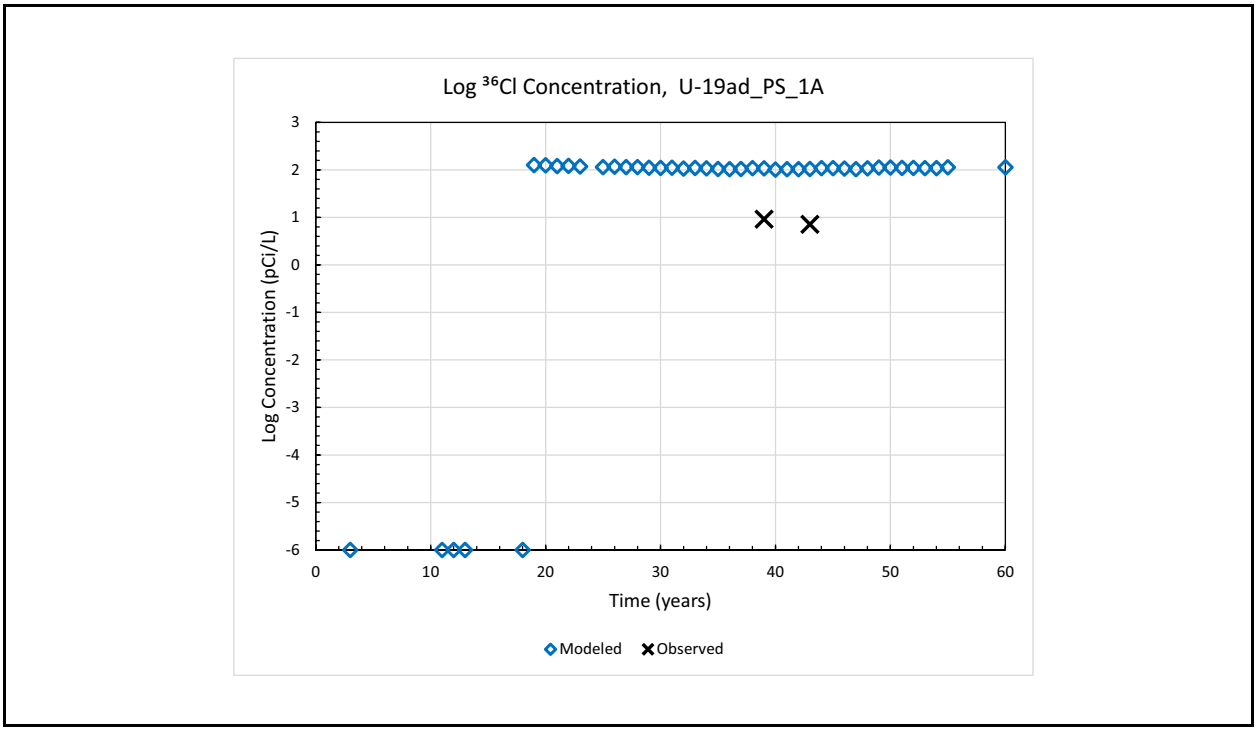

Figure H-80
Modeled and Measured ^{36}Cl Concentrations versus Time at U-19ad_PS_1A

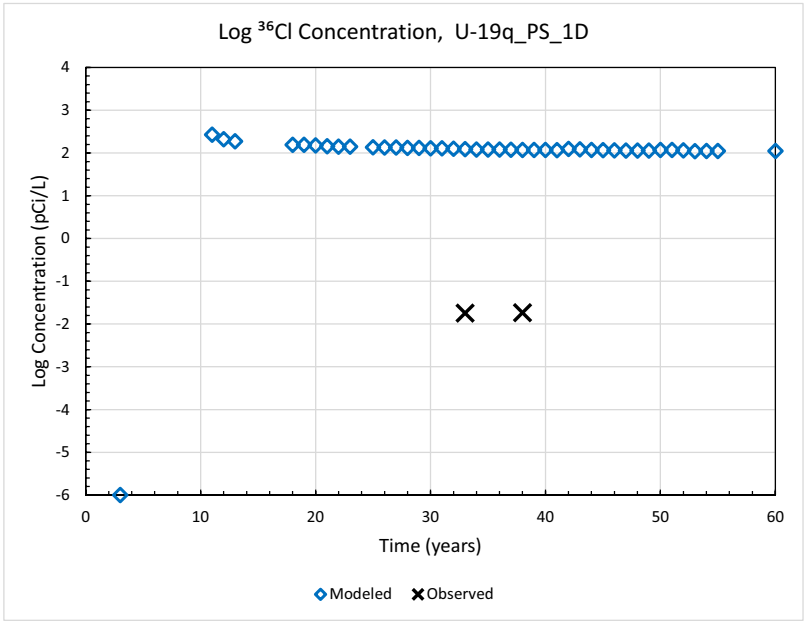

Figure H-81
Modeled and Measured ^{36}Cl Concentrations versus Time at U-19q_PS_1D

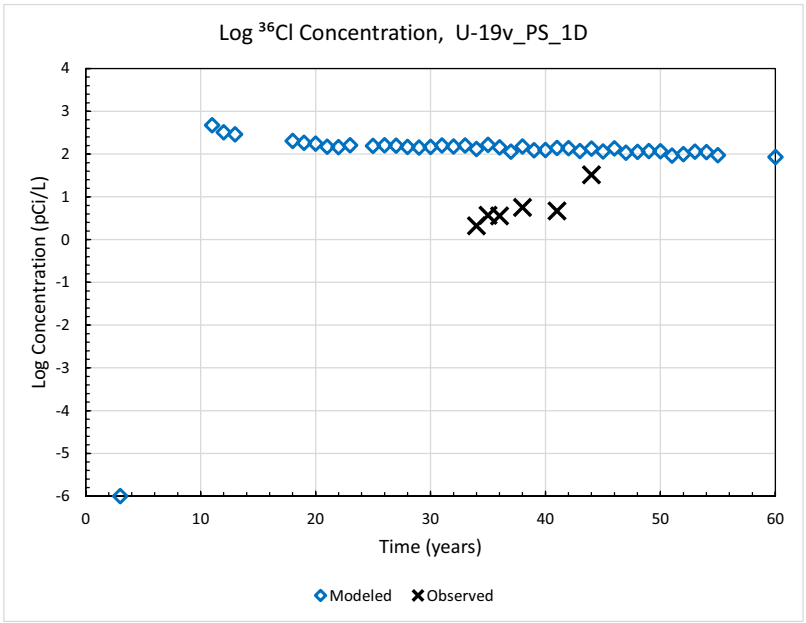

Figure H-82
Modeled and Measured ^{36}Cl Concentrations versus Time at U-19v_PS_1D

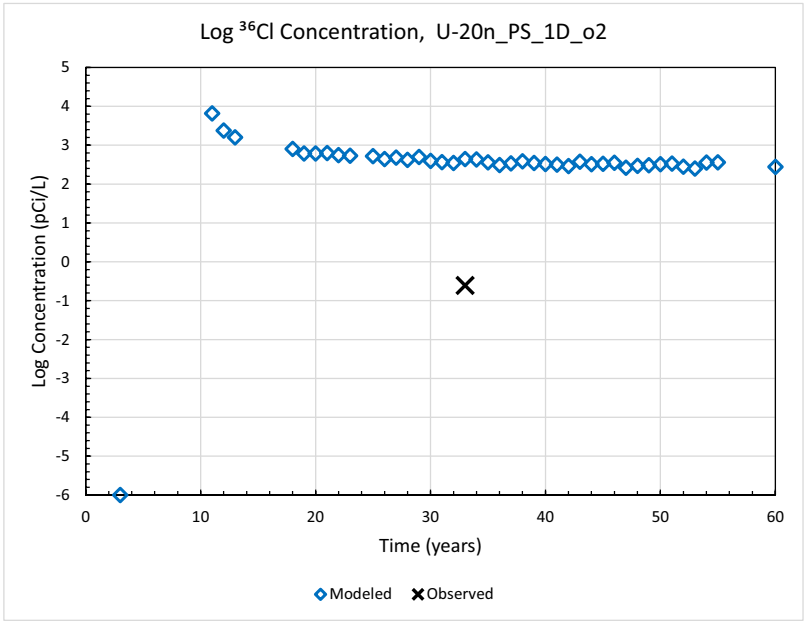

Figure H-83
Modeled and Measured ^{36}Cl Concentrations versus Time at U-20n_PS_1D_o2

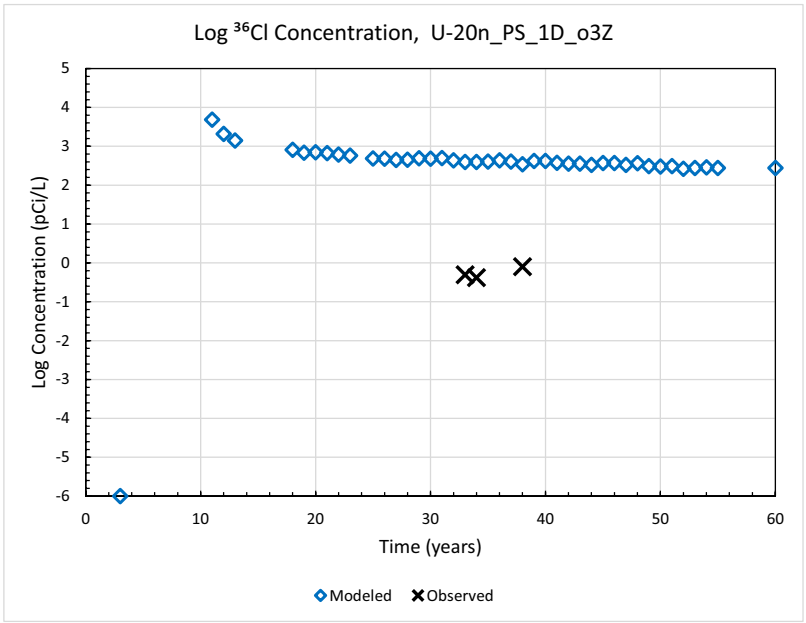

Figure H-84
Modeled and Measured ^{36}Cl Concentrations versus Time at U-20n_PS_1D_o3Z

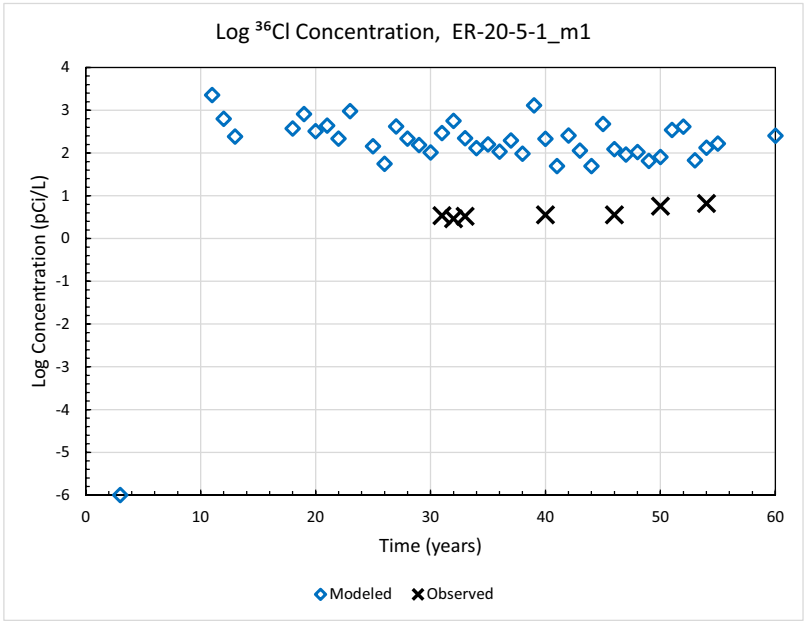

Figure H-85
Modeled and Measured ^{36}Cl Concentrations versus Time at ER-20-5-1_m1

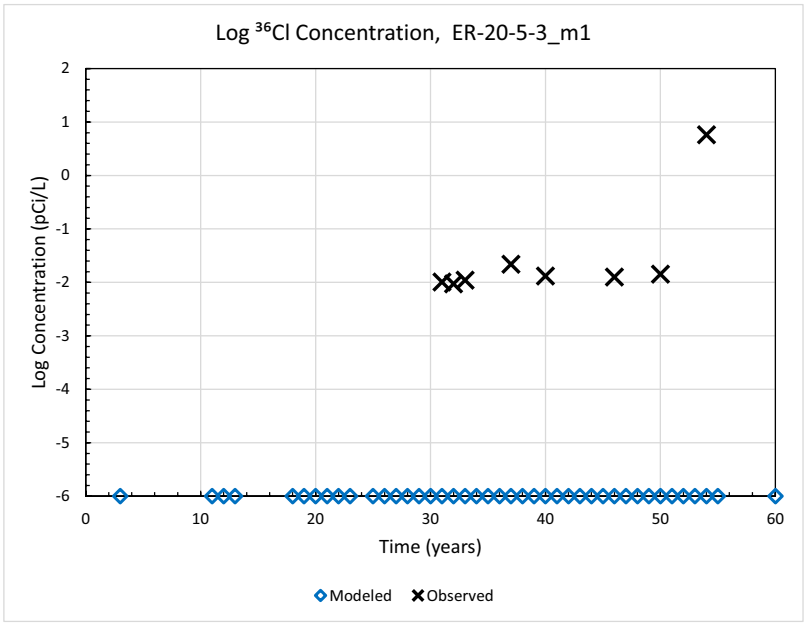

Figure H-86
Modeled and Measured ^{36}Cl Concentrations versus Time at ER-20-5-3_m1

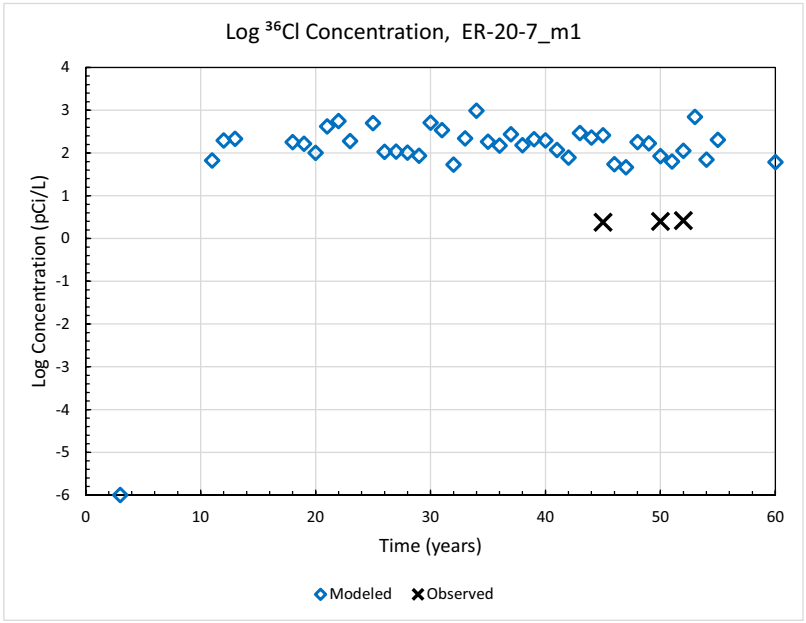

Figure H-87
Modeled and Measured ^{36}Cl Concentrations versus Time at ER-20-7_m1

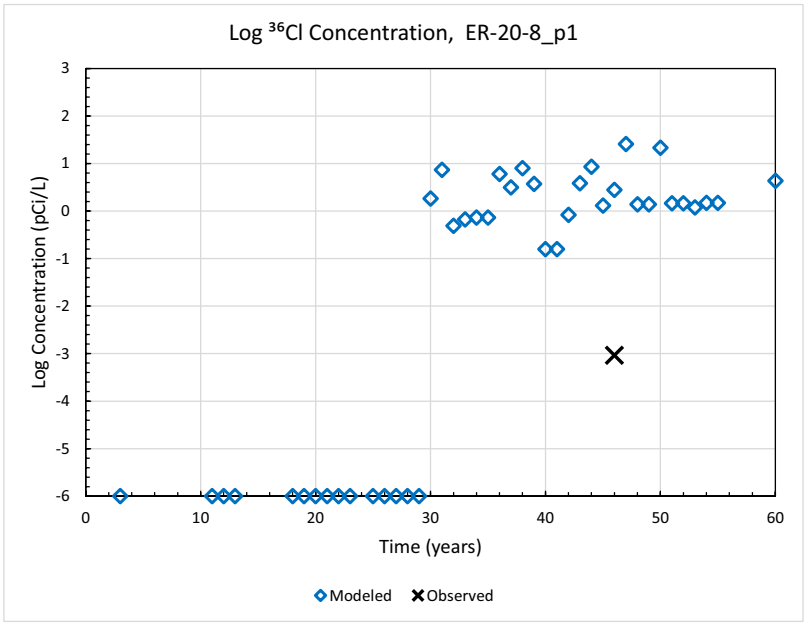

Figure H-88
Modeled and Measured ^{36}Cl Concentrations versus Time at ER-20-8_p1

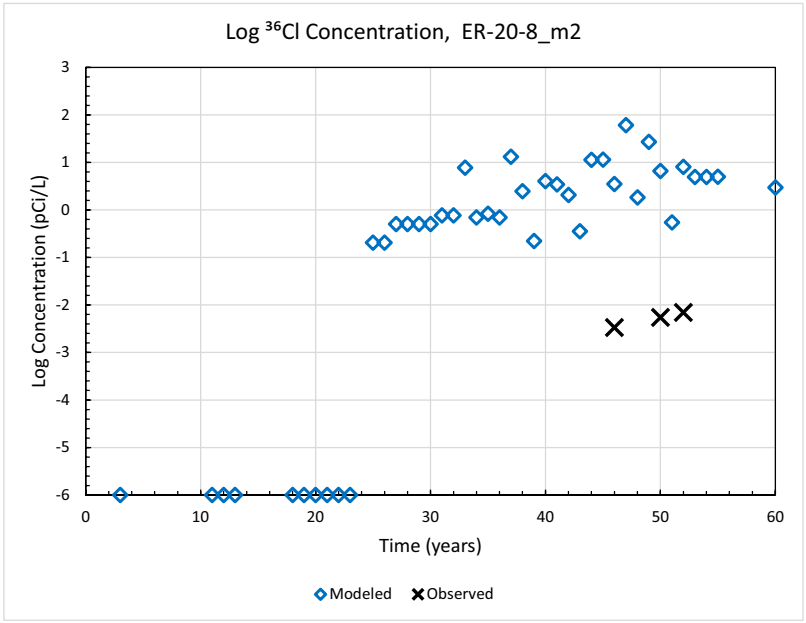

Figure H-89
Modeled and Measured ^{36}Cl Concentrations versus Time at ER-20-8_m2

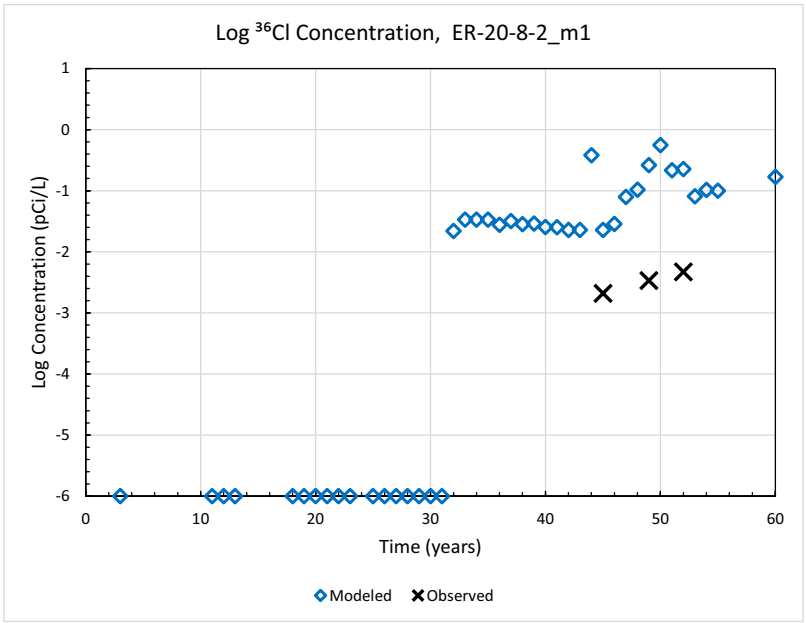

Figure H-90
Modeled and Measured ^{36}Cl Concentrations versus Time at ER-20-8-2_m1

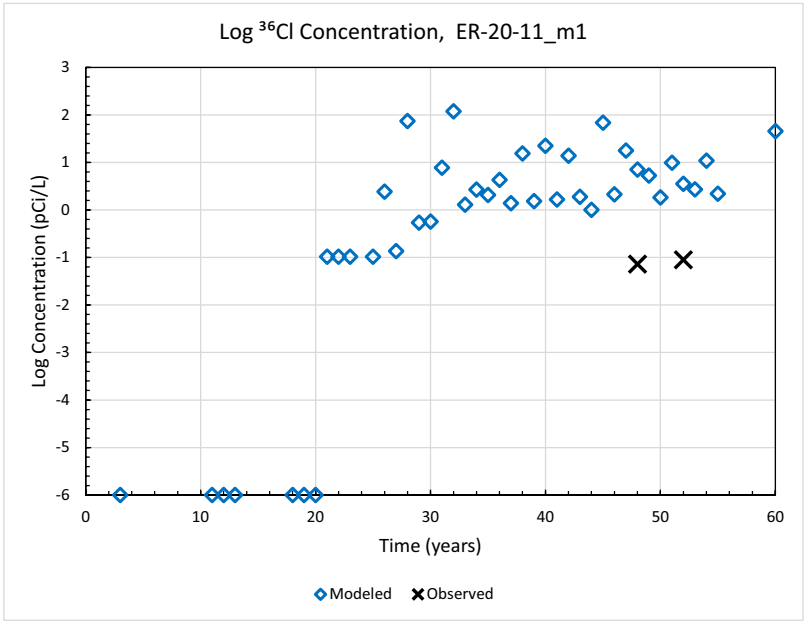

Figure H-91
Modeled and Measured ^{36}Cl Concentrations versus Time at ER-20-11_m1

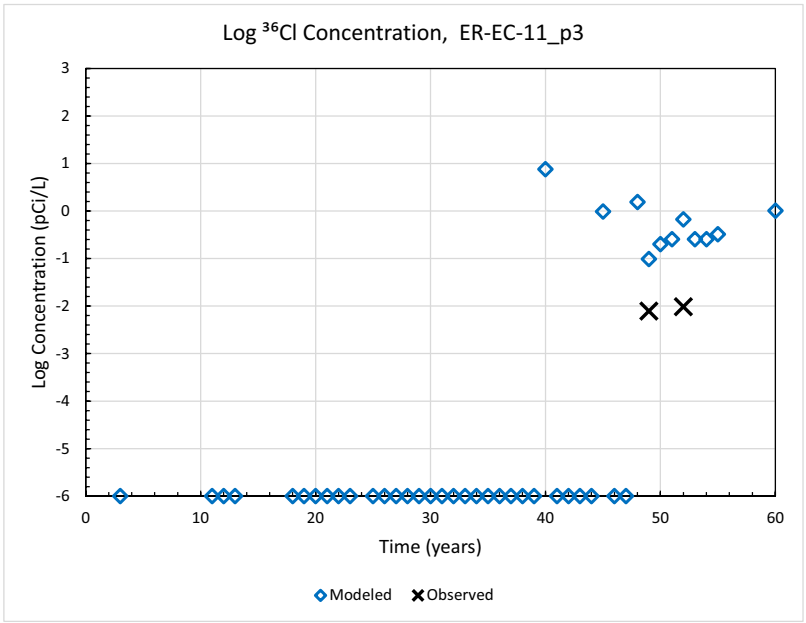

Figure H-92
Modeled and Measured ^{36}Cl Concentrations versus Time at ER-EC-11_p3

H.1.4 Modeled and Measured ^{90}Sr Concentrations versus Time from Calibrated PM CAU Transport Model

Figures H-93 through H-100 present plots of modeled and measured ^{90}Sr concentrations versus time, over the first 60 years (encompassing all observation times), from the calibrated PM CAU transport model at locations with observed ^{90}Sr. The log of concentration is used to compare modeled and measured (observed) values. Zero values were approximated with a value of 1E-06, resulting in a log value of -6. Modeled concentrations are displayed for two cases: one using minimum K_d for all zones (blue diamonds) and one using maximum K_d for all zones (red circles). As expected, higher concentrations are observed for the case with minimum K_d.

There is good agreement at U-19ad PS 1A (CHANCELLOR), where the modeled concentration range spans a range of values that is near the measured value at the upper end to a value that underpredicts by approximately 1 order of magnitude. At the other postshot locations, the modeled concentration range overpredicts measured values by a range of 1 to several orders of magnitude. This suggests that ^{90}Sr source mass input to the PM CAU transport model may be conservatively high at the sources that contribute RNs at these observation locations (CAMEMBERT and CHESHIRE).

At ER-20-12, downgradient of HANDLEY, all ^{90}Sr observations are zero (or below detection limit), but the model shows high concentrations, indicating poor agreement at this location. This suggests that ^{90}Sr source mass input to the PM CAU transport model at HANDLEY may be conservatively high.

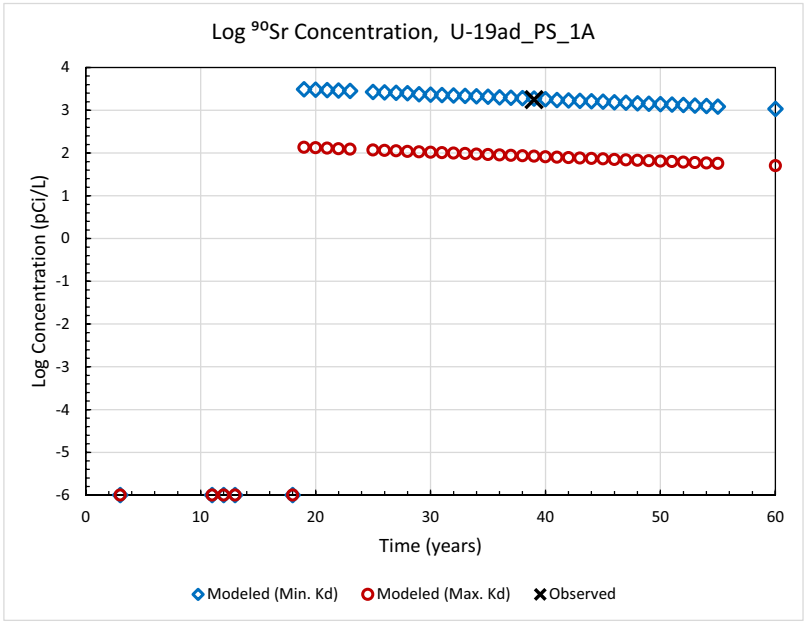

Figure H-93
Modeled and Measured ^{90}Sr Concentrations versus Time at U-19ad_PS_1A

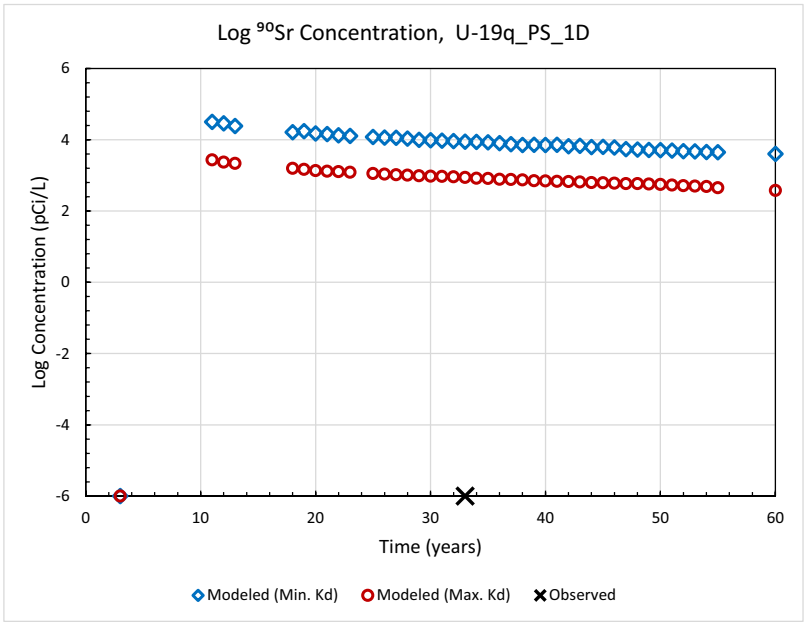

Figure H-94
Modeled and Measured ^{90}Sr Concentrations versus Time at U-19q_PS_1D

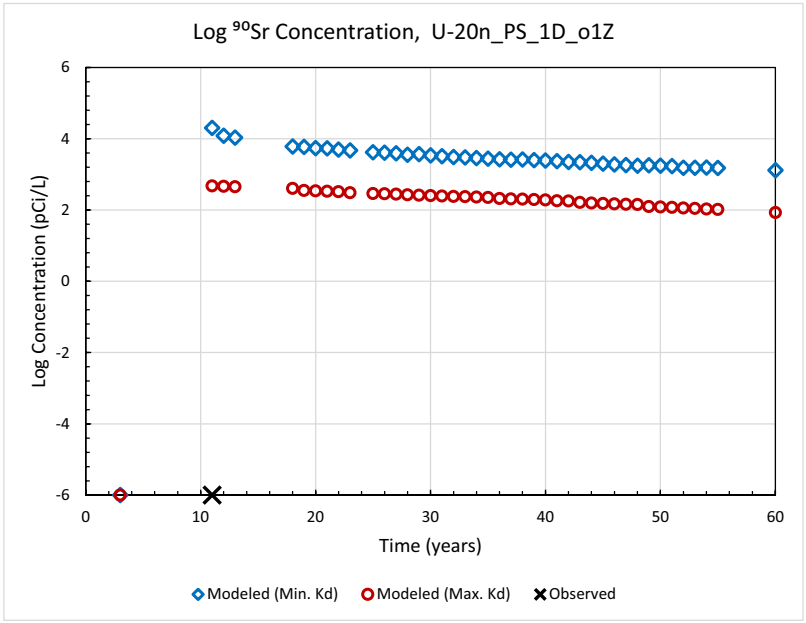

Figure H-95
Modeled and Measured ^{90}Sr Concentrations versus Time at U-20n_PS_1D_o1Z

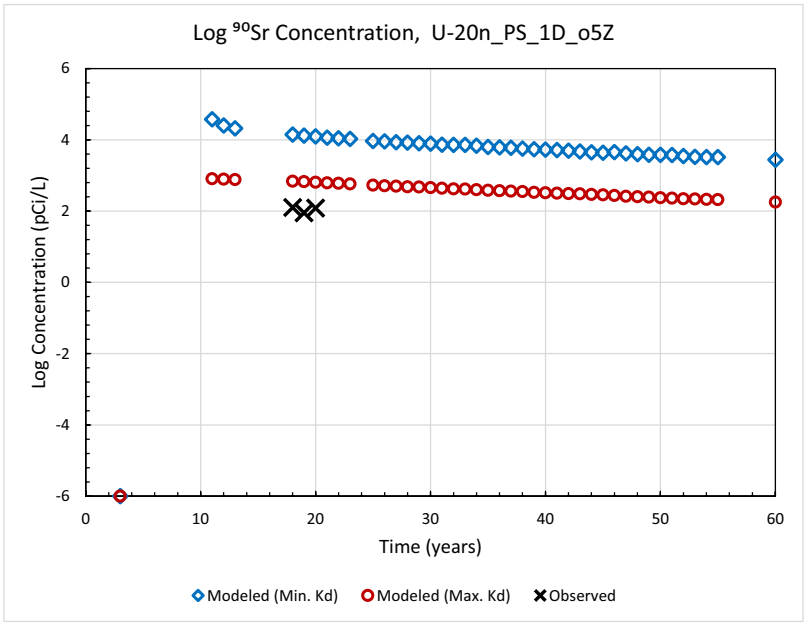

Figure H-96
Modeled and Measured ^{90}Sr Concentrations versus Time at U-20n_PS_1D_o5Z

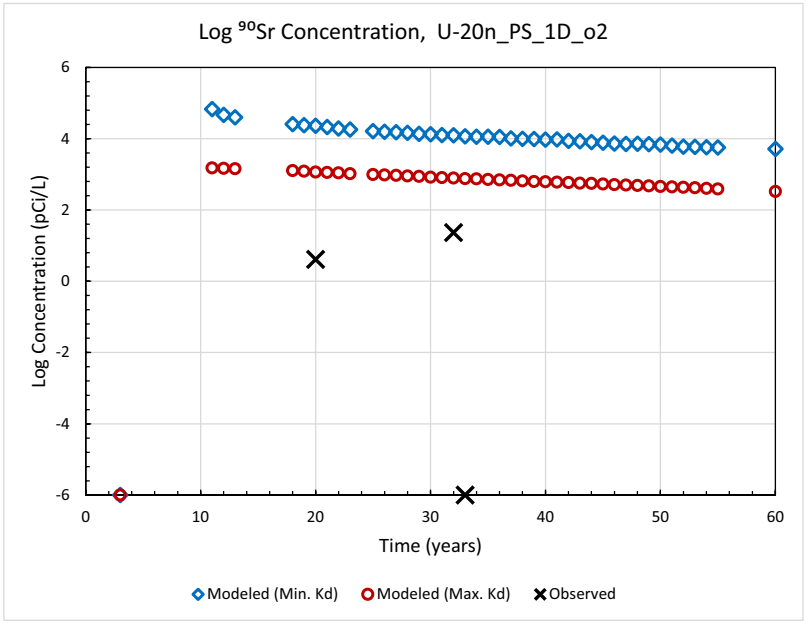

Figure H-97
Modeled and Measured ^{90}Sr Concentrations versus Time at U-20n_PS_1D_o2

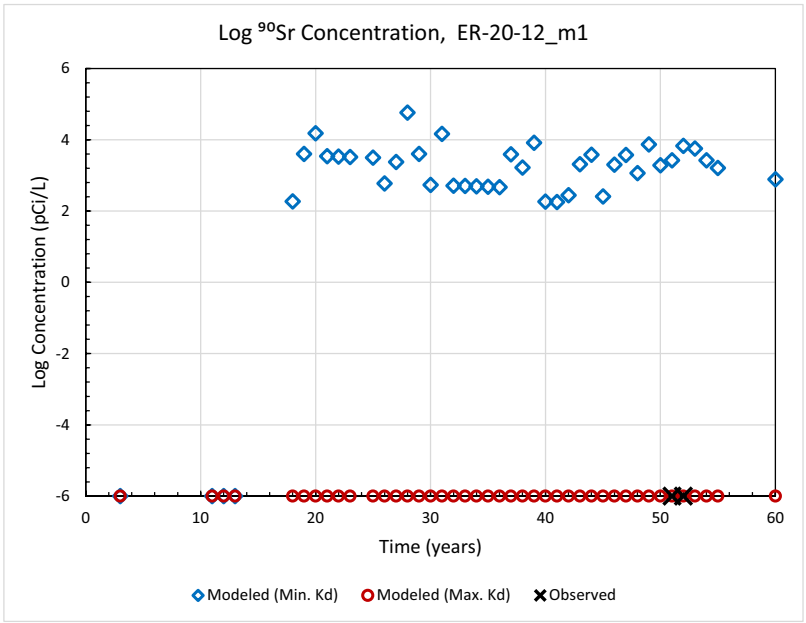

Figure H-98
Modeled and Measured ^{90}Sr Concentrations versus Time at ER-20-12_m1

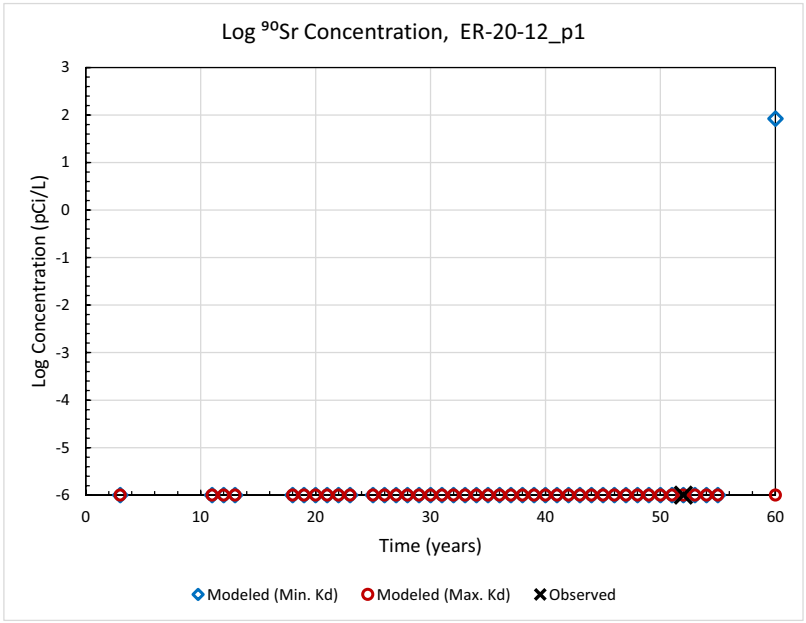

Figure H-99
Modeled and Measured ^{90}Sr Concentrations versus Time at ER-20-12_p1

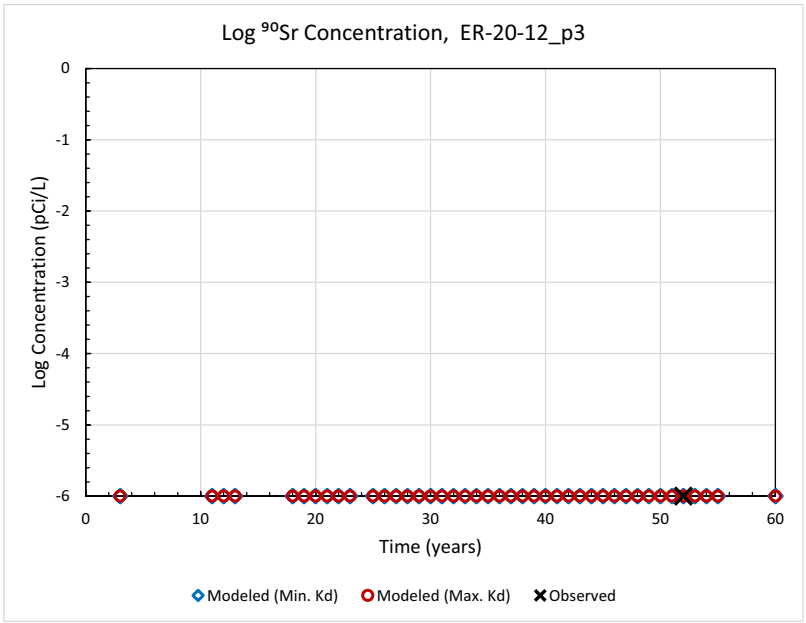

Figure H-100
Modeled and Measured ^{90}Sr Concentrations versus Time at ER-20-12_p3

H.1.5 Modeled and Measured ^{99}Tc Concentrations versus Time from Calibrated PM CAU Transport Model

Figures H-101 through H-119 present plots of modeled and measured ^{99}Tc concentrations versus time, over the first 60 years (encompassing all observation times), from the calibrated PM CAU transport model at locations with observed ^{99}Tc. The log of concentration is used to compare modeled and measured (observed) values. Zero values were approximated with a value of 1E-06, resulting in a log value of -6.

At the postshot locations, good agreement between measured and modeled values is achieved at U-19ad PS 1A (CHANCELLOR). The model overpredicts ^{99}Tc concentrations by 3 orders of magnitude at U-19q PS 1D (CAMEMBERT) and by 2 to 3 orders of magnitude at U-19v PS 1D (ALMENDRO). At CHESHIRE, fairly good agreement is achieved at U-20n PS 1D_o5Z, U-20n PS 1D_o2, and U-20n PS 1D_m2, with the model overpredicting ^{99}Tc concentrations by less than an order of magnitude. However, the model overpredicts at the remaining CHESHIRE locations by up to several orders of magnitude. These results suggest that ^{99}Tc source mass input to the PM CAU transport model at CHESHIRE may be conservatively high.

Near the Bench, good agreement is achieved at ER-20-11_m1. The model overpredicts ^{99}Tc concentrations at the other observation locations by up to several orders of magnitude. These results suggest that ^{99}Tc source mass input to the PM CAU transport model may be conservatively high at the sources that contribute RNs at these observation locations. The model predicts no ^{99}Tc at ER-20-5-3_m1. As discussed in Section 5.5.1.3, the poor agreement at ER-20-5-3_m1 is likely due to the deeper flow path from BENHAM passing to the east of the defined observation nodes.

Near HANDLEY, the model overpredicts ^{99}Tc concentrations at ER-20-12_m1 (in the PBRCM) and ER-20-12_p1 (in the BRA), although fairly good agreement is achieved for one observation at ER-20-12_p1. However, the model shows no ^{99}Tc at ER-20-12_p3 (in the CHLFA5). These results are somewhat consistent with the modeled ^{3}H concentrations at ER-20-12 (see Figure 5-32), except that modeled ^{3}H values at ER-20-12_m1 and ER-20-12_p1 were much closer to observed values. This suggests that ^{99}Tc source mass input to the PM CAU transport model at HANDLEY may be conservatively high.

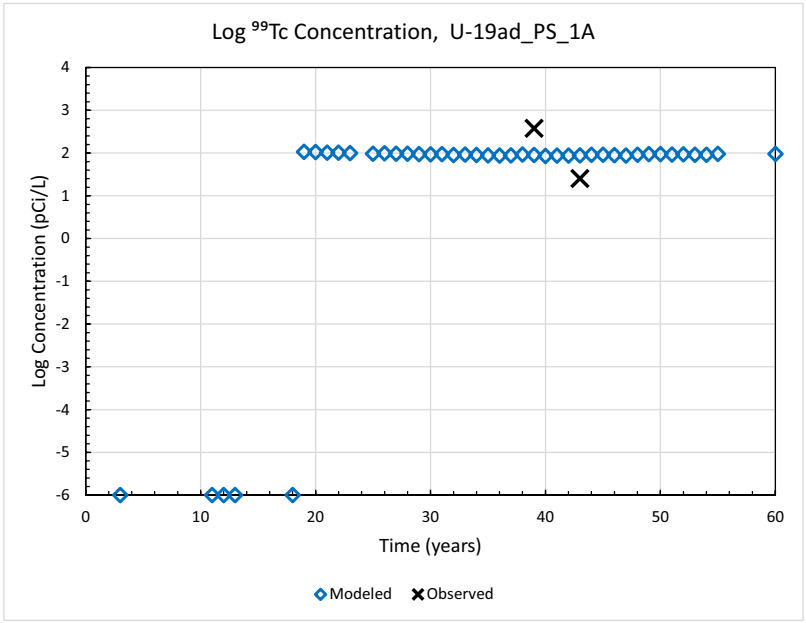

Figure H-101
Modeled and Measured ^{99}Tc Concentrations versus Time at U-19ad_PS_1A

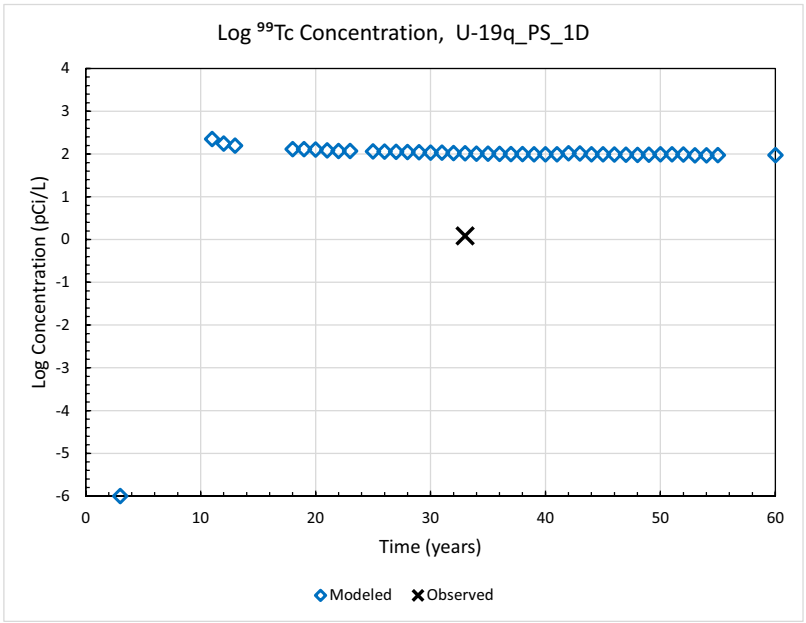

Figure H-102
Modeled and Measured ^{99}Tc Concentrations versus Time at U-19q_PS_1D

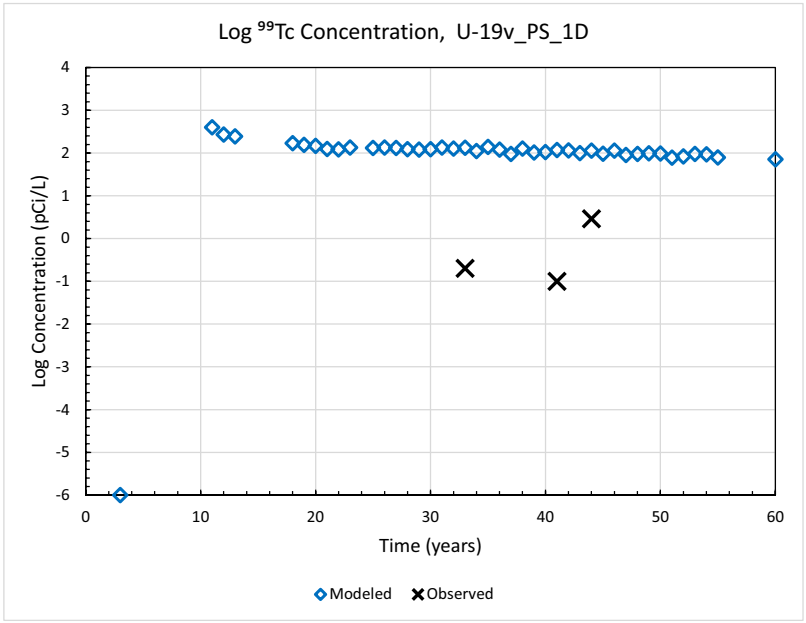

Figure H-103
Modeled and Measured ^{99}Tc Concentrations versus Time at U-19v_PS_1D

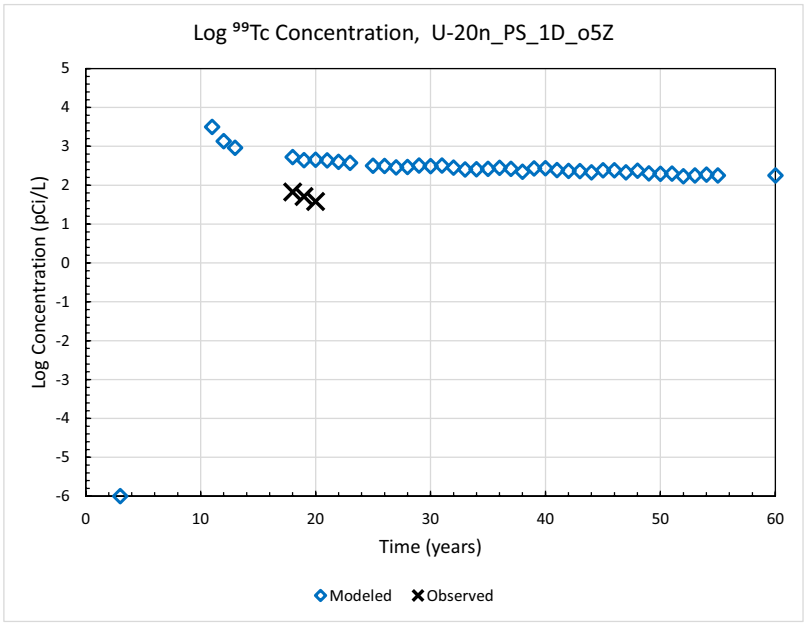

Figure H-104
Modeled and Measured ^{99}Tc Concentrations versus Time at U-20n_PS_1D_o5Z

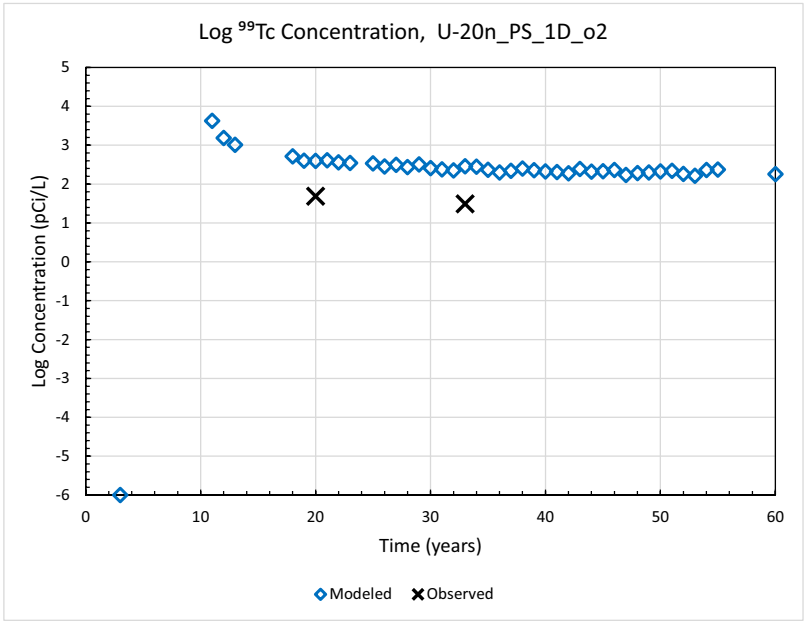

Figure H-105
Modeled and Measured ^{99}Tc Concentrations versus Time at U-20n_PS_1D_o2

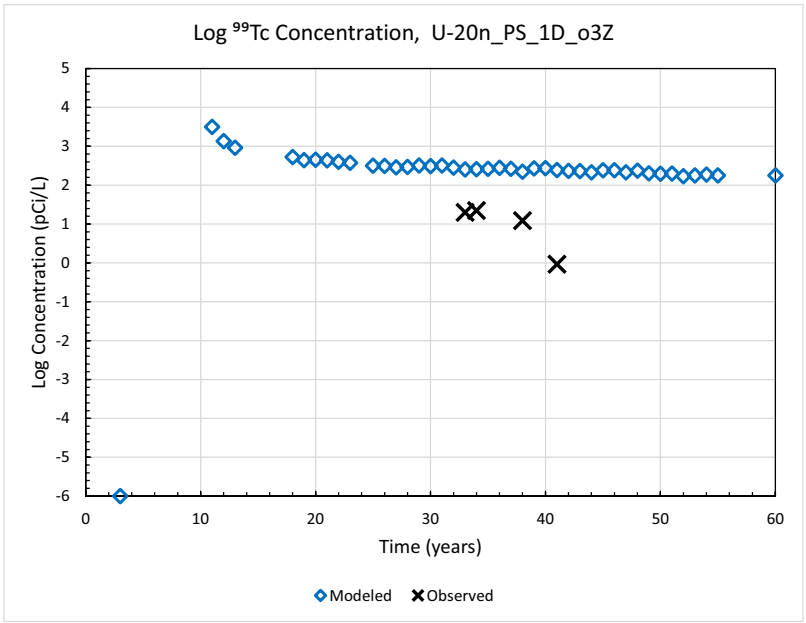

Figure H-106
Modeled and Measured ^{99}Tc Concentrations versus Time at U-20n_PS_1D_o3Z

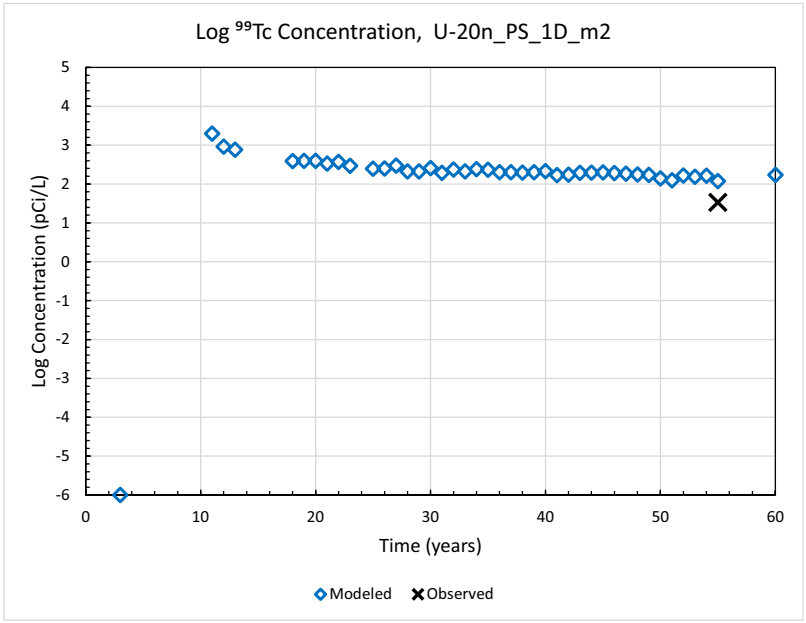

Figure H-107
Modeled and Measured ^{99}Tc Concentrations versus Time at U-20n_PS_1D_m2

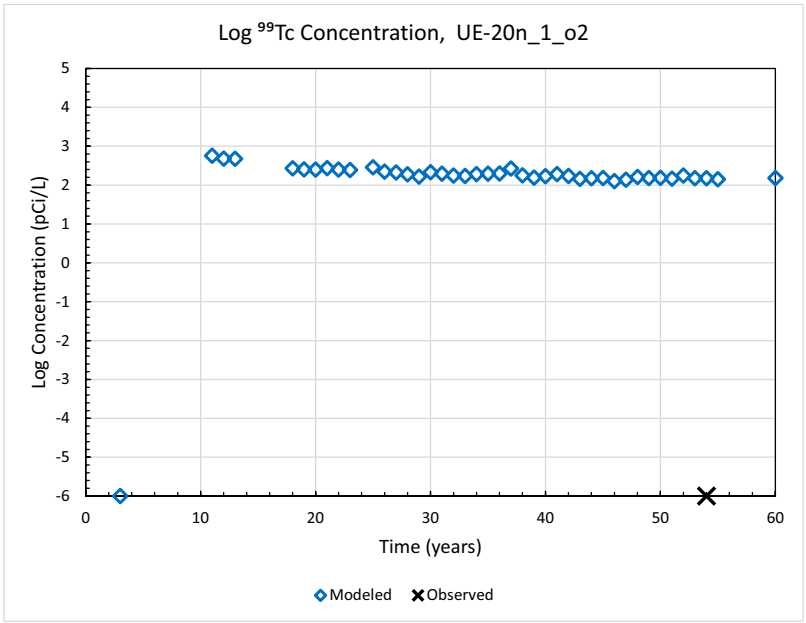

Figure H-108
Modeled and Measured ^{99}Tc Concentrations versus Time at UE-20n_1_o2

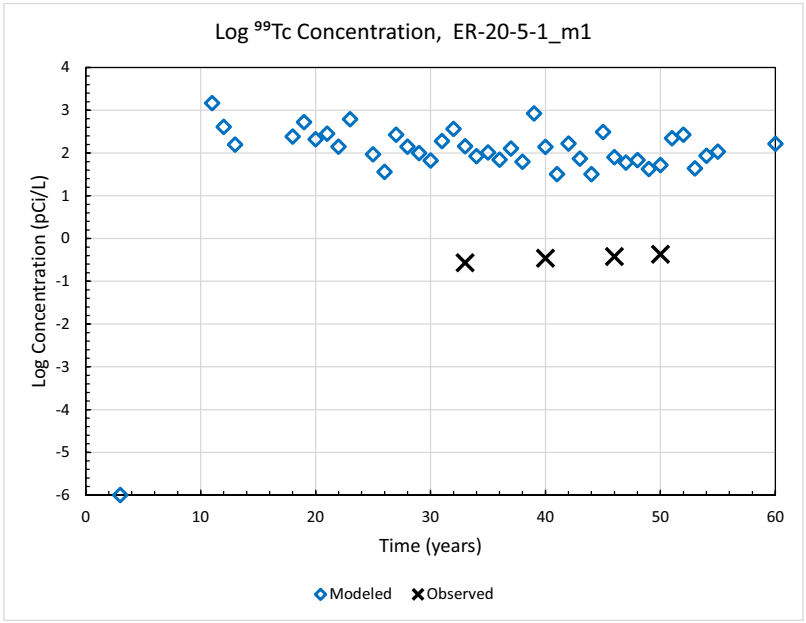

Figure H-109
Modeled and Measured ^{99}Tc Concentrations versus Time at ER-20-5-1_m1

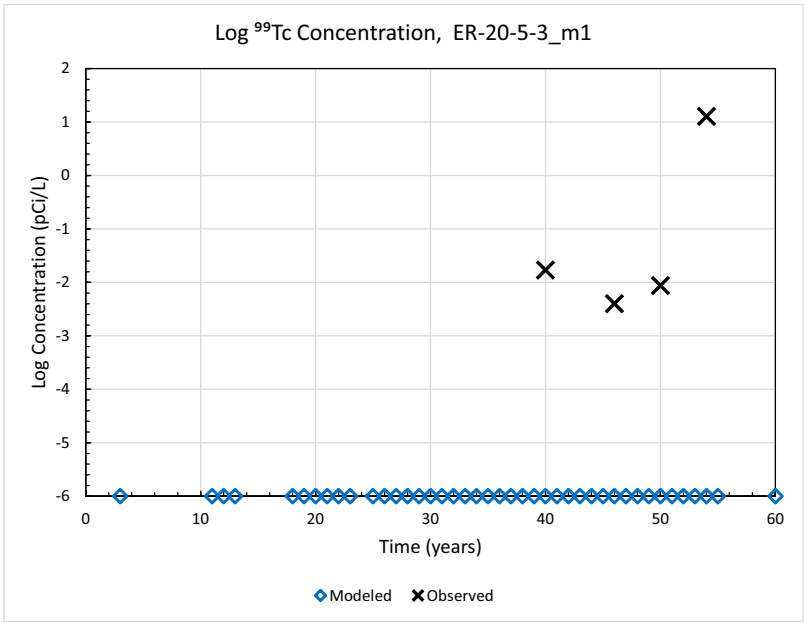

Figure H-110
Modeled and Measured ^{99}Tc Concentrations versus Time at ER-20-5-3_m1

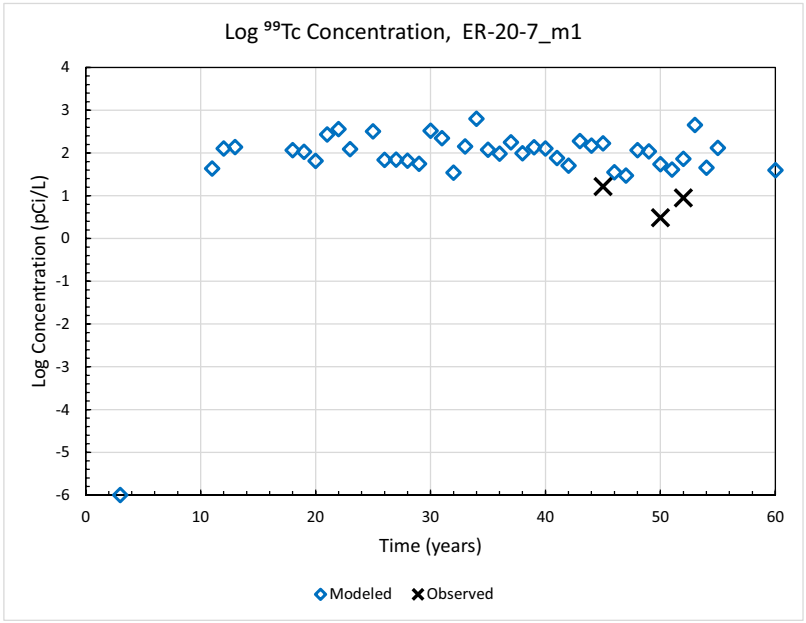

Figure H-111
Modeled and Measured ^{99}Tc Concentrations versus Time at ER-20-7_m1

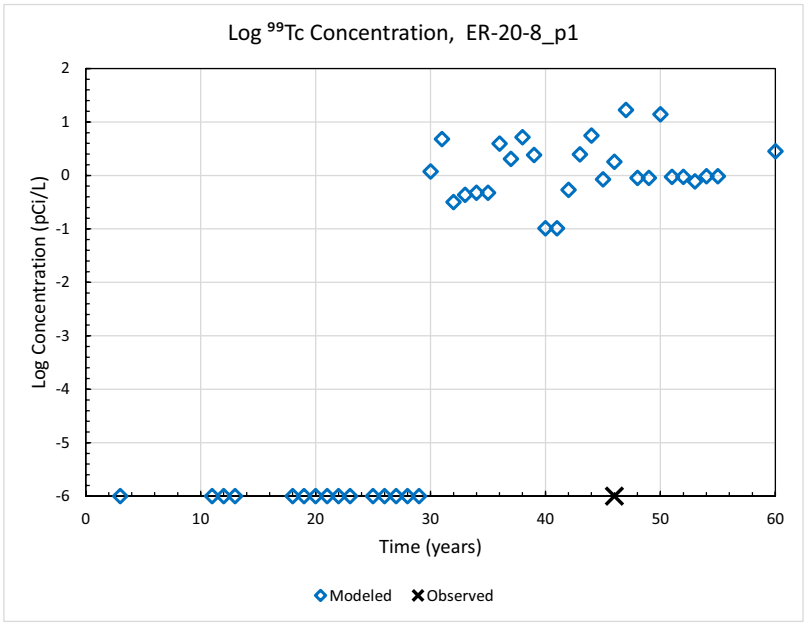

Figure H-112
Modeled and Measured ^{99}Tc Concentrations versus Time at ER-20-8_p1

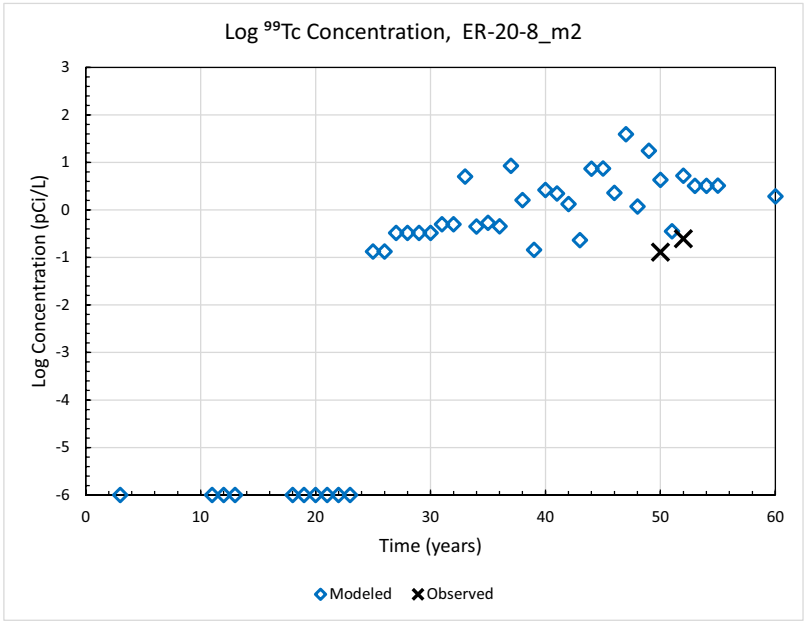

Figure H-113
Modeled and Measured ^{99}Tc Concentrations versus Time at ER-20-8_m2

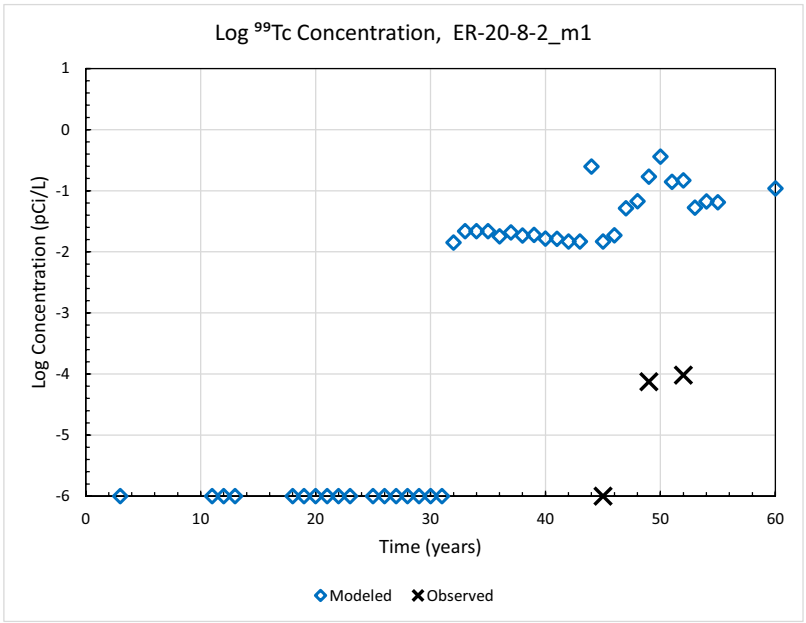

Figure H-114
Modeled and Measured ^{99}Tc Concentrations versus Time at ER-20-8-2_m1

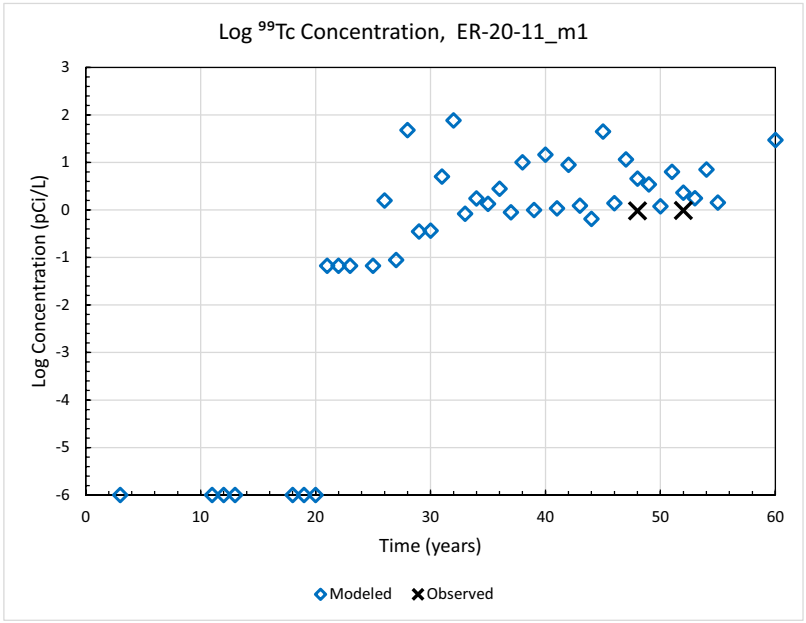

Figure H-115
Modeled and Measured ^{99}Tc Concentrations versus Time at ER-20-11_m1

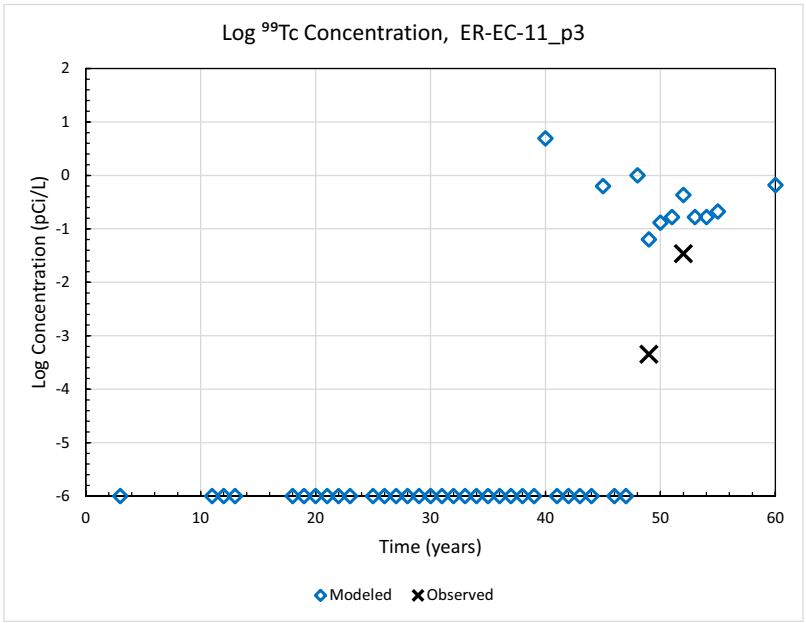

Figure H-116
Modeled and Measured ^{99}Tc Concentrations versus Time at ER-EC-11_p3

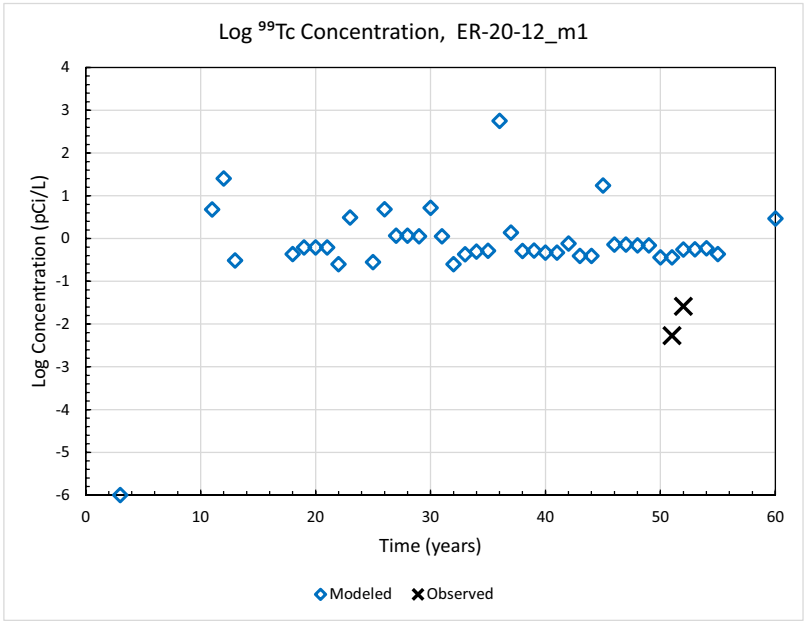

Figure H-117
Modeled and Measured ^{99}Tc Concentrations versus Time at ER-20-12_m1

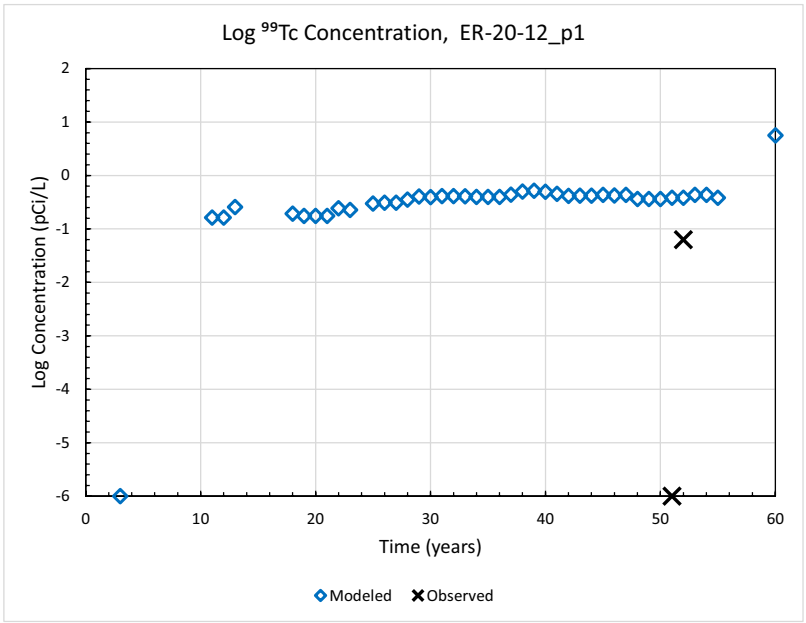

Figure H-118
Modeled and Measured ^{99}Tc Concentrations versus Time at ER-20-12_p1

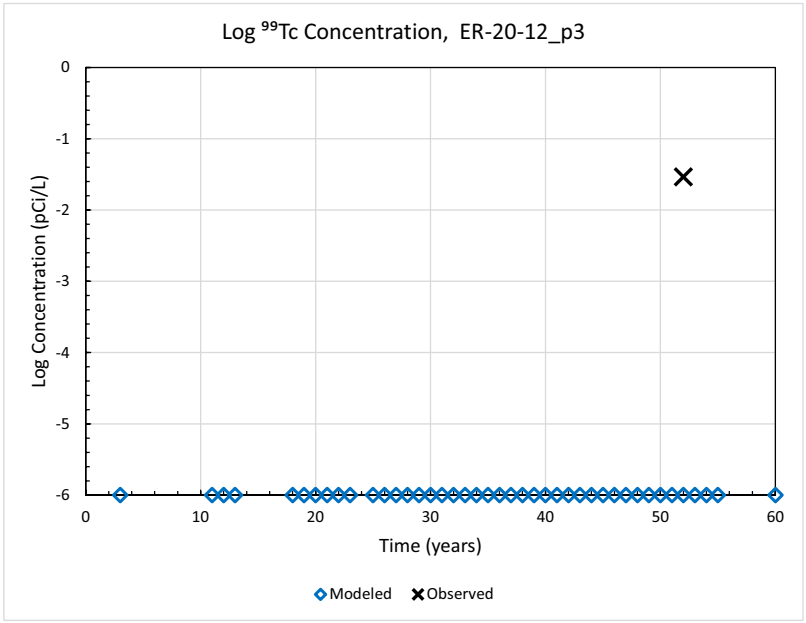

Figure H-119
Modeled and Measured ^{99}Tc Concentrations versus Time at ER-20-12_p3

H.1.6 Modeled and Measured ^{129}I Concentrations versus Time from Calibrated PM CAU Transport Model

Figures H-120 through H-137 present plots of modeled and measured ^{129}I concentrations versus time, over the first 60 years (encompassing all observation times), from the calibrated PM CAU transport model at locations with observed ^{129}I. The log of concentration is used to compare modeled and measured (observed) values. Zero values were approximated with a value of 1E-06, resulting in a log value of -6.

Good agreement between measured and modeled values is achieved at U-19ad PS 1A (CHANCELLOR) and U-19v PS 1D (ALMENDRO), with the model underpredicting ^{129}I concentrations by less than 1 order of magnitude at these locations. At U-20n PS 1D (CHESHIRE), the model overpredicts ^{129}I concentrations by approximately 1 order of magnitude. The observed values of ^{129}I at UE-20n_1 (CHESHIRE) is zero (or below detection limit), but the model calculates a concentration of 0.829 pCi/L (log value of -0.0814) at this location. The model also overpredicts ^{129}I concentrations at U-19q PS 1D (CAMEMBERT) by 2 to 3 orders of magnitude. These results suggest that ^{129}I source mass input to the PM CAU transport model at CHESHIRE and CAMEMBERT may be conservatively high.

Near the Bench, at ER-20-5-1 (in the TSA), ER-20-7 (in the TSA), ER-20-11 (in the BA), ER-EC-11_p3 (in the BA), and ER-20-8-2 (in the SPA) good agreement between measured and modeled values is achieved with the model overpredicting ^{129}I concentrations within 1 order of magnitude at these locations. At ER-20-8_p1 (in the CHZCM) and ER-20-8_m2 (in the TCA) the model overpredicts ^{129}I concentrations by 2 to 3 orders of magnitude. The model predicts no ^{129}I at ER-20-5-3_m1 (in the CHLFA5). As discussed in Section 5.5.1.3, the poor agreement at ER-20-5-3_m1 is likely due to the deeper flow path from BENHAM passing to the east of the defined observation nodes.

Near HANDLEY, the model overpredicts ^{129}I concentrations at ER-20-12_m1 (in the PBRCM) and ER-20-12_p1 (in the BRA) by approximately 2 orders of magnitude. However, the model shows no ^{129}I at ER-20-12_p3 (in the CHLFA5). These results are somewhat consistent with the modeled ^{3}H concentrations at ER-20-12 (see Figure 5-32), except that modeled ^{3}H values at ER-20-12_m1 and

ER-20-12_p1 were much closer to observed values. This suggests that ^{129}I source mass input to the PM CAU transport model at HANDLEY may be conservatively high.

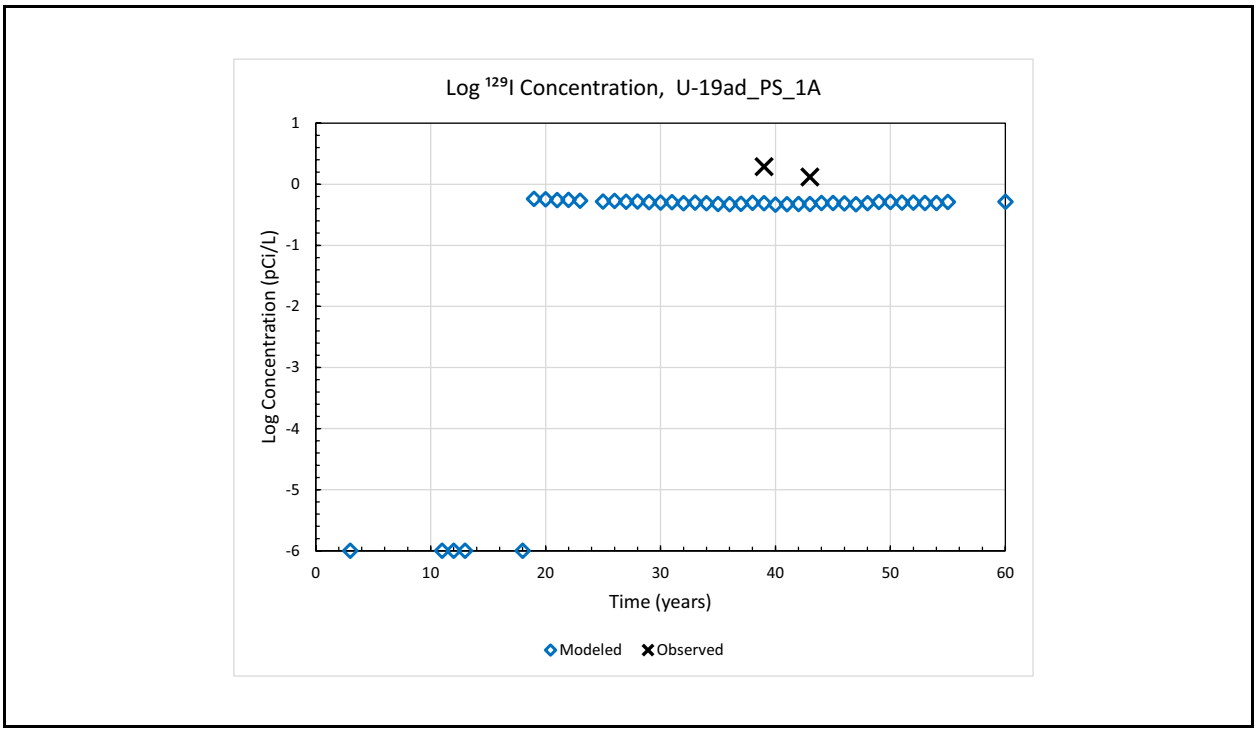

Figure H-120
Modeled and Measured ^{129}I Concentrations versus Time at U-19ad_PS_1A

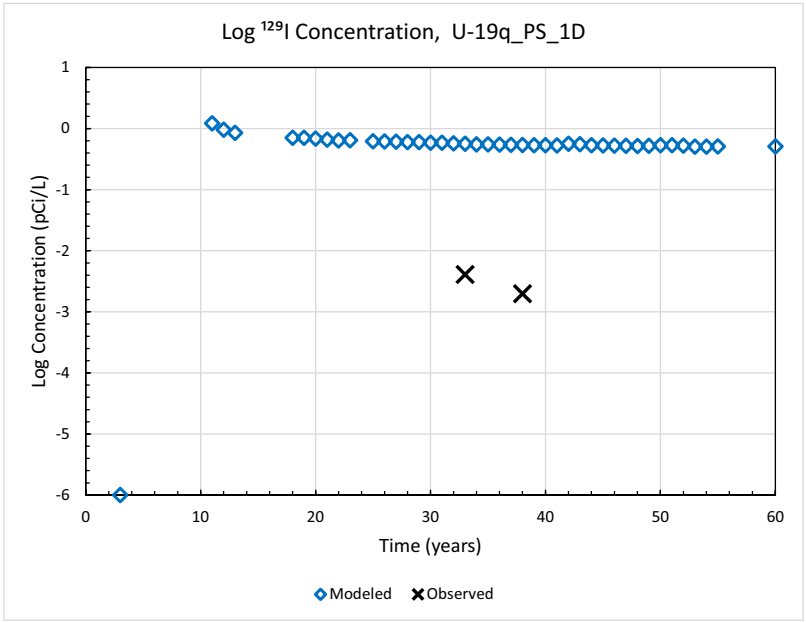

Figure H-121
Modeled and Measured ^{129}I Concentrations versus Time at U-19q_PS_1D

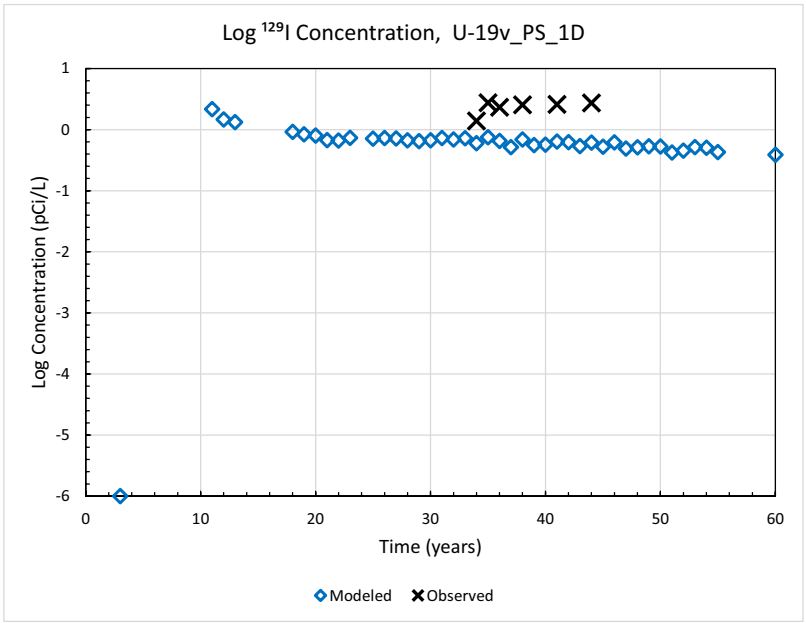

Figure H-122
Modeled and Measured ^{129}I Concentrations versus Time at U-19v_PS_1D

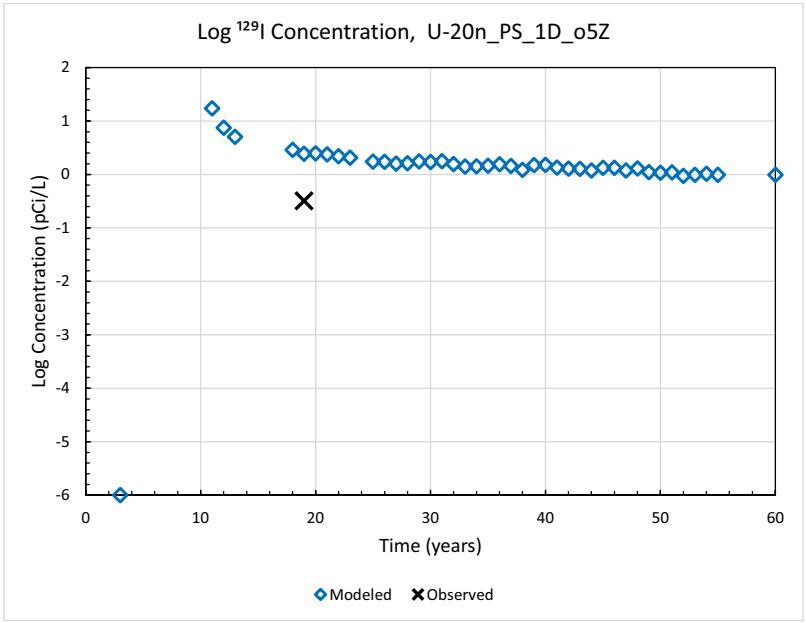

Figure H-123
Modeled and Measured ^{129}I Concentrations versus Time at U-20n_PS_1D_o5Z

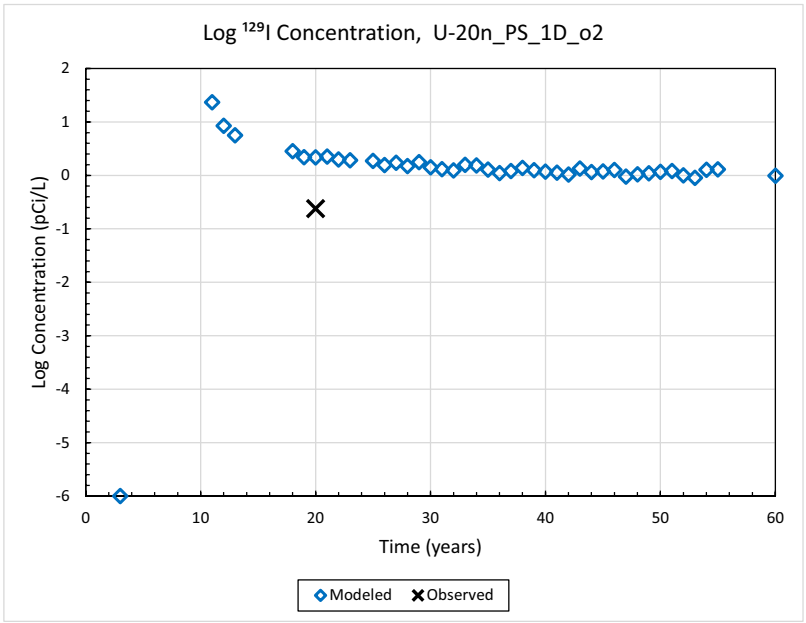

Figure H-124
Modeled and Measured ^{129}I Concentrations versus Time at U-20n_PS_1D_o2

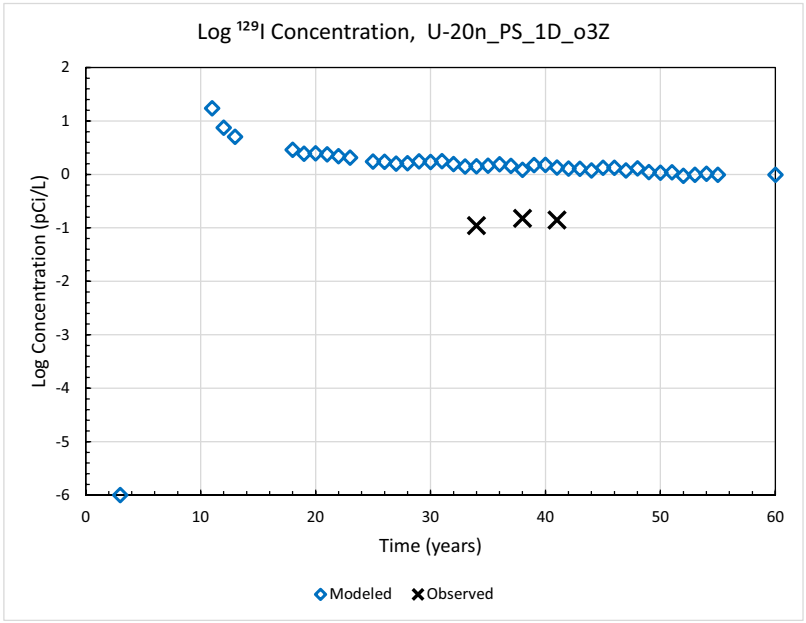

Figure H-125
Modeled and Measured ^{129}I Concentrations versus Time at U-20n_PS_1D_o3Z

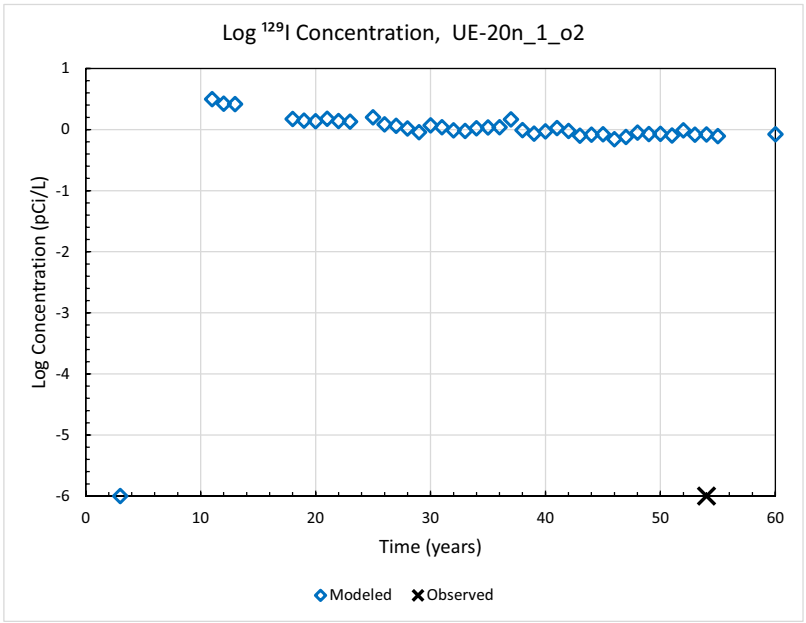

Figure H-126
Modeled and Measured ^{129}I Concentrations versus Time at UE-20n_1_o2

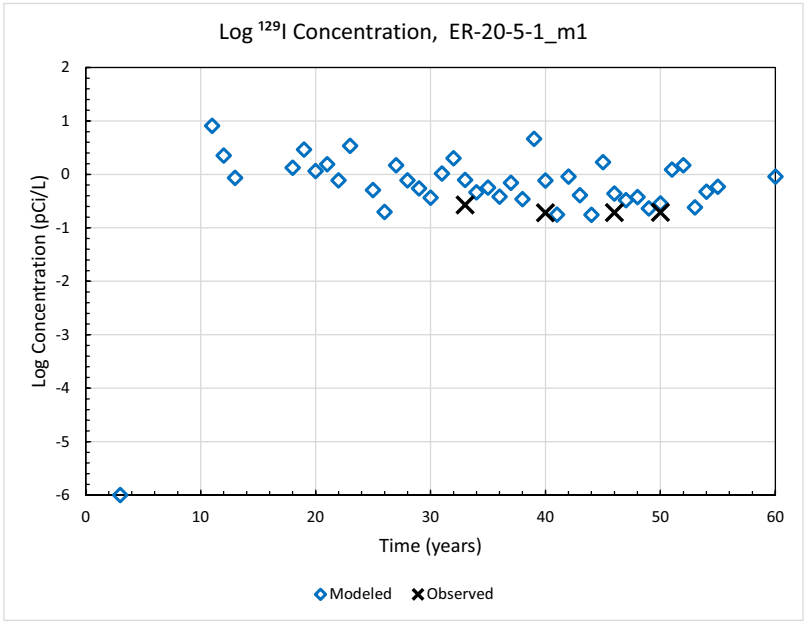

Figure H-127
Modeled and Measured ^{129}I Concentrations versus Time at ER-20-5-1_m1

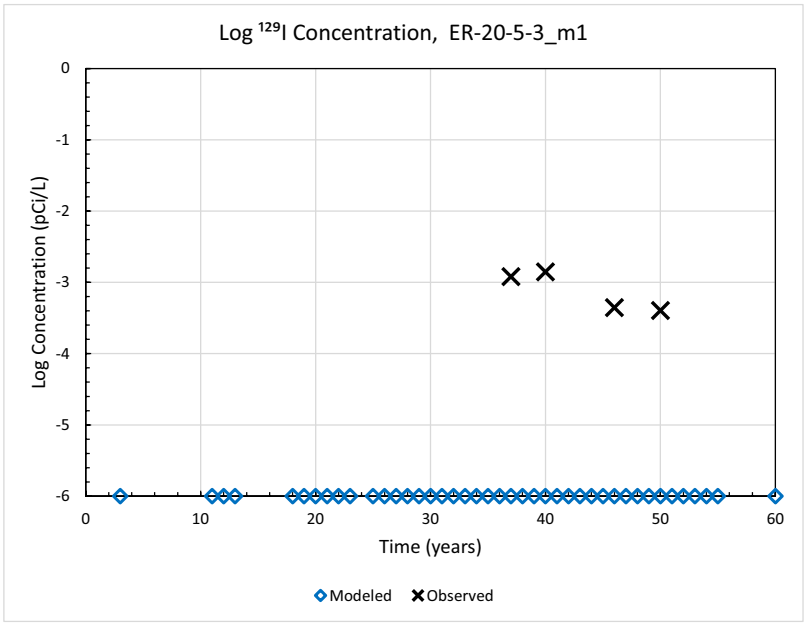

Figure H-128
Modeled and Measured ^{129}I Concentrations versus Time at ER-20-5-3_m1

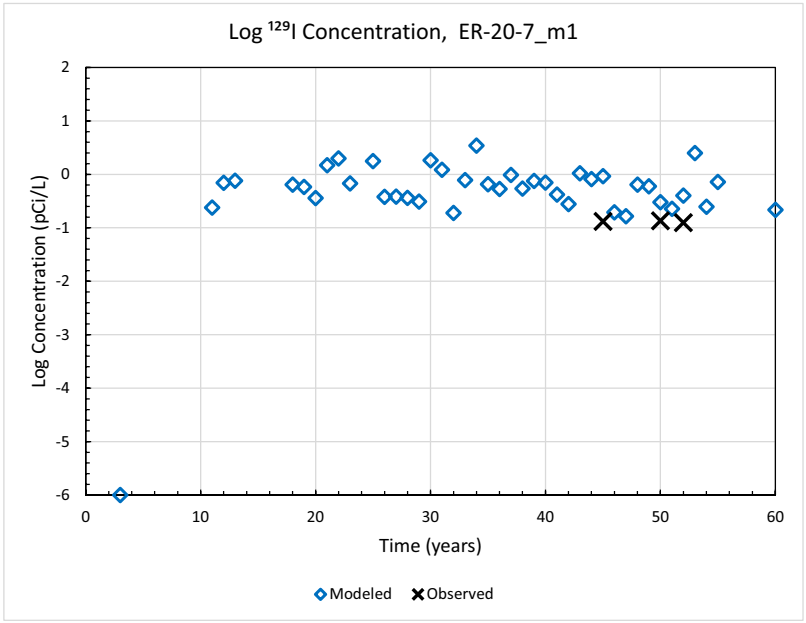

Figure H-129
Modeled and Measured ^{129}I Concentrations versus Time at ER-20-7_m1

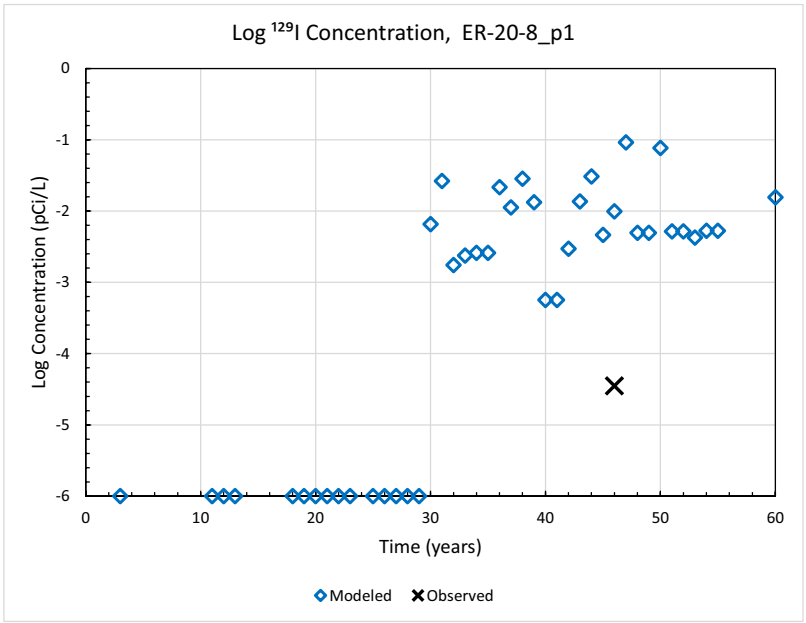

Figure H-130
Modeled and Measured ^{129}I Concentrations versus Time at ER-20-8_p1

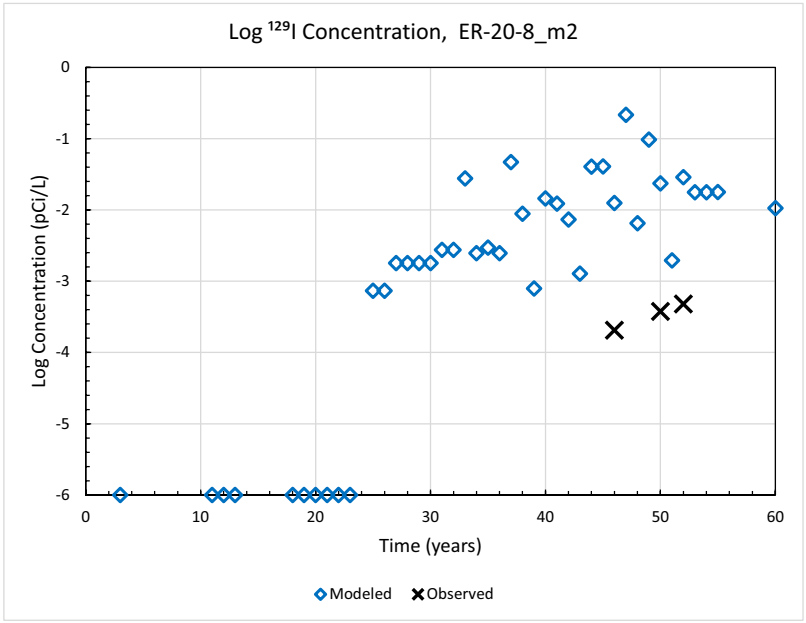

Figure H-131
Modeled and Measured ^{129}I Concentrations versus Time at ER-20-8_m2

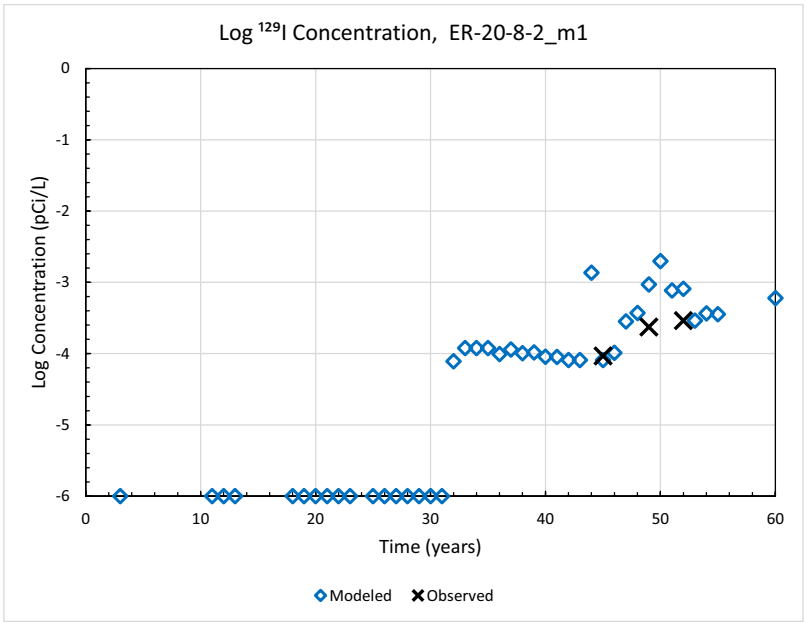

Figure H-132
Modeled and Measured ^{129}I Concentrations versus Time at ER-20-8-2_m1

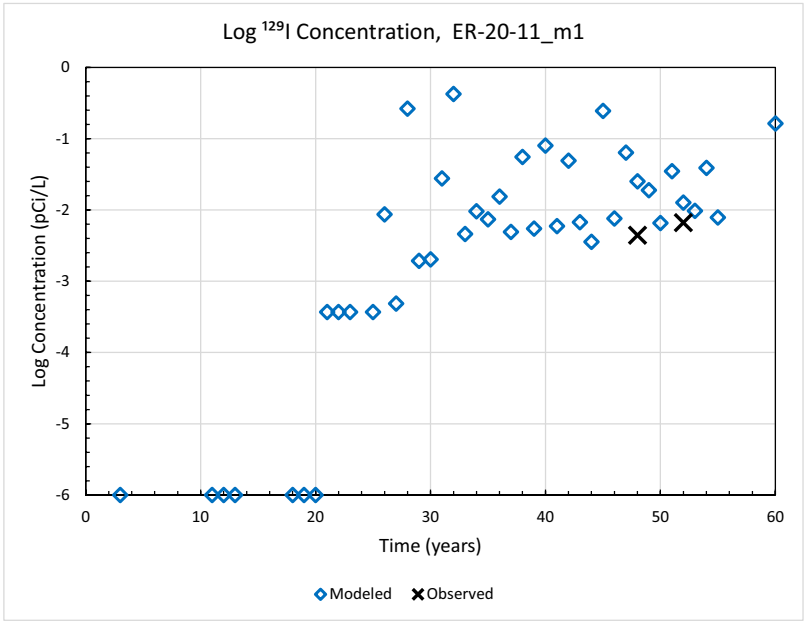

Figure H-133
Modeled and Measured ^{129}I Concentrations versus Time at ER-20-11_m1

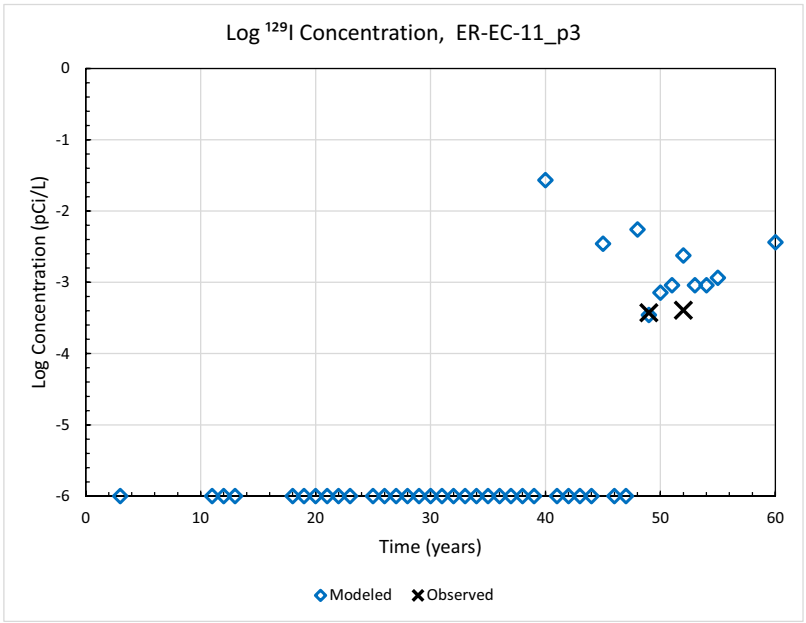

Figure H-134
Modeled and Measured ^{129}I Concentrations versus Time at ER-EC-11_p3

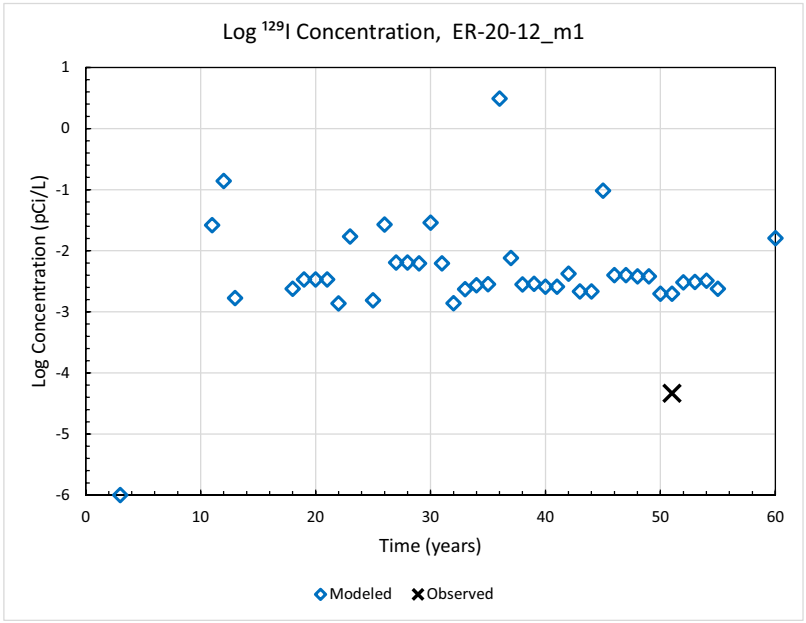

Figure H-135
Modeled and Measured ^{129}I Concentrations versus Time at ER-20-12_m1

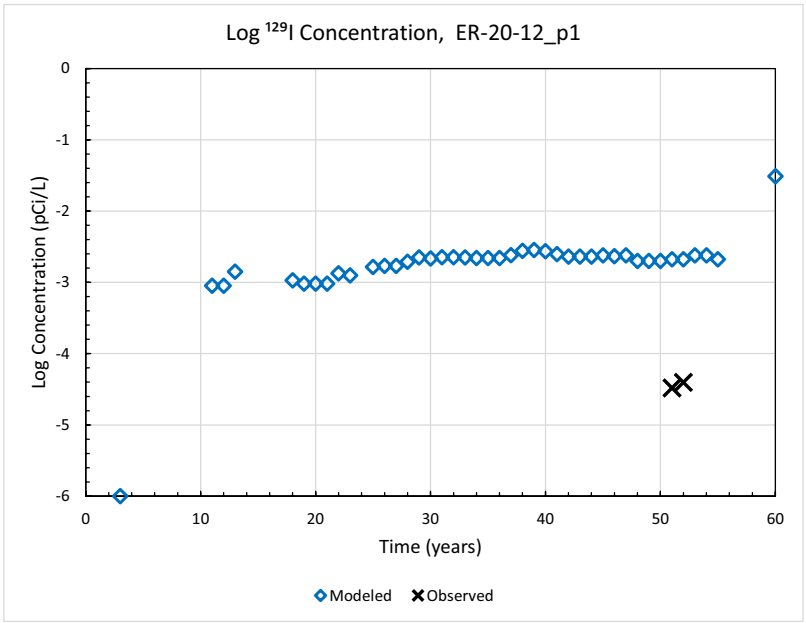

Figure H-136
Modeled and Measured ^{129}I Concentrations versus Time at ER-20-12_p1

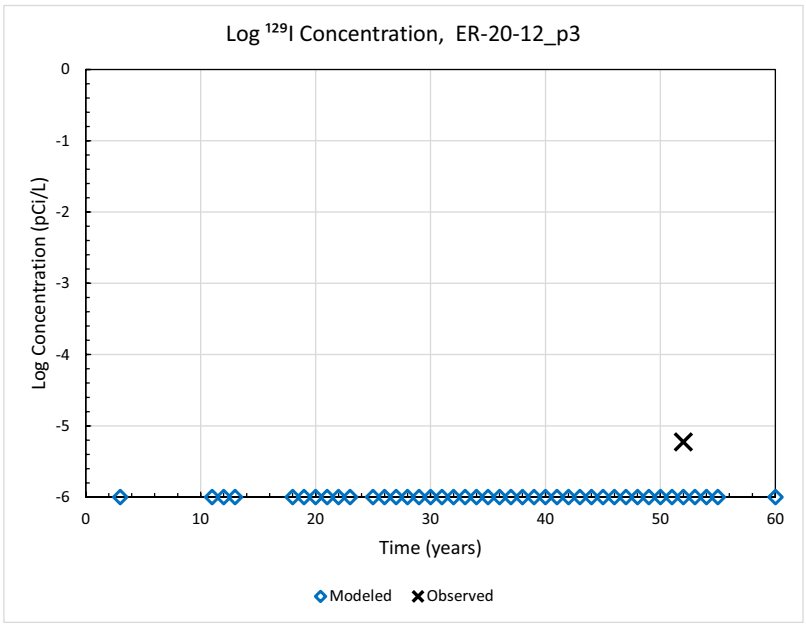

Figure H-137
Modeled and Measured ^{129}I Concentrations versus Time at ER-20-12_p3

H.1.7 Modeled and Measured ^{137}Cs Concentrations versus Time from Calibrated PM CAU Transport Model

Figures H-138 through H-146 present plots of modeled and measured ^{137}Cs concentrations versus time, over the first 60 years (encompassing all observation times), from the calibrated PM CAU transport model at locations with observed ^{137}Cs. The log of concentration is used to compare modeled and measured (observed) values. Zero values were approximated with a value of 1E-06, resulting in a log value of -6. Modeled concentrations are displayed for two cases: one using minimum K_d for all zones (blue diamonds) and one using maximum K_d for all zones (red circles). As expected, higher concentrations are observed for the case with minimum K_d.

There is good agreement at U-19q PS 1D (CAMEMBERT) where the observed ^{137}Cs concentrations are bracketed by the range of modeled ^{137}Cs concentrations. Modeled results at CHESHIRE (U-20n PS 1D and UE-20n_1) are varied. There is good agreement at U-20n PS 1D_o5Z and U-20n PS 1D_o3Z where the observed ^{137}Cs concentrations are bracketed by the range of modeled ^{137}Cs concentrations. There is also fairly good agreement at U-20n PS 1D_m2, where the range of modeled ^{137}Cs concentrations is less than observed value by approximately an order of magnitude. At U-20n PS 1D_o2, 5 of the 11 observations are bracketed by the range of modeled ^{137}Cs concentrations, and the remaining observations are overpredicted by 2 to 3 orders of magnitude. At UE-20n_1 (CHESHIRE) only one observation is bracketed by the range of modeled ^{137}Cs concentrations, with the remaining observations being underpredicted by the range of modeled ^{137}Cs concentrations.

Near the Bench, the model overpredicts ^{137}Cs concentrations at ER-20-5-1(in the TSA) by 2 to 3 orders of magnitude. The model predicts no ^{137}Cs at ER-20-5-3_m1 (in the CHLFA5). As discussed in Section 5.5.1.3, the poor agreement at ER-20-5-3_m1 is likely due to the deeper flow path from BENHAM passing to the east of the defined observation nodes.

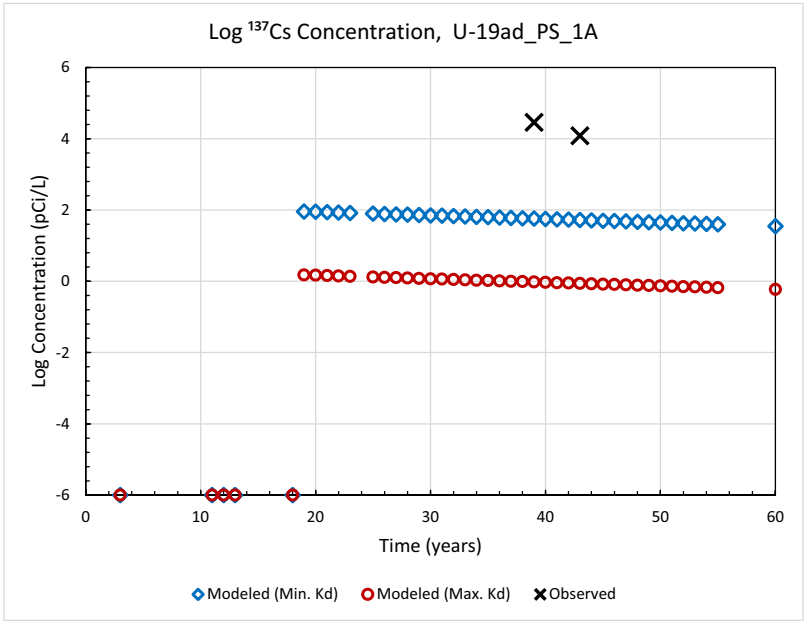

Figure H-138
Modeled and Measured ^{137}Cs Concentrations versus Time at U-19ad_PS_1A

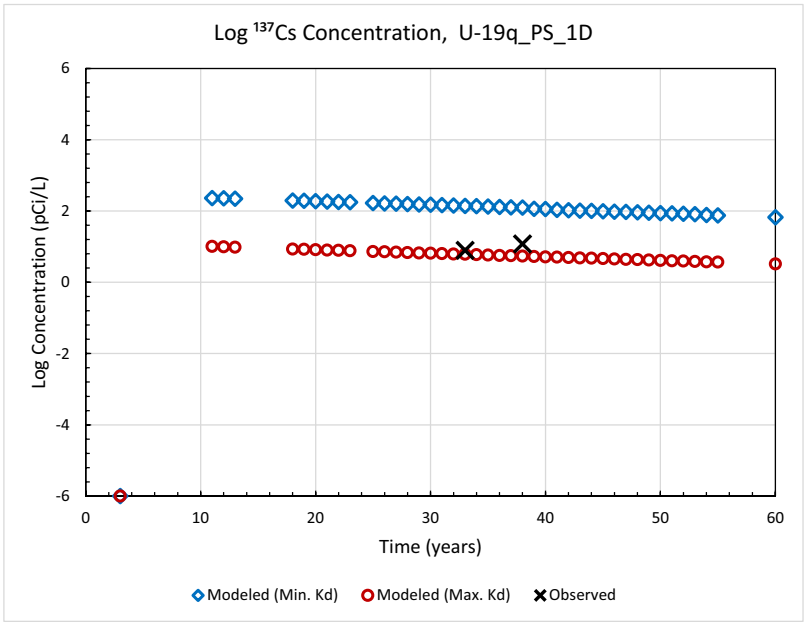

Figure H-139
Modeled and Measured ^{137}Cs Concentrations versus Time at U-19q_PS_1D

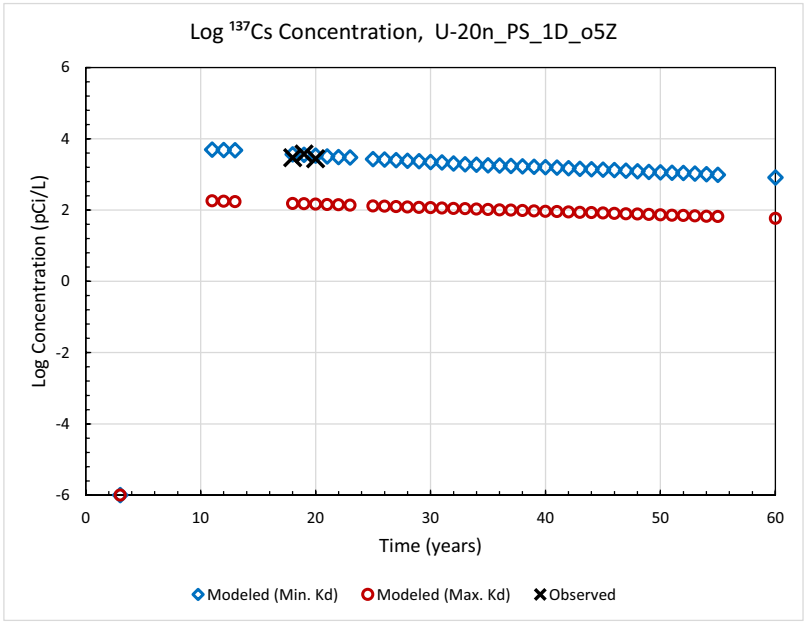

Figure H-140
Modeled and Measured ^{137}Cs Concentrations versus Time at U-20n_PS_1D_o5Z

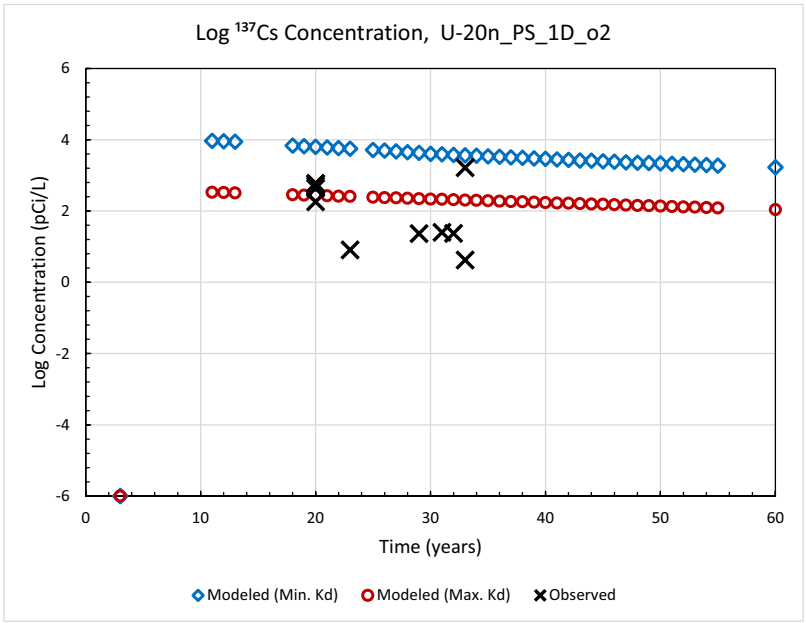

Figure H-141
Modeled and Measured ^{137}Cs Concentrations versus Time at U-20n_PS_1D_o2

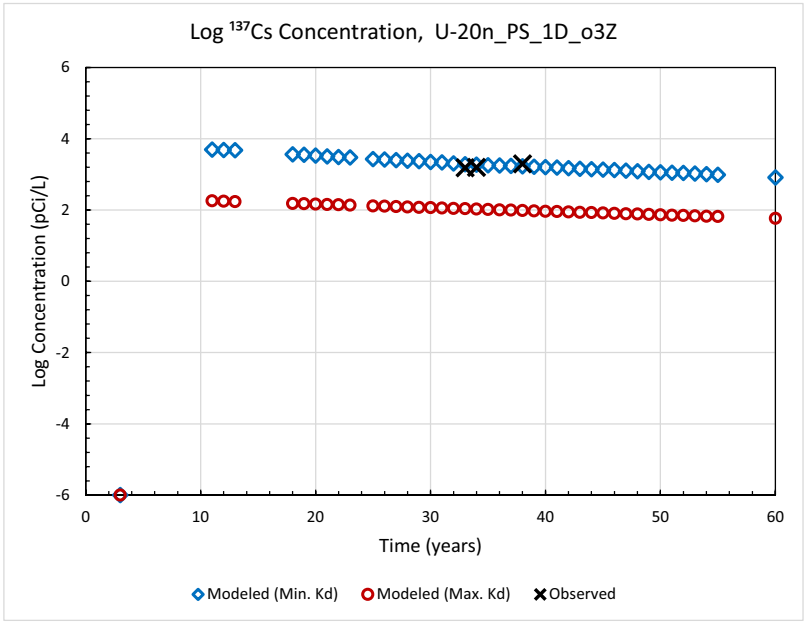

Figure H-142
Modeled and Measured ^{137}Cs Concentrations versus Time at U-20n_PS_1D_o3Z

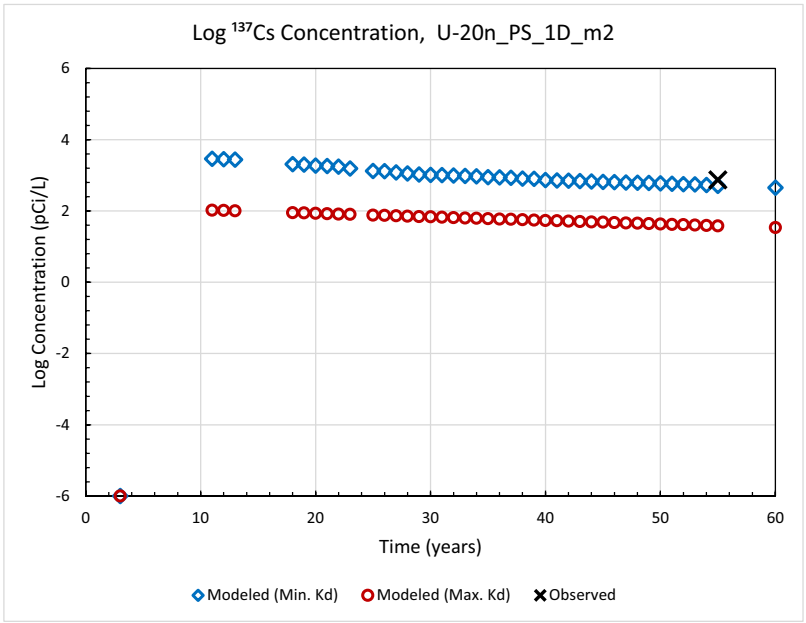

Figure H-143
Modeled and Measured ^{137}Cs Concentrations versus Time at U-20n_PS_1D_m2

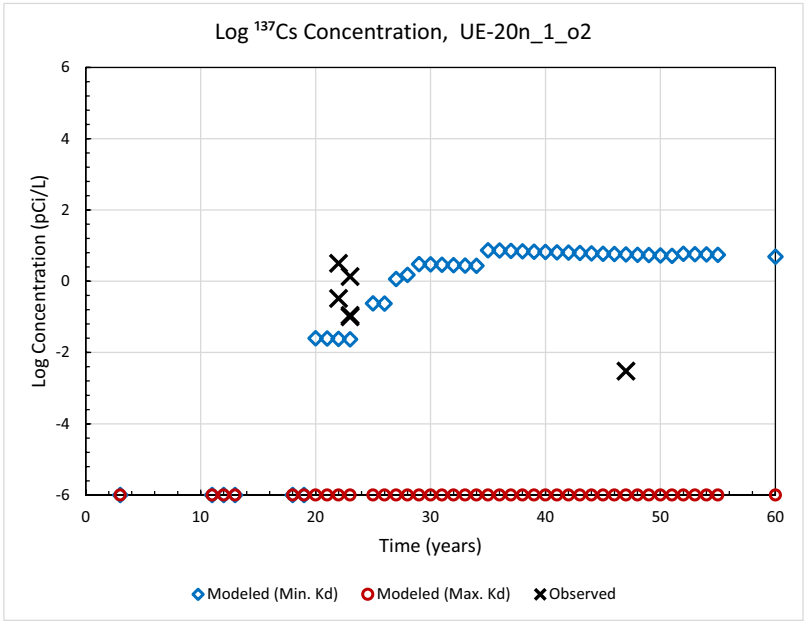

Figure H-144
Modeled and Measured ^{137}Cs Concentrations versus Time at UE-20n_1_o2

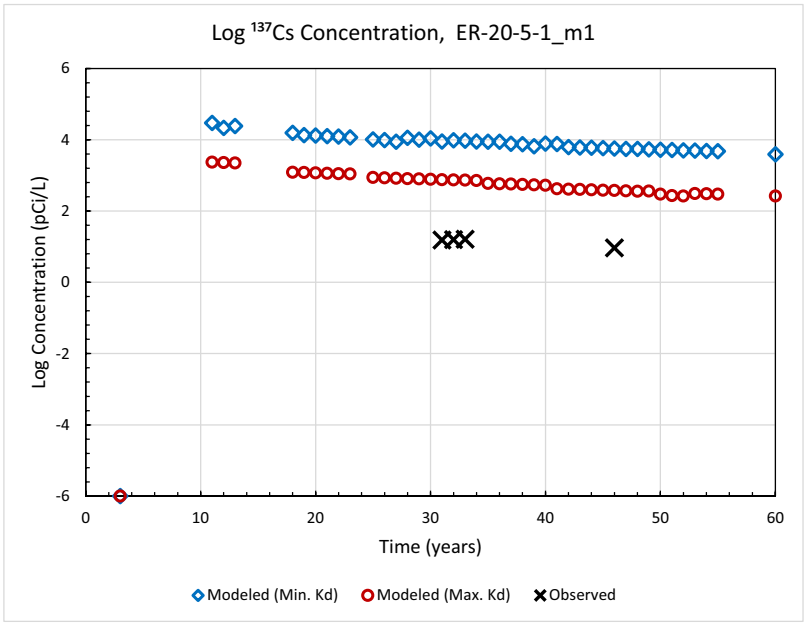

Figure H-145
Modeled and Measured ^{137}Cs Concentrations versus Time at ER-20-5-1_m1

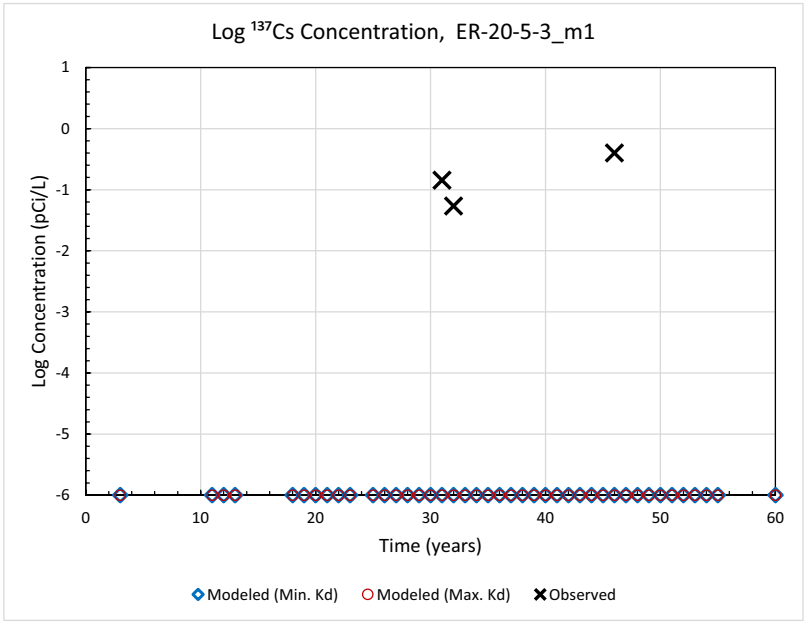

Figure H-146
Modeled and Measured ^{137}Cs Concentrations versus Time at ER-20-5-3_m1

H.1.8 Modeled and Measured U (Total) Concentrations versus Time from Calibrated PM CAU Transport Model

Figures H-147 through H-165 present plots of modeled and measured U (total) concentrations versus time, over the first 60 years (encompassing all observation times), from the calibrated PM CAU transport model at locations with observed U. The log of concentration is used to compare modeled and measured (observed) values. Zero values were approximated with a value of 1E-06, resulting in a log value of -6. Observations of U are reported as total U; thus forward runs of ^{232}U, ^{233}U, ^{234}U, and ^{238}U were made independently, and the resulting concentrations were summed for comparison to observed values. Modeled concentrations are displayed for two cases: one using minimum K_d for all zones (blue diamonds) and one using maximum K_d for all zones (red circles). As expected, higher concentrations are observed for the case with minimum K_d, except at ER-20-12_m1 where the opposite is observed.

There is good agreement at U-19q PS 1D (CAMEMBERT) where the observed U (total) concentrations are bracketed by the range of modeled U (total) concentrations. At CHESHIRE, there is good agreement at UE-20n_1and U-20n PS 1D_m2, where the observed U (total) concentrations are bracketed by the range of modeled U (total) concentrations. There is fairly good agreement at U-20n PS 1D_o2 and U-20n PS 1D_o3Z, where the range of modeled U (total) concentrations overpredicts observed U (total) concentrations by up to 2 orders of magnitude. The most recent observation at U-20n PS 1D_o2 shows no U (or below detection limit) where the modeled concentration ranges from 2.51 µg/L to 19.1 µg/L (0.399 to 1.28 in log space). At most of the observations at U-19v PS 1D (ALMENDRO) the model overpredicts by up to 3 orders of magnitude. The earliest observations at U-19v PS 1D show no U (or below detection limit) where the modeled concentration ranges from 2.14 µg/L to 14.0 µg/L (0.33 to 1.15 in log space). At U-19ad PS 1A (CHANCELLOR) the model underpredicts by up to 2 orders of magnitude.

Near the Bench, at ER-20-5-1 (in the TSA) and ER-20-7 (in the TSA), good agreement between measured and modeled U (total) concentrations is achieved with the ranges of modeled concentrations bracketing observations on the higher sides of the ranges. The model predicts no U at ER-20-5-3_m1 (in the CHLFA5). As discussed in Section 5.5.1.3, the poor agreement at ER-20-5-3_m1 is likely due to the deeper flow path from BENHAM passing to the east of the defined observation nodes. At locations further downgradient, ER-20-8_p1 (in the CHZCM),

ER-20-8_m2 (in the TCA), ER-20-8-2 (in the SPA), ER-20-11 (in the BA), and ER-EC-11_p3 (in the BA), the model generally underpredicts U (total) concentrations by up to several orders of magnitude.

Near HANDLEY, the model underpredicts U (total) concentrations at ER-20-12_m1 (in the PBRCM) and ER-20-12_p1 (in the BRA) by 2 to 3 orders of magnitude. There is poor agreement at ER-20-12_p3 (in the CHLFA5), where the model shows no U although it has been observed. The poor agreement at ER-20-12_p3 is similar to poor agreement with ^{3}H results.

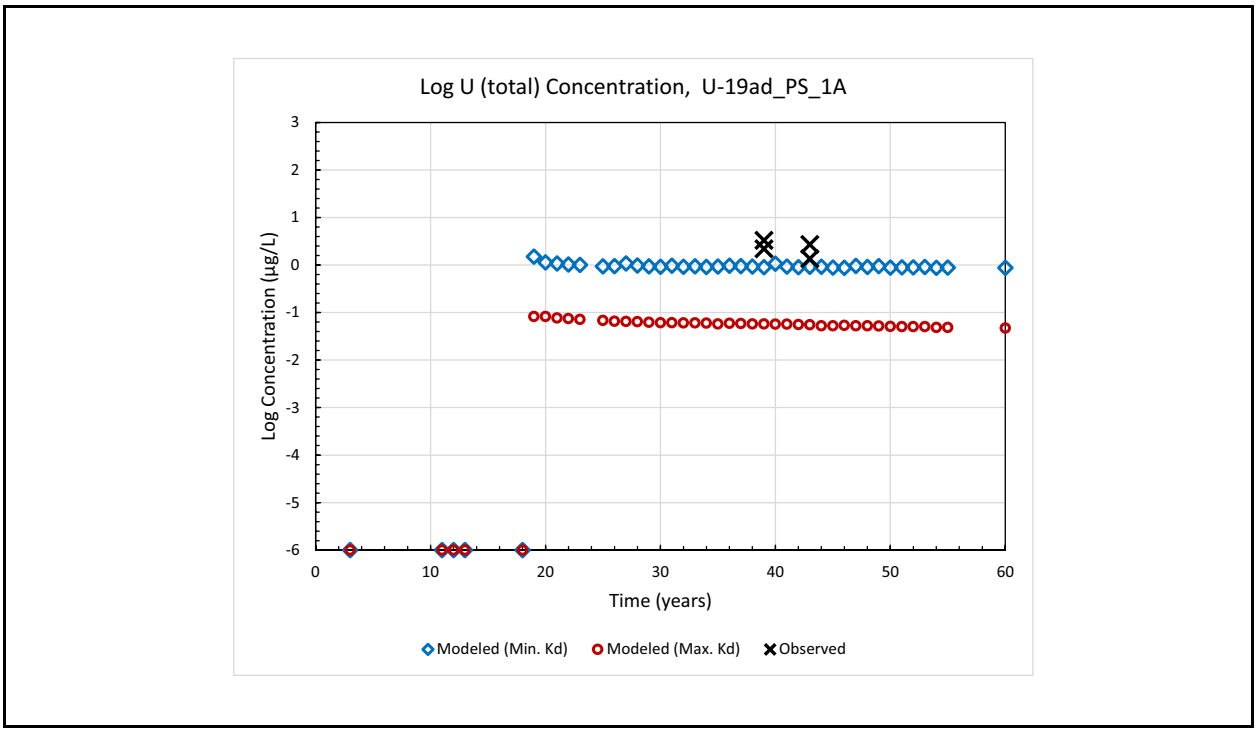

Figure H-147
Modeled and Measured U (Total) Concentrations versus Time at U-19ad_PS_1A

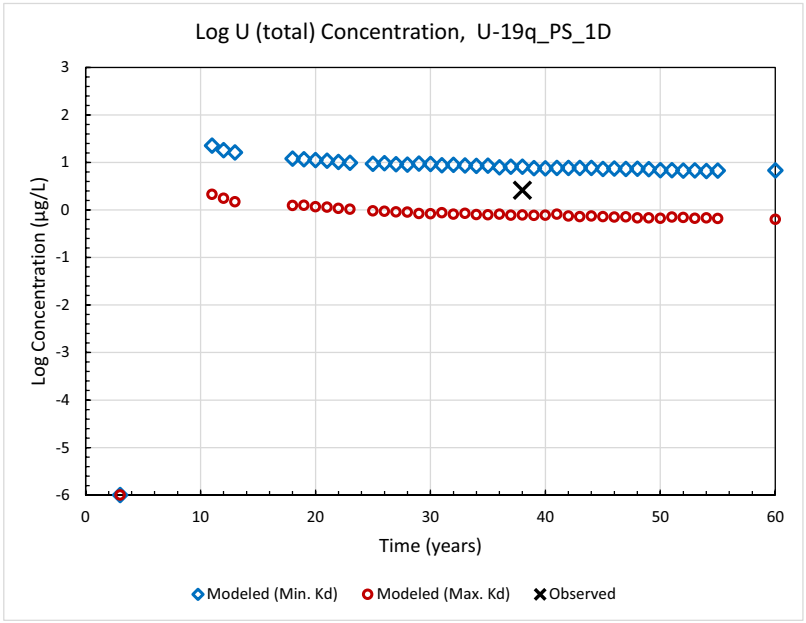

Figure H-148
Modeled and Measured U (Total) Concentrations versus Time at U-19q_PS_1D

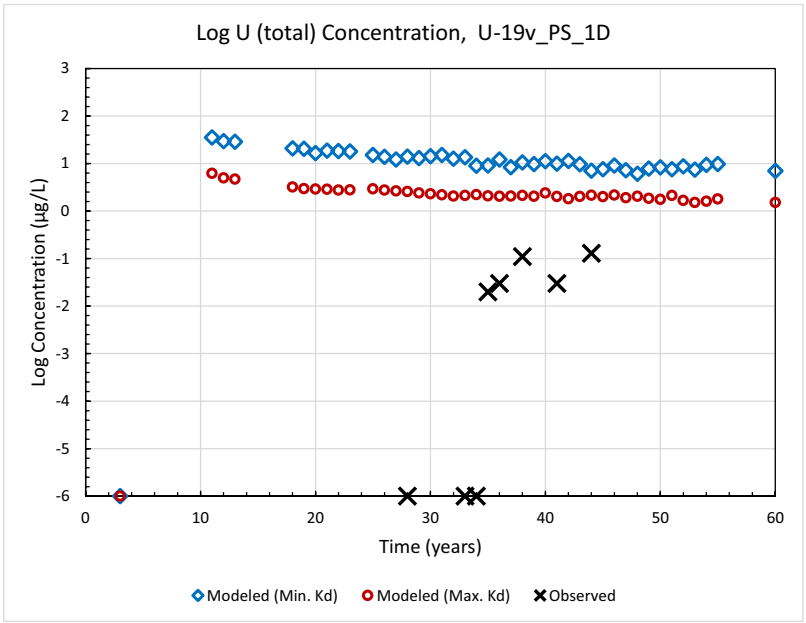

Figure H-149
Modeled and Measured U (Total) Concentrations versus Time at U-19v_PS_1D

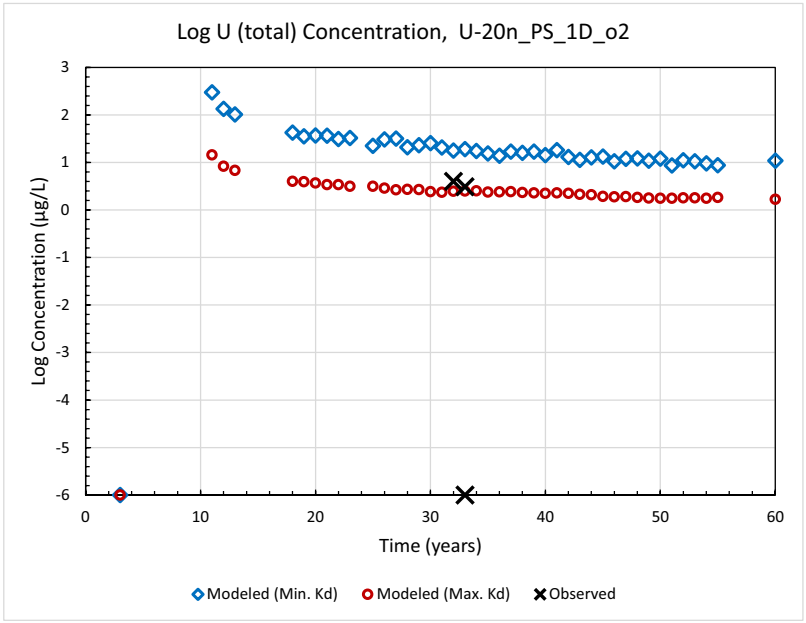

Figure H-150
Modeled and Measured U (Total) Concentrations versus Time at U-20n_PS_1D_o2

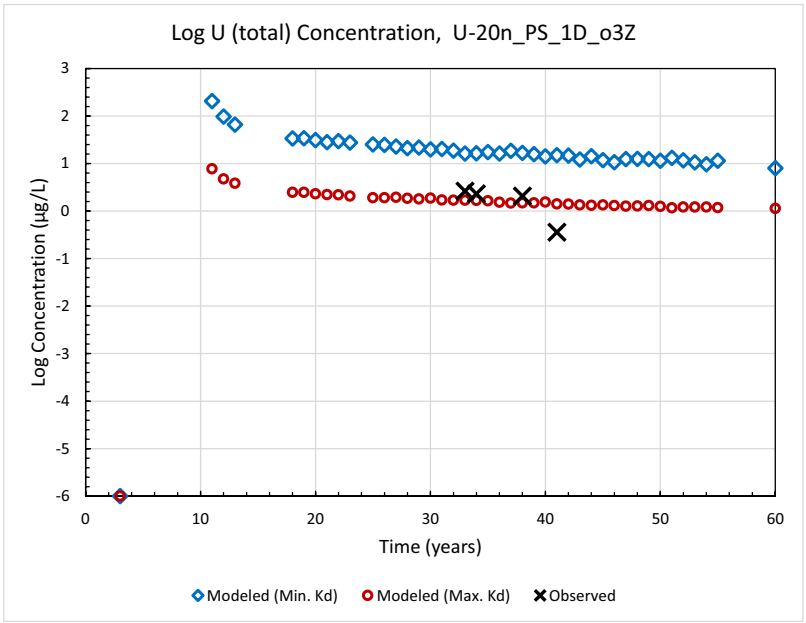

Figure H-151
Modeled and Measured U (Total) Concentrations versus Time at U-20n_PS_1D_o3Z

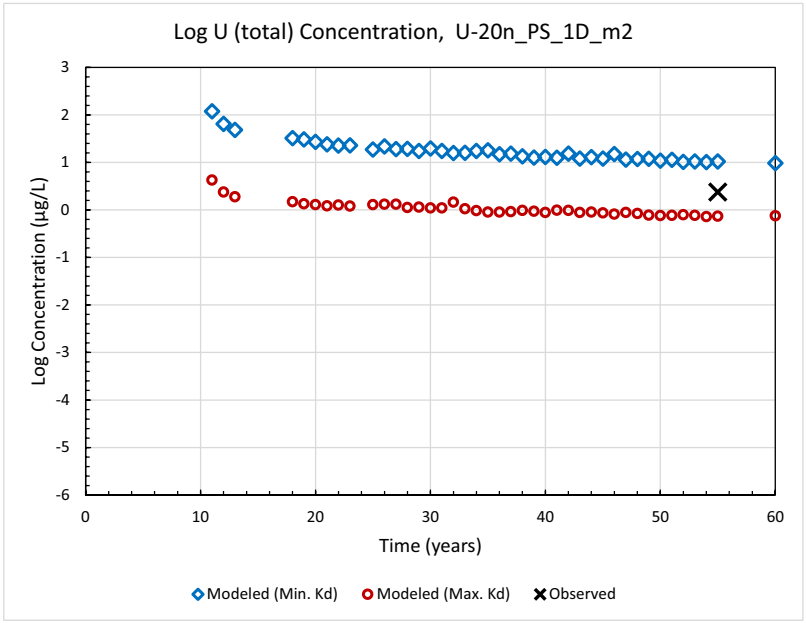

Figure H-152
Modeled and Measured U (Total) Concentrations versus Time at U-20n_PS_1D_m2

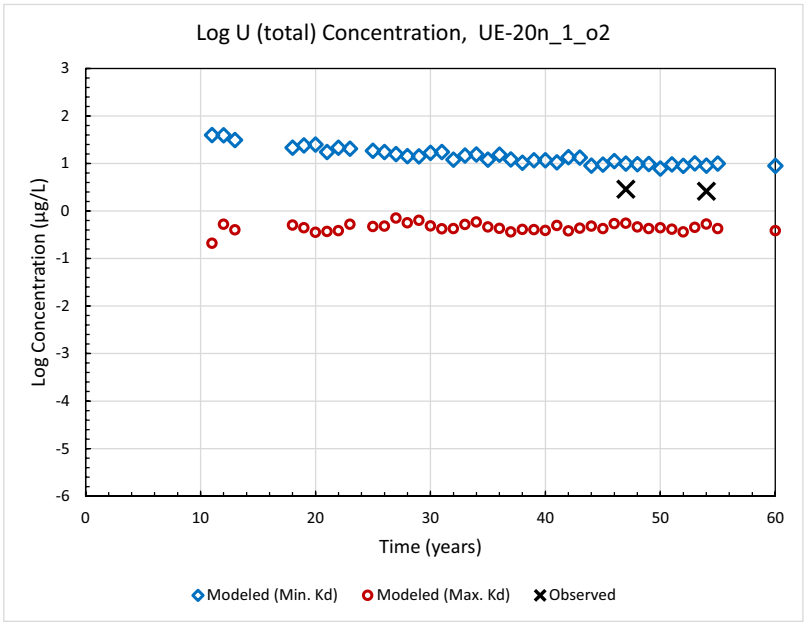

Figure H-153
Modeled and Measured U (Total) Concentrations versus Time at UE-20n_1_o2

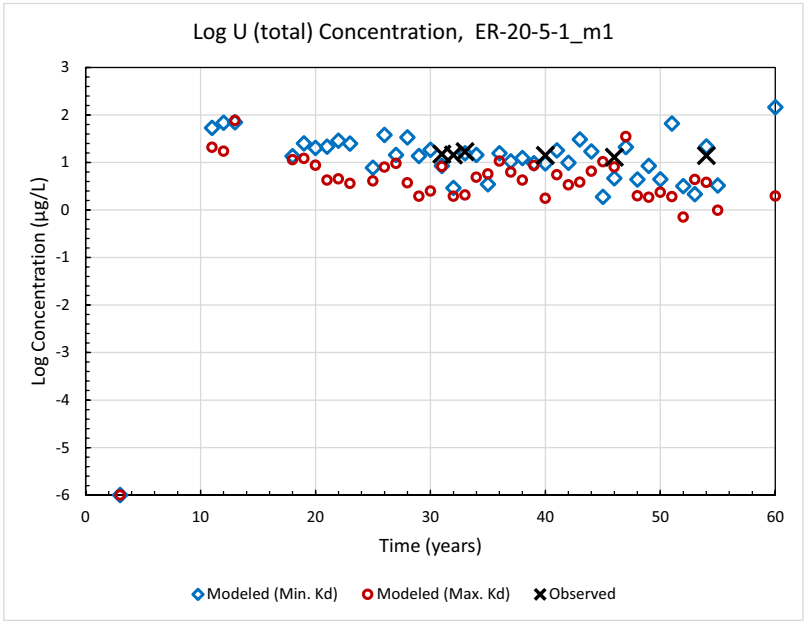

Figure H-154
Modeled and Measured U (Total) Concentrations versus Time at ER-20-5-1_m1

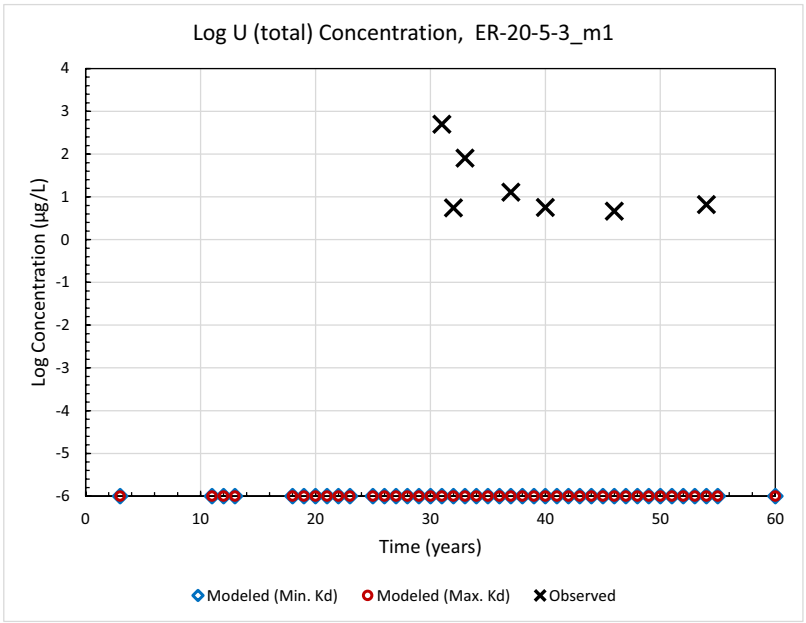

Figure H-155
Modeled and Measured U (Total) Concentrations versus Time at ER-20-5-3_m1

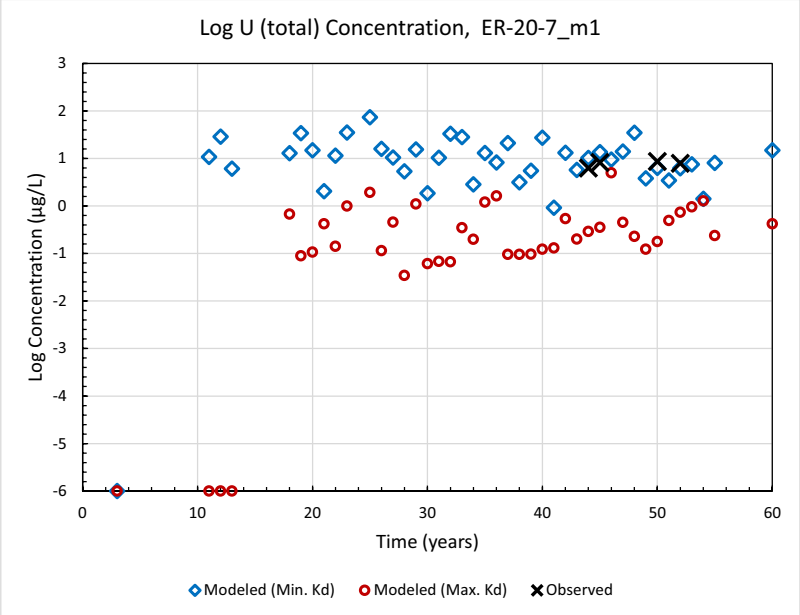

Figure H-156
Modeled and Measured U (Total) Concentrations versus Time at ER-20-7_m1

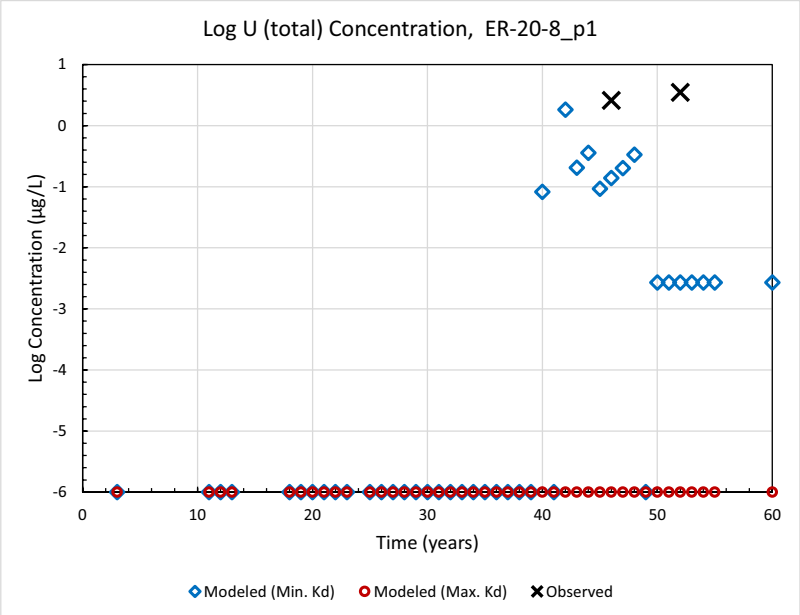

Figure H-157
Modeled and Measured U (Total) Concentrations versus Time at ER-20-8_p1

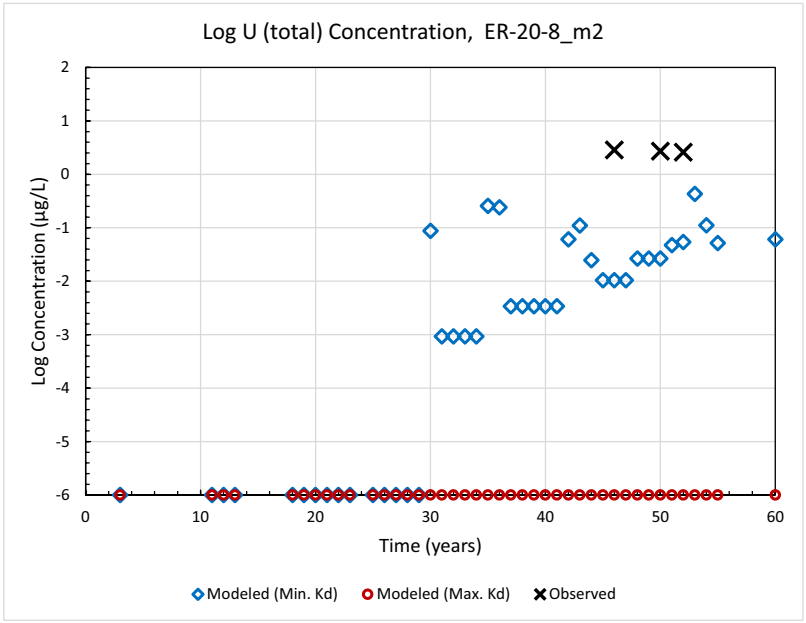

Figure H-158
Modeled and Measured U (Total) Concentrations versus Time at ER-20-8_m2

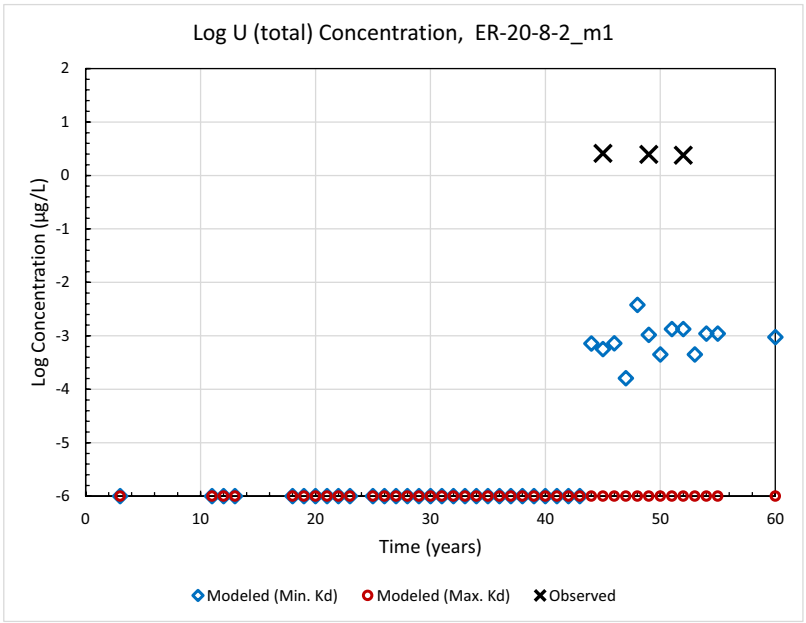

Figure H-159
Modeled and Measured U (Total) Concentrations versus Time at ER-20-8-2_m1

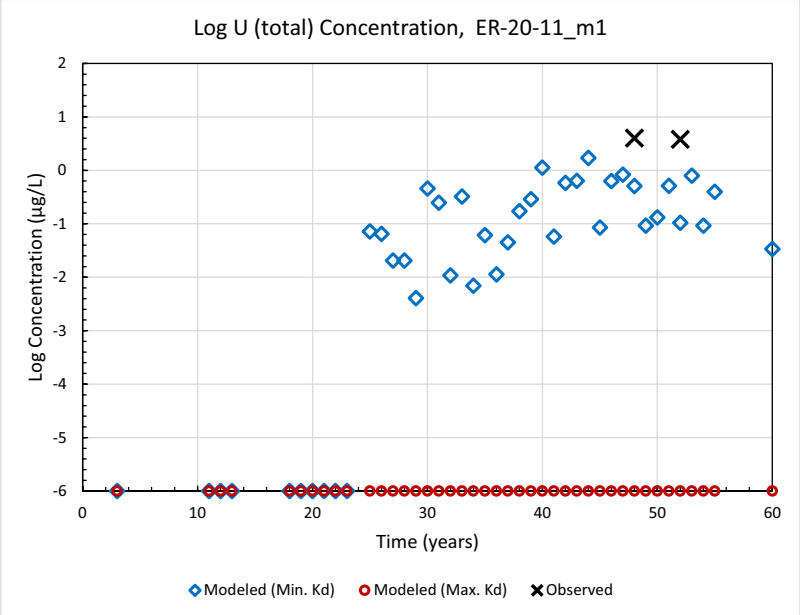

Figure H-160
Modeled and Measured U (Total) Concentrations versus Time at ER-20-11_m1

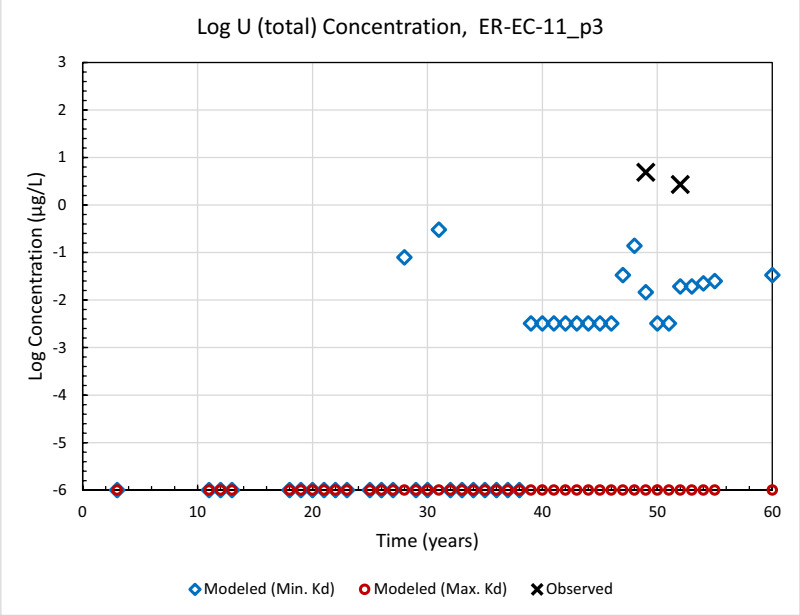

Figure H-161
Modeled and Measured U (Total) Concentrations versus Time at ER-EC-11_p3

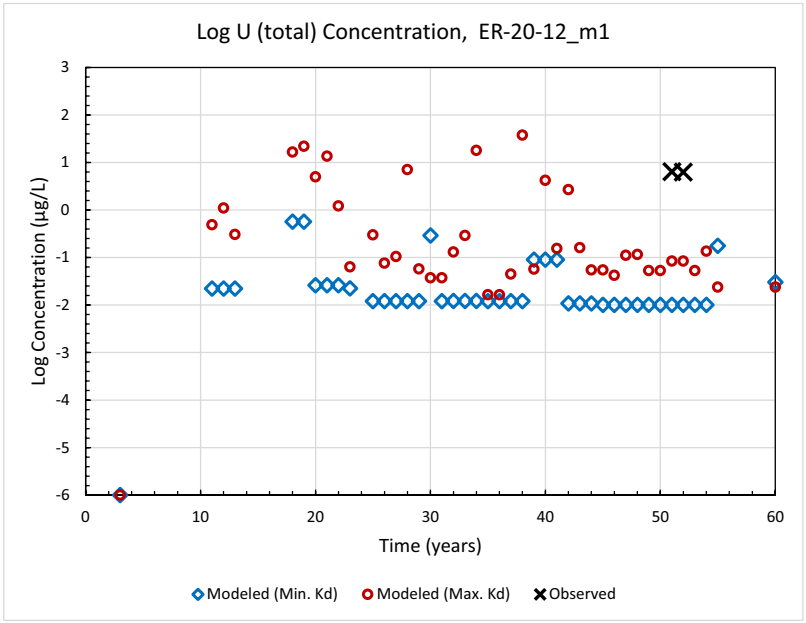

Figure H-162
Modeled and Measured U (Total) Concentrations versus Time at ER-20-12_m1

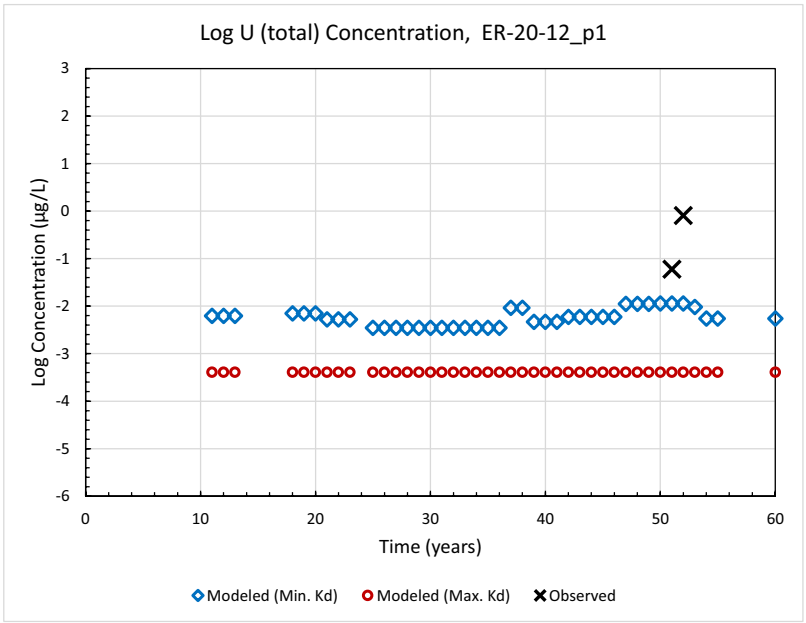

Figure H-163
Modeled and Measured U (Total) Concentrations versus Time at ER-20-12_p1

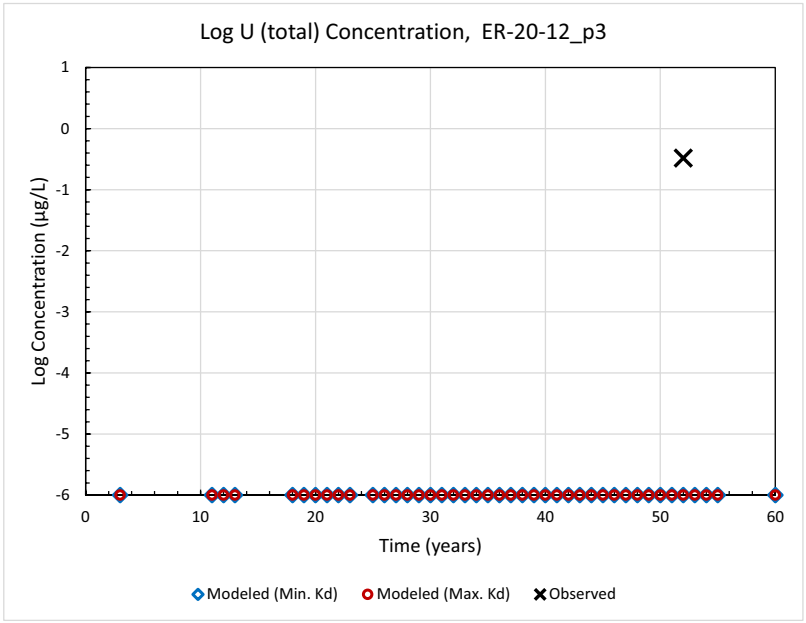

Figure H-164
Modeled and Measured U (Total) Concentrations versus Time at ER-20-12_p3

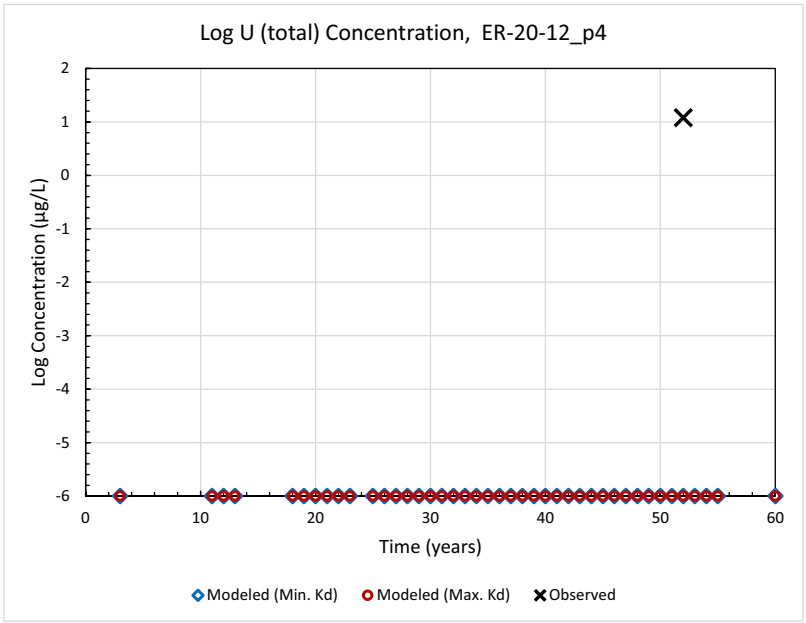

Figure H-165
Modeled and Measured U (Total) Concentrations versus Time at ER-20-12_p4

H.1.9 Modeled and Measured $^{239/240}$Pu Concentrations versus Time from Calibrated PM CAU Transport Model

Figures H-166 through H-185 present plots of modeled and measured $^{239/240}$Pu concentrations versus time, over the first 60 years (encompassing all observation times), from the calibrated PM CAU transport model at locations with observed $^{239/240}$Pu. The log of concentration is used to compare modeled and measured (observed) values. Zero values were approximated with a value of 1E-06, resulting in a log value of -6. Observations of Pu are reported as $^{239/240}$Pu; thus forward runs of ^{239}Pu and ^{240}Pu were made independently, and the resulting concentrations were summed for comparison to observed values. Modeled concentrations are displayed for two cases: one using minimum K_d for all zones (blue diamonds) and one using maximum K_d for all zones (red circles).

The model overpredicts $^{239/240}$Pu concentrations at all postshot observation locations. At U-19ad PS 1A (CHANCELLOR) the range of modeled values overpredicts $^{239/240}$Pu concentrations by 1 to 2 orders of magnitude. At U-19q PS 1D (CAMEMBERT), the range of modeled values overpredicts $^{239/240}$Pu concentrations by 3 to 4 orders of magnitude. At U-19v PS 1D (ALMENDRO) the range of modeled $^{239/240}$Pu concentrations in log space is typically between 2.8 and 3.3, even for the observations where there is no Pu. Non-zero observations are overpredicted by 2 to 4 orders of magnitude. At U-20n PS 1D (CHESHIRE), the range of modeled $^{239/240}$Pu concentrations in log space is typically between 2.6 and 3.3, even for the observations where there is no Pu. Non-zero observations are overpredicted by 3 to 4 orders of magnitude. The large overprediction of $^{239/240}$Pu concentrations at the postshot observation locations suggests that the ^{239}Pu and ^{240}Pu source masses input to the PM CAU transport model at these locations may be conservatively high.

At ER-20-5-1 (in the TSA) the model overpredicts $^{239/240}$Pu concentrations by approximately 1 to 3 orders of magnitude. At ER-20-7 (further downgradient in the TSA), the model overpredicts $^{239/240}$Pu concentrations by approximately 2 to 5 orders of magnitude. The fact that modeled $^{239/240}$Pu concentrations in the TSA increase further downgradient indicates that not enough attenuation of Pu is occurring in the modeled fractured TSA, suggesting that the assumptions regarding the transport of colloidal Pu (i.e., reduced matrix sorption and reduced matrix diffusion) may be too conservative.

At locations further downgradient, ER-20-8_p1 (in the CHZCM), ER-20-8_m2 (in the TCA), ER-20-8-2 (in the SPA), ER-20-11 (in the BA), and ER-EC-11_p3 (in the BA), there is no observed

Pu, but the model predicts $^{239/240}$Pu concentrations similar to what is observed at ER-20-5-1 and ER-20-7. These results also suggest that not enough attenuation of Pu is occurring in the model and that the assumptions regarding the transport of colloidal Pu (i.e., reduced matrix sorption and reduced matrix diffusion) may be too conservative.

Near HANDLEY, at both ER-20-12_p3 and PM-3_p2 the model predicts no Pu, which agrees with observations at this location. These results are consistent with results from other RNs at ER-20-12_p3 and PM-3_p2. At ER-20-12_m1, ER-20-12_p1, and PM-3_p1, there is no observed Pu. However, the model predicts $^{239/240}$Pu concentrations up to 7.5 pCi/L at ER-20-12_m1, $^{239/240}$Pu concentrations up to 2.2 pCi/L at ER-20-12_p1, and $^{239/240}$Pu concentrations up to 3.4 pCi/L at PM-3_p1. These results suggest that (1) the ^{239}Pu and ^{240}Pu source masses input to the PM CAU transport model at HANDLEY may be conservatively high, and/or (2) not enough attenuation of Pu is occurring in the model and that the assumptions regarding the transport of colloidal Pu (i.e., reduced matrix sorption and reduced matrix diffusion) may be too conservative.

For a continuously acting source, transported concentrations at a downgradient location would be expected to be higher for the case with minimum K_d and/or minimum diffusion coefficient, compared to the case with maximum K_d and/or maximum diffusion coefficient. This is because the reduced sorption and/or reduced diffusion increases the Pu mass in flowing fractures. However, for a finite duration pulse source like that used in the simulations presented in this report, for solutes that undergo matrix diffusion and sorption, the expected trend can be reversed at times beyond the arrival of the peak at the downgradient observation locations. This is because the solute mass that was diffused/ sorbed in the matrix while the solute concentrations in the flowing fractures were higher (prior to the peak arrival) back-diffuses into the fractures when the fracture concentrations drop below those in the matrix. Such behavior has been reported in the literature both at NNSS (e.g., Reimus and Haga, 1999) and other sites (e.g., Hess et al., 2002). This explains the overlap and/or reversal of the data points representing high and low K_d values for Pu reported in Figures H-169, H-170, H-171, H-172, H-173, H-175, H-176, H-177, H-179, and H-181, representing observation locations 20n_PS_1D_o5Z, U-20n_PS_1D_o2, U-20n_PS_1D_o3Z, U-20n_PS_1D_m2, ER-20-5-1_m1, ER-20-7_m1, ER-20-8_p1, ER-20-8_m2, ER-20-11_m1, and ER-20-12_m1.

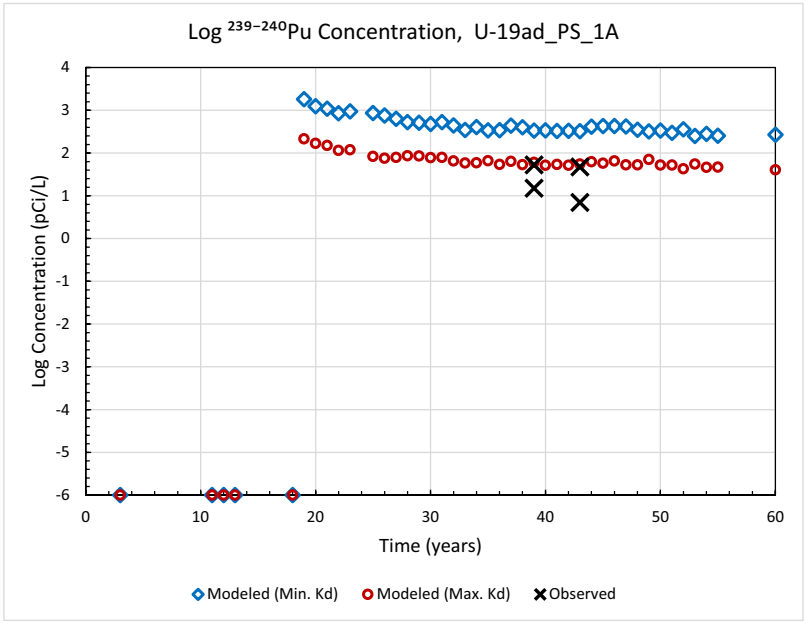

Figure H-166
Modeled and Measured $^{239/240}$Pu Concentrations versus Time at U-19ad_PS_1A

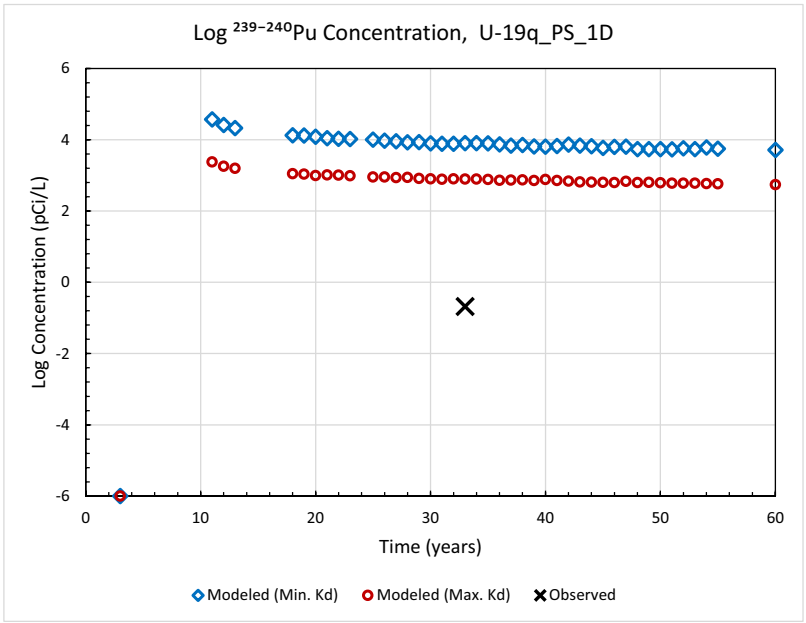

Figure H-167
Modeled and Measured $^{239/240}$Pu Concentrations versus Time at U-19q_PS_1D

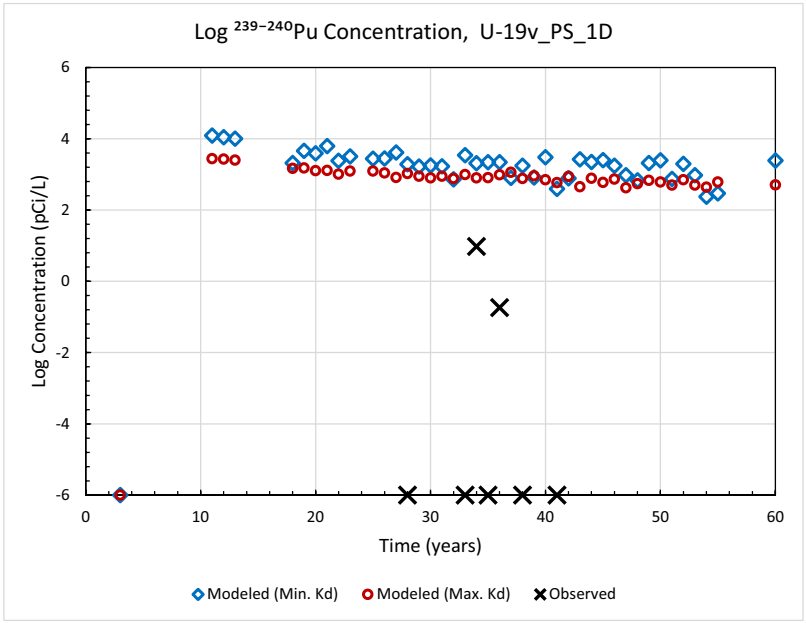

Figure H-168
Modeled and Measured $^{239/240}$Pu Concentrations versus Time at U-19v_PS_1D

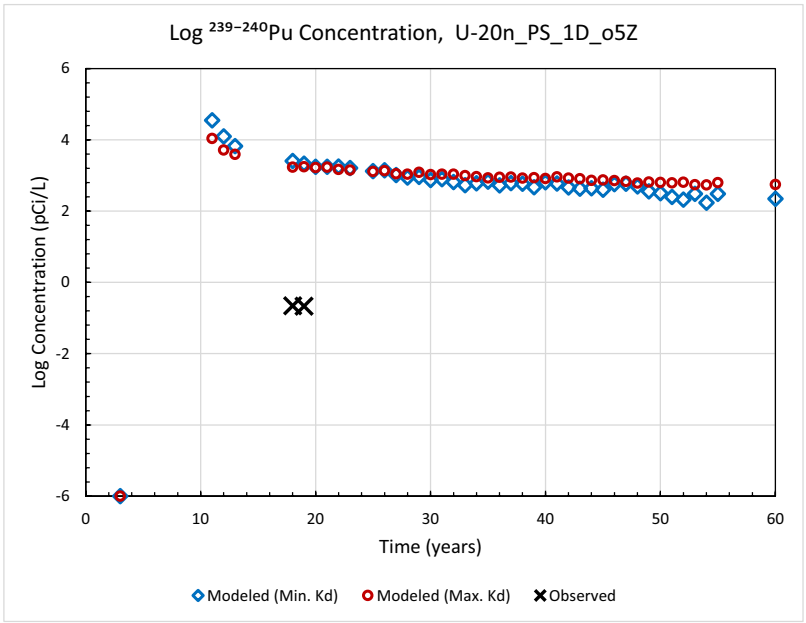

Figure H-169
Modeled and Measured $^{239/240}$Pu Concentrations versus Time at U-20n_PS_1D_o5Z

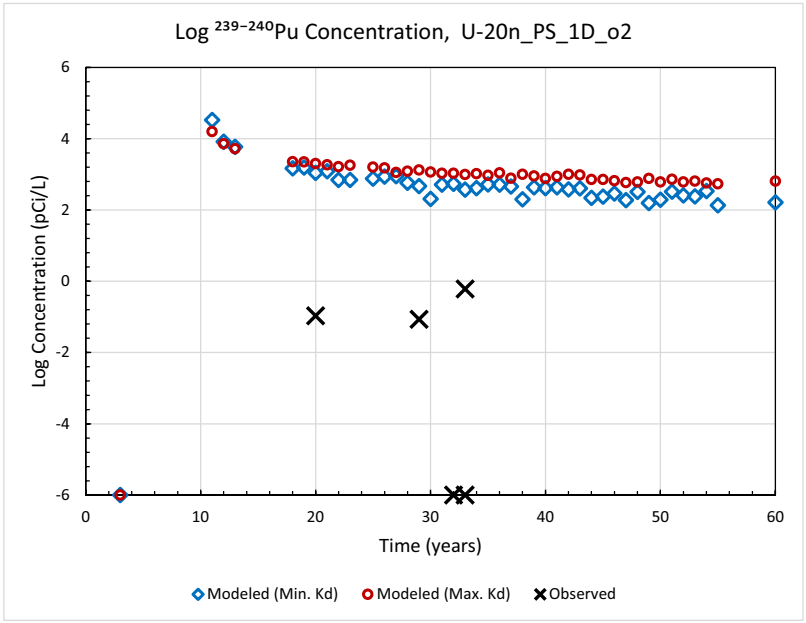

Figure H-170
Modeled and Measured $^{239/240}$Pu Concentrations versus Time at U-20n_PS_1D_o2

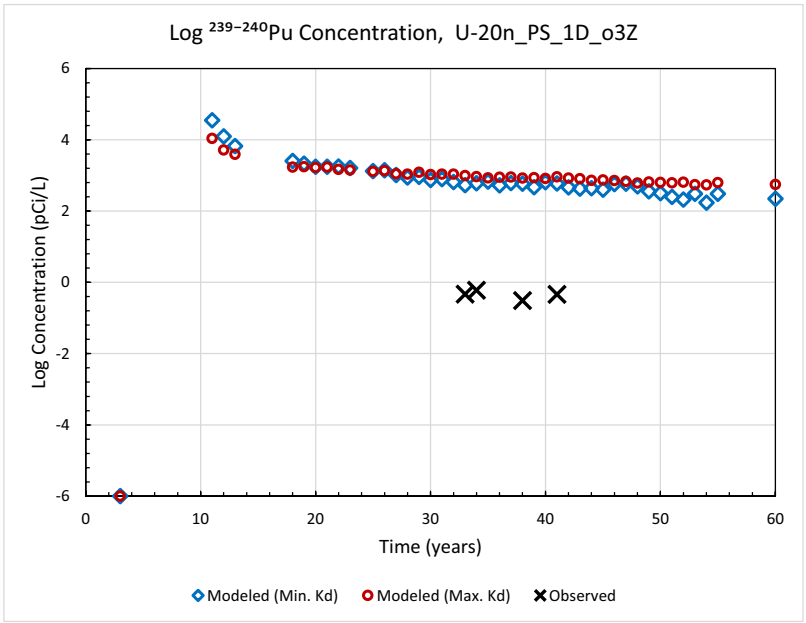

Figure H-171
Modeled and Measured $^{239/240}$Pu Concentrations versus Time at U-20n_PS_1D_o3Z

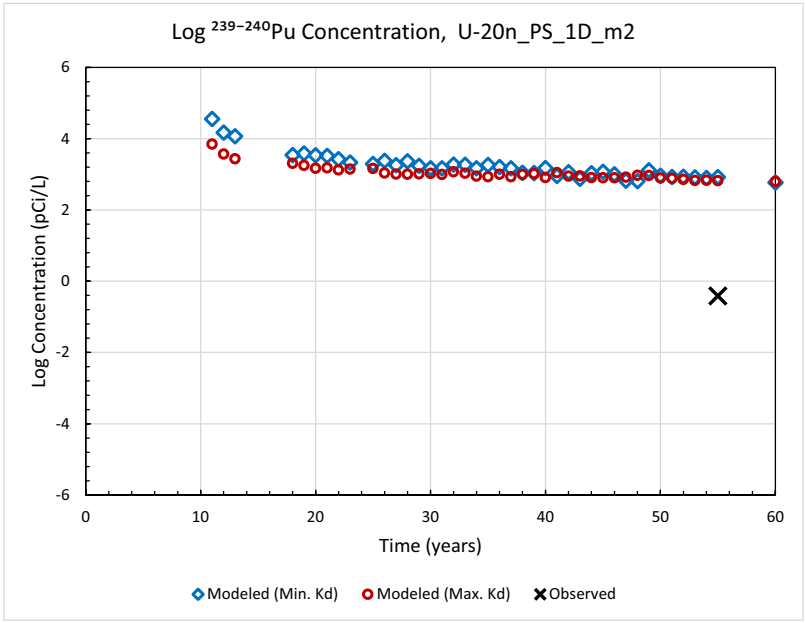

Figure H-172
Modeled and Measured $^{239/240}$Pu Concentrations versus Time at U-20n_PS_1D_m2

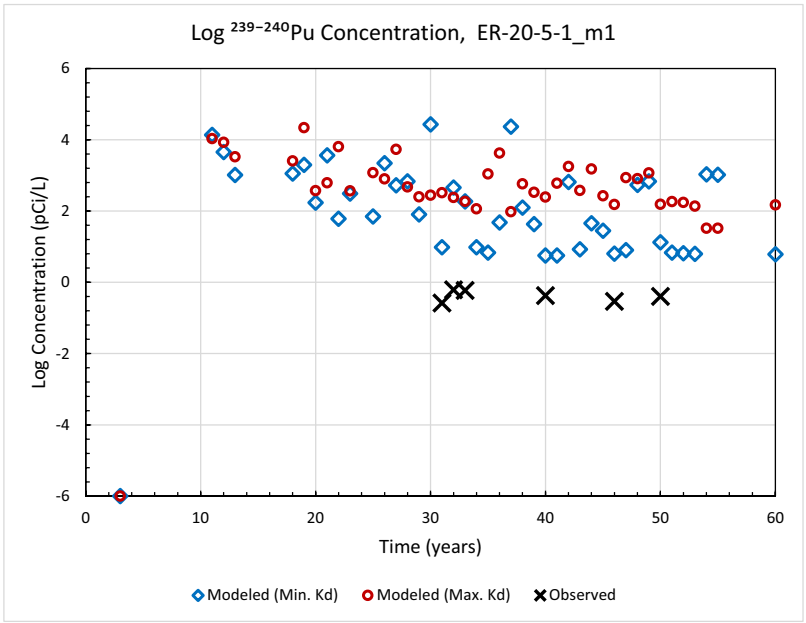

Figure H-173
Modeled and Measured $^{239/240}$Pu Concentrations versus Time at ER-20-5-1_m1

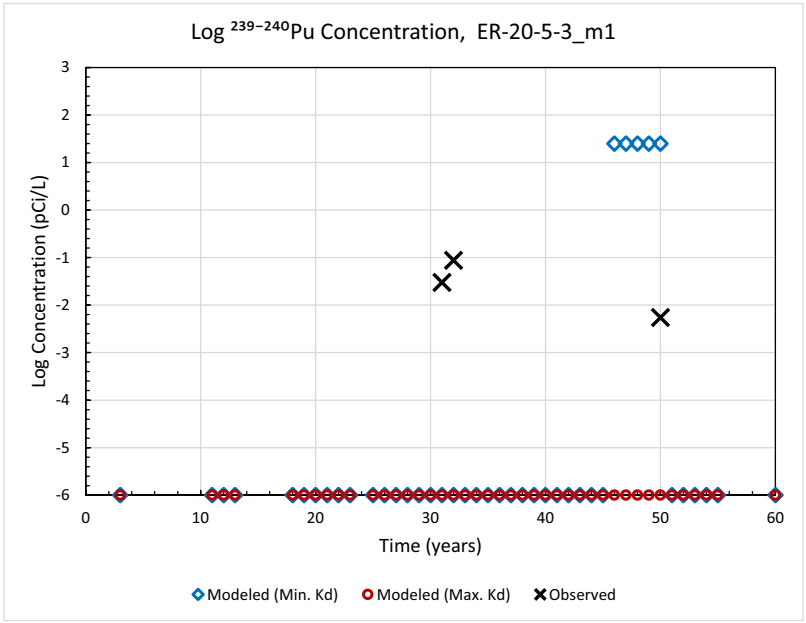

Figure H-174
Modeled and Measured $^{239/240}$Pu Concentrations versus Time at ER-20-5-3_m1

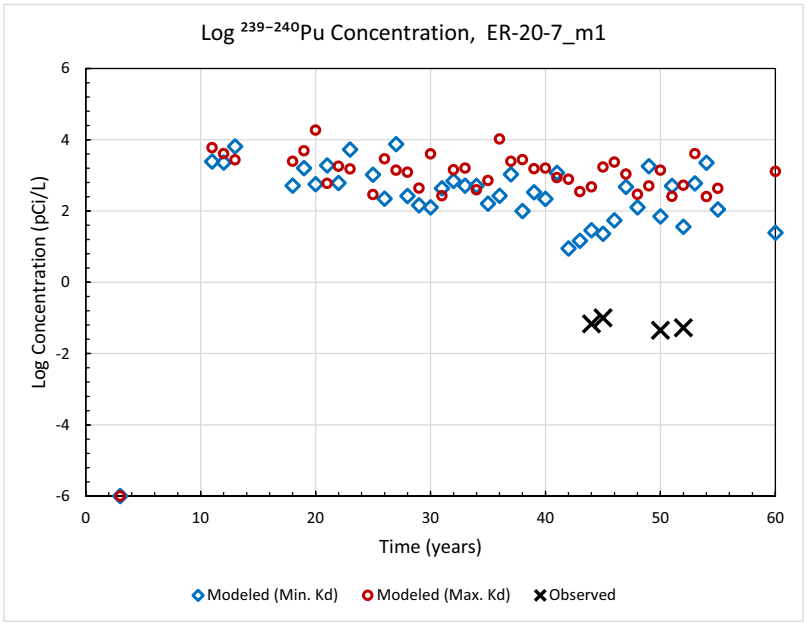

Figure H-175
Modeled and Measured $^{239/240}$Pu Concentrations versus Time at ER-20-7_m1

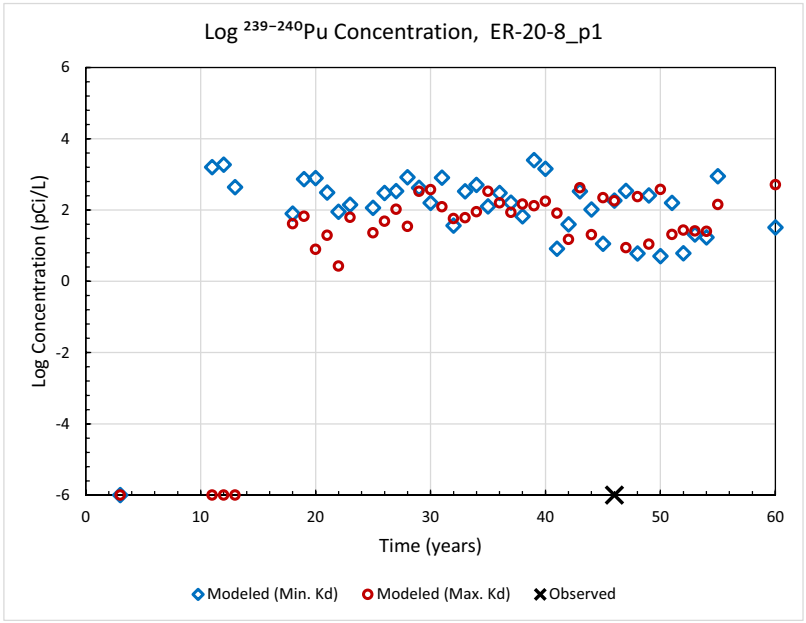

Figure H-176
Modeled and Measured $^{239/240}$Pu Concentrations versus Time at ER-20-8_p1

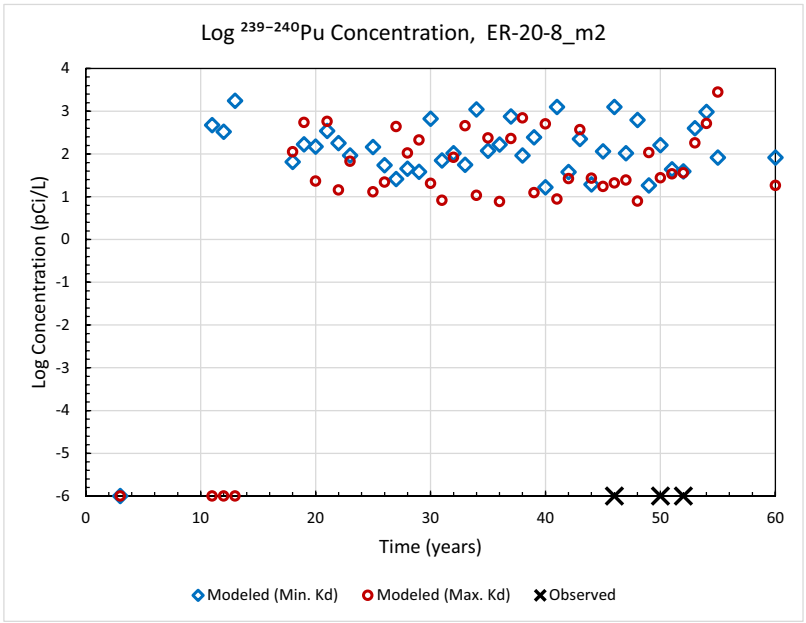

Figure H-177
Modeled and Measured $^{239/240}$Pu Concentrations versus Time at ER-20-8_m2

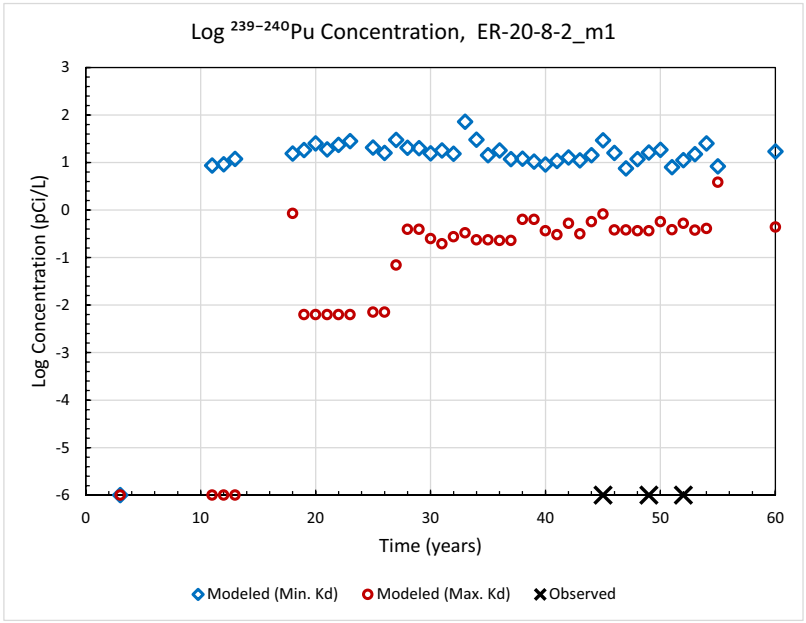

Figure H-178
Modeled and Measured $^{239/240}$Pu Concentrations versus Time at ER-20-8-2_m1

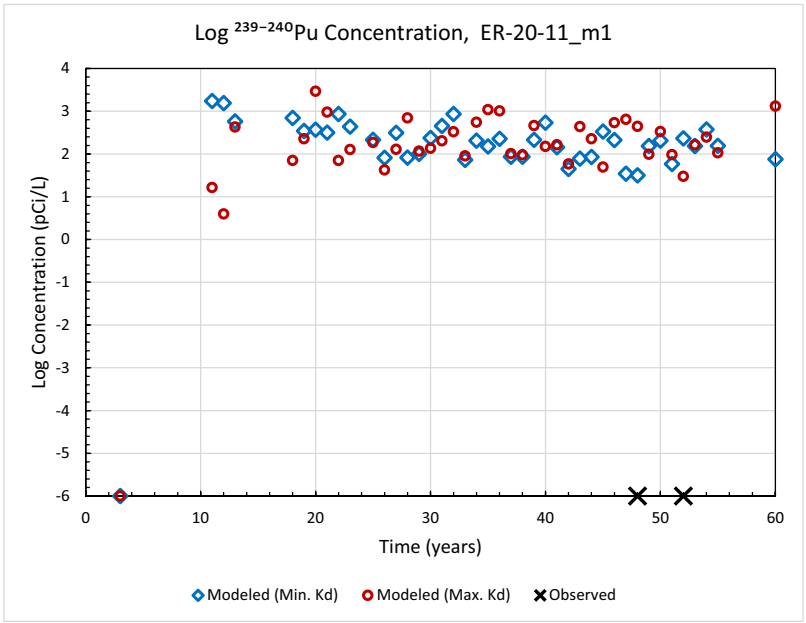

Figure H-179
Modeled and Measured $^{239/240}$Pu Concentrations versus Time at ER-20-11_m1

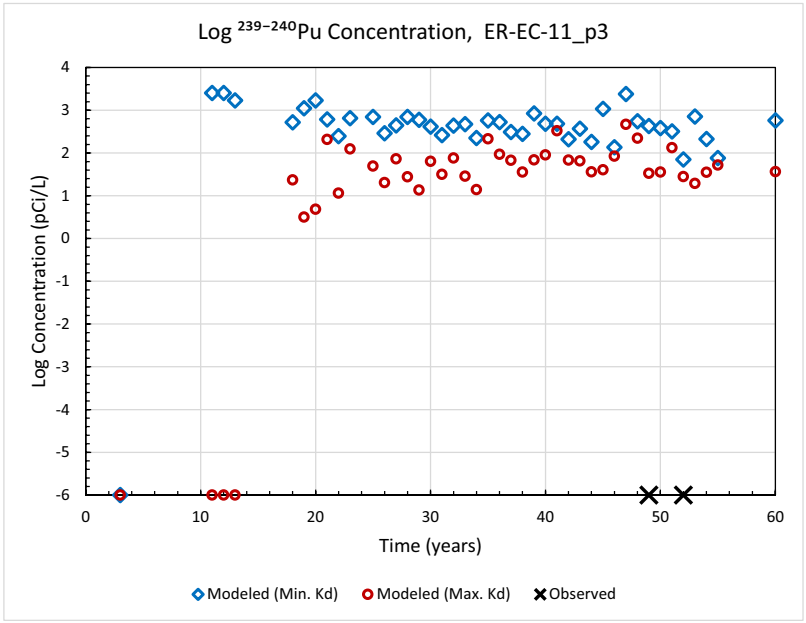

Figure H-180
Modeled and Measured $^{239/240}$Pu Concentrations versus Time at ER-EC-11_p3

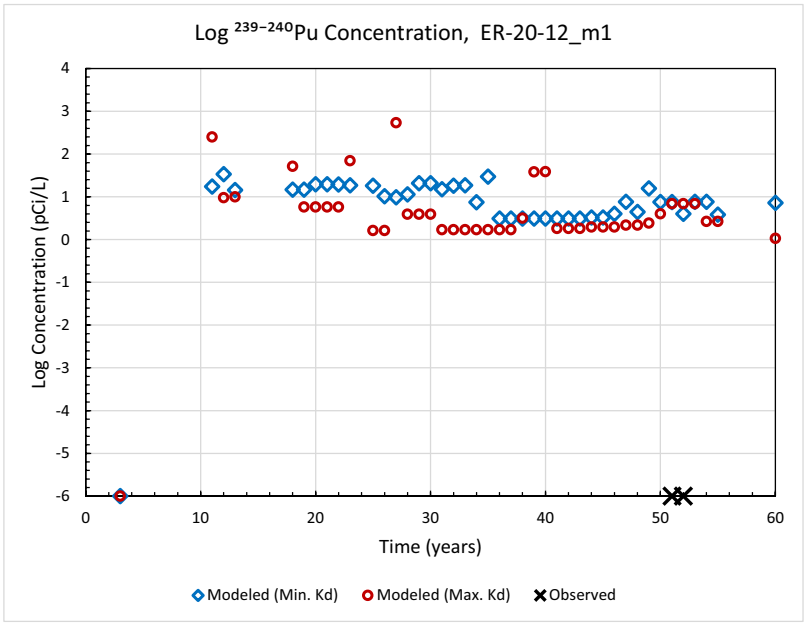

Figure H-181
Modeled and Measured $^{239/240}$Pu Concentrations versus Time at ER-20-12_m1

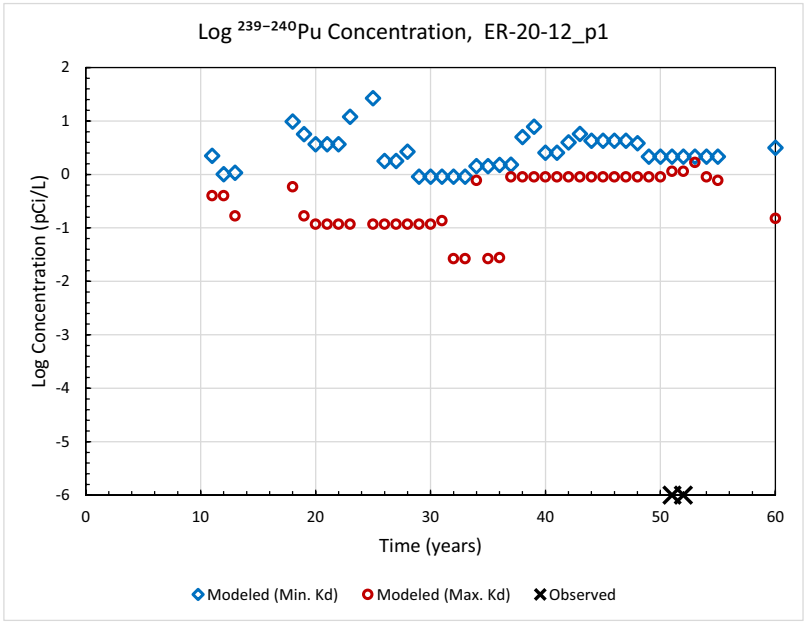

Figure H-182
Modeled and Measured $^{239/240}$Pu Concentrations versus Time at ER-20-12_p1

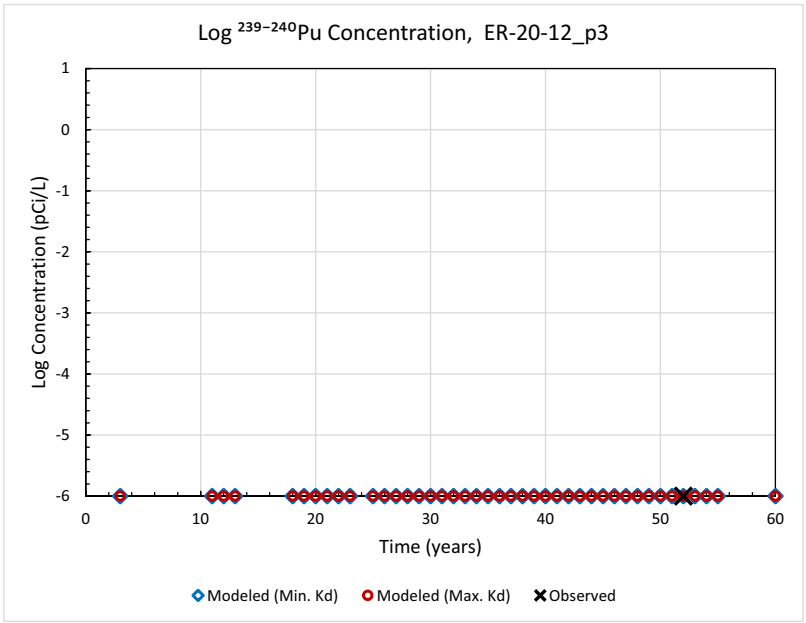

Figure H-183
Modeled and Measured $^{239/240}$Pu Concentrations versus Time at ER-20-12_p3

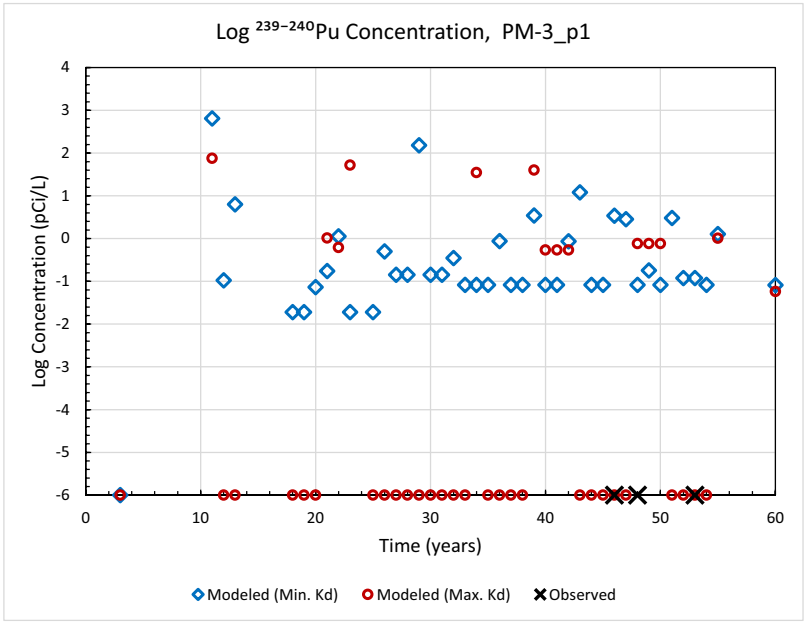

Figure H-184
Modeled and Measured $^{239/240}$Pu Concentrations versus Time at PM-3_p1

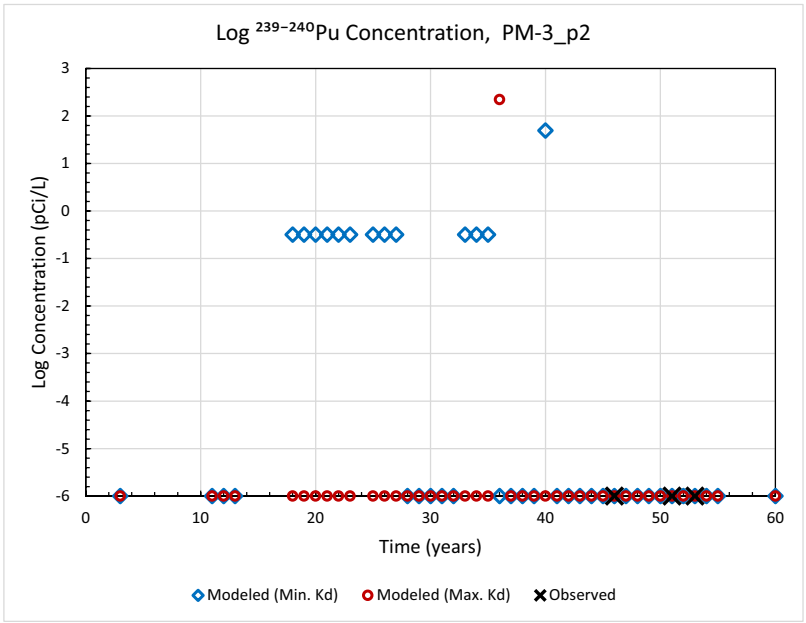

Figure H-185
Modeled and Measured $^{239/240}$Pu Concentrations versus Time at PM-3_p2

H.1.10 Modeled $^{239/240}$Pu Concentrations versus Time from Calibrated PM CAU Transport Model at Locations Not Observed for Pu

Figures H-186 through H-196 present plots of modeled $^{239/240}$Pu concentrations versus time, over the first 60 years (encompassing all observation times), from the calibrated PM CAU transport model at locations that have not been observed for Pu. The log of concentrations are plotted, with zero values approximated with a value of 1E-06, resulting in a log value of -6. Observations of Pu are reported as $^{239/240}$Pu; thus forward runs of ^{239}Pu and ^{240}Pu were made independently, and the resulting concentrations were summed for comparison to observed values. Modeled concentrations are displayed for two cases: one using minimum K_d for all zones (blue diamonds) and one using maximum K_d for all zones (red circles).

For a continuously acting source, transported concentrations at a downgradient location would be expected to be higher for the case with minimum K_d and/or minimum diffusion coefficient, compared to the case with maximum K_d and/or maximum diffusion coefficient. This is because the reduced sorption and/or reduced diffusion increases the Pu mass in flowing fractures. However, for a finite duration pulse source like that used in the simulations presented in this report, for solutes that undergo matrix diffusion and sorption, the expected trend can be reversed at times beyond the arrival of the peak at the downgradient observation locations. This is because the solute mass that was diffused/ sorbed in the matrix while the solute concentrations in the flowing fractures were higher (prior to the peak arrival) back-diffuses into the fractures when the fracture concentrations drop below those in the matrix. Such behavior has been reported in the literature both at NNSS (e.g., Reimus and Haga, 1999) and other sites (e.g., Hess et al., 2002). This explains the overlap and/or reversal of the data points representing high and low K_d values for Pu reported in Figures H-191 and H-196, representing observation locations U-20n_PS_1D_o1Z and UE-20n_1_o2.

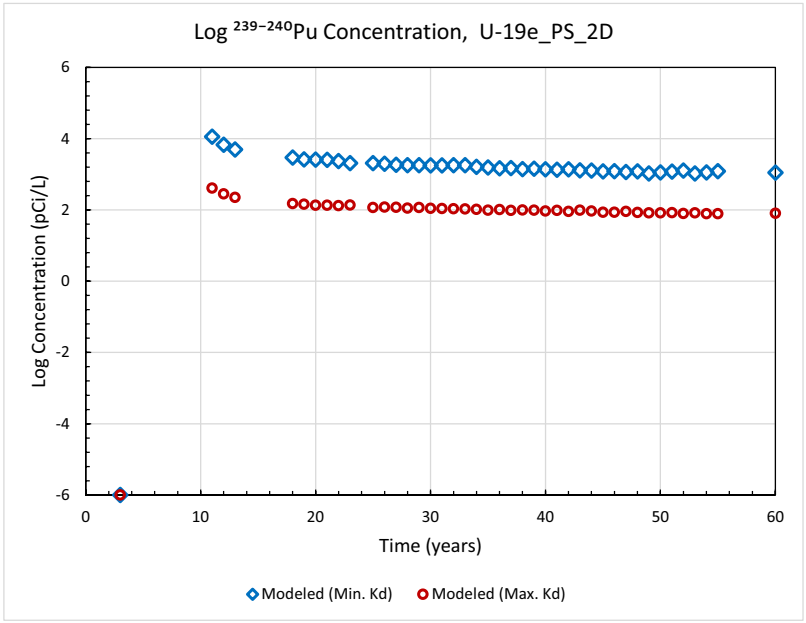

Figure H-186
Modeled $^{239/240}$Pu Concentrations versus Time at U-19e_PS_2D

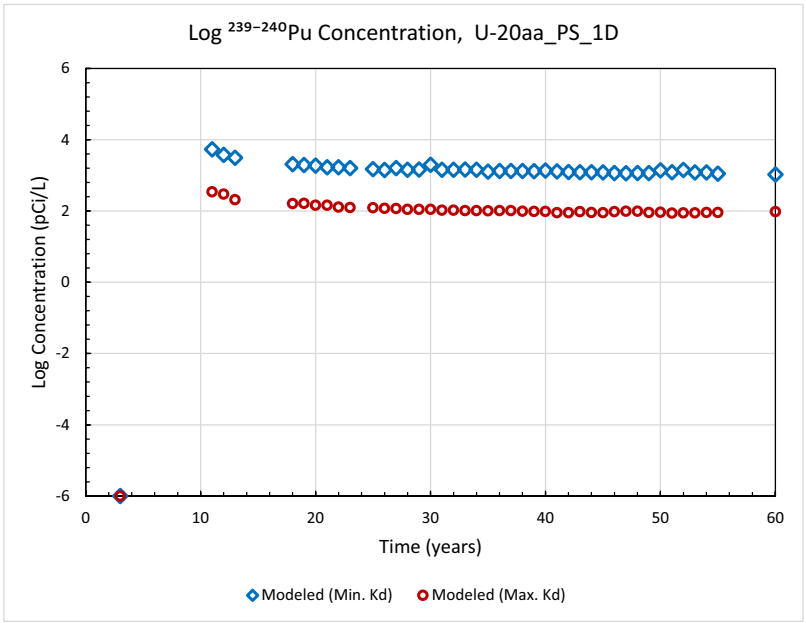

Figure H-187
Modeled $^{239/240}$Pu Concentrations versus Time at U-20aa_PS_1D

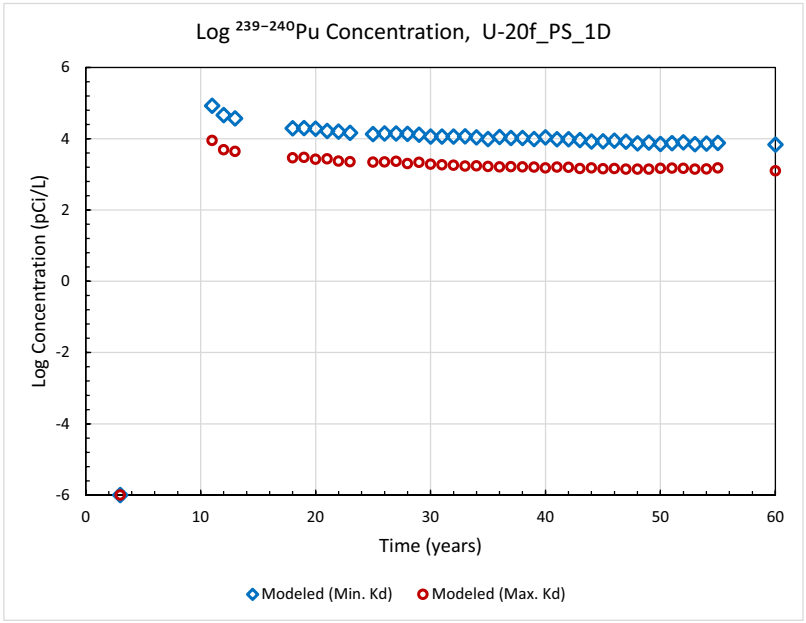

Figure H-188
Modeled $^{239/240}$Pu Concentrations versus Time at U-20f_PS_1D

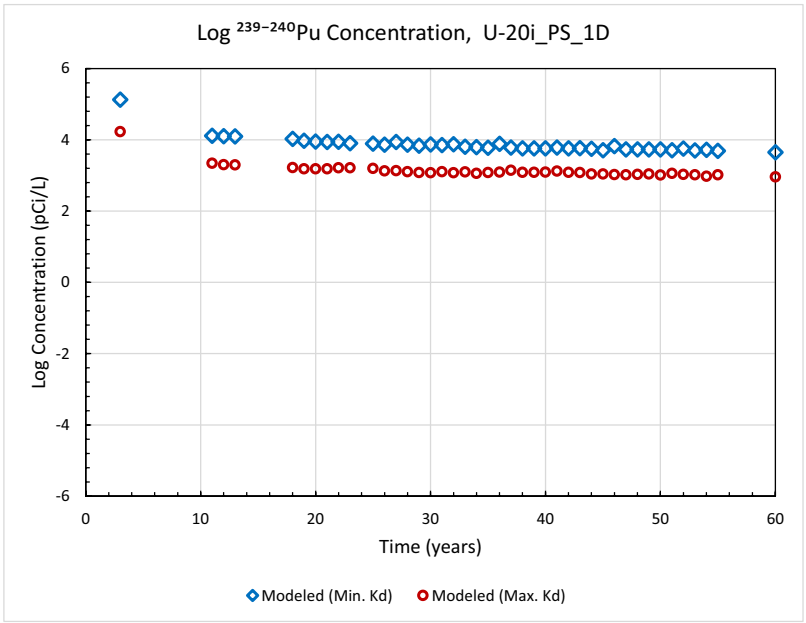

Figure H-189
Modeled $^{239/240}$Pu Concentrations versus Time at U-20i_PS_1D

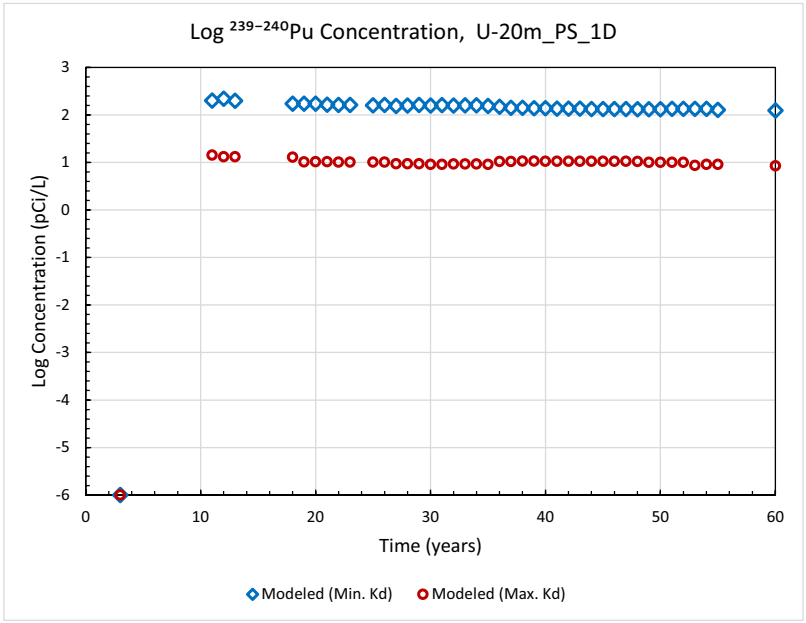

Figure H-190
Modeled $^{239/240}$Pu Concentrations versus Time at U-20m_PS_1D

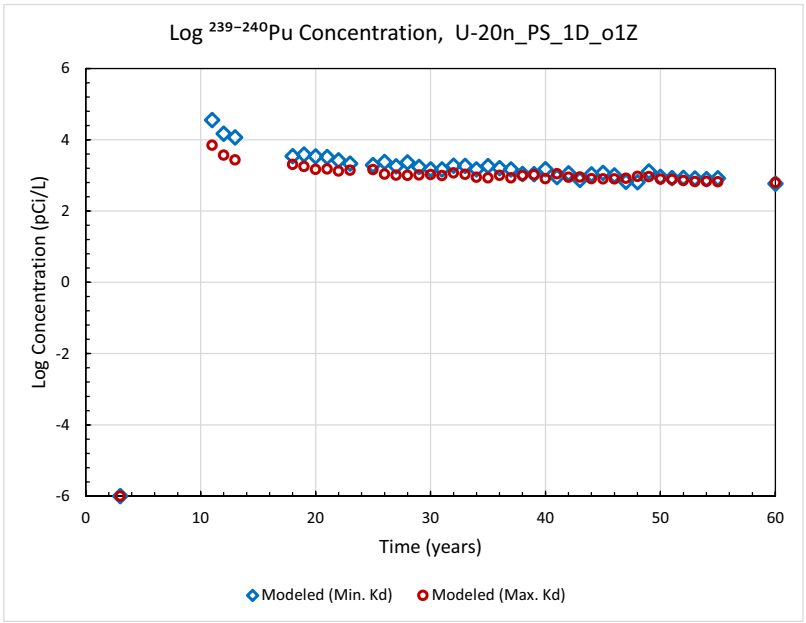

Figure H-191
Modeled $^{239/240}$Pu Concentrations versus Time at U-20n_PS_1D_o1Z

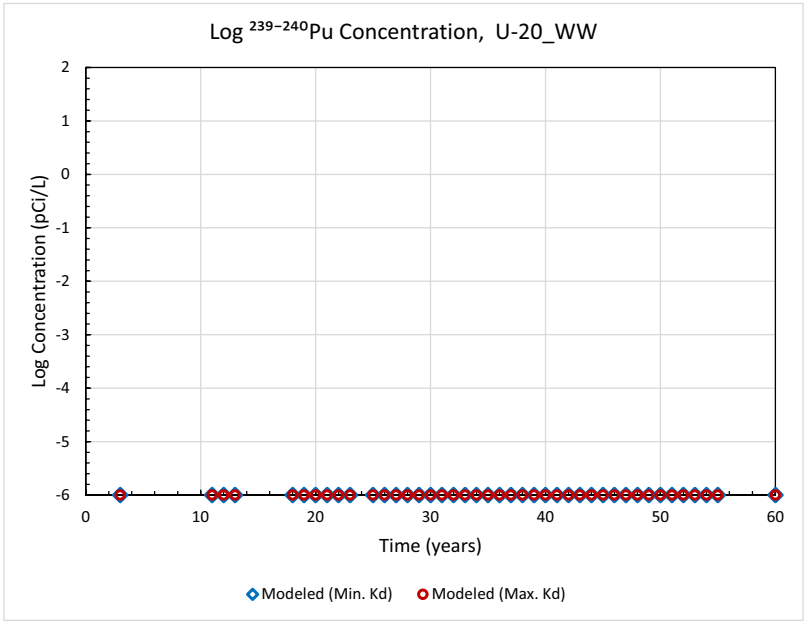

Figure H-192
Modeled $^{239/240}$Pu Concentrations versus Time at U-20_WW

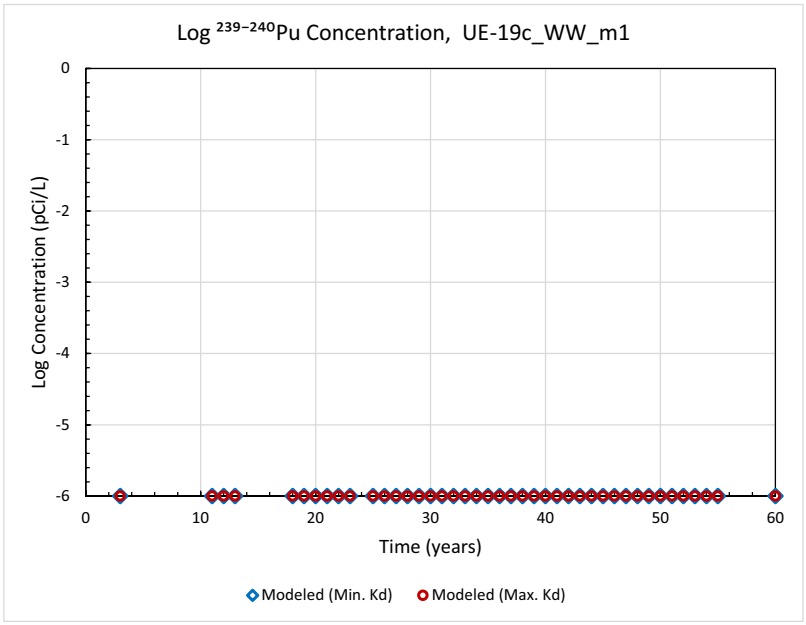

Figure H-193
Modeled $^{239/240}$Pu Concentrations versus Time at UE-19c_WW_m1

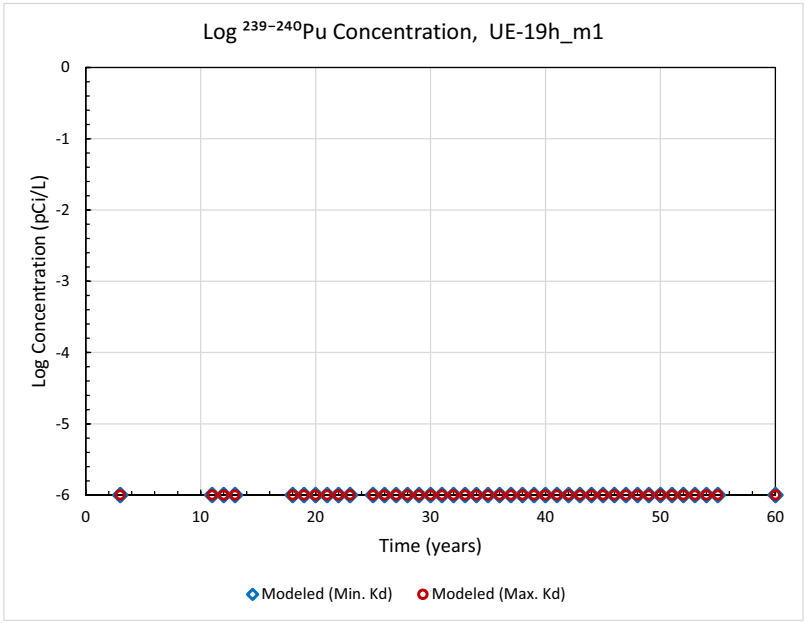

Figure H-194
Modeled $^{239/240}$Pu Concentrations versus Time at UE-19h_m1

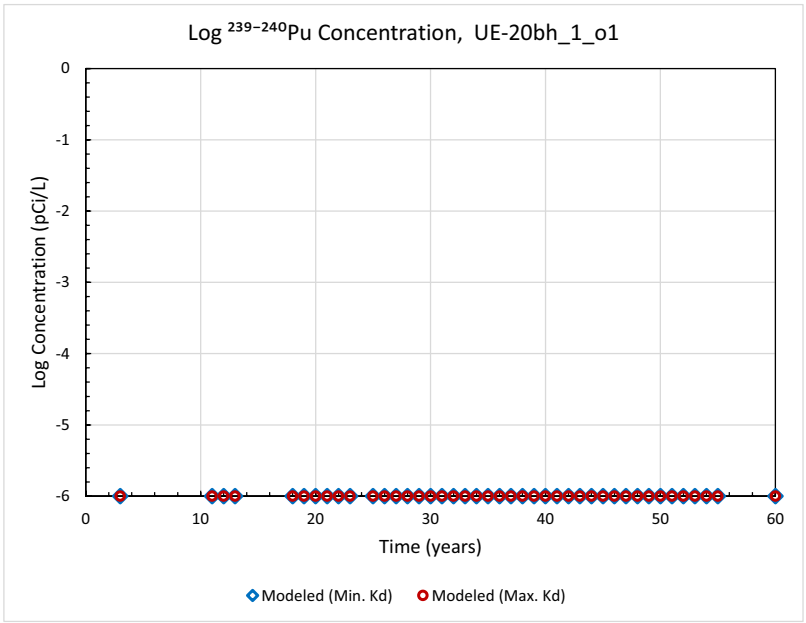

Figure H-195
Modeled $^{239/240}$Pu Concentrations versus Time at UE-20bh_1_o1

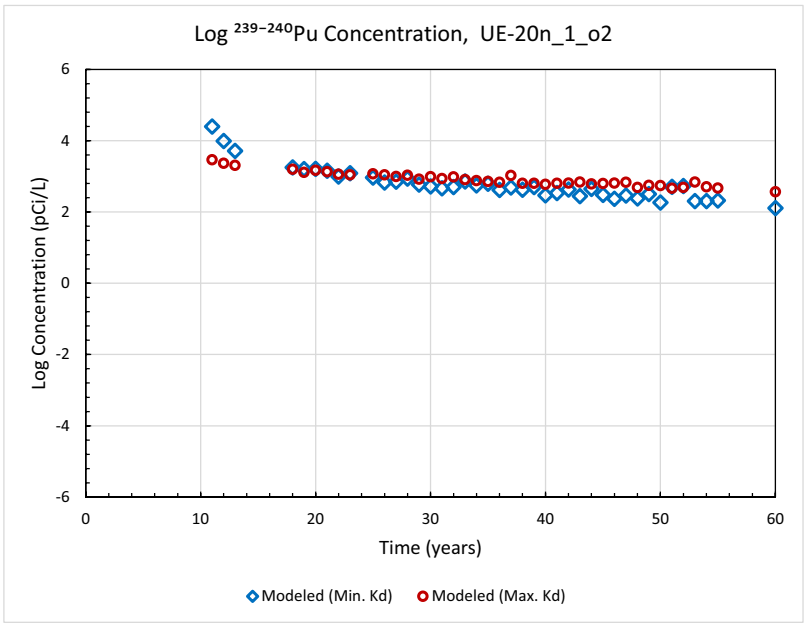

Figure H-196
Modeled $^{239/240}$Pu Concentrations versus Time at UE-20n_1_o2

H.2.0 References

Hess, K.H., J.A. Davis, D.B. Kent, and J.A. Coston. 2002. “Multispecies Reactive Tracer Test in an Aquifer with Spatially Variable Chemical Conditions, Cape Cod, Massachusetts: Dispersive Transport of Bromide and Nickel.” In *Water Resources Research*, Vol. 38(8): pp. 1161. Washington, DC: American Geophysical Union.

Reimus, P.W., and M.J. Haga. 1999. *Analysis of Tracer Responses in the BULLION Forced-Gradient Experiment at Pahute Mesa, Nevada*, LA-13615-MS. Los Alamos, NM: Los Alamos National Laboratory.

Appendix I

Nevada Division of Environmental Protection Comments

(26 Pages)

NEVADA ENVIRONMENTAL MANAGEMENT OPERATIONS ACTIVITY
DOCUMENT REVIEW SHEET

1. Document Title/Number: Groundwater Flow and Contaminant Transport Model of Corrective Action Units (CAUs) 101 and 102: Central and Western Pahute Mesa, Nye County, Nevada				2. Document Date: March, 2022
3. Revision Number: Rev 0				4. Originator/Organization: Environmental Management Nevada Program
5. Responsible EM Nevada Program Activity Lead: John Myers				6. Date Comments Due: May 13, 2022
7. Review Criteria:				
8. Reviewer/Organization Phone No.: Christine Andres (NDEP), Britt Jacobson (NDEP Contractor)				9. Reviewer's Signature:
10. Comment Number/Location		11. Type[a]	12. Comment	13. Comment Response
1.	Page ES-5, Third Paragraph, Third Sentence		Please explain in the text why these forecasts are intentionally made overly conservative.	Rephrased the sentence to: "The modeling basis of these forecasts is biased toward overestimating the potential contaminant transport when faced with sparse data that may be subject to alternative interpretations, or when the conceptual model is likely to lead to significant increase in computational burden."
2.	Page ES-6, Fourth Bullet, Second Sentence		Please explain in the text the information used to state that the uncertainty in the boundary condition is not likely to be a major factor in the overall uncertainty.	Inserted: "The uncertainty in the boundary flux is shown in Fenelon et al. (2016) to be about ±150 acre-feet per year (ac-ft/yr), or 2.5 percent of the total basin flow. The total discharge is estimated to be 5,900 ac-ft/yr with about a 15 percent uncertainty. Compared with parameter uncertainty in hydraulic conductivity, porosity, diffusion and sorption parameters, and source concentration, the amount of boundary flux uncertainty is much smaller…"

[a]Comment Types: M = Mandatory, S = Suggested.
Return Document Review Sheets to Environmental Management Nevada Program Operations Activity, Attn: QAC, M/S NSF 505

NEVADA ENVIRONMENTAL MANAGEMENT OPERATIONS ACTIVITY
DOCUMENT REVIEW SHEET

1. Document Title/Number: Groundwater Flow and Contaminant Transport Model of Corrective Action Units (CAUs) 101 and 102: Central and Western Pahute Mesa, Nye County, Nevada				2. Document Date: March, 2022
3. Revision Number: Rev 0				4. Originator/Organization: Environmental Management Nevada Program
5. Responsible EM Nevada Program Activity Lead: John Myers				6. Date Comments Due: May 13, 2022
7. Review Criteria:				
8. Reviewer/Organization Phone No.: Christine Andres (NDEP), Britt Jacobson (NDEP Contractor)				9. Reviewer's Signature:
10. Comment Number/Location		11. Type[a]	12. Comment	13. Comment Response
3.	Page ES-7, First Bullet, First Sentence		Are the alternative model formulations the same as the several hydrologic conceptual model alternatives on Page ES-6, First Bullet, Second Sentence? Please clarify throughout the Document.	They are not the same. Revised the first bullet on p. ES-7 to this: "During the calibration process, it was determined that distinct alternative HFMs were not needed to achieve calibration because the observed heterogeneity of flow properties was substantial and provided a sufficient range of values for calibration. Rather than develop alternative HFMs, the approach chosen during flow calibration was to add hydraulic conductivity heterogeneity by subdividing (laterally or vertically) some HSUs into smaller sub-HSUs with distinct material properties. Several alternative hydrologic conceptual models were also investigated that included an alternative that identified faults as distinct flow regimes separate from the HSUs." Also revised the first bullet on p. ES-6 to this: "The Phase I PM-OV HFM used separate, fully functioning alternative HFMs to address uncertainty associated with hydrogeologically significant non-unique interpretations incorporated into the Phase I HFM (see Section 6.0 in BN, 2002). Phase II work took a different approach to uncertainty analysis by testing techniques that exploit the functionality of EarthVision (Dynamic Graphics, 2015) to help understand and evaluate the potential hydrologic effects of uncertainty associated with certain aspects of the PM-OV HFM. A technique was used in which the team assessed the uncertainty associated with fault offsets and the juxtaposition of hydrostratigraphic units (HSUs) across certain faults at PM (DOE-EM, 2020). PM CAU flow model calibration evaluated several hydrologic conceptual model alternatives that included subdividing (laterally or vertically) some HSUs into smaller sub-HSUs with distinct material properties. The flow model included an alternative that identified faults as distinct flow regimes separate from the HSUs."

[a]Comment Types: M = Mandatory, S = Suggested.
Return Document Review Sheets to Environmental Management Nevada Program Operations Activity, Attn: QAC, M/S NSF 505

4.	Page ES-8, Modeling Approach, First Paragraph, First Sentence		Please explain and/or reference in the text the information used to indicate when the forecasts are likely to affect the RN transport especially when data are sparse or may be subject to alternative interpretations or when the conceptual model is likely to lead to significant increase in computational burden.	Changed the paragraph to read: "Model development was guided by the need to be as realistic as practically feasible in selecting hydrogeologic features, flow processes, transport processes, and parameter distributions for inclusion in the model, while keeping in mind the purpose of PM CAU flow and transport modeling, which is to support the UGTA corrective action strategy objective of forecasting CBs. The philosophy adopted in model development was to be conservative in the modeling assumptions when, judged on the basis of theoretical and numerical considerations, they were likely to affect the forecast extent and magnitude of RN transport, especially when data were sparse or may be subject to alternative interpretations or when the conceptual model was likely to lead to significant increase in computational burden. This philosophy led to the decision to use models or parameter values that, while reproducing many realistic features of the system (such as observed basin discharge, hydraulic heads, transmissivities, flow paths, ^{3}H concentrations at several observation wells, and transit times) tend to overestimate the potential contaminant transport. Confidence in the PM CAU flow model was established, and our understanding of the flow system was supported by calibration of the model to observed hydraulic data. Confidence in the transport model was increased by demonstrating that the model could be calibrated to observed ^{3}H data with parameter values selected within ranges of parameter uncertainty. The choice of the conservative assumptions was evaluated, when practically feasible, against the model outcomes to determine if the result was sensitive to the assumptions. The forecast contaminant transport overestimation was demonstrated by comparing modeled contaminant transport with contaminant concentration observations at and downgradient from test cavities. For example, consider colloid-facilitated transport of plutonium (Pu). As a conservative approximation, filtration and retardation of the colloids are ignored because colloid filtration process is not well-quantified. The model conservatism could be reduced with more detailed considerations of colloid transport, but that would significantly increase the complexity and numerical demands of the model. The current PM CAU model forecasts Pu transport at levels well above observations, but rather than refining the model at this time, the conservative results are accepted as they provide an additional level of protection or buffer."
5.	Page ES-8, Modeling Approach, First Paragraph, Second Sentence		Please explain in the text how the philosophy to overestimate RN transport aids in the understanding of the flow and transport for this CAU.	Replaced the text in first paragraph as follows: "Confidence in the PM CAU flow model was established, and our understanding of the flow system was supported by calibration of the model to observed hydraulic data. Confidence in the transport model was increased by demonstrating that the model could be calibrated to observed ^{3}H data with parameter values selected within ranges of parameter uncertainty. The choice of the conservative assumptions was evaluated, when practically feasible, against the model outcomes to determine if the result was sensitive to the assumptions. The forecast contaminant transport overestimation was demonstrated by comparing modeled contaminant transport with contaminant concentration observations at and downgradient from test cavities."

[a]Comment Types: M = Mandatory, S = Suggested.
Return Document Review Sheets to Environmental Management Nevada Program Operations Activity, Attn: QAC, M/S NSF 505

NEVADA ENVIRONMENTAL MANAGEMENT OPERATIONS ACTIVITY
DOCUMENT REVIEW SHEET

1. Document Title/Number: Groundwater Flow and Contaminant Transport Model of Corrective Action Units (CAUs) 101 and 102: Central and Western Pahute Mesa, Nye County, Nevada	2. Document Date: March, 2022
3. Revision Number: Rev 0	4. Originator/Organization: Environmental Management Nevada Program
5. Responsible EM Nevada Program Activity Lead: John Myers	6. Date Comments Due: May 13, 2022
7. Review Criteria:	
8. Reviewer/Organization Phone No.: Christine Andres (NDEP), Britt Jacobson (NDEP Contractor)	9. Reviewer's Signature:

10. Comment Number/Location		11. Type[a]	12. Comment	13. Comment Response
6.	Page ES-16, Contaminant Boundaries, First Paragraph, First Sentence		Based on Page ES-14, Second Paragraph, First Sentence, the PM transport model was developed using the base case flow model. Please explain in the text the effect on, or uncertainties in, the contaminant boundaries developed using alternative flow models when the transport model was calibrated using the base case.	Calibration of the transport model to the base case had no effect on the CB calculations because CB used the full ranges of uncertainty for the parameter values. Changed text to read: "CBs used the full ranges of uncertainty for the parameter values. CBs were calculated for the PM CAU transport model using the base case PM CAU flow model, and for transport models using the two alternative flow models with alternative recharge distributions and the alternative flow model that contained all faults as defined in the PM-OV HFM. All four of these transport models employed the "base case" source term as defined in Carle et al. (2020) for the 15 selected RNs. For each of the four transport models described in the previous sentence, Monte Carlo probabilistic simulations were conducted by varying the effective porosity, fracture aperture, tortuosity, and matrix sorption coefficients over the ranges of values in the transport data document (TDD) (Navarro, 2021a). Dispersion was modeled in all of these simulations using longitudinal, horizontal transverse, and vertical transverse dispersivity values of 150 m, 15 m, and 1.5 m." Also changed the second-to-last paragraph of "Modeling Results," first sentence to read: "The transport model using the base case flow model with transport parameter values within ranges identified in Navarro (2021a) was successfully calibrated to ^{3}H observations in groundwater samples collected from open intervals in numerous wells in the model area. The transport model was not recalibrated to the alternative flow models. Although transport model calibration using the alternative flow models would have created additional permissive sets of transport parameters, those parameters are not used directly in the CB calculations. Rather, the CB calculations use the full range of uncertainty for each model parameter. Recalibration of the transport model using the alternative flow models would not have changed the CB forecasts."

[a]Comment Types: M = Mandatory, S = Suggested.
Return Document Review Sheets to Environmental Management Nevada Program Operations Activity, Attn: QAC, M/S NSF 505

NEVADA ENVIRONMENTAL MANAGEMENT OPERATIONS ACTIVITY
DOCUMENT REVIEW SHEET

1. Document Title/Number: Groundwater Flow and Contaminant Transport Model of Corrective Action Units (CAUs) 101 and 102: Central and Western Pahute Mesa, Nye County, Nevada	2. Document Date: March, 2022
3. Revision Number: Rev 0	4. Originator/Organization: Environmental Management Nevada Program
5. Responsible EM Nevada Program Activity Lead: John Myers	6. Date Comments Due: May 13, 2022
7. Review Criteria:	
8. Reviewer/Organization Phone No.: Christine Andres (NDEP), Britt Jacobson (NDEP Contractor)	9. Reviewer's Signature:

10. Comment Number/Location		11. Type[a]	12. Comment	13. Comment Response
7.	Page ES-25, First Full Paragraph, Second Sentence		Please explain in the text how the model forecasts are expected to be an "adequate" representation of the CB ensemble within the next 1,000 years.	Deleted the wording.
8.	Page 1, Section 1.0, Second Paragraph, Last Sentence		The Navarro, 2021c report does not contain the initial RN concentrations needed for the flow and transport modeling. Please indicate where this missing data is documented.	This sentence has been deleted. It was out of place given the context of this section. Sections 1.3 and 1.4 list supporting documents. Initial RN masses, not concentrations, are input to the 3-D PM CAU transport model. As noted in Section 5.1.3, the available mass of RNs at each detonation location is calculated from the yield-weighted fraction of the inventory in Finnegan et al. (2016), using the maximum of the announced yield range given in DOE/NV 209--Rev. 16 (NNSA/NFO, 2015b) (except for HANDLEY, for which the minimum of the yield range is used), and decay-corrected using the method described in Tompson et al. (2019).
9.	Page 3, Section 1.0, Partial Paragraph on Top of Page, First and Second Full Sentences		Please explain in the text how the lack of representation of the actual extent of contamination in groundwater provides confidence in the flow and transport model and understanding of the system.	Replaced the last sentence: "Calibration of the PM CAU model to a range of observational data using the parameter values within ranges of parameter uncertainty and the similarity of the resulting groundwater flow paths to observed ^{3}H migration paths provided confidence that the PM CAU flow model adequately simulates observed hydraulic conditions in the PM-OV flow system and supports understanding of the flow system. The probabilistic forecasts of the CB were generated using the full range of transport parameter uncertainty rather than narrowing on the calibrated values. Hence, they are larger than would be expected on the basis of calibrated parameter values and are protective of human health."

[a]Comment Types: M = Mandatory, S = Suggested.
Return Document Review Sheets to Environmental Management Nevada Program Operations Activity, Attn: QAC, M/S NSF 505

NEVADA ENVIRONMENTAL MANAGEMENT OPERATIONS ACTIVITY
DOCUMENT REVIEW SHEET

1. Document Title/Number: Groundwater Flow and Contaminant Transport Model of Corrective Action Units (CAUs) 101 and 102: Central and Western Pahute Mesa, Nye County, Nevada	2. Document Date: March, 2022
3. Revision Number: Rev 0	4. Originator/Organization: Environmental Management Nevada Program
5. Responsible EM Nevada Program Activity Lead: John Myers	6. Date Comments Due: May 13, 2022
7. Review Criteria:	
8. Reviewer/Organization Phone No.: Christine Andres (NDEP), Britt Jacobson (NDEP Contractor)	9. Reviewer's Signature:

10. Comment Number/Location		11. Type[a]	12. Comment	13. Comment Response
10.	Page 67, Section 3.0, Second Paragraph, Last Sentence		Please explain in the text why a more conservative approach was selected when faced with choices. How does this philosophy correlate with the need to produce realistic flow and transport forecasts?	Replace the last sentence: "Confidence in the PM CAU flow and transport model was increased by calibration of the model to observed hydraulic and RN data using the parameter values within ranges of parameter uncertainty. The philosophy adopted in model development was to be conservative in the modeling assumptions when they were likely, judged on the basis of theoretical and numerical considerations, to affect the forecast extent and magnitude of RN transport, especially when data were sparse or may be subject to alternative interpretations or when the conceptual model was likely to lead to significant increase in computational burden. This philosophy led to the decisions regarding models or parameter values that lead to a calibrated PM CAU flow and transport model that, while realistically reproducing many hydraulic and transport aspects of the system, tends to overestimate the potential contaminant transport. Since the calibrated transport model parameters represent the realistic case, the CB calculations using the full range of parameter uncertainty encompass the realistic case as well as forecasting up to a 95 percent case."

[a]Comment Types: M = Mandatory, S = Suggested.
Return Document Review Sheets to Environmental Management Nevada Program Operations Activity, Attn: QAC, M/S NSF 505

NEVADA ENVIRONMENTAL MANAGEMENT OPERATIONS ACTIVITY
DOCUMENT REVIEW SHEET

1. Document Title/Number: Groundwater Flow and Contaminant Transport Model of Corrective Action Units (CAUs) 101 and 102: Central and Western Pahute Mesa, Nye County, Nevada				2. Document Date: March, 2022
3. Revision Number: Rev 0				4. Originator/Organization: Environmental Management Nevada Program
5. Responsible EM Nevada Program Activity Lead: John Myers				6. Date Comments Due: May 13, 2022
7. Review Criteria:				
8. Reviewer/Organization Phone No.: Christine Andres (NDEP), Britt Jacobson (NDEP Contractor)				9. Reviewer's Signature:
10. Comment Number/Location		11. Type[a]	12. Comment	13. Comment Response
11.	Page 76, Section 4.1.2, Third Paragraph, Last Sentence		Please include in the text where the ET estimate is documented.	Added reference to Reiner et al., 2002. Changed beginning of the paragraph to read: "A best estimate for groundwater discharges to springs and seeps in Oasis Valley is 5,900 ac-ft/yr (7,268,800 m^3/yr) and may range from 5,000 to 6,800 ac-ft/yr (Fenelon et al., 2016). Laczniak et al. (2001) performed a Monte Carlo uncertainty analysis of groundwater discharge for DVRFS3 and estimated a discharge range of approximately 4,200 to 8,900 ac-ft/yr within the PM-OV groundwater basin. Both studies cite the source of the discharge data as Reiner et al. (2002). However, the lower- and upper-end values estimated by Laczniak et al. (2001) are unlikely because these estimates represent the low-probability input parameters on the tails of the parameter distributions used in the analysis." Changed second-to-last sentence to read: "The best estimate of total recharge generated within the PM-OV groundwater basin…."
12.	Page 84, Section 4.1.4.1, Table 4-1		For HSUs CHLFA and PBRCM, a standard deviation based on two points is not appropriate. Please modify this table.	Column with standard deviation removed from Table 4-1.
13.	Page 91, Section 4.1.5, Second Bullet, Last Sentence		Is the 2010 well discharge included or used in the modeling? Please clarify.	Added statement: "Water production is assumed to be negligible compared to total basin flow and is not included in the flow models."

[a]Comment Types: M = Mandatory, S = Suggested.
Return Document Review Sheets to Environmental Management Nevada Program Operations Activity, Attn: QAC, M/S NSF 505

NEVADA ENVIRONMENTAL MANAGEMENT OPERATIONS ACTIVITY
DOCUMENT REVIEW SHEET

1. Document Title/Number: Groundwater Flow and Contaminant Transport Model of Corrective Action Units (CAUs) 101 and 102: Central and Western Pahute Mesa, Nye County, Nevada				2. Document Date: March, 2022
3. Revision Number: Rev 0				4. Originator/Organization: Environmental Management Nevada Program
5. Responsible EM Nevada Program Activity Lead: John Myers				6. Date Comments Due: May 13, 2022
7. Review Criteria:				
8. Reviewer/Organization Phone No.: Christine Andres (NDEP), Britt Jacobson (NDEP Contractor)				9. Reviewer's Signature:
10. Comment Number/Location		11. Type[a]	12. Comment	13. Comment Response
14.	Page 94, Section 4.2.2, Third Paragraph, Fourth Sentence		This sentence needs to be reworded for clarity.	Deleted the fifth sentence. Changed fourth sentence to read: "A low hydraulic conductivity deep aquifer zone was defined at depths greater than 2,500 ft (762 m) below the water table, which allows areas of transmissive aquifer within 2,500 ft of the water table where needed to match observed drawdowns from aquifer testing and deep ^{3}H measurements." Changed the first four sentences of Section 4.2.2 to: "The largest transmissivity and majority of flow generally occurs in the first 1,600 ft (488 m) below the water table (Jackson et al., 2021). However, areas of deep conductive aquifer are present in the PM subsurface. Garcia et al. (2017) estimated that 70 percent of the transmissivity at Well ER-EC-11 occurs between 1,000 and 3,000 ft (305 to 914 m) below the water table, and ^{3}H has been measured within the lower completion Well ER-20-12 at a depth of approximately 2,500 ft (762 m) below the water table due to an apparently permeable pathway from the HANDLEY test (Jackson, 2021). A low hydraulic conductivity deep aquifer zone was defined at depths greater than 2,500 ft (762 m) of the water table, which allows areas of transmissive aquifer within 2,500 ft of the water table where needed to match observed drawdowns from aquifer testing and deep ^{3}H measurements."

[a]Comment Types: M = Mandatory, S = Suggested.
Return Document Review Sheets to Environmental Management Nevada Program Operations Activity, Attn: QAC, M/S NSF 505

NEVADA ENVIRONMENTAL MANAGEMENT OPERATIONS ACTIVITY
DOCUMENT REVIEW SHEET

1. Document Title/Number: Groundwater Flow and Contaminant Transport Model of Corrective Action Units (CAUs) 101 and 102: Central and Western Pahute Mesa, Nye County, Nevada				2. Document Date: March, 2022
3. Revision Number: Rev 0				4. Originator/Organization: Environmental Management Nevada Program
5. Responsible EM Nevada Program Activity Lead: John Myers				6. Date Comments Due: May 13, 2022
7. Review Criteria:				
8. Reviewer/Organization Phone No.: Christine Andres (NDEP), Britt Jacobson (NDEP Contractor)				9. Reviewer's Signature:
10. Comment Number/Location		11. Type[a]	12. Comment	13. Comment Response
15.	Page 95, Section 4.2.3, Second Paragraph, Fourth Sentence		Please include in the text the basis of the increase in recharge by a factor of ten. How does this increase in recharge effect the water balance? Please include a discussion in the text.	Added the following discussion: "A factor of 10 increase in the amount of recharge near Black Mountain was estimated by matching the travel times of ^{3}H from HANDLEY to Wells ER-20-12 and PM-3. Travel time calculations used an effective porosity of 0.01, which resulted in flow path velocities consistent with ^{3}H migration distances downgradient of the BENHAM and TYBO nuclear tests measured in Wells ER-20-5, ER-20-7, ER-20-11, and ER-EC-11. A value of 0.01 for porosity is relatively large compared to data from tracer tests and fracture data, and represents an effective transport porosity that uses a larger value to approximate the retarding effects of matrix diffusion. A factor of 10 increase of recharge near Black Mountain increased the total basin flow by approximately 12 percent. Fenelon et al. (2016) estimated the uncertainty of total basin flow to be approximately 15 percent."
16.	Page 99, Section 4.2.4.1, First Full Paragraph, First Sentence		Please indicate the location where the hydraulic gradients are documented or referenced.	Added the following: "The hydraulic gradients were calculated from the water-level data of Jackson et al. (2021) using the straight-line distance between wells." Citation added to Table C-4 of the HDD: Navarro, 2021b: *Hydrologic Data for the Groundwater Flow and Contaminant Transport Model of Corrective Action Units 101 and 102: Central and Western Pahute Mesa, Nye County, Nevada. Rev 01*. N/0002653-073.

[a]Comment Types: M = Mandatory, S = Suggested.
Return Document Review Sheets to Environmental Management Nevada Program Operations Activity, Attn: QAC, M/S NSF 505

NEVADA ENVIRONMENTAL MANAGEMENT OPERATIONS ACTIVITY
DOCUMENT REVIEW SHEET

1. Document Title/Number: Groundwater Flow and Contaminant Transport Model of Corrective Action Units (CAUs) 101 and 102: Central and Western Pahute Mesa, Nye County, Nevada	2. Document Date: March, 2022
3. Revision Number: Rev 0	4. Originator/Organization: Environmental Management Nevada Program
5. Responsible EM Nevada Program Activity Lead: John Myers	6. Date Comments Due: May 13, 2022
7. Review Criteria:	
8. Reviewer/Organization Phone No.: Christine Andres (NDEP), Britt Jacobson (NDEP Contractor)	9. Reviewer's Signature:

10. Comment Number/Location		11. Type[a]	12. Comment	13. Comment Response
17.	Page 101, Section 4.2.4.1, First Paragraph, Last Sentence		Please explain in the text why the specified value of transmissivity (100m2/day) was selected and the reason this value was applied to the entire model thickness.	Added the following discussion and a reference to Halford and Jackson (2020). "The approximate threshold of 100 m^2/day to determine whether the well screen thickness or entire model thickness is used to calculate model transmissivity from model hydraulic conductivity was taken from the approach used by Halford and Jackson (2020) for the DVRFS3 modeling and simple reasoning that larger pumping rates draw water from a thicker section of the aquifer. Halford and Jackson (2020) state: "For aquifer tests where transmissivity was less than 1,000 ft^2/d or small volumes of water were pumped, the contributing thickness was limited to the well screen length. For aquifer tests where transmissivity exceeded 1,000 ft^2/d or large volumes (more than 100,000 gal) of water were pumped (Halford and others, 2006), the contributing thickness was the aquifer thickness from the DV3 hydrogeologic framework model." "
18.	Page 112, Figure 4-14		This Figure shows simulated travel time (days) ranging from <10k to 90k southwest from PM-3. What is the basis for this range in simulated travel time in this area when there are no downgradient wells?	The basis for the range in simulated travel time is simulations from the model calibrated to all available data throughout the model domain, particularly the general agreement of flow path travel times between HANDLEY and Wells ER-20-12 and PM-3 with ^3H travel times. It is acknowledged that uncertainty in the flow and transport model results in the vicinity of HANDLEY, ER-20-12, and PM-3 will continue to be evaluated in future discussions.

[a]Comment Types: M = Mandatory, S = Suggested.
Return Document Review Sheets to Environmental Management Nevada Program Operations Activity, Attn: QAC, M/S NSF 505

NEVADA ENVIRONMENTAL MANAGEMENT OPERATIONS ACTIVITY
DOCUMENT REVIEW SHEET

1. Document Title/Number: Groundwater Flow and Contaminant Transport Model of Corrective Action Units (CAUs) 101 and 102: Central and Western Pahute Mesa, Nye County, Nevada				2. Document Date: March, 2022
3. Revision Number: Rev 0				4. Originator/Organization: Environmental Management Nevada Program
5. Responsible EM Nevada Program Activity Lead: John Myers				6. Date Comments Due: May 13, 2022
7. Review Criteria:				
8. Reviewer/Organization Phone No.: Christine Andres (NDEP), Britt Jacobson (NDEP Contractor)				9. Reviewer's Signature:
10. Comment Number/Location		11. Type[a]	12. Comment	13. Comment Response
19.	Page 128, Section 4.3.2, Fourth sentence		This sentence indicates that a recharge increase for Black Mountain was required to calibrate the base case model. Please explain in the text the impact to the water balance with this increase in recharge. Also see the sentence beginning on the bottom of Page 152 and continuing on the top of Page 153.	Added after the fourth sentence: "A factor of 10 increase of recharge near Black Mountain increased the total basin flow by approximately 12 percent, which is within the estimated uncertainty of total basin flow of approximately 15 percent given by Fenelon et al. (2016)." Added after the last sentence: "The recharge near Black Mountain was not increased in the INFILv3 and DVRFS3 alternative recharge models; both have higher recharge in the Black Mountain area compared to the original recharge distribution from Fenelon et al. (2016) used in the base case model prior to the increase. Also see comment 15 response.

[a]Comment Types: M = Mandatory, S = Suggested.
Return Document Review Sheets to Environmental Management Nevada Program Operations Activity, Attn: QAC, M/S NSF 505

NEVADA ENVIRONMENTAL MANAGEMENT OPERATIONS ACTIVITY
DOCUMENT REVIEW SHEET

1. Document Title/Number: Groundwater Flow and Contaminant Transport Model of Corrective Action Units (CAUs) 101 and 102: Central and Western Pahute Mesa, Nye County, Nevada				2. Document Date: March, 2022
3. Revision Number: Rev 0				4. Originator/Organization: Environmental Management Nevada Program
5. Responsible EM Nevada Program Activity Lead: John Myers				6. Date Comments Due: May 13, 2022
7. Review Criteria:				
8. Reviewer/Organization Phone No.: Christine Andres (NDEP), Britt Jacobson (NDEP Contractor)				9. Reviewer's Signature:
10. Comment Number/Location		11. Type[a]	12. Comment	13. Comment Response
20.	Page 145, Section 4.4.2, Second Paragraph, Fourth Sentence		Please explain in the text why the models were made overly conservative when the metric used for evaluating groundwater flow paths from the different models was the minimum distance of any flow path endpoint to the Springdale Lower Well at 200 years.	Added at the end of Section 4.4.2: "Distance to the Springdale Lower Well is a convenient metric for nearness of contamination to the receptors, and it can be used regardless of source locations. Focusing on the various flow models under discussion, only INFILv3 recharge model using a recharge boundary condition from Middleton et al. (2019) is possibly overly conservative by having a total basin flow at the upper bounds of possible basin flows. However, the INFILv3 modeling of Middleton et al. (2019) used daily data from 26 meteorological stations in the NNSS area to constrain the water balance. The INFILv3 modeling also used shallow water-table fluctuations to evaluate model estimates of deep net infiltration beneath canyons and performed comparisons between estimates of modeled net infiltration with infiltration estimates based on the chloride mass balance method. All flow models, including the INFILv3 recharge model, have good agreement with steady-state heads, drawdowns from well development and testing, total basin flow, hydraulic gradients, and interpreted flow path directions from geochemistry data and RN concentrations." Added a discussion of the possible range in total basin flow to Section 4.1.2 (see comment 21 response) and additional discussion of the Middleton et al. (2019) modeling to Section 4.3.2.2.
21.	Page 155, Section 4.5, Second Bullet, Second Sentence		Please document in the text the possible range in total basin flow.	Added the following discussion to Section 4.1.2: "A best estimate for groundwater discharges to springs and seeps in Oasis Valley is 5,900 ac-ft/yr (7,268,800 m^3/yr) and may range from 5,000 to 6,800 ac-ft/yr (Fenelon et al., 2016). Laczniak et al. (2001) performed a Monte Carlo uncertainty analysis of groundwater discharge for DVRFS3 and estimated a discharge range of approximately 4,200 to 8,900 ac-ft/yr within the PM-OV groundwater basin. Both studies cite the source of the discharge data as Reiner et al. (2002). However, the lower- and upper-end values estimated by Laczniak et al. (2001) are unlikely because these estimates represent the low-probability input parameters on the tails of the parameter distributions used in the analysis."

[a]Comment Types: M = Mandatory, S = Suggested.
Return Document Review Sheets to Environmental Management Nevada Program Operations Activity, Attn: QAC, M/S NSF 505

NEVADA ENVIRONMENTAL MANAGEMENT OPERATIONS ACTIVITY
DOCUMENT REVIEW SHEET

1. Document Title/Number: Groundwater Flow and Contaminant Transport Model of Corrective Action Units (CAUs) 101 and 102: Central and Western Pahute Mesa, Nye County, Nevada	2. Document Date: March, 2022
3. Revision Number: Rev 0	4. Originator/Organization: Environmental Management Nevada Program
5. Responsible EM Nevada Program Activity Lead: John Myers	6. Date Comments Due: May 13, 2022
7. Review Criteria:	
8. Reviewer/Organization Phone No.: Christine Andres (NDEP), Britt Jacobson (NDEP Contractor)	9. Reviewer's Signature:

10. Comment Number/Location		11. Type[a]	12. Comment	13. Comment Response
22.	Page 200, Section 5.4, Second Paragraph, Fifth Sentence		Was the possible effect or error introduced by this averaging evaluated? If so, where is it documented and if not, please explain why there was no need to evaluate it.	Inserted in the text: "The flow model is an approximation of the HFM, and the transport model is a slightly different approximation of the HFM. The flow model uses artificial stairstepping, as necessitated by MODFLOW, to approximate the water table surface and HSU horizons. The transport model uses sloping planes to approximate the same water table surface and HSU horizons, as necessitated by WALKABOUT. Both approximations are necessitated by the computational methods used in the codes. At a vertical interface between two adjacent cells, the z-coordinates of cell interface vertices are the averages of respective common vertices. Velocities at respective common vertices are calculated by averaging the vertices' velocities from all adjacent cells with the same common vertices. This type of averaging is valid whether or not the grid layer is stairstepping or completely horizontal. This methodology is different from what is used in the USGS MODPATH 7 code, which was developed by the USGS specifically to perform particle tracking based on MODFLOW 6 simulations. MODPATH 7 can be used to simulate advection; however, it does not have the capability to perform all the necessary transport process simulation (e.g., dispersion, matrix diffusion, radioactive decay) and was not selected. The adopted methodology yields excellent results when material properties are homogeneous. The PM CAU model has a high degree of heterogeneity. Because of vertices averaging, heterogeneity can give rise to slightly different local velocity distributions. The combined effects of the heterogeneity and z-coordinate averaging at the site scale were investigated and documented in Appendix E of the report by comparing results based on MODPATH 7 and WALKABOUT. As indicated in Appendix E, it was found that flow patterns and directions based on WALKABOUT and MODPATH 7 were similar, with some differences noted between the flow paths calculated by the two codes due to the high degree of heterogeneity in the PM CAU model."

[a]Comment Types: M = Mandatory, S = Suggested.
Return Document Review Sheets to Environmental Management Nevada Program Operations Activity, Attn: QAC, M/S NSF 505

NEVADA ENVIRONMENTAL MANAGEMENT OPERATIONS ACTIVITY
DOCUMENT REVIEW SHEET

1. Document Title/Number: Groundwater Flow and Contaminant Transport Model of Corrective Action Units (CAUs) 101 and 102: Central and Western Pahute Mesa, Nye County, Nevada				2. Document Date: March, 2022
3. Revision Number: Rev 0				4. Originator/Organization: Environmental Management Nevada Program
5. Responsible EM Nevada Program Activity Lead: John Myers				6. Date Comments Due: May 13, 2022
7. Review Criteria:				
8. Reviewer/Organization Phone No.: Christine Andres (NDEP), Britt Jacobson (NDEP Contractor)				9. Reviewer's Signature:
10. Comment Number/Location		11. Type[a]	12. Comment	13. Comment Response
23.	Page 229, Section 5.5.1.3, First Paragraph, Last Sentence		Was the observation location shifted to the west to test or evaluate this statement? If so, where is it documented and if not, please explain in the text why this evaluation was not needed.	There is a typo in this paragraph: the deeper flow path is to the east of the chosen observation location for ER-20-5-3. The text has been changed to correct this. A new figure has been added after Figure 5-21 that displays the modeled vs. measured ^{3}H concentrations from the calibrated model at ER-20-5-3 using an observation location that has been adjusted one node to the east. Additional discussion has been added to clarify that this adjusted observation location was not used in the calibration.
24.	Page 248, Section 5.5.1.3.2, Second Paragraph, Last Partial Sentence		Was the adjustment by one node made to evaluate this statement? If so, where is it documented and if not, please explain in the text why this evaluation was not needed.	A new figure has been added after Figure 5-44 in Section 5.5.1.3 (where the ^{3}H results for ER-20-1 are first presented) that displays the modeled vs. measured ^{3}H concentrations from the calibrated model at ER-20-1 using an observation location that has been adjusted one node to the east. Additional discussion has been added to clarify that this adjusted observation location was not used in the calibration. In Section 5.5.1.3.2, a reference to the new figure in Section 5.5.1.3 has been added.
25.	Page 263, Section 5.5.1.4.2, First Paragraph, Last Sentence		Was there any other possible explanation suggested? If so, please include it in the text.	Inserted in the text: "In the discussion of calibrated ^{3}H results in Section 5.5.1.3, it is stated that the observation locations at the postshot holes are coincident with nodes where the source particles are located, meaning that very little transport has occurred between source locations and measurement locations. Because of this and because ^{36}Cl is nonsorbing, the only feasible explanation for the overprediction of ^{36}Cl at some postshot locations is that the source mass input to the model at these locations is high."

[a]Comment Types: M = Mandatory, S = Suggested.
Return Document Review Sheets to Environmental Management Nevada Program Operations Activity, Attn: QAC, M/S NSF 505

NEVADA ENVIRONMENTAL MANAGEMENT OPERATIONS ACTIVITY
DOCUMENT REVIEW SHEET

1. Document Title/Number: Groundwater Flow and Contaminant Transport Model of Corrective Action Units (CAUs) 101 and 102: Central and Western Pahute Mesa, Nye County, Nevada				2. Document Date: March, 2022
3. Revision Number: Rev 0				4. Originator/Organization: Environmental Management Nevada Program
5. Responsible EM Nevada Program Activity Lead: John Myers				6. Date Comments Due: May 13, 2022
7. Review Criteria:				
8. Reviewer/Organization Phone No.: Christine Andres (NDEP), Britt Jacobson (NDEP Contractor)				9. Reviewer's Signature:
10. Comment Number/Location		11. Type[a]	12. Comment	13. Comment Response
26.	Page 278, Section 5.5.2, First Paragraph, Last Sentence		For the three alternatives calibrated, is the 10x Black Mountain recharge included?	Added the following discussion to Section 5.5.2: "The base case and all-faults alterative flow models use the same recharge boundary condition, which includes increased recharge near Black Mountain. The recharge near Black Mountain was not modified in the INFILv3 and DVRFS3 alternative recharge models, which both have higher recharge in the Black Mountain area compared to the original recharge distribution from Fenelon et al. (2016) used in the base case model before modification." Also added more discussion of the recharge boundary conditions used by the alternative models in Sections 4.3.1 and 4.3.2.
27.	Page 298, Figure 5-86		In the Figure, the CB of the Base Case off the NNSS is at shallower depths. Please explain in the text how these depths compare to the screened intervals of the surrounding monitoring wells?	For the base case model, further discussion has been added at the end of Section 5.5.2.1.1 (after Figure 5-86 is introduced) to compare depths to screened intervals in wells located within the CB just outside the NNSS boundary. Similar discussion has been added at the end of Sections 5.5.2.1.2 (for INFILv3 alternative case), 5.5.2.1.3 (for DVRFS3 alternative case), and 5.5.2.1.4 (for all-faults alternative case).

[a]Comment Types: M = Mandatory, S = Suggested.
Return Document Review Sheets to Environmental Management Nevada Program Operations Activity, Attn: QAC, M/S NSF 505

NEVADA ENVIRONMENTAL MANAGEMENT OPERATIONS ACTIVITY
DOCUMENT REVIEW SHEET

1. Document Title/Number: Groundwater Flow and Contaminant Transport Model of Corrective Action Units (CAUs) 101 and 102: Central and Western Pahute Mesa, Nye County, Nevada				2. Document Date: March, 2022
3. Revision Number: Rev 0				4. Originator/Organization: Environmental Management Nevada Program
5. Responsible EM Nevada Program Activity Lead: John Myers				6. Date Comments Due: May 13, 2022
7. Review Criteria:				
8. Reviewer/Organization Phone No.: Christine Andres (NDEP), Britt Jacobson (NDEP Contractor)				9. Reviewer's Signature:
10. Comment Number/Location		11. Type[a]	12. Comment	13. Comment Response
28.	Page 325, Section 5.6.5, First Paragraph, Last Sentence		Is it correct to infer from this sentence that 20,000 particles will be used for transport modeling or is this sentence just stating a result?	Yes. Sentence has been changed to read, "Using 10 times the number of particles used in the Monte Carlo simulations…" A statement has been added at the beginning of Section 5.6.5 to clarify that the calibration and Monte Carlo simulations used up to 20,000 particles. Similarly, a statement has been added at the beginning of Section 5.6.4 to clarify that the calibration and Monte Carlo simulations used the average melt glass percentage. Similarly, a statement has been added at the beginning of Section 5.6.3 to clarify that the calibration and Monte Carlo simulations used a longitudinal dispersivity of 150 m, a transverse horizontal dispersivity of 15 m, and a transverse vertical dispersivity of 1.5 m.
29.	Page 329, Section 5.6.6, Last Paragraph, Third Sentence		Were conclusions similar to those from RM/SM and expected at PM indeed observed at PM as indicated in this sentence? Please indicate in the text.	Section 5.6.6 has been deleted because it does not provide additional insights into PM CAU model sensitivity.

[a]Comment Types: M = Mandatory, S = Suggested.
Return Document Review Sheets to Environmental Management Nevada Program Operations Activity, Attn: QAC, M/S NSF 505

NEVADA ENVIRONMENTAL MANAGEMENT OPERATIONS ACTIVITY
DOCUMENT REVIEW SHEET

1. Document Title/Number: Groundwater Flow and Contaminant Transport Model of Corrective Action Units (CAUs) 101 and 102: Central and Western Pahute Mesa, Nye County, Nevada				2. Document Date: March, 2022
3. Revision Number: Rev 0				4. Originator/Organization: Environmental Management Nevada Program
5. Responsible EM Nevada Program Activity Lead: John Myers				6. Date Comments Due: May 13, 2022
7. Review Criteria:				
8. Reviewer/Organization Phone No.: Christine Andres (NDEP), Britt Jacobson (NDEP Contractor)				9. Reviewer's Signature:
10. Comment Number/Location		11. Type[a]	12. Comment	13. Comment Response
30.	Page 336, Section 5.8, Paragraph below Bullets, First Sentence		This statement about forecasted CB ensemble is presented before the forecasted CB ensemble is presented in Section 6. The summary on this page concerns observations made from the PM CAU transport model results. Please move this sentence to a more appropriate place in the Document.	The CB ensemble is first presented in Section 5.7. The location of this statement in the summary is appropriate. This statement has been incorporated into the bulleted list and references to appropriate figures in Section 5.7 have been added.
31.	Page 354, Section 7.1, Partial Paragraph at Top of Page, Last Sentence		Please explain how "adequately" is determined, who makes this determination, and for what application (i.e., location of monitoring wells, determination of the contaminant boundaries based on the ensembles, realism of the flow and transport system in the Pahute Mesa modeling domain)?	Deleted "adequately." Reworded the sentence to read, "The calibration used a range of observational data, and the similarity of the resulting groundwater flow paths to observed ^{3}H migration paths increased confidence in the ability of the PM CAU flow model to simulate observed hydraulic conditions in the PM-OV flow system."

[a]Comment Types: M = Mandatory, S = Suggested.
Return Document Review Sheets to Environmental Management Nevada Program Operations Activity, Attn: QAC, M/S NSF 505

NEVADA ENVIRONMENTAL MANAGEMENT OPERATIONS ACTIVITY
DOCUMENT REVIEW SHEET

1. Document Title/Number: Groundwater Flow and Contaminant Transport Model of Corrective Action Units (CAUs) 101 and 102: Central and Western Pahute Mesa, Nye County, Nevada				2. Document Date: March, 2022
3. Revision Number: Rev 0				4. Originator/Organization: Environmental Management Nevada Program
5. Responsible EM Nevada Program Activity Lead: John Myers				6. Date Comments Due: May 13, 2022
7. Review Criteria:				
8. Reviewer/Organization Phone No.: Christine Andres (NDEP), Britt Jacobson (NDEP Contractor)				9. Reviewer's Signature:
10. Comment Number/Location		11. Type[a]	12. Comment	13. Comment Response
32.	Page E-17, Section E.4.1, Equations (E-5a) and (E-5b)		The last portions of the two equations are the same. Please clarify in the text, otherwise this may imply that the velocities in the x and y directions are the same.	Typos in the bi term and in the K_H term. Also defined Kx, Ky, and Kz. Corrected pp E-17 and E-18 as follows:

[a]Comment Types: M = Mandatory, S = Suggested.
Return Document Review Sheets to Environmental Management Nevada Program Operations Activity, Attn: QAC, M/S NSF 505

E.4.0 Transfer of Information from Cell Centroids to Cell Vertices

MODFLOW6 calculates hydraulic heads and intercell fluxes at respective cell centroids and across respective cell common faces. To use Walkabout for particle tracking, it is essential that all the information be transferred to the cell vertices. This requirement can be achieved by connecting all the vertices of each MODFLOW cell through tetrahedral subdivision (Figure E-3), thereby transforming the MODFLOW cells into a finite-element mesh with tetrahedral elements.

For each node 'i' of the finite-element mesh, a nodal head (head at a vertex) may be calculated as an average over the cell centroids of the MODFLOW6 cells connected to the node by the equation:

$$H_i = \frac{1}{n_i}\left(\sum_{j=1}^{n} H_{ij}\right) \qquad \text{(E-1)}$$

where:
H_i = Average head at node i;
H_{ij} = Head at node i due to cell j;
n_i = Number of cells with node i as one of the connected nodes

E.4.1) Calculations of Hydraulic Gradients and Velocities

In each tetrahedral finite element, the variation of head is governed by the equation, using the upper case 'I' to denote the local number of the node with the global number 'i':

$$\hat{H} = \left(\sum_{I=1}^{4} N_I H_I\right) \qquad \text{(E-2)}$$

where:
$\hat{H}$ = Head at any point (x,y,z) within a tetrahedral element;
H_I = Head at node I. Here the index upper case 'I' is being used with respect to the specific finite element under consideration, to corresponding to the global node number 'i' given in Eq. E-1;
N_I = Basis function within the element associated with node I of a tetrahedral element

The linear basis function associated with the node I in Equation E-2 is given by Zienkiewicz and Cheung (1967):

$$N_I = a_I + b_I x + c_I y + d_I z \qquad \text{(E-3)}$$
$$\sum N_I = 1$$

where:
a_I, b_I, c_I, d_I = Constants;
x, y, z = Cartesian coordinates

The constants in Equation E-3 in a tetrahedral element, defined by Nodes with global numbers i, j, m, and p (corresponding to local numbers I, J, M and P) (see Figure E-2) are defined by the following:

$$a_I = \frac{1}{6V}det\begin{bmatrix} x_j & y_j & z_j \\ x_m & y_m & z_m \\ x_p & y_p & z_p \end{bmatrix} \qquad \text{(E-4a)}$$

$$b_I = \frac{1}{6V}det\begin{bmatrix} 1 & y_j & z_j \\ 1 & y_m & z_m \\ 1 & y_p & z_p \end{bmatrix} \qquad \text{(E-4b)}$$

$$c_I = \frac{1}{6V}det\begin{bmatrix} x_j & 1 & z_j \\ x_m & 1 & z_m \\ x_p & 1 & z_p \end{bmatrix} \qquad \text{(E-4c)}$$

$$d_I = \frac{1}{6V}det\begin{bmatrix} x_j & y_j & 1 \\ x_m & y_m & 1 \\ x_p & y_p & 1 \end{bmatrix} \qquad \text{(E-4d)}$$

$$V = \frac{1}{6}det\begin{bmatrix} 1 & x_i & y_i & z_i \\ 1 & x_j & y_j & z_j \\ 1 & x_m & y_m & z_m \\ 1 & x_p & y_p & z_p \end{bmatrix} \qquad \text{(E-4e)}$$

where:
det = Determinant;
V = Volume of the tetrahedral element

Velocities in the x, y, and z directions, v_{xe}, v_{ye}, and v_{ze}, in tetrahedral element e, defined by Nodes i, j, m, and p, with Kx, Ky, Kz hydraulic conductivity in x,y,z directions, are given by

$$v_{xe} = -\frac{K_x}{\theta}\frac{\partial H}{\partial x} \approx -\frac{K_x}{\theta}\frac{\partial \hat{H}}{\partial x} = -\frac{K_x}{\theta}\sum_{I=1}^{4} b_I H_I \qquad \text{(E-5a)}$$

[a]Comment Types: M = Mandatory, S = Suggested.
Return Document Review Sheets to Environmental Management Nevada Program Operations Activity, Attn: QAC, M/S NSF 505

NEVADA ENVIRONMENTAL MANAGEMENT OPERATIONS ACTIVITY
DOCUMENT REVIEW SHEET

1. Document Title/Number: Groundwater Flow and Contaminant Transport Model of Corrective Action Units (CAUs) 101 and 102: Central and Western Pahute Mesa, Nye County, Nevada				2. Document Date: March, 2022
3. Revision Number: Rev 0				4. Originator/Organization: Environmental Management Nevada Program
5. Responsible EM Nevada Program Activity Lead: John Myers				6. Date Comments Due: May 13, 2022
7. Review Criteria:				
8. Reviewer/Organization Phone No.: Christine Andres (NDEP), Britt Jacobson (NDEP Contractor)				9. Reviewer's Signature:
10. Comment Number/Location		11. Type[a]	12. Comment	13. Comment Response
33.	Page E-18, Section E.4.1, Equations (E-7a) and (E-7b)		The last portions of the two equations are the same. Please clarify in the text, otherwise this may imply that the velocities in the x and y directions are the same. Also, how is the fv factor obtained?	7-a and 7-b are not the same. 7-a has Vx and 7-b has Vy. Added definition of fv.
34.	Page E-20, Section E.4.3, Second Paragraph, Last Sentence		Please include a discussion in the text of how the boundary element correction in Equation E-7 is determined?	Added after Equation E-7c: "Nodal velocities at boundary nodes in the above equations may be found by extrapolating from interior nodes. Alternatively, they can be determined using known flow conditions along the boundaries."
35.	Page E-25 of Appendix E, Section E.5.2.1, First Full Paragraph, Last Sentence		Equation (E-9) on Page E-27 is an analytical equation; it does not have a correction. Please clarify this in the text.	Added to text: "Note that Equation (E-9) is an analytical solution that operates between x = 3 m and 12 m, and does not include any of the aforementioned corrections."

[a]Comment Types: M = Mandatory, S = Suggested.
Return Document Review Sheets to Environmental Management Nevada Program Operations Activity, Attn: QAC, M/S NSF 505

NEVADA ENVIRONMENTAL MANAGEMENT OPERATIONS ACTIVITY
DOCUMENT REVIEW SHEET

Listed below are additional revisions identified by Navarro UGTA Activity participants after the NDEP review.

Comment Number/Location		Comment	Comment Response
36	Page ES-4, para 1	You may want to add the FFACO statement so the basis for corrective action alternative isn't just cost: Finally, the important potential risks from radiological contamination of groundwater are to workers, the public, and the environment; and exposure to these risks requires access to groundwater.	Added.
37	ES-5, para 3	It is not clear how the calculations "minimize health risks". Overly conservative forecasts don't really minimize risk. Used to develop use-restrictions?	Changed to “planning tools intended to facilitate regulatory decisions designed to protect the health and safety of the public.”
38	ES-5, para 3, last sentence	Delete “planned”	Deleted.
39	ES-6, 2nd bullet, 6th line	Change: base range” to range of base case”	Changed.
40	ES-7,1st bullet in the second set of bullets	Remove excess space	Removed.
41	ES-10, 1st full para, 2nd line	Change ‘exists’ to ‘exist’	Changed.
42	ES-10, 2nd para, 9th line	Change PM-OV to PM CAU	Changed.
43	Pp ES-12, 1st full para, 6th line	Change were to was	Stet change (subjunctive mood for condition contrary to fact).
44	Pp ES-14, 3rd line	Insert (INFILv3 and DVRFS3)	Inserted.
45	Pp ES-14, 1st para	Change PM-OV to PM CAU	Changed.
46	Fig ES-7, legend	Maybe add a note: values greater than 1 exceed the MCL	Changed legend to “Concentration relative to MCL.”
47	Fig ES-7, legend	Insert ‘Deep” in ‘PM Detonations’	Inserted.
48	Fig ES-7	Delete “MCL = 1….”	Deleted.
49	Fig ES-7 caption	Delete ‘contamination form calibration’	Changed caption to “Simulated Extent of ^{3}H from Calibrated PM CAU Transport Model at 55 Years (2020).”

[a]Comment Types: M = Mandatory, S = Suggested.
Return Document Review Sheets to Environmental Management Nevada Program Operations Activity, Attn: QAC, M/S NSF 505

NEVADA ENVIRONMENTAL MANAGEMENT OPERATIONS ACTIVITY
DOCUMENT REVIEW SHEET

Listed below are additional revisions identified by Navarro UGTA Activity participants after the NDEP review.

Comment Number/Location		Comment	Comment Response
50	Fig ES-9 legend	Insert ‘deep’ in ‘PM Detonations’	Inserted.
51	Pp ES-20 3rd para, line 2	120 years is stated above	Changed to 120.
52	Pp ES-20, 3rd para, line 4	This is confusing. Above it is stated that the extent of contamination is dominated by Pu, then I-129 and Cl-36. Does the extent of this migration not exceed the extent of the CB? It seems that at least Pu-239 exceeds its MCL.	Explanation added in the previous paragraph: “Note that while the time-dependent extent of contamination is dominated by different RNs at different times, the maximum extent of contamination at any time (within 1,000 years) for other RNs does not exceed that experienced by ^{3}H at times earlier than 120 years. Hence, the CB is dominated by ^{3}H.”
53	Fig ES-10 legend	Insert ‘deep’ in ‘PM Detonations’	Changed.
54	Fig ES-10 title	CB depth below the Water Table? Contamination has not really been defined.	Changed title to include “(as Determined by MCL Exceedance for Relevant RNs).” Similar change in Figures ES-11, 12, and 13.
55	Fig ES-11 legend	Insert ‘deep’ in ‘PM Detonations’	Changed.
56	1.0, pp 1, 3rd para	Calculations can’t really minimize health risks to downgradient water users.	Text modified; inserted “as planning tools.”
57	Fig 1-1	All UGTA CAUs are shown	Added “Note: Other UGTA CAUs are shown for reference.”
58	1.1.1, Pp 7, 2nd para	Change 2021 to 2022	Changed.
59	Fig 2-7 caveat	Add ‘minimum for HANDLEY’	Corrected as suggested.
60	Fig 2-15 title	Check Fig # from Lu et al	Changed to 63.
61	Fig 4-15 notes	Identifiability Index ???	Changed “Hydraulic conductivity” to “Identifiability Index.”
62	Fig 4-33, note under B	Specific storage ?	Changed.
63	Pp 180, Tbl 5-3 bottom 2 row	Check values	Corrected.
64	Pp 183, Tbl 5-4 1st and 2nd row and TCA_w row	Check values	Corrected.

[a]Comment Types: M = Mandatory, S = Suggested.
Return Document Review Sheets to Environmental Management Nevada Program Operations Activity, Attn: QAC, M/S NSF 505

NEVADA ENVIRONMENTAL MANAGEMENT OPERATIONS ACTIVITY
DOCUMENT REVIEW SHEET

Listed below are additional revisions identified by Navarro UGTA Activity participants after the NDEP review.

Comment Number/Location		Comment	Comment Response
65	Pp 186 Tbl 5-5 FCULFA5 row	Check values	Corrected.
66	Pp 187 Tbl 5-5 last row	check value	Corrected.
67	5.2.2.6.2, pp 188, 2nd sentence	This is not exactly correct and this sentence needs to be replaced. The fracture aperture statistics cited in Navarro (2021a) changed slightly from draft Rev. 0 (April, 2021) to final Rev 1 (July, 2021). Values used in transport model were from draft Rev. 0. Tim needs to add discussion on how standard deviation values were estimated, and explain why values in Table 5-6 are slightly different than in Rev 1 of TDD (Navarro, 2021a).	Explanation has been added.
68	Pp 202, Section 5.5.1, third paragraph, second sentence	Missing citation of NNSA/NFO, 2015b.	Added citation of NNSA/NFO, 2015b.
69	Pp 214, second paragraph	Description of selection of observation locations in the transport model grid is a little too specific and does not apply to all such observation locations.	Adjusted language to reflect all such observation locations.
70	Figure 5-54	“Concentration Relative to MCL” or clarify below. “Log Plot relative to MCL” is not clear.	Changed color legend heading to “Concentration Relative to MCL.”
71	Table 5-11	1. Typos found 2. N/A = Not applicable. Should be not analyzed, right? Also, why are zeros reported? Are these representing nondetects? 3. Tc-99 observations are missing	Corrected typos. Removed unnecessary rows. Added Tc-99 observations. Changed "N/A" to "--". Added the following notes to bottom of table: “-- = Not analyzed Note: Observed values below the analytical detection level are reported as zero.”
72	Table 5-11, row for U-19ad_PS_1A	Observed concentrations for 239/240Pu are reversed for listed dates.	Corrected.

[a]Comment Types: M = Mandatory, S = Suggested.
Return Document Review Sheets to Environmental Management Nevada Program Operations Activity, Attn: QAC, M/S NSF 505

NEVADA ENVIRONMENTAL MANAGEMENT OPERATIONS ACTIVITY
DOCUMENT REVIEW SHEET

Listed below are additional revisions identified by Navarro UGTA Activity participants after the NDEP review.

Comment Number/Location		Comment	Comment Response
73	Figures 5-55, 5-57, and 5-59	These samples are collected from Postshot holes not near them except UE-20n 1.	Agree that samples are collected from postshot holes. However, due to grid resolution, the modeled concentrations are near the postshot holes, not at the specific postshot hole locations. Changed "near" to "for the" (throughout) since results are presented for these locations. Added note to figure (and all similar figures) that while UE-20n_1 is not a postshot hole, it is included for convenience.
74	Pp 314, Section 5.6.1, third from last sentence	Change “several dozen of” to “many”	Changed.
75	Pp 377, fifth reference	There appears to be two references combined.	Separated references.
76	Page 188, Section 5.2.2.6.2, First Paragraph, Last Sentence	Some of the minimum and maximum fracture aperture values cited in Table 5-6 do not exactly match those from Navarro (2021a). Explanation of the differences needs to be added to the text.	Added explanation of the differences and that the expected impact of these differences on the contaminant boundary calculations is negligible.
77	Section 5.5.1.4 and Appendix H	Tc-99 results are missing from the report.	Inserted new section after Section 5.5.1.4.3 and inserted new section after Section H.1.4 containing Tc-99 results.
78	Section 4.2.4.1, last para, sentence 2 and last sentence	Delete segments that include Boxcar fault	Deleted.
79	Section 4.2.4.2, ”Model Parameters”, pp 122 2nd para, 2nd sentence	Corrections: UPCU instead of TCA and add after “PBRCM” – ‘than TCA’	Corrected.
80	Section 4.2.4.2, ” Model Parameters”, pp 122, 3rd para, 9th and 10th line	Change 9.6 to 10 km; 3.2 to 2.1 km	Changed.
81	Section 4.3.1, 3rd para	After 2nd sentence add “Boundary conditions for the all-faults alternative model are the same as for the base case model, which includes increased recharge near Black Mountain.”	Added.

[a]Comment Types: M = Mandatory, S = Suggested.
Return Document Review Sheets to Environmental Management Nevada Program Operations Activity, Attn: QAC, M/S NSF 505

Listed below are additional revisions identified by Navarro UGTA Activity participants after the NDEP review.

Comment Number/Location		Comment	Comment Response
82	Section 4.3.1, last para of the section, last sentence, pp 128,	Change 9.1 to 9.9 km, change 3.8 to 4 km	Changed.
83	Section 4.3.2.1, 2nd para, last sentence	Change 9.3 to 9.7 km	Changed.
84	Section 4.3.2.2, pp 134, 2nd para, 7th and 8th sentences	Change to "Fenelon et al. (2016) estimated the discharge to springs and seeps to range from approximately 5,000 to 6,800 acre-ft/yr. Laczniak et al. (2001) performed a Monte Carlo uncertainty analysis of groundwater discharge for Death Valley Regional Flow System and estimated a discharge range of approximately 4,200 to 8,900 acre-ft/yr within the PM-OV groundwater basin."	Changed.
85	4.3.2.2, pp 135, 1st para, 3rd line	Delete "and residuals"	Deleted.
86	4.3.2.2, pp 135, 1st para, 6th line	Delete "allowing a better agreement with observed values"	Deleted.
87	4.3.3, last para of the section, pp 139	Change 9.1 to 8.7 km, 4.1 to 3.3 km	Changed.
88	4.4.2.1, last para of the section, lines 6 & 7 from bottom	Delete sentence regarding INFILv3	Deleted.
89	4.4.2.2, 2nd para, 1st sentence	Delete "…'except within the INFILv3 recharge alternative model, where water levels in Area 19 were not markedly changed'.	Deleted.

[a]Comment Types: M = Mandatory, S = Suggested.
Return Document Review Sheets to Environmental Management Nevada Program Operations Activity, Attn: QAC, M/S NSF 505

NEVADA ENVIRONMENTAL MANAGEMENT OPERATIONS ACTIVITY
DOCUMENT REVIEW SHEET

Listed below are additional revisions identified by Navarro UGTA Activity participants after the NDEP review.			
Comment Number/Location		Comment	Comment Response
90	4.4.2.2,2nd para, 2nd sentence	Change to read:" Water levels within Area 20 east of the Purse fault and the Bench area were not markedly changed by removing the increased Black Mountain recharge in all models, except within the unconfined model. Removing the increased Black Mountain recharge uniformly lowered heads by approximately 10 m throughout Areas 19 and 20 in the unconfined model."	Changed.
91	4.5, bullet 4,5,6	Move bullet # 4,5,6 after 1st bullet	Moved.
92	4.5 bullet 1	Add in the end "and an unconfined alternative conceptualization of the model's upper boundary condition"	Added.
93	4.5, bullet 7, 3rd line	Change from "off the NNSS" to 'towards oasis valley'.	Changed.
94	4.5, bullet 7, last line	Delete "and the barrier Boxcar fault structure"	Deleted.
95	4.5, bullet 11, 3rd line	Add "from tests"	Added.
96	Sections 5.5.1.4.x where x = 1,2,5,6,7,8	Change "BENHAM passing to the west" to "BENHMA passing to the east"	Changed.

[a]Comment Types: M = Mandatory, S = Suggested.
Return Document Review Sheets to Environmental Management Nevada Program Operations Activity, Attn: QAC, M/S NSF 505

Library Distribution List

	Copies
U.S. Department of Energy Office of Scientific and Technical Information P.O. Box 62 Oak Ridge, TN 37831-0062	1 (Uncontrolled, electronic copy)
Southern Nevada Public Reading Facility c/o Nuclear Testing Archive P.O. Box 98521, M/S 400 Las Vegas, NV 89193-8521	2 (Uncontrolled, electronic copies)
Manager, Northern Nevada FFACO Public Reading Facility c/o Nevada State Library & Archives 100 N. Stewart Street Carson City, NV 89701-4285	1 (Uncontrolled, electronic copy)